

**RIKEN**  
**Accelerator**  
**Progress Report**

2003

vol. 37

独立行政法人 理化学研究所

RIKEN



# CONTENTS

	Page
<b>I. PREFACE</b> .....	1
<b>II. OPERATION OF ACCELERATORS</b>	
RILAC operation .....	3
RRC and AVF operation .....	5
CGS operation .....	7
Operation of the tandem accelerator .....	9
<b>III. RESEARCH ACTIVITIES</b>	
<b>1. Nuclear Physics</b>	
Spontaneous-fission half-lives for heavy and superheavy nuclei .....	11
Application of the generalized two-center cluster model to $^{10}\text{Be}$ and $^{12}\text{Be}$ .....	12
Tensor correlation in neutron halo nuclei .....	13
$^{16}\text{O} + ^{16}\text{O}$ nature of the superdeformed band of $^{32}\text{S}$ and the evolution of the molecular structure .....	14
$^{12}\text{C} + ^{12}\text{C} \rightarrow ^8\text{Be}_{\text{g.s.}} + ^{16}\text{O}_{\text{g.s.}}$ resonance reaction and multicluster states of highly excited $^{24}\text{Mg}$ nucleus .....	15
Effect of halo structure on $^{11}\text{Be} + ^{12}\text{C}$ elastic scattering .....	16
A search for a unified effective interaction for Monte Carlo shell model calculations (V) .....	17
Ground states in even-even nuclei using random interactions .....	18
Triaxiality of neutron-rich Mg isotopes .....	19
Charge- and parity-projected Hartree-Fock method for strong tensor correlation and its application to the alpha particle .....	20
Chiral sigma model with pion mean field in finite nuclei .....	21
Accurate calculations for few-nucleon systems using low-momentum interactions .....	22
Shell structure in nuclei around $^{16}\text{O}$ and $^{24}\text{O}$ described using modern nucleon-nucleon interactions .....	23
Modified Hartree-Fock-Bogoliubov theory at finite temperature .....	24
Pairing effect on the giant dipole resonance width at low temperature .....	25
Three-dimensional rotation of even-even triaxial nuclei .....	26
Required accuracy of mass and half-life measurements planned at future RI-beam facilities to understand the r-process nucleosynthesis .....	27
Comparison of prolate and oblate explosions in core-collapse supernovae .....	28
Properties of a relativistic equation of state for collapse-driven supernovae .....	29
Proton-nucleus elastic scattering and the equation of state of nuclear matter .....	30

A search for the effect of nuclear outer surface in proton-nucleus elastic scattering .....	31
The behavior of matter at high baryon density .....	32
The EMC effect in an effective quark theory for nuclear matter .....	33
Invariant-mass spectroscopy for condensed $\bar{K}$ nuclear clusters to be formed as residues in relativistic heavy-ion collisions .....	34
Chiral symmetry in the light-cone field theory .....	35
Electron cooling by electron beam of anisotropic velocity distribution with variable Coulomb logarithm .....	36
Electron cooling by two-temperature electron beam with extremely cold longitudinal temperature .....	37
Cooling rate of ion beam by electron cooling with flat electron velocity distribution with variable Coulomb logarithm .....	38
Ultimate temperature and cooling time of ion beam by electron cooling: Dependence on Coulomb logarithm .....	39
Mathematical tools for electron cooling by electron beam with strongly anisotropic velocity distribution .....	40
Superheavy hydrogen ${}^5\text{H}$ .....	41
Experimental evidence for existence of ${}^7\text{H}$ .....	42
Experimental evidence for a specific structure of ${}^8\text{He}$ .....	43
Measurement of the vector analyzing power for the $\vec{p} + {}^6\text{He}$ , 71 MeV/nucleon elastic scattering using spin-polarized solid proton target .....	44
Experimental test of Bell's inequality <i>via</i> the ( $d$ , ${}^2\text{He}$ ) reaction .....	45
Spectroscopy of ${}^{13}\text{B}$ <i>via</i> ${}^4\text{He}({}^{12}\text{Be}, {}^{13}\text{B}\gamma)$ .....	46
${}^{11}\text{C}(p, \gamma){}^{12}\text{N}$ reaction studied by the Coulomb dissociation method .....	47
Molecular states in ${}^{12}\text{Be}$ and ${}^{14}\text{Be}$ .....	48
Isomeric $0^+$ state in ${}^{12}\text{Be}$ .....	49
Coulomb and nuclear breakup of ${}^{11}\text{Li}$ .....	50
Measurement of reaction cross section for ${}^{17}\text{C}$ and finite-range Glauber model analysis .....	51
Measurement of the reaction cross section for ${}^{17}\text{B}$ .....	52
Mean lifetime of the first excited state in ${}^{16}\text{C}$ .....	53
In-beam gamma spectroscopy and search for isomeric states in ${}^{17,19}\text{C}$ .....	54
In-beam $\gamma$ -ray spectroscopy of Ne isotopes .....	55
Excited states in ${}^{27}\text{F}$ .....	56
Gamma-ray spectroscopy of ${}^{23}\text{F}$ with proton transfer reaction .....	57
Gamma-ray spectroscopy of ${}^{22}\text{O}$ with $\alpha$ inelastic scattering .....	58
Invariant-mass spectroscopy of ${}^{16}\text{B}$ .....	59

Inelastic scattering of $^{15}\text{B}$ and $^{17}\text{B}$ .....	60
Proton inelastic scattering of $^{19}\text{C}$ .....	61
First excited state of $^{30}\text{Ne}$ studied by proton inelastic scattering in reversed kinematics .....	62
Search for low lying dipole strength in the neutron rich nucleus $^{26}\text{Ne}$ .....	63
Direct measurement of the astrophysical reaction $^{14}\text{O}(\alpha, p)^{17}\text{F}$ .....	64
Study of astrophysically important resonance states in $^{26}\text{Si}$ and $^{27}\text{P}$ using radioactive ion beams .....	65
Study of the resonant state in $^{23}\text{Al}$ relevant to the stellar $^{22}\text{Mg}(p, \gamma)^{23}\text{Al}$ reaction .....	66
Beta decay half-lives of neutron-rich Cr, Mn, Fe, and Co isotopes .....	67
Investigation of resonant states in $^{23}\text{Al}$ and $^{22}\text{Mg}$ using RI beams .....	68
Study of the $^{26}\text{Si}(p, \gamma)^{27}\text{P}$ reaction by the Coulomb dissociation method .....	69
One-neutron halo structure in $^{15}\text{C}$ .....	70
$g$ -factor measurement for $^{19}\text{N}$ .....	71
Development of low energy $^8\text{Li}$ beam at CRIB .....	72
Production of low-energy secondary beam for secondary reactions .....	74
Development of $^{17}\text{N}$ secondary beam II .....	75
Electromagnetic transition matrix elements of proton-rich $^{46}\text{Cr}$ , $^{50}\text{Fe}$ , and $^{54}\text{Ni}$ studied by Coulomb excitation .....	76
Intermediate-energy Coulomb excitation of neutron-rich Ge isotopes around $N = 50$ ...	77
Production cross sections of neutron-rich Ca and Ni isotopes formed by fragmentation of a 63 A MeV $^{86}\text{Kr}$ beam .....	78
Lifetime of a new high-spin isomer in $^{150}\text{Dy}$ .....	79
Production and decay properties of $^{272}111$ and its daughter nuclei .....	80
Electron scattering from unstable nuclei by a novel SCRIT method .....	81
Development of liquid hydrogen target for EPR experiment at SMART .....	82
Evidence for a deeply bound kaonic system $K^-ppn$ in the $^4\text{He}$ (stopped $K^-, n$ ) reaction .....	84
Experimental signature of in-medium mass modification of vector mesons at normal nuclear density .....	85
Nuclear mass number dependence of inclusive $\omega$ and $\phi$ meson production in 12 GeV $p$ -A collisions .....	86
Geant4 simulation for the KEK-PS E325 spectrometer .....	87
Response of the HXD-II detector to cosmic heavy ions .....	88
Dimuon measurement in the NA60 experiment at CERN/SPS .....	89
First measurement of muon transfer reactions with argon ions implanted in solid deuterium films .....	90

Measurement of the magnetic field effect in muon catalyzed fusion .....	91
<b>2. Atomic and Solid-State Physics</b>	
SF <sub>6</sub> dielectric molecules: Electron and positron scattering dynamic properties and possible applications .....	93
H <sup>+</sup> + CH <sub>2</sub> collisions below the 1.5 keV regime .....	94
Resonant coherent excitation of 2s electron of Li-like Fe and Ni ions .....	95
Elastic wave from fast Xe-ion irradiation on solids .....	96
Effect of GeV-ion irradiation on Fe-Ni invar alloys .....	97
Evaluation of single-event effect in power MOSFET .....	98
Collective luminescence of extremely dense electron-hole pairs created in ion tracks in insulators .....	99
Comparative study on electron-hole plasma formed in heavy-ion irradiated MgO and CdS .....	101
A new type of positron accumulator in UHV utilizing a high-density electron plasma and an ion cloud .....	102
Soft X-ray spectroscopy of 2.3 keV/u N <sup>6+</sup> ions transmitted through a Ni microcapillary .....	103
Coincidence measurements of X rays and final charge state of highly charged ions transmitted through a microcapillary .....	104
Multiple-electron processes in close single collisions of Ne <sup>q+</sup> (q = 2, 5, 7, and 9) with Ar at 14 keV .....	105
Photodissociation for recovery of Ca <sup>+</sup> ions lost by chemical reactions in an ion trap ...	106
Experimental apparatus for X-ray spectroscopy with highly charged ion beam produced by laser ion source .....	107
μSR study on magnetic property of [Pd(dmit) <sub>2</sub> ] salts .....	109
A change in the Cu-spin fluctuations studied by μSR in La <sub>2-x</sub> Sr <sub>x</sub> CuO <sub>4</sub> at approximately 100 K .....	110
<b>3. Radiochemistry and Nuclear Chemistry</b>	
<sup>99</sup> Ru Mössbauer spectroscopic study of CaRuO <sub>3</sub> (1) .....	111
Reactions of <sup>57</sup> Mn implanted in solid oxygen .....	112
Accumulation of various trace elements in <i>Lotus japonicus</i> using the multitracer technique .....	113
Effects of carnosine (β-alanyl-L-histidine) on the absorption of various trace elements in rats .....	114
Effects of carnosine (β-alanyl-L-histidine) on the absorption of iron in rats .....	115
Multitracer screening of trace elements in brains of mice injected with lipopolysaccharide .....	116
Pharmacokinetic study on gastrointestinal absorption and blood disposition of vanadium ions in healthy rats using radiotracer method .....	117

Uptake of $^{65}\text{Zn}$ in various trophoblast cells .....	118
Metal-binding factor responsible for variation of concentration of trace elements under Zn-deficient condition .....	119
Uptake of metals in cisplatin-resistant lung cancer cell line .....	120
Relationship of reactive oxygen species generation with DNA binding and DNA cleaving activities of metallothioneins I and II .....	121
Investigation of intracellular kinetics of copper in HepG2 cell lines .....	122
Comparison of technetium and rhenium uptake rates from nutrient solution by radish .....	123
Removal of technetium and other trace elements by bacteria living in surface water covering paddy fields .....	124
Improved separation of Ba and Mg ions in the alkaline earth group using the centrifugal partition chromatograph .....	125
Improved extractive separability of metal ions with sulfonated crown ethers .....	127
Study on Re and Os removal from seawater to sediments using multitracer technique and X-ray absorption near-edge structure .....	128
Anion-exchange behavior of element 104, rutherfordium .....	130
Performance of a gas-jet-coupled multitarget system for multitracer production .....	132
Development of a new target system for online multitracer preparation .....	134
Preliminary study on olfactory transport of a multitracer produced in Ti target .....	135
Multitracer imaging in plants by GREI system .....	136
Implementation of GREI system with DOI measurement capability .....	137
Three-dimensional imaging by GREI system .....	138
Reconstruction methods for GREI .....	139
A note on the reconstruction method for GREI .....	140
Image reconstruction method with compensation for scattering angular uncertainty in MT-GEI .....	141
<b>4. Radiation Chemistry and Radiation Biology</b>	
Exposure of frozen human cells to heavy ions .....	143
Effects of heavy-ion irradiation on DNA replication in mammalian cells .....	144
Effect of heavy ions on the activation of DNA double-strand break repair proteins .....	145
High dose of heavy-ion beams cause <i>p53</i> -dependent cell death .....	146
Effect of heavy-ion beam irradiation on mutation induction in <i>Arabidopsis thaliana</i> ...	147
Isolation of light stress response mutants of <i>Arabidopsis thaliana</i> by heavy ion beam irradiation .....	148
Hormesis of heavy-ion irradiation to lettuce .....	149
Mutation induction by heavy-ion beam in asparagus .....	150

Effect of heavy-ion beam irradiation on apple and Japanese pear .....	151
Effects of heavy-ion beam irradiation on regeneration of shoots from stem segments in spray-type chrysanthemum ( <i>Dendranthema grandiflorum</i> (Ramat.) Kitamura) .....	152
<b>5. Instrumentation</b>	
Performance of strip Ge telescope for in-beam $\gamma$ -ray spectroscopy .....	153
Development of NaI(Tl) calorimeter for charged particles .....	155
Development of triggerable focal plane detector with particle identification capabilities .....	156
Development of superconducting series junction detectors for heavy ions .....	157
Performance study of the big ion chamber .....	159
Design of 4-layer magnetic shield for spin maser experiment .....	160
Detector R&D for the beta neutrino correlation experiment .....	161
Performance of a multiple-reflection time-of-flight mass spectrometer .....	163
Numerical investigation of the “fair-wind gas cell” concept for slow RI-beam production at RIKEN .....	165
FOV and angular response of the APEX onboard French-Brazilian microsatellite .....	167
Accelerator test of charge particle detectors for a satellite instrument STEP-F .....	168
Design of an RF beam splitter for a time-sharing beam delivery to BigRIPS and RIPS .....	170
Test experiment on the low-energy RI extraction system .....	171
On-line collection of $^8\text{Li}$ ions from the projectile fragment separator using an rf ion guide system (III) .....	173
Design of RI extraction system with a static electric field .....	175
Development of slow muon beam line at the RIKEN-RAL muon facility .....	176
Preparation of self-supporting boron films .....	177
R&D study of a self-confining radioactive ion target (SCRIT) .....	179
Loop-gap resonator for polarized proton target .....	181
Feasibility study of monolithic SSD for measurement of low energy nuclear reaction with GEANT4 simulation .....	183
A fast data acquisition front-end using an FPGA device .....	185
Present status of data acquisition system ‘BabarDAQ’ for nuclear physics experiments .....	187
Network and computing environment for RIKEN Accelerator Research Facility .....	189
<b>6. Material Analysis</b>	
Application of an in-air high-resolution PIXE system to direct speciation of Cr and Fe .....	191
Gamma rays from iron, aluminum and rock targets bombarded by 210 MeV protons ...	193

## 7. RIKEN-BNL Collaboration

QCD and dimensional deconstruction .....	195
Single spin asymmetry in inclusive $D$ meson production at RHIC .....	196
$\Delta g(x)$ uncertainty from prompt photon production at RHIC Spin .....	197
On a negative $A_{LL}^{\pi}$ at moderately large $\mathbf{p}_{\perp}$ .....	198
Threshold resummation for heavy-flavor photo-production .....	199
The parton structure of the nucleon and precision determination of the Weinberg angle in neutrino scattering .....	200
Energy loss of leading parton in hot QGP .....	201
Power counting in the high density effective theory .....	202
Interplay between soft and hard hadronic components for identified hadrons at RHIC .....	203
Hadronization at RHIC: Recombination <i>vs.</i> fragmentation? .....	204
New signature of the QCD critical point .....	205
Pseudogap of color superconductivity .....	206
Color ferromagnetic phase at finite quark density .....	207
Kinetic equation for $\phi^4$ theory with generalized Kadanoff-Baym ansatz .....	208
Charge symmetry breaking in few-nucleon systems .....	209
Lattice chiral symmetry with hopping interactions .....	210
Comparison of matrix model and lattice data for the QCD Dirac operator at nonzero chemical potential .....	211
Calculations of correlators and spectral function and properties of QGP .....	212
MEM analysis of the thermal glueball from SU(3) lattice QCD .....	213
Lattice study of pion electromagnetic form factor with domain wall fermions .....	214
Application of DWF to heavy-light mesons .....	215
Static potential with dynamical domain-wall quarks .....	216
Kaon B parameter from two-flavor dynamical domain wall fermions .....	217
Kaon matrix elements in domain-wall QCD with DBW2 gauge action .....	218
Lattice study of negative-parity baryon spectrum .....	219
Nucleon on the lattice .....	220
Status of the QCDOC computer project .....	221
The RHIC spin program: Where are we? .....	222
The PHENIX run 2003 and early results .....	223
Measurement of $J/\psi$ with PHENIX muon arms in 2003 p+p collisions .....	224
Single muon analysis of polarized proton-proton collision at $\sqrt{s} = 200$ GeV .....	225



Identified hadron spectra in $\sqrt{s_{NN}} = 200$ GeV p+p collisions at RHIC-PHENIX .....	226
Measurement of relative luminosity in polarized proton collision at PHENIX .....	227
Measurement of $A_N$ of inclusive particles by PHENIX BBC with tagged very forward neutron in polarized pp collisions at $\sqrt{s} = 200$ GeV .....	228
Measurement of longitudinal double spin asymmetry for $\pi^0$ 's in proton-proton collisions at $\sqrt{s} = 200$ GeV from RHIC PHENIX Run 3 .....	229
Measurement of $\pi^0$ production in p+p and Au+Au collisions at $\sqrt{s_{NN}} = 200$ GeV .....	231
Simulation studies for the Si-Vertex Tracker at PHENIX photon-jet production in $pp$ collisions at $\sqrt{s} = 200$ GeV .....	232
Charged hadron analysis in proton-proton collisions at $\sqrt{s} = 200$ GeV .....	233
Background study of direct photon production in proton-proton collisions at $\sqrt{s} = 200$ GeV with PHENIX .....	234
Radial flow study from identified hadron spectra in Au+Au collisions at $\sqrt{s_{NN}} = 200$ GeV .....	235
Single electron measurement in $\sqrt{s_{NN}} = 200$ GeV Au+Au collisions .....	236
Particle composition at high $p_T$ in Au+Au collisions at $\sqrt{s_{NN}} = 200$ GeV .....	237
$\pi^0$ event anisotropy in $\sqrt{s_{NN}} = 200$ GeV Au+Au collisions .....	238
Measurement of fluctuations in event-by-event $N_{ch} - N_\gamma$ balance .....	239
Search for non-hadronic sources of photons in Au+Au collisions at $\sqrt{s_{NN}} = 200$ GeV at RHIC-PHENIX .....	240
AGS snake .....	241
Detection of very small angle proton-proton elastic scattering for absolute polarimetry at RHIC .....	243
Polarimetry in RHIC and AGS from Run-03 .....	245
PHENIX local polarimeter, RUN III .....	246
Dead layer thickness measurement of Si detectors for the RHIC pC CNI polarimeter ..	247
$J/\Psi$ production in pp and d-Au collisions in PHENIX muon arms .....	248
PHENIX silicon upgrade project .....	249
Development of silicon pixel detectors for the PHENIX experiment .....	250
Development of silicon strip detector for PHENIX silicon vertex tracker .....	251
Development of pilot readout electronics for the PHENIX pixel detector .....	253
Semileptonic decays of open charm and beauty in the PHENIX central arm with the silicon vertex detector upgrade .....	254
Muon trigger upgrade with W production for PHENIX muon arms .....	255
eRHIC: Progress and status .....	256
CCJ operation in 2002–2003 .....	257
Azimuthal asymmetries in fragmentation processes at Belle .....	259

Progress on precision measurement of fragmentation functions at Belle .....	260
Development of trigger and DAQ system for SVD2.0 at Belle .....	261
<b>8. Miscellaneous</b>	
Pumping $^{229m}\text{Th}$ by hollow-cathode discharge .....	263
Study on beam instability due to space charge oscillation during longitudinal bunch compression .....	264
<b>IV. DEVELOPMENT OF ACCELERATOR FACILITIES</b>	
Production of intense $^{58}\text{Fe}$ and $^{64}\text{Ni}$ beams using MIVOC method .....	265
Optimization of magnetic field configuration for the production of Ar ions from RIKEN 18 GHz ECR ion source .....	267
Emittance measurement for intense beam of heavy-ions from RIKEN 18 GHz ECRIS ..	269
Control system for a Hyper ECR ion source .....	271
Improvement of power supplies for RARF beam transport magnets .....	273
Design of vacuum pumping unit for RIBF beam transport lines .....	275
Longitudinal emittance measurement of the RRC beam .....	276
Expansion of the control system for RARF .....	277
N-DIM as controller of devices for beam transport .....	279
HIS:The radiation safety interlock system for the RIKEN RI Beam Factory .....	281
Charge strippers for the RIKEN RI-Beam Factory .....	283
Low-power test of the IRC flattop resonator .....	284
Status of booster ring cyclotrons for the RIKEN RI Beam Factory .....	285
Magnetic field perturbations from the injection and the extraction elements of the RIKEN SRC and their correction .....	287
Cranes for RIBF .....	289
Current status of the control system development at RIKEN RI-Beam Factory .....	291
Status of the BigRIPS separator project .....	293
Design study of the high-power production target for the Big-RIPS separator .....	295
Design of an air-core type superconducting quadrupole for the BigRIPS separator .....	297
Gas-cooled current lead with multiple electrodes for BigRIPS superconducting quadrupoles .....	299
Design of radiation shielding for the BigRIPS separator .....	301
Conceptional design of the high-power beam dumps for BigRIPS .....	303
Prototype of the high-power beam dump for BigRIPS .....	305
Rf system with HOM damped cavity using SiC microwave absorbers for electron storage ring .....	306

Measurement of rf characteristics of magnetic-alloy-loaded cavity using cut-core configuration .....	308
Development of an HTS-SQUID DC current monitor .....	310
Feasibility of projectile-fragment-beam separation from a secondary beam in a storage ring .....	312
Numerical simulation of crystalline ion beam .....	314
<b>V. RADIATION MONITORING</b>	
Routine work for radiation safety in the ring cyclotron facility .....	317
<b>VI. LIST OF PUBLICATIONS</b> .....	319
<b>VII. LIST OF PREPRINTS</b> .....	331
<b>VIII. PAPERS PRESENTED AT MEETINGS</b> .....	333
<b>IX. LIST OF SYMPOSIA</b> .....	352
<b>X. LIST OF SEMINARS</b> .....	354
<b>XI. LIST OF PERSONNEL</b> .....	360
<b>AUTHOR INDEX</b>	

## I. PREFACE

This issue of RIKEN Accelerator Progress Report reports research activities of the RIKEN Accelerator Research Facility (RARF) up to October 2003. The research programs involve a variety of fields such as nuclear physics, nuclear chemistry, radiation biology, atomic physics, condensed matter physics, plant mutation, material characterization, application to space science, accelerator physics and engineering, laser technology, and computational technology in terms of accelerator or radiation application. These activities involved a few hundred researchers from domestic and foreign institutions together with laboratories and Centers in RIKEN.

Major research activities of the RARF are based on the heavy-ion accelerator complex consisting of the  $K = 540$  MeV RIKEN Ring Cyclotron (RRC), the energy variable heavy-ion linear accelerator (RILAC), and the  $K = 70$  MeV azimuthally varying field (AVF) cyclotron. Heavy-ion beams of a variety of elements with energies ranging from a few A MeV to 135 A MeV are provided. The two-injector machines (AVF and RILAC) are equipped with ECR heavy-ion sources. Vector and tensor polarized deuterons are also available. The three accelerators have been used in various configurations. The RRC operates either with the AVF or the RILAC as the injector. The AVF has been providing beams of ions of mass numbers up to 60, whereas the RILAC can accelerate heavier ions. An energy booster called CSM (Charge State Multiplier) has been installed in collaboration with CNS, the University of Tokyo, so that the maximum beam energy from the RILAC has been raised. This enabled to deliver high-intensity beams of intermediate mass elements such as Kr up to 64 A MeV from RRC. In addition, RILAC and RRC can be operated separately, when the AVF is used to inject ions to the RRC. This allows for long runs with RILAC beams like the experiment of super-heavy element search. Two thirds of the RRC research beam time is used for nuclear physics and nuclear astrophysics, and remaining one third is used for atomic physics, material science, nuclear chemistry, radiation biology and others. The AVF beam time was also used for fields other than nuclear physics.

The RARF carries many international collaborations. Among them are two large-size collaboration programs using overseas accelerator facilities: one is the muon science project at ISIS in collaboration with the Rutherford-Appleton Laboratory (RAL), and the other is the spin physics program at RHIC in collaboration with the Brookhaven National Laboratory (BNL). The pulsed muon-beam facility at ISIS has been oper-

ating steadily. At the RHIC facility, the first data from longitudinally polarized proton collisions have been obtained. Other smaller collaborations using foreign facilities are underway at Lanzho (China), Dubna (Russia), CERN (Switzerland/France), GSI (Germany), TRIUMF (Canada), and MSU (United States). We have collaborated with the CNS for installing the low-energy RI beam separator (CRIB) to use the low-energy beam from the AVF. Light RI beams of a few A MeV are now available as a CNS/RIKEN facility, and several experiments have been performed.

Highlights of the year for the research at RARF are as follows. (1) Experiments for super-heavy element search have been performed. Alpha-decay chains from residues of the  $^{64}\text{Ni} + ^{209}\text{Bi}$  fusion reaction have been observed, and production of the element  $^{272}[111]$  has been confirmed. Together with earlier results at GSI, properties of the decays have been revealed. An experiment to search for the element 113 is underway. (2) The lifetime of the first excited state in  $^{16}\text{C}$  has been measured. Its extraordinarily large value together with the large neutron excitation component extracted from the  $^{16}\text{C} + ^{208}\text{Pb}$  inelastic scattering results indicate anomalous dynamics of  $^{16}\text{C}$  excitation. (3) The  $^{19}\text{N}$  magnetic moment has been measured. (4) New techniques are being developed to accumulate slow RI ions from the fragment separator. The highest efficiency of around 3% was achieved for the method based on the gas-filled rf-ion guide. (5) A novel technic of TOF mass spectroscopy is being developed. Mass accuracy of 0.7 ppm has been achieved. (6) The reaction cross section for C isotopes ( $^{14,15,17}\text{C}$ ) and half lives for Cr, Mn, Fe, and Co isotopes have been measured. (6) Behavior of neutron-rich  $N = 20$  isotopes was studied. The energy of the first excited state in  $^{30}\text{Ne}$ , which was measured by a  $(p,p'\gamma)$  experiment in reversed kinematics, indicates that the neutron shell closure disappears in this nucleus. (7) The rf deflector, which was installed in the last year, has been successfully used for experiments with proton-rich RI beams.

The RI Beam Factory project is in progress. The building for the cyclotrons and fragment separators has been completed, and the experimental facility building is being built. Most of the main components of the cyclotrons IRC and SRC has been fabricated, and their installation in the building has been started. The first production of RI beams are foreseen in the year 2006.

T. Motobayashi

*Leader, Accelerator-based Research Group  
RIKEN Accelerator Research Facility*

## RILAC operation

E. Ikezawa, M. Kase, S. Kohara, O. Kamigaito, T. Nakagawa, M. Fujimaki, M. Nagase, T. Kageyama, N. Fukunishi, N. Sakamoto, H. Okuno, N. Inabe, M. Wakasugi, M. Kobayashi-Komiyama, M. Kidera, S. Yokouchi, A. Yoneda, H. Ryuto, M. Hemmi, I. Yokoyama, Y. Higurashi, T. Aihara,\* T. Ohki,\* H. Hasebe,\* H. Yamauchi,\* A. Uchiyama,\* K. Oyamada,\* A. Goto, and Y. Yano

During this reporting period, RILAC has been in steady operation and has supplied various ion beams for various experiments. Table 1 shows the statistics for RILAC operation from January 1 through December 31, 2003. Table 2 summarizes the number of days allotted to different research groups. The percentage of beam time used by the RIKEN Ring Cyclotron (RRC) was approximately 31% of the total. The  $^{40}\text{Ar}$ ,  $^{48}\text{Ca}$ ,  $^{58}\text{Ni}$ ,  $^{86}\text{Kr}$ ,  $^{136}\text{Xe}$ , and  $^{181}\text{Ta}$  ions accelerated by RILAC were injected into RRC. Among these, the  $^{40}\text{Ar}$ ,  $^{48}\text{Ca}$ ,  $^{86}\text{Kr}$ , and  $^{136}\text{Xe}$  ions were accelerated by RILAC together with the charge-state multiplier (CSM) A1 and A2 cavities and injected into RRC with a harmonic number of 8.

Research experiments on superheavy elements have been carried out with a gas-filled recoil isotope separator (GARIS) at the e3 beam line. The total beam service time for the experiments was 2413.3 hours.

Tables 3 and 4 show the statistics for the numbers of days on which RILAC ion beams were delivered using the Cockcroft-Walton injector with an 8 GHz ECR ion source (NEOMAFIOS) and using the RFQ linac with an 18 GHz ECR ion source, respectively. The ion beams of 10 elements were used for the experiments and beam acceleration tests.

Table 1. Statistics for RILAC operation from January 1 through December 31, 2003.

	No. of Days	%
Beam time	216	59.2
Overhaul and improvement	56	15.3
Periodic inspection and repair	45	12.3
Scheduled shutdown	48	13.2
Total	365	100

Table 2. Beam time allocated to different research groups.

	No. of Days	%
Atomic physics	4	1.9
Nuclear physics	134	62.0
Radiation chemistry	7	3.2
Material analysis and development	2	0.9
Accelerator research	3	1.4
Beam transport to RRC	66	30.6
Total	216	100

\* SHI Accelerator Service, Ltd.

Table 3. Statistics for RILAC ion beams delivered using the Cockcroft-Walton injector with an 8 GHz ECR ion source (NEOMAFIOS).

Ion	Mass	Charge state	No. of Days
Ar	40	8	2
Ni	58	9	3
Kr	86	18	1
Ta	181	16	2
Total			8

Table 4. Statistics for RILAC ion beams delivered using the RFQ linac with an 18 GHz ECR ion source.

Ion	Mass	Charge state	No. of Days
N	14	3	1
Ar	40	8, 11	14
Ca	48	11	10
Ni	58	9	6
Ni	64	13	52
Zn	70	16	82
Kr	84	17	2
Kr	86	18	17
Xe	136	18, 20, 26, 27	19
Ta	181	20, 24	5
Total			208

We carried out the following machine improvements during this reporting period.

- (1) The power supplies for the drift tube magnets used in the No. 1, No. 2 and No. 3 cavities and for the quadrupole magnets installed after each cavity were replaced with new ones, because they were worn out from many years of operation. Each new magnet power supply is of the switching type and has a network IO (NIO) interface.
- (2) In the beam transport line between the No. 1 and No. 6 cavities, the Faraday cups, the beam profile monitors and the phase probes were replaced with new ones in order to improve their strengths against the high beam intensity extractable from an 18 GHz ECR ion source. They were mounted on a new diagnostic chamber.
- (3) The vacuum system using the turbomolecular pumps of 150 l/s was newly installed in the beam transport line between the No. 1 and No. 6 cavities. In the experimental room, the vacuum

system for the beam transport line was also replaced with a new one.

- (4) The power supplies for the dipole magnets (A-DM2, A-DM-3 and GARIS-D) were remodeled by replacing the current shunt with the DC current transformer.<sup>1)</sup>

We experienced the following machine problems during this reporting period.

- (1) In the rf power amplifier of the RFQ linac, the rf contact finger was melted due to the excessive rf current. The rf power amplifier was improved this summer.
- (2) The 18 GHz ECR ion source was splashed with water due to the presence of a small hole in the cooling pipe of the water jacket for the hexapole magnet.
- (3) In the No. 2, No. 5, and No. 6 cavities, a thin

copper sheet (10 cm wide, 7 cm long, and 0.3 mm thick) used for electric contact melted because of the excessive rf current with parasitic oscillation.

The beam transport line of the RFQ linac with the 18 GHz ECR ion source will be modified for the RIKEN RI beam factory project during January through February, 2004. Another 18 GHz ECR ion source will be installed in parallel with the existing 18 GHz ECR ion source in the near future. Thus the beam transport line of the Cockcroft-Walton injector with the 8 GHz ECR ion source (NEOMAFIOS), which has been used for many years, will be dismantled.

#### References

- 1) M. Nagase et al.: RIKEN Accel. Prog. Rep. **37**, 273 (2004).

## RRC and AVF operation

M. Kase, T. Kageyama, M. Nagase, S. Kohara, T. Nakagawa, E. Ikezawa, M. Fujimaki, N. Inabe, H. Okuno, O. Kamigaito, M. Kidera, H. Ryuto, M. Kobayashi-Komiyama, N. Fukunishi, N. Sakamoto, M. Wakasugi, Y. Ohshiro,<sup>\*1</sup> A. Yoneda, Y. Higurashi, I. Yokoyama, S. Yokouchi, H. Isshiki,<sup>\*2</sup> N. Tsukiori,<sup>\*2</sup> K. Takahashi,<sup>\*2</sup> T. Maie,<sup>\*2</sup> R. Ohta,<sup>\*2</sup> K. Kobayashi,<sup>\*2</sup> M. Nishida,<sup>\*2</sup> Y. Kotaka,<sup>\*2</sup> S. Fukuzawa,<sup>\*2</sup> A. Goto, and Y. Yano

The RARF accelerators (RRC, AVF and RILAC) were operated under special budgetary conditions in 2003. To keep the RIBF construction schedule, the operation budget was reduced by 30%. Moreover, on the operation budget, the energy source for the accelerators was switched from electricity to gas fuel due to the introduction of a new power-generation scheme described below.

The co-generation system (CGS) of the RI Beam Factory was installed in the spring of 2003 and the gas turbine in the CGS has started to generate a power of 6300 kW routinely since April. To reduce the power cost, the accelerators use electricity from the CGS only in the daytime of weekdays and Saturday, and use commercial power during the other periods when the charge is quite low. The accelerators had a scheduled long shutdown (more than 40 days) in the summer and will have another two-month shutdown in the winter of 2004.

In November and December, experiments using beams of the RILAC-RRC combination were postponed, and the experiment to search for a super-heavy element ( $Z = 113$ ) exclusively used beams from RILAC.

For the above reasons, the operation hours of the RIKEN Ring Cyclotron (RRC) in 2003 was slightly shorter than the previous years, as shown in Table 1. Figure 1 shows the history of the RRC operation from 1996 to 2003. The RRC routinely provided a beam time of 3789 hr throughout 2003.

Table 2 shows the statistics of beam time used for each beam course. Ninety-six experiments were carried out in 2003 using the RRC beams. Among them,

Table 1. Statistics of RRC and AVF operation from Jan. to Dec. 2003.

Operation time of RRC	5684 hr
Beam Service Time	3739 hr
Machine troubles	239 hr
Nuclear Physics Experiment	74%
Non-nuclear Physics Experiment	26%
RILAC-RRC Operation	11%
AVF-RRC Operation	89%
Operation time of AVF standalone	1582 hr
Beam Service Time	1192 hr

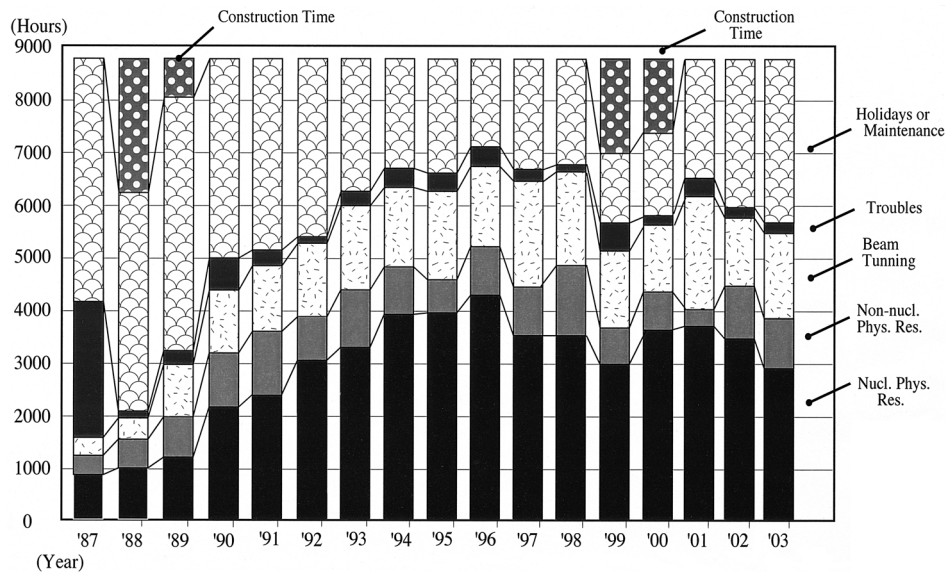


Fig. 1. Statistics of RRC operation from 1996 to 2003.

<sup>\*1</sup> Center for Nuclear Study, University of Tokyo

<sup>\*2</sup> SHI Accelerator Service, Ltd.

Table 2. RRC and AVF beam time for each course in 2003.

Target room	Total time (hr)	No. of experiments
E1	100 (257)	6 (6)
E2	117 (157)	3 (4)
E3	342 (275)	13 (15)
E4 (SMART)	538 (327)	9 (5)
E5	286 (273)	40 (29)
E6 (RIPS)	2342 (3114)	25 (31)
AVF (CO3)	158 <sup>§</sup>	5 <sup>§</sup>
E7 (CRIB)	1034 <sup>§</sup> (467 <sup>§</sup> )	16 <sup>§</sup> (8)

<sup>§</sup>AVF stand-alone only, and used for CNS of the University of Tokyo. Figures in parentheses are data in 2002.

twenty-five experiments using RI beams from RIPS were carried out in the E6 room and they used a total beam time of 2342 hr, that is, 63% of the total beam time.

A total beam time of 1034 hr is used by the Center for Nuclear Study (CNS) of the University of Tokyo. It was the second year since the physics experiments for university students started based on the RIKEN-CNS collaboration agreement. In autumn, four days were spent for these experiments.

The hyper-ECR ion source has been used routinely for injection of the AVF in collaboration with the CNS, university of Tokyo. It took charge of the production of beams such as  $^{12}\text{C}$ ,  $^{14}\text{N}$ ,  $^{16}\text{O}$ , and  $^{20}\text{Ne}$ , being used for 60% of the total beam time of the AVF. The performance of the 10 GHz ECR ion source has not been as

good as before for the production of high-charge-state ions, since it has problems on the hexa-pole magnet and extraction system.

The high-intensity nature of RRC beams enables us to provide experimental opportunities like the use of a parallel beam with an angular divergence less than 10 microradians. These parallel beams were used in ion-channeling experiments performed in the E2 experimental vault. The typical intensity of the parallel beam is several hundreds of particles per second. The power supplies of beam transport magnets were modified to improve the long-time stability of these high-precision beams. Their current detectors were converted from a Zeranin shunts into DCCT (DC current transformer).

We upgraded the EPICS base programs running on the server computer for accelerator operation from version R3.13.1 to R3.13.8 in the summer of 2003. It is expected that we can add new convenient applications supported by the EPICS community such as an operation archiver to our control system.

It was determined that the use of SMART in the E4 target room will be terminated in the summer of 2005 to install one of the cyclotrons (fRC) of RIBF.

The beam chamber of RRC is being evacuated with fourteen sets of 10000l/s cryogenics vacuum pumps. Five of them had been out of order after more than 10000 hr use. The helium compressors for these pumps were renewed in the summer of 2003. At the same time, careful maintenance was carried out for the cryopumps in RARF.



## CGS operation

H. Hasebe,\* K. Yamaguchi, T. Fujinawa, T. Maie,\* K. Oyamada,\* E. Ikezawa, M. Kase, and Y. Yano

The RI Beam Factory (RIBF) requires a gas turbine co-generation system (CGS)<sup>1)</sup> to increase the reliability of the power supply, the He-cryogenic system, vacuum system and super-conducting magnets perform poorly with any interruption of the power supply. The gas turbine generates electric power from fuel energy and supplies it to the above systems with top priority. By utilizing gas heat exhaustion from the gas turbine, the CGS will also supply cooled water to the cooling system of the RIBF accelerators as well as to the building air-conditioning system. The whole system is schematically shown in Fig. 1. Photographs of the gas turbine and the overview of the CGS are shown in Fig. 2 and Fig. 3, respectively.

The contract for the CGS construction was signed with Mitsubishi Electric Co. in Jan. 2002. The installation of the CGS was started in July 2002 on the open space of the first floor of the RIBF accelerator building, and was completed in Feb. 2003. After inspections and tests had been conducted, the generation of maximum power (6.3 MW) was achieved at the end of March 2003. The opening ceremony was held at the beginning of April with the chairman of the board of Directors in attendance, and routine operation started after that.

Until the RIBF is completed in 2005, the CGS will supply electric power mainly to the RARF accelerators (RRC, AVF and RILAC) during the daytime on weekdays including Saturday. At night and on holidays and Sundays, the CGS is out of service, because the rates for commercial electric power are very low during these periods. On the other hand, this year the

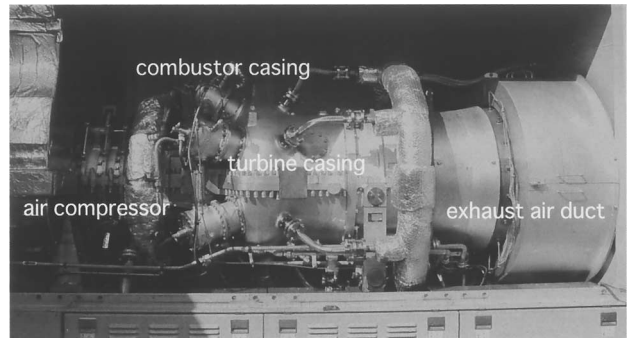


Fig. 2. Photograph of the gas turbine. Air flows from the left-hand side to the right hand side. Three sets of gas inlets and igniters are seen in the middle. The turbine is usually mounted inside the heavy container, which functions as a silencer.



Fig. 3. Over view of the CGS.

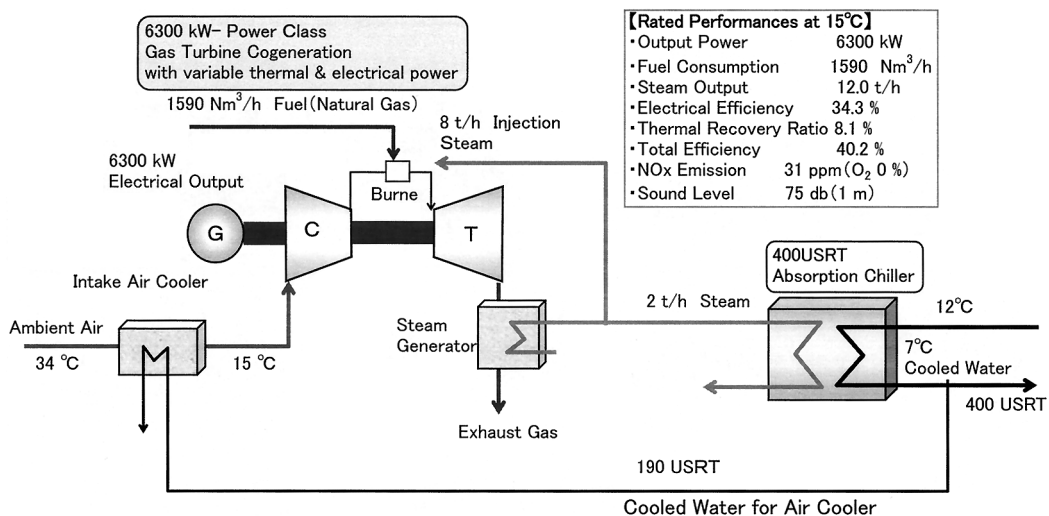


Fig. 1. Schematic diagram of the 6300-kW-power class gas turbine cogeneration system with variable thermal and electrical power.

\* SHI Accelerator Service, Ltd.

use of the exhausted heat is limited to dehumidifying the accelerator building.

The daily operation schedule of the CGS is as follows. An operator pushes the start button at 7:45 am in the CGS control room in the Nishina Memorial Building. The gas turbine is ignited at 7:50 am and, after the rotation of turbine reaches up to 14,000 rpm, the generator is started and synchronized to commercial electric power line at 8:00 am. The full power of 6.3 MW is achieved around 8:45 am by using as much output steam as possible. The stop button of the CGS is pushed at 9:40 pm and the generator is cut off from commercial electric power line at 10:00 pm. The CGS is totally stopped at 10:30 pm. The operation statistics from April to the end of October are shown in Table 1.

We have encountered some premature failures and the operation was occasionally interrupted. The bianual inspection was carried out in Sept. 2003, and an annual one is scheduled for Feb. 2004. Self-dependence operations were accidentally initiated on Sept. 3. and Oct. 2. The fist operation was triggered by an interruption of the power supply due to a lightning strike and the second, by an instant vantage reduction. In both cases, the fully automatic system for providing non-stop power supply worked successfully in the RIBF accelerator building.

RIKEN signed a new electric power contract with TEPCO in Oct. 2003. The contract peak power was reduced from 23.4 MW to 18 MW. This downsizing

Table 1. Statistics of CGS operation from April to the end of October, 2003.

	No. of Days	%
Operation time	176	82.2
Scheduled shutdown	29	13.6
Overhaul and improvement	9	4.2
Total	214	100

Cost		
Electric out put power	13,877,360 KWh	151,981,901 yen
Used gas of the CGS	3,544,958 Nm <sup>3</sup>	136,423,900 yen
Profit		15,558,001 yen

Unit rate	
Electrical output only	10.12 yen/kWh
Inc heat recovery (200 kW)	9.85 yen/kWh

has resulted in savings of more than 60 million yen per year. However a full day of operation of what will be required during the summer in 2004 to keep this contract. In Feb. 2004, the CGS will starts to supply cooled water to the Nishina Memorial Bldg. and the Linac Bldg. mainly for the air-conditioning systems of the existing accelerator vaults. It is expected that the profits of the CGS will grow somewhat in 2004.

#### References

- 1) T. Fujinawa et al.: RIKEN Accel. Prog. Rep. **36**, 310 (2003).

## Operation of the tandem accelerator

T. Kobayashi and K. Ogiwara

The 1.7 MeV tandem accelerator (pelletron) was operated for a total of 119 days for experiments, except for the time required for machine inspection and beam test (36 days), during the annual reporting period from Nov. 1, 2002 to Oct. 31, 2003.

Experimental studies on the following subjects were performed, and are still in progress.

- (1) Nuclear reaction analysis (NRA) (61 days)
  - (a) Lattice location of hydrogen in Nb-based alloys by means of the channeling method
- (2) Particle-induced X-ray emission (PIXE) (38 days)
  - (a) Development of a highly sensitive high-resolution in-air PIXE system for chemical state analysis
  - (b) Trace element analysis of biological and environmental samples using energy dispersive X-ray spectrometry
  - (c) Characterization of the II-VI ternary semiconducting crystals
- (3) Rutherford backscattering spectroscopy (RBS) and Elastic recoil detection (ERD) analysis (20 days)
  - (a) RBS analysis of polymers and carbon materials containing metallic nanoparticles
  - (b) ERD analysis of diamond-like carbon (DLC) thin films determining hydrogen contents

The total time in days, which was spent for each experiment, is shown in parentheses.

# Spontaneous-fission half-lives for heavy and superheavy nuclei

H. Koura\*

[Spontaneous fission, Lifetimes]

Our group has constructed and is developing a method of estimating the potential energy surface for spontaneous fission<sup>1)</sup> using a method of calculating shell energies in a nuclear mass formula.<sup>2,3)</sup> In this formula, the shell energy of a deformed nucleus is expressed as a sum of an appropriate mixture of spherical shell energies and an average deformation energy. The potential energy surface for spontaneous fission can be obtained by considering not only the equilibrium shapes but also the intermediated ones. With the above energy surfaces, we estimate the spontaneous-fission half-lives. We take the one-dimensional WKB method as a virtual particle with an even-odd hindrance factor. That is,

$$\begin{aligned} & \log_{10} \frac{T_{\text{sf}}}{s} \\ &= \log_{10} \left( 1 + \exp \left[ \frac{2}{\hbar} K \right] \right) + \log_{10}(N_{\text{Coll}}) - 0.159 \\ & \quad + h\delta_{\text{odd}Z} + h\delta_{\text{odd}N} - \Delta_{\text{oo}}\delta_{\text{odd}Z}\delta_{\text{odd}N}, \end{aligned} \quad (1)$$

with

$$K = \int \sqrt{2k\mu(V(\xi) - E_{\text{gs}})} d\xi. \quad (2)$$

Here,  $\mu$  is a reduced mass of the symmetric fission fragments. The path  $\xi$  is described by the differential of the deformation parameters  $\alpha$  as

$$d\xi = r_0 A^{\frac{1}{3}} d\alpha, \quad (3)$$

and taken to proceed to the lowest energy towards the prolate shapes. In this study, we take the  $\alpha_2, \alpha_4, \alpha_6$  deformations in the range  $-0.2 < \alpha_2 < 0.5$ .

Among the above parameters, we take  $r_0 = 1.2$  fm, and  $N_{\text{Coll}} = 10^{20,38}$ . The value of  $k$  in Eq. (2) is adjusted to reproduce the experimental  $T_{\text{sf}}$  for even-even nuclei. The values of  $h$  and  $\Delta_{\text{oo}}$  in Eq. (1) are adjusted for odd- $A$  and odd-odd nuclei after fixed  $k$ . The results are  $k = 6.90$ ,  $h = 3.54$ , and  $\Delta_{\text{oo}} = 3.0$ . Figure 1 shows experimental and calculated  $\log_{10}(T_{\text{sf}}/(s))$  for even-even nuclei. The root-mean-square deviation from experimental ones is 3.33.

Figure 2 shows the most dominant decay modes calculated from the above estimation. We can find that the region of fissioning nuclei is located in three areas: the nuclei near the proton-drip line with  $130 \lesssim N \lesssim 150$ , the nuclei with  $Z \approx 106$  and  $N \approx 168$ , and the nuclei with  $N \gtrsim 184$  and  $N/Z \lesssim 1.9$ .

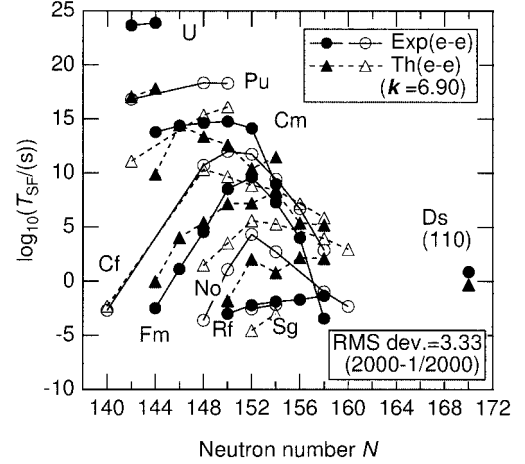
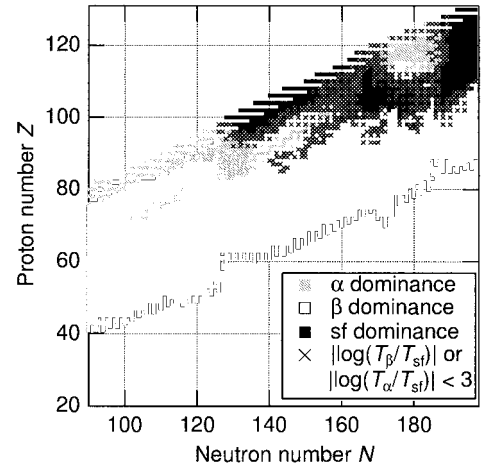
Fig. 1. Experimental and calculated  $\log_{10}(T_{\text{sf}}/(s))$ .

Fig. 2. Shortest partial half-lives among  $\alpha$ -decay ( $\alpha$ ),  $\beta$ -decay ( $\beta$ ) and spontaneous fission (sf).  $\alpha$ : Calculated from formula (B) in Ref. 4.  $\beta$ : Calculated from the gross theory.<sup>5)</sup> sf: This work. The Q values of KUTY's formula are used for the first two calculations.

## References

- 1) H. Koura et al.: RIKEN Accel. Prog. Rep. **35**, 26 (2002).
- 2) H. Koura et al.: Nucl. Phys. A **674**, 44 (2000).
- 3) H. Koura et al.: RIKEN Accel. Prog. Rep. **36**, 9 (2003).
- 4) H. Koura: J. Nucl. Radiochem. Sci. **3**, 201 (2002).
- 5) T. Tachibana et al.: Proc. Int. Conf. on Exotic Nuclei and Atomic Masses, Arles, France, 1995-6, edited by M. de Saint Simon et al. (Editions Frontueres, Gif-sur-Yvette, 1995) p. 763.

\* Advanced Research Institute for Science and Engineering, Waseda University

Application of the generalized two-center cluster model to  $^{10}\text{Be}$  and  $^{12}\text{Be}$ M. Ito,<sup>\*1</sup> K. Katō,<sup>\*2</sup> and K. Ikeda

[NUCLEAR STRUCTURE, cluster model, Unstable nuclei]

Recent experiments strongly indicate the existence of the resonant states which dominantly decay to the  $^6\text{He} + ^6\text{He}$  and  $\alpha + ^8\text{He}$  channels in the excited states of  $^{12}\text{Be}$ .<sup>1)</sup> In  $^{10}\text{Be}$  and  $^{14}\text{Be}$ , similar resonances, decaying to  $^4\text{He} + ^6\text{He}$  and  $^6\text{He} + ^8\text{He}$ , respectively, have also been reported in recent experiments.<sup>1,2)</sup> These experiments strongly suggest the existence of exotic cluster states consisting of the respective He-isotope clusters. Furthermore, the molecular orbital has been shown to provide a good description of the low-lying states of Be isotopes as emphasized by recent studies.<sup>3)</sup> Therefore, it is important to understand both the molecular-orbital formations and the possible appearance of the  $^6\text{He}$  and  $^8\text{He}$  cluster states consistently.

In order to understand the formation of these different configurations equally, we proposed a “generalized two-center cluster model” (GTCM)<sup>4)</sup> and applied it to  $^{10}\text{Be} = \alpha + \alpha + 2n$ . In this model, the total wave function is expressed in terms of a linear combination of the “atomic-orbitals states” having the  $(\alpha+n)+(\alpha+n)$  and  $\alpha + (\alpha + 2n)$  structures. The  $\alpha$  particle is described by the  $(0s)^4$  configuration in the harmonic oscillator potential (HO) and the valence neutrons are specified by the atomic orbitals in which the neutrons are localized at one of  $\alpha$  cores with  $0p_i$  orbitals ( $i = x, y, z$ ) in the same HO potential. The constructed atomic-orbitals states are fully antisymmetrized and projected to the eigenstates of the total spin and the parity. The superposition of the atomic-orbital states can generate the molecular orbitals at a small  $\alpha$ - $\alpha$  distance as well as the asymptotic cluster states of  $\alpha + ^6\text{He}$  and  $^5\text{He} + ^5\text{He}$  at a large  $\alpha$ - $\alpha$  distance.

The calculated energy surfaces are shown in Fig. 1.<sup>4)</sup> We have found that at a short  $\alpha$ - $\alpha$  distance ( $S \leq 4.5$  fm), the valence neutrons form the molecular orbitals (MO), while in an asymptotic region ( $S \geq 6$  fm), the valence neutrons are localized at one of  $\alpha$  cores leading to the formation of the dinuclear states with the  $\alpha + ^6\text{He}$  or  $^5\text{He} + ^5\text{He}$  configuration. In these states,  $^6\text{He}$  or  $^5\text{He}$  has an intrinsic spin and couples to each other with relative spin  $L$ , which just corresponds to the so-called “weak-coupling states” (WS). In addition, at  $S = 4.5$ – $6$  fm, we have found that the system has an intermediate coupling scheme between MO and WS. We also solved the  $\alpha$ - $\alpha$  relative motions and confirmed that the energy gains for the three local minimums in the surfaces of A, B and C amount to approximately 1–2 MeV.

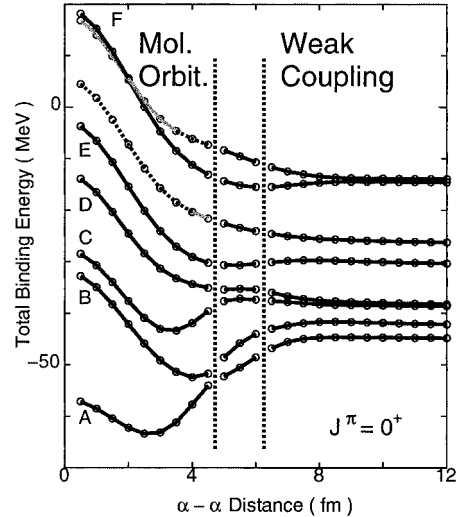


Fig. 1. Adiabatic energy surfaces in  $^{10}\text{Be}$ . The solid surfaces of A, B, C, D, E and F have a dominant component of  $(\pi_{3/2}^-)^2$ ,  $(\sigma_{1/2}^+)^2$ ,  $(\pi_{1/2}^-)^2$ ,  $(\pi_{3/2}^+)^2$ ,  $(\pi_{1/2}^+\sigma_{1/2}^+)$  and  $(\pi_{1/2}^+)^2$ , respectively, while the dotted and thin surfaces have a dominant component of  $(\pi_{1/2}^-\sigma_{1/2}^-)$  and  $(\sigma_{1/2}^-)^2$ , respectively.

Therefore, this model naturally describes the formation of the MO at a short  $\alpha$ - $\alpha$  distance as well as that of WS at an asymptotic region, which was generated by the change of the orbitals for the valence neutrons around two  $\alpha$  cores. This model also predicts the appearance of the pure  $\alpha + ^6\text{He}_{g.s.}$  and  $\alpha + ^6\text{He}(2_1^+)$  cluster states in the  $J^\pi = 1^-$  and  $J^\pi = 6^+$  states, respectively, which were not discussed in previous studies. The adiabatic energy surfaces of  $^{12}\text{Be}$  with  $J^\pi = 0^+$  was also calculated. We have found that the  $^6\text{He}_{g.s.} + ^6\text{He}_{g.s.}$  cluster configuration is enhanced in the third excited surface. This result suggests that the  $0_3^+$  state will be interpreted in terms of the molecular state of this configuration. The extension of GTCM to high spins where the resonances are observed is now under way.

## References

- 1) M. Freer et al.: Phys. Rev. C **63**, 034301 (2001).
- 2) A. Saito et al.: Prog. Theor. Phys. Suppl. **146**, 615 (2002).
- 3) Itagaki et al.: Phys. Rev. C **61**, 044306 (2000).
- 4) M. Ito, K. Kato, and K. Ikeda: Phys. Lett. B, in press.

<sup>\*1</sup> Institute of Physics, University of Tsukuba

<sup>\*2</sup> Division of Physics, Graduate School of Science, Hokkaido University

# Tensor correlation in neutron halo nuclei

T. Myo,<sup>\*1</sup> K. Katō,<sup>\*2</sup> and K. Ikeda

[NUCLEAR STRUCTURE, Unstable nuclei, Cluster model, Tensor force]

Tensor force is an important component in nuclear force and plays an important role in the nuclear structure. For example, the contribution of the tensor force in the binding energy of  ${}^4\text{He}$  is comparable to that of the central force,<sup>1)</sup> and triplet-even part is dominant.

In this report, we investigate the role of tensor force in the structures of the two neutron halo nuclei  ${}^6\text{He}$  and  ${}^{11}\text{Li}$ . In most theoretical studies of these nuclei, the core+ $n+n$  model is often used, where the core nucleus is treated as inert, such as the  $(0s)^4$  configuration of  ${}^4\text{He}$  for  ${}^6\text{He}$ . However, under this assumption, tensor force cannot be incorporated in the core nucleus or in the coupling to the core and valence parts. Therefore, the effects of tensor force in the two neutron halo nuclei have not been realized yet. For  ${}^{11}\text{Li}$  and  ${}^{10}\text{Li}$ , the lowering of the  $1s$  orbit near the  $0p$  orbit has been discussed, however, the essential mechanism of this phenomenon is still unclear. It is of interest to examine the effect of the correlation induced by tensor force on this problem.

We examine what kind of correlation tensor force (tensor correlation) produces. Tensor force tends to change the parity of the nucleon single particle orbit due to the operator of  $(\boldsymbol{\sigma} \cdot \boldsymbol{r})$ . This originates from the nature of the pion (pseudoscalar meson) because tensor force mostly comes from the one-pion-exchange potential. Then, in  ${}^4\text{He}$ , the  $0s$  and  $0p$  orbits can be coupled by tensor force and the description of  ${}^4\text{He}$  is extended to  $(0s)^4 + (0s)^2(0p)^2$ . The amount of dissolution of  ${}^4\text{He}$  can be estimated to be about 10% of the  $D$ -state probability by the exact four-body calculation.

The  $2p$ - $2h$  excitation from  $0s$  to  $0p$  orbits is also applicable in  ${}^9\text{Li}$ . In  ${}^{11}\text{Li}$  and  ${}^{10}\text{Li}$ , the mixing of such configurations in  ${}^9\text{Li}$  couples to the motion of the  $p$ -wave valence neutron. This produces the Pauli-blocking effect, and the total energies of  $p$ -wave configurations of  ${}^{10}\text{Li}$  and  ${}^{11}\text{Li}$  are lost, which may be sufficient to cause the energy to degenerate to that of  $s$ -wave configurations. Then, we expect that tensor correlation can be important to produce the halo structure.

We show the effect of tensor correlation in the calculation of  ${}^4\text{He}$ , where we use the harmonic oscillator wave function, and set the length parameter of the  $0s$  orbit as 1.4 fm to fit the charge radius with the  $(0s)^4$  configuration. The length parameter of the  $0p$  orbit is free to include the higher shell component effectively. For effective  $NN$  interactions, we use the Minnesota,

Furutani<sup>2)</sup> and G3RS forces for the central, tensor, and LS parts, respectively. These are used in the cluster model calculation. Since the Minnesota force includes the effect of tensor force, we adjust the triplet-even part of this force to fit the binding energy of  ${}^4\text{He}$ .

In Table 1, we show the results of  ${}^4\text{He}$  with three length parameters of  $0p$  orbit. It is found that when the  $0p$  orbit shrinks, the contribution of tensor force and the  $2p$ - $2h$  probability become large. In particular, the  $0p_{1/2}$  orbit is well mixed *via*  $0^-$  coupling to the  $0s_{1/2}$  orbit. This is related to the pion nature.

We also analyze the  $p$ -wave resonances of  ${}^5\text{He}$  by solving the coupled channel problem of  ${}^4\text{He}+n$ , where the length parameter of  $0p$  orbit of  ${}^4\text{He}$  is 1.0 fm. Since Pauli blocking mainly occurs in the  $1/2^-$  state due to the  $0p_{1/2}$  component in  ${}^4\text{He}$ , doublet splitting of  $1/2^- - 3/2^-$  is induced in  ${}^5\text{He}$ . A folding potential is used between  ${}^4\text{He}$  and  $n$  without an LS interaction. The results of resonant poles are shown in Table 2, where KKNN is the phenomenological  ${}^4\text{He}$ - $n$  potential that fits the observed phase shifts.<sup>3)</sup> Our model produces half of the observed splitting, which is consistent with other studies.<sup>4)</sup> From the results, the LS interaction of  ${}^4\text{He}$ - $n$  should be reexamined, and the structures of  ${}^6\text{He}$  related to the  $0p_{1/2}$  orbit can be improved.

Tensor correlation and Pauli principle strongly affect the properties of the  $0p_{1/2}$  orbit. This is crucial in the inversion problem in  ${}^{11}\text{Li}$  and  ${}^{10}\text{Li}$ .

Table 1. Results of  ${}^4\text{He}$  wave functions.

length of $0p$ orbit [fm]	1.8	1.4	1.0
$\langle V_{\text{tensor}} \rangle$ [MeV]	-1.6	-6.4	-33.1
$2p$ - $2h$ [%]	1.8	5.2	18.6
$(0p_{1/2})^2$	0.7	3.5	14.8
$(0p_{3/2})^2$	0.3	0.1	0.2
$(0p_{3/2})(0p_{1/2})$	0.8	1.6	3.6

Table 2. Splitting energies in  ${}^5\text{He}$  from two models.

	Present	KKNN
$3/2^-$	(0.74, 0.45)	(0.74, 0.60)
$1/2^-$	(1.45, 0.94)	(2.13, 5.84)

## References

- 1) Y. Akaishi et al.: Int. Rev. Nucl. Phys. **4**, 259 (1988).
- 2) H. Furutani et al.: Prog. Theor. Phys. **62**, 981 (1979).
- 3) H. Kanada et al.: Prog. Theor. Phys. **61**, 1327 (1979).
- 4) T. Terasawa: Prog. Theor. Phys. **23**, 87 (1960).

<sup>\*1</sup> Research Center for Nuclear Physics, Osaka University

<sup>\*2</sup> Division of Physics, Graduate School of Science, Hokkaido University

# $^{16}\text{O} + ^{16}\text{O}$ nature of the superdeformed band of $^{32}\text{S}$ and the evolution of the molecular structure

M. Kimura and H. Horiuchi\*

[Nuclear structure, Cluster structure]

Recently, a rather conclusive result of the properties of  $^{16}\text{O} + ^{16}\text{O}$  molecular resonance was obtained by macroscopic models<sup>1)</sup> using the unique potential. These studies gave the following results for the lowest three rotational bands whose principal quantum numbers are  $N = 24, 26$  and  $28$ . The lowest Pauli-allowed rotational band ( $N = 24$ ) starts from the  $0^+$  state located at approximately 9 MeV in the excitation energy, and the energy gap between the  $N = 24$  and  $N = 26$  bands and that between  $N = 26$  and  $N = 28$  bands are both approximately 10 MeV. In Ref. 1, it is proposed that the observed  $^{16}\text{O} + ^{16}\text{O}$  molecular states correspond to the third band ( $N = 28$ ). Aside from the molecular bands, the superdeformed state of  $^{32}\text{S}$  has also been studied by many authors using the mean-field theories,<sup>2,3)</sup> and one of their interests is the relationship between the superdeformed state of  $^{32}\text{S}$  and the  $^{16}\text{O} + ^{16}\text{O}$  molecular structure. It is notable that these calculations predict that the superdeformed band starts from the  $0^+$  located at approximately 8 to 10 MeV which agrees with the energy of the  $N = 24$  band head obtained from the unique optical potential. Therefore, it is sufficiently conceivable and has been pointed out by some authors<sup>1)</sup> that the superdeformed band and the lowest Pauli-allowed  $^{16}\text{O} + ^{16}\text{O}$  molecular band ( $N = 24$ ) are identical.

In the present study, we aim at clarifying the relationship between the superdeformed state and the  $^{16}\text{O} + ^{16}\text{O}$  molecular structure. The objectives of the present study are summarised as follows. (1) To what extent are the superdeformed state and the  $^{16}\text{O} + ^{16}\text{O}$  molecular structure related? In the unique optical potential analysis, the factors which distort the  $^{16}\text{O} + ^{16}\text{O}$  cluster structure, such as the effect of the spin-orbit force and the formation of the deformed mean-field, are renormalised into the optical potential. Therefore, when we treat these factors accurately using the full microscopic model, the pure  $^{16}\text{O} + ^{16}\text{O}$  structure will be distorted and can be understood as the superdeformed state of  $^{32}\text{S}$ . (2) Do the excited states exist in which the excitation energy is spent to excite the relative motion between the clusters? Do they correspond to the  $N = 26$  and  $28$  bands obtained from the unique optical potential? When we consider that the superdeformed states of  $^{32}\text{S}$  have a considerable amount of the  $^{16}\text{O} + ^{16}\text{O}$  component, we can expect the excitation mode in which the excitation energy is used to excite the relative motion between clusters.

To investigate these points, we need to apply the framework which can deal with the superdeformed state (largely deformed one-body field) and the molecular structure (two-center structure with the spherical subunits) at the same time. We have studied these points with the deformed-base AMD+GCM framework<sup>4)</sup> which are appropriate for studying the interplay of the deformed mean-field structure and the cluster structure.

In this report, we mention the prominent feature of our results, and readers are directed to Ref. 5 for more detailed discussions. The obtained superdeformed wave function shows the large effect of the distortion of the  $^{16}\text{O} + ^{16}\text{O}$  cluster structure. Namely, the superdeformed state obtained by the deformed-base AMD is more deeply bound than the pure  $^{16}\text{O} + ^{16}\text{O}$  state by about 10 MeV because of the energy gain in the density-dependent force and spin-orbit force. The non vanishing expectation value of the spin-orbit force at the superdeformed minimum directly indicates the distortion of the  $^{16}\text{O} + ^{16}\text{O}$  structure and the formation of the deformed one-body field. However, the obtained superdeformed wave function still has a considerable  $^{16}\text{O} + ^{16}\text{O}$  component which amounts to approximately 50%. By superposing the obtained wave functions, we have obtained three rotational bands which correspond to the  $N = 24, 26$  and  $28$  bands. The lowest band ( $N = 24$ ) has a mixed character of the  $^{16}\text{O} + ^{16}\text{O}$  structure and deformed mean-field structure and its excitation energy agrees well with the superdeformed state obtained by the mean-field calculations. In the  $N = 26$  and  $N = 28$  bands, we have found that the amount of the  $^{16}\text{O} + ^{16}\text{O}$  component increases markedly and these two bands have an almost pure  $^{16}\text{O} + ^{16}\text{O}$  structure. At the same time, these band members are fragmented into several states and the assignment of the  $N = 28$  band members to the observed  $^{16}\text{O} + ^{16}\text{O}$  molecular resonances appears plausible.

## References

- 1) S. Ohkubo and K. Yamashita: Phys. Rev. C **66**, 021301(R) (2002).
- 2) M. Yamagami and K. Matsuyanagi: Nucl. Phys. A **672**, 123 (2000).
- 3) R. R. Rodríguez-Guzmán, J. L. Egido, and L. M. Robledo: Phys. Rev. C **62**, 054308 (2000).
- 4) M. Kimura: Phys. Rev. C **69**, 052404 (2004).
- 5) M. Kimura and H. Horiuchi: nucl-th/0311061.

\* Department of Physics, Kyoto University

# $^{12}\text{C}+^{12}\text{C} \rightarrow ^8\text{Be}_{\text{g.s.}}+^{16}\text{O}_{\text{g.s.}}$ resonance reaction and multicluster states of highly excited $^{24}\text{Mg}$ nucleus

 M. Takashina, M. Ito,\*<sup>1</sup> and Y. Sakuragi\*<sup>2</sup>

 [nuclear reaction,  $\alpha$ -transfer reaction, cluster structure]

In this decade, interesting resonance-like structures have been observed in the excitation functions of  $^{12}\text{C}+^{12}\text{C}$  collisions leading to multicluster exit channels ( $3\alpha+3\alpha$ ,  $3\alpha+^{12}\text{C}$ ,  $2\alpha+^{16}\text{O}$ , etc.),<sup>1)</sup> particularly around  $E_{\text{c.m.}} = 32.5$  MeV. These experimental data suggest the existence of a new multicluster state of a highly excited  $^{24}\text{Mg}$  nucleus. In the present study, we investigate resonance-like structures observed in a  $^{12}\text{C}+^{12}\text{C} \rightarrow ^8\text{Be}_{\text{g.s.}}+^{16}\text{O}_{\text{g.s.}}$   $\alpha$ -transfer reaction by coupled-channel Born approximation (CCBA). The distorted waves are given by coupled-channel (CC) calculations of the  $^{12}\text{C}+^{12}\text{C}$  and  $^8\text{Be}+^{16}\text{O}$  systems, using double-folding interactions based on microscopic cluster-model wave functions<sup>2)</sup> for  $^{12}\text{C}$ ,  $^8\text{Be}$  and  $^{16}\text{O}$ . The T-matrix element of the transfer reaction process is calculated by Born approximation.

Figure 1 compares the calculated angle-averaged differential cross section for the  $^{12}\text{C}+^{12}\text{C} \rightarrow ^8\text{Be}_{\text{g.s.}}+^{16}\text{O}_{\text{g.s.}}$  reaction with experimental data.<sup>1)</sup> The calculation well reproduces the resonance structures, particularly in higher excitation energies. The characteristic enhancement at 90 degrees in the angular distributions (inset) at  $E_{\text{c.m.}} = 32.5$  and 28.7 MeV on-resonance energy (indicated by arrows) is also well reproduced. Figure 2 shows the same cross section (solid line) as that shown on Fig. 1 divided into contributions from individual reaction paths. It is observed that the channels with an  $(\alpha-\alpha)+(\alpha-^{12}\text{C})$ -type four-cluster structure have a dominant contribution in reproducing the resonance structures, and by further analysis, it is found that the peak at  $E_{\text{c.m.}} = 32.5$  MeV is attributed to the four-cluster resonance state produced in the  $^8\text{Be}+^{16}\text{O}$  in-

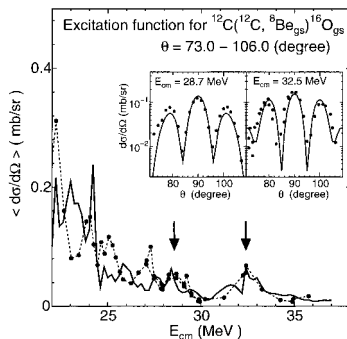


Fig. 1. Excitation function of the  $^{12}\text{C}+^{12}\text{C} \rightarrow ^8\text{Be}_{\text{g.s.}}+^{16}\text{O}_{\text{g.s.}}$   $\alpha$ -transfer reaction, and angular distributions (inset) at the energies indicated by arrows.

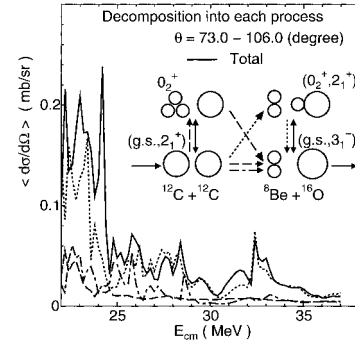


Fig. 2. Contribution from each transfer process. The solid curve is the same as that in Fig. 1.

elastic scattering. These results strongly suggest that  $(\alpha-\alpha)+(\alpha-^{12}\text{C})$ -type four-cluster resonance structures are produced in this  $\alpha$ -transfer reaction.

We also investigate the rotational band formed in the final  $^8\text{Be}+^{16}\text{O}$  system. The result is shown in Fig. 3. We observe many resonance states with three-cluster (open circles) and four-cluster structures (solid circles), although most of them cannot be observed clearly in Fig. 1. The resonance peaks at  $E_{\text{c.m.}} = 32.5$  MeV and 28.7 MeV in the  $\alpha$ -transfer reaction (Fig. 1) are found to reflect the resonances indicated by arrows in Fig. 3.

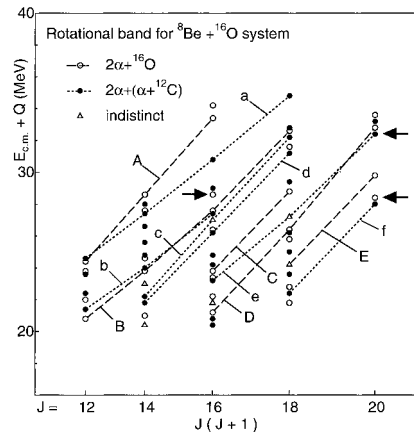


Fig. 3. Rotational band of the  $^8\text{Be}+^{16}\text{O}$  system.

## References

- 1) A. H. Wuosmaa et al.: Phys. Rev. Lett. **68**, 1295 (1992); R. A. Le Marechal et al.: Phys. Rev. C **55**, 1881 (1997); M. Aliotta et al.: Z. Phys. A **354**, 119 (1996).
- 2) M. Kamimura: Nucl. Phys. A **351**, 456 (1981); S. Okabe: unpublished; M. Takashina: Ph. D. Thesis, Osaka City University (2003).

\*1 Institute of Physics, Tsukuba University

\*2 Department of Physics, Osaka City University



# Effect of halo structure on $^{11}\text{Be}+^{12}\text{C}$ elastic scattering

M. Takashina and Y. Sakuragi\*

[NUCLEAR REACTION, Unstable nuclei]

Nuclear reactions involving neutron-rich nuclei have been important subjects in nuclear physics. Particularly, in light halo-nucleus-induced reactions, it is very interesting to study how the halo structure affects the reaction mechanisms. In the present study, we analyze the typical one-neutron halo nucleus  $^{11}\text{Be}$  elastic scattering on  $^{12}\text{C}$  at  $E/A = 49.3$  MeV.

Because of the weakly bound feature, the breakup process of the incident halo nucleus  $^{11}\text{Be}$  into  $^{10}\text{Be}+n$  is expected to be important. To describe its dynamical breakup effect accurately, one needs to treat the  $^{11}\text{Be}+^{12}\text{C}$  scattering as, at least, a three-body problem. Therefore, we apply the continuum-discretized coupled-channels (CDCC) method,<sup>1)</sup> which is one of the practical and reliable methods for studying the three-body reaction process.

In the CDCC method, the continuum-energy two-body breakup states of the projectile nucleus are approximately represented in terms of a finite number of discretized states in the prescription called *the method of momentum bins*. The discretized breakup states can be treated in the same manner as conventional discrete-excited states, and coupled-channel equations are numerically solved in the standard manner to obtain the transition matrix elements for elastic scattering and breakup reactions.

The result of the CDCC calculation is shown in Ref. 2, and is found to reproduce well the experimental data. The results of further investigation<sup>2)</sup> indicate that the breakup effect is dominated by the coupling to the  $p$ - and  $d$ -wave breakup states. Among the  $p$ -wave breakup states, the second bin ( $\hat{E}_x = 0.954$  MeV, where  $\hat{E}_x$  represents the mean energy of the bin) has the largest contribution, while in the  $d$ -wave, the bin containing the resonance state at  $E_x = 1.778$  MeV has the largest contribution. The large effect of resonance breakup can be understood from the good overlapping of localized-resonance wave function with the ground state one. However, the overlap integral of the continuum wave function with the ground state one is not so large.

To clarify the reason why the second bin of the  $p$ -wave continuum breakup state has a large contribution, we investigate the coupling potential. First, we define a function  $F_{p2,gs}^{\lambda=1}(r, R)$  as

$$F_{p2,gs}^{\lambda=1}(r, R) = \Phi_{p2}(r) V_1(r, R) \Phi_{gs}(r), \quad (1)$$

where  $V_1(r, R)$  represents the potential between core ( $^{10}\text{Be}$ ) and target (c-T), or that between neutron and

target (n-T) with multipolarity  $\lambda = 1$ .  $r$  and  $R$  represent the separation between core and neutron, and that between the center-of-mass of  $^{11}\text{Be}$  and target nucleus, respectively.  $\Phi_\alpha(r)$  is the  $^{10}\text{Be}+n$  wave function in state  $\alpha$ . Integrating  $F_{p2,gs}^{\lambda=1}(r, R)$  over  $r$  and summing the c-T and n-T components, we obtain the coupling potential between the ground state and the second bin of  $p$ -wave continuum state as a function of  $R$ .

Figure 1 shows  $F_{p2,gs}^{\lambda=2}(r, R)$  as a function of  $r$ .  $R$  is fixed at 5.0 fm. It is found that the c-T component represented by a solid curve has a large amplitude in the long-range region, while the n-T components represented by the dotted curve is localized in the short-range region. Since these two components are summed when calculating the coupling potential, the short-range parts cancel each other. However, the long-range part of the c-T component survives, resulting in comparable magnitude of coupling potential with the  $d$ -wave resonance breakup. This large amplitude of the c-T component is due to the long-range tail of the valence neutron wave function of the ground state. Namely, the large contribution from the  $p$ -wave breakup state is a notable property characteristic of the halo-nucleus-induced reaction.

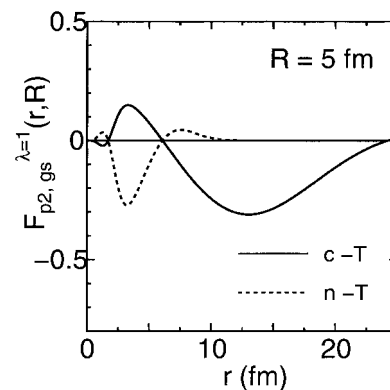


Fig. 1.  $F_{p2,gs}^{\lambda=1}(r, R)$  defined in Eq. (1) as a function of the separation  $r$  between neutron and core nucleus.  $R$  represents the separation between the center-of-mass of  $^{11}\text{Be}$  and target nucleus, and is fixed at 5.0 fm. The solid and dotted curves represent the core-target (c-T) and neutron-target (n-T) components, respectively.

## References

- 1) Y. Sakuragi, M. Yahiro, and M. Kamimura: Prog. Theor. Phys. Suppl. **89**, 136 (1986).
- 2) M. Takashina, S. Takagi, Y. Sakuragi, and Y. Iseri: Phys. Rev. C **67**, 037601 (2003).

\* Department of Physics, Osaka City University

# A search for a unified effective interaction for Monte Carlo shell model calculations (V)

M. Honma,<sup>\*1</sup> T. Otsuka,<sup>\*2,\*3</sup> B. A. Brown,<sup>\*4</sup> and T. Mizusaki<sup>\*5</sup>

[Shell model, Effective interaction]

The Monte Carlo shell model (MCSM)<sup>1)</sup> has enabled us to study various nuclear structure in a huge shell-model space. For this purpose, we have developed an effective interaction GXPF1<sup>2,3)</sup> for the full  $pf$ -shell calculations. We have tested GXPF1 in detail from various viewpoints such as binding energies, electro-magnetic moments and transitions, and excitation spectra. The semi-magic structure has been successfully described for  $N$  or  $Z = 28$  nuclei, suggesting the existence of significant core-excitations in low-lying non-yrast states as well as in high-spin yrast states. The results of  $N = Z$  odd-odd nuclei have also confirmed the reliability of GXPF1 in the isospin dependent properties.

In this report, as an example, we show the results for  $^{56}\text{Ni}$ . Most of shell-model calculations were carried out in a conventional way by using the shell-model code MSHELL,<sup>4)</sup> which enables calculations with  $M$ -scheme dimensions of up to  $\sim 10^8$  on recent powerful computers. We can handle essentially all low-lying states in the  $pf$ -shell nuclei with a minimal truncation of the model space. We took  $t = 7$  truncated subspace, where the truncation order  $t$  denotes the maximum number of nucleons which are allowed to be excited from the  $f_{7/2}$  orbit to higher three orbits  $p_{3/2}$ ,  $f_{5/2}$  and  $p_{1/2}$ . The agreement between the experiment and the calculation is rather good. The results are consistent with those of MCSM shown in Fig. 2 of Ref. 2, confirming the reliability of the MCSM calculations.

GXPF1 predicts<sup>2)</sup> the deformed 4p-4h band<sup>5)</sup> as  $0_3^+$ ,  $2_2^+$ ,  $\dots$ . Special care should be taken concerning the convergence of the calculation for such a deformed 4p-4h band, since the present truncation scheme is obviously not suitable for describing strongly deformed states, as discussed in Ref. 6 for the case of the FPD6<sup>7)</sup> interaction. Figure 1 shows the calculated energies and quadrupole moments of the lowest two  $2^+$  states as a function of the truncation order  $t$ . It can be seen that the 4p-4h state  $2_2^+$  is not completely converged even in the  $t = 7$  subspace, which corresponds to the  $M$ -scheme dimension of 89285264. In the same figure, the MCSM results are also shown, where 25 bases were searched for each eigenstate. The MCSM energy of

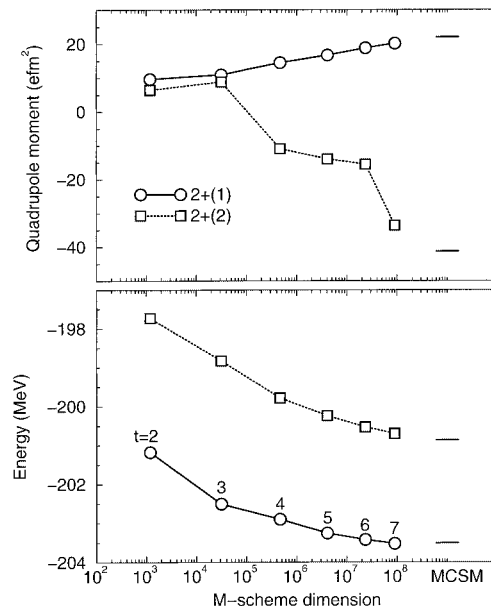


Fig. 1. Convergence of the calculated energies (lower panel) and quadrupole moments (upper panel) as functions of the truncation order  $t$  for the lowest two  $2^+$  states of  $^{56}\text{Ni}$ . Horizontal lines show the corresponding MCSM results.

the yrast  $2^+$  state is almost the same as that of the  $t = 7$  calculation, which shows reasonable convergence. On the other hand, for  $2_2^+$  states, the MCSM energy is lower than the  $t = 7$  result by about 0.2 MeV, and should be more accurate. The electric quadrupole moment is  $Q(2_2^+) = -41.2 \text{ efm}^2$  in the MCSM calculation, while it is  $-33.6$  in the present  $t = 7$  result. Similar results are obtained for the 4p-4h  $0_3^+$  state. Thus, for the description of such deformed states where a lot of mixing among various spherical configurations occurs, the MCSM calculation is more efficient and suitable, because certain basis states can be sampled from and around local minima.

## References

- 1) T. Otsuka et al.: Phys. Rev. Lett. **81**, 1588 (1998).
- 2) M. Honma et al.: Phys. Rev. C **65**, 061301(R) (2002).
- 3) M. Honma et al.: RIKEN Accel. Prog. Rep. **33**, 16 (2000); RIKEN Accel. Prog. Rep. **34**, 15 (2001); RIKEN Accel. Prog. Rep. **35**, 12 (2002); RIKEN Accel. Prog. Rep. **36**, 21 (2003).
- 4) T. Mizusaki: RIKEN Accel. Prog. Rep. **33**, 14 (2000).
- 5) D. Rudolph et al.: Phys. Rev. Lett. **82**, 3763 (1999).
- 6) T. Mizusaki et al.: Nucl. Phys. A **704**, 190c (2002).
- 7) W. A. Richter et al.: Nucl. Phys. A **523**, 325 (1991).

<sup>\*1</sup> Center for Mathematical Sciences, University of Aizu

<sup>\*2</sup> Department of Physics, University of Tokyo

<sup>\*3</sup> Center for Nuclear Study, University of Tokyo

<sup>\*4</sup> National Superconducting Cyclotron Laboratory and Department of Physics and Astronomy, Michigan State University, USA

<sup>\*5</sup> Institute of Natural Sciences, Senshu University

# Ground states in even-even nuclei using random interactions

N. Shimizu and T. Otsuka<sup>\*1,\*2</sup>

[Nuclear Shell Model, Quantum Chaos]

The random matrix theory has been investigated to study the quantum chaos and nuclear physics, the object of which is the quantum many-body system. In the 1950s, Wigner introduced the random Hamiltonian matrix, whose elements are random numbers obeying a Gaussian distribution in order to describe the level distribution of highly excited nuclear states.<sup>1)</sup> The level distribution had been the main topic of the random matrix theory, until Johnson *et al.* discovered the “ $J = 0$  dominance” of the ground state provided by a random Hamiltonian matrix.<sup>2)</sup>

The  $J = 0$  dominance means that the angular momentum,  $J$ , of the ground state of even-even nuclei obtained by a random Hamiltonian matrix favors zero, although the subspace having  $J = 0$  is very small in comparison with the entire Hilbert space. All the realistic even-even nuclei are known to have  $J = 0$  ground states experimentally, and the origin of the  $J = 0$  dominance is considered to be the pairing correlation and time reversal symmetry. However, the random interaction without time reversal symmetry was shown to reproduce the  $J = 0$  dominance,<sup>3)</sup> and its investigation is still of interest. We discuss some properties of the  $J = 0$  dominance in this report.

Table 1 shows the ground state probability of the  $sd$ -shell nuclei with  $N$  valence particles having angular momentum zero ( $P(J = 0)$ ). The Hamiltonian is taken

Table 1. Probability that the angular momentum of ground states will be zero (middle row) as compared to the ratio of the dimension of the  $J = 0$  subspace to that of the entire Hilbert space (lower row). The system consists of  $N$  identical particles in the  $sd$ -shell. The  $sd$ -shell consists of  $1d_{3/2}$ ,  $1d_{5/2}$ , and  $2s_{1/2}$ . The probabilities are obtained by 1000 runs of TBRE Hamiltonians.

$N$	2	4	6
$P(J = 0)$	14.0%	56.6%	71.3%
model space	21.4%	11.1%	9.9%

as the two-body random ensemble, or TBRE.<sup>2)</sup>  $P(J = 0)$  increases markedly with increasing  $N$ , while the  $J = 0$  ratio of all states decreases.  $P(J = 0)$  generally increases with increasing dimension of the entire model space, while the ratio of the  $J = 0$  subspace decreases. Then,  $P(J = 0)$  of a half-filled system tends to be the highest probability.

Table 2 shows the  $P(J = 0)$  and the ratio of the  $J = 0$  subspace of  $pf$ -shell nuclei. Whereas they show a similar behavior to  $sd$ -shell nuclei for the values of  $N = 0, 2, 4, 6$ , and  $8$ , the  $P(J = 0)$  of  $N = 10$  suddenly decreases. This is mainly caused by the  $f_{7/2}$  single particle orbit, which does not favor the  $J = 0$  ground state. For example,  $P(J = 0)$  of  $N = 4$  in  $f_{7/2}$  is 17.7%, which is far smaller than those of other single- $j$  shell systems.<sup>4)</sup> The occupation probability of the  $f_{7/2}$  orbit of the  $N = 10$  system is larger than that of the  $N = 8$  system, thus the  $P(J = 0)$  of  $N = 10$  is suppressed. The result that the  $pf$ -shell without  $f_{7/2}$  does not show such suppression supports this consideration.

This study is part of the RIKEN-CNS collaboration project on large-scale nuclear structure calculation.

Table 2. Same as Table 1 except that this is for the  $pf$ -shell. The  $pf$ -shell consists of  $1f_{7/2}$ ,  $1f_{5/2}$ ,  $2p_{1/2}$  and  $2p_{3/2}$ .

$N$	2	4	6	8	10
$P(J = 0)$	11.3%	42.6%	55.7%	60.3%	50.6%
model space	13.3%	5.0%	3.5%	2.9%	2.7%

## References

- 1) E. P. Wigner: Ann. Math. **67**, 325 (1958).
- 2) C. W. Johnson, G. F. Bertsch, and D. J. Dean: Phys. Rev. Lett. **80**, 2749 (1998).
- 3) R. Bijker, A. Frank, and S. Pittel: Phys. Rev. C **60**, 021302 (1999).
- 4) Y. M. Zhao and A. Arima: Phys. Rev. C **64**, 041301 (2001).

<sup>\*1</sup> Department of Physics, University of Tokyo

<sup>\*2</sup> Center for Nuclear Study, University of Tokyo

# Triaxiality of neutron-rich Mg isotopes

Y. Utsuno,\*<sup>1</sup> T. Otsuka,\*<sup>2,\*3</sup> T. Mizusaki,\*<sup>4</sup> and M. Honma\*<sup>5</sup>

[NUCLEAR STRUCTURE, Shell model, Unstable nuclei]

Owing to recent experiments of in-beam  $\gamma$ -ray spectroscopy for neutron-rich Mg isotopes  $^{32,34}\text{Mg}$ ,<sup>1,2)</sup> the structure of these nuclei can be discussed in more detail apart from the disappearance of the  $N = 20$  magic structure. Although both of them are regarded as well deformed nuclei from the measured low  $2_1^+$  energy levels, the ratios of  $E_x(4_1^+)$  to  $E_x(2_1^+)$  are rather different, *i.e.*, 2.6 and 3.2 for  $^{32,34}\text{Mg}$ , respectively.<sup>1,2)</sup> The latter is very close to the value of the rigid axially symmetric rotor, whereas the former is not. In this study, we investigate how this difference occurs by large-scale shell-model calculation using the Monte Carlo shell model (MCSM). The numerical computations have been carried out with the Alphleet and Alphleet-2 parallel computer systems as a RIKEN-CNS collaboration project on large-scale nuclear structure calculation.

The shell-model Hamiltonian used in this study is the same as that of our previous works.<sup>3)</sup> Figure 1 compares the energy levels and  $B(E2)$  values between the experiment and MCSM. The observed difference

in  $E_x(4_1^+)/E_x(2_1^+)$  is well reproduced, similarly to the excitation energies and the  $B(E2)$  values. We also calculate the non-yrast states, and find a difference between those nuclei: the  $2_2^+$  level of  $^{32}\text{Mg}$  drops closely to the  $4_1^+$  level, and is connected to the  $2_1^+$  level with a moderately large  $B(E2)$  value.

In order to examine the deviation from the rigid axially symmetric rotor, the potential energy surface (PES) is calculated within the shell-model space and using the same Hamiltonian as illustrated in Fig. 2. The PES of  $^{32}\text{Mg}$  is more  $\gamma$  unstable than that of  $^{34}\text{Mg}$ , and after the angular-momentum projection, the energy minimum moves to  $\gamma \sim 20^\circ$ . This  $\gamma$  value accounts for the shell-model result in Fig. 1, comparing to the asymmetric rigid rotor model. On the other hand,  $^{34}\text{Mg}$  appears to be a rather good symmetric rotor. The present result demonstrates that our shell-model calculation is capable of describing not only the shell structure but also the deformation giving rise to more detailed properties.

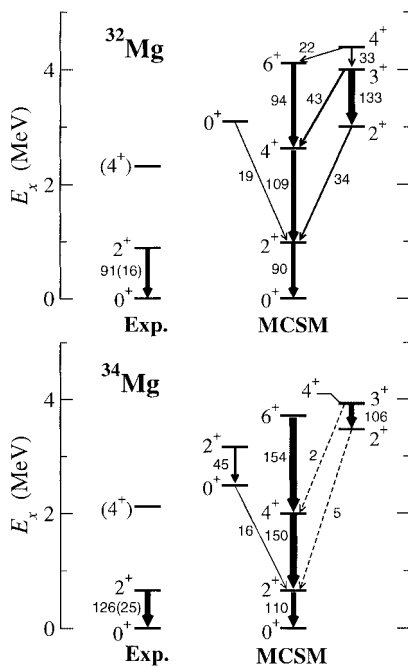


Fig. 1. Experimental energy levels and  $B(E2)$  values of  $^{32,34}\text{Mg}$  (Exp.) compared with those of the MCSM calculation (MCSM). The numbers near the arrows denote the  $B(E2)$  in  $e^2 \text{fm}^4$ .

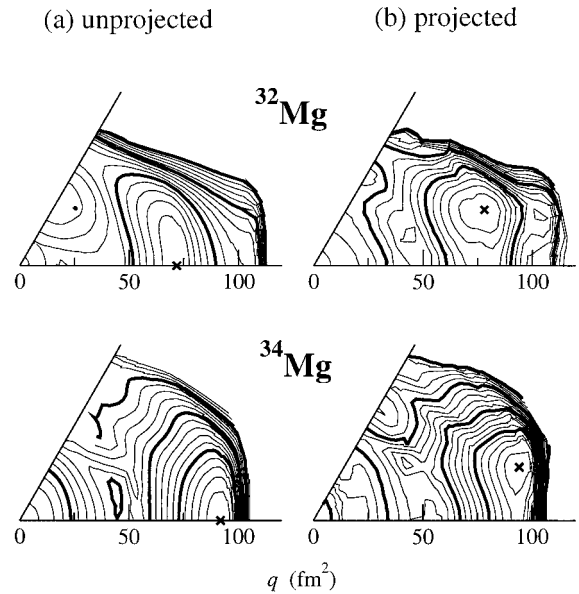


Fig. 2. Comparison of the potential energy surfaces of  $^{32,34}\text{Mg}$  (a) without and (b) with the angular momentum projection onto  $I = 0$ . The thin and thick lines are drawn at intervals of 0.3 and 1.5 MeV, respectively.

## References

- 1) K. Yoneda et al.: Phys. Lett. B **499**, 233 (2001).
- 2) F. Azaiez et al.: AIP Conf. Proc. **481**, 243 (1998).
- 3) Y. Utsuno, T. Otsuka, T. Mizusaki, and M. Honma: Phys. Rev. C **60**, 054315 (1999); Phys. Rev. C **64**, 011301(R) (2001).

\*<sup>1</sup> Japan Atomic Energy Research Institute  
 \*<sup>2</sup> Department of Physics, University of Tokyo  
 \*<sup>3</sup> Center for Nuclear Study, University of Tokyo  
 \*<sup>4</sup> Institute of Natural Sciences, Senshu University  
 \*<sup>5</sup> Center for Mathematical Sciences, University of Aizu

# Charge- and parity-projected Hartree-Fock method for strong tensor correlation and its application to the alpha particle

S. Sugimoto, K. Ikeda, and H. Toki\*

[NUCLEAR STRUCTURE, Mean field model,  $^4\text{He}$ ]

We propose a mean-field framework in which the charge and the parity symmetries of single-particle states are broken. We break these symmetries to incorporate the correlation induced by the tensor force into the nuclear mean field. The tensor force is mediated by the pion. Recently, we proposed a new method of treating the pion in the relativistic mean field (RMF) theory by breaking the parity symmetry of the nuclear mean field.<sup>1)</sup> In the previous paper,<sup>1)</sup> we applied this idea to the RMF theory and showed that the correlation induced by the pion is obtained by this method.

Because the pion is an isovector meson, a single-particle state in the mean field changes its charge state when it emits or absorbs a charged pion. This feature indicates that the isovector nature of the pion can be treated by introducing charge-mixed single-particle states. The dominant part of the tensor force is of the  $\tau_1 \cdot \tau_2$ -type, and therefore, the charge mixing is important when we treat the tensor force in a nuclear mean-field model.

The total wave function consisting of charge- and parity-mixed single-particle states does not have a definite parity and charge number, and therefore, the charge and parity projections need to be performed. For an  $A$ -nucleon system, we assume the total wave function to be a Slater determinant of  $A$  particles. We perform the charge and the parity projections on the charge- and parity-mixed total wave function and take the variation of each single-particle state. As a result, the charge- and parity-projected Hartree-Fock (CPPHF) equation, which is a Hartree-Fock-like equation, for each single-particle state is obtained. We solve it self-consistently.

We show the results for the alpha particle in Table 1. We take as the nucleon-nucleon potential the Volkov No. 1 force<sup>2)</sup> for the central part, and the G3RS force<sup>3)</sup> for the noncentral part. Here, we reduce the attractive part of the Volkov No. 1 force in the  $^3\text{E}$  channel by multiplying it by the factor  $x_{\text{TE}}$ . We also multiply the  $\tau_1 \cdot \tau_2$  part of the tensor force by the factor  $x_{\text{T}}$ . The factors,  $x_{\text{TE}}$  and  $x_{\text{T}}$ , are determined to reproduce the binding energy of the alpha particle in the CPPHF method. In the table, we show three cases. The first one is the result of the simple Hartree-Fock (HF) method, the second one is that of the parity-projected Hartree-Fock (PPHF) method, and the third one is that of the charge- and parity-projected Hartree-Fock (CPPHF) method. In the PPHF case, only the parity

Table 1. Results for the  $0^+$  state of the alpha particle for various cases. The potential energy ( $\langle \hat{v} \rangle^{(+;2)}$ ), the kinetic energy ( $\langle \hat{T} \rangle^{(+;2)}$ ), and the total energy ( $E^{(+;2)}$ ) are given.  $\langle \hat{v}_{\text{C}} \rangle^{(+;2)}$ ,  $\langle \hat{v}_{\text{T}} \rangle^{(+;2)}$ ,  $\langle \hat{v}_{\text{LS}} \rangle^{(+;2)}$ , and  $\langle \hat{v}_{\text{Coul}} \rangle^{(+;2)}$  are the expectation values for the central, tensor, LS, and Coulomb potentials, respectively.

	HF	HF	PPHF	CPPHF
$x_{\text{T}}$	1.0	1.5	1.5	1.5
$x_{\text{TE}}$	1.0	0.81	0.81	0.81
$\langle \hat{v}_{\text{C}} \rangle^{(+;2)}$ (MeV)	-76.67	-56.85	-61.31	-64.75
$\langle \hat{v}_{\text{T}} \rangle^{(+;2)}$ (MeV)	0.00	0.00	-10.91	-30.59
$\langle \hat{v}_{\text{LS}} \rangle^{(+;2)}$ (MeV)	0.00	0.00	0.67	1.91
$\langle \hat{v}_{\text{Coul}} \rangle^{(+;2)}$ (MeV)	0.83	0.76	0.78	0.85
$\langle \hat{v} \rangle^{(+;2)}$ (MeV)	-75.84	-56.10	-70.76	-92.58
$\langle \hat{T} \rangle^{(+;2)}$ (MeV)	48.54	39.98	49.67	64.39
$E^{(+;2)}$ (MeV)	-27.30	-16.12	-21.09	-28.19

projection is performed, but in the CPPHF case, both the charge and the parity projections are performed. In the simple HF case, the expectation value of the tensor force becomes zero. However, in the PPHF case, the tensor correlation becomes finite. If we perform the charge projection further, we can obtain much more attractive energy from the tensor force. The energy from the tensor force in the CPPHF case is about three times larger than that in the PPHF case. In the PPHF case, only the  $\tau_0\tau_0$  part of the tensor force is active, but in the CPPHF case, all the  $\tau_+\tau_-$ ,  $\tau_-\tau_+$ , and  $\tau_0\tau_0$  terms of the tensor force can contribute to the nuclear mean field.

From these results, we can see that, by combining the mixing of parities and charges and the projections, we are able to treat the tensor force in a mean-field framework. Here, we note that the projections need to be performed before the variation, because even if we assume the charge and the parity mixings in the simple HF method, we do not obtain a charge- and parity-mixed wave function as a result of a self-consistent calculation.

We are now trying to apply our method to heavier systems and we can show the result in the near future.

## References

- 1) H. Toki, S. Sugimoto, and K. Ikeda: Prog. Theor. Phys. **108**, 903 (2002).
- 2) A.B. Volkov: Nucl. Phys. **74**, 33 (1965).
- 3) R. Tamagaki: Prog. Theor. Phys. **39**, 91 (1968).

\* Research Center for Nuclear Physics, Osaka University

# Chiral sigma model with pion mean field in finite nuclei<sup>†</sup>

Y. Ogawa,<sup>\*1</sup> H. Toki, S. Tamenaga,<sup>\*1</sup> H. Shen,<sup>\*2</sup> A. Hosaka,<sup>\*1</sup> S. Sugimoto, and K. Ikeda

[Chiral symmetry, Linear sigma model, Finite pion mean field, Relativistic mean field theory,  
Magic number, Extended chiral sigma model]

A theoretical framework to treat explicitly the pion mean field in finite nuclei has been developed by introducing parity mixed intrinsic single particle states.<sup>1)</sup> The purpose of this study is to investigate the properties of finite nuclei and the role of the pion using a chiral sigma model within the relativistic mean field theory. Chiral symmetry is known to be the most important symmetry in hadron physics, which is described well in a linear sigma model.<sup>2)</sup> The pion, which was introduced by Yukawa as the mediator of the nuclear force,<sup>3)</sup> received its foundation through spontaneous chiral symmetry breaking.<sup>4)</sup> We then attempted to understand the nuclei based on the fundamental symmetry in hadron physics. We reconstructed an extended chiral sigma (ECS) model Lagrangian in non-linear realization, in which the nucleon and omega meson masses are generated dynamically by sigma condensation in vacuum.<sup>5)</sup> All the parameters of the chiral sigma model are essentially fixed from hadron properties in free space.

This model gives good saturation properties, which are the density  $\rho = 0.141 \text{ fm}^{-3}$  and the energy per particle  $E/A = -16.1 \text{ MeV}$ . The incompressibility in this case, however, is determined to be very large,  $K = 650 \text{ MeV}$ . Furthermore, both scalar and vector potentials, which are related to the strength of spin-orbit interaction, are approximately one-half of the phenomenological<sup>6)</sup> ones.

We have applied this model to finite nuclei ( $N = Z$  even-even mass from  $N = 16$  up to 34). We have solved the coupled equations for nucleon and mesons by iterative calculations.<sup>1)</sup> The ECS model without the pion mean field indicates that the magic number appears at  $N = 18$  instead of  $N = 20$ . This is due to the large incompressibility in the nuclear matter. This property leads to the  $1s$ -orbit pushed up anomalously. We note that this problem originates from the ECS model treated in the present framework. We expect to eliminate this problem in our future work.

Another result obtained is that the magic number does not appear at  $N = 28$ . This is due to another characteristic property of this model, which leads to the small spin-orbit interaction. Energy splittings between spin-orbit partners are small and have a negligible role in producing the magic effect at  $N = 28$ .

On the basis of this point, it is very important to introduce the pion mean field. Pionic correlations due to the finite pion mean field are expressed by coherent  $0^-$  particle-hole excitations,<sup>1)</sup> by which the coupling of different parity levels,  $l$  and  $l' = l \pm 1$ , with the same total spin  $j$  in the shell model language is induced. In this mechanism, only the highest  $j$  spin level does not find a partner in lower major shells. Once nucleons start to occupy this level, these nucleons are able to find partners in higher major shells. The highest spin level is  $f_{7/2}$  in this mass region and the nucleons in this level are used for the  $0^-$  particle-hole excitations into  $g_{7/2}$ . The number of particles to be used in the pionic correlation increases as the nucleon number in the  $f_{7/2}$  level increases until  $^{56}\text{Ni}$ , where the  $f_{7/2}$  state is completely occupied. For the nuclei above  $^{56}\text{Ni}$ , the upper shells of  $f_{5/2}$  are to be occupied and those states are not used from the  $d_{5/2}$  state due to Pauli blocking. Hence, the pionic correlation becomes maximum at  $^{56}\text{Ni}$ . This is the reason why  $^{56}\text{Ni}$  obtains the largest pionic correlation energy, which leads to the appearance of the magic effect at  $N = 28$ . Due to the pionic correlation, parity partners, ( $s_{1/2}$  and  $p_{1/2}$ ), ( $p_{3/2}$  and  $d_{3/2}$ ) and ( $d_{5/2}$  and  $f_{5/2}$ ), are pushed out, and consequently, spin-orbit partners are split largely similar to those of ordinary spin-orbit splittings.

The chiral sigma model determines the nuclear property with only a small adjustment of the parameters in the Lagrangian. The energy splitting between spin-orbit partners is caused by the pionic correlation which is completely a different mechanism from the case of the spin-orbit interaction introduced phenomenologically.

## References

- 1) H. Toki, S. Sugimoto, and K. Ikeda: Prog. Theor. Phys. **108**, 903 (2002).
- 2) M. Gell-Mann and M. Levy: Nuovo Cimento **16**, 705 (1960).
- 3) H. Yukawa: Proc. Phys.-Math. Soc. Jpn. **17**, 48 (1935).
- 4) Y. Nambu and G. Jona-Lasinio: Phys. Rev. **122**, 345 (1961); Phys. Rev. **124**, 246 (1961).
- 5) J. Boguta: Phys. Lett. B **120**, 34 (1983); Phys. Lett. B **128**, 19 (1983).
- 6) Y. Sugahara and H. Toki: Nucl. Phys. A **579**, 557 (1994).

<sup>†</sup> Condensed from the article in Prog. Theor. Phys. **111**, 75 (2004).

<sup>\*1</sup> Research Center for Nuclear Physics, Osaka University

<sup>\*2</sup> Department of Physics, Nankai University, China

## Accurate calculations for few-nucleon systems using low-momentum interactions

S. Fujii,<sup>\*1</sup> H. Kamada,<sup>\*2</sup> R. Okamoto,<sup>\*2</sup> and K. Suzuki<sup>\*2</sup>

[Low-momentum interaction,  $G$  matrix, Faddeev equation]

One of the fundamental objectives in nuclear structure calculations is to describe nuclear properties, starting with realistic nucleon-nucleon interactions. Since this kind of interaction has a repulsive core at a short distance, one has been forced to derive an effective interaction or  $G$  matrix in a model space for a nucleus from the realistic interaction, except for precise few-nucleon structure calculations.

Recently, Bogner *et al.* has proposed a low-momentum interaction which is constructed in momentum space for a two-nucleon system from a realistic nucleon-nucleon interaction, using conventional effective interaction theory or a renormalization group technique.<sup>1)</sup> They have shown that the low-momentum interaction conserves the properties of the original interaction, such as the half-on-shell  $T$  matrix and the phase shift within a cutoff momentum  $\Lambda$  which limits the low-momentum region. The low-momentum interactions for the typical  $\Lambda = 2.1 \text{ fm}^{-1}$  corresponding to  $E_{\text{lab}} \simeq 350 \text{ MeV}$  are almost the same and are not dependent on the realistic interactions employed. Thus, as a *unique* low-momentum interaction, the low-momentum interaction at approximately  $\Lambda = 2.1 \text{ fm}^{-1}$  has been employed directly in nuclear structure calculations, such as the shell-model and Hartree-Fock calculations. The calculated results are similar to the case of the  $G$  matrix taking account of the short-range correlation, Pauli-blocking effect, and the state dependence for each nucleus.

Since the low-momentum interaction can be commonly used in various structure calculations in contrast to the  $G$  matrix case, there has been increasing application of the low-momentum interaction. However, Bogner *et al.*'s results of structure calculations using the low-momentum interaction show the dependence on the cutoff momentum at around  $\Lambda = 2.1 \text{ fm}^{-1}$ .

One of the central aims of the present work is to investigate the  $\Lambda$  dependence in structure calculations for few-nucleon systems for which precise calculations can be performed, and confirm the validity of the low-momentum interaction in the structure calculation by comparing the obtained results with *exact* values. As an accurate method for the structure calculation, we use the Faddeev and Yakubovskiy equations.

In Fig. 1, the dependence of the calculated ground-state energies of  ${}^3\text{H}$  on the cutoff momentum  $\Lambda$  is shown as one of the calculated results. The low-momentum interaction for each  $\Lambda$  constructed from the CD-Bonn potential is employed in the Faddeev calculation. For simplicity, only the  $np$  interaction is used for all the channels, and the  $S$ -wave approximation is employed. The result for "exact line" denotes the *exact* solution for the Faddeev equation under the above assumptions. We see that the calculated result of approximately  $\Lambda = 2.1 \text{ fm}^{-1}$  proposed by Bogner *et al.* cannot reproduce the *exact* value. In order to reach the *exact* value within an accuracy of 50 keV, we need values larger than  $\Lambda \simeq 5 \text{ fm}^{-1}$ . More detailed results concerning the validity of the low-momentum interaction will be reported in a separate paper.<sup>2)</sup>

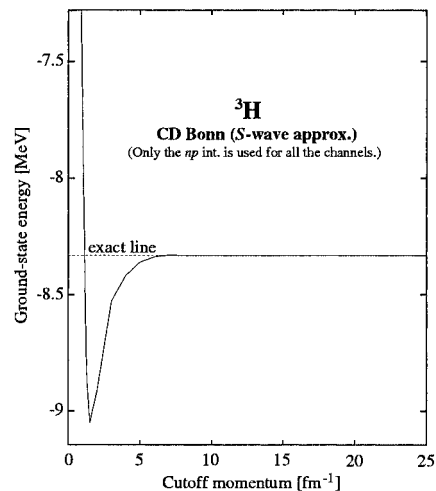


Fig. 1. Dependence of calculated ground-state energies of  ${}^3\text{H}$  on the cutoff momentum  $\Lambda$  for the CD-Bonn potential, exact line: the *exact* solution for the Faddeev equation.

### References

- 1) S. K. Bogner, T. T. S. Kuo, and A. Schwenk: Phys. Rep. **386**, 1 (2003).
- 2) S. Fujii, E. Epelbaum, R. Okamoto, K. Suzuki, H. Kamada, and W. Glöckle: in preparation.

<sup>\*1</sup> Department of Physics, University of Tokyo

<sup>\*2</sup> Department of Physics, Kyushu Institute of Technology

# Shell structure in nuclei around $^{16}\text{O}$ and $^{24}\text{O}$ described using modern nucleon-nucleon interactions

S. Fujii,<sup>\*1</sup> R. Okamoto,<sup>\*2</sup> and K. Suzuki<sup>\*2</sup>

[Shell structure, Single-particle level, Effective interaction]

The shell structure which is closely related to the single-particle level is one of the fundamental properties in nuclei. When we calculate the energies of single-particle levels in neutron- or proton-rich nuclei, it would be desirable that the calculation formalism is based on the particle basis. The advantages of the particle-basis formalism are that the Coulomb force can be treated accurately for the proton-proton channel and effects of charge dependence of realistic nuclear forces are taken into account in structure calculations. In the particle-basis formalism, one can obtain the energy differences between proton and neutron levels for not only  $N \simeq Z$  nuclei but also neutron- or proton-rich nuclei in the same manner.

As one of the methods for solving nuclear many-body problems, we have developed the unitary-model-operator approach (UMOA). Recently, we have extended the formulation of the UMOA from the isospin basis to the particle one,<sup>1)</sup> and applied it to the calculations of binding energies and single-particle energies in nuclei near the  $N = Z$  nucleus  $^{16}\text{O}$  and the neutron-rich nucleus  $^{24}\text{O}$ .

We have employed modern nucleon-nucleon interactions such as the CD-Bonn potential based on the meson-exchange model which have high accuracy to reproduce nucleon-nucleon scattering data and deuteron properties. In addition, we have also used the next-to-next-to-next-to-leading order ( $N^3\text{LO}$ ) potential based on chiral perturbation theory which has recently been constructed by Entem and Machleidt.<sup>2)</sup> Although nucleon-nucleon interactions based on chiral perturbation theory are defined essentially in a low-momentum region compared with the meson-exchange potentials, the  $N^3\text{LO}$  potential can accurately reproduce the nucleon-nucleon data below  $E_{\text{lab}} \simeq 300$  MeV. Therefore, the  $N^3\text{LO}$  potential as well as other high-precision nucleon-nucleon interactions can be used in nuclear structure calculations.

In Fig. 1, the calculated results of single-particle energies for the ground states of  $^{17}\text{O}$ ,  $^{23}\text{O}$ , and  $^{25}\text{O}$  using the CD-Bonn potential are illustrated. The results are shown separately for the cases with and without the three-body cluster (3BC) effect which is one of the higher-order many-body contributions to the single-

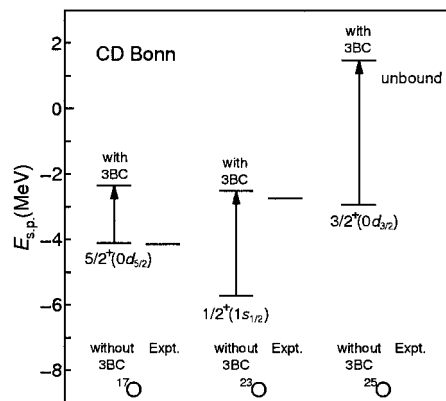


Fig. 1. Calculated single-particle energies for the ground states of  $^{17}\text{O}$ ,  $^{23}\text{O}$ , and  $^{25}\text{O}$  with the CD-Bonn potential.

particle energy. The present study is the first attempt at clarifying the 3BC effect on the single-particle energy in neutron-rich nuclei.

It can be seen that the 3BC effect makes significant repulsive contributions to the single-particle energies and increases as the mass number increases. The strong repulsive effect is favorable for the neutron-rich nuclei  $^{23}\text{O}$  and  $^{25}\text{O}$  to reproduce the experimental values. On the contrary, the result for  $^{17}\text{O}$  becomes worse in comparison with the experimental value when the 3BC effect is taken into account. We have confirmed that the results for the  $N^3\text{LO}$  potential show the same tendency as those for the CD-Bonn potential.

It is notable that a genuine three-body force is not included in the present calculation. The genuine three-body force would show attractive effects on the single-particle energies, and would have different contributions between the  $N \simeq Z$  and neutron-rich nuclei because of the isospin and density dependences. In order to obtain definite conclusions, large-scale structure calculations are in progress.

## References

- 1) S. Fujii, R. Okamoto, and K. Suzuki: nucl-th/0311053.
- 2) D. R. Entem and R. Machleidt: Phys. Rev. C **68**, 041001 (2003).

<sup>\*1</sup> Department of Physics, University of Tokyo

<sup>\*2</sup> Department of Physics, Kyushu Institute of Technology



# Modified Hartree-Fock-Bogoliubov theory at finite temperature<sup>†</sup>

N. Dinh Dang and A. Arima

[NUCLEAR STRUCTURE, Hartree-Fock-Bogoliubov theory, finite temperature]

This work has derived the modified Hartree-Fock-Bogoliubov (MHFB) theory at finite temperature, which conserves the unitarity relation of the generalized particle-density matrix. This has been done by including the thermal fluctuation of the quasiparticle number microscopically in the quasiparticle-density matrix. It has been shown that the latter can also be obtained by applying the secondary Bogoliubov transformation discussed in Refs. 1 and 2. The MHFB equations at finite temperature have been then derived following the standard variational procedure. Its Bardeen-Cooper-Schrieffer (BCS) limit yields the modified BCS (MBCS) equations, which have been derived previously in Refs. 1 and 2 using the above-mentioned secondary Bogoliubov transformation. Apart from being able to restore the unitarity transformation, this secondary transformation helps the modified quasiparticle random-phase approximation (QRPA) to completely restore the Ikeda sum rule for Fermi and Gamow-Teller transitions, which has been violated within the renormalized QRPA.

The illustration of the MHFB theory has been presented within the MBCS theory by calculating the neutron pairing gap and thermodynamic quantities for <sup>120</sup>Sn. Detailed analyses of the results obtained show that the calculations for open-shell nuclei within the MBCS theory need to be carried out using the entire single-particle spectrum, which includes both bound and quasibound levels in a large configuration space of about 7 major shells up to 126–184 one. When the use of a reduced spectrum is unavoidable, the reduction should be done symmetrically from both side of the chemical potential  $\bar{\mu}$  so that the distribution of quasiparticle-occupation number can be properly taken into account as it is symmetric with respect to  $\bar{\mu}$ . The MBCS gap decreases monotonously with in-

creasing  $T$  and does not vanish even at  $T \sim 5$  MeV. The discontinuity in the BCS heat capacity at the critical temperature  $T_c$  is also completely washed out, showing no signature of superfluid-normal phase transition. The temperature dependences of level density and level-density parameter are also smooth.

The behavior of the MBCS gap as a function of  $T$  is found in qualitative agreement with that given by the macroscopic treatment using the Landau theory of phase transitions in the sense that both gaps do not collapse at the critical temperature of the BCS superfluid-normal phase transition. However, quantitative discrepancies between microscopic and macroscopic approaches are evident. In the low-temperature region, due to the microscopic interplay between quantal and thermal components, the MBCS gap starts to decrease at a higher  $T$  with increasing  $T$  as compared to the macroscopically averaged gap  $\langle \Delta \rangle$ . At high temperatures  $T > 2$  MeV, the MBCS gap continues to decrease, while  $\langle \Delta \rangle$  remains nearly constant and even start to increase with increasing  $T$ .

The MBCS equations also show that thermal fluctuations can induce a pairing gap even for closed-shell nuclei. Results obtained using a single-particle space restricted to hole orbitals have shown that such a thermally induced gap increases with increasing temperature. However, its magnitude is negligible compared with the gap in open-shell nuclei. Therefore, it can be safely put to be equal to zero at  $T \leq 5$ –6 MeV.

## References

- 1) N. Dinh Dang and V. Zelevinsky: Phys. Rev. C **64**, 064319 (2001).
- 2) N. Dinh Dang and A. Arima: Phys. Rev. C **67**, 014304 (2003).

<sup>†</sup> Condensed from the article in Phys. Rev. C **68**, 014318 (2003)

## Pairing effect on the giant dipole resonance width at low temperature<sup>†</sup>

N. Dinh Dang and A. Arima

[NUCLEAR STRUCTURE, Hartree-Fock-Bogoliubov theory, finite temperature]

Intensive experimental studies of highly-excited nuclei during the last two decades have shown that the width of the giant dipole resonance (GDR) increases sharply with increasing the temperature  $T$  from  $T > 1$  MeV up to  $\simeq 3$  MeV. At higher  $T$  a width saturation has been reported. The increase of the GDR width with  $T$  is described reasonably well within the thermal shape-fluctuation model<sup>1)</sup> and the phonon damping model (PDM).<sup>2)</sup> The thermal shape-fluctuation model assumes an adiabatic coupling of GDR to quadrupole degrees of freedom with deformation parameters  $\beta$  and  $\gamma$  induced by thermal fluctuations and high spins in the intrinsic frame of reference. The PDM considers the coupling of the GDR to particle-particle and hole-hole configurations at  $T \neq 0$  as the mechanism of the width increase and saturation. The PDM calculates the GDR width and strength function directly in the laboratory frame without any need for an explicit inclusion of thermal fluctuation of shapes.

In general, pairing was neglected in the calculations for hot GDR as it was believed that the gap vanishes at  $T = T_c < 1$  MeV according to the temperature Bardeen-Cooper-Schrieffer (BCS) theory. However, it has been shown in Ref. 3 that thermal fluctuations smear out the superfluid-normal phase transition in finite systems so that the pairing gap survives up to  $T \gg 1$  MeV. This has been confirmed microscopically in the recent modified Hartree-Fock-Bogoliubov theory at finite  $T$ ,<sup>4)</sup> whose limit is the modified-BCS theory.<sup>5)</sup>

Very recently the  $\gamma$  decays were measured in coincidence with  $^{17}\text{O}$  particles scattered inelastically from  $^{120}\text{Sn}$ .<sup>6)</sup> A GDR width of around 4 MeV has been extracted at  $T = 1$  MeV, which is smaller than the value of  $\sim 4.9$  MeV for the GDR width at  $T = 0$ . This result and the existing systematic for the GDR width in  $^{120}\text{Sn}$  up to  $T \simeq 2$  MeV are significantly lower than the prediction by the thermal shape-fluctuation model. Based on this, Ref. 6 concluded that the narrow width observed in  $^{120}\text{Sn}$  at low  $T$  is not understood. The aim of the present work is to show that it is thermal pairing that causes the narrow GDR width in  $^{120}\text{Sn}$  at low  $T$ . For this purpose we include the thermal pairing gap obtained from the modified-BCS theory<sup>4,5)</sup> in the PDM,<sup>2)</sup> and carry out the calculations for the GDR width in  $^{120}\text{Sn}$  at  $T \leq 5$  MeV. In difference with the gap given within the conventional BCS theory, which collapses at  $T_c \simeq 0.79$  MeV, the modified-BCS gap

never vanishes, but monotonously decreases with increasing  $T$  up to  $T \simeq 5$  MeV. The results obtained show that thermal pairing indeed plays an important role in lowering the width at  $T \leq 2$  MeV as compared to the value obtained without pairing. This improves significantly the overall agreement between theory and experiment, including the width at  $T = 1$  MeV extracted in the latest experiment<sup>6)</sup> (See Fig. 1).

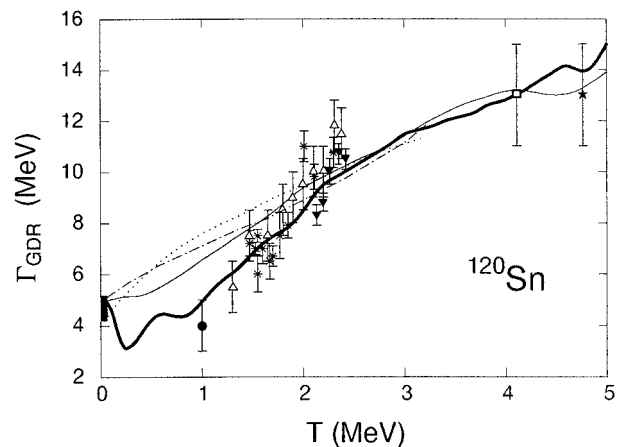


Fig. 1. GDR width  $\Gamma_{\text{GDR}}$  as functions of  $T$  for  $^{120}\text{Sn}$ . The thin and thick solid lines show the PDM results obtained without and including the thermal pairing gap, respectively. Solid circles are the low- $T$  data from Ref. 6. The predictions by two versions of the thermal shape-fluctuation model<sup>1)</sup> are shown as the dash-dotted and thin dotted lines.

### References

- 1) W. E. Ormand, P. F. Bortignon, and R. A. Broglia: Phys. Rev. Lett. **77**, 607 (1966); W. E. Ormand et al.: Nucl. Phys. A **614**, 217 (1997); D. Kusnezov, Y. Alhassid, and K.A. Snover: Phys. Rev. Lett. **81**, 542 (1998).
- 2) N. D. Dang and A. Arima: Phys. Rev. Lett. **80**, 4145 (1998); N. D. Dang and A. Arima: Nucl. Phys. A **636**, 427 (1998).
- 3) L. G. Moretto: Phys. Lett. B **40**, 1 (1972).
- 4) N. Dinh Dang and A. Arima: Phys. Rev. C **68**, 014318 (2003).
- 5) N. Dinh Dang and V. Zelevinsky: Phys. Rev. C **64**, 064319 (2001); N. Dinh Dang and A. Arima: Phys. Rev. C **67**, 014304 (2003).
- 6) P. Heckman et al.: Phys. Lett. B **555**, 43 (2003).

<sup>†</sup> Condensed from the article in Phys. Rev. C **68**, 044303 (2003)

# Three-dimensional rotation of even-even triaxial nuclei<sup>†</sup>

M. Oi\* and P. M. Walker\*

[NUCLEAR STRUCTURE, 3d-cranking model, Rapidly rotating nuclei]

Nuclei in the  $A \simeq 130$  region are now of special interest because it is suggested that a new form of nuclear rotation can be expected: a chiral rotation.<sup>1)</sup> This three-dimensional rotation was predicted at first in odd-odd systems, such as  $^{134}_{59}\text{Pr}_{75}$ , whose total angular momentum is built by a particle and a hole in valence orbitals in addition to a triaxial rotor, under an assumption of the irrotational-flow moment of inertia. Their angular momentum vectors point along the shortest ( $s$ ), longest ( $l$ ) and intermediate ( $i$ ) axes of the triaxially deformed nucleus ( $\gamma \simeq 30^\circ$ ),<sup>a)</sup> respectively. When the collective angular momentum is absent, the total angular momentum consists only of the single-particle spins. The corresponding state is called “planar” because the total angular momentum is in the  $s-l$  plane. The planar states correspond to “bandheads” of the chiral rotational bands. Rotational members built upon the planar state are classified as “aplanar” states because these states have the genuine chiral configuration. Possible experimental evidence of the nuclear chirality was reported in  $N = 75$  odd-odd isotones in the same mass region,<sup>2)</sup> through findings of pairs of near-degenerate  $\Delta I = 1$  bands (so-called “chiral doublets”).

It is an interesting question whether or not even-even nuclei can have the chiral configuration after breaking (Cooper) pairs. To realise the nuclear chirality in even-even systems, at least four quasi-particles must be excited; two neutrons and two protons. This multi-quasiparticle excited state is expected at high spin where rotation-alignment occurs due to the Coriolis force. It is likely that such a “simultaneous” aligned state would be seen at higher spin, compared with the odd-odd chiral systems. Experimentally, a candidate for chiral doublets in even-even nuclei is suggested in  $^{136}_{60}\text{Nd}_{76}$ ,<sup>3)</sup> but there is as yet no detailed theoretical analysis about the possibility of chiral solutions in even-even nuclei, except a brief conference report.<sup>4)</sup>

The original model of the nuclear chirality is based on the particle(hole)-plus-rotor model which admits the presence of a macroscopic rotor with solid triaxial deformation ( $\gamma \simeq 30^\circ$ ). Although there is no concept of a rotor in fully microscopic models like the HFB approach, the rotor spin can be treated as the collective part of angular momentum in the cranking model, which can handle the collective and single-particle angular momentum on the same footing. An analysis of the chiral configuration in odd-odd systems was carried

out through the Tilted-Axis Cranking model (TAC).<sup>1)</sup> Although each microscopic calculation (TAC) is made for given parameters of shape and pairing gaps as well as rotational frequency, these parameters are carefully determined by a macroscopic + microscopic approach (the Strutinski method) in terms of the energy minimisation.

If nuclear chirality is produced in even-even systems by four or more quasiparticle excitations, where the quasiparticles occupy orbitals with very different orientation, it is expected that the collective and individual (quasi-)particle motions would be strongly coupled through the Coriolis force. Besides, the degree of triaxial deformation can be susceptible to the influence coming from rotation-alignments at high spin, especially in those nuclei whose Fermi level is in the upper shell (*i.e.*, high- $\Omega$  Nilsson orbits).<sup>5)</sup> Therefore, if we attempt to describe the above physical situations, purely microscopic and self-consistent treatments should be made with respect to nuclear shape and pairing. In other words, for the aim of demonstrating the chirality in even-even systems, it is necessary to show the emergence of a genuine three-dimensional rotation together with the presence of substantial triaxial deformation. Furthermore, compared to odd-odd systems, it is numerically advantageous for us to study even-even systems because the treatment of pairing is more straightforward.

In this work, we performed a fully microscopic and self-consistent study of three-dimensional nuclear rotations in even-even nuclei in the  $A \simeq 130$  mass region near the yrast line, by means of the three-dimensional cranked Hartree-Fock-Bogoliubov method.<sup>6)</sup>

## References

- 1) S. Frauendorf and J. Meng: Nucl. Phys. A **617**, 131 (1997); V. I. Dimitrov, S. Frauendorf, and F. Dönau: Phys. Rev. Lett. **84**, 5732 (2000).
- 2) K. Starosta et al.: Phys. Rev. Lett. **86**, 971 (2001).
- 3) E. Mergel et al.: Eur. Phys. J. A **15**, 417 (2002).
- 4) V. Dimitrov, F. Dönau, and S. Frauendorf: nucl-th/0211063.
- 5) R. R. Hilton, H. J. Mang, and P. Ring: Phys. Rev. Lett. **43**, 1979 (1979).
- 6) T. Horibata and N. Onishi: Nucl. Phys. A **596**, 251 (1996).
- 7) P. Ring and P. Schuck: in *Nuclear Many-body Problem*, edited by W. Beiglbock et al. (Springer-Verlag, Berlin, 1980), p. 8.

<sup>†</sup> Condensed from the article in Phys. Lett. B **576**, 75 (2003)

\* Department of Physics, University of Surrey, UK

<sup>a)</sup> The Hill-Wheeler parameterization<sup>7)</sup> is employed for the quadrupole deformation parameters,  $\beta$  and  $\gamma$ , where the sign of  $\gamma$  is opposite to the Lund convention.

# Required accuracy of mass and half-life measurements planned at future RI-beam facilities to understand the r-process nucleosynthesis

Y. Motizuki, T. Tachibana,\*1 and S. Goriely\*2

[Nucleosynthesis, Nuclear mass formulae, Unstable nuclei]

To understand the r-process nucleosynthesis, we estimate the required accuracy for mass and half-life measurements planned at future RI-beam facilities, including the RI-Beam Factory. As a first rough guide for detector developments, we consider a simple requirement from a theoretical point of view as follows: The mass and half-life measurements should distinguish physical quantities predicted from semi-empirical and microscopic mass formulae, KUTY and HFB-2, respectively, within  $3\sigma$  errors at the neutron-richest nucleus on the r-process path at the  $N = 82$  shell closure. The above is the *minimum* requirement because r-process studies would not benefit if future experiments could not tell what type of mass model is appropriate for abundance calculations.

The above two mass formulae were employed because they were derived from completely opposite leading principles: the KUTY mass formula<sup>1)</sup> has an empirical gross term for macroscopic properties and spherical-basis shell terms for microscopic properties of nuclear masses. Allowing many parameters to describe the single-particle potential and nuclear structure, the KUTY model aims at explaining the nuclear masses as well as the single-particle energy-level structure as much as possible. On the other hand, HFB-2 masses<sup>2,3)</sup> were derived with the Hartree-Fock-Bogoliubov method, aiming at explaining the nuclear masses with a specific nuclear force and with much fewer number of parameters. Both models attain a good root-mean-square deviation,  $\sim 680$  keV, from the measured masses of 2135 nuclei at and close to the stability line. However, most importantly, they predict very different masses and hence give very different half-lives for nuclei relevant to the r-process which have not yet been measured.

To determine the polestar neutron-richest isotope on the r-process path among  $N = 82$  isotones, we apply an r-process path obtained under the so-called waiting-point-approximation with the KUTY masses and their half-lives calculated by the second version of the gross theory.<sup>4,5)</sup> The r-process path, simulated with a temperature of  $1.5 \times 10^9$  K and a neutron density of  $10^{24} \text{cm}^{-3}$ , determines the nuclide  $^{123}\text{Nb}$  as the polestar neutron-richest isotope. We note that the path mentioned above should be taken as a typical example.

We accordingly analyze the mass difference between

the KUTY and HFB-2 predictions for the  $N = 82$  isotones up to  $^{123}\text{Nb}$ . We conclude that the detectors for the mass measurements must have an accuracy of *at least*  $1\sigma = 250$  keV at the neutron richness of  $A/Z = 3.0$  to satisfy the above requirement. This is illustrated in Fig. 1.

The half-lives can be calculated with various methods using a set of nuclear masses. We also analyze the half-life differences derived from KUTY and HFB-2 masses and conclude that  $1\sigma = 0.15$  ms is the *minimum* requirement for the half-life measurements at the neutron richness of  $A/Z = 3.0$ . Note that not only statistical but also systematic errors should be included in the above discussion. Future measurements with smaller errors than the obtained ones here are strongly encouraged in order to develop theories of nuclear masses and half-lives: By updating the parameter values included in each model, the predictions would tend to be converged. This will highly benefit r-process studies which we do not know anything conclusive yet.

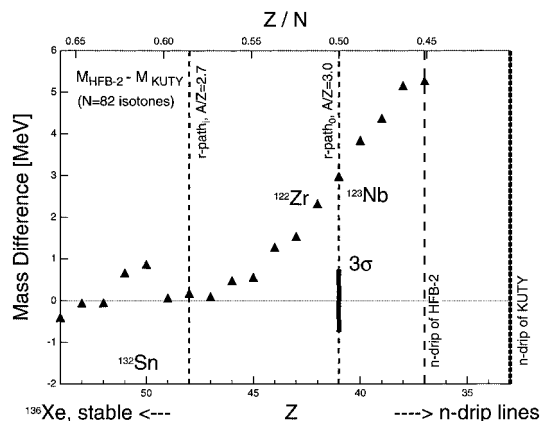


Fig. 1. Mass difference between the HFB-2 and KUTY predictions for  $N = 82$  isotones.

## References

- 1) H. Koura et al.: Nucl. Phys. A **674**, 47 (2000).
- 2) S. Goriely et al.: Phys. Rev. C **66**, 24326-1 (2002).
- 3) M. Samyn et al.: Nucl. Phys. A **700**, 142 (2001).
- 4) T. Tachibana et al.: Prog. Theor. Phys. **84**, 641 (1990).
- 5) T. Tachibana and M. Yamada: in *Proc. Int. Conf. on Exotic Nuclei and Atomic Masses*, edited by M. de Saint Simon et al. (Editions Frontieres, 1995), p. 763.

\*1 Senior High School of Waseda University

\*2 Institut d'Astronomie et d'Astrophysique, Universite Libre de Bruxelles, Belgium

## Comparison of prolate and oblate explosions in core-collapse supernovae

H. Madokoro, T. Shimizu, and Y. Motizuki

[shock waves, hydrodynamics, stars: neutron, supernova: general]

Shimizu *et al.*<sup>1)</sup> studied the effects of anisotropic neutrino radiation on the mechanism of core-collapse supernova explosions. They considered only the case in which the maximum value in the neutrino flux distribution was located at the axis of symmetry (polar axis). Janka and Keil,<sup>2)</sup> however, pointed out that the neutrino flux can have its peak on the equatorial plane. In this paper, we study the effects of the oblate neutrino heating on the explosion dynamics.

We solved hydrodynamical equations in the spherical coordinate  $(r, \theta)$ .<sup>1,3)</sup> The local neutrino flux is assumed to be<sup>3)</sup>

$$l_\nu(r, \theta) = \frac{7}{16} \sigma T_\nu^4 c_1 (1 + c_2 \cos^2 \theta) \frac{1}{r^2}, \quad (1)$$

where  $\sigma$  is the Stefan-Boltzmann constant,  $T_\nu = 4.70$  MeV is the temperature on the neutrinosphere, and  $c_2$  is a parameter which is related to the degree of anisotropy in the neutrino radiation. The value of  $c_1$  is calculated from the given  $c_2$  in such a way that the total neutrino luminosity is adjusted to that of the spherical model at the same  $T_\nu$ . The ratio of the neutrino flux along the polar axis ( $\theta = 0^\circ$ ),  $l_z$ , to that on the equatorial plane ( $\theta = 90^\circ$ ),  $l_x$ , is represented by  $l_z/l_x = 1 + c_2$ .

We studied two models: the prolate model (pro100) and the oblate model (obl091). The values of  $c_2$  for these models are chosen in such a way that the value of  $l_z/l_x$  becomes 1.1 ( $c_2 = +0.100$ ) for the prolate model and  $1/1.1 = 0.909$  ( $c_2 = -0.091$ ) for the oblate model.

Figure 1 shows the contour maps of the dimensionless entropy distribution with the velocity fields for the two models. Due to anisotropic neutrino heating, the shock front becomes prolate and largely distorted in model pro100, while it is elongated in an oblate shape in model obl091. The evolution of the explosion energy is shown in Fig. 2. It is found that the energy gain in model pro100 is much larger than that in model obl091.

The difference between the two models is attributed to the importance of the locally intense neutrino heating. In contrast to the prolate explosion, the neutrino radiation is anisotropic but its peak is not located point-like in the case of the oblate one; the heated region is distributed in a disk-like form over the equatorial plane. The efficiency of anisotropic neutrino heat-

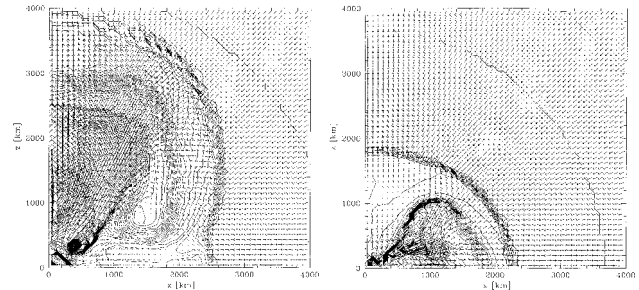


Fig. 1. Contour maps of the dimensionless entropy distribution and the velocity fields for two models, pro100 (left) and obl091 (right) at  $t \sim 280$  ms.

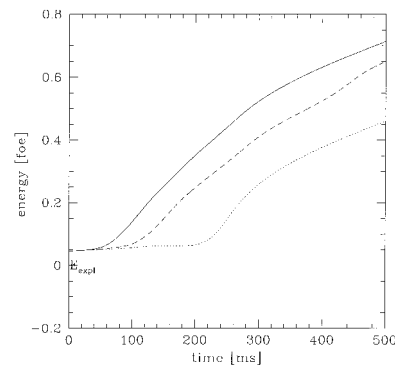


Fig. 2. Evolution of the explosion energy for model pro100 (solid line) and model obl091 (dashed line). The result of the spherical explosion (dotted line) for the same  $T_\nu$  is also shown for comparison.

ing for the oblate model is therefore considerably reduced, resulting in less energetic explosion. Our results support the statement made by Shimizu *et al.*,<sup>1)</sup> that is, locally intense neutrino heating is of great importance in producing a successful explosion.

### References

- 1) T. M. Shimizu et al.: *Astrophys. J.* **552**, 756 (2001).
- 2) H.-Th. Janka and W. Keil: *Astro-ph/9709012* (1997).
- 3) H. Madokoro, T. Shimizu, and Y. Motizuki: *Astrophys. J.* **592**, 1035 (2003).

# Properties of a relativistic equation of state for collapse-driven supernovae

K. Sumiyoshi,<sup>\*1</sup> H. Suzuki,<sup>\*2</sup> S. Yamada,<sup>\*3</sup> and H. Toki,<sup>\*4</sup>

[Dense matter, Equation of state, Supernova]

Clarifying the mechanism of core-collapse supernova explosion is fascinating. An important microphysics ingredient for supernova simulations is the equation of state (EOS) of dense matter. It determines the stellar structure, the hydrodynamics and the reaction rates through the determination of pressure, entropy and chemical compositions. Recently, a new complete EOS for supernova simulations has become available.<sup>1,2)</sup> The relativistic mean field (RMF) theory with a Thomas-Fermi approach has been applied to the derivation of the supernova EOS. The RMF theory based on the RBHF theory has been successful for reproducing the masses and radii of unstable nuclei as well as stable ones.<sup>3)</sup>

We study the characteristics of the relativistic EOS in collapse-driven supernovae<sup>4)</sup> using the general relativistic hydrodynamics<sup>5)</sup> of the gravitational collapse and bounce of supernova cores. In order to study dense matter in a dynamical situation, we perform simplified calculations of core collapse and bounce by following adiabatic collapse with a fixed electron fraction. We investigate the profiles of thermodynamical quantities and the compositions during collapse and bounce. We also perform the calculations with the Lattimer-Swesty EOS<sup>6)</sup> to compare the properties of dense matter.

The compositions during collapse at the times (1) and (2) (central densities:  $10^{11}$  and  $10^{12}$  g/cm<sup>3</sup>) are shown for the case of  $15 M_{\odot}$  model of WW95<sup>7)</sup> in Fig. 1. It can be seen that the mass fractions are substantially different between the relativistic EOS and the Lattimer-Swesty EOS. The mass fractions of alpha particles and neutrons in the relativistic EOS are larger than those in the Lattimer-Swesty EOS. The free-proton fraction is almost one order of magnitude smaller than that obtained with the Lattimer-Swesty EOS. Having a smaller fraction of free protons is favorable for the explosion since electron capture is largely reduced, leading to a stronger prompt shock.

The reduction in the free-proton fraction comes from an effect of the large symmetry energy in the RMF theory, which is constrained by systematic measurements of the masses and radii of neutron-rich nuclei. These differences of compositions should be examined further in numerical simulations of hydrodynamics with neutrino transfer by switching the two sets of EOS to

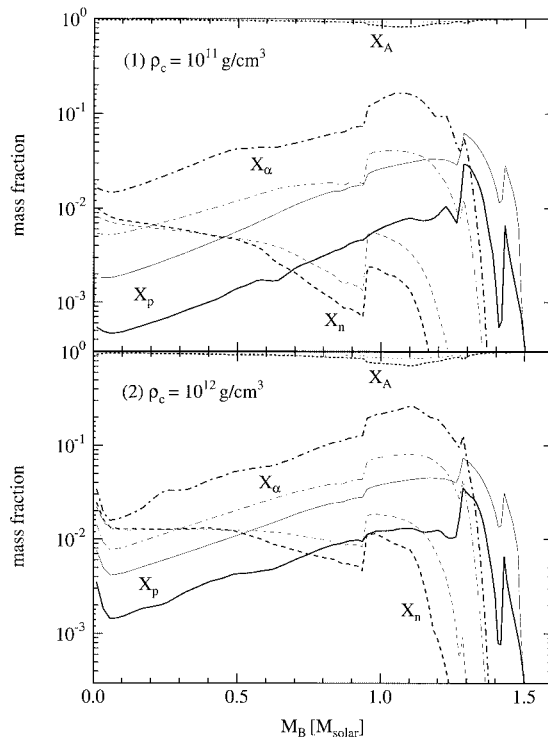


Fig. 1. The mass fractions of protons, neutrons, nuclei and alpha particles are shown as functions of baryon mass coordinates denoted by solid, dashed, dotted and dot-dashed lines, respectively. The results obtained with the relativistic EOS are shown by thick lines and the Lattimer-Swesty EOS by thin lines.

examine the role of the nuclear interaction and EOS in the mechanism of supernova explosions.

## References

- 1) H. Shen, H. Toki, K. Oyamatsu, and K. Sumiyoshi: Nucl. Phys. A **637**, 435 (1998).
- 2) H. Shen, H. Toki, K. Oyamatsu, and K. Sumiyoshi: Prog. Theor. Phys. **100**, 1013 (1998).
- 3) Y. Sugahara and H. Toki: Nucl. Phys. A **579**, 557 (1994).
- 4) K. Sumiyoshi, H. Suzuki, S. Yamada, and H. Toki: Nucl. Phys. A **730**, 227 (2004).
- 5) S. Yamada: Astrophys. J. **475**, 720 (1997).
- 6) F. D. Swesty, J. M. Lattimer, and E. S. Myra: Astrophys. J. **425**, 195 (1994).
- 7) S. E. Woosley and T. Weaver: Astrophys. J. Suppl. Ser. **101**, 181 (1995).

<sup>\*1</sup> Numazu College of Technology

<sup>\*2</sup> Faculty of Science and Technology, Tokyo University of Science

<sup>\*3</sup> School of Science and Engineering, Waseda University

<sup>\*4</sup> Research Center for Nuclear Physics, Osaka University

# Proton-nucleus elastic scattering and the equation of state of nuclear matter<sup>†</sup>

K. Iida, K. Oyamatsu,<sup>\*1</sup> and B. Abu-Ibrahim<sup>\*2</sup>

[Dense matter, Proton elastic scattering, Unstable nuclei]

We calculate differential cross sections for proton-nucleus elastic scattering by using a Glauber theory in the optical limit approximation and nucleon distributions that can be obtained in the framework of macroscopic nuclear models<sup>1)</sup> in a way dependent on the equation of state of uniform nuclear matter near the saturation density. These nuclear models reasonably reproduce empirical data for masses and radii of stable nuclei and allow for uncertainties in the values of the symmetry energy density-derivative coefficient,  $L$ , and the incompressibility of symmetric nuclear matter,  $K_0$ .

Figure 1 exhibits the results calculated for the angular distribution for proton elastic scattering off heavy stable nuclei. We can see, from comparison with the

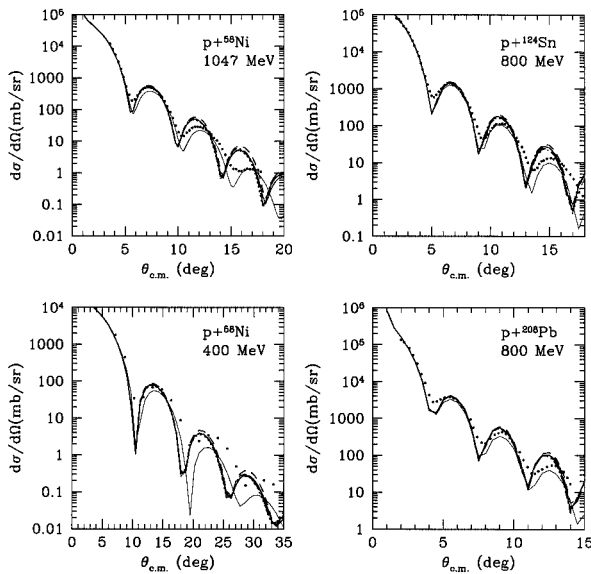


Fig. 1. Proton-nucleus elastic differential cross sections for  $^{58}\text{Ni}$  ( $T_p = 1047, 400$  MeV),  $^{124}\text{Sn}$  ( $T_p = 800$  MeV) and  $^{208}\text{Pb}$  ( $T_p = 800$  MeV). The solid, dotted, short-dashed, long-dashed and dot-dashed lines are the results calculated for  $(L, K_0) = (50, 230), (50, 180), (50, 360), (5, 230), (80, 230)$  in MeV. For comparison, we also plotted the results (thin lines) calculated from the Fermi-type nucleon distributions derived in Ref. 2. The experimental data (dots) are taken from Refs. 2–4.

empirical values, that the Glauber model is satisfactory for sufficiently high proton incident energy,  $T_p$ , and small scattering angle,  $\theta_{c.m.}$ . We thus focus on the angle and height of the first scattering peak; the values calculated for Ni isotopes are plotted in Fig. 2. We find that the peak angle decreases with  $L$  more remarkably for larger neutron excess, while the peak height increases with  $K_0$  almost independently of neutron excess. We suggest the possibility that comparison of the calculations with experimental data for the peak angle may be useful for determination of  $L$ .

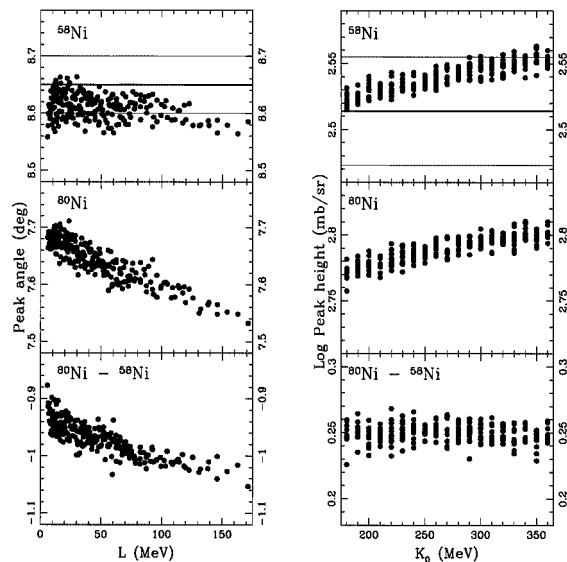


Fig. 2. The angles and heights of the scattering peak in the small angle regime, calculated as functions of  $L$  and  $K_0$  for  $p$ - $^{58}\text{Ni}$  and  $p$ - $^{80}\text{Ni}$  elastic scattering at  $T_p = 800$  MeV. The experimental angle and height including errors (from Ref. 2) are denoted by the horizontal lines (thick lines: central values, thin lines: upper and lower bounds).

## References

- 1) K. Oyamatsu and K. Iida: Prog. Theor. Phys. **109**, 631 (2003).
- 2) L. Ray, W. Rory Coker, and G. W. Hoffmann: Phys. Rev. C **18**, 2641 (1978).
- 3) R. M. Lombard, G. D. Alkharov, and O. A. Domchenkov: Nucl. Phys. A **360**, 233 (1981).
- 4) H. Sakaguchi et al.: Phys. Rev. C **57**, 1749 (1998).

<sup>†</sup> Condensed from the article in Phys. Lett. B **576**, 273 (2003)

<sup>\*1</sup> Department of Media Theories and Production, Aichi Shukutoku University

<sup>\*2</sup> Department of Physics, Cairo University, Egypt

# A search for the effect of nuclear outer surface in proton-nucleus elastic scattering

A. Kohama

[NUCLEAR REACTION, unstable nuclei]

The unstable nuclei on the neutron-rich side (neutron-rich nuclei) are often characterized as those with a large surface region generated by loosely bound valence nucleons. We have been focusing on the determination of the matter density distributions in the surface and outer regions to clarify the feature. In our previous work,<sup>1)</sup> we discussed how much we could determine the nuclear *matter* density distributions of neutron-rich nuclei from the proton elastic scatterings. We demonstrated that the matter density distribution in the surface region is determined well using relatively low-intensity beams, such as 10 [1/s].<sup>1)</sup>

For an extension of the above work, we have discussed how the density distributions in the outer surface region affect the differential cross section of the proton-nucleus elastic scattering in this work. This consideration would be useful for the analysis of nuclei whose surface structure does not change considerably when we approach the neutron drip line. This may occur for medium-heavy nuclei, such as Ni or Sn.

We have applied the Glauber approximation with the Coulomb interaction of the finite extension of the point-proton density distribution,<sup>2)</sup> and have concentrated on the observation of the behavior of the cross

section. Since the proton of small momentum transfer mostly probes the nuclear periphery, the effect of the outer surface is expected to appear in the forward direction. We have mimicked the halo structure of the neutron-rich nuclei, by artificially varying the one-neutron separation energy,  $S_n$ , from the original one, but kept the surface shape unchanged (Fig. 1). The normalization is also kept fixed.

In Fig. 2 one can see that in the forward direction where the nuclear and the Coulomb interactions compete with each other, the cross section of the halolike neutron density (the solid curve) oscillates around the one determined by the original  $S_n$  of  $^{58}\text{Ni}$  (the dashed curve), which is due to Coulomb-nuclear interference. The smaller  $S_n$  becomes, the larger the effect becomes, although the net effect is rather small. The precise measurements in the forward direction, which could be possible due to the large cross sections, will assist the minute (model-independent) determination of the density distributions of the neutron-rich nuclei.

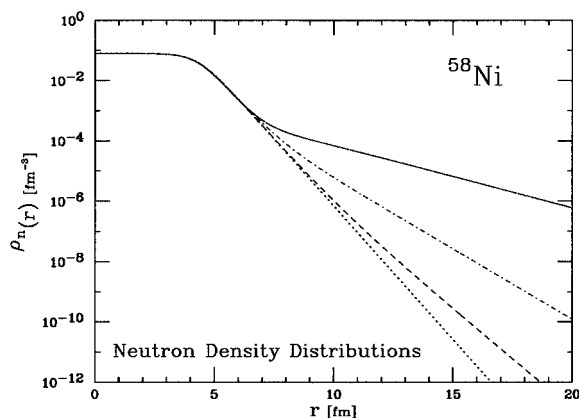


Fig. 1. Dependence of the neutron density distribution of the “mock”  $^{58}\text{Ni}$  on the variation of  $S_n$ . The dashed curve is a linear combination of the two two-parameter Fermi distributions (2pFs) with the asymptotic behavior determined by the  $S_n$  of the actual  $^{58}\text{Ni}$ . The dot-dashed curve is determined by 50% of the original  $S_n$ , and the solid curve is by 10% of the same  $S_n$ . As a reference, the one 2pF of the same surface shape is plotted by the dotted curve.

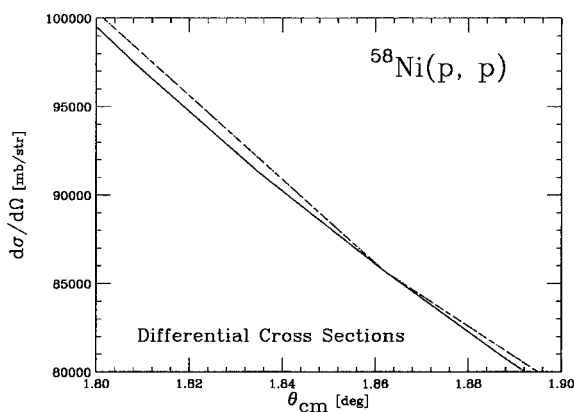


Fig. 2. Effect of the outer surface of the neutron density distribution on the proton-“mock”  $^{58}\text{Ni}$  elastic scattering cross section in the linear scale. The curves correspond to those in Fig. 1. The dot-dashed and the dashed curves are very close to each other, and cannot be identified separately by eye.

## References

- 1) A. Kohama, R. Seki, A. Arima, and S. Yamaji: J. Phys. Soc. Jpn. **72**, 2766 (2003).
- 2) R. J. Glauber: in *High-Energy Physics and Nuclear Structure*, edited by S. Devons (Plenum Press, New York, 1970), p. 207.



# The behavior of matter at high baryon density<sup>†</sup>

W. Bentz,<sup>\*1</sup> T. Horikawa,<sup>\*1</sup> N. Ishii, and A. W. Thomas<sup>\*2</sup>

[MATTER AT HIGH DENSITY, Nuclear Matter, Quark Matter]

The possibility of a phase transition from nuclear matter (NM) to quark matter (QM) at high baryon densities is of great interest in connection with neutron stars and the possible existence of quark stars. In recent works we have shown that one can consistently describe the nucleon as a quark-scalar diquark bound state,<sup>1)</sup> the equation of state (EOS) of nuclear matter (NM),<sup>2)</sup> and the transition to color superconducting quark matter (QM)<sup>3)</sup> in the framework of the Nambu-Jona-Lasinio model, which is an effective quark theory based on QCD.

The solution of the quark-diquark bound state equation gives nucleon mass  $M_N(M)$  as a function of constituent quark mass  $M$ . The effective potential for NM in the mean field approximation has the form<sup>2)</sup>  $V^{(NM)} = V_{\text{vac}} + V_N + V_\omega$ , where  $V_{\text{vac}}$  denotes the polarization of the Dirac sea of quarks,  $V_N$  arises from the Fermi motion of nucleons, and  $V_\omega$  is the contribution of the mean vector field ( $\omega_0$ ).  $M$  and  $\omega_0$  are determined so as to minimize  $V^{(NM)}$ . The effects of confinement are simulated by introducing an infrared cutoff in the proper time regularization scheme, which eliminates unphysical thresholds for the decay of the nucleon into quarks, which is very important for the stability of NM.

The effective potential for QM in the mean field approximation has the form<sup>3)</sup>  $V^{(QM)} = V_{\text{vac}} + V_Q + V_\Delta$ , where  $V_Q$  denotes the Fermi motion of quarks, and  $V_\Delta$  arises from quark pairing and depends on the color superconducting gap ( $\Delta$ ).  $M$  and  $\Delta$  are determined so as to minimize  $V^{(QM)}$ . As argued in Ref. 3, there should be no mean vector field in QM. Since QM corresponds to the deconfined phase, we do not introduce an infrared cutoff here.

Figure 1 shows the pressures for NM (solid line) and QM for several strengths of the pairing interaction ( $r_s$ ). Curve 1 corresponds to normal (non color superconducting) QM. It is clear from Fig. 1 that there is no phase transition from NM to normal QM in our model, but the scalar diquark condensation softens the EOS of QM and leads to a phase transition at a density which depends on  $r_s$ . In Fig. 2 we set  $r_s = 0.2$ , and show the pressure of the ground state as a function of baryon density. We obtain first-order transitions from vacuum (VAC) to NM, where chiral symmetry is broken and color symmetry is intact, and from NM to color superconducting QM, where chiral symmetry is

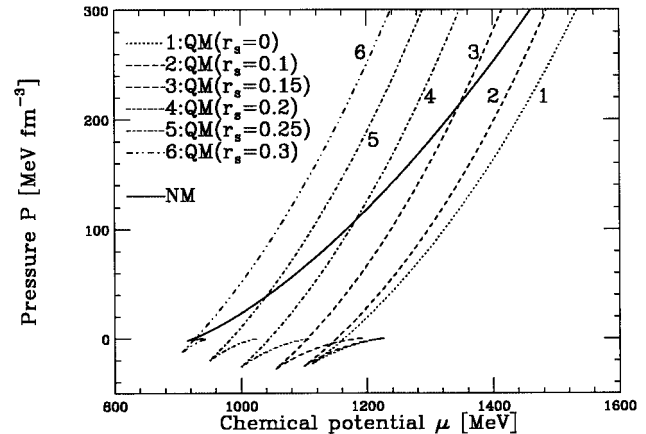


Fig. 1. Pressure as a function of chemical potential for NM (solid line) and QM at several pairing interaction strengths  $r_s$ .

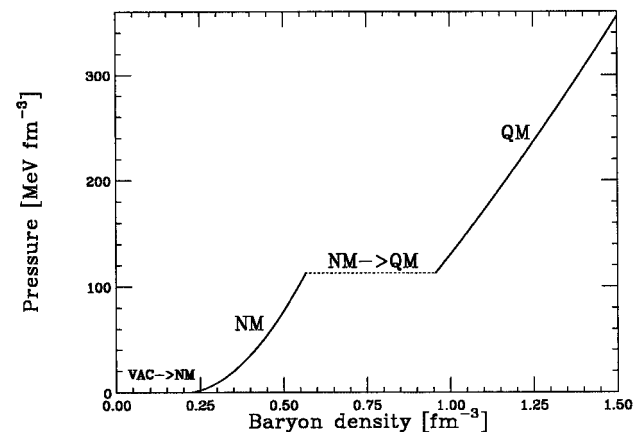


Fig. 2. Pressure of the ground state of the system as a function of baryon density for  $r_s = 0.2$ .

largely restored and color symmetry is broken.

## References

- 1) N. Ishii, W. Bentz, and K. Yazaki: Nucl. Phys. A **578**, 617 (1995).
- 2) W. Bentz and A. W. Thomas: Nucl. Phys. A **696**, 138 (2001).
- 3) W. Bentz, T. Horikawa, N. Ishii, and A. W. Thomas: Nucl. Phys. A **720**, 95 (2003).

<sup>†</sup> Condensed from the article in Nucl. Phys. A **720**, 95 (2003)

<sup>\*1</sup> Department of Physics, Tokai University

<sup>\*2</sup> Department of Physics, University of Adelaide, Australia

# The EMC effect in an effective quark theory for nuclear matter<sup>†</sup>

W. Bentz,<sup>\*1</sup> H. Mineo,<sup>\*2</sup> N. Ishii, A. W. Thomas,<sup>\*3</sup> and K. Yazaki<sup>\*4</sup>

[NUCLEAR STRUCTURE FUNCTIONS, EMC Effect, Effective Quark Theories]

In this work we will be concerned with the medium modifications of the spin-independent nuclear structure functions measured in deep inelastic scattering of leptons, that is, the EMC effect. In recent works we have shown that the quark-scalar diquark description of the single nucleon, which is based on the relativistic Faddeev approach to the Nambu-Jona-Lasinio model,<sup>1)</sup> can be combined successfully with the mean field description of the nuclear matter equation of state (NMEOS).<sup>2)</sup> This framework offers a powerful tool for investigating the origin of the EMC effect in terms of binding on the level of quarks. Here we will consider the case of infinite nuclear matter as a first step, and limit ourselves to a valence quark description.

By using the solution to the quark-diquark bound state equation, we calculate the light-cone momentum distributions (LCMDs) of quarks in a single nucleon. The LCMDs in nuclear matter are then obtained by using familiar convolution formalism. Besides the Fermi motion of nucleons, this description takes into account the effect of the mean scalar field via the density-dependent masses according to the NMEOS, and also the effect of the mean vector field ( $V_0$ ). We found that the direct effect of  $V_0$  on the LCMDs in nuclear matter can be expressed as<sup>3)</sup>  $f_{q/A}(x_A) = \frac{\epsilon_F}{E_F} f_{q/A0}(x'_A = \frac{\epsilon_F}{E_F} x_A - \frac{V_0}{E_F})$ , where  $f_{q/A0}(x'_A)$  is the LCMD for  $V_0 = 0$ , and  $\epsilon_F = E_F + 3V_0$  ( $E_F = \sqrt{M_N^2 + p_F^2}$ ) is the nucleon Fermi energy with  $M_N$  the effective nucleon mass. The actual calculations are carried out in the proper time regularization scheme which avoids unphysical quark decay thresholds for the nucleon.

The medium modifications of the isoscalar valence quark distribution at the saturation density of our NMEOS are shown in Fig. 1 for the low energy scale  $Q_0 = 0.4$  GeV. The dotted line shows the distribution in a free nucleon, the dashed line shows the result including the mean scalar field, the dotted-dashed line shows the result including the Fermi motion of nucleons, and the solid line also includes the mean vector field. It is clear from Fig. 1, and also from the scale transformation given above, that the effect of the mean vector field is to narrow the LCMD, leading to a de-

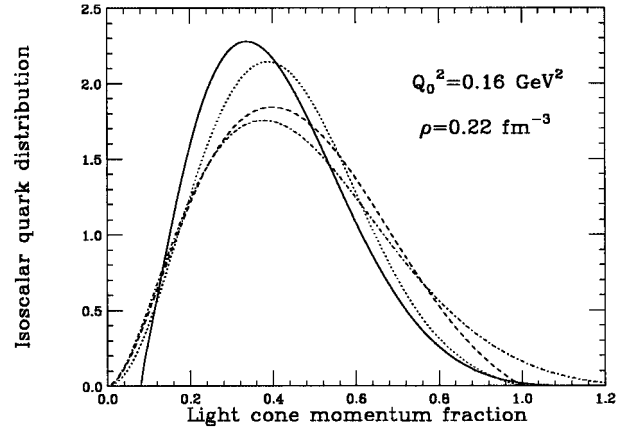


Fig. 1. Isoscalar LCMD of quarks. For explanation of the lines, see text.

pletion in the valence quark region and to an enhancement at smaller values of the Bjorken variable. Figure 2 shows the resulting EMC ratio in comparison to nuclear data extrapolated to the nuclear matter case. We see that the calculation can reproduce the main features of the EMC effect, namely the suppression at large  $x$  and the enhancement at smaller  $x$ .

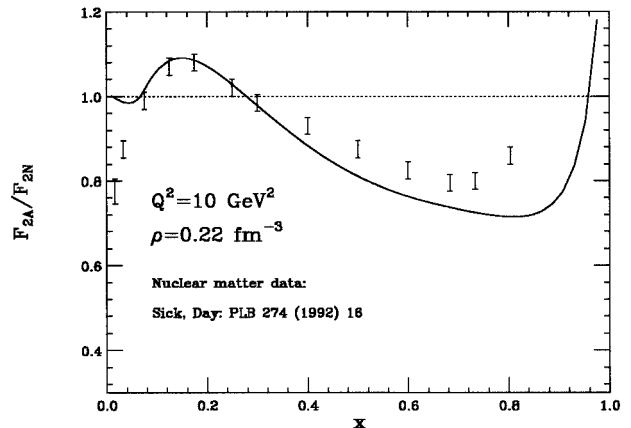


Fig. 2. EMC ratio in isospin symmetric nuclear matter.

## References

- 1) N. Ishii, W. Bentz, and K. Yazaki: Nucl. Phys. A **578**, 617 (1995).
- 2) W. Bentz and A. W. Thomas: Nucl. Phys. A **696**, 138 (2001).
- 3) H. Mineo, W. Bentz, N. Ishii, A. W. Thomas, and K. Yazaki: Nucl. Phys. A, in press.

<sup>†</sup> Condensed from an article by H. Mineo, W. Bentz, N. Ishii, A. W. Thomas, and K. Yazaki, Nucl. Phys. A, in press.

<sup>\*1</sup> Department of Physics, Tokai University

<sup>\*2</sup> Department of Physics, National Taiwan University, Taiwan

<sup>\*3</sup> Department of Physics, University of Adelaide, Australia

<sup>\*4</sup> Department of Physics, Tokyo Woman's Christian University

# Invariant-mass spectroscopy for condensed $\bar{K}$ nuclear clusters to be formed as residues in relativistic heavy-ion collisions

T. Yamazaki, A. Doté,\* and Y. Akaishi\*

[kaonic nuclei, dense nuclei, heavy-ion reactions, quark-gluon plasma]

Recently, exotic nuclear systems involving a  $\bar{K}$  ( $K^-$  or  $\bar{K}^0$ ) as a constituent have been studied theoretically by Akaishi and Yamazaki (AY).<sup>1,2)</sup> Using a phenomenological  $\bar{K}N$  interaction combined with the method of Antisymmetrized Molecular Dynamics, as developed by Doté *et al.*,<sup>3)</sup> we predict that few-body double- $\bar{K}$  nuclei, such as  $pp\bar{K}^-K^-$  and  $ppn\bar{K}^-K^-$ , as well as single- $\bar{K}$  nuclei, are tightly bound compact systems with large binding energies and ultrahigh nucleon densities. The results are summarized in Table 1.

We point out that such dense  $\bar{K}$  nuclear clusters can be produced as residual fragments in relativistic heavy-ion collisions,<sup>4)</sup> since the  $\bar{K}$  clusters are by themselves dense. They are likely to be in a deconfined quark-gluon phase, as in QGP, and thus, they will be spontaneously formed, like clusterized islands, remaining in an expanding hadron gas medium throughout the freeze-out phase (see Fig. 1) and that their invariant masses can be reconstructed from their decay particles.<sup>4)</sup> The decay modes which can be kinematically reconstructed are as follows:

$$(i) \quad ppK^- \rightarrow \Lambda + p,$$

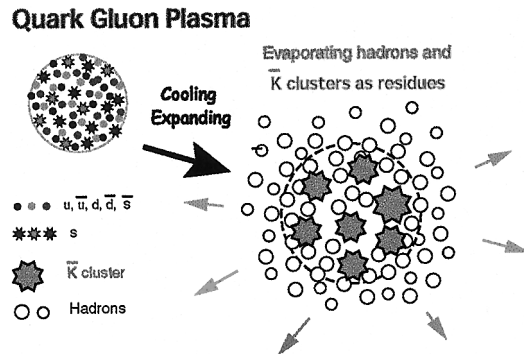


Fig. 1. Quark gluon plasma and its transition to evaporating hadron gases with heavy and dense residues of  $\bar{K}$  clusters. Dense  $\bar{K}$  can be identified by their decays.

- (ii)  $ppnK^- \rightarrow \Lambda + d,$
- (iii)  $pppK^- \rightarrow \Lambda + p + p,$
- (iv)  $ppnnK^- \rightarrow \Lambda + t,$
- (v)  $pppnK^- \rightarrow \Lambda + {}^3\text{He},$
- (vi)  $ppK^-K^- \rightarrow \Lambda + \Lambda,$
- (vii)  $pppK^-K^- \rightarrow \Lambda + \Lambda + p,$
- (viii)  $pppnK^-K^- \rightarrow \Lambda + \Lambda + d.$

Table 1. Summary of predicted  $\bar{K}$  clusters.  $M$ : total mass [MeV].  $E_K$ : total binding energy [MeV].  $\Gamma_K$ : decay width [MeV].  $\rho(0)$ : nucleon density at the center of the system [ $\text{fm}^{-3}$ ].  $R_{\text{rms}}$ : root-mean-square radius of the nucleon system [fm].

$\bar{K}$ cluster	$Mc^2$ [MeV]	$E_K$ [MeV]	$\Gamma_K$ [MeV]	$\rho(0)$ [ $\text{fm}^{-3}$ ]	$R_{\text{rms}}$ [fm]
$pK^-$	1407	27	40	0.59	0.45
$ppK^-$	2322	48	61	0.52	0.99
$pppK^-$	3211	97	13	1.56	0.81
$ppnK^-$	3192	118	21	1.50	0.72
$ppppK^-$	4171	75	162	1.68	0.95
$pppnK^-$	4135	113	26	1.29	0.97
$ppnnK^-$	4135	114	34		1.12
$ppK^-K^-$	2747	117	35		
$ppnK^-K^-$	3582	221	37	2.97	0.69
$pppnK^-K^-$	4511	230	61	2.33	0.73

The condition for observing the free decay of a  $\bar{K}$  cluster with a decay width  $\Gamma_K$  is

$$\tau_K = \hbar/\Gamma_K > \tau_f, \quad (1)$$

where  $\tau_f$  is the freeze-out time. For  $\Gamma_K = 20$  MeV,  $\tau_K \sim 10$  fm/c, which is marginally longer than the estimated freeze-out time,  $\tau_f \sim 5$  fm/c.

## References

- 1) Y. Akaishi and T. Yamazaki: Phys. Rev. C **65**, 044005 (2002).
- 2) T. Yamazaki and Y. Akaishi: Phys. Lett. B **535**, 70 (2002).
- 3) A. Doté, H. Horiuchi, Y. Akaishi, and T. Yamazaki: arXiv:nucl-th/0207085.
- 4) T. Yamazaki, A. Doté, and Y. Akaishi: arXiv:nucl-th/0310085.

\* Institute of Particle and Nuclear Studies, High Energy Accelerator Research Organization (KEK)

# Chiral symmetry in the light-cone field theory

F. Lenz,<sup>\*1</sup> M. Thies,<sup>\*1</sup> K. Ohta,<sup>\*2</sup> and K. Yazaki<sup>\*3</sup>

[HADRON PHYSICS, Chiral Symmetry, Light-Cone, Ward-Takahashi Identity]

As a continuation and generalization of the work reported last year,<sup>1)</sup> chiral symmetry and its spontaneous breakdown in light-cone field theory are studied with a Lagrangian of the following structure,

$$\begin{aligned} \mathcal{L} = & i\varphi^\dagger D_+ \varphi + i\chi^\dagger D_- \chi + \frac{i}{\sqrt{2}} (\chi^\dagger D_m \varphi - \varphi^\dagger D_m^\dagger \chi) \\ & + \mathcal{L}_{\text{int}}(\varphi, \chi), \end{aligned} \quad (1)$$

where

$$D_m = \sigma_3 D_1 + iD_2 - i\sigma_1 m. \quad (2)$$

The covariant derivative,  $D$ , couples the fermions to an external gauge field, which can be made dynamical by an obvious generalization. Only the spinor  $\varphi$  is dynamical since no time derivative of  $\chi$  is present. We start our investigations with the generating functional

$$\begin{aligned} Z[\eta, \gamma] = & \int D[\varphi, \chi] \left\{ i \int d^4x \right. \\ & \left. \cdot (\mathcal{L} + \eta^\dagger \varphi + \varphi^\dagger \eta + \gamma^\dagger \chi + \chi^\dagger \gamma) \right\}. \end{aligned} \quad (3)$$

We use the form in which four-fermion interactions are eliminated in favor of two auxiliary bosonic fields,  $\sigma$  and  $\pi$ . By integrating the constrained variable  $\chi$  and defining  $D_\perp$  as

$$D_\perp = \sigma_3 D_1 + iD_2 - ig(\sigma\sigma_1 + \pi\sigma_2) - im\sigma_1, \quad (4)$$

the generating functional becomes

$$Z[\eta, \gamma] = \int D[\varphi, \sigma, \pi] \exp \{ iS[\varphi, \sigma, \pi] + is[\eta, \gamma] \}, \quad (5)$$

with action and source terms given respectively by

$$\begin{aligned} S[\varphi, \sigma, \pi] &= \int d^4x \left( i\varphi^\dagger D_+ \varphi + i\chi^\dagger D_- \chi - \frac{1}{2}(\sigma^2 + \pi^2) \right), \\ s[\eta, \gamma] &= \int d^4x \left( \eta^\dagger \varphi + \varphi^\dagger \eta + \gamma^\dagger \chi + \chi^\dagger \gamma + \gamma^\dagger \frac{i}{D_-} \gamma \right). \end{aligned}$$

Here, the composite field  $\chi$  is defined as

$$\chi = \chi[\varphi] = -\frac{1}{\sqrt{2}D_-} D_\perp \varphi. \quad (6)$$

The spontaneous break down of the chiral symmetry is defined by the expectation values of the auxiliary fields,

$$\langle \sigma \rangle = \frac{M}{g}, \quad \langle \pi \rangle = 0, \quad (7)$$

implying a nonvanishing chiral condensate  $\langle 0|\bar{\psi}\psi|0\rangle$ .

To study the consequences of this assumed breakdown of the chiral symmetry, we consider the following infinitesimal nonlocal transformation of the fundamental fields  $\varphi(x)$  with  $x_\perp$ -independent  $\alpha$ .

$$\delta\varphi(x) = i\alpha(x^+, x^-)\Sigma_3\varphi(x) \quad (8)$$

with

$$\Sigma_3 = D_M^{-1} [\sigma_3, D_M] = \frac{2M^2\sigma_3 - 2iM\vec{\sigma}_\perp\vec{\partial}_\perp}{-\Delta_\perp + M^2}. \quad (9)$$

The operator  $\Sigma_3$  coincides with the pion operator at zero transverse momentum which can be derived in the NJL model by solving the light-cone BS equation explicitly in ladder approximation.<sup>2)</sup> If we neglect the fluctuations of the auxiliary fields  $\sigma$  and  $\pi$ ,  $\chi$  transforms only in the presence of a nonvanishing bare quark mass,

$$\delta\chi = i\alpha(x^+, x^-)\frac{\sqrt{2}m}{D_-}\sigma_2\varphi. \quad (10)$$

With the above transformation, we obtain a chiral Ward-Takahashi identity, which leads to the Gell-Mann-Oakes-Renner(GOR) relation.

$$\begin{aligned} 0 = & \int D[\varphi] e^{iS[\varphi, \sigma, \pi]} \left[ \int d^2x_\perp (\varphi^\dagger \sigma_2 \chi + \chi^\dagger \sigma_2 \varphi)(y) \right. \\ & \cdot \left\{ \partial_+ (\varphi^\dagger \Sigma_3 \varphi)(x) + \sqrt{2}m(\chi^\dagger \sigma_2 \varphi + \varphi^\dagger \sigma_2 \chi)(x) \right\} \\ & \left. - \delta(x^+ - y^+) \delta(x^- - y^-) (\varphi^\dagger \Sigma_3 \sigma_2 \chi - \chi^\dagger \sigma_2 \Sigma_3 \varphi)(y) \right]. \end{aligned}$$

We have succeeded in connecting the meson field operator to the generator of a unitary  $x^\pm$ -dependent transformation. Further analyses in the Fourier-transformed forms confirm that the pion dominance does hold in the chiral limit and the GOR relation is correctly obtained.

## References

- \*1 Institute for Theoretical Physics, University of Erlangen, Germany
- \*2 Institute of Physics, University of Tokyo
- \*3 College of Arts and Sciences, Tokyo Woman's Christian University

- 1) F. Lenz, M. Thies, K. Ohta, and K. Yazaki: RIKEN Accel. Prog. Rep. **36**, 44 (2003).
- 2) W. Bentz, T. Hama, T. Matsuki, and K. Yazaki: Nucl. Phys. A **651**, 143 (1999).

# Electron cooling by electron beam of anisotropic velocity distribution with variable Coulomb logarithm

H. Amemiya, H. Tsutsui, and T. Katayama

[Electron cooling, Anisotropic velocity distribution, Coulomb logarithm]

The aim of the present paper is to obtain the cooling rate of an ion beam by an electron beam with the longitudinal electron temperature being very low due to the beam acceleration.

For an ion traveling with a velocity  $V$  in electrons with a velocity distribution  $f(v)$ , the loss rate of kinetic energy  $dE_p/dt$  and the rate of energy increment  $dE_t/dt$  become in the beam frame

$$\frac{dE_p}{dt} = -\frac{4\pi Q}{m} V \int L_c \cdot \frac{1}{U^2} \vec{U} f(\vec{v}) d\vec{v}, \quad (1)$$

$$\frac{dE_t}{dt} = \frac{4\pi Q}{M} \int L_c \cdot \frac{1}{U} f(\vec{v}) d\vec{v}, \quad (2)$$

where  $Q = N_e Z^2 e^4 / (4\pi\epsilon_o)^2$ ,  $N_e$  is the electron density,  $M$  is the ion mass,  $m$  is the reduced mass  $m_e M / (M + m_e)$ ,  $Z$  is the charge state of the ion, and  $U$  is the relative velocity between the ion and electrons.  $L_c$  is the Coulomb logarithm given by  $\ln(\lambda_{eff} / \rho_m)$ , where  $\rho_m$  is the minimum impact parameter  $Z e^2 / (4\pi\epsilon_o m U^2)$  which depends on  $U$  and  $\lambda_{eff}$  is the effective Debye length which varies with the angle  $\theta$  of the ion velocity vector to the beam axis due to the anisotropic velocity distribution of electrons. Therefore, contrary to the previous cases,<sup>1,2)</sup>  $L_c$  is variable and placed inside the integrals.

With the acceleration of electrons to the energy  $E_o$ , the longitudinal electron temperature  $T_o$  becomes

$$\kappa T_o = (\kappa T_e)^2 / 2(\gamma + 1) E_o, \quad (3)$$

where  $T_e$  is the electron temperature in the transverse direction and near the cathode temperature,  $\sim 10^3$  K. For the case of  $E_o = 100$  keV,  $T_e = 10^3$  K, Eq. (3) gives  $T_o = 2 \times 10^{-4}$  K. However, due to the plasma effect, it is heated to

$$\kappa T_o = m \omega_p^2 d^2 / 4\pi = e^2 N_e^{1/3} / 4\pi\epsilon_o, \quad (4)$$

where  $\omega_p$  is the angular plasma frequency and  $d$  the average distance. For a typical case of  $N_e = 10^8$  cm<sup>-3</sup>, Eq. (4) gives  $T_o \sim 0.78$  K. The noise of the power supply is neglected.

The Debye length  $\lambda_{eff}$  becomes anisotropic as

$$\lambda_{eff} = \lambda [\cos^2 \theta + \eta^2 \sin^2 \theta]^{1/2}; \quad \tan \theta = \beta / \alpha. \quad (5)$$

where  $\lambda = (\epsilon_o \kappa T_e / N_e e^2)^{1/2}$  and  $\eta^2 = T_o / T_e$ .  $\alpha$  and  $\beta$  are velocities of the ion in the longitudinal and transverse directions normalized by  $s_t = (2\kappa T_e / m_e)^{1/2}$ , respectively. Hence, the Coulomb logarithm  $L_c$  can be divided as

$$L_c = L_o + (3/2)L(\theta) + \ln(U/s_t)^2, \quad (6)$$

$$L(\theta) = \ln[\cos^2 \theta + \eta^2 \sin^2 \theta], \quad (7)$$

where  $L_o = \ln(6N_D/Z) + \ln(m/m_e)$  and  $N_D = N_e(4\pi/3)\lambda^3$  are constants.

Next, the dimensionless potentials  $\phi_1$  and  $\phi_2$  defined previously<sup>3,4)</sup> to obtain the cooling and heating rates for ions with  $\rho^2 = \alpha^2 + \beta^2$  are calculated. Namely,

$$\phi_1(\rho) = -\int \frac{1}{(U/s)} f(\vec{v}) d\vec{v}, \quad (8)$$

$$\phi_2(\rho) = -\int \frac{\ln(U/s)^2}{(U/s)} f(\vec{v}) d\vec{v}. \quad (9)$$

Substituting Eqs. (8) and (9) into Eqs. (1) and (2), we obtain the rates of energy change in the  $\theta$  direction as

$$\begin{aligned} \frac{dE_p(\theta)}{dt} &= -C \left\{ (L_o + 2)\rho \nabla \phi_1 + \frac{3}{2} L(\theta) \rho \nabla \phi_1 + \rho \nabla \phi_2 \right\} \\ & \quad (10) \end{aligned}$$

$$\frac{dE_t(\theta)}{dt} = -C \frac{m}{M} \left\{ L_o \phi_1 + \frac{3}{2} L(\theta) \phi_1 + \phi_2 \right\}. \quad (11)$$

where  $C = 4\pi Q / ms$ ,  $s = (2\kappa T_e / m)^{1/2}$ ,  $\phi_1 = \phi_1(\rho, \theta)$ ,  $\phi_2 = \phi_2(\rho, \theta)$ ,  $\rho \nabla \phi_1 = \alpha \nabla_\alpha \phi_1 + \beta \nabla_\beta \phi_1$ , and  $\rho \nabla \phi_2 = \alpha \nabla_\alpha \phi_2 + \beta \nabla_\beta \phi_2$ .

Equations (10) and (11) indicate cooling and heating rates of an ion for any form of  $f(v)$ .  $L(\theta)$  and  $\phi_2$  denote corrections to previous theories<sup>1,2)</sup> which consider only the effects of  $\phi_1$  and  $L_o$ . If  $f(v)$  is isotropic, our previous result<sup>3,4)</sup> is recovered by putting  $\rho = \alpha$  and  $L(\theta) = 0$ .

It should be noted that the electron-cooling theory is valid only for  $L_c > 0$ . Applying this to  $L(\theta)$  in Eq. (7) for a small  $\eta$  ( $\sim 0$ ), we have the requisite condition as  $\sin \theta < [1 - \exp(-L_o)]^{1/2}$ . The allowable upper limit angle  $\theta_c$  becomes  $\theta_c = 82.2^\circ$  for  $L_o = 2$  and  $\theta_c = 89.6^\circ$  for  $L_o = 5$ . As  $L_o$  is larger, the theory almost covers  $\theta_c$  up to  $\pi/2$ .

The present theory accounts for the velocity and angle dependences of  $dE_p/dt$  and  $dE_t/dt$  for a given electron beam of  $f(v)$ ,  $N_e$  and  $E_o$ .

## References

- 1) H. Poth: Phys. Rep. **196**, 135 (1990).
- 2) I. N. Meshkov: Phys. Part. Nucl. **25**, 631 (1994).
- 3) H. Amemiya, T. Tanabe, and T. Katayama: J. Phys. Soc. Jpn. **73**, 617 (2004).
- 4) H. Amemiya, T. Tsutsui, and T. Katayama: RIKEN Accel. Prog. Rep. **36**, 45 (2003).

# Electron cooling by two-temperature electron beam with extremely cold longitudinal temperature

H. Amemiya, H. Tsutsui, and T. Katayama

[Electron cooling, Two-temperature velocity distribution, Coulomb logarithm]

In a previous study, the cooling and heating rates of an ion by an electron beam with a general anisotropic velocity distribution have been obtained.<sup>1)</sup> This study is intended to meet the experimental requirements for electron cooling. As a typical electron velocity distribution  $f(v)$ , the two-temperature Maxwellian type is considered.

$$f(u, t) du dt = \frac{2\pi t}{\pi^{3/2}} \exp(-u^2) \exp(-t^2) du dt. \quad (1)$$

Here,  $u = v_p/s_p$ ,  $t = v_t/s_t$ ,  $s_p = (2\kappa T_o/m)^{1/2}$ ,  $s_t = (2\kappa T_t/m)^{1/2} \sim (2\kappa T_e/m)^{1/2}$ ,  $v_p$  and  $v_t$  are electron velocities in the longitudinal (beam direction,  $x$ ) and transverse (on the  $y$ - $z$  surface) directions,  $T_e$  is the electron temperature in the source, and  $T_o$  and  $T_t$  are the electron temperatures in the beam in the directions of  $u$  and  $t$ , respectively.

Normalizing the ion velocities  $V_p$  and  $V_t$  in the  $x$  and  $y$  directions as  $\alpha = V_p/s_t$  and  $\beta = V_t/s_t$ , we have the relative velocity  $U$  between the ion and electrons.

$$D^{1/2} = \sqrt{(\alpha - u\eta)^2 + (\beta + t)^2 - 4\beta t \sin^2 \psi}, \quad (2)$$

Here,  $\eta = s_p/s_t = (T_o/T_t)^{1/2}$  and  $\psi = (\pi - \chi)/2$ ,  $\chi$  being the angle between  $V_t$  and  $v_t$ . The functions  $\phi_n(\alpha, \beta; \eta)$  for the cooling and heating rates<sup>2)</sup> become as follows ( $n = 1, 2$ ).

$$\phi_n = -\frac{4}{\pi^{3/2}} \int \frac{[\ln(U/s_t)]^{n-1} e^{-u^2} t e^{-t^2}}{D^{1/2}} du dt d\psi, \quad (3)$$

$$\nabla_\alpha \phi_1 = \frac{4}{\pi^{3/2}} \int \frac{(\alpha - u\eta) e^{-u^2} t e^{-t^2}}{D^{3/2}} du dt d\psi, \quad (4)$$

$$\begin{aligned} \nabla_\beta \phi_1 \\ = \frac{4}{\pi^{3/2}} \int \frac{[(\beta + t) - 2\beta t \sin^2 \psi] e^{-u^2} t e^{-t^2}}{D^{3/2}} du dt d\psi, \end{aligned} \quad (5)$$

where integrals are triple for  $u = -\infty$  to  $\infty$ ,  $t = 0$  to  $\infty$  and  $\psi = 0$  to  $\pi/2$ . For  $\nabla_\alpha \phi_2$  and  $\nabla_\beta \phi_2$ , integrands are multiplied by  $-(2 - \ln D)$  to those of  $\nabla_\alpha \phi_1$  and  $\nabla_\beta \phi_1$ .

Usually  $\eta$  is small,  $\sim 1/40$ . In the case of  $\eta = 0$ , the integral on  $u$  is decoupled and using  $K(k)$  and log-elliptic integral  $L(k)$  defined before,<sup>1)</sup> we obtain

$$\phi_1 = -\frac{4}{\pi} \int_0^\infty \frac{t e^{-t^2}}{\Delta^{1/2}} K(k) dt, \quad (6)$$

$$\phi_2 = -\frac{4}{\pi} \left\{ \int_0^\infty \frac{\ln \Delta \cdot t e^{-t^2}}{\Delta^{1/2}} K(k) dt \right. \quad (7)$$

$$\left. + \int_0^\infty \frac{t e^{-t^2}}{\Delta^{1/2}} L(k) dt \right\},$$

where  $k^2 = 4\beta t/\Delta$ ,  $\Delta = \alpha^2 + (\beta + t)^2$ . For the ion moving parallel to the beam axis ( $\beta = 0$ ),  $k = 0$ ,  $K = \pi/2$  and  $L = 0$ . Then,

$$\phi_1 = -\sqrt{\pi} \exp(\alpha^2) [1 - \operatorname{erf}(\alpha)], \quad (8)$$

$$\nabla_\alpha \phi_1 = 2(1 + \alpha\phi_1), \quad \nabla_\alpha \phi_2 = 2(\ln(\alpha^2) + \alpha\phi_2), \quad (9)$$

and  $\nabla_\beta \phi_{1,2} = 0$ .  $\phi_2$  are numerically obtained.

Figure 1 shows  $-\phi_1$  and  $-\phi_2$  related to the heating rate *vs.*  $\rho = (\alpha^2 + \beta^2)^{1/2}$  for some  $\theta = \tan^{-1}(\beta/\alpha)$  compared with the isotropic case,<sup>1)</sup>  $\eta = 1$ .

Figure 2 shows  $-\rho * \nabla \phi_{1,2} = \alpha \nabla_\alpha \phi_{1,2} + \beta \nabla_\beta \phi_{1,2}$  related to the cooling rate *vs.*  $\rho$  for some  $\theta$  compared with the case of  $\eta = 1$ .

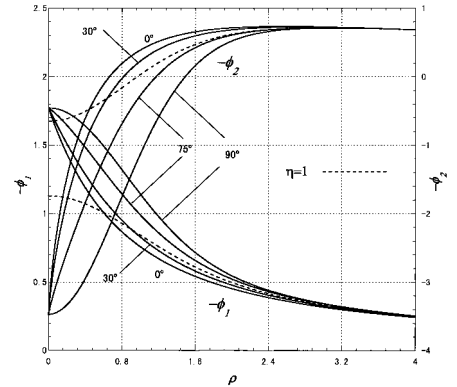


Fig. 1.  $-\phi_1$  and  $-\phi_2$  *vs.*  $\rho$  for some  $\theta$ .

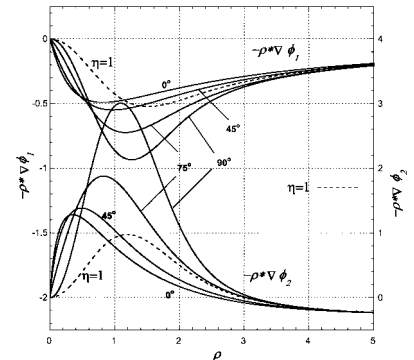


Fig. 2.  $-\rho * \nabla \phi_{1,2} = \alpha \nabla_\alpha \phi_{1,2} + \beta \nabla_\beta \phi_{1,2}$  *vs.*  $\rho$  for some  $\theta$ .

## References

- 1) H. Amemiya, H. Tsutsui, and T. Katayama: RIKEN Accel. Prog. Rep. **36**, 45 (2003).
- 2) H. Amemiya, H. Tsutsui, and T. Katayama: RIKEN Accel. Prog. Rep. **37**, 36 (2004).

# Cooling rate of ion beam by electron cooling with flat electron velocity distribution with variable Coulomb logarithm

H. Amemiya, H. Tsutsui, and T. Katayama

[Electron cooling, Cooling rate, Flat distribution, Ion beam, Coulomb logarithm]

In previous studies on electron cooling (EC)<sup>1,2</sup> the rate of energy change of a single ion by an electron beam of anisotropic velocity distribution  $f(v)$  has been obtained. Using this, the cooling and heating rates of an ion beam can be obtained through integration over an ion velocity distribution  $F(V)$ . Here,  $F(V)$  is taken typically as Maxwellian with a temperature  $T_i$ . In the beam frame,  $F(V)$  is expressed in the reduced form as

$$F(\sigma, \theta) d\sigma d\theta = \frac{4}{\pi\sqrt{\pi}} \sigma^2 \exp(-\sigma^2) d\sigma \sin \theta d\theta, \quad (1)$$

where  $\sigma = V/s_i$ ,  $s_i = (2\kappa T_i/M)^{1/2}$ ,  $M$  is ion mass and  $\theta$  ( $= 0$  to  $\pi/2$ ) is the angle of ion velocity to the beam axis.

The cooling and heating rates lead to<sup>1,2</sup>

$$\begin{aligned} \frac{d\bar{E}_p(\theta)}{dt} &= -C \int_0^\infty F(\sigma) \left[ \left( L_o + 2 + \frac{3}{2} L(\theta) \right) \rho \nabla \phi_1 \right. \\ &\quad \left. + \rho \nabla \phi_2 \right] d\sigma, \end{aligned} \quad (2)$$

$$\begin{aligned} \frac{d\bar{E}_t(\theta)}{dt} &= -C \frac{m}{M} \int_0^\infty F(\sigma) \left[ \left( L_o + \frac{3}{2} L(\theta) \right) \phi_1 + \phi_2 \right] d\sigma. \end{aligned} \quad (3)$$

where  $\phi_1$  and  $\phi_2$  are functions of  $\rho$  and  $\theta$ , and  $C = 4\pi Q/ms$ ,  $s = (2\kappa T_e/m)^{1/2}$ ,  $Q = N_e Z^2 e^4 / (4\pi \epsilon_o)^2$ ,  $L_o = \ln(6mN_D/m_e Z)$ ,  $N_D = N_e(4\pi/3)\lambda^3$ ,  $\lambda = \epsilon_o \kappa T_e / N_e e^2$ , and  $m^{-1} = m_e^{-1} + M^{-1}$ .

We define cooling and heating functions as

$$W_{p1,2}(\rho, \theta) \equiv - \int_0^\infty F(\sigma) [\rho \nabla \phi_{1,2}(\rho, \theta)] d\sigma, \quad (4)$$

$$W_{t1,2}(\rho, \theta) \equiv - \int_0^\infty F(\sigma) \phi_{1,2}(\rho, \theta) d\sigma. \quad (5)$$

Therefore, Eqs. (2) and (3) can be reduced to

$$\begin{aligned} \frac{d\bar{E}_p(\theta)}{CL_o dt} &= \left\{ W_{p1}(\theta) \left[ 1 + \frac{3}{2} \frac{L(\theta)}{L_o} \right] \right. \\ &\quad \left. + [2W_{p1}(\theta) + W_{p2}(\theta)]/L_o \right\}, \end{aligned} \quad (6)$$

$$\frac{d\bar{E}_t(\theta)}{CL_o dt} = \frac{m}{M} \left\{ W_{t1}(\theta) \left[ 1 + \frac{3}{2} \frac{L(\theta)}{L_o} \right] + W_{t2}(\theta)/L_o \right\}. \quad (7)$$

In the conventional case ( $\eta = 1$ ),<sup>3,4</sup>  $W_{p2} = W_{t2} = 0$

and  $W_{p1}$  and  $W_{t1}$  lead to

$$W_{p1} = -\frac{2}{\sqrt{\pi}} \frac{\xi}{(\xi^2 + 1)^{3/2}}, \quad W_{t1} = \frac{2}{\sqrt{\pi}} \frac{\xi}{(\xi^2 + 1)^{1/2}}. \quad (8a, b)$$

Figure 1 shows  $W_{p1}$  and  $W_{p2}$  vs.  $\xi = s_e/s_i$  for  $\theta = 0$  to  $\pi/2$  in the case of completely flat distribution  $\eta = 0$ .

Figure 2 shows  $W_{t1}$  and  $W_{t2}$  vs.  $\xi = s_e/s_i$  for  $\theta = 0$  to  $\pi/2$  for  $\eta = 0$ . It is seen that except in the range of very small  $\xi$ ,  $W_{p2}$  and  $W_{t2}$  are opposite in sign to  $W_{p1}$  and  $W_{t1}$ , respectively. In the storage ring, the ion beam broadens by the intrabeam scattering (IB).<sup>5</sup> An equilibrium ion temperature will be reached after numerous repetitions of EC and IB.

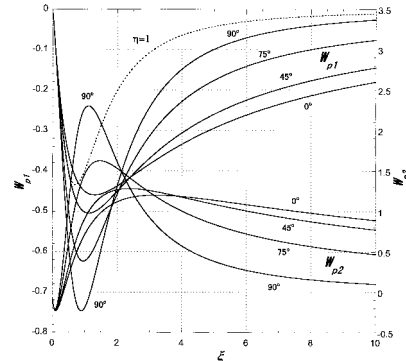


Fig. 1.  $W_{p1}$  and  $W_{p2}$  vs.  $\xi = s_e/s_i$  for some  $\theta$ .

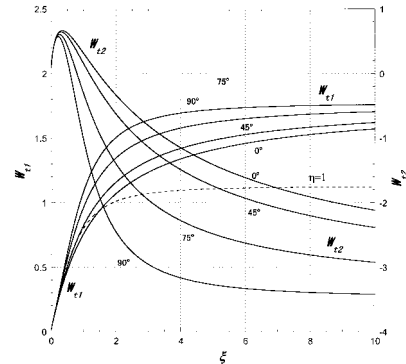


Fig. 2.  $W_{t1}$  and  $W_{t2}$  vs.  $\xi = s_e/s_i$  for some  $\theta$ .

## References

- 1) H. Amemiya, H. Tsutsui, and T. Katayama: RIKEN Accel. Prog. Rep. **36**, 45–47 (2003).
- 2) H. Amemiya, H. Tsutsui, and T. Katayama: RIKEN Accel. Prog. Rep. **37**, 36, 37 (2004).
- 3) H. Poth: Phys. Rep. **196**, 135 (1990).
- 4) I. N. Meshkov: Phys. Part. Nucl. **25**, 631 (1994).
- 5) J. D. Bjorken and S. K. Mtingwa: Part. Accel., **13**, 115 (1983).

# Ultimate temperature and cooling time of ion beam by electron cooling: Dependence on Coulomb logarithm

H. Amemiya, H. Tsutsui, and T. Katayama

[Electron cooling, Cooling rate, Flat distribution, Ion beam, Coulomb logarithm]

Using the cooling and heating functions of an ion beam,<sup>1,2)</sup> the effective cooling rate  $R(\theta, \xi)$  of an ion beam with a temperature  $T_i$  is given by

$$\frac{d\kappa T_i}{(CL_o)dt} = R(\xi, \theta), \quad (1)$$

$$R(\xi, \theta) = (W_{p1} + \varepsilon W_{t1}) \left( 1 + \frac{3L(\theta)}{2L_o} \right) + \frac{2W_{p1} + W_{p2} + \varepsilon W_{t2}}{L_o}. \quad (2)$$

Here  $\theta$  is the angle of the ion velocity to the beam axis,  $L_o$  is the constant part of Coulomb logarithm,  $C = 4\pi Q/ms$  where  $s = (2\kappa T_e/m)^{1/2}$  and  $Q = N_e Z^2 e^4 / (4\pi \varepsilon_o)^2$ ,  $L(\theta) = \ln[\cos^2 \theta + \eta^2 \sin^2 \theta]$  where  $\eta^2 = T_o/T_e$ ,  $T_o$  ( $\sim 1$  K) and  $T_e$  ( $\sim 10^3$  K) being longitudinal and lateral electron temperatures,  $\varepsilon = m_e/M$ ,  $m^{-1} = m_e^{-1} + M^{-1}$  and  $W_{p1,2}$  and  $W_{t1,2}$  are the cooling and heating functions of ion beam obtained.<sup>1,2)</sup>

Figure 1 shows  $R(\theta, \xi)$  vs.  $\xi = s_e/s_i$ , where  $s_e = (2\kappa T_e/m_e)^{1/2}$  and  $s_i = (2\kappa T_i/M)^{1/2}$ , in the case of a flattened electron velocity distribution  $f(v)$  ( $\eta = 0$ ) for  $^{238}\text{U}$  together with isotropic  $f(v)$  ( $\eta = 1$ ) with  $L_o$  as a parameter.  $R < 0$  corresponds to the cooling of ions. In typical experiments,  $\eta^2$  is  $\sim 10^{-3}$  ( $\eta^2 = T_o/T_e$ , longitudinal and lateral electron temperatures  $T_o \sim 1$  K and  $T_e \sim 10^3$  K). Therefore, the assumption of  $\eta = 0$  is a good approximation. The effects of  $W_{t1,2}$  are smaller than those of  $W_{p1,2}$  and appear only near thermal equilibrium:  $R = 0$ .

Due to the angular dependence of cooling, the temperature of the ion beam becomes anisotropic. The critical  $\xi$  at  $R = 0$  corresponds to the ultimate ion temperature  $T_{i\infty}$ . When  $L_o$  is not large, ions with large  $\theta$  are cooled only to a certain limit.

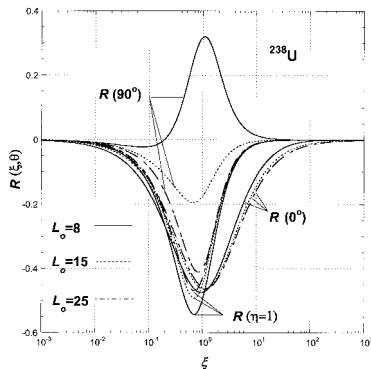
Fig. 1. Cooling rate  $R(\xi, \theta)$  vs.  $\xi$  for some  $L_o$  values.

Figure 2 shows ultimate  $T_{i\infty}$  vs.  $L_o$  for  $^{238}\text{U}$ . Above a certain  $L_o$ , a marked decrease in  $T_{i\infty}$  is observed and then  $T_{i\infty}$  reaches a very small value. A marked contrast from the case of  $\eta = 1$  (dotted curve) is observed, suggesting the importance of the effects of flat  $f(v)$  and  $L(\theta)$ . It is favorable to choose large  $L_o$  to achieve effective cooling for all  $\theta$  values.

For large  $L_o$ , the first term of the right-hand side of Eq. (2) becomes predominant.  $T_{i\infty}$  can be estimated from the balance

$$W_{p1} + \varepsilon W_{t1} \sim 0. \quad (3)$$

Substituting  $W_{t1} \sim \pi^{1/2} - (4/\pi^{1/2}) \cos \theta / \xi$  and  $W_{p1} \sim -(4/\pi^{1/2}) \cos \theta / \xi$ , we obtain, from Eq. (3),

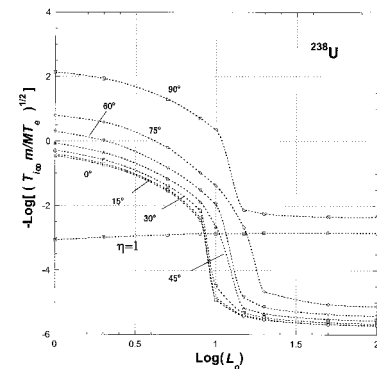
$$\frac{\cos \theta}{\xi} = \frac{\pi}{4} \varepsilon \quad \text{or} \quad \frac{T_{i\infty}}{T_e} = \frac{\pi^2}{16 \cos^2 \theta} \frac{m_e}{M}. \quad (4)$$

Then, the minimum  $T_{i\infty}$  is  $0.62(m_e/M)T_e$  at  $\theta = 0$  and decreases with  $\theta$ . Near  $\theta = \pi/2$ ,  $T_i$  decreases slowly but its value is smaller than in the isotropic case up to  $\theta = \cos^{-1}(\varepsilon^{1/2}\pi/4)$  as long as  $L(\theta) > -2L_o/3$ .

Defining  $\tau = t(CL_o/\kappa T_e)m_e/M$ , we obtain

$$\frac{d\xi(\theta)}{d\tau} = -\frac{1}{2}\xi^3 R(\xi, \theta) \quad \text{or} \quad \tau = -\int_{\xi_o}^{\xi} \frac{2d\xi}{\xi^3 R(\xi, \theta)}. \quad (5)$$

Here,  $\xi_o$  corresponds to the initial ion beam temperature. The cooling time scale is proportional to  $N_e Z^2 / M$  and the integral gives a modification factor that depends on the angle.

Fig. 2. Ultimate ion temperature  $T_{i\infty}$  vs.  $L_o$  for  $^{238}\text{U}$ .

## References

- 1) H. Amemiya, H. Tsutsui, and T. Katayama: RIKEN Accel. Prog. Rep. 36, 45–47 (2003).
- 2) H. Amemiya, H. Tsutsui, and T. Katayama: RIKEN Accel. Prog. Rep. 37, 36–38 (2004).



# Mathematical tools for electron cooling by electron beam with strongly anisotropic velocity distribution

H. Amemiya, H. Tsutsui, and T. Katayama

[Mathematical tool, Electron cooling, Electron beam, Ion beam, Magnetic field]

The present note is concerned with new functions and integrals associated with electron cooling (EC), particularly the anisotropic velocity distribution, and the effects of magnetic field are treated.

Due to acceleration, the electron beam is strongly anisotropic. A parameter  $\eta = s_p/s_t = (T_o/T_e)^{1/2}$  has been introduced to represent the anisotropy, where  $s_p$  and  $s_t$  are electron thermal velocities in the longitudinal and lateral directions, respectively, and  $T_o$  and  $T_e$  respective electron temperatures. The results of the case  $T_o = 0$  or  $\eta = 0$  have already been given.<sup>1)</sup> The cooling functions  $\phi_1$  and  $\phi_2$  and the gradients  $\nabla_{\alpha,\beta}\phi_{1,2}$  for small  $\eta$  can be given by Taylor expansion.

Optimum cooling occurs when the ion velocity is parallel to the beam axis ( $\alpha > 0, \beta = 0$ ),  $\alpha$  and  $\beta$  being the longitudinal and lateral velocities normalized by  $s_e$ . In this ideal case, we can put  $k = 0$  ( $k^2 = 4\beta t/\Delta$ ,  $\Delta = \alpha^2 + (\beta + t)^2$ ). In a previous note,<sup>2)</sup> the log-elliptic integrals L and M and their derivatives  $L_n$  and  $L_{Sn}$  were introduced. Those without log are the elliptic integrals K and E and their derivatives  $K_n$  and  $K_{Sn}$ .<sup>3)</sup> It follows for  $k = 0$  that  $E = K = K_3 = K_5 = \pi/2$ ,  $K_{S3} = K_{S5} = \pi/4$ , and  $M = L = L_3 = L_5 = L_S = L_{S3} = L_{S5} = 0$ .  $\phi_{1,2}$  and  $\nabla_{\alpha,\beta}\phi_{1,2}$  become

$$\begin{aligned} \phi_1(\alpha, 0; \eta) &= - \int_{-\infty}^{\infty} \exp[-u^2 + (\alpha - u\eta)^2] \operatorname{erfc}(|\alpha - u\eta|) du, \end{aligned} \quad (1)$$

$$\begin{aligned} \phi_2(\alpha, 0; \eta) &= -2 \int_{-\infty}^{\infty} \exp[-u^2 + (\alpha - u\eta)^2] Lx(|\alpha - u\eta|) du. \end{aligned} \quad (2)$$

Here, we define new integrals as

$$Lx(x) \equiv \int_x^{\infty} \ln t \cdot \exp(-t^2) dt. \quad (A)$$

$$I_{2n-1} = \int_0^{\infty} \frac{\exp(-x)}{\sqrt{\alpha^2 + x}^{2n-1}} dx, \quad n = 1, 2, 3, \dots \quad (B)$$

$$J_{2n-1} = \int_0^{\infty} \frac{\ln[\alpha^2 + x] \exp(-x)}{\sqrt{\alpha^2 + x}^{2n-1}} dx, \quad n = 1, 2, 3, \dots \quad (C)$$

Then, we have  $-\phi_1 = I_1$ ,  $-\phi_2 = J_1$ , and for  $\alpha \gg u\eta$   $\nabla_{\alpha}\phi_1 = \alpha I_3$ ,  $\nabla_{\alpha}\phi_2 = \alpha(-2I_3 + J_3)$ , and their derivatives (denoted as prime) over  $\eta$  are

$$\phi_1'(\alpha, 0; 0) = \frac{\eta}{2} I_3, \quad \phi_2'(\alpha, 0; 0) = \eta \left( -I_3 + \frac{J_3}{2} \right). \quad (3)$$

$$\begin{aligned} \nabla_{\alpha}\phi_1'(\alpha, 0; 0) &= 3\alpha\eta I_5, \\ \nabla_{\alpha}\phi_2'(\alpha, 0; 0) &= \alpha\eta[8I_5 - 3J_5], \\ \nabla_{\beta}\phi_{1,2}'(\alpha, 0; \eta) &= \nabla_{\beta}\phi_{1,2}'(\alpha, 0; \eta) = 0. \end{aligned} \quad (4)$$

The opposite case  $\alpha \ll u\eta$  occurs near the temperature equilibrium where the expansion is not applied.

Due to the oscillatory motion of electrons in the magnetic field, the Coulomb logarithm is modified as<sup>4)</sup>

$$\ln \Lambda = \int_{\rho_m/v_e}^{1/\omega_p} \frac{d\tau}{\tau} \cos \omega\tau, \quad (6)$$

where  $v_e = (\kappa T_e/m_e)^{1/2}$ ,  $\omega$  and  $\omega_p$  are the angular electron cyclotron and plasma frequencies, and  $\rho_m$  the minimum impact parameter. Equation (6) becomes

$$\ln \Lambda = \int_{\rho_m}^{\lambda_D} \frac{1}{r} dr - 2 \int_{\rho_m(v/v_e)}^{\lambda_D(v/v_e)} \frac{\sin^2(r/2r_L)}{r} dr, \quad (7)$$

where  $r = v\tau$ ,  $v$  being the velocity of individual electron,  $r_L = v/\omega$  and  $\lambda_D = v_e/\omega_p$ .

We define a new function  $\Sigma(x)$  as

$$\Sigma(x) = \int_0^x \frac{\sin^2 \xi}{\xi} d\xi, \quad (D)$$

which is 0 at  $x = 0$  and increases with  $x$  and approaches to  $(\ln(2x) + \gamma)/2 - \sin(2x)/4x$  at large  $x$ . Inflections appear at points  $2x = \tan x$ . Then,

$$\ln \Lambda = \ln \left( \frac{\lambda_D}{\rho_m} \right) - 2[\Sigma(\xi_2) - \Sigma(\xi_1)]. \quad (8)$$

where  $\xi_1 = \omega\rho_m/2v_e$  and  $\xi_2 = \omega\lambda_D/2v_e = \omega/2\omega_p$ . The first term of RHS is the Coulomb logarithm  $L_c$  without magnetic field, while the second term gives the gyration effect.

## References

- 1) H. Amemiya, H. Tsutsui, and T. Katayama: RIKEN Accel. Prog. Rep. **37**, 36–39 (2004).
- 2) H. Amemiya, H. Tsutsui, and T. Katayama: RIKEN Accel. Prog. Rep. **36**, 47 (2003).
- 3) M. Abramovitz and I. A. Stegun: *Handbook of Mathematical Functions with Formulas, Graphs and Mathematical Tables*, 9th ed. (Dover, New York, 1970).
- 4) I. P. Shkalovsky, T. W. Johnston, and M. P. Bachinsky: *The Particle Kinetics of Plasmas* (Addison-Wesley, London, etc., 1966).

## Superheavy hydrogen ${}^5\text{H}^\dagger$

A. A. Korshennikov, M. S. Golovkov, I. Tanihata, A. M. Rodin,<sup>\*1</sup> A. S. Fomichev,<sup>\*1</sup> S. I. Sidorchuk,<sup>\*1</sup>  
 S. V. Stepanov,<sup>\*1</sup> M. L. Chelnokov,<sup>\*1</sup> V. A. Gorshkov,<sup>\*1</sup> D. D. Bogdanov,<sup>\*1</sup> R. Wolski,<sup>\*1</sup>  
 G. M. Ter-Akopian,<sup>\*1</sup> Yu. Ts. Oganessian,<sup>\*1</sup> W. Mittig,<sup>\*2</sup> P. Roussel-Chomaz,<sup>\*2</sup>  
 H. Savajols,<sup>\*2</sup> E. A. Kuzmin,<sup>\*3</sup> E. Yu. Nikolskii,<sup>\*3</sup> and A. A. Ogloblin<sup>\*3</sup>

[NUCLEAR REACTION,  $p({}^6\text{He}, {}^2\text{He}){}^5\text{H}$ ,  $E = 36\text{A MeV}$ , Nuclear structure]

The very neutron-rich nucleus  ${}^5\text{H}$  having an extreme fraction of neutrons,  $N/Z = 4$ , has been the object of research for more than 40 years. Numerous early experiments attempted to observe a particle-stable  ${}^5\text{H}$ , either by its beta activity or by direct detection of  ${}^5\text{H}$ , thus finally proving its instability. Later experiments focused on unbound  ${}^5\text{H}$ . However, the existence of  ${}^5\text{H}$  resonance remained unclear.

In the present paper, we report on an experimental study of  ${}^5\text{H}$ . We applied a technique that resembles the missing-mass method, but with detection of an unstable recoil nucleus. In conventional missing-mass experiments, the binary reaction  $A(b, c)D$  is studied, and by detecting nucleus  $c$ , one obtains the excitation energy spectrum of the residual system  $D$ . Generally speaking, the more neutron-rich system  $D$  we want to study, the more proton-rich nucleus  $c$  has to be detected. As a result, nucleus  $c$  can even be unstable, *e.g.*,  ${}^6\text{Be}$ , that decays into  $p+p+\alpha$ , or singlet-state  ${}^2\text{He}$ , that decays into  $p+p$ . Nevertheless, we can deal with the unstable nucleus  $c$ , if all particles from its decay are detected. Having kinematically complete information on the unstable system  $c$ , we can reconstruct the excitation energy in the residual nucleus  $D$  and can perform its spectroscopy.

The reaction  $p({}^6\text{He}, {}^2\text{He}){}^5\text{H}$  was chosen for the search for  ${}^5\text{H}$ . It is reasonable to expect that neutrons in the ground state of  ${}^5\text{H}$  occupy the same orbitals as those in  ${}^6\text{He}$ . Hence, by removing one proton from  ${}^6\text{He}$ , we should selectively populate the ground state  $1/2^+$  of  ${}^5\text{H}$ . In other interesting reactions, such as  $t(t, p){}^5\text{H}$  and  $t({}^6\text{He}, {}^4\text{He}){}^5\text{H}$ , the two-neutron transfer is expected to populate also excited states  $5/2^+$  and  $3/2^+$ , which are predicted by theoretical calculations. These broad excited states will render more difficult, if not impossible, the identification of the ground state.

To detect all particles from the decay of the unstable recoil system  $c$  in the reaction  $A(b, c)D$ , we built the RIKEN telescope, which is a stack of solid-state

strip detectors. This telescope enables the measurement of angles, energy losses and energies of several particles detected in coincidence. The detectors have an annular hole for the beam. With this geometry, decay products of the system  $c$  can be detected at small angles in the laboratory system in inverse kinematics typical for many experiments with secondary beams.

The secondary beam of  ${}^6\text{He}$  at 36 A MeV was obtained using the fragment separator ACCULINA at JINR (Dubna). Two plastic scintillators were used for the identification of each particle of the secondary beam and for the measurement of its energy by time-of-flight. The trajectory of  ${}^6\text{He}$  was measured by two multiwire proportional chambers. We used a cryogenic target from GANIL (France), which was filled with hydrogen gas at a temperature of 35 K and pressure of 10 atm. The two protons originating from the decay of  ${}^2\text{He}$  were detected in coincidence by the RIKEN telescope. Besides protons, we also detected tritons from the decay  ${}^5\text{H} \rightarrow t+n+n$ , using a downstream telescope which consisted of a large-area SSD detector and a BGO crystal.

The key of this experiment was the combination of the exotic  ${}^6\text{He}$  beam provided by the fragment separator ACCULINA (Dubna, Russia), the hydrogen cryogenic target from GANIL (France), and the detection system based on the telescope of ringlike solid-state strip detectors (RIKEN).

The excitation energy spectrum obtained for this reaction shows a peak corresponding to a resonance  ${}^5\text{H}$  at  $1.7 \pm 0.3\text{ MeV}$  above the  $n+n+t$  threshold with a width of  $1.9 \pm 0.4\text{ MeV}$ . The angular distribution of the  $p({}^6\text{He}, {}^2\text{He}){}^5\text{H}$  reaction was measured as well as the energy correlation of two protons. The former has a shape consistent with the angular momentum transfer  $l = 0$  expected for the population of  ${}^5\text{H}_{g.s.}(1/2^+)$ , while the latter confirms the emission of the  ${}^2\text{He}$  virtual state in the reaction studied.

<sup>†</sup> Condensed from Phys. Rev. Lett. **87**, 092501 (2001)

<sup>\*1</sup> Joint Institute for Nuclear Research, Russia

<sup>\*2</sup> Grand Accelérateur National D'Ions Lourds, France

<sup>\*3</sup> Kurchatov Institute, Russia

## Experimental evidence for existence of ${}^7\text{H}^\dagger$

A. A. Korshennikov, E. Yu. Nikolskii, E. A. Kuzmin, A. Ozawa, K. Morimoto, F. Tokanai, R. Kanungo, I. Tanihata, N. K. Timofeyuk,<sup>\*1</sup> M. S. Golovkov,<sup>\*2</sup> A. S. Fomichev,<sup>\*2</sup> A. M. Rodin,<sup>\*2</sup> M. L. Chelnokov,<sup>\*2</sup> G. M. Ter-Akopian,<sup>\*2</sup> W. Mittig,<sup>\*3</sup> P. Roussel-Chomaz,<sup>\*3</sup> H. Savajols,<sup>\*3</sup> E. Pollacco,<sup>\*4</sup> A. A. Ogloblin,<sup>\*5</sup> and M. V. Zhukov<sup>\*6</sup>

[NUCLEAR REACTION,  $p({}^8\text{He}, pp){}^7\text{H}$ ,  $E = 61.3$  A MeV, Nuclear structure]

Progress in experimental technique including usage of secondary beams of short-lived radioactive nuclei has enabled studies of exotic nuclear systems in the vicinity and beyond the neutron drip line. Recently, experimental studies of  ${}^5\text{H}$  have been performed in the reactions  $p({}^6\text{He}, {}^2\text{He}){}^5\text{H}$ ,<sup>1)</sup>  $t(t, p){}^5\text{H}$ ,<sup>2)</sup> and  $d({}^6\text{He}, {}^3\text{He}){}^5\text{H}$ .<sup>3)</sup> These three measurements show a peak of  ${}^5\text{H}$  at  $\sim 1.8$  MeV above the decay threshold into  $t + 2n$ . Another recent experiment<sup>4)</sup> devoted to  ${}^5\text{H}$  show a  ${}^5\text{H}$  peak at relatively higher energy. Due to the known systematics of helium isotopes, where  ${}^8\text{He}$  having two more neutrons than  ${}^6\text{He}$  is more bound relative to the separation of two neutrons than  ${}^6\text{He}$ , and where  ${}^7\text{He}$  is less unbound than  ${}^5\text{He}$ , the results for  ${}^5\text{H}$  allow us to speculate that  ${}^7\text{H}$  may exist as a state in the vicinity of the  $t + 4n$  decay threshold.

Hardly  ${}^7\text{H}$  exists as a bound state. In numerous measurements performed previously using the  $\Delta E$ - $E$  method, the region of hydrogen and helium isotopes was studied in detail and no hyperbole of the bound  ${}^7\text{H}$  in two-dimensional  $\Delta E$ - $E$  plots was observed. However,  ${}^7\text{H}$  may exist as an unstable state. Being close to the threshold,  ${}^7\text{H}$  could be a particularly interesting system. It should undergo the unique five-particle decay into the  $t + 4n$  channel and its width may be very narrow. An extreme fraction of neutrons in  ${}^7\text{H}$ ,  $N/Z = 6$ , is comparable with that in neutron stars.

The experimental search for unstable  ${}^7\text{H}$  presents a difficult task, and this resonance has never been observed. Recent theoretical calculation of  ${}^7\text{H}$  within the seven-body hyperspherical functions method suggests that  ${}^7\text{H}$  can be unbound with respect to the  $t + 4n$  decay by 840 keV.<sup>5)</sup>

We carried out an additional attempt to estimate the energy range for  ${}^7\text{H}$  to be measured. In the present calculations, we used the K-harmonics approach and calculated  ${}^3,5,7\text{H}$  and  ${}^4,6,8\text{He}$  as A-body systems trying to reproduce the binding energies of  ${}^3,5\text{H}$  and  ${}^4,6,8\text{He}$  simultaneously. As a result, we obtained for the  ${}^7\text{H}$

energy relative to the  $t + 4n$  threshold an estimate of about 3 MeV as an upper limit.

Considering the experimental search for  ${}^7\text{H}$ , we considered the following. It is reasonable to suppose that neutrons in the ground state of  ${}^7\text{H}$  occupy the same orbitals as those in  ${}^8\text{He}$ . Hence, by removing one proton from  ${}^8\text{He}$ , we should obtain a good chance of populating the ground state  $1/2^+$  of  ${}^7\text{H}$ . Consequently, we have chosen the reaction  $p({}^8\text{He}, pp){}^7\text{H}$  for the experimental search for  ${}^7\text{H}$ .

The experiment was performed at RIKEN using a secondary beam of  ${}^8\text{He}$  produced by the fragment separator RIPS from the fragmentation of a primary beam of  ${}^{18}\text{O}$ . The obtained secondary  ${}^8\text{He}$  beam had a very high intensity of  $\sim 300000$  particles per second and an energy of 61.3 A MeV with an energy spread of 2.6 A MeV. (The beam energy and parameters of the measuring system were optimized in computer simulations preceding the experiment.)

As a proton target, we used a cryogenic target from GANIL (France), which was filled with hydrogen gas at a temperature of 35 K and a pressure of 10 atm. The target thickness was  $6 \times 10^{21}$  protons/cm<sup>2</sup>.

The two protons originating from the reaction  $p({}^8\text{He}, pp){}^7\text{H}$  were detected in coincidence by the RIKEN telescope which is a stack of Si strip detectors. This telescope enables for the detection of several particles in coincidence, identification of each particle and measurement of their energies and angles.

Experimental results obtained in the pp-coincidences show a very interesting feature: a very rapid increase in the  ${}^7\text{H}$  spectrum near the  $t + 4n$  threshold. The experimental spectrum increases near the threshold even more sharply than a two-body phase-space. This provides a strong indication of the possible existence of the  ${}^7\text{H}$  state near the  $t + 4n$  threshold. For further studies of  ${}^7\text{H}$ , apart from the  $p({}^8\text{He}, pp){}^7\text{H}$  reaction, reactions  $d({}^8\text{He}, {}^3\text{He}){}^7\text{H}$  and  $t({}^8\text{He}, {}^4\text{He}){}^7\text{H}$  also seem to be promising.

<sup>†</sup> Condensed from the article in Phys. Rev. Lett. **90**, 082501 (2003)

<sup>\*1</sup> University of Surrey, UK

<sup>\*2</sup> Joint Institute for Nuclear Research, Russia

<sup>\*3</sup> Grand Accélérateur National D'Ions Lourds, France

<sup>\*4</sup> Département D'Astrophysique, de Physique des Particules, de Physique Nucléaire et de L'Instrumentation Associée, France

<sup>\*5</sup> Kurchatov Institute, Russia

<sup>\*6</sup> Chalmers University of Technology and Göteborg University, Sweden

### References

- 1) A. A. Korshennikov et al.: Phys. Rev. Lett. **87**, 092501 (2001).
- 2) M. S. Golovkov et al.: Phys. Lett. B **556**, 70 (2003).
- 3) G. M. Ter-Akopian et al.: under preparation for publication.
- 4) M. Meister et al.: Nucl. Phys. A **723**, 13 (2003).
- 5) N. K. Timofeyuk: Phys. Rev. C **65**, 064306 (2002).

## Experimental evidence for a specific structure of ${}^8\text{He}^\dagger$

A. A. Korshennikov, E. Yu. Nikolskii, E. A. Kuzmin, A. Ozawa, K. Morimoto, F. Tokanai, R. Kanungo, I. Tanihata, N. K. Timofeyuk,<sup>\*1</sup> M. S. Golovkov,<sup>\*2</sup> A. S. Fomichev,<sup>\*2</sup> A. M. Rodin,<sup>\*2</sup> M. L. Chelnokov,<sup>\*2</sup> G. M. Ter-Akopian,<sup>\*2</sup> W. Mittig,<sup>\*3</sup> P. Roussel-Chomaz,<sup>\*3</sup> H. Savajols,<sup>\*3</sup> E. Pollacco,<sup>\*4</sup> A. A. Ogloblin,<sup>\*5</sup> and M. V. Zhukov<sup>\*6</sup>

[NUCLEAR REACTION,  $p({}^8\text{He}, t){}^6\text{He}_{g.s.}$ ,  $p({}^8\text{He}, t){}^6\text{He}^*(2^+)$ ,  $E = 61.3\text{ A MeV}$ , Nuclear structure]

We investigated the two-neutron transfer reaction  $p({}^8\text{He}, t)$  populating the ground and excited  $2^+$  state of  ${}^6\text{He}$ . The experiment was performed at RIKEN using a secondary beam of  ${}^8\text{He}$  produced by the fragment separator RIPS from the fragmentation of a primary beam of  ${}^{18}\text{O}$ . The obtained secondary  ${}^8\text{He}$  beam had an intensity of  $\sim 300000$  pps and an energy of  $61.3\text{ A MeV}$ . As a proton target we used a cryogenic target from GANIL (France), which was filled with a hydrogen gas at a temperature of  $35\text{ K}$  and a pressure of  $10\text{ atm}$ . The target thickness was  $6 \times 10^{21}$  protons/cm<sup>2</sup>. The recoil triton from the  $p({}^8\text{He}, t)$  reaction was detected using the RIKEN telescope which is a stack of Si strip detectors. In addition we detected  ${}^6\text{He}$  nuclei and  $\alpha$  particles from the decay of  ${}^6\text{He}^*(2^+)$  into  $\alpha + 2n$  using a downstream detection system consisting of a dipole magnet and plastic scintillators.

Let us first consider the simplest assumption on the structure of  ${}^8\text{He}$  (below we will see that in reality another configuration is realized in  ${}^8\text{He}$ ). If the ground state of  ${}^8\text{He}$  would contain subsystem  ${}^6\text{He}$  mainly in the state  $0^+$ , then the  ${}^8\text{He}(p, t)$  reaction would populate preferentially  ${}^6\text{He}_{g.s.}(0^+)$ . The cross section for the population of  ${}^6\text{He}^*(2^+)$  would be some order of magnitude lower, because the latter would be the second order process. It requires a two-neutron peak-up from  ${}^8\text{He}$ , such as in  $p({}^8\text{He}, t){}^6\text{He}_{g.s.}$ , but in addition, in this case, the  ${}^6\text{He}(0^+)$  subsystem should be excited to the  $2^+$  state. As a result, the cross section of the  $p({}^8\text{He}, t){}^6\text{He}^*(2^+)$  reaction would be suppressed.

The obtained experimental data show that in reality, the situation is just the opposite: the cross section of

the  $p({}^8\text{He}, t){}^6\text{He}^*(2^+)$  reaction is higher than that of  $p({}^8\text{He}, t){}^6\text{He}_{g.s.}$ . It denotes that the ground state of  ${}^8\text{He}$  contains the subsystem  ${}^6\text{He}$  in the  $2^+$  state with a large weight.

Qualitatively, it is consistent with the consideration of  ${}^8\text{He}$  in a simple model shown in Ref. 1, where a five-body ( $\alpha + 4n$ ) wave function of  ${}^8\text{He}$  was constructed with the four antisymmetrized neutrons in the  $p_{3/2}$  states relative to the  $\alpha$  core. Within this model, one can strictly investigate the spin-parity of the  ${}^6\text{He}$  subsystem in  ${}^8\text{He}$ . As a result we obtained weights for various  $J^\pi$  in the  ${}^6\text{He}$  subsystem:  $P(0^+) = \frac{1}{6}$ ,  $P(1^+) = 0$ ,  $P(2^+) = \frac{5}{6}$ ,  $P(3^+) = 0$ . That is, the excited  $2^+$  state of  ${}^6\text{He}$  is predominant in the  ${}^8\text{He}$  ground state wave function.

Finally, note that recently in Dubna (Russia) the  $(p, t)$  reaction was investigated at a lower energy of the  ${}^8\text{He}$  beam,  $26\text{ A MeV}$ , and also, a cross section for the  ${}^6\text{He}^*(2^+)$  channel higher than that for  ${}^6\text{He}_{g.s.}$  was observed. Also, an indication on the  ${}^6\text{He}(2^+) + 2n$  configuration in the ground state of  ${}^8\text{He}$  was previously obtained in fragmentation of  ${}^8\text{He}$  in the C target.<sup>2)</sup>

In summary, the  $p({}^8\text{He}, t)$  reaction populating the ground and excited  $2^+$  state of  ${}^6\text{He}$  was investigated. The obtained results suggest a specific structure of the ground state of  ${}^8\text{He}$  containing the subsystem  ${}^6\text{He}$  in the  $2^+$  state with a large weight.

### References

- 1) M. V. Zhukov, A. A. Korshennikov, and M. H. Smedberg: Phys. Rev. C **50**, R1 (1994).
- 2) K. Markenroth, M. Meister, B. Eberlein et al.: Nucl. Phys. A **679**, 462 (2001).

<sup>†</sup> Condensed from the article in Phys. Rev. Lett. **90**, 082501 (2003)

<sup>\*1</sup> University of Surrey, UK

<sup>\*2</sup> Joint Institute for Nuclear Research, Russia

<sup>\*3</sup> Grand Accelérateur National D'Ions Lourds, France

<sup>\*4</sup> Département D'Astrophysique, de Physique des Particules, de Physique Nucléaire et de L'Instrumentation Associée, France

<sup>\*5</sup> Kurchatov Institute, Russia

<sup>\*6</sup> Chalmers University of Technology and Göteborg University, Sweden

# Measurement of the vector analyzing power for the $\vec{p} + {}^6\text{He}$ , 71 MeV/nucleon elastic scattering using spin-polarized solid proton target

M. Hatano,<sup>\*1</sup> T. Wakui,<sup>\*2</sup> H. Sakai,<sup>\*1,\*2</sup> T. Uesaka,<sup>\*2</sup> A. Tamii,<sup>\*3</sup> T. Kawabata,<sup>\*2</sup> N. Aoi, H. Iwasaki,<sup>\*1</sup>  
Y. Yanagisawa, T. Ohnishi, K. Sekiguchi, K. Yako,<sup>\*1</sup> H. Okamura,<sup>\*4</sup> N. Sakamoto, Y. Satou,<sup>\*5</sup>  
K. Suda,<sup>\*6</sup> Y. Maeda,<sup>\*1</sup> T. Saito,<sup>\*1</sup> H. Kuboki,<sup>\*1</sup> K. Itoh,<sup>\*6</sup> T. Ikeda,<sup>\*6</sup> T. K. Onishi,<sup>\*1</sup>  
M. Sasano,<sup>\*1</sup> Y. Ichikawa,<sup>\*1</sup> N. Matsui,<sup>\*5</sup> and D. Suzuki<sup>\*1</sup>

[polarized solid proton target, RI-beam experiment]

For our RI-beam experiments, we have constructed a new spin-polarized solid proton target system. The most significant advantage of our target is its applicability in a low magnetic field of 100 mT and at liquid N<sub>2</sub> temperature. In July 2003, the first experiment using the RI-beam, that is, a vector analyzing power ( $A_y$ ) measurement in  $\vec{p} + {}^6\text{He}$  elastic scattering at 71 MeV/nucleon, was carried out. The measured angular region was 40° to 75° in the center-of-mass system. The aim was to determine the spin-orbit potential between protons and  ${}^6\text{He}$ . In this paper, an overview of the experiment is reported.

As a target material, we used a single crystal of naphthalene (C<sub>10</sub>H<sub>8</sub>). Protons in the naphthalene crystal were polarized by means of a pulsed dynamic nuclear polarization method.<sup>1,2)</sup> For details regarding the proton polarizing system see Refs. 3 and 4.

The experiment was performed using RIPS at the RIKEN Ring Cyclotron Facility. The  ${}^6\text{He}$  beam was produced by a fragmentation reaction of a  ${}^{12}\text{C}$  beam with an energy of 92 MeV/nucleon penetrating a 1.39 g/cm<sup>2</sup> Be target. The energy of the  ${}^6\text{He}$  beam was degraded by an aluminum degrader with a thickness of 0.32 g/cm<sup>2</sup> to an energy of 71 MeV/nucleon. The purity of the secondary beam was 95%, and the intensity was 170 kcps on average.

The secondary beam bombarded the polarized proton target with a thickness of 113 mg/cm<sup>2</sup>. The target was placed approximately 1 m downstream of the F3 focal point.

To detect leading particles (mainly  ${}^6\text{He}$ ), we used a forward-counter placed approximately 1 m downstream of the target. The forward-counter consisted of a multiwired drift chamber (MWDC) and three layers of plastic scintillator hodoscopes placed downstream of the MWDC. The MWDC was used to measure the trajectory of the leading particles. The plastic scintillator hodoscopes were used to identify the leading particle with the standard  $\Delta E$ - $E$  method.

To detect recoil protons, a pair of backward-counters was used. One was for the left-hand event and the other was for the right-hand event. Each counter consisted of two 5-mm strip silicon detectors (X-PSD, Y-PSD) and plastic scintillators. The PSDs were set perpendicular to each other and used to obtain two-dimensional-position information on recoiled particles. The particle identification of recoiled particles were performed with the  $\Delta E$  information from the PSDs and  $E$  information from plastic scintillators. To discriminate background events scattered,  ${}^6\text{He}$  particles and recoiled protons were detected in coincidence. In such a coincidence detection, one can select the elastic scattering events only by identifying the  ${}^6\text{He}$  particles at the forward-counter, since  ${}^6\text{He}$  does not have a bound excited state.

Figure 1 shows the asymmetry of  $\vec{p} + {}^6\text{He}$  elastic scattering events measured at 40° in the center-of-mass system. The horizontal axis corresponds to the angle of scattered  ${}^6\text{He}$  particles. Figure 1 (a) and (b) show summaries of the data when the proton polarization was “UP” and “DOWN” respectively. The data analysis to deduce  $A_y$  and the differential cross section is now in progress.

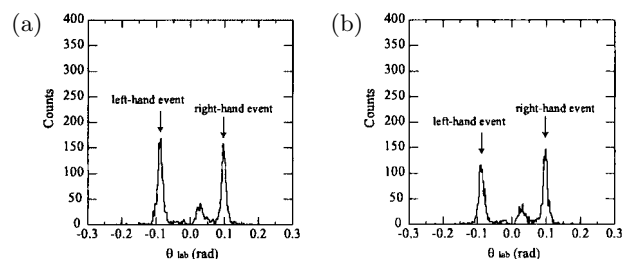


Fig. 1. Asymmetry measured at 40° in the center-of-mass system. (a) when the proton polarization was “UP”. (b) when the proton polarization was “DOWN”.

## References

- 1) A. Henstra et al.: Phys. Lett. A **134**, 134 (1988).
- 2) M. Iinuma et al.: Phys. Rev. Lett. **84**, 171 (2000).
- 3) M. Hatano et al.: RIKEN Accel. Prog. Rep. **36**, 48 (2003).
- 4) T. Wakui et al.: RIKEN Accel. Prog. Rep. **37**, 181 (2004).

<sup>\*1</sup> University of Tokyo

<sup>\*2</sup> Center for Nuclear Study, University of Tokyo

<sup>\*3</sup> Research Center for Nuclear Physics, Osaka University

<sup>\*4</sup> Tohoku University

<sup>\*5</sup> Tokyo Institute of Technology

<sup>\*6</sup> Saitama University

## Experimental test of Bell's inequality *via* the ( $d$ , $^2\text{He}$ ) reaction

T. Saito,<sup>\*1</sup> H. Sakai,<sup>\*1,\*2</sup> T. Ikeda,<sup>\*3</sup> K. Itoh,<sup>\*3</sup> T. Kawabata,<sup>\*2</sup> H. Kuboki,<sup>\*1</sup> Y. Maeda,<sup>\*1</sup> N. Matsui,<sup>\*4</sup>  
M. Sasano,<sup>\*1</sup> Y. Satou,<sup>\*4</sup> K. Sekiguchi, K. Suda,<sup>\*3</sup> A. Tamii,<sup>\*5</sup> T. Uesaka,<sup>\*2</sup> and K. Yako<sup>\*1</sup>

[Bell's inequality, ( $d$ ,  $^2\text{He}$ ) reaction]

Since the discovery of Bell's inequality (BI),<sup>1)</sup> many experiments have been performed up to now to verify the violation of BI and to establish the correctness of the quantum mechanical description of nature. It should be noted that, even though BI was originally derived from a consideration on correlation of two spin  $\frac{1}{2}$  particles in a spin singlet ( $^1S_0$ ) state, most of the experiments performed so far have employed polarization-correlation of two photons.

The only one exception using spin  $\frac{1}{2}$  particles is the experiment by Laméhi-Rachti and Mittig (LRM).<sup>2)</sup> LRM measured spin-correlations of proton pairs produced by 13.5 MeV  $pp$ -elastic  $S$ -wave scattering. Although their results agreed with quantum mechanics and violated the classical limits of BI, There are some problems in their estimation of the systematic errors. The incident proton energy is so high that their estimation of effects by the mixture of the spin triplet states in the final two protons is not sufficient.

We are planning to test BI by measuring spin-correlation of proton pairs produced by the ( $d$ ,  $^2\text{He}$ ) reaction. Here we define a  $^2\text{He}$  as a pair of protons coupled in the  $^1S_0$  state by the final state interaction. Use of ( $d$ ,  $^2\text{He}$ ) reaction has following advantages: (1) In the case of LRM's experiment, the relative energy of the two protons was fixed kinematically, while the ( $d$ ,  $^2\text{He}$ ) reaction enables us to select as small relative energy as possible. Hence we can produce high purity of  $^1S_0$ -state proton pairs. (2) Since the kinetic energy of the protons in the laboratory frame is high, the proton polarizations can be measured easily.

We have performed experiments at RIKEN in 2003. We measured the  $^1\text{H}(d, ^2\text{He})n$  reaction at 270 MeV. The beam was injected into a liquid hydrogen target<sup>3)</sup> of 70 mg/cm<sup>2</sup> thick.  $^2\text{He}$  scattered at  $0^\circ$  were momentum analyzed by a spectrometer SMART and detected with a proton polarimeter EPOL placed at the second focal plane of SMART. Typical beam intensity was 0.3 nA and we detected  $^2\text{He}$  at the rate of 1–1.5 kcps. An example of the energy spectrum is shown in Fig. 1.

A schematic view of EPOL is presented in Fig. 2. EPOL consists of three multi-wire drift chambers (MWDCs), two sets of plastic scintillator hodoscopes and an analyzer target (5.0 cm thick carbon block).

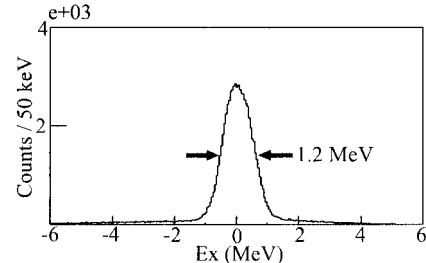


Fig. 1. Typical excitation energy spectrum of  $^1\text{H}(d, ^2\text{He})n$  reaction at  $E_d = 270$  MeV.

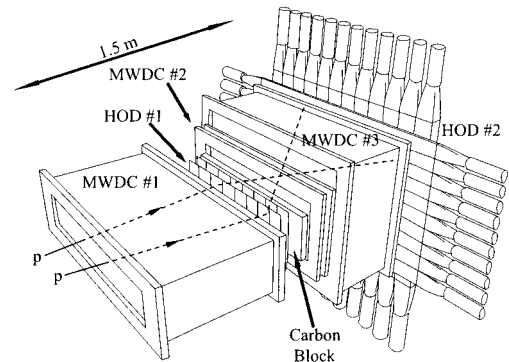


Fig. 2. Schematic view of the proton polarimeter EPOL.

The incident pairs of protons are simultaneously scattered from the analyzer target. By measuring the left-right asymmetry of the scattering for each proton, spin-correlation function  $\Pi(\vec{a}, \vec{b}) = \langle \vec{\sigma}_1 \cdot \vec{a} \vec{\sigma}_2 \cdot \vec{b} \rangle$  can be derived, where  $\vec{a}$  and  $\vec{b}$  are the direction of the reference axes of the spin measurement, and  $\vec{\sigma}_1$  and  $\vec{\sigma}_2$  are the Pauli matrices of each proton. If the angle between the two axes  $\vec{a}$  and  $\vec{b}$  is  $45^\circ$ , quantum mechanical prediction is  $|\Pi_{\text{QM}}(45^\circ)| = \frac{1}{\sqrt{2}}$ , whereas the classical limit by BI is  $|\Pi_{\text{BI}}(45^\circ)| \leq \frac{1}{2}$ . Thus, the violation of Bell's inequality can be tested.

We have obtained data enough to verify the violation of Bell's inequality by five standard deviations. Data analysis is now in progress.

### References

- 1) J. S. Bell: *Physics* **1**, 195 (1964).
- 2) M. Laméhi-Rachti and W. Mittig: *Phys. Rev. D* **14**, 2543 (1976).
- 3) T. Ikeda et al.: *RIKEN Accel. Prog. Rep.* **37**, 82 (2004).

<sup>\*1</sup> Department of Physics, University of Tokyo

<sup>\*2</sup> Center for Nuclear Study, University of Tokyo

<sup>\*3</sup> Department of Physics, Saitama University

<sup>\*4</sup> Course of Fundamental Physics, Tokyo Institute of Technology

<sup>\*5</sup> Research Center for Nuclear Physics, Osaka University

Spectroscopy of  $^{13}\text{B}$  via  $^4\text{He}(^{12}\text{Be}, ^{13}\text{B}\gamma)$ 

S. Ota,<sup>\*1</sup> S. Shimoura,<sup>\*2</sup> H. Iwasaki,<sup>\*3</sup> M. Kurokawa, S. Michimasa,<sup>\*2</sup> S. Kubono,<sup>\*2</sup> T. Teranishi,<sup>\*2</sup> M. Notani,<sup>\*2</sup> M. Tamaki,<sup>\*2</sup> T. Murakami,<sup>\*1</sup> N. Iwasa,<sup>\*4</sup> T. Motobayashi, Y. Yanagisawa, T. Minemura, S. Takeuchi, T. Gomi,<sup>\*5</sup> K. Yamada,<sup>\*5</sup> A. Saito,<sup>\*5</sup> H. Baba,<sup>\*5</sup> Y. U. Matsuyama,<sup>\*5</sup> S. Kanno,<sup>\*5</sup> E. Takeshita,<sup>\*5</sup> K. Demichi,<sup>\*5</sup> K. Hasegawa,<sup>\*5</sup> K. Kurita,<sup>\*5</sup> H. Sakurai,<sup>\*3</sup> N. Aoi, E. Ideguchi,<sup>\*2</sup> A. Odahara,<sup>\*6</sup> T. Fukuchi,<sup>\*2</sup> K. Miller,<sup>\*7</sup> Z. Elekes, and M. Ishihara

[NUCLEAR REACTION,  $^4\text{He}(^{12}\text{Be}, ^{13}\text{B}\gamma)$ , transfer reaction, in-beam  $\gamma$ -ray spectroscopy]

The disappearance of regular magic numbers in neutron-rich nuclei has been one of the most interesting phenomena. Focusing on the  $N = 8$  magicity, we have studied  $^{13}\text{B}$ , where the spins even for low-lying states have not been assigned.<sup>1-4)</sup>

We measured the differential cross section of the proton transfer reaction  $^4\text{He}(^{12}\text{Be}, ^{13}\text{B}\gamma)$ , which is expected to populate the proton single particle state. We assigned the spin and parity of the highest bound excited state for the first time.

The experiment was performed at RIPS beam line in RIKEN. A primary beam of  $^{18}\text{O}$  at 100 MeV/nucleon bombarded a 1.85 g/cm<sup>2</sup>-thick  $^9\text{Be}$  target. A secondary beam of  $^{12}\text{Be}$  was produced as the fragment and separated by the RIPS. Its intensity and energy were  $2 \times 10^5$  particles/s and 50 MeV/nucleon, respectively. The  $^{12}\text{Be}$  was identified event-by-event via a TOF- $\Delta E$  method with two plastic scintillators and bombarded a 120 mg/cm<sup>2</sup>-thick liquid helium target. Outgoing particles were measured by a hodoscope which consists of 13- $\Delta E$  and 16- $E$  plastic scintillators and identified by the TOF- $\Delta E$ - $E$  method. The TOF was the flight time between the target and a  $\Delta E$  plastic scintillator.

Excited states in  $^{13}\text{B}$  were identified by de-excitation  $\gamma$  rays, which were detected by an array of segmented-Ge detectors<sup>5)</sup> and the DALI (II) system.<sup>6)</sup> The array of segmented-Ge consists of six segmented-Ge detectors located 140 degrees to the beam direction. The DALI (II) system consists of 75 NaI (TI) detectors at forward angles. The detection efficiency of Ge detectors was 0.17% for the 1.332-MeV  $\gamma$  ray from  $^{60}\text{Co}$  source and that of DALI (II) was 9.8% for the 661.6-keV  $\gamma$  ray from  $^{137}\text{Cs}$  source. The energy resolutions of Ge detectors and the DALI (II) system, were 16 keV ( $\sigma$ ) and 55 keV ( $\sigma$ ) respectively, for the Doppler-corrected 2.1-MeV  $\gamma$  ray from moving ( $\beta \sim 0.3$ )  $^{12}\text{Be}$ .

The differential cross section of the  $^4\text{He}(^{12}\text{Be}, ^{13}\text{B}\gamma)$  reaction for the 4.8-MeV excited state of  $^{13}\text{B}$  is indi-

cated by closed circles in Fig. 1. Three curves were obtained by zero-range DWBA calculations with assumptions of transfer angular momenta  $l = 0, 1$ , and 2. The set of optical potentials<sup>7,8)</sup> used in the calculation is listed in Table 1. The experimental angular distribution is fitted with the DWBA calculation with  $l = 0$ , which indicates that the transferred angular momentum was  $l = 0$ . Since the ground state of  $^{12}\text{Be}$  is  $0^+$ , we assigned  $J^\pi = 1/2^+$  to the 4.8-MeV excited state. Further analysis is in progress.

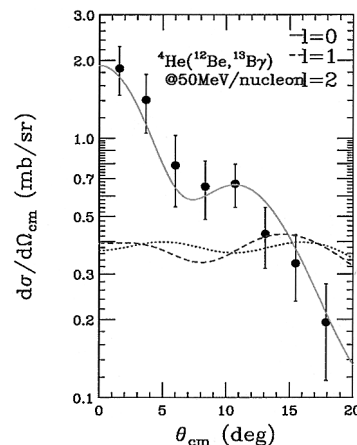


Fig. 1. Differential cross section of  $^4\text{He}(^{12}\text{Be}, ^{13}\text{B}\gamma)$  reaction.

Table 1. Optical potentials used in DWBA calculations. (a:  $^4\text{He}+^{12}\text{C}^{7)}$ , b:  $^3\text{He}+^{12}\text{C}^{8)}$

	$V_0$ (MeV)	$r_V$ (fm)	$a_V$ (fm)	$W_0$ (MeV)	$r_W$ (fm)	$a_W$ (fm)
a	75.680	1.277	0.728	13.880	1.885	0.425
b	108.47	1.020	0.828	18.483	1.171	0.594

## References

- 1) F. Ajzenberg-Selove et al.: Phys. Rev. C **17**, 1283 (1978).
- 2) V. Guimarães et al.: Phys. Rev. C **61**, 064609 (2000).
- 3) N. Aoi et al.: Phys. Rev. C **66**, 014301 (2002).
- 4) R. Kalpakcieva et al.: Eur. Phys. J. A **7**, 451 (2000).
- 5) S. Shimoura et al.: CNS Annu. Rep. **2001**, 5.
- 6) S. Takeuchi et al.: RIKEN Accel. Prog. Rep. **36**, 148 (2003).
- 7) A. Ingemarsson et al.: Nucl. Phys. A **676**, 3 (2000).
- 8) A. Ingemarsson et al.: Nucl. Phys. A **696**, 3 (2001).

\*1 Department of Physics, Kyoto University  
 \*2 Center for Nuclear Study, University of Tokyo  
 \*3 Department of Physics, University of Tokyo  
 \*4 Department of Physics, Tohoku University  
 \*5 Department of Physics, Rikkyo University  
 \*6 Nishinohon Institute of Technology  
 \*7 Michigan State University, USA

# $^{11}\text{C}(p,\gamma)^{12}\text{N}$ reaction studied by the Coulomb dissociation method

T. Minemura, T. Motobayashi, S. Shimoura,<sup>\*1</sup> H. Murakami,<sup>\*2</sup> Y. Ando,<sup>\*2</sup> Y. Yanagisawa, Y. Iwata,<sup>\*3</sup> S. Ozawa, S. Takeuchi, Y. Higurashi, K. Yamada,<sup>\*2</sup> T. Gomi,<sup>\*2</sup> M. Serata,<sup>\*2</sup> H. Kobayashi,<sup>\*2</sup> T. Teranishi,<sup>\*1</sup> N. Aoi, M. Hirai,<sup>\*4</sup> H. Iwasaki,<sup>\*4</sup> N. Imai, N. Iwasa,<sup>\*5</sup> M. Uesaka, H. Akiyoshi, Zs. Fülöp,<sup>\*6</sup> H. Sakurai,<sup>\*4</sup> K. Yoshida, Z. Liu,<sup>\*7</sup> and M. Ishihara

[NUCLEAR REACTIONS:  $^{208}\text{Pb}(^{12}\text{N}, ^{11}\text{C} p)^{208}\text{Pb}$ , Coulomb dissociation]

The importance of the radiative capture reaction,  $^{11}\text{C}(p,\gamma)^{12}\text{N}$ , at low energies has been discussed in connection with an astrophysical nuclear burning process called the hot pp chain.

There are two resonant states in  $^{12}\text{N}$  of astrophysical interest: the first excited state with  $J^\pi = 2^+$  at  $E_{\text{ex}} = 0.960$  MeV, and the second one with  $2^-$  at 1.19 MeV. In terms of astrophysical implications, the most important property is the radiative width ( $\Gamma_\gamma$ ) of the 1.19 MeV state.

Experiments have been performed at RIKEN using the secondary beam line, RIPS. A 77.0 MeV/nucleon  $^{12}\text{N}$  radioactive beam was produced through a fragmentation reaction of a primary 135 MeV/nucleon  $^{16}\text{O}$  beam. A 30 mg/cm<sup>2</sup>  $^{208}\text{Pb}$  target was bombarded by a secondary  $^{12}\text{N}$  beam. Protons and  $^{11}\text{C}$  produced in the  $^{12}\text{N}$  dissociation were detected by a plastic-scintillator hodoscope with an active area of  $1 \times 1$  m<sup>2</sup> located 5.1 m downstream of the target. The energy of the fragment was determined by its measured mass and the velocity obtained from the TOF. The complete kinematics of the reaction products, the total energy and relative momentum vector of the  $p+^{11}\text{C}$  system were thus fully determined. To measure  $\gamma$  rays emitted from excited states of  $^{11}\text{C}$  in the channel of  $^{12}\text{N} \rightarrow p+^{11}\text{C}^*$ , a  $\gamma$ -ray detector system called DALI (Detector Assembly for Low Intensity radiation), consisting of 64 NaI(Tl) scintillators, was placed around the target.

Figure 1(a) shows the comparison between the experimental relative energy spectrum for the  $^{11}\text{C}(p,\gamma)^{12}\text{N}$  reaction and the calculation considered E1 interference effect. The two resonants and nonresonant contributions are plotted separately. The direct capture cross section for the E1 transition has been calculated using the direct capture component of the ANC measurement result.<sup>1)</sup> The bump observed at around 0.6 MeV by the experimental relative-energy spectrum is mainly due to the E1 excitation of  $^{12}\text{N}$  from the  $1^+$  ground state to the  $2^-$  state at  $E_{\text{ex}} =$

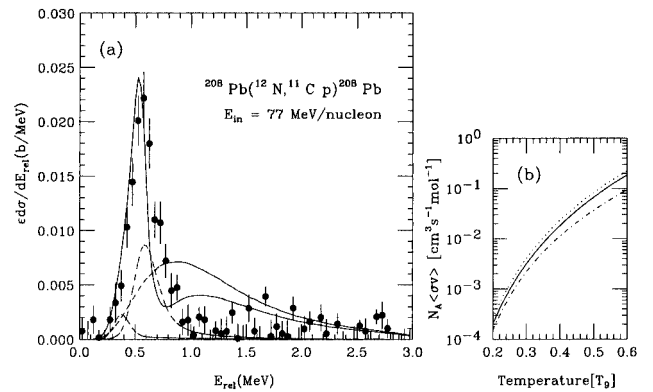


Fig. 1. (a) Comparison between relative energy and E1 interference effect. (b) Reaction rate for the  $^{12}\text{N}(p,\gamma)^{11}\text{C}$  reaction.

1.19 MeV. The present result ( $\Gamma_\gamma = 13.0 \pm 0.5$  meV) considered E1 interference effect is consistent with that of the Coulomb dissociation experiment at GANIL<sup>2)</sup> ( $\Gamma_\gamma = 6^{+7}_{-3.5}$  meV), but the accuracy is markedly improved. Also, the E1 interference effect was not considered in the GANIL result. The radiative width measured in the present experiment is in between the two different predictions by Wiescher *et al.*<sup>3)</sup> ( $\Gamma_\gamma = 2$  meV) and Descouvemont and Baraffe<sup>4)</sup> ( $\Gamma_\gamma = 45$  or 49 meV). The  $^{11}\text{C}(p,\gamma)^{12}\text{N}$  reaction rate is shown in Fig. 1(b). The solid curve is our updated reaction rate summed for direct capture and second resonance. The dotted curve is from Tang *et al.*,<sup>1)</sup> and the dash-dotted line is the result treated as noninterfering in Ref. 2.

## References

- 1) X. Tang et al.: Phys. Rev. C **67**, 015804 (2003).
- 2) A. Lefebvre et al.: Nucl. Phys. A **592**, 69 (1995).
- 3) M. Wiescher et al.: Astrophys. J. **343**, 352 (1989).
- 4) P. Descouvemont et al.: Nucl. Phys. A **646**, 261 (1999).

<sup>\*1</sup> Center for Nuclear Study, University of Tokyo

<sup>\*2</sup> Rikkyo University

<sup>\*3</sup> National Institute of Radiological Sciences

<sup>\*4</sup> University of Tokyo

<sup>\*5</sup> Tohoku University

<sup>\*6</sup> ATOMKI, Hungary

<sup>\*7</sup> Institute of Modern Physics, China



Molecular states in  $^{12}\text{Be}$  and  $^{14}\text{Be}$ 

A. Saito,<sup>\*1</sup> S. Shimoura,<sup>\*2</sup> S. Takeuchi, T. Motobayashi, T. Minemura, Y. U. Matsuyama,<sup>\*1</sup> H. Baba,<sup>\*1</sup> H. Akiyoshi, Y. Ando,<sup>\*1</sup> N. Aoi, Zs. Fülöp,<sup>\*3</sup> T. Gomi,<sup>\*1</sup> Y. Higurashi, M. Hirai,<sup>\*4</sup> K. Ieki,<sup>\*1</sup> N. Imai, N. Iwasa,<sup>\*5</sup> H. Iwasaki,<sup>\*6</sup> Y. Iwata,<sup>\*4</sup> S. Kanno,<sup>\*1</sup> H. Kobayashi,<sup>\*1</sup> S. Kubono,<sup>\*2</sup> M. Kunibu,<sup>\*1</sup> M. Kurokawa, Z. Liu, S. Michimasa,<sup>\*2</sup> T. Nakamura,<sup>\*7</sup> S. Ozawa, H. K. Sakai,<sup>\*1</sup> H. Sakurai,<sup>\*6</sup> M. Serata,<sup>\*1</sup> E. Takeshita,<sup>\*1</sup> T. Teranishi,<sup>\*2</sup> K. Ue,<sup>\*2</sup> K. Yamada,<sup>\*1</sup> Y. Yanagisawa, and M. Ishihara

[NUCLEAR REACTIONS:  $^{12}\text{C}(^{14}\text{Be}, ^6\text{He}+^6\text{He})\text{X}$ ,  $^4\text{He}(^{12}\text{Be}, ^6\text{He}+^6\text{He})^4\text{He}$ ]

Excited states in neutron-rich beryllium isotopes were investigated using radioactive beams of  $^{14}\text{Be}$  and  $^{12}\text{Be}$  to bombard carbon and liquid helium targets, respectively. The invariant-mass method and the angular-correlation techniques were employed to measure the excitation energies and spins of excited states above the  $^6\text{He}+^6\text{He}$  and  $^6\text{He}+^8\text{He}$  thresholds in  $^{12}\text{Be}$  and  $^{14}\text{Be}$ , respectively. The details of the  $^{14}\text{Be}+^{12}\text{C}$  experiment are described in Ref. 1.

Figure 1(a) shows the decay energy spectrum of  $^6\text{He}+^6\text{He}$  in the two-neutron removal reaction of the  $^{14}\text{Be}$  beam on the  $^{12}\text{C}$  target. Two peaks were observed at 1.7 MeV and 2.7 MeV, which correspond to 11.8 MeV and 12.8 MeV, respectively, in addition to known levels at 14.9 MeV and 16.1 MeV.<sup>2)</sup> The spectrum was considered to include a large contribution of the continuum background. Therefore it is difficult to apply the angular correlation techniques for the observed peaks to determine the spins of the excited states. Inelastic scattering of the  $^{12}\text{Be}$  beam on the liquid helium target was performed to obtain more precise information on the highly excited states in  $^{12}\text{Be}$ .

The experiment was carried out at RIPS in the RIKEN Accelerator Research Facility. The secondary beam of  $^{12}\text{Be}$  at 60 A MeV was produced by a fragmentation reaction of the  $^{18}\text{O}$  beam at 100 A MeV on a beryllium target. The average intensity of the secondary beam was  $3 \times 10^4$  particles per second. The thickness of the secondary target was 250 mg/cm<sup>2</sup>. Reaction products of helium isotopes were measured and identified using a hodoscope of a plastic scintillator array with an active area of  $1 \times 1$  m<sup>2</sup> placed 3.9 m downstream of the secondary target.

Figure 1(b) shows the decay energy spectrum of  $^6\text{He}+^6\text{He}$  in the  $^{12}\text{Be}+^4\text{He}$  reaction. Two strong peaks are seen at 0.8 MeV and 1.2 MeV, which were not identified in Fig. 1(a), in addition to the weak bump

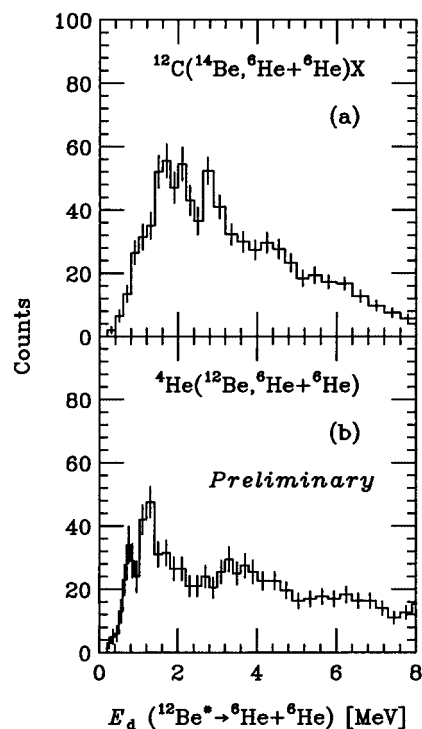


Fig. 1. Decay energy spectra of  $^{12}\text{Be}^* \rightarrow ^6\text{He}+^6\text{He}$  in the (a)  $^{14}\text{Be}+^{12}\text{C}$  and (b)  $^{12}\text{Be}+^4\text{He}$  reactions.

at approximately 1.7 MeV. The peak at 2.7 MeV in Fig. 1(a) is not seen in Fig. 1(b). To determine the spins of these levels, the analyses of angular distribution of the excited  $^{12}\text{Be}$  are in progress.

## References

- 1) A. Saito et al.: RIKEN Accel. Prog. Rep. **35**, 55 (2002); RIKEN Accel. Prog. Rep. **36**, 62 (2003).
- 2) M. Freer et al.: Phys. Rev. Lett. **82**, 1383 (1999).

<sup>\*1</sup> Department of Physics, Rikkyo University

<sup>\*2</sup> Center for Nuclear Study, University of Tokyo

<sup>\*3</sup> ATOMKI, Hungary

<sup>\*4</sup> National Institute of Radiological Science

<sup>\*5</sup> Department of Physics, Tohoku University

<sup>\*6</sup> Department of Physics, University of Tokyo

<sup>\*7</sup> Department of Physics, Tokyo Institute of Technology

## Isomeric $0^+$ state in $^{12}\text{Be}^\dagger$

S. Shimoura,<sup>\*1</sup> A. Saito,<sup>\*2</sup> T. Minemura, Y. U. Matsuyama,<sup>\*2</sup> H. Baba,<sup>\*2</sup> H. Akiyoshi, N. Aoi, T. Gomi,<sup>\*2</sup>  
 Y. Higurashi, K. Ieki,<sup>\*2</sup> N. Imai, N. Iwasa,<sup>\*3</sup> H. Iwasaki,<sup>\*1</sup> S. Kanno,<sup>\*2</sup> S. Kubono,<sup>\*1</sup> M. Kunibu,<sup>\*2</sup>  
 S. Michimasa,<sup>\*1</sup> T. Motobayashi, T. Nakamura,<sup>\*4</sup> H. Sakurai,<sup>\*5</sup> M. Serata,<sup>\*2</sup> E. Takeshita,<sup>\*2</sup>  
 S. Takeuchi, T. Teranishi,<sup>\*1</sup> K. Ue,<sup>\*1</sup> K. Yamada,<sup>\*2</sup> Y. Yanagisawa,  
 M. Ishihara, and N. Itagaki<sup>\*5</sup>

[Isomeric state,  $\gamma$ - $\gamma$  correlation, Radioactive beam experiment]

An isomeric  $0^+$  state in  $^{12}\text{Be}$  was found at  $E_x = 2.24$  MeV. The isomer was identified by measuring two coincident  $\gamma$ -rays from an in-flight  $^{12}\text{Be}$  nucleus, produced by the projectile fragmentation of  $^{18}\text{O}$  on a Be target at 100 A MeV. Its spin was determined to be  $0^+$  by the angular correlation of the two  $\gamma$ -rays.

The experiment was performed at the RIKEN Accelerator Research Facility. A primary beam of  $^{18}\text{O}$  projectiles at 100 A MeV bombarded a 2-g/cm<sup>2</sup>-thick Be target. The  $^{12}\text{Be}^{(*)}$  nuclides at 60 A MeV were selected by the RIKEN Projectile Fragment Separator (RIPS).<sup>1)</sup> Two plastic scintillators at the second (F2) and third (F3) focal points of the RIPS were used for identifying the  $^{12}\text{Be}$  event by event using the time-of-flight (TOF) between the two scintillators and the pulse heights. Gamma rays were detected by an array of 68 NaI(Tl) scintillators (DALI) about 70 cm downstream of the F3 scintillator. Timing signals of NaI(Tl) were used to discriminate the true coincidence from the accidental one, and to evaluate the vertex point from which the  $\gamma$ -ray was emitted. The vertex point was used for Doppler-shift corrections event by event. The  $^{12}\text{Be}$  nucleus after decay was detected by a plastic scintillator hodoscope with a  $1 \times 1$  m<sup>2</sup> active area located 4 m downstream of DALI. The hodoscope consisted of a 5-mm-thick  $\Delta E$  plane and a 60-mm-thick  $E$  plane.

We analyzed events where two NaI(Tl) scintillators made signals from in-flight  $^{12}\text{Be}$  particles. After the Doppler-shift correction, we found a new 0.14 MeV transition coincident with the 2.1 MeV transition ( $2^+ \rightarrow 0_1^+$ ), resulting in a new state at about 0.14 MeV above the  $2^+$  state, *i.e.*, an isomeric state at  $E_x = 2.24$  MeV.

In order to determine the spin of the new state, we have examined an azimuthal angular correlation

of these two  $\gamma$ 's with respect to the direction of the  $^{12}\text{Be}$  momentum. Figure 1 shows the observed angular correlation together with a theoretical prediction assuming a cascade decay of  $0_2^+ \rightarrow 2_1^+ \rightarrow 0_1^+$ . We conclude the isomeric state has spin  $0^+$  based on the excellent fit.

We also observed coincident 0.51 MeV  $\gamma$ -rays originated from the annihilation of positrons, which are to be produced in the  $e^+e^-$  pair decay of the  $0_2^+ \rightarrow 0_1^+$  transition. From the relative yields of the 0.14 MeV and 0.51 MeV  $\gamma$ -rays, the branching ratio of the  $0_2^+ \rightarrow 2^+ \rightarrow 0_1^+$  and  $0_2^+ \rightarrow 0_1^+$  transitions are deduced to be  $(83 \pm 2)\%$  and  $(17 \pm 2)\%$ , respectively.

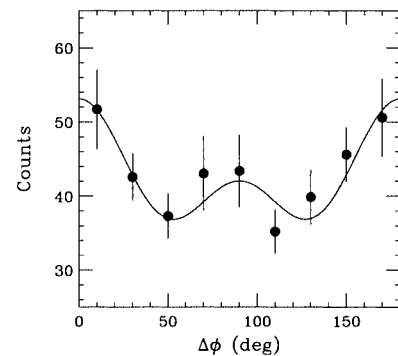


Fig. 1. Azimuthal angular correlation pattern of 2.1 MeV and 0.14 MeV  $\gamma$ -rays. The solid line denotes the theoretical prediction assuming the  $0^+ \rightarrow 2^+ \rightarrow 0^+$  transition.

### References

- 1) T. Kubo et al.: Nucl. Instrum. Methods Phys. Res. B **70**, 309 (1992).

<sup>†</sup> Condensed from the article in Phys. Lett. B **560**, 31 (2003)

<sup>\*1</sup> Center for Nuclear Study, University of Tokyo

<sup>\*2</sup> Department of Physics, Rikkyo University

<sup>\*3</sup> Faculty of Science, Tohoku University

<sup>\*4</sup> Department of Applied Physics, Tokyo Institute of Technology

<sup>\*5</sup> Department of Physics, University of Tokyo

## Coulomb and nuclear breakup of $^{11}\text{Li}$

A. M. Vinodkumar,<sup>\*1</sup> T. Nakamura,<sup>\*1</sup> N. Fukuda, T. Sugimoto,<sup>\*1</sup> M. Miura,<sup>\*1</sup> Y. Kondo,<sup>\*1</sup> T. Kobayashi,<sup>\*2</sup>  
 N. Aoi, N. Imai, T. Kubo, T. Gomi,<sup>\*3</sup> A. Saito,<sup>\*3</sup> H. Sakurai,<sup>\*4</sup> S. Shimoura,<sup>\*5</sup> D. Bazin,<sup>\*6</sup>  
 H. Hasegawa,<sup>\*3</sup> H. Baba,<sup>\*3</sup> T. Motobayashi, T. Yakushiji,<sup>\*2</sup> Y. Yanagisawa,  
 K. Yoneda,<sup>\*6</sup> K. Watanabe,<sup>\*2</sup> Y. X. Watanabe,<sup>\*7</sup> and M. Ishihara

[NUCLEAR REACTIONS:  $^{12}\text{C}(^{11}\text{Li}, ^9\text{Li} \text{ nX})$ , Nuclear breakup]

$^{11}\text{Li}$  is one of the two neutron halo nuclei extensively studied for Coulomb dissociation experimentally and theoretically.<sup>1-6</sup> However, these measurements and theories were not able to provide a conclusive picture regarding the structure of  $^{11}\text{Li}$  as well as the reaction mechanism involved.  $^{11}\text{Li}$  Coulomb and nuclear dissociation has been investigated by Ieki *et al.*<sup>1,2</sup> (MSU data), Shimoura *et al.*<sup>3</sup> (RIKEN data), and Zinser *et al.*<sup>4</sup> (GSI data), at 28 A MeV, 43 A MeV and 280 A MeV, respectively. The  $B(E1)$  distributions derived from these three measurements shows discrepancies among each other. The GSI data shows a second bump at approximately 2.5 MeV in the  $B(E1)$  distribution. However, RIKEN data do not show such a bump. In this preliminary report, we present the analysis of  $^9\text{Li}$  in coincidence with one neutron produced in the breakup on a carbon target.

We have carried out a kinematically complete experiment using the RIPS spectrometer at RIKEN. A  $^{11}\text{Li}$  secondary beam of 70.34 A MeV energy bombarded lead and carbon targets of 347 mg/cm<sup>2</sup> thickness and 377 mg/cm<sup>2</sup> thickness respectively. The time of flight of the beam was measured using a thin plastic detector at the achromatic focus and the RF signal. The fragment was bent by a large acceptance dipole magnet and traced using a drift chamber and hodoscopes (7 numbers). The momentum vectors of the fragment were reconstructed from the time of flight and tracking information. The neutrons were detected using 4 walls of plastic scintillators. The intrinsic efficiency and conditions for eliminating crosstalk events were obtained from a separate experiment in which we used a proton beam ( $^7\text{Li}(p, n)$  reaction). The experimental details are presented in a previous report.<sup>7</sup>

The invariant mass spectrum of the  $^{10}\text{Li}$  is reconstructed from the momenta of the charged particle and neutron. In Fig. 1, the relative energy between  $^9\text{Li}$  and

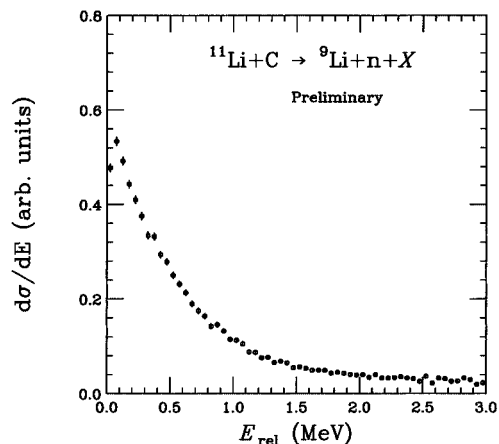


Fig. 1. The two body relative energy spectra obtained in the  $^{11}\text{Li} + \text{C} \rightarrow ^9\text{Li} + \text{n} + \text{X}$  reaction.

one neutron (invariant mass spectra of  $^{10}\text{Li}$ ) obtained using a carbon target is shown. In the relative energy spectra, at close to zero relative energy, more strength was observed compared with the GSI measurement. Presently we are investigating the physical significance of this low-energy strength. Also the analysis of the  $^9\text{Li}$  in coincidence with two neutrons is in progress.

### References

- 1) K. Ieki *et al.*: Phys. Rev. Lett. **70**, 730 (1993).
- 2) D. Sackett *et al.*: Phys. Rev. C **48**, 118 (1993).
- 3) S. Shimoura *et al.*: Phys. Lett. B **348**, 29 (1995).
- 4) M. Zinser *et al.*: Nucl. Phys. A **619**, 151 (1997).
- 5) T. Kobayashi *et al.*: Phys. Lett. B **232**, 51 (1989).
- 6) I. J. Thompson and M. V. Zhukov: Phys. Rev. C **49**, 1904 (1994).
- 7) T. Nakamura *et al.*: RIKEN Accel. Prog. Rep. **35**, 57 (2002).

<sup>\*1</sup> Tokyo Institute of Technology

<sup>\*2</sup> Department of Physics, Tohoku University

<sup>\*3</sup> Department of Physics, Rikkyo University

<sup>\*4</sup> Department of Physics, University of Tokyo

<sup>\*5</sup> Center for Nuclear Study, University of Tokyo

<sup>\*6</sup> Michigan State University, USA

<sup>\*7</sup> High Energy Accelerator Research Organization (KEK)

# Measurement of reaction cross section for $^{17}\text{C}$ and finite-range Glauber model analysis

C. Wu,<sup>\*1</sup> Y. Yamaguchi,<sup>\*2</sup> A. Ozawa,<sup>\*3</sup> R. Kanungo, T. Suzuki,<sup>\*4</sup> D. Q. Fang,  
T. Suda, T. Ohnishi, M. Fukuda,<sup>\*5</sup> N. Iwasa,<sup>\*6</sup> T. Ohtsubo,<sup>\*2</sup> T. Izumikawa,<sup>\*2</sup>  
R. Koyama,<sup>\*2</sup> W. Shinozaki,<sup>\*2</sup> M. Takahashi,<sup>\*2</sup> and I. Tanihata

[ $^{17}\text{C}$ , reaction cross section  $\sigma_R$ , density distribution, finite-range Glauber Model]

The reaction cross sections  $\sigma_R$  at low energies have been proved to be more sensitive to the nuclear density at the surface because of large nucleon-nucleon total cross sections. Like  $^8\text{B}$ , although measurements of the interaction cross section  $\sigma_I$  at relativistic energies did not show significant enhancement, measurements of  $\sigma_R$  at low energies revealed the necessity of a long proton tail.<sup>1)</sup> Motivated by this, we measured  $\sigma_R$  of  $^{17}\text{C}$  at 79 A MeV by the transmission method. The density distribution of  $^{17}\text{C}$  has been investigated by fitting the present result of  $\sigma_R$  and previous experimental data of  $\sigma_I$ <sup>2)</sup> using the Glauber model.

The experiment was performed at RIPS of RIKEN. Secondary  $^{17}\text{C}$  beam was produced by projectile fragmentation of primary-beam  $^{22}\text{Ne}$  at 110 A MeV on production target Be. Before the reaction target (carbon) at F2, particle identification was achieved by the standard  $B\rho - \Delta E - \text{TOF}$  method, in which  $B$  was the magnetic field of D<sub>2</sub>,  $\Delta E$  was the energy loss in F2SSD and TOF was the time of flight between F1PPAC and F2Plastic. After the reaction target, the TOF- $\Delta E-E$  method was used to identify particles. TOF was the time of flight between F2Plastic and F3Plastic.  $\Delta E$  and  $E$  were energy loss in the IC (ion chamber) and total energy deposit in NaI(Tl), respectively. In addition, we used a set of veto detectors around NaI(Tl) to detect the emitted charged particles or neutrons from reactions in NaI(Tl).

To measure  $\sigma_R$  by the transmission method, the quantities of incident  $^{17}\text{C}$ ,  $N_{in}$ , and outgoing nonreacted  $^{17}\text{C}$ ,  $N_{out}$ , should be determined. In our work,  $N_{in}$  was determined by particle identification before the reaction target. To determine  $N_{out}$ , the number of other fragments,  $N_{frag}$  (like  $^{16}\text{C}$ ,  $^{15}\text{C}$ ,  $^{14}\text{C}$ ), and that of inelastic  $^{17}\text{C}$ ,  $N_{inel}$ , from reactions in the target were subtracted from the total number of outgoing particles with  $Z = 6$ . The present result of  $\sigma_R$  for  $^{17}\text{C}$  is shown in Fig. 1(b) by the closed square.

The finite-range Glauber Model (FRGM)<sup>3)</sup> has been employed to probe the density distribution of  $^{17}\text{C}$ . All results are shown in Fig. 1. We assumed that the density of  $^{17}\text{C}$  was (1) HO density, the size parameter

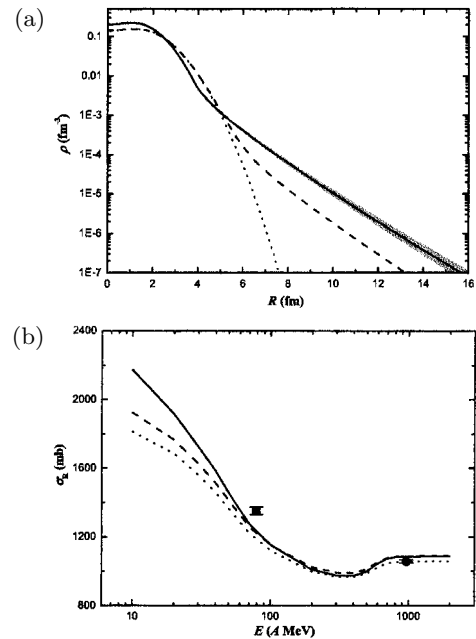


Fig. 1. (a) Density distribution of  $^{17}\text{C}$ . (b) Results of  $\sigma_R$  and FRGM calculation.

$\alpha_{HO}$  of which was obtained by fitting  $\sigma_I$  at high energy, as shown by the dotted line; (2) a HO core and a Yukawa tail, in which  $\alpha_{HO}$  and the crossing radius were the same as those of  $^{16}\text{C}$ ,<sup>3)</sup> as shown by the solid line; (3) core ( $^{16}\text{C}$ ) plus single-particle density, assuming a mixture of s- and d-waves of the valence neutron. A dominant d-wave ( $77 \pm 21\%$ ) was found from the best fit shown by the dash line.

In conclusion, the existence of a tail in the density distribution of  $^{17}\text{C}$  is suggested to explain the large reaction cross section data. Based on the assumption of a core plus single-particle density, d-wave dominance is favored in the best fit, which is in agreement with other measurements.<sup>4,5)</sup>

## References

- 1) M. Fukuda et al.: Nucl. Phys. A **656**, 209 (1999).
- 2) A. Ozawa et al.: Nucl. Phys. A **691**, 599 (2001).
- 3) T. Zheng et al.: Nucl. Phys. A **709**, 103 (2002).
- 4) V. Maddalena et al.: Phys. Rev. C **63**, 024613 (2001).
- 5) U. Datta Pramanik et al.: Phys. Lett. B **551**, 63 (2003).

<sup>\*1</sup> Peking University, China

<sup>\*2</sup> Niigata University

<sup>\*3</sup> Tsukuba University

<sup>\*4</sup> Saitama University

<sup>\*5</sup> Osaka University

<sup>\*6</sup> Tohoku University

## Measurement of the reaction cross section for $^{17}\text{B}$

Y. Yamaguchi,<sup>\*1</sup> C. Wu,<sup>\*2</sup> A. Ozawa,<sup>\*3</sup> T. Suzuki,<sup>\*4</sup> T. Ohnishi, T. Suda, M. Fukuda,<sup>\*5</sup> D. Q. Fang, R. Kanungo, N. Iwasa,<sup>\*6</sup> T. Ohtsubo,<sup>\*1</sup> T. Izumikawa,<sup>\*1</sup> W. Shinozaki,<sup>\*1</sup> R. Koyama,<sup>\*1</sup> M. Takahashi,<sup>\*1</sup> S. Watanabe,<sup>\*1</sup> and I. Tanihata

[NUCLEAR REACTIONS,  $^{17}\text{B}$ , measured reaction cross section]

The neutron-rich nucleus  $^{17}\text{B}$  has been considered as the two-neutron halo nucleus due to its weak binding energy of valence two-neutron,<sup>1)</sup> large *r.m.s* matter radius<sup>2)</sup> and narrow momentum distribution for  $^{15}\text{B}$  fragment from the breakup of  $^{17}\text{B}$ .<sup>3)</sup> Therefore it is interesting to study the nucleon density distribution of  $^{17}\text{B}$ . In order to deduce the nucleon density distribution, we have measured the reaction cross section at 77A MeV by using a transmission method.

The experiment was performed at RIKEN Projectile Fragment Separator (RIPS).<sup>4)</sup> The primary beam of  $^{22}\text{Ne}$  with 110 A MeV, accelerated by the RIKEN Ring Cyclotron (RRC), was used to impinge on Be or Ta targets to produce  $^{17}\text{B}$  as the secondary beam through the projectile fragmentation reaction. The RIPS was operated in an achromatic mode with an Al wedge degrader and the momentum acceptance of 1.0%. The Particle IDentification (PID) before the carbon reaction target ( $377\text{ mg/cm}^2$ ), which was placed at F2 of RIPS, was performed by the  $B\rho$ - $\Delta E$ -TOF standard method for each of the fragments. Magnetic rigidity ( $B\rho$ ) was determined by using the position information of PPACs. The magnetic fields at the two dipoles were monitored by NMR probes. The energy loss ( $\Delta E$ ) was measured by a silicon detector ( $50 \times 50 \times 0.15\text{ mm}^3$ ) placed at F2. The Time-Of-Flight (TOF) information before the reaction target was determined from the *rf*-signal and the timing signal of the plastic scintillator (0.5 mm thickness) placed at F2. The background contamination of other particles was estimated to be  $10^{-4}$  in the offline analysis. After the reaction target, a quadropole-triplet was used to transport and focus the beam onto F3. The PID after the reaction target was performed by the TOF- $\Delta E$ - $E$  method. The TOF information was determined between the two plastic scintillators at F2 and F3. The  $\Delta E$  was measured by the ion chamber<sup>5)</sup> which was placed at F3. The total energy ( $E$ ) was measured by the  $3''\phi \times 6\text{ cm}$  NaI(Tl) detector placed at the end of the beam line with a reaction suppressor.<sup>6)</sup>

The reaction cross section ( $\sigma_R$ ) for  $^{17}\text{B}$  was calculated using the following equation,

$$\sigma_R = -\frac{1}{t} \ln \left( \frac{R_{in}}{R_{out}} \right) \quad (1)$$

where  $t$  is the thickness of the reaction target in the unit of atom/cm<sup>2</sup>,  $R_{in}$  and  $R_{out}$  are the ratios of the number of outgoing particles to that of the incident particles with and without the reaction target, respectively. We did find a large enhancement of  $\sigma_R$  for  $^{17}\text{B}$ , compared with that of the expected value by Kox's formula calculation. Kox's formula can reproduce the  $\sigma_R$  for stable nuclei well.<sup>7)</sup> The ratios of the experimental  $\sigma_R$  for  $^{17}\text{B}$  to the expected value from Kox's formula are shown in Fig. 1. At low energy, the enhancement of  $\sigma_R$  is much larger than that at high energy. This effect suggests the existence of a low-density tail at a large distance from the center of the nucleus.

The nucleon density distribution of  $^{17}\text{B}$  will be deduced by using the energy dependence of the measured cross sections. The data analysis is still in progress with Glauber-model calculation.

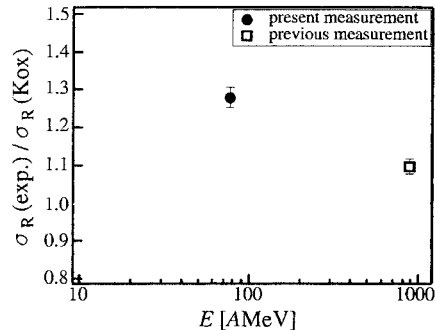


Fig. 1. The ratios of the experimental  $\sigma_R$  to the expected value from Kox's formula calculation for  $^{17}\text{B}$  are plotted as a function of the incident beam energy. The closed circle denotes the data point obtained in this work. The open square is obtained from Ref. 2.

### References

- 1) G. Audi et al.: Nucl. Phys. A **624**, 1 (1997).
- 2) T. Suzuki et al.: Nucl. Phys. A **658**, 313 (1999).
- 3) T. Suzuki et al.: Phys. Rev. Lett. **89**, 12501-1 (2002).
- 4) T. Kubo et al.: Nucl. Instrum. Methods Phys. Res. B **70**, 309 (1992).
- 5) Y. Yamaguchi et al.: RIKEN Accel. Prog. Rep. **36**, 161 (2003).
- 6) T. Suda et al.: RIKEN Accel. Prog. Rep. **35**, 171 (2002).
- 7) S. Kox et al.: Phys. Rev. C **35**, 35 (1987).

<sup>\*1</sup> Niigata University  
<sup>\*2</sup> Peking University, China  
<sup>\*3</sup> Tsukuba University  
<sup>\*4</sup> Saitama University  
<sup>\*5</sup> Osaka University  
<sup>\*6</sup> Tohoku University

## Mean lifetime of the first excited state in $^{16}\text{C}$

N. Imai, H. J. Ong,<sup>\*1</sup> N. Aoi, H. Sakurai,<sup>\*1</sup> K. Demichi,<sup>\*2</sup> H. Kawasaki,<sup>\*2</sup> H. Baba,<sup>\*2</sup> Zs. Dombrádi,<sup>\*3</sup> Z. Elekes,<sup>\*3</sup> N. Fukuda, Zs. Fülöp,<sup>\*3</sup> A. Gelberg,<sup>\*4</sup> T. Gomi,<sup>\*2</sup> H. Hasegawa,<sup>\*2</sup> K. Ishikawa,<sup>\*6</sup> H. Iwasaki,<sup>\*5</sup> E. Kaneko,<sup>\*2</sup> S. Kanno,<sup>\*2</sup> T. Kishida, Y. Kondo,<sup>\*6</sup> T. Kubo, K. Kurita,<sup>\*2</sup> S. Michimasa,<sup>\*5</sup> T. Minemura, M. Miura,<sup>\*6</sup> T. Motobayashi, T. Nakamura,<sup>\*6</sup> M. Notani,<sup>\*3</sup> T. K. Onishi,<sup>\*1</sup> A. Saito,<sup>\*2</sup> S. Shimoura,<sup>\*5</sup> T. Sugimoto,<sup>\*6</sup> M. K. Suzuki,<sup>\*1</sup> E. Takeshita,<sup>\*2</sup> S. Takeuchi, M. Tamaki,<sup>\*5</sup> K. Yoneda,<sup>\*7</sup> H. Watanabe, and M. Ishihara

[NUCLEAR REACTIONS:  $^9\text{Be}(^{16}\text{C}, ^{16}\text{C}^*)^9\text{Be}$   $E = 34.6\text{ MeV/u}$ , RSM]

We measured the mean lifetime of the first excited state of  $^{16}\text{C}$  using a new experimental technique. The mean lifetime is directly related to the  $B(E2)$  value of the nucleus, which reflects the quadrupole collectivity of charge distribution in the nucleus.

The new technique essentially follows the concept of the recoil shadow method (RSM),<sup>(1)</sup> in which the emission point of the de-excitation  $\gamma$ -ray is located and the  $\gamma$ -ray intensity is recorded as a function of the flight distance of the de-exciting nucleus. By utilizing an intermediate-energy radioactive-isotope beam, the flight velocity of the de-exciting nucleus is close to half the light velocity even after the secondary reaction. With such a high velocity, the flight distance over 100 ps corresponds to a macroscopic length of about 1.7 cm. The present shadow method provides a wide range of applicability, extending to lifetimes of around 20 ps.

The beam of  $^{16}\text{C}$  was produced by projectile fragmentation of a 100 MeV/u  $^{18}\text{O}$  beam with a thick 1850 mg/cm<sup>2</sup> Be target. The  $^{16}\text{C}$  beam was separated by the RIPS beam line and bombarded onto a thick 370 mg/cm<sup>2</sup> Be target. In the middle of the target, the energy of the beam was 34.6 MeV/u. The typical secondary beam intensity was 200 kHz.

The de-excitation  $\gamma$ -rays from the inelastically excited  $^{16}\text{C}$  nuclei were detected by an array of thirty-two NaI(Tl) detectors. The array was divided into two rings, R1 and R2. R1 (R2) was composed of 14 (18) NaI(Tl) detectors and was placed at 121 (102) degrees from the center of the target position with respect to the beam axis. In order to implement the RSM concept, we placed a lead slab of 5 cm-thickness just downstream of R2. The upstream surface of the lead slab was defined as  $z = 0.0\text{ cm}$  for later description. Due to the screening effect of this slab, effective  $\gamma$ -ray efficiencies of R1 and R2 are different. The magnitude of the difference depends on the point of  $\gamma$ -ray emission

along the beam axis. Thus, the mean lifetime can be deduced from the  $\gamma$ -ray yield ratio (R1/R2).

The measurements were performed with two target positions,  $z = 0.0$  and 1.0 cm, to verify the deduced mean lifetime. The R1/R2 ratios as a function of mean lifetime  $\tau$  are shown as solid lines in Fig. 1. These functions were obtained by the Monte Carlo simulation. The simulation includes the measured emittance of the beams and scattering angles, and the calculated angular distribution of de-excitation  $\gamma$ -rays. The measured R1/R2 ratios are also presented in Fig. 1. From the overlapped areas, the values of  $\tau$  were determined to be  $92 \pm 22\text{ ps}$  and  $63 \pm 17\text{ ps}$ , respectively, for data obtained at the two target positions. As the final value, we adopted a weighted average of these two values. The uncertainty mentioned above is attributed to statistical error. By adding systematic error quadratically, we determined  $\tau = 77 \pm 24\text{ ps}$ . The present mean lifetime is anomalously long by an order of magnitude compared with any predicted value. A paper which summarizes the present results has been submitted to Physical Review Letters.

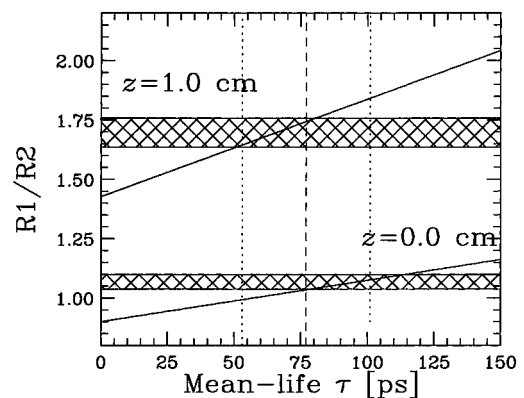


Fig. 1. Gamma-ray yield ratio of R1 to R2 as a function of mean lifetime of  $^{16}\text{C}(2_1^+)$ . Hatched boxes indicate the measured R1/R2 ratios for the two target positions,  $z = 0.0$  and 1.0 cm. Dashed line indicates the mean value of the adopted  $\tau$ , while dotted lines represent the 1-sigma error region.

<sup>\*1</sup> University of Tokyo  
<sup>\*2</sup> Rikkyo University  
<sup>\*3</sup> ATOMKI, Hungary  
<sup>\*4</sup> University of Koeln, Germany  
<sup>\*5</sup> Center for Nuclear Study, University of Tokyo  
<sup>\*6</sup> Tokyo Institute of Technology  
<sup>\*7</sup> National Superconducting Cyclotron Laboratory at Michigan State University, USA

### References

- 1) H. Backe et al.: Z. Phys. A **285**, 159 (1978).

# In-beam gamma spectroscopy and search for isomeric states in $^{17,19}\text{C}$

R. Kanungo, Z. Elekes,<sup>\*1</sup> H. Baba,<sup>\*2</sup> Zs. Dombrádi,<sup>\*3</sup> Zs. Fülöp,<sup>\*3</sup> J. Gibelin,<sup>\*2</sup> A. Horvath,<sup>\*4</sup> Y. Ichikawa,<sup>\*5</sup> E. Ideguchi,<sup>\*6</sup> N. Iwasa,<sup>\*7</sup> H. Iwasaki,<sup>\*5</sup> S. Kawai,<sup>\*2</sup> Y. Kondo,<sup>\*8</sup> T. Motobayashi, M. Notani,<sup>\*6</sup> T. Ohnishi, A. Ozawa,<sup>\*9</sup> H. Sakurai,<sup>\*5</sup> S. Shimoura,<sup>\*6</sup> E. Takeshita,<sup>\*2</sup> S. Takeuchi, I. Tanihata, Y. Togano,<sup>\*2</sup> C. Wu,<sup>\*10</sup> Y. Yamaguchi,<sup>\*11</sup> Y. Yanagisawa, A. Yoshida, and K. Yoshida

[gamma spectroscopy, proton inelastic scattering, isomer]

The study of unstable nuclei has become indispensable in recent times for nuclear structure studies. The  $p$ - $sd$  shell neutron-rich nuclei exhibit interesting features such as enhanced interaction cross section, which suggests the presence of some exotic structures.

It has been interesting to note that although the reaction observables such as the interaction cross section and the longitudinal momentum distribution for one neutron removal have been well understood for the  $p$ -shell nuclei such as  $^{11}\text{Li}$  and  $^{11}\text{Be}$ , there exists some anomaly in understanding the ground state spin of the nucleus  $^{19}\text{C}$ .<sup>1)</sup> Several experimental studies suggest an abnormal spin of  $1/2^{+2,3)}$  for this nucleus. However, several attempts to measure the magnetic moment for this nucleus has not yet yielded any confirmation on this spin assignment.<sup>4)</sup>

Recent investigations at GANIL showed an interesting observation of a prompt gamma transition at  $\sim 200$  keV for  $^{19}\text{C}$ .<sup>5)</sup> This triggered considerable interest since it corresponds to the de-excitation of a very short-lived state. According to shell model calculations and single particle excitation estimates, a long-lived state is expected as the first excited state for  $^{19}\text{C}$  having a ground state spin  $1/2^{+}$ . It thus became interesting to look for the existence of a low-lying isomeric state in  $^{19}\text{C}$ . For a comparative study, we also investigated the nuclei  $^{17}\text{C}$  and  $^{17}\text{B}$ .

It was also necessary to have a re-confirmation for the existence of the 200 keV gamma transition through a different method of excitation. Since the threshold in the GANIL measurement was quite close to 200 keV, it was interesting to investigate the possibilities of prompt gamma transitions of lower energy.

Our experiment was directed towards these goals. The experiment was designed to search for both the prompt gamma transition and gamma decay from the isomeric state simultaneously. The prompt gamma detection was carried out by in-beam gamma spec-

troscopy where a secondary beam of  $^{19,17}\text{C}$  was excited through proton inelastic scattering ( $p,p'$ ) from liquid  $\text{H}_2$  target.

The experimental setup is schematically shown in Fig. 1. The secondary beam of  $^{19,17}\text{C}$  was produced by fragmentation of a  $^{22}\text{Ne}$  primary beam with a  $1.864\text{ gm/cm}^2$  Be target.  $^{17}\text{B}$  was retained as a contaminant fragment in the  $^{19}\text{C}$  setting. The secondary beam after scattering from a liquid  $\text{H}_2$  target was identified and stopped in a stack of silicon detectors. The prompt gamma transitions from the excited states of the secondary beam, populated by inelastic ( $p,p'$ ) scattering, were detected by an array of  $\text{NaI(Tl)}$  detectors surrounding the  $\text{H}_2$  target. The threshold was 20–40 keV.

To detect gamma rays from the possible isomeric transition, germanium clover detectors were placed outside the plastic scintillators. For the same purpose,  $\text{NaI(Tl)}$  crystals were placed at  $0^\circ$  to the beam. Beta rays from decay of  $^{17,19}\text{C}$  ground state were detected by plastic scintillators surrounding the silicon stack for reducing the background in the gamma-ray detectors. The time gate for detection of isomeric transition was  $500\ \mu\text{sec}$ . The gamma energy threshold was set  $\sim 30$  keV to focus on low-lying excited states.

A discussion on some preliminary observations for ( $p,p'$ ) is reported in Ref. 6. Further analysis of experimental results is in progress.

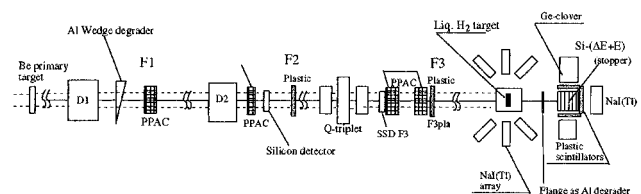


Fig. 1. Schematic figure of the experimental setup.

<sup>\*1</sup> On leave from ATOMKI, Hungary  
<sup>\*2</sup> Department of Physics, Rikkyo University  
<sup>\*3</sup> Institute of Nuclear Research, ATOMKI, Hungary  
<sup>\*4</sup> Eotvos Lorand University, Hungary  
<sup>\*5</sup> Department of Physics, University of Tokyo  
<sup>\*6</sup> Center for Nuclear Study, University of Tokyo  
<sup>\*7</sup> Department of Physics, Tohoku University  
<sup>\*8</sup> Department of Physics, Tokyo Institute of Technology  
<sup>\*9</sup> Institute of Physics, University of Tsukuba  
<sup>\*10</sup> Peking University, China  
<sup>\*11</sup> Niigata University

## References

- 1) R. Kanungo et al.: Nucl. Phys. A **677**, 171 (1998).
- 2) V. Maddalena et al.: Phys. Rev. C **63**, 024613 (2001).
- 3) T. Nakamura et al.: Phys. Rev. Lett. **83**, 1112 (1999).
- 4) K. Asahi et al.: private communication.
- 5) M. Lewitowicz: Nucl. Phys. A **722**, 67c (2003).
- 6) Z. Elekes et al.: RIKEN Accel. Prog. Rep. **37**, 61 (2004).

## In-beam $\gamma$ -ray spectroscopy of Ne isotopes

K. Ishikawa,<sup>\*1</sup> J. Gibelin,<sup>\*2</sup> K. Yoshida, T. Nakamura,<sup>\*1</sup> D. Beaumel,<sup>\*2</sup> N. Aoi, H. Baba,<sup>\*3</sup> Y. Blumenfeld,<sup>\*2</sup>  
 Z. Elekes, N. Fukuda, T. Gomi,<sup>\*3</sup> Y. Kondo,<sup>\*1</sup> A. Saito,<sup>\*3</sup> Y. Satou,<sup>\*1</sup> E. Takeshita,<sup>\*3</sup> S. Takeuchi,  
 T. Teranishi,<sup>\*4</sup> Y. Togano,<sup>\*3</sup> V. Lima,<sup>\*2</sup> Y. Yanagisawa, A. M. Vinodkumar,<sup>\*1</sup>  
 T. Kubo, and T. Motobayashi

[NUCLEAR REACTIONS, Al( $^{26}\text{Ne}$ ,  $^{26-x}\text{Ne}^*$ ), Pb( $^{26}\text{Ne}$ ,  $^{26-x}\text{Ne}^*$ ), in-beam  $\gamma$ -ray spectroscopy, Coulomb dissociation]

We performed the study of the low-lying  $E1$  strength of the neutron-rich  $^{26}\text{Ne}$  nucleus by using the Coulomb dissociation and excitation reactions. The dipole strength is expected to be much more fragmented below the giant dipole resonance region.<sup>1)</sup> In the case of  $^{26}\text{Ne}$ , the low-lying excitation is suggested to be a pygmy of the giant dipole resonance. In this report, we present a preliminary result of the Coulomb excitation part in which we search for such resonance below the one-neutron emission threshold.

The experiment was performed at RIKEN Projectile-fragment Separator RIPS. The primary beam of  $^{40}\text{Ar}$  at 95 MeV/nucleon bombarded a 2-mm-thick Be target to produce the secondary beam of  $^{26}\text{Ne}$ . The average intensity and purity of the  $^{26}\text{Ne}$  beam were about 6 kcps and 80%, respectively, with 58 MeV/nucleon just before the reaction target. The secondary beam was identified through energy loss and time-of-flight measurements. The scattering angles of incoming particles were determined by two PPAC's located upstream of the reaction target. Pb and Al targets having thicknesses of 230 mg/cm<sup>2</sup> and 130 mg/cm<sup>2</sup>, respectively, were used for estimating the Coulomb and nuclear excitation components. Particle identification of the fragments passing through the target was performed using four-layer Si strip detectors composed of  $\Delta E$  and  $E$  counters located at about 1.2 m downstream of the target. The first two layers were composed of 8 Si detectors which were used for position detection. The position and intrinsic energy resolution of  $\Delta E$  counters were 5 mm and 2% (FWHM), respectively. The last two layers were the  $E$  counter composed of 8 Si(Li) detectors with 3 mm thickness, and an intrinsic energy resolution of 3% (FWHM). The neutrons produced in the reaction were detected by the neutron wall. The neutron wall had 4 layers located 3 m downstream of the target. Each layer had 29 plastic scintillators. The analysis of the neutrons is not used here and is reported elsewhere. The  $\gamma$ -rays emitted from

outgoing nuclei were detected by 152 NaI detectors, DALI2. For 2 MeV  $\gamma$ -rays, the efficiency is calculated to be around 10% with an intrinsic energy resolution of 7% (FWHM).

A preliminary  $\gamma$ -ray spectrum for the  $^{26}\text{Ne} + \text{Pb}$  reaction is shown in Fig. 1. The Doppler shift due to the velocity of  $^{26}\text{Ne}$  is corrected for. We have observed a peak at 2020 keV corresponding to the excitation to the first  $2^+$  state. The  $B(E2)$  of this transition was previously measured at MSU,<sup>2)</sup> so that we can use this excitation as a reference. Further analysis to extract the  $E1$  strength below the one-neutron threshold is now in progress.

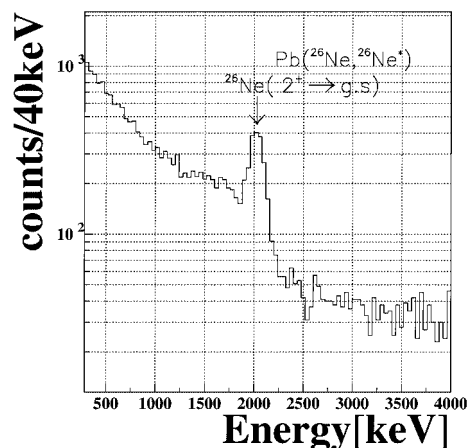


Fig. 1. Energy spectrum of Doppler-corrected  $\gamma$ -rays detected in coincidence with the  $^{26}\text{Ne}$  ejectile. The peak at around 2020 keV is clearly seen.

### References

- 1) A. Leistenschneider et al.: Phys. Rev. Lett. **86**, 24 (2001).
- 2) B. V. Pritychenko et al.: Phys. Lett. B **461**, 322 (2001).

<sup>\*1</sup> Department of Physics, Tokyo Institute of Technology

<sup>\*2</sup> Institut de Physique Nuclaire, France

<sup>\*3</sup> Department of Physics, Rikkyo University

<sup>\*4</sup> Center for Nuclear Study, University of Tokyo



## Excited states in $^{27}\text{F}$

Z. Elekes,<sup>\*1</sup> Zs. Dombrádi,<sup>\*2</sup> A. Saito,<sup>\*3</sup> N. Aoi, H. Baba,<sup>\*3</sup> K. Demichi,<sup>\*3</sup> Zs. Fülöp,<sup>\*2</sup> J. Gibelin,<sup>\*4</sup> T. Gomi,<sup>\*3</sup> H. Hasegawa,<sup>\*3</sup> N. Imai,<sup>\*5</sup> M. Ishihara, H. Iwasaki,<sup>\*5</sup> S. Kanno,<sup>\*3</sup> S. Kawai,<sup>\*3</sup> T. Kishida, T. Kubo, K. Kurita,<sup>\*3</sup> Y. U. Matsuyama,<sup>\*3</sup> S. Michimasa,<sup>\*5</sup> T. Minemura, T. Motobayashi, M. Notani,<sup>\*5</sup> T. Ohnishi,<sup>\*5</sup> H. J. Ong,<sup>\*5</sup> S. Ota,<sup>\*6</sup> A. Ozawa,<sup>\*7</sup> H. K. Sakai,<sup>\*3</sup> H. Sakurai,<sup>\*5</sup> S. Shimoura,<sup>\*5</sup> E. Takeshita,<sup>\*3</sup> S. Takeuchi, M. Tamaki,<sup>\*5</sup> Y. Togano,<sup>\*3</sup> K. Yamada,<sup>\*3</sup> Y. Yanagisawa, and K. Yoneda

[NUCLEAR STRUCTURE, Unstable nuclei,  $^{27}\text{F}$  excited states]

It is known that the last bound oxygen neutron-rich nucleus is  $^{24}\text{O}$ , while adding one more proton even the  $^{31}\text{F}$  is bound.<sup>1)</sup> A straightforward way of understanding this phenomena is to assume that the  $\nu d_{3/2}$  neutron orbit is unbound in oxygen isotopes, while the additional proton in the fluors can make bound this state. This assumption is enough to explain the existence of  $^{27,29}\text{F}$ , but for understanding the bound nature of  $^{31}\text{F}$  additional assumptions are needed. In terms of shell model, sudden lowering of multiparticle multi-hole states may be an explanation.<sup>2)</sup> If this is valid, its traces must be seen also in the lighter F isotopes. In  $^{27}\text{F}$  the first excited state is expected to be unbound in the  $usd^3$  approximation, while allowing for particle-hole excitations to the  $fp$  shell, a bound excited state in  $^{27}\text{F}$  is expected. To search for such states we studied the  $^{27}\text{F}(p,p'\gamma)$  reaction.

In the present experiment a 94 A MeV energy primary beam of  $^{40}\text{Ar}$  with 60 pnA intensity hit a  $^{181}\text{Ta}$  production target of 0.5 cm thickness. The reaction products were momentum and mass analyzed by the RIPS<sup>4)</sup> fragment separator. The secondary beam included neutron-rich  $^{24}\text{O}$ ,  $^{25,26,27}\text{F}$ ,  $^{27,28,29,30}\text{Ne}$  and  $^{29,30,31,32}\text{Na}$  nuclei. The RIPS was operated at 6% momentum acceptance. The total intensity was about 100 cps having a  $^{27}\text{F}$  intensity of 4 cps on average. The identification of incident beam species was performed by means of energy loss, time-of-flight and magnetic rigidity ( $B\rho$ ).<sup>5)</sup>  $^{27}\text{F}$  particles could be fully separated from other nuclei. The secondary beam was transmitted to a liquid hydrogen target<sup>6)</sup> at the final focus of RIPS. The average areal density of the hydrogen was  $210\text{ mg/cm}^2$ . The position of the incident particles was determined by two PPACs placed at F3 upstream the target. The scattered particles were detected and identified by a PPAC and a silicon telescope. The telescope consisted of three layers with thicknesses of 0.5, 0.5 and 1 mm. The Z identification was performed by TOF-energy loss method. Based on  $\Delta E$ - $E$  information

isotope separation was carried out among the different fluorine isotopes.  $^{27}\text{F}$  nuclei represented a distinct peak and they were well separated from other products emerged by neutron removal reactions in the liquid hydrogen target. The new DALI2 setup including 146 NaI(Tl) scintillator detectors,<sup>7)</sup> surrounded the target to detect de-exciting  $\gamma$  rays emitted by the inelastically scattered nuclei. Figure 1 is the Doppler-corrected  $\gamma$ -ray spectra for  $^{27}\text{F}$  nuclei. The plot shows three peaks at around 450, 750 and 1200 keV. Though the statistics are low, it is straightforward that the energy sum of the first two peaks gives the energy of the third one. These results suggest that at least two excited states are bound in  $^{27}\text{F}$ .

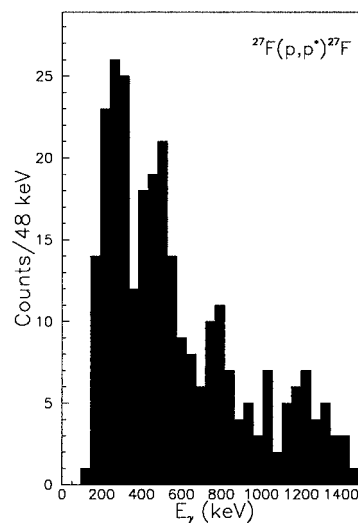


Fig. 1. Doppler-corrected spectra of  $\gamma$ -rays emerging from  $^{27}\text{F}(p,p')^{27}\text{F}$  reaction.

### References

- 1) H. Sakurai et al.: Phys Lett. B **448**, 1147 (1990).
- 2) Y. Utsuno et al.: Phys. Rev. C **64**, 011301 (2001).
- 3) T. Otsuka et al.: Eur. Phys. J. A **15**, 151 (2002).
- 4) T. Kubo et al.: Nucl. Instrum. Methods Phys. Res. B **70**, 309 (1992).
- 5) H. Sakurai et al.: Phys. Lett. B **448**, 180 (1999).
- 6) H. Akiyoshi et al.: RIKEN Accel. Prog. Rep. **32**, 167 (1999).
- 7) H. Hasegawa et al.: RIKEN Accel. Prog. Rep. **35**, 169 (2002).

<sup>\*1</sup> On leave from Institute of Nuclear Research, ATOMKI, Hungary

<sup>\*2</sup> Institute of Nuclear Research, ATOMKI, Hungary

<sup>\*3</sup> Rikkyo University

<sup>\*4</sup> Institut de Physique Nucléaire, France

<sup>\*5</sup> University of Tokyo

<sup>\*6</sup> Kyoto University

<sup>\*7</sup> University of Tsukuba

# Gamma-ray spectroscopy of $^{23}\text{F}$ with proton transfer reaction

S. Michimasa,<sup>\*1</sup> S. Shimoura,<sup>\*1</sup> H. Iwasaki,<sup>\*2</sup> M. Tamaki,<sup>\*1</sup> N. Aoi, H. Baba,<sup>\*3</sup> N. Iwasa,<sup>\*4</sup> S. Kanno,<sup>\*3</sup>  
 S. Kubono,<sup>\*1</sup> K. Kurita,<sup>\*3</sup> M. Kurokawa, T. Minemura, T. Motobayashi, M. Notani,<sup>\*1</sup>  
 H. J. Ong,<sup>\*2</sup> S. Ota,<sup>\*5</sup> A. Saito,<sup>\*3</sup> H. Sakurai,<sup>\*2</sup> S. Takeuchi,  
 E. Takeshita,<sup>\*3</sup> Y. Yanagisawa, and A. Yoshida

[NUCLEAR REACTION:  $^4\text{He}(^{22}\text{O}, ^{23}\text{F}^*)$ , Transfer reaction, In-beam  $\gamma$ -ray spectroscopy]

Neutron-rich fluorine isotopes are interesting in their features. A recent discovery revealed that the stability of neutron-rich isotopes remarkably changes between oxygen and fluorine isotopes.<sup>1)</sup> The fluorine isotopes are extended up to  $^{31}\text{F}$  with  $N = 22$  beyond the magic number of  $N = 20$  while the heaviest oxygen isotope is  $^{24}\text{O}$  with  $N = 16$ . This feature may indicate that a strong attraction works between a valence proton on the  $d_{5/2}$  shell and valence neutrons in fluorine isotopes. To ensure this feature, it is essential to know the proton shell structures in fluorine isotopes as a function of neutron number. One-proton transfer reactions are effective tools for investigating proton shell structure. We have, hence, measured de-excitation  $\gamma$ -rays from the excited states in  $^{23}\text{F}$  via the proton transfer reaction,  $^4\text{He}(^{22}\text{O}, ^{23}\text{F})$ .

The experiment was performed at the RIPS beam line in RIKEN. The  $^{40}\text{Ar}$  ions were accelerated up to 63 MeV/nucleon by the linear accelerator scheme of RFQ-RILAC-CSM-RRC. The maximum intensity of the primary beam was achieved up to 800 pA. The primary target was  $^9\text{Be}$  with a thickness of 1 mm. The unstable  $^{22}\text{O}$  beam was produced by their projectile fragmentation reaction, and bombarded a liquid helium target<sup>2)</sup> of 100 mg/cm<sup>2</sup> with Havar foil windows. The mean energy of  $^{22}\text{O}$  was 35 MeV/nucleon, and its intensity was  $2 \times 10^3$  particles/s on average. The  $^{22}\text{O}$  ions and contaminating beam particles were identified event-by-event using  $\Delta E$  and TOF. Reaction products were identified from TOF,  $\Delta E$ , and  $E$ , which were measured by a telescope consisting of 9 SSDs and 36 NaI(Tl) scintillators.<sup>3)</sup> The masses of the products were determined with the resolution of 0.3 mass unit. Furthermore, de-excited  $\gamma$ -rays from the reaction products were detected by 150 NaI(Tl) scintillators<sup>4)</sup> surrounding the secondary target. The  $\gamma$ -ray detector system has the energy resolution of 8% ( $\sigma$ ) for 3.2-MeV  $\gamma$ -rays from  $^{22}\text{O}$  traveling with  $\beta \sim 0.27$ , and the efficiency of 14.5% for 1.33-MeV  $\gamma$ -rays from a  $^{60}\text{Co}$  standard source.

A Doppler-corrected  $\gamma$ -ray energy spectrum obtained via the  $^4\text{He}(^{22}\text{O}, ^{23}\text{F})$  reaction is shown in

Fig. 1. The  $\gamma$ -ray energies were reconstructed by summing up the energies of multiple  $\gamma$ -rays detected in neighboring NaI(Tl) crystals. In the present experiment, we observed five de-excited  $\gamma$ -rays at 0.9, 2.3, 2.9, 3.4, and 4.1 MeV. The 3.4-MeV  $\gamma$ -ray was observed for the first time in the present experiment. The 2.3-MeV, 2.9-MeV, and 4.1-MeV  $\gamma$ -rays were expected to be de-excitation ones to the ground state from the excited states reported in Ref. 5. It was also confirmed that the  $\gamma$ -rays at 0.9 and 2.9 MeV were members of the cascade decay reported in Ref. 6.

In further analysis, we will deduce the orbital angular momenta of these excited states from the angular distributions for the proton transfer reaction.

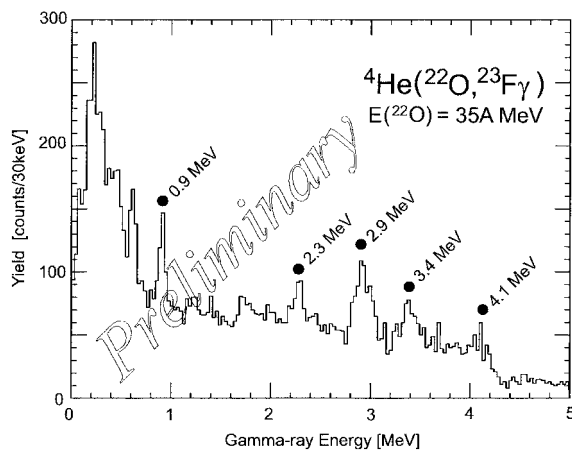


Fig. 1. De-excitation  $\gamma$ -ray energy spectrum of  $^{23}\text{F}$  obtained from the  $^4\text{He}(^{22}\text{O}, ^{23}\text{F}\gamma)$  reaction.

## References

- 1) H. Sakurai et al.: Phys. Lett. B **448**, 180 (1999).
- 2) H. Akiyoshi et al.: RIKEN Accel. Prog. Rep. **34**, 193 (2001).
- 3) M. Tamaki et al.: CNS-REP-59, 76 (2003).
- 4) S. Takeuchi et al.: RIKEN Accel. Prog. Rep. **36**, 148 (2003).
- 5) N. A. Orr et al.: Nucl Phys. A **491**, 457 (1989).
- 6) D. Guillemaud-Mueller: Eur. Phys. J. A **13**, 63 (2002).

\*1 Center for Nuclear Study, University of Tokyo

\*2 Department of Physics, University of Tokyo

\*3 Department of Physics, Rikkyo University

\*4 Department of Physics, Tohoku University

\*5 Department of Physics, Kyoto University

# Gamma-ray spectroscopy of $^{22}\text{O}$ with $\alpha$ inelastic scattering

M. Tamaki,<sup>\*1</sup> S. Shimoura,<sup>\*1</sup> H. Iwasaki,<sup>\*2</sup> S. Michimasa,<sup>\*1</sup> N. Aoi, H. Baba,<sup>\*3</sup> N. Iwasa,<sup>\*4</sup> S. Kanno,<sup>\*3</sup>  
 S. Kubono,<sup>\*1</sup> K. Kurita,<sup>\*3</sup> M. Kurokawa, T. Minemura, T. Motobayashi, M. Notani,<sup>\*1</sup>  
 H. J. Ong,<sup>\*2</sup> S. Ota,<sup>\*5</sup> A. Saito,<sup>\*3</sup> H. Sakurai,<sup>\*2</sup> S. Takeuchi, E. Takeshita,<sup>\*3</sup>  
 Y. Yanagisawa, and A. Yoshida

[NUCLEAR REACTION:  $\text{He}(^{22}\text{O}, ^{22}\text{O}\gamma)$ ,  $\alpha$  Inelastic Scattering, In-beam  $\gamma$ -ray spectroscopy]

The spectroscopy of neutron-rich oxygen isotopes has attracted much attention, since information on nuclear structure such as single-particle levels and collectivities can be studied as a function of neutron numbers in proton-magic nuclei. In the few experimental studies on the  $^{22}\text{O}$  nucleus so far, where measurements of de-excitation  $\gamma$  rays from inelastic scattering of a Au target<sup>1)</sup> and a fragmentation reaction<sup>2)</sup> have been reported. In order to obtain more spectroscopic information on the  $^{22}\text{O}$ , we have performed an experiment on an  $\alpha$  inelastic scattering in inverse kinematics by measuring de-excitation  $\gamma$  rays coincident with the  $^{22}\text{O}$  ejectile. Here the  $\alpha$  inelastic scattering on a spin-0 nucleus can populate several excited states having natural parities<sup>3)</sup> which can be determined by the analysis of angular distributions of differential cross sections depending on the transferred angular momenta.

The experiment was performed at the RIKEN Accelerator Research Facility. The  $^{22}\text{O}$  beam was produced by fragmentation of a 63 MeV/nucleon  $^{40}\text{Ar}$  primary beam incident on a beryllium target of 180 mg/cm<sup>2</sup> thickness. Fragments were separated by the RIPS separator. The  $^{22}\text{O}$  beam was identified event-by-event using the TOF- $\Delta E$  method. The TOF was the flight time between two plastic scintillators at the second (F2) and third (F3) focal planes of the RIPS. The  $\Delta E$  was measured with a 325- $\mu\text{m}$  Si detector installed at F2. The average intensity of the  $^{22}\text{O}$  beam was  $2 \times 10^3$  cps, and its purity was 37%. The  $^{22}\text{O}$  beam bombarded a liquid helium target of 100 mg/cm<sup>2</sup> thickness sealed using 6  $\mu\text{m}$  havar foils of 30 mm diameter.<sup>4)</sup> The energy of the  $^{22}\text{O}$  beam was 35 MeV/nucleon at the center of the secondary target. The scattering angles of outgoing particles were determined by three PPACs. Two of them were installed upstream and the other was installed downstream of the secondary. The particle identification of outgoing products from the secondary target was performed using TOF,  $\Delta E$  and  $E$  information measured using a telescope consisting of a Si array and a NaI(Tl) array.<sup>5)</sup> The excited states in  $^{22}\text{O}$  were identified by de-excitation  $\gamma$  rays which were detected by the DALI(II) system<sup>6)</sup> which consists of 150 NaI(Tl) crystals surrounding the secondary target.

Figure 1 shows the doppler-shift-corrected energy spectra of  $\gamma$  rays from the  $^4\text{He}(^{22}\text{O}, ^{22}\text{O}\gamma)$  reaction. In Fig. 1 (a), two peaks are clearly observed at 3.2 and 1.4 MeV. The 3.2-MeV  $\gamma$  ray corresponds to the  $\gamma$  ray which was reported in Refs. 1 and 2. In order to identify a cascade transition, we examined a  $\gamma$  ray spectrum coincident with the 3.2-MeV  $\gamma$ -ray which is the strongest transition as shown in Fig. 1 (b). It is clear that the 1.4-MeV  $\gamma$  ray corresponds to a member of a cascade transition through the first excited state as speculated in Ref. 2. These results indicate that there are two excited states at 3.2 and 4.6 MeV. In order to assign spins to these states the analysis of the angular distributions for the inelastic scattering is now in progress.

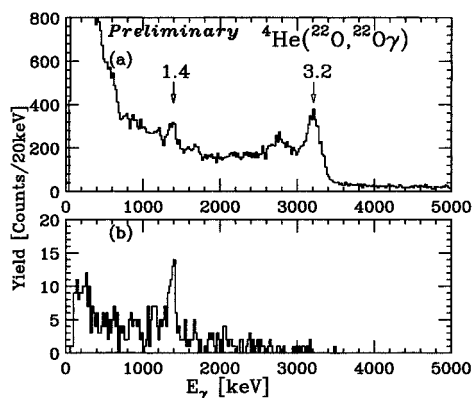


Fig. 1. (a) Doppler-shift-corrected energy spectrum of  $\gamma$  rays from the  $^4\text{He}(^{22}\text{O}, ^{22}\text{O}\gamma)$  reaction. (b) The  $\gamma$ -ray energy spectrum coincident with 3.2-MeV  $\gamma$  ray.

## References

- 1) P. G. Thirolf et al.: Phys. Lett. B **485**, 16 (2000).
- 2) F. Azaiez et al.: Nucl. Phys. A **704**, 37 (2002).
- 3) H. Baba et al.: CNS-REP-59, 17 (2003).
- 4) H. Akiyoshi et al.: RIKEN Accel. Prog. Rep. **34**, 193 (2001).
- 5) M. Tamaki et al.: CNS-REP-59, 76 (2003).
- 6) S. Takeuchi et al.: RIKEN Accel. Prog. Rep. **36**, 148 (2003).

<sup>\*1</sup> Center for Nuclear Study, University of Tokyo

<sup>\*2</sup> Department of Physics, University of Tokyo

<sup>\*3</sup> Department of Physics, Rikkyo University

<sup>\*4</sup> Department of Physics, Tohoku University

<sup>\*5</sup> Department of Physics, Kyoto University

Invariant-mass spectroscopy of  $^{16}\text{B}$ 

T. Sugimoto,<sup>\*1</sup> T. Nakamura,<sup>\*1</sup> N. Fukuda, M. Miura,<sup>\*1</sup> Y. Kondo,<sup>\*1</sup> N. Aoi, H. Baba,<sup>\*2</sup> D. Bazin,<sup>\*3</sup>  
 T. Gomi,<sup>\*2</sup> H. Hasegawa,<sup>\*2</sup> N. Imai, T. Kobayashi,<sup>\*4</sup> T. Kubo, T. Motobayashi, A. Saito,<sup>\*2</sup>  
 H. Sakurai,<sup>\*5</sup> S. Shimoura,<sup>\*6</sup> A. M. Vinodkumar,<sup>\*1</sup> K. Watanabe,<sup>\*4</sup> Y. X. Watanabe,<sup>\*7</sup>  
 T. Yakushiji,<sup>\*4</sup> Y. Yanagisawa, K. Yoneda,<sup>\*3</sup> and M. Ishihara

[NUCLEAR REACTIONS:  $\text{C}(^{17}\text{B}, ^{15}\text{B}nX)$ , Nuclear breakup]

The nuclear structure of  $^{17}\text{B}$ , which is a Borromean nucleus, has been studied by investigating the unbound subsystem<sup>1,2)</sup> of  $^{16}\text{B}$ . In this report, we show the preliminary result of the relative energy spectrum of the  $^{15}\text{B} + n$  system studied using nuclear breakup reactions. In the spectrum, we observed the possible ground state of the  $^{16}\text{B}$  nucleus.

The experiment was performed at the radioactive beam facility RIPS. The secondary  $^{17}\text{B}$  beam was produced by the fragmentation of  $^{22}\text{Ne}$  at 110 MeV/nucleon. The secondary beam was identified event by event using the time-of-flight (TOF)- $\Delta E$  method. The secondary carbon target (377 mg/cm<sup>2</sup>) was bombarded by  $^{17}\text{B}$  with a central energy of 75 MeV/nucleon.  $^{17}\text{B}$  were broken up into charged particles and neutrons, and these fragments were measured in coincidence.<sup>3,4)</sup>

The outgoing charged fragments were measured using a magnetic spectrometer, which consists of a dipole magnet, two drift chambers, and a hodoscope. The downstream drift chamber contains five and four planes for the measurement of horizontal ( $x$ ) and vertical ( $y$ ) positions, respectively. The average position resolutions were approximately 350 and 310  $\mu\text{m}$  (FWHM), respectively. The time resolution of the hodoscope was 420 ps (FWHM). The mass number and atomic number of the fragment were identified by using the TOF information between the target and hodoscope, the energy loss signal in the hodoscope, and the tracking information of the drift chamber. The momentum vectors of the outgoing fragments were reconstructed from the reaction point upon the target, the traced rays obtained from the drift chamber, and the TOF information. The outgoing neutrons were detected with an array of 54 plastic scintillator rods. These rods were arranged into two walls in order to separate events from crosstalk. The momentum vectors of neutrons were reconstructed from TOF and hit positions of neutrons.

Figure 1 shows the preliminary result of the relative energy spectrum of the  $^{15}\text{B} + n$  system. The estimated

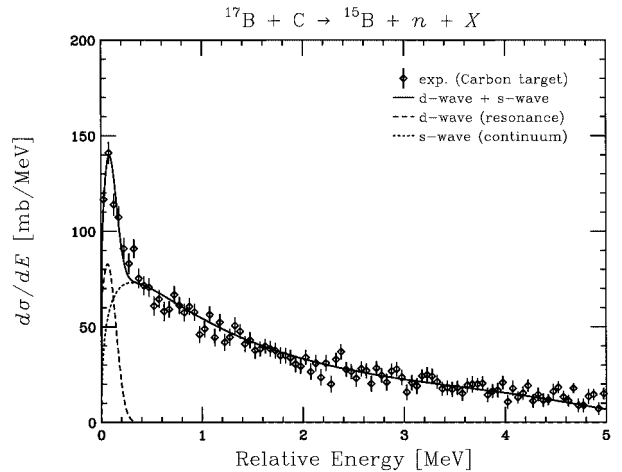


Fig. 1. Preliminary result of the relative energy spectrum of  $^{15}\text{B} + n$  system. A narrow peak can be seen in the low-energy part of this spectrum. This peak is a candidate for the ground state of  $^{16}\text{B}$ . The estimated relative-energy resolution is  $\Delta E_{\text{rel}} = 0.32\sqrt{E_{\text{rel}}}$  MeV.

relative-energy resolution is  $\Delta E_{\text{rel}} = 0.32\sqrt{E_{\text{rel}}}$  MeV. In the spectrum, a narrow peak at 70 keV is observed. Assuming that the narrow peak is a  $1d$  resonance and the remaining part is a continuum  $2s$  component, we fit the experimental result using the theoretical model based on Ref. 5. The energy of the peak is consistent with the result reported in Ref. 6. This peak can be a candidate of the ground state of  $^{16}\text{B}$ .

## References

- 1) M. Zinser et al.: Nucl. Phys. A **619**, 151 (1997).
- 2) P. Santi et al.: Phys. Rev. C **67**, 24606 (2003).
- 3) T. Nakamura et al.: RIKEN Accel. Prog. Rep. **35**, 57 (2002).
- 4) T. Sugimoto et al.: RIKEN Accel. Prog. Rep. **36**, 67 (2003).
- 5) G. F. Bertsch et al.: Phys. Rev. C **57**, 1366 (1998).
- 6) R. Kalpakchieva et al.: Eur. Phys. J. A **7**, 451 (2000).

<sup>\*1</sup> Tokyo Institute of Technology

<sup>\*2</sup> Rikkyo University

<sup>\*3</sup> National Superconducting Cyclotron Laboratory, Michigan State University, USA

<sup>\*4</sup> Tohoku University

<sup>\*5</sup> University of Tokyo

<sup>\*6</sup> Center for Nuclear Study, University of Tokyo

<sup>\*7</sup> Institute of Particle and Nuclear Studies, High Energy Accelerator Research Organization (KEK)

## Inelastic scattering of $^{15}\text{B}$ and $^{17}\text{B}$

Y. Kondo,<sup>\*1</sup> T. Nakamura,<sup>\*1</sup> N. Fukuda, T. Sugimoto,<sup>\*1</sup> M. Miura,<sup>\*1</sup> N. Aoi, N. Imai, T. Kubo, T. Kobayashi,<sup>\*3</sup> T. Gomi,<sup>\*4</sup> A. Saito,<sup>\*4</sup> H. Sakurai,<sup>\*2</sup> S. Shimoura,<sup>\*2</sup> D. Bazin,<sup>\*5</sup> H. Hasegawa,<sup>\*4</sup> H. Baba,<sup>\*4</sup> T. Motobayashi, T. Yakushiji,<sup>\*3</sup> Y. Yanagisawa, K. Yoneda, K. Watanabe,<sup>\*3</sup> Y. X. Watanabe,<sup>\*6</sup> and M. Ishihara

[NUCLEAR REACTIONS:  $\text{C}(^{15}\text{B}, ^{15}\text{B}^*)$ ,  $\text{C}(^{17}\text{B}, ^{17}\text{B}^*)$ , in-beam gamma-ray spectroscopy]

Bound excited states of  $^{15}\text{B}$  and  $^{17}\text{B}$  were studied by the inelastic scattering with a carbon target. We used a method of in-beam gamma-ray spectroscopy. Neutron-rich B isotopes are considered to have a unique feature such as halo and/or cluster structure. In a previous theoretical study, it was predicted that, with increase in a neutron number, B isotopes have clustering structure.<sup>1)</sup> The two-neutron halo structure of  $^{17}\text{B}$  was observed recently.<sup>2)</sup>

In-beam gamma-ray spectroscopy with a radioactive ion beam is a powerful tool to study a broad range of neutron-rich nuclei even extending to the neutron drip line. In this method, the gamma ray from an excited projectile is measured with a scattered ejectile in coincidence. By correcting the Doppler shift due to a velocity of the projectile, one can determine rather precisely an excitation energy and a transition probability of the bound excited states. In addition, we also measured a scattering angle of a particle. This information is useful to determine the transition multipolarity.

The experiment was performed at the radioactive-isotope beam separator, RIPS.  $^{15}\text{B}$  and  $^{17}\text{B}$  beams delivered from the RIPS were bombarded on a carbon target with a thickness of  $377\text{ mg/cm}^2$ . The carbon target was employed populating the excited states of  $^{15}\text{B}$  and  $^{17}\text{B}$ . The energies of the  $^{15}\text{B}$  and  $^{17}\text{B}$  beam were  $72\text{ MeV/u}$  at the middle of the target. The experimental setup is described in Ref. 3.

The first excited states in  $^{15}\text{B}$  and  $^{17}\text{B}$  were observed to be  $1.35(1)\text{ MeV}$  and  $1.07(1)\text{ MeV}$ , respectively, for the first time. In coincidence with these gamma transitions, angular distributions of the inelastically scattered  $^{15}\text{B}$  and  $^{17}\text{B}$  were extracted. Figure 1 shows angular distributions of the inelastically scattered  $^{15}\text{B}$  and  $^{17}\text{B}$  in c.m. frame. We compared the data with the calculation by using a coupled channel calculation

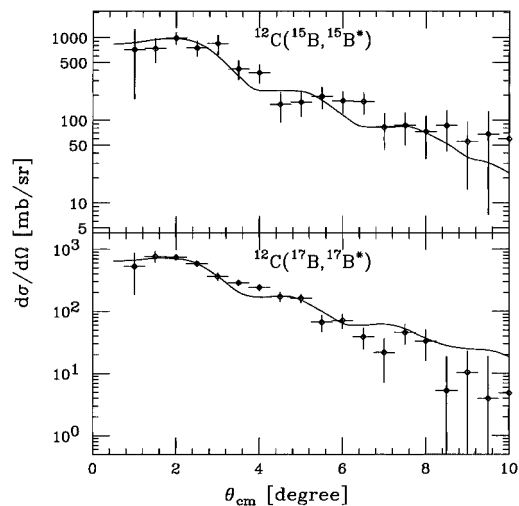


Fig. 1. Angular distributions of the inelastically scattered  $^{15}\text{B}$  and  $^{17}\text{B}$ . Lines show calculated distributions using the ECIS code with the assumption of a pure E2 transition.

code ECIS97. In this calculation, we used the optical potential parameters determined for the  $^{16}\text{O} + ^{12}\text{C}$  reaction.<sup>4)</sup> The calculated distribution well matched with the experimental data when we assumed a pure E2 transition. Further analysis is now in progress.

### References

- 1) Y. Kanada-En'yo and H. Horiuchi: *Phys. Rev. C* **52**, 647 (1995).
- 2) T. Suzuki et al.: *Phys. Rev. Lett.* **89**, 12501 (2002).
- 3) Y. Kondo et al.: *RIKEN Accel. Prog. Rep.* **36**, 65 (2003).
- 4) M.-E. Brandan: *Phys. Rev. Lett.* **60**, 784 (1988).

<sup>\*1</sup> Tokyo Institute of Technology

<sup>\*2</sup> University of Tokyo

<sup>\*3</sup> Tohoku University

<sup>\*4</sup> Rikkyo University

<sup>\*5</sup> National Superconducting Cyclotron Laboratory, Michigan State University, USA

<sup>\*6</sup> High Energy Accelerator Research Organization (KEK)

## Proton inelastic scattering of $^{19}\text{C}$

Z. Elekes,<sup>\*1</sup> Zs. Dombrádi,<sup>\*2</sup> R. Kanungo, H. Baba,<sup>\*3</sup> Zs. Fülöp,<sup>\*2</sup> J. Gibelin,<sup>\*4</sup> Á. Horváth,<sup>\*5</sup> E. Ideguchi,<sup>\*6</sup> Y. Ichikawa,<sup>\*6</sup> N. Iwasa,<sup>\*7</sup> H. Iwasaki,<sup>\*6</sup> S. Kanno,<sup>\*3</sup> S. Kawai,<sup>\*3</sup> Y. Kondo,<sup>\*3</sup> T. Motobayashi, M. Notani,<sup>\*6</sup> T. Ohnishi,<sup>\*6</sup> A. Ozawa, H. Sakurai,<sup>\*6</sup> S. Shimoura,<sup>\*6</sup> T. Suzuki,<sup>\*3</sup> E. Takeshita,<sup>\*3</sup> S. Takeuchi, I. Tanihata, Y. Togano,<sup>\*3</sup> C. Wu,<sup>\*8</sup> Y. Yamaguchi,<sup>\*3</sup> Y. Yanagisawa, A. Yoshida, and K. Yoshida

[NUCLEAR STRUCTURE, Unstable nuclei, proton inelastic scattering,  $^{19}\text{C}$ ,  $^{17}\text{B}$ , excited] states

The isotope  $^{19}\text{C}$  is a good candidate for a one-neutron halo nucleus since it has a low binding energy and a possible spin 1/2 ground state. Several experiments aimed at exploring the structure of  $^{19}\text{C}$  by Coulomb dissociation,<sup>1)</sup> parallel momentum distribution,<sup>2)</sup> reaction cross section<sup>3)</sup> *e.g.* in Ref. 1–3, for example, have been carried out. The results suggest the expected halo structure; however, an open question remains regarding the configuration of the unpaired neutron. Experimental information on excited levels might help to further understand the nuclear structure of  $^{19}\text{C}$  since these levels are rarely studied.

We have studied the  $^{19}\text{C}(p, p')$  reaction, which is expected to excite possible low-lying states even if they are difficult to reach through electromagnetic interaction.

The experiment was carried out at the RIKEN radioactive isotope separator RIPS.<sup>4)</sup> A  $^{22}\text{Ne}$  primary beam of 100 pA intensity and 110 A MeV energy hit a  $^9\text{Be}$  production target of 0.8 cm thickness. After momentum and mass analysis, the secondary cocktail beam including  $^{19}\text{C}$  at 20% and  $^{17}\text{B}$  at 25% was transmitted to a liquid hydrogen target of 190 mg/cm<sup>2</sup> average thickness.<sup>5)</sup> The mean energies of  $^{19}\text{C}$  and  $^{17}\text{B}$  isotopes were calculated to be 49.4 and 43.8 A MeV, respectively, from the incident energies and the energy loss in the target. The total beam intensity was around 800 cps and the momentum acceptance was set to 6%. The incident nuclei could be fully separated from each other by energy loss and time-of-flight measurements. The beam focus was monitored by two PPACs placed upstream of the secondary target. The scattered isotopes were identified using a silicon telescope consisting of three layers with thicknesses of 0.5, 2.0 and 2.0 mm. The  $\Delta E$ - $E$  method was used for the separation of the different carbon and boron isotopes.  $^{19}\text{C}$  and  $^{17}\text{B}$  were well separated from other products emerging in neutron removal reactions in the liquid

hydrogen target. The 158 NaI(Tl) scintillator detectors of the DALI2 array<sup>6)</sup> surrounded the target and detected the de-exciting  $\gamma$  rays emitted by the inelastically scattered nuclei. The threshold was set to 30 keV taking into account the Doppler effect. Figure 1 is the Doppler-corrected  $\gamma$  ray spectra for  $^{19}\text{C}$  and  $^{17}\text{B}$  nuclei. Some peaks, including the ones reported earlier for  $^{19}\text{C}$ <sup>7)</sup> and  $^{17}\text{B}$ ,<sup>8)</sup> were observed. Further analysis and assignment of these peaks is now in progress.

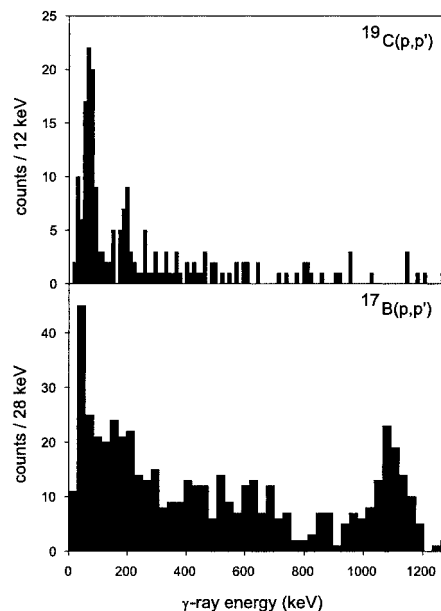


Fig. 1. Doppler-corrected spectra of  $\gamma$  rays emerging from  $^{19}\text{C}(p, p')$   $^{19}\text{C}$  (upper panel) and  $^{17}\text{B}(p, p')$   $^{17}\text{B}$  (lower panel) reactions.

### References

- 1) T. Nakamura et al.: Phys. Rev. Lett. **83**, 1112 (1999).
- 2) R. Kanungo et al.: Nucl. Phys. A **701**, 378c (2002).
- 3) A. Ozawa et al.: RIKEN Accel. Prog. Rep. **32**, 83 (1998).
- 4) T. Kubo et al.: Nucl. Instrum. Methods Phys. Res. B **70**, 309 (1992).
- 5) H. Akiyoshi et al.: RIKEN Accel. Prog. Rep. **32**, 167 (1998).
- 6) H. Hasegawa et al.: RIKEN Accel. Prog. Rep. **35**, 169 (2001).
- 7) M. Stanoiu: Thesis, Univ. Caen, code:tel-00002775 (2003).
- 8) Y. Kondo et al.: RIKEN Accel. Prog. Rep. **36**, 65 (2003).

<sup>\*1</sup> On leave from Institute of Nuclear Research (ATOMKI), Hungary  
<sup>\*2</sup> Institute of Nuclear Research (ATOMKI), Hungary  
<sup>\*3</sup> Rikkyo University  
<sup>\*4</sup> Institut de Physique Nucléaire, France  
<sup>\*5</sup> Eötvös Lóránd University, Hungary  
<sup>\*6</sup> University of Tokyo  
<sup>\*7</sup> Tohoku University  
<sup>\*8</sup> Peking University, China

# First excited state of $^{30}\text{Ne}$ studied by proton inelastic scattering in reversed kinematics<sup>†</sup>

Y. Yanagisawa, M. Notani,<sup>\*1</sup> H. Sakurai,<sup>\*2</sup> M. Kunibu,<sup>\*3</sup> H. Akiyoshi, N. Aoi, H. Baba,<sup>\*3</sup> K. Demichi,<sup>\*3</sup> N. Fukuda, H. Hasegawa,<sup>\*3</sup> Y. Higurashi, M. Ishihara, N. Iwasa,<sup>\*4</sup> H. Iwasaki,<sup>\*2</sup> T. Gomi,<sup>\*3</sup> S. Kanno,<sup>\*3</sup> M. Kurokawa, Y. U. Matsuyama,<sup>\*3</sup> S. Michimasa,<sup>\*1</sup> T. Minemura, Y. Mizoi, T. Nakamura,<sup>\*5</sup> A. Saito,<sup>\*3</sup> M. Serata,<sup>\*3</sup> S. Shimoura,<sup>\*1</sup> T. Sugimoto,<sup>\*5</sup> E. Takeshita,<sup>\*3</sup> S. Takeuchi, K. Ue,<sup>\*2</sup> K. Yamada,<sup>\*3</sup> K. Yoneda,<sup>\*6</sup> and T. Motobayashi

[Nuclear structure,  $^{30}\text{Ne}$ , Proton inelastic scattering, Unstable nuclei]

An interesting aspect of nuclei around  $N = 20$  is the transition from spherical to deformed shapes in a region centered at  $Z \sim 11$  and  $N \sim 21$ , which is referred to as the ‘island of inversion’.<sup>1)</sup> We report on the first measurement of the first excited state of  $^{30}\text{Ne}$ , which is expected to be the last even-even  $N = 20$  nucleus.

In-beam  $\gamma$  spectroscopy using fast radioactive beams has been carried out by some methods in recent years. We have employed it with proton inelastic scattering in reversed kinematics using a liquid-hydrogen target by detecting de-excitation  $\gamma$  rays in coincidence with scattered particles. This method is advantageous because of the high experimental efficiency in determining the locations of low-lying excited states. Compared to the high- $Z$  targets used in Coulomb excitation, the number of target atoms per  $\text{g}/\text{cm}^2$  in liquid hydrogen is substantially larger, typically by two orders of magnitude.

The experiment was performed using the RIPS.<sup>2)</sup> A primary  $^{40}\text{Ar}$  beam of 94 MeV/nucleon with a typical intensity of 60 pnA bombarded a  $^{181}\text{Ta}$  target with a thickness of  $641 \text{ mg}/\text{cm}^2$ . To reduce the amount of beam impurities, an aluminum wedged degrader having a mean thickness of  $321 \text{ mg}/\text{cm}^2$  was installed on the momentum dispersive focal plane (F1). Secondary ions were collected using the optimized magnetic rigidity setting for  $^{30}\text{Ne}$  and with the full momentum acceptance of the RIPS ( $\pm 3\%$ ). The intensity of the  $^{30}\text{Ne}$  beam with an average incident energy of 56 MeV/nucleon was obtained to be 0.2 cps with the contamination of  $^{29}\text{Ne}$ ,  $^{31}\text{Na}$  and  $^{32}\text{Na}$  beams. A liquid hydrogen target<sup>3)</sup> was placed at the final focus of the RIPS to excite the projectiles. The thickness of the hydrogen target cell was 24 mm and the entrance and exit windows were made of 6.6- $\mu\text{m}$ -thick Havar foil. The resultant areal density of hydrogen was  $186 \text{ mg}/\text{cm}^2$  on average. Scattered particles were detected and identified by a PPAC and a silicon-detector

telescope located about 50 cm downstream of the target. In the DALI setup, sixty-eight NaI(Tl) scintillators were placed around the target to detect the de-excitation  $\gamma$  rays emitted from the excited nuclei.

The energy of the de-excitation  $\gamma$  rays from  $^{30}\text{Ne}$  with the Doppler correction was obtained to be 791(26) keV, by measuring the  $^{30}\text{Ne}$  secondary beams in coincidence with scattered particles. Considering this systematic trend, the 791 keV  $\gamma$  ray is consistent with the  $2^+ \rightarrow 0^+$  de-excitation in  $^{30}\text{Ne}$ , leading to the first  $2^+$  energy  $E(2^+)$  of 791 keV.

The quadrupole deformation parameter of the 791 keV state was extracted by a coupled channel calculation using the ECIS79 code in the framework of the standard symmetric rotational model. By taking the  $\gamma$ -ray detection efficiency into account, the corresponding experimental cross section of the 791 keV transition was calculated to be  $30 \pm 18 \text{ mb}$ . By comparing the calculated and experimental cross sections, the deformation parameter  $\beta_2^{p,p'} = 0.58_{-0.22}^{+0.16}$  was obtained. Under the assumption that electromagnetic deformation is the same as nuclear one ( $\beta_2^{p,p'} = \beta_2^{\text{em}}$ ), the reduced E2 transition probability  $B(E2)$  was estimated to be  $460 \pm 270 e^2 \text{ fm}^4$ .

In summary, the first excited state of the very neutron-rich nucleus  $^{30}\text{Ne}$  was measured for the first time. In-beam  $\gamma$  spectroscopy was applied using proton inelastic scattering and a liquid hydrogen target. The observed energy of 791(26) keV for  $^{30}\text{Ne}$  is the lowest among the  $2^+$  energies of even-even  $N = 20$  isotones, suggesting a large deformation of  $^{30}\text{Ne}$ , and that the  $^{30}\text{Ne}$  nucleus thus belongs to the ‘island of inversion.’ The  $B(E2)$  value estimated from the (p, p') cross section also supports this conclusion.

## References

- 1) E. K. Warburton et al.: Phys. Rev. C **41**, 1147 (1990).
- 2) T. Kubo et al.: Nucl. Instrum. Methods Phys. Res. B **70**, 309 (1992).
- 3) H. Akiyoshi et al.: RIKEN Accel. Prog. Rep. **32**, 167 (1999).

<sup>†</sup> Condensed from the article in Phys. Lett. B **556**, 84 (2003)

<sup>\*1</sup> Center for Nuclear Study, University of Tokyo

<sup>\*2</sup> Department of Physics, University of Tokyo

<sup>\*3</sup> Department of Physics, Rikkyo University

<sup>\*4</sup> Department of Physics, Tohoku University

<sup>\*5</sup> Department of Physics, Tokyo Institute of Technology

<sup>\*6</sup> Department of Physics, Michigan State University, USA

# Search for low lying dipole strength in the neutron rich nucleus $^{26}\text{Ne}$

J. Gibelin,<sup>\*1,\*2</sup> K. Yoshida, D. Beaumel,<sup>\*1</sup> N. Fukuda, N. Aoi, H. Baba,<sup>\*2</sup> Y. Blumenfeld,<sup>\*1</sup> Z. Elekes, T. Gomi,<sup>\*2</sup> K. Ishikawa,<sup>\*3</sup> Y. Kondo,<sup>\*3</sup> T. Kubo, V. Lima,<sup>\*1</sup> T. Motobayashi, T. Nakamura,<sup>\*3</sup> A. Saito,<sup>\*2</sup> Y. Satou,<sup>\*3</sup> E. Takeshita,<sup>\*2</sup> S. Takeuchi, T. Teranishi,<sup>\*4</sup> Y. Togano,<sup>\*2</sup> A. M. Vinodkumar,<sup>\*3</sup> and Y. Yanagisawa

[Nuclear structure, Coulomb excitation,  $^{26}\text{Ne}$ ]

We measured Coulomb excitation in  $^{26}\text{Ne}$  to investigate low lying E1 strength in  $^{26}\text{Ne}$ , for which some predictions exist,<sup>1)</sup> using the invariant mass method.

In this experiment,  $^{26}\text{Ne}$  was selected by the RIKEN Projectile fragment Separator (RIPS) after a 2-mm-thick Be production target was bombarded with a 95 MeV/n  $^{40}\text{Ar}$  beam. We thus required a secondary  $^{26}\text{Ne}$  beam with an energy of 58 MeV/n, an average rate of 10 kcps and a purity of 80%. The main contaminant was  $^{29}\text{Mg}$ . In order to obtain information on the contributions of E1 *vs.* E2 and Coulomb *vs.* nuclear excitations, measurements have been performed using Pb and Al targets. The Pb target being more charged is expected to induce more Coulomb excitation than Al, which is used to subtract the nuclear reaction part. Hence, we used secondary targets of 230 mg/cm<sup>2</sup> Pb and 130 mg/cm<sup>2</sup> Al.

Secondary beam momentum vectors were obtained by tracking with two parallel-plate avalanche counters placed before the target and using time-of-flight (TOF) information between the production target (RF signal) and a 5 mm plastic scintillator located downstream of the RIPS F2 focal point. The detection setup at the last focal point is represented on Fig. 1. The momenta and energies of outgoing charged fragments were measured using a telescope placed at 1.2 m upstream of the target and consisted of two layers (X and Y) of 8 silicon strip detectors (SSD) that can determine a position with a precision of 5 mm and an energy loss (dE) of 2% (FWHM). The last layer used 3-mm-thick Si(Li) (8 pieces) from the charged-particle detector, MUST,<sup>2)</sup> which provided a 3% (FWHM) precision on the energy (E).

In-beam  $\gamma$  rays were detected using a  $4\pi$ - $\gamma$ -detector, DALI,<sup>3)</sup> which consisted of 152 NaI detectors placed around the target. For 2 MeV  $\gamma$  rays, its efficiency is calculated to be approximately 10% with a precision of 7% (FWHM). The hodoscope for neutron detection was a cross-shape array of 4 layers of 29 plastic rods each, placed 3.5 m downstream of the target. Each layer was composed of 13 [2.1 m  $\times$  6 cm  $\times$  6 cm] and 2 times 8 [1.1 m  $\times$  6 cm  $\times$  6 cm] rods. Its total intrinsic efficiency was calculated to be  $\sim$ 25%. Finally, 29 plastic rods, sensitive to charged particles, covered the active hodoscope front face in order to be used as vetoes

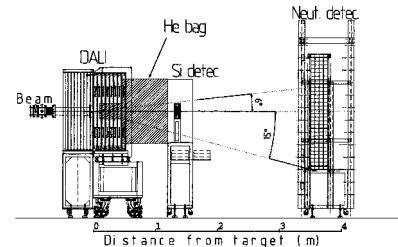


Fig. 1. Overview of the whole setup.

and active beam stoppers. The position is expected to be determined with a precision of 6 cm (FWHM) and the energy, from TOF information, with 4% (FWHM).  $^{26}\text{Ne}$  was identified using TOF, charged fragments with dE-E method and neutron by suppressing simultaneous events in veto.

The data obtained are still under analysis but the rate of triple coincidence ( $^{26}\text{Ne}$  beam  $\otimes$   $^{25}\text{Ne}$  in silicon  $\otimes$  neutron) measured during the experiment is approximately 1 event per minute. This is compatible with the results of simulations, assuming an excitation of 8 MeV and 10% of the energy weighted sum rule for ECIS cross-section ( $\sim$ 120 mb) calculation. Shown in Fig. 2 are preliminary results for the distribution of relative energy between  $^{25}\text{Ne}$  and neutron. Based on the neutron emission threshold for  $^{26}\text{Ne}$  being at 5.6 MeV, the energy of interest here should be approximately 2.5 MeV.

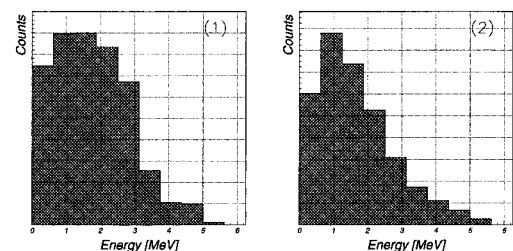


Fig. 2. Preliminary results for relative energy distribution between  $^{25}\text{Ne}$  and neutron: (1) using runs with Pb target and by weighted subtraction from no-target runs; (2) detection efficiency weighted summation from Pb-target runs, in coincidence with  $\gamma$  emitted from  $^{25}\text{Ne}^*$ .

## References

- 1) Z. Ma: Private communication.
- 2) Y. Blumenfeld et al.: Nucl. Instrum. Methods Phys. Res. A **421**, 471 (1999).
- 3) S. Takeuchi et al.: RIKEN Accel. Prog. Rep. **36**, 148 (2002).

\*1 Institut de Physique Nuclaire, France

\*2 Department of Physics, Rikkyo University

\*3 Department of Physics, Tokyo Institute of Technology

\*4 Center for Nuclear Study, University of Tokyo



# Direct measurement of the astrophysical reaction $^{14}\text{O}(\alpha, p)^{17}\text{F}$

M. Notani,<sup>\*1</sup> S. Kubono,<sup>\*1</sup> T. Teranishi,<sup>\*1</sup> Y. Yanagisawa, S. Michimasa,<sup>\*1</sup> K. Ue,<sup>\*1</sup> T. Minemura, Zs. Fülöp,<sup>\*2</sup> J. J. He,<sup>\*1</sup> H. Iwasaki,<sup>\*3</sup> H. Baba,<sup>\*4</sup> M. Tamaki,<sup>\*1</sup> S. Shimoura,<sup>\*1</sup> N. Hokoïwa,<sup>\*5</sup> Y. Wakabayashi,<sup>\*5</sup> T. Sasaki,<sup>\*5</sup> T. Fukuchi,<sup>\*5</sup> A. Odahara,<sup>\*6</sup> Y. Gono,<sup>\*5</sup> E. K. Lee,<sup>\*7</sup> K. I. Hahn,<sup>\*7</sup> J. Y. Moon,<sup>\*8</sup> C. C. Yun,<sup>\*8</sup> J. H. Lee,<sup>\*8</sup> C. S. Lee,<sup>\*8</sup> and S. Kato<sup>\*9</sup>

[NUCLEAR REACTIONS  $^{14}\text{O}(\alpha, p)^{17}\text{F}$ , Unstable nuclei, Nuclear astrophysics]

Explosive hydrogen burning of light nuclei occurs in a hot and dense stellar environment such as those of novae and X-ray bursts. As a starting point of the rapid proton-capture (rp-) process, nuclear reactions in the breakout process from the hot-CNO cycle are highly interesting in the field of nuclear astrophysics.<sup>1)</sup> At high temperatures, the  $^{14}\text{O}(\alpha, p)^{17}\text{F}$  ( $p, \gamma$ ) $^{18}\text{Ne}$  ( $\alpha, p$ ) $^{21}\text{Na}$  reaction sequence can provide a path way into the rp-process. Therefore, the rate of the  $^{14}\text{O}(\alpha, p)^{17}\text{F}$  reaction is important for understanding the breakout process. This reaction has been studied via only indirect methods and time-reverse reaction so far. A direct measurement of the  $^{14}\text{O}(\alpha, p)^{17}\text{F}$  reaction is difficult since it requires an intense low-energy  $^{14}\text{O}$  beam and a helium gas target.

The experiment was performed using the CNS radioactive ion beam separator (CRIB),<sup>2)</sup> which was recently installed by CNS, in the RIKEN accelerator research facility. A primary beam of  $^{14}\text{N}$  was accelerated up to an energy of 8.4 A MeV in the RIKEN AVF cyclotron with  $K = 70$ . The maximum intensity of the beam was 300 pnA. The primary beam bombarded a  $\text{CH}_4$  gas target with a thickness of 1.3 mg/cm<sup>2</sup>. The target gas was confined in a small chamber with entrance and exit windows made of 2.2- $\mu\text{m}$  Havar foils. A secondary beam of  $^{14}\text{O}$  was produced by the  $^1\text{H}(^{14}\text{N}, ^{14}\text{O})\text{n}$  reaction. An energy degrader of 10- $\mu\text{m}$ -thick mylar foil was installed at the momentum dispersive focal plane (F1) to remove background light ions from the secondary beam. A horizontal slit was set to select the  $^{14}\text{O}$  particles at a mean energy of 6.40 A MeV after the degrader with the momentum acceptance of 1%.

At the achromatic focal plane (F2), a series of detectors and a secondary target were installed in a vacuum chamber. The setup consisted of two parallel-plate avalanche counters (PPACs), a helium gas target with a thickness of 3.57 mg/cm<sup>2</sup>, and a silicon-detector stack with thicknesses of 0.02, 0.07, 1.5 and 1.5 mm. Particle identification was performed for each event

on the basis of time of flight (TOF) between the two PPACs. The purity of the  $^{14}\text{O}$  beam was 85% at F2.

A cold helium gas target was bombarded with the  $^{14}\text{O}$  beam at an incident energy of 43 MeV. The helium gas was confined in a 50-mm-long cell with two windows of 2.2- $\mu\text{m}$ -thick Havar foils. It was kept at a pressure of 0.6 atm and was cooled to 30 K. The target was chosen to be as thin as possible, but sufficiently thick to stop the  $^{14}\text{O}$  nuclei in it. The novel helium gas target was designed offering ten times larger density than at room temperature. This design results in exceedingly compactness and thus makes it possible to effectively apply the thick-target method.<sup>3)</sup> The reaction products emitted from the helium target were identified by the  $\Delta E$ - $E$  method, using the telescope of four silicon detectors located at 0°.

From the proton spectrum, the reaction cross sections were obtained in the energy range of 0.8–3.8 MeV in the center-of-mass system of  $^{14}\text{O} + \alpha$ . Eight resonances are clearly identified in the data which correspond to previously observed states at 6.15, 6.29, 7.05, 7.12, 7.35, 7.62, 7.95 and 8.30 MeV in  $^{18}\text{Ne}$ .<sup>4)</sup> In addition, we newly observed a peak related to the  $^{14}\text{O}(\alpha, p)^{17}\text{F}^*$  reaction leading to the  $1/2^+$  first-excited state in  $^{17}\text{F}$ , which undergoes a resonance at around  $E_x(^{18}\text{Ne}) = 7.1$  MeV, as shown in Fig. 1. Further analysis is in progress.

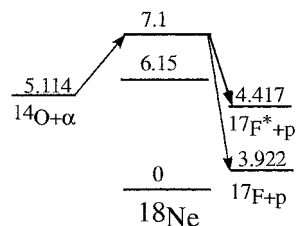


Fig. 1. Level scheme in  $^{18}\text{Ne}$ .

## References

- 1) R. K. Wallace and S. E. Woosley: *Astrophys. J. Suppl. Ser.* **45**, 389 (1981).
- 2) Y. Yanagisawa et al.: *RIKEN Accel. Prog. Rep.* **34**, 183 (2001).
- 3) K. P. Artemov et al.: *Sov. J. Nucl. Phys.* **52**, 408 (1990).
- 4) K. I. Hahn et al.: *Phys. Rev. C* **54**, 1999 (1996).

\*1 Center for Nuclear Study, University of Tokyo

\*2 ATOMKI, Hungary

\*3 University of Tokyo

\*4 Rikkyo University

\*5 Kyushu University

\*6 Nishinippon Institute of Technology

\*7 Ewha Womans University, Korea

\*8 Chun-Ang University, Korea

\*9 Yamagata University

## Study of astrophysically important resonance states in $^{26}\text{Si}$ and $^{27}\text{P}$ using radioactive ion beams

J. Y. Moon,<sup>\*1</sup> C.-S. Lee,<sup>\*1</sup> J.-H. Lee,<sup>\*1</sup> C. C. Yun,<sup>\*1</sup> J. C. Kim,<sup>\*2</sup> M. Youn,<sup>\*2</sup> S. Kubono,<sup>\*3</sup> T. Teranishi,<sup>\*3</sup>  
J. J. He,<sup>\*3</sup> M. Notani,<sup>\*3</sup> S. Nishimura, M. Kurata-Nishimura, S. Kato,<sup>\*4</sup>  
V. Guimarães,<sup>\*5</sup> and R. F. Lihitenthaler<sup>\*5</sup>

[Nucleoastrophysics, radioactive ion beam,  $^{26}\text{Si}$ ,  $^{27}\text{P}$ ]

1.809 MeV gamma rays, observed by COMPTEL of CGRO, are known to be produced when  $^{26}\text{Al}(\text{g.s})$   $\beta$ -decays to the first excited state in  $^{26}\text{Mg}$  followed by de-exciting to its ground state. Their sources are not clearly identified yet. In thermonuclear runaway under explosive hydrogen burning, the  $^{25}\text{Al}(\text{p}, \gamma)^{26}\text{Si}$  reaction hinders production of  $^{26}\text{Al}(\text{g.s.})$  and thus its nuclear structural information, such as excitation energy and spin parity is needed to calculate the reaction rate and estimate its contribution. In spite of previous experimental efforts, spins of some states including those at  $E_x = 6.470$  MeV, 6.880 MeV and 7.019 MeV have not been clarified yet.<sup>1,2)</sup> The  $^{26}\text{Si}(\text{p}, \gamma)^{27}\text{P}$  reaction prevents production of  $^{26m}\text{Al}$ . It has been suggested that high-temperature novae ( $T \geq 0.4$  GK) are hot sufficiently to establish an equilibrium between  $^{26}\text{Al}(\text{g.s})$  and  $^{26m}\text{Al}$ .<sup>3)</sup> Thus, resonance states in  $^{27}\text{P}$  should be studied to determine the reaction rate of  $^{26}\text{Si}(\text{p}, \gamma)^{27}\text{P}$ . Thus far, only one state at 1.199 MeV above the proton threshold has been reported.<sup>4)</sup>

The radioactive beams used in this experiment were obtained by the CNS radioactive ion beam separator (CRIB). A  $^{24}\text{Mg}^{8+}$  primary beam, accelerated by the RIKEN AVF cyclotron ( $K = 70$ ), bombarded a  $^3\text{He}$  gas target at 7.434 A MeV. The thickness of the  $^3\text{He}$  gas target was 0.32 mg/cm<sup>2</sup>. With  $^3\text{He}(^{24}\text{Mg}, \text{n})^{26}\text{Si}^*(\text{p})^{25}\text{Al}$  and  $^3\text{He}(^{24}\text{Mg}, \text{n})^{26}\text{Si}$ , two kinds of radioactive beams were produced and used for the measurement of elastic scattering  $^1\text{H}(^{25}\text{Al}, \text{p})^{25}\text{Al}$  and  $^1\text{H}(^{26}\text{Si}, \text{p})^{26}\text{Si}$ . Secondary beams were identified using TOF between two PPACs on the achromatic focal plane (F2), beam energy and TOF between the production target and the PPACb on the F2 plane. With a slit on the momentum-dispersive focal plane (F1), the purities of secondary beams were enhanced. Additionally, an energy degrader of 2.6  $\mu\text{m}$  mylar was used to achieve another particle separation. The properties of secondary beams are shown in Table 1. The secondary beams bombarded a polyethylene ( $\text{CH}_2$ ) target of 8.24 mg/cm<sup>2</sup>, and fully stopped in the target. To detect recoiled protons, two sets of silicon counter telescopes, which consist of a 75  $\mu\text{m}$  position-

Table 1. The properties of secondary beams on target (averaged).

	Energy(A MeV)	Intensity (kcps)	Purity (%)
$^{25}\text{Al}$	3.44	9.325	4.72
$^{26}\text{Si}$	3.95	1.573	0.7

sensitive silicon detector (PSD) and 1500  $\mu\text{m}$  surface barrier silicon detector (SSD), were installed at 0° and 17°. They were also used as  $\Delta E$ - $E$  telescopes to distinguish them from other recoiled particles, such as  $\alpha$  and heavy ions. In the second set at 17°, additional SSD was added to reject the proton with high energy. In this experiment, we used the thick-target method to examine a wide excitation energy range in  $^{26}\text{Si}$  and  $^{27}\text{P}$ , where the incident beam can have different energies in the target and interact with the target until its energy is fully absorbed. The secondary beams had energies of 3.4407 A MeV for the  $^{25}\text{Al}$  beam and 3.9575 A MeV for the  $^{26}\text{Si}$  beam on the target. Under these conditions, we succeeded in our investigation up to  $E_x = 8.8243$  MeV and  $E_x = 4.7109$  MeV above the proton threshold. Also, a carbon target was used to eliminate the contribution of carbon in the  $\text{CH}_2$  target from the proton spectrum of the  $\text{CH}_2$  target. The energy calibration of the detector was performed with protons whose energy was determined by the CRIB magnetic setting. We observed some peaks below  $E_x = 8.120$  MeV in the  $^{25}\text{Al} + \text{p}$  elastic scattering spectrum. Above 8.120 MeV, we could not identify a resonant structure because of a large contaminant. For the  $^{26}\text{Si} + \text{p}$  elastic scattering spectrum, we also observed several peaks even with low counting statistics. Now data analysis is in progress. R-matrix analysis will be performed to determine the spins and the excitation energies of the resonance states.

### References

- 1) D. W. Bardayan et al.: Phys. Rev. C **65**, 032801(R) (2002).
- 2) J. A. Caggiano et al.: Phys. Rev. C **65**, 055801 (2002).
- 3) A. Coc, M.-G. Porquet, and F. Nowacki: Phys. Rev. C **61**, 015801 (1999).
- 4) J. A. Caggiano et al.: Phys. Rev. C **64**, 025802 (2001).

<sup>\*1</sup> Department of Physics, Chung-Ang University, Korea

<sup>\*2</sup> Department of Physics, Seoul National University, Korea

<sup>\*3</sup> Center for Nuclear Study, Graduate School of Science, University of Tokyo

<sup>\*4</sup> Department of Physics, Yamagata University

<sup>\*5</sup> Instituto de Física, Universidade de São Paulo, Brazil

## Study of the resonant state in $^{23}\text{Al}$ relevant to the stellar $^{22}\text{Mg}(p,\gamma)^{23}\text{Al}$ reaction

T. Gomi,<sup>\*1</sup> T. Motobayashi, Y. Ando,<sup>\*1</sup> N. Aoi, H. Baba,<sup>\*1</sup> K. Demichi,<sup>\*1</sup> Z. Elekes,<sup>\*2</sup> N. Fukuda, Zs. Fülöp,<sup>\*2</sup> U. Futakami,<sup>\*1</sup> H. Hasegawa,<sup>\*1</sup> Y. Higurashi, K. Ieki,<sup>\*1</sup> N. Imai, M. Ishihara, K. Ishikawa,<sup>\*3</sup> N. Iwasa,<sup>\*4</sup> H. Iwasaki,<sup>\*5</sup> S. Kanno,<sup>\*1</sup> Y. Kondo,<sup>\*3</sup> T. Kubo, S. Kubono,<sup>\*6</sup> M. Kunibu,<sup>\*1</sup> K. Kurita,<sup>\*1</sup> Y. U. Matsuyama,<sup>\*1</sup> S. Michimasa,<sup>\*6</sup> T. Minemura, M. Miura,<sup>\*3</sup> H. Murakami,<sup>\*1</sup> T. Nakamura,<sup>\*3</sup> M. Notani,<sup>\*6</sup> S. Ota,<sup>\*7</sup> A. Saito,<sup>\*1</sup> H. Sakurai,<sup>\*5</sup> M. Serata,<sup>\*1</sup> S. Shimoura,<sup>\*6</sup> T. Sugimoto,<sup>\*3</sup> E. Takeshita,<sup>\*1</sup> S. Takeuchi, Y. Togano,<sup>\*1</sup> K. Ue,<sup>\*5</sup> K. Yamada,<sup>\*1</sup> Y. Yanagisawa, K. Yoneda, and A. Yoshida

[NUCLEAR REACTIONS:  $^{208}\text{Pb}(^{23}\text{Al}, ^{22}\text{Mg} p)^{208}\text{Pb}$ , Coulomb dissociation]

We have performed an experiment to study the stellar  $^{22}\text{Mg}(p,\gamma)^{23}\text{Al}$  reaction using the Coulomb-dissociation method. This reaction is relevant to the nucleosynthesis of the  $\gamma$ -ray emitter  $^{22}\text{Na}$  in Ne novae. In the energy region of astrophysical interest, the first excited state of  $^{23}\text{Al}$  is known to be located at an excitation energy of 0.528 MeV.<sup>1)</sup> However, there is no experimental data for the strength of the resonant capture through this first excited state. In the present work, we aimed at determining the radiation width of this resonant state.

The experiment was performed at the RIPS beam line. A secondary beam of  $^{23}\text{Al}$  at 50 MeV/nucleon produced by the projectile fragmentation of  $^{28}\text{Si}$  bombarded a Pb target. The products of the breakup reaction,  $^{22}\text{Mg}$  and a proton, were detected respectively using silicon counter telescopes and a plastic scintillator hodoscope located 50 cm and 3 m downstream of the target. In order to deduce the relative energy of the breakup reaction products measured in coincidence, we measured the momentum vectors of the particles. A stack of sixty-eight NaI(Tl) scintillators (DALI) was placed around the target to measure deexcitation  $\gamma$ -rays from  $^{22}\text{Mg}$  in its excited states, the contribution of which should be subtracted to extract the Coulomb dissociation cross section of interest. The details of the experimental setup can be found in Ref. 2.

The relative energy spectrum obtained for the  $^{208}\text{Pb}(^{23}\text{Al}, ^{22}\text{Mg} p)^{208}\text{Pb}$  reaction is shown in Fig. 1. We deduced this spectrum after subtracting the contribution of the dissociation process leading to higher states in  $^{22}\text{Mg}$  using the information from the  $\gamma$ -ray detector array. Therefore, this spectrum is for the process in which  $^{23}\text{Al}$  disintegrates to the ground state of  $^{22}\text{Mg}$  through excited states in  $^{23}\text{Al}$ . In this spectrum, the first excited state of  $^{23}\text{Al}$  corresponds to the peak

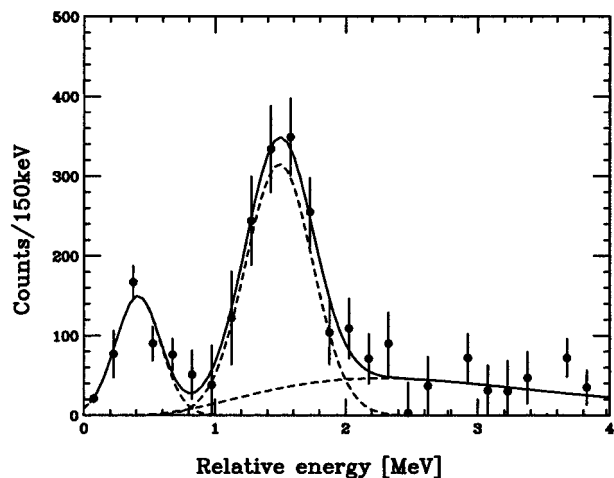


Fig. 1. Relative energy spectrum obtained for the  $^{208}\text{Pb}(^{23}\text{Al}, ^{22}\text{Mg} p)^{208}\text{Pb}$  reaction. The solid curve represents the result of a fitting with two Gaussian functions and a distribution assuming a nonresonant component. The dashed curves show each component.

around 400 keV. We obtained the cross section of the Coulomb dissociation through the first excited state of  $^{23}\text{Al}$  as 4.4 mb. Supposing that the spin and parity of  $^{23}\text{Al}$  are  $5/2^+$  for the ground state and  $1/2^+$  for the first excited state, the cross section corresponds to  $\Gamma_\gamma = 7.2 \times 10^{-7}$  eV with an error of 20%.

In order to evaluate the influence of the  $^{22}\text{Mg}(p,\gamma)^{23}\text{Al}$  reaction on the network calculation for thermonuclear runaway, we consider the competition with  $\beta$  decay of  $^{22}\text{Mg}$ . According to the temperature and density condition predicted by nova models,<sup>3)</sup> the main reaction flow favors the  $\beta$  decay rather than the proton capture on  $^{22}\text{Mg}$ .

### References

- 1) J. A. Caggiano et al.: Phys. Rev. C **64**, 025802 (2001).
- 2) T. Gomi et al.: RIKEN Accel. Prog. Rep. **36**, 82 (2003).
- 3) C. Iliadis et al.: Astrophys. J. Suppl. Ser. **142**, 105 (2002).

\*1 Rikkyo University

\*2 ATOMKI, Hungary

\*3 Tokyo Institute of Technology

\*4 Tohoku University

\*5 University of Tokyo

\*6 Center for Nuclear Study, University of Tokyo

\*7 Kyoto University

# Beta decay half-lives of neutron-rich Cr, Mn, Fe, and Co isotopes

S. Nishimura, Y. Nishi, M. A. Famiano,\*<sup>1</sup> M. Kurata-Nishimura, R. N. Boyd,\*<sup>2</sup> M. E. Howard,\*<sup>2</sup>  
D. Reitzner,\*<sup>2</sup> E. E. Smith,\*<sup>2</sup> and I. Tanihata

[Beta decay, Half-life, r-Process]

The neutron-rich nuclei far from stability are expected to play a key role in the r-process nucleosynthesis. At present, however, the study of these nuclei in relation to their half-lives, Q values, and neutron-emission probabilities is limited by their low production rates.

Our primary experiment was carried out at the RIKEN Ring Cyclotron (RRC). The neutron-rich V, Cr, Mn, Fe, Co, and Ni isotopes were produced by the fragmentation of a 63 MeV  $^{86}\text{Kr}^{32+}$  beam, of mean intensity  $1\ \mu\text{A}$ , onto a  $^9\text{Be}$  target of  $375\ \mu\text{m}$  thickness. Figure 1(a) shows the nuclei identified using high-resolution TOF detectors<sup>1)</sup> and a  $150\ \mu\text{m}$  silicon detector. The beta-ray detection system, which consists of ion stopper plates attached on the rotating wheel and high-efficiency position-sensitive detectors,<sup>2,3)</sup> was installed at the end of the beam line. The event associations between the implanted nuclei and the beta decays were achieved using the precise position measurement of incident nucleus and the beta-decay points on the stopper plates. The beta-decay time spectrum in correlation with the implantation of  $^{65}\text{Mn}$  isotope is shown in Fig. 1(b). The cutoff time after 250 ms is determined by the acceptance of the beta-ray detectors. The half-lives of nuclei were extracted by considering the four parameters in the fitting procedure: the half-lives of the mother and daughter nuclei, the beta detection efficiency, and the background rate over the collecting time. The half-lives of daughter nuclei have been obtained from Ref. 4. The background from the decay of long-lived nuclei is estimated by the event-mixing method. Our preliminary results of half-lives for the neutron-rich  $^{63,64}\text{Cr}$ ,  $^{65,66}\text{Mn}$ ,  $^{67,68}\text{Fe}$ , and

$^{69,70}\text{Co}$  nuclei are summarized in Table 1. In addition, the results from other experiments<sup>4)</sup> and theoretical predictions<sup>5)</sup> are listed for comparison. The discrepancy between the experimental values and the theoretical predictions support the overabundances of  $^{64}\text{Ni}$  in certain inclusions of meteorites.<sup>6)</sup>

Our first measurement of the half-lives of massive nuclei above 63–70 amu successfully demonstrated the possibility of reconstructing the beta-decay spectra of rare isotopes under high intensities of mixed beam at the RIBF. Here, the application of the plastic material instead of the silicon detector for the isotope implantation was aimed to avoid the potential problem of radiation damage on the detector itself together with the minimization of the accumulated contaminants from the daughters. Further upgrade of the system is planned by introducing additional detectors,  $\text{CaF}_2(\text{Eu})$ ,  $\text{NaI}(\text{Tl})$ , and Ge, which enable us to measure the energies of beta and gamma rays simultaneously as well as to reduce the accidental backgrounds in the detectors.

Table 1. Preliminary results of half-lives of  $^{63,64}\text{Cr}$ ,  $^{65,66}\text{Mn}$ ,  $^{67,68}\text{Fe}$ , and  $^{69,70}\text{Co}$  nuclei. Also presented are the results from other experiments<sup>4)</sup> and theoretical predictions.<sup>5)</sup>

RI	$T_{1/2}^{R322n}$ (ms)	$T_{1/2}^{\text{Exp.}}$ (ms)	$T_{1/2}^{\text{Theo.}}$ (ms)
$^{70}\text{Co}$	135 $\begin{smallmatrix} +11 \\ -9 \end{smallmatrix}$	120	47.5
$^{69}\text{Co}$	197 $\begin{smallmatrix} +80 \\ -29 \end{smallmatrix}$	216	76.6
$^{68}\text{Fe}$	155 $\begin{smallmatrix} +34 \\ -18 \end{smallmatrix}$	155	767.3
$^{67}\text{Fe}$	597 $\begin{smallmatrix} +209 \\ -100 \end{smallmatrix}$	470	1139
$^{66}\text{Mn}$	103 $\begin{smallmatrix} +44 \\ -33 \end{smallmatrix}$	66	23.1
$^{65}\text{Mn}$	85 $\begin{smallmatrix} +10 \\ -9 \end{smallmatrix}$	88	28.9
$^{64}\text{Cr}$	61 $\begin{smallmatrix} +60 \\ -19 \end{smallmatrix}$	44	153.9
$^{63}\text{Cr}$	161 $\begin{smallmatrix} +104 \\ -91 \end{smallmatrix}$	113	96.6

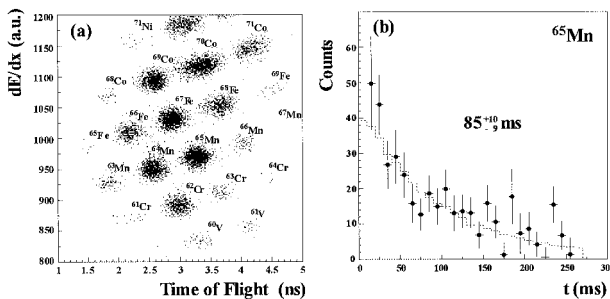


Fig. 1. (a) Identification of the nuclei produced in the experiment by their energy loss ( $dE/dx$ ) and time of flight (TOF). (b) Preliminary beta-decay spectrum of  $^{65}\text{Mn}$ .

\*<sup>1</sup> National Superconducting Cyclotron Laboratory, USA

\*<sup>2</sup> Ohio State University, USA

## References

- 1) S. Nishimura et al.: Nucl. Instrum. Methods Phys. Res. A **510**, 377 (2003).
- 2) M. A. Famiano, Y. Nishi, S. Nishimura, and I. Tanihata: Nucl. Instrum. Methods Phys. Res. A **496**, 248 (2003).
- 3) S. Nishimura et al.: Nucl. Phys. A **718**, 214c (2003).
- 4) T. Horiguchi, T. Tachibana, H. Koura, and J. Katakura: Chart of the Nuclides, Japan Atomic Energy Research Institute (2000).
- 5) P. Möller, J. R. Nix, and K.-L. Kratz: At. Data and Nucl. Data Tables **66**, 131 (1997).
- 6) O. Sorlin et al.: Nucl. Phys. A **719**, 193c (2003).

## Investigation of resonant states in $^{23}\text{Al}$ and $^{22}\text{Mg}$ using RI beams

J. J. He,<sup>\*1</sup> S. Kubono,<sup>\*1</sup> T. Teranishi,<sup>\*1</sup> M. Notani,<sup>\*1</sup> H. Baba,<sup>\*2</sup> S. Nishimura, J. Y. Moon,<sup>\*3</sup>  
 M. Kurata-Nishimura, S. Michimasa,<sup>\*1</sup> H. Iwasaki,<sup>\*4</sup> Y. Yanagisawa, N. Hokoikiwa,<sup>\*5</sup>  
 M. Kibe,<sup>\*5</sup> J. H. Lee,<sup>\*3</sup> S. Kato,<sup>\*6</sup> Y. Gono,<sup>\*5</sup> and C. S. Lee<sup>\*3</sup>

[Proton Resonant State, Nuclear Astrophysics]

During the early stage of the rp process, both the  $^{22}\text{Mg}(p, \gamma)^{23}\text{Al}$  and  $^{21}\text{Na}(p, \gamma)^{22}\text{Mg}$  reactions play a very important role.<sup>1-4</sup> They possibly influence the production of  $\gamma$ -emitter  $^{22}\text{Na}$  in Ne-rich novae.<sup>5,6</sup> In the present study, we aimed at directly investigating proton resonant states in  $^{23}\text{Al}$  and  $^{22}\text{Mg}$  by the elastic scattering of  $^{22}\text{Mg}$  and  $^{22}\text{Na}$  RI beams on a thick proton target, respectively.

Previously, excited states in  $^{23}\text{Al}$  were studied by the  $^{24}\text{Mg}(^7\text{Li}, ^8\text{He})^{23}\text{Al}$  reaction,<sup>2</sup> but there was no direct measurement of proton resonant states in  $^{23}\text{Al}$  yet. Excited states in  $^{22}\text{Mg}$  were investigated in many experiments,<sup>4</sup> including that on the elastic scattering of a  $^{21}\text{Na}$  beam at 1.4 MeV/nucleon performed at TRIUMF, and three proton resonance states at 6.332, 6.617 and 6.813 MeV were observed.<sup>5</sup>

The experiment was carried out using the CNS radioactive ion beam separator (CRIB), as described elsewhere.<sup>7,8</sup> A  $^{20}\text{Ne}^{8+}$  primary beam was accelerated up to an energy of 8.11 MeV/nucleon at the RIKEN AVF cyclotron ( $K = 70$ ) with an average intensity of approximately 200 pA. The primary beam bombarded a  $^3\text{He}$  gas target with a thickness of 0.36 mg/cm<sup>2</sup>, where a  $^{22}\text{Mg}$  secondary beam was produced by the  $^3\text{He}(^{20}\text{Ne}, ^{22}\text{Mg})n$  reaction. Fortunately, a  $^{21}\text{Na}$  radioactive ion beam was also produced.

The radioactive beams were separated by the CRIB with an energy degrader, 5.43- $\mu\text{m}$ -thick Mylar foil, which was installed at the momentum dispersive focal plane (F1) to eliminate light particles. Furthermore, an F1 horizontal slit was used to select  $^{22}\text{Mg}$  particles with a momentum deviation of 1%. After the energy degradation, the energy of  $^{22}\text{Mg}$  particles was determined to be 5.93 MeV/nucleon. At the same magnetic rigidity ( $B\rho$ ) setting, the energy of  $^{21}\text{Na}$  particles was determined to be 5.46 MeV/nucleon.

At the achromatic focal plane (F2), a setup for the elastic scattering measurement was installed inside a vacuum chamber.<sup>9</sup> The setup consisted of two parallel-plate avalanche counters (PPACs), a thick 7.87 mg/cm<sup>2</sup>  $(\text{CH}_2)_n$  target and three sets of  $\Delta E$ - $E$  silicon telescopes. The first set of  $\Delta E$ - $E$  silicon telescopes was installed at 0° (covering a scattering angle

from  $-5^\circ$  to  $5^\circ$ ), consisting of a 75- $\mu\text{m}$ -thick position-sensitive detector (PSD1) and two Si detectors with a thickness of 1.5 mm each. The second set was installed at 16° (covering a scattering angle from 11° to 21°), consisting of a 75- $\mu\text{m}$ -thick position-sensitive detector (PSD2) and a Si detector with a thickness of 1.48 mm. The third set was installed at  $-23^\circ$  (covering a scattering angle from  $-18^\circ$  to  $-28^\circ$ ), consisting of a 73- $\mu\text{m}$ -thick position-sensitive detector (PSD3) and a Si detector with a thickness of 1.5 mm. As for PSD1, double-sided strips (16  $\times$  16 strips) were used to determine two-dimensional hit positions, while for PSD2 and PSD3, only horizontal  $x$  strips were used.

On the secondary target, the beam spot widths were 15 mm (FWHM) horizontally and 11 mm (FWHM) vertically. The horizontal and vertical angular widths of the two beams were 28 mrad (FWHM) and 33 mrad (FWHM), respectively. The energies of  $^{22}\text{Mg}$  and  $^{21}\text{Na}$  beams were 4.38 MeV/nucleon and 4.00 MeV/nucleon on the secondary target, respectively, and their width was 0.12 MeV/nucleon (FWHM).

The protons piling out of the  $(\text{CH}_2)_n$  target were accumulated for about 53 hours. Furthermore, the measurement was performed with an equivalent thickness of the C target to evaluate the background contribution of the reactions of beam particles with C atoms in the  $(\text{CH}_2)_n$  target. The proton energies were calibrated using secondary proton beams separated by CRIB at several energy points.

At present, the center-of-mass energy ( $E_{cm}$ ) of elastic scattering was reconstructed, whose resolution is about 30–50 keV (FWHM) with an error of 15–30 keV as a function of the  $E_{cm}$  energies. Now, the R-matrix analysis is in progress to reduce the resonance parameters of the observed resonant states.

### References

- 1) J. A. Caggiano et al.: Phys. Rev. C **64**, 025802 (2001).
- 2) N. Bateman et al.: Phys. Rev. C **63**, 035803 (2001).
- 3) A. A. Chen et al.: Phys. Rev. C **63**, 065807 (2001).
- 4) C. Ruiz et al.: Phys. Rev. C **65**, 042801 (2002).
- 5) I. Iyudin et al.: Astron. Astrophys. **300**, 422 (1995).
- 6) M. Wiescher et al.: J. Phys. G **25**, 133 (1999).
- 7) S. Kubono et al.: Eur. Phys. J. A **13**, 217 (2002).
- 8) T. Teranishi et al.: Phys. Lett. B **556**, 27 (2003).
- 9) J. J. He et al.: CNS Ann. Rep. **2002**, 1.

<sup>\*1</sup> Center for Nuclear Study, University of Tokyo

<sup>\*2</sup> Department of Physics, Rikkyo University

<sup>\*3</sup> Department of Physics, Chun-Ang University, Korea

<sup>\*4</sup> Department of Physics, University of Tokyo

<sup>\*5</sup> Department of Physics, Kyushu University

<sup>\*6</sup> Department of Physics, Yamagata University

## Study of the $^{26}\text{Si}(p, \gamma)^{27}\text{P}$ reaction by the Coulomb dissociation method

Y. Togano,<sup>\*1</sup> T. Gomi,<sup>\*1</sup> T. Motobayashi, Y. Ando,<sup>\*1</sup> N. Aoi, H. Baba,<sup>\*1</sup> K. Demichi,<sup>\*1</sup> Z. Elekes, N. Fukuda, Zs. Fülöp,<sup>\*2</sup> U. Futakami,<sup>\*1</sup> H. Hasegawa,<sup>\*1</sup> Y. Higurashi, K. Ieki,<sup>\*1</sup> N. Imai, M. Ishihara, K. Ishikawa,<sup>\*3</sup> N. Iwasa,<sup>\*4</sup> H. Iwasaki,<sup>\*5</sup> S. Kanno,<sup>\*1</sup> Y. Kondo,<sup>\*3</sup> T. Kubo, S. Kubono,<sup>\*5</sup> M. Kunibu,<sup>\*1</sup> K. Kurita,<sup>\*1</sup> Y. U. Matsuyama,<sup>\*1</sup> S. Michimasa,<sup>\*5</sup> T. Minemura, M. Miura,<sup>\*3</sup> H. Murakami,<sup>\*1</sup> T. Nakamura,<sup>\*3</sup> M. Notani,<sup>\*5</sup> S. Ota,<sup>\*6</sup> A. Saito,<sup>\*1</sup> H. Sakurai,<sup>\*7</sup> M. Serata,<sup>\*1</sup> S. Shimoura,<sup>\*5</sup> T. Sugimoto,<sup>\*3</sup> E. Takeshita,<sup>\*1</sup> S. Takeuchi, K. Ue,<sup>\*7</sup> K. Yamada,<sup>\*1</sup> Y. Yanagisawa, K. Yoneda, and A. Yoshida

[ $^{208}\text{Pb}(^{27}\text{P}, p^{26}\text{Si})^{208}\text{Pb}$ , Coulomb dissociation, Nuclear astrophysics]

We have carried out an experiment to study the  $^{26}\text{Si}(p, \gamma)^{27}\text{P}$  reaction using the Coulomb dissociation of  $^{27}\text{P}$ . The gamma decay width of the first excited state in  $^{27}\text{P}$  was measured because of its astrophysical interest.

The  $^{26}\text{Si}(p, \gamma)^{27}\text{P}$  reaction is one of the key reactions in the nucleosynthesis in Ne-rich novae. The rate of this reaction must be known to evaluate the amount of  $^{26}\text{Al}$  (g.s.). This reaction is also important for estimating the mass evolution to heavier elements. The  $^{27}\text{P}$  production in Ne-rich novae mainly depends on resonant capture via the first excited state in  $^{27}\text{P}$  at 1.2 MeV, because the state is close to the Gamow window. Therefore, we aimed at determining the gamma decay width of the first excited state in  $^{27}\text{P}$  in order to reveal the strength of the resonant capture in this reaction.

The experiment was performed at the RIPS beam line at the RIKEN Accelerator Research Facility. The secondary beam of  $^{27}\text{P}$  at 57 MeV/nucleon was produced by the fragmentation of a 115 MeV/nucleon  $^{36}\text{Ar}$  beam on a  $^9\text{Be}$  target. The beam of  $^{27}\text{P}$  bombarded a 125 mg/cm<sup>2</sup> Pb target. The products of the breakup reaction,  $^{26}\text{Si}$  and proton, were detected using silicon telescopes and a plastic scintillator hodoscope, respectively. Details of the experimental setup are described in Ref. 1. The angle of products and the energy of  $^{26}\text{Si}$  were measured by the silicon telescopes. The time of flight of the proton was determined using the plastic scintillator hodoscope.

The relative energy spectrum was obtained from the measured momentum vectors of products. The preliminary spectrum is shown in Fig. 1. The peaks were observed at 0.34 MeV and 0.8 MeV which correspond respectively to the first and second excited states at 1.2 MeV and 1.6 MeV in  $^{27}\text{P}$  reported in Ref. 2. We also found another peak at 1.2 MeV that did not correspond to any known state.

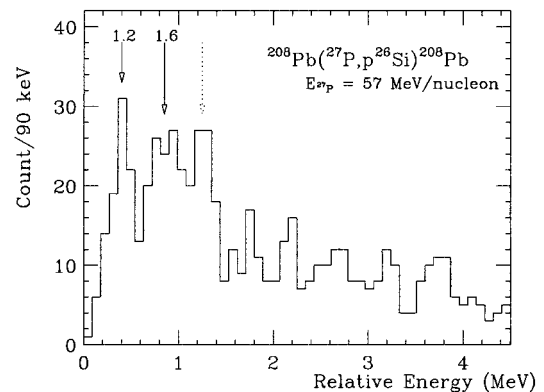


Fig. 1. Preliminary relative energy spectrum of the  $^{208}\text{Pb}(^{27}\text{P}, p^{26}\text{Si})^{208}\text{Pb}$  reaction. The peak at 0.34 MeV corresponds to the first excited state in  $^{27}\text{P}$  at 1.2 MeV.

We obtained the cross section of the first excited state of  $^{27}\text{P}$  to be 5 mb with a statistical error of about 25%. Supposing that the spin and parity of the first excited state in  $^{27}\text{P}$  is  $3/2^+$ , the transition between the first excited state and the ground state is by M1/E2 multipolarity. Since the E2 component was strongly enhanced in the Coulomb dissociation, the experimental cross section is exhausted via the E2 excitation. To extract the total gamma decay width, the M1 component was estimated using the mixing ratio,  $E2/M1 = 0.048$ , from the mirror transition in  $^{27}\text{Mg}$ . The gamma decay width of the first excited state thus deduced preliminarily was determined to be  $3.5 \pm 0.6$  (stat) meV. This result is consistent with the value estimated on the basis of a shell model calculation.<sup>2)</sup> It also indicates that this reaction does not contribute significantly to the amount of  $^{26}\text{Al}$  (g.s.).

### References

- 1) T. Gomi et al.: RIKEN Accel. Prog. Rep. **36**, 82 (2003).
- 2) J. A. Caggiano et al.: Phys. Rev. C **64**, 025802 (2001).

<sup>\*1</sup> Rikkyo University  
<sup>\*2</sup> ATOMKI, Hungary  
<sup>\*3</sup> Tokyo Institute of Technology  
<sup>\*4</sup> Tohoku University  
<sup>\*5</sup> Center for Nuclear Study, University of Tokyo  
<sup>\*6</sup> Kyoto University  
<sup>\*7</sup> University of Tokyo

# One-neutron halo structure in $^{15}\text{C}$

D. Q. Fang,<sup>\*1</sup> T. Yamaguchi, T. Zheng,<sup>\*2</sup> A. Ozawa, M. Chiba,<sup>\*3</sup> R. Kanungo, T. Kato, K. Morimoto, T. Ohmishi, T. Suda, Y. Yamaguchi,<sup>\*4</sup> A. Yoshida, K. Yoshida, and I. Tanihata

[Measured reaction cross section, measured fragment momentum distribution, halo structure]

Discrepancies have been found in the momentum distribution and interaction cross section ( $\sigma_{\text{I}}$ ) measurements for  $^{15}\text{C}$ .<sup>1)</sup> We measured the fragment momentum distribution and reaction cross section ( $\sigma_{\text{R}}$ ) of  $^{14,15}\text{C}$  at 83 A MeV to study the halo structure in  $^{15}\text{C}$ .

The experiment was performed at the Riken Projectile Fragment Separator (RIPS). The primary beam of 110 A MeV  $^{22}\text{Ne}$  was used to produce the secondary beams of  $^{14,15}\text{C}$ . Before the carbon reaction target (370 mg/cm<sup>2</sup>) installed at F2, particle identification was carried out by the  $B\rho$ - $\Delta E$ -TOF method. TOF was determined from F1-PPAC and a plastic scintillator (0.5 mm thick) at F2.  $\Delta E$  was measured using two Si detectors (each 150  $\mu\text{m}$  thick). After the reaction target, the TOF- $\Delta E$ - $E$  method was used for particle identification. Another plastic (1.5 mm thick) at F3 gave the stop signal of the TOF from F2 to F3. Three Si detectors (each 150  $\mu\text{m}$  thick) were used to measure  $\Delta E$ .  $E$  was measured using a NaI(Tl) detector.

The fragment momentum distributions from  $^{14,15}\text{C}$  breakup are shown in Fig. 1. A Lorentzian function was used to fit  $^{15}\text{C} \rightarrow ^{14}\text{C}$  distributions. A Gaussian function was used to fit  $^{15}\text{C} \rightarrow ^{13}\text{C}$  and  $^{14}\text{C} \rightarrow ^{13}\text{C}$  distributions. The FWHMs were determined to be  $71 \pm 9$  MeV/c (Fig. 1 (a)),  $223 \pm 28$  MeV/c (Fig. 1 (b)) and  $195 \pm 21$  MeV/c (Fig. 1 (c)) after unfolding the Gaussian-shaped system resolution.

A few-body Glauber model analysis for the one-neutron removal process of  $^{14,15}\text{C}$  was performed.<sup>2)</sup> We assumed a core + n structure for  $^{14,15}\text{C}$ . The density distribution of the core was supposed to be HO with its size parameter adjusted to reproduce  $\sigma_{\text{I}}$  at high energies.<sup>1)</sup> The wave function of the valence neutron was calculated by solving the eigenvalue problem in a Woods-Saxon potential. For  $^{14}\text{C}$ , the calculated momentum distributions can reproduce the ex-

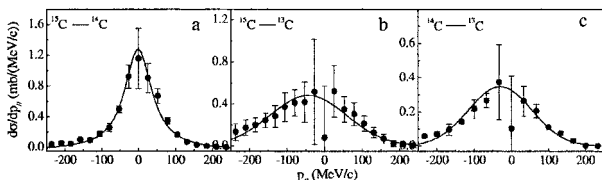


Fig. 1. Fragment longitudinal momentum distributions in the projectile rest frame for  $^{15}\text{C} \rightarrow ^{14}\text{C}$  (a),  $^{15}\text{C} \rightarrow ^{13}\text{C}$  (b) and  $^{14}\text{C} \rightarrow ^{13}\text{C}$  (c).

periment data well. For  $^{15}\text{C}$ , contributions from different breakup sequences were considered. In the best-fitted results, the contribution of the d wave to a one-neutron removal cross section ( $\sigma_{1n}$ ) was  $4_{-4}^{+10}\%$ . It is consistent with the results from a previous experiment in which the d wave contributed only 2% to  $\sigma_{1n}$ .<sup>3)</sup> Our analysis suggests that the contribution from the  $1d_{5/2}$  orbit in the ground state of  $^{15}\text{C}$  is very small.

The  $\sigma_{\text{R}}$  values for  $^{14}\text{C}$  and  $^{15}\text{C}$  are determined to be  $1075 \pm 61$  mb and  $1319 \pm 40$  mb, respectively. A strong increase from  $^{14,16}\text{C}$  is exhibited in  $\sigma_{\text{R}}$  measured at 83 A MeV for  $^{15}\text{C}$ .<sup>4)</sup> The effective density distribution of  $^{15}\text{C}$  was extracted using the finite-range Glauber model.<sup>4)</sup> The HO plus  $v(p_{1/2})$  neutron was used for the  $^{14}\text{C}$  core with the p wave distribution obtained from the above wave function calculation. The HO size parameter was adjusted to reproduce the  $\sigma_{\text{R}}$  of  $^{14}\text{C}$  at 83 A MeV. Then the depth of the potential was changed arbitrarily in calculating the wave function of the valence neutron so as to reproduce the  $\sigma_{\text{R}}$  of  $^{15}\text{C}$  at 83 A MeV. The fitted densities are compared with the calculated s and d wave distributions in Fig. 2. A long tail is necessary to explain the measured  $\sigma_{\text{R}}$  of  $^{15}\text{C}$ . The extracted tail agrees with the s wave distribution much better than the d wave. We can conclude that the s wave is dominant in the ground state of  $^{15}\text{C}$  based on the analysis of both  $\sigma_{\text{R}}$  and momentum distribution data from this experiment. This is a strong evidence of the halo structure in this nucleus.

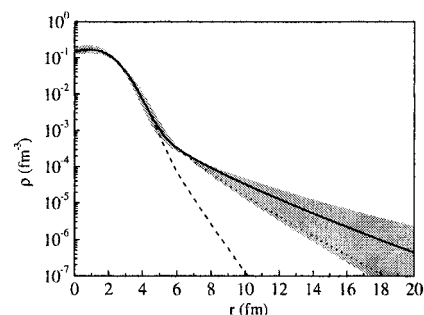


Fig. 2. Density distribution of  $^{15}\text{C}$ . The solid line is a best-fit result. The dotted and dashed lines show the calculated s and d wave distributions. The shaded area represents the error of  $\sigma_{\text{R}}$  from both  $^{15}\text{C}$  and  $^{14}\text{C}$ .

## References

- 1) A. Ozawa et al.: Nucl. Phys. A **691**, 599 (2001).
- 2) T. Yamaguchi et al.: Nucl. Phys. A **724**, 3 (2003).
- 3) V. Maddalena et al.: Nucl. Phys. A **682**, 332c (2001).
- 4) T. Zheng et al.: Nucl. Phys. A **709**, 103 (2002).

<sup>\*1</sup> Shanghai Institute of Nuclear Research, China  
<sup>\*2</sup> Department of Technical Physics, Peking University, China  
<sup>\*3</sup> Department of Physics, Tohoku University  
<sup>\*4</sup> Department of Physics, Niigata University

# $g$ -factor measurement for $^{19}\text{N}$

D. Kameda,<sup>\*1</sup> K. Asahi, H. Ueno, A. Yoshimi, H. Miyoshi,<sup>\*1</sup> H. Watanabe, T. Haseyama, K. Shimada,<sup>\*1</sup>  
G. Kato,<sup>\*1</sup> S. Emori,<sup>\*1</sup> G. Kijima,<sup>\*1</sup> J. Murata,<sup>\*2</sup> and Y. Kobayashi

[NUCLEAR STRUCTURE,  $^{19}\text{N}$ , Spin polarization,  $\beta$ -NMR method]

In contrast to the well known observation that almost all of the measured nuclear magnetic moments are found inside the Schmidt lines due to the core polarization effect, the magnetic moment of  $^{15}\text{N}$  and also that of  $^{17}\text{N}$ <sup>1)</sup> fall outside the Schmidt lines. Considering the increased number of neutrons in the  $sd$ -shell, the magnetic moment for  $^{19}\text{N}$  should be even larger for  $^{17}\text{N}$ . Shell models predict, in fact, that the magnetic moment for  $^{19}\text{N}$  is larger than that of  $^{17}\text{N}$  as shown later.

The experiment was performed at the RIKEN Accelerator Research Facility. The  $^{19}\text{N}$  activity was obtained from the fragmentation of a  $^{22}\text{Ne}$  projectile at an energy of 110 MeV/nucleon on a carbon target of 546 mg/cm thickness. By using the projectile-fragment separator RIPS, the  $^{19}\text{N}$  nuclide was separated from other fragments. In order to produce spin polarization, only those with emission angles  $2.6^\circ$ – $6.0^\circ$  and outgoing momenta 8.18–8.69 GeV/c were accepted. The  $^{19}\text{N}$  fragments were implanted in a graphite stopper to which a static field  $B_0 = 200.12$  mT was applied and an RF field was supplied to induce a nuclear magnetic resonance.

In Fig. 1, the effect of a spin flip by the resonance is

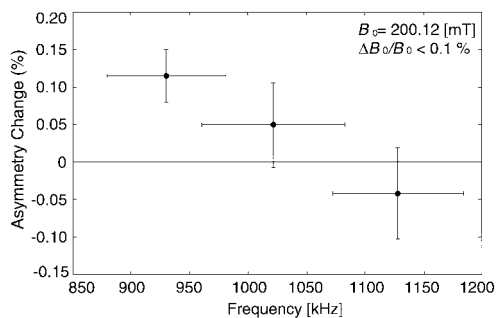


Fig. 1. Observed NMR spectrum of  $^{19}\text{N}$  in a graphite stopper. Three data points are shown as filled circles. The vertical axis is the up/down count ratio of  $\beta$ -rays detected by plastic scintillators which were placed above and below the stopper. The vertical bars on each point show the statistical error of the  $\beta$ -ray count. The horizontal bars are a sweep width over which the frequency of the field was varied for each data point in order to flip the  $^{19}\text{N}$  spin [the Adiabatic Fast Passage (AFP) method].

observed in the leftmost data point with a deviation of  $3.2\sigma$  from the zero level, where the  $\sigma$  is a standard deviation. The result indicates that there is the  $g$  factor for  $^{19}\text{N}$  within the region of  $g = 0.58$ – $0.64$  which is derived from the sweep width of the frequency as shown in Fig. 1. The centroid of the resonance could be beyond the left side of the sweep region due to the finite resonance width. The possible deviation mainly comes from the field inhomogeneity, as shown in the Fig. 1, and the ratio of the field magnitude of the static field to that of the rf field, of which the value is 0.25%. These deviations are negligibly small compared with the present accuracy of the  $g$  factor.

The present  $g$  factor for  $^{19}\text{N}$  is significantly smaller than the shell model predictions.<sup>2)</sup> In Fig. 2, a systematic trend is observed: The shell models predict  $|g|$  factors as monotonically increasing with increasing number of neutrons  $n$  in the  $sd$  shell. The experimental  $|g|$  certainly follows this trend up to  $n = 2$  (*i.e.*,  $^{17}\text{N}$ ). The experimental  $|g|$  for  $^{19}\text{N}$ , however, abruptly decreases. The reason for this anomalous  $n$  dependence is not known.

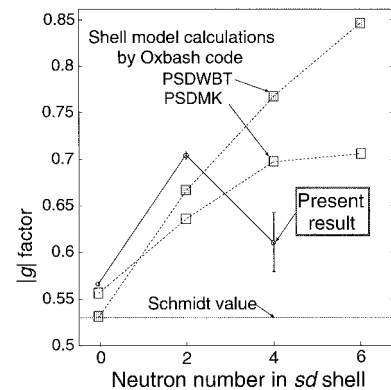


Fig. 2. Experimental (circle with error bars) and theoretical (square)  $|g|$  factor for the odd-mass N isotopes. The magnetic moment is obtained from  $\mu = g\mu_N I$  where  $I$  and  $\mu_N$  are the nuclear spin and nuclear magneton, respectively. The spin parity of  $^{19}\text{N}$  was assumed to be  $1/2^-$  in the calculation.

## References

- 1) H. Ueno et al.: Phys. Rev. C **53**, 2142 (1996).
- 2) B. A. Brown, A. Etchengoyen, and W. D. Rae: Computer code OXBASH, Michigan State University Cyclotron Laboratory Report, No. 524 (1986).

<sup>\*1</sup> Department of Physics, Tokyo Institute of Technology

<sup>\*2</sup> Department of Physics, Rikkyo University



## Development of low energy $^8\text{Li}$ beam at CRIB

M. Kurata-Nishimura, S. Nishimura, T. Teranishi,<sup>\*1</sup> M. Notani,<sup>\*1</sup> J. J. He,<sup>\*1</sup> H. Baba,<sup>\*2</sup>  
S. Michimasa,<sup>\*1</sup> S. Kubono,<sup>\*1</sup> and I. Tanihata

[Astrophysics, Nucleosynthesis, Unstable nuclei]

The inhomogeneous big bang model<sup>1,2)</sup> has succeeded in predicting the synthesis of heavy elements in contrast to the standard primordial nucleosynthesis model which makes reasonably accurate predictions of the light element abundances. In the inhomogeneous big bang model,  $^4\text{He}(t, \gamma)^7\text{Li}(n, \gamma)^8\text{Li}(\alpha, n)^{11}\text{B}(n, \gamma)^{12}\text{B}(\beta\nu)^{12}\text{C}$  is considered to be a dominant flow path to explain the synthesis of  $^{12}\text{C}$  and heavy elements in the very early universe. Recently, it has also been identified to play an important role in r-process nucleosynthesis occurring in supernova explosions.<sup>3)</sup> In both environments, it is claimed to determine the reaction cross section in a direct reaction with the center of mass energy less than 1 MeV. In that sequence, the  $^8\text{Li}(\alpha, n)^{11}\text{B}$  reaction gives large ambiguity caused by the short life of  $^8\text{Li}$ . Some previous experiments were conducted to determine this reaction cross section<sup>4-6)</sup>; however, the results of these experiments were not in qualitative agreement with each other. Moreover, measurements of the low-energy cross section below 1 MeV/n, which is the most important energy region, have not been conducted yet due to difficulty of handling low-energy beams.

In RIKEN cyclotron, an in-flight low-energy radioisotope beam separator<sup>7-9)</sup> (CRIB) has been constructed to study unstable nuclear structures and nuclear reactions for astrophysics, through a collaboration between RIKEN and the Center of Nuclear Study (CNS). Since the energy of the RI beam produced by the in-flight method is almost equivalent that of a primary beam which is more than a few MeV/n, it is necessary to insert a thick degrader in the beam line to reduce the energy to 1 MeV/n. It is expected that the energy straggling and beam profile degeneration will be a crucial problem. In this article, we will report results of an experiment to develop a low-energy  $^8\text{Li}$  beam in CRIB. In addition, the neutron background level will be noted.

An unstable  $^8\text{Li}$  beam is created by an inversed reaction of  $^7\text{Li}(d, p)^8\text{Li}$ . The primary beam of  $^7\text{Li}^{2+}$  is accelerated to an energy of 3.14 MeV/nucleon by the RIKEN AVF cyclotron with the beam current of 100 pA. The primary beam is focused at the F0 plane where deuteron gas target of 0.39 mg/cm<sup>2</sup> is located. A removable aluminum foil with a thickness of 40  $\mu\text{m}$  is placed upstream of the gas target cell in order to reduce the beam energy. The produced  $^8\text{Li}$  beams are

separated from  $^7\text{Li}$  in the D1 magnetic field traveling to a momentum-dispersive focal plane (F1). The ions path through an F1 slit are transported to the second focal plane (F2) where two delayed-line PPACs and SSD are installed to identify ions and to measure the energy spread and beam profile. Mylar foil degraders with thickness of 0, 10, 29 and 50  $\mu\text{m}$  are placed on a stepping motor in front of the PPACs. For the purpose of estimating the neutron background level, four liquid scintillation counters are prepared; three are placed near the F2 chamber and the other is placed 6 m downstream from the F2 chamber.

The particle identification without any degrader is shown in Fig. 1. The  $^8\text{Li}$  ions are clearly separated from  $^7\text{Li}$  ion.

Several thicknesses of energy degrader are used in attempts to reduce  $^8\text{Li}$  beam energy. The beam properties for each energy degrader configuration are summarized in Table 1.

The maximum  $^8\text{Li}$  beam intensity of  $5.1 \times 10^5$  is obtained for a 100 pA  $^7\text{Li}$  beam without any degrader. At the energy of 1.57 MeV corresponding to  $E_{cm} = 0.52$  MeV for the  $^8\text{Li}(\alpha, n)^{11}\text{B}$  reaction, the  $^8\text{Li}$  beam purity of 99.5% and the intensity of  $4 \times 10^4$  is obtained. The energy straggling and beam profile

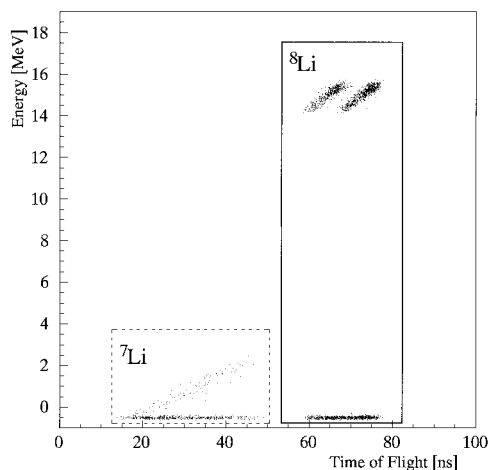


Fig. 1. Particle identification of  $^8\text{Li}$ . Horizontal axis and vertical axis indicate time of flight between two PPACs and the energy deposit in the SSD, respectively. Two clusters in the  $^8\text{Li}$  region are known to be caused by the problem of double timing triggers. Some ions shows zero energy deposit on SSD due the relatively small acceptance of SSD.

<sup>\*1</sup> Center for Nuclear Study, University of Tokyo

<sup>\*2</sup> Department of Physics, Rikkyo University

Table 1. Summary of  $^8\text{Li}$  beam properties for several configurations.

Degrader			$^8\text{Li}$					
Place	Material	T [ $\mu\text{m}$ ]	Energy [MeV]	dE/E [%]	$\sigma_x$ [mm]	$\sigma_y$ [mm]	Purity [%]	Intensity [cps]/100 pA
no	no	no	15.3	1.29	16.1	12.8	78.6	$5 \times 10^5$
F2	Mylar	10	13.0	1.40	17.1	14.1	98.7	$4 \times 10^4$
F2	Mylar	29	9.21	2.55	19.9	17.8	99.5	$4 \times 10^4$
F2	Mylar	50	1.57	21.40	29.6	24.9	99.5	$4 \times 10^4$
F0	Al	40	4.22	11.3	—	26.6	57.0	$3 \times 10^4$

could be improved by adapting a degrader at F1 and adjusting the slit size at F1 and F2.

Furthermore, the neutron background with the order of 1000 cps is expected from the primary target through the  $^7\text{Li}(d, n)$  reaction. However, it is found to be 20 cps even at the side close to the primary target. In this case, signal to noise ratio of the neutron can be estimated as 1/100 which is acceptable for this experiment.

#### References

1) M. J. Balbes et al.: Phys. Rev. Lett. **71**, 3931 (1993).

- 2) N. Hata et al.: Phys. Rev. Lett. **75**, 3977 (1995).
- 3) M. Terasawa et al.: Astrophys. J. **562**, 470 (2001).
- 4) X. Gu et al.: Phys. Lett. B **343**, 31 (1995).
- 5) R. N. Boyd et al.: Phys. Rev. Lett. **68**, 1283 (1992).
- 6) Y. Mizoi et al.: Phys. Rev. C **6206**, 5801 (2000).
- 7) S. Kubono et al.: Eur. Phys. J. A **13**, 217 (2002).
- 8) T. Teranishi et al.: CNS-REP-39 (2001).
- 9) S. Watanabe et al.: CNS-REP-48 (2002).

## Production of low-energy secondary beam for secondary reactions

E. Ideguchi,<sup>\*1</sup> H. Baba,<sup>\*2</sup> T. Fukuchi,<sup>\*1</sup> C. Ishida,<sup>\*3</sup> H. Iwasaki,<sup>\*4</sup> T. Komatsubara,<sup>\*5</sup> T. Kubo,  
M. Kurokawa, S. Michimasa,<sup>\*1</sup> K. Morimoto, M. Niikura,<sup>\*1</sup> T. Ohnishi, S. Ota,<sup>\*6</sup> A. Ozawa,<sup>\*5</sup>  
S. Shimoura,<sup>\*1</sup> T. Suda, M. Tamaki,<sup>\*1</sup> I. Tanihata, and K. Yoshida

[NUCLEAR REACTION,  ${}^9\text{Be}({}^{37}\text{P}, \text{xn})^{46-x}\text{K}$ , Unstable nuclei]

Studies of high-spin states in atomic nuclei by in-beam gamma-ray spectroscopy have provided detailed information on the nuclear structure. In such studies, high-spin states are achieved mostly through a fusion reaction using a combination of a stable-isotope beam and a stable-isotope target, since large angular momentum can be brought to the nucleus of interest in the reaction. However, nuclei produced in the fusion reaction are limited, in many cases, to the proton-rich side relative to the  $\beta$ -stability line. In the neutron-rich nuclei, unprecedented phenomena such as the disappearance of the shell gap<sup>1)</sup> and the onset of a new magic number<sup>2)</sup> have recently been observed. These phenomena are ascribable to the change of the nuclear structure on the neutron-rich side, but this region, particularly at high spin, have not been studied well so far. It would be desirable to extend the experimental study of high-spin states and carry out a systematic investigation covering from the proton-rich to the neutron-rich region. By utilizing a neutron-rich beam in the fusion reaction, nuclei will be produced in the neutron-rich side and the region available for high-spin studies will be largely expanded. In order to actualize this method, an experiment to produce a low-energy secondary beam ( $\sim 6$  MeV/nucleon), which is indispensable for inducing the fusion reaction, was performed at the RIKEN accelerator research facility.

In the experiment, a secondary  ${}^{37}\text{P}$  beam was produced at the RIPS facility<sup>3)</sup> in RIKEN by the fragmentation reaction of an  ${}^{40}\text{Ar}$  beam impinging on a  ${}^9\text{Be}$  target 1.5 mm thick. The primary  ${}^{40}\text{Ar}$  beam of 63 MeV/nucleon with a typical intensity of 60 pA was provided by the RIKEN Ring cyclotron. An aluminum wedge with a mean thickness of 221 mg/cm<sup>2</sup> placed at the momentum-dispersive focal plane (F1) was used to achieve a clear isotope separation and to lower the energy of the fragment to 26 MeV/nucleon. The energy of the  ${}^{37}\text{P}$  beam was further lowered to  $\sim 6$  MeV/nucleon by placing an aluminum rotatable degrader 0.425 mm thick at the achromatic focal plane (F2). The energy of the beam was optimized by adjusting the rotation angle of the degrader relative to the beam direction. By operating RIPS at the maximum values of momentum acceptance and solid angle, a typ-

ical intensity of  $2.0 \times 10^5$  counts per second for the  ${}^{37}\text{P}$  beam was obtained at F2. Particle identification of the secondary beam was carried out by the time-of-flight (TOF)- $\Delta E$  method, and it was found that an almost pure  ${}^{37}\text{P}$  beam was obtained. The TOF and  $\Delta E$  information was obtained from the timing of the plastic scintillator relative to the RF signal of the cyclotron and from the energy loss in the 0.5-mm-thick silicon detector placed at F2, respectively. The  ${}^{37}\text{P}$  beam was transported to the final focal plane (F3) and irradiated on the secondary  ${}^9\text{Be}$  target 10  $\mu\text{m}$  thick in order to induce the secondary fusion reaction,  ${}^9\text{Be}({}^{37}\text{P}, \text{xn})^{46-x}\text{K}$ . The intensity of the  ${}^{37}\text{P}$  beam at F3 was about  $1.0 \times 10^5$  counts per second. Two PPAC counters<sup>4)</sup> were placed up stream of the secondary target in order to profile the image and the incident angle of the beam on the target, as well as to determine energy from TOF information relative to the plastic timing at F2, event by event. Another PPAC counter was also placed down stream of the target to detect recoil nuclei produced in the secondary reaction and to measure the TOF. Figure 1 shows the energy spectrum of the  ${}^{37}\text{P}$  beam at the secondary target position. The beam spot size (FWHM) at the target was found to be 42 mm and 18 mm, respectively, in horizontal and vertical directions. Gamma rays emitted in the secondary reaction were measured by the CNS Ge detector array<sup>5)</sup> placed around the secondary target at angles between  $70^\circ$  and  $110^\circ$ . The analysis of the data obtained for the secondary reaction is in progress.

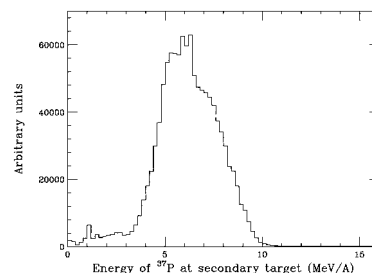


Fig. 1. Energy spectrum of the  ${}^{37}\text{P}$  beam at secondary target position deduced from TOF information.

### References

- 1) T. Motobayashi et al.: Phys. Lett. B **346**, 9 (1995).
- 2) A. Ozawa et al.: Phys. Rev. Lett. **84**, 5493 (2000).
- 3) T. Kubo et al.: Nucl. Instrum. Methods B **461**, 309 (1992).
- 4) H. Kumagai et al.: Nucl. Instrum. Methods A **470**, 562 (2001).
- 5) S. Shimoura et al.: CNS Annu. Rep. **2001**, 5.

<sup>\*1</sup> Center for Nuclear Study, University of Tokyo

<sup>\*2</sup> Department of Physics, Rikkyo University

<sup>\*3</sup> Department of Physics, Royal Institute of Technology

<sup>\*4</sup> Department of Physics, University of Tokyo

<sup>\*5</sup> Department of Physics, Tsukuba University

<sup>\*6</sup> Department of Physics, Kyoto University

## Development of $^{17}\text{N}$ secondary beam II

A. Odahara,<sup>\*1</sup> Y. Wakabayashi,<sup>\*2</sup> Y. Gono,<sup>\*2</sup> T. Fukuchi,<sup>\*3</sup> N. Hokoïwa,<sup>\*2</sup> M. Kibe,<sup>\*2</sup> T. Teranishi,<sup>\*3</sup>  
 S. Kubono,<sup>\*3</sup> M. Notani,<sup>\*3</sup> Y. Yanagisawa, S. Michimasa,<sup>\*3</sup> J. J. He,<sup>\*3</sup> H. Iwasaki,<sup>\*4</sup> S. Shimoura,<sup>\*3</sup>  
 H. Watanabe, T. Kishida, E. Ideguchi,<sup>\*3</sup> H. Baba,<sup>\*5</sup> S. Nishimura, M. Kurata-Nishimura,  
 J. Y. Moon,<sup>\*6</sup> and S. Kato<sup>\*7</sup>

[RI beam,  $\gamma$ -ray spectroscopy, nuclear structure]

A secondary beam of  $^{17}\text{N}$  was developed using the low-energy radioisotope beam separator (CRIB)<sup>1)</sup> of the Center for Nuclear Study (CNS), University of Tokyo, in order to search for high-spin isomers in  $N = 51$  isotones. Since nuclei with  $Z < 40$  of  $N = 51$  isotones are close to the stability line, it is difficult to produce high-spin states of nuclei using reactions by combinations of stable beams and targets. Therefore, it is very effective to use the radioisotope beam. By means of the  $\gamma$  spectroscopy method, high-spin isomers can be searched for in the nuclei  $^{90}\text{Y}$ ,  $^{89}\text{Sr}$  and  $^{88}\text{Rb}$  produced by the  $\alpha 5n$ ,  $\alpha p 5n$  and  $2\alpha 3n$  channels of the  $^{82}\text{Se} + ^{17}\text{N}$  reaction, respectively.

High-spin isomers of  $N = 51$  isotones are expected to be shape isomers stemmed from a sudden shape change from near spherical to an oblate shape. They may also be expected to have stretch coupled configurations resulting from the breaking of a neutron magic 50 core, as a similar type of isomerism observed in  $N = 83$  isotones.<sup>2)</sup> The configurations of these isomers in  $N = 51$  isotones are considered to be  $[\nu(d_{5/2}g_{7/2}h_{11/2})\pi(g_{9/2}^2)]_{39/2}^-$  for odd nuclei and  $[\nu(d_{5/2}g_{7/2}h_{11/2})\pi(p_{1/2}g_{9/2}^2)]_{20}^+$  for odd-odd nuclei.

A secondary  $^{17}\text{N}$  beam was produced by using the CRIB<sup>1)</sup> which consists of two dipole (D1, D2), three quadrupole (Q1, Q2, Q3) and two small correction magnets (M1, M2). A  $^9\text{Be}$  primary target of  $2.3\text{ mg/cm}^2$  was bombarded by a  $^{18}\text{O}^{8+}$  primary beam of  $126.4\text{ MeV}$  to obtain a  $^{17}\text{N}$  beam. An  $^{18}\text{O}^{6+}$  beam was accelerated by the AVF cyclotron in RIKEN. The charge states of the beam particles were converted by using C foil which was set before a bending magnet to eliminate  $^{12}\text{C}^{4+}$  contamination in the primary beam. The beam intensity was  $0.4\text{ p}\mu\text{A}$  at the primary target.

A parallel plate avalanche counter (PPAC) was set on a dispersive focal plane (F1) for beam monitoring. In order to identify reaction products, a PPAC and a  $1.5\text{ mm}$  thick Si detector were installed on an achromatic focal plane (F2). These detectors were located at  $681$  and  $731\text{ mm}$  downstream of Q3, respectively. Secondary target of  $^{82}\text{Se}$  of  $4.9\text{ mg/cm}^2$  was placed at  $1251\text{ mm}$  downstream of Q3. Two clover Ge detectors

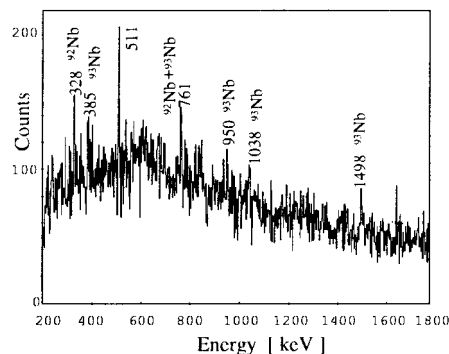


Fig. 1. Projection spectrum of  $\gamma\gamma$  coincidence.

were set at  $40\text{ mm}$  apart from the secondary target to measure  $\gamma$ -rays emitted from nuclei which were produced by the secondary fusion reaction. A plastic scintillator was placed at  $597\text{ mm}$  downstream of the secondary target in order to detect the secondary beam.

The acceptance solid angle was set to be  $5.6\text{ msr}$  by a slit downstream of F0. The energy of  $^{17}\text{N}$  recoiling out of a primary target was  $109.1 \pm 0.8\text{ MeV}$ . A  $B\rho$  value of D1 was set to be  $0.886\text{ Tm}$  to select a  $^{17}\text{N}^{7+}$  beam. Momentum acceptance was restricted to  $2.2\%$  by a rectangular slit at F1. The  $^{18}\text{O}$  primary beam was stopped by the slit at F1.

Particle identification was performed by using energies of reaction products and time differences of RF and F2-PPAC signals. The energy of  $^{17}\text{N}^{7+}$  was deduced to be  $104 \pm 2\text{ MeV}$ . As the Si detector was moved out during the  $\gamma$ -ray measurement,  $^{17}\text{N}^{7+}$  and  $^{17}\text{O}^{7+}$  could not be separated. The intensity and fraction of the  $^{17}\text{N}^{7+}$  and  $^{17}\text{O}^{7+}$  mixed beam were  $1.5 \times 10^5$  particles/s and  $33\%$ , respectively.

A total number of events of  $2.1 \times 10^8$  was collected during the measurement for 2.4 days. Data acquisition started when F2-PPAC and one Ge detector were hit. A plastic scintillator signal was used to veto the secondary beams passed through the target without making a secondary reaction. Only the data with the signals of the cocktail beam of  $^{17}\text{N}$  and  $^{17}\text{O}$  at F2 were accumulated. Although the background level originating from the thermal neutron capture  $\gamma$ -rays was 200 times higher than the counts of peaks coming from the secondary fusion reaction, seven transitions belonging to  $^{92}\text{Nb}$  and  $^{93}\text{Nb}$  were observed, as shown in Fig. 1.

### References

- 1) S. Kubono et al.: Eur. Phys. J. A **13**, 217 (2002).
- 2) Y. Gono et al.: Eur. Phys. J. A **13**, 5 (2002).

\*1 Nishinippon Institute of Technology

\*2 Kyushu University

\*3 Center for Nuclear Study, University of Tokyo

\*4 Department of Physics, University of Tokyo

\*5 Rikkyo University

\*6 Chung-Ang University, Korea

\*7 Yamagata University

# Electromagnetic transition matrix elements of proton-rich $^{46}\text{Cr}$ , $^{50}\text{Fe}$ , and $^{54}\text{Ni}$ studied by Coulomb excitation

K. Yamada,<sup>\*1</sup> T. Motobayashi, N. Aoi, H. Baba,<sup>\*1</sup> K. Demichi,<sup>\*1</sup> Z. Elekes, J. Gibelin,<sup>\*2</sup> T. Gomi,<sup>\*1</sup>  
 H. Hasegawa,<sup>\*1</sup> N. Imai, H. Iwasaki,<sup>\*3</sup> S. Kanno,<sup>\*1</sup> T. Kubo, K. Kurita,<sup>\*1</sup> Y. U. Matsuyama,<sup>\*1</sup>  
 S. Michimasa,<sup>\*4</sup> T. Minemura, M. Notani,<sup>\*4</sup> T. K. Onishi,<sup>\*3</sup> H. J. Ong,<sup>\*3</sup> S. Ota,<sup>\*5</sup> A. Ozawa,<sup>\*6</sup>  
 A. Saito,<sup>\*1</sup> H. Sakurai,<sup>\*3</sup> S. Shimoura,<sup>\*4</sup> E. Takeshita,<sup>\*1</sup> S. Takeuchi, M. Tamaki,<sup>\*4</sup>  
 Y. Togano,<sup>\*1</sup> Y. Yanagisawa, K. Yoneda,<sup>\*7</sup> and I. Tanihata

[NUCLEAR STRUCTURE,  $B(E2)$ , Unstable nuclei, Coulomb excitation,  $M_n/M_p$ ]

The measurement of proton as well as neutron multipole matrix elements in exotic nuclei is one of the incisive methods of studying the dynamical properties of nuclear states, and has received increased attention. The proton and neutron multipole elements are defined<sup>1)</sup> as

$$M_{p(n)}(T_z) = \langle J_f T T_z | \sum_{p(n)} r_i^\lambda Y_\lambda(\Omega_i) | J_i T T_z \rangle$$

$$= \frac{1}{2} [M_0(T_z) \pm M_1(T_z)], \quad (1)$$

where  $M_0(T_z)$  and  $M_1(T_z)$  are the matrix elements in an isospin representation. The multipole matrix element  $M_p$  is related to the reduced electromagnetic matrix element  $B(E\lambda; J_i \rightarrow J_f)$  by

$$B(E\lambda; J_i \rightarrow J_f) = |M_p(T_z)|^2 / (2J_i + 1). \quad (2)$$

Therefore, the proton multipole matrix element  $M_p$  can be determined via the measurement of the electromagnetic transition strength. On the other hand, the neutron multipole matrix element  $M_n$  can be obtained by comparing electromagnetic transitions in mirror nuclei.<sup>1)</sup>

As reported previously,<sup>2)</sup> we performed the first measurement of  $B(E2; 0_{g.s.}^+ \rightarrow 2_1^+)$  in the proton-rich nuclei of  $^{46}\text{Cr}$ ,  $^{50}\text{Fe}$ , and  $^{54}\text{Ni}$  in order to clarify the structures around the  $Z = 20$ –28 region systematically. The details of the experiment were described in Ref. 2.

Figure 1 shows the Doppler-corrected energy spectra of  $\gamma$  rays from  $^{46}\text{Cr}$ ,  $^{50}\text{Fe}$ , and  $^{54}\text{Ni}$ . A single distinct peak is observed in each spectrum of  $^{40}\text{Cr}$  and  $^{50}\text{Fe}$ ; their level energies are consistent with results of recent studies.<sup>3,4)</sup> In the spectrum of  $^{54}\text{Ni}$ , we can find a peak at energy of around 1400 keV which corresponds to the unknown level of  $^{54}\text{Ni}$ . In order to extract  $B(E2; 0_{g.s.}^+ \rightarrow 2_1^+)$  values, these spectra were fitted by the function  $y = af(E_\gamma) + \exp(-b \times E_\gamma + c)$ , where  $f(E_\gamma)$  is the line shape obtained by Monte-Carlo calculation. The results of fitting for  $^{46}\text{Cr}$  and  $^{50}\text{Fe}$  are shown by curves in Fig. 1. The matrix elements

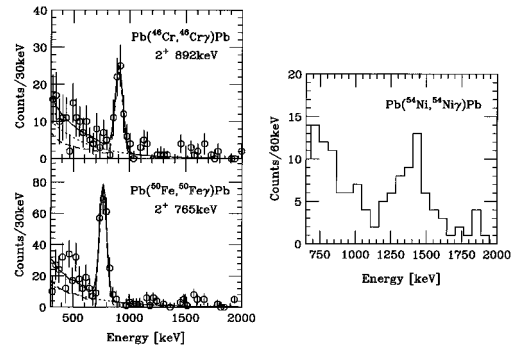


Fig. 1. The Doppler-corrected  $\gamma$  spectra from Coulomb excitation of  $^{46}\text{Cr}$ ,  $^{50}\text{Fe}$ , and  $^{54}\text{Ni}$ .

$B(E2; 0_{g.s.}^+ \rightarrow 2_1^+)$  were derived from the  $\gamma$  yield with the help of a distorted-wave calculation, assuming pure E2 Coulomb excitation. The preliminary results for  $B(E2; 0_{g.s.}^+ \rightarrow 2_1^+)$  were  $19.9 \pm 4.2$  W.u. and  $25.8 \pm 4.9$  W.u. for  $^{46}\text{Cr}$  and  $^{50}\text{Fe}$ , respectively. These errors include the ambiguities associated with the fitting procedure and common systematic uncertainties. In order to examine the validity of our method,  $B(E2; 0_{g.s.}^+ \rightarrow 2_1^+)$  of  $^{44}\text{Ti}$ ,  $^{48}\text{Cr}$ , and  $^{52}\text{Fe}$  in the secondary beam was extracted and compared with known spectroscopic information. The present results of  $21.9 \pm 2.8$  W.u. and  $19.2 \pm 3.5$  W.u. for  $^{44}\text{Ti}$  and  $^{48}\text{Cr}$  are considerably variant to their adopted  $B(E2; 0_{g.s.}^+ \rightarrow 2_1^+)$  values of  $13 \pm 4$  W.u. and  $31 \pm 4$  W.u., respectively.

However, the result of  $16.4 \pm 2.1$  W.u. for  $^{52}\text{Fe}$  is consistent with a recent measurement by Yurkewicz et al.,<sup>5)</sup> which gives  $B(E2; 0_{g.s.}^+ \rightarrow 2_1^+) = 14.2 \pm 1.8$  W.u.

Comparing the present results of  $B(E2; 0_{g.s.}^+ \rightarrow 2_1^+)$  with those of mirror nuclei, we can obtain  $M_n/M_p$  values of  $0.99 \pm 0.11$  and  $0.88 \pm 0.09$  for  $^{46}\text{Cr}$  and  $^{50}\text{Fe}$ , respectively. Both the  $M_n/M_p$  values are close to  $N/Z$ , suggesting collective aspects of these nuclei. Detailed comparisons of the present results and theoretical calculations are under way.

## References

- 1) A. M. Bernstein et al.: Phys. Rev. Lett. **42**, 425 (1979).
- 2) K. Yamada et al.: RIKEN Accel. Prog. Rep. **36**, 85 (2003).
- 3) P. E. Garrett et al.: Phys. Rev. Lett. **87**, 132502 (2001).
- 4) S. M. Lenzi et al.: Phys. Rev. Lett. **87**, 122501 (2001).
- 5) K. L. Yurkewicz et al.: Phys. Rev. to be published.

<sup>\*1</sup> Department of Physics, Rikkyo University  
<sup>\*2</sup> Institut de Physique Nucléaire, France  
<sup>\*3</sup> Department of Physics, University of Tokyo  
<sup>\*4</sup> Center for Nuclear Study, University of Tokyo  
<sup>\*5</sup> Department of Physics, Kyoto University  
<sup>\*6</sup> Institute of Physics, University of Tsukuba  
<sup>\*7</sup> National Superconducting Cyclotron Laboratory, Michigan State University

## Intermediate-energy Coulomb excitation of neutron-rich Ge isotopes around $N = 50$

H. Iwasaki,<sup>\*1</sup> N. Aoi, S. Takeuchi, S. Ota,<sup>\*2</sup> H. Sakurai,<sup>\*1</sup> M. Tamaki,<sup>\*3</sup> T. K. Onishi,<sup>\*1</sup> E. Takeshita,<sup>\*4</sup>  
H. J. Ong,<sup>\*1</sup> N. Iwasa,<sup>\*5</sup> H. Baba,<sup>\*4</sup> Z. Elekes, T. Fukuchi,<sup>\*3</sup> Y. Ichikawa,<sup>\*1</sup> M. Ishihara, S. Kanno,<sup>\*4</sup>  
R. Kanungo, S. Kawai,<sup>\*4</sup> T. Kubo, K. Kurita,<sup>\*4</sup> S. Michimasa,<sup>\*3</sup> T. Motobayashi, M. Niikura,<sup>\*3</sup> A. Saito,<sup>\*4</sup>  
Y. Satou,<sup>\*6</sup> S. Shimoura,<sup>\*3</sup> H. Suzuki,<sup>\*1</sup> M. K. Suzuki,<sup>\*1</sup> Y. Togano,<sup>\*4</sup> and Y. Yanagisawa

[NUCLEAR REACTIONS:  $^{76,78,80,82}\text{Ge} + \text{Pb}$ , Coulomb excitation]

We have studied intermediate-energy Coulomb excitation of neutron-rich Ge isotopes around  $N = 50$  using secondary beams of  $^{76-82}\text{Ge}$  incident on Pb and C targets. Among the various reactions recently applied for  $\gamma$ -ray spectroscopy with radioactive-ion beams,<sup>1-6)</sup> Coulomb excitation affords unique opportunities for measuring both energies and transition probabilities  $B(E2)$  for the low-lying  $2^+$  states. The aim of the present experiment is to investigate such E2 properties of the neutron-rich Ge isotopes, which enable us to depict systematic trends of the collective behavior toward the neutron magic number  $N = 50$ . In addition, two-step excitation at an intermediate energy has been studied to examine a possible access to higher excited states. Here, we report the experimental arrangement.

The experiment was performed at the RIPS beam line in RIKEN. The radioactive beams of  $^{76-82}\text{Ge}$  were produced by fragmentation of a 63 A MeV  $^{86}\text{Kr}$  beam on a 66.2-mg/cm<sup>2</sup>-thick  $^9\text{Be}$  target. A maximum intensity of 100 pA was achieved for the primary  $^{86}\text{Kr}$  beam, owing to the recently developed acceleration scheme of the RRC with the RFQ+RILAC+CSM injection system. The reaction fragments were collected and analyzed by RIPS. As an energy degrader, we used a curved aluminum plate, which is equivalent in thickness along the beam line to a 65 mg/cm<sup>2</sup> wedge-shaped degrader. Particle identification of the incident beam was carried out event-by-event by measuring magnetic rigidity ( $B\rho$ ), time-of-flight (TOF), and energy loss ( $\Delta E$ ). The positions at the momentum-dispersive focal plane of RIPS were measured by a parallel plate avalanche counter (PPAC) to determine the  $B\rho$  value. The TOF between the production target and the final focal plane (F3) of RIPS was obtained from the RF signal of the accelerator and the 0.01-mm-thick plastic scintillator placed at F3. The  $\Delta E$  information was provided by the 100- $\mu\text{m}$ -thick silicon detector placed at the second focal plane of RIPS. The accuracy in the particle identification of the Ge isotopes was around 0.9% and 0.2% (r.m.s.), respectively, for the  $Z$  and  $A/Z$  determinations. The typical secondary-beam

intensities were around 6 kcps for  $^{76}\text{Ge}$ , 2 kcps for  $^{78}\text{Ge}$ , 1 kcps for  $^{80}\text{Ge}$ , and 100 cps for  $^{82}\text{Ge}$  in the separate  $B\rho$  settings optimized for each isotope. Pb targets were placed at F3 and were used to excite the projectiles. The position and incident angles of the beam at F3 were measured by two sets of PPAC placed upstream of the target. To evaluate the possible contributions of nuclear excitations, additional measurements with C targets were also performed.

De-excitation  $\gamma$  rays were detected by an array of 158 NaI(Tl) scintillators<sup>7)</sup> surrounding the target. The energy and efficiency calibrations of the array were made using standard  $^{22}\text{Na}$ ,  $^{60}\text{Co}$ , and  $^{137}\text{Cs}$  sources. The overall photopeak efficiency and energy resolution were found to be 30% and 9% (FWHM), respectively, for a 661-keV  $\gamma$  ray as measured with the  $^{137}\text{Cs}$  source.

Scattered particles were detected by a Si telescope and a NaI(Tl) calorimeter located 75 cm and 1.5 m downstream of the secondary target. The Si telescope consisted of 16 silicon detectors placed in a  $4 \times 4$  matrix. The size of each detector was 5 cm  $\times$  5 cm  $\times$  325  $\mu\text{m}$ . The NaI(Tl) calorimeter, the details of which are described elsewhere,<sup>8)</sup> comprised 132 NaI(Tl) crystals arranged in a  $12 \times 12$  matrix except for three crystals at each corner. Each crystal has a rectangular shape with the size of 31  $\times$  31  $\times$  50 mm<sup>3</sup>. The Si telescope provided energy-loss ( $\Delta E$ ) information, while the NaI(Tl) calorimeter served as an  $E$  counter. The atomic number of the outgoing particles was thus identified by the  $\Delta E$ - $E$  method. The whole counter was located in a vacuum chamber to minimize the energy loss in the material between the Si and NaI(Tl) detectors. The present setup covered a solid angle of approximately 8 degrees. The scattering angle was determined by the hit positions in the two PPAC at F3 and the NaI(Tl) calorimeter.

An analysis of the data is now in progress.

### References

- 1) T. Motobayashi et al.: Phys. Lett. B **346**, 9 (1994).
- 2) H. Iwasaki et al.: Phys. Lett. B **491**, 8 (2000).
- 3) T. Glasmacher et al.: Nucl. Phys. A **693**, 90 (2001).
- 4) K. Yoneda et al.: Phys. Lett. B **499**, 233 (2001).
- 5) F. Azaiez: Nucl. Phys. A **704**, 37c (2002).
- 6) Y. Yanagisawa et al.: Phys. Lett. B **566**, 84 (2003).
- 7) S. Takeuchi et al.: RIKEN Accel. Prog. Rep. **36**, 148 (2003).
- 8) M. Tamaki et al.: CNS-REP-59, 76 (2003).

<sup>\*1</sup> Department of Physics, University of Tokyo

<sup>\*2</sup> Department of Physics, Kyoto University

<sup>\*3</sup> Center for Nuclear Study, University of Tokyo

<sup>\*4</sup> Department of Physics, Rikkyo University

<sup>\*5</sup> Department of Physics, Tohoku University

<sup>\*6</sup> Department of Physics, Tokyo Institute of Technology

## Production cross sections of neutron-rich Ca and Ni isotopes formed by fragmentation of a 63 A MeV $^{86}\text{Kr}$ beam

H. Iwasaki,<sup>\*1</sup> H. Nishino,<sup>\*1</sup> K. Tsurusaki,<sup>\*1</sup> H. Sakurai,<sup>\*1</sup> T. K. Onishi,<sup>\*1</sup> N. Aoi, E. Takeshita,<sup>\*2</sup> Y. Ichikawa,<sup>\*1</sup> H. Baba,<sup>\*2</sup> Z. Elekes, T. Fukuchi,<sup>\*3</sup> M. Ishihara, N. Iwasa,<sup>\*4</sup> S. Kanno,<sup>\*2</sup> R. Kanungo, S. Kawai,<sup>\*2</sup> T. Kubo, K. Kurita,<sup>\*2</sup> S. Michimasa,<sup>\*3</sup> T. Motobayashi, M. Niikura,<sup>\*3</sup> H. J. Ong,<sup>\*1</sup> S. Ota,<sup>\*5</sup> A. Saito,<sup>\*2</sup> Y. Satou,<sup>\*6</sup> S. Shimoura,<sup>\*3</sup> H. Suzuki,<sup>\*1</sup> M. K. Suzuki,<sup>\*1</sup> S. Takeuchi, M. Tamaki,<sup>\*3</sup> Y. Togano,<sup>\*2</sup> and Y. Yanagisawa

[NUCLEAR REACTIONS:  $^9\text{Be}(^{86}\text{Kr}, X)$ ,  $E(^{86}\text{Kr}) = 63 A \text{ MeV}$ ; Measured production cross sections of  $^{51-53}\text{Ca}$  and  $^{72-75}\text{Ni}$ ]

We have measured production cross sections of neutron-rich nuclei formed by the fragmentation of a 63 A MeV  $^{86}\text{Kr}$  beam. Previous studies<sup>1,2)</sup> have investigated  $^{86}\text{Kr}$ -induced reactions with  $^9\text{Be}$  targets at 500 A MeV<sup>1)</sup> and 66 A MeV.<sup>2)</sup> They reported production cross sections of neutron-rich nuclei along the  $N = 50$  line and estimated the cross section for the doubly magic nucleus  $^{78}\text{Ni}$ . The present work extends the experimental information to neutron-rich Ca and Ni isotopes, which allows us to examine the feasibility of the secondary-beam experiments with these nuclei.

The experiment was performed using a  $^{86}\text{Kr}$  primary beam accelerated up to 63 A MeV by the RIKEN Ring Cyclotron (RRC) incident upon a 66.2-mg/cm<sup>2</sup>-thick  $^9\text{Be}$  target. The linear accelerator complex of the RFQ+RILAC+CSM scheme was used as an injector to RRC, which facilitated an intense  $^{86}\text{Kr}$  beam with a maximum intensity of 100 pA.

The reaction fragments were collected and analyzed by the RIPS spectrometer. The momentum acceptance and solid angle of RIPS were set at 0.5% and 5 msr, respectively. The fragments were transported to the final focal plane (F3) of RIPS and stopped in four layers of 0.5-mm-thick silicon detectors. The arrival timing at F3 was measured by a parallel plate avalanche counter (PPAC) set immediately upstream of the silicon detectors.

Particle identification of the fragments was performed on the basis of time-of-flight (TOF), energy loss ( $\Delta E$ ), and total kinetic energy (TKE) measurements. The TOF was determined from the RF signal of the accelerator and the PPAC. The  $\Delta E$  information was obtained by the first silicon detector, while the whole detectors provided the TKE measurement.

Five different settings of magnetic rigidity in the range of 2.85–3.03 Tm were employed to obtain differential cross sections. The production cross section for each fragment was determined by a fit of the observed momentum distribution to an asymmetric Gaussian distribution.

Figure 1 shows the production cross sections obtained for neutron-rich Ca and Ni isotopes. The data are also compared with the production cross sections in the  $^{238}\text{U}$ -fission reaction<sup>3)</sup> as well as the results of the empirical parametrization (EPAX2).<sup>4)</sup> The  $^{86}\text{Kr}$ -induced cross sections are smaller than the  $^{238}\text{U}$ -fission cross sections by more than two orders of magnitude. It is also found that the  $^{86}\text{Kr}$ -induced cross sections have large mass-number (or  $N/Z$  ratio) dependence, even stronger than that of the EPAX2 predictions. Further investigation is of great importance for establishing a reliable prediction toward very neutron-rich nuclei such as  $^{78}\text{Ni}$ .

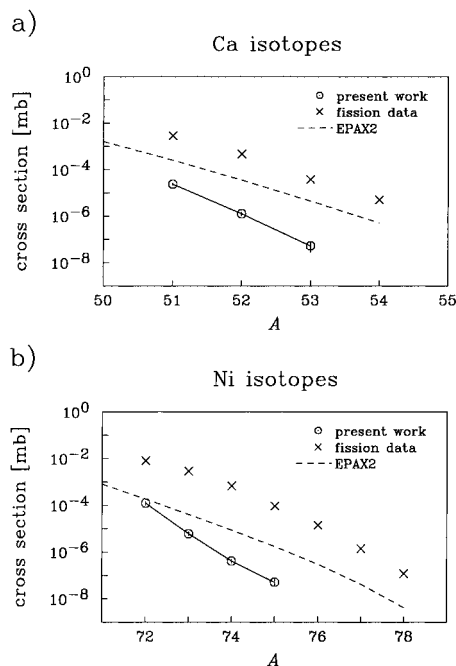


Fig. 1. Production cross sections of a) Ca and b) Ni isotopes plotted as a function of mass number ( $A$ ).

### References

- 1) M. Weber et al.: Nucl. Phys. A **578**, 659 (1994).
- 2) N. Aoi et al.: RIKEN Accel. Prog. Rep. **35**, 75 (2002).
- 3) M. Bernas: AIP Conf. Proc. **455**, 664 (1998).
- 4) K. Sümmerer and B. Blank: Phys. Rev. C **61**, 034607 (2000).

<sup>\*1</sup> Department of Physics, University of Tokyo  
<sup>\*2</sup> Department of Physics, Rikkyo University  
<sup>\*3</sup> Center for Nuclear Study, University of Tokyo  
<sup>\*4</sup> Department of Physics, Tohoku University  
<sup>\*5</sup> Department of Physics, Kyoto University  
<sup>\*6</sup> Department of Physics, Tokyo Institute of Technology

# Lifetime of a new high-spin isomer in $^{150}\text{Dy}$

H. Watanabe, Y. Wakabayashi,\*<sup>1</sup> Y. Gono,\*<sup>1</sup> T. Fukuchi,\*<sup>2</sup> H. Ueno, W. Sato,\*<sup>3</sup> A. Yoshimi, D. Kameda,\*<sup>4</sup>  
H. Miyoshi,\*<sup>4</sup> T. Kishida, Y. Kobayashi, T. Morikawa,\*<sup>1</sup> S. Motomura, O. Kashiya,\*<sup>1</sup>  
K. Saito,\*<sup>1</sup> A. Odahara,\*<sup>5</sup> and K. Asahi \*<sup>4</sup>

[NUCLEAR STRUCTURE,  $^{150}\text{Dy}$ , High-spin isomer, Lifetimes]

High-spin states in  $^{150}\text{Dy}$  have been studied using two types of experiments. In the first experiment, the nucleus  $^{150}\text{Dy}$  was produced *via* the  $^{141}\text{Pr}(^{16}\text{O}, \text{p}6\text{n})$  reaction with an energy of 165 MeV provided by the SF cyclotron at the Center for Nuclear Study, University of Tokyo. Five HPGe detectors with BGO anti-Compton shields were arranged around the target. The experimental data were acquired when at least two Compton-suppressed Ge detectors were fired concurrently. Figure 1 shows a partial decay scheme confirmed in this experiment. The second experiment was carried out with a 6 mg/cm<sup>2</sup> natural Mg target irradiated by a  $^{132}\text{Xe}$  beam accelerated up to an energy of 7.0 MeV/u by the RIKEN Ring Cyclotron. The beam burst was pulsed with an interval of 1  $\mu\text{s}$  and a width of  $\leq 1$  ns. The reaction products which recoiled out the target with a mean velocity of  $0.07c$  were gathered on a lead stopper placed 7 cm downstream from the target. It took approximately 3 ns for the recoil nuclei to pass between the target and the stopper. The production target was shielded by lead blocks so that

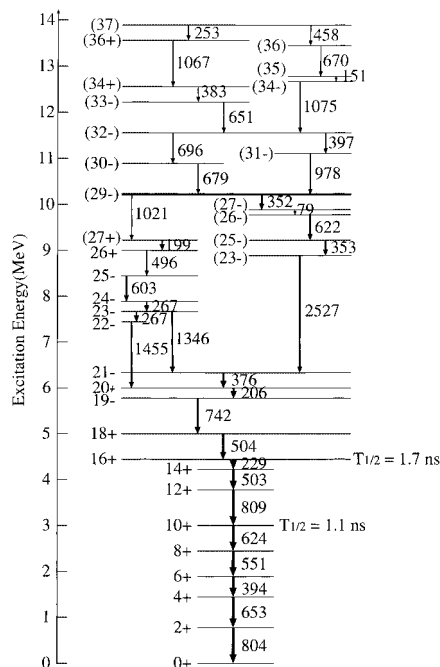


Fig. 1. Partial level scheme of  $^{150}\text{Dy}$ .

the prompt  $\gamma$  rays were not observed by Ge detectors. The combination of the pulsed beam and the recoil-shadow method<sup>1)</sup> with the inverse-kinematic reaction allowed us to measure only  $\gamma$  rays emitted *via* isomeric states whose half-lives ranged from a few nanoseconds to sub microseconds. Five HPGe detectors were used to measure the delayed  $\gamma$  rays from the stopper position.

Comparing the  $\gamma$ - $\gamma$ -gated spectra for  $^{150}\text{Dy}$  measured in both experiments, the  $\gamma$  rays deexciting the states higher than the  $E_{ex} = 10.3$  MeV level could be clearly observed in the first experiment (Fig. 2 (A)), while only the transitions below that state were detected with the recoil-shadowing setup (Fig. 2 (B)). This indicates that the 10.3 MeV state has a half-life of more than a few nanoseconds. The half-life of this isomeric state has been determined to be  $T_{1/2} = 1.6 \pm 0.6$  ns using the conventional centroid-shift method.<sup>2)</sup>

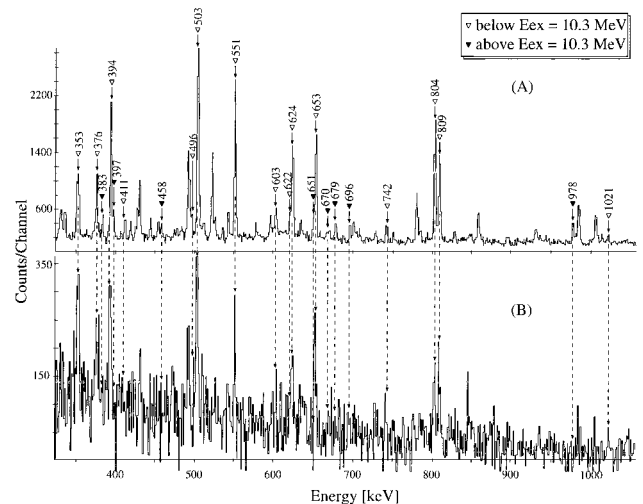


Fig. 2.  $\gamma$ - $\gamma$  coincidence spectra for  $^{150}\text{Dy}$  measured at (A) the target position in the first experiment, (B) the stopper position with the recoil-shadowing geometry in the second experiment. Both figures were created by summing up spectra gated by 742, 206, 1455, 1346 keV transitions. The energies are noted for the  $\gamma$  rays below (open triangle) and above (solid triangle) the  $E_{ex} = 10.3$  MeV state in  $^{150}\text{Dy}$ .

\*<sup>1</sup> Department of Physics, Kyushu University  
\*<sup>2</sup> Center for Nuclear Study, University of Tokyo  
\*<sup>3</sup> Graduate School of Science, Osaka University  
\*<sup>4</sup> Tokyo Institute of Technology  
\*<sup>5</sup> Nishinippon Institute of Technology

## References

- 1) J. Thirion and V. L. Telegdi: Phys. Rev. **92**, 1253 (1953).
- 2) W. Andrejtscheff et al.: Nucl. Instrum. Methods **204**, 123 (1982).



# Production and decay properties of $^{272}111$ and its daughter nuclei

K. Morita, K. Morimoto, D. Kaji, S. Goto, H. Haba, E. Ideguchi, J. C. Peter, R. Kanungo, K. Katori, H. Koura, H. Kudo, T. Ohnishi, A. Ozawa, T. Suda, K. Sueki, I. Tanihata, F. Tokanai, H. Xu, A. V. Yeremin, A. Yoneda, A. Yoshida, Y.-L. Zhao, and T. Zheng

[ $^{272}111$ , production and decay, excitation function, gas-filled recoil separator]

The search for the heaviest elements is one of the most important challenges in nuclear physics. We installed a gas-filled recoil separator (GARIS)<sup>1</sup> for the research on the heaviest elements at an experimental hall of the RIKEN Linear Accelerator Facility. As the first attempt using the separator, we studied the production and decay of an isotope  $^{271}\text{Ds}$  ( $Z = 110$ ) using the  $^{208}\text{Pb} + ^{64}\text{Ni} \rightarrow ^{271}\text{Ds} + \text{n}$  reaction in 2002.<sup>2)</sup> In the present work, we investigated the production and decay of  $^{272}111$  using  $^{209}\text{Bi} + ^{64}\text{Ni} \rightarrow ^{272}111 + \text{n}$  reaction. The synthesis of this nuclide was reported by Hofmann *et al.*<sup>3,4)</sup> using the same reaction as that in the present work. The present result presents the first clear confirmation for the discovery of  $^{272}111$  and its  $\alpha$ -decay products,  $^{264}\text{Bh}$  and  $^{268}\text{Mt}$ .

The measurement was made at three different beam energies, 320, 323 and 326 MeV. The reaction products in flight were separated from the incident beam through GARIS. The products were then implanted into the position-sensitive semiconductor detector placed at the focus of GARIS. The energy and position signals from implantations and subsequent decays of the products were used for data analysis. Targets were prepared by vacuum evaporation of metallic bismuth on carbon backing foils of  $30 \mu\text{g}/\text{cm}^2$  thickness. The thickness of the bismuth layer was approximately  $280 \mu\text{g}/\text{cm}^2$ . The targets were covered by a  $10\text{-}\mu\text{g}/\text{cm}^2$ -thick carbon to protect the target from sputtering. Other experimental setups were almost the same as those described in Ref. 2.

We have observed 14  $\alpha$ -decay chains in total, which were assigned, on the basis of their energies and time correlations, to subsequent decays from  $^{272}111$  produced in the  $^{209}\text{Bi}(^{64}\text{Ni}, 1\text{n})$  reaction. The decay chains observed in the present experiment are summarized in Fig. 1. The numbers in parenthesis in the figure denote the numbers of observed events. Three decay chains ended by spontaneous fission decays. The fission events are also indicated in the figure. Half-lives and  $\alpha$ -decay energies measured in the present experiment for  $^{272}111$ ,  $^{264}\text{Bh}$ , and  $^{268}\text{Mt}$  are shown in the figure. The observed half-life of  $^{272}111$ ,  $3.8^{+1.4}_{-0.8}$  ms, is more than two times longer than the value of  $1.6^{+1.1}_{-0.5}$  ms reported in Ref. 4, while that of  $^{268}\text{Mt}$ ,  $21^{+8}_{-5}$  ms, is two times shorter than the value of  $42^{+29}_{-12}$  ms reported in the reference.

Cross sections of the  $^{209}\text{Bi}(^{64}\text{Ni}, 1\text{n})$  reaction were deduced from the numbers of the observed events,

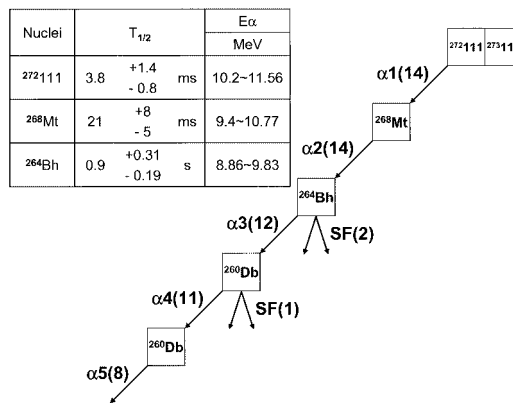


Fig. 1. Summary of the observed decay chains. The numbers in parenthesis denote the numbers of observed events.

target thicknesses, beam doses, and the efficiency of GARIS. Results are summarized in Table 1. The first three decay chains are excluded from the analysis of excitation function because of the target deterioration occurring for those events. The efficiency of GARIS was assumed to be 80%. In Table 1,  $E_{lab}$  denotes the projectile energy at the middle of the target. The errors in the cross sections are only statistical ones at 68% confidence level. The cross section value obtained in the present experiment agrees well with the value reported in Ref. 4.

Table 1. Summary of the reaction of  $^{64}\text{Ni}$  on  $^{209}\text{Bi}$ .

$E_{proj}$ MeV	Thickness <sup>§1</sup> $\mu\text{g}/\text{cm}^2$	$E_{lab}^{\text{§2}}$ MeV	dose $10^{18}$	Observed events	$\sigma$ pb
320.0	250	317.5	2.0	3	$2.6^{+2.3}_{-1.5}$
323.0	290	320.3	4.9	8	$2.5^{+1.2}_{-0.9}$
326.0	300	323.2	2.5	0	$0.0^{+1.1}_{-0.0}$

<sup>§1</sup>average target thickness

<sup>§2</sup>at the middle of the target

## References

- 1) K. Morita et al.: RIKEN Accel. Prog. Rep. **36**, 196 (2003).
- 2) K. Morita et al.: RIKEN Accel. Prog. Rep. **36**, 90 (2003); RIKEN Accel. Prog. Rep. **36**, 91 (2003).
- 3) S. Hofmann et al.: Z. Phys. A **350**, 281 (1995).
- 4) S. Hofmann et al.: Eur. Phys. J. A **14**, 147 (2002).

## Electron scattering from unstable nuclei by a novel SCRIT method

T. Suda, M. Wakasugi, T. Koseki, T. Emoto, T. Ohnishi, H. Takeda, and K. Kurita\*

[NUCLEAR STRUCTURE, Unstable nuclei, electron scattering, SCRIT]

Electron scattering is one of the most precise probes for studying the internal structure of atomic nuclei. In particular, elastic electron scattering provides precise spatial charge distribution in a nucleus, which plays an essential role in our understanding of the nuclear structure.

We have been discussing possible ways of realizing electron scattering off radioactive isotopes (RI) in order to study their internal structure.<sup>1-3)</sup> Recently, a novel scheme has been proposed, which employs a well-known ion-trapping phenomenon in electron storage rings at synchrotron radiation (SR) facilities. Ion trapping is a phenomenon where ionized residual gases by an electron beam are trapped by the circulating beam itself. It is known that this ion trapping effect seriously reduces the performances of the SR facilities, such as causing shorter beam lifetime and beam instability.

Our novel method is to produce a localized RI target on the electron beam by the ion trapping effect in a storage ring, SCRIT (Self Confined RI Target).<sup>4,5)</sup> RI ions are injected from an external ion source.

Numerical simulations have shown that the SCRIT system may provide sufficiently high luminosity for elastic electron scattering:  $10^{28}/\text{cm}^2/\text{s}$  being achievable for  $10^8/\text{s}$  ion injection with a 500 mA electron beam current.

The following issues, however, have to be examined experimentally.

- Does the SCRIT concept really work?
- Can we determine the luminosity accurately?
- Does the detection system properly work near a high-current stored beam such as 500 mA?

A test experiment is to be carried out at an existing electron storage ring, KSR, at Kyoto University. A SCRIT system equipped with an electron detection system has been recently constructed for this experiment.

The SCRIT system consists of an ion source for (stable) Sn nucleus and electrodes placed along the beam line for longitudinal ion trapping. The externally injected ions are trapped transversely by the circulating electron beam, and longitudinally by the electrodes placed along the beam line. The electron detection system consists of a drift chamber, a set of plastic scintillators and calorimeters, as shown in Fig. 1. They are arranged to detect elastically scattered electrons in the angular range of 30–80 degrees from a spatially

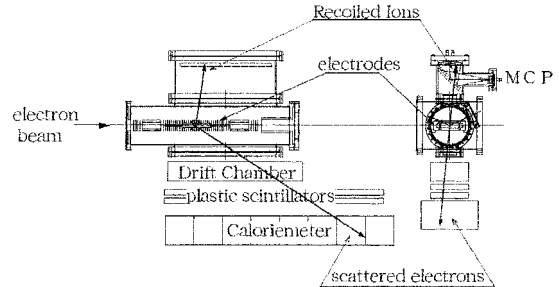


Fig. 1. SCRIT chamber with planned detection system. The ion source is not shown.

extended SCRIT of approximately 15 cm.

The luminosity is monitored by detecting bremsstrahlung  $\gamma$ -ray downstream of the straight section, where the SCRIT system is installed.

The momentum transfer under this kinematics with 100 MeV stored electron beam corresponds to 50–120 MeV/c, where the elastic cross section for Sn is larger than 100 mb/sr. The maximum counting rate of the e+Sn elastic scattering is expected to be 1/s for the expected luminosity of  $10^{25}/\text{cm}^2/\text{s}$ . The SCRIT system is ready to be installed at one of the straight sections of KSR in the beginning of 2004.

In the future, we plan to install a recoiled-ion detection system, as shown in Fig. 1. By taking coincidences with the electron arm, the elastic scattering events can be unambiguously identified. In addition, the time-of-flight information of recoiled ions provides their mass, since one knows the recoil momentum simply from the electron scattering angle. The recoiled-ion detector, where an MCP is a candidate, must not face the circulating beam directly in order to avoid expected backgrounds of UV lights from SR and Moeller electrons. Instead, MCPs detect secondary electrons emitted from a metal foil that catches the recoiled ions.

### References

- 1) T. Suda et al.: RIKEN Accel. Prog. Rep. **33**, 52 (2000).
- 2) T. Suda et al.: RIKEN Accel. Prog. Rep. **34**, 49 (2001).
- 3) T. Suda: A proposal for RIKEN RI Beam Factory (F01-23, 2001).
- 4) M. Wakasugi: to be published in Proc. Int. Workshop on Beam Cooling and Related Topics, Yamanashi, 2003-5, in press.
- 5) M. Wakasugi: Proc. 14th Symp. on Accelerator Science and Technology, Tsukuba, 2003-12, in press.

\* Rikkyo University

## Development of liquid hydrogen target for EPR experiment at SMART

T. Ikeda,<sup>\*1</sup> T. Saito,<sup>\*2</sup> H. Sakai,<sup>\*2</sup> T. Uesaka,<sup>\*3</sup> T. Kawabata,<sup>\*3</sup> K. Yako,<sup>\*2</sup> and K. Itoh <sup>\*1</sup>

Einstein Podolsky Rosen (EPR) paradox is famous as one of the problems of quantum mechanics. We have challenged this problem by measuring the spin correlation of a spin-singlet proton pair produced *via* the (*d*, <sup>2</sup>He) reaction at intermediate energy.<sup>1)</sup>

As a production target in this investigation, a hydrogen target is most appropriate because of its simplicity and its liability to the spin and isospin flips. Thus, we have developed a liquid hydrogen target for this measurement.

The target consisted of a cryogenic refrigerator, a target cell, a thermal shield, and driving gears for moving and rotating the target (Fig. 1). The target cell was attached to the cold head of the cryogenic refrigerator and placed in the scattering chamber of the E4 experimental area. The cell used was made of aluminum to avoid unnecessary activation and to keep the thermal conductivity high.

From the estimated production rate of <sup>2</sup>He and true-to-accidental coincidence ratio under the actual experimental setup, it was determined that the thickness of the target was 70 mg/cm<sup>2</sup>. Aramid foils of 20 mm diameter and 12.5 μm thickness were used as the windows of the target.

The thermal shield made of aluminum attached to the first stage of the refrigerator prevented the target cell from the effect of thermal radiation from surrounding materials at room temperature.

This target was used in the experiment for 270 MeV deuteron beams. The operation temperature and inner pressure of the liquid hydrogen target were 15 K and

0.4 atm, respectively.

Figure 2 shows the target inner pressure and temperature during the experiment. The peaks of this graph appeared when the target was moved. The cause of this phenomenon is not known yet.

This graph indicates that the fluctuation of target temperature was small for a long time; hence, the effects of beams and thermal radiation were very small. It is possible to use this target for a long time.

Figure 3 shows the excitation energy spectrum of

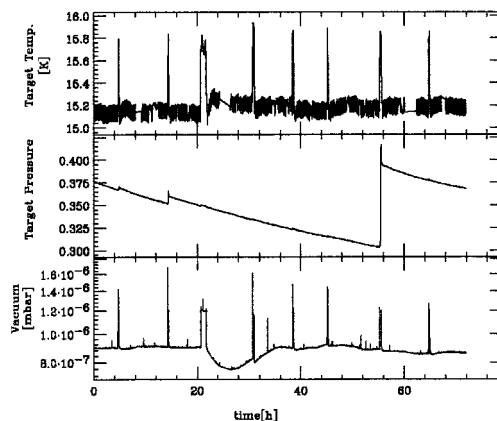


Fig. 2. Target temperature, inner pressure and vacuum degree in scattering chamber.

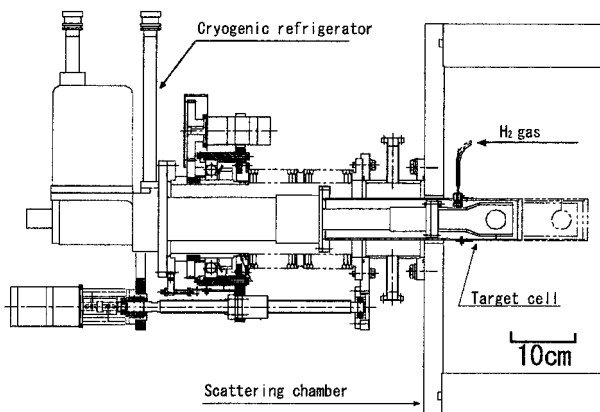


Fig. 1. Liquid hydrogen target system.

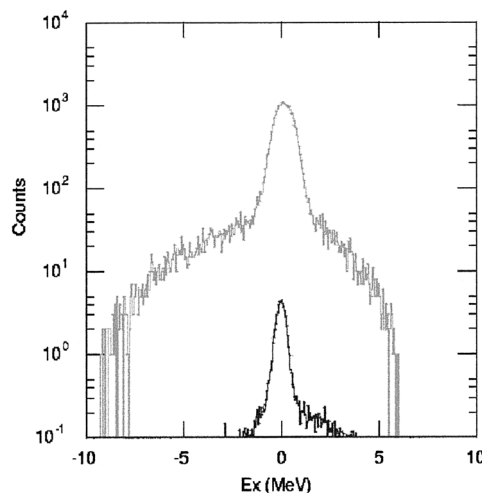


Fig. 3. Excitation energy spectrum of remaining neutron. The upper line indicates the spectrum of the liquid hydrogen target, while the lower one indicates the spectrum of the empty target cell.

<sup>\*1</sup> Department of Physics, Saitama University  
<sup>\*2</sup> Department of Physics, University of Tokyo  
<sup>\*3</sup> Center for Nuclear Study, University of Tokyo

the remaining neutron of the  $H(d, {}^2\text{He})n$  reaction. The spectra with and without liquid hydrogen in the target cell were compared. We observe from this figure that the ratio of true events from liquid hydrogen to background events from the aramid foil window is more than 100; thus, the background from the aramid foil is sufficiently small to be ignored in this experiment.

Hence, it is concluded that the target has a high stability and a high  $S/N$  ratio in the EPR paradox experiment.

#### References

- 1) T. Saito et al.: RIKEN Accel. Prog. Rep. **37**, 45 (2004).

## Evidence for a deeply bound kaonic system $K^-ppn$ in the ${}^4\text{He}$ (stopped $K^-, n$ ) reaction<sup>†</sup>

H. Ota, H. Bhang,<sup>\*1</sup> G. Franklin,<sup>\*2</sup> K. Gomikawa,<sup>\*3</sup> R. S. Hayano,<sup>\*3</sup> T. Hayashi,<sup>\*4</sup> M. Iwasaki, K. Ishikawa,<sup>\*4</sup> S. Ishimoto,<sup>\*5</sup> K. Itahashi, T. Katayama,<sup>\*4</sup> Y. Kondo,<sup>\*4</sup> Y. Matsuda, T. Nakamura,<sup>\*4</sup> S. Okada, B. Quinn,<sup>\*2</sup> M. Sato,<sup>\*4</sup> M. Shindo,<sup>\*3</sup> H. So,<sup>\*1</sup> P. Strasser, T. Sugimoto,<sup>\*4</sup> K. Suzuki,<sup>\*6</sup> S. Suzuki,<sup>\*5</sup> T. Suzuki,<sup>\*3</sup> D. Tomono,<sup>\*4</sup> A. M. Vinodkumar,<sup>\*4</sup> E. Widmann,<sup>\*3</sup> T. Yamazaki, and T. Yoneyama<sup>\*4</sup>

[NUCLEAR STRUCTURE, Kaon-baryon interactions, Chiral symmetries]

The kaonic hydrogen X-ray measurement at KEK<sup>1)</sup> strongly suggests the attraction of the  $\bar{K}N$  interaction in the  $I = 0$  channel. Now  $\Lambda(1405)$  can be interpreted as a bound state of  $K^-$  and a proton. Recently, Akaishi and Yamazaki developed a phenomenological  $\bar{K}N$  interaction using the  $\bar{K}N$  scattering length and energy/width of  $\Lambda(1405)$  and predicted that very deeply bound kaonic nuclear states —  $B_K \geq 100$  MeV — are formed in light nuclei. Due to its strong binding, a major  $\bar{K} + N \rightarrow \Sigma + \pi$  decay channel is forbidden; hence the state is considered to have a narrow width of  $\Gamma \sim 30$  MeV.<sup>2)</sup> In addition, due to the  $K^-p$  strong attraction, the kaonic nuclei forms an extremely dense system with a central density of 8–10 times the normal nuclear density,<sup>3)</sup> where we can expect the restoration of the chiral symmetry.

In the present experiment, we measured the energy spectrum of neutron by means of TOF from the  ${}^4\text{He}$  (stopped  $K^-, n$ ) reaction. If the narrow bound state of  $K^-ppn$  is formed, a mono-energetic neutron should be emitted *via* the  $K^- + {}^4\text{He} \rightarrow K^-ppn + n$  reaction.<sup>4)</sup> We placed  $2\text{ m}^3$  of plastic scintillation counter arrays at 2 m from the helium target for neutron TOF measurement. Absolute timing calibration was carried out using  $\gamma$  rays and an overall resolution of  $\Delta(1/\beta) = 0.04(\sigma)$  was achieved, which corresponds to  $\sigma = 6$  MeV neutron energy resolution at  $p_n \sim 500$  MeV/c. We also required that a charged particle is emitted from the target region in the trigger level. Both the incoming kaon and outgoing charged particle tracks were measured by the drift chambers and the reaction point was determined by the vertex between the two trajectories. By determining the distance of the closest approach ( $DCA$ ) of the two trajectories and selecting  $DCA \neq 0$  events, we can detect charged pions from the weak decay of hyperons ( $\Lambda \rightarrow N\pi$  or  $\Sigma \rightarrow N\pi$  decay). Also we can roughly identify the direction of hyperon emission from this  $DCA$  analysis.

In the high-momentum region of the neutron spectrum, backgrounds predominantly originate from the  $K^-$  two-nucleon absorption process ( $K^-NN \rightarrow YN$ ;  $Y \rightarrow N\pi$ ). Simulation shows that neutron direction from the background process does not correlate to that of hyperon emission, whereas the  $\Sigma$  from the  $K^-ppn \rightarrow \Sigma NN$  decay of the kaonic nucleus tends to go backward to the formation neutron. Figure 1 shows the comparison of  ${}^4\text{He}$  (stopped  $K^-, n$ ) spectra in coincidence with backward/forward  $\Sigma$  emission. (Charged pions from the  $\Lambda$  tend to have a smaller momentum, thus we eliminated them by selecting a “fast” charged pion.) The comparison of the two spectra reveals a peak at  $\sim 470$  MeV/c in the “backward” spectrum. The excess over the background is estimated to be  $3.6\sigma$  and is statistically significant. Hence, we have found evidence of strongly bound kaonic nuclei, whose major decay mode is  $K^-ppn \rightarrow \Sigma NN$ . The binding energy and width are obtained as  $B_K = 165 \pm 4$  MeV and  $\Gamma < 25$  MeV, respectively.

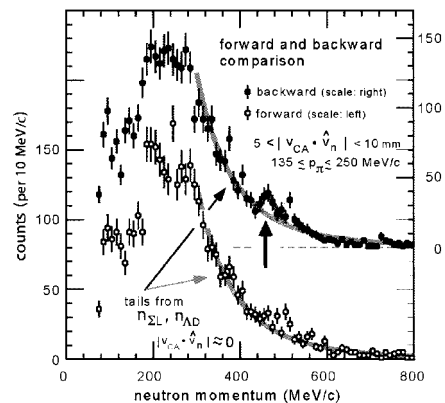


Fig. 1. Neutron spectra from the  ${}^4\text{He}$ (stopped  $K^-, n$ ) reaction in coincidence with backward/forward  $\Sigma$  emission. Arrow indicates the  $K^-ppn$  bound state.

<sup>†</sup> Condensed from the article submitted to Phys. Lett. B; Preprint nucl-ex/0310018

<sup>\*1</sup> Department of Physics, Seoul National University, Korea  
<sup>\*2</sup> Department of Physics, Carnegie Mellon University, USA  
<sup>\*3</sup> Department of Physics, University of Tokyo  
<sup>\*4</sup> Department of Physics, Tokyo Institute of Technology  
<sup>\*5</sup> Institute of Particle and Nuclear Studies, High Energy Accelerator Research Organization (KEK)  
<sup>\*6</sup> GSI, Germany

### References

- 1) M. Iwasaki et al.: Phys. Rev. Lett. **78**, 3067 (1997).
- 2) Y. Akaishi and T. Yamazaki: Phys. Rev. C **65**, 044005 (2002).
- 3) A. Dote et al.: Prog. Theor. Phys. Suppl. **146**, 508 (2003).
- 4) M. Iwasaki et al.: Nucl. Instrum. Methods Phys. Res. A **473**, 286 (2001).

# Experimental signature of in-medium mass modification of vector mesons at normal nuclear density

R. Muto, H. En'yo, M. Naruki,\* F. Sakuma,\* T. Tabaru and S. Yokkaichi, for the KEK-PS E325 Collaboration

[QCD, chiral symmetry, normal nuclear density, mass modification, vector meson]

We measured invariant mass spectra of  $e^+e^-$  pairs produced in 12-GeV p+A interaction to investigate the in-medium mass modification of vector mesons. Modifications of mass spectra, even at normal nuclear density, have been predicted by many theories as a precursor of the QCD chiral phase transition.

The experiment was carried out at the KEK-PS EP1-B beam line. The data gathering ended in March 2002. We already performed event reconstruction for all of the obtained data with refined calibration parameters for drift chambers. We also performed event generation using cascade code JAM<sup>1)</sup> and detailed detector simulation using Geant 4<sup>2)</sup> to analyze the obtained mass spectra.<sup>3)</sup> In these analyses, we used approximately 130,000 cpu-hours of the excellent cpu power of RIKEN CC-J,<sup>4)</sup> which is originally built for the RHIC spin physics.

The invariant mass spectra of  $e^+e^-$  pairs are shown in Fig. 1 for carbon and copper targets. The gray lines are the best-fit results of cocktails of known hadronic sources with a combinatorial background. The significant excess can be seen on the low mass side of the clear peak from decays of  $\omega$  mesons in free space, which is located at  $0.78 \text{ GeV}/c^2$ . The obtained  $\rho/\omega$

ratios from the fit results are statistically consistent with zero for both targets, which is much smaller than the known  $\rho/\omega$  ratio, unity, in p+p interactions in almost the same energy.<sup>5)</sup> This fact implies that most of the  $\rho$  mesons are modified to the lower mass region in nuclear matter.

Next, we examined the velocity and nuclear size dependences of this excess. We divided the data into two groups at  $\beta\gamma = 2.2$  of the mesons. We fitted each spectrum in the same scheme and obtained the abundances of  $\omega$  and the excess. Here, the excess was integrated in the mass region from  $0.5$  to  $0.8 \text{ GeV}/c^2$ . We also considered the mass acceptance of the spectrometer by Monte Carlo calculation. Figure 2 shows the velocity dependence of the ratio of the excess to the  $\omega$  for each target. The excess increases in the lower velocity region and is larger in the heavier target (copper) data than in the lighter target (carbon) data. These tendencies are geometrically and kinematically consistent with a picture of meson-mass modification in a nucleus, since slowly moving mesons in a larger nucleus have a larger probability of decaying inside a nucleus.

We are setting up a model calculation on the basis of a theoretical prediction to reproduce the observed spectrum quantitatively.

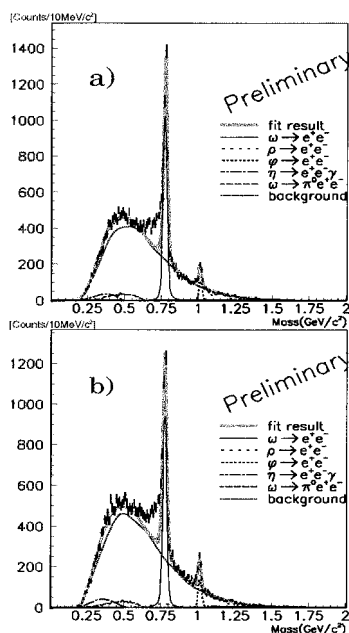


Fig. 1. Invariant mass spectra of the 2002  $e^+e^-$  data. a) is for the carbon target and b) is for the copper target.

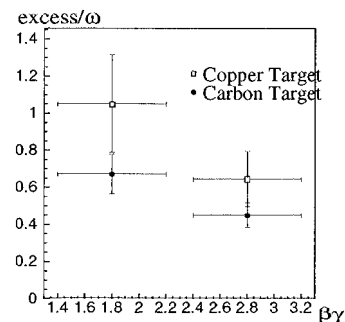


Fig. 2. Velocity and target nucleus dependences of the ratio of the excess to the  $\omega$ . The vertical axis is the ratio, while the horizontal axis is the average  $\beta\gamma$  value.

## References

- 1) <http://quark.phy.bnl.gov/~ynara/jam/>
- 2) <http://wwwasd.web.cern.ch/wwwasd/geant4/geant4.html>
- 3) F. Sakuma et al.: RIKEN Accel. Prog. Rep. **37**, 87 (2004).
- 4) S. Yokkaichi et al.: RIKEN Accel. Prog. Rep. **37**, 257 (2004).
- 5) V. Brobel et al.: Phys. Lett. B **48**, 73 (1974).

\* Department of Physics, Kyoto University

# Nuclear mass number dependence of inclusive $\omega$ and $\phi$ meson production in 12 GeV $p$ -A collisions

T. Tabaru, H. En'yo, R. Muto, M. Naruki, F. Sakuma, and S. Yokkaichi, for the KEK-PS E325 Collaboration

[Mass number dependence, Vector Meson]

It has been theoretically predicted that the vector meson masses could be modified as a consequence of the partial restoration of the chiral symmetry at finite density and/or finite temperature.<sup>1)</sup> We measured the decays of  $\omega \rightarrow e^+e^-$ ,  $\phi \rightarrow e^+e^-$  and  $\phi \rightarrow K^+K^-$  in 12 GeV  $p$ +A interactions. At the low-mass side of the  $\omega$  meson mass (0.55–0.75 GeV/c<sup>2</sup>) we have observed the excess of  $e^+e^-$  pairs in  $p$ -Cu collisions, which could not be explained by the known hadronic sources.<sup>2)</sup>

Since the predicted mass modification depends on nuclear matter density, it is important to understand how the production and decay points are distributed inside a nucleus. We therefore studied the production mechanism of the  $\omega$  and  $\phi$  mesons, by measuring the nuclear mass number dependence ( $\alpha$ ) obtained by the usual parametrization,  $\sigma(A) = \sigma_0 A^\alpha$ , where  $\sigma(A)$  is the cross section and  $A$  is the target mass number.

The experiment was performed using the EP1-B beam line of the 12 GeV proton synchrotron of the High Energy Accelerator Research Organisation (KEK). The 12 GeV proton beam was delivered onto polyethylene (CH<sub>2</sub>), carbon (C) and copper (Cu) targets, and the produced  $e^+e^-$  and  $K^+K^-$  pairs were measured by the newly built spectrometer. The acceptances for  $\phi \rightarrow K^+K^-$  decays covered 0.5–1.5 in the rapidity ( $y$ ) and 0.4–1.6 GeV/c in the transverse momentum ( $p_T$ ), and those for decays of  $\omega \rightarrow e^+e^-$  and  $\phi \rightarrow e^+e^-$  covered 0.3–1.7 in  $y$  and 0–1.1 GeV/c in  $p_T$ .

The kaon ID was performed with the time of flight measured by three types of plastic scintillation counters, the momentum measured by drift chambers, and the hit association by aerogel Čerenkov counters, whose refractive index was 1.034. The electron ID was performed by cascade operation of gas Čerenkov counters using iso-butane with a refractive index of 1.0019 and electromagnetic lead-glass calorimeters. The purity of the final  $K^+K^-$  samples was  $89.8 \pm 2.4\%$ , and that of the final  $e^+e^-$  samples was  $79.5 \pm 0.2\%$ .

The measured invariant mass spectra consisted of correlated pairs from resonance decays and uncorrelated pairs of combinatorial background. We evaluated the background by mixing events. The spectral shapes of the correlated pairs and the spectrometer acceptance were estimated by feeding the result of the nuclear cascade simulation, JAM,<sup>3)</sup> into the detector simulation. By fitting these spectral shapes to the present data, we obtained consistent results for the  $\phi$  produc-

tion cross sections between the decays of  $\phi \rightarrow e^+e^-$  and  $\phi \rightarrow K^+K^-$ , as shown in Fig. 1. We also obtained the  $\omega$  production cross section of  $1.4 \pm 0.6$  mb in  $p$ - $p$  collisions by subtracting the C target data from the CH<sub>2</sub> data, which was consistent with the previous measurement of  $1.80 \pm 0.25$  mb for  $\rho^0$  meson.<sup>4)</sup> It is known that the productions of  $\rho^0$  and  $\omega$  have almost the same cross sections in this energy region.<sup>4)</sup>

From the data of the C and the Cu targets, we obtained the  $\alpha$  of  $0.83 \pm 0.07$  for the  $\omega$  production and that of  $1.1 \pm 0.2$  for the  $\phi$  production measured in the dielectron decay. In the decay of  $\phi \rightarrow K^+K^-$ , we obtained the  $\alpha$  of  $1.01 \pm 0.08$ .

Although JAM overestimates these measured cross sections by factors of 8.93 for  $\omega$  and 2.88 for  $\phi$ , it reproduced the observed  $\alpha$ ,  $y$  and  $p_T$  distributions of these mesons fairly well. By examining the cascade processes in JAM, the large  $\alpha$  values in the present data can be explained by the large contributions of the secondary and tertiary interactions in a nucleus.

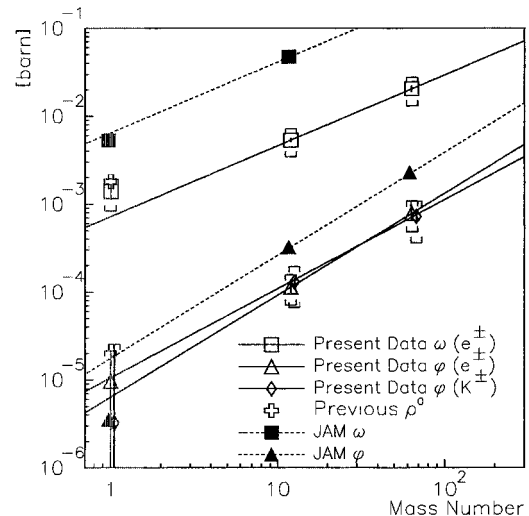


Fig. 1. Meson production cross sections as functions of target mass number.

## References

- 1) T. Hatsuda and S. H. Lee: Phys. Rev. C **46**, R34 (1992).
- 2) K. Ozawa et al.: Phys. Rev. Lett. **86**, 5019 (2001).
- 3) Y. Nara et al.: Phys. Rev. C **61**, 024901 (1999).
- 4) V. Blobel et al.: Phys. Lett. B **48**, 73 (1974).

# Geant4 simulation for the KEK-PS E325 spectrometer

F. Sakuma,\* H. En'yo, M. Naruki,\* R. Muto, T. Tabaru, and S. Yokkaichi, for KEK-PS E325 Collaboration

[Geant4, vector meson, in-medium modification]

We performed an experiment at the KEK proton synchrotron to measure the invariant mass spectra of  $\rho$ ,  $\omega$  and  $\phi$  mesons through their  $e^+e^-$  or  $K^+K^-$  decays in 12 GeV p + A interactions. The data acquisition was completed in March 2002, and we have observed in-medium modification of the  $\rho$  and/or  $\omega$  mesons at normal nuclear-matter density for the first time.<sup>1,2)</sup>

To analyze the obtained mass spectra, we have to evaluate the mass shape from known hadronic sources. The mass shape could be deformed by the detector acceptance and the energy loss effects of electrons flying through the spectrometer. To evaluate such effect, we performed detailed detector simulation using the Geant4 toolkit.<sup>3)</sup> For electrons and positrons, Geant4 provides a realistic simulation of ionization losses, Coulomb multiple scattering and Bremsstrahlung. The list of materials is summarized in Table 1.<sup>4)</sup> All wires in the drift chambers are input one at a time (total of 20,000 wires).

Table 1. List of materials input to the simulation code.

Counter	material	radius [mm]	thickness X [mm]	rad length $X_0$ [mm]	X/ $X_0$ [%]
Target	target (C)	–	1.00	188.5	0.531
	target (Cu)x4	–	0.08x4	14.4	0.556x4
VTC	Ar-C <sub>2</sub> H <sub>6</sub> (50:50)	0.00	245.00	177608.0	0.138
	Wire-inner (Be-Cu) <sup>§</sup>	–	0.018	15.8	0.114
	Wire-inner (Au-W) <sup>§</sup>	–	0.0004	3.5	0.011
	Wire-outer (Be-Cu) <sup>§</sup>	–	0.024	15.8	0.152
	Wire-outer (Au-W) <sup>§</sup>	–	0.0006	3.5	0.017
	Mylar	245.00	0.05	287.4	0.017
	air	245.05	134.95	305225.0	0.044
STC	scintillator	380.00	5.00	424.3	1.178
	lapping	385.00	0.20	287.0	0.070
	air	385.20	14.80	305225.0	0.005
CDC	Mylar	400.00	0.05	287.4	0.017
	Ar-C <sub>2</sub> H <sub>6</sub> (50:50)	400.05	479.95	177608.0	0.270
	Wire (Be-Cu) <sup>§</sup>	–	0.031	15.8	0.196
	Wire (Au-W) <sup>§</sup>	–	0.0005	3.5	0.014
	Mylar	880.00	0.05	287.4	0.017
FGC	air	880.05	19.90	305225.0	0.007
	Mylar	899.95	0.05	287.4	0.017
	isobutane	900.00	660.00	181801.0	0.363
	acrylic mirror	1560.00	3.00	382.7	0.784
BDC	aluminum cover	1563.00	1.00	88.9	1.125
	air	1564.00	5.95	305225.0	0.002
	Mylar	1569.95	0.05	287.4	0.017
	Ar-C <sub>2</sub> H <sub>6</sub> (50:50)	1570.00	80.00	177608.0	0.045
	Wire (Be-Cu) <sup>§</sup>	–	0.010	15.8	0.063
	Wire (Au-W) <sup>§</sup>	–	0.0001	3.5	0.003

<sup>§</sup> X is average of wire thickness through the flight path of particles. However, in the simulation, all wires are input one at a time.

We generated vector mesons from the nuclear cascade code JAM.<sup>5)</sup> Vector mesons decayed to the  $e^+e^-$  or  $K^+K^-$  pair, and this pair is traced in the detector simulator. We obtained the simulated hit data smeared with the measured chamber resolution, and analyzed them using the source code used to analyze read data. Figure 1 shows the  $e^+e^-$  pair trajectory from  $\omega$  meson decay in the E325 spectrometer.

The invariant mass resolution of  $6.1 \pm 0.3 \text{ MeV}/c^2$  is obtained in the  $\omega \rightarrow e^+e^-$  decay from the detector simulation. This result reproduces the real resolution of approximately  $7.4 \pm 0.5 \text{ MeV}/c^2$ . With this realistic simulation, we have confirmed the observed excess, which is expected as a consequence of in-medium modification and which, cannot be explained by any trivial detector effects. The observed excess is at least 40% of the  $\omega$ -peak yield<sup>6)</sup> while the detector effect is 10% at most.

To expedite the analysis, we have used CC-J at RIKEN. We would like to thank the members of the Radiation Laboratory for their support.

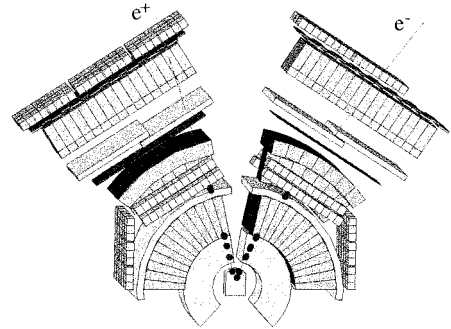


Fig. 1.  $e^+e^-$  pair trajectory from  $\omega$  meson decay in E325 spectrometer.

## References

- 1) K. Ozawa et al.: Phys. Rev. Lett. **86**, 5019 (2001).
- 2) M. Naruki et al.: Nucl. Phys. A **721**, 297 (2003).
- 3) <http://geant4.web.cern.ch/geant4/>
- 4) M. Sekimoto et al.: Nucl. Instrum. Methods Phys. Res. A **516**, 390 (2004).
- 5) Y. Nara et al.: Phys. Rev. C **61**, 024901 (1999).  
<http://quark.phy.bnl.gov/ynara/jam/>
- 6) R. Muto et al.: RIKEN Accel. Prog. Rep. **37**, 85 (2004).

\* Department of Physics, Kyoto University



## Response of the HXD-II detector to cosmic heavy ions

M. Kawaharada,<sup>\*1</sup> M. Kokubun,<sup>\*1</sup> K. Makishima, S. Hong, Y. Terada, H. Miyasaka,<sup>\*2</sup> K. Yamaoka,<sup>\*3</sup>  
M. Ohno,<sup>\*4</sup> Y. Fukazawa,<sup>\*4</sup> H. Inoue,<sup>\*5</sup> and T. Takahashi<sup>\*5</sup>

[Iron ion, BGO, HXD-II]

The Hard X-ray Detector (HXD-II) is one of the instruments onboard the *Astro-E2* satellite, scheduled for launch in February 2005. The HXD-II probes the universe in the energy range of 10–600 keV with a sensitivity an order of magnitude better than those of previous missions.<sup>1)</sup> The HXD-II consists of well-type  $4 \times 4$  GSO( $\text{Gd}_2\text{SiO}_5:\text{Ce}$ )/BGO( $\text{Bi}_4\text{Ge}_3\text{O}_{12}$ ) phoswich counters called ‘Well-counter units’, each of which works independently as an extremely low background hard X-ray detector. The counters form an anticoincidence system, and are further surrounded by 20 pillar-shaped BGO counters called ‘Anti-counter units’.

In orbit, the HXD-II is exposed to various cosmic rays. The dominant components of these rays are protons and helium ions of which the count rate is  $\sim 100$  Hz per unit, and the energy deposit is  $\sim 100$  MeV. Although heavier ions are rare,  $\sim 0.01$  Hz, they could deposit up to  $\sim \text{GeV}$  *via* minimum ionization. The HXD-II has been designed and developed by fully taking these large frequent signals into account.<sup>2,3)</sup>

On November 17–18 2002, we carried out a ground experiment at the E3 beamline of the RIKEN ring cyclotron as shown in Fig. 1. The objectives of the experiment were 1) examining the precise shape and amount of the BGO scintillation activated by heavy ions, 2) the effect of secondary particles on a Well-counter unit when heavy ions hit surrounding units, and 3) confirming the response of the Well-counter unit and the flight-compatible analog electronics to real heavy ions. For these purposes, we accelerated  $^{56}\text{Fe}$  ions to  $\sim 90$  MeV/nucleon, at a rate of 3–4 Hz so that individual pulses could be examined. The ioniza-

tion loss of these ions in BGO is  $\sim 20$  GeV/cm, and a total kinetic energy of 5 GeV is deposited in  $\ll 1$  cm. Therefore, we can simulate the energy delivered by minimum-ionizing heavy nuclei in the orbit.

Firstly, we attached a BGO block ( $2 \times 2 \times 2 \text{ cm}^3$ ) on one end of an acrylic light guide ( $5 \text{ cm} \times 20 \text{ cm} \times 5 \text{ mm}$ ), which was glued to a flight-compatible PMT to prevent it from being exposed to the ion beam. The measured pulse heights of the  $^{56}\text{Fe}$  events are 0.7 V at a high voltage of  $-1000$  V, and 1.9 V at  $-1200$  V. To investigate detailed structures in the pulses, we magnified and averaged the anode output at  $-1200$  V. Over a time range of 2.5–7.5  $\mu\text{s}$ , no particular deviation from a smooth waveform, such as ringing, was observed. This implies that the BGO crystal itself behaves normally for heavy ions, just like for  $\gamma$  rays but with a much larger output. Referring to calibration isotopes, we determined that the BGO scintillation for the 90 MeV/nucleon  $^{56}\text{Fe}$  ion is equivalent to  $\sim 500$  MeV in terms of  $\gamma$ -ray response. In other words, the quenching factor is  $\sim 0.1$ .

Secondly, we placed a Well-counter unit behind an Anti-counter unit, and irradiated them with the  $^{56}\text{Fe}$  beam through a plastic scintillator used for triggers. We set an oscilloscope so that it triggered on the coincidence between the plastic scintillator output and the leading edge of the Well-counter output. We actually observed simultaneous events with various anode output pulse heights, ranging from 60 to 500 mV. These events were scintillations of secondary particles created in the Anti-counter unit. If we assume that they are protons and their quenching factor is the same as that of heavy ions, namely 0.1, their typical kinetic energy is estimated as  $\sim 60$  MeV. Correcting this value for the energy loss in the  $\sim 4$ -cm-thick BGO of the Anti-counter unit, we estimate their initial energy to be  $\sim 170$  MeV. Therefore, each ion in the beam is inferred to produce a few tens secondary particles when hitting an Anti-counter.

Finally, we irradiated the ion beam to the Well-counter unit at the supplied voltage of 900 V. The anode output was observed to clamp at 3 V, while the Well amplifier output saturated at 4.3 V with an overshoot level of 2.4 V. These results confirm the designed responses of the Well-counter unit to large pulses.

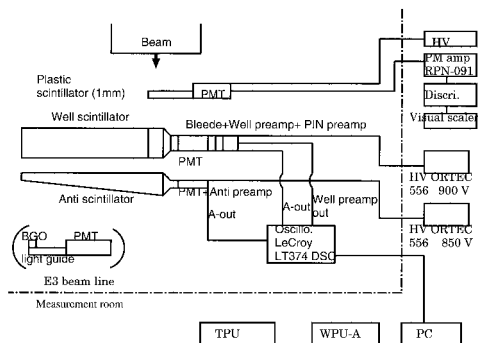


Fig. 1. Experimental setup in the E3 beamline.

<sup>\*1</sup> University of Tokyo

<sup>\*2</sup> University of Delaware, USA

<sup>\*3</sup> Aoyama Gakuin University

<sup>\*4</sup> Hiroshima University

<sup>\*5</sup> Japan Aerospace Exploration Agency (JAXA)

### References

- 1) T. Kamae et al.: Proc. SPIE **2806**, 314 (1996).
- 2) T. Takahashi et al.: Proc. SPIE **3445**, 155 (1998).
- 3) C. Tanihata et al.: Proc. SPIE **3765**, 645 (1999).

# Dimuon measurement in the NA60 experiment at CERN/SPS

H. Ohnishi, for the NA60 Collaboration

[High-energy heavy-ion collisions, Quark Gluon Plasma]

The NA60 experiment<sup>1)</sup> measures the  $J/\psi$  suppression pattern in high-energy In-In collisions at CERN Super Proton Synchrotron (SPS). Comparing the pattern measured in this new experiment to the pattern measured in Pb-Pb collisions,<sup>2)</sup> we should be able to determine the critical scale for the onset of deconfined parton condensation, and distinguish between a parton percolation transition that should occur as a function of the number of nucleons participating in the collision, and a thermal transition that should depend on the reached local energy density. Moreover, NA60 is designed to measure muons arising from positions displaced with respect to the primary collision vertex, thereby identifying open charm meson decays and allowing the first clear measurement of the open charm production cross section in heavy-ion collisions. The complementary analysis extracts a clean sample of prompt intermediate mass dimuons, where thermal dimuons can be searched.<sup>3)</sup> The NA60 experiment comprises a muon spectrometer and Zero degree calorimeter (ZDC) previously used in the NA50 experiment with a new detector, a silicon pixel vertex telescope, placed in the target region. The details can be found elsewhere.<sup>1)</sup> The silicon pixel vertex telescope consists of eight 4-chip pixel planes followed by 4 large tracking stations, which are made from two 8-chip pixel planes. The readout chips were developed for the ALICE and LHC-B experiments<sup>4)</sup> and are radiation tolerance up to 30 Mrad. Each pixel chip is bump-bonded to a  $300\ \mu\text{m}$  thick silicon sensor which contains a matrix of  $32 \times 256$  pixels of  $50 \times 425\ \mu\text{m}^2$  size.

In June 2002, NA60 was first used to collect physics data taking using a  $400\ \text{GeV}/c$  proton beam incident on Be, In and Pb targets. The reconstructed dimuon mass distribution after matching the muon from the muon spectrometer with the charged tracks in the vertex telescope is shown in Fig. 1. The mass resolution is found to be approximately 25 and 30 MeV for the  $\omega$  and  $\phi$  peaks, respectively. Furthermore, as seen in Fig. 1, the acceptance for the low-mass dimuon pairs is extended down to very low  $p_T$  which allows us to explore the window of low mass dileptons where the CERES collaboration observed a strong anomalous excess of low-mass electron pairs.<sup>5)</sup> These results confirmed the feasibility of the experiment and gave a good outlook for the subsequent runs with proton and Indium beams.

In the physics run in October 2003, we collected the first data of heavy-ion collisions induced by indium

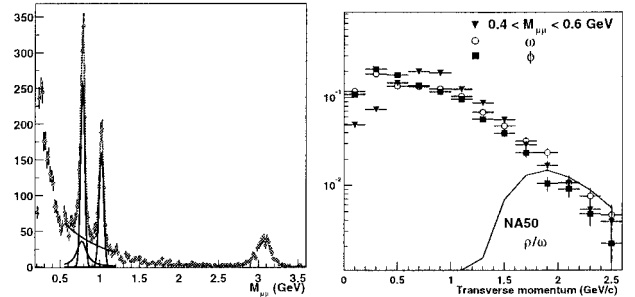


Fig. 1. Left figure shows, dimuon mass distribution for p-Pb collisions; Right figure shows  $p_T$  distributions measured in different mass windows.

ions on  $158\ \text{GeV}/c$  per nucleon on indium targets. Figure 2 shows a typical In-In collision event reconstructed with the NA60 vertex telescope. This figure illustrates that the NA60 vertex telescope was operating well during the heavy-ion data collection period. The analysis of the data is in progress, to answer the question whether quark gluon plasma formed in the matter created by heavy-ion collisions at CERN SPS.

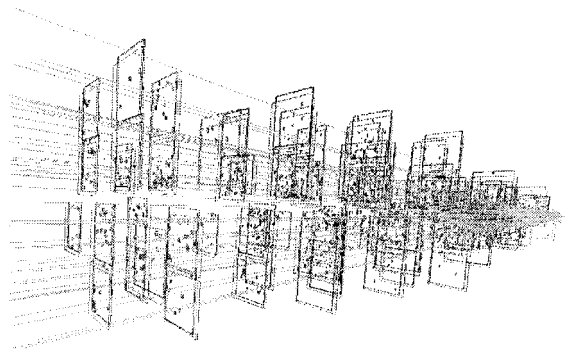


Fig. 2. Tracking of charged particles produced in one Indium-Indium collision and traversing the silicon pixel telescope.

## References

- 1) NA60 Collaboration: CERN/SPSC 2000-010, March 2000.
- 2) M. C. Abreu et al.: Phys. Lett. B **447**, 28 (2000).
- 3) R. Rapp and E. Shuryak: Phys. Lett. B **473**, 13 (2000).
- 4) W. Snoeys et al.: Nucl. Instrum. Methods Phys. Res. A **465**, 176 (2001); K. Wyllie et al.: Proc. 5th Workshop on Electronics for LHC Experiments, Snowmass, USA, 1999-9 (CERN, 1999), p. 93.
- 5) G. Agakishiev et al.: Phys. Lett. B **422**, 405 (1998).

# First measurement of muon transfer reactions with argon ions implanted in solid deuterium films

P. Strasser, K. Nagamine,\* T. Matsuzaki, K. Ishida, Y. Matsuda, K. Itahashi, and M. Iwasaki

[Muonic atom spectroscopy, Solid hydrogen film, Ion implantation]

Muonic atom spectroscopy<sup>1)</sup> has for many years played an important role in establishing and refining nuclear structure models, and has been successfully used to study stable nuclei. Muonic X-ray measurements can yield very precise and absolute values for the charge radii and other ground-state properties. We proposed the cold (solid) hydrogen film method<sup>2)</sup> to extend muonic atom spectroscopy to the use of nuclear beams, including in the future RI beams, and to produce radioactive muonic atoms. This method would allow studies of unstable nuclei by means of the muonic X-ray method at facilities where both intense  $\mu^-$  and RI beams would be available. The basic concept is to stop both beams simultaneously in a solid hydrogen ( $H_2/D_2$ ) film, followed by the direct muon transfer reaction to higher  $Z$  nuclei to form radioactive muonic atoms. An experimental program has been initiated at the RIKEN-RAL muon facility to experimentally establish the feasibility of this method.<sup>3)</sup> An experimental setup ( $\mu A^*$ ) was constructed to implant stable ions in solid hydrogen films.<sup>4)</sup> The first results with implanted argon ions have recently been obtained.

Two different target configurations were investigated. At first, a two-layer arrangement was used. The primary layer made of 0.5-mm  $H_2/D_2$  is used to efficiently stop 27 MeV/c  $\mu^-$  followed by  $p\mu$  formation,  $p\mu$  to  $d\mu$  transfer and  $d\mu$  emission with the help of the Ramsauer-Townsend effect in the diffusion of the  $d\mu$  atoms, while the second layer made of pure  $D_2$  (several  $\mu m$  thick) with implanted Ar ions is used to confine the production region of muonic argon ( $\mu Ar$ ) atoms to an optimized film thickness. This scheme would require a smaller amount of implanted ions. The germanium energy spectra shown in Fig. 1(a) very clearly indicates  $\mu Ar$   $2p \rightarrow 1s$  transition X-rays at 644 keV from

the muon transfer reaction. Approximately  $10^{16}$  Ar ions per  $cm^2$  were implanted in a  $D_2$  thickness of  $5 \mu m$  using alternate implantation and  $D_2$  deposition, which corresponded to an average concentration of 500 ppm. At this concentration, all  $d\mu$  atoms emitted from the primary  $H_2/D_2$  layer are expected to transfer very rapidly. Only “short” delayed events are observed, mainly due to the diffusion time of the  $d\mu$  atoms before reaching the added  $D_2$  layer. The triangular peaks observed at 596 keV and 691 keV result from inelastic neutron excitation of the Ge isotope nuclei within the detector itself.<sup>5)</sup> The neutrons are produced following  $\mu^-$  capture on nuclei.

Later, a pure  $D_2$  layer was used, and each Ar implantation was separated from the next by depositing about  $20 \mu m$  of  $D_2$  to make a total  $D_2$  layer thickness of 0.5 mm. Each implantation region had a thickness of only  $0.1 \mu m$  with a local concentration of 1000 ppm. The average Ar concentration throughout the  $D_2$  layer was around 5 ppm, corresponding to approximately the same amount as used in the previous target. Figure 1(b) clearly shows that even with an inhomogeneous target, very strong muon transfer events can be detected. Due to the strong reduction of the Bragg cross section at low  $d\mu$  collision energies in solid  $D_2$ ,<sup>6)</sup> the  $d\mu$  atom mean free path is strongly increased to nearly 10–20  $\mu m$  below  $\sim 1$  meV, resulting in a high  $d\mu$  atom mobility and a very long diffusion length. Preliminary analysis shows that the 644 keV X-ray disappearance rate is consistent with an average Ar concentration of 5 ppm. At this concentration, most of the muon transfer is delayed, and the S/N ratio can be greatly improved by selecting only delayed events.

This first test experiment was performed with a large amount of implanted Ar ions. Further measurements are planned with reduced Ar concentrations to study the muon transfer reaction and investigate the diffusion process of  $d\mu$  atoms in solid. This effect will limit the minimum layer thickness that can be used in the two-layer arrangement without being affected by  $d\mu$  atom loss.

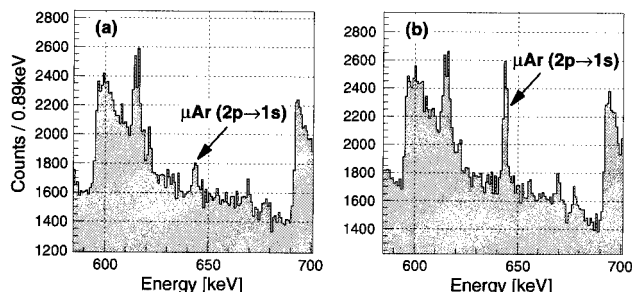


Fig. 1. Total energy spectra measured with (a) 0.5-mm  $H_2/D_2 \oplus 7\text{-}\mu m D_2(Ar)$ , and (b) 0.5-mm  $D_2(Ar)$ .

\* Meson Science Laboratory, High Energy Accelerator Research Organization (KEK)

## References

- 1) L. Schaller: *Z. Phys. C* **56**, S48 (1992).
- 2) P. Strasser et al.: *Hyperfine Interact.* **119**, 317 (1999).
- 3) P. Strasser et al.: *Nucl. Phys. A* **722**, 523c (2003).
- 4) P. Strasser et al.: *Nucl. Instrum. Methods Phys. Res. A* **460**, 451 (2001).
- 5) E. Gete et al.: *Nucl. Instrum. Methods Phys. Res. A* **388**, 212 (1997).
- 6) A. Adamczak: *Hyperfine Interact.* **119**, 23 (1999).

# Measurement of the magnetic field effect in muon catalyzed fusion

K. Ishida, T. Matsuzaki, M. Iwasaki, Y. Matsuda, K. Nagamine,<sup>\*1</sup> N. Kawamura,<sup>\*1</sup> H. Imao,<sup>\*2</sup>  
M. Kato,<sup>\*3</sup> H. Sugai,<sup>\*3</sup> M. Tanase,<sup>\*3</sup> and G. H. Eaton<sup>\*4</sup>

[Muon catalyzed fusion]

Muon catalyzed fusion ( $\mu$ CF) has been studied under a variety of D/T target conditions since the start of the RIKEN-RAL  $\mu$ CF experiment in 1995. One of the main interests in the study of  $\mu$ CF is the improvement of energy production efficiency, which can be achieved by larger  $\lambda_c$  (cycling rate of  $\mu$ CF process) and smaller  $W$  (muon loss per cycle). However, there are some experimental conditions whose effect on  $\mu$ CF has not been studied sufficiently, and the magnetic field is one of them. While  $\mu$ CF experiments at PSI, LAMPF and Dubna were mostly carried out without a magnetic field,  $\mu$ CF experiments at RIKEN-RAL were all carried out under a strong magnetic field of 2.4 T only, because this is the field where the muon beam is best focussed to the D/T target which has a size of only 1 cm<sup>3</sup>.

Theoretically, it is not common to presume that the magnetic field would affect the reactions of muonic atoms, since the magnetic field effect on the energy level is very small compared with the energy scale of the muonic atoms. However, there were several theoretical investigations predicting the possible magnetic field effect on the muon-to-alpha sticking, which is the main source of muon loss in  $\mu$ CF.

Melezhik and Schmelcher proposed<sup>1)</sup> that a magnetic field would stimulate transitions between the  $lm$  sublevels of a moving  $(\alpha\mu)^+$  ion formed by muon-to-alpha sticking. The field-stimulated transitions can compete with other processes such as muon stripping from the  $(\alpha\mu)^+$  ion and may change the effective sticking probability. Another calculation indicates the magnetic field effect on the muon-to-alpha sticking through the contribution of convoy muons.<sup>2)</sup> There can be, although with a small probability ( $\sim 0.5\%$ ), a convoy muon produced after fusion, which moves slightly ahead of the alpha particle but is not initially captured. The alpha particles may finally catch up with some of the convoy muons and result in sticking. A magnetic field reduces the probability of recombination of muon and alpha particles by separating the tracks of oppositely charged particles. Thus it is important to study experimentally whether there is any indication of the magnetic field effect to test these predictions.

The experiment was performed under four magnetic

fields (0, 1.2, 2.4 and 3.3 T) for liquid D/T with a tritium concentration of 30%. Fusion neutrons and various muonic X-rays were detected while the number of stopping muons were determined by counting the muon-decay electrons. The result is summarized in Fig. 1.

As expected, the muon stopping rate was significantly reduced at 0 and 1.2 T compared with that at 2.4 T. Even with this large difference in measurement conditions, the cycling rate and the muon loss probability, which is mainly due to the muon-to-alpha sticking, were almost independent of the field within  $\pm 5\%$  for the liquid D/T.  $K_\alpha$  X-ray yield slightly increased with magnetic field by 30% ( $2.5\sigma$ ). The result is opposite to that predicted based on convoy effect,<sup>2)</sup> of decreasing muon-to-alpha sticking and X-ray yield as magnetic field is increased. On the other hand, the stimulated transition<sup>1)</sup> enhances 2s-2p mixing in  $(\alpha\mu)^+$  and increases the  $K_\alpha$  emission and thus it is consistent with, or at least does not contradict, our result. In order to further confirm the magnetic field effect on  $\mu$ CF and its dependence on the target condition, measurement of the magnetic field effect in solid D/T is in progress.

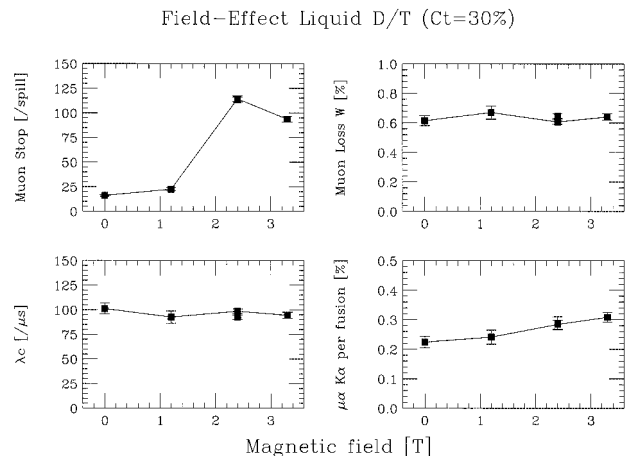


Fig. 1. Preliminary result on field dependence of the number of muons stopped in liquid D/T target,  $\mu$ CF cycling rate ( $\lambda_c$ ), muon loss per cycle ( $W$ ), and the amount of  $\alpha\mu$   $K_\alpha$  X-ray per fusion.

<sup>\*1</sup> Meson Science Laboratory, Institute of Materials Structure Science, High Energy Accelerator Research Organization (KEK)

<sup>\*2</sup> Department of Physics, University of Tokyo

<sup>\*3</sup> Tokai Research Establishment, Japan Atomic Energy Research Institute

<sup>\*4</sup> Rutherford Appleton Laboratory, UK

## References

- 1) V. S. Melezhik and P. Schmelcher: Phys. Rev. A **59**, 4264 (1999).
- 2) B. Muller, H. E. Rafelski, and J. Rafelski: Phys. Rev. A **40**, 2839 (1989).

# SF<sub>6</sub> dielectric molecules: Electron and positron scattering dynamic properties and possible applications

C. Makochekanwa\* and M. Kimura

SF<sub>6</sub>, sulfur hexafluoride, is a man-made gas, and is presently one of the most widely and extensively used gases for commercial and research applications.<sup>1)</sup> Therefore, its various physical and chemical properties, and dynamical behavior under various application conditions have been broadly studied. However, it is also now known as one of the most serious greenhouse gases since it is an efficient absorber of infrared radiation at wavelengths near 10.5  $\mu\text{m}$ , and is solidly stable in chemical and photolytic reactions and hence, remains permanently once released in air. Hence, concerns over its environmental impact have newly generated interest for performing a more comprehensive study of this gas. Accordingly, we have undertaken a comparative study of electron and positron scattering from this molecule from 0.6 eV to 1000 eV. By investigating electron and positron scattering comparatively, more detailed underlying physics of spectroscopic and dynamical aspects is expected to emerge and also critical evaluation of electron scattering cross-section data becomes possible.

Earlier studies on dynamical aspects of this molecule include, total cross-section measurements by electron and positron impact by Dabaneh *et al.*,<sup>2)</sup> and swarm experiments by Christophorou *et al.*<sup>1)</sup> Phelps and Van Brunt have compiled all available data of electron impact, and published a complete set of cross-section data for a wide range of energy from 1 meV to 1 keV.<sup>3)</sup>

Although agreement between the present results and earlier ones reported by Dabaneh *et al.* on both electron and positron scattering cross sections for SF<sub>6</sub> is found to be good, this study covers more extended impact energies, compared to those of Ref. 2.

Total cross-section measurements for 0.4–1000 eV by electron and 0.2–1000 eV by positron impacts were performed using an absorption type time-of-flight apparatus as in our previous works.<sup>4)</sup> The present results for total cross sections (TCSs) and elastic cross sections (ECSs) are shown for electron and positron impact in Fig. 1(a) and (b), respectively. The result of elastic cross section was obtained theoretically by using the continuum multiple-scattering (CMS) method.<sup>5)</sup>

## References

- 1) L. G. Christophorou, J. K. Olthoff, and D. S. Green: National Institute of Standards and Technology (NIST) Technical Note **1425**, 1 (1997).
- 2) M. S. Dabaneh, Y.-F. Hsieh, W. E. Kauppila, C. K. Kwan, S. J. Smith, T. S. Stein, and M. N. Uddin: *Phys. Rev. A* **38**, 1207 (1988).
- 3) A. V. Phelps and R. J. Van Brunt: *J. Appl. Phys.* **64**, 4269 (1988).
- 4) O. Sueoka, S. Mori, and A. Hamada: *J. Phys. B* **27**, 1453 (1994).
- 5) M. Kimura and H. Sato: *Comments At. Mol. Phys.* **26**, 333 (1991).

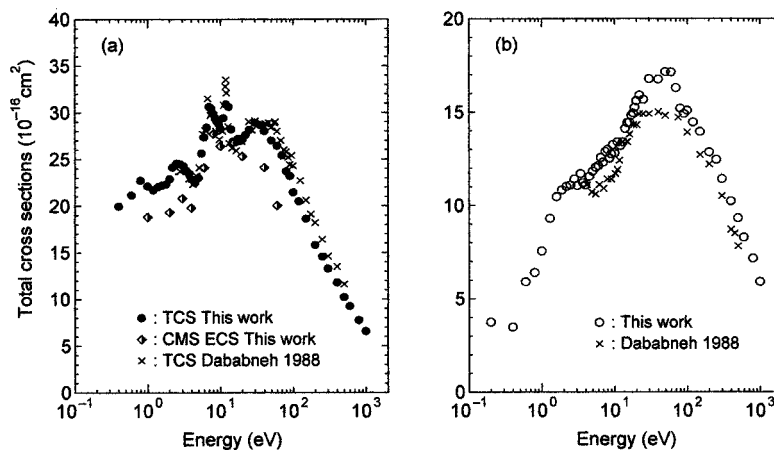


Fig. 1. SF<sub>6</sub> total cross sections for (a) electron and (b) positron scattering.

\* Graduate School of Science and Engineering, Yamaguchi University

# H<sup>+</sup> + CH<sub>2</sub> collisions below the 1.5 keV regime

H. Suno,<sup>\*1</sup> M. Kimura,<sup>\*1</sup> R. J. Buenker,<sup>\*2</sup> A. Watanabe,<sup>\*3</sup> and I. Shimamura

Electron capture in collisions of ions with atoms in the low-keV-energy regions is one of the most important processes in experimental and theoretical atomic physics as well as in applications to astrophysics and fusion research. Relatively comprehensive studies have been carried out for a variety of atomic targets and various charged projectiles in a wide range of collision energies (meV to keV), but those for molecular targets are still scarce, both experimentally and theoretically.

This report concerns a rigorous theoretical investigation of the electron capture process in the collision of H<sup>+</sup> ions with CH<sub>2</sub> molecules in the region below a few keV. This hydrocarbon molecule, CH<sub>2</sub>, exist in various atmospheric and astrophysical environments. It also plays a key role in various molecular reactions involving carbon atoms in the universe. We consider four different scattering conditions for collision dynamics: (i) the proton approaches the C atom along the bisector of the H-C-H bond angle, passing the midpoint of the H-H line; (ii) it travels along the same line as in (i), but in the opposite direction; (iii) the proton approaches the C atom in the H-C-H plane and perpendicularly to the bisector of the H-C-H bond angle; (iv) the proton approaches the C atom perpendicularly to the H-C-H plane.

The adiabatic potential-energy curves are calculated by the multireference single- and double-excitation configuration-interaction (MRD-CI) method,<sup>1,2</sup> with configuration selection and energy extrapolation employing the Table-CI algorithm.<sup>3</sup> The *ab initio* calculations are performed for each of the four configurations mentioned above. Scattering dynamics is studied on the basis of the fully quantum formulation of a molecular-orbital expansion method. The total scattering wave function is described in an adiabatic representation as an expansion in products of electronic and nuclear wave functions and the electron translation factor. Substitution of the total scattering wave function into the stationary Schrödinger equation and transformation to the diabatic representation<sup>4</sup> yield the coupled equations

$$\left[ \frac{1}{2\mu} \Delta_{RI} - V^d(R) + EI \right] X^d(R) = 0, \quad (1)$$

where  $k = (2\mu E)^{1/2}$  is the momentum of the projectile,  $\mu$  the reduced mass of the system,  $I$  the identity matrix,  $V^d$  the diabatic potential-energy matrix, and  $X^d(R)$  the nuclear wave function in the diabatic representation. The coupled equations (1) are solved nu-

merically to obtain the scattering  $S^l$  matrix for each partial wave  $l$ .<sup>5</sup> The differential cross section is then given by

$$\frac{d\sigma(\theta)}{d\Omega} = \frac{1}{4k^2} \left[ \sum_l (2l+1) \{ \delta_{if} - S_{if}^l \} P_l(\cos\theta) \right]^2, \quad (2)$$

where  $\theta$  is the scattering angle in the center of mass coordinates.

The differential cross sections for electron capture are shown in Fig. 1 for all four molecular configurations (i)–(iv), for scattering angles of 0°–180° at 1.5 keV. For all cases, the differential cross sections oscillate rapidly when  $\theta \leq 5^\circ$ , while they are all relatively smooth when  $5^\circ \leq \theta \leq 25^\circ$ . We noted that the magnitude of the differential cross section for case (i) is nearly the same as that for case (ii) in the region  $\theta \leq 30^\circ$ . For all cases, oscillatory structures are present when  $\theta \geq 30^\circ$ .

In conclusion, the dependences on the molecular orientation—The steric effects—are conspicuous in H<sup>+</sup> + CH<sub>2</sub> collisions.

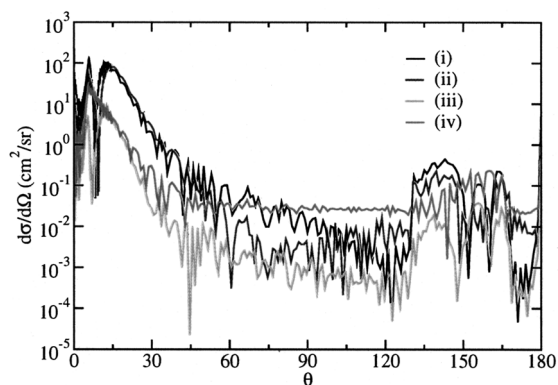


Fig. 1. Differential cross sections for electron capture for the four molecular configurations (described in the text) at 1.5 keV.

## References

- 1) R. J. Buenker and S. D. Peyrimhoff: *Theor. Chim. Acta* **35**, 33 (1974).
- 2) R. J. Buenker: *Int. J. Quantum Chem.* **29**, 435 (1986).
- 3) R. J. Buenker: *Proc. Workshop on Quantum Chemistry and Molecular Physics*, Wollongong, Australia, edited by P. Burton (University Press, Wollongong, 1980).
- 4) M. Kimura and N. F. Lane: *Adv. At. Mol. Opt. Phys.* **26**, 79 (1989).
- 5) B. H. Bransden: *Atomic Collision Theory* (Benjamin, New York, 1983).

<sup>\*1</sup> Faculty of Engineering, Yamaguchi University

<sup>\*2</sup> Theoretische Chemie, Bergische Universität-Gesamthochschule Wuppertal, Germany

<sup>\*3</sup> Faculty of Science, Ochanomizu University

# Resonant coherent excitation of 2s electron of Li-like Fe and Ni ions

T. Ikeda, Y. Nakai, Y. Kanai, T. Kambara, N. Fukunishi, T. Azuma,<sup>\*1</sup> K. Komaki,<sup>\*2</sup>  
C. Kondo,<sup>\*2</sup> and Y. Yamazaki

When the energy difference between two levels of ion channeling through a crystal agrees with the energy of a “virtual-photon” of the periodic crystal field, the ion is resonantly excited. This is referred to as the “resonant coherent excitation (RCE)”. In the case of ion channeling in the (220) plane of a Si crystal, the transition energy,  $E_{trans}$ , is given by the equations  $k \cos \theta/a + l \sin \theta/(a/\sqrt{2}) = E_{trans}/hc\gamma\beta$  in the case that  $\theta$  is the angle between the incident beam and the [001] axis and  $k \cos \theta/(a/\sqrt{2}) + l \sin \theta/a = E_{trans}/hc\gamma\beta$  in the case that  $\theta$  is the angle between the incident beam and the [110] axis. Here,  $k$  and  $l$  are integers,  $a$  is the lattice constant,  $c\beta$  is the ion velocity,  $\gamma = 1/\sqrt{1-\beta^2}$ , and  $h$  is the Planck constant. Many RCE experiments have been performed but no RCE experiments on the outer-shell electrons of systems with three or more electrons have been reported to the best of our knowledge. Azuma and coworkers have found that resonances are quite sharp in a series of RCE experiments using the planar-channeling of relativistic H-like and He-like heavy ions.<sup>1-4</sup> Therefore, we can expect a sharp resonance structure also for the RCE of a 2s electron of Li-like heavy ions.

We measured the 2s electron RCE at the  $n = 3$  states of 83 MeV/u Fe<sup>23+</sup> and 72 MeV/u Ni<sup>25+</sup> ions. The experimental setup was described in other reports.<sup>5,6</sup> A 7- $\mu\text{m}$ -thick Si (001) crystal was vertically mounted so that the beam direction was near the [001] axis for Fe<sup>23+</sup> and this crystal foil was 45° inclined so that the beam direction was near the [110] axis for Ni<sup>25+</sup>. The ions emerging from the crystal were deflected by an analyzing magnet downstream of the Si target in order to separate the final charge states. A two-dimensional position-sensitive detector (2D-PSD) was located 8 m downstream of the analyzing magnet, which detected Li-like, He-like, H-like and bare ions.

Electrons in the excited state are much more easily stripped in the crystal target than those in the ground state. Therefore, the fraction of surviving Li-like ions,  $f(\text{Li-like}) = N(\text{Li-like})/[N(\text{Li-like}) + N(\text{He-like}) + N(\text{H-like}) + N(\text{bare})]$ , should decrease when the Li-like ions are resonantly excited, where  $N$  is the number of Li-like, He-like, H-like and bare ions emerging from the crystal. The survival fraction  $f(\text{Li-like})$  was measured as a function of rotation angle  $\theta$ . Figure 1 shows  $f(\text{Li-like})$  for Ni<sup>25+</sup> under the resonance condition of  $(k, l) = (1, 1)$ , where  $\theta$  is the angle from the [110] axis. Five resonance dips can be observed. For Fe<sup>23+</sup>, a similar resonance dip structure was also obtained.

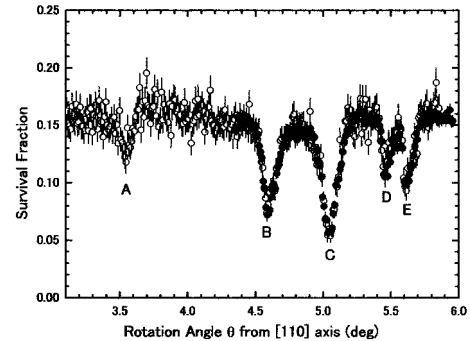


Fig. 1. Survival fraction  $f(\text{Li-like})$  for 72 MeV/u Ni<sup>25+</sup> under the resonance condition of  $(k, l) = (1, 1)$ . Open circles and solid circles correspond to different experimental runs.

By comparing the transition energy of each dip with spectroscopic data, we assigned dip A to the transition from  $2s_{1/2}$  to  $3s_{1/2}$ , dip B from  $2s_{1/2}$  to  $3p_{1/2}$ , dip C from  $2s_{1/2}$  to  $3p_{3/2}$ , dip D from  $2s_{1/2}$  to  $3d_{3/2}$  and dip E from  $2s_{1/2}$  to  $3d_{5/2}$ . Surprisingly, the resonance dips corresponding to optically forbidden transitions (dip-A, dip-D and dip-E) can be observed as well as optically allowed transitions (dip-B and dip-C). Here, an optically allowed transition denotes the E1 transition and an optically forbidden transition is any other transition. We are considering two possible reasons for the observation of the optically forbidden transitions: (1) The transitions from the 2s state to the 3s and 3d states become less and less optically forbidden as the distance from the channel center increases, due to E1 transition *via* the 3p component in the Stark-mixed 3s and 3d states. (2) In the crystal periodic field, transitions with a large momentum transfer become more important. It is thought that transitions with a large momentum transfer occur far from the channel center. Therefore purely optically forbidden transitions become more important with increasing distance from the channel center.

## References

- 1) T. Azuma et al.: Phys. Rev. Lett. **83**, 528 (1999).
- 2) T. Azuma: Phys. Scr. T **80**, 79 (1999).
- 3) T. Azuma et al.: Phys. Scr. T **92**, 61 (2001).
- 4) K. Komaki et al.: Nucl. Instrum. Methods Phys. Res. B **146**, 19 (1998).
- 5) Y. Nakai et al.: RIKEN Accel. Prog. Rep. **36**, 96 (2003).
- 6) Y. Nakai et al.: Nucl. Instrum. Methods Phys. Res. B **205**, 784 (2003).

<sup>\*1</sup> Department of Physics, Tokyo Metropolitan University

<sup>\*2</sup> Institute of Physics, University of Tokyo

## Elastic wave from fast Xe-ion irradiation on solids

T. Kambara, Y. Kanai, T. M. Kojima, Y. Nakai, Y. Yamazaki, A. Yoneda, and K. Kageyama\*

When a fast heavy ion passes through a solid, it deposits its kinetic energy through electronic excitations which may result in temporary or permanent atomic displacements in the lattice. Such atomic displacements, besides thermal expansion, can generate stress and strain along the ion path inside the bulk. On the other hand, the ion irradiation might result in the ejection of atoms or molecules from the surface to vacuum, and the recoil of the ejection stresses the surface. In either case, the stress and strain generated by the irradiation propagate in the bulk as elastic waves, which can be detected by ultrasonic sensors at a distance of more than 30 mm. The source of the stress can be located by precise measurements of the propagation time of the elastic waves.

We have performed such seismological analyses of irradiation effects by fast heavy ions on solids at the RIKEN Ring Cyclotron. Solid targets were irradiated with single-bunch heavy-ion beams, and waveforms from piezoelectric ultrasonic sensors were observed with an oscilloscope. Results with a 3.8 GeV Ar beam on various solids have been reported previously,<sup>1)</sup> where the depth of the elastic wave correlated with the range of the ions in the material calculated with the TRIM code.<sup>2)</sup>

Here, we report another experiment to locate the source of the elastic waves generated by 3.54 GeV  $^{136}\text{Xe}$  ions. The experiment setup is almost the same as that described previously: A 10-mm-thick plate of sample material is irradiated by a single-bunch ion beam and the generated elastic waves are detected at the back of the plate. The present experiment requires more precision in the source-position measurement since the range of the Xe ion (approximately 0.3 mm) is much shorter than that of the Ar ion (approximately 4.2 mm). Since the uncertainty of the propagation-time measurement is mainly due to the signal delay of about 80 ns caused by the piezoelectric sensors and amplifiers, we have performed complementary measurements with a pulse YAG laser to cancel the delay. Since the laser is absorbed in metal within  $1\ \mu\text{m}$  from the surface, the laser-generated waves travel across the sample from surface to surface. If the ion irradiation generates elastic waves inside the sample, the waves travel in the sample to the sensor by a shorter distance, as shown in Fig. 1. The difference in elastic-wave arrival time between the ion and laser irradiations corresponds to the depth of the ion-generated waves.

Before and after the ion irradiation on an Al sample, we irradiate the sample using a laser with an energy of 0.3–0.5 mJ/pulse. The acquisition of the waveform

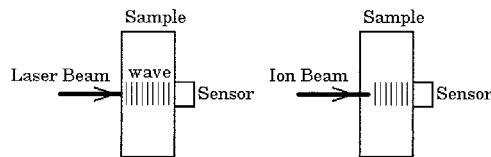


Fig. 1. Schematics of beam and sensor setups for laser (left) and ion (right) irradiations.

is triggered by the reflected light signals from a photodiode. In both ion and laser measurements, the setup of the sensors and the amplifiers are unaltered. Figure 2 shows the onset of the longitudinal waveforms by the Xe-ion (upper) and YAG laser (lower) irradiations. The origin of the time axis is set to the impingement with corrections for the differences in cable length and flight time of the ions. The waveform by the ion beam is normalized to  $10^4$  ions per bunch.

The onset of the ion-generated elastic wave is ahead of that of the laser-generated wave by about  $45 \pm 5$  ns. Since the velocity of the longitudinal wave in this sample has been determined to be 6514 m/s, this delay time corresponds to a source depth of about  $293 \pm 32\ \mu\text{m}$ . It is in good agreement with the range of the Xe ions of  $288\ \mu\text{m}$  calculated with the TRIM code.

The shape of the elastic wave onset pulse is different between the ion and laser irradiations: It is broader for the ion than the laser irradiation. The precision of the delay time is limited by the slow increase in the elastic wave by the ion irradiation. In the ion irradiation, the source region of the elastic wave should spread over the ion range, and the analyses of the waveform could reveal the distribution of the radiation-induced stress.

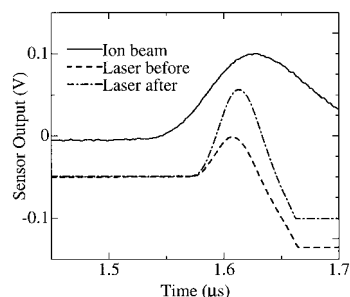


Fig. 2. Elastic waveforms at the onset of the longitudinal wave by 3.54-GeV Xe ions (upper) and YAG laser (lower).

### References

- 1) T. Kambara et al.: Nucl. Instrum. Methods Phys. Res. B **193**, 371 (2002).
- 2) J. F. Ziegler, J. P. Biersack, and U. Littmark: *The Stopping and Range of Ions in Solids* (Pergamon Press, New York, 1985).

\* Department of Mechanical Engineering, Saitama University



## Effect of GeV-ion irradiation on Fe-Ni invar alloys

F. Ono,<sup>\*1</sup> A. Iwase,<sup>\*2</sup> S. Komatsu,<sup>\*1</sup> H. Kanamitsu,<sup>\*1</sup> Y. Chimi,<sup>\*3</sup> N. Ishikawa,<sup>\*3</sup> and T. Kambara

Fe-Ni alloys with a Ni-concentration approximately 35 at% are called invar alloys that are known to exhibit various anomalies in both mechanical and magnetic properties.<sup>1)</sup> These anomalies are as follows: very small thermal expansion coefficient, anomalous decrease in the spontaneous magnetization from the Slater-Pauling curve, and very large pressure dependence of the Curie temperature  $T_C$ . These anomalies are associated with the instability of the ferromagnetic condition of the 3d-electrons.<sup>2)</sup> The Curie temperatures of Fe-Ni invar alloys were reported to decrease<sup>3)</sup> with pressure at a high rate of  $-36$  K/GPa. Therefore, high-energy ion irradiation is expected to introduce a large positive change in  $T_C$  through the negative pressure associated with the irradiation-induced lattice expansion.

The effect of high-energy ion beam irradiation on  $T_C$  of Fe-31.9 at%Ni invar alloy was investigated and reported to increase with irradiation dose.<sup>4,5)</sup> In these reports, unfortunately, the data before irradiation are missing. Therefore, it was not possible to check whether the dose-dependence of  $T_C$  is linear. In this report, we present a full curve of the dose-dependence of  $T_C$ .

Thin rectangular plates of Fe-30at%Ni Invar alloy were prepared. The irradiations were carried out at room temperature with 3.8 GeV Ta ions to the ion-fluence of the order of  $10^{13}/\text{cm}^2$  using the RIKEN Ring Cyclotron. Observed ac-susceptibility-temperature curves before and after the irradiations

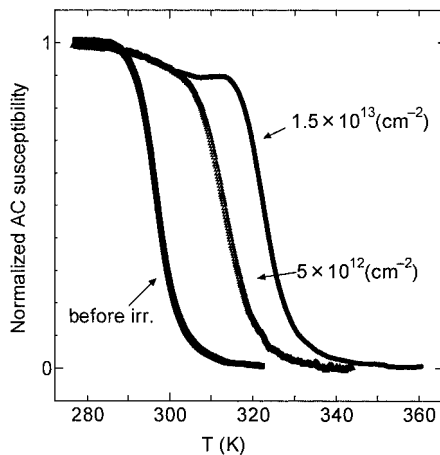


Fig. 1. Temperature dependence of ac susceptibilities for Fe-30 at%Ni invar alloys before and after irradiation with 3.8 GeV Ta ions to a dose of up to  $1.5 \times 10^{13}$  ions/cm<sup>2</sup>.

are shown in Fig. 1. The ac susceptibility decreases suddenly at the Curie temperature. In this figure it is evident that  $T_C$  increases with irradiation dose. The dose dependence of  $T_C$  is shown in Fig. 2, where a sublinear relationship is clearly seen.

This sublinear effect indicates that there are at least 2 or more origins<sup>6,7)</sup> that contribute to the increase in  $T_C$ . A possible mechanism is the lattice expansion associated with the introduction of pointlike defects and tracks along the paths of ion beams. Because the pressure dependence of  $T_C$  in Fe-Ni Invar alloys is large and negative,  $T_C$  increases with the negative pressure. Another mechanism is compositional changes induced by irradiation.

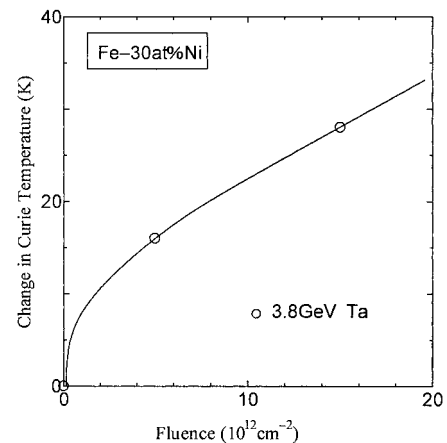


Fig. 2. Change in Curie temperature with irradiation dose in Fe-30 at%Ni invar alloy.

### References

- 1) For example, see: *The Invar Effect: A Centennial Symposium*, edited by J. Wittenauer (The Minerals, Metals & Materials Society, Warrendale, 1997).
- 2) P. Entel, E. Hoffmann, P. Mohn, K. Schwarz, and V. L. Moruzzi: *Phys. Rev. B* **47**, 8706 (1993).
- 3) S. Endo, M. Nishino, and F. Ono: *Sci. Technol. High Pressure* **2**, 850 (2000).
- 4) F. Ono, A. Iwase, Y. Hamatani, Y. Motoshimizu, N. Ishikawa, Y. Chimi, Y. Mukumoto, and T. Kambara: *RIKEN Accel. Prog. Rep.* **35**, 96 (2002).
- 5) A. Iwase, Y. Hamatani, Y. Mukumoto, N. Ishikawa, Y. Chimi, T. Kambara, C. Mueller, R. Neumann, and F. Ono: *RIKEN Accel. Prog. Rep.* **36**, 99 (2003).
- 6) F. Ono, Y. Hamatani, Y. Mukumoto, S. Komatsu, N. Ishikawa, Y. Chimi, A. Iwase, T. Kambara, C. Mueller, and R. Neumann: *Nucl. Instrum. Methods Phys. Res. B* **206**, 295 (2003).
- 7) A. Iwase, Y. Hamatani, Y. Mukumoto, N. Ishikawa, Y. Chimi, T. Kambara, C. Mueller, R. Neumann, and F. Ono: *Nucl. Instrum. Methods Phys. Res. B* **209**, 323 (2003).

<sup>\*1</sup> Department of Physics, Okayama University

<sup>\*2</sup> Research Institute for Advanced Science and Technology, Osaka Prefecture University

<sup>\*3</sup> Japan Atomic Energy Research Institute

## Evaluation of single-event effect in power MOSFET

N. Ikeda,<sup>\*1</sup> S. Kuboyama,<sup>\*1</sup> K. Oka,<sup>\*1</sup> H. Sato,<sup>\*1</sup> H. Ohira,<sup>\*2</sup> Y. Morishima,<sup>\*2</sup>  
 H. Otomo,<sup>\*2</sup> O. Shimada,<sup>\*2</sup> N. Inabe, and M. Kase

A power MOSFET (metal-oxide-semiconductor field-effect transistor) is a key device in a power circuit which achieves low ON-resistance and fast switching. A MOSFET to be used in space is required to have radiation hardness. Protons, heavy ions and other particles in space could cause single-event effects and lead to semiconductor device malfunction or failure. Single-event burnout (SEB) is the main concern regarding power MOSFETs. SEB is triggered by a heavy ion passing through the device when it is off. Transient current by such an ion turn on a parasitic bipolar transistor, which results in burning out of the device and its possible destruction.<sup>1)</sup> JAXA has developed a radiation-hardened power MOSFET for use in space. It has SEB tolerance up to the rated voltage (drain-source voltage,  $V_{DS}$ ). Several parameters for hardness were determined, and their performances were verified by  $^{58}\text{Ni}^{19+}$  irradiation tests using the RIKEN Ring Cyclotron. Energy, LET and the range of ions in a device were 300 MeV, 26 MeV/(mg/cm<sup>2</sup>), and 50  $\mu\text{m}$ , respectively.

The EPICS (Energetic Particle Induced Charge Spectroscopy) system developed by JAXA, was introduced to observe SEB. It collects charges of holes and electrons generated by the penetration of an ion. SEB resistance is judged on the basis of the spectra of those collected charges with  $V_{GS}$  (gate-source voltage) equal to zero and several  $V_{DS}$  values. Typically, two peaks are observed in the spectra, which are here called the 1st peak and the 2nd peak. They have different mechanisms of charge collection. The 2nd peak grows (shifts to the right) with the increase of  $V_{DS}$  and becomes the SEB peak which has a much larger collection of charges. Therefore, the performance of the 2nd peak is a good index of SEB resistance, and it is better to have a 2nd peak with smaller charges.

The upper graph in Fig. 1<sup>2)</sup> shows the spectrum of a MOSFET whose epi-layer parameters (resistivity and thickness) of have been improved. The collected charges of the 2nd peak are less than those of a reference MOSFET (lower graph). No SEB was observed up to the rated  $V_{DS}$ .

Figure 2<sup>2)</sup> shows the spectrum difference of other parameter, which is the length of an n-layer protruding out from the p-layer under the gate. SEB was observed in the longest of the three devices. The two other devices exhibit almost the same spectrum. The SEB threshold was determined from this result.

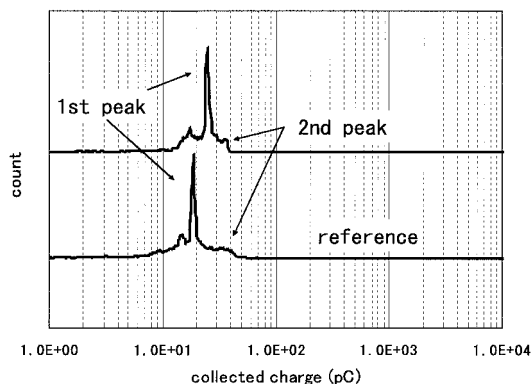


Fig. 1. SEB spectra of the 150 V power MOSFET with improved epi-layers (upper). Collected charges of 2nd peak are smaller than those of reference ( $V_{DS} = 135$  V).

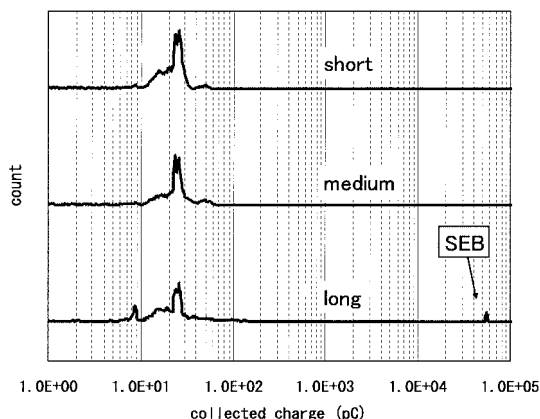


Fig. 2. SEB spectra of 250 V power MOSFETs with other parameter, which is the length of an n-layer protruding out from the p-layer under the gate. SEB occurred in the longest device ( $V_{DS} = 220$  V).

There are some other parameters for SEB, and their effectiveness for SEB tolerance was proved by the irradiation experiment at RIKEN.

### References

- 1) JAERI and NASDA Joint Research Report, Vol. 2 (1999), p. II-9.
- 2) N. Ikeda et al.: IEICE Technical Report, EE2003-40 (2003) p. 43.

<sup>\*1</sup> Japan Aerospace Exploration Agency

<sup>\*2</sup> Ryohei Technica Company

# Collective luminescence of extremely dense electron-hole pairs created in ion tracks in insulators

K. Kimura,<sup>\*1</sup> M. Koshimizu,<sup>\*1</sup> K. Asai,<sup>\*2</sup> and M. Kase

We have found ultrafast luminescence ( $\tau < 100$  ps) from incipient heavy-ion track cores in insulator crystals such as alkali halides, metal oxides, and alkaline-earth halides.<sup>1)</sup> This luminescence is the first observed collective behavior of track cores of ions, and precedes that due to known excitons or excited states of impurity or defect centers. Such luminescence can be detected using not only fast sensitive detection techniques but also the beam condition under which energetic electrons to eject further secondary electrons are negligibly small and moreover the track-core effects are major. We have developed techniques for luminescence measurements with a time resolution of 85 ps.<sup>1)</sup> To make the core effect prominent and to equalize the incident ion velocity, the equal incident ion energy of 2 MeV/nucleon was used so that we could compare the dependence on excitation density in the track cores reasonably for different ions, and moreover there is the maximum stopping power near this ion energy. Time-resolved (TR) measurements revealed ultrafast and broad luminescence preceding known luminescence bands. Furthermore, experimental results characterized the luminescence as follows, namely, its efficiency showed the super-linear increase to excitation density, the large dependence on the materials and the insensitiveness on temperatures; the decay-curve has no tail beyond the exponential, and the spectral shift from the absorption edge was the large Stokes shift. These results suggest the ultrafast luminescence corresponds to the stimulated emission caused among adjacent e-h pairs.

This report exhibits the results for a single crystal of MgO. This material is known as a unique insulator that has strong free-exciton luminescence and shallow-trapped-exciton luminescence in the vacuum ultraviolet region while it has no self-trapped excitons as are familiar in alkali halides. Under the present extremely high-density excitation, it is interesting whether free excitons can combine to form the stationary electron-hole plasma known in semiconductors, and also whether the ultrafast luminescence process is related to the radiation resistivity known in MgO. Figure 1 shows a time-integrated luminescence spectrum at 4 K obtained with cathode-ray irradiation, TR luminescence spectra at low temperature for N, Ar, and Xe ions, and that at room temperature for Ar ion, from top to bottom. The spectrum obtained us-

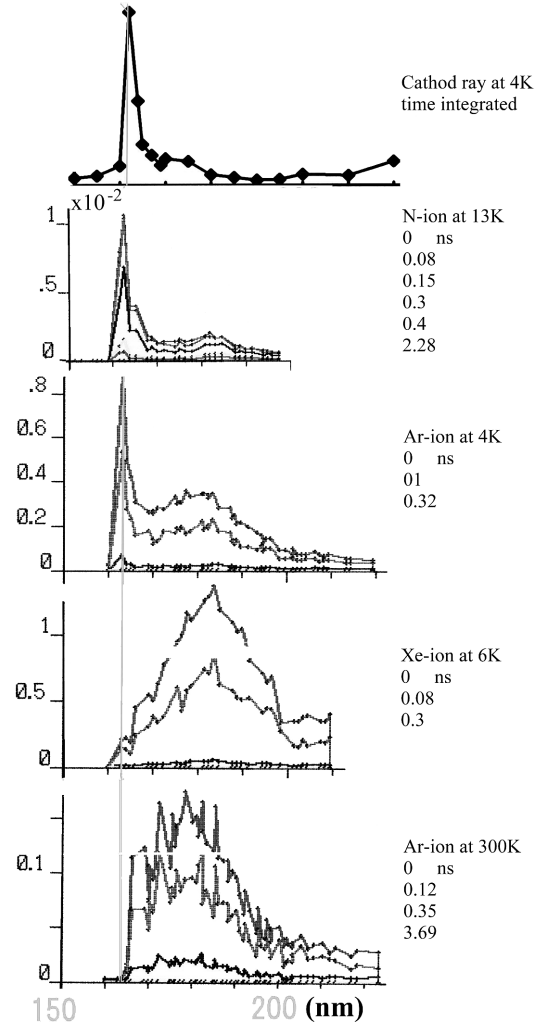


Fig. 1. Excitation-density-dependent time-resolved luminescence spectra.

ing the cathode ray exhibits a sharp band at 162 nm and a weak shallow-trapped exciton band on the right side. The 162 nm band is due to free-excitons as reported so far. In contrast, the ion irradiated MgO revealed a new broad band at 180 nm, whereas the free exciton band was quenched with increasing excitation density, namely from electron to Xe irradiation, the 180 nm band appeared and increased in its intensity, while the free exciton band increased in quenching rate and disappeared completely by Xe-ion irradiation. The TR spectra at room temperature, given at the bottom, show that luminescence efficiency of the new band does not decrease markedly whereas that of the free excitons disappeared completely. These results mean that the

<sup>\*1</sup> Department of Quantum Engineering and Systems Science, School of Engineering, University of Tokyo

<sup>\*2</sup> Department of Applied Chemistry, School of Engineering, Tohoku University

new luminescence does not originate from the free excitons but the excited species in the earlier stage before free excitons are created. Although the spectral shift looks as if it is caused by the binding energy among the free excitons, the value of 0.9 eV is too large. Otherwise, the shift associated with the trapping of the hole is reasonable. This trapping, however, is not due to tight binding (deep trap) such as the self-trapping of the hole seen in alkali halides but due to shallow one generated by orientation and displacement of  $O^{2-}$  surrounding holes ( $O^-$ ) like polarons. This situation is similar to that observed for the electron-hole plasma in alkali halides.<sup>2)</sup> Thus, the present luminescence is largely different from the e-h plasma known in laser irradiated semiconductors. However, it is not the same as that of alkali halides considering its much smaller shift from the gap energy and smaller density of e-h pairs than the case of alkali halides. The e-h plasma for MgO seems to a little expand in volume because of shallow and mobile hole-trapping.

Lastly, the present photoemission seems to account for the radiation resistivity of MgO that it reduces the defect production caused by the effect of high-density excitation. Recently, it has been reported that MgO was the lowest in the sputtering yield on metal oxides attributed to high-density excitation. The yields increased in the following order: MgO,  $Al_2O_3$ ,  $TiO_2$ , and  $SiO_2$ .<sup>3)</sup> Contrarily, yields of the e-h plasma luminescence were reverse to this.

#### References

- 1) K. Kimura, J. Kaneko, S. Sharma, W. Hong, and N. Itoh: *Phys. Rev. B* **60**, 12626 (1999); K. Kimura, S. Sharma, and A. Popov: *Radiat. Meas.* **34**, 99 (2001); *Nucl. Instrum. Methods Phys. Res. B* **191**, 48 (2002).
- 2) K. Kimura: *Nucl. Instrum. Methods Phys. Res. B* **212**, 123 (2003).
- 3) N. Matsunami, M. Sataka, A. Iwase, and S. Okayasu: *Nucl. Instrum. Methods Phys. Res. B* **209**, 288 (2003).

## Comparative study on electron-hole plasma formed in heavy-ion irradiated MgO and CdS

M. Koshimizu,\* K. Kimura,\* K. Asai,\* and M. Kase

The irradiation effects of swift heavy ions in semiconductors and insulators are characterized by high-density electronic excitation along their paths. In order to understand the dynamics of high-density excitation states, we measured the time-resolved luminescence spectra using a SISP (single ion and single photon time correlation) system, with a time resolution of 80 ps. One of the authors (K. K.) observed the luminescence bands having very short lifetimes in alumina and alkali halides.<sup>1,2)</sup> These bands can be ascribed to the multiple interaction of the high-density excited carriers analogous to electron-hole plasma (EHP) in semiconductors.<sup>3)</sup> However, the detailed discussion is still incomplete due to the difficulty in treating such an excited state in insulators with strong electron-lattice coupling.

In this study, we aim to compare the dynamics of the high-density excited carriers produced by heavy ions in MgO and CdS. In CdS, the electron-lattice coupling is very weak, and can be treated by considering the phonon scattering of the excited carriers. In contrast, in MgO, self-trapped excitons (STEs) are supposed to be stable although self-trapped holes are not formed, and a luminescence band due to free excitons is observed at low temperature.<sup>4)</sup>

In the time-resolved luminescence spectrum of CdS at 15 K induced by 2 MeV/nucleon Xe ions, the spontaneous luminescence of EHP was observed, as shown in Fig. 1. We analyzed the shape of this band in accordance with Goebel,<sup>5)</sup> and we have obtained a carrier temperature and an electron-hole concentration of 15 K and  $1.2 \times 10^{19} \text{ cm}^{-3}$ , respectively. In contrast, for the case of 2 MeV/nucleon Ar irradiation, a rather sharp luminescence band due to EHP was observed at 12 K, and the carrier density was obtained to be  $3.0 \times 10^{18} \text{ cm}^{-3}$ . This carrier density is consistent with the results of calculation on the carrier diffusion dy-

namics taking into account the optical phonon scattering of the excited carriers, the method of which is described for GaAs in Ref. 6. Therefore, the spatial behavior of the excited carriers along the ion trajectory can be described in terms of the carrier-phonon scattering.

For MgO, a free exciton (FE) band was observed when the excitation density was low in the time-resolved luminescence spectra, as shown in manuscript p. 99 in this volume of Riken Accel. Prog. Rep. As the excitation increases, the FE band disappeared and the intensity of a broad luminescence band at the low-energy side of the FE band increased rapidly. The quenching of the FE band can be analyzed quantitatively by considering the electrostatic screening of the Coulomb force responsible for the exciton formation, similarly to the case in semiconductors.<sup>3)</sup> By calculating the Mott density, at which excitons become unstable due to the electrostatic screening and the EHP is formed, the carrier density can be roughly estimated for excitation by each ion when the disappearance of the FE band takes place. By using the values of the carrier density, the spatial extent of the excited region, *i.e.*, diffusion length, can be estimated to be about as large as 200 nm. This estimation may be reasonable when one considers that a hole is not self-trapped in lattice distortion. Therefore, it is concluded that the behavior of the high-density excited carriers along the ion trajectory should be considered in terms of hole-lattice coupling, and the exciton-lattice interaction has much less importance.

From the above consideration, the broad luminescence band at the low-energy side of the FE band can be ascribed to the EHP. The Stokes shift of this band is very large compared with the EHP band in semiconductors. This difference should be due to the lattice distortions analogous to polarons. However, further consideration is necessary to clarify the EHP dynamics in insulators.

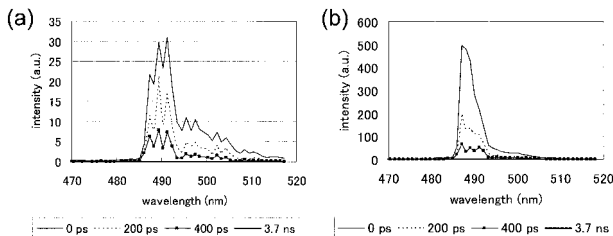


Fig. 1. Time-resolved luminescence spectra of CdS irradiated with 2.0 MeV/n Xe (a) and Ar (b).

\* Department of Applied Chemistry, School of Engineering, Tohoku University

### References

- 1) K. Kimura, S. Sharma, and A. I. Popov: Phys. Rev. B **60**, 12626 (1999).
- 2) K. Kimura, S. Sharma, and A. I. Popov: Nucl. Instrum. Methods Phys. Res. B **191**, 48 (2002).
- 3) For review, see C. Klingshirn and H. Haug: Phys. Rep. **70**, 315 (1981).
- 4) Z. A. Rachko and J. A. Valbis: Phys. Stat. Sol. (b) **98**, 161 (1979).
- 5) E. O. Goebel: Appl. Phys. Lett. **24**, 492 (1974).
- 6) M. Koshimizu, K. Asai, and H. Shibata: J. Lumin. **94**, 407 (2001).

# A new type of positron accumulator in UHV utilizing a high-density electron plasma and an ion cloud

M. Niigaki,\* T. M. Kojima, N. Oshima,\* A. Mohri, M. Inoue,\* K. Komaki,\* and Y. Yamazaki

In the previous report,<sup>1)</sup> we have introduced a new method which can accumulate positrons directly in ultra-high vacuum (UHV) with an efficiency higher than other UHV-compatible accumulators. The key of our method is to utilize a high-density electron plasma as an energy absorber of positron beams.

The setup of our system is shown in Fig. 1. It consists of a slow positron source, an electron gun, a Multi-Ring Trap (the MRT—a kind of electromagnetic trap),<sup>2)</sup> a positron remoderator, a Faraday cup and an annihilation  $\gamma$ -ray detector. Positrons and electrons are accommodated in electric potential wells (noted as range (e) and (p)) which are formed by multiring electrodes of the MRT. The  $\gamma$ -ray detector, the Faraday cup and the remoderator are used for diagnoses of charged particles. The total number of trapped positrons  $N_{e^+}$  is measured by dumping them onto the Faraday cup, and counting the number of annihilation  $\gamma$ -rays by the  $\gamma$ -ray detector. The total number of electrons  $N_{e^-}$  can be measured as the total amount of charges by collecting them at the Faraday cup or remoderator.

The positron accumulation process includes four steps: (1) formation of a high-density electron plasma in range (e) by injecting electron beams, (2) injection of positron beams of  $\sim 10^6 e^+/s$  from the slow positron source, and remoderation by the remoderator (about 10–30% of them are reemitted), (3) energy loss by Coulomb collision in the electron plasma, (4) trapping of decelerated positrons into range (p), and their self-cooling *via* synchrotron radiation.

In this method, reinjection of positrons into the remoderator after step (3) causes a considerable decrease in the overall positron population. Hence, it is important to make the positron energy loss  $\Delta K$  suffi-

ciently large in step (3) so that positrons can no longer reach the remoderator.  $\Delta K$  depends on the electron column density  $\sigma = n_{e^-} \cdot L_{e^-}$ , where  $n_{e^-}$  and  $L_{e^-}$  are density and length of the electron plasma, respectively. Large  $\Delta K$  can be achieved by using an electron plasma with large  $\sigma$ .  $\Delta K$  depends on the injection energy of reemitted positrons  $K$ , which is expressed as  $K = e(V_{RM} - V_{e^-}) + E_{RM}$ , where  $e$  is elementary charge,  $V_{RM}$  is the bias potential of the remoderator,  $V_{e^-}$  is the electrostatic potential in the electron plasma,  $E_{RM}$  ( $\sim$  a few eV) is the initial energy of positrons reemitted from the remoderator. In order to make  $\Delta K$  sufficiently large, a small  $K$  should be selected, because a smaller  $K$  allows longer collision time, and as a result, a larger momentum transfer.  $K$  can be minimized to a few eV when  $V_{RM} \approx V_{e^-}$ , and positron trapping efficiency is maximized under this condition. Another important feature is that  $10^8$  of  $H_2^+$ , created in range (p) by electron-beam injection at step (1), are utilized at step (4). Positrons collide elastically with these ions, and it enhances trapping of decelerated positrons into range (p). We found these ions enhance by 10-fold the positron trapping efficiency.

Figure 2 shows the measured positron trapping efficiency  $\varepsilon_t$  as a function of  $V_{RM}$ .  $\varepsilon_t$  is defined as the ratio of trapped positrons to those injected into the MRT. Three results are shown here: (a)  $N_{e^-} = 1.8 \times 10^{10}$ , (b)  $N_{e^-} = 1.6 \times 10^{10}$  and (c)  $N_{e^-} = 1.2 \times 10^{10}$ . All data were acquired with 50 s injection of  $10^6 e^+/s$  beams. Each peak corresponds to the “potential matching condition”, *i.e.*  $V_{RM} \approx V_{e^-}$ . It can be seen that the maximum trapping efficiency  $\varepsilon_t^{max}$  becomes higher as  $N_{e^-}$  is increased, suggesting that  $\sigma$  of the electron plasma becomes larger together with  $N_{e^-}$ . So far,  $\varepsilon_t^{max} \sim 1\%$  has been achieved.

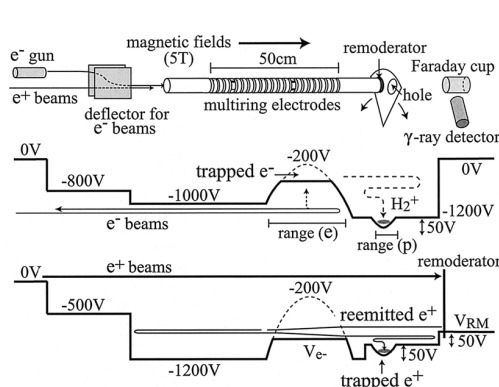


Fig. 1. Setup of the system and schematic of the total procedure.

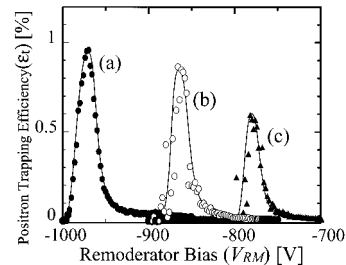


Fig. 2. Positron trapping efficiency  $\varepsilon_t$  as a function of remoderator bias  $V_{RM}$ . Solid lines are guide for eyes.

## References

- 1) N. Oshima et al.: RIKEN Accel. Prog. Rep. **36**, 111 (2003).
- 2) A. Mohri et al.: Jpn. J. Appl. Phys. **37**, 664 (1998).

\* Institute of Physics, University of Tokyo

## Soft X-ray spectroscopy of 2.3 keV/u N<sup>6+</sup> ions transmitted through a Ni microcapillary

Y. Iwai, Y. Kanai, Y. Nakai, T. Ikeda, H. Oyama, K. Ando, H. Masuda,\*<sup>1</sup>  
K. Nishio,\*<sup>1</sup> H. A. Torii,\*<sup>2</sup> K. Komaki,\*<sup>2</sup> and Y. Yamazaki

X-rays emitted from 2.3 keV/u N<sup>6+</sup> ions transmitted through a thin Ni microcapillary foil were measured using a high-resolution soft X-ray spectrometer to study the formation and relaxation dynamics of a hollow atom (ion) produced by a resonant charge transfer in ion-surface collisions. This work will be compared with a previous result involving N<sup>7+</sup> ions for the study of incident charge dependence.<sup>1)</sup>

2.3 keV/u N<sup>6+</sup> ions are supplied by a 14.5 GHz Caprice electron cyclotron resonance ion source in RIKEN.<sup>2)</sup> The microcapillary target was  $\sim 1$  mm<sup>2</sup> in area with a thickness of  $\sim 1$   $\mu$ m and had a multitude of straight holes  $\sim 200$  nm in diameter.<sup>3)</sup> The spectrometer consists of a concave grating and a charge-coupled device (CCD). For details of the spectrometer and methods of data analysis, see Ref. 4. X-ray spectra were taken at five points downstream of the target along the ion beam. The points were immediately downstream of the target ( $T = 0$ ), 0.15 mm ( $T = 0.22$  ns), 0.35 mm ( $T = 0.52$  ns), 1.00 mm ( $T = 1.50$  ns), and 2.75 mm ( $T = 4.10$  ns) downstream, where  $T$  is the time after passing through the target.

Figure 1 shows an X-ray spectrum, which was taken immediately downstream of the target for 2.3 keV/u N<sup>6+</sup> ions transmitted through the microcapillary. The eight major lines are attributed to helium-like transitions, which are summarized in Table 1.<sup>5)</sup> It is expected that the relative intensity of each transition reflects the

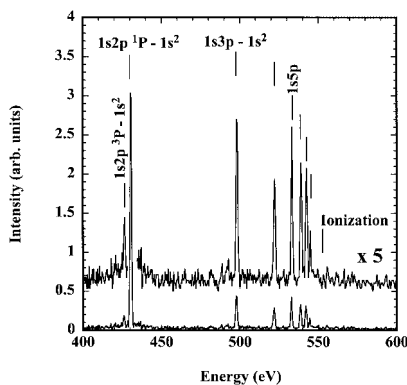


Fig. 1. Spectrum of  $K$  X-rays measured using the spectrometer immediately downstream of the target ( $T = 0$ ) for 2.3 keV/u N<sup>6+</sup> ions transmitted through a Ni microcapillary. The bars with transition terms show transition energies and N VI ionization potential energy.<sup>5)</sup>

\*<sup>1</sup> Department of Applied Chemistry, Graduate School of Engineering, Tokyo Metropolitan University

\*<sup>2</sup> Institute of Physics, Graduate School of Arts and Sciences, University of Tokyo

Table 1. Observed transition energies and electronic configurations.

Experiment	Ref. data <sup>5)</sup>	Configurations	Terms
$426.1 \pm 0.8$ eV	426.3 eV	$1s2p \rightarrow 1s^2$	$^3P_1 \rightarrow ^1S_0$
$430.4 \pm 0.8$ eV	430.7 eV	$1s2p \rightarrow 1s^2$	$^1P_1 \rightarrow ^1S_0$
$497.8 \pm 1.0$ eV	498.0 eV	$1s3p \rightarrow 1s^2$	$^1P_1 \rightarrow ^1S_0$
$521.8 \pm 1.1$ eV	521.6 eV	$1s4p \rightarrow 1s^2$	$^1P_1 \rightarrow ^1S_0$
$532.7 \pm 1.2$ eV	532.6 eV	$1s5p \rightarrow 1s^2$	$^1P_1 \rightarrow ^1S_0$
$538.7 \pm 1.2$ eV	538.5 eV	$1s6p \rightarrow 1s^2$	$^1P_1 \rightarrow ^1S_0$
$542.2 \pm 1.2$ eV	542.1 eV	$1s7p \rightarrow 1s^2$	$^1P_1 \rightarrow ^1S_0$
$544.5 \pm 1.2$ eV	544.6 eV	$1s8p \rightarrow 1s^2$	$^1P_1 \rightarrow ^1S_0$
Cf.	552.1 eV <sup>§</sup>		

§ N VI ionization potential energy

initial population and the cascade transitions of the hollow atom (ion).

Figure 2 shows the X-ray intensities for the  $1s3p - 1s^2$ ,  $1s2p \ ^1P - 1s^2$ , and  $1s2p \ ^3P - 1s^2$  transitions as a function of the time after the ion leaves the target. The decay curves indicate lifetimes in nanoseconds. Since the life of the  $1s2p \ ^1P$  transition is estimated to be in picoseconds, this result provides information on the decay process related to outer shells.<sup>6)</sup>

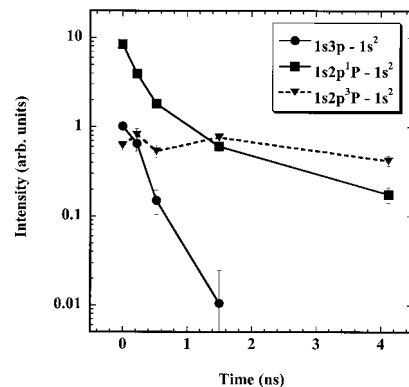


Fig. 2. X-ray decays of  $1s3p - 1s^2$ ,  $1s2p \ ^1P - 1s^2$ , and  $1s2p \ ^3P - 1s^2$  transitions.

### References

- 1) Y. Iwai et al.: Nucl. Instrum. Methods Phys. Res. B **193**, 504 (2002).
- 2) Y. Kanai et al.: Phys. Scr. T **92**, 467 (2001).
- 3) H. Masuda et al.: Appl. Phys. Lett. **71**, 2770 (1997).
- 4) Y. Iwai et al.: Nucl. Instrum. Methods Phys. Res. B **205**, 762 (2003).
- 5) R. L. Kelly: J. Phys. Chem. Ref. Data **16**, Suppl. 1 (1987).
- 6) W. R. Johnson et al.: Adv. At. Mol. Opt. Phys. **35**, 255 (1995).

# Coincidence measurements of X rays and final charge state of highly charged ions transmitted through a microcapillary

Y. Kanai, Y. Nakai, Y. Iwai, T. Ikeda, K. Nishio,\* H. Masuda,\* and Y. Yamazaki

A slow highly charged ion (HCI) passing through a microcapillary target captures target valence electrons into high- $n$  orbits while keeping inner shell vacancies. The captured electrons are stabilized through cascading down *via* photon emissions and/or Auger electron emissions. Some of the captured electrons emit X rays at the final stage of the stabilization. Ninomiya *et al.*<sup>1)</sup> found that the lifetime of the K vacancy was as long as  $10^{-9}$  s even with several electrons in the outer shells, using  $N^{6+}$  ions which have a single K vacancy. It is interesting to see how the inner shell filling process changes when the incoming ions have multiple inner shell vacancies. We have measured K (L) X rays in coincidence with the exiting charge states for 2.1 keV/u  $N^{7+}$  (2.8 keV/u Ar ions) to study the filling processes of inner shell vacancies.

The experiments were carried out at the Slow Highly Charged Ion Facility at RIKEN.<sup>2)</sup> 2.1 keV/u  $N^{7+}$  and 2.8 keV/u  $Ar^{q+}$  ( $q = 14, 13$  and  $9$ ) ions were extracted from a 14.5 GHz ECR ion source. The beams impinged on a Ni microcapillary target along the capillary axis. A Si(Li) X-ray detector was placed at  $90^\circ$  to the beam axis. A shield located between the target and the Si(Li) detector was movable along the beam direction, and limited the detection region of the X-ray emission. The X rays emitted after  $t' > t = z/v$  ( $v$ : ion velocity,  $v = 0.64$  mm/ns and  $0.74$  mm/ns for 2.1 keV/u and 2.8 keV/u, respectively) were detected, when the shield was located at  $z$ . The final charge states  $q_f$  of ions were analyzed with an electrostatic charge state analyzer. The difference between the initial  $q_i$  and final  $q_f$  charge states of ions gives the number  $s$  of the stabilized electrons after the decay processes;  $s = q_i - q_f$ . The X-ray spectra and yield coincident with the final charge state were measured as a function of the shield position  $z$ .

As shown in Fig. 1(a) for 2.8 keV/u  $Ar^{14+}$  incident,<sup>3)</sup> the X-ray yield coincidence with  $Ar^{13+}$  ions which have only one stabilized electron  $s = 1$ , decreases more rapidly than those with other charge state ions which have multiple stabilized electrons  $s > 1$ . The same tendency can be seen in Fig. 1(b) and (d) for 2.8 keV/u  $Ar^{13+}$  and 2.1 keV/u  $N^{7+}$  incident, respectively. On the other hand, this tendency is not observed in Fig. 1(c) for 2.8 keV/u  $Ar^{9+}$  incident. This difference may be due to these being different numbers of initial inner shell vacancies, because  $Ar^{14+}$ ,  $Ar^{13+}$  and  $N^{7+}$  ions have multiple inner shell (L- or K-shell) vacancies and  $Ar^{9+}$  ions have only one inner shell (K-

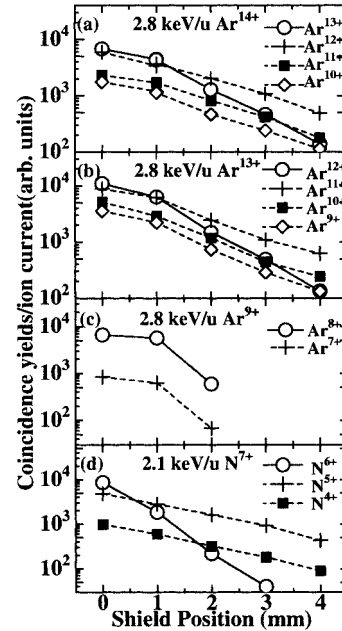


Fig. 1. Integrated delayed X-ray yields normalized by ion current as a function of the shield position for (a)  $Ar^{14+}$ , (b)  $Ar^{13+}$ , (c)  $Ar^{9+}$ , and (d)  $N^{7+}$  incident.

shell) vacancy. This speculation is supported by Ninomiya *et al.*'s results;<sup>1)</sup> they observed the same tendency in the  $N^{6+}$  incident as we observed in the  $Ar^{9+}$  incident as shown in Fig. 1(c).

We must note that the peak positions of the X-ray spectrum coincidence with the final charge state shift to a lower energy with decreasing final charge state and do not shift with the shield position.<sup>3)</sup> This result may be explained by either (1)  $(s-1)$  electrons rapidly ( $\ll 10^{-9}$  s) fill the inner shell vacancies *via* photon emissions and/or Auger electron emissions and the last electron slowly de-excites radiatively, or (2)  $(s-1)$  electrons slowly ( $\sim 10^{-9}$  s) fills the inner shell vacancies *via* Auger electron emissions and the last electron fill the inner shell vacancy by a radiative process.

We do not have sufficient experimental and theoretical information on the decay schemes to explain our results consistently. We are planning to use (1) a high-resolution X-ray spectroscopy to identify the final transition and (2) an electron spectroscopy to determine the role of the Auger process in the total decay process.

## References

- 1) S. Ninomiya *et al.*: Phys. Rev. Lett. **78**, 4557 (1997).
- 2) Y. Kanai *et al.*: Physica Scr. T **92**, 467 (2001).
- 3) Y. Kanai *et al.*: RIKEN Accel. Prog. Rep. **36**, 109 (2003).

\* Department of Applied Chemistry, Tokyo Metropolitan University



## Multiple-electron processes in close single collisions of $\text{Ne}^{q+}$ ( $q = 2, 5, 7, \text{ and } 9$ ) with Ar at 14 keV

M. Hoshino,<sup>\*1</sup> T. Kambara, Y. Kanai, S. Madzunkov,<sup>\*2</sup> R. Schuch,<sup>\*2</sup> and Y. Yamazaki

We study electron transfer in close single collisions of slow highly charged ions (HCIs) with atoms, through large-angle experiments. This work is motivated by the intrinsic interest in the multiple-electron reaction dynamics in slow and very close ion-atom collisions, in the understanding of the neutralization in HCI-surface interactions, and in the possible formation of the hollow atoms in HCI-atom collisions. Early experimental studies of very close collisions were performed with singly charged ions.<sup>1)</sup> It is expected that the reaction processes for singly and highly charged ions should be very different, that is, ionization in the former and multiple-electron transfer in the latter. Only one study on multiple-electron transfer in slow, close collisions has been done, by Herrmann *et al.*,<sup>2)</sup> for a  $\text{Ne}^{9+}$ -Ne symmetric system up to  $4.2^\circ$  at the collision energy of 90 keV. There is no experimental data on the projectile charge dependence of the outgoing ion charge state in close collisions. The charge-state distributions of recoil ions were measured for  $\text{Ne}^{q+}$  ( $q = 2, 5, 7, \text{ and } 9$ ) on Ar at a fixed projectile energy of 14 keV, or at a velocity of 0.17 atomic unit.

The experiment was carried out at a slow highly charged ion facility of RIKEN. A 14-keV  $\text{Ne}^{q+}$  ( $q = 2, 5, 7, \text{ and } 9$ ) beam from the 14.5 GHz Caprice-type ECR ion source was collimated on a localized Ar gas target from a needle. Scattered Ne ions and recoil Ar ions were detected at  $27^\circ$  and  $70^\circ$ , which correspond to  $40^\circ$  of the center of mass (CM) scattering angle, as expected from the kinematics of elastic scattering for this system. Each of the ion-detection systems consists of a time-of-flight (TOF) drift tube which is set at electrostatic potential, and a two-dimensional position-sensitive detector. For each coincidence event, the time difference between the detections of the scattered and recoil ions ( $\Delta\text{TOF}$ ) and the positions of the both ions were recorded. With the drift tube at electrostatic potential one can modulate the ion velocity and determine the outgoing charge states by  $\Delta\text{TOF}$ .

The recoil-ion charge state distributions were measured for  $\text{Ne}^{q+}$  ( $q = 2, 5, 7, \text{ and } 9$ ) on Ar, where only the drift tube for the recoil-ion detector was biased at about  $-2.0\text{ kV}$ . Figure 1 shows the results for each projectile charge state. The recoil-ion charge increases with the projectile charge.

For  $\text{Ne}^{2+}$ -Ar collision, the charge states of the recoil ion ( $q_r$ ) and scattered ion ( $q_s$ ) were measured simultaneously by applying bias on both drift tubes. In Fig. 2, the charge state distributions of scattered and recoil

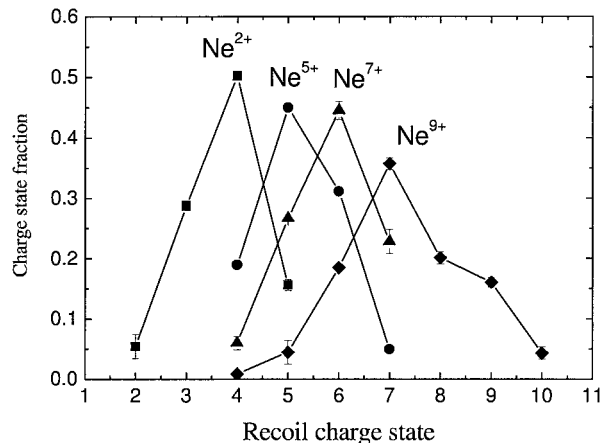


Fig. 1. The recoil ion distributions for each projectile charge. ( )  $\text{Ne}^{2+}$ , ( )  $\text{Ne}^{5+}$ , ( )  $\text{Ne}^{7+}$ , ( )  $\text{Ne}^{9+}$ .

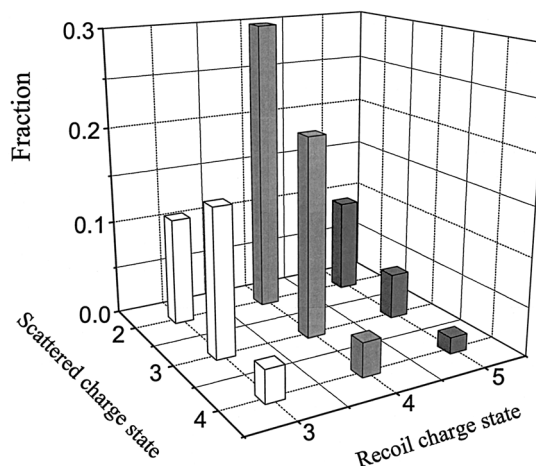


Fig. 2. The charge state distributions of scattered and recoil ions for  $\text{Ne}^{2+}$ -Ar.

ions for  $\text{Ne}^{2+}$  are shown. The most probable combination is  $(q_s, q_r) = (2, 4)$ . In such low-charge projectiles, electron capture is not observed and ionization and electron loss are the dominant reaction processes. For high incoming charges, electron capture is expected to be important.

### References

- 1) E. Everhart and Q. C. Kessel: Phys. Rev. Lett. **14**, 247 (1965).
- 2) R. Herrmann et al.: Phys. Rev. A **46**, 5631 (1992).

<sup>\*1</sup> Department of Physics, Sophia University

<sup>\*2</sup> Atomic Physics, Stockholm University, Sweden

## Photodissociation for recovery of $\text{Ca}^+$ ions lost by chemical reactions in an ion trap

K. Okada,<sup>\*1</sup> M. Wada, T. Takayanagi,<sup>\*1</sup> T. Nakamura,<sup>\*2</sup> I. Katayama,<sup>\*2</sup> and S. Ohtani<sup>\*3</sup>

An ion trap connected to an rf ion guide system will be used for cooling and trapping energetic ion beams in order to study the Bohr-Weisskopf effects of unstable alkali earth ions.<sup>1,2)</sup> One of the serious problems in such experiments is a chemical reaction of an objective isotope ion with a water molecule during the cooling process. Generally, the collision-induced dissociation (CID) technique is applied to solve the problem. But, a high-pressure noble gas must be loaded to realize the CID. Thus, photodissociation of such molecular ions will be useful as a clean dissociation method.

In this short report, we present results of photodissociation experiments when trapped  $\text{Ca}^+$  ions are lost by chemical reactions with  $\text{H}_2\text{O}$  molecules. Details of the experimental setup are described elsewhere.<sup>3)</sup> For detection of laser-induced fluorescence from  $\text{Ca}^+$  ions, we used two laser diodes with oscillation wavelengths at 397 nm and 866 nm. In order to accelerate the reaction with  $\text{H}_2\text{O}$ ,  $\text{Ca}^+$  ions were pumped into the metastable  $3^2\text{D}_{3/2}$  state by turning off the 866 nm laser, and then the  $\text{CaOH}^+$  ions are efficiently produced. An important point is that the produced  $\text{CaOH}^+$  ions are still trapped in the ion trap after the reaction. The dissociation energy of  $\text{CaOH}^+ \rightarrow \text{Ca}^+ + \text{OH}$  was estimated by the GAUSSIAN 03 program package.<sup>a)</sup> The photodissociation energy of  $\text{CaOH}^+$  is at least 4.6 eV, which corresponds to  $\lambda = 268$  nm light. A deep UV light of around 200–300 nm was extracted from a mercury xenon lamp (200 W, Hamamatsu Photonics Co. Ltd). The extracted UV light was focused on the center of the ion trap by a fused-silica lens.

In Fig. 1, we present a time spectrum of the fluorescence intensity from trapped  $\text{Ca}^+$  ions during the chemical reaction and the photodissociation processes. The wavelength distribution of the incident UV light was  $\sim 250 \pm 10$  nm, and the total power was  $\sim 50$  mW. The clear fluorescence increase, therefore the recovery of  $\text{Ca}^+$  from  $\text{CaOH}^+$ , was observed by irradiation of the UV light as shown on the right of the figure. Since we carried out the experiment using a liquid-nitrogen-cooled ion trap, the loss of reaction products was considered negligible during the experiment. Accordingly, the fluorescence intensity recovered the same level as in the initial state. The fluorescence increase as a function of UV exposure time is shown in the in-

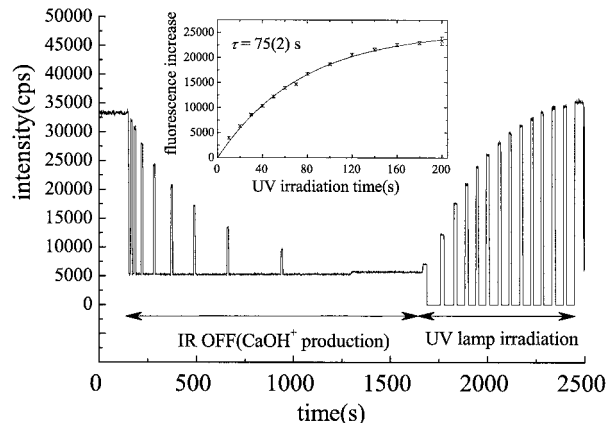


Fig. 1. A time spectrum of fluorescence from trapped  $\text{Ca}^+$  ions during the  $\text{Ca}^{+*}(\text{D}_J) + \text{H}_2\text{O} \rightarrow \text{CaOH}^+ + \text{H}$  reaction and the photodissociation process:  $\text{CaOH}^+ + h\nu \rightarrow \text{Ca}^+ + \text{OH}$ . The insert shows a rise time profile of fluorescence increase as a function of a UV exposure time.  $\text{H}_2\text{O}$  pressure:  $3 \times 10^{-6}$  Pa.

set of Fig. 1. The rise time depends on the number of  $\text{CaOH}^+$  ions and the effective photon flux for the photodissociation. The latter should vary with the peak wavelength of incident UV light. In order to roughly estimate the wavelength dependence of the photodissociation, we inserted various UV filters with different transmittance properties in the optical path. Moreover, we tried to dissociate  $\text{CaOH}^+$  ions using a pulsed 266 nm laser, which was produced by 4th harmonic generation (FHG) of a Nd: YAG pulsed laser. As a result, we could not observe any fluorescence increase by irradiation of UV light with a longer wavelength than  $\sim 255$  nm. A tunable UV laser is required for further study of the wavelength dependence.

In summary, the photodissociation method by UV or visible light from a high-power discharge lamp can be applied to dissociate molecular ions or water cluster ions containing long-lived isotope ions, such as  $^7,^{10}\text{Be}^+$  and  $^{41,45,47}\text{Ca}^+$  even in the UHV condition.

### References

- 1) M. Wada et al.: Nucl. Phys. A **626**, 365c (1997).
- 2) M. Wada et al.: RIKEN Rev., No. 31, 56 (2000).
- 3) K. Okada et al.: J. Phys. B **36**, 33 (2003).

<sup>\*1</sup> Department of Physics, Sophia University

<sup>\*2</sup> Institute for Particle and Nuclear Studies, High Energy Accelerator Research Organization (KEK)

<sup>\*3</sup> Institute for Laser Science, University of Electro-Communications

<sup>a)</sup> M. J. Frisch et al.: Gaussian Inc. (2003).

## Experimental apparatus for X-ray spectroscopy with highly charged ion beam produced by laser ion source

S. Ozawa, M. Wakasugi, M. Okamura, M. Serata,\* T. Koizumi,\* and T. Katayama

In order to measure transitions of highly charged ions, we are developing a new experimental technique which uses soft X-rays instead of laser light. In the present situation, a high-quality X-ray beam that has a resolution and intensity as high as those of laser light is only available in the facility of synchrotron radiation, thus the ion beam and the beam transport line must be moved to the facility. The intensity of the X-ray beam is several orders of magnitude less than that of laser light. Therefore, a high-current ion beam is quite important to compensate the defect.

The experimental setup is shown in Fig. 1. The Nd:YAG laser, which has a maximum power of 450 mJ/pulse and pulse duration (FWHM) of 6 ns, is used as the laser ion source. The power density of the laser radiation flux on the ion source target is estimated to be  $1.2 \times 10^{13}$  W/cm<sup>2</sup>. The maximum repetition rate of the laser is 3 Hz during operation. The ion source is applied with a maximum bias voltage of 100 kV. The ion beam produced by the laser ion source is extracted by an acceleration voltage and focused by the einzel lens. Then the charge states of the ions are selected by the dipole magnet, and the ion beam propagates to the fluorescence detector. The ion beam is focused in the fluorescence detector by the electrostatic quadrupole lens. In the detector, the ions excited by the X-ray beam decay to the ground state with emitting fluorescence photons. The resonance spectrum is obtained by scanning the X-ray energy, and the resonance energy is obtained from the spectrum. The C<sup>4+</sup> ion is chosen

for the target because this ion has an excitation energy of 300 eV which is suitable for synchrotron radiation. The level scheme of the C<sup>4+</sup> ion is shown in Fig. 2. The detector has a cryopump system for achieving high vacuum ( $4 \times 10^{-6}$  Pa) for the suppression of noise coming from the collisions of ions and residual gas molecules.<sup>1)</sup> Four microchannel plates (MCPs) of 30 mm aperture (Hamamatsu 2224-21SFX) are mounted in the detector. A faraday cup of 10 mm aperture and a beam profile viewer made of ZnS are also located in the detector.

To verify the feasibility of the X-ray spectroscopy experiment, we estimated the count rate of fluorescence photons. Figure 3 shows a signal from the faraday cup of the fluorescence detector. The apertures of the slits located in the entrance and the exit of the dipole magnet are  $20 \times 20$  mm and  $6 \times 6$  mm, respectively.

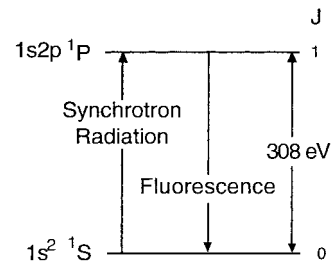


Fig. 2. Level scheme of C<sup>4+</sup> ion.

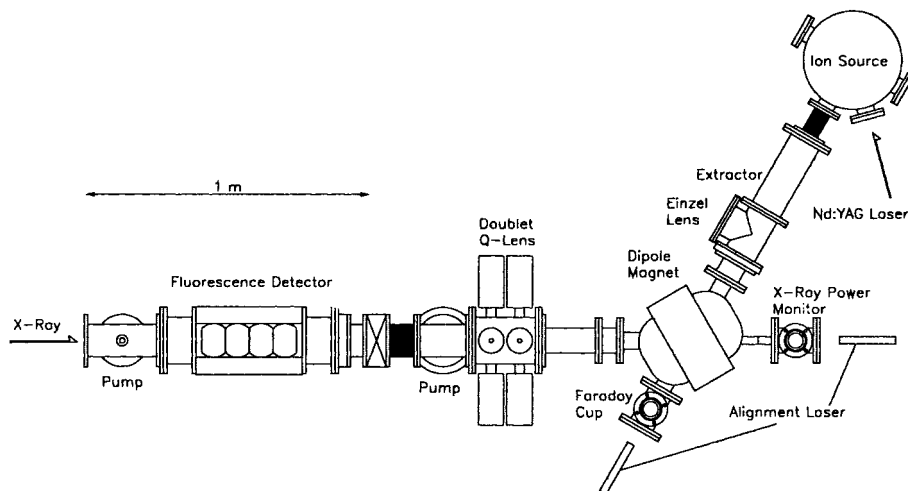


Fig. 1. Layout of the experimental setup.

\* Department of Physics, Rikkyo University

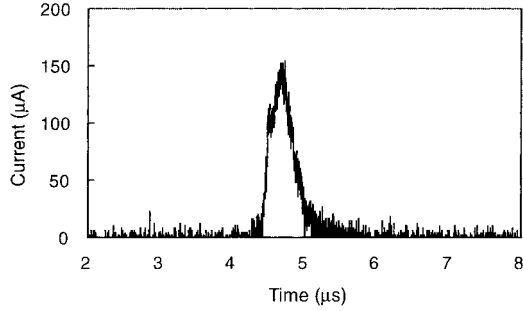


Fig. 3. Current of  $C^{4+}$  ion at the detector. Ions are accelerated by the voltage of 26 kV.

From the Fig. 3, the number of ions with a size of 10 mm is evaluated to be  $1.3 \times 10^8$  ions/bunch. The count rate of the fluorescence (CR) is calculated by the following formula. The parameters are summarized in Table 1.

$$CR = B \cdot \frac{\rho_x}{\Delta\nu} \cdot N_i \cdot t \cdot f_i \cdot R_{\text{laser}} \cdot \varepsilon_{\text{mcp}} \cdot \Omega_d \quad (1)$$

Table 1. Parameters for estimation of the signal count rate.

Spontaneous transition probability (/s)	$A$	$8.873 \times 10^{11}$
Power density of X ray ( $J/m^3$ )	$\rho_x$	$1.6 \times 10^{-5}$
Repetition rate of laser (/s)	$R_{\text{laser}}$	3
Band width of X ray (Hz)	$\Delta\nu$	$7.4 \times 10^{13}$
Quantum efficiency of MCP	$\varepsilon_{\text{mcp}}$	0.4
Solid angle of detector	$\Omega_d$	0.005
Interaction rate	$f_i$	250
Number of ions (/bunch)	$N_i$	$1.3 \times 10^8$
Interaction time (s)	$t$	$2 \times 10^{-9}$

The spontaneous transition probability (Einstein coefficient) of the target transition is  $8.873 \times 10^{11}/s$ .<sup>2)</sup> The induced transition coefficient ( $B$ ) is calculated from the spontaneous transition probability. The CR is estimated to be 0.3 cps. The X-ray intensity of  $10^{12}$  photons/s/0.1%bw is used for the estimation, because it is a realistic value for synchrotron radiation.<sup>3,4)</sup> The result indicates that the ion beam current enables us to carry out an X-ray spectroscopy experiment with synchrotron radiation. Under the present condition, the count rate of noise was measured to be 3 cps. As compared to the noise from the ion beam, the noise from the X-ray beam oscillated by synchrotron radiation is negligible. The noise from the X-ray beam was measured at the beam line (BL-16B) of KEK Photon Factory (Proposal No.2002G023).<sup>4)</sup>

By improving of the noise level, we can increase the number of incident ions to the fluorescence detector. Consequently, we can use X rays with high resolution because a high-resolution beam has an intensity lower than the value in Table 1. If an experiment with X rays with a resolution ( $E/\Delta E$ ) of 10000 is possible, the excitation energy of the target ions will be obtained in the accuracy of more than  $10^{-5}$ . In the case of the  $1s^2 2s \ ^2S_{1/2} - 1s^2 2p \ ^2P_{1/2}$  transition of  $U^{89+}$ , it corresponds to 0.001 eV, and the accuracy will be one order of magnitude higher than that in a previous experiment.<sup>5)</sup>

#### References

- 1) M. Wakasugi et al.: Nucl. Instrum. Methods Phys. Res. A **419**, 50 (1998).
- 2) [http://physics.nist.gov/cgi-bin/AtData/main\\_asd](http://physics.nist.gov/cgi-bin/AtData/main_asd)
- 3) <http://www.spring8.or.jp/>
- 4) <http://pfwww.kek.jp/>
- 5) J. Schweppe et al.: Phys. Rev. Lett. **66**, 1434 (1991).

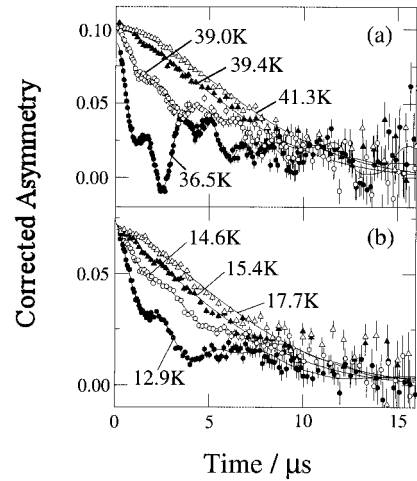
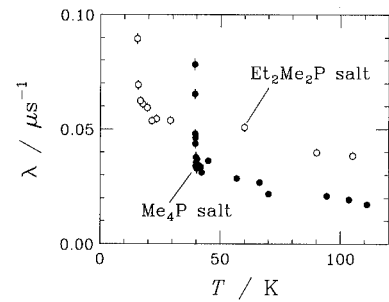
## $\mu$ SR study on magnetic property of $[\text{Pd}(\text{dmit})_2]$ salts<sup>†</sup>

S. Ohira, M. Tamura, R. Kato, I. Watanabe, and M. Iwasaki

The magnetic properties of low-dimensional quantum spin systems have been of interest in recent years. In particular, the magnetic properties of a frustrated two-dimensional (2D) Heisenberg triangular lattice antiferromagnet with  $S = 1/2$  have been discussed theoretically with much attention. However, the existing substance is only few, thus the detailed magnetic properties of these systems have not been sufficiently understood.  $[\text{Pd}(\text{dmit})_2]$  salts (dmit = 1,3-dithiol-2-thione-4,5-dithiolate) have 2D distorted triangular lattice structures with spin-1/2, thus the spin frustration operates here. Some of these salts have the antiferromagnetic (AFM) ground state.<sup>1,2)</sup> To understand the magnetic properties of such systems at finite temperatures, we carried out a muon spin relaxation ( $\mu$ SR) measurement on two salts,  $\beta'$ - $\text{Me}_4\text{P}[\text{Pd}(\text{dmit})_2]_2$  (**1**) and  $\beta'$ - $\text{Et}_2\text{Me}_2\text{P}[\text{Pd}(\text{dmit})_2]_2$  (**2**), where Me =  $\text{CH}_3$  and Et =  $\text{C}_2\text{H}_5$ .

The experiment was carried out at the RIKEN-RAL Muon Facility in the UK, using a  $^4\text{He}$  cryostat down to 1.5 K. Polycrystalline samples **1** and **2** were respectively wrapped with a silver foil to have a plate shape with  $20 \times 20 \times 1 \text{ mm}^3$ , and fixed onto the sample holder of the cryostat.

In the ZF- $\mu$ SR measurement, an AFM transition was observed at 40 K in **1** and at 15 K in **2** (Fig. 1). A muon spin relaxation due to nuclear dipole fields was observed above  $T_N$ , while muon spin precession signals were observed below  $T_N$ . The time spectra above  $T_N$  were fitted with  $A(t) = Ae^{-(\sigma t)^2}e^{-\lambda t}$ , where  $\sigma$  is the distribution width of the random internal field at the muon site, and  $\lambda$  is the muon spin relaxation rate due to dynamically fluctuating internal fields. The background has already been subtracted. The temperature dependence of  $\lambda$  for the two salts is shown in Fig. 2. We note that the AFM transition in **1** is quite sharp compared with that in **2**. The most important parameter affecting  $T_N$  in these salts is not the distance between the layers but the ratio of the small transfer integral to the large one in the layer, which shows a deviation from the regular triangular lattice. The values for **1** and **2** are 0.6 and 0.8 respectively.<sup>3)</sup> The growth of  $\xi$ , which emerges from the intralayer anisotropy, is rapidly exponential in the square lattice case, such that it yields a 3D ordering in the presence of nonzero interlayer couplings.<sup>4)</sup> Therefore, it is expected that the growth of  $\xi$  in **1** is more rapid than that in **2** as a re-

Fig. 1. ZF- $\mu$ SR time spectra of (a) **1** and (b) **2**.Fig. 2. Temperature dependences of relaxation rates of  $\text{Me}_4\text{P}$  salt (**1**) and  $\text{Et}_2\text{Me}_2\text{P}$  salt (**2**).

sult of a more distorted packing. The sharp increase in  $\lambda$  just above  $T_N$  observed for **1** is consistent with this. Our result experimentally shows how  $\xi$  grows depending on the degree of anisotropy of the triangular lattice by observing the critical behavior for the AFM ordering.

### References

- 1) T. Nakamura et al.: J. Mater. Chem. **11**, 2159 (2001).
- 2) M. Tamura and R. Kato: J. Phys.: Condens. Matter **14**, L729 (2002).
- 3) S. Rouzière et al.: Phys. Rev. B **60**, 3113 (1999).
- 4) M. Tamura and R. Kato: J. Physique IV-Proc., in press.

<sup>†</sup> Condensed from the article in J. Physique IV-Proc., in press.

# A change in the Cu-spin fluctuations studied by $\mu$ SR in $\text{La}_{2-x}\text{Sr}_x\text{CuO}_4$ at approximately 100 K

I. Watanabe, T. Adachi,\*<sup>1</sup> Y. Koike,\*<sup>1</sup> and K. Nagamine\*<sup>2</sup>

One of the fascinating models for describing the mechanism of the high- $T_c$  superconductivity is the so-called stripe model.<sup>1)</sup> This model assumes the microscopic segregation of spins and holes in the  $\text{CuO}_2$  plane forming stripes, which has theoretically been discussed to be possibly important for the occurrence of the high- $T_c$  superconductivity.<sup>2)</sup> In order to clarify the correlation between the dynamical properties of spins and holes, precise zero-field muon-spin-relaxation (ZF- $\mu$ SR) measurements have been carried out on  $\text{La}_{2-x}\text{Sr}_x\text{CuO}_4$  (LSCO) at the RIKEN-RAL Muon Facility over a wide range of hole concentrations from  $x = 0.024$  to 0.15, probing a change in Cu-spin dynamics at high temperatures of approximately 100 K at which hole domains are expected to be formed.

Time spectra measured at high temperatures are analyzed using the function of  $A_0 e^{-\lambda t} G_z(\Delta, t)$ .  $A_0$  and  $\lambda$  are the initial asymmetry at  $t = 0$  and the dynamical depolarization rate, respectively.  $G_z(\Delta, t)$  is the static Kubo-Toyabe function with a half-width of  $\Delta$  describing the distribution of the nuclear-dipole field at the muon site.

Figure 1 shows the temperature dependence of  $\lambda$  of LSCO with  $x = 0.115$ .  $\lambda$  starts to increase monotonically with decreasing temperature at approximately 100 K, showing a change in the dynamics of the Cu-spin fluctuations. For convenience, the temperature at

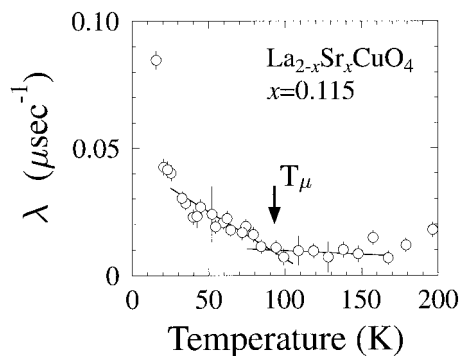


Fig. 1. Temperature dependence of the dynamical muon-spin depolarization rate,  $\lambda$ , of  $\text{La}_{2-x}\text{Sr}_x\text{CuO}_4$  with  $x = 0.115$ .

which  $\lambda$  starts to increase at a high temperature with decreasing temperature is named  $T_\mu$ , as shown by an arrow in Fig. 1. Solid lines in Fig. 1 show the best-fit results using a linear function. Figure 2 displays the  $T_\mu$ 's of all samples as open circles. The superconducting transition temperatures determined from the resistivity measurements are also displayed as open triangles.

The temperature,  $T_{\rho_{\min}}$ , at which the resistivity is the minimum is read from figures in the literature<sup>3-5)</sup> and plotted in Fig. 2 by closed triangles and squares. It is found that the  $x$  dependence of  $T_\mu$  is in good agreement with that of  $T_{\rho_{\min}}$ . This means that the origin of  $T_\mu$  is related to the localization of holes in the normal state. Therefore, the present study proves the coupling between the localization of holes and the change of dynamics of the Cu-spin fluctuations, which is an important feature of the stripe model.

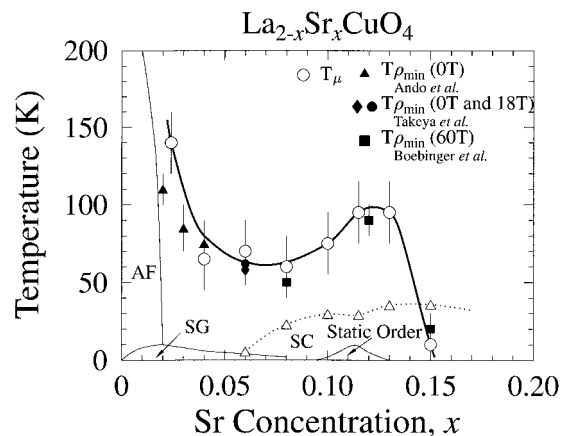


Fig. 2. Phase diagram of  $\text{La}_{2-x}\text{Sr}_x\text{CuO}_4$ . Lines are guides for the eyes.

## References

- 1) J. M. Tranquada et al.: *Nature* **375**, 561 (1995).
- 2) V. J. Emery and S. A. Kivelson: *Physica C* **235/240**, 189 (1994).
- 3) G. S. Boebinger et al.: *Phys. Rev. Lett.* **77**, 5417 (1996).
- 4) J. Takeya et al.: *Phys. Rev. Lett.* **88**, 077001 (2002).
- 5) Y. Ando et al.: *Phys. Rev. Lett.* **88**, 137005 (2002).

\*<sup>1</sup> Department of Applied Physics, Tohoku University

\*<sup>2</sup> Meson Science Laboratory, Institute of Materials Structure Science, High Energy Accelerator Research Organization (KEK)

**$^{99}\text{Ru}$  Mössbauer spectroscopic study of  $\text{CaRuO}_3$  (1)**Y. Kobayashi, T. Okada, H. Haba, S. Jimbo,\*<sup>1</sup> T. Taniguchi,\*<sup>1</sup> Y. Noro,\*<sup>2</sup> and Y. Nagata\*<sup>1</sup>

Following the discovery of unconventional superconductivity in copper-free layered perovskite  $\text{Sr}_2\text{RuO}_4$ ,<sup>1)</sup> the electronic, magnetic, and superconducting properties of ruthenium oxides (ruthenates) have been attracting strong interest in the past few years.<sup>2-5)</sup> In particular, a series of ruthenates,  $(\text{Ca}, \text{Sr})_{n+1}\text{Ru}_n\text{O}_{3n+1}$ , have been known to show a wide variety of magnetic properties, where the electron configuration of Ru ions is  $4d^4$  in the low-spin state.  $\text{SrRuO}_3$  and  $\text{CaRuO}_3$ , which are end members of this series, have nearly cubic and slightly distorted cubic perovskite structures, respectively. Although both ruthenates exhibit similar chemical and structural characteristics, their magnetic properties are quite different. The results of static magnetic measurement, neutron diffraction, and Mössbauer studies well established that  $\text{SrRuO}_3$  is an itinerant ferromagnet with a Curie temperature ( $T_c$ ) of 165 K. On the other hand, the magnetic properties of  $\text{CaRuO}_3$  at low temperatures are not yet thoroughly understood, as compared with those of  $\text{SrRuO}_3$ . The recent literature contains contradictory results, for example,  $\text{CaRuO}_3$  is a Pauli paramagnet, an exchange-enhanced paramagnet, an antiferromagnet, or spin-glass with long-range ordering.

We have applied  $^{99}\text{Ru}$  Mössbauer spectroscopy to the series  $(\text{Ca}, \text{Sr})_{n+1}\text{Ru}_n\text{O}_{3n+1}$  in order to clarify the magnetic ground state of  $\text{CaRuO}_3$  as well as to understand comprehensively the origin of the magnetic properties of this series.

As the electronic state of the ruthenates is very sensitive to the disorder around Ru ions, pure samples are required to avoid the influences of magnetic impurities and defects. Single crystals of  $\text{CaRuO}_3$  were prepared by the flux method with powdered samples as the starting material. Flux of a mixture of polycrystalline  $\text{CaRuO}_3$  and  $\text{CaCl}_2$  was fired at 1300 C for 5 h and then cooled to 1100 C at the rate of 1 C/h. After the flux was removed by washing out the crystals, the chemical composition, the X-ray diffraction pattern, the magnetization, and the electrical resistivity were measured. The above results and the characterizations were described in detail in Ref. 6.

The Mössbauer source nuclide  $^{99}\text{Rh}$  ( $T_{1/2} = 15.0$  d) was produced by the  $^{99}\text{Ru}(p, n)^{99}\text{Rh}$  reaction with 12 MeV protons accelerated by the AVF Cyclotron. Metal powder of enriched  $^{99}\text{Ru}$  was used as the target, and the irradiated target was used as the Mössbauer source with no prior heat or chemical treatment.<sup>7)</sup> As the Mössbauer  $\gamma$ -transition of  $^{99}\text{Ru}$  is as high as

90 keV, both the source and absorber of  $\text{CaRuO}_3$  were kept below 5 K.  $^{99}\text{Ru}$  Mössbauer spectra were obtained using the conventional Mössbauer spectrometer.

The temperature dependence of the magnetic susceptibility of  $\text{CaRuO}_3$  follows the Curie-Weiss law in the high-temperature region above about 50 K, but gradually deviates from the law upon lowering the temperature to 1.7 K. The effective paramagnetic moment ( $p_{eff}$ ) and the paramagnetic Curie temperature ( $\theta$ ) are derived to be  $2.82\mu_B$  and  $-77$  K, respectively.

The  $^{99}\text{Ru}$  Mössbauer spectra on  $\text{CaRuO}_3$  were measured at 5 and 2 K. The spectrum at 5 K is shown in Fig. 1. The spectra down to 2 K apparently consist of doublets with slight asymmetry, as typically observed in the case of an electric quadrupole interaction with no appreciable hyperfine magnetic interaction, and were analyzed satisfactorily under the assumption of a pure electric field gradient with an axial symmetry. The derived isomer shift and quadrupole splitting are  $-0.31$  mm/s and  $-0.33$  mm/s, respectively. Our Mössbauer results of  $\text{CaRuO}_3$  are consistent with the absence of anomaly in the magnetization measurement. Thus, on the basis of the results of the present study it is concluded that  $\text{CaRuO}_3$  has no magnetic interactions between 2 and 300 K.

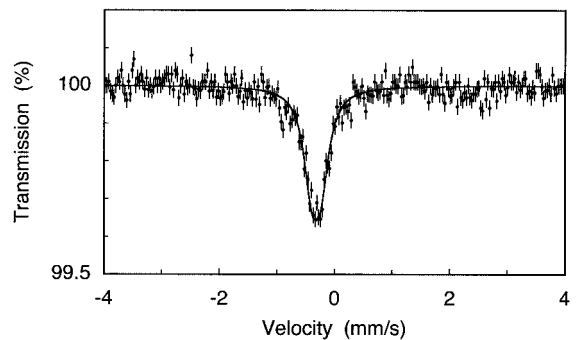


Fig. 1. A  $^{99}\text{Ru}$  Mössbauer spectrum of  $\text{CaRuO}_3$  single crystals at 5 K. The isomer shift is taken relatively to ruthenium metal.

## References

- 1) Y. Maeno et al.: Nature **372**, 532 (1994).
- 2) K. Yoshimura et al.: Phys. Rev. Lett. **83**, 4397 (1999).
- 3) H. Mukuda et al.: Phys. Rev. B **60**, 12279 (1999).
- 4) I. Felner et al.: Phys. Rev. B **62**, 11332 (2000).
- 5) I. Felner et al.: Physica B **337**, 310 (2003).
- 6) A. Koriyama et al.: J. Alloys Compd. **171**, 339 (2003).
- 7) Y. Kobayashi et al.: Inorg. Chem. **31**, 4570 (1992).

\*<sup>1</sup> Department of Physics, Aoyama Gakuin University

\*<sup>2</sup> Kawazoe Future Technology

## Reactions of $^{57}\text{Mn}$ implanted in solid oxygen

Y. Yamada,<sup>\*1</sup> Y. Kobayashi, H. Ueno, K. M. Kubo,<sup>\*2</sup> H. Watanabe, A. Yoshimi,  
H. Miyoshi,<sup>\*3</sup> D. Kameda,<sup>\*3</sup> and K. Asahi

We are planning to perform experiments to study the electronic structures of  $^{57}\text{Fe}$  atoms decayed from  $^{57}\text{Mn}$  implanted in solid oxygen by in-beam Mössbauer spectroscopy, in order to determine iron species with extraordinarily high oxidation states. Here, we briefly discuss a preliminary study on novel iron oxide species produced by laser evaporation and matrix isolation in relation to our previous study on  $^{57}\text{Mn}$  atoms implanted in  $\text{KMnO}_4$  to produce Fe(VIII) species.

Reactions of laser-evaporated iron atoms with oxygen gas, which produced various novel iron oxide species, were studied.<sup>1)</sup> Oxidation of iron is a fundamentally and chemically interesting subject because it is related to corrosion of materials and catalytic reactions. The simplest oxidation reaction of iron is the reaction of an iron atom with oxidizing gas. Thus, we investigated the reactions of laser-evaporated Fe atoms with oxygen gas by matrix isolation. Laser-evaporated iron atoms were isolated in low-temperature Ar matrices and their chemical reactions with oxygen were investigated by conventional Mössbauer spectroscopy. Reactions of these iron atoms with oxygen produced FeO, Fe(O<sub>2</sub>), FeO<sub>3</sub>, (O<sub>2</sub>)FeO<sub>2</sub>, and OFeO. While Fe(O<sub>2</sub>) maintains an O-O bond and has a side-on O<sub>2</sub> molecule, O-Fe-O has two O atoms without an O-O bond between them. In the case of laser-evaporated iron atoms, the highest oxidation state found among the iron oxide species was VI: FeO<sub>3</sub>.

The  $^{57}\text{Fe}$  atoms decayed from  $^{57}\text{Mn}$  have extremely higher energy than the laser-evaporated Fe atoms upon implantation and decay, which provides important information on chemistry under extreme conditions and on the production of novel species. We have obtained well-resolved in-beam Mössbauer spectra of  $^{57}\text{Fe}$  arising from  $^{57}\text{Mn}$  implanted in  $\text{KMnO}_4$  between 11 K and 155 K.<sup>2)</sup> A manganese atom in  $\text{KMnO}_4$  is in a VII state and forms a  $[\text{MnO}_4]^-$  tetrahedron. On the basis of the Mössbauer parameters, the  $^{57}\text{Fe}$  atoms in Mn sites in a  $[\text{MnO}_4]^-$  tetrahedron were found to have an unusually high valence state of Fe(VIII).

While  $^{57}\text{Fe}$  implanted in  $\text{KMnO}_4$  may suffer geometrical hindrances of  $[\text{FeO}_4]^-$  in a solid  $\text{KMnO}_4$  crystal,  $^{57}\text{Fe}$  implanted in solid oxygen may have less geometrical restriction of the matrix, and may react to form Fe(VIII) species with a stable geometrical structure. As the highly charged  $^{57}\text{Mn}$  atoms are implanted in

solid oxygen with high translational energy, Mn(VII) oxide species may be produced and trapped in a solid oxygen matrix, followed by a decay process forming  $^{57}\text{Fe}$  oxide species. The novel iron Fe(VIII) oxide species may have different structures from those obtained by our previous study of  $^{57}\text{Mn}$  implanted in solid  $\text{KMnO}_4$ . This experiment will confirm our finding of the unusually high valence state of Fe(VIII). Furthermore, the in-beam Mössbauer technique is very sensitive such that a very small amount of  $^{57}\text{Fe}$  can be detected. Consequently, the iron oxide species produced by implantation can be well isolated, and their simple Mössbauer spectra can be analyzed. Although various by-products are also expected to be produced, the Mössbauer parameters of various iron oxide species have been obtained by our previous experiments using the laser-evaporated iron atoms, which makes the analysis of the Mössbauer spectra easier.

Prior to the experiments of  $^{57}\text{Mn}$  implanted in solid oxygen, we performed an experiment using laser-evaporated iron atoms. Laser-evaporated  $^{57}\text{Fe}$  atoms were deposited on solid oxygen (20 K), and their Mössbauer spectra were obtained. The amount of  $^{57}\text{Fe}$  deposited on solid oxygen was varied in order to determine the effect of the products. The type of products on the surface of solid oxygen varied depending on the amount of iron atoms. When the amount of iron atoms is large, the Mössbauer spectra of the products show magnetic splitting because of the magnetically ordered iron oxide produced on the low-temperature solid oxygen surface. In contrast, when the amount of iron atoms is small, magnetic splitting is not observed in the Mössbauer spectra of the products and a doublet absorption is observed, which is attributed to the isolated single Fe(O<sub>2</sub>). It was demonstrated that laser-evaporated iron does not have sufficient translational energy for implantation in solid oxygen; rather, most of the reactions take place on the surface of solid oxygen.

### References

- 1) Y. Yamada, H. Sumino, Y. Okamura, H. Shimasaki, and T. Tominaga: *Appl. Radiat. Isot.* **52**, 157 (2000).
- 2) Y. Kobayashi, M. K. Kubo, T. Saito, H. Ueno, H. Miyoshi, K. Yoneda, W. Sato, and Y. Yamada: *J. Radioanal. Nucl. Chem.* **255**, 403 (2003).

<sup>\*1</sup> Department of Chemistry, Tokyo University of Science

<sup>\*2</sup> College of Liberal Arts, International Christian University

<sup>\*3</sup> Graduate School of Science and Engineering, Tokyo Institute of Technology



## Accumulation of various trace elements in *Lotus japonicus* using the multitracer technique

R. Hirunuma, K. Igarashi, H. Saito, Y. Miyazawa, H. Haba, H. Takeichi, T. Abe, and S. Enomoto

Newly discovered toxic metal hyperaccumulator plants (*Lotus japonicus*) hold promise for phytoremediation of toxic-metal-polluted soil and rivers.

*Lotus japonicus* has been proposed as a model leguminous plant for molecular genetic study. We report a study of uptake, distribution, and accumulation of various trace elements in *Lotus japonicus* (Miyakojima MG-20 and Gifu B-129) using the multitracer technique.

Forty seedlings of each variety (Miyakojima MG-20 and Gifu B-129) were grown on soil for about 2 months in a growth chamber under a daily 16 h light/8 h dark cycle at 25°C. After blooming and the start of seed growth, the plants were cultivated in a nutrient solution containing a multitracer prepared using an Ag target. Five plants of each variety were transplanted to a 1000 mL plastic pot containing 500 mL of the multitracer solution for 1 week. The plant samples were in contact with the solution via their roots. After 1 week, the plants were carefully removed from the solution and divided into roots, primary shoot (shoot apex; upper part; middle part; lower part), secondary shoots, flowers, pods, and seeds. The roots were washed with a nutrient solution without multitracer for one minute using an ultrasonic cleaner and dried with filter paper. These samples were dried at 60°C for 3 days. The radioactivities in these samples were determined by  $\gamma$ -ray spectrometry using high-purity Ge detectors.

The behaviors of Be, Na, Sc, V, Cr, Mn, Fe, Co, Zn, As, Se, Rb, Sr, Y, Zr, Tc, Ru, and Rh were determined. The amounts of trace elements in the whole plant and the above-ground parts are shown in Table 1. In the

Table 1. Uptake (%) of trace elements in *Lotus japonicus*.

	Uptake (%) in the whole plant		Uptake (%) in the above-ground parts	
	Miyakojima MG-20	Gifu B-129	Miyakojima MG-20	Gifu B-129
As	43	53	4.22	1.67
Be	64	68	0.29	0.04
Co	88	82	8.10	6.76
Cr	51	66	0	0
Fe	45	67	0.28	0.11
Mn	92	85	19.05	12.42
Na	18	23	6.69	2.76
Rb	68	70	51.92	46.24
Rh	46	60	0.17	0.29
Ru	48	69	0	0
Sc	54	63	0	0
Se	65	72	3.72	1.84
Sr	32	39	24.76	19.34
Tc	46	50	32.99	22.49
V	67	65	0.33	0
Y	63	71	0.55	0.12
Zn	87	81	48.32	47.03
Zr	44	61	0	0

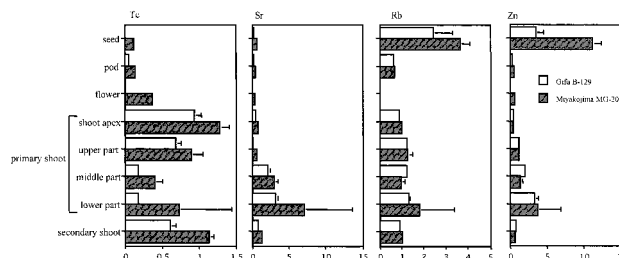


Fig. 1. Uptake ratios of Tc, Sr, Rb, and Zn into plant parts (Uptake rate (%/g) in each part/uptake rate (%/g) in whole plant).

whole plant, uptakes of all elements except Na were high. The uptakes of trace elements in the whole plant of Miyakojima MG-20 were the same as those of Gifu B-129. In the above-ground parts, Cr, Ru, Sc, and Zr were not detected, and Be, Fe, Rh, V, and Y were only slightly detected. On the other hand, uptakes of Tc, Sr, Rb, and Zn were high. Thus, while Cr, Ru, Sc, Zr, Be, Fe, Rh, V, and Y were not absorbed or absorbed only in small amounts into plants, Tc, Sr, Rb, and Zn were confirmed to be absorbed. Although Fe is an essential element, the amount of Fe absorbed into plants was nominally detectable. The uptakes of Tc, Sr, Rb, and Zn in Miyakojima MG-20 were higher than those in Gifu B-129.

Figure 1 shows the uptake ratios of Tc, Sr, Rb, and Zn into individual parts. Technetium was found to be widely distributed among primary and secondary shoots. High Tc concentration was found in primary (shoot apex and upper part) and secondary shoots. Low Tc concentration was found in seeds, pods, and flowers. Strontium was found mainly in the primary shoot. Rubidium was found to be widely distributed among all parts except the flowers. High Rb concentration was found in seeds. Zinc was found to be widely distributed among all parts. High Zn concentration was found in seeds and the primary shoot (lower part). The accumulation of Zn into seeds of Miyakojima MG-20 was the highest.

In the next experiment, the transport of various elements from soil to plants will be investigated and the transfer factor of *Lotus japonicus* will be calculated.

## Effects of carnosine ( $\beta$ -alanyl-L-histidine) on the absorption of various trace elements in rats

K. Igarashi, R. Hirunuma, H. Haba, S. Kimura\*, and S. Enomoto

Carnosine ( $\beta$ -alanyl-L-histidine) was first identified in beef extract in 1900. It is found in millimolar concentrations in skeletal muscles and brains of animals. Numerous studies have reported the specific properties of carnosine. One of the major functions of carnosine is to act as a natural antioxidant. It is an efficient oxygen scavenger and protects phage against  $\gamma$ -irradiation which causes oxidative DNA damage.<sup>1)</sup> On the other hand, carnosine has a chelating property for metals. Carnosine-metal complexes exhibit a superoxide dismutase (SOD)-like activity.<sup>2)</sup> Furthermore, the pharmacological activity of the carnosine-Zn complex has been studied in recent years.<sup>3)</sup> However, it is possible that carnosine may influence the absorption of metals.

Thus, to investigate the effects of carnosine on the absorption of metals, we determined the uptake rate of various trace elements in rats administered carnosine using a multitracer technique.

A multitracer solution was prepared from an Ag target irradiated with a heavy-ion beam of 135 MeV/nucleon accelerated in the RIKEN Ring Cyclotron. Rats were administered the multitracer solution with carnosine (dose, 10 mg/rat) into the stomach through a tube. The rats were kept in cages and sacrificed 1, 3, 6 and 24 h after carnosine administration. Then, the liver, kidney, bone, muscle, brain and blood were collected. These samples were placed in a Ge-detector, and the radioactivities of the multitracers were measured. In this study, the amounts of Co, Zn, As and Se incorporated into the various tissues and blood of rats were determined.

Figure 1 shows the uptake rates of Zn into the blood, intestine, liver, kidney, brain and muscle in rats. In both the control and the carnosine-administered rats, the rate of Zn uptake into the blood was maintained at the same level after 24 h. The amount of Zn uptake into the intestine decreased in a time-dependent manner, while those into the liver, kidney, brain and muscle increased at 24 h. The uptake rates of Zn in the blood and tissues of the carnosine-administered rats were significantly lower than those of the control rats. Similarly, the carnosine-administered rats exhibited significant decrease in uptake rates of Co into the blood and tissues compared with the control

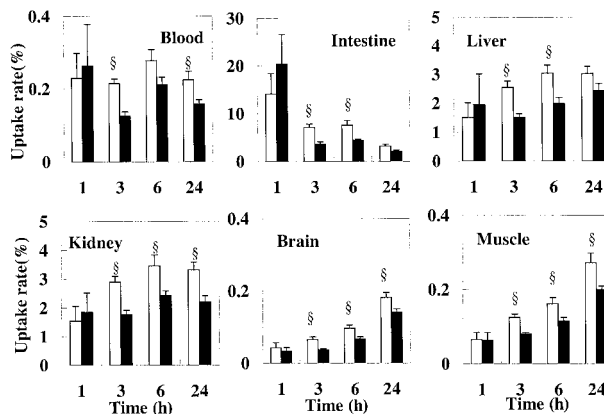


Fig. 1. The uptake rates of Zn into the blood, intestine, liver, kidney, brain and muscles in rats. □: control rats, ■: carnosine-administered rats. §Significant differences were observed between control and carnosine-administered rats ( $P < 0.05$ ).

rats. Furthermore, the carnosine-administered rats exhibited slightly reduced Se uptake rates into the blood and tissues compared with the control rats. Although, the uptake rates of As into the blood, intestine and kidney of the carnosine-administered rats were significantly lower than those of the control rats, no significant differences in As uptake rates into other tissues were observed between the carnosine-administered and control rats.

These results suggest that carnosine administration decreased uptake rates of Zn, Co, Se and As into the body. However, it is considered that the results of this study were affected by a substantial difference in administration volume between carnosine and trace elements.

### References

- 1) T. A. Dahl et al.: Photochem. Photobiol. **47**, 357 (1988).
- 2) R. Kohen et al.: Free Radical Res. Commun. **12/13**, 179 (1991).
- 3) M. Seiki et al.: Folia Pharmacologica Japonica, **95**, 257 (1990).

\* Graduate School of Human Life Sciences, Showa Women's University

## Effects of carnosine ( $\beta$ -alanyl-L-histidine) on the absorption of iron in rats

K. Igarashi, R. Hirunuma, S. Kimura,\* and S. Enomoto

Iron deficiency is probably the most frequent nutritional disorder in the world. One of the main causative factors is the poor absorption of dietary iron. There are two types of iron in food. Heme iron from meat, poultry and fish has a high intestinal absorption efficiency, because heme iron directly enters the mucosal cells. On the other hand, the intestinal absorption of nonheme iron, the main form of dietary iron, is influenced by other food components. The bioavailability of nonheme iron has been extremely low because inhibitors, such as phytic acid and polyphenols, bind nonheme iron in the intestinal lumen. The absorption rate of vegetable iron is only about 1–2%.<sup>1)</sup> Therefore, the enhancement of nonheme iron absorption is important for improving iron nutrition.

It is well established that the bioavailability of nonheme iron from foods is enhanced by vitamin, organic acid, meat, poultry and fish. Ascorbic acid and citric acid maintain iron in a more soluble and absorbable form, and prevent its binding to inhibitory ligands.<sup>2)</sup> Although meat stimulates nonheme iron absorption, the factor in meat responsible for enhancing nonheme iron absorption is yet to be identified.

A number of putative roles have been ascribed to the histidine-containing peptides. Carnosine ( $\beta$ -alanyl-L-histidine) and anserine ( $\beta$ -alanyl-3-methyl-L-histidine) are observed in millimolar concentrations in the skeletal muscles and brains of animals, although there are substantial differences in their tissue distributions. These compounds have been proposed to act as natural antioxidants *in vivo*.<sup>3)</sup> Furthermore, carnosine was reported to enhance recovery from exhaustion due to its buffering capacity.<sup>4)</sup> A significant effect of carnosine is its ability to prevent, or partly reverse, lens cataract. Recently, the pharmacological activity of the carnosine-metal complex has been studied.<sup>5)</sup>

Thus, to identify the factor in meat that enhances of the nonheme iron absorption, we determined the

effects of carnosine on the absorption of iron in rats. We used the cannulation system for investigating iron absorption in rats that were administered with carnosine because it is effective determining of the biological response to infused samples into the stomach or intestine in conscious rats.

Six-week-old male Wistar rats are purchased and housed in stainless steel cages in a temperature and light-controlled room. The method of cannula preparation is as described by Taguchi *et al.* and Spannagel *et al.*<sup>6,7)</sup> That is, the rats are anesthetized with enflurane and prepared with Silastic cannula for carnosine and iron administrations into the stomach. They are also prepared with a jugular vein cannula for collecting blood. Cannulas from the abdominal cavity are placed under the skin to exit on the back. After closure, the rats are placed in Bollman type restraint cages modified to provide the minimum restraint possible. Three days after surgery, the rats are administered carnosine and iron into the stomach simultaneously. Then the blood is collected at regular intervals, plasma and blood cells are separated by centrifugation (3000 rpm for 15 min). To determine the bioavailability of iron, serum iron concentration is measured using a kit by the Nitroso-PSAP method.<sup>8)</sup>

### References

- 1) L. Hallberg: *Ann. Rev. Nutr.* **1**, 123 (1981).
- 2) I. M. Zijp *et al.*: *Crit. Rev. Food Sci. Nutr.* **40**, 371 (2000).
- 3) M. A. Babizhayev *et al.*: *Biochem. J.* **304**, 509 (1994).
- 4) R. Harada *et al.*: *J. Jpn. Soc. Nutr. Food Sci.* **55**, 209 (2002).
- 5) M. Seiki *et al.*: *Folia Pharmacologica Japonica* **95**, 257 (1990).
- 6) S. Taguchi *et al.*: *Jpn. J. Clin. Physiol.* **24**, 241 (1994).
- 7) A. W. Spannagel *et al.*: *Am. J. Physiol.* **270**, G128 (1996).
- 8) M. Saito *et al.*: *Bunseki kagaku* **30**, 635 (1981).

\* Graduate School of Human Life Sciences, Showa Women's University

## Multitracer screening of trace elements in brains of mice injected with lipopolysaccharide

M. Ono,\* H. Yokokawa,\* S. Enomoto, and R. Amano\*

It is well known that by injection of lipopolysaccharide (LPS) in mice, the outbreak of endotoxic shock gives rise to impediments in the blood brain barrier (BBB), as described by Minami *et al.*<sup>1)</sup> However, the behavior of trace elements in the brain has not been elucidated under these impediments. In this work, we examined the movement of trace elements in the brains of mice injected with LPS using the multitracer technique.

A multitracer solution was obtained from a Ag target irradiated for two days with a <sup>12</sup>C beam at 135 MeV/nucleon accelerated in RIKEN Ring Cyclotron. Then, the Ag target was removed by chemical separation and the multitracer was prepared as a physiological saline solution. The multitracer solution contained 8 radioisotopes, namely, <sup>46</sup>Sc, <sup>54</sup>Mn, <sup>58</sup>Co, <sup>65</sup>Zn, <sup>75</sup>Se, <sup>83</sup>Rb, <sup>88</sup>Zr, and <sup>88</sup>Y.

In this screening, two mouse groups (LPS-treated and normal groups), consisting of six 12-week-old ICR mice each, were prepared. The treated mice were injected intraperitoneally with LPS at a dose of 15 mg/kg<sup>1</sup> (dissolved in the physiological saline solution). The multitracer solution was injected intravenously *via* the tail 24 hours after LPS treatment. Blood and brain samples were obtained 30 min after the multitracer injection. The blood was centrifuged to obtain the plasma fraction. The plasma and brain samples were then freeze-dried and assayed by  $\gamma$ -ray spectroscopy using high-purity Ge detectors.

Table 1 summarizes the plasma retention rate and the brain uptake rate of <sup>46</sup>Sc, <sup>54</sup>Mn, <sup>58</sup>Co, <sup>65</sup>Zn, <sup>75</sup>Se, <sup>83</sup>Rb, <sup>88</sup>Zr, and <sup>88</sup>Y. Except for <sup>88</sup>Y, no significant

difference in plasma retention rate was observed between the LPS-treated group and the normal group. On the other hand, the brain uptake rates of <sup>54</sup>Mn, <sup>58</sup>Co, <sup>65</sup>Zn, <sup>75</sup>Se, and <sup>83</sup>Rb in LPS-treated mice were markedly lower than those in normal mice. Moreover, <sup>54</sup>Mn showed a very distinctive result: the brain uptake rate was clearly decreased while the plasma retention rate was increased, as shown in Fig. 1.

From this result, LPS is considered to cause impediments in the brain movement of <sup>54</sup>Mn. We are interested in this behavior of Mn in LPS-treated mice. Further study is required to clarify the observed behavior of <sup>54</sup>Mn using the singletracer technique.

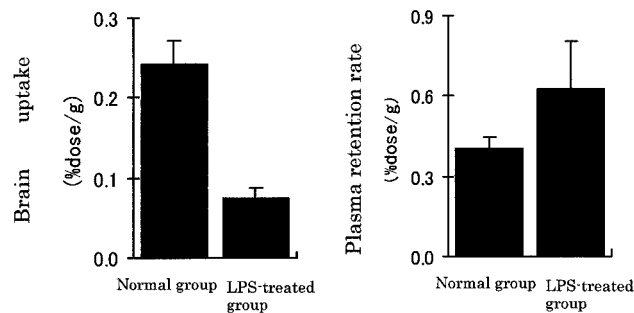


Fig. 1. <sup>54</sup>Mn brain uptake rate and plasma retention rate in mice 30 min after multitracer injection. The bar represents the mean±S.D. for six mice.

### References

- 1) T. Minami et al.: Environ. Toxicol. Pharmacol. **5**, 35 (1998).

Table 1. Brain uptake rate and plasma retention rate in mice 30 min after multitracer injection.

	Brain Uptake rate (%dose/g)		Plasma Retention rate (%dose/g)	
	Normal group	LPS-treated group	Normal group	LPS-treated group
<sup>46</sup> Sc	0.03 ± 0.006	0.04 ± 0.011	11.31 ± 1.08	11.76 ± 3.26
<sup>54</sup> Mn	0.24 ± 0.029	0.03 ± 0.007 <sup>§2</sup>	0.41 ± 0.04	0.63 ± 0.18
<sup>58</sup> Co	0.04 ± 0.009	0.08 ± 0.010 <sup>§2</sup>	1.50 ± 0.16	0.94 ± 0.18
<sup>65</sup> Zn	0.15 ± 0.014	0.04 ± 0.003 <sup>§2</sup>	0.55 ± 0.12	0.39 ± 0.20
<sup>75</sup> Se	0.03 ± 0.003	0.10 ± 0.018 <sup>§1</sup>	1.49 ± 0.18	1.15 ± 0.46
<sup>83</sup> Rb	0.07 ± 0.004	0.04 ± 0.004 <sup>§2</sup>	0.07 ± 0.02	0.09 ± 0.01
<sup>88</sup> Zr	0.01 ± 0.003	0.02 ± 0.003	6.52 ± 0.73	9.09 ± 2.82
<sup>88</sup> Y	0.01 ± 0.002	0.02 ± 0.002	3.42 ± 0.34	8.60 ± 2.84 <sup>§1</sup>

Each value represents the mean±S.D. of data from six mice. <sup>§1</sup> and <sup>§2</sup> indicate significant differences of normal group versus LPS-treated group. <sup>§1</sup>:  $P < 0.01$   
<sup>§2</sup>:  $P < 0.005$

\* School of Health Sciences, Faculty of Medicine, Kanazawa University

## Pharmacokinetic study on gastrointestinal absorption and blood disposition of vanadium ions in healthy rats using radiotracer method

H. Yasui,\* Y. Adachi,\* J. Fugono,\* H. Haba, A. Nakayama, R. Hirunuma, S. Enomoto, and H. Sakurai\*

In recent years, vanadium compounds have been demonstrated to exhibit insulinomimetic effects in *in vitro* and *in vivo* experiments, and used to treat both insulin-dependent type 1 and insulin-independent type 2 diabetes mellitus. We have reported that vanadyl complexes normalize the blood glucose level of

streptozotocin-induced type-1 diabetic rats and hereditary type-2 KK-*A<sup>y</sup>* mice.<sup>1)</sup> To understand the action mechanism of vanadium treatment, in this study, we focused on investigating the pharmacokinetics of gastrointestinal absorption and disposition of vanadium ions in the blood of healthy rats by administration of their radiotracers.<sup>2)</sup>

As shown in Fig. 1 (A), the clearance curves of <sup>48</sup>V in the blood of healthy rats receiving intravenous injection of vanadyl (<sup>48</sup>VO<sup>2+</sup>) and vanadate (<sup>48</sup>VO<sub>4</sub><sup>3-</sup>) ions were not significantly different in spite of the administration of different chemical species of vanadium ions with different oxidation states,<sup>3)</sup> probably because of the rapid reduction of vanadate to vanadyl in the blood and organs of rats which has been reported.<sup>4)</sup>

On the other hand, as shown in Fig. 1 (B), the absorption of <sup>48</sup>VO<sub>4</sub><sup>3-</sup> was found to be 3-fold higher than that of <sup>48</sup>VO<sup>2+</sup>, suggesting the chemical species-dependent transport mechanism on the gastrointestinal absorption of vanadium in animals.<sup>5)</sup> The bioavailability values of <sup>48</sup>V after oral administration of <sup>48</sup>VO<sup>2+</sup> and <sup>48</sup>VO<sub>4</sub><sup>3-</sup> ions in healthy rats were estimated to be 4.9% and 14.6%, respectively, which coincides well with the results in rats given nontracer VOSO<sub>4</sub> and NaVO<sub>3</sub>, strongly indicating the need for developing vanadium complexes with higher bioavailability which contribute to a higher hypoglycemic activity than that of vanadium ions after oral administration.

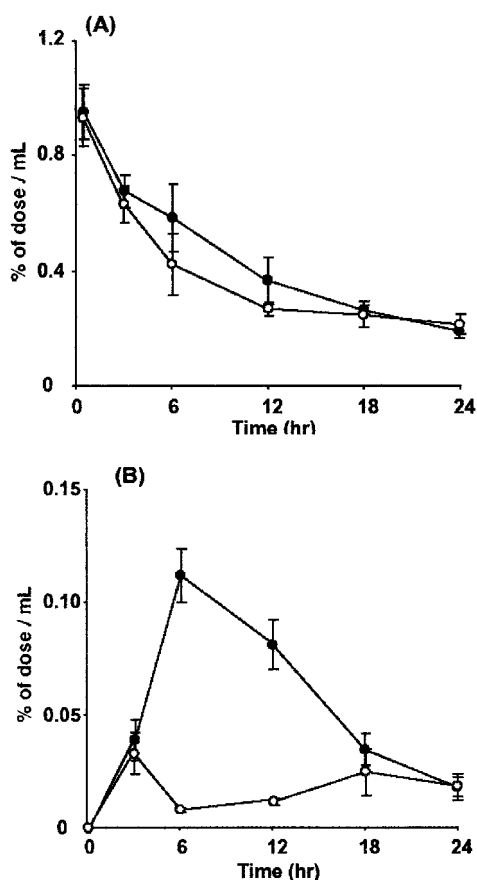


Fig. 1. Clearance curves of <sup>48</sup>V in the blood of rats given intravenous injection (A) and oral administration (B) of 500  $\mu$ L of <sup>48</sup>V solution reduced with (○; <sup>48</sup>V(IV)O<sup>2+</sup>) or without (●; <sup>48</sup>V(V)O<sub>4</sub><sup>3-</sup>) 100  $\mu$ M sodium ascorbate. Data are expressed as the means  $\pm$  SDs for 4 rats.

### References

- 1) H. Sakurai: Chem. Rec. **2**, 237 (2002); H. Sakurai et al.: Coord. Chem. Rev. **226**, 187 (2002); H. Sakurai et al.: Expert Opin. Investig. Drugs **12**, 1189 (2003).
- 2) K. Yamaoka, T. Nakagawa, and T. Uno: J. Pharmacokinetic. Biopharm. **6**, 547 (1978).
- 3) D. C. Crans and A. S. Tracey: ACS Symp. Ser. **711**, 2 (1998).
- 4) H. Sakurai, S. Shimomura, K. Fukuzawa, and K. Ishizu: Biochem. Biophys. Res. Commun. **96**, 293 (1980); M. Ding et al.: J. Inorg. Biochem. **55**, 101 (1994).
- 5) L. C. Cantley, Jr. et al.: Nature **272**, 552 (1978); A. Rolfs et al.: Curr. Opin. Gastroenterol. **17**, 177 (2001).

\* Department of Analytical and Bioinorganic Chemistry, Kyoto Pharmaceutical University

## Uptake of $^{65}\text{Zn}$ in various trophoblast cells

N. Asano,\* C. Ebihara,\* M. Kondoh,\* M. Fujii,\* S. Enomoto, and Y. Watanabe\*

Zinc is a vital metal that plays a pivotal role in the normal growth and development of the fetus. Deficiency of maternal zinc results in abnormal development of the fetus.<sup>1)</sup> During pregnancy, zinc is transferred from maternal blood to fetal blood across the placenta, and the zinc level in fetal serum is up to 2-fold higher than that in the maternal serum at the end of pregnancy.<sup>2)</sup> However, the mechanism of zinc transport in the placenta is not clear.

Zinc is a multifunctional element involved in transcription, metalloenzyme activities and maintenance of protein structure. Therefore, organisms are equipped with mechanisms for controlling intracellular zinc levels and localization. In general, intracellular zinc homeostasis is maintained by the control of zinc efflux, influx and storage. Zinc is not absorbed by simple diffusion because of its hydrophilic and highly charged properties. Zinc kinetics is regulated by specific transporters of zinc. Zinc transporters are now classified into two categories: the ZnT family of transporters, which controls zinc efflux, and the ZIP family of transporters, which controls zinc influx.<sup>3,4)</sup> For example, ZnT1 is a transporter that regulates efflux of zinc from the plasma membrane, and ZnT3 is involved in the efflux of zinc from the cytosol into the intracellular zinc pool. ZnT5 transports zinc from the cytosol into the trans-Golgi network, and ZIP1, located in the plasma membrane, plays a key role in the intracellular uptake of zinc. Deficiency of ZnT1 results in zinc toxicity and embryonic lethality, and ZnT3 is involved in the accumulation of zinc in neuron synapsis. ZnT5 plays roles in osteoblast maturation in the bone and in formation of insulin crystals by the transport of zinc into secretory granules in pancreatic  $\beta$  cells. ZnT4 functions as a transporter of zinc into breast milk during lactation in the mammary glands. Defects in ZIP4 are responsible for the onset of acrodermatitis enteropathica, an inherited disease of zinc metabolism. Thus, zinc transporters are associated with various physiological events.

The expression of some ZnT transporters, including ZnT1, ZnT2 and ZnT5, has been detected in the placenta.<sup>4,5)</sup> However, their functions have not been elucidated. Although we have investigated the expression of zinc transporters in various trophoblast cell lines, we have never examined zinc uptake. Here, we developed an assay system for measuring zinc uptake

in trophoblasts using  $^{65}\text{Zn}$ .

We used a cell culture model of human choriocarcinoma cells, BeWo and JEG-3 cells and of rodent choriocarcinoma cells, Rcho-1 cells. BeWo cells, JEG-3 cells ( $5 \times 10^5$  cells/ml), and Rcho-1 cells ( $1 \times 10^5$  cell/ml) were seeded on 24-well plates. After at least 12 hr of culture in a fetal-calf-serum-deficient medium, the cells were washed twice with HBSS solution (Ca, Mg free). Then the cells were incubated with  $5 \mu\text{M}$   $^{65}\text{ZnCl}_2$  for 1 or 30 min. The cells were washed three times with ice-cold PBS containing 1 mM EDTA, and then  $200 \mu\text{l}$  of 1% TritonX-100 was added. Radioactivity and amounts of protein in the lysate were determined. As shown in Fig. 1, the amounts of Zn uptake were different among the cells under this condition. Since zinc homeostasis is achieved through various zinc transporters, the expression profile of zinc transporters may be different among cell lines. In order to clarify the functions of zinc transporters, time-course change and dose-dependency of Zn uptake are now under consideration for the determination of Zn kinetics in trophoblasts.

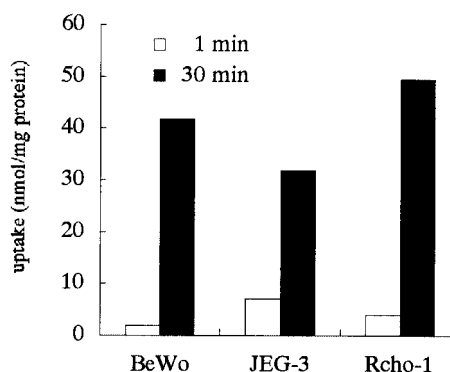


Fig. 1.  $^{65}\text{Zn}$  uptake in various trophoblast cells.

### References

- 1) J. Apgar: *Ann. Rev. Nutr.* **5**, 43 (1985)
- 2) M. Krachler et al.: *Eur. J. Clin. Nutr.* **53**, 486 (1999).
- 3) R. D. Palmiter and L. Huang: *Pflugers Arch.* **447**, 744 (2004).
- 4) J. Dufner-Beattie et al.: *J. Biol. Chem.* **278**, 50142 (2003).
- 5) J. P. Liuzzi et al.: *J. Nutr.* **133**, 342 (2003).

\* Department of Pharmaceutics and Biopharmaceutics, Showa Pharmaceutical University

## Metal-binding factor responsible for variation of concentration of trace elements under Zn-deficient condition

M. Yanaga,<sup>\*1</sup> T. Ohyama, N. Kinugawa,<sup>\*1</sup> T. Ogi,<sup>\*1</sup> M. Noguchi,<sup>\*2</sup> H. Suganuma,<sup>\*1</sup>  
K. Ishikawa,<sup>\*2</sup> R. Hirunuma, K. Takahashi, and S. Enomoto

There are many kinds of trace metal elements, such as Mn, Fe, Co, Ni, Cu and Zn, which play important roles in living organisms. Among these essential trace elements, Zn is the most important because of the variety of its biochemical and physiological actions. Previously, we determined the concentrations of trace elements in the subcellular fractions of livers of Zn-deficient mice by instrumental neutron activation analysis in order to investigate the influence of Zn deficiency on the biological behavior of trace elements.<sup>1)</sup> In this work, the Zn concentration in the nuclear fraction of Zn-deficient mice, which were fed with a Zn-deficient diet during the growth period, was lower than that of control mice. Furthermore, in the supernatant fraction, an increase in the concentrations of many of the analyzed elements was recognized in comparison with those of the control mice. However, in adult mice, which were fed with a Zn-deficient diet for 3 weeks from 8 weeks of age, such trend was not observed, although the Co concentrations in all subcellular fractions were higher than those of control as seen in growing mice. The change in concentration of trace elements should be related to the change in the concentration of metal-binding proteins. Therefore, in the present work, we attempt to analyze the affinity between trace elements and Zn-binding proteins which induce the variation of the concentrations of trace elements under the Zn-deficient condition.

Sixteen 8-week-old male mice of ICR strain were divided into two groups. Eight mice were fed with a Zn-deficient diet and the other eight with the control diet. After three weeks of treatment, their livers were removed. Eight livers of each group were altogether homogenized with Tris-HCl buffer (25 mM, pH 7.4), and then, centrifuged for 65 min at 105,000 g to remove supernatant fractions. Then, an aliquot of the supernatant fraction of each group was divided into 35 fractions by gel filtration chromatography with Sephadex G-100 using Tris-HCl buffer as eluent at a flow rate of 10 ml/h. The concentrations of trace elements and the protein content in each fraction were determined by ICP-MS and BCA protein assay method, respectively. The fractions which have high Zn to protein ratios (marked A, B and C in Fig. 1) were poured into centrifuge filter tubes, and then a multitracer solution was added. After centrifugation, the radioac-

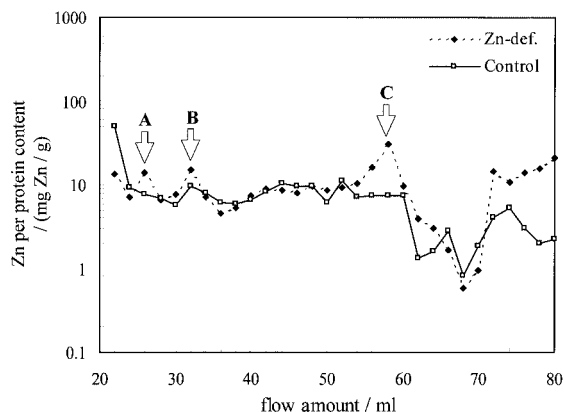


Fig. 1. Zinc to protein ratio in each fraction separated by gel filtration chromatography.

tivities in the filters and filtrates were measured using HPGe detectors. Radioactivities detected in filters indicate binding amounts and those in filtrates released amounts. The distributions of four elements (Se, Zn, Co, and Mn) are summarized in Fig. 2. As shown in Fig. 2, the binding amounts of three elements, namely, Se, Co and Mn, in fraction B of Zn-deficient mice were higher than those of control mice. This may indicate the existence of proteins which have great affinity to these elements in this fraction.

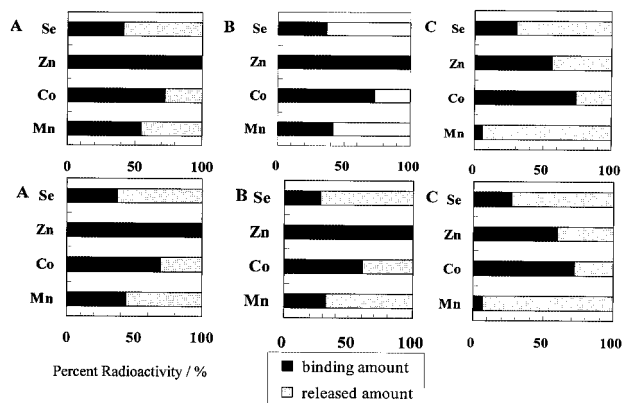


Fig. 2. Affinity between trace elements and proteins in fractions A, B, C in supernatant fraction of livers of mice. (upper: Zn-deficient mice, lower: control mice)

### References

- 1) T. Ohyama, M. Koike, T. Ogi, Y. Kawamoto, H. Maetsu, H. Suganuma, M. Noguchi, K. Ishikawa, R. Hirunuma, S. Enomoto, and M. Yanaga: Proc. Int. Symp. on Bio-Trace Elements 2002, Joint Symp. RIKEN and Yamanashi Institute of Environmental Science, Wako and Fuji-yoshida, 2002-10, (RIKEN, 2003) p. 80.

<sup>\*1</sup> Radiochemistry Research Laboratory, Faculty of Science, Shizuoka University

<sup>\*2</sup> Department of Biology and Geosciences, Faculty of Science, Shizuoka University

## Uptake of metals in cisplatin-resistant lung cancer cell line

T. Suzuki,<sup>\*1</sup> K. Ishibashi,<sup>\*1</sup> T. Togawa,<sup>\*1</sup> S. Ohata,<sup>\*1</sup> N. Sato,<sup>\*1</sup> K. Nishio,<sup>\*2</sup> R. Hirunuma,  
H. Haba, S. Enomoto, and S. Tanabe<sup>\*1</sup>

The molecular mechanism of cisplatin resistance has been revealed to be “multifunctional”, such as decreased accumulation, increased intracellular detoxification and increased DNA repair ability. Decreased accumulation of cisplatin was observed in non-small cell lung cancer (NSCLC) cell lines resistant to cisplatin. There was a good correlation between the intracellular amount of platinum and sensitivity to cisplatin. This evidence suggests that intracellular accumulation is a major determinant of cisplatin resistance, at least in NSCLC cell lines.<sup>1)</sup> Previously, it was reported that cisplatin enters the cells in an ATP-dependent manner. However, the molecular mechanism of cisplatin uptake is still unclear. In this study, to investigate the cisplatin uptake mechanisms associated with cisplatin resistance, we determined the uptakes of various metals in cisplatin-resistant cell lines.

We modified the methods described by Yanagiya *et al.*<sup>2)</sup> and used the human NSCLC cell line, PC-9 and its cisplatin-resistant subline, PC-9/CDDP. Cell lines were grown in RPMI1640 supplemented with 10% FBS. A radioactive multitracer (MT) solution was obtained from a Ag target irradiated in the RIKEN Ring Cyclotron. Then MT solution was added to the cells in a serum-free medium and incubated for 2 hr. After incubation, the cells were separated from the medium and the radioactivities were determined using a Ge detector.

Figure 1 shows the uptakes of metals in the cisplatin-resistant and parental cell lines exposed to multitracer for 2 hr. As, Be, Co, Cr, Fe, Mn, Rb, Rh, Ru, Sc, Se, Sr, V, Y, Zn and Zr were detected in both cell lines.

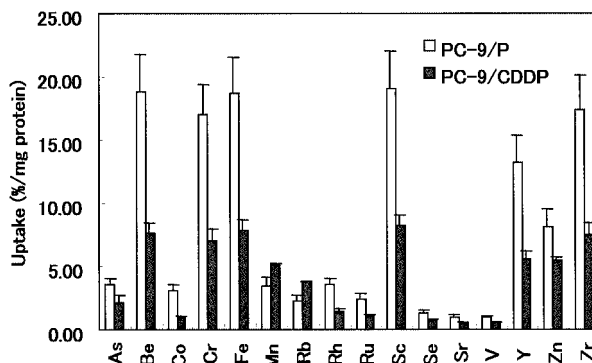


Fig. 1. Uptakes of metals in lung cancer cell lines. Cisplatin-resistant cell line (closed column) and parental cell line (open column) were exposed to multitracer for 2 hr.

The uptakes of Mn and Rb in the cisplatin-resistant cell line were higher than in the parental cell line. However, the uptakes of other metals, particularly Co were down-regulated in the cisplatin-resistant cell line. In conclusion, the multitracer technique gave some evidence of decreasing metal uptake in the cisplatin-resistant cell line, but further studies are needed to determine the molecular target for a metal transporter including a cisplatin transporter.

### References

- 1) T Suzuki et al.: *Curr. Drug Metab.* **2**, 363 (2001).
- 2) T. Yanagiya et al.: *Life Sci.* **65**, PL177 (1999).

<sup>\*1</sup> Department of Analytical Biochemistry, Meiji Pharmaceutical University

<sup>\*2</sup> Project Ward, National Cancer Center Hospital



## Relationship of reactive oxygen species generation with DNA binding and DNA cleaving activities of metallothioneins I and II

A. Nakayama and S. Enomoto

Copper (Cu) plays a central role in biological systems. Excess Cu, however, is cytotoxic to cells through hydroxyl radical ( $\bullet\text{OH}$ ) generation by reacting with reactive oxygen species (ROS) such as  $\text{H}_2\text{O}_2$ .<sup>1,2)</sup> In the case of excessive Cu accumulation, some metal-binding proteins are induced to protect organs. Among them, metallothionein (MT) is one of the most important proteins. Such MTs have four isoforms, MT-I, MT-II, MT-III, and MT-IV. Among these isoforms, MT-I and MT-II are expressed ubiquitously in living systems. On the other hand, Cu accumulates more highly in the tumor portion of hepatocellular carcinoma.<sup>3)</sup> Thus, Cu is considered to be associated with tumor development. In contrast, the MT concentration decreases in the tumor portion.<sup>3)</sup> However, high MT levels are found in the nuclei of malignant cells.<sup>4)</sup> The above observations suggest that  $\bullet\text{OH}$  generation through the reaction between Cu-MT and ROS induces DNA cleavage and induces cancer development. Thus, we investigated whether Cu-MT induces DNA cleavage.

The reactivities of various metal containing MT-I and -II to superoxide anion ( $\bullet\text{O}_2^-$ ) and  $\text{H}_2\text{O}_2$  were estimated by the ESR-spin-trapping method and NBT assay. DNA cleaving activity was evaluated by agarose gel electrophoresis, and interaction between MT and DNA was estimated by immunoprecipitation.

During the investigation, our results showed that only Cu-containing MT could react with  $\bullet\text{O}_2^-$  and  $\text{H}_2\text{O}_2$  to generate  $\bullet\text{OH}$ . Cu-MT-II has higher reactivity to  $\bullet\text{O}_2^-$  than Cu-MT-I, while their reactivities to  $\text{H}_2\text{O}_2$  appeared to be the same (Figs. 1 and 2). Such observations suggested that Cu is closely associated with the development and/or progression of cancer because Cu easily reacts with ROS and generates  $\bullet\text{OH}$ .

We then investigated the DNA cleaving activity of MTs. Cu-MTs were able to react with pBR322 plasmid DNA regardless of  $\text{H}_2\text{O}_2$  addition. In addition, the bands containing Cu-MTs and the pBR322 reaction mixture were smeared, and the smeared band disappeared with the addition of SDS, followed by the appearance of a new band that shifted above. This result suggested that Cu-MTs could form a complex with pBR322 and cleave DNA strands. The formation of the Cu-MT-pBR322 complex was confirmed by an immunoprecipitation method. The result showed that pBR322 was coprecipitated with Cu-MTs, suggesting that Cu-MTs could form a complex with DNA.

Thus, we proposed that an increase in cellular Cu concentration leads to the formation of Cu-MTs, which are transported to the nuclei of cancerous cells, where

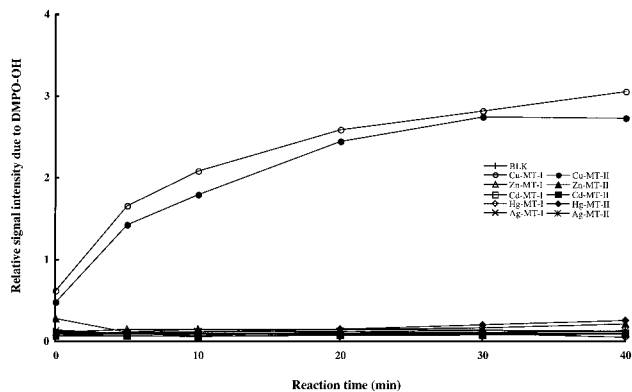


Fig. 1. Time-dependent  $\bullet\text{OH}$  generation in the systems of various MTs (225  $\mu\text{g}/\text{mL}$ ) and  $\text{H}_2\text{O}_2$  (225  $\mu\text{M}$ ) at room temperature.

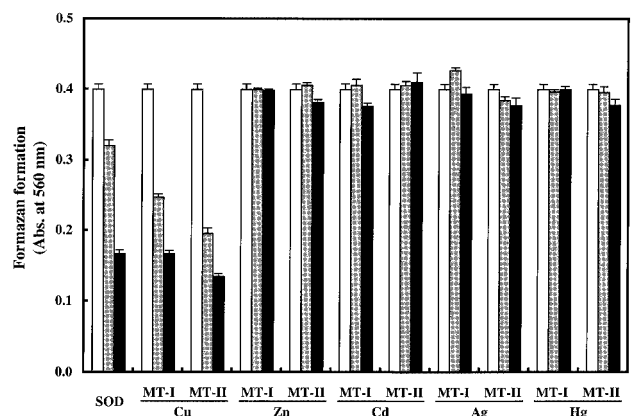


Fig. 2. Concentration-dependent  $\bullet\text{O}_2^-$ -scavenging activities of SOD and MTs. Each column represents mean  $\pm$ S.D. of three experiments. Open bar, dashed bar, and closed bar represent the concentrations at 0, 5, and 10, in U/mL or  $\mu\text{g}/\text{mL}$  of SOD or MTs, respectively.

Cu-MTs bind with and then cleave genomic DNA *via*  $\bullet\text{OH}$  generation in the vicinity of the DNA. This series of reactions leads to mutation, DNA cleavage and, finally, cancer.

### References

- 1) H. Sakurai et al.: *Biochem. Biophys. Res. Commun.* **184**, 1393 (1992).
- 2) A. Nakayama et al.: *Biomed. Res. Trace Elem.* **13**, 78 (2002).
- 3) A. Nakayama et al.: *J. Trace Elem. Exp. Med.* **15**, 31 (2002).
- 4) I. Tashiro-Ito et al.: *Liver* **17**, 300 (1997).

## Investigation of intracellular kinetics of copper in HepG2 cell lines

A. Nakayama, H. Haba, and S. Enomoto

Copper is an essential redox active metal that serves as a cofactor in various enzymes such as cytochrome c oxidase, Cu, Zn superoxide dismutase, ceruloplasmin, and lysyl oxidase.<sup>1)</sup> An excess of copper, however, induces cytotoxicity due to its proclivity to participate in Fenton-like reactions that lead to the generation of highly reactive hydroxyl radicals.<sup>2)</sup> It has been reported that copper stimulates the proliferation and migration of human endothelial cells,<sup>3)</sup> and also the development of human cancer.<sup>4)</sup>

Recently, it has been reported that organisms have developed sophisticated mechanisms of maintaining the balance between essential and toxic copper levels. Studies of the copper uptake mechanism in human cells have shown that copper is transported by two high-affinity copper transport proteins, Ctr1 and Ctr3. Within cells, copper is distributed to specific subcellular components or proteins by copper chaperones that include Hah1, which delivers copper to ceruloplasmin, Cox17, which in turn delivers copper to mitochondrial cytochrome c oxidase, and CCS, which inserts copper into Cu, Zn superoxide dismutase.<sup>5)</sup>

However, the molecular mechanisms underlying the alteration of intracellular copper distribution in diseased cells are poorly understood, because the utilization of radioactive copper isotope is generally difficult. Thus, we attempted to produce the <sup>67</sup>Cu with the longest half-life ( $t_{1/2} = 61.7$  h) among radioactive copper isotopes and to investigate the intracellular copper kinetics using <sup>67</sup>Cu.

<sup>67</sup>Cu was introduced *via* the <sup>70</sup>Zn(p,  $\alpha$ ) reaction according to the method reported by Jamriska *et al.*<sup>6)</sup> In brief, an enriched <sup>70</sup>Zn target (80%) was irradiated with a 0.96  $\mu$ A proton beam (proton energy: 12.8 MeV) for 1 h and <sup>67</sup>Cu was separated from the unreacted target and by-products, <sup>67</sup>Ga and <sup>56</sup>Co, by anion-exchange chromatography. The resulting solution containing <sup>67</sup>Cu was heated to dryness and stocked until use. The dried <sup>67</sup>Cu was completely dissolved in a small amount of 1 M HCl, and diluted with Dulbecco's modified Eagle's medium (DMEM) supplemented with fetal bovine serum (FBS) at the time of use.

We used the human hepatocellular carcinoma cell line, HepG2, and its Cu chaperone knock-down mu-

tants (Hah1<sup>-</sup>- and hCCS<sup>-</sup>-Hep G2) to investigate the kinetics of intracellular copper, because the characteristics of HepG2 cells has been well investigated. Hah1 (human ATX1 (antioxidant protein1) homolog1) is a copper-binding protein and mediates copper homeostasis by donating Cu to the P-type ATPase, ATP7A and ATP7B which transport Cu to the secretory pathway for incorporation into secretory proteins and cellular export.<sup>7)</sup> hCCS (human copper chaperone for superoxide dismutase) donates Cu to the antioxidant enzyme containing Cu and Zn, superoxide dismutase.<sup>8)</sup>

HepG2 cells were grown in DMEM supplemented with 10% FBS. Then, 100 kBq of <sup>67</sup>Cu was added to the medium and the cells were incubated for 12 h. After incubation, the cells were disrupted with lysis buffer (20 mM EDTA, 100 mM NaCl, and 1% SDS in 50 mM Tris-HCl buffer, pH 7.5) to obtain cytosols. The cytosols were analyzed by sodium dodecyl sulfate - polyacrylamide gel electrophoresis (SDS-PAGE) and two-dimensional polyacrylamide gel electrophoresis (2D-PAGE) to evaluate the intracellular kinetics of copper. By these methods, the proteins are rapidly separated on the basis of the molecular mass in the case of SDS-PAGE and on the basis of the isoelectric point and molecular mass in the case of 2D-PAGE. The radioactive copper was detected using a bioimaging analyzer BAS-2500 (Fuji Photo Film Co., Ltd., Japan).

Although useful information has not yet been obtained at present, important information regarding copper cytotoxicity as well as the development and progression of cancer is expected to be obtained in the near future.

### References

- 1) M. C. Linder: *Biochemistry of Copper* (Plenum Publishing, New York, 1991).
- 2) B. Halliwell and J. M. C. Gutteridge: *Biochem. J.* **219**, 1 (1984).
- 3) G. F. Hu: *J. Cell. Biochem.* **69**, 326 (1998).
- 4) A. Nakayama *et al.*: *J. Trace Elem. Exp. Med.* **15**, 31 (2002).
- 5) M. Marjorette *et al.*: *J. Biol. Chem.* **275**, 33244 (2000).
- 6) D. J. Jamriska *et al.*: *J. Radioanal. Nucl. Chem.* **195**, 263 (1995).
- 7) I. H. Hung *et al.*: *J. Biol. Chem.* **273**, 1749 (1998).
- 8) V. C. Cizewski *et al.*: *J. Biol. Chem.* **272**, 23469 (1997).

## Comparison of technetium and rhenium uptake rates from nutrient solution by radish

K. Tagami,\* S. Uchida,\* R. Hirunuma, H. Haba, and S. Enomoto

Naturally occurring Re is mostly found in earth-surface materials in trace concentrations. Because of the chemical similarities of Re and Tc, Re transfer factors from soil to plant can be a Tc surrogate in the natural environment. Among Tc isotopes,  $^{99}\text{Tc}$  is of potential long-term importance in the environment because it has a long half-life of  $2.1 \times 10^5$  y and is produced in the fissions of  $^{235}\text{U}$  and  $^{239}\text{Pu}$  at relatively high ratios. Tc is considered to be highly mobile in biogeochemical cycles; indeed, having the highest transfer factor (TF) in plants among nonnutrient elements<sup>1,2)</sup> makes Tc peculiar. However, the TFs of Tc obtained from recent field observations<sup>3,4)</sup> have been lower than those obtained from laboratory studies.<sup>1,2)</sup> Technetium chemical forms in the environment presumably play an important role in determining the fate of Tc in soil to plant systems, although the amount of  $^{99}\text{Tc}$  in the natural environment is determined to be very low.

Although the amount of Re in the environment is higher than that of  $^{99}\text{Tc}$ , no data are available for terrestrial plant samples. This is primarily due to Re being one of the rarest elements in the earth's crust so that its measurement is difficult. We think that a terrestrial plant absorbs Re at a high rate, the same as that found for Tc. However, the uptake behavior for Tc and Re was not clarified. Therefore, a radiotracer experiment using the multitracer technique<sup>5)</sup> was carried out in this preliminary study. The uptake rates of Tc and Re by plants were estimated using nutrient solutions.

Radish seedlings were grown in a nutrient solution culture. The plants were placed in a greenhouse at 21°C and exposed to normal daylight conditions for 30 d. Uniform-size plants were transplanted to 120-mL plastic vessels each containing 40 or 60 mL of new nutrient solution with multitracers including  $^{95\text{m}}\text{TcO}_4^-$  and  $^{183}\text{ReO}_4^-$ . The plants were in contact with the solution through their fine roots. After 1, 3 and 7 d of contact, the plants were carefully removed from the solution. The fine roots were rinsed twice with 300 mL of deionized water and gently wiped with paper towels. The plants were used for another study. The nutrient solutions were passed through 0.22- $\mu\text{m}$  filters and radioactivities were measured using a Ge detecting system (Seiko EG&G Ortec).

The physicochemical forms of Re in plants are not known, but there are several reports on those of Tc.<sup>e.g.,6)</sup> Technetium is taken up by plants through their roots as  $\text{TcO}_4^-$ , which is the most stable chem-

ical form in water under aerobic conditions, and Tc is translocated to the leaves. Therefore, we expect that Re could also be taken up as  $\text{ReO}_4^-$ , which is also the most stable chemical form. After the 1- and 7-d exposure periods, the volume of the nutrient solution that remained in the vessels decreased by 8% and 20%, respectively. The vaporization of the nutrient solution directly from the vessel would be negligible because it was covered with a polystyrene foam board, thus the reduction was due to plant transpiration. The average concentration ratios for  $^{95\text{m}}\text{Tc}$  and  $^{183}\text{Re}$  obtained after and before ( $C/C_0$ ) the 7-d exposure period in the nutrient solutions were  $1.03 \pm 0.03$  and  $0.88 \pm 0.12$ , respectively. As shown in Fig. 1, the concentration ratios for the samples determined after the 1-d and 3-d exposure periods were the same, that is, the  $^{95\text{m}}\text{Tc}$  and  $^{183}\text{Re}$  concentrations did not change during the experimental period. In our previous study using a 24-h exposure period, the same results were obtained for Re.<sup>7)</sup> The results suggest that Tc and Re uptake rates by the plants are almost the same as the water uptake rate.

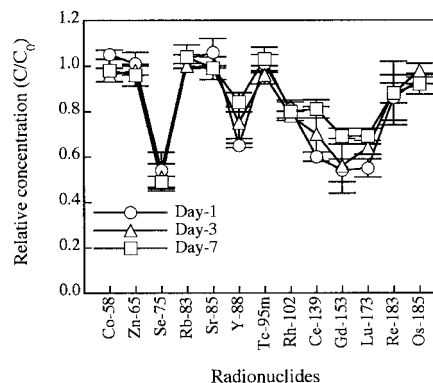


Fig. 1. Relative concentrations of radionuclides in nutrient solutions after planting radish for 1, 3 and 7 d.

### References

- 1) R. E. Wildung, T. R. Garland, and D. A. Cataldo: *Health Phys.* **32**, 314 (1977).
- 2) F. O. Hoffman, C. T. Garten, Jr., J. W. Huckabee, and D. M. Lucas: *J. Environ. Qual.* **11**, 134 (1982).
- 3) N. Green and B. T. Wilkins: *Sci. Total. Environ.* **173/174**, 385 (1995).
- 4) S. Uchida and K. Tagami: *Appl. Radiat. Isot.* **53**, 69 (2000).
- 5) F. Ambe: *J. Radioanal. Nucl. Chem.* **243**, 21 (2000).
- 6) G. C. Krijger, A. V. Harms, R. Leen, T. G. Verburg, and B. Wolterbeek: *Environ. Exp. Bot.* **42**, 69 (1999).
- 7) K. Tagami and S. Uchida: *J. Radioanal. Nucl. Chem.* **255**, 547 (2003).

\* Office of Biospheric Assessment for Waste Disposal, National Institute of Radiological Sciences

## Removal of technetium and other trace elements by bacteria living in surface water covering paddy fields

N. Ishii,\* K. Tagami,\* S. Enomoto, and S. Uchida\*

Technetium ( $^{99}\text{Tc}$ , half-life:  $2.1 \times 10^5$  y) is a radioactive contaminant in marine<sup>1)</sup> and terrestrial environments.<sup>2)</sup> It is normally present as pertechnetate ( $\text{TcO}_4^-$ ), which is both highly soluble and mobile in these environments. In addition, this chemical form is available to plants. These characteristics of Tc raise concerns about the transfer of  $^{99}\text{Tc}$  from plants to human beings.

Recently, we have found the formation of insoluble Tc in surface water covering paddy fields.<sup>3)</sup> In flooded paddy fields, therefore, the transfer amount of Tc to paddy rice may be smaller than previously thought.

In this report, we describe the contributions of microorganisms to the insoluble Tc formation in the surface water of paddy fields. In addition to Tc, trace elements, which behave similar to the Tc, were investigated by the multitracer technique.

A typical Japanese paddy soil, gray lowland soil, was air-dried and sieved using a 2 mm mesh. The soil sample was flooded for 7 d under a light-dark condition. After the incubation, only the surface water covering paddy soil was collected into a new tube, and then the water sample (pH 6.3) was used without any treatment following radioactive tracer experiments. A part of the water sample was treated by fungicide or bactericide immediately after the water sample collection.<sup>3)</sup>

A carrier-free  $^{95\text{m}}\text{Tc}$  solution was prepared from niobium foils irradiated by 40 MeV alpha-particles from a cyclotron. A multitracer solution containing radioisotopes of 14 elements ( $^{46}\text{Sc}$ ,  $^{58}\text{Co}$ ,  $^{65}\text{Zn}$ ,  $^{75}\text{Se}$ ,  $^{83}\text{Rb}$ ,  $^{85}\text{Sr}$ ,  $^{88}\text{Y}$ ,  $^{95}\text{Nb}$ ,  $^{139}\text{Ce}$ ,  $^{143}\text{Pm}$ ,  $^{153}\text{Gd}$ ,  $^{173}\text{Lu}$ ,  $^{175}\text{Hf}$ , and  $^{183}\text{Re}$ ) was prepared from a thin gold foil irradiated by a heavy-ion beam of 135 MeV nucleon<sup>-1</sup> from the RIKEN Ring Cyclotron. Both solutions were sterilized by filtration through a 0.2- $\mu\text{m}$  pore-size membrane. That is, all of the radioactive tracers were in the soluble form when the experiments were started.

The radioactive tracer solutions were added to the untreated and treated surface water samples and were incubated for 4 d in the dark. To examine the removal ratio of the tracers, the water samples with tracers were passed through a 0.2- $\mu\text{m}$ -pore-size filter after the incubation, and the radioactivity of tracers in the filtrate was determined with a Ge detecting system. The tracers, which removed by the filtration, were defined as insoluble form. The removal ratio of each tracer was calculated by the difference in the radioactivity of tracers between "total" and "filtrate" determinations.

The formation of insoluble Tc in the surface water

covering gray lowland soil was determined. After 4 d from the addition of soluble  $^{95\text{m}}\text{TcO}_4^-$ ,  $70.4 \pm 4.5\%$  of the  $^{95\text{m}}\text{Tc}$  was removed from the surface water sample by the filtration. The data showed the possibility that soluble  $\text{TcO}_4^-$  changes to insoluble Tc in surface water of paddy fields in a short time. The formation of insoluble Tc in the surface water may be one of the mechanisms for the Tc accumulation in paddy soils.

In flooded paddy fields, the accumulation of Tc in the soils was experimentally demonstrated by Tagami and Uchida.<sup>4)</sup> They reported that microorganisms indirectly contributed to the accumulation through the consumption of molecular oxygen by their respiration. In addition to the results for the flooded paddy soil experiments, the contributions of microorganisms on the insoluble Tc formation in the surface water sample were determined. When the activity of fungi was inhibited by the addition of fungicide to the surface water, the removal ratio of Tc was  $80.9 \pm 0.3\%$ . In contrast, the addition of bactericide resulted in a decrease in the removal ratio to  $16.6 \pm 3.0\%$ . Thus bacteria living in the surface water would cause the insoluble Tc formation.

Among the 14 elements in the multitracer,  $^{65}\text{Zn}$  and  $^{95}\text{Nb}$  showed a similar removal pattern to that of the  $^{95\text{m}}\text{Tc}$ . The behavior of both radionuclides in the surface water samples seemed to be controlled by bacteria.

$^{65}\text{Zn}$  was completely removed from both the untreated and fungicide samples. The removal pattern of  $^{65}\text{Zn}$  may be explained by the importance of Zn for living bacteria as a cofactor for numerous enzymes.

Approximately 65% of  $^{95}\text{Nb}$  was removed from the untreated surface water. The removal ratio increased slightly by the addition of fungicide. For the bactericide sample, the removal ratio of  $^{95}\text{Nb}$  was approximately 35% of the total  $^{95}\text{Nb}$  added. The Tc insolubilizing bacteria may be used for remediation of the solution contaminated by both Nb and Tc.

Re and Tc are in the same manganese group. Both Tc and Re can exist in heptavalent compounds under aerobic conditions. Thus Re would be expected to behave similarly to Tc, but no similar removal patterns were found between these two elements.

### References

- 1) V. Smith et al.: *J. Environ. Radioact.* **56**, 269 (2001).
- 2) K. Tagami and S. Uchida: *J. Nucl. Radiochem. Sci.* **3**, 1 (2002).
- 3) N. Ishii and K. Tagami: *Radioisotopes* **52**, 475 (2003).
- 4) K. Tagami and S. Uchida: *Chemosphere* **33**, 217 (1996).

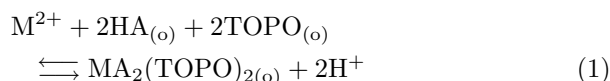
\* Office of Biospheric Assessment for Waste Disposal, National Institute of Radiological Sciences

## Improved separation of Ba and Mg ions in the alkaline earth group using the centrifugal partition chromatograph

Y. Komatsu,<sup>\*1</sup> M. Sekita,<sup>\*2</sup> H. Kokusen,<sup>\*1</sup> T. Tanemoto,<sup>\*1</sup> M. Iiyama,<sup>\*1</sup>  
H. Yamada,<sup>\*2</sup> S. Umetani,<sup>\*3</sup> and S. Enomoto

The ring cyclotron of the RIKEN Accelerator produces multitracers which include about 50 radioactive elements useful in the fields of biotechnology and medical technology, and other applications. The accelerator provides us useful information and the multiple elements; however, if all elements were to be used in the tracer technique, some would have a negative effect to the specimen and thus it would become very difficult to analyze the results. Thus, it is necessary to chemically separate the desirable elements from the produced tracer elements. In order to obtain the desirable elements, we applied the centrifugal partition chromatography (CPC) technique in the solvent extraction system.<sup>1)</sup> We have been successful in separating potassium (K) and calcium (Ca) ions, which belong to different groups in the periodic table, by means of this technique, during the course of developing an automation technique for the chemical separation.<sup>1)</sup> In this study, we report the results of the separation of barium (Ba) and magnesium (Mg) ions, which belong to the same alkaline earth group, by improving this CPC technique.

In the case of the separation of K and Ca ions,<sup>1)</sup> Ca ions can be extracted by adding thenoyl-trifluoroacetone (TTA) as an extractant and Tri-n-octylphosphine oxide (TOPO) as an adductance from the aqueous phase to the organic solution, although K ions pass through the CPC device. After all of the K ions have passed through the CPC device, the Ca ion in the organic phase can be back-extracted to the aqueous phase by adding acid to the solution. Thus the K and Ca ions can be completely separated.<sup>1)</sup> However, regarding the separation of Ba and Mg ions, they belong to the same group of the periodic table, and thus it is expected to be much more difficult to separate them completely than the case of K and Ca ions. In order to overcome this difficulty, we have focused our attention on the difference between the distribution coefficients of Ba and Mg in the equilibrium;



where HA means TTA and 'o' denotes the organic phase. According to Eq. (1), both Ba and Mg ions will be extracted to the organic phase by adding TTA and

TOPO; however, if acid (proton) is added, the reaction will go from the right-hand side to the left in Eq. (1). The distribution coefficients of Ba and Mg differ by almost 3 orders of magnitude, and thus it is possible to back-extract Ba ions prior to the back-extraction of Mg ions by adjusting the pH of the solution.

In the first stage, TTA and TOPO were filled in organic phase (cyclohexane) with an aqueous solution containing no metal ions for the stationary (organic) phase, and then the second aqueous solution containing Ba and Mg ions for the mobile phase was flowed into the CPC device. By applying centrifugal force within the CPC device, the Ba and Mg ions in the mobile (aqueous) phase were moved into the stationary phase by forming a metal complex with TTA-TOPO.

In the next stage, nitric acid solution with controlled pH was flowed into the mobile phase of the CPC device. Since the pH of the solution in the CPC device was changed from 5.51 to 3.77, the Ba ion forming TTA-TOPO chelates in the stationary phase were back-extracted to the mobile phase in accordance with Eq. (1). Due to their having a smaller distribution coefficient than Mg ions, only Ba ions in the mobile phase are directly moved (back-extracted) into the fraction collector, while Mg ions were left in the stationary phase within the CPC device. Every 5 minutes, each 5 cm<sup>3</sup> solution was flowed to the sampling tubes in the fraction collector in order to monitor the amount of Ba and Mg ions during experiments. The measured amounts of Ba and Mg ions versus the volume of effluent from the CPC device are shown in Fig. 1. One can see in Fig. 1 that only Ba ions were extracted from the 28th (140 ml) to 42nd (210 ml) samplings.

Finally, nitric acid solution with lower pH, that is, stronger acid, was added to the mobile phase at the 47th sampling time (235 ml). Since the pH of the solution in the CPC device was changed to 1.06 at most,

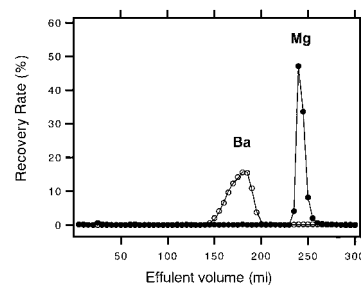


Fig. 1. Measured recovery rate of Mg and Ba in percent versus the effluent volume (cm<sup>3</sup>) from the CPC device.

\*1 Department of Environmental Systems Engineering, Kanazawa Institute of Technology

\*2 Advanced Materials Laboratory, National Institute for Materials Science

\*3 Institute for Chemical Research, Kyoto University

this is a stronger acid region than the preceding stage of 3.77, the Mg ions forming TTA-TOPO chelates in the stationary phase were then back-extracted into the mobile phase similarly to the Ba ions. As can be seen in Fig. 1, the peak of the percentage of Ba ions appeared at about the 37th (185 ml) sampling from the beginning of sampling. The Mg ions can be back-extracted after the extraction of Ba ions was completed from the 47th (235 ml) to 55th (275 ml) samplings.

It can be concluded that the Ba and Mg ions were completely separated and recovered in this improved method using the CPC device together with the pH control of the mobile phase solution.

#### References

- 1) Y. Komatsu, M. Sekita, R. M. Fujii, H. Yamada, S. Umetani, and S. Enomoto: RIKEN Accel. Prog. Rep. **36**, 207 (2003).

## Improved extractive separability of metal ions with sulfonated crown ethers

S. Umetani,<sup>\*1</sup> Y. Komatsu,<sup>\*2</sup> H. Yamada,<sup>\*3</sup> and S. Enomoto

A new type of water-soluble sulfonated crown ether has been prepared. The extractive separability of lanthanide ions was found to improve by adding the sulfonated crown ethers into the aqueous phase. The number of water molecules in the first coordination sphere of the central  $\text{Eu}^{3+}$  in the complex was determined by a laser-induced luminescence study. In addition, fluorescence spectra were measured to evaluate the structure of the complexes. The stabilization of the complexes formed is discussed, taking into account an outer-sphere electrostatic attraction between the sulfonic acid group and the metal ion. It can also be expected that the unique extractability is applicable to the separation of multitracers produced by an accelerator.

A new type of sulfonated crown ether (Fig. 1) has been synthesized, 3'-sulfobenzo-12-crown-4 (SB12C4), 3'-sulfobenzo-15-crown-5 (SB15C5), 3'-sulfobenzo-18-crown-6 (SB18C6), di(3'-sulfo)-dibenzo-18-crown-6 (DSDB18C6), di(3'-sulfo)-dibenzo-21-crown-7 (DSDB21C7) and di(3'-sulfo)-dibenzo-24-crown-8 (DSDB24C8), and the complexation reaction of these crown ethers with lanthanide metal ions in aqueous solution have been investigated. The complex formation constants,  $\beta$ , of lanthanide ions with the sulfonated crown ethers in aqueous solution were determined by analyzing the distribution of lanthanide ions in the D2EHPA/cyclohexane solvent extraction system in the presence and absence of the crown ether. All of the sulfonated crown ethers show appreciable complexation with lanthanide ions. The present results are unforeseen and would support the significant contribution of the sulfonic acid group to the complexation.

The stability of the resulting complex increases with increasing in the number of the sulfonic acid groups in the following order: 18C6 < SB18C6 < DSDB18C6. It can be considered that the outer-sphere interaction between the sulfonic acid group and the metal ion can contribute to the complexation stability. Moreover, for

mono- and disulfonated crown ether complexes, the stability varies in the order, SB18C6 < SB15C5 < SB12C4 and DSDB18C6 < DSDB21C7 < DSDB24C8. The stability of the complexes cannot be explained only on the basis of the concept of a "size-fitting effect", although it is known that the cavity size of 18C6 (radius, 1.34–1.43 Å) is similar to the ionic size of the lighter lanthanide ions. The  $\log \beta$  values are plotted against the reciprocal of the ionic radius. It is found that  $\beta$  for all of the sulfonated crown ether complexes with lanthanide ions decreases gradually with increasing the atomic number. This indicates that the cavity size is not the significant factor that governs the complexation behavior with lanthanide ions.

The separation factor between  $\text{La}^{3+}$  and  $\text{Yb}^{3+}$  in the absence of any crown ether is 5.34, and this increases when the crown ethers are added to the aqueous phase as ion-size selective masking reagents. It is clear that the sulfonated crown ethers are much more effective ion-size selective masking reagents than 18C6. The best value is given by SB12C4 at 6.63. It is also found that the sulfonated crown ethers are effective for the heavier lanthanides.

The hydration number,  $n_{\text{H}_2\text{O}}^{\circ}$ , of  $\text{Eu}^{3+}$  can be determined from the decay constants of the luminescent excited state of  $\text{Eu}^{3+}$  in the crown ether complex.<sup>1)</sup> In general, it could be expected that the number of hydrated water molecules around the central metal ion decreases with the strong binding of the inner-sphere interaction-type armed crown ethers to the metal ion. However, the opposite tendency is seen in the results; for the complexes of the 18-membered crown ethers and  $\text{Eu}^{3+}$ ,  $n_{\text{H}_2\text{O}}^{\circ}$  increases with increasing number of sulfonic acid groups (SB18C6 < DSDB18C6); that is,  $n_{\text{H}_2\text{O}}^{\circ}$  increases with increasing stability of the complex. The  $n_{\text{H}_2\text{O}}^{\circ}$  value also increases in the order, SB18C6 < SB15C5 < SB12C4, for the monosulfonated crown ethers, the same order in which their  $\log \beta$  values increase. The  $n_{\text{H}_2\text{O}}^{\circ}$  value for the disulfonated crown ether complex slightly increases with the cavity size.

The unusual stability of lanthanide ions with the sulfonated crown ethers which have one or two binding sites is dominated by two primary factors: (1) ion-dipole interaction between the metal ion and the crown ether donating oxygens and (2) the long-range interaction between the metal ion and the sulfonic acid group. These synergistic effects should be considered.

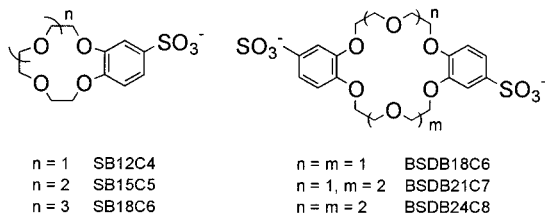


Fig. 1. Sulfonated crown ethers.

<sup>\*1</sup> Institute for Chemical Research, Kyoto University

<sup>\*2</sup> Faculty of Engineering, Kanazawa Institute of Technology

<sup>\*3</sup> Advanced Materials Laboratory, National Institute for Material Science

### References

- 1) T. Kimura and G. R. Choppin: *J. Alloys Compd.* **213/214**, 313 (1994).

## Study on Re and Os removal from seawater to sediments using multitracer technique and X-ray absorption near-edge structure

M. Ito,\* Y. Takahashi,\* H. Haba, S. Enomoto, and H. Shimizu\*

Rhenium and Os abundances have been reported to be approximately 8 pg/g<sup>1)</sup> and 0.01 pg/g,<sup>2)</sup> respectively, in seawater and 20–190 ng/g and 0.2–0.7 ng/g, respectively, in black shale,<sup>3)</sup> with <sup>187</sup>Re/<sup>188</sup>Os ratios of approximately 4300 in seawater and 500–1500 in black shale. These data indicate the Re/Os fractionation during Re and Os removal from seawater to black shale. Here, the sorption experiments of Re and Os on sediments from seawater was conducted using the radioactive nuclides <sup>183</sup>Re and <sup>185</sup>Os in a multi-tracer. Rhenium and Os species incorporated in the sediments were studied using Re L<sub>III</sub>-edge and Os L<sub>III</sub>-edge XAFS.

The nuclides <sup>183</sup>Re and <sup>185</sup>Os were obtained from Au targets irradiated with <sup>12</sup>C or <sup>14</sup>N ions using the RIKEN Ring Cyclotron. The Au target was dissolved with aqua regia, which was evaporated at 60–100°C for two hours under vacuum. Most of Os was separated into distilled solution. Rhenium mainly remained in the residue after the evaporation for Os separation. Gold, matrix in the residue, was extracted into ethyl acetate. Rhenium remaining in the aqueous phase during the solvent extraction was separated from other

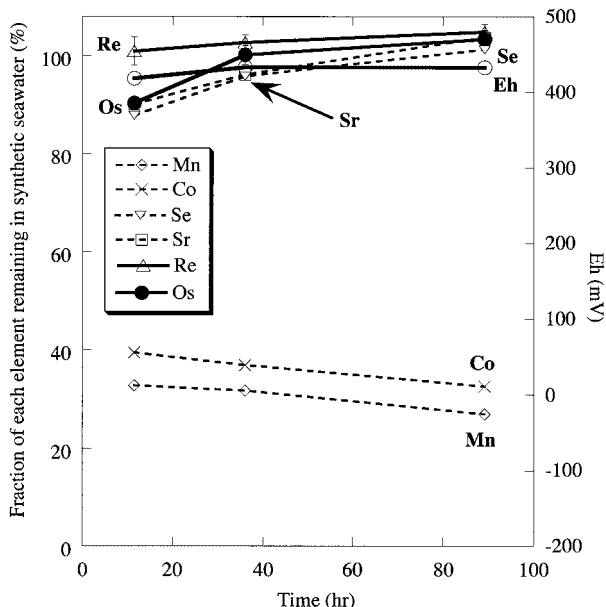


Fig. 2. Time dependence of Eh and fraction of each element remaining in synthetic seawater in the presence of Tokyo Bay sediments free from organic matter. The organic matter was removed by burning at 980°C. Synthetic seawater: 12.0 g; Tokyo Bay Sediments free from organic matter: 3.00 g.

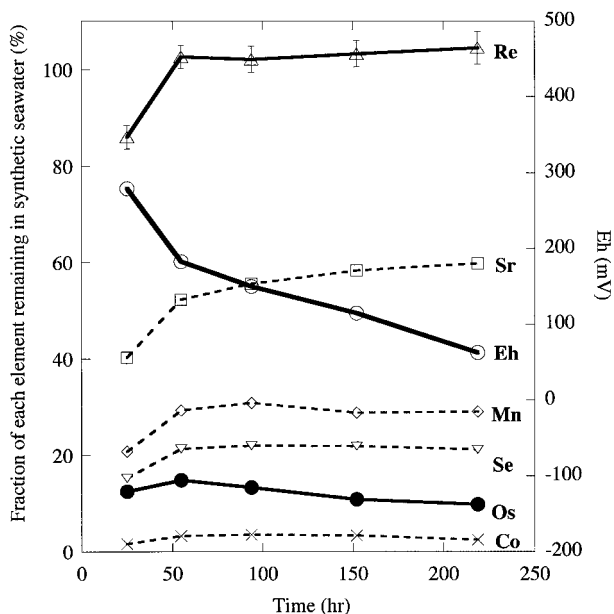


Fig. 1. Time dependence of Eh and fraction of each element remaining in synthetic seawater in the presence of Tokyo Bay sediments under mildly oxic condition. Synthetic seawater: 12.0 g; Tokyo Bay Sediments: 3.00 g.

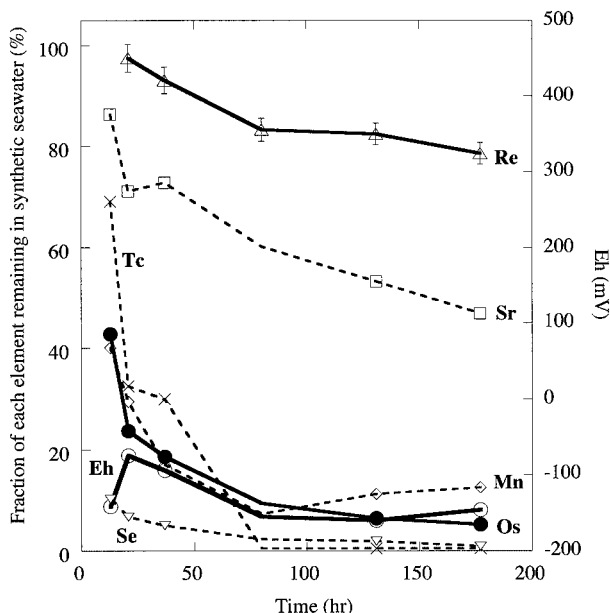


Fig. 3. Time dependence of Eh and fraction of each element remaining in synthetic seawater in the presence of Tokyo Bay sediments under reducing condition. Synthetic seawater: 12.0 g; Tokyo Bay Sediments free from organic matter: 3.00 g.

\* Department of Earth and Planetary Systems Science, Graduate School of Science, Hiroshima University



cations using a cation-exchange resin, where Re is not adsorbed on the resin. The Os and Re fractions were mixed prior to their use in the sorption experiments.

In the sorption experiments on Tokyo Bay sediments (total organic carbon content: 2.07%) from synthetic seawater under different Eh conditions, the removal behavior of Os from seawater into sediments was shown to be different from that of Re. Osmium was removed into sediments even under mildly oxic conditions (Eh = 300 mV and pH 7.5) (Fig. 1), but not removed into sediments free from organic carbon (Fig. 2). This suggests that Os in seawater directly interacts with organic matter in sediments. On the other hand, Re was incorporated into the sediments only under strongly anoxic conditions produced by the addition of glucose (Fig. 3). This suggests that removal of Re into sediments depends on anoxic conditions rather than the effect of organic matter.

Speciation of Re and Os added into the Tokyo Bay sediments under anoxic conditions was conducted by

XAFS. XANES spectra suggested that the oxidation number of Os sorbed on the sediments was trivalent, even though Os was doped into synthetic seawater as  $\text{Os(IV)Cl}_6^{2-}$  and  $\text{Os(VIII)O}_4$ . Since octavalent Os has been considered as the main dissolved species in the ocean,<sup>2)</sup> the reductive reaction of Os can be an important factor in the accumulation of Os in anoxic sediments. This is consistent with the labile character of trivalent cation which is readily sorbed on various metal oxides and complexed with natural organic polyacids.

#### References

- 1) D. Colodner, J. Sachs, G. Ravizza, K. K. Turekian, J. Edmond, and E. Boyle: *Earth Planet. Sci. Lett.* **117**, 205 (1993).
- 2) S. Levasseur, J. Birck, and C. F. Allegre: *Science* **282**, 272 (1998).
- 3) G. Ravizza, K. K. Turekian, and B. J. Hay: *Geochim. Cosmochim. Acta* **55**, 3741 (1991).

## Anion-exchange behavior of element 104, rutherfordium

H. Haba, K. Tsukada,<sup>\*1</sup> M. Asai,<sup>\*1</sup> A. Toyoshima,<sup>\*1,\*2</sup> K. Akiyama,<sup>\*1</sup> I. Nishinaka,<sup>\*1</sup> M. Hirata,<sup>\*1</sup> T. Yaita,<sup>\*1</sup> S. Ichikawa,<sup>\*1</sup> Y. Nagame,<sup>\*1</sup> K. Yasuda,<sup>\*1</sup> Y. Miyamoto,<sup>\*1</sup> T. Kaneko,<sup>\*1</sup> S. Goto,<sup>\*3</sup> S. Ono,<sup>\*3</sup> T. Hirai,<sup>\*3</sup> H. Kudo,<sup>\*3</sup> M. Shigekawa,<sup>\*2</sup> A. Shinohara,<sup>\*2</sup> Y. Oura,<sup>\*4</sup> H. Nakahara,<sup>\*4</sup> K. Sueki,<sup>\*5</sup> H. Kikunaga,<sup>\*6</sup> N. Kinoshita,<sup>\*6</sup> N. Tsuruga,<sup>\*6</sup> A. Yokoyama,<sup>\*6</sup> M. Sakama,<sup>\*7</sup> S. Enomoto, M. Schädel,<sup>\*8</sup> W. Bröchle,<sup>\*8</sup> and J. V. Kratz<sup>\*9</sup>

The increasingly strong relativistic effect on the valence electrons of transactinide elements is expected to induce deviations in chemical properties from the periodicity based on lighter homologues in the periodic table. The first transactinide element, rutherfordium (Rf), is considered to be a group-4 member with the ground-state electronic configuration of [Rn]5f<sup>14</sup>6d<sup>2</sup>7s<sup>2</sup>, though relativistic calculations have predicted different configurations such as 6d<sup>2</sup>7s<sup>2</sup>, 7s<sup>2</sup>7p<sup>2</sup>, and 6d7s<sup>2</sup>7p.<sup>1)</sup> The nuclide <sup>261</sup>Rf, which has a half-life of 78 s,<sup>2)</sup> can be used for chemical studies of Rf. The production rate of <sup>261</sup>Rf is of the order of one atom per minute under typical experimental conditions, which forces us to perform rapid and repetitive chromatographic experiments with single atoms. Previously, we investigated the anion-exchange behavior of Rf together with those of lighter homologues of group-4 elements Zr and Hf in 4.0–11.5 M HCl and 8.0 M HNO<sub>3</sub> solutions.<sup>3)</sup> It was found that the adsorption trends of Rf in HCl and HNO<sub>3</sub> are very similar to those of Zr and Hf, indicating that Rf is a typical group-4 member. Reported in this paper is our recent result of the successive anion-exchange study of Rf in 1.9–13.9 M HF solutions.

The carrier-free radiotracers of <sup>89</sup>Zr and <sup>175</sup>Hf were produced in the <sup>89</sup>Y(*p*, *n*) and <sup>175</sup>Lu(*p*, *n*) reactions, respectively, using a 14-MeV proton beam from the RIKEN K70 AVF Cyclotron. The anion-exchange resin used was MCI GEL CA08Y, supplied by Mitsubishi Chemical Corporation, a strongly basic quaternary-amine polymer with the particle size of 22 ± 2 μm. 10–200 mg of CA08Y and 3 mL of 0.97–26.4 M HF solution containing 50 μL of the tracer solution were placed in a polypropylene tube and shaken for 100 min at 20°C. After centrifugation, 1 mL of the aqueous phase was pipetted into a polyethylene tube and subjected to γ-ray spectrometry using a Ge detector. As a standard sample, 50 μL of the tracer solution was diluted to 1 mL of 0.1 M HF in another polyethylene tube. The distribution coefficient *K*<sub>d</sub> in unit of

mL g<sup>-1</sup> was obtained using  $K_d = A_r V_s / A_s W_r$ , where *A*<sub>r</sub> and *A*<sub>s</sub> are the radioactivities in the resin and the solution, respectively, and *V*<sub>s</sub> is the volume of the acid solution and *W*<sub>r</sub> is the mass of the dry resin.

Isotope <sup>261</sup>Rf was produced in the <sup>248</sup>Cm(<sup>18</sup>O, 5*n*) reaction using a 94-MeV <sup>18</sup>O beam delivered from the JAERI tandem accelerator. A <sup>248</sup>Cm target of 610 μg cm<sup>-2</sup> thickness was prepared by electrodeposition onto a 2.4 mg cm<sup>-2</sup> thick Be foil. Beam intensity was approximately 0.3 particle μA. Reaction products recoiling out of the target were transported by a He/KCl gas-jet system to the Automated Ion-exchange separation apparatus coupled with the Detection system for Alpha spectroscopy (AIDA).<sup>3,4)</sup> Two different micro-columns, 1.6 i.d. × 7.0 mm and 1.0 i.d. × 3.5 mm, were filled with the CA08Y resin. After the deposition for 125 s, Rf was dissolved in 240 (260)<sup>a)</sup> μL of 13.9, 11.6, 7.7, 5.8, 4.8, and 3.9 (3.0, 2.4, and 1.9) M HF and fed into the column at a flow rate of 0.74 (1.0) mL min<sup>-1</sup>. The effluent was collected on a Ta dish as Fraction 1 and evaporated to dryness using hot He gas and a halogen heat lamp. The remaining Rf in the column was eluted with 210 (200) μL of 4.0 M HCl. This effluent was collected on another Ta dish and evaporated to dryness as Fraction 2. The pair of Ta dishes, Fractions 1 and 2, was automatically transferred to an α spectrometry station equipped with eight 600 mm<sup>2</sup> PIPS detectors. All events were registered event by event. To investigate the on-line anion-exchange behavior of Zr and Hf, isotopes <sup>85</sup>Zr and <sup>169</sup>Hf were simultaneously produced in the <sup>nat</sup>Ge(<sup>18</sup>O, *xn*) and <sup>nat</sup>Gd(<sup>18</sup>O, *xn*) reactions, respectively. The anion-exchange experiments were performed with AIDA at 3.9–17.4 M HF under the same experimental conditions as those with <sup>261</sup>Rf. The effluents were assayed by γ-ray spectrometry with Ge detectors.

From ion-exchange experiments performed 849, 631, 322, 271, 179, 532, 465, 501, and 476 times at 13.9, 11.6, 7.7, 5.8, 4.8, 3.9, 3.0, 2.4, and 1.9 M HF, respectively, a total of 266 α events from 78-s <sup>261</sup>Rf (8.28 MeV)<sup>2)</sup> and its daughter 25-s <sup>257</sup>No (8.22, 8.27, and 8.32 MeV)<sup>2)</sup> were registered in the energy range of 8.00–8.36 MeV, including 25-time-correlated α pairs. From the activities *A*<sub>1</sub> and *A*<sub>2</sub> observed in Fractions 1 and 2, respectively, the percent adsorption (%*ads*) on CA08Y was evaluated using %*ads* = 100 *A*<sub>2</sub> / (*A*<sub>1</sub> + *A*<sub>2</sub>).

<sup>\*1</sup> Advanced Science Research Center, Japan Atomic Energy Research Institute

<sup>\*2</sup> Graduate School of Science, Osaka University

<sup>\*3</sup> Faculty of Science, Niigata University

<sup>\*4</sup> Graduate School of Science, Tokyo Metropolitan University

<sup>\*5</sup> Department of Chemistry, University of Tsukuba

<sup>\*6</sup> Faculty of Science, Kanazawa University

<sup>\*7</sup> School of Health Sciences, University of Tokushima

<sup>\*8</sup> Gesellschaft für Schwerionenforschung, Germany

<sup>\*9</sup> Institut für Kernchemie, Universität Mainz, Germany

<sup>a)</sup> The values given in parenthesis refer to the condition when the 1.0 i.d. × 3.5 mm column was used.

Then, the %ads values of Rf were transformed into  $K_d$  values based on the smooth relationship between the %ads values of  $^{85}\text{Zr}$  and  $^{169}\text{Hf}$  and the  $K_d$  values of  $^{89}\text{Zr}$  and  $^{175}\text{Hf}$ .<sup>5)</sup>

In Fig. 1, the variation of the  $K_d$  value of Rf is shown by closed squares as a function of HF concentration, [HF], together with those of  $^{89}\text{Zr}$  and  $^{175}\text{Hf}$  shown by open squares and open circles, respectively. As shown in Fig. 1, the  $K_d$  values of Zr and Hf are identical with each other and both decrease with an increase of [HF].

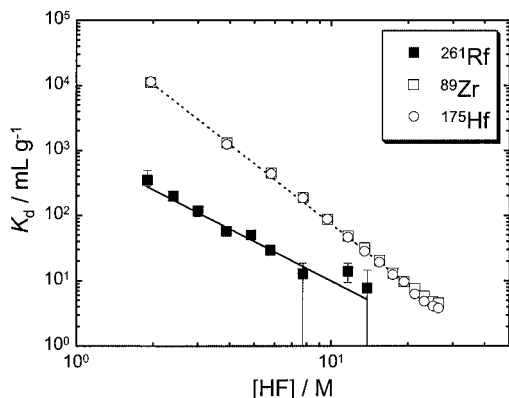


Fig. 1. Variations of the distribution coefficient values ( $K_d$ ) of  $^{261}\text{Rf}$ ,  $^{89}\text{Zr}$ , and  $^{175}\text{Hf}$  on CA08Y as a function of HF concentration, [HF]. Linear relationships with slopes  $-2.0 \pm 0.3$  for Rf and  $-3.0 \pm 0.1$  for Zr and Hf in the log  $K_d$ -log [HF] plot are indicated by the solid and dotted lines, respectively.

A linear relationship with a slope of  $-3.0 \pm 0.1$  was found in the log  $K_d$ -log [HF] plot shown by a dashed line. As HF is a weak acid, equilibrations among HF,  $\text{H}^+$ ,  $\text{F}^-$ , and  $\text{HF}_2^-$  in the solution are established following the two chemical relations:  $\text{H}^+ + \text{F}^- \leftrightarrow \text{HF}$  and  $\text{HF} + \text{F}^- \leftrightarrow \text{HF}_2^-$ .<sup>6)</sup> Above 1 M,  $[\text{HF}_2^-]$  is more than one order of magnitude higher than  $[\text{F}^-]$ , and the decrease of  $K_d$  with [HF] is explained as displacement of the metal complexes from the binding sites of the resin with  $\text{HF}_2^-$ . Although the  $K_d$  values of Rf also decrease linearly with [HF], they are apparently smaller than those of Zr and Hf. Also noted is that the slope of  $-2.0 \pm 0.3$  of the plot of log  $K_d$  vs. log [HF] for Rf differs from that for Zr and Hf, implying that different anionic species are formed. The relativistic molecular density functional calculations on the fluoride complexes of Rf, Zr, and Hf are under study in our group to interpret the remarkable difference in the anion-exchange behavior and to discuss the influence of relativistic effects on the fluoride complexation of Rf.

#### References

- 1) M. Schädel (ed.): *The Chemistry of Superheavy Elements* (Kluwer Academic Publishers, Dordrecht, 2003).
- 2) R. B. Firestone and V. S. Shirley: *Table of Isotopes, 8th ed.* (John Wiley & Sons, New York, 1996).
- 3) H. Haba et al.: *J. Nucl. Radiochem. Sci.* **3**, 143 (2002).
- 4) Y. Nagame et al.: *Czech. J. Phys. Suppl. A* **53**, A299 (2003).
- 5) H. Haba et al.: *J. Am. Chem. Soc.*, in press.
- 6) P. M. Plaisance and R. Guillaumont: *Radiochim. Acta* **12**, 32 (1969).

## Performance of a gas-jet-coupled multitarget system for multitracer production

H. Haba, K. Igarashi, D. Kaji,\* R. Hirunuma, and S. Enomoto

Since 1991,<sup>1)</sup> the RIKEN multitracer technique has been successfully applied in investigations of the behavior of various elements in the fields of chemistry, biology, medicine, engineering, and environmental science. By using the falling ball system,<sup>1)</sup> radionuclides of a large number of elements were simultaneously produced from metallic targets such as Ti, Ag, and Au irradiated with a 135 MeV/nucl. <sup>14</sup>N (or <sup>12</sup>C, <sup>16</sup>O) beam from the RIKEN Ring Cyclotron (RRC). After the irradiation, these radionuclides were chemically separated from the target material,<sup>1,2)</sup> and then carrier-free and salt-free multitracer solutions were applied to various experiments.

Recently, we have installed a gas-jet-coupled multitarget system on the E3b beam line of RRC as an alternative to the falling ball system. A schematic of this system is shown in Fig. 1. In the first chamber, the 135 MeV/nucl. <sup>14</sup>N (or <sup>12</sup>C, <sup>16</sup>O) beam from RRC passes through a HAVAR vacuum window of 6 μm thickness, and enters 30 multitarget of about 1 μm in thickness with 10 mm spacings. The recoiling multitracers are stopped in He gas, attached to aerosols such as NaCl, KCl, and C, and are continuously transported through a Teflon capillary to a chemistry room, where the multitracers are collected on a glass filter. Then, the multitracer solutions are obtained simply by wash-

ing the filter with a suitable solution. Lastly, the <sup>14</sup>N beam enters the thick metallic targets such as Ti, Ag, and Au, which are about 200 μm in thickness, in the second chamber. After the irradiation, the long-lived multitracers were chemically separated using the same procedure as applied previously.<sup>1,2)</sup>

Advantages of the present system are as follows. (1) The multitracers are separated from the target material without chemical separation and transported to the chemistry room within a few seconds. Thus, radionuclides with short half-lives of less than 1 min are available for tracer experiments. (2) The targets with various chemical compositions are prepared by electrodeposition or vacuum-evaporation techniques. The composition of the radionuclides in the multitracer can be optimized by changing the target material and its array. (3) The radionuclides of interest can be easily concentrated by using a liquid chromatography apparatus based on ion exchange or solvent extraction. (4) All of the targets are continuously cooled with He gas during the irradiation. Thus, the beam intensity of ~1 μA is acceptable, though the maximum in the falling ball system was approximately 0.1 μA due to the irradiation in a vacuum chamber.

The performance of the gas-jet-coupled multitarget system was investigated using the 30 multiple

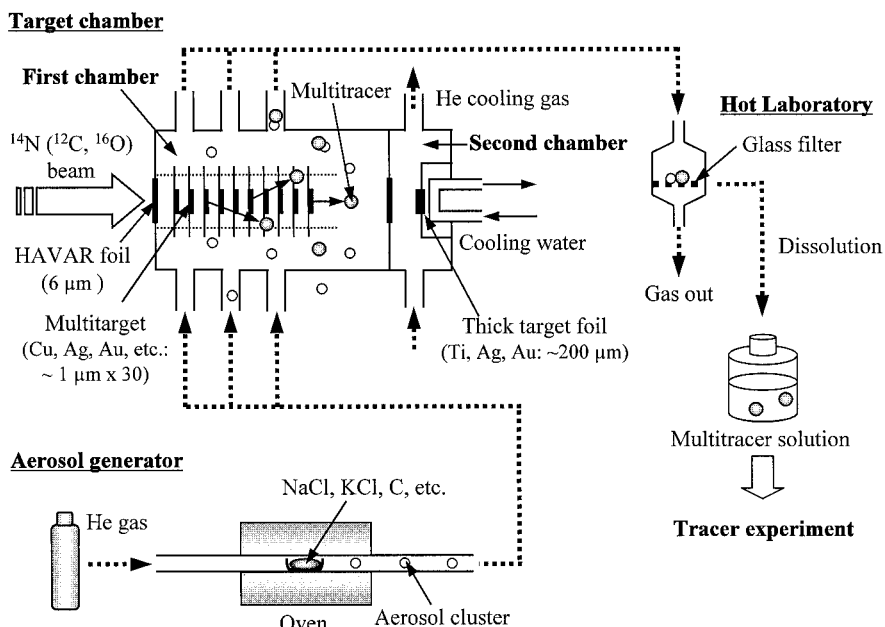


Fig. 1. Schematic of the gas-jet-coupled multitarget system for multitracer production.

\* Center for Nuclear Study, University of Tokyo

$^{nat}\text{Cu}$  target of  $2\ \mu\text{m}$  in thickness irradiated with the  $135\ \text{MeV/nucl. } ^{14}\text{N}$  beam of  $50\ \text{pnA}$  in intensity. The multitracers recoiling out of the target were stopped in He gas ( $\sim 80\ \text{kPa}$ ), attached to KCl aerosols generated by sublimation of the KCl powder at  $640^\circ\text{C}$ , and continuously transported through a Teflon capillary ( $2.0\ \text{mm i.d.}$ ,  $10\ \text{m}$  long) to the Hot Laboratory just beneath the E3 irradiation room. The aerosols were collected on a glass filter ADVANTEC GB-100R for  $15\ \text{min}$ . The flow rate of the He carrier gas was  $2.0\ \text{L min}^{-1}$ . In the same irradiation, one Cu foil of  $2\ \mu\text{m}$  thickness and  $15\times 15\ \text{mm}^2$  size sandwiched by one pair of Kapton foils of  $50\ \mu\text{m}$  thickness and  $20\times 20\ \text{mm}^2$  size, which collected the recoiling nuclei from the target, was irradiated in the second chamber. After the irradiation, the glass filter, the Cu target, and the Kapton catchers were subjected to  $\gamma$ -ray spectrometry with a Ge detector.

The radioactivities of the 52 nuclides of 18 elements produced from  $^{nat}\text{Cu}$  were identified in the glass filter. This number of nuclides is quite large as compared with the 11 nuclides of 10 elements produced from  $^{nat}\text{Cu}$  by the falling ball system.<sup>3)</sup> The radionuclides with short half-lives ( $T_{1/2} < \sim 1\ \text{min}$ ) such as  $^{25}\text{Na}$  ( $59.1\ \text{s}$ ),  $^{35}\text{P}$  ( $47.3\ \text{s}$ ),  $^{40}\text{Cl}$  ( $1.35\ \text{min}$ ), and  $^{58\text{m}}\text{Mn}$  ( $65.3\ \text{s}$ ) were found to be applicable for tracer experiments. On the other hand, the 28 radionuclides varying from  $^{61}\text{Cu}$  to  $^{24}\text{Na}$  were identified in both the Cu target and the Kapton catchers. For these nuclides, the recoil efficiency  $\varepsilon_r$  and the gas-jet efficiency  $\varepsilon_g$  were calculated according to the equations  $\varepsilon_r = 100N_{\text{Kapton}}/(N_{\text{Kapton}} + N_{\text{Cu target}})$  and  $\varepsilon_g = 100N_{\text{Glass filter}}/30N_{\text{Kapton}}$ ,  $N$  being the number of atoms, respectively. The  $\varepsilon_r$  and  $\varepsilon_g$  values are shown in Fig. 2 as a function of the mass difference ( $\Delta A$ ) between a product and a target ( $A = 65$ ), and are represented by open and closed circles, respectively. The  $\varepsilon_r$  values increase smoothly with an increase of  $\Delta A$ , reflecting both the increasing kinetic energy and the decreasing stopping power of Cu for the product nuclei. The  $\varepsilon_g$  values are about 30% for the product nuclei with  $\Delta A = \sim 5$  and decrease to about 10% with an increase of  $\Delta A$ . It is interesting to note that the  $\varepsilon_g$

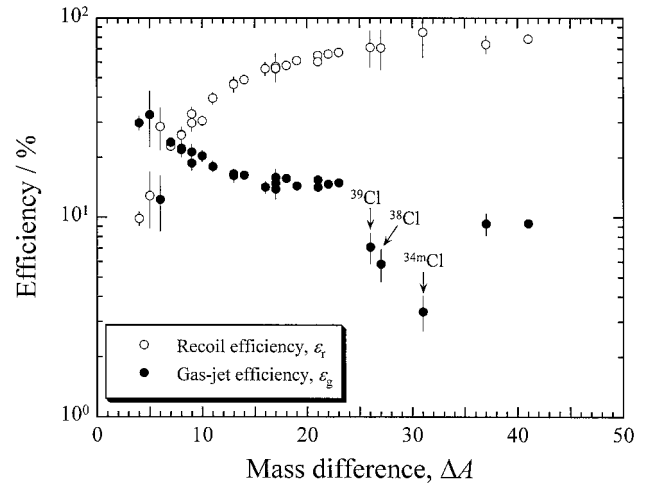


Fig. 2. Variation of the recoil efficiency  $\varepsilon_r$  and the gas-jet efficiency  $\varepsilon_g$  as a function of the mass difference  $\Delta A$ .

values of chlorine isotopes of  $^{39}\text{Cl}$ ,  $^{38}\text{Cl}$ , and  $^{34\text{m}}\text{Cl}$  are appear to be smaller than the systematic trend from other products. The hot chlorine atom may interact with Cl atoms of the aerosol and form a gaseous  $\text{Cl}_2$ , which cannot be collected on the glass filter.

In separate experiments, the long-lived multitracers were produced from  $200\text{-}\mu\text{m}$ -thick  $^{nat}\text{Ag}$  and  $300\text{-}\mu\text{m}$ -thick  $^{197}\text{Au}$  targets using the  $135\ \text{MeV/nucl. } ^{14}\text{N}$  beam with the maximum intensity of  $0.6\ \mu\text{A}$ , which was more than six times the limit of the falling ball system. Thus, the production efficiency of the multitracer was markedly enhanced. The entire target chamber was surrounded with  $150\text{-mm}$ -thick iron and  $300\text{-mm}$ -thick concrete blocks in order to shield the neutrons and  $\gamma$ -rays from the targets and the beam dump. The radiation dose in the E3 room during the multitracer production was decreased to about one fourth of that of the previous system.

#### References

- 1) S. Ambe et al.: Chem. Lett. **1991**, 149.
- 2) S. Ambe: RIKEN Rev., No. 13, 3 (1996).
- 3) S. Ambe et al.: Anal. Sci. **7**, Suppl., 317 (1991).

## Development of a new target system for online multitracer preparation

M. Yatsukawa,<sup>\*1</sup> Y. Kasamatsu,<sup>\*1</sup> H. Kikunaga,<sup>\*2</sup> N. Kinoshita,<sup>\*2</sup> S. Shibusawa,<sup>\*3</sup> T. Hashimoto,<sup>\*2</sup> M. Arai,<sup>\*3</sup> K. Ninomiya,<sup>\*1</sup> A. Yokoyama,<sup>\*3</sup> W. Sato,<sup>\*1</sup> N. Takahashi,<sup>\*1</sup> S. Enomoto, S. Shibata,<sup>\*4</sup> and A. Shinohara<sup>\*1</sup>

The multitracer technique enables simultaneous tracing of a number of elements in biological and chemical systems. This technique is therefore useful in various fields such as medicine, pharmacology, biology, chemistry, and environmental science. For the supply of a multitracer solution, however, chemical separation must be performed after several-day cooling of the target irradiated with high-energy heavy ions. For the rapid preparation of a wider variety of elements, we have developed a new target system for the online preparation of multitracer elements.

On the basis of our previous data for the yield and recoil property,<sup>1,2)</sup> we have designed a special irradiation apparatus shown in Fig. 1. The target foil is placed in the chamber filled with a catcher solution. While the target is irradiated with a heavy-ion beam, radioactive nuclides recoil out of the foil. Then the recoils are caught in the solution to be transported to the solution reservoir.

Test experiments with the target fragmentation reaction were performed using HIMAC (Heavy Ion Medical Accelerator in Chiba) at National Institute of Radiological Sciences with a <sup>12</sup>C beam (290 MeV/nucleon). Five sheets of Nb foils of 11.3 mg/cm<sup>2</sup> thickness were employed as the target and spaced at intervals of 0.4 mm. Ion exchange water and pH5 and pH3 acetic acid solutions were used as catcher solvents to investigate the pH dependence of the yield. During the irradiation for 20 minutes, each of the solvents was circulated in the chamber for the homogenization of the solutions. After the irradiation, we immediately recovered the multitracer solutions and measured the radioactivities in them with a Ge detector placed away from the irradiation room.

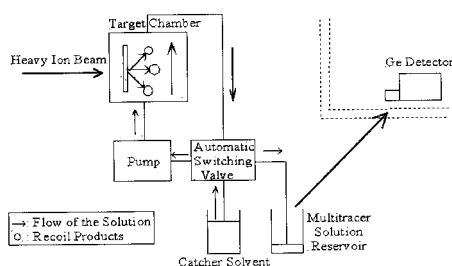


Fig. 1. New target system for online multitracer production.

<sup>\*1</sup> Graduate School of Science, Osaka University

<sup>\*2</sup> Graduate School of Natural Science and Technology, Kanazawa University

<sup>\*3</sup> Faculty of Science, Kanazawa University

<sup>\*4</sup> National Institute of Radiological Sciences

Table 1 shows the yields of detected elements, expressed in the form of relative values to those for the stacked catcher foils.<sup>1)</sup> We found that the yields of the recoil products from the target foils tend to increase with decreasing pH of the solution: water < pH5 < pH3 acetic acid solutions. The yields of the detected elements are plotted in Fig. 2 as a function of the solubility of each metal-hydroxide solution.<sup>3),a)</sup> We can see a correlation between the yields and the solubilities of the metal hydroxides. In order to achieve reproducibility, further experiments are to be carried out at the RIKEN Accelerator Research Facility.

Table 1. Elemental yields of the recoil products recovered by solution catchers. The average values are shown for the elements corresponding to two or more nuclides.

Element	Detected Nuclide (Half Life)	Water / %	pH5 / %	pH3 / %
Na	<sup>24</sup> Na (14.96 h)	42 ± 6	90 ± 10	79 ± 9
Mg	<sup>27</sup> Mg (9.46m)	33 ± 4	79 ± 11	74 ± 11
Al	<sup>29</sup> Al (6.6m)	14 ± 4	41 ± 8	36 ± 8
Cl	<sup>38</sup> Cl (37.18m), <sup>39</sup> Cl (56m)	33 ± 6	61 ± 9	73 ± 11
Sc	<sup>44</sup> Sc (3.92h)	N. D.	36 ± 4	53 ± 5
Mn	<sup>52m</sup> Mn (21m)	33 ± 9	48 ± 10	54 ± 11
Co	<sup>62m</sup> Co (14m)	N. D.	N. D.	57 ± 18
Cu	<sup>60</sup> Cu (23m)	28 ± 5	37 ± 6	61 ± 10
As	<sup>70</sup> As (53m)	26 ± 4	37 ± 6	58 ± 9
Se	<sup>72</sup> Se (7.1h)	N. D.	N. D.	18 ± 2
Br	<sup>74g</sup> Br (25.4m), <sup>74m</sup> Br (46m)	68 ± 14	86 ± 20	90 ± 20
Kr	<sup>77</sup> Kr (1.24h)	N. D.	65 ± 3	73 ± 3
Rb	<sup>82m</sup> Rb (6.3h)	N. D.	45 ± 5	49 ± 5
Y	<sup>84m</sup> Y (40m), <sup>86g</sup> Y (14.74h) <sup>86m</sup> Y (48m)	N. D.	55 ± 3	88 ± 4

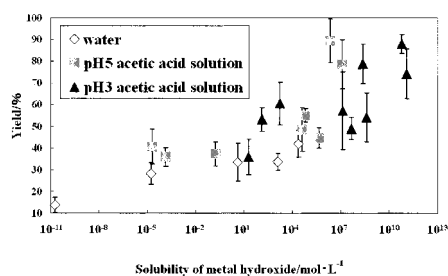


Fig. 2. Correlation of the elemental yields of the recoil products with the solubilities of the metal hydroxides.

### References

- 1) A. Yokoyama et al.: *Radiochim. Acta* **89**, 703 (2001).
- 2) A. Yokoyama et al.: *HIMAC-042*, 95 (2001).
- 3) *Kagaku Binran*, 4th edition edited by M. Oki et al. (The Chemical Society of Japan, Tokyo, 1993), p. II-161.

a) For the solubility products of the metal hydroxides, the solubilities were calculated for each pH of the solutions using literature values adopted in Ref. 3.

## Preliminary study on olfactory transport of a multitracer produced in Ti target

Y. Kanayama,\* H. Haba, R. Hirunuma, S. Enomoto, and R. Amano\*

Olfactory receptor neurons are in contact with the environment *via* the olfactory epithelium, moreover, the neurons connect with the olfactory bulb *via* axons. The axonal transport provides a pathway by which some proteins, viruses, and rarely metals directly enter the brain. Little information is available on the transport of metal ions *via* the olfactory pathway, although  $\text{Mn}^{2+}$ , which has a similar property to  $\text{Ca}^{2+}$  was reported to be accumulated in the olfactory bulb *via* this pathway.<sup>1)</sup>

In our previous studies, 24 hours after intranasal administration, we noted the anomalously high accumulation of  $^{83}\text{Rb}^+$  in the brain among 16 radionuclides in the multitracer produced in the Ag target.<sup>2)</sup> Furthermore, we demonstrated that  $^{86}\text{Rb}^+$ ,  $^{137}\text{Cs}^+$ , and  $^{201}\text{Tl}^+$ , which are  $\text{K}^+$ -mimic ions, are unilaterally accumulated and transported to the olfactory bulb and cortices after unilateral intranasal administration.<sup>3)</sup> These findings clearly indicate that these ions are transported *via* the olfactory pathway. Interestingly, it seems that the speed of transport differs depending on the ion, for example  $\text{Rb}^+$  transport is faster than  $\text{Mn}^{2+}$  transport. However, underlying mechanisms and physiological roles of the axonal transport of  $\text{K}^+$  and  $\text{Ca}^{2+}$  are poorly understood. In this research, we attempted to apply a multitracer produced in Ti target, which enables simultaneous tracing of  $^{24}\text{Na}^+$ ,  $^{28}\text{Mg}^{2+}$ ,  $^{43}\text{K}^+$ , and  $^{47}\text{Ca}^{2+}$ , for clarifying their olfactory transport.

A multitracer was obtained from a Ti target of 2  $\mu\text{m}$  thickness irradiated with a 135 MeV/nucl.  $^{14}\text{N}$  beam of 300 pA for 3 hours using RIKEN Ring Cyclotron. The multitracer solution for administration contained radionuclides of  $^{24}\text{Na}^+$ ,  $^{28}\text{Mg}^{2+}$ ,  $^{43}\text{K}^+$ , and  $^{47}\text{Ca}^{2+}$  in the physiological saline solution. Eight-week-old male ICR mice were subjected to either intranasal (IN) or intravenous (IV) administration of the multitracer solution. In the IN-group, the solution was administered only into the right nostril to clarify whether the route of tracer delivery is *via* the olfactory pathway. Six hours after the administration, the blood (BL), liver (LI), and brain were separately obtained. The brain was then divided into the right and left sides, and further divided into three regions which were the olfactory bulb (OB), the forebrain including the olfactory cortex (FB), and all the remaining brain (RB). Activities were measured by  $\gamma$ -ray spectrometry using pure Ge detectors and the uptake rates were determined in terms of the administered dose per wet weight

(%dose/g).

Figure 1 shows the  $^{24}\text{Na}^+$ ,  $^{28}\text{Mg}^{2+}$ , and  $^{43}\text{K}^+$  uptake rates. No significant differences were observed between the right and left sides of the three brain regions. This indicates that the multitracer solution can penetrate the nasal septum. The  $^{43}\text{K}^+$  uptake rates in the ROB and LOB in the IN-group seemed to be higher than in the IV-group, and agreed with our previous data of the  $\text{K}^+$ -mimic ions.<sup>3)</sup> Moreover, a similar tendency was observed in the  $^{28}\text{Mg}^{2+}$  uptake rates. The results indicate that  $\text{Mg}^{2+}$  and  $\text{K}^+$  are directly transported *via* the olfactory pathway. In contrast,  $^{24}\text{Na}^+$  uptake rates were low, and there was no significant difference between IN- and IV-groups. As for  $^{47}\text{Ca}^{2+}$ , activities were not detected except in blood samples of the IV-group ( $0.42 \pm 0.09\%$ dose/g).

Novel knowledge on the ion transportation *via* the olfactory pathway strongly indicates the usefulness of the multitracer produced in the Ti target for investigating the biobehavior of  $\text{Na}^+$ ,  $\text{K}^+$ , and  $\text{Mg}^{2+}$  simultaneously.

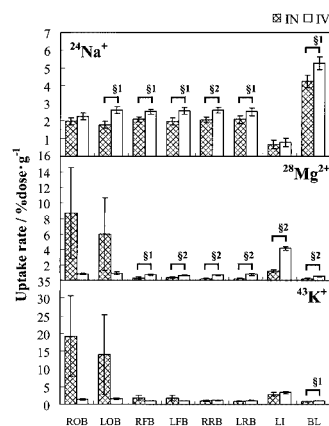


Fig. 1. Uptake rates (%dose/g) of  $^{24}\text{Na}^+$ ,  $^{28}\text{Mg}^{2+}$ , and  $^{43}\text{K}^+$  in the blood, liver, and brain regions following intranasal (IN) or intravenous (IV) administration of a multitracer. In IN administration the multitracer was instilled only into the right nostrils of the mice. OB: olfactory bulb; FB: forebrain; RB: remaining brain; BL: blood; LI: liver; R: right side; L: left side. The errors are standard deviations for three samples. Significance levels: §1  $p < 0.05$ , §2  $p < 0.01$ , IN *vs.* IV.

### References

- 1) S. Durston et al.: NeuroImage **16**, 449 (2002).
- 2) Y. Kanayama et al.: RIKEN Accel. Prog. Rep. **36**, 123 (2003).
- 3) Y. Kanayama et al.: Eur. J. Nucl. Med. Mol. Imaging. **30** suppl. 2, S296 (2003).

\* School of Health Sciences, Faculty of Medicine, Kanazawa University

## Multitracer imaging in plants by GREI system

S. Motomura, R. Hirunuma, K. Igarashi, H. Haba, H. Takeichi, M. Kibe,\*<sup>1</sup> Y. Gono, A. Odahara,\*<sup>2</sup> S. Enomoto, and Y. Yano

We have instrumented a prototype of the  $\gamma$ -ray emission imaging<sup>1)</sup> (GREI) system. The GREI system makes it possible to visualize the distribution of mixed radioisotopes (RIs) simultaneously and nondestructively. On the other hand, the RI Beam Factory (RIBF) project is in progress at RIKEN Accelerator Research Facility. The RIBF provides a great variety of RIs in the form of accelerated heavy-ion beams. The GREI system, combined with the RIBF, will give rise to a new methodology in biology, nuclear medicine, and so forth.

In order to prove the feasibility of the GREI system by examples, we have performed experiments to visualize the RIs distributed in soybean samples. In this report, we present the results for two samples, SB-1 and SB-2 (Fig. 1), administered with the following RIs: (1) 40-kBq  $^{65}\text{Zn}$ ; (2) 630-kBq  $^{137}\text{Cs}$ , 140-kBq  $^{59}\text{Fe}$  and 50-kBq  $^{65}\text{Zn}$ . The measurements of SB-1 and SB-2 were carried out for 113 and 25 hours, respectively. Each sample was fixed on a plane 1.5 cm apart from the center of the front detector.

The sections of the cones defined for each event were accumulated on the plane where the sample was fixed, in order to obtain the two-dimensional image of the RIs. This image is called a simple back-projection (SBP). The SBP image for SB-1 is shown in Fig. 2 (a). The smeared image in the SBP was deconvoluted assuming that the point-spread function (PSF) was shift-invariant. We call the resultant image DABP (deconvolution after back-projection). The DABP image for SB-1 is shown in Fig. 2 (b).

The  $\gamma$ -ray spectrum measured by the GREI system for SB-2 is shown in Fig. 3 (a). The peaks of the intrinsic  $\gamma$  rays for each RI are clearly separated in the spec-

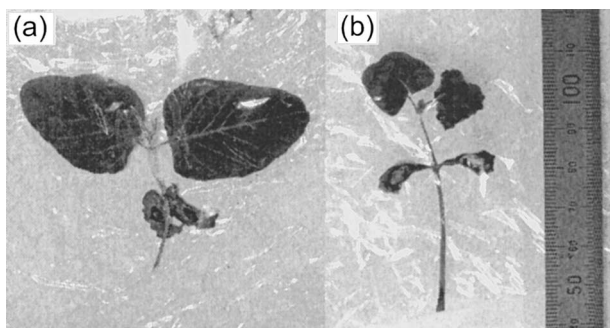


Fig. 1. Photographs of soybean plants administered with RIs. (a) SB-1. (b) SB-2.

\*<sup>1</sup> Graduate School of Science, Kyushu University

\*<sup>2</sup> Nishinippon Institute of Technology

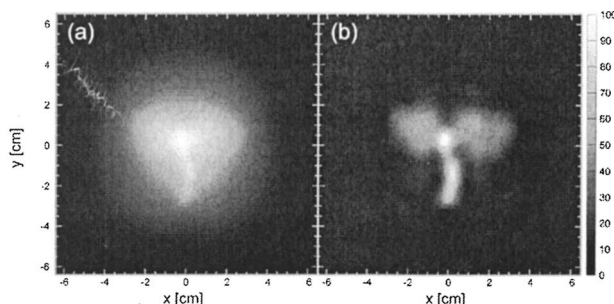


Fig. 2. Results of imaging  $^{65}\text{Zn}$  in SB-1. (a) SBP image. (b) DABP image.

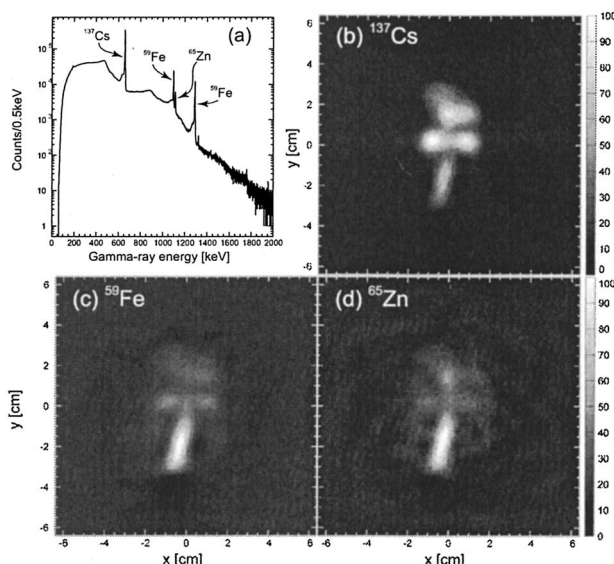


Fig. 3. Results of imaging the RIs in SB-2. (a) The  $\gamma$ -ray spectrum measured by the GREI system. (b)–(d) DABP images of each RI.

trum. By setting energy gates at each peak, DABP images were obtained for each RI (Fig. 3 (b)–(d)). It was successfully observed that each RI has a different distribution in SB-2.

The development of the GREI system is still in progress in order to improve the position resolution and the sensitivity, including an accurate treatment of the PSF, which is significantly dependent on the position in reality.

### References

- 1) S. Motomura and S. Enomoto: J. Clin. Exper. Med. **205**, 884 (2003).



# Implementation of GREI system with DOI measurement capability

S. Motomura, M. Kibe,<sup>\*1</sup> Y. Gono, A. Odahara,<sup>\*2</sup> H. Takeichi, S. Enomoto, and Y. Yano

The Compton camera proposed for  $\gamma$ -ray emission imaging<sup>1,2)</sup> (GREI) consists of two sets of double-sided orthogonal-strip (DSOS) germanium (Ge) detectors which are arranged in parallel. The dimensions of the DSOS Ge detectors are 39 mm  $\times$  39 mm  $\times$  10 mm and 39 mm  $\times$  39 mm  $\times$  20 mm for the front and rear detectors, respectively. The strip pitch is 3 mm for both detectors. The transverse position of a  $\gamma$ -ray interaction point (TOI) in the DSOS Ge detector is determined by a combination of the anode and cathode strips with the accuracy given by the width of the strip. It is also possible to determine the depth of the  $\gamma$ -ray interaction point (DOI) by taking into account the time difference between the signals from the anode and cathode.<sup>3,4)</sup>

We have fabricated a prototype of the GREI system which is able to utilize the DOI information. Timing filter amplifiers (TFAs) and constant fraction discriminators (CFDs) were employed in order to generate the timing pulses from each output of the preamplifiers. The time constants of the TFAs were 500 ns and 60 ns for differentiation and integration, respectively. The fraction for the CFDs was 0.5. The delay time for the CFDs was 50 ns, which was the upper limit of the modules.

In order to check the performance of the system, we measured  $\gamma$  rays from a point source of  $^{152}\text{Eu}$  placed in front of the Compton camera. Histograms of the time difference between the signals from the anode and the cathode were constructed for some intrinsic  $\gamma$  rays of  $^{152}\text{Eu}$  by setting energy gates at each peak. A result for the energy gate at 122 keV is shown in Fig. 1. The origin of the time difference was set where is maximum. As shown in Fig. 1, the dependence of the count on time difference has good agreement with the attenuation curve of 122-keV  $\gamma$  ray in Ge crystal assuming that the time differences of 0 ns and 140 ns correspond to the DOI values of 0 cm and 1 cm, respectively. This implies that DOI can be measured directly from the time difference. In addition, it was found that the range of the time difference is constant even when the  $\gamma$ -ray energy is changed. Because of this fact, the algorithm for DOI measurement has become very simple. This is an advantage of using CFD.

The effect of DOI measurement was investigated by obtaining simple back-projection (SBP) images of a point source of  $^{65}\text{Zn}$ , which emits 1115-keV  $\gamma$  rays. The source was placed 4.9 cm away from the center of the front detector. Two-dimensional (2D) SBP images were obtained by accumulating the sections of the cones defined event by event on the plane where the

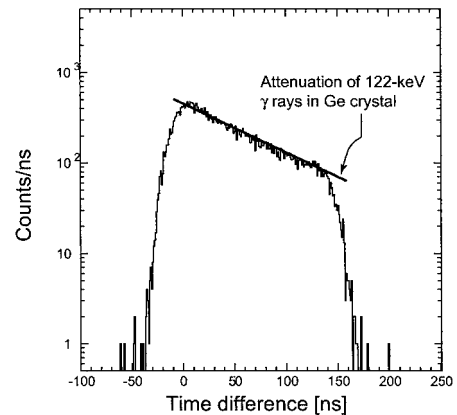


Fig. 1. Histogram of the time difference between the signals from the anode and cathode strips. The energy gate was set at the 122-keV  $\gamma$ -ray peak. The time differences of 0 ns and 140 ns are assumed to correspond to the DOI values of 0 cm and 1 cm, respectively.

source was located. The full-width at half maximum (FWHM) of the 2D-SBP was 8 mm when DOIs were fixed at the half depth of each detector. On the other hand, the FWHM of the 2D-SBP was 6 mm when DOIs were measured from the time difference.

The effect of DOI measurement becomes more significant when TOI is measured more accurately. 2D-SBP images of the  $^{65}\text{Zn}$  point source under the same conditions as in the above experiment were obtained by simulation using GEANT when: (1) TOIs were fixed at the center of each strip and (2) TOIs were assumed to be measured with an accuracy of 0.2 mm in FWHM. When the TOIs were fixed, the FWHMs of the 2D-SBP images were 8 and 6 mm for the fixed and measured DOIs, respectively. These values agreed well with the results of the experiment. When the TOIs were assumed to be measured with an accuracy of 0.2 mm, on the other hand, the FWHMs of the 2D-SBP images were 6 and 2 mm for the fixed and measured DOIs, respectively. We have already developed a method of measuring TOI more accurately than the width of the strip. This method utilizes signals from the strips adjacent to the strip used for DOI measurement. The implementation of this device is in progress.

## References

- 1) S. Motomura and S. Enomoto: *J. Clin. Exper. Med.* **205**, 884 (2003).
- 2) Y. F. Yang et al.: *IEEE Trans. Nucl. Sci.* **48**, 656 (2001).
- 3) S. Motomura et al.: *RIKEN Accel. Prog. Rep.* **36**, 154 (2003).
- 4) M. Momayzei et al.: *Proc. SPIE* **3768**, 530 (1999).

<sup>\*1</sup> Graduate School of Science, Kyushu University

<sup>\*2</sup> Nishinippon Institute of Technology

## Three-dimensional imaging by GREI system

S. Motomura, H. Takeichi, M. Kibe,\*<sup>1</sup> Y. Gono, A. Odahara,\*<sup>2</sup> S. Enomoto, and Y. Yano

The Compton camera for  $\gamma$ -ray emission imaging<sup>1)</sup> (GREI) consists of double-sided orthogonal-strip (DSOS) germanium (Ge) detectors which are arranged in parallel. The GREI system makes it possible to obtain three-dimensional (3D) images of radioisotopes (RIs) distributed in a sample by measuring the sample from only one direction. This is an advantage of employing a Compton camera system.

In order to examine the feasibility of 3D imaging using the GREI system, we produced 3D simple back-projection (3D-SBP) images by simulations using GEANT. The 3D-SBP images were obtained by accumulating three-dimensionally the cones defined for each event. The depth of a  $\gamma$ -ray interaction point in the DSOS Ge detector was assumed to be measured with an accuracy of 1 mm in the full width at half maximum. A point source of 1115 keV  $\gamma$ -rays was positioned at the origin of the coordinate axes. The Compton camera was located on the  $z$ -axis. The distance between the source and the center of the first DSOS Ge was 6.9 cm. In addition, we performed simulations of 3D-SBP by employing two Compton cameras. The second Compton camera was located on the  $x$ -axis with the same distance from the source as that of the first Compton camera.

The 3D-SBP images (the section on the  $y = 0$  surface) produced by the above simulation are shown in Fig. 1. One can see that their shape is distorted. Note that these images are not the final images that we intend to obtain; they are used as point-spread functions (PSFs) when 3D images are deconvoluted.

The quality of these images was evaluated on the basis of their Fourier power spectrum (Fig. 2). When the spatial frequency is higher than  $f_c$ , as indicated in Fig. 2, the Fourier power is dominated by the random noise contained in the image. Thus the component of the image cannot be reconstructed if the frequency is

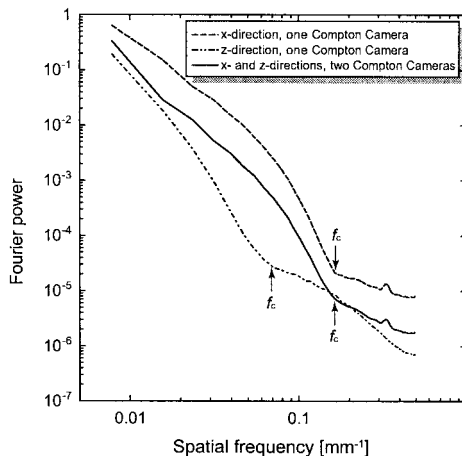


Fig. 2. Fourier power spectra of PSFs.

higher than  $f_c$ . When only one Compton camera is used,  $f_c$  in the  $z$ -direction is much lower than that in the  $x$ -direction. When two Compton cameras are used, on the other hand,  $f_c$  in the  $z$ -direction is improved to the same level as that in the  $x$ -direction. Therefore, it is advantageous to use two Compton cameras for obtaining 3D images.

In addition, an example of 3D imaging using the GREI system is shown in Fig. 3. A 3D-SBP was obtained from measured data first, then deconvoluted by a shift-invariant PSF. The image of the RI was successfully visualized three-dimensionally.

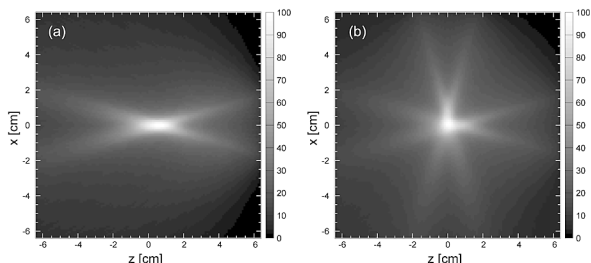


Fig. 1. Slices of 3D-SBP images on  $y = 0$  surface. (a) One Compton camera. (b) Two Compton cameras.

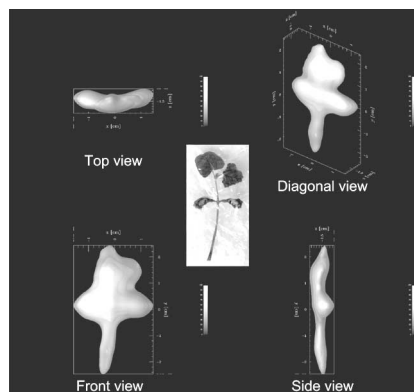


Fig. 3. 3D image of  $^{137}\text{Cs}$  distributed in a soybean sample. Photograph of the sample is also shown at the center.

### References

1) S. Motomura and S. Enomoto: J. Clin. Exper. Med. **205**, 884 (2003).

\*<sup>1</sup> Graduate School of Science, Kyushu University  
 \*<sup>2</sup> Nishinippon Institute of Technology

## Reconstruction methods for GREI

H. Takeichi, S. Motomura, R. Hirunuma, K. Igarashi, S. Enomoto, and Y. Yano

Reconstruction methods for emission imaging were examined and a version of maximum likelihood expectation-maximization (MLEM) algorithm for  $\gamma$  ray emission imaging (GREI) was implemented.

The development of computed tomography (CT) has been one of the most remarkable achievements in medical imaging physics. The internal structure of a three-dimensional sample can be reconstructed from a set of two-dimensional projections through computation, enabling precise and nondestructive measurement of the shape and location of an object inside, such as an organ or a tumor.

CT application to an imaging modality other than X ray such as emission tomography and magnetic resonance imaging provided not only considerable diagnostic information but also problems specific to the new technique. In the case of GREI, unlike the collimated emission imaging, views from varying viewpoints are obtained not by rotating the detector but by accumulating data with various scattering angles following Compton kinematics; therefore, the images are ‘merged’ and not separated into different projection images. The data is in a six-dimensional space where each  $\gamma$  ray is represented by a set of six parameters: three for the location of the interaction, one for the scattering angle, and two for the orientation of the  $\gamma$  ray. Each  $\gamma$  ray defines a cone surface on which the source lies instead of a line in the reconstruction. In this report, problems associated with the ‘merged cone’ representation and the solution will be described.

The easiest reconstruction method is simple back projection (SBP), in which the cone surface is simply ‘drawn’ in the reconstruction space, representing the probability distribution or the uncertainty of the location of the source. When all the cone surfaces are overlaid, they collectively describe the estimation of the source distribution, namely, the reconstruction. Just as the estimated source location is ‘smeared’ along the line of projection in the collimated emission imaging, the estimated source is distributed uniformly over the surface of the cone in SBP-GREI. Although this may provide an impression that SBP-GREI is skewed in a complicated manner, with a number of  $\gamma$  rays, the blur is described by a smooth point spread function (PSF), which can be either measured experimentally or estimated by simulation. Because PSF depends on the energy that determines the scattering angle, it is specific to a nuclide.

An improved reconstruction method, therefore, is deconvolution after back projection (DABP), in which

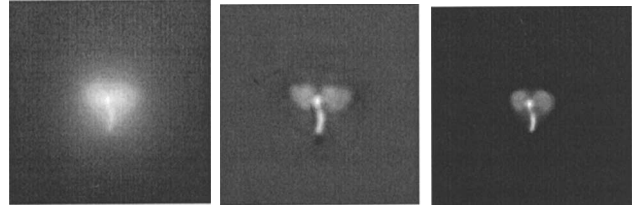


Fig. 1. Sample images obtained by SBP, DABP, and MLEM.

the blur is removed from SBP by deconvolving PSF. Although this may appear valid as long as only a planar-thin sample such as a slice is imaged and the estimation of  $z$  is not critical, such as astrophysics applications of the Compton camera, DABP suffers from severe distortion in three-dimensional reconstruction of a volumetric sample. This is because PSF is not shift-invariant along the  $z$ -axis, although it is roughly shift-invariant along the  $x$ - and  $y$ -axes except at the periphery of the detector. The radius of the circle defined as a cross section of the cone increases linearly with increasing distance from the detector, introducing different blurs at different depths, so that PSF is  $z$ -dependent. Note that an analytical distortion compensation is difficult because the required compensation depends on the true source distribution estimated.

Therefore, we implemented an iterative MLEM algorithm for GREI. The idea of MLEM is to iteratively update the estimated source distribution depending on a correction term. The correction term is defined as the ratio of the actual projection to the forward projection of the current estimate and back-projected into the reconstruction space using the probability of a  $\gamma$  ray being emitted from a location in the sample space and detected at a location in the projection. The probability can be estimated by simulation or calculated analytically in some cases.

Figure 1 shows images obtained by different reconstruction methods. From left to right, the SBP, DABP, and MLEM images of a young soybean shoot administered with  $^{65}\text{Zn}$  single tracer are shown. Instead of the exact PSF, a Butterworth filter was used in DABP to reduce high spatial frequency noise. MLEM is the result of  $> 700$  iterations. The MLEM image appears less noisy than the DABP image.

In summary, MLEM is implemented as an initial reconstruction method for GREI. Improvements in estimation accuracy and computational efficiency are under consideration.

## A note on the reconstruction method for GREI

H. Takeichi

The relationship between image reconstruction and statistical data analysis in an application of  $\gamma$  ray emission imaging (GREI) to functional brain imaging is discussed and their integration, cascaded expectation maximization (CEM), is proposed.

Estimation is always accompanied by error, which needs to be minimized. In its minimization, it is important to identify its characteristic property and take an appropriate strategy depending on the property. In functional brain mapping by emission imaging, for example, the result of the statistical data analysis depends partially on the choice of the image reconstruction method. This may be because the nature as well as the magnitude of the error depends on the reconstruction method. In other words, when the image reconstruction is designed, the manner in which the reconstructed image is used needs to be considered. In this report, the nature of the error in two image reconstruction methods for GREI and two data analysis methods in functional brain imaging are described and their relationship is discussed.

As described elsewhere in this volume, there are two types of reconstruction methods: analytical and iterative. The analytical method is a shift-invariant deconvolution called deconvolution after back projection (DABP), and the iterative method involves iterative error estimation and propagation using a shift-invariant or a shift-variant probability relating the projection and the reconstruction, called maximum likelihood expectation-maximization (MLEM). Only the effect of an error in the estimated point spread, *i.e.* point spread imperfection (PSI) will be considered. PSI is uniformly distributed over the entire image in DABP, because it is in the shift-invariant deconvolution kernel, while PSI can be nonuniformly distributed and confined to a neighborhood in MLEM, because it can be localized to a subset of the probabilities relating the projection and the reconstruction. Although MLEM is more advantageous than DABP with respect to image reconstruction itself, it is also important to examine their relative superiority and inferiority with respect to their application.

In functional brain imaging, the effect of an experimental manipulation is evaluated by generating a map that represents a change in the metabolism or the regional cerebral blood flow due to the manipulation at each location in the brain. There are two methods for generating the map: model-based and data-driven.

In the model-based method, the effect is measured in terms of the mean signal difference between the activation state and the resting state at each location.

The Student's t-test is often performed with a correction for multiple comparisons. This is called general linear model (GLM) because it assumes that the experimental effect is linear. The model is described as follows:

$$X = \beta G + \varepsilon$$

where  $X$  is the data *i.e.* the signal at each location at each time point,  $\beta$  is the coefficient for the magnitude of the effect at each location,  $G$  is the time course of the effect, and  $\varepsilon$  is the residual error. In this case,  $G$  is given and  $\beta$  is estimated and compared with  $\varepsilon$ .

In the data-driven method, the effect is characterized as a coherent mean signal difference between the states at a set of locations. The most significant difference between the model-based method and the data-driven method is that the former uses an extrinsic model *i.e.* the time course of the experimental manipulation for the identification of the effect, while the latter uses an intrinsic criterion *i.e.* the statistical independence between the effects for their identification. A popular definition of independence is the absence of correlation, which is identified by analyzing covariance. This is called principal component analysis (PCA). A revised definition is the absence of mutual information, which can be identified by analyzing the 'co-kurtosis' or higher order statistics. This is called independent component analysis (ICA). In both cases, the analysis is described as follows:

$$X = \beta G$$

where the residual error is omitted because it is not essential in this analysis.

A critical difference between GLM and ICA with respect to the image reconstruction method is that while the effect is evaluated for each location in GLM, it is evaluated for each set of locations in ICA. Because GLM is a highly localized analysis, it is more susceptible to the localized PSI in MLEM than to the distributed PSI in DABP. In contrast, because ICA is less localized, the influence of localized PSI in MLEM is less severe than GLM.

In addition, as ICA can be implemented by an expectation maximization algorithm, there is a possibility of performing cascaded expectation maximization (CEM) by combining the image reconstruction (MLEM) and the statistical data analysis (ICA). By establishing a direct link between the measurement and the application, CEM enables an adaptive and real-time analysis of a complex system.

## Image reconstruction method with compensation for scattering angular uncertainty in MT-GEI

M. Hirasawa,<sup>\*1</sup> T. Tomitani,<sup>\*1</sup> S. Shibata,<sup>\*1</sup> S. Motomura, S. Enomoto, Y. Gono,<sup>\*2</sup> and Y. Yano

The MT-GEI (multitracer gamma-ray emission imager) has been developed to image living-body tomograms of multitracers produced at the RIKEN Ring Cyclotron. Multitracer imaging can be attained using an imaging device based on the Compton camera principle. The MT-GEI consists of two three-dimensional position-sensitive  $\gamma$ -ray detectors. The  $\gamma$  ray emitted from the each tracer undergoes Compton scattering in the first detector followed by photoelectric absorption in the second detector. The direction of the  $\gamma$  ray can be confined to a cone whose vertex, axis and vertex angle are determined by the scattering point, the scattering ray line and twice the Compton scattering angle, respectively. The scattering angle is calculated from the deposited energies using the Compton formula. However, the calculated angle includes uncertainty due to the finite energy resolution of the first detector and the Doppler broadening of the Compton electron energy in the first detector. Figure 1 shows the dependence of the angular uncertainty in the MT-GEI on the emitted  $\gamma$ -ray energy for scattering angles of 10, 20 and 30 degrees. As the energy increases, the uncertainty decreases rapidly and tends to level off to 2 or less degrees in FWHM beyond 300 keV.

An image reconstruction method using the cone data obtained by the MT-GEI was developed first without

compensating for the above angular uncertainty.<sup>1)</sup> The algorithm has been revised to compensate for the uncertainty as<sup>2)</sup>

$$\alpha_n(\cos \omega) \equiv \int_{-1}^1 d\langle \mathbf{s}, \mathbf{t} \rangle Br_t(\mathbf{s}, \mathbf{t}; \omega) P_n(\langle \mathbf{s}, \mathbf{t} \rangle), \quad (1)$$

$$H_n \equiv \int_{\cos \omega_2}^{\cos \omega_1} d \cos \omega h(\cos \omega) \alpha_n(\cos \omega)^2, \quad (2)$$

and

$$f(\mathbf{s}) \approx \int_{\cos \omega_2}^{\cos \omega_1} d \cos \omega \int_S d\Omega_t \times \sum_{n=0}^{n_{\max}} \frac{2n+1}{4\pi} \frac{\alpha_n(\cos \omega)}{H_n} P_n(\langle \mathbf{t}, \mathbf{s} \rangle) g(\mathbf{t}; \omega), \quad (3)$$

where  $f(\mathbf{s})$  denotes the relative tracer density line integrated on a line with  $\mathbf{s}$  in its direction unit vector, and  $g(\mathbf{t}; \omega)$  represents the number density of cone data with  $\mathbf{t}$  in its axial (scattering)-direction unit vector with half of its vertex (calculated scattering) angle  $\omega$ . Furthermore,  $P_n$  and  $h$  denote the Legendre function of  $n$ -th degree and the Klein-Nishina formula, respectively, and  $\Omega_t$  and  $\langle \mathbf{s}, \mathbf{t} \rangle$  are the solid angle with  $\mathbf{t}$  in its direction unit vector and the inner product of  $\mathbf{s}$  and  $\mathbf{t}$ , respectively.  $Br$  describes the scattering angular uncertainty defined by

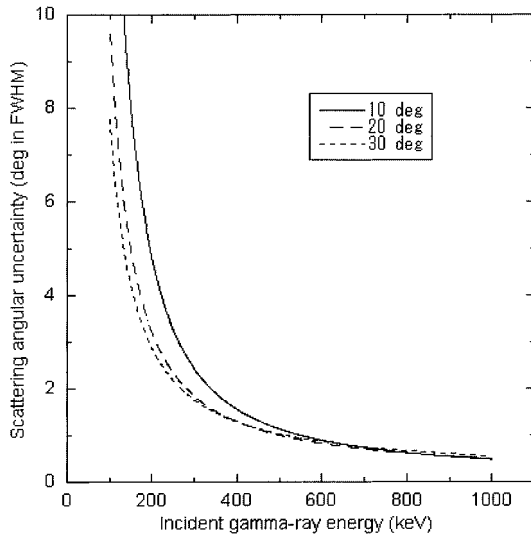


Fig. 1. Dependence of scattering angular uncertainty in MT-GEI on incident  $\gamma$ -ray energy. Solid, dashed and dotted curves correspond to the scattering angles of 10, 20 and 30 degrees, respectively.

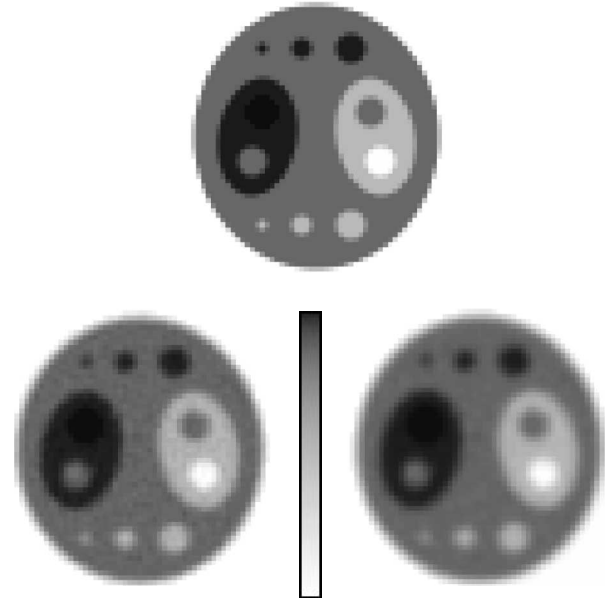


Fig. 2. Reconstructed images with (left) and without (right) compensation from the simulated cone data for MT-GEI. The top is the original phantom.

<sup>\*1</sup> National Institute of Radiological Sciences

<sup>\*2</sup> Kyushu University

$$Br(\mathbf{s}, \mathbf{t}; \omega) \equiv \frac{1}{\sqrt{2\pi} \sigma \sin \omega} \exp \left\{ -\frac{(\langle \mathbf{s}, \mathbf{t} \rangle - \cos \omega)^2}{2(\sigma \sin \omega)^2} \right\}, \quad (4)$$

where  $\sigma$  is the standard deviation of the scattering angular uncertainty.

Figure 2 shows the reconstructed distribution images with and without compensation for the angular uncertainty. The  $10^8$  cone data obtained by the MT-GEI, with 10 to 30 degrees in the calculated scattering angle, are simulated using a digital phantom emitting 364 keV  $\gamma$  rays. The reconstructed image with compen-

sation has higher spatial resolution but greater noise than that without compensation.<sup>3,4)</sup>

#### References

- 1) T. Tomitani and M. Hirasawa: *Phys. Med. Biol.* **47**, 2129 (2002).
- 2) M. Hirasawa and T. Tomitani: *Phys. Med. Biol.* **48**, 1009 (2003).
- 3) T. Tomitani and M. Hirasawa: *IEEE Trans. Nucl. Sci.* **50**, 1602 (2003).
- 4) M. Hirasawa and T. Tomitani: *Proc. 2003 IEEE NSS/MIC*, M14-303 (2004).

## Exposure of frozen human cells to heavy ions

F. Yatagai, H. Ryuto, N. Fukunishi, and F. Hanaoka

Exposure to ionizing radiation (IR) induces various types of DNA lesion including base damage, cross-linking, and DNA single- and double-strand breaks (DSBs). DSBs were originally considered to be the critical cytotoxic lesions. We have recently established a gene mutation assay system whose target is the autosomal heterozygous thymidine kinase (*TK*) locus in the human lymphoblastoid cell line TK6.<sup>1)</sup> This assay system enables the detection of genetic alterations at the chromosome level as loss of the functional allele (or loss of heterozygosity (LOH)). Using this assay system, we succeeded in the (10 cGy) detection of IR-specific hemizygous LOHs (interstitial deletions).<sup>2)</sup> The 22 keV/ $\mu\text{m}$  C ion beam irradiation has shown higher induction of such an LOH event than X-ray irradiation,<sup>3)</sup> probably due to an efficient production of DSBs by C ions compared to X-rays.<sup>4)</sup>

The direct effect of an accelerated heavy ion beam on DNA can be well estimated by the irradiation of frozen cells, because the indirect effect mediated by free radicals can be suppressed under such a frozen condition. Furthermore, the long-period preservation of cells by freezing is convenient for detecting the genetic effects of low-dose and low-dose-rate irradiation. The above LOH assay system appears to be very useful for elucidating genetic changes in IR-irradiated frozen cells. The preliminary results obtained are described below.

The viability of TK6 cells was estimated from plating efficiency (PE) (Table 1), which was determined by the limiting dilution method as previously described.<sup>1-3)</sup> TK6 cells were exposed to IR under the

frozen condition ( $-80^\circ\text{C}$ ) and preserved at the same temperature after the exposure.

The relative PE of the cells preserved for one week after the 2 Gy X-ray exposure was 20% that of unirradiated cells, indicating a percentage higher than 8% in our previous experiment under the suspension-culture conditions. Such higher viability was also observed after the 2 Gy C ion irradiation, as determined by the relative PEs of 17% and 6% under the frozen and suspension conditions, respectively. These results strongly suggest that the indirect effect of irradiation on cell killing is suppressed by the exposure to freezing condition. Similar tendency was obtained with one month preservation. The viability was not reduced by the 10 cGy irradiation in any case (Table 1).

The  $\text{TK}^-$  mutation frequencies for the cells irradiated with C ions under the frozen condition and preserved as frozen were also determined by the method as previously described<sup>1-3)</sup> (Table 2).

In contrast to the reduction in the cell killing effect of C ion exposure under the frozen condition as described above, the enhancement of mutation frequency was similar or rather higher than that in the cell-suspension case in our previous study.<sup>3)</sup> A higher induction of mutation was observed with a longer preservation. Our future analyses for the LOH events detected as  $\text{TK}^-$  mutations can be expected to contribute to the basic understanding of direct-hit DNA damage as well as the estimation of the genetic effects of low-dose irradiation.

Table 2. Mutation frequencies for cells irradiated with C ions under the frozen condition and preserved as frozen.

Frozen period after C ion exposure	Mutation Frequency ( $\times 10^{-5}$ ) "PE (%) [Relative value]"		
	0 Gy	0.1 Gy	2.0 Gy
2 days	1.4	1.6	6.0
	"23 [1.0]"	"17 [0.74]"	"18 [0.78]"
1 month	1.9	5.1	17
	"21 [1.0]"	"16 [0.76]"	"11 [0.52]"

Table 1. Reduction in the viability of cells irradiated under the frozen condition and preserved by freezing after the irradiation.

Radiation (Frozen <sup>§</sup> )	Plating Efficiency (%) [Relative]			
	0 Gy	0.1 Gy	0.5 Gy	2.0 Gy
X-rays (1 week)	25 [1.0]	21 [0.84]	13 [0.52]	5.1 [0.20]
X-rays (1 month)	6.1 [1.0]	5.6 [0.92]	3.8 [0.63]	4.3 [0.70]
C ions (1 week)	8.3 [1.0]	8.8 [1.06]	6.4 [0.77]	1.4 [0.17]
C ions (1 month)	10 [1.0]	8.5 [0.85]	8.3 [0.83]	5.2 [0.52]

<sup>§</sup> Period of freezing after radiation exposure

### References

- 1) M. Honma et al.: Mol. Carcinog. **28**, 203 (2000).
- 2) S. Morimoto et al.: Radiat. Res. **157**, 533 (2002).
- 3) S. Morimoto et al.: J. Radiat. Res. **43** Suppl. 163 (2002).
- 4) G. Taucher-Sholtz and G. Kraft: Radiat. Res. **151**, 595 (1999).

## Effects of heavy-ion irradiation on DNA replication in mammalian cells

M. Izumi, T. Tsukada, M. Tomita, N. Fukunishi, H. Ryuto, F. Yatagai, and F. Hanaoka

Eukaryotic cells have surveillance mechanisms, or checkpoint pathways, which detect damaged DNA or ongoing DNA replication and block cell cycle progression in order to allow sufficient time for repair of damaged DNA or to complete replication. In response to a moderate dose of ionizing radiation, the overall rate of DNA replication in an asynchronously growing mammalian cell culture is reduced by ~50% within 30 min.<sup>1)</sup> This response is mainly caused by inhibiting subsequent initiation at origins of replication, while allowing forks already in progress to continue.<sup>1)</sup> Recent studies have shown that mammalian cells exposed to ionizing radiation such as X-rays activate the ATM kinase, which triggers two parallel cascades that cooperate to inhibit DNA synthesis, although further studies are necessary to identify the downstream targets of these cascades.<sup>2)</sup> In this study, we examined the cell cycle progression and the rate of DNA synthesis of human lymphoblastoid TK6 cells after irradiation with carbon ions (LET: 22 keV/ $\mu$ m).

When TK6 cells were irradiated with 1 Gy of carbon beam, most cells were arrested at G1 or G2 phase 16 h after irradiation (Fig. 1). The rate of bromodeoxyuridine (BrdU) incorporation did not change after irradiation and S phase progressed without retardation. These results indicate that TK6 cells undergoing DNA replication did not respond to ionizing radiation levels that were able to block cells in G1 or G2 phase. This S phase specific resistance against DNA damage appears to occur in budding yeast as well.<sup>3)</sup> It has been reported that replication forks pause frequently during a normal S phase, often leading to parental strand breakage.<sup>4,5)</sup> The threshold necessary for the checkpoint activation may be elevated during S phase so that damage arising from normal fork progression does not cause cell cycle arrest.

On the other hand, the rate of BrdU incorporation was suppressed when cells were irradiated at higher dose. Interestingly, the suppression in the late S phase was observed even at 3 Gy (Fig. 1, white arrows), whereas the suppression in the early S phase required 5 Gy irradiation (Fig. 1, black arrow). The different sensitivities between early S phase and late S phase may be due to the different chromatin structures, *i.e.*, the higher levels of irradiation are necessary for

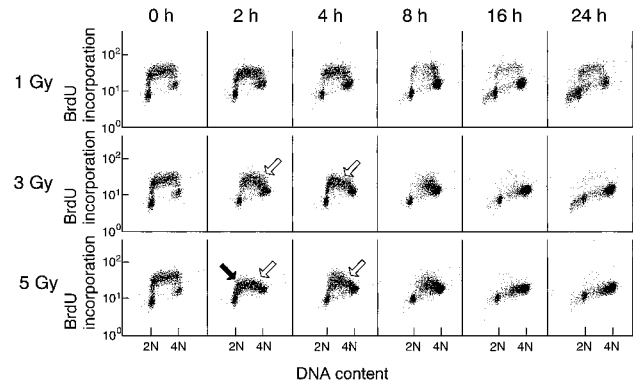


Fig. 1. Rate of DNA synthesis and cell cycle progression of TK6 cells after carbon-ion irradiation (1, 3, or 5 Gy). TK6 cells were pulse-labeled with 10  $\mu$ g/ml bromodeoxyuridine (BrdU) for 30 min at indicated hours after irradiation and stained with FITC-conjugated anti-BrdU antibody. Chromosomal DNA was stained with propidium iodide. BrdU incorporation and DNA content (2N, 4N) were measured by flow cytometric analysis. White arrows indicate the suppressed DNA replication in the late S phase. The black arrow indicates the suppressed DNA replication in the early S phase.

suppressing DNA synthesis when the euchromatic regions are replicated. Alternatively, the different stages of S phase provoke different checkpoint responses with respect to the components or the activated levels of checkpoint pathways. At present, we are analyzing the checkpoint response after heavy-ion irradiation in more detail.

### References

- 1) J. M. Larner, H. Lee, and J. L. Hamlin: *Mol. Cell. Biol.* **14**, 3 (1994).
- 2) J. Falck, J. H. J. Petrini, B. R. Williams, J. Lukas, and J. Bartek: *Nat. Genet.* **30**, 290 (2002).
- 3) K. Shimada, P. Pasero, and S. M. Gasser: *Genes Dev.* **16**, 3236 (2002).
- 4) A. M. Deshpande and C. S. Newlon: *Science* **272**, 1030 (1996).
- 5) Y. Wang, M. Vujcic, and D. Kowalski: *Mol. Cell. Biol.* **21**, 4938 (2001).



## Effect of heavy ions on the activation of DNA double-strand break repair proteins

M. Tomita, A. Naruto,\* T. Tsukada, M. Izumi, N. Fukunishi, H. Ryuto, and F. Yatagai

DNA double-strand breaks (DSBs) are the most lethal damage induced by ionizing radiation. Accelerated heavy ions have been shown to induce DNA clustered damage, which is two or more DNA lesions induced within a few helical turns. The higher biological effectiveness of heavy ions could be caused predominantly by the induction of complex DNA clustered damage, leading to nonrepairable DSBs.<sup>1)</sup> In mammalian cells, DSBs are repaired by mainly two distinct and complementary mechanisms, namely, non-homologous end-joining (NHEJ) and homologous recombination (HR).<sup>2)</sup> DNA-dependent protein kinase (DNA-PK) is composed of a catalytic subunit (DNA-PKcs) and DNA-binding heterodimers (Ku70 and Ku86). DNA-PK acts as a sensor of DSB for the NHEJ, since DNA-PK is activated to bind to the ends of double-stranded DNA.<sup>3)</sup> Cells defective in each of the DNA-PK components are extremely radiosensitive. It has been reported that human radiosensitive malignant glioma M059J cells do not express DNA-PKcs.<sup>4)</sup> To elucidate the physiological role of DNA-PK in the cellular response to heavy-ion-induced DSBs, we examined the sensitivity of M059J cells and control M059K cells, which have a normal level of DNA-PKcs expression, to accelerated heavy ions.

Figure 1 shows the clonogenic surviving fractions of M059K and M059J cells irradiated with 250 kV X-rays, 135 MeV/u carbon ions (C ions) at 80 keV/ $\mu$ m, 490 MeV/u silicon ions (Si ions) at 200 keV/ $\mu$ m, 95 MeV/u argon ions (Ar ions) at 300 keV/ $\mu$ m and 90 MeV/u iron ions (Fe ions) at 1000 keV/ $\mu$ m. The surviving fractions were determined by a colony formation assay. DNA-PKcs-defective M059J cells were more sensitive to both X-rays and heavy ions than

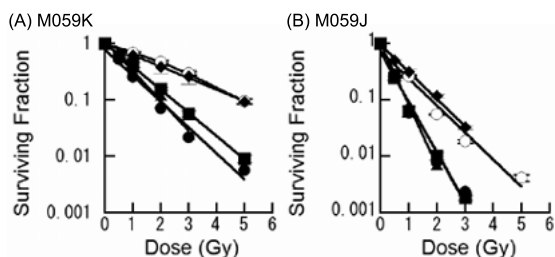


Fig. 1. Cell survival curves for M059K (A) and M059J (B) cells irradiated with X-rays (2 keV/ $\mu$ m, open circle), C ions (80 keV/ $\mu$ m, solid box), Si ions (200 keV/ $\mu$ m, solid triangle), Ar ions (300 keV/ $\mu$ m, solid circle) or Fe ions (1000 keV/ $\mu$ m, solid diamond).

control M059K cells. The radiosensitivities of both M059K and M059J cells to C, Si and Ar ions were higher than those to X-rays and Fe ions. The lower cell-killing efficiency of Fe ions than those of C, Si and Ar ions was caused by particle energy deposition in excess of cell killing, usually named the over-killing effect.

The relative biological effectiveness (RBE) were calculated using the dose leading to 10% cell survival ( $D_{10}$ ) from cell survival curves. Figure 2 shows the relationship between LET and RBE. In general, the RBE increased with LET, reaching maximum, and then decreased.<sup>5)</sup> The RBE of M059J cells, however, was significantly lower than that of M059K cells. The peak RBE values were 2.01 and 2.93 for M059K cells, and 1.76 and 1.84 for M059J cells at 80 keV/ $\mu$ m and 300 keV/ $\mu$ m, respectively. Previously, we have reported that HR-related proteins, NBS1 and histone H2AX, recognized heavy-ion-induced DNA clustered damage.<sup>6)</sup> Our present and previous results suggest that both HR and NHEJ play important roles in the repair of the heavy-ion-induced DSBs, and that the cellular RBE is partly determined by the cellular DNA repair capacity.

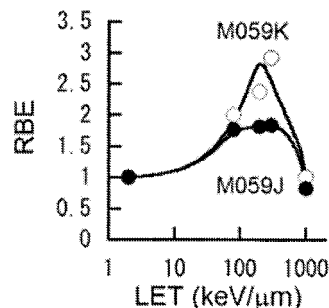


Fig. 2. Relative biological effectiveness (RBE) of accelerated heavy ions in M059K and M059J cells. The RBE values were calculated using the dose leading to 10% cell survival ( $D_{10}$ ) from cell survival curves.

### References

- 1) E. A. Blakely and A. Kronenberg: *Radiat. Res.* **150**, S126 (1998).
- 2) K. K. Khanna and S. P. Jackson: *Nat. Genet.* **27**, 247 (2001).
- 3) G. C. M. Smith and S. P. Jackson: *Genes Dev.* **13**, 916 (1999).
- 4) S. Lees-Miller et al.: *Science* **267**, 1183 (1995).
- 5) Y. Furusawa et al.: *Radiat. Res.* **154**, 485 (2000).
- 6) M. Tomita et al.: *RIKEN Accel. Prog. Rep.* **36**, 133 (2003).

\* Laboratory of Environmental and Molecular Biology, Tokyo University of Pharmacy and Life Science

## High dose of heavy-ion beams cause *p53*-dependent cell death

T. Tsukada, M. Tomita, N. Fukunishi, H. Ryuto, and M. Izumi

It is well known that the tumor suppressor gene *p53* promotes cell cycle arrest or apoptosis after DNA damage.<sup>1)</sup> *P53* is one of the target substrate of activated ATM kinase in X-ray irradiation, related to the cascade of repair of the damaged DNA. Heavy-ion beams have been known to induce clustered DNA damage efficiently, and it is considered that such severe damage is difficult to repair.

To clarify the *p53* functions at cellular responses after exposure to heavy-ion beams, we used two human B-lymphoblast cell lines derived from the same donor but differing in the *p53* status: TK6 (wild-type *p53*), and NH32 (*p53* deficient) and examine the viabilities of these cells after the irradiation.

In our previous report, there are no significant differences in apoptotic rate between TK6 and NH32 at 3 Gy of C ions (22 keV/ $\mu$ m) or Fe ions.<sup>2)</sup> However, exposure to heavy-ion beams, such as C ions or Fe ions, induced *p53* expression,<sup>3)</sup> suggesting that *p53* may also play an important role in cellular responses induced by heavy-ion beams. In this study, we examined the involvement of *p53* in the cell death process in more detail.

Cells were exposed to heavy-ion beams (C ions: 22 keV/ $\mu$ m or 80 keV/ $\mu$ m, Fe ions: 1000 keV/ $\mu$ m, Ar ions: 300 keV/ $\mu$ m) at doses of 1, 3, 5, 10 Gy (C ions: 22 keV/ $\mu$ m, Fe ions) and 1, 2, 3, 5 Gy (C ions: 80 keV/ $\mu$ m) and 0.5, 1, 2, 3, 5, 10 Gy (Ar ions). Apoptosis was determined by the externalization of phosphatidylserine and was measured as annexin V-positive cells by flow cytometry.

Figure 1 shows the percentage of annexin V-positive cells, which included apoptotic cells (annexin V+, PI-) and late phase apoptotic cells or necrotic cells (annexin V+, PI+). Lower doses of heavy-ion beams (C ions: 1, 3 Gy, Fe ions: 1, 3 Gy, Ar ions: 0.5, 1 Gy) caused cell death in TK6 (wild-type *p53*) or NH32 (*p53* deficient), however, there were no significant differences in the percentage of cell death between TK6 and NH32. On the other hand, higher doses of heavy-ion beams (C ions: 5, 10 Gy, Fe ions: 5, 10 Gy, Ar ions: 2, 3, 5, 10 Gy) induced extensive cell death in TK6. In contrast, cell death was triggered at a significantly lower percentage in NH32. Moreover, percentages of both annexin V+, PI- cells and annexin V+, PI+ cell increased following higher-dose irradiation in TK6. This suggests that *p53* is involved in the process of cell death, which may include not only apoptosis but also necrosis caused by high-dose of each high-LET (22, 80, 300, 1000 keV/ $\mu$ m). Alternatively, it was reported that there must be a difference in DNA

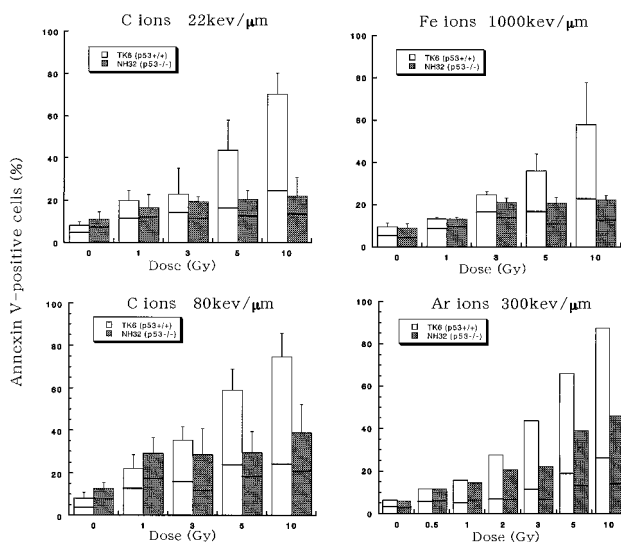


Fig. 1. Phosphatidylserine externalization in TK6 (*p53*+/+) and NH32 (*p53*-/-) cells 24 hour after irradiation with C ions (22 keV/ $\mu$ m or 80 keV/ $\mu$ m), Fe ions (1000 keV/ $\mu$ m) or Ar ions (300 keV/ $\mu$ m). Cells ( $5 \times 10^5$ ) were labeled with annexin V-FITC and propidium iodide (PI), and analyzed by flow cytometry. Apoptosis is expressed as the percentage of cells positive for annexin V-FITC. The lower part of each column indicates annexin V(+), PI(-) cells (apoptotic cells), the upper part of each column indicates annexin V(+), PI(+) cells (late phase of apoptotic cells and necrotic cells). Each column shows the average data (except Ar ions) of both annexin V(+), PI(-) cells and annexin V(+), PI(+) cells.

replication damage between irradiation with a low dose and that with a high dose of C-ion beams.<sup>4)</sup> The suppression of the late S phase was observed at both 3 Gy and 5 Gy, whereas the suppression of the early S phase required 5 Gy irradiation in TK6.<sup>4)</sup> Therefore, our result suggests that *p53* may also be involved in specific pathways of checkpoint or replication of euchromatic regions.

### References

- 1) T. Jacks et al.: *Curr. Biol.* **4**, 1 (1994).
- 2) T. Tsukada et al.: *RIKEN Accel. Prog. Rep.* **36**, 131 (2003).
- 3) S. Morimoto et al.: *RIKEN Accel. Prog. Rep.* **34**, 177 (2001).
- 4) M. Izumi et al.: *RIKEN Accel. Prog. Rep.* **37**, 144 (2004).

## Effect of heavy-ion beam irradiation on mutation induction in *Arabidopsis thaliana*

H. Saito, T. Matsuyama, Y. Y. Yamamoto, T. Abe, and S. Yoshida

Since high linear energy transfer (LET) heavy-ion beams cause clustered damages including DNA double-strand breaks,<sup>1)</sup> they seem to be more effective for inducing mutations than low LET radiation such as X-rays,  $\gamma$ -rays and electrons. In basic plant sciences, mutants defective in a biological process provide useful tools for genetic analysis. *Arabidopsis thaliana* (*Arabidopsis thaliana*) is one of the model plants and often used in such genetic analyses. To achieve effective mutagenesis of *Arabidopsis*, we evaluated the conditions of heavy-ion beam irradiation on mutation induction.

Dry seeds of *Arabidopsis* ecotype Columbia (about 250  $\mu\text{m}$  in diameter) were packed with Hybri-Bag Hard (95  $\mu\text{m}$  thickness, Cosmo Bio Co., Ltd.) to provide a monolayer of the seeds for homogenous irradiation. They were irradiated with  $^{12}\text{C}$ ,  $^{20}\text{Ne}$ ,  $^{40}\text{Ar}$  and  $^{56}\text{Fe}$  ions with a dose range of 5 to 400 Gy. These ions were accelerated up to 135, 135, 95 and 90 MeV/nucleon, and their LETs were 23, 61, 280 and 630 keV/ $\mu\text{m}$ , respectively. Furthermore, to determine the effects of the LETs of heavy ions on mutagenesis, the LET of C ion beams was increased to 63 keV/ $\mu\text{m}$  after passing through a set of absorbers in the range shifter. All LETs were calculated at the seed surface. The irradiated  $M_1$  seeds were incubated on 1/2 MS agar medium at 4°C in darkness for 3 days for vernalization and then at 22°C under continuous illumination. The germination rate (number of germinated seeds per total number of incubated  $M_1$  seeds) was determined 2 to 3 weeks after the initiation of incubation. True leaf-developed seedlings were transplanted to plastic trays (13  $\times$  9 cm) containing soil. Eleven seedlings were planted in each tray and cultured at 22°C under continuous illumination in the greenhouse. The flowering rate (number of flowering plants per total number of incubated  $M_1$  seeds) was determined one month after the transfer.  $M_2$  seeds were harvested from self-pollinated  $M_1$  plants in each tray.  $M_2$  seeds were similarly collected and incubated under the same condition as that for germinating  $M_1$  seeds. The frequencies of albino plants (number of albino plants per total number of germinated  $M_2$  seedlings) were measured after most seedlings expanded cotyledons.

In the control seeds without irradiation, the germination rate was 97.1% and all seedlings flowered until one month after transfer to soil. The effects of heavy-ion beam irradiation on mutagenesis in *Arabidopsis* are shown in Table 1. Germination of  $M_1$  plants was not affected by irradiation with any ions at the doses tested. However, the decrease in the flowering rate of  $M_1$  plants was observed in accordance with the in-

Table 1. Effect of heavy-ion beams on mutation induction in *Arabidopsis*.

Ion	LET (keV/ $\mu\text{m}$ )	Dose (Gy)	No. of $M_1$ seeds <sup>§1</sup>	Germination rate of $M_1$ plants (%)	Flowering rate of $M_1$ plants (%)	% of albino $M_2$ plants
Control	—	—	680	97.1 $\pm$ 2.5	97.1 $\pm$ 2.5	0.07 $\pm$ 0.07
C	23	50	371	93.5 $\pm$ 4.0	93.5 $\pm$ 4.0	0.16 $\pm$ 0.1
		100	256	86.0 $\pm$ 2.5	83.1 $\pm$ 0.8	0.48 $\pm$ 0.4
		150	210	89.3 $\pm$ 3.9	87.3 $\pm$ 4.3	0.34 $\pm$ 0.1
		200	279	94.2 $\pm$ 1.0	81.2 $\pm$ 0.7	0.53 $\pm$ 0.1
		400	255	91.1 $\pm$ 4.2	34.2 $\pm$ 11.6	nd <sup>§2</sup>
C	63	50	439	95.8 $\pm$ 0.5	94.8 $\pm$ 0.6	0.80 $\pm$ 0.1
		100	455	98.1 $\pm$ 0.6	93.1 $\pm$ 1.8	1.35 $\pm$ 0.4
		150	446	92.3 $\pm$ 3.7	91.4 $\pm$ 3.2	1.92 $\pm$ 0.4
		200	413	98.2 $\pm$ 0.5	19.2 $\pm$ 17.1	nd
		400	358	96.0 $\pm$ 1.6	0.8 $\pm$ 0.1	nd
Ne	61	50	515	97.6 $\pm$ 0.4	94.9 $\pm$ 1.9	0.30 $\pm$ 0.2
		100	412	92.9 $\pm$ 3.9	91.8 $\pm$ 3.5	1.02 $\pm$ 0.4
		150	390	91.8 $\pm$ 5.4	90.3 $\pm$ 4.4	1.67 $\pm$ 0.7
		200	393	88.5 $\pm$ 7.9	83.2 $\pm$ 8.9	0.39 $\pm$ 0.1
		400	301	87.2 $\pm$ 6.3	3.0 $\pm$ 1.9	nd
Ar	280	5	580	97.9 $\pm$ 1.1	89.5 $\pm$ 2.1	0.20 $\pm$ 0.1
		10	567	94.2 $\pm$ 5.3	88.2 $\pm$ 4.8	0.32 $\pm$ 0.1
		20	479	94.6 $\pm$ 4.3	91.4 $\pm$ 4.3	0.26 $\pm$ 0.1
		50	499	97.6 $\pm$ 2.1	92.2 $\pm$ 2.0	1.37 $\pm$ 0.3
		100	445	93.9 $\pm$ 4.0	1.2 $\pm$ 1.2	nd
		150	452	92.6 $\pm$ 5.9	0	nd
		200	341	95.5 $\pm$ 3.7	0	nd
Fe	640	5	410	97.0 $\pm$ 0.3	96.6 $\pm$ 0.2	0.10 $\pm$ 0.1
		10	408	93.8 $\pm$ 1.9	93.5 $\pm$ 2.0	0.35 $\pm$ 0.3
		20	341	92.9 $\pm$ 4.2	88.2 $\pm$ 4.2	0.17 $\pm$ 0.1
		50	324	95.6 $\pm$ 3.0	94.4 $\pm$ 3.1	0.42 $\pm$ 0.2
		100	226	94.1 $\pm$ 1.8	74.9 $\pm$ 4.7	1.09 $\pm$ 1.0
		150	196	91.4 $\pm$ 3.4	5.9 $\pm$ 5.9	nd
200	210	86.9 $\pm$ 6.4	0	nd		

<sup>§1</sup> Total number of irradiated  $M_1$  seeds from three experiments.

<sup>§2</sup> Data were not determined.

crease in doses. For most  $M_1$  plants after high-dose irradiation, growth-decreased plants produced a few seeds. Among the irradiation conditions using the different energies of C ions, LET of 63 keV/ $\mu\text{m}$  was more effective for inducing albino plants. Similar frequencies of albino plants were observed for both irradiation treatments by C ions with LET of 63 keV/ $\mu\text{m}$  and by Ne ions with LET of 61 keV/ $\mu\text{m}$ . Also, the same doses were required for higher frequencies. It has been reported that the lethality rate after ion beam irradiation was affected by LET in *Arabidopsis*: Ne or Ar ions with LET higher than 350 keV/ $\mu\text{m}$  were more effective than 113 keV/ $\mu\text{m}$  C ions.<sup>2)</sup> The LET of ion beams seems to be an important factor for the efficient mutagenesis of plants. More detailed studies using several ions at different LETs are in progress.

In the present study, not only albino plants but also several morphologically abnormal plants, such those with variegation, pale green color, longer hypocotyl and higher anthocyanin accumulation, were isolated in the  $M_2$  generation derived from seeds irradiated by all ion beams tested. Molecular analyses of mutated genes to clarify the effect of ions and their LETs are also in progress using these mutants.

### References

- 1) D. T. Goodhead: Int. J. Radiat. Biol. **65**, 7 (1994).
- 2) N. Shikazono et al.: Radiat. Environ. Biophys. **41**, 159 (2002).

## Isolation of light stress response mutants of *Arabidopsis thaliana* by heavy ion beam irradiation

Y. Y. Yamamoto, T. Abe, and S. Yoshida

Plants utilize sunlight for photosynthesis, and thus light is indispensable for plant growth. On the other hand, exposure of plants to high-intensity light, called high light (HL), harms their photosynthetic apparatus. Development of a protective mechanism against HL is one of the prerequisites for plant survival on the land. It is known that the adaptation of higher plants is achieved in part by the regulation of gene expression.<sup>1)</sup> However, little is known about how plants recognize HL environments and alter their gene expression profile accordingly. Our research aims to elucidate the molecular mechanisms behind the perception of HL environments and the subsequent signal transduction leading to gene activation. Because the perception is suggested to occur in the chloroplast and the gene activation in the nucleus,<sup>2,3)</sup> the HL signal is considered to be transduced in an *inter* organellar fashion, which is one of the unique characteristics of this signaling system.

Recent studies have revealed that the HL response is mediated by at least two independent pathways, and one of which leads to the activation of *ELIP* genes<sup>2)</sup> encoding antistress proteins that protect plants from light stress. Therefore, the activation of *ELIP* genes by HL is one of the strategies for plant survival in HL environments. To identify the components involved in HL-activated gene expression, we decided to take the genetic approach. An established transgenic *Arabidopsis* line carrying a firefly luciferase reporter gene, *ELIP2::LUC*, activates luciferase-based bioluminescence in response to HL.<sup>2)</sup> The response of the reporter can be monitored in a nondisruptive manner, therefore, this assay system is suitable for the screening of mutants defective in the HL response.

Because heavy ion beam irradiation tends to cause short (1 to 10 bps) deletions in the genome,<sup>4)</sup> it is expected to provide null mutants due to frameshift. Such mutants would be suitable for investigating gene-function relationships. Dry seeds of the reporter line were irradiated with a  $C^{6+}$  beam at a dose of 150 Gy. The treated seeds were grown in a greenhouse to provide self-crossed  $M_2$  generation.  $M_2$  seedlings were grown at a light intensity higher than that of the optimal growth conditions for *Arabidopsis* (50–70 W/m<sup>2</sup>), thereby causing light stress. Under this stressful condition, light-stress-sensitive lines were screened for by visual inspection as an indication of paler color of leaves than wild type. From the screening, 69 lines were identified as light stress-sensitive mutants out of approximately 2,100 irradiated  $M_1$  lines. The identified mutants were grown, and 46 lines were fertile, providing

$M_3$  seeds.

The  $M_3$  seeds of the 46 lines were subjected to luciferase-based *in vivo* assays for HL response.<sup>2)</sup> Three types of responses of the mutants were predicted: normal response, as in the wild type, weak response, and strong response. As shown in Table 1, as much as 96% (44/46) of the mutants had a normal HL response. This suggests that although HL-sensitive mutants suffer more light stress than the wild type under HL, generally such physiological conditions do not cause an enhanced HL response. This indicates that light stress causing gene activation can be monitored by a specific parameter(s) that is not influenced by most of the analyzed mutants. As exceptions, two mutant lines showing an enhanced HL response (Table 1, Table 2) did alter such a parameter(s). Analyses of these mutants are expected to provide information on sensing mechanisms in HL environments by plants.

Table 1. Summary of the mutant screening.

Category	Line number
HL-sensitive <sup>§1</sup>	46
Higher transcriptional response to HL <sup>§2</sup>	2
Lower transcriptional response to HL <sup>§2</sup>	0

<sup>§1</sup> Determined by visual inspection of leaves grown under continuous light at 50 W/m<sup>2</sup> for 1 to 2 weeks. <sup>§2</sup> Determined by the LUC-based gene expression analysis in response to HL (light intensity of 150 W/m<sup>2</sup> for 3 h).

Table 2. HL response of the isolated mutants.

line	HL response <sup>§</sup>
Wild type	1.00
Mutant 1	5.00±2.48
Mutant 2	3.09±1.57

<sup>§</sup> Relative value determined by the LUC-based gene expression analysis in response to HL (light intensity of 150 W/m<sup>2</sup> for 3 h). Standard deviations are also shown.

### References

- 1) M. Kimura, Y. Y. Yamamoto, M. Seki, T. Sakurai, M. Sato, T. Abe, S. Yoshida, K. Shinozaki, and M. Matsui: *Photochem. Photobiol.* **77**, 226 (2003).
- 2) M. Kimura, T. Yoshizumi, K. Manabe, Y. Y. Yamamoto, and M. Matsui: *Genes Cells* **6**, 607 (2001).
- 3) M. Kimura, K. Manabe, T. Abe, S. Yoshida, M. Matsui, and Y. Y. Yamamoto: *Photochem. Photobiol.* **77**, 668 (2003).
- 4) N. Shikazono, Y. Yokota, S. Kitamura, C. Suzuki, H. Watanabe, S. Tano, and A. Tanaka: *Genetics* **163**, 1449 (2003).

## Hormesis of heavy-ion irradiation to lettuce

I. Honda,\* K. Kikuchi,\* H. Saito, Y. Miyazawa, T. Abe, and S. Yoshida

In 1980, Luchey<sup>1)</sup> described radiation hormesis as promotive effects in many living things by their exposure to low doses of X-ray,  $\gamma$ -ray, and radiation from many radioactive nuclei. He presented more than one thousand examples of hormesis and advocated its utilization for improving of all living organisms. In general, however, the effects were not significant and have thus been sometimes regarded as not holding great potential.

Miura *et al.*<sup>2)</sup> examined the possibility of utilizing radiation hormesis in cultivating some vegetables. They found that lettuce seed germination at a high temperature was promoted by low-dose  $\gamma$ -ray irradiation, and indicated that this effect may contribute to improving the lettuce productivity, which normally requires the preparation of well-grown seedlings for machine transplantation in practical field cultivation. However, the effect they demonstrated in the germination of lettuce was so small as to be considered negligible.

Recently, a heavy-ion irradiation (HII) of plants has been frequently utilized as a new method to induce mutation in plants. Abe extensively applied HII technology for various plants and reported that mutation rates after HII were higher than that of  $\gamma$ -ray irradiation.<sup>3)</sup> On the other hand, the hormesis-like effect of HII has been never examined. In this study, we examined whether HII shows hormesis-like effects or not.

Dry seeds of lettuce cv. cisco (Takii Seed Inc.) were irradiated by  $^{12}\text{C}$ - and  $^{20}\text{Ne}$ -ion beams (135 MeV/u) at a dose range of 3 to 300 Gy. Effects of HII on the growth rate were examined under normal cultivation conditions in soil. Seeds irradiated with less than 30 Gy by both heavy-ions grew well, but their growth was severely inhibited after irradiation above 100 Gy. To examine hormesis effects, low-dose irradiation was conducted in a dose range from 0.1 Gy to 30 Gy, and the effects were examined by conducting a seed germination test.

Fifty seeds were sown in each petri dish (9 cm) containing a two-layer filter paper and 4 ml of distilled water, incubated at 35°C in the dark, and their germinations were examined daily. At least four dishes were used in each single experiment to obtain the germination rates. As shown in Fig. 1, the germination rates of lettuce one day after imbibition were 8–20% even in nonirradiated (0 Gy) seeds. The germination rates of 0.1 Gy  $^{12}\text{C}$ - and 3 Gy  $^{20}\text{Ne}$ -ion beam irradiated seeds were slightly higher than those of the control experiment. Incubation was continued for more 3 days, but only few seeds germinated additionally in

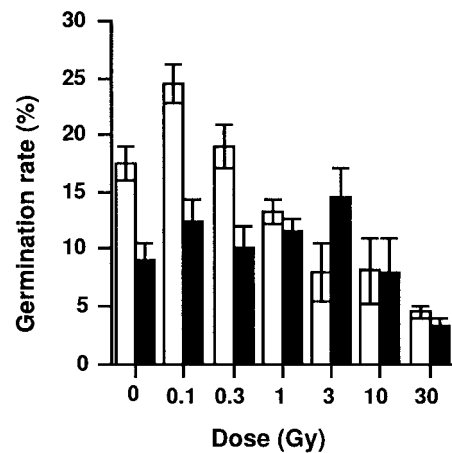


Fig. 1. Effects of heavy-ion irradiation on the seed germination of lettuce one day after imbibition. Open and closed bars indicate the effects of  $^{12}\text{C}$ - and  $^{20}\text{Ne}$ -ion beam irradiation, respectively. The incubation temperatures for  $^{12}\text{C}$ - and  $^{20}\text{Ne}$ -ion samples were 34°C and 35°C, respectively. Error bar indicates standard error.

every experiment, representing slightly higher germination rates for these irradiated seeds. These seeds were stored at 4°C for two days after the above examination, and re-incubated at 25°C for two days. This re-incubation resulted in the germination of more than 90% of the remaining seeds. These results may indicate that ion-beam irradiation has a certain effect of breaking dormancy in lettuce seeds which is induced by high temperature.<sup>4)</sup> As the decrease in the uniformity of lettuce seedlings growth expressed by this dormant like effect in germination sometimes leads to economic loss in practical cultivation under high temperature conditions, as suggested by the results there is a possibility that ion-beam irradiation may be useful for increasing lettuce productivity. Further studies on suitable ions, doses and other HII methods are required to conclude the existence of HII hormesis as well as to gain an understanding of its mechanisms.

### References

- 1) T. D. Luchey: *Hormesis with Ionizing Radiation* (CRC Press Inc., Boca Raton, 1980).
- 2) S. Miura, H. Yamazaki, and M. Hamano: Proc. 26th Int. Horticultural Congress, Toronto, Canada, 2002-8, (International Society of Horticultural Science, 2002), p. 550.
- 3) T. Abe: *Breed. Res.* **5** Suppl. 2, 58 (2003).
- 4) D. Gray: *J. Hortic. Sci.* **50**, 349 (1975).

\* National Institute of Vegetable and Tea Science

## Mutation induction by heavy-ion beam in asparagus

P.-Y. Yun,\* S.-Y. Kim,\* A. Kanno,\* T. Kameya,\* T. Abe, Y. Miyazawa, H. Saito, and S. Yoshida

It has been reported that many types of mutation can be induced by heavy-ion irradiation, such as dwarfism, chlorophyll deficiency, sterility, and aberrance in floral organ. Floral mutations are very important in studying the molecular genetic mechanism of flower development. Asparagus (*Asparagus officinalis* L.) is a dioecious plant and is the economically most important species in the genus *Asparagus* due to its edible shoots. It has sex chromosomes called X and Y, XY in male and XX in female.<sup>1)</sup> Male and female flowers have both stamens and carpels during the hermaphrodite developmental stages, whereas sex differentiation appears to be the result of the selective abortion of stamens in female flowers and carpels in male flowers. In this study, we attempted to induce dioecious asparagus floral mutation by heavy-ion beam irradiation (C, N, Ne).

Asparagus (cv Mary Washington 500 W) was used as the plant material. The seeds of asparagus were grown on the MS medium until germination. For N- and Ne-ion irradiation, 15 germinated seeds were selected, and for C-ion irradiation, 33 seeds were selected per individual experiments of irradiation. One week after germination, germinated seeds were irradiated with C, N and Ne ions within a range of 5 to 50 Gray. The linear energy transfer of the C, N and Ne ions corresponded to 22, 30, 63 Kev/mm, respectively. Two days after irradiation, irradiated seedlings were sown in the soil.

Survival rates are shown in Fig. 1. From these results, we suppose that Ne-ion beam has a stronger effect on the survival of asparagus than C- and N-ion beams. The numbers of flowering plants (male, female) and plants with modified flowers are shown in the Table 1. We could obtain various floral modifications of asparagus plants following the irradiation with heavy-ion beam (Fig. 2). Most plants did not have the same floral modifications and only some flowers are modified in a plant. However, mutant BN27, which was induced by N-ion (20 Gy) irradiation, had tepals that did not dehiscence, and no pollens were released even when the flowers became mature. These characteristics were stable for 3 years and the shape of all flowers was iden-

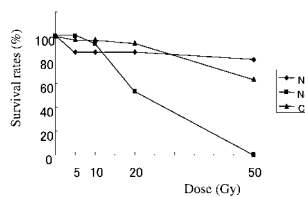


Fig. 1. Survival rates of asparagus plants irradiated with C-, N- and Ne-ion beams.

Table 1. Observation of asparagus irradiated by heavy-ion beam.

Ion	Dose (Gy)	Number of flowering plants				Number of plants with modified flowers		
		Total	unflowering	Male	Female	Total	Male	Female
Control	0	15	0	9	6	0	0	0
Ne	5	7	0	5	2	2	2	0
	10	7	1	4	2	3	3	0
	20	5	0	3	2	0	0	0
	50	0	0	0	0	0	0	0
	5	9	1	5	3	1	1	0
N	10	7	0	3	4	0	0	0
	20	12	4	6	2	2	2	0
	50	5	1	2	2	0	0	0
	5	18	4	7	7	3	1	2
	10	16	2	10	4	2	1	1
C	20	26	7	14	5	2	2	0
	50	11	2	6	3	0	0	0

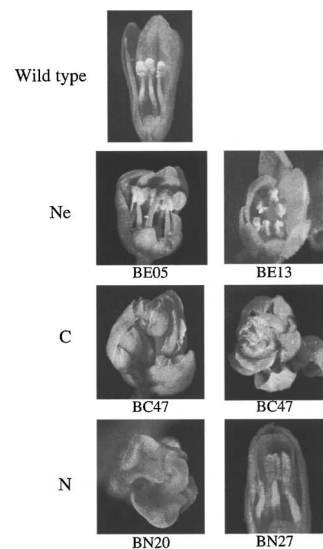


Fig. 2. Various asparagus floral modifications were obtained following C-, N- and Ne-ion beam irradiation. The flower of BE05 has modified filaments, BE13 and BN20 have additional tepals, BC47 has flowers in a flower, and BN27 shows no opening of tepals and their dehiscence and no release of pollens.

tical in mutant BN27. The dehiscence program probably requires the activation of many genes, including those that encode hydrolytic enzymes required for cell death, such as RNase, proteases, and cellulases.<sup>2-4)</sup> In addition to the examination of pollen sterility, we are also studying the relationship between the floral identity gene and floral modification in asparagus mutant BN27.

### References

- 1) H. Löptien: Zeitschrift für Pflanzenzüchtung **82**, 162 (1979).
- 2) C. J. Keijzer: New Phytol. **105**, 487 (1987).
- 3) L. L. Bonnerr and H. G. Dickenson: New Phytol. **113**, 97 (1989).
- 4) E. del Campillo and L. N. Lewis: Plant Physiol. **99**, 1015 (1992).

\* Graduate School of Life Sciences, Tohoku University

## Effect of heavy-ion beam irradiation on apple and Japanese pear

Y. Ito,\* T. Abe, H. Saito, Y. Miyazawa, T. Takyu,\* H. Yamanouchi,\* and S. Yoshida

In fruit tree crops, mutation breeding has played an important role in providing the specific characteristics such as host-specific toxin disease resistance and fruit maturity. It has been difficult, however, to obtain mutants having other important agricultural characteristics by artificial induction. In recent years, the effects of heavy-ion beam irradiation in mutation induction were reported to be different from gamma-ray irradiation in ornamental flower crops. Thus, the difference in the characteristics of mutation induction between heavy-ion beam irradiation and gamma-ray irradiation on tree fruit crops must be studied for the improvement of their mutation breeding. In this study, the effects of heavy-ion beam irradiations on apple and Japanese pear were investigated.

The dormant scions of apple (cv. Fuji) and Japanese pear (cv. Kosui) were used as the irradiation materials. The scions were cut to a length of approximately 6 cm and packed 7 each in polyethylene bags and irradiated with carbon ( $^{12}\text{C}^{6+}$ , 135 MeV/u) and neon ( $^{20}\text{Ne}^{10+}$ , 135 MeV/u) ions. For adjusting the linear energy transfer (LET) of both ions to approximately 8 mm in depth from the surface of the scions, an absorber was inserted before reaching the materials. Keeping the 8 mm penetration, the maximum LET values at the surface of the materials were 42.0 keV/ $\mu\text{m}$  for carbon ions and 84.1 keV/ $\mu\text{m}$  for neon ions. Forty-nine scions were used for each dose exposure, and were grafted onto the rootstocks in April 2002. Aodai No.3 was used as the apple rootstock and the seedlings of *Pyrus betulaefolia* as the Japanese pear rootstock. The rate of new shoot grown (survived) scions and visible mutation were investigated in the summers of 2002 and 2003.

The survival rate decreased with increasing exposure dose. From the obtained dose-response curves (Fig. 1), the lethal dose 50 (LD<sub>50</sub>) for apple was estimated at approximately 18 Gy of carbon-ion irradiation and approximately 8 Gy of neon-ion irradiation. LD<sub>50</sub> for Japanese pear was estimated to be approximately 13 Gy of carbon-ion irradiation and approximately 8 Gy of neon-ion irradiation (Fig. 2). Abnor-

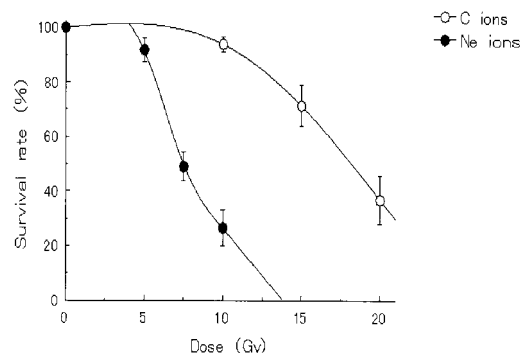


Fig. 1. Survival rate curves for ion beam irradiation on apple (cv. Fuji).

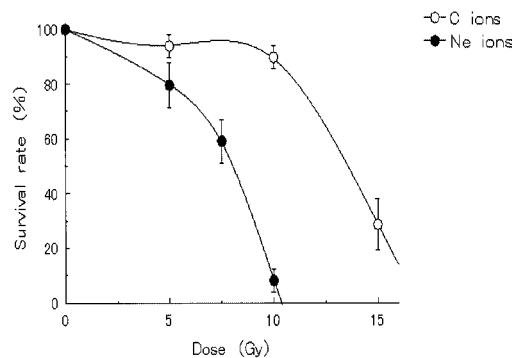


Fig. 2. Survival rate curves for ion beam irradiation on Japanese pear (cv. Kosui).

mal shapes in the first leaves were observed, but the new leaves following them showed normal shapes in most surviving plants. One variegated leaf (partly chlorophyll deficient) mutant of apple was observed after 7.5 Gy of neon-ion irradiation. Further observations are required to determine visible mutation rate by heavy-ion beam irradiation in fruit tree crops, due to possible chimeric structures. Using DNA analysis and other methods, we are now selecting the mutants which show self-compatibility or low tree height habit.

\* National Institute of Agrobiological Sciences

## Effects of heavy-ion beam irradiation on regeneration of shoots from stem segments in spray-type chrysanthemum (*Dendranthema grandiflorum* (Ramat.) Kitamura)

K. Suzuki,\* Y. Takatsu,\* T. Gonai,\* Y. Miyazawa, H. Saito, T. Abe, S. Yoshida, and M. Kasumi\*

Mutation breeding has been used to improve with minimum changes original cultivars of various plant species. Recently, heavy-ion beam irradiation was reported as an excellent breeding technique for ornamental plants, such as dahlia,<sup>1)</sup> verbena<sup>2)</sup> and chrysanthemum.<sup>3)</sup> Spray-type chrysanthemum is one of the major cut flowers in Japan, and its various characteristics have been improved by conventional hybridization methods. To change one or two characteristics, such as flower color and flowering time, we attempted to use heavy-ion beam irradiation as a mutation breeding technique. In the present study, we investigated the effects of heavy-ion beam irradiation on the regeneration of shoots from stem segments in several varieties of spray-type chrysanthemum.

Eighteen varieties cultivated in Ibaraki prefecture were used for this experiment. Stem segments, 2 mm long and vertically cut in half, were placed on a shoot regeneration medium consisting of MS basal medium supplemented with 2 mg/l IAA, 0.2 mg/l BA and solidified 4 g/l gellum gum. Three to 7 days after the culture, stem segments were irradiated with <sup>12</sup>C ion beams (135 MeV/nucleon, LET 23 keV/μm) at doses

of 3, 7, 10, and 20 Gy. Fifty to 150 segments were irradiated in each experiment. Thirty days after the culture, the number of regenerated shoots was counted and the rate of shoot regeneration was calculated.

The frequency of shoot regeneration decreased with increasing irradiation dose. No regenerated shoot was observed after 20 Gy irradiation except for 'Chiyo.' The significant difference in half lethal dose (LD<sub>50</sub>) was observed among varieties. The number of varieties with an LD<sub>50</sub> value of less than 3 Gy was four, that with 3–7 Gy was five, that with 7–10 Gy was seven, and that with 10–20 Gy was two (Table 1).

The LD<sub>50</sub> value in 18 varieties of chrysanthemum has become apparent in this experiment, and we are now further investigating the characteristics such as flower color and flowering time.

### References

- 1) M. Hamatani et al.: RIKEN Accel. Prog. Rep. **34**, 169 (2001).
- 2) K. Suzuki et al.: RIKEN Accel. Prog. Rep. **35**, 129 (2002).
- 3) S. Nagatomi et al.: Breed. Res. **48** Suppl. 1, 220 (1998).

Table 1. Effects of heavy-ion beam irradiation on the regeneration of shoots from stem segments in varieties of chrysanthemum.

Dose (Gy)	Shoot regeneration rate (%)					
	Korogi <sup>1)</sup>	Sakiko <sup>1)</sup>	Subaru <sup>1)</sup>	Tomoshihi <sup>1)</sup>	Benikomachi <sup>2)</sup>	Duet <sup>2)</sup>
0	47.9	54.5	36.3	59.0	65.0	52.0
3	5.8	1.0	10.5	18.7	37.8	37.8
7	6.3	0.0	3.0	4.3	21.6	9.5
10	0.0	0.0	1.1	0.0	5.5	1.1
20	0.0	0.0	0.0	0.0	0.0	0.0
	Okinamaru <sup>2)</sup>	Hajime <sup>2)</sup>	Nonko <sup>2)</sup>	Beachball <sup>3)</sup>	Kosuzu <sup>3)</sup>	Nagisa <sup>3)</sup>
0	63.5	25.0	43.0	81.0	30.0	20.6
3	56.7	26.3	22.7	– <sup>§</sup>	–	7.1
7	23.9	7.1	5.1	44.8	15.8	12.9
10	2.2	2.2	2.2	2.2	0.0	0.0
20	0.0	0.0	0.0	0.0	0.0	0.0
	Natsuhikari <sup>3)</sup>	Sasayaki <sup>3)</sup>	Satobue <sup>3)</sup>	Shirofune <sup>3)</sup>	Chiyo <sup>4)</sup>	Haruka <sup>4)</sup>
0	76.0	95.0	72.0	38.2	100.0	100.0
3	65.1	68.5	67.0	63.4	–	–
7	55.7	67.7	34.2	29.3	–	–
10	16.5	1.1	40.0	1.4	93.7	94.4
20	0.0	0.0	0.0	0.0	16.4	0.0

1) The LD<sub>50</sub> value is less than 3 Gy, 2) 3–7 Gy, 3) 7–10 Gy, 4) 10–20 Gy, respectively.

<sup>§</sup> The symbol '–' indicates no data.

\* Plant Biotechnology Institute, Ibaraki Agricultural Center



## Performance of strip Ge telescope for in-beam $\gamma$ -ray spectroscopy

M. K. Suzuki,\* T. K. Onishi,\* H. J. Ong,\* H. Suzuki,\* Y. Ichikawa,\* N. Imai, N. Aoi, H. Iwasaki,\* and H. Sakurai\*

We are developing a strip germanium telescope<sup>1)</sup> (SGT) for in-beam  $\gamma$ -ray spectroscopy using fast RI beams ( $\beta \simeq 0.4$ ). Improvements have been made with emphasis on the resolution and the signal-to-noise ratio by modifying the signal readout of the SGT and applying a Compton active shield. In this article, we briefly describe the design of the SGT. We also report the performance study of the SGT using a 100 A MeV  $^{18}\text{O}$  beam as well as using standard  $\gamma$ -ray sources, and thus demonstrate the usefulness of the SGT in in-beam  $\gamma$ -ray spectroscopy.

The central design concept of the SGT is the combination of a high-efficiency detector and a position-sensitive detector. The schematic of the SGT is shown in Fig. 1. The high-efficiency detector is composed of a  $70 \phi \times 70 \text{ mm}^3$  coaxial crystal. The position-sensitive detector comprises a  $50 \times 50 \times 20 \text{ mm}^3$  planar crystal with 25 2-mm-wide electrodes which can read out signals individually. The reaction position can be determined on the hit patterns of signals without the need for analysing the pulse shapes. The position information is used for the Doppler-shift correction.

The intrinsic energy resolutions of individual strips and coaxial crystals are typically 2.5 keV (FWHM) for 1408 keV  $\gamma$ -rays. As discussed in a previous report,<sup>1)</sup> the resolution of the energy sum is typically 10 keV for multihits events where two or more strips have signals. The poor resolution of the multihit events is mainly due to the crosstalk between neighbouring strips. The crosstalk is not due to the so-called mirror charge effect. We thus added the readout for the total-charge signal from the opposite side of the planar crystal. As a result, the energy sum resolution was improved to 6 keV. The energy resolution is sufficient for the

analyses of the Doppler correction, although it cannot compete with the intrinsic resolution.

The basic performance characteristics of the SGT were measured with standard  $\gamma$ -ray sources;  $^{60}\text{Co}$ ,  $^{137}\text{Cs}$ ,  $^{133}\text{Ba}$ , and  $^{152}\text{Eu}$ . The data were obtained with each source placed 63 mm distant from the SGT. The full-energy peak efficiencies of the SGT are shown in Fig. 2 for the following cases: (A) a  $\gamma$ -ray is absorbed in the planar crystal, (B) a  $\gamma$ -ray is Compton-scattered in the planar crystal and then absorbed in the coaxial crystal, and (C) both of (A) and (B). The errors were determined to be typically 5% mainly from the uncertainties of the activities of the sources. The efficiencies for 1 MeV  $\gamma$ -rays in cases (A), (B), and (C) were respectively  $2.5 \times 10^{-3}$ ,  $1.8 \times 10^{-3}$ , and  $4.3 \times 10^{-3}$ . The energy resolutions are shown in Fig. 3. In each case, the overall resolutions of the SGT were dominated by

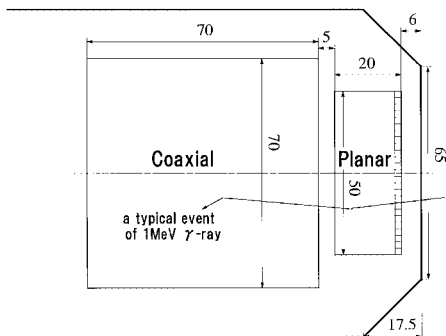


Fig. 1. Schematic of the telescope.

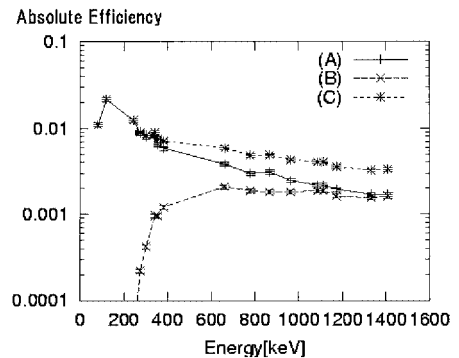


Fig. 2. Efficiencies measured in the following cases: (A) a  $\gamma$ -ray is absorbed in the planar crystal, (B) a  $\gamma$ -ray is Compton-scattered in the planar crystal and then absorbed in the coaxial crystal, and (C) both of (A) and (B).

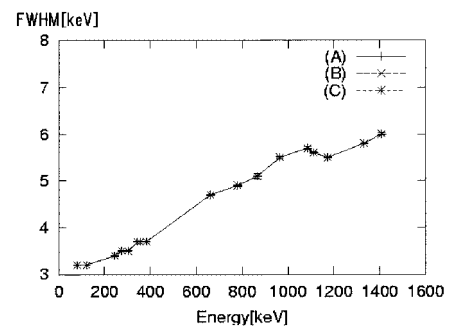


Fig. 3. The energy resolutions.

\* University of Tokyo

the energy sum resolution.

To demonstrate the performance of the SGT for an actual in-beam experiment, we tested the SGT in an inelastic scattering experiment of  $^{18}\text{O}$  ( $E = 100$  A MeV,  $\beta = 0.42$ ) with a 0.5-mm-thick Be target at RIPS. The SGT is located perpendicular to the beam line and 63 mm distant from the target. In this study, we applied the Compton active shield around the SGT with an array of 30 NaI(Tl) detectors. The  $\gamma$ -ray emission angle for the Doppler shift correction was determined by measuring the directions of scattered particles and  $\gamma$ -rays. Two parallel plate avalanche counters were placed 524 mm and 865 mm downstream of the target to determine the direction of scattered particles and the beam-hit position at the target. The  $\gamma$ -ray direction was obtained from the  $\gamma$ -ray reaction position in the SGT and the beam-hit position.

Figure 4 shows the spectra of  $\gamma$ -rays measured in coincidence with  $^{18}\text{O}$  beams. The upper panel shows the spectra in the laboratory frame and the lower one shows the spectra in the moving frame with  $\beta = 0.42$ . The hatched spectra are obtained under the condition that the Compton active shield is not fired. Note that background levels due to Compton scattering were re-

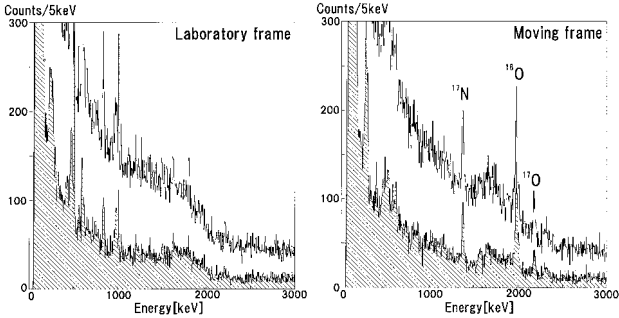


Fig. 4. Spectra of  $\gamma$ -rays measured in coincidence with  $^{18}\text{O}$  beams. The upper panel shows the spectra in the laboratory frame. The lower panel shows the spectra in the moving frame with  $\beta = 0.42$ . The hatched spectra are obtained under the condition that the Compton active shield is not fired.

duced by a factor of 3.

In the moving-frame spectra, full-energy peaks are observed around 1370 keV, 1980 keV, and 2180 keV, which correspond to the transitions  $\frac{3}{2}^- \rightarrow \frac{1}{2}^-$  in  $^{17}\text{N}$ ,  $2^+ \rightarrow 0^+$  in  $^{18}\text{O}$ , and  $\frac{1}{2}^- \rightarrow \frac{1}{2}^+$  in  $^{17}\text{O}$ , respectively. The excitation energies, the energy resolutions of the observed peaks and the observed yields are summarised in Table 1. The resolutions for 1–2 MeV  $\gamma$ -rays are determined to be approximately 1.5%.

The Compton-suppression condition causes more reduction of the 2183 keV  $\gamma$ -ray yield compared with other  $\gamma$ -rays, because the  $\gamma$ -ray is part of the cascade process of  $\frac{1}{2}^- \rightarrow \frac{1}{2}^+$  (2183 keV) and  $\frac{1}{2}^+ \rightarrow \frac{5}{2}^+$  (870 keV) in  $^{17}\text{O}$ . On the other hand, the peak around 870 keV cannot be observed clearly. The reason is that the long lifetime of the  $\frac{1}{2}^+$  state ( $\simeq 180$  ps) broadens the peak.

On the basis of the equation for the Doppler-shift correction,

$$E_{Dc} = \gamma(1 - \beta \cos \theta_{lab})E_{lab} \quad (1)$$

the resolution of  $E_{Dc}$  is approximated using

$$\begin{aligned} \left(\frac{\delta E_{Dc}}{E_{Dc}}\right)^2 &= \left(\frac{\delta E_{lab}}{E_{lab}}\right)^2 \\ &+ \left(\frac{\beta\gamma^2(\beta - \cos \theta_{lab})}{1 - \beta \cos \theta_{lab}}\right)^2 \left(\frac{\delta\beta}{\beta}\right)^2 \\ &+ \left(\frac{\beta \sin \theta_{lab}}{1 - \beta \cos \theta_{lab}}\right)^2 (\delta\theta_{lab})^2. \end{aligned} \quad (2)$$

Each variation is evaluated as  $\frac{\delta E_{lab}}{E_{lab}} \simeq 0.5\%$  at around 2000 keV,  $\frac{\delta\beta}{\beta} \simeq 2.0\%$  due to the energy loss in the target, and  $\delta\theta_{lab} \simeq 1\text{--}6\%$  due to the width of a strip and the thickness of the planar crystal. With all these terms assigned to Eq. (2), the resolution was calculated to be 1.3%, which is consistent with the measured value of 1.5%.

#### References

- 1) M. K. Suzuki et al.: RIKEN Accel. Prog. Rep. **36**, 156 (2003).

Table 1. Properties of peaks in the spectra in the moving frame with  $\beta = 0.42$ .

$E_\gamma$ (keV)	FWHM	Counts			Transition
		not suppressed	suppressed	suppression loss	
1374	18 keV (1.3%)	388	287	26%	$\frac{3}{2}^- \rightarrow \frac{1}{2}^-$ in $^{17}\text{N}$
1981	30 keV (1.5%)	829	677	18%	$2^+ \rightarrow 0^+$ in $^{18}\text{O}$
2183	32 keV (1.5%)	219	122	44%	$\frac{1}{2}^- \rightarrow \frac{1}{2}^+$ in $^{17}\text{O}$

## Development of NaI(Tl) calorimeter for charged particles

M. Niikura,<sup>\*1</sup> S. Shimoura,<sup>\*1</sup> H. Iwasaki,<sup>\*2</sup> S. Michimasa,<sup>\*1</sup> M. Tamaki,<sup>\*1</sup> S. Ota,<sup>\*3</sup> and H. Baba<sup>\*4</sup>

A new NaI(Tl) calorimeter is developed in order to measure charged particles produced in nuclear reactions with RI beams. This calorimeter was designed for extending studies of unstable nuclei to a heavier mass region,  $A = 50\text{--}100$  at RIKEN projectile-fragment separators (RIPS). The detector is also aimed at measuring a particle at higher energies of more than a few hundred MeV/nucleon at the RI-beam factory in the near future.

The calorimeter consists of a maximum of 132 NaI(Tl) crystals with photomultiplier tubes (PMTs), which are arranged in a  $12 \times 12$  matrix except for three crystals at each corner. Figures 1 and 2 show schematic views of the calorimeter and each NaI(Tl) detector setup, respectively. A NaI(Tl) crystal has a rectangular shape of  $31 \times 31 \times 50 \text{ mm}^3$ . The thickness of 50 mm is adopted for detecting light particles up to approximately 100 MeV/nucleon or heavy ions up to a few hundred MeV/nucleon. The front face is covered with thin 7- $\mu\text{m}$ -thickness Haver foil to reduce the

energy losses of charged particles which degrade the energy resolution. For higher count rate detection, each PMTs in the center of the calorimeter ( $6 \times 6$  matrix) is equipped with three-stage boosters. To measure accurate energies of charged particles and to minimize the energy loss in flight, the detector is operated in vacuum. An O-ring between the light guide and the flange maintains the vacuum in a chamber.

In order to measure the energy resolution of NaI(Tl) crystal for charged particles, we performed a test experiment in the CRIB facility<sup>1)</sup> using the 25-MeV  $\alpha$  beam and the 90-MeV  $^{14}\text{N}$  beam. The observed energy resolution of a NaI(Tl) scintillator is mainly determined by the intrinsic energy resolution of the scintillators and the position dependence of the light collection in a crystal. To define a hit position of NaI(Tl) crystal, we used a 1-mm- $\phi$  collimeter for the  $\alpha$  beam and a tracking detector installed upstream of the detector for the  $^{14}\text{N}$  beam. The energy resolutions at the center of the crystal were 0.60% and 0.91% for the  $\alpha$  and  $^{14}\text{N}$  beams, respectively. We also observed a difference between output pulse height from PMTs at the center and the corner of the crystal. The typical differences were 1–5% for the  $\alpha$  beam and 2–3% for the  $^{14}\text{N}$  beam.

We carried out an experiment to test the performance of the NaI(Tl) detector for higher energy by the  $\Delta E$ - $E$  method using a combination of  $3 \times 3$  matrix Si detectors ( $\Delta E$ ) and the  $6 \times 6$  matrix calorimeter ( $E$ ). The result of the particle identification has been reported in Ref. 2. In this experiment, the intrinsic energy resolution of the scintillators was estimated to be  $0.8 \pm 0.1\%$  ( $\sigma$ ) for the 560-MeV  $^{23}\text{F}$  secondary beam, and the position dependence of pulse height was observed as 0.1–0.3%. In the present estimation, we took into account the effect of energy straggling in the Si detector which was estimated as  $0.42 \pm 0.06\%$  ( $\sigma$ ).

The intrinsic energy resolution of the NaI(Tl) scintillator is so high that the energy straggling of the  $\Delta E$  detector determines the resolution of the particle identification. The position dependence of the light collection in the NaI(Tl) crystal decreases in a higher energy region.

### References

- 1) Y. Yanagisawa et al.: RIKEN Accel. Prog. Rep. **34**, 183 (2001).
- 2) M. Tamaki et al.: CNS Annu. Rep. **2002**, 76.

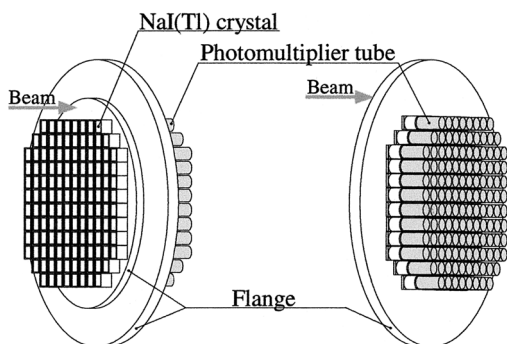


Fig. 1. Schematic view of NaI(Tl) calorimeter.

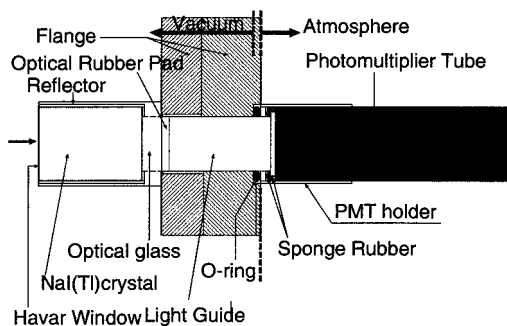


Fig. 2. Schematic view of the setup.

<sup>\*1</sup> Center for Nuclear Study, University of Tokyo

<sup>\*2</sup> Department of Physics, University of Tokyo

<sup>\*3</sup> Department of Physics, Kyoto University

<sup>\*4</sup> Department of Physics, Rikkyo University

## Development of triggerable focal plane detector with particle identification capabilities

K. Itahashi, H. Geissel,<sup>\*1</sup> A. Gillitzer,<sup>\*2</sup> K. Gomikawa,<sup>\*3</sup> R. S. Hayano,<sup>\*3</sup> M. Iwasaki, K. Lindberg,<sup>\*4</sup> M. Shindo,<sup>\*3</sup> P.-E. Tegner,<sup>\*4</sup> H. Weick,<sup>\*1</sup> and T. Yamaguchi,<sup>\*1</sup>

We have been developing a new type of self-triggering detector with particle identification capabilities. The detector TORCH will be used as the focal plane detector for the spectroscopy experiment of  $\eta$ - and  $\omega$ - bound  $^{11}\text{B}$  nuclei in the nuclear reaction  $^{12}\text{C}(d, ^3\text{He})$ . The experiment belongs to a series of spectroscopy experiments of meson-bound states in nuclei<sup>1-3</sup> and will be performed at the Fragment Separator (FRS) in the SIS-18 synchrotron of the GSI, Germany. In the experiment, the proton background rate due to the incident deuteron breakup is expected to be higher than 100 MHz at the dispersive focal plane, whereas the signal  $^3\text{He}$  rate is to be of the order of 1 Hz. Since no existing detector works under these conditions, we developed a detector system which has the proton rejection capability of  $> 10^8$  with the  $^3\text{He}$  detection efficiency of  $> 90\%$ . The detector will be placed at the focal plane and has a position resolution of  $< 2\text{ mm}$  (FWHM).

The largest difficulty in this experiment is the high background rate of protons. Since we have to employ a high intensity deuteron beam of  $1 \times 10^{11}/s$  and a thick target of  $1\text{ g/cm}^2$ , the focal plane detector is exposed to  $\sim 100\text{ MHz}$  of protons. Our strategy to eliminate the background and to find the signal  $^3\text{He}$  is based on the difference of the Cherenkov emission angle. Since the magnetic rigidities of the background protons and the signal  $^3\text{He}$  are the same, they have different velocities  $\sim 0.94c$  for proton and  $\sim 0.87c$  for  $^3\text{He}$ .

The detector mainly consists of a radiator, a segmented light guide, and 16 1-inch photomultipliers. The horizontal acceptance is about 24 cm (See Fig. 1). We have carefully chosen the radiator material of UV Lucite (with the refractive index of  $\sim 1.5$ ). The Cherenkov photons originating in the  $^3\text{He}$  ions distribute to 3 or 4 cells of the light guide whereas those originating in protons are almost totally reflected at the inner surface of the radiator and rarely reach the photomultipliers. About 40 photons are detected by the photomultipliers in the case of  $^3\text{He}$ . Taking the weighted average of the detected photons, the incident position of  $^3\text{He}$  is measured with a resolution of  $\sim 2\text{ mm}$  (FWHM).

We made a test experiment in the realistic environment of the FRS by employing deuteron and  $^{12}\text{C}$  beams. The tested points are (1) position resolu-

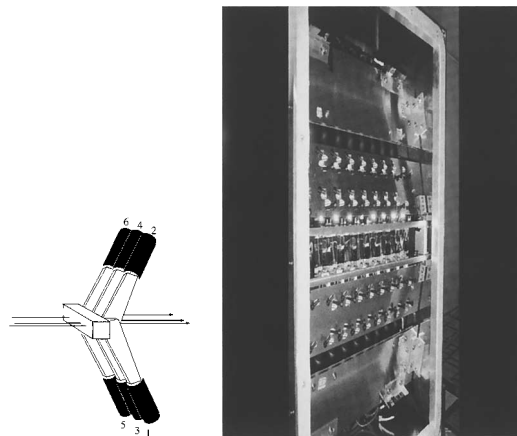


Fig. 1. Schematic design of TORCH and a photograph of its interior.

tion, (2) proton rejection capability and helium detection efficiency, and (3) time resolution. We installed a set of drift chambers with 2.5 mm cell size before the TORCH detector (TORCH-S2) at the mid-focus region of the FRS and another TORCH detector (TORCH-S4) at the end-focus region.

We correlated the drift chamber measured position to the TORCH measured position and found satisfactory linearity of the position measurement. The overall position resolution is estimated to be about 2 mm (FWHM) however small structures due to the segmentation are still visible. With the background proton rate of  $\sim 100\text{ MHz}$ , TORCH detectors provided sufficiently clean trigger of about 1 kHz by the coincidence of the two TORCHs. The time resolution was about 1 ns (FWHM), and by applying a cut in the TOF spectrum between the mid- and end-focus,  $^3\text{He}$  is identified almost free of background.

The test result shows the TORCH detector sufficiently fulfills our requirement. We improve its capability by adding high-voltage boosters in the photomultipliers to ensure the performance under a high background rate. Calibration measurement of the detector is being started in November 2003 and we will complete the final preparation for the main experiment scheduled in January 2004.

### References

- 1) H. Geissel et al.: Phys. Rev. Lett. **88**, 122301 (2002).
- 2) K. Suzuki et al.: Phys. Rev. Lett. **92**, 072302 (2004).
- 3) M. Iwasaki et al.: submitted to Phys. Lett. B.

<sup>\*1</sup> Gesellschaft für Schwerionenforschung, Germany

<sup>\*2</sup> FZ-Jülich, Institut für Kernphysik, Germany

<sup>\*3</sup> Department of Physics, The University of Tokyo

<sup>\*4</sup> Department of Physics, Stockholm University, Sweden

# Development of superconducting series junction detectors for heavy ions

H. Sato, M. Kurakado, Y. Takizawa, S. Shiki, and H. M. Shimizu

Series arrays of superconducting tunnel junctions (STJs) have a potential to realize a better energy resolution and linearity at an energy of several tens of MeV in experiments which use heavy ions. The STJ is a kind of Josephson junction which has a sandwich structure of superconductor-insulator-superconductor thin layers. The typical size of a single junction is  $110\ \mu\text{m}\phi$ . Series arrays of STJs are fabricated on a sapphire substrate.

Ions are detected in the following manner with STJs. Ions are implanted into the substrate using a beam collimator. The deposited energy generates phonons. The phonons distribute in the substrate and are then absorbed by STJ arrays which surround the detection area. The absorbed phonons break Cooper pairs in the superconducting layers of the STJs and a current signal is produced by tunneling through a barrier.<sup>1,2)</sup> Because the mean energy to break one Cooper pair is meV (for example, 2.6 meV for Nb), a better energy resolution than that obtained with semiconductor detectors such as those of Si can be realized.<sup>3,4)</sup>

One of the suitable applications of our STJs is in the experiment which searches for superheavy elements. Usually Si detectors are used in these experiments to measure the energy of  $\alpha$  particles in order to identify the superheavy elements.<sup>5)</sup> However, if a spontaneous fission event occurs, it is difficult to measure its released energy (around 100 MeV) with a good energy resolution and linearity because of the condensation of electron-hole pairs in the Si detector within a very small area. On the other hand, because our STJ arrays typically consist of thousands of junctions, the energy which is detected by each single junction is small. Therefore, STJ arrays maintain a good energy resolution and linearity. We have started to develop arrays of STJs, and in this paper, we report on the present status of the development of the detectors.

We adopt the series array of Nb-based STJs for these detectors and four series arrays are fabricated on a chip whose size is  $6\ \text{mm} \times 6\ \text{mm}$  (Fig. 1).<sup>6)</sup> The structure of the STJs is shown in Fig. 2. A center area of the chip ( $1.5\ \text{mm} \times 1.5\ \text{mm}$ ) is surrounded by STJ arrays and phonons generated by energy deposition in this area are absorbed by them. The energy spectra of  $\alpha$  particles are obtained by summing signals from the four STJ arrays.

We evaluated the characteristics of the detector by using the  $^{241}\text{Am}$   $\alpha$  source (5.486 MeV). An STJ chip was attached on a copper plate which had a hole (1 mm in diameter) at the center of it. The copper plate was mounted in a cryostat to be cooled to 0.35 K. The

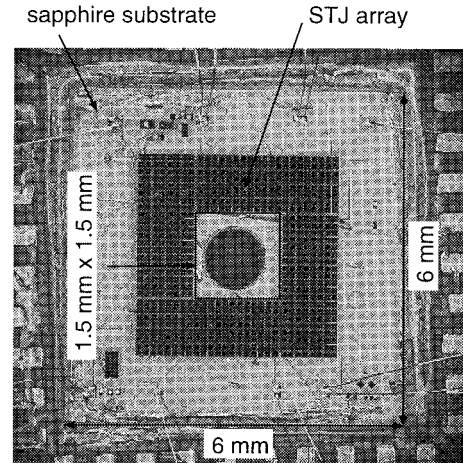


Fig. 1. Photograph of a series-array STJ chip. Each array contains 160 junctions.

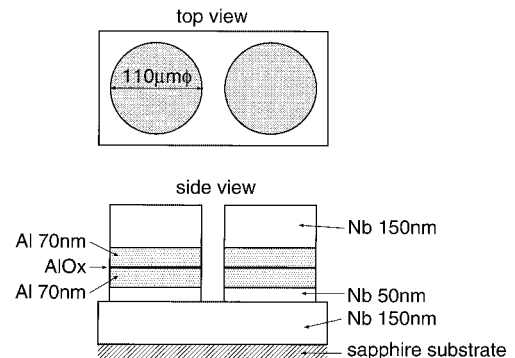


Fig. 2. Schematic view of one element of the STJ arrays.

$^{241}\text{Am}$   $\alpha$  source was also mounted in the cryostat and the chip was irradiated by  $\alpha$  particles from the back surface of the chip (Fig. 3). Each STJ array was connected to the charge preamplifiers independently. Only coincident signals from the four STJ arrays are acquired as true events.

The accumulation of the sum of four signals from the STJ arrays creates an energy spectrum of  $\alpha$  particles. However, the obtained pulse height of the signal depends on the detected position. This position dependence of pulse height broadens the peak width if we sum all events. To prevent this effect, we introduced the position correction method in data analysis.<sup>6)</sup> By using the signals from array-1 and array-3 in Fig. 4, the  $x$  position of an event was defined by  $x = x_2/(x_1 + x_2)$ , and from the signals from array-2 and array-4, the

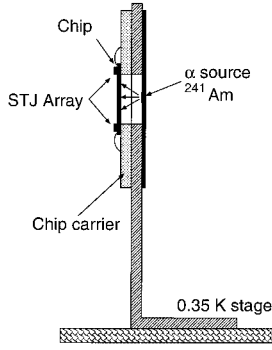


Fig. 3. Experimental setup of the cryostat cold stage.

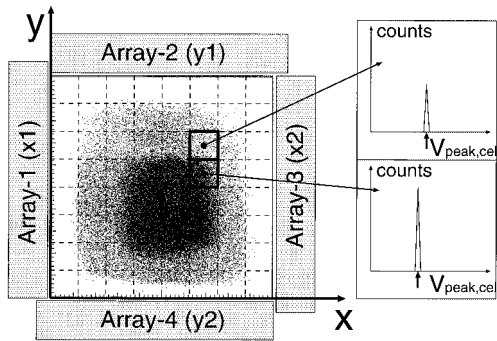


Fig. 4. Segmentation of the effective area for the position dependence correction analysis.

$y$  position was defined as  $y = y_1/(y_1 + y_2)$ , where  $x_1$ ,  $y_1$ ,  $x_2$  and  $y_2$  represent the pulse heights of the signals from array-1, array-2, array-3 and array-4, respectively. Then, we obtained a two-dimensional scattered plot. The  $x$ - $y$  scattered plot of the irradiated area was divided into  $45 \times 45$  cells and a spectrum was created using events  $V_{cell}$  in each cell (Fig. 4). The peak position ( $V_{peak, cell}$ ) of each spectrum and the maximum value ( $V_{max}$ ) among  $V_{peak, cell}$  are defined. Then the correction coefficient of each cell was calculated as  $R = V_{max}/V_{peak, cell}$  and the spectrum was rebuilt as  $V'_{cell} = R \times V_{cell}$ . By summing  $V'_{cell}$  of all cells, we obtained the corrected energy spectrum. In this correction, actually, the data of the cells which have less than 10 events were not used for rejecting any inaccuracy of the definition of  $V_{peak, cell}$ .

Figure 5 (a) shows the energy spectrum of the sum of the signals from the four arrays without correction. On the other hand, Fig. 5 (b) shows the energy spectrum obtained by applying the position correction. By comparing these two spectra, we can find that the peak width was sharpened by the correction. As a result, we obtained an energy resolution of 0.5% in full width at

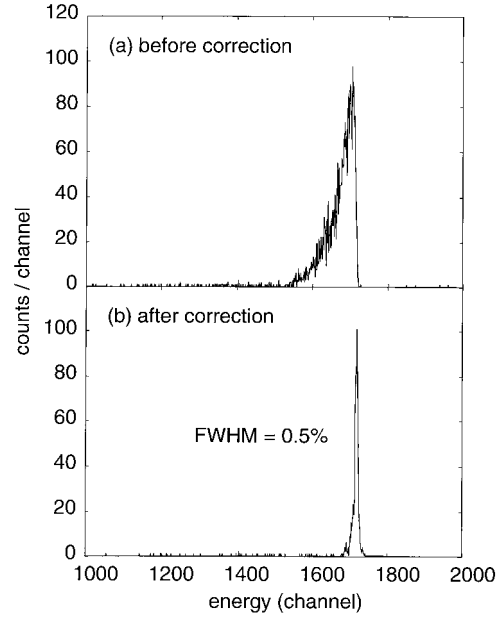


Fig. 5. Energy spectra of  $\alpha$  particles (5.486 MeV) emitted from  $^{241}\text{Am}$ . (a) is obtained by summing signals from four STJ arrays. (b) is obtained after applying position correction on (a). The energy resolution of (b) is 0.5% in FWHM.

half maximum (FWHM).

We are also testing larger chips whose size is  $12 \text{ mm} \times 12 \text{ mm}$  and effective area is  $8 \text{ mm} \times 8 \text{ mm}$ . With this chip, we obtained a resolution of 3.5% in FWHM for  $\alpha$  particles from  $^{241}\text{Am}$ . Therefore, in order to improve the energy resolution, detailed studies on the relationships among the phonon speed in the substrate, size of the effective area, formation of STJ arrays and substrate materials are required.

## References

- 1) M. Kurakado, A. Matsumura, T. Takahashi, S. Ito, R. Katano, and Y. Isozumi: Rev. Sci. Instrum. **62**, 351 (1991).
- 2) M. Kurakado, D. Ohsawa, R. Katano, S. Itoh, and Y. Isozumi: Rev. Sci. Instrum. **68**, 3685 (1997).
- 3) M. Kurakado: Nucl. Instrum. Methods **196**, 275 (1982).
- 4) M. Frank, C. A. Mears, S. E. Labov, F. Azgui, M. A. Lindeman, L. J. Hiller, H. Netel, and A. Barfknecht: Nucl. Instrum. Methods Phys. Res. A **370**, 41 (1996).
- 5) Yu. Ts. Oganessian et al.: Phys. Rev. C **63**, 011301(R) (2000).
- 6) M. Kurakado, S. Kamihirata, A. Kagamihata, K. Hirota, H. Hashimoto, H. Sato, H. Hotchi, H. M. Shimizu, and K. Taniguchi: Nucl. Instrum. Methods Phys. Res. A **506**, 134 (2003).

## Performance study of the big ion chamber

K. Sugawara,<sup>\*1</sup> K. Kimura,<sup>\*2</sup> T. Akiyama,<sup>\*1</sup> D. Fang, M. Hosoi,<sup>\*1</sup> T. Izumikawa,<sup>\*3</sup> T. Ohnishi, T. Ohtsubo,<sup>\*3</sup> A. Ozawa, W. Shinozaki,<sup>\*3</sup> T. Suzuki,<sup>\*1</sup> A. Takisawa,<sup>\*3</sup> C. Wu, Y. Yamaguchi,<sup>\*3</sup> and I. Tanihata

We have reported the performance of the big ion chamber (IC), which is used to identify the atomic number ( $Z$ ) of secondary beams under the high counting rate of up to 500 kHz.<sup>1,2)</sup> This IC will be used to search for the proton halo in  $^{23}\text{Al}$  at the second focal plane (F2) of RIPS, instead of the conventional SSD, where the high counting rate of several tens of kHz is predicted. To use the IC at RIPS, we enlarged the IC size, 780 (length)  $\times$  376 (width)  $\times$  330 (height) mm<sup>3</sup>, and entrance window, 200 mm in diameter. In this paper, we report the result of a test experiment to study the dependence of energy resolution on position as well as on counting rate.

The experiment was carried out at the E1C beam line. The newly constructed big IC filled with P-10 gas at a pressure of  $9.88 \times 10^4$  Pa (741 Torr) was located just behind the F2 vacuum chamber. The anode voltage was set at 500 V. A plastic scintillation counter for the time-of-flight (TOF) measurement was put close to the IC. An SSD was used for particle identification under the lower counting rate less of than a few kHz. In addition, a PPAC and two PPACs were placed at F1 and F2 foci, respectively, to monitor the beam profile. We used secondary beams produced through the fragmentation of the  $^{40}\text{Ar}$  primary beam (95 MeV/nucleon) impinging on a Be production target. The particle was identified by the conventional method to measure the time-of-flight (TOF), the energy loss ( $\Delta E$ ) and the magnetic rigidity for each fragment. A typical  $Z$  distribution obtained by the IC is shown in Fig. 1.

The position dependence of the energy resolution ( $\Delta Z/Z$ , where  $\Delta Z$  denotes FWHM of the peak in

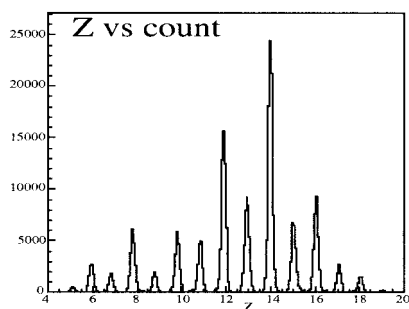


Fig. 1.  $Z$  spectrum on  $A/Z = 2$  obtained from the IC. The horizontal axis is the atomic number ( $Z$ ) of the fragment, and the vertical axis is the counting number. The counting rate was 666 Hz.

<sup>\*1</sup> Saitama University

<sup>\*2</sup> Nagasaki Institute of Applied Science

<sup>\*3</sup> Niigata University

the atomic-number spectrum) was measured by moving the big IC perpendicular to the beam axis, either by  $\pm 50$  mm in the horizontal or by +50 mm in the vertical direction. As seen in Fig. 2 (a), the  $Z$ -resolution at off-centers, 50 mm shifted horizontally and vertically, differs by 0.03% and 0.06%, respectively, from the  $Z$ -resolution measured at the center. Therefore, we confirmed that the big IC does not have any significant position dependence.

The rate dependence of  $\Delta Z/Z$  was also examined by changing the beam intensity from 666 Hz to 330 kHz. Figure 2 (b) shows the  $Z$ -resolution for  $Z = 8, 10$ , and 14 fragments as a function of counting rates. As seen in Fig. 2 (b), the difference in  $\Delta Z/Z$  obtained at 666 Hz and that at 34 kHz is less than 0.1%. However  $\Delta Z/Z$  at 330 kHz is worse by 0.5% compared to that at 666 Hz. The behavior of  $\Delta Z/Z$  against the high rate of more than several  $\times 10^4$  Hz may be attributed to the properties of the counting gas, such as the drift velocity of electrons and ions. This result shows the same trend with that of the previous experiment.<sup>1,2)</sup> Further studies are necessary.

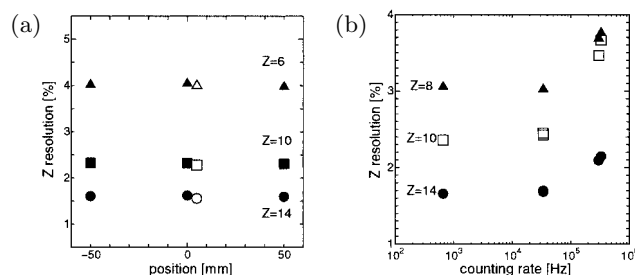


Fig. 2. (a)  $Z$  resolution of IC as a function of IC position relative to the beam. The triangle, square, and circle indicate the resolution for  $Z = 6, 10$  and 14, respectively. Open symbols indicate resolutions obtained with the position setting of +50 mm vertically. The positive value on the horizontal axis corresponds to the right-hand side of the geometry, viewing from upstream of beam line. (b)  $Z$  resolution of IC as a function of counting rates. The counting rate was changed from 666 Hz to 330 kHz. The closed triangle, open square and closed circle indicate the data for  $Z = 8, 10$  and 14, respectively.

### References

- 1) Y. Yamaguchi et al.: RIKEN Accel. Prog. Rep. **36**, 161 (2002).
- 2) K. Kimura et al.: to be published.

## Design of 4-layer magnetic shield for spin maser experiment

A. Yoshimi, K. Asahi, S. Emori,\* and M. Tsukui\*

Nuclear spin precession sometimes serves as an exclusive tool for fundamental physics studies such as the search for the T-violating electric dipole moment (EDM) in nuclei. The developments of laser-polarized noble gas nuclei and the self-sustained nuclear spin maser with the hyperpolarized nuclei are in progress.<sup>1)</sup> The nuclear spin maser, where the spin precession is continued beyond the intrinsic transverse relaxation time by the feedback system, is advantageous for detecting the small frequency shift of the spin precession that is required for EDM search.

In such experiments homogeneity and stability of the magnetic field are important for observing the spin precession phase with high accuracy. We designed a 4-layer magnetic shield for suppressing the field penetration from the external environment. The shield is cylindrical for performing the maser experiment. The noble gas sample confined in a glass cell, an oven chamber for optical pumping, and a solenoid coil are to be located inside the shield.

The shielding factor is mainly determined by permeability and the cylinder's geometry. The shield was made of Permalloy (JIS mark: PC, 1.5 mm thickness) which has a high initial permeability of approximately  $1 \times 10^5$ . The shielding factor strongly depends on the ratio between length ( $l$ ) and diameter ( $d$ ) of the cylinder. The shield's geometry is shown in Fig. 1. Each  $l/d$  ratio is chosen to be approximately 4.0. In order to suppress the field penetration from the open end of the cylinder, a large value of  $l/d$  is advantageous. On the other hand, field penetration from the middle area of the cylinder's shell into the shielded area increases when the cylinder becomes long. The  $l/d$  ratio of 4.0 is considered to be most appropriate for the maximum axial shielding factor.<sup>2)</sup>

The existing theory for the magnetic shielding factor only describes the transverse shielding factor of infinitely long cylindrical shield. Therefore, the estimation of shielding was numerically calculated using the two-dimensional electromagnetic field calculation

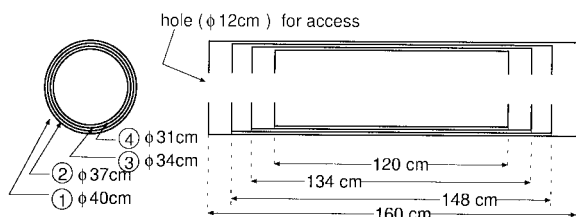


Fig. 1. Geometry of the 4-layer cylindrical magnetic shield.

code POISSON. The calculated field lines are shown in Fig. 2. The calculated field strength in the center of the shield in the presence of an external magnetic field of  $30 \mu\text{T}$  (equivalent to the earth's magnetic field strength) is summarized in Table 1. The estimated shielding factors reach  $4 \times 10^{-4}$  and  $3 \times 10^{-7}$  for the axial and transverse directions, respectively.

The 4-layer shield was constructed and the shielding effect was roughly measured with a flux gate magnetometer. The measurement was performed for the externally applied field of  $B_{\text{ext}} = 30 \mu\text{T}$ . Since the shielding factor is large for the constructed shield, the residual magnetic field inside the 4-layer shield was below the detection limit ( $< 1 \text{ nT}$ ). The residual fields were also separately measured for each single-layer shield, and the measured fields for each shield ranged from 240–300 nT in the transverse direction of the cylinder and from 900–1000 nT in the axial direction. These values agreed with those calculated by POISSON within a factor of 2. The discrepancy between the measurements and the calculation is considered to come from finite residual magnetization in the Permalloy and from a slight field penetration from joint points of cylindrical shields. We expect that the field fluctuation due to the external magnetic field can be suppressed to smaller than  $10 \text{ pT}$ .<sup>3)</sup> We are now preparing the equipment combined with a high-precision magnetometry for the spin maser experiment.

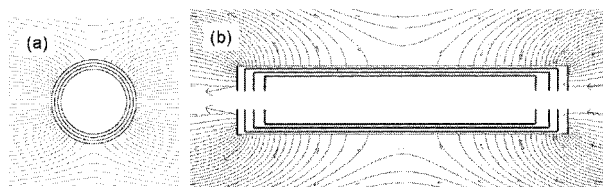


Fig. 2. Calculated magnetic field flux. (a) Transverse field. (b) Longitudinal field.

Table 1. Calculated field strength in the shield center.

direction/layer	1	1+2	1+2+3	1+2+3+4
axial (nT)	500	100	30	10
transverse (nT)	200	5	0.2	0.01

### References

- 1) A. Yoshimi and K. Asahi: RIKEN Accel. Prog. Rep. **36**, 173 (2003).
- 2) E. Paperno, H. Koike, and I. Sasada: MAG-99-28, 7 (1999).
- 3) A. Yoshimi, K. Asahi et al.: Phys. Lett. A **304**, 13 (2002).

\* Department of Physics, Tokyo Institute of Technology



## Detector R&D for the beta neutrino correlation experiment

J. Murata,<sup>\*1</sup> K. Asahi, T. Haseyama, D. Kameda,<sup>\*2</sup> K. Kurita,<sup>\*1</sup> H. Miyoshi,<sup>\*2</sup>  
K. Shimada,<sup>\*2</sup> H. Ueno, H. Watanabe, and A. Yoshimi

Next generation precision beta decay experiments aiming test of the standard model using stopped RI beams which is going to be produced with huge intensity at the RIKEN-RIBF is presented. Appearance of some physics beyond the standard model is predicted at just below the current experimental sensitivities in the beta decay observables by SUSY or GUT.<sup>1)</sup> The prime motivation of the present measurement is to reach the highest sensitivity aiming the discovery of the physics beyond the standard model.<sup>2,3)</sup>

The present schematic design of the experimental setup to measure beta neutrino angular correlation and to search time reversal symmetry violation, is shown in Fig. 1. In-flight beta decay from the stopped RI-atomic beam<sup>4)</sup> is going to be observed. As shown in Fig. 1, the detector setup consists of beta tracking detectors and position sensitive microchannel plate (MCP) recoil ion detectors. Another possible choice for the secondary electron multiplier is microsphere plate, however, we use MCP as the first prototype device. The beta momentum vector is determined using the planar drift chamber and scintillation counters. The decay vertex position is defined using the beta-ray straight-line track information and the atomic beam profile. The vertex position resolution is dominated by the wide atomic beam profile of around a few mm. For the recoil ions do not have sufficient kinetic energy to hit the MCPs, a static electric field is applied to accelerate the recoil ions before hitting the MCPs. Using a cross-wire helical delay line anode, two-dimensional

hitting position information for the recoil ions on the MCPs can be obtained. The initial ion position at the ground-level grid, just before entering the acceleration field, can then be extracted using a particle trajectory calculation inside the electric field. Together with the decay vertex information, the recoil ion track in the free volume can be determined. The kinetic energy of the recoil ion can be extracted by a TOF measurement between the electron hitting timing and the MCP hitting timing.

Most of the previous and ongoing beta neutrino angular correlation experiments are based on single measurements of the recoil energy spectra using ion traps.<sup>5-7)</sup> The disadvantage of the present in-flight measurement is the low statistics and the difficulty of the coincident measurement with the beta particle. On the other hand, our advantage is the high sensitivity on the so-called  $a$  parameter (beta neutrino angular correlation coefficient) thanks to the direct determination of the beta and neutrino emission angle in the coincident experiment. In Fig. 2, event-generator-based simulation results are shown, comparing the expected deviation from  $a = 1$  to  $a = 0.9$ , on the single recoil ion energy spectra and the beta neutrino relative angular distribution with same statistics of  $10^5$  events. Figure 2 shows that the direct measurement of the relative emission angle enables a highly sensitive angular correlation coefficient measurement.

A prototype position-sensitive recoil ion MCP detector using a helical cross wire delay line anode has been

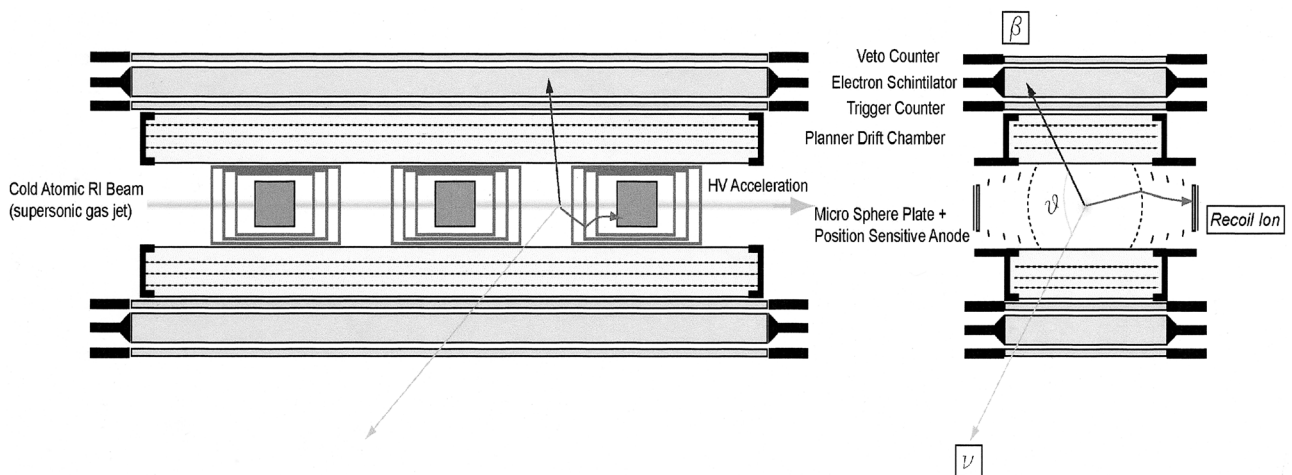


Fig. 1. Detector setup for the beta neutrino angular correlation measurement.

<sup>\*1</sup> Department of Physics, Rikkyo University

<sup>\*2</sup> Department of Physics, Tokyo Institute of Technology

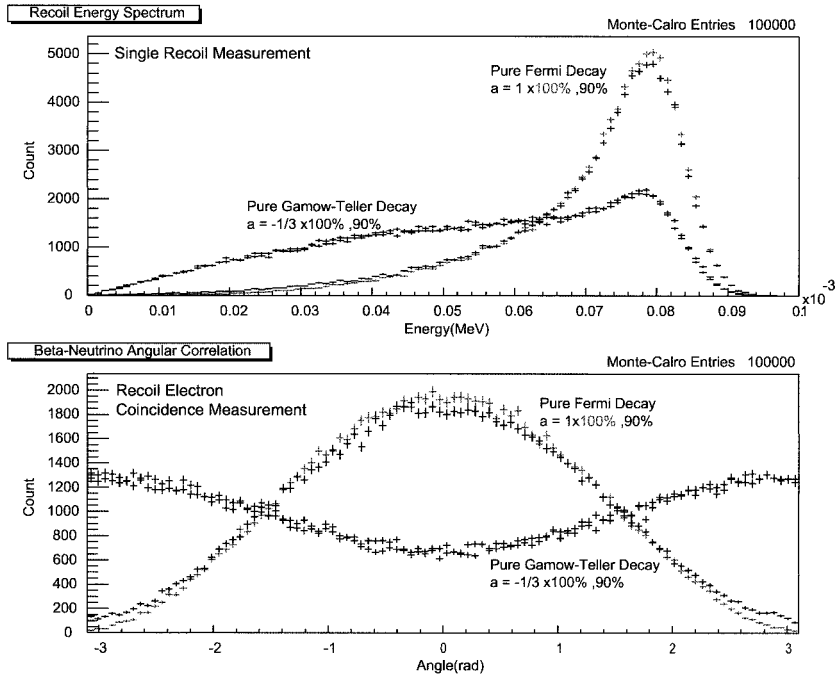


Fig. 2. Simulation results comparing single recoil ion measurement and direct emission angle measurement.

built without the acceleration field, showing a position resolution of around 100 microns, which is sufficiently good for the current purpose. A study of two-dimensional position detection and overall position resolution combined with the acceleration field is under way. The fabrication of the planar drift chamber with delay line readout is already started, and is expected to be completed and tested within 2003. Detector and RI-atomic beam facilities will be completed before the first RIBF beam by utilizing the current RIKEN accelerator, and we will start data production at RIBF from its initial stage.

#### References

- 1) B. R. Holstein and S. B. Treiman: Phys. Rev. D **66**, 010001 (2003); H. Abele: Nucl. Instrum. Methods Phys. Res. A **440**, 499 (2000).
- 2) J. Murata et al.: RIKEN Accel. Prog. Rep. **34**, 246 (2001) and references therein.
- 3) J. Murata: to be published in Czech. J. Phys. **53** (2003).
- 4) H. Miyoshi et al.: RIKEN Accel. Prog. Rep. **36**, 193 (2003) and the references therein.
- 5) J. S. Allen et al.: Phys. Rev. **116**, 134 (1959).
- 6) C. H. Johnson et al.: Phys. Rev. **132**, 1149 (1963).
- 7) E. G. Adelberger et al.: Phys. Rev. Lett. **86**, 1299 (1999).

# Performance of a multiple-reflection time-of-flight mass spectrometer

Y. Ishida, M. Wada, Y. Matsuo, I. Tanihata, A. Casares,\* and H. Wollnik\*

In order to determine nuclear binding energies of short-lived nuclei, we have developed a multiple-reflection time-of-flight mass spectrometer (MR-TOF).<sup>1)</sup> In the MR-TOF, ions are repeatedly reflected between two coaxially arranged electrostatic ion mirrors. These ions are passed up to 700 times between the ion mirrors. Within this system, the overall ion flight time can be 3 ms and the overall flight distance more than 100 m. There are no intensity losses in the grid-free ion mirrors. The transmission is limited only by angle scattering of the ions by residual gas atoms. The achieved mass resolving power exceeded  $m/\Delta m \approx 40,000$ .

The CO-N<sub>2</sub>-C<sub>2</sub>H<sub>4</sub> mass triplet is used to check the accuracy of the MR-TOF. This triplet contains ions of masses  $m_{CO} = 27.994915$  u,  $m_{N_2} = 28.006148$  u,  $m_{C_2H_4} = 28.031300$  u and thus features mass differences of  $m_{CO} - m_{N_2} \approx 0.011233$  u  $\approx 10.4638$  MeV/c<sup>2</sup> and  $m_{C_2H_4} - m_{N_2} \approx 0.025152$  u  $\approx 23.4290$  MeV/c<sup>2</sup>. The obtained spectrum in Fig. 1 shows a mass-resolving power of  $m/\Delta m \approx 25,000$  for ions that had undergone 245 reflections corresponding to the flight time of about 905  $\mu$ s. Using the masses of CO and N<sub>2</sub> as reference masses, the mass of C<sub>2</sub>H<sub>4</sub> is 28.031276(42) u which differs from the correct value by 22 keV/c<sup>2</sup> or 0.85 ppm. Also, from the masses of CO and C<sub>2</sub>H<sub>4</sub> that of N<sub>2</sub> was determined as 28.006153(19) u which is 5.1 keV/c<sup>2</sup> or 0.2 ppm larger than the correct value. Naturally, the value determined by interpolation is more accurate and precise than that by extrapolation. It can be seen that the relative positions of the reference peaks to the unknown one in the spectrum are important for accurate and precise mass determination, as well as the resolving power.

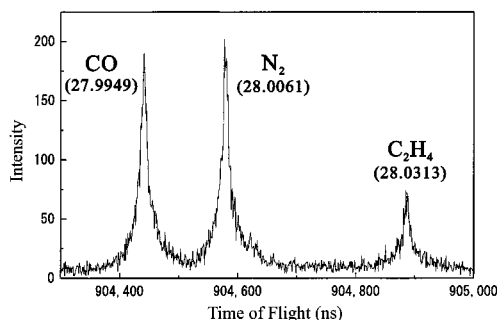


Fig. 1. The mass spectrum of a mixture of CO, N<sub>2</sub> and C<sub>2</sub>H<sub>4</sub> as obtained in the MR-TOF. The mass-resolving power of  $m/\Delta m \approx 25,000$  in FWHM is achieved after 245 reflections in this spectrum. Assuming two of these masses to be known, we can determine the third one with an accuracy of < 1 ppm.

A large variety of exotic nuclei can be produced and separated in-flight using the RIKEN projectile fragment separator (RIPS) or Big RIPS in the RIKEN RI-beam factory project. Those energetic ions are injected into an RF ion-guide system and are thermalized.<sup>2)</sup> The ions are extracted from this system and guided to the MR-TOF for mass spectrometry. We plan to collect the ions in a bunching device before they are injected to the MR-TOF. In such a setup the used electron-impact ion source will be replaced by a small Paul trap.

Ions must be well confined and well cooled before injection to the MR-TOF, otherwise the energy spread of injecting ions becomes wider. The MR-TOF itself can compensate such an energy spread up to the second order when an appropriate setup is selected,<sup>3)</sup> but not the higher order effect. If the energy spread is larger than several percent, the higher order effect is not negligible, so that the mass-resolving power becomes lower than 20,000. Also, the density of the buffer gas into the Paul trap is important. If we inject ions continuously into the trap, dense buffer gas is necessary because ions must lose their energy within the length of the trap. However, the dense gas causes energy loss of the extracting ions due to gas collision. Therefore, a pulsed ion beam is necessary for efficient transport to the trap. While the pressure in the MR-TOF must be kept lower than  $10^{-7}$  mbar, the cooling of ions within the trapped period of  $\sim 1$  ms requires the pressure of the buffer gas to be at least  $10^{-3}$  mbar. As a result, the mean free path is about ten times larger than the trapped region.

A quadratic Paul trap and a linear Paul trap are considered for the device mentioned above. The linear Paul trap has a greater phase-space acceptance and is much easier to operate. For example, the RF applied to the ring electrode of the quadratic Paul trap results in a time-varying force along the longitudinal axis or the axis along which the ions are injected and subsequently extracted. Ions must be injected carefully into the Paul trap by synchronizing the injection with the RF applied. However, the RF applied to the rods of the linear trap creates no such time-varying force along the longitudinal axis, and therefore the RF-phase criterion is not critical. Clark *et al.* compared the linear trap with the quadratic trap as the collecting and cooling device before ions are transported to a Penning trap.<sup>4)</sup> The typical efficiency with the quadratic trap was 15%, whereas, they obtained 80% or better with the linear trap.

We construct a linear Paul trap and investigate its matching to the MR-TOF and the behavior of the ions in the linear trap are calculated by SIMION 7.<sup>5)</sup> The

\* Oak Ridge National Laboratory, USA

calculated ion trajectory in the linear trap is shown in Fig. 2. Such a calculation is useful for determining the

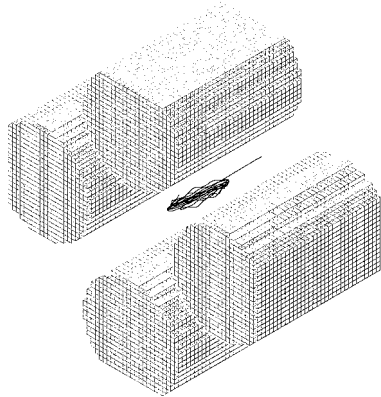


Fig. 2. The ion trajectory in a linear Paul trap calculated by SIMION 7. The ion was trapped by switching the voltage of an endcap electrode (not shown).

appropriate parameter. We find that it is possible to load the pulsed ions from the RF ion-guide system effectively by switching the voltage of the endcap of the trap. As the axial length of the trap becomes longer, the acceptance of the pulsed ion beam becomes higher, however, the mass-resolving power of the MR-TOF becomes lower. Therefore, we design a 2-stage linear trap to separate the loading part and the extraction part.

#### References

- 1) Y. Ishida et al.: RIKEN Accel. Prog. Rep. **36**, 184 (2003).
- 2) M. Wada et al.: Nucl. Instrum. Methods Phys. Res. B **204**, 570 (2003).
- 3) H. Wollnik: J. Mass Spectrom. **34**, 991 (1999).
- 4) J. Clark et al.: Nucl. Instrum. Methods Phys. Res. B **204**, 487 (2003).
- 5) D. A. Dahl: Int. J. Mass Spectrom. **200**, 3 (2000).

# Numerical investigation of the “fair-wind gas cell” concept for slow RI-beam production at RIKEN

M. Wada and V. L. Varentsov\*

A slow-RI-beam facility is planned as one of the primary facilities in the RIKEN RI-beam factory. Developments for the efficient and fast deceleration and cooling of energetic RI beams provided by a projectile fragment separator are under way using a large gas catcher cell and an *rf ion guide*.<sup>1)</sup> They have achieved an overall efficiency of 5% for collecting a 100 MeV/nucleon  $^8\text{Li}$  beam,<sup>2)</sup> which corresponds to an extraction efficiency of 40%. It is hard to increase the efficiency beyond 10% since the stopping capability of the present gas cell, which is 2 m in length and filled with 133 mbar He gas, is limited to  $\sim 12\%$  for such light nuclei. The maximum gas pressure in the cell is restricted by the possible amplitude of the rf gradient electric field applied to the rf ion guide.

A novel concept, named the *fair-wind gas cell*, has been recently proposed,<sup>3,4)</sup> in which the transport of ions through the stopping cell is carried out by a gas flow without using any electric fields. This is similar to an original IGISOL scheme, but the extremely high gas flow rate here enables the use of 1 bar gas pressure and provides fast ion transport through the stopping cell even if its length is as large as 1 m. The collection of ions behind the exit hole of the cell, where the gas pressure is still nearly as high as that inside the stopping cell, should be performed using an rf funnel. It is not obvious that possible rf gradient electric fields applied to the rf-funnel will provide a sufficient barrier force for transporting ions to the entrance of a miniature supersonic nozzle. That is why we have performed detailed ion trajectory simulations, whose results are presented in this short report.

The principle scheme of the *fair-wind gas cell* combined with an extraction rf funnel<sup>5)</sup> is shown in Fig. 1. The large axial symmetric gas cell consists of a stopping chamber and an extraction chamber, which are connected through a central hole. An energetic RI beam enters through an entrance window into the stopping chamber, where the ions are decelerated and thermalized in a buffer gas. The *fair-wind gas cell* concept is based on the use of an intensive compulsory buffer gas flow through the cell combined with an rf funnel. For this purpose, there are annular slits on the side surfaces of the stopping and extraction chambers, which serve as the gas inlet and outlet, respectively. An intensive compulsory gas flow through the cell is maintained by the pressure difference between these slits that is maintained by pumping. Since the flow rate of high-purity helium is extremely high (typically, it is 10–30 bar l/s), the gas inlet and outlet should be con-

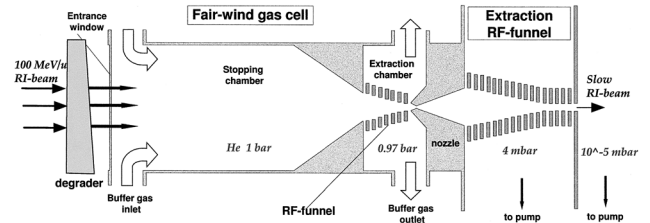


Fig. 1. Principle scheme of the *fair-wind gas cell* and extraction rf-funnel system. The gas cell sizes, which we used in simulations, are as follows: the length of the stopping chamber is 1000 mm; the length of the extraction chamber is 100 mm; the inner cell diameter is 150 mm; the widths of the inlet and outlet slits are 20 mm; the half-angle of conical part of the stopping chamber is  $45^\circ$  and the stopping chamber exit hole diameter is 16.6 mm.

nected to a closed recycling system through an oil-free pump and a gas-purification system.

The stopped ions are transported by the gas flow through the stopping chamber into the extraction chamber, where the rf funnel is placed on the axis between the stopping chamber exit hole and the supersonic nozzle (see Fig. 1). Most of the buffer gas flowing through the cell is evacuated from the extraction chamber through the outlet slit (see Fig. 1) passing through the gaps between rf-funnel rings when the repelling force due to an rf field gradient confines the ions inside this funnel. It should be emphasized that there is no need here for any additional DC field to drag the ions through the buffer gas, as it is used in conventional gas cell techniques. Then the ions are carried by a supersonic gas jet out of the nozzle into the next rf funnel, where a high-speed buffer gas flow effectively transports the ions through this second rf funnel into a high-vacuum region.

The operation of the *fair-wind gas cell* + extraction rf-funnel system was investigated by detailed numerical simulations. First, gas dynamic simulations were performed for both the *fair-wind gas cell* at 1 bar helium buffer gas pressure and the extraction rf funnel at 4 mbar background gas pressure (the computer code used is described in Ref. 6. Then the results of these gas dynamic calculations were incorporated into the Monte Carlo code<sup>1)</sup> for microscopic ion-beam trajectory simulations under the combined effect of the buffer gas flow and electric fields of the rf funnels.

The results of the gas dynamic simulations of the helium gas flow inside the *fair-wind gas cell* are shown

\* Radium Institute, Russia

in Fig. 2. The rf funnel consists of 152 thin metal ring electrodes separated by gaps. The thicknesses of the rings and gaps are 0.3 mm (only every 5th ring is shown in Fig. 2). The entrance and exit rf-funnel apertures are 16.6 mm and 1.2 mm, which correspond to the diameters of the stopping chamber exit hole and the entrance aperture of the supersonic nozzle, respectively. For simulations, we used the same converging-diverging nozzle geometry as that used in Refs. 3 and 4. The axial gas velocity in the cylindrical part of the stopping chamber is approximately 3.5 m/s. The gas velocity is considerably increased in the conical part of the stopping chamber and continues to increase inside the rf funnel (approximately 160–200 m/s) down to the supersonic nozzle entrance. The inlet gas pressure is 1.0 bar, while the outlet gas pressure is 0.96 bar. The total gas flow rate through the *fair-wind gas cell* is 26.5 bar l/s. At the same time, the gas flow rate through the nozzle is only 129 mbar l/s.

The results of the Monte Carlo simulation are shown in Figs. 3 and 4. Figure 3 shows typical ion trajectories in the rf funnel and Fig. 4 shows the transmission efficiencies of  $^8\text{Li}$  and  $^{133}\text{Cs}$  ions, which we have cho-

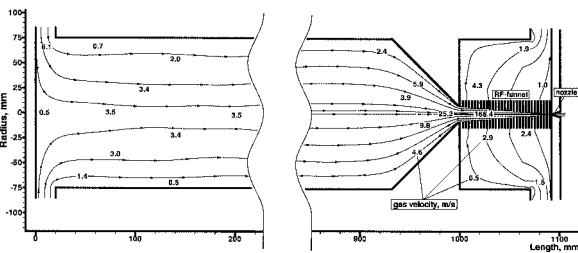


Fig. 2. He gas velocity flow field inside the *fair-wind gas cell*. Arrowhead lines are gas streamlines. Details are in the text.

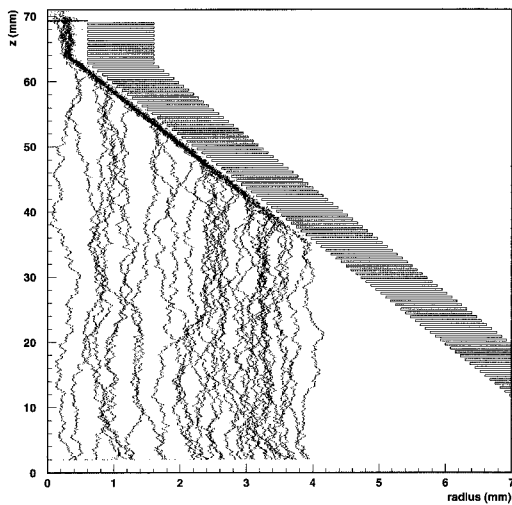


Fig. 3. Typical ion trajectories in the rf funnel of the *fair-wind gas cell*.

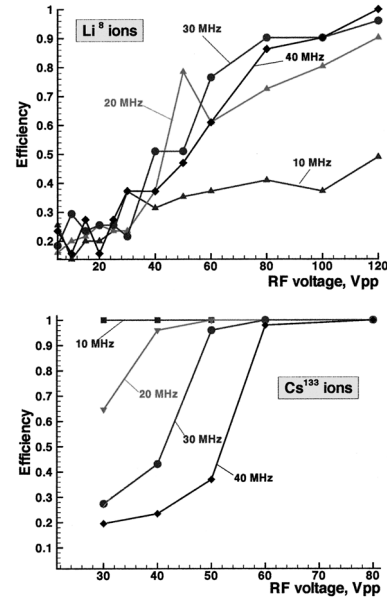


Fig. 4. Transmission efficiencies of  $^8\text{Li}$  and  $^{133}\text{Cs}$  ions through the rf-funnel of the *fair-wind gas cell* as functions of rf frequency and the rf amplitude applied to the ring electrodes.

sen as representatives of light and heavy ions, through the rf funnel of the *fair-wind gas cell* as functions of the rf frequency and the rf amplitude applied to the ring electrodes. One can see that, at adequate rf voltages applied to the funnel electrodes, most of the ions are transported through the funnel even at 1 bar buffer gas pressure. This occurs because an effective repelling force due to the rf gradient electric field in this case is larger than the *dragging force* of the buffer gas flowing out through the gaps between the funnel rings.

The presented numerical simulations support the *fair-wind gas cell* concept. Further investigations should be performed to clarify some other possible problems, such as space-charge effects in the stopping chamber at a high RI-beam intensity. A *real* experiment using a proof-of-principle model is also planned at the present RIKEN facility.

#### References

- 1) M. Wada et al.: Nucl. Instrum. Methods Phys. Res. B **204**, 570 (2003).
- 2) A. Takamine et al.: RIKEN Accel. Prog. Rep. **37**, 173 (2004).
- 3) V. L. Varentsov and D. Habs: Nucl. Instrum. Methods Phys. Res. A **496**, 286 (2003).
- 4) V. L. Varentsov and M. Wada: Proc. COOL03, to be published in Nucl. Instrum. Methods Phys. Res. B.
- 5) V. L. Varentsov: SHIPTRAP Collaboration Workshop, Mainz, Germany, 2001-3, unpublished.
- 6) V. L. Varentsov and A. A. Ignatiev: Nucl. Instrum. Methods Phys. Res. A **413**, 447 (1998).

## FOV and angular response of the APEX onboard French-Brazilian microsatellite

H. Miyasaka,<sup>\*1</sup> H. Kato, K. Makishima, U. B. Jayanthi,<sup>\*2</sup> T. Tamagawa, K. Yamaoka,<sup>\*3</sup> I. Sakurai, S. Hong,<sup>\*4</sup> M. Nakajima,<sup>\*5</sup> M. Kohama, Y. Terada, J. Kotoku,<sup>\*6</sup> and Y. Uchihori<sup>\*7</sup>

We report on the angular response of the APEX onboard the French-Brazilian microsatellite with beam calibration results. Since preliminary beam calibration results, APEX features and observation objectives have been reported previously,<sup>1-3</sup> we will not describe their details here. Note that the schedule for launching has been postponed to mid-2006 instead of the end of 2003 because of a recent Brazilian rocket accident.

The APEX is a radiation monitor, consisting of only four PIN diodes (D1–D4), that observes alpha, proton and electron fluxes around several MeV at the altitude of  $\sim 750$  km of the equatorial region. The APEX has a  $\pm 15$  degrees opening angle of view (FOV). Even with a shield to maintain this FOV, a high-energy particle can easily penetrate the detector through the shield from an unexpected direction. To avoid this, we used a multithreshold discriminator and coincident logic. From the FOV and the energy responses, we determined the geometric factor (G-factor;  $\text{cm}^2\cdot\text{sr}$ ) of the APEX to be  $\sim 0.0076 \text{ cm}^2\cdot\text{sr}$  by Monte Carlo simulation. The G-factor is an important characteristic of the detector for determining fluxes of cosmic rays in real observation. We examined this from accelerator experiments. However, the particle from the accelerators has a parallel direction and not an isotropic distribution; therefore, we examined the angular energy responses and angular particle detection efficiency separately. We performed beam experiments at E3A facilities in RIKEN Ring Cyclotron with 135 MeV/nucleon  $\text{H}_2^+$ . Figures 1 and 2 show examples of the results for angular energy responses and detection efficiency, respectively.

Figure 1 shows a normalized deposited energy of detector 2 (D2) at each incidence angle. This has been normalized at the deposited energy at  $0^\circ$ . Note that the error has been estimated from the standard deviation of the D2 output. This result can be simply expressed as  $1/\cos(x)$  with incidence angle  $x$  by a dash line in Fig. 1. Even from this simple model, we can see a quite good agreement with the experimental results, however, there are some systematic deviation at large incidence angles. This is caused by an energy increase at the detector or Al window.

Figure 2 shows the angular efficiency as the count

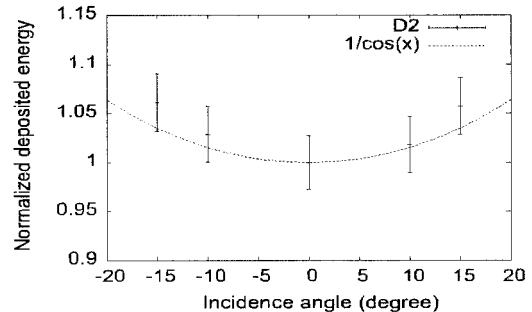


Fig. 1. D2 deposited energy at each incidence angle normalized at 0 degrees. The dashed line represents the expected deposited energy.

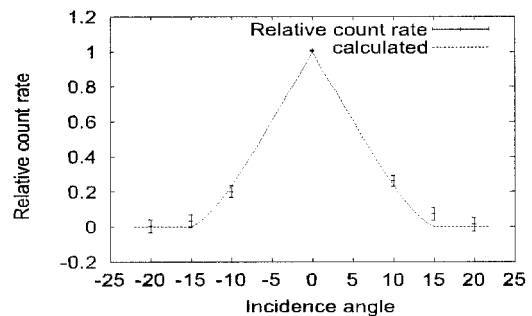


Fig. 2. D4 count rate relative to the input count rate at each incidence angle. The dashed line represents the response calculated from the APEX geometry.

rate of D4 relative to the input count rate at each incidence angle. The dash line represents the efficiency calculated from the APEX detector's geometry. Also from this result, we can see a good agreement between our experimental and calculated results.

Finally from these results, we confirm the expected performance of the APEX. Using this G-factor, for example, we can estimate the count rate of proton at the edge of SAA (South Atlantic Anomaly as a well-known radiation belt region) as  $\sim 100$  counts/sec.

### References

- 1) U. B. Jayanthi: submitted to Adv. Space Res.
- 2) T. Kohno et al.: RIKEN Accel. Prog. Rep. **31**, 168 (1998).
- 3) H. Miyasaka et al.: RIKEN Accel. Prog. Rep. **36**, 170 (2003).

\*1 University of Delaware, USA

\*2 Instituto Nacional de Pesquisas Espaciais, Brazil

\*3 Aoyama Gakuin University

\*4 Saitama University

\*5 Nihon University

\*6 University of Tokyo

\*7 National Institute of Radiological Sciences

## Accelerator test of charge particle detectors for a satellite instrument STEP-F

O. Dudnik,<sup>\*1</sup> T. Goka,<sup>\*2</sup> H. Matsumoto,<sup>\*2</sup> M. Fujii,<sup>\*3</sup> V. Persikov,<sup>\*1</sup> T. Malykhina,<sup>\*1</sup> and H. Kato

Japanese-Ukrainian collaboration in space research includes the testing and calibration of detectors and analogue electronics of the STEP-F instrument.<sup>1)</sup> It is a satellite spectrometer-telescope for high-energy charged particles, which was developed in Ukraine to study the solar cosmic rays and dynamics of the Earth's radiation belts onboard the Russian spacecraft "Coronas-Photon". The instrument consists of a detector unit installed on the external surface of the spacecraft, and a digital data processing unit located in a hermetic module. The detector unit (Fig. 1) contains two identical silicon position-sensitive matrix detectors D1 and D2, and two CsI(Tl) scintillator crystal detectors viewed using large-area photodiodes (D3) and a photomultiplier tube (D4). Each element of the silicon matrix is a separate autonomous semiconductor detector, and has its own analogue signal shaping amplifier. Some operational characteristics of the instrument are presented in Table 1.

Calibration measurements of each type of detector were carried out by the RIKEN Ring Cyclotron by using  $\alpha$ -particle beams of energy  $E = 100$  MeV/nucleon and H<sub>2</sub> ion beams of energy 70 MeV/nucleon. Aluminum absorbers of thickness 21, 25, 30, 35 and 36 mm were used to obtain various energies of the incident  $\alpha$ -particles. Measurements without an absorber were also carried out. The pulse amplitudes from detectors D2 and D3 corresponding to the incident  $\alpha$ -particle energies 62.5, 84, 164, 214, 254, and 400 MeV were obtained in the experimental energy spectra. Simultaneously, computer simulations of energy losses by the

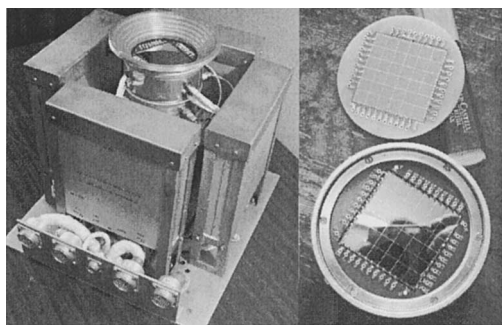


Fig. 1. Common view of detector unit and position-sensitive silicon matrices of the satellite spectrometer-telescope STEP-F.

<sup>\*1</sup> Kharkiv National University, Ukraine  
<sup>\*2</sup> Japan Aerospace Exploration Agency, Tsukuba Space Center  
<sup>\*3</sup> FAM Science Co., Ltd.

Table 1. Operational characteristics of the instrument.

Event Logic <sup>§</sup>	Energy Range (MeV)	Measurements
$D1\overline{D2}D3D4$	Electrons: 0.2–0.45, Protons: 3.5–7.3, Alphas: 13.7–29.5	Intensities of particles in the full field of view
$D1D2\overline{D3}D4$	Electrons: 0.45–0.55, Protons: 7.3–9.9, Alphas: 29.5–40.1	Energy and angular distribution of particles
$D1D2D3\overline{D4}$	Electrons: 1.2–16, Protons: 14.5–61, Alphas: 62–249	Energy and angular distribution of particles in 10 differential energy channels
$D1D2D3D4$	Electrons: > 16.8, Protons: > 64, Alphas: > 262	Angular distributions and integral intensities of particles

<sup>§</sup>  $D1D2$  means logical coincidence,  $D1\overline{D2}$  means logical anti-coincidence .

Cern GEANT4 Toolkit in the detectors by  $\alpha$ -particles in the energy range 10–410 MeV were carried out for a small number of particles ( $N = 10$ ) with variable steps of input energy. Figure 2 shows results of the simulation as well as experimental data (in volts) for detector D3, which is used as an E-detector in the  $dE/dx$ - $E$  technique. The comparison of simulation results with experimental data allowed us to verify the energy ranges of  $\alpha$ -particles recorded by the detectors. Alpha particles with energies up to 13.7 MeV are stopped by the shielding aluminium foil placed immediately above the first silicon matrix D1, while  $\alpha$ -particles with energies in the ranges 40.5–62 MeV, and 248.5–262 MeV are stopped in the coating materials of the scintillation

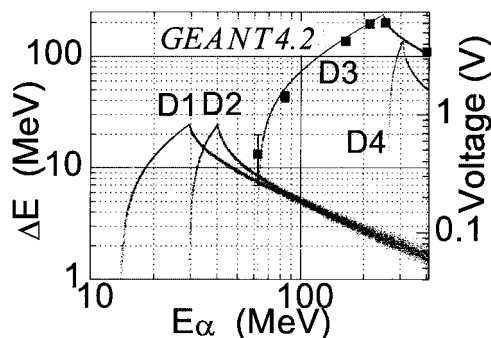


Fig. 2. Simulation results of deposited energies (solid curves) compared to the experimental data (dots) of pulse amplitudes from  $\alpha$ -particle signals.



detectors D3 and D4. Excluding these energy gaps, particles with energies from 13.7 MeV to 262 MeV are stopped in the active detector materials and make contributions to the pulse amplitudes of analogue signals.

In order to study the effects of secondary particles on detector signals, the energy spectra from most of the D1 and D2 matrix elements were obtained by using a 140 MeV H2 ion beam. The axis of the beam was directed in parallel to the telescope axis and was displaced to peripheral elements 7, 8, 9, and 11 of the matrices as shown in Fig. 3 (the beam is indicated by the circle). These elements registered 58, 36, 3 and 2.5% of particles, respectively, which is consistent with the present beam size of 5 mm. Figure 4 shows a typical spectrum measured from element #7 of matrix 1.

Protons of energy  $E = 70$  MeV compose the major part of a beam as is shown in Fig. 4. In counting the number of particles detected by each element of the matrix, either protons (crosshatched region in Fig. 4) or secondary particles with energies less than 70 MeV were taken into account. The number of particles recorded during the calibration process by element #7 of each matrix is taken as a relative unit.

The total quantities of particles recorded in most of the elements in both matrices are presented in Fig. 5. Both primary beam particles and secondaries produced in the aluminium foil above D1 and in detectors D1, D2 and D3 (albedo particles), are taken into account. To indicate the differences in the number of particles

detected by various elements, a logarithmic scale is used on the vertical axis. Figure 5 shows that particles were mainly recorded by elements 7, 8, 9 and 11 (crosshatched columns) and in a negligible number — ( $< 1\%$ ) — by closely neighboring elements.

Computer simulations were also performed for the same configuration of elements in terms of both silicon matrices and direction of the beam axis. One hundred and fifty thousand primary protons at the energy of 70 MeV were simulated. The number of recorded particles in each element of the matrices was calculated by the technique used in the experiment, and was normalised to the number of particles in element #7, as in the experiment. Figure 5 presents simulation results, giving the number of primary protons and secondary particles recorded in the elements of two matrices (light columns). Figure 5 shows a fairly good agreement between the experimental data and simulation. A conclusion may also be drawn that the effects of secondary particles in detector signals are almost negligible when operating at high primary particle energies. In particular, the number of secondary albedo particles produced in the scintillation detector D3 is negligible. Therefore, the error in the counting rate of the D2 detector due to the production of secondary species in the D3 scintillator at high energies of charged primary particles will be small.

This work is supported by the Science and Technology Center in Ukraine (STCU Grant N 1578).

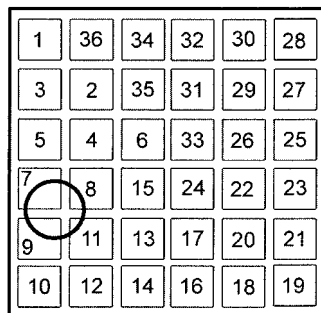


Fig. 3. Beam projection on the elements of the silicon matrix. Spatial scale is preserved.

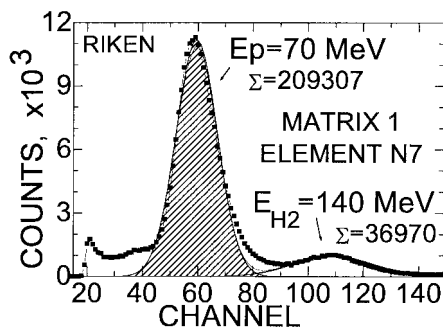


Fig. 4. Spectrum of ions H2 and decay products from element #7 of matrix 1.

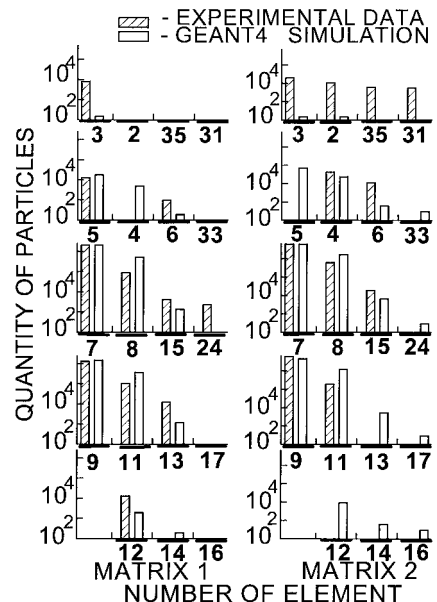


Fig. 5. The number of particles in each element of both matrices after passage of H2 beam (experimental data and results of simulation).

#### References

- 1) O. V. Dudnik, T. Goka et al.: Adv. Space Res., **32**, 2367 (2003).

## Design of an RF beam splitter for a time-sharing beam delivery to BigRIPS and RIPS

H. Ueno, A. Yoshimi, and K. Asahi

In the RIBF configuration, medium- and heavy-mass beams can be accelerated up to the energy of  $E = 115$  AMeV with IRC. When a beam-transport line from IRC to RIPS in the existing facility is constructed, intense beams with a wide range of atomic number can be also provided to RIPS as well as BigRIPS. The energy region around 100 AMeV is preferred in experiments utilizing the fragment-induced spin polarization because of its mechanism, as well as the material science with radioactive-isotope beams (RIBs).<sup>1)</sup>

We are proposing the operation in the time-sharing scheme between BigRIPS and RIPS by using a present RF beam splitter system, whose schematic layout is shown in Fig. 1. The extracted beam from IRC is introduced into the RF beam splitter system. The basic structure of the system is similar to that of the existing RF beam deflector system.<sup>2)</sup> A high voltage is applied to vertically arranged parallel electrodes at a frequency of 9–22 MHz, which is adjusted to one-half of the cyclotron frequency. The system deflects each extracted particle bunch up and down at angles of  $\pm\theta_{\text{def}}$  alternately. Here, a static magnetic field is applied to the beam on the horizontal plane perpendicular to the incoming beam, which changes the beam angles of  $-\theta_{\text{def}}$  and  $+\theta_{\text{def}}$  into  $-2\theta_{\text{def}}$  and 0, respectively. The required magnetic field strength is  $\sim 0.04$  T. Then the beam is introduced into a Lambertson-type septum magnet,<sup>3)</sup> which is located downstream of the RF beam splitter.

The Lambertson magnet is a special dipole that contains two areas for a beam. One area has a magnetic field and bends the beam. The other area is shielded from the field and the beam simply passes through it. The  $\theta = 0^\circ$  beam goes to SRC through a tunnel built in the pole of the magnet. The single operation of BigRIPS can be easily carried out only by turning off the RF beam splitter system: the beam simply goes to

SRC through the tunnel of the Lambertson magnet. In this beam-sharing scheme, the beam is delivered to SRC at a period of 91–222 ns depending on the cyclotron frequency. This beam evolution period is very short so that the beam loading effects are considered negligible. On the other hand, the  $\theta = -2\theta_{\text{def}}$  beam goes through the pole gap of the Lambertson magnet. The pole gap is slanted off the horizontal plane. The Lambertson magnet deflects the beam by 20 degrees. Then the beam is introduced into the beam-transport line connected to RIPS. The maximum magnetic rigidity of the beam-transport line from IRC to RIPS is designed to be  $B\rho = 4.2$  Tm. This value is sufficiently large to accept the beam extracted from IRC except for the very heavy ions near uranium.

The existing RF deflector is a type of quarter-wavelength coaxial resonator with an upright fixed-length cavity.<sup>2)</sup> The frequency is adjusted with the capacity tuner attached on the side. We have designed a similar type of resonator, but the cathode cavity is tuned with a sliding RF short plate. In this configuration, the width of the system becomes narrower, thus the system is only 1 m wide, whereas the RF deflector is 2.4 m wide. Since the lateral space for the installation of the RF beam splitter is limited at the exit of IRC, the present configuration is suitable.

In our design, the maximum high voltage of 150 kV is applied to the electrode with a length of 1000 mm and a gap of 30 mm. Based on a model calculation, where the transmission-line model of the distributed constant circuit is taken into account in the one-dimensional approximation, the power loss of the cavity is expected to be less than 50 kW.<sup>4)</sup> This power loss does not cause serious problems to the cooling of the cavity.

At the entrance of the Lambertson magnet, which is placed 2 m downstream the RF beam splitter, the beams of  $^{86}\text{Kr}^{35+}$  and  $^{136}\text{Xe}^{52+}$  with an energy of 115 AMeV are deflected by 42 mm and 39 mm from the central trajectory, respectively. These values are expected to be sufficiently large to construct the Lambertson magnet.

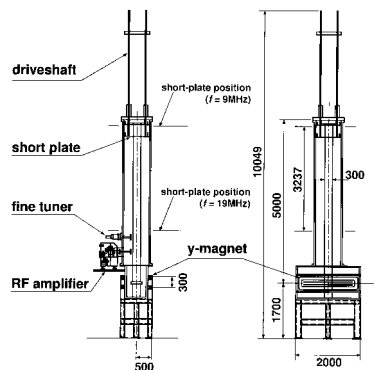


Fig. 1. A schematic layout of the RF beam splitter system.

### References

- 1) Y. Kobayashi et al.: Eur. Phys. J. A **13**, 243 (2002); W. Sato et al.: J. Radioanal. Nucl. Chem. **255**, 183 (2003).
- 2) K. Yamada et al.: RIKEN Accel. Prog. Rep. **34**, 201 (2001); K. Yamada et al.: RIKEN Accel. Prog. Rep. **35**, 147 (2002); K. Yamada et al.: RIKEN Accel. Prog. Rep. **36**, 190 (2003).
- 3) L. W. Olesiuk et al.: IEEE Trans. Nucl. Sci. **NS-20**, 428 (1973).
- 4) H. Miyazaki: Private communication (2003).

## Test experiment on the low-energy RI extraction system

H. Miyoshi,\*<sup>1</sup> K. Asahi,\*<sup>1</sup> K. Shimada,\*<sup>1</sup> A. Yoshimi, D. Kameda,\*<sup>1</sup> H. Ueno,  
H. Watanabe, T. Haseyama, J. Murata,\*<sup>2</sup> S. Emori,\*<sup>1</sup> G. Kato,\*<sup>1</sup>  
G. Kijima,\*<sup>1</sup> M. Tsukui,\*<sup>1</sup> and Y. Kobayashi

Spin polarized low-energy radioactive isotope (RI) beams are useful not only in nuclear physics but also in materials and surface physics. We are developing a device that produces a spin polarized low-energy RI beam based on the *atomic beam resonance technique*. A prototype, including a fragment stopping and collecting gas chamber, a jet separator, an atomic-beam forming nozzle and a spin-selecting sextupole magnet is almost completed. At present, we are detailing the design of the fragment stopping and collecting gas chamber.<sup>1)</sup>

In the present paper, we report on test experiments on the chamber using a RI beam delivered by the fragment separator RIPS.

The schematic setup used for the test experiments is illustrated in Fig. 1. The pressure of helium gas in the RI stopping gas chamber was approximately 600 Torr. We chose a beam of <sup>31</sup>Al ions produced by the fragmentation of an <sup>40</sup>Ar projectile at an energy of 95 MeV/nucleon on a 3.5-mm-thick Beryllium target. The intensity of the <sup>40</sup>Ar primary beam was approximately 50 pA. The intensity of the <sup>31</sup>Al beam was approximately 10<sup>4</sup> particles/sec at the entrance of chamber. Using the rotating degrader, we adjusted the energy of <sup>31</sup>Al ions at the entrance of the chamber such that which were safely stopped in the He gas volume.

Figure 2 illustrates the system of detectors employed as a  $\beta$ -ray tracking system. The system consisted of two layers: the first layer had 12 plastic scintillators (45 × 0.5 × 210 mm) and the second layer had 30 plastic scintillators (25 × 25 × 200 mm).

The stopping chamber involved 50 electrodes with which a static electric field was applied in order to extract the stopped ions. The detailed arrangement is described elsewhere.<sup>1)</sup> The experimental result is summarized in Fig. 3.

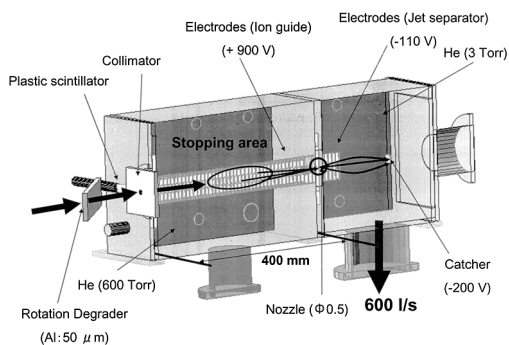


Fig. 1. Schematic view of experimental setup.

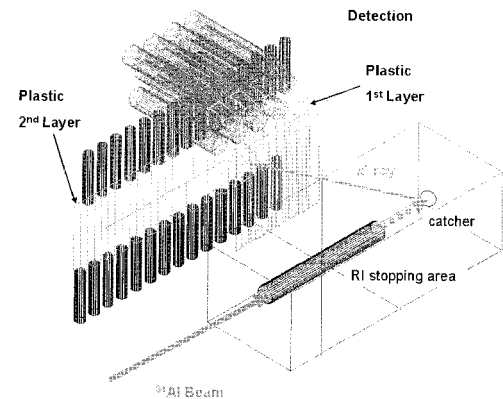


Fig. 2. The  $\beta$ -ray tracking system. The beam transport and energy regions of the incident <sup>31</sup>Al ions were so arranged that the region in the gas where the <sup>31</sup>Al ions were stopped is distributed indicated by the shaded cylinder. The cylindrical region was surrounded by an array of 50 ring electrodes with an inner diameter of 20 mm. After extraction using the electrodes, ions reached the catcher in the second chamber.  $\beta$ -rays emitted from the <sup>31</sup>Al ions were detected by the first and second plastic scintillator layers. From the two positions extracted from the two scintillator layers, the source point was deduced.

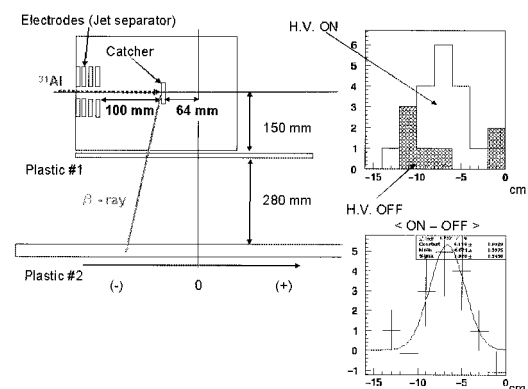


Fig. 3. The left part shows a schematic view of the downstream chamber which is called a *jet separator*. The right two panels show the deduced position distribution of the source points along the h.v. beam axis; the upper one being the distributions with the electrodes voltages on and off, and the lower one being their difference. A peak point is observed at around the  $-70$  mm position. This is consistent with the position of the catcher which is shown in the left panel.

\*<sup>1</sup> Department of Physics, Tokyo Institute of Technology

\*<sup>2</sup> Department of Physics, Rikkyo University

Considering the chamber walls and the  $\beta$ -ray energy, the  $\beta$ -ray emitted from the first chamber could not be counted by the tracking system. Moreover, because of the resolution of the tracking system, we could distinguish the position of catcher. From the result of Fig. 3 and calculations, the extraction efficiency for the  $^{31}\text{Al}$  incident at the stopping gas chamber was determined to be  $3.8 \times 10^{-4}$ . In deducing this number, the efficiency of the  $\beta$ -ray detection with the plastic scintillator telescope array and its solid angle were taken into account. The obtained value for the extraction efficiency is not large at the present test experiment. The loss by extraction efficiency might come from possibly incomplete stopping in the stopping gas chamber, irregular focusing caused by the electrodes, neutralization of ions due to contaminations in the chamber or diffusion of ions in the second transportation chamber.

The second test experiment was performed in September. The aim of the test experiment was to exclude the above possible efficiency losses, for example, in this experiment, we employed  $^{34}\text{P}$  ions and the

pressure of He gas was approximately 1200 Torr. We confirmed that contamination was less than 1 ppb by measuring gas impurity using a quadrupole mass spectrometer (PFEIFFER QMG 422). When the number of counts of He is  $10^7$  counts at QMG 422 at approximately  $10^{-6}$  Torr, the number of counts of sum of contaminations is less than  $10^2$  counts. During the filling of He gas in the chamber, other contaminations were not increased. To improve the collection efficiency, we changed the partition of the applied voltages at the electrodes. As for the detectors, we installed a trigger counter ( $210 \times 800 \times 5$  mm) to detect  $\beta$ -ray from  $^{34}\text{P}$  with a high  $S/N$  ratio and a veto counter to exclude the background. The details of the electrodes and their characteristics are described elsewhere.<sup>1)</sup> The analysis of the obtained data is now in progress.

#### References

- 1) K. Shimada et al.: RIKEN Accel. Prog. Rep. **37**, 175 (2004).

## On-line collection of $^8\text{Li}$ ions from the projectile fragment separator using an rf ion guide system (III)

A. Takamine,<sup>\*1</sup> M. Wada, Y. Ishida, T. Nakamura,<sup>\*2</sup> T. Kambara, H. Ohyama, Y. Kanai, T. M. Kojima, Y. Nakai, N. Oshima,<sup>\*1</sup> A. Yoshida, T. Kubo, Y. Matsuo, Y. Fukuyama, K. Okada,<sup>\*3</sup> T. Sonoda,<sup>\*4</sup> S. Ohtani,<sup>\*5</sup> K. Noda,<sup>\*6</sup> H. Kawakami,<sup>\*2</sup> I. Katayama,<sup>\*2</sup> Y. Yamazaki, H. Wollnik,<sup>\*7</sup> V. Varentsov,<sup>\*8</sup> and P. Hosteins

The projectile fragment separator provides a wide variety of short-lived RI ions which are partially not restricted to their chemical properties and lifetimes. The beam energy and quality is, however, are not adequate for low-energy beam experiments, in particular, for trapping experiments. We have been working on technical developments for obtaining a low-energy beam from an energetic RI beam leaving a projectile fragment separator using the rf ion guide system.

The rf ion guide system consists of an energy degrader, a large He buffer gas cell and an rf ring electrode assembly. The energetic RI beams ( $\sim 100$  MeV/nucleon) coming from the fragment separator pass through two wedged degraders of variable angle and thickness. The medium energy beam ( $\sim 2$  MeV/nucleon) thus obtained is then injected into a large He gas cell for stopping and thermalization. The high ionization potential of He allows for keeping the RI ions in the singly charged state. The stopped ions can be extracted by the dc field applied between the cell as the anode and the exit as the cathode. In the rf ion guide, the cathode electrode consists of many ring electrodes to which rf voltages are applied in addition to dc potentials, with the idea that the average force due to the rf gradient field drives the ions away from the electrodes. The extracted ions can be transported by SPIG<sup>1)</sup> through a number of differential pumping sections toward experimental instruments in an ultrahigh vacuum.

We have tested several different geometries of the rf ion guide setup on-line with 100-MeV/nucleon  $^8\text{Li}$  beams provided by the RIKEN projectile fragment separator RIPS.<sup>2,3)</sup> Thus far, the maximum overall efficiency of 1% and the maximum yield of approximately 2,000  $^8\text{Li}$  ions per second were obtained.<sup>3)</sup> We report here the recent test experiment with a new gas cell geometry (Fig. 1). In the new gas cell, a linear dc field can be applied in the entire region of the cell in order to increase the effective volume (Fig. 2) and an extraction electrode assembly with a new rf carpet is

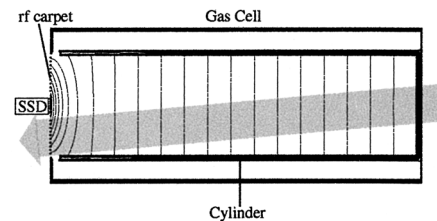


Fig. 1. New gas cell ( $40\text{ cm}\phi \times 2\text{ m}$ ). The linear dc field is generated. Lines represent equipotential lines and the big arrow indicates the injecting  $^8\text{Li}$  beam which is intentionally inclined to the cell in order to avoid injecting fast  $^8\text{Li}$  ions into SSD behind the exit nozzle.

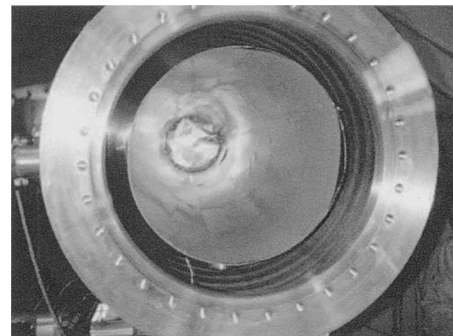


Fig. 2. Cu cylinder installed in the gas cell. A linear dc field is produced by electrodes on printed circuit boards mounted in the Cu cylinder. The Cu cylinder is connected to a cryogenic head to cool the cylinder.

placed at the bottom of the cell. Since the detector for  $^8\text{Li}$  is still mounted just behind the extraction nozzle, the cell is inclined so as to avoid injecting fast  $^8\text{Li}$  ions directly into the detector. The new rf carpet consists of an outer part and a central part. We apply rf voltages with dc offsets to the central part while a simple dc potential gradient is applied to the outer part. The central part has 160 ring electrodes, the interval of which is 0.28 mm with an exit nozzle of 0.7 mm in diameter.

Figure 3 shows the overall efficiency and yield as a function of the incoming  $^8\text{Li}$  beam intensity. The maximum overall efficiency of 3.6% was achieved when the beam intensity was low at the highest dc field. However, a decrease was observed as the beam intensity was increased, and three lines converged to the line whose yield was nearly proportional to the square root

\*1 Graduate School of Arts and Sciences, University of Tokyo

\*2 Institute of Particle and Nuclear Studies, High Energy Accelerator Research Organization (KEK)

\*3 Department of Physics, Sophia University

\*4 Cyclotron and Radioisotope Center, Tohoku University

\*5 Institute for Laser Science, University of Electro-Communications

\*6 National Institute for Radiological Science

\*7 University of Giessen, Germany

\*8 Radium Institute, Russia

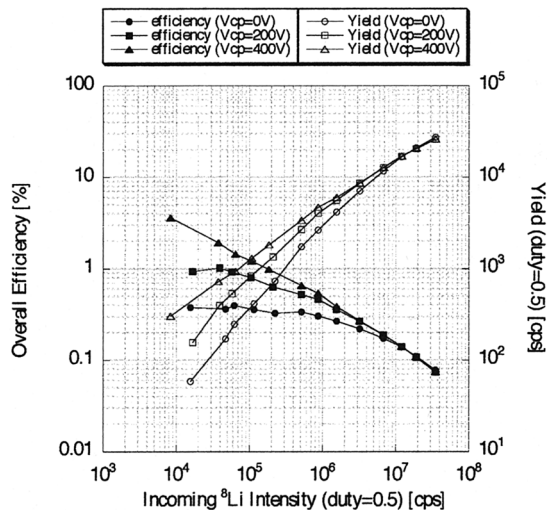


Fig. 3. Overall efficiency and yield of extracted  $^8\text{Li}$  ions as a function of intensity of incoming  $^8\text{Li}$  from RIPS. The rf voltage on the rf carpet was  $150 V_{p.p.}$ . “ $V_{cp}$ ” is defined as the potential difference between the two edges of the cylinder, the inside of which a linear dc field is generated. (Even if  $V_{cp} = 0$  V, penetration fields from the rf carpet exist inside the cylinder.) A maximum yield of 26,000 cps was obtained when the incoming beam intensity was highest.

of the incoming  $^8\text{Li}$  intensity. We also obtained a time profile<sup>3)</sup> of extracted  $^8\text{Li}$  by deconvoluting the time spectrum of the delayed  $\alpha$ -decay of  $^8\text{Li}$  (Fig. 4).

Since the mobility of  $^8\text{Li}$  at 100 Torr He gas is  $152 \text{ cm}^2\text{V}^{-1}\text{s}^{-1}$ , it should take only 600 ms for a  $^8\text{Li}$  ion to travel a 2 m distance when  $V_{cp} = 400$  V. The time spectrum in Fig. 4 shows the presence of slower components, which suggests that the dc field is weakened by the space charge effect due to the presence of charged particles (mainly  $\text{He}^+$ ) produced by injected beams.

The yield dependence on the intensity can be explained in two different ways. One is that the phenomenon is due to the recombination process between the  $^8\text{Li}$  ions and electrons which are produced by injected ion beams. It is because such a process can be described using the rate equation

$$\frac{dn}{dt} = -\alpha n^2 + Q \quad (1)$$

with  $n$  is the ion density,  $\alpha$  the effective recombination coefficient and  $Q$  the ionizing rate, and then the equilibrium density  $n_{eq} = \sqrt{\frac{Q}{\alpha}}$ . The other is that the phenomena is due to the space charge effect. The fact that the yield curves in Fig. 3 converge when the beam

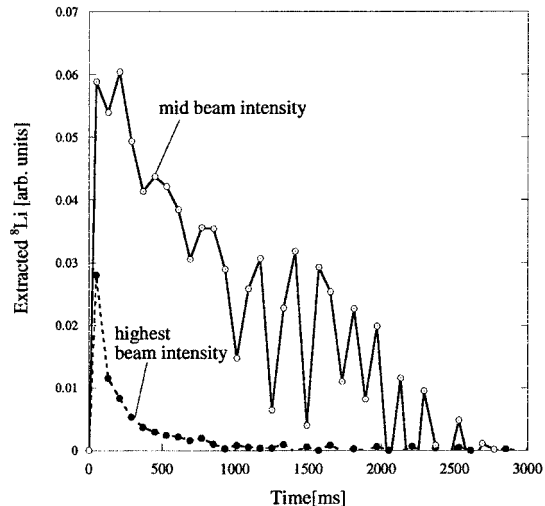


Fig. 4. Time profile of the  $^8\text{Li}$  ions when  $V_{cp} = 400$  V at two beam intensities. Each profile is normalized to the sum is equal to the efficiency. This shows that ions can be extracted far from the exit.

intensity is high supports this explanation. As can be seen from the time spectrum at the highest beam intensity, the fraction of slow components is small. Thus, the extractive volume seems to be restricted to the region just in front of the rf carpet where the dc field applied to the cylinder is less effective. When the beam intensity is low, on the other hand, the space charge effect should not be significant, then the extractive volume can be expanded to the entire cylinder. However, extraction time which depends on the  $V_{cp}$  causes another loss of  $^8\text{Li}$  ions due to their lifetime. The yield dependence on  $V_{cp}$  at the lowest beam intensity supports this explanation. For the moment, we could not judge which one is the dominant effect. Further investigation on this problem is required.

The absolute intensity of the low-energy  $^8\text{Li}$  was more than 26,000 atoms per second, which is sufficient for various experiments. Since a similar intensity is expected for  $^{11}\text{Be}$  ions, we will begin the precision spectroscopy of the hyperfine structure of the trapped  $^{11}\text{Be}$  isotope aiming at studying the Bohr-Weisskopf effect.<sup>4)</sup>

#### References

- 1) H. Xu et al.: Nucl. Instrum. Methods Phys. Res. A **333**, 274 (1993).
- 2) M. Wada et al.: Nucl. Instrum. Methods Phys. Res. B **204**, 570 (2003).
- 3) M. Wada et al.: RIKEN Accel. Prog. Rep. **36**, 194 (2003).
- 4) T. Nakamura et al.: Opt. Commun. **205**, 329 (2002).

## Design of RI extraction system with a static electric field

K. Shimada,\*<sup>1</sup> K. Asahi, H. Miyoshi,\*<sup>1</sup> A. Yoshimi, H. Ueno, J. Murata,\*<sup>2</sup> Y. Kobayashi, K. Sakai,\*<sup>1</sup>  
H. Watanabe, T. Haseyama, D. Kameda,\*<sup>1</sup> S. Emori,\*<sup>1</sup> G. Kato,\*<sup>1</sup> G. Kijima,\*<sup>1</sup> and M. Tsukui\*<sup>1</sup>

A method for producing slow neutral radioactive isotope (RI) beams and for measuring their electromagnetic moments is under development, which is expected to be applied generally to the whole region of the nuclear chart. The method is essentially based on the atomic beam resonance technique,<sup>1)</sup> and has a few advantages over the fragmentation-based polarization method which has so far been employed in nuclear moment measurements in light unstable nuclei. A key issue for the successful application of the present method to RI produced in the projectile-fragmentation (PF) reaction is the formation of a slow neutral RI beam<sup>2)</sup> from the PF reaction products which have inevitably high kinetic energies.

To produce slow RI beam, the RI ions produced by the PF reaction are introduced into a high-pressure helium volume where most of them are eventually stopped (Fig. 1). In this volume, we apply a parallel and rather strong electric field, so that the stopped RI ions are swiftly separated from the plasma region around the track of the RI ions and are drifted downstream. Close to the end of this volume, the field lines are compressed into a small-diameter bundle at the outlet orifice by increasing the field strength. The RI ions drift following the field lines and are thus compressed into the orifice. In the region close to the orifice, there exists helium gas flowing going out of the orifice, and because of a converging corn placed upstream of the orifice, the flow velocity rapidly increases and helps the RI ions to be transported through the orifice. As soon as the RI ions and the carrier helium gas enter the downstream chamber (jet-separator (JS) chamber), the RI ions are forced to proceed further downstream by a strong parallel electric field, while the helium gas is evacuated using a high-power vacuum pumping system. In the section placed after this, the neutralization is achieved by the passage of the ion beam through the charge exchange gas,<sup>3)</sup> but the details are under investigation.

In the present work, we designed and fabricated an RI extraction chamber. The first chamber for RI-stopping and RI-drifting volume involves electrodes consisting of 36 stainless-steel discs and intervening ceramic spacers. The upstream 33 electrodes are 1-mm-thick discs

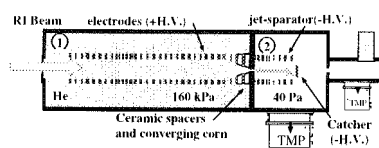


Fig. 1. Schematic picture of the gas stopping chamber.

\*<sup>1</sup> Department of Physics, Tokyo Institute of Technology

\*<sup>2</sup> Department of Physics, Rikkyo University

of 58 mm in diameter with respective inner openings of 20 mm in diameter. The remaining three (34th, 35th and 36th) electrodes have inner openings of 15 mm, 10 mm and 5 mm in diameter, respectively. The ceramic spacers located close to the nozzle have a tapered hole and form the converging corn. This corn suppresses the discharge between electrodes, so that we could apply 2.1 kV to the last electrode. The orifice of the nozzle is as low as 0.2 mm in diameter. This diameter is chosen to increase the pressure of the first chamber, so that approximately 70% of the energetically spread RI ions sent from RIPS stop there. The second chamber is the JS chamber, which consists of the same electrodes as those in the first chamber. The total voltage applied to these electrodes is  $-700$  V. The pressure stays at 40 Pa which is  $2.5 \times 10^{-4}$  times as low as that in the first chamber.

A static electric field calculated with POISSON code<sup>a)</sup> and the tracks of the drift of the incident ions simulated in a computer are shown in Fig. 2. In this simulation, the total voltages applied to electrodes in the first chamber and in the second chamber are 2.4 kV and  $-700$  V, respectively. In addition, the current of the incident beam of approximately  $10^{-14}$  A is so small that a charge of ions attached to the ceramic spacer is ignored. The electric fields in the first chamber start with as low as 8 V/cm, and in the final electrode it rapidly increases to 2.3 kV/cm. As a result, the drifting ions converge into the nozzle. For example, ions which stopped at a radial distance of 10 mm from the axis of the cylindrical stopping gas volume converge at a radial distance of 0.6 mm just before the orifice. Since the velocity of the outgoing He flow is much larger than the ion drift velocity due to the electric field the ions converged into such radii are expected to be transported through the nozzle.

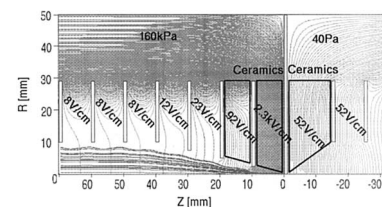


Fig. 2. The electric field and the track of the drift of the incident ions near the nozzle.

### References

- 1) H. Miyoshi et al.: RIKEN Accel. Prog. Rep. **34**, 181 (2001).
- 2) H. Miyoshi et al.: RIKEN Accel. Prog. Rep. **35**, 143 (2002).
- 3) T. M. DeTurck et al.: Nucl. Instrum. Methods Phys. Res. B **172**, 293 (2000).

a) The Los Alamos Accelerator Code Group

## Development of slow muon beam line at the RIKEN-RAL muon facility

Y. Matsuda, P. Bakule, K. Nagamine, Y. Miyake, K. Shimomura, S. Makimura, P. Strasser,  
T. Matsuzaki, K. Ishida, and M. Iwasaki

We have been developing a slow muon beam line at experimental port 3 in the RIKEN-RAL muon facility. The objective of this project is to construct a beam line that provides low-energy positive muon beam (1–10 keV) with a superior resolution of beam energy and time structure. Such beam can extend the scope of the  $\mu$ SR technique to thin films, multi-layered structures, and extremely small samples, which are all important both scientifically and commercially. For example, Giant Magnetic Resistance was first reported in multilayers consisting of ferromagnetic layers and a thin nonmagnetic metallic layer, and its discovery has led to many industrial applications. In these systems, the magnetisations of the layers are coupled through electron spin density of the spacer layer. Various measurements have been carried out to understand this interlayer exchange coupling, but a probe for studying the induced spin polarisation in the nonmagnetic intermediate layer is still lacking. Using slow muons, we would be able to carry out depth-resolved  $\mu$ SR measurement in order to detect magnetic field distribution in the intermediate layer.

These potentials of slow muons are widely recognised in major muon facilities, and several methods of generating slow muons have been proposed.<sup>1,2)</sup> We adopted the resonance ionization method developed at Meson Science Laboratory of High Energy Accelerator Research Organization.<sup>2)</sup> This method is based on the observation that a few percent of muons injected into a hot tungsten film are emitted from its surface as thermalised muonium atoms with kinematic energies of approximately 0.2 eV. Then we irradiated two ionizing lasers; 122 nm Lyman- $\alpha$  wavelength for exciting muonium atoms from 1S state to 2P state and 355 nm wavelength for stripping electrons from 2P state to generate free muons, which were extracted and transported to the sample position.

This scheme is particularly suitable for pulsed muon beam facilities, where a bunch of muons is delivered at a repetition rate of 20–50 Hz and a timing width of 100–150 nsec. Intense short-pulsed lasers can be synchronised to muon beams to generate pulsed slow muon bunches whose timing width is much smaller than that of the initial muon beam, thus providing an excellent energy resolution of the beam and an excellent time resolution on the  $\mu$ SR spectrum.

We reported our first observation of slow muon beam at the RIKEN-RAL muon facility in our previous reports.<sup>3,4)</sup> Since then, we have improved our laser system by introducing a phase-matching scheme for the

generation of ionizing VUV laser and optimised transport optics to minimise loss in our beam line.<sup>4)</sup> At the last beam time in April 2003, we observed slow muon beam with an intensity of 5/sec, which is more than 100 times larger than our previous results. The advantage of the laser resonant ionization method is demonstrated in Fig. 1; the timing width of the beam is less than 10 nsec, whereas that of our initial muon beam is about 150 nsec. The obtained width of 10 nsec is much better than that obtained in another experiment<sup>5)</sup> at the ISIS EU muon beam line using the cyrosolid moderator method,<sup>1)</sup> in which the timing width of the initial beam is conserved in the slow muon beam. Slow muon yield dependence on laser power was measured, and no saturation was observed for both 122 nm and 355 nm lasers, leading us to expect a further increase in the yield by further improvement of laser power. A work on upgrading the 355 nm laser is currently being undertaken.

In coming beam time, our plan is to measure beam size at the sample position and optimize beam transport optics using this information. A position sensitive MCP (Roentdek 40DLD MCP) has been installed and tested at the sample position for such purpose. A design work for the  $\mu$ SR spectrometer is also currently being carried out, and we plan to install it in the spring of 2004.

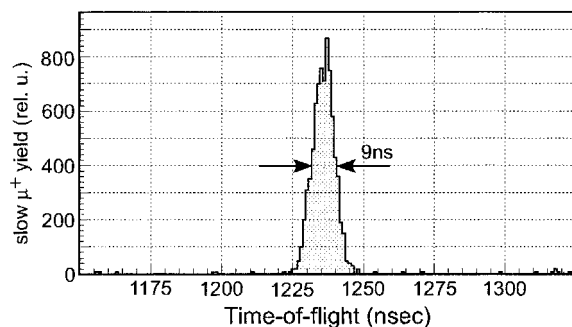


Fig. 1. Typical time-of-flight spectrum of slow muon beam obtained at the RIKEN-RAL muon facility.

### References

- 1) E. Morenzoni et al.: Phys. Rev. Lett. **72**, 2794 (1994).
- 2) K. Nagamine et al.: Phys. Rev. Lett. **74**, 4811 (1995).
- 3) Y. Matsuda et al.: RIKEN Accel. Prog. Rep. **35**, 138 (2002); Y. Matsuda et al.: J. Phys. G **29**, 2039 (2003).
- 4) P. Bakule et al.: Spectrochim. Acta, Part B **58**, 1019 (2003).
- 5) K. Trager et al.: Physica B **289/290**, 662 (2000); K. Trager: Ph.D. Thesis, Universitat Heidelberg (1999).



## Preparation of self-supporting boron films

S. Ozawa and M. Hamagaki

In nuclear physics experiments, self-supporting boron films are required as targets for projectile fragmentation. We developed a new method of preparing self-supporting boron films by sputtering with an electron-beam-excited plasma (EBEP).<sup>1)</sup>

A schematic of the experimental setup is shown in Fig. 1. The principle of preparing boron films is described in Ref. 2. The boron target is heated sufficiently to become a conductor by several minutes of electron beam bombardment. At this point, the target temperature is 1100°C, which is maintained until the end of deposition. The boron target temperature is measured using an optical pyrometer. The substrates are placed on a copper table whose temperature is controlled from 20 to 250°C. The temperature of the table is measured using a thermocouple (not shown in Fig. 1). The sputtering target is a boron tablet ( $\phi$  40 mm  $\times$  5 mm) with a purity of 99%. The tablet is covered with carbon in order to supply bias voltage (see Fig. 2). The material applied with bias voltage is sputtered by  $\text{Ar}^+$  ions which are accelerated by the bias voltage when the material comes into contact with plasma. Hence all of the materials, except the boron tablet, must be covered by an insulator to prevent them from being sputtered by  $\text{Ar}^+$  ions with the bias voltage. As shown in Fig. 2, the carbon support and the copper feedthrough are covered with an insulator to prevent them from being sputtered by  $\text{Ar}^+$  ions with the bias voltage. The insulator cover for the target, which was made of hexagonal boron nitride, has an aperture of 28 mm because the diameter of the electron beam is approximately 30 mm. The feedthrough is covered with ceramics tubes. Three kinds of substrate, namely, tantalum, Pyrex glass, and silicon, are used in the experiment. To stop deposition, the electron beam is stopped and the bias voltage is turned off. Then the films are left to cool for more

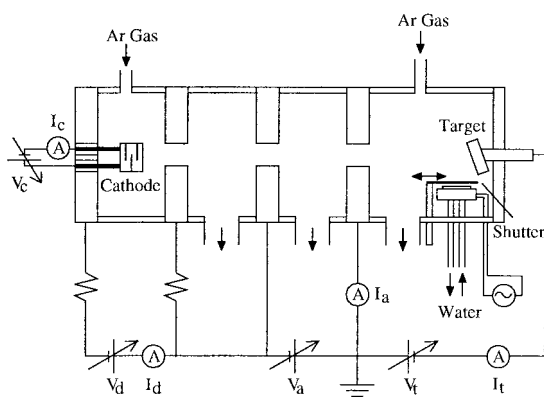


Fig. 1. Schematic of the experimental setup.

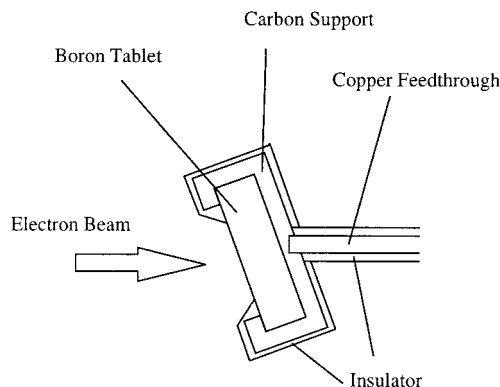


Fig. 2. Schematic of the target. Only the boron surface was sputtered by argon ions with energy equivalent to the applied voltage. Previously, the carbon support was not covered by an insulator and was consequently sputtered by argon ions.

than one hour in vacuum.

In the present experiment, a boron film of  $330 \mu\text{g}/\text{cm}^2$  was obtained on a silicon substrate after one hour of deposition at  $V_t = -280 \text{ V}$  and  $I_t = 0.76 \text{ A}$ . The deposition rate in the present experiment was  $0.4 \text{ nm/s}$ , and the temperature of the substrate was  $20^\circ\text{C}$ . However, films exceeding  $140 \mu\text{g}/\text{cm}^2$  started flaking on Pyrex glass substrates, as was observed in our previous study,<sup>2)</sup> even though the sputtering rate and substrate temperature were the same as in the case of silicon substrates. Boron films on tantalum substrates also start flaking off at approximately this thickness in the present experiment, whereas boron films on silicon substrates can be much thicker. The surface of the glass substrate is smooth, but its thermal conductivity is low. The surface of the tantalum substrate is rough. The roughness and the thermal conductivity of the surface are thought to be more important than the kind of material. Silicon wafers have a smooth surface and high thermal conductivity.

To prepare self-supporting boron films,  $\text{LaCl}_3$  and  $\text{NiCl}_2$  were tested for use in the present experiment.  $\text{LaCl}_3$  is commonly used as a water-soluble compound in the preparation of self-supporting carbon films. However, it was found that  $\text{LaCl}_3$  is not useful for separating boron films from the substrate because La forms a compound with boron.  $\text{NiCl}_2$  was used for preparing self-supporting boron films.

Boron films on the tantalum substrate were prepared for EPMA. The boron film thickness was  $70 \mu\text{g}/\text{cm}^2$ . In the previous experiment,<sup>2)</sup> EPMA showed that the boron film contained carbon, nitrogen, and oxygen. In addition, we must investigate copper which is included

in the feedthrough, the components of the stainless steel (SUS304) used for the target-holding flange, and the components of the Pyrex glass vacuum chamber. We chose five kinds of spectrum crystals in order to detect all elements contained in the boron film. The typical EPMA spectra of the elements which were detected as impurities in our previous experiment<sup>2)</sup> are shown in Fig. 3. The upper spectrum was obtained by diffraction using an LDE-1H crystal that detects carbon, nitrogen and oxygen. The LDE-2 crystal detects boron,

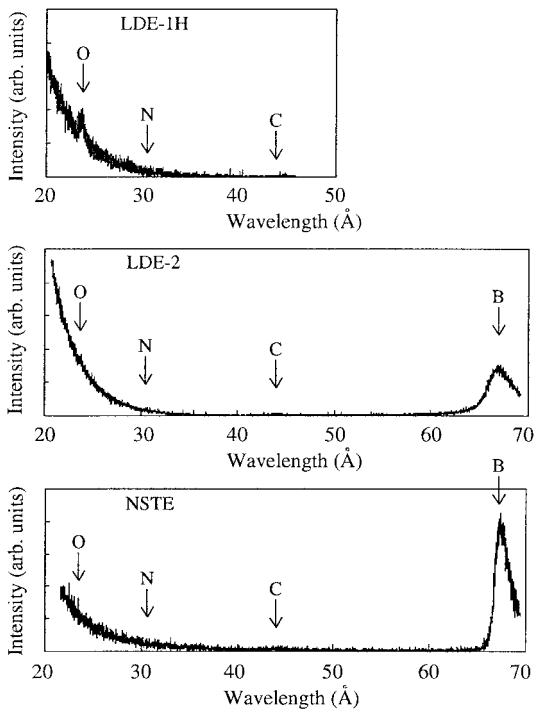


Fig. 3. EPMA spectrum of boron film. Three spectra were obtained by diffraction of LDE-1H, LDE-2, and NSTE. In the spectra, the positions of boron, carbon, oxygen, and nitrogen peaks are indicated by arrows.

carbon, nitrogen and oxygen, as does the NSTE crystal. An oxygen peak can be observed in the LDE-1H spectrum because the LDE-1H crystal has a high sensitivity that enables it to detect oxygen absorbed on the surface of the films. The oxygen peak cannot be observed in other spectra. Carbon and nitrogen are not observed in any of the spectra. By using other two crystals to detect other elements (copper, tantalum, and ingredients of stainless steel and Pyrex glass), only the tantalum peak can be observed. This is because the energy of the electron beam (15 keV) from the EPMA apparatus is sufficiently high for the beam to pass through the boron film and reach the tantalum substrate. These results show that the amount of impurities in the boron films is less than the EPMA detection limit.

A boron target without insulators was used in our previous experiment,<sup>2)</sup> and the amount of carbon in boron films was more than 30%. After the carbon support of the boron tablet was covered with an insulator, the amount of carbon in boron films was reduced to below the EPMA detection limit. In our previous experiment,<sup>2)</sup> we introduced nitrogen gas into the vacuum chamber, and exposed the films to atmosphere immediately after stopping deposition. As a result, nitrogen and oxygen were considered to contain the boron films. In the present experiment, to reduce the amounts of nitrogen and oxygen, films were left to cool for more than one hour after turning off the bias voltage. The purity of almost 100% was achieved as a result of the following improvements to the method of preparing boron films: (1) the sputtering target was covered with boron nitride and (2) the films were left to cool for more than one hour in vacuum after the deposition.

#### References

- 1) M. Hamagaki et al.: *Jpn. J. Appl. Phys.* **33**, 4369 (1994).
- 2) S. Ozawa and M. Hamagaki: *RIKEN Accel. Prog. Rep.* **36**, 186 (2003).

# R&D study of a self-confining radioactive ion target (SCRIT)

M. Wakasugi, T. Emoto, T. Koseki, K. Kurita, T. Ohnishi, T. Suda, H. Takeda, and Y. Yano

We propose a new colliding system of electrons and radioactive (unstable nuclei) ions, in which a high-energy electron beam collides with its self-confining RI ion target (SCRIT) formed in an electron storage ring.<sup>1,2)</sup> Ions in the SCRIT are transversely confined by repetitious transverse focusing kicks given by electron bunches and drift back and forth with very low velocity between two electrostatic mirrors placed a certain distance apart. The concept of the electron-RI colliding system with the SCRIT is schematically shown in Fig. 1. In this paper, the performance of the SCRIT as a target and the achievable luminosity are estimated by numerical simulation, and the status of the R&D study is described.

In the numerical simulation we deal with a 500-MeV electron scattering off intriguing double-magic  $^{132}\text{Sn}$  nuclei as an example of its practical applications. The parameters used in the present calculation are listed in Table 1. We take three kinds of potentials into account in calculating the motion of ions. The first is the time-dependent negative potential produced by an electron bunch that comes in the SCRIT periodically. The second is an additional positive electrostatic potential (mirror potential) for confining ions longitudinally. The third is a positive potential produced by the confined ion cloud itself. We numerically solve the equations of motion of each sample ion in the superposition of these potentials. Atomic processes in

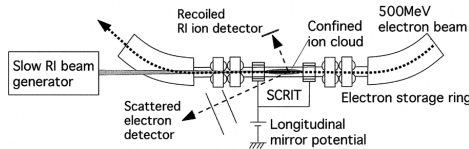


Fig. 1. Electron-RI colliding system with the SCRIT.

Table 1. Parameters in the present simulations.

RI ion	
Elements	$^{132}\text{Sn}$
Initial kinetic energy and spread (keV)	$10 \pm 0.1$
Pulse length at injection (cm)	4.0
Initial r.m.s. emittance ( $\pi$ mm · mrad)	10.0
Transverse r.m.s. beam size (mm)	1.0
$\sigma_{ix} = \sigma_{iy} = \sigma_{ir}$	
Longitudinal length of ion cloud (mm)	about 130
Electron Beam	
Number of electrons in a bunch $N_e$	$10^{10}$
r.m.s. beam size $\sigma_{ex} = \sigma_{ey} = \sigma_{er}$ (mm)	1.0
r.m.s. bunch length $\sigma_{ez}$ (mm)	15.0
Energy (MeV)	500.0
RF frequency (MHz)	500.0
Vacuum at the SCRIT (Pa)	$10^{-10}$
Mirror Potential	
Structure of electrodes	Register divided ring electrodes
Maximum voltage at electrode (kV)	20.0

the SCRIT, for example, charge-state multiplication by electron beam impact, nuclear decay, and residual-gas ion capture are considered in the calculation. Details of the calculation are described in Refs. 1 and 2.

Time-evolution of the number of confined ions ( $N_i$ ) in the SCRIT is shown in Fig. 2 for several cases of the number of initially injected ions ( $N_{inj}$ ). In the short time range ( $\ll 1$  ms) immediately after the injection of ions, the  $N_i$  quickly decreases with time and approaches to approximately  $3 \times 10^8$  for the case of  $N_{inj} > 3 \times 10^8$ , as shown in Fig. 2(a). The line density of ions in the SCRIT at the saturation is about 14% of the time-averaged electron line density of  $1.67 \times 10^8 \text{ cm}^{-1}$ . In longer time range (see Fig. 2(b)), the  $N_i$  further decreases with increasing average charge state. We found that the time evolution of the  $N_i$  depends on the number of injected ions  $N_{inj}$ , and  $10^7$ – $10^8$  ions can be confined in the SCRIT for a few seconds. The time-dependent luminosity in these cases is shown in Fig. 3, which is defined in this calculation as

$$L(t) = f_{rf} \int_0^{3\sigma_{er}} \int_0^{2\pi} \left\{ \left( \int_{-\infty}^{\infty} \rho_e(r, z) dz \right) \right.$$

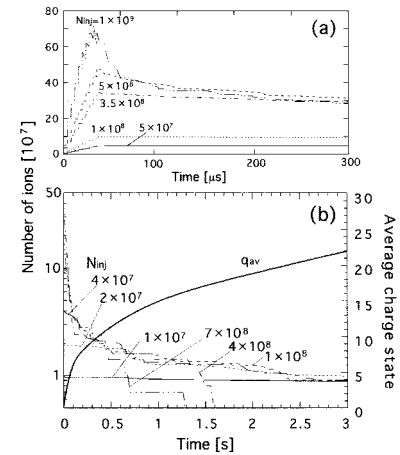


Fig. 2. Time-evolution of the number of confined ions in short time range (a) and longer time range (b).

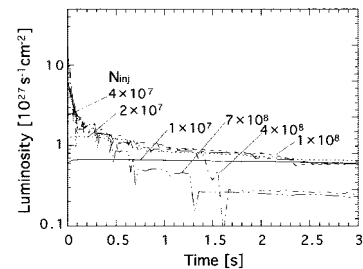


Fig. 3. Time-dependent luminosity.

$$\times \left( \int_{-\infty}^{\infty} \rho_i(r, z, t) dz \right) \} r dr d\theta, \quad (1)$$

where  $\rho_e(r, z)$  is the density distribution of the electron bunch, which is a Gaussian distribution, and  $\rho_i(r, z, t)$  is that of the confined ion cloud obtained in each time step of the calculation. The luminosity can be kept at more than  $10^{27} \text{ s}^{-1} \cdot \text{cm}^{-2}$  for a few seconds. During the measurement of the electron-RI scattering, we repeat the ion-injection and the release with the appropriate period ( $\tau_{cycle}$ ), and the time-averaged luminosity is calculated in the unit cycle as

$$L = \frac{1}{\tau_{cycle}} \int_0^{\tau_{cycle}} L(t) dt. \quad (2)$$

The time-averaged luminosity depends on the  $N_{inj}$  and the  $\tau_{cycle}$ . The  $N_{inj}$  is a function of the production rate ( $N_{prod}$ ), the total injection efficiency ( $\varepsilon_{total}$ ), and the  $\tau_{cycle}$  as

$$N_{inj} = N_{prod} \varepsilon_{total} \tau_{life} \left\{ 1 - \exp \left( -\frac{\tau_{cycle}}{\tau_{life}} \right) \right\}, \quad (3)$$

where  $\tau_{life}$  is the nuclear lifetime ( $\tau_{life} = 40 \text{ s}$  for  $^{132}\text{Sn}$ ). Assuming  $\varepsilon_{total} = 0.1\%$ , the time-averaged luminosities are shown in Fig. 4 as a function of the  $N_{prod}$  for several cases of the  $\tau_{cycle}$ . When a very large amount of ions are injected, the ions are heated up immediately after injection by a space charge effect and escape out more rapidly as shown in Fig. 2(b) and Fig. 3. That is the reason why the luminosity curve for each case has a peak in Fig. 4. The dashed line is a trace of the maximum values for these cases of the  $\tau_{cycle}$ . This line indicates achievable luminosity under the present conditions. If we have the production rate of more than  $10^{10} \text{ s}^{-1}$  and choose an optimum period of the injection cycle, the SCRIT gives us the luminosity of more than  $10^{27} \text{ s}^{-1} \cdot \text{cm}^{-2}$ , which is a sufficient value for the measurement of the nuclear charge distribution of  $^{132}\text{Sn}$ .<sup>3)</sup>

The SCRIT device has been constructed to demonstrate our idea. Photographs of the SCRIT system are shown in Fig. 5. It consists of a pulse ion source, an ion transport line, an ion injector electrode system, a beam position monitor (BPM) for the electron beam, and the SCRIT electrode system. The pulse

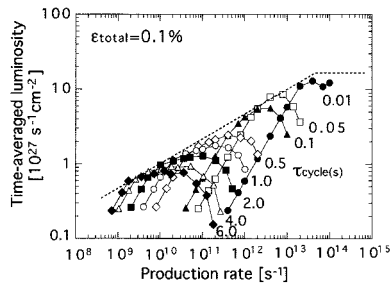


Fig. 4. Time-averaged luminosity for several  $\tau_{cycle}$  as a function of production rate.

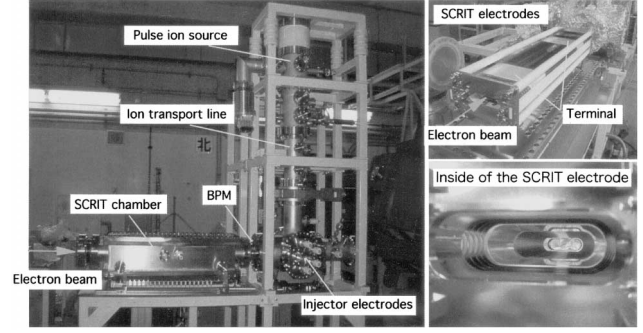


Fig. 5. Photographs of the SCRIT system and the SCRIT electrodes.

ion beam ( $\text{Sn}^{1+}$ ) is produced by a laser ablation process using a pulse YAG laser and accelerated up to 10 keV. The ion transport line includes four steering electrodes, two Einzel lenses, and a Faraday cup. The injector electrode is a 90-degree electrostatic deflector and merges the ion beam to the electron beam orbit, which is measured by the BPM. The SCRIT electrode system is shown in the right-hand side of the figure; it is a register-divided ring-electrode system having 40 thin electrodes and 2 terminal electrodes. The upper and lower parts of these electrodes have a mesh structure with 93% opening rate so that recoiled ions and scattered electrons can pass through the electrodes without any obstacles. Every electrode is connected to a high-voltage feed-through and we can create any form of longitudinal potential in the SCRIT region by applying an appropriate voltage to each electrode. At both terminal electrodes, the highest voltage is applied and a potential well for ion trapping is formed between the terminals. When a pulse ion beam is injected, the potential wall at the injector side is reduced by a fast switching system.

The vacuum condition of the SCRIT devices is important because the electron storage ring in which the SCRIT will be installed works under the vacuum of lower than  $10^{-7} \text{ Pa}$  and the lifetime of the stored electron beam strongly depends on the vacuum condition. After one-day baking at the temperature of  $250^\circ\text{C}$ , the vacuum of the SCRIT chamber was determined to be  $3 \times 10^{-8} \text{ Pa}$  by evacuating with two ion pumps having an evacuation velocity of 500 l/s per each.

The SCRIT devices will be installed in the electron storage ring (KSR) at Kyoto University and the test experiment for ion trapping will begin in 2004.

## References

- 1) M. Wakasugi et al.: to be published in Proc. Int. Workshop on Beam Cooling and Related Topics, Yamanashi, 2004-5.
- 2) M. Wakasugi et al.: Proc. 14th Symp. on Accelerator Science and Technology, Tsukuba, 2003-11 (KEK, Tsukuba, Japan, 2003), p. 17.
- 3) T. Suda et al.: RIKEN Accel. Prog. Rep. **37**, 81 (2004).

## Loop-gap resonator for polarized proton target

T. Wakui,<sup>\*1</sup> M. Hatano,<sup>\*2</sup> H. Sakai,<sup>\*1,\*2</sup> A. Tamii,<sup>\*3</sup> and T. Uesaka<sup>\*1</sup>

A polarized solid proton target using a crystal of naphthalene doped with pentacene has been developed.<sup>1)</sup> The target is unique among polarized solid targets in that protons in the crystal can be polarized in a magnetic field of 0.3 T or lower and at a temperature of 77 K or above. This feature allows the target to be used in RI beam experiments, which are usually carried out under the inverse kinematic condition. The first experiment with the <sup>6</sup>He beam of 71 MeV/nucleon was carried out in July 2003.<sup>2)</sup> The target system for the experiment is described in Ref. 3.

For polarizing protons, a large population difference which appears on the lowest triplet state in pentacene by optical excitation is transferred to protons by a technique based on cross-relaxation between electron and proton spins.<sup>4)</sup> This method, which was originally called the integrated solid effect,<sup>4)</sup> utilizes electron spin resonance (ESR) with adiabatic fast passage (AFP). That is, an external magnetic field is adiabatically swept through an ESR line during microwave irradiation. In the AFP, the effective Larmor frequency,  $\omega_{\text{eff}}$ , in a coordinate system rotating with the frequency of the microwave,  $\omega$ , is given as

$$\omega_{\text{eff}} = \sqrt{\omega_{\text{R}}^2 + (\omega_{\text{s}} - \omega)^2}, \quad (1)$$

where  $\omega_{\text{R}}$  is the Rabi frequency,  $\omega_{\text{R}} = \gamma_{\text{s}} H_1$ , and  $\omega_{\text{s}}$  is the Larmor frequency of electrons. At the point where  $\omega_{\text{s}} = \omega$ , the effective frequency is dependent only on the amplitude of the oscillating field. If we adjust the amplitude of the oscillating field so that the effective frequency of electrons is equal to that of protons, we fulfill the Hartmann-Hahn condition for cross-relaxation. Here, the exchange of spin polarization takes place owing to the dipolar interaction between electron and proton spins. As a result, polarization is transferred from the electron to the proton.

For polarization transfer, a cylindrical microwave cavity with a resonance frequency of 9.1 GHz has been used in the prototype proton polarizing system.<sup>1)</sup> The cylindrical cavity is enclosed by thick copper walls which prevent low-energy recoiled protons from reaching the detectors. Thus, we introduced a copper-film loop-gap resonator (LGR)<sup>5)</sup> instead of the cylindrical cavity so that recoiled protons can reach the detectors. The LGR is made of a 25- $\mu\text{m}$ -thick Teflon sheet which is coated on both sides with copper metal with the thickness of 4.4  $\mu\text{m}$  each. The copper is etched to create capacitive gaps due to overlapping regions of copper, as shown in Fig. 1(a). The etched sheet

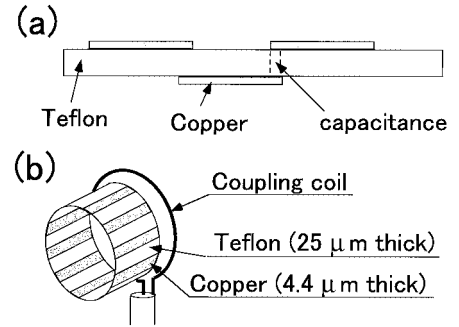


Fig. 1. (a) Schematic view of the etched Teflon sheet. The overlap of copper regions on the two surfaces of Teflon sheet creates capacitive gaps. (b) Schematic view of the LGR. The LGR is inductively coupled to a microwave circuit using a coupling coil.

is formed into a cylindrical loop, which acts as an inductive element. The LGR is inductively coupled to a microwave circuit using a coupling coil, as shown in Fig. 1(b). Inductance,  $L$ , and capacitance,  $C$ , can be calculated using the semi-empirical equations<sup>5,6)</sup>

$$L = \left\{ \left( 0.2 \frac{2r}{z} - 0.45 \right) \frac{2r}{z} + 1 \right\} \mu_0 \pi \frac{r^2}{z} \quad (2)$$

$$C = \kappa_e \epsilon_0 \frac{(w+t)(z+t)}{nt}, \quad (3)$$

where  $r$  is the radius,  $z$  is the length of the LGR,  $\mu_0$  is the magnetic permeability,  $\kappa_e$  is the dielectric constant of the Teflon sheet,  $\epsilon_0$  is the permittivity,  $w$  is the gap width,  $t$  is the gap thickness, and  $n$  is the number of gaps.

To produce an oscillating magnetic field with the sufficient amplitude to fulfill the Hartmann-Hahn condition, the LGR should be designed so that its diameter and length are small compared with a quarter-wavelength,  $\lambda/4$ , of the microwave. If the dimensions are close to  $\lambda/4$ , the LGR will act as an antenna and emit radiation, which greatly decreases the quality factor of the LGR. Indeed, we could not find the resonance for the LGR designed to have the resonant frequency of 9 GHz with the diameter of 8 mm. In addition, the diameter of the LGR had to be enlarged to 16 mm for the experiment with <sup>6</sup>He beam. Thus, we lowered the microwave frequency to 3 GHz, making allowance for further enlargement of the diameter in a future experiment.

Figure 2 shows a plan for the LGR of the designed frequency of 2.3 GHz. The designed frequency was chosen by taking into account the large deviation reported for frequencies lower than 3 GHz, which is up to 20%.<sup>5)</sup> The diameter and the length were 16 mm and 20 mm,

<sup>\*1</sup> Center for Nuclear Study, University of Tokyo

<sup>\*2</sup> Department of Physics, University of Tokyo

<sup>\*3</sup> Research Center for Nuclear Physics, Osaka University

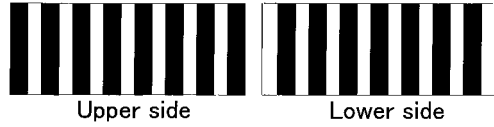


Fig. 2. Plan for upper and lower sides of the LGR designed using Eqs. (2) and (3). The designed frequency is 2.3 GHz. The solid black regions represent copper remaining on Teflon sheet after etching.

respectively. The number of gaps was 15. When the LGR was mounted in the target system, unwanted resonances from other conductive components around the LGR appeared. To prevent these unwanted resonances, the LGR was covered with a cylindrical shield made of aluminum with the thickness of  $12\ \mu\text{m}$ . Figure 3 shows the input reflection coefficient measured as a function of the frequency at the temperature of 100 K. The measured resonant frequency was 2.78 GHz at room temperature. When the LGR was cooled to

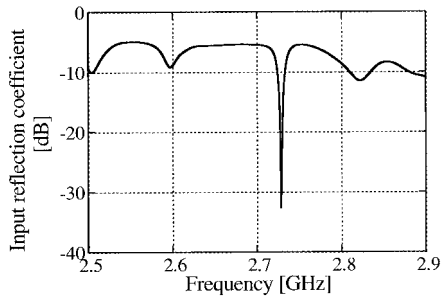


Fig. 3. Input reflection coefficient measured at the temperature of 100 K using a vector network analyzer. The resonant frequency is 2.73 GHz.

100 K, the resonant frequency changed to 2.73 GHz.

To prove the effectiveness of the LGR in polarization transfer, we measured the polarization rate at the beginning of buildup as a function of the incident microwave power. Figure 4 shows the result of the measurement. The polarization rate increases rapidly and reaches a maximum at 1.0 Watt. This shows that the LGR produces an oscillating field with the sufficient amplitude to transfer the polarization from the electron to the proton.

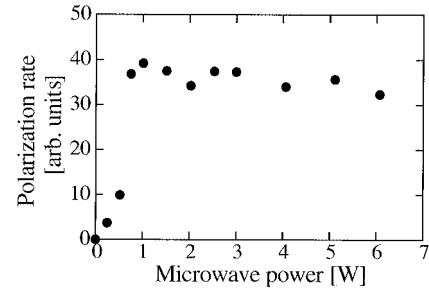


Fig. 4. Dependence of the polarization rate on the incident microwave power. The most efficient transfer of polarization occurs at the power of 1.0 Watt.

#### References

- 1) T. Wakui et al.: RIKEN Accel. Prog. Rep. **34**, 194 (2001).
- 2) M. Hatano et al.: RIKEN Accel. Prog. Rep. **37**, 44 (2004).
- 3) M. Hatano et al.: RIKEN Accel. Prog. Rep. **36**, 48 (2003).
- 4) A. Henstra et al.: Phys. Lett. A **134**, 134 (1988).
- 5) B. T. Ghim et al.: J. Magn. Reson. A **120**, 72 (1996).
- 6) G. A. Rinard et al.: J. Magn. Reson. A **105**, 137 (1993).

## Feasibility study of monolithic SSD for measurement of low energy nuclear reaction with GEANT4 simulation

M. Kurata-Nishimura, S. Nishimura, S. Kubono,\* and I. Tanihata

The inhomogeneous big bang model<sup>1,2)</sup> enabled the successful prediction of the synthesis of heavy elements compared with the standard primordial nucleosynthesis model which makes reasonably accurate predictions of light-element abundances. In the inhomogeneous big bang model,  ${}^4\text{He}(t, \gamma){}^7\text{Li}(n, \gamma){}^8\text{Li}(\alpha, n){}^{11}\text{B}(n, \gamma){}^{12}\text{B}(\beta, \nu){}^{12}\text{C}$  is considered to be a dominant flow path for explaining the synthesis of  ${}^{12}\text{C}$  and heavy elements in the very early universe. Recently, the above sequence of reactions has also been identified to play an important role in r-process nucleosynthesis occurring in supernova explosion.<sup>3)</sup> In both environments, it is claimed that the reaction cross section must be determined in the direct reaction with center of mass energy less than 1 MeV. In that sequence, the  ${}^8\text{Li}(\alpha, n){}^{11}\text{B}$  reaction is the source of large ambiguity caused by the short decay time of  ${}^8\text{Li}$ . Previously, several experiments were conducted to determine this reaction cross section,<sup>4-6)</sup> however, the results of those experiments were not in qualitative agreement with each other. Moreover, the measurements of the low-energy cross section below 1 MeV/n, which is the most important energy region, have not been conducted yet due to the difficulty in handling low-energy beams.

In an experiment performed at TRIUMF in 2001,<sup>7)</sup> it is concluded that the  ${}^8\text{Li}$  beam trigger is necessary for rejecting a huge amount of background in a neutron spectrum. In order to overcome this problem, we have been developing detectors and also low-energy  ${}^8\text{Li}$  beam. In May, 2003, we performed an experiment to develop low-energy  ${}^8\text{Li}$  beam using an in-flight low-energy radioisotope beam separator<sup>8,9)</sup> (CRIB) in RIKEN-CNS. The results are reported elsewhere.<sup>10)</sup>

In the present report, we propose the detection of not only  ${}^8\text{Li}$  but also  ${}^{11}\text{B}$  produced by the reaction through particle identification. Because  ${}^8\text{Li}$  from elastic scattering would contaminate a true event, even if a neutron is detected by a liquid scintillator with a pulse shape discriminator which is able to identify a neutron or  $\gamma$ -ray, a recommended means of identifying low-energy ions is the  $dE/dx$ - $E$  method. However, a  $dE/dx$  detector must be as thin as possible so as not to stop ions in the first detector. Conventionally, a gas counter is used for such a thin detector. Recently, a monolithic SSD detector with an outer geometry is  $15 \times 10 \text{ mm}^2$  has been developed.<sup>11)</sup> This detector consists of  $1 \mu\text{m}$  pad readout SSD and  $508 \mu\text{m}$  SSD. Signals from the first and second layers could be used to measure  $dE/dx$  and a total energy deposit, respectively. Such a thin SSD detector

has never been produced. In this article, a feasibility study of the monolithic SSD detector for the measurement of  ${}^8\text{Li}(\alpha, n){}^{11}\text{B}$  reaction using GEANT4 simulation code<sup>12)</sup> is reported.

In the above simulation code, a gas target is filled with helium gas at a pressure of 100 Torr and a length of 3 cm. The 8 monolithic SSDs are placed at the end cap of the gas target. A  ${}^8\text{Li}$  beam with an energy of 0.2 MeV/u reacts with helium nuclei along the beam axis and  ${}^{11}\text{B}$  is emitted.

The result of this simulation is shown in Fig. 1. In the upper part of the figure, the  ${}^{11}\text{B}$  detected by the monolithic SSD is shown. In the GEANT4 simulation code,  ${}^{11}\text{B}$  is generated at the same amount in the ground state and in the first, second and third excited states.  ${}^{11}\text{B}$  in the ground and the first excited states are clearly separated, while those in the second and third excited states are impossible to distinguish. At the same time, elastic scattering is also simulated in the code as is seen in the lower part of the figure.  ${}^8\text{Li}$  and  $\alpha$  nuclei are also clearly identified in this plot.

From this simulation result, we conclude that monolithic SSD is capable of inclusive measurement in a low-energy reaction. To measure branching ratio to higher excited states, neutron detectors are necessary. We have started testing the monolithic SSD using an  $\alpha$  source.

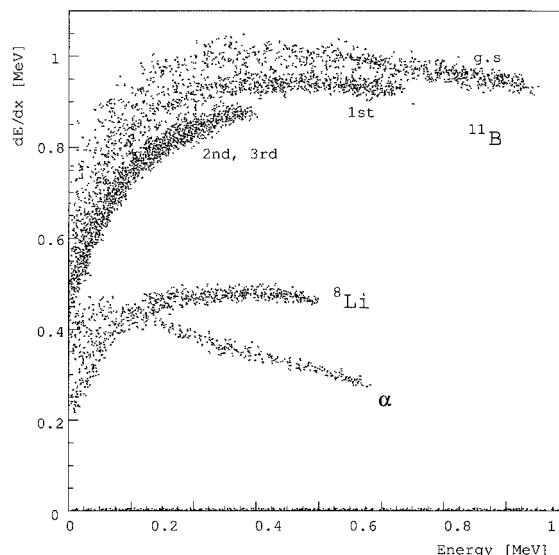


Fig. 1.  $dE/dx$  and  $E$  detected by monolithic SSD simulated for  ${}^8\text{Li}(\alpha, n){}^{11}\text{B}$  reaction.

### References

- 1) M. J. Balbes et al.: Phys. Rev. Lett. **71**, 3931 (1993).

\* Center of Nuclear Study, University of Tokyo

- 2) N. Hata et al.: Phys. Rev. Lett. **75**, 3977 (1995).
- 3) M. Terasawa et al.: Astrophys. J. **562**, 470 (2001).
- 4) X. Gu et al.: Phys. Lett. B **343**, 31 (1995).
- 5) R. N. Boyd et al.: Phys. Rev. Lett. **68**, 1283 (1992).
- 6) Y. Mizoi et al.: Phys. Rev. C **6206**, 5801 (2000).
- 7) M. K-Nishimura et al.: RIKEN Accel. Prog. Rep. **35**, 80 (2002).
- 8) S. Kubono et al.: Eur. Phys. J. A **13**, 217 (2002).
- 9) T. Teranishi et al.: CNS-REP-39, October (2001) p. 1.
- 10) M. Kurata-Nishimura et al.: RIKEN Accel. Prog. Rep. **36**, 168 (2003).
- 11) A. Musumarra et al.: Nucl. Instrum. Methods Phys. Res. A **409**, 414 (1998).
- 12) Geant4 collaborations: <http://geant4.web.cern.ch/geant4/>



## A fast data acquisition front-end using an FPGA device

M. Wada

A fast data acquisition (DAQ) front-end was developed for laser microwave spectroscopy experiments for laser-cooled ions in an ion trap. In this experiment, laser-induced fluorescence (LIF) photons are detected by a position-sensitive photon-counting camera, Hamamatsu PIAS-TI, used for observing an image of each trapped ion.<sup>1)</sup> Many commercial DAQ systems or interface cards can be used for the simple observation of such ion crystal images. However, for spectroscopy experiments, many additional data, such as microwave frequency, time after laser pulse, and so on, should be acquired simultaneously with the photon data and recorded event by event for correlation analyses. There is no such commercial DAQ, and moreover, traditional CAMAC systems are not sufficient in terms of performance, in particular, in terms of the dead time. The counting rate of the LIF measurement is often high, typically up to 40 kcps, since a laser-cooled ion frequently repeats the excitation-deexcitation cycles with a maximum rate of  $10^8 \text{ s}^{-1}$ . If the dead time for each event is  $20 \mu\text{s}$ , approximately 80% of data is be lost. Thus, we set  $\sim 2 \mu\text{s}$  as an allowable dead time per event, which prevents the use of any software-based acquisition front-end.

Buffering acquired-event data for translating random data to blocked data, the so-called *de-randomization*, is an important concern in the DAQ design. Usually, the buffer is located in the front-end, which allows the use of a standard interface to the back-end computer, such as Ethernet, Firewire, USB2 or SCSI. In this case, only a high throughput is required of the interface for the *de-randomized* data transfer. In the present DAQ design, however, we use a FIFO buffer of a commercial PCI interface board, ADLink PCI7300A,<sup>a)</sup> as the *de-randomizing* buffer, which simplifies the architecture of the front-end. Since PCI7300A accepts a 32-bit data input every 50 ns as long as the 16 kwords FIFO buffer is not yet full, the dead time due to the data transfer to the buffer is negligible.

Figure 1 shows the functional diagram of the DAQ front-end. It has eight 12-bit ADCs for analog inputs (Analog Devices, ADS-7818), four 32-bit binary counters and 8-bit auxiliary digital inputs for tag data, and a 32-bit output port for transferring the event data to PCI7300A in the back-end computer. A data acquisition is initiated by the 'Trig-in' signal, then the sequencer latches counters and digital inputs and asserts 'Conv' signal to begin AD conversion. The latched digital data are immediately sent to PCI7300A with 'Strobe' signals while the AD conversions are processed

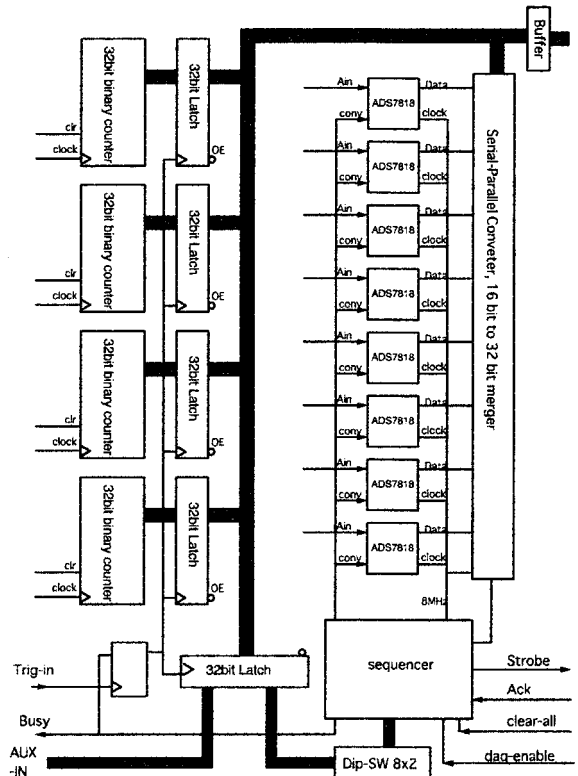


Fig. 1. Functional block diagram of the DAQ front-end.

concurrently. When AD conversions are completed, these data are also transferred. These functions can be simply realized using an FPGA (Field Programmable Gate Array) device shown in Fig. 2. All the logic circuits can be constructed in the FPGA, so that only AD converters and electrical buffers are the devices aside

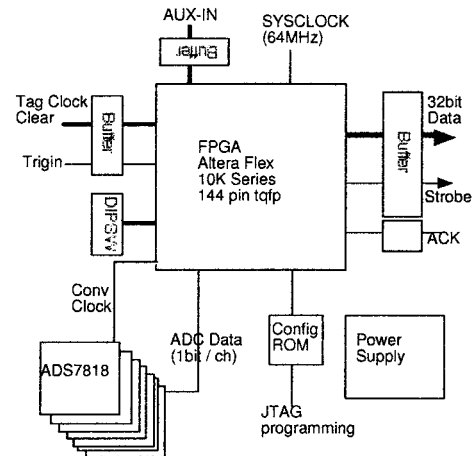


Fig. 2. Physical block diagram of the DAQ front-end.

<sup>a)</sup> <http://www.adlinktech.com/>

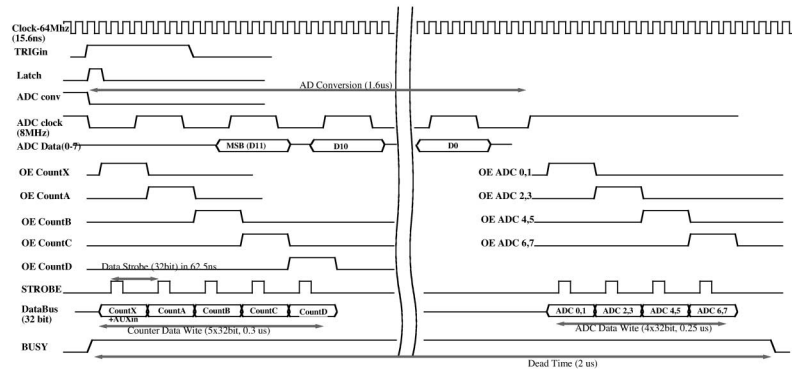


Fig. 3. Timing chart of the DAQ front-end.

from the FPGA. The timing chart of the front-end device is also shown in Fig. 3.

The functions of the FPGA can be configured using HDL (Hardware Description Language), Verilog-HDL, and the source code is, then, compiled by software tools which are usually provided by the FPGA device vendor free of charge. We used an ALTERA Flex series FPGA, EPF10K30ATC144-3; MAX+PLUS II Advanced Synthesis and MAX+PLUS II Baseline are the relevant tools for the FPGA device.<sup>b)</sup> The compiled code can be written in a configuration ROM using the same tools through a JTAG port even when the system is in operation. One can easily modify the configuration when one wants to change the structure of the event data, for instance. Its flexibility is similar to that of a software-based acquisition device, but it is indeed a hardware device.

An example data structure of an event which is used in a laser-microwave spectroscopy experiment is shown in Fig. 4. In this case, only three ADCs are used to record the position and amplitude of the detected photon. In addition, five counters and an 8-bit auxiliary input data are recorded. The event size is six 32-bit words, so that the required throughput when the average event rate is 40 kcps is 240 kwords/s (0.96 Mbytes/s). Although PCI7300A is capable of transferring the data in the bus-master DMA (direct memory access) mode, the vendor provide drivers only

sync code (8)	AUXin (8)	Event Counter (16)	
0001	1 MHz real time clock (28)		
0010	Time since Laser Chop (28)		
0011	Laser Chop Counter (12)	Microwave Step Counter (16)	
0100	Y position (12)	X position (12)	
0101	Amplitude (12)		

Fig. 4. Typical event data structure.

for Windows and a few Linux versions and any source codes are not opened. We wrote a simple driver for PCI7300A under a real-time extended Linux, Linux-RTAI,<sup>c)</sup> which does not yet support the bus-master DMA mode. The total throughput including writing-overhead to a storage device is as high as 750 kwords/s (3 Mbytes/s), which is sufficient for the present purpose.

The back-end computer so far used is a simple data server. It acquires the data from the front-end device and stores the data to a hard disk drive, while some online analyses are performed to produce spectra for monitoring purposes. Human interfaces for controlling the acquisition procedure and monitoring the spectra are carried out by LabVIEW programs on the other PCs connected to the back-end computer via ethernet.

A fast DAQ front-end for high counting rate experiments was developed with minimum effort, budget, and time using an FPGA device and a commercial PCI interface card. The dead time per event is as small as  $2 \mu\text{s}$  and the total throughput of the entire system is 750 kwords/s. The dead time is mainly determined by the relatively slow conversion time of the AD converter chip, and one can use faster ADCs if necessary. If one needs more AD converters, only one input per channel should be added to the FPGA configuration and one needs a small increase in the dead time, 62.5 ns per extra two channels. Another extension for using multiple front-end devices is also possible. In this case, tag words such as an event counter and an accelerator's rf frequency counter, should be used for identification of the event at the event builder. The advantages of developing our own DAQ system are the flexibility and extendability. In particular, the use of an FPGA device allows flexible configuration as if it were a software-based system, but it runs at hardware speed.

#### References

- 1) T. Nakamura et al.: Opt. Commun. **205**, 329 (2002).

<sup>b)</sup> <http://www.altera.com/support/licensing/>

<sup>c)</sup> <http://www.rtai.org>

## Present status of data acquisition system ‘BabarDAQ’ for nuclear physics experiments

H. Baba,<sup>\*1</sup> S. Takeuchi, K. Yamada,<sup>\*1</sup> Y. Sakamoto,<sup>\*1</sup> K. Ieki,<sup>\*1</sup> and S. Shimoura<sup>\*2</sup>

We have introduced a data acquisition system (DAQ) BabarDAQ.<sup>1)</sup> This system has been widely used for nuclear physics experiments with the RIKEN projectile-fragment separator (RIPS) and the CNS RI-beam separator (CRIB) in the RIKEN Accelerator Research Facility.

Recently, we developed detector arrays: the NaI(Tl) detector array for in-beam  $\gamma$ -ray spectroscopy,<sup>2)</sup> the NaI(Tl) calorimeter for charged particles,<sup>3)</sup> and the segmented Ge detector array,<sup>4)</sup> each of which has signals of more than a few hundred channels. CAEN VME-type ADC modules are used in order to handle plenty of signals, because the conventionally used CAMAC-type LeCroy FERA system is out of production. Therefore we have modified BabarDAQ to use the hybrid system of CAMAC and VME.<sup>5)</sup>

The characteristics of BabarDAQ are cost efficiency, flexibility and good performance. The features of this system are as follows.

- Uses standard CAMAC and VME modules only.
- Uses personal computers (PCs) with Linux OS.
- Real-Time Linux OS for driving CAMAC and VME.
- Network distributed data processing.
- Includes useful analysis software.

This system is divided into three main components: the CAMAC & VME driver (*Driver*), the DAQ controller (*Controller*), and some on-line analyzers (*Analyzer*). These components can be distributed among some PCs that communicate with each other through an ethernet. The typical configuration is shown in Fig. 1. The *Driver-PC* is working under Real-Time Linux (RTLinux)<sup>6)</sup> which is a real-time extension of

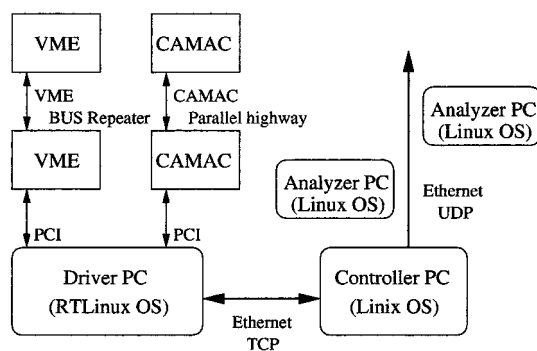


Fig. 1. Configuration of BabarDAQ system.

Linux Kernel. RTLinux has been released under the GNU General Public License and the RTLinux Open Patent License, and can be used for free. Using a real-time OS, the system can be kept running for a long time with stability and high efficiency.

The *Driver-PC* reads out data from CAMAC and VME modules through the bus controllers and accumulates data into a buffer. This system can handle several bus controllers: TOYO CC/7700 + CC/PCI, Kinetic systems K3922 + K2915 PCI, SBS Bit3 618/620 PCI to VME bus adapter, and Wiener VMEMM + PCIADA. When one buffer becomes full, one block of data is transferred to the *Controller-PC* with the TCP/IP protocol. Using the double-buffer method, data read out from the CAMAC and VME modules can be performed during the data transfer process to the *Controller-PC*. Unless both the buffers become full during the data transfer, dead time is not induced.

The *Controller-PC* receives the data from the *Driver-PC* and puts the data into storage devices. Then, the *Controller-PC* distributes data to some *Analyzer-PCs* with the UDP/IP protocol. This process does not affect the data acquisition performance.

The *Analyzer-PC* writes the transferred data from the *Controller-PC* into a shared memory, and ANAPAW or some other on-line software use on-line block data through the shared memory.

ANAPAW is a useful analysis software which runs under Linux OS and has been developed together with BabarDAQ. It has been used as the on-line and off-line analysis software in RIPS and CRIB experiments in recent years, and provided us with an easy and fast analysis in both on- and off-line analyses.

ANAPAW consists of three components as shown in Fig. 2. The first is the PAW<sup>7)</sup> component. Users can use not only ANAPAW commands but also PAW commands for analysis. The second is the ANAPAW library which has a main analysis routine pro-

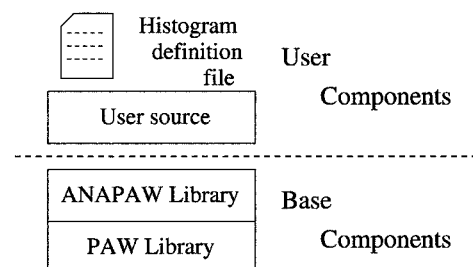


Fig. 2. Overview of ANAPAW components.

<sup>\*1</sup> Department of Physics, Rikkyo University

<sup>\*2</sup> Center for Nuclear Study, University of Tokyo

Table 1. Access times of CAMAC and VME from developed device driver.

CAMAC	TOYO CC/7700 + CC/PCI	Kinetic K3922 + K2915
no data transfer	4.1 $\mu$ s	7.8 $\mu$ s
single read	6.3 $\mu$ s	10.2 $\mu$ s
single write	6.0 $\mu$ s	9.9 $\mu$ s
quasi block read	4.8 $\mu$ s/ch + 1.6 $\mu$ s	
block read		2.6 $\mu$ s/ch + 8.0 $\mu$ s
VME	Wiener VMEMM + PCIADA	SBS Bit3 620 PCI-VME
32 bit single read	1.9 $\mu$ s	2.4 $\mu$ s
32 bit single write	1.2 $\mu$ s	2.0 $\mu$ s
32 bit DMA read		0.4 $\mu$ s/ch + 1.9 $\mu$ s

viding original analysis commands and I/O routines. Basically the I/O routines of ANAPAW are created to adapt BabarDAQ with a shared memory and a semaphore which are able to send and receive data between BabarDAQ and ANAPAW. Once the I/O routines are modified to fit another DAQ system, on-line analysis is available in the system. The last is the user-source component which is modified by experimental users to match with experimental conditions. This component consists of a main routine and analysis routines. The main routine is executed by an event-loop routine in ANAPAW to check an event size and to put detector data into analysis routines. The analysis routines convert raw data to numerical data and calculate physical values. In addition, an NTUPLE format is available by modifying an NTUPLE-I/O routine in the user-source component.

For on-line use, ANAPAW reads out data from a shared memory in the *Analyzer-PC*, while it reads out data from files for off-line analysis. During on/off-line analysis, users prepare and modify histogram definition files. In those files, one-dimensional (1D) and two-dimensional (2D) histograms, logical gates and 1D/2D gates are defined. Periodical displays of 1D histograms and scatter plots are available and operation for histograms is also available using ANAPAW commands. Since the environments of off-line analysis are the same as those of on-line analysis, users can utilize experimental parameters and histogram definition files for off-line analysis.

We report the performance of the *Driver* below. The *Driver* detects a CAMAC LAM signal or a VME IRQ signal every 40  $\mu$ s using the RTLinux periodic task to

determine the end of module conversion. While the periodic task in standard Linux takes up to 600  $\mu$ s to start a handler, there could easily be a more than 20 ms latency. On the other hand, the RTLinux periodic task can run within 35  $\mu$ s of its scheduled time. Therefore, the response time of the CAMAC LAM signal or VME IRQ signal by the RTLinux periodic task is 20  $\mu$ s on average. In addition, we have developed device drivers that run under RTLinux to access every controller. Access times of CAMAC and VME through each controller are shown in Table 1.

The main source of dead time in BabarDAQ is the access time of CAMAC and VME modules. It increases in proportion to the number of readout channels, because only one CPU reads every channel one-by-one. To reduce the dead time, we are developing an eventbuild-type DAQ system in which some CPUs read out data in parallel and construct complete event data later. The new eventbuild-type DAQ system will be implemented during the year 2004.

#### References

- 1) H. Baba et al.: RIKEN Accel. Prog. Rep. **34**, 221 (2001).
- 2) S. Takeuchi et al.: RIKEN Accel. Prog. Rep. **36**, 148 (2003).
- 3) M. Tamaki et al.: CNS-REP-59, July (2003), p. 76.
- 4) S. Shimoura et al.: CNS-REP-45, July (2002), p. 5.
- 5) H. Baba and S. Shimoura: CNS-REP-45, July (2002), p. 53.
- 6) M. Barabanov and V. Yodaiken: Linux Journal **34**, 19 (1997).
- 7) CERN Program Library : unpublished.

# Network and computing environment for RIKEN Accelerator Research Facility

T. Ichihara, Y. Watanabe, K. Yoshida, and A. Yoshida

The advanced computer network<sup>1)</sup> started operation in 2002 at the RIKEN Accelerator Research Facility (RARF). After that, RIKEN was connected to the Super Sinet (Sinet Information Network)<sup>2)</sup> at the bandwidth of 1 Gbps in July 2003. The previous bandwidth of the Wide Area Network connection was 100 Mbps. As a result, a huge amount of data can be transferred *via* the Internet using the newly connected Super Sinet.

Figure 1 shows the current configuration of the RARF advanced computer network. Between the RARF internal network and external Internet, a firewall (PIX 525) has been installed to maintain security. The bandwidth of the RARF firewall and RIKEN central LAN switch was increased from 100 Mbps to 1 Gbps in order to correspond to the increased bandwidth of the Super Sinet.

Figure 2 shows the current configuration of the UNIX cluster servers of RARF for general users. Nine nodes of UNIX servers, four of which are True 64 UNIX (alpha), three of which are RedHat Linux and two of which are Solaris, are connected *via* the Gigabit or 100Mbps Ethernet. RARFAXP is the central server for e-mail, text processing, user home pages and general computing. RARFAX1, RARFAX2 and RARFLX1-3 are used mainly for intensive data analysis, large-scale calculations and user terminals. RARFSUN is a gateway computer for accessing the internal private network of RARF using SSH. RARFNFS0 is a dedicated Network File Service (NFS) server which is equipped with 2.8 TB + 1.7 TB Raid5 work disks. The Veritas File System (VxFS), which is a logging file system, was installed for the raid file systems in order to achieve high performance in file operation.

Secure Shell (SSH) protocol has been installed for all the nodes. The use of SSH is requested for remote login and file transfer to ensure security against network packet sniffing. The Secure Sockets Layer (SSL)-encrypted Internet Message Access Protocol (IMAPS) service is available at the RARFAXP. In order to pre-

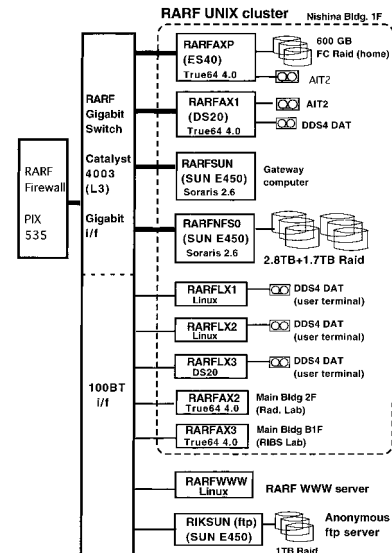


Fig. 2. Configuration of the RARF UNIX cluster.

vent virus infections *via* e-mail, a virus-detecting and -eliminating system is installed in the node RARFAXP.

Most of the RARF users have e-mail addresses of *username@rarf.riken.jp* or *username@riken.jp*.

The first one represents an e-mail address of the RARF mail server (RARFAXP) and the second one represents an e-mail address of the RIKEN mail server (postman). Note that the operation of the e-mail forwarding service to the RARF VMS system, which forwards e-mail sent to the old VMS systems (RIKVAX and RIKAXP), was terminated in November 2003.

An anonymous ftp service is operating at RIKSUN (ftp.riken.go.jp) which archives 1 TB of useful software for research, including Linux and TeX distributions, GNU software and large collections of free software for PC, Macintosh and UNIX systems.

## References

- 1) T. Ichihara et al.: RIKEN Accel. Prog. Rep. **36**, 199 (2002).
- 2) <http://www.sinet.ad.jp/>

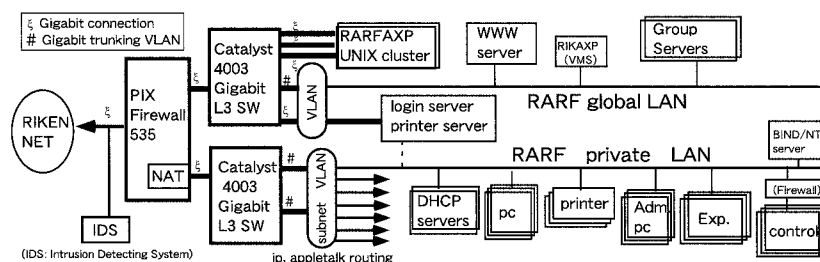


Fig. 1. Configuration of the RARF Advanced Network.

## Application of an in-air high-resolution PIXE system to direct speciation of Cr and Fe

K. Maeda, K. Hasegawa,<sup>\*1</sup> H. Hamanaka,<sup>\*2</sup> M. Tsuji,<sup>\*3</sup> and S. Muraio<sup>\*4</sup>

Particle-induced X-ray emission (PIXE) analysis with high energy resolution is one of the most effective tools for direct investigations of chemical bonding states of atoms in target materials. We have developed a compact spectrometer system consisting of an analyzing crystal and a position-sensitive proportional counter (PSPC) for high-resolution PIXE measurements in air of atmospheric pressure.<sup>1)</sup> The system is most appropriate for K-X rays of third-period elements. As for the main components, it is possible to distinguish chemical species within five seconds. A small quantity of the sample, 1 mg and 10 mm<sup>2</sup>, is sufficient for measurements.

This time we have examined the feasibility of this system for the direct speciation of 3d transition elements. We report here the preliminary results obtained from the measurements of the K $\beta$  spectra of Cr and Fe.

The experimental setup presented in the previous report<sup>2)</sup> is used. A target sample is placed in air and bombarded with a 2.1 MeV proton beam of 3 mm diameter, which is extracted from a vacuum beam line through a 7- $\mu$ m-thick Al exit window. X-rays are diffracted by a cylindrically curved crystal of v. Hamos geometry and detected by the PSPC. A narrow slit of 0.4 mm width is placed between the target and the crystal, at a position very close to the proton beam spot on the target. Third-order diffraction by a Ge (111) crystal of 150 mm in radius of curvature ( $r$ ) was used for the measurements of Cr K $\beta$ , while first-order diffraction by a LiF (420) crystal of 200 mm  $r$  was used for the measurements of Fe K $\beta$ . Proton beam current was 30–60 nA. A gas mixture of Xe:CO<sub>2</sub> (9:1) was used as the counter gas.

Figure 1 shows the Cr K $\beta$  spectra of Cr metal and Cr<sub>2</sub>O<sub>3</sub>. A difference in chemical state between the metal and oxide Cr is observed in a relative intensity of a low-energy satellite K $\beta$ '. The main line K $\beta$ <sub>1,3</sub> results from the 3p–1s electron transition. The satellite K $\beta$ ' is explained by the promotion of unpaired 3d electrons to the conduction band or by the exchange interaction between unpaired 3d electrons and 3p holes.<sup>3–5)</sup> Thus, K $\beta$ ' can be used as a good indicator of the bonding states of 3d elements.

As well as the K $\beta$  spectra of Cr, a difference in K $\beta$ '

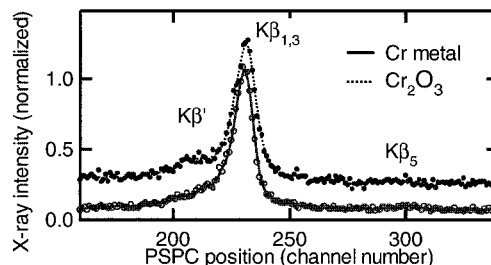


Fig. 1. Cr K $\beta$  spectra. Diffraction angle  $\theta$  is  $\sim 74^\circ$ . One channel corresponds to 0.53 eV around the K $\beta$ <sub>1,3</sub> line (5.95 keV).

intensity is clearly observed between the Fe K $\beta$  spectra of the metal and oxide, as shown in Fig. 2.

The difference in intensity distribution of spectrum between two oxides, Fe<sub>2</sub>O<sub>3</sub> (Fe<sup>3+</sup>) and FeO (Fe<sup>2+</sup>), is small. In addition, a high background mainly caused by  $\gamma$ -rays emitted from the Al exit foil masks the difference. However, after background subtraction, nor-

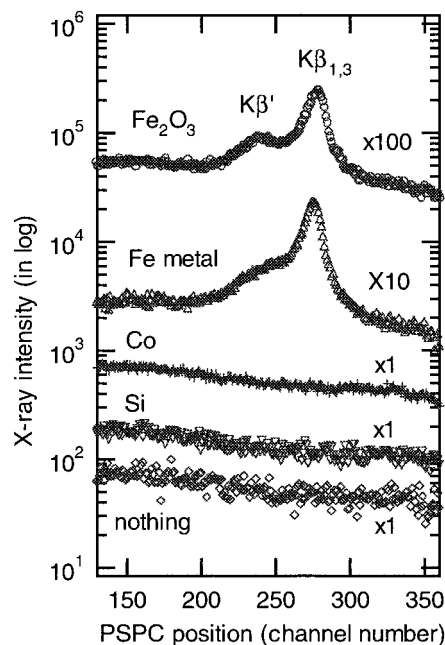


Fig. 2. Fe K $\beta$  spectra of Fe metal and Fe<sub>2</sub>O<sub>3</sub>, and background spectra measured with Co and Si targets and without a target. Diffraction angle  $\theta$  is  $\sim 77^\circ$ . One channel corresponds to 0.38 eV around the K $\beta$ <sub>1,3</sub> line (7.06 keV). The accumulated beam charges are 80  $\mu$ C for Fe, 200  $\mu$ C for Fe<sub>2</sub>O<sub>3</sub>, 200  $\mu$ C for Co, 70  $\mu$ C for Si, and 20  $\mu$ C for the case without a target.

<sup>\*1</sup> MIS Ltd.

<sup>\*2</sup> Faculty of Engineering, Hosei University

<sup>\*3</sup> Research Center for Carbon Recycling and Utilization, Tokyo Institute of Technology

<sup>\*4</sup> Institute for Geo-Resources and Environment, National Institute of Advanced Industrial Science and Technology (AIST)

malization and smoothing of the measured spectra, the difference became evident, as shown in Fig. 3. In accordance with the data obtained by the X-ray fluorescence method,<sup>3)</sup> the  $K\beta'$  intensity of  $Fe_2O_3$  is slightly higher than that of  $FeO$ . The PIXE measurement was also carried out using a green biotite sample shown in Fig. 3. The  $K\beta$  spectrum of the sample resembles that of  $FeO$ , which is in consistent with the generally accepted explanation of the oxidation state (2+) of Fe in biotite.

We have assured that the background of the Fe  $K\beta$  spectra is markedly reduced by a factor of 4, when a

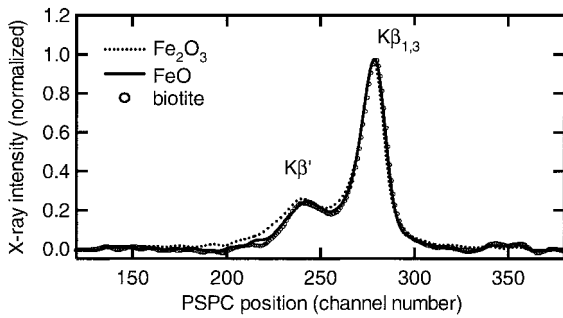


Fig. 3. Fe  $K\beta$  spectra of  $Fe_2O_3$ ,  $FeO$  and green biotite. The biotite was collected from the Tosham polymetallic deposit, India.

7- $\mu$ m-thick Kapton foil is used as the exit window instead of the Al foil. However, Kapton is not as strong as Al against damage caused by proton impact. Probably the beam current should be maintained at less than 20 nA for the Kapton window. On the other hand, the Al window withstands the proton beam of > 100 nA. The  $K\beta$  spectra shown in Figs. 1–3 were obtained at the accumulated beam charge of 70–300  $\mu$ C and the measuring time of 20–80 min. The sensitivity of the speciation of the 3d elements using this system is not as good as that of the third-period elements. However, it is expected that the sensitivity could be much improved if a multistacked PSPC assembly with a large sensitive area<sup>6)</sup> is combined with a curved crystal of Johann or Johansson geometry.

#### References

- 1) K. Maeda et al.: Adv. X-Ray Chem. Anal. Jpn. **34**, 89 (2003).
- 2) K. Maeda et al.: RIKEN Accel. Prog. Rep. **36**, 205 (2003).
- 3) A. S. Koster and G. D. Rieck: J. Phys. Chem. Solids **31**, 2505 (1970).
- 4) K. Tsutsumi et al.: Phys. Rev. B **13**, 929 (1976).
- 5) H. Eba and K. Sakurai: Adv. X-Ray Chem. Anal. Jpn. **33**, 253 (2002).
- 6) K. Hasegawa et al.: Trans. Soc. Instrum. Control Eng., **39**, 11 (2003).

# Gamma rays from iron, aluminum and rock targets bombarded by 210 MeV protons

E. Shibamura,<sup>\*1</sup> N. Hasebe,<sup>\*2</sup> M. Kobayashi,<sup>\*2</sup> T. Miyachi,<sup>\*2</sup> H. Okada,<sup>\*2</sup> T. Hiramoto,<sup>\*2</sup> S. Murasawa,<sup>\*2</sup>  
A. Nagashima,<sup>\*2</sup> O. Okudaira,<sup>\*2</sup> N. Yamashita,<sup>\*2</sup> and J. Yasutani<sup>\*2</sup>

Planetary bodies bombarded by cosmic rays emit  $\gamma$  rays with energies characteristic to surface materials. Measuring the  $\gamma$  rays determines the chemical concentration of the planetary surface. Remote sensing  $\gamma$ -ray spectroscopy has been employed to study planetary bodies,<sup>1-4</sup> for example, by Japanese lunar orbiter SELENE. Nuclear spectroscopic analysis,<sup>5</sup> however, requires quantitative data on major elements over a wide range of concentrations. To improve the analysis, beam experiments with protons simulating the cosmic-ray exposure play an important role.

Cosmic-ray irradiation environments of planetary surfaces are simulated using proton beams and thick targets.<sup>6</sup> We used four thick targets, namely, Fe and Al targets, which are  $0.5 \times 0.5 \times 0.5 \text{ m}^3$  in volume, and gabbro and granite targets, which are  $0.7 \times 0.7 \times 0.7 \text{ m}^3$  in volume. Each target was irradiated with 210 MeV proton beams from the Riken Ring Cyclotron.  $\gamma$  rays from the targets were observed using a Ge detector with a volume of  $113 \text{ cm}^3$  placed 25 cm away from the irradiated surface.

A typical energy spectrum of  $\gamma$  rays in the Fe target is shown in Fig. 1 together with that calculated by Geant4. There were high background  $\gamma$  rays whose sources include naturally radioactive materials as well as  $\gamma$  rays induced by recoiled protons and neutrons from massive materials in the experimental facility. The ratios of major peak areas in the experiment to

those in the calculation are shown in Fig. 2. The experimental values are lower than the calculated ones except the peak at 1238 keV. The differences are not fully understood, but are in part explained by the simplification of material disposition in the calculation and surrounding materials in the exposure room. The nuclear data libraries for generating neutron-induced  $\gamma$  rays would be acceptable regarding the major peaks from the Fe target. Some minor peaks in the calculation are not seen in the experiment. The values employed in the libraries for other nuclides were deficient, implying the necessity to improve the  $\gamma$ -ray- and neutron-related libraries. This experiment provides fundamental data for calibrating the SELENE GRS and nuclear library, which will be beneficial to lunar and planetary  $\gamma$ -ray spectroscopies. Further experiments, however, are necessary to improve the accuracy of planetary  $\gamma$ -ray spectroscopy.

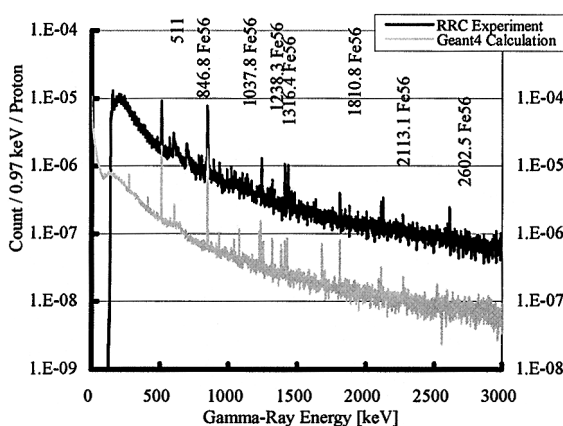


Fig. 1. Comparison of energy spectra of gamma rays from Fe target between experiment (left axis) and calculation (right axis).

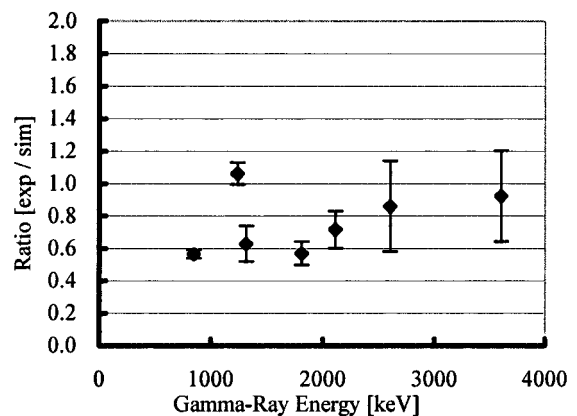


Fig. 2. Ratios of peak areas in experiment to those in calculation.

## References

- 1) T. M. Harrington et al.: Nucl. Instrum. Methods **118**, 401 (1974).
- 2) W. C. Feldman et al.: Nucl. Instrum. Methods Phys. Res. A **422**, 562 (1999).
- 3) W. V. Boynton et al.: Science **297**, 81 (2002).
- 4) N. Hasebe et al.: Adv. Space Res. **23**, 1837 (1999).
- 5) R. C. Reedy: Proc. 9th Lunar Planetary Science Conf., (1978) p. 2961.
- 6) N. Yamashita et al.: Adv. Space Res. **31**, 2359 (2003).

<sup>\*1</sup> College of Health Science, Saitama Prefectural University

<sup>\*2</sup> Advanced Research Institute for Science and Engineering, Waseda University



# QCD and dimensional deconstruction

M. A. Stephanov\*

In this work we consider an effective theory describing pions and a tower of vector and axial vector mesons based on a large number of hidden local symmetries. In the limit  $K \rightarrow \infty$  this theory can be viewed as a discretization (or, deconstruction) of a classical 5d Yang-Mills theory. Several nontrivial properties of the hadronic resonances, such as, e.g., vector meson dominance have a simple explanation within the model.

The model under consideration in Ref. 1 is described by the following Lagrangian

$$\mathcal{L} = \sum_{k=1}^{K+1} f_k^2 \text{Tr} |D_\mu \Sigma^k|^2 - \sum_{k=1}^K \frac{1}{2} \text{Tr} (F_{\mu\nu}^k)^2. \quad (1)$$

The covariant derivatives are defined as

$$D_\mu \Sigma^k = \partial_\mu \Sigma^k - i(gA_\mu)^{k-1} \Sigma^k + i\Sigma^k (gA_\mu)^k. \quad (2)$$

A shorthand notation is used for the product of the gauge field  $A_\mu = A_\mu^a \tau^a / 2$  and its coupling constant:  $g_k A_\mu^k \equiv (gA_\mu)^k$ . We assume  $A_\mu^0 = A_\mu^{K+1} = 0$ .

The model contains  $K + 1$  nonlinear sigma model fields  $\Sigma^k \in \text{SU}(2)$  (or, in general,  $\text{SU}(N_f)$ ), interacting via  $K$  gauge boson fields  $A_\mu^k$ . The model has a chiral  $\text{SU}(2) \times \text{SU}(2)$  symmetry and an  $\text{SU}(2)^K$  local symmetry. This model is a natural generalization of models of hidden local symmetry.<sup>2)</sup>

Consider the limit  $K \rightarrow \infty$ . In this case we can replace the discrete variable  $k$  by a continuum variable which we shall call  $u$ :  $u = (k - \frac{K}{2})a$ . If the limit  $K \rightarrow \infty$  is performed in the following way  $K \rightarrow \infty$ , and  $a \rightarrow 0$ , while  $Ka \equiv 2u_0$  is fixed, then  $u$  becomes a continuum replacement for  $k$ . If the  $f_k$  and  $g_k$  are smooth functions of  $k$  we can also replace them by functions of  $u$ .

The continuum limits for important physical quantities in terms of the functions  $f(u)$  and  $g(u)$  are as follows. The pion decay constant is given by  $4f_\pi^{-2} = \int_{-u_0}^{+u_0} du f^{-2}(u)$ .

The vector/axial vector resonance masses are given by the eigenvalues of

$$g(f^2(gb_n)')' = -m_n^2 b_n. \quad (3)$$

with Dirichlet boundary conditions  $b_n(\pm u_0) = 0$  (since we set  $A_\mu^0 = A_\mu^{K+1} = 0$ ).

The coupling of the  $n$ -th vector meson to 2 pions is given by

$$g_{n\pi\pi} = \frac{f_\pi^2}{4} \int_{-u_0}^{+u_0} \frac{du}{f^2(u)} g(u) b_n(u). \quad (4)$$

From this equation it can be easily seen that the coupling of higher vector mesons are suppressed by the

overlap integral of fast oscillating wave-function  $b_n(u)$  and smooth  $g(u)/f^2(u)$ . This provides a natural explanation of the observed vector meson dominance of the pion formfactor.

The theory with  $K \gg 1$  can be also considered as a discretized (or deconstructed<sup>3)</sup>) five-dimensional continuum gauge theory in curved spacetime. The variable  $u$  plays the role of the fifth dimension and  $\Sigma$ 's can be interpreted as the corresponding gauge field link variables,  $\Sigma^k \approx 1 + iaA_5(u)$ . The action of the model can be written as:

$$S = - \int d^5x \sqrt{|g|} \frac{1}{2g^2} \text{Tr} F_{\hat{\mu}\hat{\nu}} F^{\hat{\mu}\hat{\nu}}, \quad (5)$$

where  $\hat{\mu}, \hat{\nu}$  are 5d Lorentz indices and  $|g|$  is the determinant of the metric tensor. The metric has a warped form, with  $f^2 g^2$  playing the role of the warp factor

$$ds^2 = -du^2 + f^2 g^2 \eta_{\mu\nu} dx^\mu dx^\nu. \quad (6)$$

The correlators of conserved currents in this theory can be computed by using a prescription essentially identical to the AdS/CFT one. Namely, the generating functional for the correlation functions of the currents is equal to the action of a solution to the classical field equations, with the sources serving as the boundary values for the classical fields.

For a metric which at the boundaries,  $u \rightarrow \pm\infty$ , approaches AdS<sub>5</sub> form, i.e.,  $f(u) \rightarrow (\Lambda/g_5)e^{|u|}$ , with  $g(u) \rightarrow g_5$ , the vector-vector current polarization operator is given by:

$$\Pi_V(Q^2) = -\frac{1}{g_5^2} \ln(Q^2), \quad Q^2 \gg \Lambda^2. \quad (7)$$

Matching this to QCD result

$$\Pi_V(Q^2) = -\frac{N_c}{24\pi^2} \ln(Q^2), \quad (8)$$

where  $N_c$  is the number of colors, one obtains

$$\frac{1}{g_5^2} = \frac{N_c}{24\pi^2}. \quad (9)$$

In particular, this means that such a theory is weakly coupled when  $N_c \rightarrow \infty$ . It is natural to expect this property from a theory dual to QCD.

## References

- 1) D. T. Son and M. A. Stephanov: arXiv:hep-ph/0304182.
- 2) M. Bando, T. Kugo, S. Uehara, K. Yamawaki, and T. Yanagida: Phys. Rev. Lett. **54**, 1215 (1985); M. Bando, T. Fujiwara, and K. Yamawaki: Prog. Theor. Phys. **79**, 1140 (1988).
- 3) N. Arkani-Hamed, A. G. Cohen, and H. Georgi: Phys. Rev. Lett. **86**, 4757 (2001).

\* Physics Department, University of Illinois at Chicago, USA

# Single spin asymmetry in inclusive $D$ meson production at RHIC

K. Sudoh

Direct measurement of the polarized strange quark density is crucial for the understanding of the flavor structure of the polarized parton distribution functions (PDFs) and provides a clue to resolving the proton spin puzzle. The charged current reaction such as  $W^\pm$  production is effective for extracting the flavor decomposed PDFs, because the  $W^\pm$  boson changes the flavor of partons.

Here, we propose charm quark production in parity-violating processes. In  $s$ -channel  $W$  production, there are processes,  $\Delta u(\Delta\bar{d}) + \bar{d}(u) \rightarrow W^+ \rightarrow \bar{s}c$ , which are similar to those of conventional  $W$  production. Moreover, there are processes,<sup>a)</sup>  $\Delta s(\Delta u) + u(s) \rightarrow dc$ ,  $\Delta s(\Delta\bar{d}) + \bar{d}(s) \rightarrow \bar{u}c$ , and  $\Delta s(\Delta\bar{s}) + \bar{s}(s) \rightarrow \bar{c}c$ , in the  $t, u$ -channel  $W$  exchange process, and  $\Delta s(\Delta g) + g(s) \rightarrow W^-c$  in charm-associated  $W$  production, which are sensitive to the polarized strange quark distribution  $\Delta s(x, Q^2)$ . In the unpolarized case, there are additional parity-conserving processes which are pure QCD processes:  $gg \rightarrow \bar{c}c$  and  $q\bar{q} \rightarrow \bar{c}c$ . Therefore, in order to examine the sensitivity of  $\Delta s(x, Q^2)$ , we investigated inclusive  $D$  meson production in unpolarized proton-polarized proton collisions at RHIC.

The single spin asymmetry is defined as

$$A_L^D \equiv \frac{[d\sigma_- - d\sigma_+]/dp_T}{[d\sigma_- + d\sigma_+]/dp_T} = \frac{d\Delta\sigma/dp_T}{d\sigma/dp_T}, \quad (1)$$

where  $d\sigma_{-(+)}$  is the spin-dependent differential cross section with negative (positive) helicity for protons.  $p_T$  is the transverse momentum of  $D$  meson. The cross sections and asymmetry are calculated in the PHENIX acceptance; the rapidity range  $|\eta| \leq 0.35$ , and  $Q^2$  is set as  $p_T^2$ .

We show the cross sections in Fig. 1 as a function of  $p_T$  at  $\sqrt{s} = 500$  GeV. The upper bold line and four lower lines represent the unpolarized cross section and the polarized cross sections, respectively. For the polarized PDFs, we adopted the following four

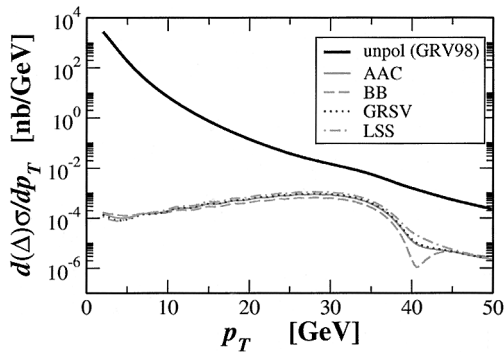


Fig. 1. The  $p_T$  distribution of cross sections for the process  $p\bar{p} \rightarrow DX$  at  $\sqrt{s} = 500$  GeV.

parametrizations; AAC,<sup>1)</sup> BB,<sup>2)</sup> GRSV,<sup>3)</sup> LSS.<sup>4)</sup> The unpolarized cross section is dominated by the QCD gluon-gluon fusion process, and it rapidly decreases with  $p_T$ . On the other hand, the polarized cross sections do not strongly depend on  $p_T$ . Note that the polarized cross sections are dominated by the  $u$  quark-associated process, since the momentum fractions for both protons are integrated in this analysis.

In Fig. 2, the single spin asymmetries are shown at  $\sqrt{s} = 500$  GeV with various parametrization models of the polarized PDFs. The expected statistical error in Fig. 2 is estimated using the designed data of the beam polarization ( $P = 70\%$ ), the integrated luminosity ( $\mathcal{L} = 800 \text{ pb}^{-1}$ ), and the reconstruction efficiency ( $\varepsilon = 50\%$ ), together with the value of the unpolarized cross section. We can see that the parametrization model dependence on asymmetry is measurable in large  $p_T$  regions. Therefore, it might provide another test of the parametrization model of the polarized PDFs.

However, the sensitivity of  $\Delta s(x, Q^2)$  is small, since the valence quark contribution is dominant in the  $x$ -integrated asymmetry. Some kinematical improvements to extract  $\Delta s(x, Q^2)$  are needed.

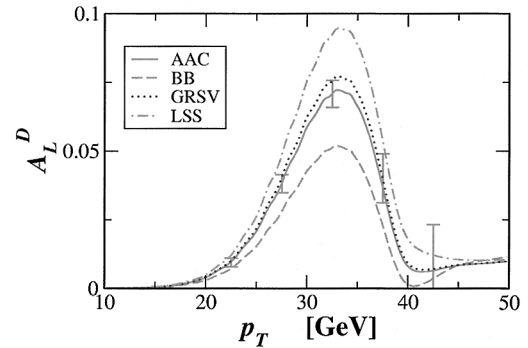


Fig. 2. Single spin asymmetries with statistical error expected at  $\sqrt{s} = 500$  GeV and  $\mathcal{L} = 800 \text{ pb}^{-1}$ .

## References

- 1) Asymmetry Analysis Collaboration, Y. Goto et al.: Phys. Rev. D **62**, 034017 (2000).
- 2) J. Blümlein and H. Böttcher: Nucl. Phys. B **636**, 225 (2002).
- 3) M. Glück, E. Reya, M. Stratmann, and W. Vogelsang: Phys. Rev. D **63**, 094005 (2001).
- 4) E. Leader, A. V. Sidorov, and D. B. Stamenov: Eur. Phys. J. C **23**, 479 (2002).

<sup>a)</sup> In the numerical calculation, all processes such as Cabbibo corrections, neutral current interaction diagrams, and interferences among  $W$ ,  $Z^0$ , and  $\gamma$  are included in a leading order of the coupling constant.

# $\Delta g(x)$ uncertainty from prompt photon production at RHIC Spin

M. Hirai

Determination of polarized gluon distribution  $\Delta g(x)$  from polarized deep inelastic scattering (DIS) data is insufficient, since the gluon contribution is indirect and small.<sup>1)</sup> One of the processes that the gluon distribution predominantly contributes to is the prompt photon production which is measured by the RHIC Spin. This report explains the effectiveness of this process for the  $\Delta g(x)$  determination in terms of uncertainties of polarized parton distribution functions (PDFs).

In order to indicate the constraint of prompt photon data on the gluon distribution, I compare the uncertainty of spin asymmetry  $A_{LL}^\gamma$  with expected statistical errors. The asymmetry uncertainty indicates the accuracy of a predicted value with polarized PDFs, which comes from PDF uncertainties. On the other hand, the expected statistical error can be estimated using well-determined unpolarized PDFs, which means a constriction for the asymmetry uncertainty.

The spin asymmetry is defined as the cross section ratio  $A_{LL}^\gamma = \Delta\sigma/\sigma$ . By the factorization theorem, the polarized cross section  $\Delta\sigma$  is expressed as

$$\frac{d\Delta\sigma}{dp_T} = \sum_{a,b} \Delta f_a(x_1) \otimes \Delta f_b(x_2) \otimes \frac{d\Delta\hat{\sigma}^{ab}}{dp_T}, \quad (1)$$

where  $\otimes$  denotes the convolution integral.  $\Delta\sigma^{ab}$  is the partonic cross section ( $a + b \rightarrow \gamma + X$ ), which is precisely calculated by perturbative QCD. In order to reduce a theoretical uncertainty, this cross section is calculated at the next-to-leading order.<sup>2)</sup> The cross section is integrated over the rapidity bin  $|\eta| < 0.35$ . This rapidity cut corresponds to the acceptance of the PHENIX detector.  $\Delta f_a(x)$  is the polarized PDF of the parton  $a$ . The uncertainty of the cross section comes from these polarized PDF uncertainties, which are estimated by the Hessian method.

On the other hand, the expected statistical error  $\delta A_{LL}^\gamma$  can be estimated by

$$\delta A_{LL}^\gamma = \frac{1}{P_1 P_2 \sqrt{\mathcal{L}_{int} \sigma}}, \quad (2)$$

where  $\sigma$  is the unpolarized cross section integrated over each  $p_T$  bin,  $P_{1,2}$  is the beam polarization ( $P_1 = P_2 = 0.7$ ), and  $\mathcal{L}_{int}$  is the integrated luminosity (320 and 800 pb<sup>-1</sup> at  $\sqrt{s} = 200$  and 500 GeV, respectively). These values are taken from design values of an RHIC Spin experiment.<sup>3)</sup>

Figure 1 shows a comparison between asymmetry uncertainty and expected statistical errors at  $\sqrt{s} = 200$  and 500 GeV. The covered area with dashed curves is obtained by current polarized PDF uncertainties,<sup>1)</sup> and the asymmetry uncertainty is mostly composed of gluon uncertainty. In practice, the asymmetry uncertainty from quark and antiquark distributions is

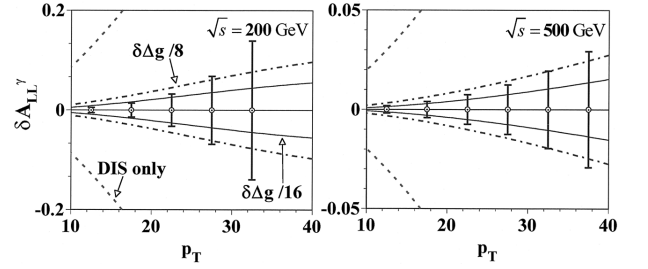


Fig. 1. Comparison between the asymmetry uncertainty and expected statistical errors.

smaller than the statistical errors. This indicates that the gluon uncertainty is primarily constricted by including the prompt photon data.

Furthermore, the covered area with solid curves is estimated by the constricted gluon uncertainty with overhaul factor 1/16 and all quark and antiquark uncertainties. This factor corresponds to the statistical errors in the region  $p_T = 10\text{--}20$  GeV.  $x_T (= 2p_T/\sqrt{s})$  would approximate the Bjorken  $x_{Bj}$  around the central region, thus this fact means that these data constrain the gluon distribution in the specific  $x_{Bj}$  region:  $x_{Bj} = 0.1\text{--}0.2$  at  $\sqrt{s} = 200$  GeV and  $0.04\text{--}0.08$  at 500 GeV.

Finally, the constricted uncertainties of the gluon distribution and the spin asymmetry are shown in Fig. 2. Although these factors are roughly estimated, this figure indicates that the prompt photon production is effective for reducing the gluon uncertainty.

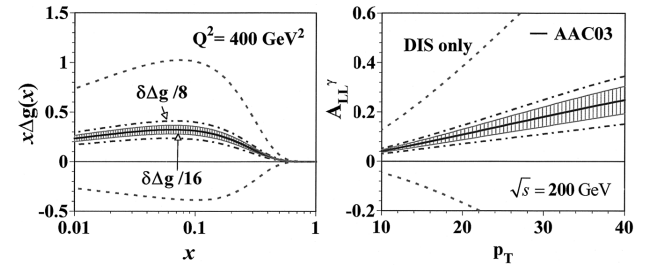


Fig. 2. Uncertainties from DIS data and prompt photon data. Left figure shows the polarized gluon distribution with its uncertainty, and right figure is the spin asymmetry. Shaded area is estimated with the factor 1/16.

## References

- 1) M. Hirai, S. Kumano, and N. Saito, Asymmetry Analysis Collaboration: hep-ph/0312112.
- 2) L. E. Gordon and W. Vogelsang: Phys. Rev. D **48**, 3136 (1993).
- 3) G. Bunce et al.: Ann. Rev. Nucl. Part. Sci. **50**, 525 (2000).

# On a negative $A_{LL}^\pi$ at moderately large $p_\perp$ <sup>†</sup>

W. Vogelsang

The determination of the nucleon's polarized gluon density is a major goal of current experiments with longitudinally polarized protons at RHIC.<sup>1)</sup> It can be accessed through measurement of the spin asymmetries

$$A_{LL} = \frac{d\Delta\sigma}{d\sigma} = \frac{d\sigma^{++} - d\sigma^{+-}}{d\sigma^{++} + d\sigma^{+-}}, \quad (1)$$

for high transverse momentum ( $p_\perp$ ) reactions such as  $pp \rightarrow \pi X$ . In Eq. (1),  $\sigma^{++}$  ( $\sigma^{+-}$ ) denotes the cross section for scattering of two protons with same (opposite) helicities. High  $p_\perp$  implies large momentum transfer, and the cross sections for such reactions may be factorized into long-distance pieces that contain the desired information on the (spin) structure of the nucleon, and short-distance parts that describe the hard interactions of the partons and are amenable to QCD perturbation theory (pQCD). Very recently the PHENIX collaboration has presented first preliminary data<sup>2)</sup> for  $A_{LL}^\pi$ . They are consistent with a significant (up to a few per cent) negative asymmetry in the region  $p_\perp \sim 1 \div 4$  GeV. Even though the experimental uncertainties are still large and leave room for a different behavior of  $A_{LL}^\pi$ , the new data motivate us to entertain the unexpected possibility of  $A_{LL}^\pi$  being negative. As we will show now, within pQCD at leading power, there is a lower bound on the asymmetry of about  $-10^{-3}$ .

We consider the LO cross section integrated over all rapidities  $\eta$  and take Mellin moments in  $x_T^2 = 4p_\perp^2/S$  of the cross section:

$$\Delta\sigma^\pi(N) \equiv \int_0^1 dx_T^2 (x_T^2)^{N-1} \frac{p_\perp^3 d\Delta\sigma^\pi}{dp_\perp}. \quad (2)$$

One finds:

$$\Delta\sigma^\pi(N) = \sum_{a,b,c} \Delta a^{N+1} \Delta b^{N+1} \Delta \hat{\sigma}_{ab}^{c,N} D_c^{\pi,2N+3}, \quad (3)$$

where the  $\Delta \hat{\sigma}_{ab}^{c,N}$  are the  $\hat{x}_T^2$ -moments of the partonic cross sections and, as usual,  $f^N \equiv \int_0^1 dx x^{N-1} f(x)$  for the parton distribution and fragmentation functions. Explicitly, the dependence on the moments  $\Delta g^N$  is

$$\Delta\sigma^\pi(N) = (\Delta g^{N+1})^2 \mathcal{A}^N + 2\Delta g^{N+1} \mathcal{B}^N + \mathcal{C}^N. \quad (4)$$

Here,  $\mathcal{A}^N$  represents the contributions from  $gg \rightarrow gg$  and  $gg \rightarrow q\bar{q}$ ,  $\mathcal{B}^N$  the ones from  $qg \rightarrow qg$ , and  $\mathcal{C}^N$  those from the (anti)quark scatterings.

Being a quadratic form in  $\Delta g^{N+1}$ ,  $\Delta\sigma^\pi(N)$  possesses an extremum, given by the condition

$$\mathcal{A}^N \Delta g^{N+1} = -\mathcal{B}^N. \quad (5)$$

The coefficient  $\mathcal{A}^N$  is positive, and Eq. (5) describes a minimum of  $\Delta\sigma^\pi(N)$ , with value

$$\Delta\sigma^\pi(N) \Big|_{\min} = -(\mathcal{B}^N)^2 / \mathcal{A}^N + \mathcal{C}^N. \quad (6)$$

It is then straightforward to perform a numerical Mellin inversion of this minimal cross section. The minimal asymmetry resulting from this exercise is negative indeed, but very small: in the range  $p_\perp \sim 1 \div 4$  GeV its absolute value does not exceed  $10^{-3}$ . The  $\Delta g$  in Eq. (5) that minimizes the asymmetry is shown in Fig. 1, compared to  $\Delta g$  of the GRSV LO “standard” set.<sup>3)</sup> One can see that it has a node and is smaller than the GRSV one, except at large  $x$ .

Even though we have made some approximations in deriving the bound in Eq. (6), we do believe that it exhibits the basic difficulty with a sizable negative  $A_{LL}^\pi$  at moderate  $p_\perp$ : the fact that the cross section is a quadratic form in  $\Delta g$  effectively means that it is bounded from below. Effects like NLO corrections,<sup>4)</sup> choice of scales, and realistic range of rapidity may be thoroughly addressed in a “global” NLO analysis of the data, taking into account the results from polarized DIS as well. We have performed such an analysis, and it confirms the findings of our simple example above.

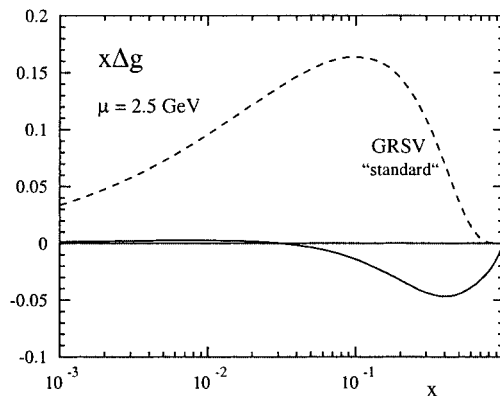


Fig. 1.  $\Delta g(x, \mu = 2.5 \text{ GeV})$  resulting from Eq. (5) (solid). The dashed line shows the GRSV LO “standard”  $\Delta g$ .<sup>3)</sup>

## References

- 1) G. Bunce, N. Saito, J. Soffer, and W. Vogelsang: *Annu. Rev. Nucl. Part. Sci.* **50**, 525 (2000).
- 2) A. Bazilevsky: talk presented at the Xth Workshop on High Energy Spin Physics (Spin-03), Dubna, Russia, 2003-9.
- 3) M. Glück et al.: *Phys. Rev. D* **63**, 094005 (2001).
- 4) B. Jäger et al.: *Phys. Rev. D* **67**, 054005 (2003).

<sup>†</sup> Condensed from the article in hep-ph/0310197, accepted for publication in *Phys. Rev. Lett.*

# Threshold resummation for heavy-flavor photo-production

H. Yokoya\*<sup>1</sup> and W. Vogelsang\*<sup>2</sup>

The polarized gluon distribution function  $\Delta g(x, Q^2)$  may play an important role for understanding the spin structure of the nucleon. Data from polarized DIS, accumulated over more than two decades, constrain  $\Delta g$  only very little. There are several new experiments now dedicated to accessing gluon polarization. One reaction, to be studied by COMPASS at CERN, is  $\vec{\mu}\vec{p} \rightarrow c\bar{c}X$ , polarized heavy-flavor production. Here one takes advantage of the photon-gluon fusion process which is expected to dominate the cross section.

First-order QCD corrections to  $\gamma g \rightarrow c\bar{c}$  were found to be sizable.<sup>1,2)</sup> This raises questions concerning the relevance of yet higher orders. We address this issue by considering all-order threshold resummation corrections to the reaction. The perturbative expansion for the photon-gluon fusion cross section reads:

$$(\Delta)\hat{\sigma}_{\gamma g}(\rho) = \frac{e_Q^2 \alpha \alpha_s(m^2)}{m^2} \left[ (\Delta)f_{\gamma g}^{(0)}(\rho) + 4\pi\alpha_s(m^2)(\Delta)f_{\gamma g}^{(1)}(\rho) + \dots \right], \quad (1)$$

where  $\rho = 4m^2/\hat{s}$  and we have chosen the renormalization scale as the mass  $m$  of the heavy quark.  $f^{(0)}$  is the leading order (LO) contribution, and  $f^{(1)}$  is the next-to-leading order (NLO) coefficient functions. Near partonic threshold,  $\rho \rightarrow 1$ ,  $f^{(1)}$  develops large logarithmic terms,  $\propto \ln^2(8\beta^2)$  and  $\ln(8\beta^2)$ , where  $\beta = \sqrt{1-\rho}$ . These are associated with soft-gluon emission.

We perform resummation of these threshold corrections following the method used by Bonciani *et al.*<sup>3)</sup> We go to Mellin moment space,  $f_N = \int_0^1 d\rho \rho^{N-1} f(\rho)$ , where the threshold region corresponds to  $N \rightarrow \infty$  and the large logarithms appear as  $\ln^2 N$  or  $\ln N$ . The resummed coefficient function is given by

$$(\Delta)f_N^{\text{res}} = \left( (\Delta)f_N^{(0)} + 4\pi\alpha_s(m^2)(\Delta)f_N^{\text{Coul.}} \right) \times \left( 1 + \frac{\alpha_s(m^2)}{\pi} C \right) \Delta_{N+1}(\alpha_s(m^2)), \quad (2)$$

where  $f_N^{\text{Coul.}}$  corresponds to the Coulomb gluon exchange contribution, and  $C$  is a constant. The radiative factor  $\Delta_N$  has an exponential form. It gives all the threshold logs. Its explicit form is given in Ref. 3.

The unpolarized coefficient functions are shown in Fig. 1, *versus*  $\eta = (1-\rho)/\rho$ . At small  $\eta$ , *i.e.* near threshold, the NLO contribution strongly increases the cross section, compared to LO. The  $O(\alpha_s)$  expansion of the resummed result is in good agreement with full

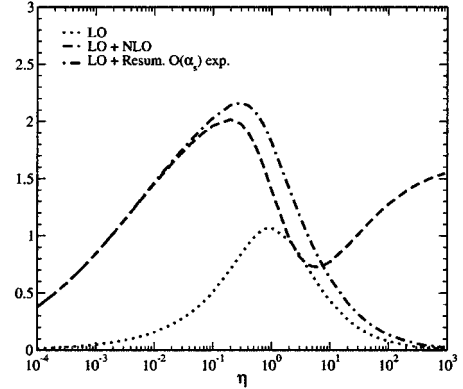


Fig. 1. Coefficient functions for the unpolarized cross section at LO (dotted), LO+NLO (dashed), and for the  $O(\alpha_s)$  expansion of the resummed result (dot-dashed).

NLO, except of course at large  $\eta$ .

The polarized coefficient functions are shown in Fig. 2. We find similar features as in the unpolarized case.

Our results demonstrate that the NLO correction is dominated by the threshold logarithms. This justifies their all-order resummation as given by Eq. (2), for which we hope to publish results in the near future.

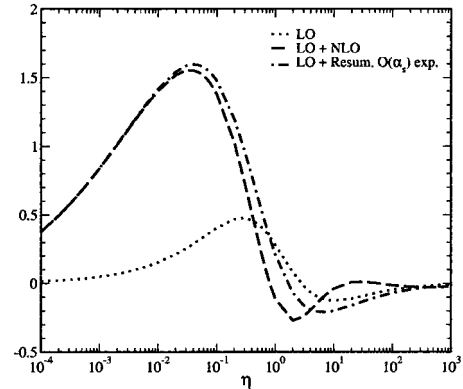


Fig. 2. Same as Fig. 1, but for the polarized case.

## References

- 1) R. K. Ellis and P. Nason: Nucl. Phys. B **312**, 551 (1989).
- 2) I. Bojak and M. Stratmann: Phys. Lett. B **443**, 411 (1998); Nucl. Phys. B **540**, 345 (1999).
- 3) R. Bonciani *et al.*: Nucl. Phys. B **529**, 424 (1998).

\*<sup>1</sup> Department of Physics, Hiroshima University

\*<sup>2</sup> Physics Department, Brookhaven National Laboratory, USA

# The parton structure of the nucleon and precision determination of the Weinberg angle in neutrino scattering<sup>†</sup>

S. Kretzer

An important open question in particle physics in recent years has been the significance of the “NuTeV anomaly”—a  $3\sigma$  deviation of the measured  $\sin^2\theta_W$  ( $0.2277 \pm 0.0013 \pm 0.0009$ ) reported in Ref. 1 from the “standard model value” ( $0.2227 \pm 0.00037$ ), based on the world average of other measurements. No consistent picture has yet emerged in spite of an extensive literature on this subject.<sup>2)</sup> The measurement in Ref. 1 is closely related to measuring the Paschos-Wolfenstein ratio,<sup>3)</sup> which provides the theoretical underpinning of the analysis. For an isoscalar target, the parton model relates the Paschos-Wolfenstein ratio  $R^-$  to the Weinberg angle by

$$R^- \equiv \frac{\sigma_{\text{NC}}^\nu - \sigma_{\text{NC}}^{\bar{\nu}}}{\sigma_{\text{CC}}^\nu - \sigma_{\text{CC}}^{\bar{\nu}}} \simeq \frac{1}{2} - \sin^2\theta_W. \quad (1)$$

For the accuracy required to test the consistency of the SM, one needs a quantitative analysis based on a thorough revision of the relevant perturbative cross sections<sup>4)</sup> and non-perturbative parton distribution functions.<sup>5)</sup>

A particularly elusive source of uncertainty so far<sup>2)</sup> has been that associated with a possible strangeness asymmetry in the parton structure of the nucleon. A positive (negative) asymmetry, as measured by the momentum integral

$$[S^-] \equiv \int dx x [s(x) - \bar{s}(x)], \quad (2)$$

would reduce (increase) the NuTeV discrepancy. A devoted global analysis of parton distribution functions<sup>5)</sup> has now indicated that this asymmetry is of order  $|[S^-]| \lesssim 10^{-3}$ . The sign of  $[S^-]$  cannot be determined reliably from global data: The central fit in Ref. 5 prefers a positive value but for a conservative theoretical error estimate a broad range around the best fit value has to be considered. To quantify the impact of these new findings on  $R^-$ , we combine them with a recently completed state-of-the-art program for calculating neutrino cross sections in next-to-leading-order QCD, including target mass and charm mass corrections.<sup>4)</sup> The results are summarized in Table 1. The shift based on the central fit B can bridge up to about  $1.5\sigma$  of the overall  $3\sigma$  discrepancy between the NuTeV result and the world average of other measurements of

Table 1. Shifts in  $R^-$ , calculated with PDF sets of Ref. 5 (with non-zero  $[S^-]$ ) compared to the value with the CTEQ6M set ( $[S^-] = 0$ ). A positive (negative)  $\delta R^-$  corresponds to an increase (decrease) of the extracted  $\sin^2\theta_W$  along Eq. (1).

fit	$[S^-] \times 100$	$\chi_{\text{dimuon}}^2$	$\chi_{\text{inclusiveI}}^2$	$\delta R^-$
B <sup>+</sup>	0.540	<b>1.30</b>	0.98	-0.0065
A	0.312	1.02	0.97	-0.0037
B	0.160	1.00	1.00	-0.0019
C	0.103	1.01	1.03	-0.0012
B <sup>-</sup>	-0.177	<b>1.26</b>	<b>1.09</b>	0.0023

$\sin^2\theta_W$ . For fits with higher  $[S^-]$ , such as “A”, it is possible to reduce the discrepancy to within  $1\sigma$ .

More input on  $[s(x) - \bar{s}(x)]$  would, of course, be helpful in pinning down the contribution of the strangeness asymmetry to  $\delta R^-$ . Measurements of associated production of charmed jets and  $W^\pm$ -bosons at the Tevatron, at RHIC or at the future LHC would increase our knowledge of  $s(x)$  and  $\bar{s}(x)$ . In principle it seems also feasible to study  $[s(x) - \bar{s}(x)]$  on the lattice. Unfortunately, the most relevant moment  $[S^-]$  does not correspond to a local operator and cannot be calculated on the lattice.

The uncertainties in the QCD theory which relates  $R^-$  to  $\sin^2\theta_W$  are a comparatively large and unfortunate mismatch with the high statistical precision of the NuTeV data.<sup>1)</sup> Within the uncertainty bounds, the results of this study suggest that the new dimuon data, the Weinberg angle measurement, and other global data sets used in QCD parton structure analysis can all be consistent within the standard model of particle physics.

## References

- 1) NuTeV Collaboration, G. P. Zeller et al.: Phys. Rev. Lett. **88**, 091802 (2002).
- 2) S. Davidson, S. Forte, P. Gambino, N. Rius, and A. Strumia: JHEP **0202**, 037 (2002).
- 3) E. A. Paschos and L. Wolfenstein: Phys. Rev. D **7**, 91 (1973).
- 4) S. Kretzer and M. H. Reno: Phys. Rev. D **69**, 034002 (2004).
- 5) F. Olness et al.: RBRC-329.

<sup>†</sup> Condensed from the article in RBRC-328, submitted to Phys. Rev. Lett.

# Energy loss of leading parton in hot QGP<sup>†</sup>

S. Jeon\*

In highly relativistic heavy ion collisions, production of hard  $p_T$  partons precedes most other processes, simply because the time scale of the production is short,  $\tau \sim 1/p_T$ . In particular, the production of hard secondary partons precedes the formation of a quark-gluon plasma (QGP). Therefore, the produced hard partons find themselves in an environment far different from a vacuum. The interaction between the parton and the environment influences the final spectrum of high  $p_T$  hadrons in a nontrivial manner. In particular, if the QGP is very dense, we expect energy loss, leading to an energy dependent suppression of the high  $p_T$  spectrum, a phenomenon called “jet quenching.” The extent of jet quenching can be used to learn about the QGP. Experimentally, the CERN SPS exhibited little evidence of jet quenching, but RHIC has revealed a rather dramatic suppression of high  $p_T$  pions.

Theoretically, it is well established that the main energy loss mechanism of a fast parton is the bremsstrahlung of gluons in the medium. The strength of the bremsstrahlung in medium depends on a coherence effect called the Landau-Pomeranchuk-Migdal (LPM) effect.<sup>1–9</sup>

The purpose of this paper is to revisit the energy loss calculation with particular emphasis on two points. (i) Bremsstrahlung energy loss is dominated by hard emissions. Therefore, the distribution of final energies is as broad as the mean energy loss. To account for this, we directly evolve the spectrum of the partons as they undergo bremsstrahlung energy loss using a kinetic equation. (ii) At realistic parton energies one cannot take the LPM effect to be *parametrically* large. Therefore, we will use the formalism developed by Arnold, Moore and Yaffe (AMY),<sup>10</sup> which correctly treats the LPM effect (up to  $O(g_s)$  corrections) at all energies  $E_{\text{gluon}} > g_s T$ .

In Fig. 1, we show the ratio of the final and the initial quark spectrum calculated in two ways. The solid and dashed curves are the result of directly solving the full equation, and the dotted and dash-dot curves were obtained by evolving particle energies according to a  $dE/dx$  approximation. With the plasma temperature of about 0.4 GeV, the energy range shown corresponds to about 6 GeV to 20 GeV, with a time range of 0.5 fm to 1.5 fm.

In this way, we have demonstrated that the LPM-suppressed bremsstrahlung can in fact explain the qualitative features of the high  $p_T$  experimental data obtained from RHIC. This is in contrast to previ-

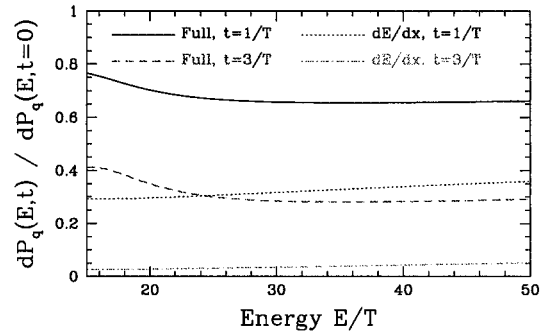


Fig. 1. The ratios of the final and the initial momentum spectra for quarks. The black and red (solid) curves are calculated by solving the full equation. The blue and green (dashed) curves are calculated by first calculating  $dE/dt$ .

ous findings. This difference is due to two features of our treatment. First, we determine the distribution of the final energies that an energetic parton can end up with, rather than using the mean. This is important when the initial spectrum is steeply falling. Second, we do not assume that the LPM effect is *parametrically* large from the beginning, but use a treatment which correctly handles the transition between Bethe-Heitler and LPM regimes. Since this transition occurs at emitted gluon energies of  $\sim 10T$ , such a treatment is necessary. We find that the ratio  $R$  of the data to the  $pp$ -based expectations initially decreases with energy, reaches a minimum at around  $30T$ , and then rises slowly thereafter.

## References

- 1) M. Gyulassy and X. Wang: Nucl. Phys. B **420**, 583 (1994).
- 2) R. Baier et al.: Nucl. Phys. B **483**, 291 (1997).
- 3) R. Baier et al.: Nucl. Phys. B **531**, 403 (1998).
- 4) B. G. Zakharov: JETP Lett. **63**, 952 (1996).
- 5) M. Gyulassy, P. Levai, and I. Vitev: Nucl. Phys. B **594**, 371 (2001); Phys. Rev. Lett. **85**, 5535 (2000); Phys. Lett. B **538**, 282 (2002).
- 6) I. Vitev and M. Gyulassy: Phys. Rev. Lett. **89**, 252301 (2002).
- 7) R. Baier et al.: JHEP **0109**, 033 (2001).
- 8) E. Wang and X. N. Wang: Phys. Rev. C **64**, 034901 (2001).
- 9) S. Jeon, J. Jalilian-Marian, and I. Sarcevic: Nucl. Phys. A **723**, 467 (2003).
- 10) P. Arnold, G. D. Moore, and L. G. Yaffe: JHEP **0111**, 057 (2001); JHEP **0206**, 030 (2002); JHEP **0301**, 030 (2003).

<sup>†</sup> Condensed from the article in hep-ph/0309332. Work done with Guy Moore in McGill University. Submitted to Phys. Rev. Lett.

\* Physics Department, McGill University, Canada

# Power counting in the high density effective theory<sup>†</sup>

T. Schäfer\*

The study of hadronic matter in the regime of high baryon density has led to the theoretical prediction of several new phases of strongly interacting matter, such as color superconducting quark matter and color-flavor locked matter. These phases may be realized in nature in the cores of neutron stars. In order to study this possibility quantitatively we would like to develop a systematic framework that will allow us to determine the exact nature of the phase diagram as a function of the density, temperature, the quark masses, and the lepton chemical potentials, and to compute the low energy properties of these phases.

Such a framework is provided by effective field theory. At high baryon density the relevant degrees of freedom are particle and hole excitations which move with the Fermi velocity  $v$ . Since the momentum  $p \sim v\mu$  is large, typical soft scatterings cannot change the momentum by very much. An effective field theory of particles and holes in QCD<sup>1)</sup> is given by

$$\mathcal{L} = \sum_v \psi_v^\dagger (iv \cdot D) \psi_v - \frac{1}{4} G_{\mu\nu}^a G_{\mu\nu}^a + \dots, \quad (1)$$

where  $v_\mu = (1, \vec{v})$ . The field describes particles and holes with momenta  $p = \mu\vec{v} + l$ , where  $l \ll \mu$ . We will write  $l = l_0 + l_\parallel + l_\perp$  with  $\vec{l}_\parallel = \vec{v}(\vec{l} \cdot \vec{v})$  and  $\vec{l}_\perp = \vec{l} - \vec{l}_\parallel$ . In order to take into account the entire Fermi surface we have to cover the Fermi surface with patches labeled by the local Fermi velocity. The number of such patches is  $n_v \sim (\mu^2/\Lambda_\perp^2)$  where  $\Lambda_\perp \ll \mu$  is the cutoff on the transverse momenta  $l_\perp$ .

Higher order corrections have additional derivatives, or more powers of the fields. At  $O(1/\mu)$  we encounter terms like  $\psi_v^\dagger D_\perp^2 \psi_v$  and  $\psi_v^\dagger \sigma^{\mu\nu} G_{\mu\nu}^\perp \psi_v$ . At  $O(1/\mu^2)$  we find four fermion operators like  $(\psi_{v_1} \Gamma \psi_{v_2})(\psi_{v_3}^\dagger \Gamma' \psi_{v_4}^\dagger) \delta(\sum_i v_i)$ . Four fermion operators describe large angle scatterings that are not accounted for by the leading order, collinear, interaction given in Eq. (1).

In the following we wish to discuss the power counting associated with the high density effective theory.<sup>2,3)</sup> We will count powers of the small momentum  $l$ . Complications arise because not all loop diagrams scale as  $l^4$ . In fermion loops sums over patches and integrals over transverse momenta can combine to give integrals that are proportional to the surface area of the Fermi sphere,

$$\frac{1}{2\pi} \sum_{\vec{v}} \int \frac{d^2 l_\perp}{(2\pi)^2} = \frac{\mu^2}{2\pi^2} \int \frac{d\Omega}{4\pi}. \quad (2)$$

These loop integrals scale as  $l^2$ , not  $l^4$ . In the following we will refer to loops that scale as  $l^2$  as “hard loops” and loops that scale as  $l^4$  as “soft loops”. In order to take this distinction into account we define  $V_k^S$  and  $V_k^H$  to be the number of soft and hard vertices of scaling dimension  $k$ . A vertex is called soft if it contains no fermion lines. In order to determine the  $l$  counting of a general diagram in the effective theory we remove all gluon lines from the graph. We denote the number of connected pieces of the remaining graph by  $N_C$ . Using Euler identities for both the initial and the reduced graph we find that the diagram scales as  $l^\delta$  with

$$\delta = \sum_i [(k-4)V_k^S + (k-2-f_k)V_k^H] + E_Q + 4 - 2N_C. \quad (3)$$

Here,  $f_k$  denotes the number of fermion fields in a hard vertex, and  $E_Q$  is the number of external quark lines. We observe that in general the scaling dimension  $\delta$  increases with the number of higher order vertices, but there are two important exceptions.

First we observe that the number of disconnected fermion loops,  $N_C$ , reduces the power  $\delta$ . Each disconnected loop contains at least one power of the coupling constant,  $g$ , for every soft vertex. As a result, fermion loop insertions in gluon  $n$ -point functions spoil the power counting if the gluon momenta satisfy  $l \sim g\mu$ . This implies that for  $l < g\mu$  the high density effective theory becomes non-perturbative and fermion loops in gluon  $n$ -point functions have to be resummed. This is the familiar hard dense loop (HDL) resummation.<sup>4)</sup>

The second observation is that the power counting for hard vertices is modified by a factor that counts the number of fermion lines in the vertex. Using Eq. (3) it is easy to see that four-fermion operators without extra derivatives are leading order ( $k-2-f_k=0$ ), but terms with more than four fermion fields, or extra derivatives, are suppressed. This result is familiar from the effective field theory analysis of theories with short range interactions.<sup>5)</sup>

## References

- 1) D. K. Hong: Phys. Lett. B **473**, 118 (2000).
- 2) T. Schäfer: Nucl. Phys. A **728**, 251 (2003).
- 3) T. Schäfer: Proc. 2nd Int. Workshop on Quantum Chromodynamics: Theory and Experiment, Conversano, Italy, 2003-6 (2003), eConf C030614:038.
- 4) E. Braaten and R. D. Pisarski: Phys. Rev. D **45**, 1827 (1992).
- 5) R. Shankar: Rev. Mod. Phys. **66**, 129 (1994).

<sup>†</sup> Condensed from the article in Nucl. Phys. A **728**, 251 (2003)

\* North Carolina State University, USA



# Interplay between soft and hard hadronic components for identified hadrons at RHIC

T. Hirano and Y. Nara\*

A vast body of data has already been collected and analyzed during the past few years at the Relativistic Heavy Ion Collider (RHIC) in Brookhaven National Laboratory for the complete understanding of dense QCD matter.<sup>1)</sup> In the collider experiments, perturbative QCD (pQCD) processes become important in intermediate-high  $p_T$  regions. One of the most important new physics in heavy ion collisions at RHIC energies is to study the propagation of (mini-)jets in dense QCD matter. Jet quenching has been proposed<sup>2)</sup> as a possible signal of deconfined nuclear matter, the quark gluon plasma (QGP). Recent data at RHIC indicate that yields for both neutral pions<sup>3,4)</sup> and charged hadrons<sup>5-7)</sup> at high  $p_T$  in central Au + Au collisions are suppressed relative to the  $pp$  scaled by the number of binary collisions or large centrality spectra. However, protons do not seem to be quenched in the moderate  $p_T$  range.<sup>8)</sup>

We investigate the transverse dynamics in Au + Au collisions at  $\sqrt{s_{NN}} = 200$  GeV by emphasizing upon the interplay between soft and hard hadronic components through  $p_T$  spectra for identified hadrons. From hydrodynamics combined with traversing mini-jets which go through jet quenching in the hot medium, we calculate the interactions of hard jets with the soft hydrodynamic components (the hydro+jet model).<sup>9)</sup> We obtain the  $p_T$  spectra for pions, kaons, and protons from hydrodynamic and minijet contributions. Both soft (hydro) and hard (minijets) components are found to be important for the hadron spectra in the transverse momentum of the range around  $2 \lesssim p_T \lesssim 5$  GeV/c, depending on the hadron mass. We can define the crossing point of transverse momentum  $p_{T,cross}$  at which the yield from the soft part is identical to that from the hard part.  $p_{T,cross}$  increases with the mass of particles because of the effect of radial flow. In central collisions, we find  $p_{T,cross} \sim 1.8, 2.7,$  and  $3.7$  GeV/c for pions, kaons, and protons, respectively. Figure 1 shows the nuclear modification factors

$$R_{AA} = \left( \frac{dN^{A+A}}{dp_T dy} \right) / \left( N_{coll} \frac{dN^{p+p}}{dp_T dy} \right), \quad (1)$$

for pions, kaons, and protons, respectively, in Au + Au collisions at RHIC for impact parameters  $b = 2.0, 5.5,$  and  $7.2$  fm. We find that protons are not suppressed ( $R_{AA} \sim 1$ ) in the momentum range of  $1.5 < p_T < 2.5$  GeV/c. Pions, on the contrary, are largely suppressed for all momentum range. Since the crossing point  $p_{T,cross}$  depends on the hadronic species,  $R_{AA}$  only for pions reflects the jet quenching effect in this

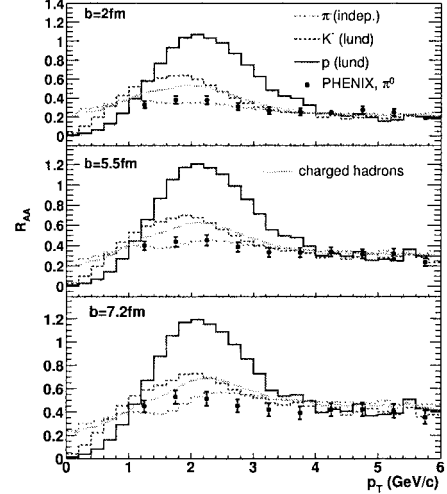


Fig. 1. The nuclear modification factors  $R_{AA}$  for  $\pi^-$  (short dashed),  $K^-$  (long dashed), and  $p$  (solid).  $R_{AA}$  for charged hadrons is also shown in dotted lines. Data are obtained by the PHENIX Collaboration.<sup>4)</sup>

momentum region.  $p_{T,cross} \sim 3.7$  GeV/c for protons leads to  $R_{AA} \sim 1$  due to the soft component which is pushed from the low to high  $p_T$  regions by radial flow. This does not mean the absence of jet quenching for protons. The interplay between radial flow and jet quenching can give an interpretation of recent puzzling data for proton nuclear modification factors.

## References

- 1) Proc. 16th Int. Conf. on Ultrarelativistic Nucleus-Nucleus Collisions, Quark Matter 2002: Nucl. Phys. A **715** (2003).
- 2) M. Gyulassy and M. Plümer: Phys. Lett. B **243**, 432 (1990); X.-N. Wang and M. Gyulassy: Phys. Rev. Lett. **68**, 1480 (1992); M. Gyulassy and X.-N. Wang: Nucl. Phys. B **420**, 583 (1994); X.-N. Wang, M. Gyulassy, and M. Plümer: Phys. Rev. D **51**, 3436 (1995).
- 3) PHENIX Collaboration, K. Adcox et al.: Phys. Rev. Lett. **88**, 022301 (2002).
- 4) PHENIX Collaboration, S. S. Adler et al.: Phys. Rev. Lett. **91**, 072301 (2003).
- 5) STAR Collaboration, C. Adler et al.: Phys. Rev. Lett. **89**, 202301 (2002).
- 6) STAR Collaboration, J. Adams et al.: nucl-ex/0305015.
- 7) PHENIX Collaboration, K. Adcox et al.: Phys. Lett. B **561**, 82 (2003).
- 8) PHENIX Collaboration, S. S. Adler et al.: nucl-ex/0305036.
- 9) T. Hirano and Y. Nara: Phys. Rev. C **66**, 041901(R) (2002); Phys. Rev. Lett. **91**, 082301 (2003).

\* Department of Physics, University of Arizona, USA

# Hadronization at RHIC: Recombination *vs.* fragmentation?<sup>†</sup>

S. A. Bass,<sup>\*1</sup> R. J. Fries,<sup>\*2</sup> B. Müller,<sup>\*1</sup> and C. Nonaka<sup>\*1</sup>

Data from the Relativistic Heavy Ion Collider (RHIC) have shown a strong nuclear suppression of the pion yield at transverse momenta larger than 2 GeV/c in central Au+Au collisions, compared with  $p+p$  interactions.<sup>1,2)</sup> The emission of protons and antiprotons does not appear to be similarly suppressed, and the  $p/\pi^+$  ratio reaches or even exceeds unity for transverse momenta above 2 GeV/c. These results lack a consistent explanation in the standard picture of hadron production at high transverse momentum, which assumes that hadrons are created by the fragmentation of energetic partons. Whereas the observed suppression of the pion yield is attributed to the energy loss of partons during their propagation through the hot and dense matter created in the nuclear collision — a phenomenon commonly referred to as jet quenching<sup>3)</sup> — the absence of a similar effect in the proton spectrum is puzzling.<sup>4)</sup>

In Ref. 5 we have shown that hadron production at momenta of a few GeV/c in an environment with a high density of partons occurs by recombination, rather than fragmentation, of partons. Recombination always dominates over fragmentation for an exponentially falling parton spectrum, but fragmentation wins out eventually, when the spectrum takes the form of a power law.

Starting point of our calculation is the assumption that the constituent quark transverse momentum distribution at hadronization is given by the superposition of a thermal distribution for low and intermediate momenta and a pQCD based power-law contribution for large transverse momenta.

The normalization of the thermal part of the spectrum is adjusted to fit the measured inclusive spectrum of charged hadrons from PHENIX, as shown in the upper frame of Fig. 1. The parameters of the pQCD contribution are fixed by a minijet calculation.<sup>5)</sup>

The lower frame of Fig. 1 shows our prediction for the  $p/\pi^+$  ratio. The rapid drop of its value in the range 4–5 GeV/c is an unambiguous prediction of our model, due to the onset of parton fragmentation. Experiments at RHIC have not yet been able to probe this  $P_T$  range, because the identification of protons has not been feasible beyond 4 GeV/c. The identification of hyperons is possible to higher  $P_T$ , and indications of a rapid drop in the  $\Lambda/K_s^0$  ratio have been found.<sup>2)</sup>

We find that the competition between recombination and fragmentation of partons can explain several

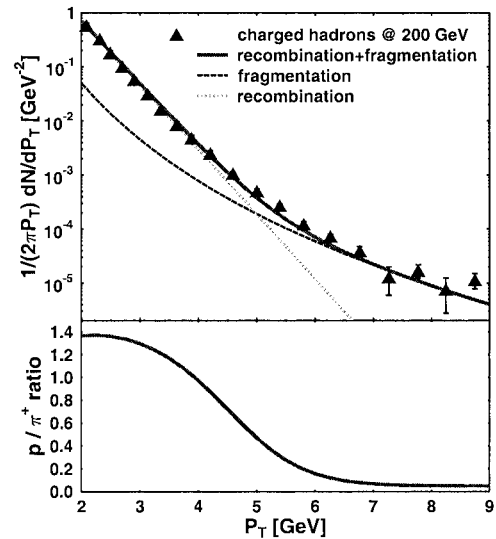


Fig. 1. Top: inclusive  $P_T$  spectrum of charged hadrons in central Au + Au collisions at  $\sqrt{s_{NN}} = 200$  GeV. Bottom: ratio of protons to  $\pi^+$  as a function of  $P_T$ .

of the surprising features of the published data. In particular, the proton excess at intermediate  $P_T$ , the different nuclear suppression observed in pion and proton spectra, and the different saturation thresholds in the elliptic flow, are easily explained. We predict that all baryon spectra will exhibit a rapid transition around 5 GeV/c to a region dominated by parton fragmentation. Finally, our scenario requires the assumption of a thermalized partonic phase characterized by an exponential momentum spectrum. Such a phase may be appropriately called a quark-gluon plasma.

## References

- 1) PHENIX Collaboration, K. Adcox et al.: Phys. Rev. Lett. **88**, 022301 (2002); Phys. Rev. Lett. **88**, 242301 (2002); Phys. Rev. Lett. **89**, 092302 (2002).
- 2) STAR Collaboration, C. Adler et al.: Phys. Rev. Lett. **86**, 4778 (2001); Phys. Rev. Lett. **89**, 092301 (2002); nucl-ex/0210033.
- 3) M. Gyulassy and X. Wang: Nucl. Phys. B **420**, 583 (1994); R. Baier et al.: Nucl. Phys. B **484**, 265 (1997).
- 4) PHENIX Collaboration, J. Velkovska: J. Phys. G **30**, S 151 (2004).
- 5) R. J. Fries, B. Müller, C. Nonaka, and S. A. Bass: Phys. Rev. Lett. **90**, 202303 (2003).

<sup>†</sup> Condensed from the article in Phys. Rev. Lett. **90**, 202303 (2003)

<sup>\*1</sup> Department of Physics, Duke University, USA

<sup>\*2</sup> Department of Physics, University of Minnesota, USA

## New signature of the QCD critical point

Y. Hatta<sup>\*1</sup> and M. A. Stephanov<sup>\*2</sup>

Recently, there has been considerable interest, both theoretically and experimentally, in the critical point considered to exist in the phase diagram of QCD at finite temperature and baryon chemical potential. The first proposal of observables for discovering the critical point in experiments is given in Ref. 1. It was predicted that enormous fluctuations of the sigma meson field associated with the second order phase transition could be reflected in the event-by-event fluctuation of pion observables through the pion-sigma coupling.

Here we propose a new observable<sup>2)</sup> for discovering the critical point; the event-by-event fluctuation of the *net proton number*, *i.e.*, the number of protons minus the number of antiprotons observed. Our starting point is the fact that the baryon number susceptibility

$$\chi_B = \frac{1}{VT} \langle (\delta B)^2 \rangle, \quad (1)$$

where  $V$  and  $T$  are the volume and the temperature, respectively, and  $\delta B$  is the baryon number measured relative to the equilibrium value, diverges at the critical point. If we could measure all the baryons in the experiments, the event-by-event fluctuation of the baryon number would be a signature of the end-point. Unfortunately, it is very difficult to detect the neutrons in ultrarelativistic heavy-ion collision experiments, which makes the measurement of the baryon number fluctuation virtually impossible. However, we argue that due to the peculiar nature of the critical point, the proton number fluctuation alone correctly reflects the divergence of  $\chi_B$ .

A simple symmetry argument shows that, in the presence of isospin symmetry, the isospin number susceptibility

$$\chi_I = \frac{1}{VT} \langle (\delta I)^2 \rangle, \quad (2)$$

is finite at the critical point. One can also show that the electric charge susceptibility is divergent and the ratio of the singular parts of the susceptibilities is

$$\chi_B : \chi_I : \chi_Q = 4 : 0 : 1. \quad (3)$$

We wish to relate the susceptibilities  $\chi_B$ ,  $\chi_I$  and  $\chi_Q$  to the observable particle number fluctuations. For simplicity, we shall limit our discussion by considering only protons, neutrons and pions. In hadron language, the susceptibilities may be written as

$$\chi_B = \frac{1}{VT} \langle (\delta N_{p-\bar{p}} + \delta N_{n-\bar{n}})^2 \rangle,$$

$$\chi_I = \frac{1}{VT} \left\langle \left( \frac{1}{2} \delta N_{p-\bar{p}} - \frac{1}{2} \delta N_{n-\bar{n}} + \delta N_{\pi^+ - \pi^-} \right)^2 \right\rangle,$$

$$\chi_Q = \frac{1}{VT} \langle (\delta N_{p-\bar{p}} + \delta N_{\pi^+ - \pi^-})^2 \rangle, \quad (4)$$

where we introduced the notation  $N_{p-\bar{p}} \equiv N_p - N_{\bar{p}}$  for the net proton number fluctuation. Similar notations are used for neutrons and pions.

Observing that the singularity in the susceptibilities is caused by the exchange of the sigma meson which is an isospin singlet, one can single out the net contribution to the singular part:

$$\chi_B = \frac{4}{VT} \langle \delta N_{p-\bar{p}} \delta N_{p-\bar{p}} \rangle,$$

$$\chi_I = 0,$$

$$\chi_Q = \frac{1}{VT} \langle \delta N_{p-\bar{p}} \delta N_{p-\bar{p}} \rangle. \quad (5)$$

Namely, the singular part of the charge fluctuation comes from the protons. The pions do not contribute to the singular part because of a cancellation. We see also that the proton number fluctuation completely reflects the singularity of the baryon number susceptibility, which justifies its use as a sensible probe for the QCD critical point.

A simple estimate of the net proton number fluctuation is given by calculating the correlator

$$\langle \delta n_{\mathbf{p}} \delta n_{\mathbf{k}} \rangle, \quad (6)$$

where  $n_{\mathbf{p}}$  is the net proton number in the momentum bin labeled by the value  $\mathbf{p}$ . The main feature of such calculations<sup>2)</sup> is that the singularity coming from the exchange of the sigma meson is enhanced by the proton loop effect. Thus, if the critical density of the end-point is large, as suggested by several model calculations and lattice simulations, our effect could be very large. Experimentally, separating protons and measuring proton fluctuations is a feasible task in the RHIC as well as in the SPS detectors. A direct measurement of the proton number fluctuation as a function of the  $\sqrt{s}$  of the collision is both feasible and is less affected by other effects. The correlation of such a measurement with other proposed signatures (such as  $p_t$  fluctuations<sup>1)</sup>) would lead to the discovery of the QCD critical point.

### References

- 1) M. A. Stephanov, K. Rajagopal, and E. V. Shuryak: Phys. Rev. Lett. **81**, 4816 (1998).
- 2) Y. Hatta and M. A. Stephanov: Phys. Rev. Lett. **91**, 102003 (2003).

<sup>\*1</sup> Department of Physics, Kyoto University

<sup>\*2</sup> Department of Physics, University of Illinois, USA

# Pseudogap of color superconductivity<sup>†</sup>

M. Kitazawa,<sup>\*1</sup> T. Koide,<sup>\*2</sup> T. Kunihiro,<sup>\*3</sup> and Y. Nemoto

Recently considerable attention has been being paid to color superconductivity (CS) at large chemical potential ( $\mu$ ) but with relatively low temperature ( $T$ ) of QCD. At relatively low density, the strong coupling nature of QCD may make the so-called Ginzburg region so wide that precursory fluctuations of a pair field may give rise to physically significant effects even above the critical temperature ( $T_c$ ).<sup>1)</sup> The existence of the large fluctuations suggests that CS may share some basic properties with high- $T_c$  superconductivity (HTSC). One of the characteristic phenomena of HTSC is the existence of a pseudogap, *i.e.*, the anomalous depression of the density of states (DOS) as a function of fermion energy  $\omega$  around a Fermi surface above  $T_c$ . We show that the pseudogap of the quark density of states is actually formed in hot quark matter as a precursory phenomenon of CS based on a low-energy effective theory, the Nambu-Jona-Lasinio (NJL) model.

DOS is calculated from the spectral function of a single quark. A fluctuating diquark pair field develops a collective mode at  $T$  above but in the vicinity of  $T_c$ .<sup>1)</sup> Our point in this work is that the soft mode contributes to the self-energy of the quark field, thereby it can markedly modify the spectral function and DOS resulting a pseudogap.

A numerical calculation of the self-energy of a quark  $\Sigma_-$  shows that as momentum  $k$  varies from  $k_F$ , the peak of  $|\text{Im}\Sigma_-|$  at  $\omega \approx 0$  moves along  $\omega \approx -k + \mu$ . This indicates that quasiparticles with this energy are dumped modes.  $\text{Im}\Sigma_-$  describes a decay process of a quark to a hole and a diquark,  $q \rightarrow h + (qq)$ , where the hole is on-shell with free dispersion relation  $\omega_h = \mu - |\mathbf{k}_h|$ . The essential point for pseudogap formation is that the above process is enhanced when the diquark  $(qq)$  forms a collective mode; the diquark soft mode  $(qq)_{\text{soft}}$  has a prominent strength at negligible energy  $\omega_s$  and momentum  $\mathbf{k}_s$  near  $T_c$ . Owing to the energy-momentum conservation, the energy momentum of the decaying particle  $(\omega_p, \mathbf{k}_p)$  should satisfy  $\omega_p + \omega_h = \omega_s \simeq 0$  and  $\mathbf{k}_p + \mathbf{k}_h = \mathbf{k}_s \simeq 0$ . This indicates that when the decaying particle has almost the same energy as a free quark,  $|\text{Im}\Sigma_-(\mathbf{k}, \omega)|$  is largest.

The spectral function is shown in Fig. 1. One can see two families of peaks around  $\omega = \omega_-(k) \approx k - \mu$  and  $\omega = -k - \mu$ , which correspond to the quasiparticle peaks of the quarks and anti-quarks, respectively. A notable point is that the quasiparticle peak has a clear

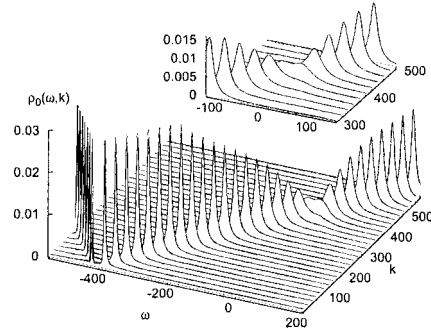


Fig. 1. Spectral function at  $\mu = 400$  MeV and  $\varepsilon = 0.01$ .

depression around  $\omega = 0$ , *i.e.*, the Fermi energy. The mechanism of the depression is easily understood in terms of the characteristic properties of the self-energy mentioned above.

Figure 2 shows DOS at  $\mu = 400$  MeV and various reduced temperatures  $\varepsilon = (T - T_c)/T_c$ . As anticipated, one can see a significant depression of DOS, *i.e.*, the pseudogap, around Fermi energy  $\omega = 0$ . One sees that the smaller  $\varepsilon$ , the more significant the rate of depression. The clear pseudogap structure survives even at  $\varepsilon = 0.05$ . One may thus conclude that there is a pseudogap region within the QGP phase above  $T_c$  up to  $T = (1.05 \sim 1.1)T_c$  at  $\mu = 400$  MeV, for instance.

Our result obtained for a three-dimensional system tells us that a considerable pseudogap can be formed without the help of the low dimensionality as in HTSC and that pseudogap phenomena in general may be universal in any strong coupling superconductivity.

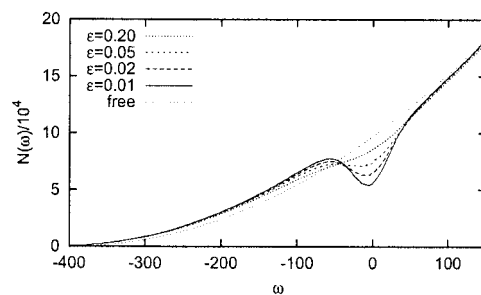


Fig. 2. Density of states at  $\mu = 400$  MeV and various  $\varepsilon$  values. The dotted line shows these of free quarks.

## References

- 1) M. Kitazawa, T. Koide, T. Kunihiro, and Y. Nemoto: Phys. Rev. D **65**, 091504(R) (2002).

<sup>†</sup> Condensed from the article in arXiv:hep-ph/0309026

<sup>\*1</sup> Department of Physics, Kyoto University

<sup>\*2</sup> Institut für Theoretische Physik, J. W. Goethe-Universität, Germany

<sup>\*3</sup> Yukawa Institute for Theoretical Physics, Kyoto University

## Color ferromagnetic phase at finite quark density

M. Ohtani, A. Iwazaki,<sup>\*1</sup> O. Morimatsu,<sup>\*2</sup> and T. Nishikawa<sup>\*2</sup>

A phase diagram of quark and hadronic matter is considered to have a rich structure for finite temperature and density. The restoration of chiral symmetry and deconfinement transition have drawn much attention for understanding systems with strong interaction. Color superconductors are a topic of great interest and are expected to be realized for high-density and low-temperature regions. However, using only indirect information by astronomical observations, we must speculate on color superconductors which may exist in compact stars. In heavy ion collisions, it is difficult to create sufficiently dense quark matter to confirm its signals. Accordingly, phases and their properties of quark/hadrons for finite density are still open to discussion, though the deeply bound kaonic nucleus is promising for studying high-density matter.<sup>1)</sup> In view of the situation, we report here the realizability of a new phase — color ferromagnetic phase — in cold dense quark matter.

In non-Abelian gauge theory, a perturbative vacuum is known to be unstable against condensation of a color magnetic field.<sup>2)</sup> In fact, the one-loop effective potential implies spontaneous generation of the color magnetic field. The color magnetic field can be set to be in the maximal Abelian subalgebra by a gauge transformation and off-diagonal components of a gluon can be treated as charged matter with spin 1. Then, the energy of the transverse motion of an off-diagonal gluon is quantized in Landau levels. However, the energy of the gluonic state in the lowest Landau level has an imaginary part and hence the system with a spontaneous color magnetic field is found to be unstable.<sup>3)</sup> Although the physical significance of this instability for the real nonperturbative vacuum is not understood yet, it has been recently shown<sup>4,5)</sup> that the color ferromagnetic state becomes stable by forming a specific configuration of off-diagonal gluons in quark matter.

Here we note that this state is analogous to the quantum Hall state (QHS) of electrons because both of them are accompanied by the magnetic field and are effectively reduced to a two-dimensional system. The dimensional reduction of the color ferromagnetic state is justified from the fact that the most unstable mode is spatially uniform along the color magnetic field and only this mode is relevant for the stability of the state. Therefore, to analyze the color ferromagnetic state, we adopt Chern-Simons theory which is used to study the quantum Hall system of electrons.<sup>6)</sup>

In the Chern-Simons theory, an elementary particle is expressed by composite fields: a bosonized matter

field and the Chern-Simons field. The Chern-Simons field is introduced to carry a property of the particle statistics: the exchange phase of particle permutation is reproduced by the Chern-Simons flux. In our case, off-diagonal gluons are expressed by composite fields.

In the case of QHS of electrons, Chern-Simons flux cancels out the imposed magnetic field, so that total flux on the bosonized electron vanishes. In the same way, we can consider “the quantum Hall state of off-diagonal gluons”, where the Chern-Simons flux is set to be equal to the color magnetic field. We showed that the color ferromagnetic state along with the QHS of off-diagonal gluons is stable in cold dense quark matter. We predict that this new phase lies between the hadronic phase and color superconducting phase for low-temperature regions.

Furthermore, we consider a vortex excitation on the QHS associated with the color ferromagnetic phase.<sup>7)</sup> For the electron system, quasi-particles with fractional charge are excited on the QHS<sup>8)</sup> and they are described as vortex excitations in the Chern-Simons formalism. The excitation energy is correlated with the plateau width of Hall resistance and the stability of the state. Similarly, the vortex excitation in the QHS of gluons plays an important role in the color ferromagnetic phase. We solve the equations for a vortex configuration under the color magnetic field and estimate the excitation energy of the vortex. We find that the vortex energy decreases as quark density is diminished. This indicates that the color ferromagnetic state transforms to the hadronic phase with vortex excitations for lower density.

In summary, we emphasize the possibility of a new phase, the color ferromagnetic state along with QHS of the off-diagonal gluon for a high-density region, which will give a new clue for understanding the properties of dense quark matter.

### References

- 1) Y. Akaishi, A. Doté, and T. Yamazaki: Prog. Theor. Phys. Suppl. No. 149, 221 (2003); M. Iwasaki et al.: nucl-ex/0310018.
- 2) G. K. Savvidy: Phys. Lett. B **71**, 133 (1977).
- 3) N. K. Nielsen and P. Olesen: Nucl. Phys. B **144**, 376 (1978); Phys. Lett. B **79**, 304 (1978).
- 4) A. Iwazaki, O. Morimatsu, T. Nishikawa, and M. Ohtani: Phys. Lett. B **579**, 347 (2004).
- 5) A. Iwazaki and O. Morimatsu: Phys. Lett. B **571**, 61 (2003).
- 6) S. C. Zhang, T. H. Hansson, and S. Kivelson: Phys. Rev. Lett. **62**, 82 (1989).
- 7) A. Iwazaki, O. Morimatsu, T. Nishikawa, and M. Ohtani: in preparation.
- 8) R. B. Laughlin: Phys. Rev. Lett. **50**, 1395 (1983).

<sup>\*1</sup> Department of Physics, Nishogakusha University

<sup>\*2</sup> Institute of Particle and Nuclear Studies, High Energy Accelerator Research Organization (KEK)

# Kinetic equation for $\phi^4$ theory with generalized Kadanoff-Baym ansatz

T. Ikeda

Recently, quantum field theories in and out of thermal equilibrium have been extensively studied, motivated by heavy-ion collision experiments ongoing at RHIC and upcoming at LHC, (p)reheating in early universe and so on. We investigate the decay of a single particle excitation of  $\phi^4$  theory whose Lagrangian is  $(\partial_\mu\phi)^2/2 - g^2\phi^4$ , in 3 + 1 dimensions and the spatially homogeneous case, using kinetic equations with and without memory effects.

Nonequilibrium properties are often studied on the basis of Boltzmann-like equations. Those equations, however, are not applicable to strongly correlated plasmas. Kadanoff-Baym (KB) equations for two-point Green's functions are useful for studying correlated plasmas, which are usually difficult to solve directly due to two-time correlation. Therefore, it is easier to analyze kinetic equations for Wigner distribution function  $N$  which is derived from KB equations in the equal time limit. When deriving kinetic equations, we encounter the reconstruction problem: How can two-point Green's functions be expressed as a function of  $N$ ? While the simplest solution is the Kadanoff-Baym (KB) ansatz which cannot explain memory effects, we have a more general solution, the generalized Kadanoff-Baym (GKB) ansatz which can take into account such effects properly.<sup>1)</sup> Memory effects are expected to play an important role in correlated systems.

Within the 3-loop level for the two-particle irreducible (2PI) effective action, we obtain two different self-energies.<sup>2)</sup> The leading order one contributes to the thermal mass which is obtained by solving the gap equation self-consistently. Self-energies in the next-to-leading order (NLO) correspond to the scattering processes, leading to damping of a single particle excitation.

With the above self-energies and the quasiparticle approximation for the spectral function, we obtained kinetic equations in time representation:

$$\partial_t \delta N(p, t) = -2\gamma(p, t)\delta N(p, t), \quad (1)$$

for the KB ansatz and

$$\partial_t \delta N(p, t) = -2\gamma(p, t)\delta N(p, 0) - 2 \int_0^t dz_0 \gamma(p, z_0 - t) \partial_{z_0} \delta N(p, z_0), \quad (2)$$

for the GKB ansatz.<sup>3)</sup> Here,  $\delta N$  is a deviation from the thermal distribution function, and  $\gamma(p, t)$  is a time-dependent damping rate which can be calculated using the gap of NLO self-energies.

Figure 1 shows the numerical results of  $\delta N$  as a function of time. For weak coupling  $g = 0.1$ , dampings of excitation in KB and GKB ansatz are in good agreement, and are both exponential. In this case, there is no memory effect due to the separation of scales: the relaxation time is much larger than the time scale at which oscillation of  $\gamma(t)$  ends. For moderately large coupling  $g = 1.0$ , memory effects make the relaxation time faster, as shown in the middle panel. For the strongest coupling  $g = 1.6$  in our calculation,  $\delta N$  oscillates around zero and an amplitude of the oscillation damps slower than the case without memory effects.<sup>3)</sup> Thus, memory effects influence the decay of the excitation differently as the coupling strength changes.

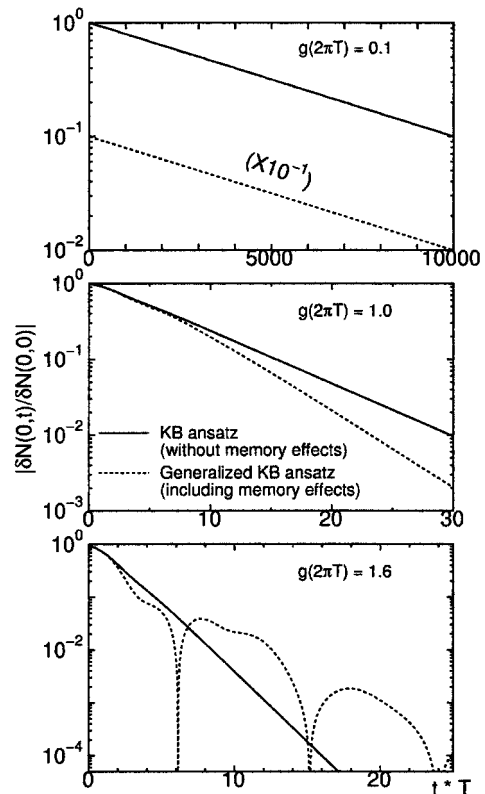


Fig. 1. Deviations from thermal distribution for  $p = 0$  with KB and generalized KB ansatz are plotted as a function of time for three values of coupling constant.

## References

- 1) P. Lipavsky, V. Spicka, and B. Velicky: Phys. Rev. B **34**, 6933 (1986).
- 2) J. Berges and J. Cox: Phys. Lett. B **517**, 369 (2001).
- 3) T. Ikeda: hep-ph/0401045 (accepted for publication in Phys. Rev. D).

# Charge symmetry breaking in few-nucleon systems<sup>†</sup>

U. van Kolck\*

Two-flavor QCD is nearly invariant under the SU(2) group of isospin transformations. Charge symmetry is a rotation of  $\pi$  around the  $y$  axis in isospin space, which is broken by the difference in up-down quark masses and by electromagnetic effects.

These sources of CSB manifest themselves in various guises in the low-energy effective theory of QCD. One of the most important consequences is the proton-neutron mass splitting  $\Delta m_N = m_p - m_n = -1.3$  MeV, which receives contributions from both quark-mass difference —denoted  $\delta m_N$ — and electromagnetism —denoted  $\bar{\delta} m_N$ . Although there are several estimates of these two contributions, there is no firm experimental information on their sizes: at least one other suitable CSB observable is needed to separate them.

One can show<sup>1)</sup> that the approximate chiral symmetry of QCD implies that there are two sets of pion-nucleon interactions with strengths fixed by  $\delta m_N$  and  $\bar{\delta} m_N$ , respectively. In Ref. 2 it was suggested that these interactions would give important contributions to the front-back asymmetry in the reaction  $pn \rightarrow d\pi^0$  near threshold. Assuming  $\bar{\delta} m_N > 0$  as in most models, it was predicted that these contributions would be 1–2 times larger, but in the opposite direction, than the sum of other, more conventional mechanisms. This

prediction has recently been confirmed at TRIUMF.<sup>3)</sup>

An estimate of the contributions from these interactions to the CSB reaction  $dd \rightarrow \alpha\pi^0$  near threshold suggested that it could be observed at IUCF. Indeed, for the first time an unambiguous signal was seen above background, resulting in a cross-section of about 10 pb.<sup>4)</sup> A group of theorists including the present author is now working on a more accurate calculation.<sup>5)</sup>

Given their importance in pion production, it is natural to investigate the effect of these interactions in nuclear forces. The corresponding two-pion exchange two-nucleon potential is the dominant non-short-range CSB interaction, and it has been calculated in Ref. 6. Its effects on CSB observables are small.

## References

- 1) U. van Kolck: *Few-Body Systems Suppl.* 9, 444 (1995).
- 2) U. van Kolck, J. A. Niskanen, and G. A. Miller: *Phys. Lett. B* **493**, 65 (2000).
- 3) A. K. Opper et al.: *Rhys. Rev. Lett.* **91**, 212302 (2003).
- 4) E. J. Stephenson et al.: *Phys. Rev. Lett.* **91**, 142302 (2003).
- 5) A. Gårdestig et al.: to appear in *Phys. Rev. C*, nucl-th/0402021.
- 6) J. L. Friar, U. van Kolck, G. L. Payne, and S. A. Coon: *Phys. Rev. C* **68**, 024003 (2003).

<sup>†</sup> This research was supported in part by the DOE and by the Alfred P. Sloan Foundation

\* University of Arizona, USA

# Lattice chiral symmetry with hopping interactions<sup>†</sup>

T. Sugihara

In contrast with the great success of the lattice gauge theory, lattice fermions remain a long-standing problem. Naive discretization causes the species doubling problem.<sup>1)</sup> The situation does not change regardless of how the lattice spacing is reduced as long as the space-time derivative is modeled as a naive difference. Many attempts have been made to resolve the doubling problem.<sup>1-6)</sup> Wilson removed doublers at low energy by introducing an interaction that mixes left- and right-handed fermions.<sup>1)</sup> However, unwanted degeneracy persists at high energy and chiral symmetry is explicitly broken. To fix these problems, Kaplan modified Wilson's fermion with an extra dimension<sup>4)</sup> and succeeded in realizing approximate chiral symmetry. However, the cost of numerical calculations based on it is high. If we can develop a method of performing such calculations without an extra dimension, the calculation time decreases largely and a deeper understanding of quantum field theory becomes possible.

The lattice fermion has another serious problem. The lattice fermion propagator deviates from the continuum one even if doublers are removed with existing techniques such as Kaplan's fermion. We need to modify the discretized propagator somehow so that it will

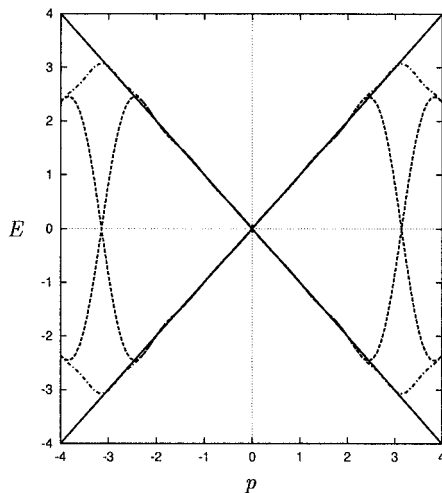


Fig. 1. The solid line plots the correct energy  $\pm p$  from the continuum theory. The dashed line plots the function  $\pm s(p)$  modified with the Lanczos factor. The dot-dashed line plots the function  $\pm k(p)$  modified with the Lanczos factor. The function  $\pm k(p)$  almost agrees with  $\pm p$  in the fundamental region  $|p| \leq \pi$  except for a small deviation around momentum  $|p| \sim 2.3$ . The dispersion relation of the continuum theory has been reproduced approximately.

be as close as possible to the continuum propagator.

In this work, based on a Hamiltonian formalism, we introduce ultralocal hopping interactions to remove doublers and improve the momentum dependence of fermion energy in the (1 + 1)-dimensional free Dirac fermion (see Fig. 1). On the basis of the continuum theory, we know the correct momentum dependence of the energy. We start from momentum space and return to real space via discrete Fourier transform. Approximate chiral symmetry is realized at low energy (see Fig. 2). Explicit breaking of chiral symmetry has been compressed to high energy. In future works, it should be precisely checked whether the insertion of gauge interactions affects chiral properties.

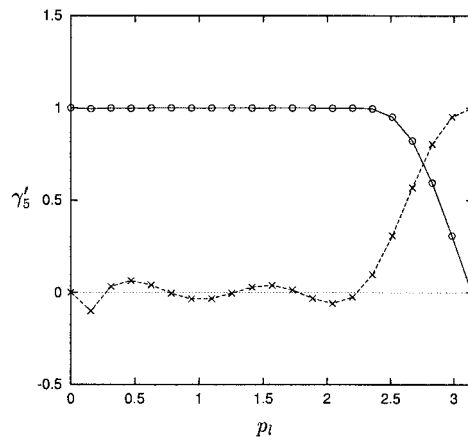


Fig. 2. The matrix elements of  $\gamma'_5$  are plotted as functions of momentum  $p_l$  modified with the Lanczos factor. The functions are plotted on the right-half plane of momentum space  $p_l \geq 0$ . The circles are plots of the diagonal (1,1) element of  $\gamma'_5$ . The crosses are plots of the negative off-diagonal (1,2) element of  $\gamma'_5$ . The solid and dashed lines are plotted as visualguides. The Dirac fermion has approximate chiral symmetry because  $\gamma'_5$  almost commutes with the Hamiltonian at low energy.

## References

- 1) K. G. Wilson: in *New Phenomena in Subnuclear Physics*, edited by A. Zichichi (Plenum, New York, 1977) p.13.
- 2) J. Kogut and L. Susskind: *Phys. Rev. D* **11**, 395 (1975).
- 3) S. D. Drell, M. Weinstein, and S. Yankielowicz: *Phys. Rev. D* **14**, 487 (1976).
- 4) D. B. Kaplan: *Phys. Lett. B* **288**, 342 (1992); M. F. Golterman, K. Jansen, and D. B. Kaplan: *Phys. Lett. B* **301**, 219 (1993).
- 5) H. Neuberger: *Phys. Lett. B* **417**, 141 (1998); *Phys. Lett. B* **427**, 353 (1998).
- 6) M. Lüscher: *Phys. Lett. B* **428**, 342 (1998).

<sup>†</sup> Condensed from the article in *Phys. Rev. D* **68**, 034502 (2003)



# Comparison of matrix model and lattice data for the QCD Dirac operator at nonzero chemical potential

G. Akemann\*<sup>1</sup> and T. Wettig\*<sup>2</sup>

QCD at nonzero density is important in a variety of physical situations, such as relativistic heavy-ion collisions or neutron stars. While considerable progress has recently been made in several directions, Monte Carlo simulations at real chemical potential  $\mu > 0$  are not feasible at large volumes because the weight function is complex. To obtain a better theoretical understanding of this situation, we have studied the (complex) eigenvalues of the QCD Dirac operator in a particular random matrix model and on the lattice. The model<sup>1)</sup> is defined by the partition function

$$Z_\nu(\tau; \{m_f\}) = \int_{\mathbb{C}} \prod_{j=1}^N dz_j dz_j^* |z_j|^{2|\nu|+1} \prod_{f=1}^{N_f} (z_j^2 + m_f^2) \times e^{-\frac{N}{1-\tau^2} [ |z_j|^2 - \frac{\tau}{2} (z_j^2 + z_j^{*2}) ]} \prod_{k>l}^N |z_k^2 - z_l^2|^2 \quad (1)$$

given in terms of  $N$  eigenvalues  $z_j$ . Here, the  $m_f$  are quark masses,  $\nu$  is the topological charge, and  $\tau$  determines the degree of nonhermiticity. We have  $\mu^2 = 1 - \tau^2$  by comparing Eq. (1) with the matrix model of Ref. 2. From Eq. (1) analytical results can be derived for the distribution of the small Dirac eigenvalues. Two regimes have to be distinguished. In the region of weak nonhermiticity, we have  $\mu^2 N \equiv \alpha^2 \sim \mathcal{O}(1)$  and obtain for  $N \rightarrow \infty$  and  $N_f = 0$ <sup>1)</sup>

$$\rho_{\text{weak}}(\xi) = \frac{\sqrt{\pi\alpha^2}}{\text{erf}(\alpha)} |\xi| \exp\left[-\frac{(\Im m \xi)^2}{\alpha^2}\right] \times \int_0^1 dt e^{-\alpha^2 t} J_{|\nu|}(\sqrt{t}\xi) J_{|\nu|}(\sqrt{t}\xi^*), \quad (2)$$

where the eigenvalues have been rescaled according to  $\xi = \sqrt{2}Nz$ . In the region of strong nonhermiticity, we have  $\mu \sim \mathcal{O}(1)$  and obtain<sup>1)</sup>

$$\rho_{\text{strong}}(\xi) = \sqrt{2\pi} |\xi| \exp(-|\xi|^2) I_{|\nu|}(|\xi|^2) \quad (3)$$

with rescaled eigenvalues  $\xi = \sqrt{N/(1-\tau^2)} z$ .

The conjecture is that the model of Eq. (1) is in the same universality class as QCD, in which case Eqs. (2) and (3) should agree with lattice data. We have tested this conjecture by computing large ensembles of spectra for the staggered Dirac operator at several values of  $\mu$  and lattice volume  $V$ . We worked at  $N_f = 0$

and  $\beta = 5.0$ , see Ref. 3 for the justification of these choices. We effectively have  $\nu = 0$  because the staggered Dirac operator does not have exact zero modes at strong coupling. Some of our results are shown in Figs. 1 and 2 (the histograms represent lattice data, the solid curves the analytical predictions). Note that the data have been rescaled by a factor proportional to the average level spacing in the same way as in Eqs. (2) and (3). We observe good agreement between theory and lattice data in both regimes. This confirms the existence of the two different scaling limits and indicates that the model of Eq. (1) may be capable of describing QCD. Recent calculations<sup>4)</sup> for the model of Ref. 2 at weak nonhermiticity found small numerical differences between the two models which deserve further study.

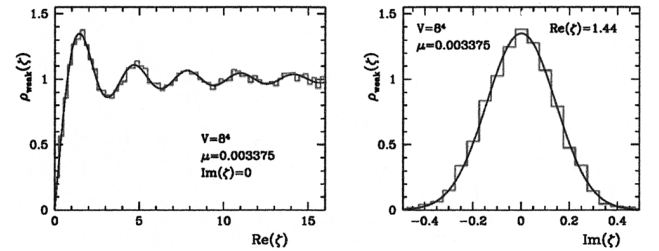


Fig. 1. Density of small Dirac eigenvalues in the regime of weak nonhermiticity, cut along the real axis (left) and parallel to the imaginary axis (right).

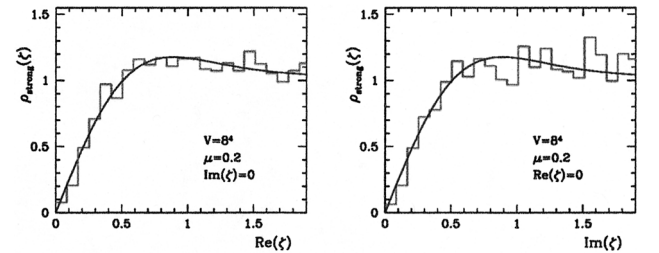


Fig. 2. Density of small Dirac eigenvalues in the regime of strong nonhermiticity, cut along the real (left) and imaginary (right) axes.

## References

- 1) G. Akemann: Phys. Rev. Lett. **89**, 072002 (2002); J. Phys. A **36**, 3363 (2003).
- 2) M. A. Stephanov: Phys. Rev. Lett. **76**, 4472 (1996).
- 3) G. Akemann and T. Wettig: hep-lat/0308003.
- 4) K. Splittorff and J. J. M. Verbaarschot: hep-th/0310271.

\*<sup>1</sup> Service de Physique Théorique, Commissariat de l'Energie Atomique/Direction des Sciences de la Matière/Service de Physique Théorique Saclay, Unité de recherche associée au Centre National de la Recherche Scientifique, France

\*<sup>2</sup> Department of Physics, Yale University, USA

## Calculations of correlators and spectral function and properties of QGP

S. Datta,<sup>\*1</sup> O. Kaczmarek,<sup>\*1</sup> F. Karsch,<sup>\*1</sup> P. Petreczky,<sup>\*2</sup> K. Petrov,<sup>\*2</sup> I. Wetzorke,<sup>\*3</sup> and F. Zantow<sup>\*1</sup>

Properties of heavy quarkonia at finite temperature have been a longstanding problem as it was suggested that they can be used as a signature of Quark Gluon Plasma (QGP) in heavy ion collisions.<sup>1)</sup> The properties of heavy quarkonia have been studied using potential models.<sup>1,2)</sup> Lattice calculation of the charmonia spectral function become available only recently.<sup>3-5)</sup>

We have calculated charmonia spectral functions in quenched QCD (*i.e.* without dynamical quarks) in pseudo-scalar, vector, scalar and axial-vector channels corresponding to  $\eta_c$ ,  $J/\psi$ ,  $\chi_{c0}$  and  $\chi_{c1}$  states respectively. Spectral function have been calculated from temporal lattice correlation function using the Maximum Entropy Method (MEM).<sup>6)</sup> We have used isotropic lattices with the lattice spacing  $a^{-1} = 9.72 \text{ GeV}^7)$  and  $a^{-1} = 4.86 \text{ GeV}^8)$  in our calculations. We have found that the correlation function show large changes across the deconfinement temperature,  $T_c$ , in the scalar and axial-vector channel, while in the pseudo-scalar and vector channels only small changes were observed. Correspondingly, no peaks in the scalar and axial-vector spectral functions due to  $\chi_{c0}$  and  $\chi_{c1}$  states for  $T > T_c$  were found, while the  $\eta_c$  and  $J/\psi$  peaks in the pseudo-scalar and vector spectral functions are clearly observable at least up to temperatures  $1.5T_c$ . Moreover, it seems, that the properties of ground state charmonia are not strongly affected by deconfinement. These findings are in agreement with the calculations done using anisotropic lattices.<sup>4,5)</sup>

Naturally the question arises how far the existence of charmonia states well above the deconfinement temperature can be understood in terms of color screening. On quite general grounds it is expected that the color forces between static quark and antiquark are exponentially screened beyond some distance  $R_{sc}$ . In perturbation theory  $R_{sc} = 1/(g(T)T)$  (if dynamical quarks are absent), with  $g(T)$  being the temperature dependent gauge coupling. Non-perturbatively color screening phenomenon was studied in terms of the color averaged free energy  $F_{av}(R, T)$  (Polyakov loop correlator).<sup>9,10)</sup> Very small screening radius was found in these studies, which would indicate the dissolution of all charmonia states. However, the free energy of static quark-antiquark pair depends on whether this pair is in color singlet or color octet state. Thus in order to make contact with charmonium physics at finite

temperature the singlet free energy need to be studied non-perturbatively. This was done in great details in Refs. 11 and 12. Furthermore, the singlet free energy contains also contribution from the entropy  $S_1(R, T)$ ,  $F_1(R, T) = U_1(R, T) - TS_1(R, T)$ .<sup>11,12)</sup> The internal energy  $U_1(R, T)$  is most closely related to the concept of static potential at  $T = 0$  and it turns out that the screening length extracted from this quantity is larger than those extracted from  $F_{av}$  or  $F_1$ . It reaches the zero temperature  $J/\psi$  radius only around  $2T_c$ . Thus from the analysis of  $U_1(R, T)$  one would conclude, that charmonia state may exist up to temperatures  $2T_c$  in accordance with lattice studies of the charmonium spectral functions.

All the studies discussed above were done in quenched QCD. In order to make connection with heavy ion phenomenology the effect of dynamical quarks need to be studied. For the charmonium spectral functions this cannot be done with present computer resources (it would require about 10 Teraflops computing power). However, the effect of dynamical quarks on singlet free energy of static quark-antiquark pair can be estimated and will serve a valuable input for quarkonium physics at finite temperature. Some preliminary studies in this direction have already been done<sup>12)</sup> and more detailed study with three different lattice spacings and variety of quark masses is in progress.<sup>13)</sup>

In conclusion, we have studied charmonium properties at finite temperature using MEM as well as the singlet free energy of a static quark antiquark pair. These studies indicate quite complex color screening phenomenon in QGP.

### References

- 1) T. Matsui and H. Satz: Phys. Lett. B **178**, 416 (1986).
- 2) F. Karsch et al.: Z. Phys. C **37**, 617 (1988); S. Digal et al.: Phys. Rev. D **64**, 094015 (2001).
- 3) S. Datta et al.: Nucl. Phys. B (Proc. Suppl.) **119**, 487 (2003).
- 4) T. Umeda et al.: hep-lat/0211003.
- 5) M. Asakawa et al.: hep-lat/0308034.
- 6) M. Asakawa, Y. Nakahara, and T. Hatsuda: Prog. Part. Nucl. Phys. **46**, 459 (2001).
- 7) P. Petreczky et al.: hep-lat/0309191.
- 8) P. Petreczky: hep-lat/0310059.
- 9) O. Kaczmarek et al.: Phys. Rev. D **62**, 034021 (2000).
- 10) F. Karsch et al.: Nucl. Phys. B **605**, 579 (2001).
- 11) O. Kaczmarek et al.: Phys. Lett. B **543**, 41 (2002).
- 12) O. Kaczmarek et al.: hep-lat/0309121.
- 13) P. Petreczky and K. Petrov: work in progress.

<sup>\*1</sup> Fakultät für Physik, Universität Bielefeld, Germany

<sup>\*2</sup> Physics Department, Brookhaven National Laboratory, USA

<sup>\*3</sup> John von Neuman Institute for Computing and DESY Zeuthen, Germany

## MEM analysis of the thermal glueball from SU(3) lattice QCD

N. Ishii and H. Suganuma\*

Near the critical temperature  $T_c$ , one expects various onsets of the deconfinement transition in the QCD vacuum such as the reduction of the string tension and the partial chiral restoration. As a consequence, some hadrons are expected to exhibit the pole-mass reduction near  $T_c$ , as suggested by effective-model studies.<sup>1-4)</sup> Indeed, these changes are considered as important precritical phenomena of the QCD phase transition in RHIC experiments, and corresponding lattice QCD calculations were attempted at the quenched level recently.<sup>5-8)</sup> In this paper, we consider  $0^{++}$  glueball, whose pole-mass reduction is suggested by an effective model based on the dual Meissner picture of color confinement.<sup>4)</sup>

In general, to study the pole mass of a hadron in lattice QCD, one first constructs a temporal correlator as  $G(\tau) = \langle \phi(\tau)\phi(0) \rangle$ , and then resorts to its spectral representation as  $G(\tau) = \int_0^\infty d\omega K(\tau, \omega)A(\omega)$ , where  $K(\tau, \omega) \equiv \frac{\cosh(\omega(\beta/2 - \tau))}{\sinh(\beta\omega/2)}$ ,  $\beta \equiv 1/T$ , and  $A(\omega)$  is the spectral function with its spatial momentum projected to zero, *i.e.*,  $A(\omega) \equiv A(\omega, \vec{p} = \vec{0})$ . Each peak position of  $A(\omega)$  corresponds to a pole mass of a hadron at  $T > 0$ . Usually, to extract  $A(\omega)$  from  $G(\tau)$ , one adopts an ansatz to perform a fit analysis. The most popular ansatz is the delta function, which is justified as long as the peak is sufficiently narrow. At  $T > 0$ , even a bound state may acquire a thermal width through the interaction with the heat bath, which can be considered with an advanced Breit-Wigner ansatz.<sup>8)</sup> Although the latter is rigid at low temperature, the shape of the spectral function may become complicated near and beyond  $T_c$ . In this case, it may be less trivial to figure out a proper ansatz. Hence, it is desirable to perform the maximum entropy analysis of the glueball correlator at finite temperature,<sup>9)</sup> because it provides us with a numerical procedure to reconstruct  $A(\omega)$  directly from lattice QCD Monte Carlo results.<sup>10,11)</sup>

The glueballs are known to give only negligibly weak contributions to the ordinary plaquette-plaquette correlator. To overcome this, we adopt a spatially extended glueball operator generated by the smearing method with a  $\rho$  of suitable size.<sup>8)</sup> Note that the smearing method has a shortcoming, that is, it may create an unphysical bump in the spectral function. However, since the actual low-lying glueball is a definite bound state in quenched QCD below  $T_c$ , the problem of unphysical bump is not serious. This is because the pole position in the complex  $\omega$  plane is unaffected by a particular choice of the operators.<sup>8)</sup>

We reconstruct  $A(\omega)$  for the smeared glueball correlator normalized as  $G(\tau = 0) = 1$ .

We adopt the Shannon-Jaynes entropy as  $S \equiv \int_0^\infty \left[ A(\omega) - m(\omega) - A(\omega) \log \left( \frac{A(\omega)}{m(\omega)} \right) \right]$ , where  $m(\omega)$  is real and positive, referred to as the default model function.  $m(\omega)$  is required to reproduce the asymptotic behavior of  $A(\omega)$  as  $\omega \rightarrow \infty$ . We adopt the  $O(\alpha_s^0)$  perturbative expression as  $m(\omega) = N\omega^4 \exp\{-\omega^2/4\}$ , where the normalization factor  $N$  is determined to mimic  $G(\tau = 0) = 1$ , *i.e.*,  $1 = \int_0^\infty d\omega K(\tau = 0, \omega)m(\omega)$ .

In Fig. 1, we show the reconstructed spectral functions of the lowest  $0^{++}$  glueball at  $T = 130, 253,$  and  $275$  MeV. We use 5,500 to 9,900 gauge configurations generated by Wilson action with  $\beta_{\text{lat}} = 6.25$  and the renormalized anisotropy  $\xi \equiv a_s/a_t = 4$ . The critical temperature is estimated as  $T_c \simeq 280$  MeV from Polyakov loop susceptibility. Since the error bar estimated by following Ref. 11 turns out to be unreasonably small, we do not show it to avoid unnecessary confusion. For a reasonable estimate, the jackknife error estimator should be used.<sup>12)</sup> In Fig. 1, we see the tendency that the peak becomes broader with increasing temperature below  $T_c$ , which is consistent with the Breit-Wigner analysis of the thermal glueball correlator.<sup>8)</sup>

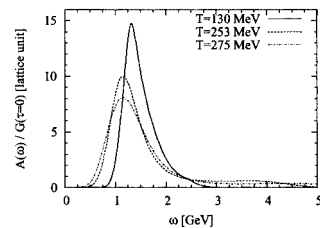


Fig. 1. Reconstructed spectral functions of the lowest  $0^{++}$  glueball at  $T = 130, 253,$  and  $275$  MeV.

## References

- 1) T. Hashimoto et al.: Phys. Rev. Lett. **57**, 2123 (1986).
- 2) T. Hatsuda et al.: Phys. Rev. Lett. **55**, 158 (1985).
- 3) T. Hatsuda et al.: Phys. Rev. D **47**, 1225 (1993).
- 4) H. Ichie et al.: Phys. Rev. D **52**, 2944 (1995).
- 5) QCD-TARO Collaboration: Phys. Rev. D **63**, 054501 (2001).
- 6) T. Umeda et al.: Int. J. Mod. Phys. A **16**, 2215 (2001).
- 7) N. Ishii et al.: Phys. Rev. D **66**, 014507 (2002).
- 8) N. Ishii et al.: Phys. Rev. D **66**, 094506 (2002).
- 9) N. Ishii et al.: Nucl. Phys. B (Proc. Suppl.) **129/130C**, in press (hep-lat/0309102).
- 10) M. Jarrell et al.: Phys. Rep. **269**, 133 (1996).
- 11) M. Asakawa et al.: Prog. Part. Nucl. Phys. **46**, 459 (2001).
- 12) N. Ishii et al.: work in progress.

\* Department of Physics, Tokyo Institute of Technology

# Lattice study of pion electromagnetic form factor with domain wall fermions<sup>†,††</sup>

Y. Nemoto

The pion electromagnetic (EM) form factor is one of the simplest quantities in QCD. Some new experiments on this quantity at relatively large momentum transfers are under way.<sup>1)</sup> While there exists a few lattice computations, none of them respect the chiral symmetry sufficiently well. The new experimental data with small errors might not only impose strong restrictions on some phenomenological models, but give stringent test of lattice QCD. We calculate the pion EM form factor in the quenched lattice QCD using domain wall fermions (DWF) with several momentum transfers which partially cover the above experiments. The DWF enables us to access lighter quark masses than ever, because it has good chiral properties which are quite important for the Nambu-Goldstone bosons such as the pion.

We employ the DWF action for the quark action. The number of sites in the fifth direction is  $L_5 = 12$  and the domain wall height  $M_5 = 1.8$ . Quark masses are taken to be  $m_q a = 0.08, 0.06, 0.04$  and  $0.02$  whose pion masses in the physical unit are approximately 760, 660, 540 and 390 MeV, respectively. The gauge action is a renormalization-group-improved gauge action called DBW2 with the lattice size  $16^3 \times 32$ . The gauge coupling is taken to be  $\beta = 0.87$ , which gives the lattice spacing  $a^{-1} \sim 1.3$  GeV and a sufficient spatial lattice volume  $V = (2.4 \text{ fm})^3$  for a pion. The number of configurations is 100. The explicit chiral symmetry breaking due to the finiteness of the fifth direction  $L_5$  is characterized by the residual mass  $m_{\text{res}}$ . Our result of  $m_{\text{res}}$  after the chiral extrapolation is about 1.5 MeV, which is much smaller than the quark masses  $m_f$ .

The pion EM form factor  $F_\pi(Q^2)$  is defined by  $F_\pi(Q^2)(p_\mu + p'_\mu) = \langle \pi^+(p) | j_\mu | \pi^+(p') \rangle$ , where  $q^2 = -Q^2 = (p - p')^2$  and  $j_\mu$  is the EM current. We note  $F_\pi(0)$  is the electric charge of a pion and we employ this relation as a numerical check. The computation method for the three-point function is as follows. We use an appropriate smeared source and a local sink. The separation between the source and the sink is 24 in the lattice unit. A momentum is injected at the sink and flows into the current insertion, i.e., only one quark propagator has a non-zero momentum. This method is statistically efficient for small momentum transfers. The presently calculated momentum transfers of the form factor are  $\vec{p} = (0, 0, 0), (1, 0, 0)$  and

$(1, 1, 0)$  in the unit of  $2\pi/La$  with the spatial lattice size  $L$ . They correspond to physical values of  $Q^2 = 0, 0.26, \text{ and } 0.53 \text{ GeV}^2$ , respectively. Larger momentum transfers will be investigated in the near future. We employ the sequential source technique when solving the quark propagator with the finite momentum.

The EM current used here is the local current which is not conserved on the lattice and requires operator renormalization before comparing with the matrix element in the continuum. We have calculated the renormalization factor of the axial vector current,  $Z_A$ , nonperturbatively using lattice QCD.  $Z_A$  is equal to the vector current factor  $Z_V$  in DWF and its chiral-extrapolated value is  $Z_A = 0.7798(5)$ .

All the fitted results of the pion EM form factor after the renormalization are summarized in Table 1. We see excellent agreement with unity for  $Q^2 = 0$  for the numerical check. Quark mass dependence of the form factors with the finite momenta seems to be rather small, although they have relatively large statistical errors.

We have calculated the pion electromagnetic form factor using the quenched DWF and DBW2 gauge action. Because of the good chiral and scaling properties of the action, we have investigated lighter quark masses than ever. The present results with small momentum transfers show a rather small quark mass dependence.

Calculations at larger momentum transfers are necessary for obtaining a functional form of the form factor to be compared with experiments, or models such as vector meson dominance. Such calculations are now under way.

Table 1. Fitted results of the pion EM form factor for each  $Q^2$  [GeV<sup>2</sup>] and quark mass (100 configurations).

$m_f a$	$Q^2 = 0$	$Q^2 = 0.26$	$Q^2 = 0.53$
0.08	1.003(19)	0.783(24)	0.603(48)
0.06	1.010(22)	0.779(31)	0.583(73)
0.04	1.013(27)	0.761(44)	0.564(138)
0.02	1.011(34)	0.689(77)	n/a

## References

- 1) The Jefferson Lab F(pi) Collaboration, J. Volmer et al.: Phys. Rev. Lett. **86**, 1713 (2001); H. P. Blok, G. M. Huber, and D. J. Mack: arXiv:nucl-ex/0208011.

<sup>†</sup> Condensed from the article in Nucl. Phys. (Proc. Suppl.) to be published; hep-lat/0309173

<sup>††</sup> This work was carried out under RBC Collaboration. We thank RIKEN, Brookhaven National Laboratory and the U.S. Department of Energy for providing the facilities essential for the completion of this work.

# Application of DWF to heavy-light mesons<sup>†</sup>

N. Yamada, for the RBC Collaboration

Domain wall fermions<sup>1,2)</sup> (DWF) are expected to have a negligible  $O(a)$  error as well as better control over chiral extrapolations. Simulating light quarks using DWF benefits from these advantages and has been successfully used in the light hadron system.<sup>3-5)</sup> It is, then, natural to consider its application to the massive quarks. We have started the simulation of  $D$  mesons using DWF for both heavy and light quarks. In the following we will present a progress report on this study.

The gauge configurations are generated with the quenched DBW2 gauge action<sup>6)</sup> with  $\beta = 1.22$  on  $24^3 \times 48$  sites. The lattice spacing  $a^{-1} = 2.86(9)$  GeV is obtained using  $m_\rho = 770$  MeV. We set the extension of the fifth dimension and the domain wall height to  $L_s = 10$  and  $aM_5 = 1.65$ , respectively. The light and heavy quark masses range in  $0.008 \leq am_{lq} \leq 0.040$  and  $0.1 \leq am_{hq} \leq 0.5$ , respectively. Data presented below is obtained with 20 configurations. The errors given below are statistical only, unless otherwise specified.

The pseudo-scalar meson mass  $m_D$  is used to fix  $am_{\text{charm}}$ . After the chiral extrapolation and interpolation in heavy quark mass, we find  $am_{\text{charm}} = 0.380(4)$ . The mass splitting of  $m_{D_s} - m_D$  is, then, obtained as

$$m_{D_s} - m_D = 114(6) \text{ MeV}. \quad (1)$$

While this value is about 15% larger than the experimental value ( $m_{D_s} - m_D = 99$  MeV), quenching may account for much of the discrepancy.

The lattice calculation of the 1S hyperfine splitting has been a long standing problem because the lattice results are significantly smaller than the experimental values, independent of the heavy quark action adopted. In this work we obtain  $m_{D^*} - m_D = 69(6)$  MeV and  $m_{D_s^*} - m_{D_s} = 70(4)$  MeV. Comparing to the experimental results of  $m_{D^*} - m_D = 142$  MeV and  $m_{D_s^*} - m_{D_s} = 144$  MeV, we see that this problem persists when using DWF.

The leptonic decay constants  $f_{PS}$  are obtained in a standard way. Since relevant correlation functions are still noisy, the resulting decay constants depend on the fit ranges by as much as 10% which we take as a systematic error in the following analysis. Figure 1 shows the chiral behavior of the decay constant at  $am_{hq} = 0.4$ . Since the data with lightest light quark looks suspicious, we performed linear extrapolations with and without this data point. The difference between the two extrapolations are taken as a systematic error again. After interpolation to  $am_{hq} = am_{\text{charm}}$ , we obtain

$$f_D^{\text{latt}} = 200(9)_{(-21)}^{(+20)} \text{ MeV}, \quad (2)$$

<sup>†</sup> Condensed from the article in Proc. 21th Int. Symp. on Lattice Field Theory (Lattice2003)

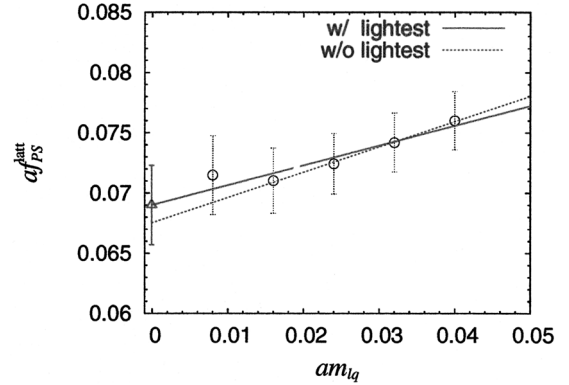


Fig. 1. The chiral extrapolation of the pseudo-scalar decay constant at  $am_{hq} = 0.4$ .

$$f_{D_s}^{\text{latt}} = 216(7)(22) \text{ MeV}, \quad (3)$$

where the systematic errors are summed up in quadrature. At present we quote the lattice bare values since the renormalization constant has not been available yet.

The SU(3) flavor breaking ratio of the decay constant is one of the quantities for which lattice QCD can attain a high precision. We can anticipate that the on-going charm experiments make it possible to measure this ratio at a few % accuracy, and so this is a good quantity for which to compare the lattice result with the experimental one although the uncertainties in  $m_s$ , the chiral extrapolation and quenching effects must first be under control. Our current result is

$$f_{D_s}/f_D = 1.08(3)_{(-0)}^{(+2)}. \quad (4)$$

We have started an exploratory study of massive DWF aiming at precision lattice calculations of the  $D$  meson system. To this purpose, we need to understand scaling violations well, especially those induced by relatively larger mass parameters. We also need more statistics to have better control over chiral extrapolations.

## References

- 1) D. B. Kaplan: Phys. Lett. B **288**, 342 (1992).
- 2) Y. Shamir: Nucl. Phys. B **406**, 90 (1993); V. Furman and Y. Shamir: Nucl. Phys. B **439**, 54 (1995).
- 3) T. Blum et al.: arXiv:hep-lat/0007038.
- 4) CP-PACS Collaboration, A. Ali Khan et al.: Phys. Rev. D **63**, 114504 (2001).
- 5) Y. Aoki et al.: arXiv:hep-lat/0211023.
- 6) T. Takaishi: Phys. Rev. D **54**, 1050 (1996).

# Static potential with dynamical domain-wall quarks<sup>†</sup>

K. Hashimoto\* and T. Izubuchi\*

We report our ongoing calculation for the static quark potential<sup>1)</sup> on two-flavor lattice QCD with domain-wall quarks.<sup>2)</sup> This project with dynamical quarks has two purposes: (i) determination of lattice spacing,  $a$ , from the Sommer's scale  $r_0 = R_0 a \approx 0.50 \text{ fm}$ <sup>3)</sup> and (ii) observation of *string breaking* which is expected at large distance between quark and anti-quark due to the pair creation of dynamical quarks. Domain-wall fermion is one of the most ideal lattice formulation of fermions which preserves symmetry of chiral and flavor rotations even at  $a > 0$  in a good approximation.

The static potential,  $V(\vec{R})$ , is the potential energy between infinitely heavy quark and anti-quark separated by  $\vec{R}$  in spacial direction and is obtained from the Wilson loop,  $W(\vec{R}, T)$ ,

$$\langle W(\vec{R}, T) \rangle \sim C_0 \exp(-V(\vec{R})T) + C_1 \exp(-V'(\vec{R})T) \quad (1)$$

The calculation of  $W(\vec{R}, T)$  is done on configurations generated using two-flavor dynamical domain-wall fermion with  $L_s = 12$ ,  $M_5 = 1.8$ . Dynamical quark masses are  $m_f = 0.02$ ,  $0.03$  and  $0.04$  which correspond to  $m_\pi/m_\rho = 0.54(1)$ ,  $0.60(1)$  and  $0.64(1)$  respectively. We employ the improved gauge action, DBW2, with  $\beta = 0.80$  on  $16^3 \times 32$  lattices. Inverse of the lattice spacing from rho meson mass turns out to be  $a^{-1} \sim 1.8 \text{ GeV}$ . We implement *Bresenham algorithm*<sup>4)</sup> of Computer Graphics which allows one to obtain the geodesic path connecting the ends of  $\vec{R} = (N_1, N_2, N_3)$  on lattice, where  $N_i$  are any three integers.

The static potential  $V(\vec{R})$  is obtained from  $V(\vec{R}) = \ln(W(\vec{R}, t_{\min})/W(\vec{R}, t_{\min} + 1))$  by omitting the second term in Eq. (1).  $t_{\min}$  is selected as the smallest time distance to the plateau of  $V(\vec{R})$ . We measure  $V(\vec{R})$  with  $|\vec{R}| < 10$ . Then the physical parameters are obtained from fitting function:

$$V(\vec{R}) = \sigma |\vec{R}| - C_F \frac{\alpha_S}{|\vec{R}|} + V_0, \quad (2)$$

$$R_0 = \sqrt{\frac{1.65 - C_F \alpha_S}{\sigma}},$$

where  $\sigma$  is the string tension and  $\alpha_S$  is the QCD coupling constants. Our preliminary results of the fits with the number of configuration used and the fit ranges are tabulated in (Table 1). The lack of statistics (especially for  $m_f = 0.04$ ) currently prevent us from more accurate determination as well as the information of the excited state  $C_1$ ,  $V'$  in Eq. (1).

<sup>†</sup> Work done with the RBC Collaboration

\* Institute for Theoretical Physics, Kanazawa University

Table 1. Preliminary results of fits for each dynamical quark mass (statistical error only).

$m_f$	0.02	0.03	0.04
# of conf.	820	410	130
# of traj./conf.	5	10	10
(The length of MD time per one trajectory is 0.5)			
$r_{\min}$	$\sqrt{2}$	$\sqrt{2}$	$\sqrt{2}$
$r_{\max}$	$\sqrt{62}$	$\sqrt{56}$	$\sqrt{56}$
$t_{\min}$	4	4	4
$\sigma$	0.08420(153)	0.08514(202)	0.08360(430)
$C_F \alpha_S$	0.3579(60)	0.3488(88)	0.3629(183)
$R_0$	3.917(27)	3.909(34)	3.924(74)

We measured  $r_0 \times (V(r) - V(r_0))$  as a function of  $r/r_0$  on  $N_F = 0$  quenched lattice (DBW2,  $\beta = 1.04$ ,  $a^{-1} \sim 2 \text{ GeV}$ )<sup>5)</sup> and that on  $N_F = 2$  dynamical ( $m_f = 0.02$ ) lattice in Fig. 1. One could see a deeper Coulomb potential for  $N_F = 2$  (blank square) than that of quenched (filled circle) at small  $r$  ( $\ll r_0$ ). This difference is consistent with the milder running of the strong coupling constant in  $N_F = 2$  theory as a consequence of the quark's contribution to the vacuum polarization:  $\alpha_S(r, N_F = 0) < \alpha_S(r, N_F = 2)$ .

At large  $|\vec{R}|$  and  $T$ , the static potential is poorly determined as seen from statistical errors in Fig. 1. The smearing procedure (APE and/or HYP) is under way in order to maximize the overlap of the QCD string in  $W(\vec{R}, T)$  by which one might obtain the scale with better accuracy. Also by controlling the overlap to the states in this way one might obtain enhanced informations about the excited state which is hoped to bring the signal of the string breaking.

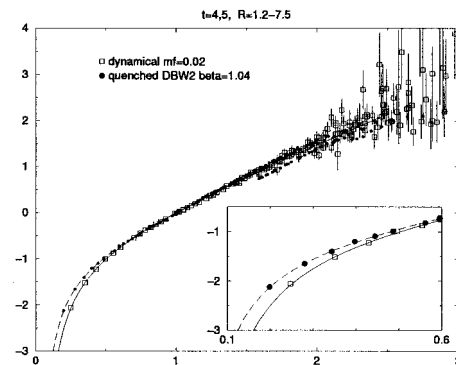


Fig. 1.  $r_0 \times (V(r) - V(r_0))$  vs.  $(r/r_0)$  on  $N_F = 0$  (quenched) and  $N_F = 2$  dynamical ( $m_f = 0.02$ ) lattices.

## References

- 1) G. S. Bali: Phys. Rep. **343**, 1 (2001).
- 2) RBC Collaboration, T. Izubuchi: Nucl. Phys. B. (Proc. Suppl.) **119**, 813 (2003); RBC Collaboration, C. Dawson: hep-lat/0310055 (2003).
- 3) R. Sommer: Nucl. Phys. B **411**, 839 (1994).
- 4) B. Bolder et al.: Phys. Rev. D **63**, 074504 (2001).
- 5) RBC Collaboration, Y. Aoki et al.: hep-lat/0211023 (2002).

# Kaon B parameter from two-flavor dynamical domain wall fermions<sup>†</sup>

T. Izubuchi,\* for the RBC Collaboration

The kaon B parameter,  $B_K$ , is an essential bridge between  $K_0-\bar{K}_0$  mixing experiments and the Cabibbo-Kobayashi-Maskawa matrix. Employing domain wall fermions (DWF) as dynamical quarks would diminish the unphysical operator mixing and  $O(a)$  errors as well as the systematic errors from quenched approximation.

Using an improved HMC algorithm for DWF, we have generated three ensembles of lattices of size  $16^3 \times 32$  for two-flavor QCD with degenerate dynamical masses of  $m_{\text{dyn}} = 0.02, 0.03, 0.04$ , which are roughly corresponding to 60, 90, 120 MeV quark masses in  $\overline{\text{MS}}$  2 GeV respectively.  $a^{-1} = 1.81(6)$  GeV from the rho mass in  $m_{\text{dyn}}$  to the chiral limit.<sup>1)</sup>

We evaluate the bag parameter,  $B_{\text{PS}}$  ( $B_K = B_{\text{PS}}$  when the pseudoscalars have the kaon mass), by the conventional method, where the ratio of a three-point Green's function and two pseudoscalar-axial-vector correlators is taken. In Fig. 1, we show our results for  $B_{\text{PS}}^{\text{lat}}$  for degenerate valence quark masses for each different value of  $m_{\text{dyn}}$ . The filled points in the figure have  $m_{\text{dyn}} = m_{\text{val}}$ . Our simplest result to report for  $B_K$  comes from extrapolating the  $m_{\text{val}} = m_{\text{dyn}}$  points in Fig. 1 to  $m_f = \bar{m}_s/2 \equiv 0.018$ . (A pseudoscalar with two quarks with  $m_f = \bar{m}_s/2$  has the mass of the kaon.) We perform this extrapolation using the partially quenched formula

$$B_{\text{PS}}(m) = b_0 \left( 1 - \frac{6}{(4\pi f)^2} \left( M_{\text{PS}}^2 \log \frac{M_{\text{PS}}^2}{\Lambda_{\chi\text{PT}}^2} \right) \right) + b_1 M_{\text{PS}}^2, \quad (1)$$

fitting the three points with  $m_{\text{val}} = m_{\text{dyn}}$ , and find  $B_K^{\text{lat}} = 0.541(9)$  (statistical error only), with a small

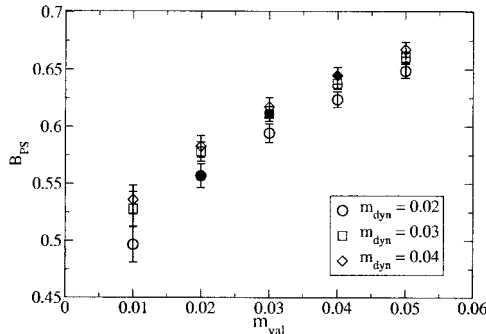


Fig. 1.  $B_{\text{PS}}^{\text{lat}}$  for different valence and dynamical masses. The filled symbols have  $m_{\text{val}} = m_{\text{dyn}}$ .

$\chi^2/\text{d.o.f.}$  Note that we are using the known coefficient of the chiral logarithm and  $\Lambda_{\chi\text{PT}} = 1$  GeV. The statistical error in the lattice spacing gives an additional 2% systematic error in the value of  $B_K^{\text{lat}}$ , due to the uncertainty in the strange quark mass.

We have also fit the dependence of  $B_{\text{PS}}$  on  $m_{\text{val}}$  to (1) for each fixed  $m_{\text{dyn}}$ , using the five values for  $m_{\text{val}}$ . The interpolated values for  $B_K^{\text{lat}}$  ( $m_{\text{val}} = \bar{m}_s/2, m_{\text{dyn}}$ ) are 0.537(11), 0.557(9) and 0.568(10) for  $m_{\text{dyn}} = 0.02, 0.03$  and 0.04 respectively.

We calculate  $\hat{B}_K$ , the renormalization group invariant (RGI) parameter, from  $B_K^{\text{lat}}$  via the multiplicative renormalization

$$\hat{B}_K = Z^{\text{RGI,RI-MOM}}(\mu) \times (Z_Q^{\Delta S=2}(\mu a)/Z_A^2(\mu a)) B_K^{\text{lat}}(a) \quad (2)$$

A similar equation is used for  $B_K^{\overline{\text{MS}}}$ . Using NPR at  $m_{\text{val}} = m_{\text{dyn}}$  we find  $Z^{\text{RGI,RI-MOM}} Z_Q^{\Delta S=2}/Z_A^2 = 1.29(4)$  and  $Z^{\overline{\text{MS,RI-MOM}}} Z_Q^{\Delta S=2}/Z_A^2 = 0.93(2)$  at  $\mu = 2$  GeV, which agree with the one loop perturbative calculation<sup>4)</sup> very well.

The preliminary results of our initial calculation of  $B_K$  with dynamical domain wall fermions is summarized for each dynamical lattice in Table 1. We see a trend toward lower values as the dynamical quark mass is reduced. We have likely underestimated our statistical error, due to the long autocorrelation times, and we have not yet studied chiral/continuum/volume extrapolations. However, it is clear that these dynamical DWF calculations are possible with current computers and hold promise for the next generation of computers.

Table 1. Preliminary results for renormalized  $B_K$  from valence quark extrapolations. For  $m_{\text{dyn}} = 0.02, 0.03$  and 0.04 a 2% scale error has been included in the error on the renormalized quantities.

$m_{\text{dyn}}$	$B_K^{\text{lat}}$	$B_K^{\overline{\text{MS}}}(2\text{GeV})$	$\hat{B}_K$
0.02	0.537(11)	0.499(22)	0.692(34)
0.03	0.557(9)	0.518(20)	0.719(32)
0.04	0.568(10)	0.529(21)	0.733(34)
$\infty$	RBC <sup>2)</sup>	0.536(6)	
$\infty$	CP-PACS <sup>3)</sup>	0.564(14)	

## References

- 1) RBC Collaboration, T. Izubuchi: Nucl. Phys. B, (Proc. Suppl.) **119**, 813 (2002); RBC Collaboration, C. Dawson: hep-lat/0310055 (2003).
- 2) T. Blum et al.: hep-lat/0110075 (2001).
- 3) A. Ali Khan et al.: Phys. Rev. D **64**, 114506 (2001).
- 4) S. Aoki et al.: Phys. Rev. D **67**, 094502 (2003).

<sup>†</sup> Condensed from the article in hep-lat/0310058

\* Institute for Theoretical Physics, Kanazawa University

# Kaon matrix elements in domain-wall QCD with DBW2 gauge action<sup>†</sup>

J. Noaki

Calculation of the weak matrix elements on the lattice is one of the important step in the theoretical treatment of the non-leptonic kaon decays which has CP asymmetry. In order to examine some of systematic errors which were not controlled in previous works,<sup>1,2)</sup> we are performing an extensive quenched numerical simulation on lattices with rather fine spacing using the combination of domain-wall fermion and the DBW2 gauge action. This choice improves chiral symmetry and allows us to examine the effect of the charmed quark on the lattice as well as the scaling violation.

In Table 1, simulation parameters used in this calculation and preliminary results of the basic quantities are summarized.<sup>3)</sup> The value of residual quark mass as small as  $m_{\text{res}} \lesssim 0.3 \text{ MeV}$  demonstrates the good chiral symmetry. Therefore, it is expected that the chiral symmetry breaking effects due to the finite  $L_s$  are negligible at least as to the local operator for Kaon B-parameter.  $B_K$  can be obtained on the lattice as a ratio of the matrix elements of the local operator  $Q_{\Delta S=2} = [\bar{s}\gamma_\mu(1-\gamma_5)d]^2$  and the axial current  $A_4$ . Fit function  $B_K = \xi_0[1 + Cm_f a \ln(m_f a)] + \xi_1 m_f a$  is demonstrated to fit well with  $\chi^2/\text{dof} = 0.76$ , where the coefficient  $C$  is obtained analytically. Taking only statistical errors into account, our preliminary results are

$$\begin{aligned} B_K^{\text{latt}}(m_f a = 0.0155) &= 0.552(11), \\ B_K^{\text{RI-MOM}}(\mu = 2 \text{ GeV}) &= 0.542(11), \\ B_K^{\text{MS, NDR}}(\mu = 2 \text{ GeV}) &= 0.549(11), \\ \hat{B}_K &= 0.764(15). \end{aligned}$$

In the step of non-perturbative renormalization, we observed that all elements of the amputated four-point function in the chirality basis were less than 0.2% of the  $(VV + AA, VV + AA)$  element which corresponds

Table 1. Simulation parameters and preliminary results of basic quantities.

lattice size:	$24^3 \times 48$
gauge coupling:	$\beta = 1.22$ ,
#sweeps:	5,000 ( $B_K$ ), 10,000 ( $K \rightarrow \pi$ , meson)
domain-wall parameters:	$M_5 = 1.65$ , $L_s = 10$
light quark mass:	$m_f a = 0.008 - 0.040$ , in step of 0.008
charmed quark mass:	$m_c a = 0.08, 0.12, 0.16, 0.20, 0.30, 0.40, 0.50$
#configs.:	77 ( $B_K$ ), 23 (NPR), 42 ( $m_{\text{res}}$ ), 50 ( $K \rightarrow \pi$ , meson)
<hr/>	
$a^{-1} = 2.86(9) \text{ GeV}$ ( $m_f a = 0$ , $m_\rho = 770 \text{ MeV}$ )	
$m_{\text{res}} a = 9.73(4) \cdot 10^{-5}$ ( $m_f a = 0$ )	

<sup>†</sup> Condensed from the article hep-lat/0309175

to  $Z_{B_K}$ . Our result of  $B_K^{\text{MS}}(\mu = 2 \text{ GeV})$  is consistent with CP-PACS<sup>4)</sup> and the previous work of RBC.<sup>2)</sup>

In  $\Delta I = 1/2$  rule, matrix element of  $Q_2 = (\bar{s}u)_L(\bar{u}d)_L$  dominates the decay amplitude and the charmed operator  $Q_{2c} = (\bar{s}c)_L(\bar{c}d)_L$  also have contribution through the GIM mechanism. For these operators, the slope of the  $K \rightarrow \pi$  matrix element as a function of  $m_f a$  are in proportion to  $K \rightarrow \pi\pi$  matrix elements at the lowest order of chiral perturbation theory,<sup>5)</sup> where the unphysical effect must be subtracted:

$$\langle \pi^+ | Q_i | K^+ \rangle_{\text{subt}} = \langle \pi^+ | Q_i - \alpha_i Q_{\text{subt}} | K^+ \rangle, \quad (1)$$

In Fig. 1,  $K \rightarrow \pi$  matrix elements of  $Q_2$  (left) and  $Q_{2c} = (\bar{s}u)_L(\bar{u}d)_L$  (right) before and after the subtraction are shown. In particular, one finds that the slope of the subtracted matrix element of  $Q_{2c}$  is much smaller than that of  $Q_2$ . It might mean a minor contribution of  $\langle \pi\pi | Q_{2c} | K \rangle$  to  $\Delta I = 1/2$  rule.

Another important value for the test of Standard Model,  $\epsilon'/\epsilon$ , also can be obtained in this calculation. Since it requires much more statistics than we have so far, our calculation is still ongoing.

We thank RIKEN, BNL and the U.S. DOE for providing the facilities essential for the completion of this work.

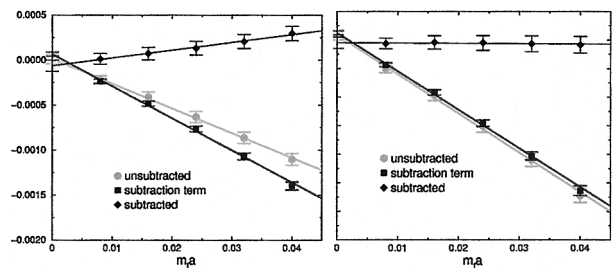


Fig. 1.  $K \rightarrow \pi$  matrix elements of  $Q_2^{(0)}$  (left) and  $Q_{2c}$  (right, with  $m_c a = 0.40$ ) as a function of  $m_f a$ . Circles, squares and diamonds are standing for unsubtracted matrix elements, subtraction term and subtracted matrix elements, respectively.

## References

- 1) CP-PACS Collaboration, J. Noaki et al.: Phys. Rev. D **68**, 014501 (2003).
- 2) RBC Collaboration, T. Blum et al.: Phys. Rev. D **68**, 114506 (2003).
- 3) RBC Collaboration, J. Noaki: Nucl. Phys. B (Proc. Suppl.) **119**, 362 (2003).
- 4) CP-PACS Collaboration, A. Ali Khan et al.: Phys. Rev. D **64**, 114506 (2001).
- 5) C. Bernard et al.: Phys. Rev. D **32**, 2343 (1985).



# Lattice study of negative-parity baryon spectrum

Y. Nemoto, N. Nakajima,<sup>\*1</sup> H. Matsufuru,<sup>\*2</sup> and H. Suganuma<sup>\*3</sup>

Excited state baryons are still less known than the ground state ones both theoretically and experimentally. From a theoretical point of view, the conventional quark model reproduces the low-lying excited states of baryons fairly well. However, it has still not been resolved how the quark model is derived from the first principle of the strong interaction, QCD. To gain deeper insight into the connection between QCD and the quark model, it is meaningful to compute the spectra of excited baryons from lattice QCD, and compare them with the results of the quark model.

We investigate the low-lying negative-parity baryons in the  $SU(3)$  flavor octet, decuplet and singlet with the standard Wilson gauge action and the  $O(a)$  improved Wilson quark actions. For accurate measurements of the masses of the negative-parity baryons, we have adopted quenched anisotropic  $SU(3)$  lattice QCD, in which the temporal lattice spacing is finer than the spatial one.<sup>1)</sup> The simulation parameters are as follows. The sizes of the lattices are  $12^3 \times 96$  ( $\beta = 5.75$ ,  $a_\sigma^{-1} = 1.034(6)$  GeV),  $16^3 \times 128$  ( $\beta = 5.95$ ,  $a_\sigma^{-1} = 1.499(9)$  GeV) and  $20^3 \times 160$  ( $\beta = 6.10$ ,  $a_\sigma^{-1} = 1.871(14)$  GeV). The scale  $a_\sigma^{-1}$  is determined from the  $K^*$  meson mass. The anisotropy is  $\xi = a_s/a_t = 4$ , where  $a_t$  is the temporal lattice spacing. On the quark mass, we adopt four different values, which roughly cover around the strange quark mass. We use the standard baryon operators which survive in the non-relativistic limit. The negative-parity baryons can also be measured by these operators using the parity projection. They are simply the parity partners of the ground-state baryons. In the source operator, each quark is smeared with the Gaussian function of the width  $\sim 0.4$  fm. The chiral extrapolation is taken linearly from lattice data.

Particular attention is paid to  $\Lambda(1405)$ , which is considered to be the flavor singlet baryon ( $qqq$  state) in the naive quark model, or the exotic penta-quark state ( $\bar{q}q-qqq$ ). We have calculated the flavor-singlet state as a three-quark state on the lattice. We show the results of the various baryon masses in the physical unit in Fig. 1 for the  $\beta = 6.10$  lattice. Note here that the flavor-singlet baryon has one strange valence quark and therefore the ambiguity from the chiral extrapolation should be less than that of the nucleon and the delta. Nevertheless, the discrepancy between the lattice result and the experimental value of  $\Lambda(1405)$  is the largest of all. Even if we take the quenching effect of

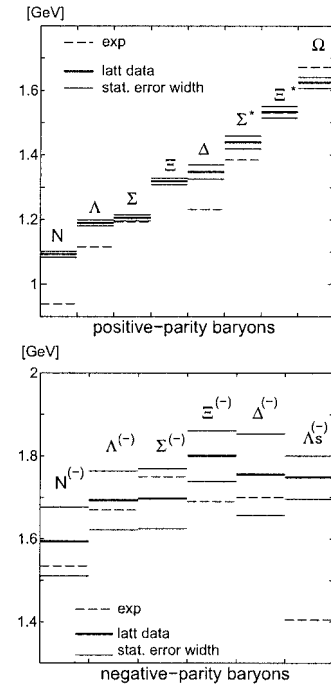


Fig. 1. Various baryon masses from the  $\beta = 6.10$  lattice.

10% level into account, this large discrepancy cannot be understood. Therefore, the numerical result for the flavor-singlet baryon exhibits different features from other channels, which indicates that it is unacceptably heavier than  $\Lambda(1405)$ . Thus, our result indicates that the three valence quark picture fails to represent the experimentally observed  $\Lambda(1405)$ , *i.e.*, the overlap with the 3Q component of  $\Lambda(1405)$  is small. The other possible candidate for  $\Lambda(1405)$  is a five-quark  $N\bar{K}$  state. Lattice simulation of the  $N\bar{K}$  (five-quark) state would be interesting even at the quenched level, where the dynamical quark-loop effect including the quark-antiquark pair creation is absent and thus the quark-level constitution of hadrons is definitely clear in the simulation.

## References

- 1) N. Nakajima, H. Matsufuru, Y. Nemoto, and H. Suganuma: AIP Conf. Proc. **594**, 376 (2001); Y. Nemoto, N. Nakajima, H. Matsufuru, and H. Suganuma: Nucl. Phys. A **721**, 879 (2003); Y. Nemoto, N. Nakajima, H. Matsufuru, and H. Suganuma: Phys. Rev. D **68**, 094505 (2003).

<sup>\*1</sup> Center of Medical Information Science, Kochi Medical School

<sup>\*2</sup> High Energy Accelerator Research Organization (KEK)

<sup>\*3</sup> Faculty of Science, Tokyo Institute of Technology

## Nucleon on the lattice

Y. Aoki,<sup>\*1</sup> S. Ohta,<sup>\*2</sup> and K. Orginos<sup>\*3</sup>

We report the nucleon structure calculations by the RIKEN-BNL-Columbia-KEK Collaboration. We have been applying a combination<sup>1)</sup> of the domain wall fermions (DWF) and the “doubly blocked Wilson 2” (DBW2) improved gauge actions to study nucleon on the lattice. The DWF preserves the chiral symmetry even at finite lattice cutoff by introducing a fifth lattice dimension in which the symmetry violation is exponentially suppressed. The DBW2 improvement helps the approach to the continuum limit.

The simplest of the electroweak matrix elements are the isovector vector ( $g_V$ ) and axial ( $g_A$ ) charges which dominate the neutron  $\beta$  decay.<sup>2)</sup> With DWF their ratio is renormalized up to  $O(a^2)$ , with  $a$  being the lattice spacing. In Fig. 1 we show the ratio as a function of the pion mass squared. The full-QCD results (diamonds) are consistent with the old quenched results (circles). This theoretical first principles calculations, which do not yet include isospin breaking effects, yields a value of  $g_A$  only a little bit below the experimental one,  $1.2670 \pm 0.0030$ . And the dependence on the quark mass is very mild. We have also calculated the moments of structure functions such as the quark momentum fraction, the first moment of the transversity, and the moment  $d_1$  of the polarized structure functions, in both quenched and full QCD.

Figure 2 shows the result of nucleon decay matrix elements. Any matrix element of nucleon decaying to pseudoscalar meson *via* dimension-six operator can be calculated from those shown in the figure. We have confirmed the consistency between (preferable but

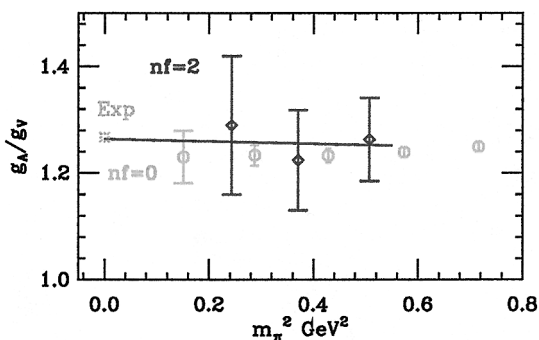


Fig. 1. Nucleon isovector axial to vector charge ratio,  $g_A/g_V$ , quenched (circle) and full QCD (diamond).

<sup>\*1</sup> Physics Department, University of Wuppertal, Germany

<sup>\*2</sup> Institute of Particle and Nuclear Studies, High Energy Accelerator Research Organization (KEK)

<sup>\*3</sup> Center for Theoretical Physics and Department of Physics, Laboratory for Nuclear Science, Massachusetts Institute of Technology, USA

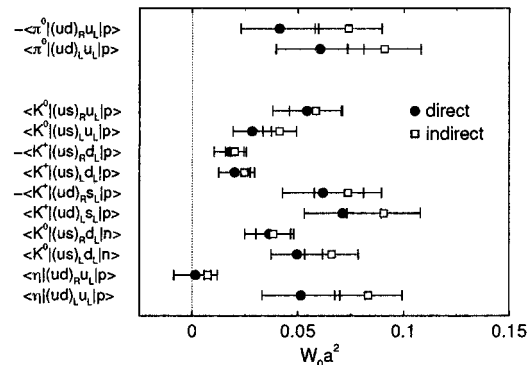


Fig. 2. Relevant form factor  $W_0$  for nucleon decay.

expensive) direct calculation and indirect one. We have performed a non-perturbative renormalization (NPR) and have shown that there are no mixing at practical level. The scheme matching calculation is underway to get matrix elements in  $\overline{\text{MS}}$  scheme. We are performing an indirect calculation on the  $N_f = 2$  dynamical domain-wall fermion configuration, which tells us the size of the quenching error in our results shown here.

To summarize, the lattice calculations with DBW2 and DWF work well for nucleon matrix elements. The axial to vector charge ratio is well reproduced to within 5% of the experimental value even with relatively heavy quark mass. The dependence on quark mass is very mild. Likewise the moments of structure functions  $\langle x \rangle_q$ ,  $d_1$ , and  $\langle 1 \rangle_{\delta q}$  all show mild linear dependence on quark mass, though some of them are yet to be renormalized. Good chiral behavior was observed in nucleon decay calculations, both for non-perturbative renormalization and matrix elements themselves. We will soon be able to report  $\overline{\text{MS}}$  estimates of these matrix elements.

## References

- 1) Y. Aoki et al.: arXiv:hep-lat/0211023; to appear in Phys. Rev. D, and references cited there in; RBC Collaboration, Y. Aoki: arXiv:hep-lat/0309152; RBC Collaboration, S. Ohta and K. Orginos: arXiv:hep-lat/0309113, and references therein.
- 2) RIKEN-BNL-Columbia-KEK Collaboration, S. Sasaki, K. Orginos, S. Ohta, and T. Blum: Phys. Rev. D **68**, 054509 (2003).

## Status of the QCDOC computer project

P. A. Boyle,<sup>\*1,\*2</sup> D. Chen,<sup>\*3</sup> N. H. Christ,<sup>\*2</sup> M. Clark,<sup>\*1</sup> S. D. Cohen,<sup>\*2</sup> C. Cristian,<sup>\*2</sup> Z. Dong,<sup>\*2</sup> A. Gara,<sup>\*3</sup>  
 B. Joó,<sup>\*1</sup> C. Jung,<sup>\*2,\*4</sup> C. Kim,<sup>\*2</sup> L. Levkova,<sup>\*2</sup> X. Liao,<sup>\*2</sup> G. Liu,<sup>\*2</sup> R. D. Mawhinney,<sup>\*2</sup> S. Ohta,<sup>\*5</sup>  
 K. Petrov,<sup>\*2,\*4</sup> T. Wettig,<sup>\*6</sup> and A. Yamaguchi<sup>\*2</sup>

The QCDOC (QCD On a Chip) project was started in 1999 as a joint effort of RIKEN, Columbia University and IBM Research to design a massively parallel super computer optimized for numerical calculations in lattice quantum chromodynamics (QCD). The architecture combines state-of-the-art system-on-a-chip technology with custom-designed logic specially optimized for lattice QCD calculations to provide computing power in the tens of TFlops range at a price/performance ratio of 1 US\$ per sustained MFlops.<sup>1-5)</sup> The British UKQCD collaboration and the US lattice community later endorsed the project.

Let us first repeat what we described last year. The QCDOC computer is a multiple-instruction, multiple-data (MIMD) machine with distributed memory, just like its predecessor, the QCDSF at Columbia University and RIKEN-BNL Research Center. While a single processing node of the QCDSF consists of seven chips assembled on a credit-card-sized board, now it is possible to integrate the components that make up a single node on a single chip, creating an application-specific integrated circuit (ASIC). The QCDOC chip is such an ASIC, consisting of a) a 500 MHz, 32-bit PowerPC 440 processor core, b) a 64-bit, 1 GFlops floating-point unit, c) 4 MBytes of embedded-DRAM memory, d) controllers for embedded and external memories, e) a nearest-neighbor serial communication unit (SCU) with latencies of 350 ns (550 ns) for supervisor (regular) transfers, overlapped between the 12 independent directions and an aggregate bandwidth of 12 Gbit/s, and f) other components such as an Ethernet controller, *etc.* Two such ASICs are mounted on a daughter board, together with two double data rate (DDR) SDRAM modules (one per ASIC, up to 2 GByte each). Thirty-two daughter boards are mounted on a mother board, and eight mother boards in a crate with two backplanes. The final machine consists of a certain number of such crates.

There are two separate networks: the physics network and the Ethernet-based auxiliary network. The physics network consists of high-speed serial links between nearest neighbors with a bandwidth of  $2 \times 500$  Mbits/s per link. The nodes are arranged in

a six-dimensional torus which allows efficient partitioning of the machine in software. The SCU in the ASIC provides direct memory access, single-bit error detection with automatic resend, and a low-latency store-and-forward mode for global operations. The Ethernet-based 100 Mbit/s auxiliary network is used for booting, diagnostics, and I/O, with an Ethernet controller integrated on the ASIC. Hubs on the mother board provide a bandwidth of 0.8 Gbit/s (decreased from 1.6 Gbit/s) off a mother board to commercial switches and the host workstation.

Development since the last year: The first five prototype ASICs were delivered by IBM in June, 2003. Many more have been produced following the successful testing of these five. The daughter board design was completed around the same time and was used extensively in testing the ASIC. We now have 96 daughter boards. The first mother board with 32 mounted daughter boards was successfully assembled and tested. Most notably the basic operating system and Dirac operator application now work on this mother board. A second mother board is being assembled, and will join the first one to test the intercommunication between them. After this test succeeds, the whole design will be signed off for the construction of production machines. We expect two 2-TFlops peak prototype configurations in early 2004, and two 10-TFlops configurations, one for RBRC and the other for UKQCD, in the summer of 2004. The US community is in the process of deciding the size of their QCDOC computer.

### References

- 1) P. A. Boyle et al.: arXiv:hep-lat/0309096.
- 2) QCDOC Collaboration, P. A. Boyle, C. Jung, and T. Wettig: arXiv:hep-lat/0306023.
- 3) P. A. Boyle et al.: Nucl. Phys. B (Proc. Suppl.) **119**, 1041 (2003).
- 4) P. A. Boyle et al.: Nucl. Phys. B (Proc. Suppl.) **106**, 177 (2002).
- 5) D. Chen et al.: Nucl. Phys. B (Proc. Suppl.) **94**, 825 (2001).

<sup>\*1</sup> Department of Physics and Astronomy, University of Edinburgh, UK

<sup>\*2</sup> Department of Physics, Columbia University, USA

<sup>\*3</sup> IBM Thomas J. Watson Research Center, USA

<sup>\*4</sup> Department of Physics, Brookhaven National Laboratory, USA

<sup>\*5</sup> Institute of Particle and Nuclear Studies, High Energy Accelerator Research Organization (KEK)

<sup>\*6</sup> Department of Physics, Yale University, USA

## The RHIC spin program: Where are we?

G. Bunce\* and H. En'yo

RHIC completed its second run with polarized proton collisions in May 2003. The first run, in 2001/2, established the first ever polarized proton collider, and provided first measurements of cross sections and spin asymmetries in this new energy range,  $\sqrt{s} = 200$  GeV, an order of magnitude above previous experiments. This first run collided transversely polarized protons. The second run introduced new spin rotators and established collisions of longitudinally polarized protons, providing first data for longitudinal asymmetries that are sensitive to the gluon polarization in the proton. In this report, we discuss what we have learned so far, where we are in our program, and the issues that we need to solve.

In the first spin run, a new method to measure the beam polarization was introduced, giving very fast measurements with excellent sensitivity. Beam polarization measurements with 3% relative polarization error were made in one minute every two hours during stored beam.<sup>1)</sup> The polarimeter was then used to monitor the polarization during commissioning. Special new magnets were added to RHIC for the spin program to prevent loss of polarization during acceleration. The sets of magnets, called Siberian Snakes, were based on a new design for RHIC, and the Siberian Snake concept had only been tested at very low energy. The polarized protons were accelerated from 24 GeV to 100 GeV with little polarization loss, and the polarization was maintained through 8 hour stores. Thus, the first run demonstrated that the key concepts and devices needed for the spin program worked and worked well.

The first run also provided important physics results at this new energy. From the PHENIX experiment, the measurement of the inclusive  $\pi^0$  cross section versus transverse momentum has been accepted for publication.<sup>2)</sup> In the letter it is shown that the cross section is described by the hard scattering of quarks and gluons from the colliding protons, over the full range measured, from  $p_T = 2\text{--}14$  GeV/c. This is a key result, confirming the theoretical basis of the spin program, even for lower  $p_T$ , where spin asymmetries can be measured at low to moderate luminosity. The result is also very important for the heavy ion program, since it demonstrates that the production of  $\pi^0$  at moderate  $p_T$  for heavy ion collisions is largely from hard scattering of quarks and gluons in the heavy ion beams.

Spin asymmetry measurements for the run, using transverse spin, showed very large spin asymmetries, for very forward neutrons,<sup>3)</sup> and for forward  $\pi^0$ .<sup>4)</sup> The neutron asymmetry was used to set up spin rotators

at PHENIX for the second RHIC run. The forward  $\pi^0$  asymmetry, observed by STAR, may lead to a new understanding of the transverse spin structure of the proton.

For the 2003 spin run, new spin rotators, designed and built for RHIC, were used for the first time. The rotators worked perfectly, providing longitudinal polarization at PHENIX and STAR. Both experiments collected the first spin asymmetry data ever for longitudinally polarized proton collisions. The PHENIX experiment reported a preliminary result for the longitudinal spin asymmetry for production of  $\pi^0$  in September.<sup>5)</sup> The asymmetry is surprisingly slightly negative, where predictions, depending on the degree of gluon polarization assumed, are positive. The result, which may indicate that the gluon polarization is small, represents an important first result, with results still to come from STAR. Future running with higher luminosity and polarization should give decisive results on the gluon polarization, a major focus for the RHIC spin program.

For the 2003 run, the luminosity was  $4 \times 10^{30}$  cm<sup>-2</sup>s<sup>-1</sup>, and polarization  $P = 0.3$ . The goals of the RHIC spin program call for 20 times higher luminosity, and  $P = 0.7$ . These goals will be the next focus of the program. Luminosity improvements are expected from selection of a new focusing value to avoid resonances and beam loss, and new vacuum pumping. Polarization improvement is expected from new Siberian Snakes that are being built for the AGS injector.

The results so far demonstrate the creation of intense beams of polarized protons, acceleration to 100 GeV with little or no polarization loss, and routine measurement of polarization. The experiments have successfully developed triggers for high luminosity collisions, and have already observed large spin asymmetries. First measurements sensitive to gluon polarization have already been reported. The next emphasis of the spin program will be to improve luminosity and polarization.

### References

- 1) O. Jinnouchi et al.: AIP Conf. Proc. **675**, 817 (2003).
- 2) PHENIX Collaboration, S. S. Adler et al.: Phys. Rev. Lett. **91**, 241803 (2003).
- 3) A. Bazilevsky et al.: AIP Conf. Proc. **675**, 584 (2003).
- 4) STAR Collaboration, J. Adams et al.: accepted by Phys. Rev. Lett.; hep-ex/0310058.
- 5) PHENIX Collaboration, S. S. Adler et al.: submitted to Phys. Rev. Lett.

---

\* Brookhaven National Laboratory, USA

# The PHENIX run 2003 and early results

M. Grosse Perdekamp,\* for the PHENIX Collaboration

We summarize the PHENIX data taking during the 2003 run of the Relativistic Heavy Ion Collider at Brookhaven National Laboratory.

The run was divided in two independent segments, colliding deuteron and gold nuclei in the first part and polarized protons in the second part of the run. The integrated luminosity for the deuteron-Gold run was  $\int L_{dAu} dt = 2.7 \text{ nb}^{-1}$  with peak luminosities reaching  $L_{dAu} = 2.2 \times 10^{28} \text{ cm}^{-2} \text{ s}^{-1}$ . In the polarized proton run  $\int L_{pp} dt = 352 \text{ nb}^{-1}$  were collected, corresponding to about  $6.6 \times 10^9$  events. Peak luminosities during the proton run reached  $L_{pp} = 6 \times 10^{30} \text{ cm}^{-2} \text{ s}^{-1}$  and the beam polarization in RHIC typically was between 30 and 35%. A detailed critique of the RHIC accelerator performance can be found in Ref. 2.

Just in time for the data taking the PHENIX detector did reach its full design configuration in January 2003. Compared to the previous data taking period in 2002 the most notable additions were 1) the North Muon Spectrometer with its muon tracker cathode chambers and muon identifier Iarocci-tube panels, 2) two forward hadron calorimeters for the event characterization in d-Au collisions and 3) scintillator hodoscopes inserted at the location of the shower maximum into the Zero Degree Calorimeter (ZDC). The combination of information from the new shower maximum detectors and the ZDC was successfully used for measurements of the beam polarization at the PHENIX collision point.

In addition to the introduction of new detector hardware an important innovation was the significant expansion of the online PHENIX computing facilities and the simultaneous introduction of a strong on-line analysis group. Partial data streams of rare event triggers with low bandwidth requirements — for example, the EMC-RICH trigger selecting events with clusters where  $E_{\text{cluster}} > 3 \text{ GeV}$  — were established by this group. The resulting data samples were used to carry out physics level analysis tasks to obtain fast feedback on the PHENIX detector performance.

At the same time the use of small partial data samples accelerated the analysis of selected physics channels of high interest: Figure 1 shows the first measurement of longitudinal double spin asymmetries in inclusive neutral pion production<sup>3)</sup> at RHIC. The size of the statistical errors does not permit to constrain the gluon polarization in the proton from our measurement. However, it is interesting to note that large negative asymmetries in  $A_{LL}^{\pi^0}$  at low  $p_T$  are not compatible with perturbative QCD.<sup>4)</sup>

Figure 2 shows the nuclear modification factor  $R_{dA}$

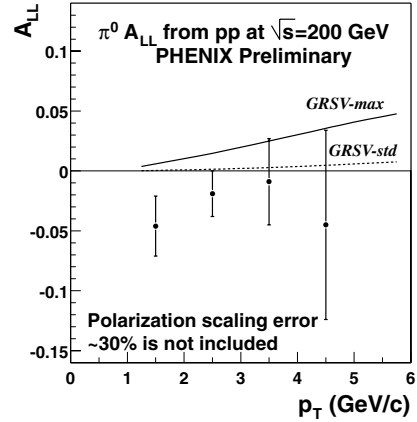


Fig. 1. The longitudinal double spin asymmetry  $A_{LL}^{\pi^0}$  observed in polarized proton collisions at RHIC. The data for  $A_{LL}^{\pi^0}$  are compared to predictions based on gluon polarizations compatible with existing DIS data.<sup>1)</sup>

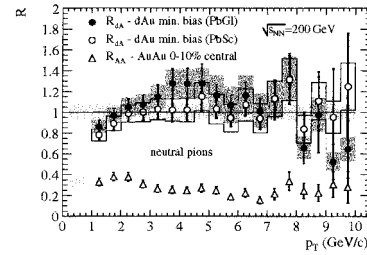


Fig. 2. The nuclear modification factor  $R_{dA}$  for the inclusive  $\pi^0$  cross section as function of the transverse momentum  $p_T$ . For comparison  $R_{AA}$  is shown for the 10% most central events.

for inclusive  $\pi^0$  production in deuteron-gold collisions.<sup>5)</sup> The absence of any suppression pattern strongly suggests that the suppression observed in gold-gold collisions is connected to final state effects due to the formation of a novel dense opaque nuclear media in heavy ion collisions instead of nuclear effects in the nucleon parton distributions. These are truly exciting results and were published within 2–3 months after data taking.

## References

- 1) M. Glück et al.: Phys. Rev. D **63**, 094005 (2001).
- 2) F. Pilat and T. Satagota: RHIC Retreat 2003, BNL, <http://www.agrshichome.bnl.gov/AP/RHIC2003/Retreat>
- 3) A. Bazilevsky: Proc. 10th Workshop on High Energy Spin Physics (Spin-03), Dubna, Russia, 2003-9, to be published.
- 4) B. Jager et al.: hep-ph/0310197.
- 5) M. Grosse Perdekamp: RHIC Users Meeting, 2003-5; S. Adler et al.: Phys. Rev. Lett. **91**, 072303 (2003).

\* University of Illinois at Urbana-Champaign, USA

## Measurement of $J/\psi$ with PHENIX muon arms in 2003 p+p collisions

N. Kamihara,<sup>\*1</sup> V. Cianciolo,<sup>\*2</sup> V. Dzordzhadze,<sup>\*3</sup> A. Glenn,<sup>\*3</sup> D. J. Kim,<sup>\*4</sup> K. Read,<sup>\*2,\*3</sup> H. D. Sato,<sup>\*5</sup>  
T.-A. Shibata,<sup>\*1</sup> and A. Taketani

The PHENIX experiment at the Relativistic Heavy Ion Collider (RHIC) is designed to explore many aspects of relativistic heavy-ion physics and high-energy spin physics. One of the most important probes for both physics is a  $J/\psi$  particle. The suppression of the  $J/\psi$  production in heavy-ion collisions is regarded as a strong indication of the formation of the quark-gluon plasma (QGP). The double longitudinal-spin asymmetry of the  $J/\psi$  production in polarized-proton collisions determines the helicity distribution of the gluon ( $\delta g$ ).

The PHENIX detector system consists of two muon arms to cover the forward rapidity region and two central arms to cover the central rapidity region. The muon arms are designed to measure di-muons from the decay of vector mesons (*e.g.*  $J/\psi$ ) and single-muons from the decay of the open heavy-flavor production and W bosons. The two muon arms cover the pseudorapidity ranges of  $-2.2 < \eta < -1.2$  (south muon arm) and  $1.2 < \eta < 2.4$  (north muon arm) with  $2\pi$  azimuthal-angle coverage.

The muon arms consist of a muon-tracker (MuTr)<sup>1,2)</sup> subsystem, which tracks trajectories of charged particles to determine the momenta of the particles, and a muon-identifier (MuID)<sup>2,3)</sup> subsystem, which identifies muons and triggers di-muon event candidates.

The south muon arm started operation during the 2001-2002 run period. In the 2003 run period, we made the north muon arm ready for operation and updated the di-muon trigger to handle both the south and north muon arms. In 2003, the PHENIX recorded a total luminosity of  $0.35 \text{ pb}^{-1}$  in longitudinally polarized proton collisions at  $\sqrt{s} = 200 \text{ GeV}$  with an average polarization of 27%.

The di-muon trigger is made using the MuID subsystem as a range counter. The trigger logic is configured by CAMAC modules and called the blue-logic trigger (BLT). The MuID subsystem is a sandwich of five wire-chamber panels and steel plates. Each wire-chamber panel has one horizontal-wire layer and one vertical-wire layer which comprise Iarocci-type plastic tubes, and there are ten layers in total. For the trigger

logic, each layer is divided into four (two horizontal and two vertical) quadrants. Two coincidence logics are configured in each quadrant: one is called the deep trigger, which is configured with eight layers inside and requires coincidence hits of seven layers, and the other is called the shallow trigger, which is configured with four layers inside and requires coincidence hits of three layers. The di-muon trigger requires one deep trigger in one quadrant and one shallow trigger in another quadrant. More detailed information about the muon trigger system is described in Ref. 4.

For a preliminary  $J/\psi$  measurement analysis, di-muon trigger events are filtered out from all the PHENIX raw data, and the di-muon invariant mass is reconstructed. Figure 1 shows a clear  $J/\psi$  mass peak at the correct invariant mass. The event reconstruction of the entire PHENIX raw data will start soon at the RHIC computing facility.

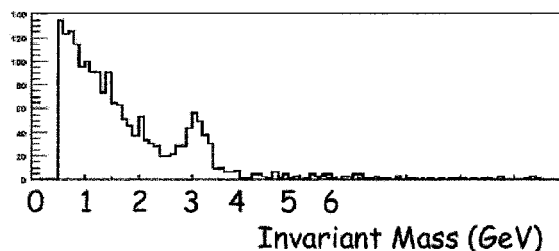


Fig. 1. Invariant mass spectrum of north muon arm. The filtered raw data was used.

### References

- 1) H. Kobayashi et al.: RIKEN Accel. Prog. Rep. **35**, 232 (2002).
- 2) A. Taketani et al.: RIKEN Accel. Prog. Rep. **35**, 224 (2002).
- 3) H. D. Sato et al.: RIKEN Accel. Prog. Rep. **35**, 225 (2002).
- 4) H. D. Sato et al.: RIKEN Accel. Prog. Rep. **36**, 240 (2003).

<sup>\*1</sup> Tokyo Institute of Technology

<sup>\*2</sup> Oak Ridge National Laboratory, USA

<sup>\*3</sup> University of Tennessee, USA

<sup>\*4</sup> Yonsei University, Korea

<sup>\*5</sup> Kyoto University

# Single muon analysis of polarized proton-proton collision at $\sqrt{s} = 200$ GeV

A. Taketani, D. S. Brown,\* O. Jinnouchi, and H. Kobayashi

It is expected that single-spin transverse asymmetry ( $A_N$ ) is zero, from naive pQCD calculation. However the Fermilab E704 experiment reported large  $A_N$  in the reactions, using transversely polarized proton beams, ( $p_{\uparrow}p \rightarrow \pi^+X$  and  $p_{\uparrow}p \rightarrow \pi^-X$ ) at  $\sqrt{s} = 19.4$  GeV.<sup>1)</sup> The origins of asymmetries are considered to be (1) initial state radiation, (2) final state radiation, (3) higher twist effect, or their combination. It is interesting to measure the  $A_N$  in the RHIC energy region at  $\sqrt{s} = 200$  GeV. We pay attention to the inclusive muon production which is the decay product of charged pion or kaon.

PHENIX collected transversely polarized proton-proton collision data at  $\sqrt{s} = 200$  GeV in Run2 from 2001 to 2002. The integrated luminosity was  $0.15$   $pb^{-1}$  and the polarizations were 14% and 17% on average.

The PHENIX muon arm mainly consists of muon tracker (MuTr) and muon identifier (MuId). It covers  $1.2 < |\eta| < 2.4$  over full azimuthal range.<sup>2)</sup> In the Run2, only the south arm, which covers  $-2.2 < \eta < -1.2$ , was installed and operated. The MuTr measures the charged particle momentum with 3 layers of chambers in the magnetic field.<sup>2)</sup> It is designed such that  $\Delta p/p \sim 3\%$  at  $p = 3\text{--}10$  GeV/c. The MuId identifies muons by using range counter that consists of 5 layers of chamber and iron absorber sandwiches. The muon detection efficiency is saturated at  $p \sim 2.5$  GeV/c. The  $\mu/\pi$  rejection factor is about  $10^{-3}$ . The MuId is also used as a trigger counter.<sup>3)</sup>

The selection criteria of muon<sup>4)</sup> are based on the quality of reconstruction, matching between MuTr and MuId segments, and event vertex position along the beam axis. The muon yield depending on the event vertex position was well explained by the decay product of charged pions and kaons.<sup>4)</sup> The 230 K tracks were selected for this analysis. Muons from open heavy flavor decay will dominate higher  $P_t$  regions.

The transverse single spin asymmetry is defined as  $A_N = \frac{1}{P} \cdot \frac{\sigma_L - \sigma_R}{\sigma_L + \sigma_R}$ , where  $P$  and  $\sigma$  are beam polarization and cross section, and indices  $R$  and  $L$  represent right and left.

We evaluated the systematic error of  $A_N$  by measuring the detector acceptance asymmetry ( $\varepsilon_\Omega$ ), and luminosity asymmetry ( $\varepsilon_B$ ).  $A_N$ ,  $\varepsilon_\Omega$ , and  $\varepsilon_B$  are described by using square root formul<sup>5)</sup> as

$$\frac{\sqrt{N_L^\uparrow N_R^\downarrow} - \sqrt{N_L^\downarrow N_R^\uparrow}}{\sqrt{N_L^\uparrow N_R^\downarrow} + \sqrt{N_L^\downarrow N_R^\uparrow}} \simeq PA_N(1 + O(\varepsilon^3)), \quad (1)$$

$$\frac{\sqrt{N_L^\uparrow N_L^\downarrow} - \sqrt{N_R^\uparrow N_R^\downarrow}}{\sqrt{N_L^\uparrow N_L^\downarrow} + \sqrt{N_R^\uparrow N_R^\downarrow}} \simeq \varepsilon_\Omega + PA_N\varepsilon + O(\varepsilon^3),$$

and

$$\frac{\sqrt{N_L^\uparrow N_R^\uparrow} - \sqrt{N_L^\downarrow N_R^\downarrow}}{\sqrt{N_L^\uparrow N_R^\uparrow} + \sqrt{N_L^\downarrow N_R^\downarrow}} \simeq \varepsilon_B + PA_N\varepsilon + O(\varepsilon^3),$$

where  $N$  is the number of events, indices  $\uparrow/\downarrow$  represent up/down beam polarizations, and  $\varepsilon$  is other asymmetries, and is expected to be less than 0.1.

$\varepsilon_\Omega$  is 30% and 40% for  $\mu^+$  and  $\mu^-$ , respectively. This is due to the dead MuTr electronics. Since detector acceptance terms during the derivation of Eq. (1) are exactly canceled out, this will be negligible on the  $A_N$  measurement unless  $\varepsilon_\Omega \sim \pm 1$ .  $\varepsilon_B$  is varied from  $-5\%$  to  $15\%$  by beam condition. Again, this will affect very small on the  $A_N$ .

We also employed the bunch shuffle method, in which bunch polarization direction is randomly shuffled, in order to estimate systematic error. Shuffled  $A_N$  should be distributed with zero average. Then the RMS of the distribution is considered to be the systematic error for  $A_N$ . It was measured as 0.01 which is comparable to statistical error.

The systematic error for  $A_N$  was evaluated. We are re-analyzing Run2 data with better reconstruction efficiency. It is expected to have 25% to 50% more muons and smaller  $\varepsilon_\Omega$ . Then error for  $A_N$  of 0.015 may be obtained. We have finished reprocessing Run2 data with better track reconstruction program and will obtain  $A_N$ .

## References

- 1) D. L. Adams et al.: Phys. Lett. **264**, 462 (1991).
- 2) H. Akikawa et al.: Nucl. Instrum. Methods Phys. Res. A **499**, 537 (2003).
- 3) H. D. Sato et al.: RIKEN Accel. Prog. Rep. **36**, 242 (2003).
- 4) A. Taketani et al.: RIKEN Accel. Prog. Rep. **36**, 228 (2003).
- 5) H. Spinka: ANL-HEP-TR99-113 (1999).

---

\* New Mexico State University, USA

# Identified hadron spectra in $\sqrt{s_{NN}} = 200$ GeV p+p collisions at RHIC-PHENIX

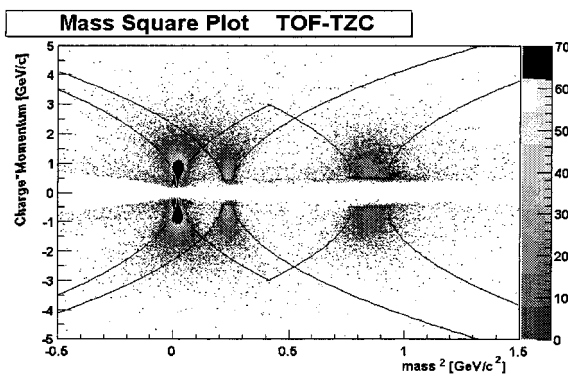
S. Kaminaga\* and S. Esumi\*

To investigate QGP formation,  $\sqrt{s_{NN}} = 200$  GeV Au+Au collisions are studied at BNL-RHIC. In Au+Au collisions, QGP phase formation and its recovery to the hadronic phase are expected. Hadron measurement reveals the final state of Au+Au collisions, and it is important to carry out systematic comparison of heavy-ion collisions with p+p collisions at the same energy.

The RHIC-PHENIX detector has a strong identification capability by means of time-of-flight measurements with high resolution.<sup>1,2)</sup> The start and stop signals for the time-of-flight measurements are given by beam-beam counter (BBC) and time-of-flight (TOF) detector. The BBC also provides the minimum-biased events by detecting a large number of particles near the beam line. In heavy-ion collisions, the BBC triggers nearly 100% of the Au+Au cross section. However, multiplicities for p+p collisions are much less than those for heavy-ion collisions, and the BBC triggers only half of the p+p collisions. Therefore a BBC-triggered p+p event sample might have an unknown trigger bias. In order to solve this problem, a time-zero counter (TZC) has been installed for p+p collisions in 2001. The TZC covers acceptance of TOF, thus it is expected that particle identification using TOF and TZC has a small trigger bias.

In this report, results of hadron analysis with TOF-TZC particle identification (PID) are shown, namely, mass square plot, mass<sup>2</sup> resolution, and  $pt$  spectra for TOF-TZC PID.

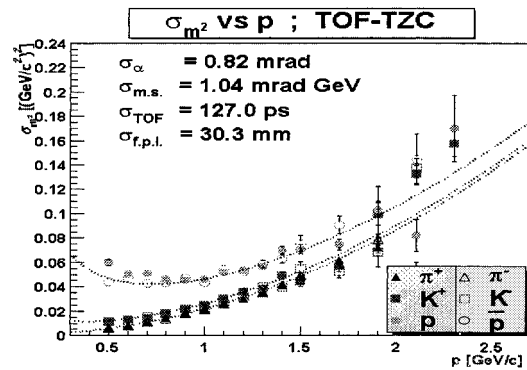
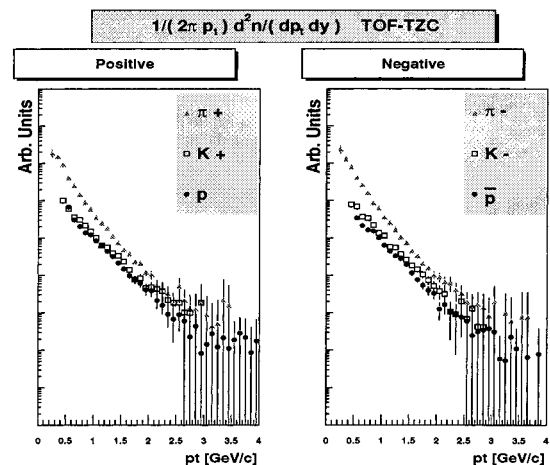
Figure 1 shows the mass<sup>2</sup> distribution with TOF-TZC PID in p+p collisions. The mass<sup>2</sup> distribution was calculated from momentum  $p$ , time of flight and flight path length. The  $2\sigma$  PID cut was applied to this

Fig. 1. Mass<sup>2</sup> vs. charge\* momentum.

analysis. The contamination correction was estimated here and applied to the spectra.

Figure 2 shows the mass<sup>2</sup> resolution for TOF-TZC PID. The  $\sigma_{TOF}$  is the resolution of the time of flight, and it is consistent to that expected from the design.

Figure 3 shows single-particle  $pt$  spectra with TOF-TZC PID in p+p collisions. These spectra have been corrected by Monte Carlo single-particle simulation. As the next step, we will study the trigger bias by comparing the BBC-triggered event sample and TZC-triggered event sample.

Fig. 2. Momentum dependence of mass<sup>2</sup> resolution. f.p.l denotes flight path length.Fig. 3. Single-particle  $pt$  spectra of identified hadrons.

## References

- 1) J. T. Mitchell et al.: Nucl. Instrum. Methods Phys. Res. A **482**, 491 (2002).
- 2) M. Aizawa et al.: Nucl. Instrum. Methods Phys. Res. A **499**, 508 (2003).

\* Department of Physics, University of Tsukuba



# Measurement of relative luminosity in polarized proton collision at PHENIX

K. Tanida, for the PHENIX Collaboration

The main purpose of the polarized proton run at PHENIX is to obtain information on the spin structure of protons by measuring the double spin asymmetry,  $A_{LL}$ , of various channels.  $A_{LL}$  is defined by the asymmetry of the reaction cross section of two longitudinally polarized particles as

$$A_{LL} = \frac{\sigma_{++} - \sigma_{+-}}{\sigma_{++} + \sigma_{+-}},$$

where  $\sigma_{++}(\sigma_{+-})$  is the cross section of a specific reaction channel with both particles having the same (opposite) helicity. Since the cross section can be written as experimental counting yield ( $N$ ) divided by integrated luminosity ( $L$ ) and overall detection efficiency ( $\epsilon$ ), which is safely assumed to be helicity independent, we can write

$$\epsilon_{LL} = \frac{N_{++} - RN_{+-}}{N_{++} + RN_{+-}}, \quad R = \frac{L_{++}}{L_{+-}},$$

where  $\epsilon_{LL}$  is the raw asymmetry and is relevant to  $A_{LL}$  through beam polarizations ( $P_B$  and  $P_Y$ ) as  $A_{LL} = \epsilon_{LL}/(P_B P_Y)$ . Here,  $R$  is called ‘‘relative luminosity’’.

In order to accurately measure  $A_{LL}$ , precise determination of  $R$  is necessary, as

$$\delta A_{LL} = \frac{1}{P_B P_Y} \frac{2N_{++}N_{+-}}{(N_{++} + RN_{+-})^2} \delta R \sim \frac{1}{2P_B P_Y} \delta R.$$

In Run 3, the average polarization was about 27% and our goal of  $A_{LL}$  accuracy was  $3 \times 10^{-3}$ , and thus  $\delta R$  must be smaller than  $4 \times 10^{-4}$ .

In the PHENIX experiment,<sup>1)</sup> relative luminosity and its accuracy were estimated as follows: We counted the number of coincidence of two Beam-Beam Counters (BBCLL1 trigger) for each bunch crossing and used it as an unnormalized luminosity for that crossing. Since BBCLL1 was free from backgrounds ( $\sim 10^{-4}$  of all triggers) and had very high statistics, it is an ideal (relative) luminosity monitor. Then we calculated  $R$  for each fill as we had all four combinations of helicities [(++), (+-), (-+), and (--)] in one fill.

To estimate the accuracy of relative luminosity, another trigger from Zero Degree Calorimeter (ZDCLL1 trigger) was used. ZDCLL1 was also free from backgrounds though its statistics was  $\sim 30$  times smaller than that of BBCLL1. Ideally, the ratio

$$r(i) = \frac{N_{ZDC}(i)}{N_{BBC}(i)}$$

is a constant independent of crossing number  $i$ . This assumption was checked by  $\chi^2$  of a fitting to

$$r(i) = C[1 + \epsilon_{LL}^{ZDC/BBC} S_B(i)S_Y(i)].$$

Here, the second term in the bracket of r.h.s. was introduced to implement the possible effect of  $A_{LL}$  in BBCLL1 and ZDCLL1, and  $S_B(i)$  and  $S_Y(i)$  represent the signs of helicity for crossing bunches [1(-1) for positive (negative) helicity].

The reduced  $\chi^2$  ( $\tilde{\chi}^2$ ) of the fitting significantly deviated from unity for most of the fills. It was found that this is mostly due to the crossing-by-crossing difference in collision Z-vertex distribution. Although the two triggers selected the same region ( $|Z_{\text{vert}}| < 30$  cm), the Z-vertex resolution of ZDCLL1 was worse ( $\sigma \sim 20$  cm) than that of BBCLL1 ( $\sigma \sim 5$  cm). Due to this difference, ZDCLL1/BBCCLL1 ratio increases as Z-vertex distribution broadens.

After correcting  $r(i)$  for this effect, the obtained  $\tilde{\chi}^2$  was consistent with unity for most of the fills, as shown in Fig. 1. As there are still fills whose reduced  $\tilde{\chi}^2$  is significantly larger than unity, we increased statistical error by  $\sqrt{\tilde{\chi}^2}$  if  $\tilde{\chi}^2 > 1$ .<sup>a)</sup>

Averaging over fills, we obtained  $\epsilon_{LL}^{\text{BBC/ZDC}} = (1.3 \pm 1.3) \times 10^{-4}$ . The error corresponds to  $\delta A_{LL} = 1.8 \times 10^{-3}$  or  $\delta R = 2.5 \times 10^{-4}$  and satisfies the Run 3 goal. We are continuing our work to further improve this analysis by studying other possible effects.

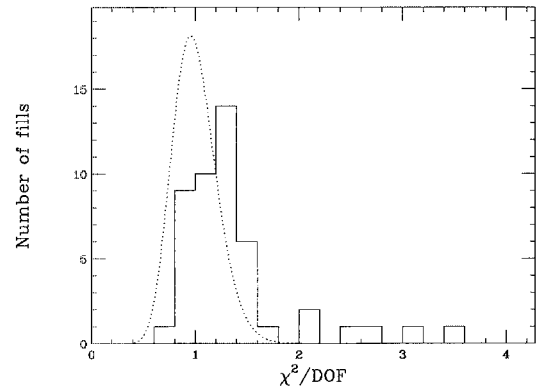


Fig. 1. Distribution of  $\tilde{\chi}^2$  ( $\chi^2/\text{DOF}$ ) after applying correction for Z-vertex width. The dotted curve is the ideal distribution, normalized to the number of analyzed fills (47).

## References

- 1) PHENIX Collaboration, K. Adcox et al.: Nucl. Instrum. Methods Phys. Res. A **499**, 469 (2003).

<sup>a)</sup> This correction gives conservative error estimation because  $\tilde{\chi}^2$  can be larger than unity by statistical fluctuation alone.

# Measurement of $A_N$ of inclusive particles by PHENIX BBC with tagged very forward neutron in polarized pp collisions at $\sqrt{s} = 200$ GeV

K. Tanida, for the PHENIX Collaboration

In the collision of transversely polarized protons at  $\sqrt{s} = 200$  GeV, it is reported<sup>1)</sup> that very forward neutron has a large single spin asymmetry ( $A_N$ ) of approximately  $-10\%$ . The mechanism of this asymmetry is of interest, and the measurement of  $A_N$  of coincident particles provides valuable information on it. For example, if the neutron asymmetry comes from diffractive-like processes, *i.e.*,

$$\vec{p} + p \rightarrow N^*(\Delta^*) + X_1, \quad N^*(\Delta^*) \rightarrow n + X_2,$$

it is expected that  $A_N$  of  $X_2$ , which is detected by forward counters, has the same sign as the neutron, and that the sign is opposite for backward particle(s),  $X_1$ .

PHENIX Beam-Beam Counter (BBC) is suitable for detecting these coincident particles since it covers forward and backward regions (pseudorapidity  $3.0 < |\eta| < 3.9$ ). Here, we describe the result on  $A_N$  in BBC with very forward neutron tagged by Zero Degree Calorimeter (ZDC). See Ref. 2 for the descriptions of the BBC, ZDC and other detectors in PHENIX.

Except that neutron hits were tagged, the analysis procedure was mostly the same as that in last year's report,<sup>3)</sup> where measurement of  $A_N$  of inclusive charged particles at BBC was described. Neutrons were selected in the following way. Because the DX magnet is located in front of ZDC, only neutral particles ( $\gamma$ ,  $n$ , and  $K_L$ ) were detected. Since ZDC has three telescope segments of 20 cm thick tungsten each and  $\gamma$ 's cannot penetrate the first segment, we were able to select hadrons by requiring a hit in at least one of the second and third segments. Contamination of  $K_L$  was estimated to be 2–3% and was neglected. We performed a realistic detector simulation and estimated the purity of neutron tagging to be 86%, with the main background being  $\gamma$ 's which hit the light guide of ZDC. For reference,  $\gamma$  tagging was also performed by selecting a hit only in the first segment; according to the same detector simulation, the purity of  $\gamma$  tagging is 52%, with a severe contamination of neutrons (42%).

We then calculated asymmetries for each beam fill, using the bunch fitting method.<sup>3)</sup> Distribution of reduced  $\chi^2$  of the fitting was consistent with the expected  $\chi^2$  distribution so that no systematic error was suggested here.

The preliminary results are  $A_N = [-4.86 \pm 0.54(\text{stat.}) \pm 0.42(\text{syst.})] \times 10^{-2}$  for particles detected by forward BBC and  $A_N = [2.46 \pm 0.59(\text{stat.}) \pm 0.21(\text{syst.})] \times 10^{-2}$  for backward particles with forward neutron tagging. The systematic error include

uncertainties in the event selection and treatment of backgrounds in neutron tagging, but not that in beam polarization. Consistency between physically equivalent measurements (*i.e.*,  $A_N$  obtained by BBC-north and BBC-south) was checked and was fine. Parity-violating asymmetry (top-bottom asymmetry) was also checked and confirmed to be consistent with zero. When the backward neutron was tagged, the asymmetries were consistent with zero in both forward and backward BBCs. The asymmetries were also consistent with zero for  $\gamma$ -tagged events after subtracting the effect of neutron contamination in the  $\gamma$  tagging.

The present results of  $A_N$  are consistent, at least qualitatively, with the simple picture of diffractive-like processes mentioned above. On the other hand, there is another possibility for the  $A_N$  of forward neutron based on the result of FNAL E704.<sup>4)</sup> They observed a positive  $A_N$  for forward  $\pi^+$  and  $\pi^0$  and a negative  $A_N$  for  $\pi^-$  at  $\sqrt{s} = 20$  GeV. Also, STAR reported that the  $A_N$  for forward  $\pi^0$  survives even at  $\sqrt{s} = 200$  GeV,<sup>5)</sup> and that they observed positive asymmetry at their BBC,<sup>6)</sup> where more  $\pi^+$  is expected than  $\pi^-$ . Hence, a possible explanation is that the neutron asymmetry is caused by a recoil of  $\pi^+$  which is kicked out of a proton. However, it is quite difficult to explain the present results by this mechanism since the  $\pi^+$  is very likely detected by BBC so that forward BBC asymmetry becomes positive. Therefore, the present result suggests the mechanism for  $A_N$  in very forward neutron is different from that of forward pions observed by FNAL E704 and STAR.

We are still working on the data analysis to understand systematic errors better. Also, analysis of data taken in FY 2003 is starting to obtain higher statistics and to measure  $A_N$  using other detectors with forward neutron tagging for better understanding of the reaction mechanism.

## References

- 1) Y. Fukao et al.: RIKEN Accel. Prog. Rep. **36**, 232 (2003).
- 2) PHENIX Collaboration, K. Adcox et al.: Nucl. Instrum. Methods Phys. Res. A **499**, 469 (2003).
- 3) PHENIX Collaboration, K. Tanida et al.: RIKEN Accel. Prog. Rep. **36**, 229 (2003).
- 4) D. L. Adams et al.: Phys. Lett. B **264**, 462 (1991).
- 5) STAR Collaboration, G. Rakness et al.: AIP Conf. Proc. **675**, 400 (2003).
- 6) STAR Collaboration, J. Kiryluk et al.: AIP Conf. Proc. **675**, 424 (2003).

# Measurement of longitudinal double spin asymmetry for $\pi^0$ 's in proton-proton collisions at $\sqrt{s} = 200$ GeV from RHIC PHENIX Run 3

A. Bazilevsky, C. Aidala,\*<sup>1</sup> F. Bauer,\*<sup>2</sup> A. L. Deshpande, Y. Goto, Y. Fukao,\*<sup>3</sup> B. Fox, T. Horaguchi,\*<sup>4</sup> K. Okada, K. Tanida, and H. Torii, for the PHENIX Collaboration

Measurement of the gluon polarization in a polarized proton is a major goal of the RHIC-Spin program. It can be probed through the longitudinal double spin asymmetry ( $A_{LL}$ ) in high  $p_T$  hadron production.<sup>1)</sup> During the year 2003 run, RHIC was successfully operated for the first time as a collider of longitudinally polarized protons at a center of mass energy of 200 GeV. We present the first PHENIX results on  $A_{LL}$  for  $\pi^0$  in four  $p_T$  bins in the range of 1–5 GeV/c obtained from the data corresponding to the integral luminosity of  $0.215 \text{ pb}^{-1}$ , the average beam polarization being 26%.

To calculate  $A_{LL}$ , we measured the number of  $\pi^0$ 's ( $N$ ) and integral luminosity ( $L$ ) from the colliding protons with the same ( $++$ ) and the opposite ( $+ -$ ) helicity:

$$A_{LL} = \frac{1}{|P_B||P_Y|} \frac{N_{++} - RN_{+-}}{N_{++} + RN_{+-}}, \quad R = \frac{L_{++}}{L_{+-}}, \quad (1)$$

where  $P_B$  and  $P_Y$  are beam polarizations.

For the relative luminosity ( $R$ ) measurements,<sup>2)</sup> we used beam-beam counters.<sup>3)</sup> The achieved relative luminosity precision was  $\delta R = 2.5 \times 10^{-4}$ , which corresponded to  $\delta A_{LL} = 1.8 \times 10^{-3}$ .

The PHENIX Local Polarimeter<sup>4)</sup> was used to measure the longitudinal component of the spin of the beams as well as to confirm the spin direction.

High  $p_T$   $\pi^0$ 's were collected using an electromagnetic-calorimeter-based high  $p_T$  photon trigger (ERT<sup>5)</sup>). The trigger efficiency for  $\pi^0$ 's varied from 6% in the 1–2 GeV/c  $p_T$  bin to 95% in the 4–5 GeV/c  $p_T$  bin. The number of  $\pi^0$ 's was obtained by integrating the counts under  $\pi^0$  peak in  $\pm 25 \text{ MeV}/c^2$  mass window in two photon invariant mass distributions. The background contribution (combinatorial+hadronic) varied from 45% in the 1–2 GeV/c  $p_T$  bin to 5% in the 4–5 GeV/c  $p_T$  bin.

The spin asymmetry for each beam fill<sup>a)</sup>  $A_{LL}^{fill}$  was calculated using Eq. (1). For the  $A_{LL}^{fill}$  error evaluation, we considered only the statistical error on  $N$ :

$$\sigma_{A_{LL}^{fill}} = \frac{1}{|P_B||P_Y|} \cdot \frac{\sigma_{N_{++}+N_{+-}}}{N_{++} + N_{+-}}. \quad (2)$$

The statistical error is given by  $\sigma_N = \sqrt{k^2 N^{ev}}$ , where

$N^{ev}$  is the number of recorded events and  $k$  is count multiplicity per event. In a ‘‘Poisson limit’’ ( $k$  is always 0 or 1)  $\sigma_N = \sqrt{N}$ .

The resulting  $A_{LL}$  was obtained after the fitting of all  $A_{LL}^{fill}$ 's to a constant. The fitting  $\chi^2$  as well as ‘‘bunch shuffling’’ technique were used to confirm the errors assigned to  $A_{LL}$ 's. In each ‘‘bunch shuffling’’ we randomly assigned the helicity sign to every bunch crossing and did the whole procedure to calculate  $A_{LL}$  and  $\chi^2$  described above. Mean values of  $\chi^2/\text{NDF}$  (NDF is the number of degrees of freedom) were very close to unity in all  $p_T$  bins. The widths of the distributions of  $A_{LL}$  values for  $N$  obtained in all bunch shuffles were consistent with errors assigned to  $A_{LL}$ 's. It denotes that errors were properly assigned to  $A_{LL}$  values. In other words, all other noncorrelated bunch-to-bunch and fill-to-fill systematic errors are much less than  $N^{\pi^0}$  statistical errors. (Certainly, it does not exclude correlated systematic errors for all bunches and fills, such as the error on polarization).

Figure 1 shows our  $A_{LL}$  results after background  $A_{LL}$  subtraction (points) as well as theory prediction curves.<sup>6)</sup> The  $A_{LL}$  of background was estimated for the counts adjacent to the  $\pi^0$  peak in two photon invariant mass distributions. The obtained sensitivity is not yet sufficient to discriminate between different gluon polarization models. The expected statistics and beam polarization in the next runs (in 2004–2005) will decrease the error bars 3–7 times.

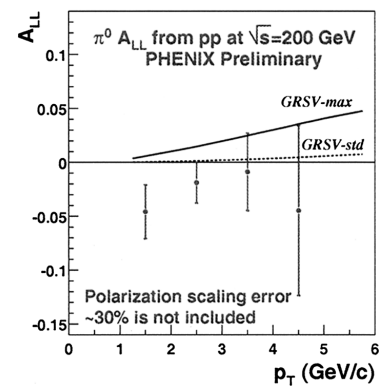


Fig. 1. The measured double spin asymmetry  $A_{LL}^{\pi^0}$  vs. the  $p_T$  with two theoretical curves shown for different gluon polarizations<sup>6)</sup>.

\*<sup>1</sup> Brookhaven National Laboratory, USA

\*<sup>2</sup> University of Riverside, USA

\*<sup>3</sup> Kyoto University

\*<sup>4</sup> Tokyo Institute of Technology

a) Each fill is characterized by a constant polarization of the beams.

## References

- 1) A. Bazilevsky et al.: RIKEN Accel. Prog. Rep. **34**, 243 (2001).
- 2) K. Tanida: RIKEN Accel. Prog. Rep. **37**, 227 (2004).
- 3) M. Allen et al.: Nucl. Instrum. Methods Phys. Res. A **499**, 549 (2003).
- 4) A. Deshpande et al.: RIKEN Accel. Prog. Rep. **37**, 246 (2004).
- 5) K. Okada et al.: RIKEN Accel. Prog. Rep. **36**, 248 (2003).
- 6) B.Jäger et al.: Phys. Rev. D **67**, 054005 (2003).

# Measurement of $\pi^0$ production in p+p and Au+Au collisions at $\sqrt{s_{NN}} = 200 \text{ GeV}^\dagger$

H. Torii, A. Bazilevsky, B. Fox, Y. Goto, and K. Okada for the PHENIX Collaboration

In this paper, two independent but strongly related topics are discussed. One is about a testing ground of the perturbative quantum chromodynamics (pQCD) theory and the other is the medium effect in heavy ion collisions, the suppression of particle production at high  $p_T$  which is predicted as a Quark Gluon Plasma (QGP) signature.<sup>1)</sup> In the first part, we will prove that our measurements in p+p collisions can be described by the pQCD theory. Next, we will compare the measured medium effect in Au+Au collisions with the p+p data. This study used PHENIX electromagnetic calorimeters, which have an azimuthal coverage of  $90^\circ + 90^\circ$  and a pseudorapidity coverage of  $\pm 0.35$ . The data were collected during the p+p and Au+Au runs in 2001–2002 at RHIC.

In Fig. 1, our results of  $\pi^0$  production in the p+p data are compared with next-to-leading order (NLO) pQCD calculations.<sup>2)</sup> The calculations have been performed with the same renormalization and factorization scales of  $p_T$  by using the CTEQ6M<sup>3)</sup> set of parton distribution functions and two sets of fragmentation functions: “Kniehl-Kramer-Pötter” (KKP)<sup>4)</sup> and “Kretzer”.<sup>5)</sup> The calculation with the former agrees with our data better than that with the latter. These two sets differ mainly in that the gluon-to-pion fragmentation function,  $D_g^\pi$ , is greater in the KKP set. This difference is exhibited primarily at low  $p_T$  because of the dominance of gluon-gluon interactions. We conclude that the  $\pi^0$  production in p+p collisions in this energy region are described well by the pQCD calculation.

In Au+Au collisions, we quantify the medium ef-

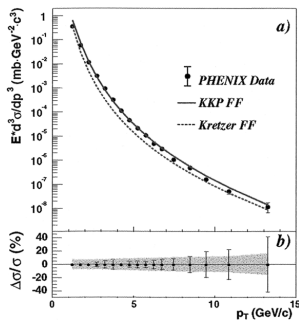


Fig. 1. a) Invariant differential cross section for inclusive  $\pi^0$  production in p+p collisions and the results of NLO pQCD calculations.<sup>2-5)</sup> See the text for details. b) The relative statistical (point) and point-to-point systematic (band) errors.

fects with the nuclear modification factor given by the ratio of the measured Au+Au invariant yields to the  $NN$ -collision-scaled p+p invariant yields:  $R_{AA} = \frac{d^2 N_{AuAu}^{\pi^0}}{N_{AuAu}^{evt} dp_T dy} / (\langle N_{coll} \rangle \times \frac{d^2 \sigma_{pp}^{\pi^0}}{\sigma_{pp}^{inel} dp_T dy})$ , where  $\langle N_{coll} \rangle$  is the average nucleon-nucleon collision estimated by the Glauber model.  $R_{AA}(p_T)$  measures the deviation of AA data from an incoherent superposition of  $NN$  collisions. Figure 2 shows  $R_{AA}$  as a function of  $p_T$  measured in the 0–10% central and 80–92% peripheral Au+Au collisions. Within errors, the peripheral collisions behave similarly to a superposition of  $NN$  collisions. The  $R_{AA}$  values for the central collisions, however, are notably below unity, as observed at 130 GeV,<sup>6)</sup> and in contrast to the enhanced high  $p_T$   $\pi^0$  production ( $R_{AA} > 1$ ) observed at CERN-SPS energies.<sup>7)</sup>

In summary, we have discovered significant suppression of the  $\pi^0$  production in the central Au+Au collisions compared to an incoherent superposition of  $NN$  collisions. This observation is consistent with the theoretical model, jet quenching, predicted as a QGP signature.<sup>1)</sup>

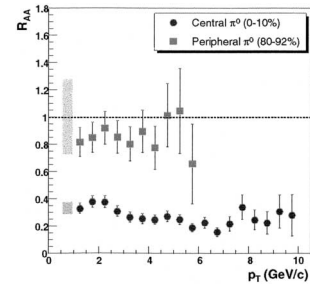


Fig. 2. Nuclear modification factor  $R_{AA}(p_T)$  in central and peripheral Au+Au collisions. Error bars include statistical and systematic errors. Shaded bands represent the quadratic sum of fractional uncertainties in Glauber calculation and  $\pi^0$  yield normalization.

## References

- 1) X. N. Wang et al.: Phys. Rev. D **44**, 3501 (1991).
- 2) F. Aversa et al.: Nucl. Phys. B **327**, 105 (1989); Private communication with W. Vogelsang.
- 3) CTEQ Collaboration, J. Pumplin et al.: J. High Energy Phys. 07(2002)012.
- 4) B. A. Kniehl et al.: Nucl. Phys. B **597**, 337 (2001).
- 5) S. Kretzer: Phys. Rev. D **62**, 054001 (2000).
- 6) PHENIX Collaboration, K. Adcox et al.: Phys. Rev. Lett. **88**, 022301 (2002).
- 7) WA98 Collaboration, M. M. Aggarwal et al.: Eur. Phys. J. C **23**, 225 (2002).

<sup>†</sup> Condensed from the article in Phys. Rev. Lett. **91**, 072301 (2003); Phys. Rev. Lett. **91**, 241803 (2003)

## Simulation studies for the Si-Vertex Tracker at PHENIX photon-jet production in $pp$ collisions at $\sqrt{s} = 200$ GeV

M. Togawa,\* Y. Akiba, H. En'yo, Y. Goto, K. Imai,\* V. L. Rykov and N. Saito\*

Direct photon production is a key process of measuring the gluon distribution of nucleons and the polarization of gluons. At RHIC energies, quark-gluon Compton scattering,  $q + g \rightarrow q + \gamma$ , is the dominant parton-level process in high- $p_T$  direct photons. In  $pp$  collisions, the cross section of this process is directly proportional to the quark and gluon densities multiplied by the pQCD cross section. Thus, measuring a direct photon together with a recoil jet is a direct and clean method of measuring the gluon density and polarization. With the present PHENIX setup, direct photons are measured with finely segmented electromagnetic calorimeters (EMCal) in central arms. However, most of the recoil jets cannot be measured due to the limited coverage of the central arms.

The Si-Vertex Tracker (VTX) is proposed as a PHENIX upgrade,<sup>1,2</sup> that works as a large solid angle charged particle tracker and the expected momentum resolution is approximately 10% for a 1 GeV/c track.<sup>3</sup> This resolution is sufficient to reconstruct the recoil jets. With the knowledge of the recoil jet, we can constrain the initial kinematics ( $x_1$  and  $x_2$ ) of incoming partons and thus determine the gluon density and polarization as a function of  $x$ .

We have studied the potential improvements due to the VTX in a Monte Carlo simulation. In this simulation, the direct photon events are generated using the PYTHIA event generator. The recoil jet is reconstructed from the charged tracks within the VTX detector acceptance ( $|\eta| < 1.2$ ), but in the opposite azimuthal direction of the direct photon. In the first step of the algorithm, tracks with momenta greater than 1.0 GeV/c at an azimuthal angle opposite to the direct photon ( $|\phi - \phi_\gamma| > \pi/2$ ) are selected. Then, the direction of the jet is estimated to be the momentum weighted average of the selected tracks.

$$\eta^{jet} = \frac{\sum \eta^i p_T^i}{\sum p_T^i}, \quad \phi^{jet} = \frac{\sum \phi^i p_T^i}{\sum p_T^i} \quad (1)$$

Next, the tracks within the cone radius,  $R = \sqrt{(\eta^{jet} - \eta^i)^2 + (\phi^{jet} - \phi^i)^2}$ , are selected ( $R < 0.5$ ). This procedure is iterated until the direction of the axis no longer changes.

From the measurement of  $\eta_{jet}$  and the transverse momentum  $p_T$  of the direct photon, the kinematics of the initial partons can be determined. Under the assumption that the  $p_T$  values of the direct photon and the recoil jet are the same, the fractional momenta of the initial partons  $x_1$  and  $x_2$  are calculated to be,

$$x_1 = \frac{p_T}{\sqrt{s}} (\exp(\eta^{jet}) + \exp(\eta^\gamma)), \quad (2)$$

$$x_2 = \frac{p_T}{\sqrt{s}} (\exp(-\eta^{jet}) + \exp(-\eta^\gamma)). \quad (3)$$

The two panels in Fig. 1 show the correlation between the  $x$  calculated as mentioned above (reconstructed  $x$ ) and its true value is from the event generator (true  $x$ ). If the recoil jet direction is not known (left panel) the best estimate for  $x$  based on the photon  $p_T$  is only loosely correlated to the true  $x$ . However, with the recoil jet reconstruction (right panel) there is a narrow correlation between the reconstructed  $x$  and true  $x$ .

In Fig. 2,  $(\text{reconstructed } x - \text{true } x)/\text{true } x$  is shown as a function of  $x_1$ , and the error bar shows these widths (RMS). In the range of  $x > 0.04$ , the  $x$  values are determined with an accuracy of  $\sim 20\%$ .

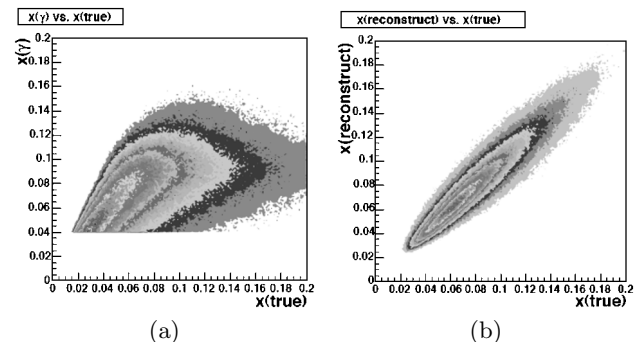


Fig. 1. Correlation between reconstructed  $x$  and true  $x$  from PYTHIA. These samples are chosen as  $\gamma_{p_T} > 4.0$  GeV/c. (a) no jet information has been used (calculated as  $2p_T/\sqrt{s}$ ). (b) is obtained using the reconstructed jet axis in the barrel VTX.<sup>1)</sup>

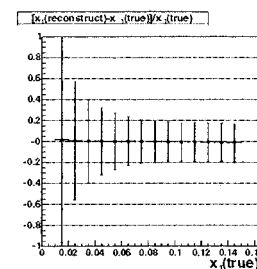


Fig. 2.  $(\text{reconstructed } x - \text{true } x)/\text{true } x$  is shown as a function of  $x_1$ , and the error bar shows these widths (RMS).<sup>1)</sup>

### References

- 1) Y. Akiba et al.: Proposal for Silicon Vertex Tracker (VTX) for the PHENIX Experiment (BNL, upon 2003).
- 2) Y. Goto et al.: RIKEN Accel. Prog. Rep. **37**, 249 (2004).
- 3) Y. Goto et al.: RIKEN Accel. Prog. Rep. **36**, 249 (2003).

\* Department of Physics, Kyoto University

# Charged hadron analysis in proton-proton collisions at $\sqrt{s} = 200$ GeV

K. Okada and J. Jia,\* for the PHENIX Collaboration

As a probe of the high-energy density matter created in relativistic heavy ion collisions, we can use charged hadrons, which are produced through the initial parton-parton interactions. With medium effects, charged hadron transverse momentum spectra are expected to be distorted from the scaling of those from inelastic nucleon-nucleon interactions.

The data of  $p + p$  collisions at a center of mass energy ( $\sqrt{s}$ ) of 200 GeV collected during the 2001–2002 run period (Run2) provide the basic knowledge for Au+Au collisions in the same energy per nucleon. In this article, we report the analysis procedure of inclusive charged hadron production with 21 million vertex triggered events.

We use the East central tracking spectrometer in PHENIX.<sup>1)</sup> The key detectors in this analysis are, from the collision point to the outside, Beam-Beam Counters (BBC), the drift chamber (DC), the pad chamber (PC1), the ring image cherenkov counter (RICH), another pad chamber (PC3), and the Electromagnetic Calorimeter (EMC). The magnetic field ( $\int \mathbf{B} \cdot d\mathbf{l} = 0.78$  [T · m]) exists inside the DC radius.

Particles reconstructed in BBC, DC, and PC1 include many fake ones. At first, PC3 hit matching is applied. Because of the absence of a tracking system inside the magnetic field in PHENIX, in the case that a photon converts to electrons in front of DC or a particle decays in flight, the kick offsets the magnetic field kick; such daughters are assigned as an incorrect momentum. Here the statistical subtraction method<sup>2)</sup> was applied. The conversion electron contamination was estimated by using RICH. The decay daughter backgrounds are mostly low momentum particles which can be bent by the residual field outside the DC radius. This results in the broadening of the PC3 hit matching. Its matching shape is independent of the appeared momentum. Figure 1 shows how background subtraction works.

For the correction of the acceptance and the momentum smearing, Monte Carlo simulation is performed. After tuning detector dead region, the correction factor defined by the ratio of number of particles reconstructed to the input is approximately 13. This is consistent with the simple estimation from  $(\Delta\eta \cdot \Delta\phi / 2\pi \cdot \epsilon_{DC+PC1} \cdot \epsilon_{PC3})^{-1} = (0.5 \cdot 0.25 \cdot 0.75 \cdot 0.82)^{-1}$ , where  $\epsilon_{DC+PC1}$  and  $\epsilon_{PC3}$  are mainly determined by the live area.

The integrated luminosity is determined from the number of BBC triggered events using an absolute calibration of the trigger cross section obtained *via* the van der Meer scan technique. From this measurement,

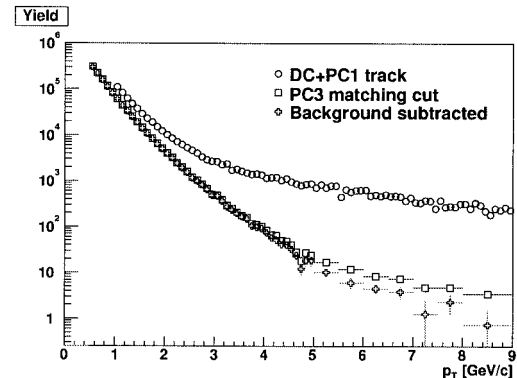


Fig. 1. Yield.

our BBC trigger is approximately half ( $21.8 \pm 0.9$  mb) of total inelastic interactions.<sup>3)</sup> The next question is about trigger bias. In the neutral pion analysis,<sup>3)</sup> events with pion production tend to be triggered by 0.75/0.52 independent of the pion momentum above 1 GeV/c. For events with charged hadron production, PC+EMC tracking is used for the BBC unbiased sample. The result is consistent with the neutral pion results, with a slight drop in the lower  $p_T$  region (Fig. 2).

This analysis will be finalized by the end of 2003.

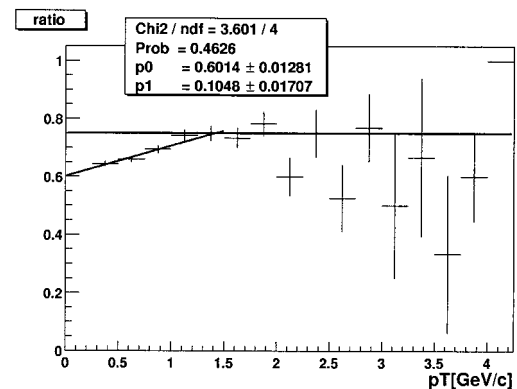


Fig. 2. BBC trigger bias study with PC track. 0.75 is the result of  $\pi^0$ . The drop in the high  $p_T$  region is due to momentum resolution of PC+EMC tracking.

## References

- 1) K. Adcox et al.: Nucl. Instrum. Methods Phys. Res. A **499**, 469 (2003).
- 2) J. Jia: Ph.D. Thesis, State University of New York at Stony Brook (2003).
- 3) S. S. Adler et al.: Phys. Rev. Lett. **91**, 241803 (2003).

\* Columbia University, USA

# Background study of direct photon production in proton-proton collisions at $\sqrt{s} = 200$ GeV with PHENIX

T. Horaguchi\* and Y. Akiba

Polarized proton-proton collisions at the Relativistic Heavy Ion Collider (RHIC) can provide information on the spin structure of the nucleon. Direct photon at high  $p_T$  is produced mainly by gluon Compton scattering ( $gq \rightarrow \gamma q$ ). The measurement of the direct photon cross section is a testing ground of perturbative QCD, and it gives us the polarized and unpolarized gluon distributions in the nucleon.

In PHENIX,<sup>1)</sup> we have collected data with an integrated luminosity of  $0.15 \text{ pb}^{-1}$  for transversely polarized proton-proton collisions with 15% average polarization in the run of 2001–2002 and  $0.35 \text{ pb}^{-1}$  for longitudinally polarized data in the run of 2003 at  $\sqrt{s} = 200$  GeV with 30% average polarization.

We analyze the 2001–2002 data of PHENIX to measure the direct photon cross section in  $pp$  collisions at RHIC. We use the electromagnetic calorimeter of central arm spectrometers for the analysis. This calorimeter consists of two subsystems, six sectors of a lead scintillator calorimeter and two sectors of a lead glass calorimeter. It is located at a radial distance of approximately 5 m from the beam line. Each of these sectors covers the pseudorapidity range of  $|\eta| < 0.35$  and an azimuthal angle of  $\Delta\phi = 22.5^\circ$ . In this analysis, we use five lead scintillator calorimeters.

In order to measure the direct photon cross section, we need to subtract a large background from the decay of  $\pi^0$  and  $\eta$  ( $\pi^0 \rightarrow \gamma\gamma, \eta \rightarrow \gamma\gamma$ ). We use the following method in search for the direct photon signal. We select a high  $p_T$  photon ( $p_T \geq 3 \text{ GeV}/c$ ) in a fiducial volume in the calorimeter. If the reconstructed mass of the photon and any other photon in the same event is close to the mass of  $\pi^0$  or  $\eta$ , the photons are rejected as “decay photons”. The remaining photons are direct photon candidates, which include some fraction of  $\pi^0$  and  $\eta$  decay photons since the rejection method is not perfect. Therefore the direct photon candidates are contaminated by the background of such “fake direct photons”. We evaluate the ratio of the “fake direct photon” relative to the “decay photon” by the detailed GEANT Monte Carlo simulation of PHENIX. We define “fake ratio”  $R_{\text{fake}}$  as

$$R_{\text{fake}}^{MC}(\pi^0) = N_{\gamma}^{MC}(\text{fake})/N_{\gamma}^{MC}(\pi^0). \quad (1)$$

Here,  $N_{\gamma}^{MC}(\pi^0)$  ( $N_{\gamma}^{MC}(\text{fake})$ ) is the number of  $\pi^0$  decay photons in the Monte Carlo simulation for which

the other photon from the same parent  $\pi^0$  is (not) detected in the calorimeter. The fake ratio for  $\eta$ ,  $R_{\text{fake}}^{MC}(\eta)$ , is defined in a similar way. We can then subtract the remaining background in the direct photon candidate by

$$N_{\gamma}^{\text{sig}} = N_{\gamma}^{\text{cand}} - R_{\text{fake}}^{MC}(\pi^0)N_{\gamma}(\pi^0) - R_{\text{fake}}^{MC}(\eta)N_{\gamma}(\eta) - N_{\gamma}^{\text{other}}. \quad (2)$$

Here,  $N_{\gamma}^{\text{sig}}$  is the number of direct photon signals,  $N_{\gamma}^{\text{cand}}$  is the number of direct photon candidates in the data,  $N_{\gamma}(\pi^0)$  ( $N_{\gamma}(\eta)$ ) is the number of identified  $\pi^0$  ( $\eta$ ) decay photons measured in the data, and  $N_{\gamma}^{\text{other}}$  is the remaining small background due to photons from hadron decays ( $\omega \rightarrow \gamma\pi^0, \eta' \rightarrow \gamma\gamma$ ) and mis-identified hadrons.

The data analysis based on this method is in progress. Figure 1 shows the “fake ratio” for  $\pi^0$  as a function of  $p_T$  calculated by the Monte Carlo simulation. We are also working to determine the correction factors (acceptance, trigger efficiency) and to estimate the systematic uncertainties of the analysis. We expect that we can soon establish the signal of the direct photon in the data and can determine its cross section.

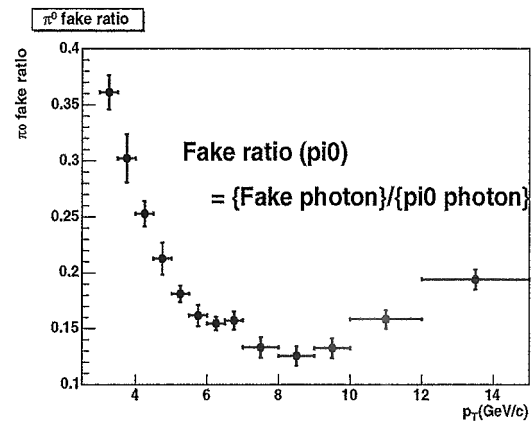


Fig. 1. “Fake ratio” for  $\pi^0$ . See the explanations in the text.

## References

- 1) K. Adcox et al.: Nucl Instrum. Methods Phys. Res. A **499**, 469 (2003).

\* Department of Physics, Tokyo Institute of Technology



# Radial flow study from identified hadron spectra in Au+Au collisions at $\sqrt{s_{NN}} = 200$ GeV

A. Kiyomichi and T. Chujo, for the PHENIX Collaboration

Heavy ion collisions at relativistic energy offer the possibility of producing highly compressed strongly interacting matter, which may form the quark gluon plasma (QGP). Identified hadron spectroscopy is an important tool for studying the collision dynamics. The momentum spectra of pions, kaons, and protons are sensitive to the dynamical evolution of the system and carry information about the radial flow velocity and thermal freeze-out condition.

PHENIX<sup>1)</sup> is one of the major experiments performed at RHIC for measuring a variety of signals from heavy-ion collisions. We have measured the transverse momentum spectra for  $\pi^\pm$ ,  $K^\pm$ ,  $p$  and  $\bar{p}$  at mid-rapidity in Au+Au collisions at  $\sqrt{s_{NN}} = 200$  GeV over a broad momentum range with various centrality selections. The detailed analysis methods and results are described in Ref. 2.

Figure 1 shows the centrality dependence of mean transverse momentum  $\langle p_T \rangle$  for  $\pi^\pm$ ,  $K^\pm$ ,  $p$  and  $\bar{p}$ . It is found that  $\langle p_T \rangle$  for all particle species increases from the most peripheral to the central collisions, and also increases with particle mass. The dependence of  $\langle p_T \rangle$  on particle mass suggests the existence of a collective hydrodynamical expansion.

The radial flow velocity ( $\beta_T$ ) and freeze-out temperature ( $T_{fo}$ ) are extracted using a phenomenological hydrodynamical model presented in Ref. 3. The invariant cross section can be expressed as

$$\frac{dN}{m_T dm_T} \propto \int_0^R r dr m_T I_0\left(\frac{p_T \sinh \rho}{T_{fo}}\right) K_1\left(\frac{m_T \cosh \rho}{T_{fo}}\right),$$

where  $I_0$ ,  $K_1$  are modified Bessel functions and  $\rho = \tanh^{-1} \beta_r$ . Here  $T_{fo}$  is the freeze-out temperature,  $R$  is the maximum radius of the expanding source at freeze-

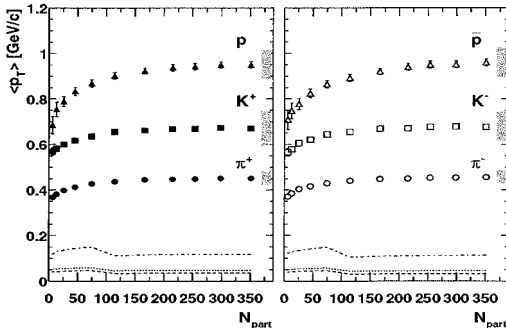


Fig. 1. Mean transverse momenta  $\langle p_T \rangle$  as a function of  $N_{part}$  for  $\pi^\pm$ ,  $K^\pm$ ,  $p$  and  $\bar{p}$ . The error bars are statistical errors. The systematic errors from cuts conditions are shown as shaded boxes on the right for each particle species.

out and  $m_T = \sqrt{p_T^2 + m^2}$  denotes the transverse mass of the particle. The transverse velocity profile  $\beta_r(r)$  is parameterized as  $\beta_r(r) = \beta_T (r/R)^n$ , with the surface velocity  $\beta_T$ .

To study the parameter correlations, we make a grid of combinations of  $T_{fo}$  and  $\beta_T$ , and perform a chi-squared minimization for each particle type. We use a linear velocity profile ( $n = 1$ ) and constant particle density distribution. The fit is performed simultaneously for all particle species in the range  $(m_T - m_0) < 1.0$  GeV. Since the experimental data include the decay of resonance, we add the decay of mesonic ( $\rho, \eta, \omega, K^*, \dots$ ) and baryonic ( $\Delta, \Lambda, \Sigma, \dots$ ) resonance effects as follows: (1) Generate resonances with the transverse momentum distribution determined by each combination of  $T_{fo}$  and  $\beta_T$ . (2) Decay them using Monte Carlo simulation, and obtain  $\pi^\pm$ ,  $K^\pm$ ,  $p$  and  $\bar{p}$  distribution. (3) Merge all particles, where the particle abundance is calculated with chemical parameters ( $T_{ch} = 177$  MeV,  $\mu_B = 29$  MeV).<sup>4)</sup>

Figure 2 shows the centrality dependence of the freeze-out temperature  $T_{fo}$  and radial flow velocity  $\beta_T$ . It is found that  $T_{fo}$  decreases and  $\beta_T$  increases from the most peripheral to mid-central collisions, and appears to saturate in the central collisions. The behavior of  $\beta_T$  is in accordance with a collective expansion picture.

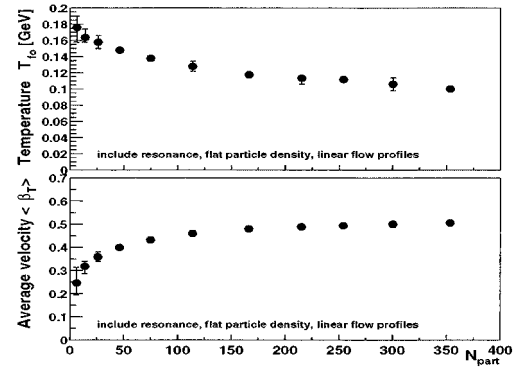


Fig. 2. Freeze-out temperature (top) and average radial flow velocity (bottom) as a function of  $N_{part}$ .

## References

- 1) PHENIX Collaboration, K. Adcox et al.: Nucl. Instrum. Methods Phys. Res. A **499**, 469 (2003).
- 2) PHENIX Collaboration, S. S. Adler et al.: Phys. Rev. C **69**, 034909 (2004).
- 3) E. Schnedermann, J. Sollfrank, and U. Heinz: Phys. Rev. C **48**, 2462 (1993).
- 4) P. Braun-Munzinger, D. Magestro, K. Redlich, and J. Stachel: Phys. Lett. B **518**, 41 (2001).

# Single electron measurement in $\sqrt{s_{NN}} = 200$ GeV Au+Au collisions

T. Hachiya\* and Y. Akiba

Heavy quarks (charm and beauty) are one of the important probes of the hot and dense matter created in high energy heavy ion collisions. They are mainly produced *via* gluon-gluon fusions in the initial stage of the collisions. Therefore, the yield of charm and beauty is sensitive to the initial gluon density.<sup>1)</sup> In central Au+Au collisions at RHIC, high  $p_T$  particles are strongly suppressed due to energy loss in the dense matter created in the collision. It is predicted that the charm quarks suffer smaller energy loss than light quarks due to the “dead cone” effect.<sup>2)</sup> This effect can be studied from the transverse momentum ( $p_T$ ) distribution of charmed particles. In addition, the open charm yield is the baseline of the  $J/\psi$  suppression<sup>3)</sup> which is one of the expected signatures of the deconfinement of quarks and gluons.

The measurement of single electrons at high  $p_T$  resulting from the semi-leptonic decays of heavy quarks ( $D \rightarrow eX$  and  $B \rightarrow eX$ ) is a useful way to study the heavy flavor production. We have studied the single electron production in Au+Au collisions at  $\sqrt{s_{NN}} = 200$  GeV. The data was recorded by the PHENIX east-arm spectrometer during the 2001 run period. The PHENIX detector is described in detail elsewhere.<sup>4)</sup> A set of beam-beam counters and zero degree calorimeters provides our minimum bias triggers and measures its collision vertex positions. The charged particle tracks are reconstructed with the drift chamber and the pad chamber which covers  $|\eta| < 0.35$  in pseudorapidity and 90 degrees in azimuthal angle. Electron identification is carried out by using the ring imaging Cherenkov detector and the electromagnetic calorimeter. The raw spectrum is corrected for the geometrical acceptance and the reconstruction and identification efficiencies determined by a detailed GEANT simulation.

The inclusive electron spectrum can be decomposed into contributions from *non-photonic* sources (charm and beauty decays) and from *photonic* sources (Dalitz decays of neutral mesons and photon conversions). In order to separate these contributions experimentally, we took a special data with a brass photon converter placed around the beam pipe. The converter increases electrons only from *photonic* sources by a fixed factor which is determined by the radiation length of the converter (1.7%). We analyzed 2.2M events of converter data and 2.5M events of no converter data. We also simulated the effect of the photon converter using a detailed GEANT simulation of the PHENIX detector. By the comparison of the real and simulated data with and without the converter, we extracted the *non-*

*photonic* component of the electron spectrum.

Figure 1 shows the invariant  $p_T$  spectrum of electrons from *non-photonic* sources in minimum bias Au+Au collisions at  $\sqrt{s_{NN}} = 200$  GeV. Here, only the statistical uncertainty is shown. The background from kaon decays and di-electron decays of light vector mesons ( $\rho$ ,  $\omega$ ,  $\phi$ ) are also evaluated using a GEANT simulation and a hadron decay generator, respectively. Those contributions are small, and they are subtracted from the *non-photonic* electron spectrum.

The dash and dot-dash lines in the Fig. 1 show the contributions from charm and beauty decays calculated by PYTHIA,<sup>5)</sup> and the solid line is the combination of the two contributions. The PYTHIA calculation is scaled from  $pp$  to Au+Au collisions using the number of binary collisions determined by a Glauber model. The data is consistent with the PYTHIA charm and beauty decays. This suggests that heavy quarks suffer smaller energy loss in the dense matter than light quarks.

A preliminary result of this analysis, with large systematic uncertainties, was presented at the QM02 conference. The present analysis has significantly reduced the systematic uncertainties. The centrality dependence of the electron yield from *non-photonic* sources and the estimation of the systematic uncertainties are in progress. We expect to publish the final result of the analysis soon.

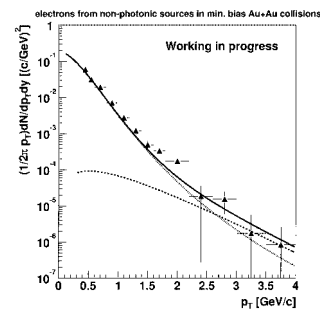


Fig. 1. Invariant  $p_T$  spectrum of electrons from *non-photonic* sources in minimum bias Au+Au collisions at  $\sqrt{s_{NN}} = 200$  GeV compared with the expected contributions from semi-leptonic decays of charm and beauty calculated by PYTHIA.

## References

- 1) B. Muller and X. N. Wang: Phys. Rev. Lett. **68**, 2437 (1992).
- 2) Y. L. Dokshitzer and D. E. Kharzeev: Phys. Lett. B **519**, 199 (2001).
- 3) T. Matsui and H. Satz: Phys. Lett. B **178**, 416 (1986).
- 4) K. Adcox et al.: Nucl. Instrum. Methods Phys. Res. A **499**, 469 (2003).
- 5) T. Sjostrand: Comput. Phys. Commun. **82**, 74 (1994).

\* Hiroshima University

# Particle composition at high $p_T$ in Au+Au collisions at $\sqrt{s_{NN}} = 200$ GeV

T. Chujo and A. Kiyomichi

High  $p_T$  hadron production originating in the fragmentation of partons with a large momentum transfer is a sensitive probe of the hottest and densest stage in the relativistic heavy-ion collisions. One of the most significant results from the Relativistic Heavy Ion Collider (RHIC) runs is that the high  $p_T$  hadron yields are largely suppressed in central Au+Au collisions with respect to the underlying number of nucleon-nucleon collisions ( $N_{coll}$ ).<sup>1)</sup> It is also found that protons and anti-protons yields near 2 GeV/c in central Au+Au collisions are comparable to that of pions,<sup>2)</sup> which suggests that a significant fraction of all particle yields is  $p$  and  $\bar{p}$  at the intermediate  $p_T$  (2–5 GeV/c) in central Au+Au collisions. We report here the results of  $p$  and  $\bar{p}$  yields and their scaling properties in Au+Au collisions at  $\sqrt{s_{NN}} = 200$  GeV measured by the PHENIX experiment at RHIC.

Figure 1 shows the  $p/\pi$  and  $\bar{p}/\pi$  ratios as a function of  $p_T$  measured at mid-rapidity in different collision centrality selections in Au+Au at  $\sqrt{s_{NN}} = 200$  GeV. We observed that there is a strong centrality dependence in  $p/\pi$  and  $\bar{p}/\pi$  ratios at the intermediate  $p_T$  region, *i.e.*, the ratios in central events are a factor of  $\sim 3$  larger than in peripheral events. The peripheral data at  $p_T > 3$  GeV/c agree well with the ratios observed in  $p + p$  collisions at lower energies and the results from gluon and quark jet fragmentation. In order to investigate the scaling behavior and yield suppression effect for  $p$  and  $\bar{p}$ , the  $N_{coll}$  scaled central to peripheral yield ratios ( $R_{CP}$ ) for protons is used. As shown in Fig. 2,  $p$  and  $\bar{p}$  are not suppressed at  $p_T = 1.5$ –4.5 GeV/c while there is a factor of 2–3 suppression for  $\pi^0$ . We also observe that  $h/\pi^0$  ratio in central events is enhanced by

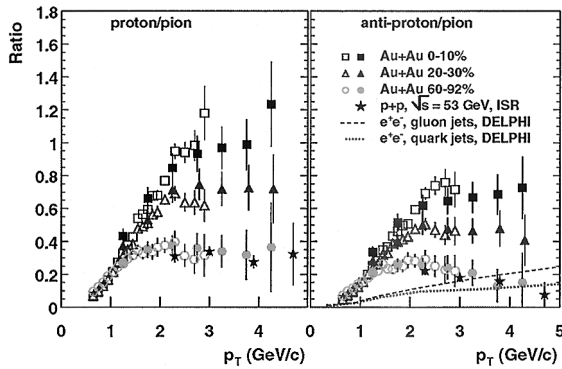


Fig. 1. Centrality dependence of  $p/\pi$  and  $\bar{p}/\pi$  ratios in Au+Au collisions at  $\sqrt{s_{NN}} = 200$  GeV.<sup>3,4)</sup>

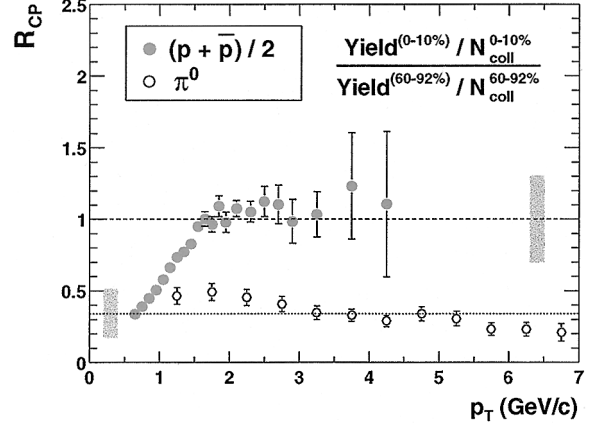


Fig. 2. Nuclear modification factor  $R_{CP}$  for  $(p+\bar{p})/2$  (filled circles) and  $\pi^0$ .<sup>3,4)</sup> Dashed and dotted lines indicate  $N_{coll}$  and  $N_{part}$  (number of participant nucleons) scaling; the shaded bars show the systematic errors on these quantities.

as much as 50% above the  $p+p$  value<sup>3)</sup> and this relative baryon enhancement is limited to  $p_T < 5$ –6 GeV/c.

It is interesting why the suppression for  $p$  and  $\bar{p}$  is absent in central Au+Au collisions. Recently the observed abundance of protons yields relative to pions in central collisions has been attributed to the recombination of quarks, rather than fragmentation.<sup>5)</sup> In this model, quark recombination for  $p$  and  $\bar{p}$  is effective up to  $p_T \simeq 5$  GeV above which fragmentation dominates for all particle species. Another explanation of the observed large baryon content invokes a hydrodynamical radial flow and the jet quenching of hard jet.<sup>6)</sup> Both theoretical models agree with data qualitatively and predict that the baryon/meson enhancement is limited to  $p_T < \sim 5$  GeV/c.

## References

- 1) PHENIX Collaboration, K. Adcox et al.: Phys. Rev. Lett. **88**, 022301 (2002).
- 2) PHENIX Collaboration, K. Adcox et al.: Phys. Rev. Lett. **88**, 242301 (2002).
- 3) PHENIX Collaboration, S. S. Adler et al.: Phys. Rev. Lett. **91**, 172301 (2003).
- 4) PHENIX Collaboration, S. S. Adler et al.: Phys. Rev. C **69**, 034909 (2004).
- 5) R. C. Hwa et al.: Phys. Rev. C **67**, 034902 (2003); R. J. Fries et al.: nucl-th/0301087; V. Greco et al.: nucl-th/0301093.
- 6) T. Hirano and Y. Nara: nucl-th/0307015.

# $\pi^0$ event anisotropy in $\sqrt{s_{NN}} = 200$ GeV Au+Au collisions

M. Kaneta and H. Torii, for the PHENIX Collaboration

Event anisotropy analysis is a powerful tool for studying the properties of the early stage of high energy heavy ion collisions. Because it provides information on collision dynamics in the early stage after heavy ion collisions. The recent results of event anisotropy analysis suggest a finite  $v_2$  (second-harmonic coefficient of Fourier expansion of azimuthal distributions) up to 6 GeV/c of transverse momentum ( $p_T$ ). Due to the particle identification method, the measurement of charged  $\pi$ ,  $K$ , and  $p$  has a limit of  $p_T$  ( $< 4$  GeV/c, thus far).<sup>1)</sup> On the other hand,  $\pi^0$  measurement using an Electro-Magnetic Calorimeter (EMC) can reach a very high  $p_T$  ( $> 10$  GeV/c).<sup>2,3)</sup> The PHENIX is an unique experiment to measure high transverse momentum  $\pi^0$  in relativistic heavy ion collisions at RHIC. We will report the results of  $\pi^0 v_2$  analysis as a function of centrality and  $p_T$  from  $\sqrt{s_{NN}} = 200$  GeV Au+Au collisions data.

Event anisotropy analysis involves the application of the Fourier expansion of particle distributions to analyze the event anisotropy of azimuthal distributions of particles. The distributions are described by,

$$E \frac{dN^3}{d^3p} = \frac{1}{2\pi} \frac{d^2N}{p_T dp_T dy} \times \left( 1 + \sum_{n=1}^{\infty} 2v_n^m \cos[n(\phi - \Phi_r)] \right), \quad (1)$$

where  $y$  is the rapidity and  $\phi$  is the azimuthal angle of the particle,  $\Phi_r$  is the reaction plane and  $v_n^m$  is the  $n$ th order of the Fourier coefficient measured by detectors. The reaction plane is defined using a Beam-Beam counter (BBC) and has a resolution due to granularity of the detector. Therefore, the  $v_n^m$  is smeared by the uncertainty of the reaction plane definition. The method of  $v_n^m$  correction we adopted is shown in Ref. 4 and real  $v_n$  will be corrected by reaction plane resolution ( $v_n = v_n^m / \sigma_n$ , where  $\sigma_n$  is the resolution for the  $n$ th harmonic). Here we will focus on the ellipticity of event anisotropy. Event anisotropy is rotation symmetric to the zero rapidity axis because of momentum conservation. Therefore the odd number of the order of harmonics will be canceled when we add positive and negative rapidity regions. Additionally, assuming a higher order of harmonics is negligible, Eq. (1) becomes

$$E \frac{dN^3}{d^3p} = \frac{1}{2\pi} \frac{d^2N}{p_T dp_T dy} \left( 1 + 2v_2^m \cos[2(\phi - \Phi_r)] \right) = C \left( 1 + 2v_2^m \cos[2(\phi - \Phi_r)] \right), \quad (2)$$

where  $C$  is a constant. Since the reaction plane is distributed uniformly, the efficiency of the detector is normalized. Hence, we can fit the number of particles as a function of  $\phi - \Phi_r$  by Eq. (2) to obtain  $v_2^m$ .

The  $\pi^0 v_2$  analysis was performed in the following steps: (1) Invariant mass calculation from two photons measured by EMC,<sup>2,3)</sup> (2) subtracting the combinatorial background by the event mixing method, (3) counting the number of  $\pi^0$  as a function of  $\phi - \Phi_r$  for each centrality,  $p_T$  bins, (4) the distribution is fitted using Eq. (2), and (5) correct  $v_2^m$  by resolution to obtain  $v_2$ . Figure 1 shows  $\pi^0 v_2$  as a function of  $p_T$  from the minimum bias data in  $\sqrt{s_{NN}} = 200$  GeV Au+Au collisions. The limit of the  $p_T$  range has been defined by statistics thus far. On the other hand, a low  $p_T$  ( $< 1$  GeV/c) has much hadron contamination in EMC. Therefore we analyzed  $\pi^0$  in  $p_T > 1$  GeV/c.

The result shown in Fig. 1 is the first measurement of an identified hadron up to  $p_T = 10$  GeV/c at RHIC.  $\pi^0 v_2$  increases with  $p_T$  and then saturates at  $p_T \sim 3$  GeV/c. Also it has a non-zero value up to  $p_T = 8$  GeV/c. PHENIX has the results of the identified charged pion  $v_2$ .<sup>5)</sup>  $\pi^0 v_2$  is consistent with the charged pion results.

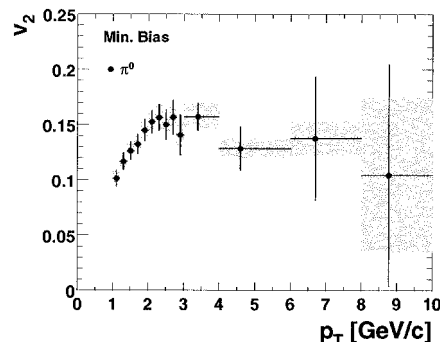


Fig. 1. PHENIX preliminary result of  $\pi^0 v_2$  as a function of  $p_T$  for minimum bias data (92% of geometrical cross-section of  $\sqrt{s_{NN}} = 200$  GeV Au+Au collisions). The error bar shows statistical error and the systematic errors are shown by gray box.

## References

- 1) K. Adcox et al.: nucl-ex/0307010.
- 2) S. S. Adler et al.: hep-ex/0304038.
- 3) S. S. Adler et al.: Phys. Rev. Lett. **91**, 072301 (2003).
- 4) A. M. Poskanzer and S. A. Voloshin: Phys. Rev. C **58**, 1671 (1998).
- 5) S. S. Adler et al.: nucl-ex/0305013.

# Measurement of fluctuations in event-by-event $N_{ch} - N_\gamma$ balance

T. Nakamura\* and K. Homma,\* for the PHENIX Collaboration

The anomalous event-by-event fluctuation of the balance between the number of produced charged and neutral pions ( $N_{\pi^\pm}, N_{\pi^0}$ ) is one of the possible signatures of the chiral phase transition followed by the creation of disoriented chiral condensates<sup>1)</sup> in high energy heavy-ion collisions.

In Au+Au collisions at  $\sqrt{s_{NN}} = 200$  GeV in the PHENIX<sup>2)</sup> experiment at RHIC, we investigate the balance between the number of charged particles and photons ( $N_{ch}, N_\gamma$ ) as a function of subdivided phase space  $x \equiv (\eta/n_\eta, \phi/n_\phi)$ , where  $n_\eta$  and  $n_\phi$  are the numbers of bins that divide the total phase space  $\eta$  and  $\phi$ . The balance is defined as

$$B(x) \equiv N_{\pi^\pm}(x) - 2N_{\pi^0}(x) \approx N_{ch}(x) - N_\gamma(x), \quad (1)$$

where  $N_{\pi^\pm}$  and  $N_{\pi^0}$  are approximated to be  $N_{ch}$  and  $N_\gamma$  in this analysis, since we assume that most statistically dominant particles are pions. Then we introduce  $\delta B(x)$ , which is defined as a differential balance normalized to the expected standard deviation  $\sigma_{\langle B(x) \rangle}$  of the balance at the subdivided phase space size.

$$\delta B(x) \equiv \frac{B(x+dx) - B(x)}{\sigma_{\langle B(x) \rangle}}, \quad (2)$$

$$\langle B(x) \rangle \equiv \langle N_{ch}(x) \rangle - \langle N_\gamma(x) \rangle, \quad (3)$$

$$\sigma_{\langle B(x) \rangle} \equiv \sqrt{\delta \langle N_{ch}(x) \rangle^2 + \delta \langle N_\gamma(x) \rangle^2}, \quad (4)$$

where,  $B(x+dx) - B(x)$  corresponds to a difference between two neighboring bins. The variance around the expected values  $\langle N_{ch}(x) \rangle$  and  $\langle N_\gamma(x) \rangle$  is expressed by the value of  $\delta B(x)$ . Then finally our observable is defined as;

$$\delta B_{max} \equiv \max |\delta B(x)|. \quad (5)$$

where a maximum  $|\delta B(x)|$  is selected among all available phase spaces in all resolution levels per event. Finding  $\delta B_{max}$  allows us to detect the most anomalous domain in a given event and to determine how anomalous the domain is compared to baseline fluctuations. Figure 1 shows  $\delta B_{max}$  distributions for each centrality and minimum bias events that correspond to 92.2% of the Au+Au inelastic cross section. The filled distributions indicate the  $\delta B_{max}$  distributions of binomial samples produced by hit map of real charged tracks and photon clusters to reflect detector conditions. We introduced these binomial distributions as a baseline fluctuations and established the correspondence between probabilities to exclude the binomial distribution and values of  $\delta B_{max}$ . Figure 2 shows the fraction of events above the 5% significance level to

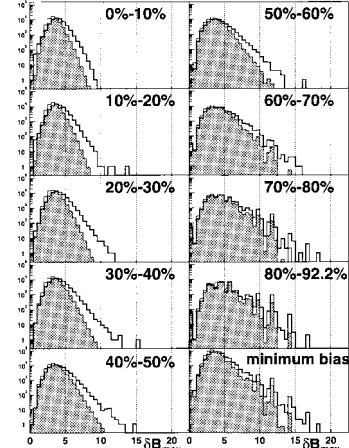


Fig. 1. Maximum differential balance ( $\delta B_{max}$ ) distributions for each centrality (solid) and binomial samples generated with exactly the same multiplicity sets ( $N_{ch}, N_\gamma$ ) (filled). The binomial distribution was normalized to the number of events in the real data.

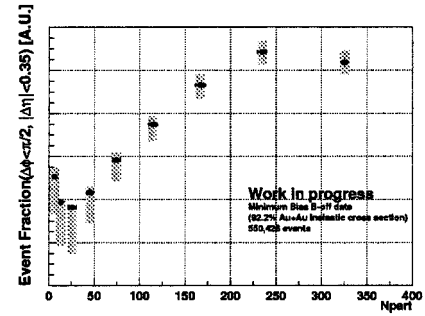


Fig. 2.  $N_{part}$  dependence of the fraction of events above the event-by-event 5% significance level from the total number of MB events analyzed, which is integrated in all resolution levels after subtracting of binomial points. The systematic errors from the selection criterion of charge tracks and photon clusters and ambiguities of the limit value as 5% significance level are shown as shaded band.

exclude the binomial fluctuations with respect to minimum bias events as a function of the number of participants ( $N_{part}$ ). It is shown that the fraction increases as  $N_{part}$  increases. The analysis to investigate the sources of the fluctuations is in progress by taking the effects of jets, flow and Bose-Einstein correlation into account.

## References

- 1) K. Rajagopal and F. Wilczek: Nucl. Phys. B **399**, 395 (1993).
- 2) K. Adcox et al.: Nucl. Instrum. Methods Phys. Res. A **499**, 469 (2003).

\* Hiroshima University

# Search for non-hadronic sources of photons in Au+Au collisions at $\sqrt{s_{NN}} = 200$ GeV at RHIC-PHENIX

T. Sakaguchi,<sup>\*1</sup> X. Camard,<sup>\*2</sup> G. David,<sup>\*3</sup> D. d'Enterria,<sup>\*4</sup> H. Hamagaki,<sup>\*1</sup> S. Kametani,<sup>\*1</sup> K. Kato,<sup>\*5</sup>  
 T. Matsumoto,<sup>\*1</sup> S. Mioduszewski,<sup>\*3</sup> K. Oyama,<sup>\*1</sup> K. Ozawa,<sup>\*1</sup> M. L. Porschke,<sup>\*3</sup> M. Tamai,<sup>\*5</sup>  
 H. Torii, and C. Woody,<sup>\*3</sup> for the PHENIX Collaboration

Thermal photons have long been considered to be an excellent probe of the early stages of the relativistic heavy ion collisions because they have a long mean free path compared to the size of the nuclear volume involved in the collisions. To extract the thermal photons,  $\gamma$ 's from known hadronic sources must be subtracted. Of the hadronic sources,  $\pi^0$  and  $\eta$  are the major contributors. The sum of the other sources is  $\sim 4\%$  of the total at around  $p_T$  of 2 GeV/c. Thus,  $\pi^0$  and  $\eta$  contributions must be correctly evaluated and subtracted from measured inclusive photons.

PHENIX<sup>1)</sup> has succeeded in measuring  $\pi^0$ 's in Au+Au collisions at  $\sqrt{s_{NN}} = 200$  GeV using the electro-magnetic calorimeter (EMCal)<sup>2)</sup> for events classified in accordance with the impact parameter of the collision. 0% corresponds to an impact parameter of 0, and 100% to that of the diameter of a gold ion. The transverse momentum spectra of  $\pi^0$  have been published,<sup>3)</sup> and those for central (0–10%) and peripheral (60–80%) events are used for this analysis. The spectra are fitted with a power-law function of  $A(1 + p_T/p_0)^{-n}$ , where  $A$ ,  $p_0$  and  $n$  are the fitting parameters. The systematic error due to fitting was estimated by moving data points up and/or down by  $p_T$ -correlated and  $p_T$ -uncorrelated errors, fitting with power-law function, and comparing with the original fit.

The  $m_T$  scaled power-law fit to  $\pi^0$  is used as a spectrum of  $\eta$ . The function is similar to the one for  $\pi^0$  except that  $p_T$  is substituted by  $(p_T^2 - m_{\pi^0}^2 + m_\eta^2)^{1/2}$ , and  $A$  by  $0.55 \times A$  according to the result from a PYTHIA calculation.<sup>4)</sup> The systematic uncertainty of the factor is 50%. The total systematic error on the sum of the yield of  $\pi^0$  and  $\eta$  is estimated to be 17–22%.

The fast Monte Carlo simulation<sup>5)</sup> was used to generate  $\gamma$ 's from  $\pi^0$  and  $\eta$ , to accumulate all  $\gamma$ 's that are in the acceptance, and to smear their energies according to the intrinsic resolution of the EMCal. The photon identification and clustering efficiency as well as the background contribution are evaluated using HIJING simulation events<sup>6)</sup> processed through a GEANT-based simulation code. The measured EMCal cluster energy distributions are corrected using the ef-

iciency and the estimate of the background to obtain the  $\gamma$  spectrum.

Figure 1 shows the ratios of the measured  $\gamma$  distributions to those calculated for both peripheral (60–80%) and central (0–10%) events at  $\sqrt{s_{NN}} = 200$  GeV. The gray bands show the systematic errors originating from  $\pi^0$  measurement,  $\eta/\pi^0$  ratio, photon identification and clustering efficiency, and the estimate of the background contributions. In this plot, the  $p_T$ -correlated systematic errors are shown as bands, and the quadrature sum of  $p_T$ -uncorrelated and statistical errors are shown as error bars. The measured distributions are consistent with the calculated distributions for both peripheral and central events within the current statistical and systematic errors.

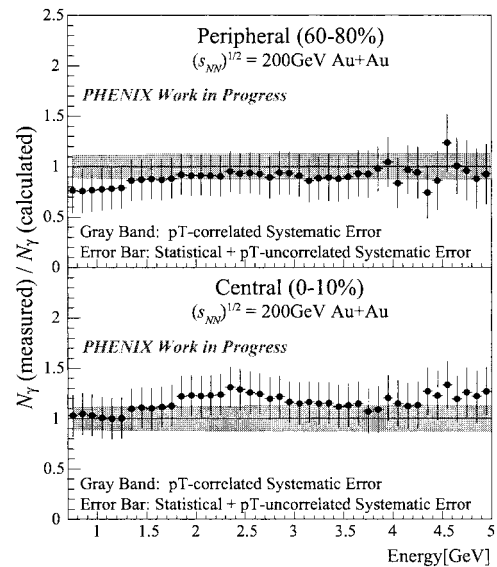


Fig. 1. Ratios of measured and calculated  $\gamma$  distributions for peripheral (upper) and central (lower) events.

## References

- 1) PHENIX Collaboration: Nucl. Instrum. Methods Phys. Res. A **499**, 469 (2003).
- 2) L. Aphecetche et al.: Nucl. Instrum. Methods Phys. Res. A **499**, 521 (2003).
- 3) S. S. Adler et al.: Phys. Rev. Lett. **91**, 072301 (2003).
- 4) T. Sjostrand: Comput. Phys. Commun. **82**, 74 (1994).
- 5) T. Sakaguchi et al.: CNS-REP-36, 35 (2001).
- 6) X.-N. Wang and M. Gyulassy: Phys. Rev. D **44**, 3501 (1991).

<sup>\*1</sup> Center for Nuclear Study, University of Tokyo

<sup>\*2</sup> Groupe Photons, SUBATECH, France

<sup>\*3</sup> Brookhaven National Laboratory, USA

<sup>\*4</sup> Columbia University, USA

<sup>\*5</sup> Advanced Research Institute for Science and Engineering, Waseda University

# AGS snake

M. Okamura and J. Takano\*

A new normal-conducting helical snake magnet for the AGS was designed and fabricated successfully and is being shipped to BNL.

The AGS synchrotron at BNL introduced a partial snake, which helps to overcome the imperfection resonances that appear during the acceleration of polarized protons. The existing partial snake is a solenoid magnet and its field rises at the same rate as that of the AGS main magnet. However, the longitudinal component of the solenoidal partial snake introduces linear coupling of the transverse coordinates of the beam. This linear coupling causes additional intrinsic resonances which affect the final polarization of the beam. To achieve high polarization in the RHIC which follows the AGS, those intrinsic overcoming resonances in the AGS is very important. In order to reduce the coupling caused by the solenoid magnet, an alternative partial snake called helical dipole magnet has been proposed. Unlike the helical dipole magnet used in RHIC,<sup>1)</sup> each of which consists of four 2.4-m-long superconducting magnets, the AGS partial helical snake is simply a single helical magnet which can be accommodated in a short straight line of the AGS.<sup>2,3)</sup>

Figure 1 shows the AGS helical dipole magnet's input to OPERA-3D (TOSCA).<sup>a)</sup> Figure 2 shows the coil shape of this magnet.

We adopted a square-shaped conductor of 14.5 mm × 14.5 mm in cross section, with a square hollow water passage of 10 mm × 10 mm. The coil has 10 turns (azimuthal direction) and 7 layers (radial direction). Total operational current is 187000 AT and the maximum field strength is 1.5 T. To meet the requirements from the AGS machine group in order to reduce the temperature rise of the cooling water, we employed parallel-pancake winding. This doubles the number of water passages, although the fabrication of the coil would become complicated.

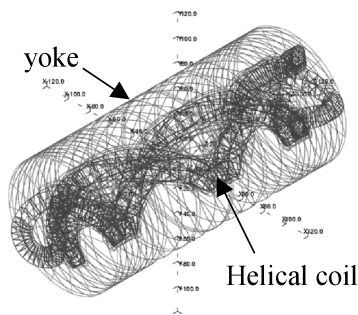


Fig. 1. Model of the helical magnet on OPERA-3D.

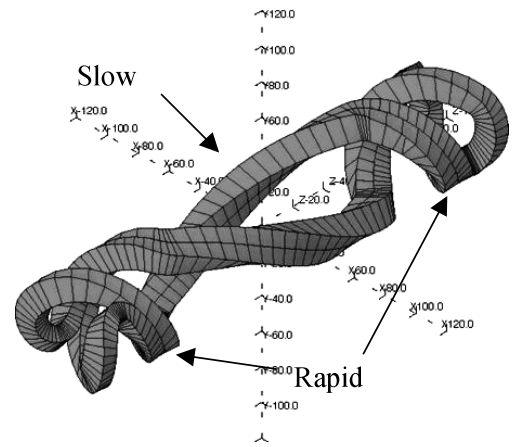


Fig. 2. Double-pitch structure of the helical coil.

In the case of the RHIC, each snake consists of four superconducting helical dipole magnets. All these magnets are mechanically identical but the operational field strengths are varied, such as 1.2 T, -4 T, 4 T, -1.2 T. The AGS helical single magnet, on the other hand, consists of two types of patterns as shown in Fig. 2: one slow pitch section and two rapid pitch sections in a magnet. Figure 3 shows the cross sections of

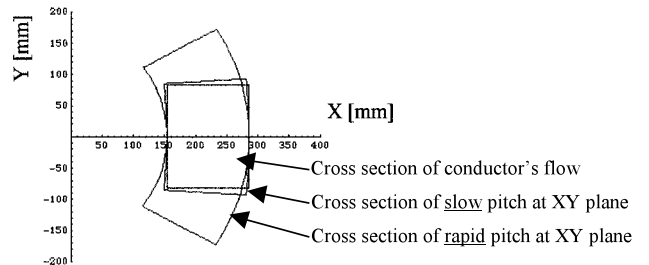


Fig. 3. Cross sections of the helical coil.

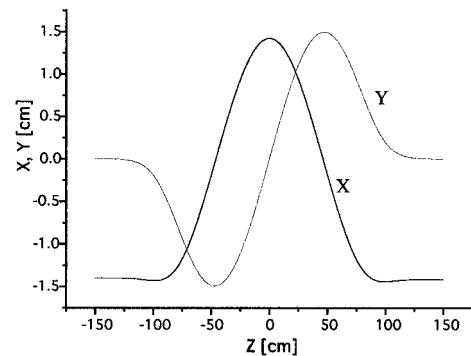


Fig. 4. Beam trajectory of  $z$  vs.  $x, y$  after optimization.

\* Tokyo Institute of Technology  
 a) Vector Fields Limited, Oxford.

the coil at  $z = \text{constant}$  plane in different pitches. The beam shift and beam deflection angle can be adjusted by choosing adequate pitch values and ratios of the two

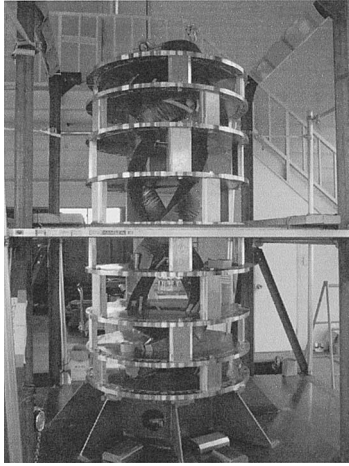


Fig. 5. AGS helical dipole magnet under construction.

patterns. Although it is rather difficult to construct this complicated structure in a single magnet, the size and cost of the snake were minimized.

To minimize the beam shift and deflection angle, the pitches and length of each section are carefully selected using OPERA-3D/TOSCA. Beam trajectories after optimization are shown in Fig. 4.

Figure 5 shows the coil alignment process in the fabrication of the helical dipole magnet. Mechanical design work and fabrication were carried out by Takano Original Magnet Co. This magnet was completed at the end of October, 2003.

We plan to measure the field quality of the magnet at BNL in collaboration with the superconducting magnet division before installation to the AGS.

#### References

- 1) W. W. MacKay et al.: AGS/RHIC/SN-80/BNL (1999).
- 2) M. Okamura et al.: Proc. EPAC 2002, Paris, France, 2002-6 (The European Physical Society, 2002) p. 2421.
- 3) M. Okamura et al.: Proc. EPAC 2000, Vienna, Austria, 2000-6 (Austrian Academy of Sciences Press, 2000) p. 2126.



# Detection of very small angle proton-proton elastic scattering for absolute polarimetry at RHIC

H. Okada,<sup>\*1</sup> A. Bravar,<sup>\*2</sup> G. Bunce,<sup>\*2</sup> K. Imai,<sup>\*1</sup> O. Jinnouchi, K. Kurita,<sup>\*3</sup> Y. I. Makdisi,<sup>\*2</sup> and N. Saito<sup>\*1</sup>

The precision measurement of beam polarization is a crucial part of the RHIC spin program. For example, two-spin longitudinal asymmetry is defined as  $A_{LL} = \frac{1}{P_{beam}^2} \varepsilon_{LL}$ , where  $\varepsilon_{LL}$  is the measured (raw) asymmetry in a particular process for the parallel and antiparallel spin configurations of polarized proton beams. A currently obtained accuracy of  $\Delta P_{beam}/P_{beam} \sim 30\%$ <sup>(1)</sup> would contribute to the uncertainty of asymmetry,  $\Delta A_{LL}/A_{LL}$ , by  $\sim 60\%$ . Since the error of asymmetry would be directly reflected on the uncertainty of the physical observables which we are trying to extract, *e.g.*, gluon polarization, it is very important to reduce the uncertainty in the beam polarization. We are now constructing the RHIC Absolute Polarimeter to achieve the best possible determination of the beam polarization.

We have chosen  $pp$  elastic scattering for the RHIC Absolute Polarimeter in the very small  $|t|$  region of 0.001–0.02 GeV<sup>2</sup>. The reason why we have chosen  $pp$  elastic scattering is that we can simply transfer the target polarization  $P_{target}$  to the beam polarization  $P_{beam}$  by comparing beam spin asymmetry with target spin asymmetry. By using a polarized gas jet target and a polarized beam simultaneously, the beam polarization can be determined at its best possible precision ( $\Delta P_{beam}/P_{beam} \approx \Delta P_{target}/P_{target}$ ) with the sufficient number of  $pp$  elastic events. We also need a high target polarization to minimize systematic errors and we have chosen the Polarized Gas Jet Target. We can expect  $P_{target}$  to be more than 90% with  $\Delta P_{target}/P_{target} < 2\text{--}3\%$ . This high (“statistical” not needed) accuracy will allow us to measure the absolute beam polarization to  $\Delta A_{LL}/A_{LL} \sim$  (“10% in ’04 and a final goal of” not needed) 6%.

We also want to extend the precision measurement to smaller  $|t|$  region. Figure 1 shows the theoretical prediction of  $A_N$  in the CNI (Coulomb Nuclear Interference) region as a function of  $|t|$ .  $A_N$  for  $pp$  elastic scattering is expected to reach  $\sim 4.5\%$  at  $|t| \approx 3 \times 10^{-3}$  GeV<sup>2</sup> and to change dynamically in a very small  $|t|$  region, 0.001–0.006 GeV<sup>2</sup>. However, there has been no measurement yet, since it is extremely difficult to identify elastic scattering in a very small angle. Figure 2 shows the correlation between proton recoil angle and  $|t|$ . Line (a) corresponds to the  $pp$  elastic scattering kinetics and lines (b) and (c) correspond to kinematical boundaries for the pion-associated production and resonance production, respectively. The shaded

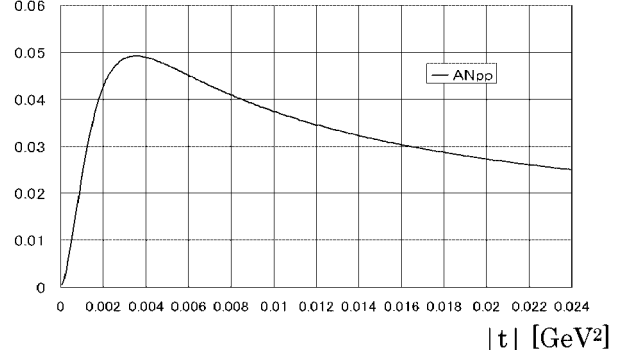


Fig. 1. Theoretical prediction for  $A_N$  as a function of  $|t|$ .

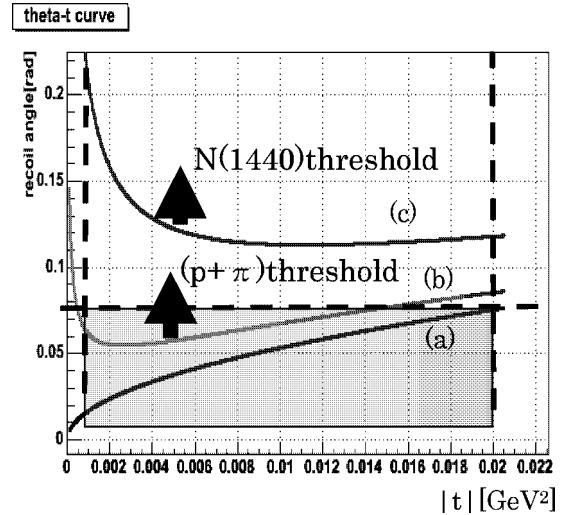


Fig. 2. Kinetic limit of the recoil proton angle *vs.*  $|t|$ . Line (a);  $pp$  elastic. Line (b); threshold of  $pp \rightarrow (p + \pi)p$ . Line (c); threshold of  $pp \rightarrow N(1440)p$ . Shaded region; detectable region for Si detectors.

region shows the detectable area of our Si detector for a recoil proton. The figure shows that our data could be significantly contaminated by pion-associated production. We expect that we should be able to overcome this problem by measuring the correlation between  $|t|$  and proton recoil angle.

As shown in Fig. 2, the main physics background is an inelastic event,  $pp \rightarrow (p\pi)p$ . The recoil angle of this event is quite different from that of an elastic event:

$$\sin \theta_R^{Xp} = \frac{M_X^2 - m_p^2}{2P_{beam} \sqrt{|t|}} + \sin \theta_R^{elastic} > \sin \theta_R^{elastic}.$$

$$\text{If } (M_X^2 - m_p^2) = (m_p + m_\pi)^2 - m_p^2$$

<sup>\*1</sup> Department of Physics, Kyoto University

<sup>\*2</sup> Brookhaven National Laboratory, USA

<sup>\*3</sup> Department of Physics, Rikkyo University

$$> 2p_{beam} \sqrt{|t|} \Delta\theta_R,$$

we can remove inelastic events by reconstructing  $M_X(|t|, \theta_R)$ , and the desired angle resolution is  $\sim 3$  mrad. Here,  $m_p$  and  $m_\pi$  are the masses of a proton and pion, respectively.  $P_{beam}$  is the momentum of the beam.

There are two methods of determining  $|t|$ . One is to measure the kinetic energy of the recoil proton, and the other is to measure the TOF of the recoil proton. In the first method, our goal in the resolution  $\Delta|t| < 1.0 \times 10^{-4} \text{ GeV}^2$  is reachable with the energy resolution of  $\Delta T_{kin} \sim 50 \text{ keV}$ , which is already established with the Si detector to be used for this measurement. In determining  $|t|$  from TOF, TOF resolution is dominated by bunch length ( $= 5 \text{ ns}$ ), since the time resolution of the Si detector is measured to be  $2 \text{ ns}$ . The typical TOF is  $\sim 80 \text{ ns}$  in  $|t| \sim 0.001 \text{ GeV}^2$ . The time resolution of  $5 \text{ ns}$  leads to  $\Delta|t| \approx 1.3 \times 10^{-4} \text{ GeV}^2$ , which is sufficient for our measurement.

The resolution of the recoil angle detection is dominated by the strip width of the Si detector. The strip width is  $1 \text{ mm}$  and the distance between the beam axis and Si detectors is  $\sim 0.8 \text{ m}$ . The angle separation between the elastic and inelastic events would be in the order of  $0.01 \text{ rad}$ , and we have a sufficient resolution.

The Jet Target<sup>2)</sup> has already been checked its high polarization at one of the collision points at RHIC, and Si detectors will be installed in February – March, 2004 for the  $pp$  run in April. We will fully commission the system in this coming run and we will obtain  $A_N$  very precisely in the next run, when we expect to have a very long  $pp$  run.

#### References

- 1) O. Jinnouchi et al.: RIKEN Accel. Prog. Rep. **36**, 237 (2003).
- 2) A. Zelenski: Proc. 10th Workshop on High Energy Spin Physics (SPIN2003), Dubna, Russia, 2003-9, to be published.

## Polarimetry in RHIC and AGS from Run-03

O. Jinnouchi, I. G. Alekseev,<sup>\*1</sup> A. Bravar,<sup>\*2</sup> G. Bunce,<sup>\*2</sup> S. Dhawan,<sup>\*3</sup> H. Huang,<sup>\*2</sup> V. Hughes,<sup>\*3</sup> G. Igo,<sup>\*4</sup> K. Kurita,<sup>\*5</sup> Z. Li,<sup>\*2</sup> W. Lozowski,<sup>\*6</sup> W. W. Mackay,<sup>\*2</sup> S. Rescia,<sup>\*2</sup> T. Roser,<sup>\*2</sup> N. Saito,<sup>\*7</sup> H. Spinka,<sup>\*8</sup> D. N. Svirida,<sup>\*1</sup> D. Underwood,<sup>\*8</sup> C. Whitten,<sup>\*4</sup> and J. Wood<sup>\*4</sup>

In the previous polarized proton run in 2001/2 at the Relativistic Heavy Ion Collider (RHIC), two RHIC polarimeters were successfully operated.<sup>1,2)</sup> They use the proton-Carbon elastic scattering process in a very small momentum transfer region  $0.005 < -t < 0.05 (\text{GeV}/c)^2$  called Coulomb Nuclear Interference (CNI).

The low polarization at the RHIC storage energy ( $\sim 11\%$  in blue and  $\sim 16\%$  in yellow on average) was of maximum concern in RHIC-Spin Run-02. The main cause was known to be due to AGS acceleration. In Run-03, a new polarimeter using the same  $pC$  CNI process was installed in AGS internally to provide fast feedback for the diagnostics in polarized proton acceleration. The setup was similar to that installed in RHIC polarimeters except, 1) The Carbon target was wider,  $\sim 600 \mu\text{m}$ , to gain a higher hit rate, 2) the distance between the target and the detector was set to be longer (25 cm) considering the longer bunch space in AGS, 3) only two silicon strip detectors (SSDs), instead of six were installed at 90-degree locations. The data acquisition uses the waveform digitizer module as in RHIC. The recoil Carbon events were stored on board memory and read out for each AGS cycle.

For the first time, the polarization measurements during energy ramping were carried out in AGS. The measured raw asymmetry is shown in Fig. 1 as a function of  $G\gamma$  where  $G$  is the anomalous magnetic moment coefficient of proton and  $\gamma$  is a Lorentz factor. Due to the solenoidal partial snake in AGS, the beam spin direction flips at imperfection resonance points, where  $G\gamma$  equals integer values. Furthermore, at four strong intrinsic resonances (*i.e.*  $G\gamma = 12 + \nu$ ,  $36 - \nu$ ,  $48 - \nu$  and  $36 + \nu$ , where  $\nu$  is the vertical betatron tune in AGS,  $\nu = 8.7$ ), the depolarization is overcome by using an ac dipole (spin flipper), and changes in the spin direction are also observed.

In addition to the nominal measurements with AGS extraction energy at  $24.3 \text{ GeV}/c$  ( $G\gamma = 46.5$ ), measurements were performed at the intermediate energies such as,  $G\gamma = 7.5$ ,  $12.5$ ,  $18.5$  and  $41.5$ . These data were collected with another internal inelastic  $pC$  polarimeter (E880) for the normalization. The data indicates a rapid change in the analyzing power  $A_N$  in

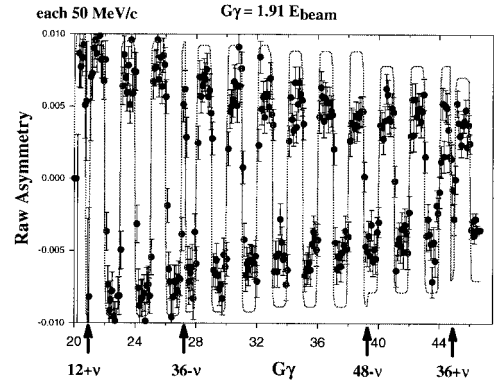


Fig. 1. A raw asymmetry measured with a new AGS CNI polarimeter as a function of beam energy (equivalent to  $G\gamma$ ) after averaging over many ramps for more than five hours. The deviation between the solid curve (spin simulation without assuming the analyzing power change) and the data points indicates that the analyzing power is not constant.

the low beam momentum regime below  $10 \text{ GeV}/c$ , and showed a quite different  $-t$  dependence compared to the nominal CNI shape. The difference of the  $-t$  dependence of  $A_N$  showed a rather asymptotic behavior in momentum above  $20 \text{ GeV}/c$ . This is consistent with the result from other measurement (E950<sup>3)</sup>) with the AGS  $21.7 \text{ GeV}/c$  polarized proton. The dependence is also confirmed at the RHIC energies of  $24.3 \text{ GeV}$  and  $100 \text{ GeV}$ , where similar results in both rings were shown.

Polarization in RHIC was significantly improved from the last run.  $29\%$  and  $25\%$  in average for Blue and Yellow rings at storage energy were established. Nevertheless, a large polarization drop was seen from the injection energy to storage energy. There were attempts made to measure the polarization along with the energy ramp in RHIC as well, to determine the depolarization point during the acceleration. Because of the lack of statistics due to technical reasons, the result was not conclusive. We will resume this measurement in the next run.

### References

- 1) O. Jinnouchi et al.: RIKEN Accel. Prog. Rep. **36**, 237 (2003).
- 2) O. Jinnouchi et al.: AIP Conf. Proc. **675**, 817 (2003).
- 3) J. Tojo et al.: Phys. Rev. Lett. **89**, 052302 (2002).

<sup>\*1</sup> Institute for Theoretical and Experimental Physics, Russia

<sup>\*2</sup> Brookhaven National Laboratory, USA

<sup>\*3</sup> Yale University, USA

<sup>\*4</sup> University of California, Los Angeles, USA

<sup>\*5</sup> Rikkyo University

<sup>\*6</sup> Indiana University Cyclotron Facility, USA

<sup>\*7</sup> Kyoto University

<sup>\*8</sup> Argonne National Laboratory, USA

## PHENIX local polarimeter, RUN III

A. Deshpande, B. Fox, Y. Fukao,\* Y. Goto, K. Tanida, M. Togawa,\* and N. Saito,\*  
for the PHENIX Collaboration

The spin physics program for double longitudinal spin measurements at the Relativistic Heavy Ion Collider (RHIC) began in 2002-3, in RUN III of the collider operation. For the first time polarized protons collided in PHENIX experimental area with longitudinal polarization.<sup>1)</sup> The stable direction of the polarized protons in the collider ring is vertical. The spin rotator magnets located around the experimental area are supposed to rotate the spin vector by 90 degrees to enable longitudinal collisions in the PHENIX Interaction Region (IR). The phenix local polarimeter was motivated by the need to confirm that the spin orientation in the IR during the run was indeed longitudinal.

A single transverse spin analyzing power in the neutron production was discovered in 2001-2 in a test setup at IP12 in RHIC.<sup>2)</sup> This surprisingly large analyzing power was discovered using a calorimeter located 18 meters from the collision point between the two beam pipes. This is the same location in which RHIC Zero Degree Calorimeters (ZDCs) are located.

Each of the RHIC ZDCs consist of 3 modules of tungsten-fiber hadronic calorimeters. The total radiation length of the 3 ZDCs is  $X_0 \sim 150$  and  $\lambda_I \sim 5.1$ . They have no transverse segmentation. Two layers (horizontal and vertical) of plastic scintillators (Shower Max Detectors or SMDs) were inserted between the 1st & the 2nd ZDC module to locate the position of the neutron hits on the surface of the first ZDC. Each of the SMD element was 1.5 cm wide. There were 7 vertical and 8 horizontal elements of these hodoscopes read by a M16 Hamamatsu photo multiplier tube.

Photons do not make it to the end of the first ZDC module and hardly give a signal on the SMDs. Neutrons traversing through the ZDC create electro magnetic shower which is detected by the SMDs. The energy deposits on the individual (1.5 cm wide) units of the SMD can be used to arrive at the position of the neutron hit on the face of the ZDC. Based on the location of the hit, left/right and up/down asymmetries were formed. We plot the  $\phi$  position of the hit along the azimuthal angle. The maxima at  $\phi = \pm\pi/2$  indicate transverse vertical polarization, a maxima at  $\phi = 0$  indicate a horizontal polarization, and no asymmetry over the entire range indicates that the polarization vector is longitudinal.

Figures 1 and 2 show the transverse spin asymmetries measured by the SMD-ZDC system calculated using position of the neutrons hit in the front of the first ZDC. In Fig. 1 the spin rotator magnets were turned off, *i.e.* the spin orientation of the proton was

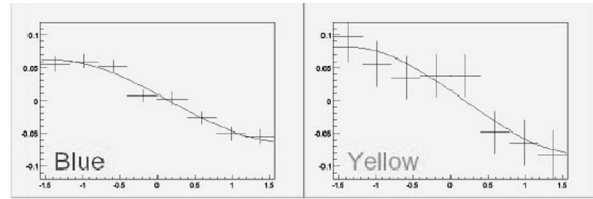


Fig. 1. The asymmetry divided by the polarization measured by PHENIX local polarimeter for transverse polarization (spin rotator magnets currents off).

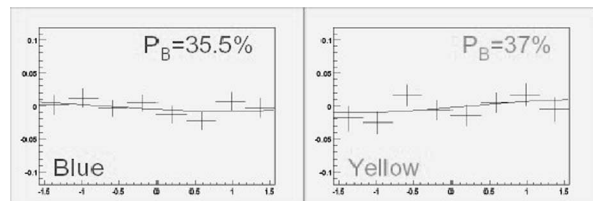


Fig. 2. The asymmetry divided by the polarization when the beams were longitudinally polarized.

transverse and vertical. When the spin rotators were turned on first we found that results consistent with radial polarization in PHENIX. Apparently, the current leads of the spin rotator magnets were switched, as such the spin rotators turned the transverse orientation of the proton beams to transverse (radial) in the IR. Discovering this very quickly and decisively was crucial to the entire RHIC Spin run last year and even for future. After correcting for this mistake, we obtained Fig. 2 in which we show the final current values at which no asymmetries were seen, while RHIC CNI polarimeter was consistently measuring  $\sim 35\%$  polarization.

After the run the above asymmetries were calculated for all good fills used in the final data analysis.<sup>1)</sup> In blue the beam polarization projection over the entire RUN III was  $P_L/P = 0.993^{+0.005}_{-0.014} \quad +0.000_{-0.090}$  while in the yellow ring it was  $P_L/P = 0.974^{+0.013}_{-0.032} \quad +0.010_{-0.090}$ , both consistent with 1.0. Further, tracking of the spin vector precession in the magnets around the experimental area confirms that the spin orientation of the protons in the bunches were indeed understood.

### References

- 1) A. Bazilevsky et al.: RIKEN Accel. Prog. Rep. **37**, 229 (2004).
- 2) Y. Fukao et al.: AIP Conf. Proc. **675**, 584 (2003).

\* Physics Department, Kyoto University

# Dead layer thickness measurement of Si detectors for the RHIC pC CNI polarimeter

S. Saito,\* H. Ueno,\* O. Jinnouchi, and K. Kurita\*

We measured the dead layer thickness of the Si detector used for the RHIC pC CNI polarimeter.<sup>1)</sup> We used the Si detector to measure recoil carbons from proton-carbon Coulomb nuclear interference (CNI) reactions and determined the polarization of proton beams. The energy loss in the dead layer was significant, because recoil carbons of interest had very low energy values of 200 to 300 keV.

The Si detector was an implantation type. The detector sensitive volume was 10 mm × 25 mm × 0.4 mm and was segmented into 12 strips which were 10 mm long and 2 mm wide. From the experimental data of the RHIC polarimeter, dead layer thickness was estimated to be approximately 40 μg/cm<sup>2</sup>, which we considered as the major source of our systematic error. To confirm this result, we carried out a direct measurement of the thickness of the dead layer to reduce energy measurement errors.

We determined the dead layer thickness by measuring the incidence angle dependence of the energy loss. We applied alpha rays from <sup>241</sup>Am to the Si detector from various angles. We assumed that the energy loss in the dead layer is proportional to the length of the alpha ray passage through the dead layer as long as the angle is less than 70° with respect to the normal incidence.

When we apply alpha rays from various angles, the energy loss in the dead layer  $\Delta E(\theta)$  can be written as

$$\Delta E(\theta) = \frac{\Delta E_0}{\cos \theta} \quad (1)$$

where  $\theta$  is the incidence angle of alpha rays and  $\Delta E_0$  is the energy loss at normal incidence.<sup>2)</sup> We defined the normal incidence as 0 degrees. The actual detector signal corresponds to the alpha total energy subtracted by the energy loss in the dead layer. The measured energy  $E_\theta$  can be written as

$$E(\theta) = E_0 - \Delta E(\theta) \quad (2)$$

where  $E_0$  is the alpha total energy. Therefore, from the formula above which describes the relationship between angles and energies detected by the Si detector, we can determine the thickness of the dead layer.

We developed a structure to set the incidence angle of alpha rays. It allows angle adjustment in 11° steps with ±1° error. The distance of the <sup>241</sup>Am source from the detector was kept at 7 cm. The detector and the Am source support structure were enclosed in a vacuum chamber and the readout electronics outside the chamber were connected by a D-Sub feedthrough.

We utilized the same preamplifier used for the RHIC polarimeter. The time constant of the shaping amplifier we used was 100 ns. We used a charge-integration-type ADC CAMAC module to obtain energy spectra.

First, we measured the energy spectra of alpha rays from the source by applying alpha rays vertically. An example of the spectra is shown in Fig. 1. The three peaks correspond to 5485.6 keV, 5442.9 keV and 5388 keV <sup>241</sup>Am alpha rays.

We can use the energy gaps among these three peaks for calibration purposes. For example, the difference between the position of the rightmost peak and that of the second peak corresponds to 42.7 keV.

Then, we measured the peak position shift when alpha rays were applied to the detector at various angles. The peak shifts because the effective thickness of the dead layer increases as the incidence angle increases. Therefore, by fitting the data with Eq. (2), we can determine the absolute dead layer thickness.

Figure 2 shows our preliminary results. We plotted the relationship between the energy peak positions and the incidence angles. The dead layer thickness we estimated was approximately 40–80 μg/cm<sup>2</sup>. We plan to stabilize the measurement to obtain final results.

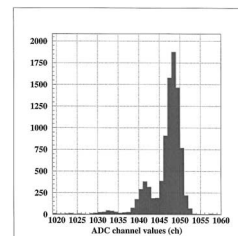


Fig. 1. An energy spectrum of <sup>241</sup>Am.

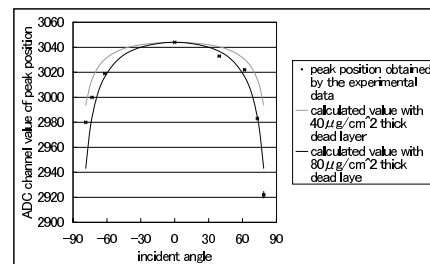


Fig. 2. Preliminary results of the incidence angle dependence of the peak position.

## References

- 1) O. Jinnouchi et al.: Proc. 15th Int. Spin Physics Symp. (SPIN 2002) Upton, USA, 2002-9 (AIP, 2003), p. 817.
- 2) G. F. Knoll: *Radiation Detection and Measurement*, 3rd ed. (Wiley, New York, 2000).

\* Department of Physics, Rikkyo University

# $J/\Psi$ production in pp and d-Au collisions in PHENIX muon arms

D. E. Fields\*

Muons are an important probe of the physics for both the heavy ion physics program (focusing on the generation, detection, characterization of the quark-gluon plasma (QGP) as well as studying the gluon distribution in nuclear matter) and the spin physics program (measuring the helicity distributions of flavor-separated quarks and antiquarks, as well as the first *direct* measurement of the gluon polarization in the nucleon<sup>1</sup>). For these purposes, the most interesting muons originate from vector meson ( $J/\Psi$ ,  $\Upsilon$ , etc.) decays, Drell-Yan decays,  $W$ -decay, and heavy flavor (c and b) meson decays. PHENIX has implemented a two-arm (North and South) muon spectrometer at high rapidity to supplement the photon, electron and hadron identification around mid-rapidity.<sup>2</sup> Although these muon arms are performing well, several upgrades are planned to improve the trigger rejection power and to discriminate single muons based upon coincident particles ( $\chi_c \rightarrow J/\Psi$ ) or offset vertices (c, b  $\rightarrow e, \mu$ ).

In RHIC Run02, data was taken with the South Muon Arm operational, and we have recently published the results of the  $J/\Psi$  analysis for di-muons and di-electrons in PHENIX. The combined analysis shown in Fig. 1 and Fig. 2 is discussed in detail in Ref. 3. The statistical accuracy available with Run02 data was insufficient to discriminate between different competing models for the  $J/\Psi$  production mechanism, although the Color Octet Model showed good agree-

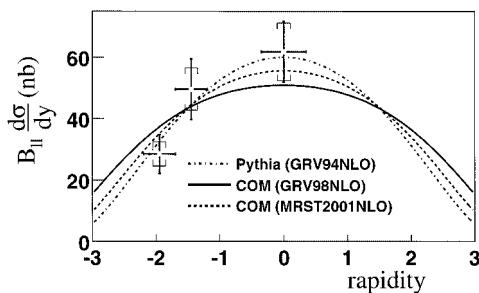


Fig. 1. Rapidity dependence of  $J/\Psi$  production in Run02 pp data. Curves are discussed in Ref. 3.

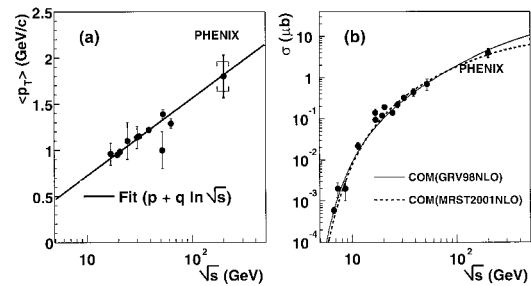


Fig. 2. Mean transverse momentum and cross-section of  $J/\Psi$  shown with other previous measurements at lower value of  $\sqrt{s}$ . Curves are discussed in Ref. 3.

ment with the transverse momentum spectrum and the collision energy dependence of the cross-section. A  $J/\Psi$  polarization measurement at PHENIX will help to make this discrimination.

For RHIC Run03, both the North and South Muon Arms were operational and took nominal integrated luminosities of  $\mathcal{L}_{int} = 2.74 \text{ nb}^{-1}$  in d-Au running and  $\mathcal{L}_{int} = 352 \text{ nb}^{-1}$  in longitudinally polarized pp running. The pp data will increase our statistics for  $J/\Psi$ s by approximately an order of magnitude over the published Run02 results. The d-Au data will allow us to help determine the effect of the initial state gluon distribution on the suppression of high transverse momentum particles seen in the Au-Au data, as well as determining the nuclear effect on the  $J/\Psi$  production mechanism, which is still undetermined.

The Run03 data analysis is nearing completion. Remaining tasks include a detailed study of the trigger efficiency, complicated by beam backgrounds and resulting high voltage depletion on the Muon Identification subsystem.

## References

- 1) G. Bunce et al.: Ann. Rev. Nucl. Part. Sci. **50**, 525 (2000).
- 2) H. Akikawa et al.: Nucl. Instrum. Methods Phys. Res. A **499**, 537 (2003).
- 3) S. S. Adler et al.: Phys. Rev. Lett. **92**, 051802 (2004).

\* University of New Mexico, USA

## PHENIX silicon upgrade project

Y. Goto, Y. Akiba, H. En'yo, K. Fujiwara,<sup>\*1</sup> J. M. Heuser, H. Kano, T. Kawasaki,<sup>\*1</sup> Z. Li,<sup>\*2</sup> H. Ohnishi, V. L. Rykov, N. Saito,<sup>\*3</sup> T. Tabaru, A. Taketani, M. Tanaka,<sup>\*4</sup> K. Tanida, M. Togawa,<sup>\*3</sup> J. Tojo, and Y. Watanabe

We have been developing silicon detectors for charged-particle tracking and precise vertex finding. A goal of the development is to construct a silicon vertex tracker subsystem for the PHENIX detector upgrade.

The silicon upgrade enables us the robust measurement of heavy-flavor production. It detects charged particles with a wide acceptance coverage and identifies them as decay products from charm- or beauty-carrying particles by the displacement of their trajectories to the collision vertex. The wide-ranging precise measurements of heavy-flavor production will significantly extend the physics program of PHENIX in both heavy-ion physics and spin physics. In heavy-ion collisions, open charm and beauty production will help to probe the high-density matter created early during the reaction.

In polarized-proton collisions, the silicon upgrade enables us to reconstruct jets over a large acceptance. The direct photon + jet measurement, as well as the heavy-flavor measurement, is a key process for the gluon polarization measurement in the proton. Although the gluon polarization measurement can be achieved using the PHENIX baseline detector, the silicon upgrade provides significantly enhanced coverage of momentum fraction of the gluon ( $x_{\text{gluon}}$ ) and overlap of the coverage by multiple channels. In proton (or deuteron) + nucleus collisions, the enhanced coverage of  $x_{\text{gluon}}$  enables us to investigate shadowing of the gluon distribution in nuclei extensively.

In order to construct a barrel detector which covers a mid-rapidity region, two types of detectors have been developed. One is a silicon strip detector<sup>1)</sup> which comprises three outer barrels with radii of 6, 8, and 10 cm. The other is a silicon pixel detector<sup>2)</sup> which comprises an innermost barrel with a radius of 2.5 cm.

The first prototype of the silicon strip sensor was tested with a beam at KEK-PS in December 2002. Based on results obtained in the beam test, a second prototype sensor has been developed. The development of readout electronics of the strip sensor is an ongoing operation with the collaboration of the Oak Ridge National Laboratory group. The sensor will be readout with the SVX4 chip which was developed by a FNAL/Berkeley collaboration. The sensor, SVX4 readout chip, and electronics are being assembled and tested. A chain test of the assembled system will be

performed with an emulated PHENIX data acquisition system on a personal computer. The basic performance of the second prototype sensor will be tested with a newly built laser test bench.

The silicon pixel detector has been developed in collaboration with the ALICE group at CERN (RIKEN–ALICE collaboration). Many tests on and evaluation of its hybrid (sensor + bump-bonded electronics) and the development of a readout electronics chain, which consists of a data bus, MCM (multichip module), and ASICs, are ongoing.<sup>3)</sup> The PHENIX hybrid and readout electronics are based on those for the ALICE experiment. The chain for the ALICE experiment was tested with a beam at CERN-SPS in November 2003. We are also collaborating with the NA60 experiment group at CERN. They have a silicon pixel detector system using ALICE hybrids. The final physics run of the NA60 experiment was performed in October and November 2003. Their silicon pixel detector worked very well.<sup>4)</sup>

Simulation studies with the PHENIX silicon upgrade has also been performed.<sup>5)</sup> The geometry of the upgraded detector was implemented in the PHENIX simulation program, and performance of the detector has been studied for the heavy-flavor and photon + jet measurements.

Aiming at approval of the PHENIX silicon upgrade project as a construction plan, the “Proposal for a Silicon Vertex Tracker (VTX) for the PHENIX Experiment” was made and submitted to Brookhaven National Laboratory in October 2003.<sup>6)</sup> This will be reviewed by the RHIC Detector Advisory Committee in November 2003.

### References

- 1) J. Tojo et al.: RIKEN Accel. Prog. Rep. **37**, 251 (2004).
- 2) J. M. Heuser et al.: RIKEN Accel. Prog. Rep. **37**, 250 (2004).
- 3) H. Kano: RIKEN Accel. Prog. Rep. **37**, 253 (2004).
- 4) H. Ohnishi et al.: RIKEN Accel. Prog. Rep. **37**, 89 (2004).
- 5) V. L. Rykov et al.: RIKEN Accel. Prog. Rep. **37**, 254 (2004); M. Togawa et al.: RIKEN Accel. Prog. Rep. **37**, 232 (2004).
- 6) Y. Akiba et al.: Proposal for a Silicon Vertex Tracker (VTX) for the PHENIX Experiment (BNL, Upton, 2003).

---

<sup>\*1</sup> Niigata University

<sup>\*2</sup> Brookhaven National Laboratory, USA

<sup>\*3</sup> Kyoto University

<sup>\*4</sup> High Energy Accelerator Research Organization (KEK)

## Development of silicon pixel detectors for the PHENIX experiment

J. M. Heuser, for the ALICE-RIKEN Collaboration

The Radiation Laboratory of RIKEN and the ALICE experiment at CERN have agreed on a collaboration on the development and production of silicon pixel detectors for a Vertex Detector upgrade of the PHENIX experiment at Brookhaven National Laboratory's Relativistic Heavy Ion Collider (RHIC). The PHENIX collaboration has started a comprehensive programme toward an upgraded experiment. Several new detector systems will provide extended detection capabilities in collisions of heavy ion and polarized proton beams when RHIC reaches full running at design luminosity in the next years. The new detector systems are essential for the access to new observables in a collider upgraded to about 20 to 40 times the design luminosity in the second half of the decade. The main PHENIX upgrade foreseen is a new Vertex Spectrometer installed between the pole faces of the central magnet. It combines high precision tracking for jet and heavy-flavor decay vertex measurement, electron identification and charged particle tracking, in its sub-systems Silicon Vertex Detector, Micro TPC and Compact Hadron Blind Detector. The Silicon Vertex Detector<sup>1)</sup> (see Fig. 1) comprises pixel detectors and novel microstrip sensors. The pixel detectors are essential in its internal layer to resolve the high track densities in heavy ion collisions.

The RIKEN group has teamed up with the ALICE collaboration at CERN to develop pixel detector modules suited for PHENIX. The ALICE collaboration is currently constructing a Silicon Pixel Detector for their Inner Tracking System.<sup>2)</sup> This application is very similar to what PHENIX plans to build. It is based on sophisticated pixel detector technology that was developed and applied at CERN over the last ten years.<sup>3)</sup> The pixel detectors are hybrid devices made from a sensor chip and a readout chip component, interconnected with microscopic solder balls ("bump bonds"). With the ALICE1LHCb pixel detector, the *pin* structure of the sensor is segmented into  $32 \times 256$  pixels of  $50 \times 425 \mu\text{m}^2$  size. Every sensor pixel connects through a  $20 \mu\text{m}$  diameter bump bond to a matching area of signal processing electronic on the radiation tolerant readout chip. Several chips can be arranged on a common sensor substrate as a building block of pixel detector modules ("ladders").

We participate in the ALICE production of thin pixel detector ladders, and work on PHENIX specific modifications to their pixel bus and pilot readout. Thin detectors are required to minimize multiple scattering of particles in the material. The sensors are directly produced in their final thickness of  $200 \mu\text{m}$ . The readout chips are initially  $750 \mu\text{m}$  thick after fabrication, and then thinned to  $150 \mu\text{m}$  during the bump

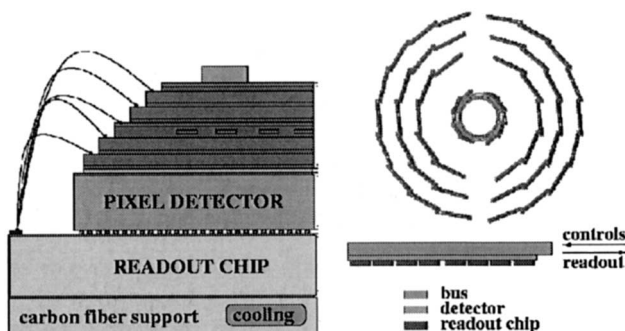


Fig. 1. The Silicon Vertex Detector of PHENIX will comprise four detection layers arranged in two half-shells. The internal layer at 2.5 cm radius just outside of a new beam pipe of reduced diameter is built from 10 pixel detector modules ("ladders"). A half-ladder comprises two sensor ladders, each with four readout chips bump-bonded to a silicon sensor substrate. The chips themselves are wire-bonded to a common readout bus. A pilot module outside of the geometrical acceptance of the sensors interfaces the half-ladder to the data acquisition and control systems. The figures are not to scale.

bonding process. We work with industrial partners to achieve high production yield. Among other challenges are the development of a small-pitch pixel bus with parallel readout branches, and a parallel pilot chip that controls this readout, in order to match the high-rate capability of the PHENIX data acquisition system.

Since two years, several members of the Radiation Laboratory are also active in the NA60 collaboration at CERN which studies prompt dimuon and charm production with proton and heavy ion beams at the SPS.<sup>4)</sup> Utilizing pixel detector technology developed for ALICE, we contributed to the development and production of NA60 specific pixel detector modules for the Pixel Vertex Spectrometer that completes the Muon Spectrometer previously used in the NA50 experiment. The pixel detectors are working well. In November, 2003, NA60 finished the physics run with Indium beams of 158 GeV per nucleon colliding with Indium targets.

### References

- 1) J. M. Heuser: Nucl. Instrum. Methods Phys. Res. A **511**, 210 (2003).
- 2) P. Chochula et al.: Nucl. Phys. A **715**, 849 (2003).
- 3) E. H. M. Heijne: Nucl. Instrum. Methods Phys. Res. A **465**, 1 (2001).
- 4) J. M. Heuser et al.: AIP Conf. Proc., **698**, 713 (2003).



## Development of silicon strip detector for PHENIX silicon vertex tracker

J. Tojo, Y. Akiba, K. Aoki,<sup>\*1</sup> H. En'yo, V. Eremin,<sup>\*2</sup> Y. Fukao,<sup>\*1</sup> Y. Goto, J.M. Heuser, T. Kawabata,<sup>\*3</sup>  
Z. Li,<sup>\*4</sup> H. Ohnishi, H. Okada,<sup>\*1</sup> V. Radeka,<sup>\*4</sup> V.L. Rykov, N. Saito,<sup>\*1</sup> F. Sakuma,<sup>\*1</sup> M. Sekimoto,<sup>\*5</sup>  
T. Tabaru, A. Taketani, K. Tanida, M. Togawa,<sup>\*1</sup> and Y. Watanabe

The silicon vertex tracker (VTX) has been proposed as one of the major upgrades of the PHENIX detector.<sup>1)</sup> An overview of the PHENIX VTX project is given in Refs. 2 and 3. In this article, we report the development of a new single-sided silicon strip detector for the outer three barrel layers of the VTX.

The “stripixel” detector concept<sup>4)</sup> developed by the BNL Instrumentation Division was applied to the first prototype sensor for the VTX. A novel feature of the stripixel concept is two-dimensional position sensitivity with single-sided processing achieved by charge sharing between two interleaved electrodes in one pixel. Collected charges are projectively read out by double layers of strips. The sensor has the size of 34.3 mm ( $r\phi$ )  $\times$  64.6 mm ( $z$ ) with a thickness of 400  $\mu\text{m}$  or 250  $\mu\text{m}$  and has two left-right mirror symmetric active areas of 30.7 mm  $\times$  30.0 mm. Each active area is composed of 384  $\times$  30 pixels with 80  $\mu\text{m}$   $\times$  1000  $\mu\text{m}$  pitch. Two interleaved spiral-shaped electrodes with the line width of 7  $\mu\text{m}$  and the line gap of 6  $\mu\text{m}$  are called the  $x$ -cell and the  $u$ -cell, respectively. A readout line called the  $x$ -strip connects 30  $x$ -cells in the  $z$ -direction, and that called the  $u$ -strip connects 30  $u$ -cells diagonally. The stereo angle between the  $x$ -strip and the  $u$ -strip is 4.6°. There are 384  $x$ -strips with wire-bonding pads on the left (right) side and 384  $u$ -strips with wire-bonding pads on the right (left) side in the left (right) active area. The wire-bonding pad pitch is 80  $\mu\text{m}$ .

Seven detectors with three 400- $\mu\text{m}$ -thick sensors and four 250- $\mu\text{m}$ -thick sensors were constructed to evaluate the stripixel sensor performance.<sup>5)</sup> Each detector consisted of one sensor, six readout chips, a base board, two fanout boards (pitch adaptors) and two SMT boards to read out the right active area of the sensor. A positive bias voltage was applied to the sensor back plane (ohmic side) through the base board. The readout chip was VA2 chip,<sup>6)</sup> an analog multiplexer chip with 128-channel charge-sensitive preamplifier-shaper circuits. Six VA2 chips (three chips for 384  $x$ -strips and three chips for 384  $u$ -strips) in one detector were sequentially read out with a VME-based data acquisition system with a set of modules, CAEN V550 and V551B, suitable for dealing with analog multiplexed signals.

The sensor performance of charge sharing, detection efficiency and position resolution has been evaluated with a <sup>90</sup>Sr  $\beta$ -source (2.283 MeV) and a test beam at KEK. In the source test, three detector telescope was operated with the source located upstream of the first detector and a plastic scintillator for the trigger located downstream of the third detector. The beam test was performed at the T1 beam line in KEK-PS, which delivered a positively charged particle beam with a momentum of 0.50–2.00 GeV/c. Seven detector telescope was operated with trigger plastic scintillators placed upstream and downstream of the telescope. One detector in the middle of the telescope could be rotated with respect to the vertical direction to change the beam incidence angle.

The charge sharing property can be characterized from the asymmetry,  $\mathcal{A}_Q = (Q_x - Q_u)/(Q_x + Q_u)$ , where  $Q_x$  and  $Q_u$  represent collected charges at the  $x$ - and  $u$ -strips, respectively. With good charge sharing, the  $\mathcal{A}_Q$  distribution should be a narrow peak with its mean at zero. Its width depends on the incident particle angle,  $\theta$ . The widest distribution is expected for perpendicular crossings,  $\theta = 0^\circ$ , and distribution becomes narrower as  $\theta$  increases. This dependence has been observed in the beam test measurements presented in three upper rows of Fig. 1. In the test with the radioactive source, the  $\mathcal{A}_Q$  distribution was effectively smeared with the electron incidence angle, resulting in its shape and width as for nonzero  $\theta$ . The narrow distributions for  $\theta = 15^\circ$  and  $30^\circ$  in the beam test represent evidence that the stripixel principle is working and that a good two-dimensional position sensitivity is achievable. However, the broad distribution for  $\theta = 0^\circ$  with two peaks at  $\mathcal{A}_Q \sim \pm 0.2$  is clear indication that, for perpendicular crossings, quite frequently, almost all of the charge is collected either at the  $x$ - or  $u$ -cell with little charge sharing. Improvement of the charge sharing property is expected by fabricating a finer stripixel structure with smaller center-to-center distances between  $x$ - and  $u$ -cells.

Detection efficiencies and signal-to-noise ( $S/N$ ) ratios were measured in the beam test. The detection efficiencies were  $\sim 97\%$  for the detectors with the 400- $\mu\text{m}$ -thick sensor and  $\sim 60\%$  for those with the 250- $\mu\text{m}$ -thick sensor. The  $S/N$  ratios were  $\sim 17$  for the 400- $\mu\text{m}$ -thick sensor and  $\sim 9$  for the 250- $\mu\text{m}$ -thick sensor. The poorer detection efficiency and the  $S/N$  ratio of the detector with the 250- $\mu\text{m}$ -thick sensor, compared to the 400- $\mu\text{m}$ -thick sensor, were mainly due to lower ioniza-

<sup>\*1</sup> Department of Physics, Kyoto University

<sup>\*2</sup> Ioffe Physico-Technical Institute of Russian Academy of Science, Russia

<sup>\*3</sup> Center for Nuclear Study, University of Tokyo

<sup>\*4</sup> Brookhaven National Laboratory, USA

<sup>\*5</sup> High Energy Accelerator Research Organization (KEK)

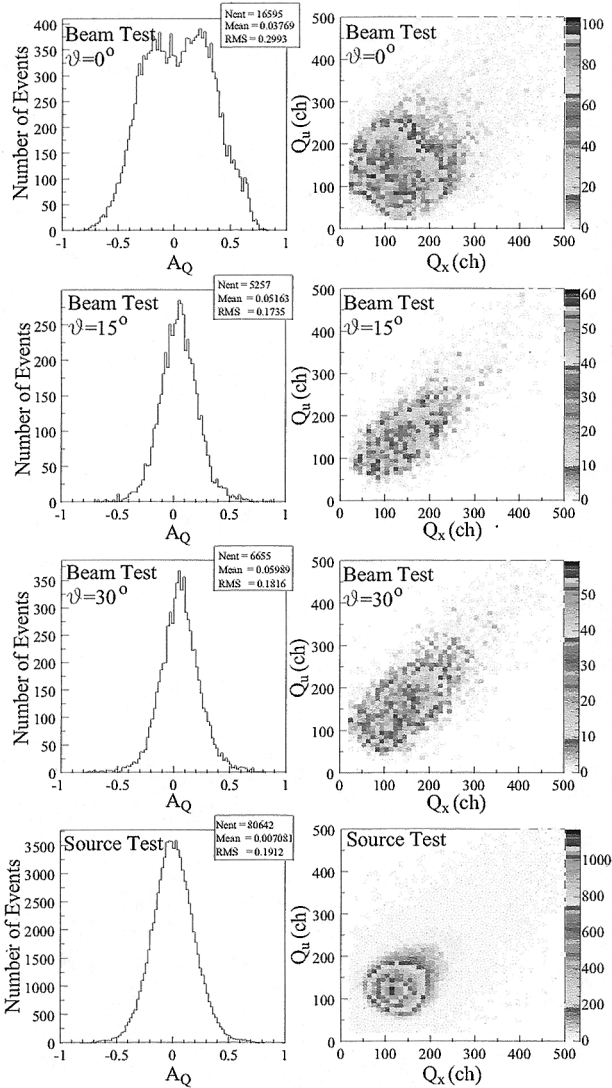


Fig. 1. The  $A_Q$  distributions and correlations between  $Q_x$  and  $Q_u$  measured in the beam test (three upper rows) and with the radioactive source (bottom row).

tion and greater electronic noise. For electronic noise, there is still room for improvement by optimizing the operating conditions. The better charge sharing between  $x$ - and  $u$ -cells in the finer structured detector will also contribute to the improvement of the detection efficiency and  $S/N$  ratio.

The position resolutions were measured in the beam test from the residuals of hits on reconstructed particle trajectories. The expected position resolutions from the pixel pitch of  $80 \mu\text{m}$  ( $r\phi$ )  $\times$   $1000 \mu\text{m}$  ( $z$ ) are  $\sigma_x = 80 \mu\text{m}/\sqrt{12} = 23 \mu\text{m}$  in the  $x$ -strip from the  $r\phi$ -direction pixel pitch,  $\sigma_z = 1000 \mu\text{m}/\sqrt{12} = 289 \mu\text{m}$  from the  $z$ -direction pixel pitch and  $\sigma_u = \sigma_x \cos \alpha \oplus \sigma_z \sin \alpha = 33 \mu\text{m}$  in the  $u$ -strip, where  $\alpha$  and  $\oplus$  repre-

sent the stereo angle between the  $x$ - and  $u$ -strips and the quadratic sum, respectively. After deconvoluting contributions of the setup geometry and multiple scattering, the measured position resolutions of the detector were  $\sigma_x \simeq 23 \mu\text{m}$  for the  $x$ -strip and  $\sigma_u \simeq 31 \mu\text{m}$  for the  $u$ -strip. These results are in the good agreement with the expectations.

To study the electrical properties of the stripixel sensor and to determine the optimum operating conditions, a laser test setup was constructed at the BNL Instrumentation Division. The study is based on the transient charge/current technique.<sup>7)</sup> A nanosecond pulsed laser coupled into a focuser through an optical fiber was operated with a pulse generator. A red laser with the wavelength of 635 nm and the penetration depth of  $3 \mu\text{m}$  in silicon was used to study the separate collection of electrons and holes. An infrared laser with the wavelength of 1060 nm and the penetration depth of  $800 \mu\text{m}$  in silicon was used to study the detector response to the charge deposition of a minimum ionizing particle. The focuser was fixed to an XYZ motorized stage. The precision of laser spot positioning with the motorized stage was  $0.5 \mu\text{m}$ . The laser spot size of approximately  $10 \mu\text{m}$  in diameter was achieved in the constructed setup. The existing setup and/or an upgraded setup which has an automatic multiaxis motor drive control will provide the basic tool for quality control of the sensors and, later, of the assembled detector ladders.

The second prototype stripixel sensors, which has the finer center-to-center distance between  $x$ -cell and  $u$ -cell lines, are under processing and are expected to show the better performance on charge sharing. The SVX4 chip<sup>8)</sup> developed for the Run IIb silicon vertex detector upgrades of the CDF and D0 detectors at the Fermilab Tevatron is planned to be used as the readout chip for the silicon strip detectors in the VTX. The detector with the second prototype sensor and the SVX4 chip is under development.

## References

- 1) K. Adcox et al.: Nucl. Instrum. Methods Phys. Res. A **499**, 469 (2003).
- 2) J. M. Heuser: Nucl. Instrum. Methods Phys. Res. A **511**, 210 (2003).
- 3) Y. Goto et al.: RIKEN Accel. Prog. Rep. **37**, 249 (2004).
- 4) Z. Li: BNL Internal Report, BNL Rep., No. 67527, 1 (2000); Z. Li et al.: RIKEN Accel. Prog. Rep. **36**, 250 (2003).
- 5) J. Tojo et al.: RIKEN Accel. Prog. Rep. **36**, 252 (2003).
- 6) <http://www.ideas.no/>
- 7) V. Eremin et al.: Nucl. Instrum. Methods Phys. Res. A **372**, 388 (1996).
- 8) <http://www-cdf.lbl.gov/users/mweber/svx4/>

## Development of pilot readout electronics for the PHENIX pixel detector

H. Kano

The Radiation Laboratory in RIKEN and the CERN ALICE Pixel group have established a joint program for the development of silicon Pixel Detectors, to be used for the upgrading of the PHENIX detector at Brookhaven National Laboratory's Relativistic Heavy Ion Collider (RHIC).

The PHENIX collaboration has started a study for an upgraded experiment. Several new detector systems will provide extended detection capabilities in collisions of heavy ion and polarized proton beams when RHIC reaches full operation at the design luminosity in the next few years. These systems are essential for the access to new observables in a collider upgraded to about 20 to 40 times the design luminosity in the second half of the decade. The main PHENIX upgrade foreseen is a new Vertex Spectrometer installed between the pole faces of the central magnet. It combines high-precision tracking for jet and heavy-flavor decay vertex measurements, electron identification and charged particle tracking in its subsystem Silicon Vertex Detector, Micro-TPC and Compact Hadron Blind Detector. The Silicon Vertex Detector comprises pixel and novel microstrip sensors. The pixel detectors in the internal layer are essential for resolving the high track densities in heavy ion collisions.

The Radiation Laboratory in RIKEN has teamed up with the ALICE collaboration at CERN to develop pixel detector and readout modules suited for PHENIX. The ALICE collaboration is currently developing a Silicon Pixel Detector for their Inner Tracking System.<sup>1)</sup> This system is similar to what PHENIX plans to upgrade. It is based on sophisticated pixel detector technology that was developed and applied at CERN over the last ten years.

The on-detector pilot readout electronics<sup>2)</sup> of the ALICE silicon pixel detector (nearly 10 million pixels) consists of 1200 readout chips bump-bonded to a silicon sensor and mounted on the front-end bus, and of 120 control (PILOT) chips mounted on multichip modules (MCM), as shown in Fig. 1, together with opto-electronic transceivers. The front-end chips are all ASICs designed in a commercial 0.25-micron process, and are used to transmit data over an optical fiber to the control room where the actual data processing and event building are performed. This system can be applied to PHENIX with minor modifications.

We joined in on component tests of the detector and the pilot readout system (MCM), and are participating in their integration test. The integration test setup is shown in Fig. 2. The tests performed on the entire on-detector readout chain and the optical communication

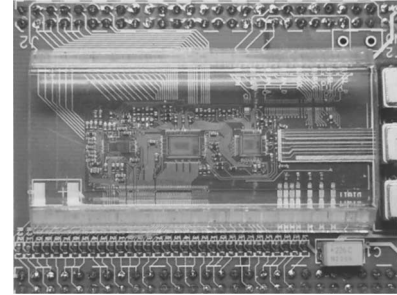


Fig. 1. Fully functional prototype multichip module (50 mm × 15 mm, green board) with all ASICs and optical package. This MCM is mounted on an adapter board.

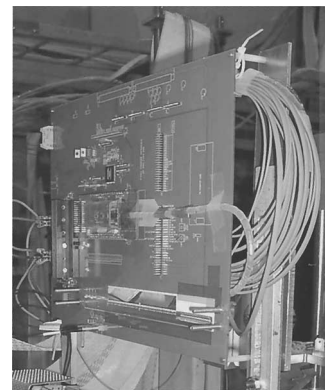


Fig. 2. Test setup of detector and on-detector readout system (MCM).

between the control room and detector proved them to be work reliable. The bidirectional optical link has been successfully tested.

We are working on the modifications of the readout control ASIC on the MCM to optimize it to the PHENIX experiment which requires much higher readout speed and data rates (40  $\mu\text{s}/\text{event}$  in PHENIX, 256  $\mu\text{s}/\text{event}$  in ALICE). The prototype ASIC has been developed for testing the additional zero-suppression circuit and wide bus to achieve higher readout speed. We have started the development of the ASIC with full functionality for the PHENIX pixel readout.

### References

- 1) P. Chochula et al.: Nucl. Phys. A **715**, 849 (2003).
- 2) A. Kluge et al.: Proc. 7th Workshop on Electronics for LHC Experiments, Stockholm, Sweden, 2001-9 (CERN, 2001), p. 95.

# Semileptonic decays of open charm and beauty in the PHENIX central arm with the silicon vertex detector upgrade

V. L. Rykov, Y. Akiba, M. D. Baker,<sup>\*1</sup> Y. Goto, J. M. Heuser, C. A. Ogilvie,<sup>\*2</sup>  
H. Ohnishi, K. Tanida, J. Tojo, and C. Woody<sup>\*1</sup>

The PHENIX detector<sup>1)</sup> at the Relativistic Heavy Ion Collider (RHIC) in BNL is designed to perform a broad study of  $A$ - $A$ ,  $p$ - $A$  and  $p$ - $p$  collisions. The prime motivation for the recently proposed Silicon Vertex Tracker (VTX) upgrade<sup>2)</sup> was to enhance PHENIX capabilities for precise measurements of heavy quark yields, which are a sensitive probe of the early stage of heavy-ion collisions and are critical for the physics goals of proton spin structure and for structure function studies in  $p$ - $A$  reactions. The semileptonic decays of charm and beauty,  $c \rightarrow e^\pm + X$  and  $b \rightarrow e^\pm + X$ , are abundant sources of electrons within the acceptance of PHENIX Central Arm.<sup>3)</sup> However, these electrons need to be separated from the background electrons, first of all from Dalitz decays and  $\gamma$ -conversions in detector material. We plan, using the VTX, to identify heavy flavor decay vertices, which are displaced from the primary event vertex by about a hundred or more microns.

The VTX (Fig. 1) represents a set of four concentric barrels of silicon detectors with a length of approximately 30 cm along the beam ( $z$ -axis). The inner most barrel at a radius of 2.5 cm consists of hybrid silicon pixel detectors<sup>4)</sup> with a pitch size of  $50 \times 425 \mu\text{m}^2$ . The outer three barrels at radii 6, 8 and 10 cm are composed of silicon strip detectors<sup>5)</sup> with two sets of stereo strips of dimension  $80 \mu\text{m} \times 3 \text{ cm}$ , creating effective pitches of size  $\Delta r\varphi \times \Delta z = 80 \times 1000 \mu\text{m}^2$ . The expected VTX resolution for the track's distance-of-closest approach (DCA) to the known primary vertex is  $\sim 20$ – $50 \mu\text{m}$  in the  $xy$ -plane. This is well below the  $c\tau$  values of  $\sim 100$ – $500 \mu\text{m}$  for charm and beauty mesons.

The power of this resolution is seen by comparing the PYTHIA+GEANT simulated DCA distributions from charm, beauty and Dalitz decays in Fig. 2. A DCA cut of  $\sim 150$ – $200 \mu\text{m}$  removes the majority of Dalitz

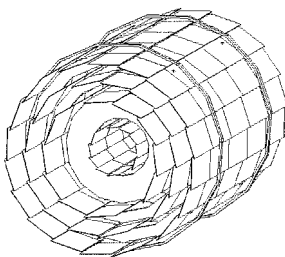


Fig. 1. The VTX schematic view.

<sup>\*1</sup> Brookhaven National Laboratory, USA

<sup>\*2</sup> Iowa State University, USA

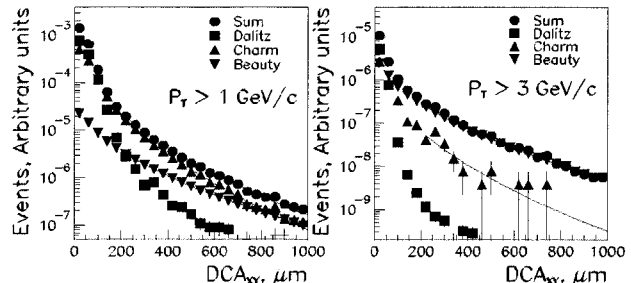


Fig. 2. DCA distributions for electrons from Dalitz, charm and beauty decays simulated through four Si layers of thickness 2% of a radiation length per layer.

contribution from the electron yield even at low electron transverse momenta,  $P_T$ , just above 1 GeV/ $c$ .

Figure 3 compares signal-to-background ratios with the DCA cut to the case of no VTX. It is apparent that using the VTX detector will dramatically reduce the systematic errors due to uncertainties in the background subtraction, thus opening the opportunity for truly model independent measurements of open heavy flavor yields.

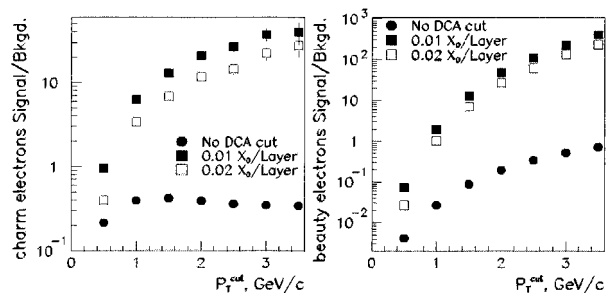


Fig. 3. Signal-to-background ratios for electrons from open charm (left) and beauty (right) as a function of electron  $P_T^{\text{cut}}$  for  $DCA_{\text{cut}} = 200 \mu\text{m}$ . Dalitz decays and  $\gamma$ -conversions are taken as a background. Shown simulation results are for VTX thickness of 1% and 2% of radiation length per layer.

## References

- 1) K. Adcox et al.: Nucl. Instrum. Methods Phys. Res. A **499**, 469 (2003).
- 2) Y. Goto et al.: RIKEN Accel. Prog. Rep. **37**, 249 (2004).
- 3) K. Adcox et al.: Phys. Rev. Lett. **88**, 192303 (2002).
- 4) J. M. Heuser et al.: RIKEN Accel. Prog. Rep. **37**, 250 (2004).
- 5) J. Tojo et al.: RIKEN Accel. Prog. Rep. **37**, 251 (2004).

# Muon trigger upgrade with W production for PHENIX muon arms

A. Taketani, K. Aoki, K. Barish,\* A. Deshpande, M. Grosse Perdekamp, N. Saito, and W. Xie\*

The intermediate weak boson W, is an excellent probe to investigate the spin structure of proton.<sup>1)</sup> The parity-violating nature of the weak interaction can provide the polarization of light quarks and antiquarks in a proton through measurements of longitudinal single-spin asymmetry,  $A_L = \frac{1}{P} \frac{\sigma_{++} - \sigma_{--}}{\sigma_{++} + \sigma_{--}}$ , where  $P$  is beam polarization. If a larger rapidity of the produced W boson is considered, it can be expressed by quark and antiquark polarizations, as well as an unpolarized parton distribution function,

$$A_L^{W^+} \approx \frac{\Delta u(x_1)}{u(x_1)}, \quad A_L^{W^-} \approx \frac{\Delta d(x_1)}{d(x_1)}, \quad \text{for } x_1 \gg x_2,$$

and

$$A_L^{W^+} \approx \frac{-\Delta \bar{d}(x_1)}{\bar{d}(x_1)}, \quad A_L^{W^-} \approx \frac{-\Delta \bar{u}(x_1)}{\bar{u}(x_1)},$$

for  $x_1 \ll x_2$ .

The PHENIX muon arm is designed to detect muons,  $P_\mu > 2 \text{ GeV}/c$  with  $1.2 < |\eta| < 2.4$  over a full azimuthal range coverage.<sup>2)</sup> Since  $M_W$  is 80 GeV, muons from W are easily identified by requiring  $P_t > 20 \text{ GeV}/c$ . Muon arm has 8 times larger acceptance than the PHENIX central arm for detecting electrons from W decays. The muon arm will act a significant role in the investigation of quark flavor decomposed spin structure function. On the other hand, the production cross section of W bosons is small, which is order of 1 nb. Thus  $\sim 10^4$  events for the muon channel are expected with  $800 \text{ pb}^{-1}$  integrated luminosity at  $\sqrt{s} = 500 \text{ GeV}$ . The design instantaneous luminosity is  $2 \times 10^{32} \text{ s}^{-1} \text{ cm}^{-2}$ . Since the total cross section of proton-proton collision is 60 mb, the event rate will be 12 MHz. PHENIX DAQ system can handle maximum 12 kHz at level 1 trigger (LV1) output for several rare event channels.<sup>3)</sup> If 2 kHz of the LV1 bandwidth is dedicated to a single muon trigger, a rejection factor of 6000 will be required. The current muon LV1 rejection factor is measured to be 250 with Run3 p-p data at  $\sqrt{s} = 200 \text{ GeV}$ . So the LV1 rejection factor must be improved by more than 24.

The muon arm consists of two major parts. One is the muon tracker (MuTr) which determines momentum using the 3 layers of cathode readout chambers in magnetic field.<sup>2)</sup> The other is muon identifier (MuId) which works as a range counter to distinguish muons from other hadrons. Also MuID is used as a trigger counter.<sup>4)</sup> The muon trigger efficiency rises from zero at 1.8 GeV/c and becomes saturated at 2.5 GeV/c. Lower momentum muons dominate trigger and reconstructed tracks.<sup>5)</sup> It is very hard to increase this momentum threshold by adding more absorber materials

due to the space limit of the PHENIX experimental hall.

There are two methods for increasing momentum threshold in order to reduce single muon trigger rate.

The one method involves using a threshold-type Čerenkov detector. Figure 1 shows the configuration of the test Čerenkov counter setup we installed at PHENIX during the Run3 proton-proton collision period and the collected data as part of the PHENIX detector. The radiator of Čerenkov is 1 atm CO<sub>2</sub> and the momentum thresholds are 3.5 GeV/c and 17 MeV/c, for the muon and the electron, respectively. The coincidences of scintillators S1 and S2, are used as the trigger signal. Electrons, which are associated with the incident muon, may fire Čerenkov counter, even if muon momentum is below Čerenkov threshold. Two aluminum plates with 5 cm thickness are expected to absorb these electron. We obtained a 3–7 rejection factor with only the Čerenkov counter by analyzing these data. This is much smaller than the required rejection factor of 24.

The other method involves using fast momentum tracking. MuTr can readout only very slowly due to its cathode strip readout feature. We consider to put additional tracking devices in front and back of the MuTr with a faster readout time. The incident muon is bent in the azimuthal direction by the radial magnetic field. By measuring the azimuthal deviation across MuTr, momentum is determined. Detailed detector simulations are used to investigate rejection factor, and optimize additional device configuration.

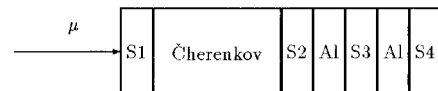


Fig. 1. Configuration of test Čerenkov counter setup: S1, S2, S3, and S4 indicate scintillation counters. Al's represent 5 cm aluminum plates. The radius of the Čerenkov cross section is 23 cm.

## References

- 1) N. S. Craigie et al.: Phys. Rep. **99**, 69 (1983); C. Bourrely et al.: Phys. Rev. D **59**, 95 (1980).
- 2) H. Akikawa et al.: Nucl. Instrum. Methods Phys. Res. A **499**, 537 (2003).
- 3) S. S. Adler et al.: Nucl. Instrum. Methods Phys. Res. A **499**, 560 (2003).
- 4) H. D. Sato et al.: RIKEN Accel. Prog. Rep. **36**, 240 (2003).
- 5) A. Taketani et al.: RIKEN Accel. Prog. Rep. **36**, 228 (2003).

\* University of California, Riverside, USA

## eRHIC: Progress and status

A. Deshpande, for the eRHIC Collaboration

The possibility of building an intense and polarized electron/positron beam facility adjacent to the Relativistic Heavy Ion Collider (RHIC) at BNL which could enable lepton-hadron Deep Inelastic Scatter (DIS) has been discussed in previous annual reports.<sup>1)</sup> We present the status and progress on this project in this paper.

The 10 GeV polarized lepton beam facility will collide with the 100 GeV heavy ion or the (up to) 250 GeV polarized proton beams at RHIC, resulting in a effective Center of Mass (CM) energy of 63 and 100 GeV for e-A and e-p collisions, respectively. Neither lepton-nucleus nor polarized e-p/n collisions have been performed above 30 GeV in CM energy. Further, it would be the first time these studies would be performed in collider geometry, enabling a systematic study of target as well as beam fragments. Because of RHIC's unique ability to vary the beam species all the way from polarized and unpolarized protons (p), unpolarized and (possibly) polarized helium (He), lithium (Li) to lead (Pb) or uranium (U), will allow an unprecedented study of fundamental and universal aspects of QCD including nucleon spin. The eRHIC facility at BNL would also be an attractive *experimental facility* because of two additional reasons: (1) All experiments could be performed with a single detector, which will enable significant reduction in the systematic uncertainties of measurements requiring comparison of results under different collision circumstances, (2) The high luminosity provided by the collider  $1 \times 10^{33} \text{ cm}^{-2} \text{ sec}^{-1}$  for e-p and a factor 100 down from that for e-A physics

Specifically, eRHIC will address the following questions related to QCD about which we presently know very little: (1) How do we understand the momentum distribution and spin content of protons and neutrons in terms of fundamental quarks and gluons? (2) While in high energy collisions quarks and gluons are involved, only hadrons are observed in the final states. Can we understand this phenomenon of hadronization? (3) What roles do quarks and gluons play in the microscopic structure of the nuclei? (4) Can we observe new phenomenon predicted by QCD involving saturation of gluons at high energies, similar to the Bose-Einstein condensation in atoms at low temperatures?

Attracted by such unique physics possibilities a large and diverse group of people have now formed a collaboration to finalize the design for eRHIC and its detectors. The electron beam design is being devel-

oped on two fronts: 1) a ring-ring design in which one adds a 10 GeV electron ring facility (injected in to by a 10 GeV super-conducting linac). The electron ring in this design will be approximately 1/3 in diameter of the RHIC, and 2) a linac-ring collider facility in which the 10 GeV linac collides with the RHIC hadron beams. It is assumed that collisions could take place at two or three beam energies between 5 and 10 GeV electron beams. Presently the first option is considered to be more probable one, but detailed design reports on both are awaited. The Ring-Ring option is being developed by the BNL-MIT/Bates collaboration with close ties with the DESY accelerator physicists. The Linac-Ring design is being developed by the BNL-JLAB accelerator physicists. A *Zeroth Design Report (ZDR)* has been requested by the BNL management by early January 2004 which will be reviewed by an external committee by mid-2004.

Based on the first versions of the accelerator lattice and IR design, the eRHIC detector WG has started studies related to the synchrotron radiation and related problems which might arise at this facility. This work needs close communication between the accelerator and physics working groups, and is being carried out through monthly meeting between people in both WGs. A detailed simulation of the IR and the synchrotron radiation related background in the present eRHIC lattice are under way and are expected to guide us to the final IR Design. These and such studies will then lead to the technology selection effort for different physical variables in terms of the detector components. There is a broad interest developing amongst the HERA-III interested physicists to do experiments at eRHIC if HERA-III program does not realize at DESY. They have joined the eRHIC detector design effort in recent past.

Having gone through various NSAC and its subcommittee reviews in the years 2002 and 2003, in November 2003, the US DoE declared<sup>2)</sup> that eRHIC would be one of the 28 "must-do" major scientific projects to pursued by the US office of Science and Technology in the next 20 years.

### References

- 1) eRHIC Collaboration, A. Deshpande: RIKEN Accel. Prog. Rep. **35**, 221, 228 (2002); RIKEN Accel. Prog. Rep. **36**, 232, 233, 236, 237, 259 (2003).
- 2) [http://www.science.doe.gov/Sub/Facilities\\_for\\_future/facilities\\_future.htm](http://www.science.doe.gov/Sub/Facilities_for_future/facilities_future.htm)

## CCJ operation in 2002–2003

S. Yokkaichi, Y. Goto, H. Hamagaki,\* T. Ichihara, O. Jinnouchi, A. Kiyomichi, Y. Watanabe, and H. En'yo

CCJ,<sup>1)</sup> RIKEN Computing Center in Japan for RHIC<sup>2)</sup> physics, started operation from June 2000 as the largest off-site computing center for the PHENIX<sup>3)</sup> experiment at RHIC. CCJ fills, in PHENIX computing, the three roles of (1) the simulation center, (2) Asian regional center and (3) center of spin physics. Recently DST (Data Summary Tape) production from raw data comes more important than simulation for CCJ role. Other smaller computing centers in PHENIX can handle only relatively small simulation data, however, only CCJ can handle several tens of TB of raw data except RCF (RHIC computing facility)<sup>4)</sup> because of our HPSS (High Performance Storage System)<sup>5)</sup> and data duplication facility built by us at RCF to transfer the data to CCJ.

Many analysis and simulation projects are being carried out at CCJ, including some PHENIX-official projects. They are shown on the web page: <http://ccjsun.riken.go.jp/ccj/proposals/>.

Within the current year, the data from PHENIX Run2 (2001/8–2002/1) and Run3 (2002/11–2003/5) were mainly analyzed. The report from each project is described in this volume.

About 50 TB of data were transported from BNL via tape media (42 TB) and network (9.1 TB) within this year. In a typical shipment of tapes, 17 TB of data are transferred in 33 days which includes tape transport by airplane, uploading to CCJ-HPSS and all limited factor of troubles. It means 6 MB/s of transfer rate on average. *Via* network, the typical transfer rate from BNL is 3–4 MB/s and approximately 12 MB/s was observed as the maximum burst rate retained in 20 minutes. In such large-scale network transfer, multi-stream transfer was mainly used with the *bbftp*<sup>6)</sup> command. The data amounts recorded at PHENIX and sent to CCJ are summarized in Table 1. Typical file sizes of the data are also shown.

The DST hierarchy in PHENIX is as follows. In each stage, the data size is reduced for easier handling. An event reconstruction process writes the DST in ‘root’<sup>7)</sup> format from the raw data. While the typical file size of raw data is 1.5 GB, DSTs are reduced to 0.6–1.8 GB. The  $\mu$ DST is written in the ‘root tree’ format and some information included in DST is dropped. Typical  $\mu$ DST size is 0.1–0.3 GB. The nanoDST(nDST)s are subsets of  $\mu$ DST which has only limited events and/or information which is selected with special interest for each group of users. The nDSTs have a size of 10–80 MB typically. In principle, we transfer all DST,  $\mu$ DST and nDST, *etc.*, from RCF to CCJ. For the raw data, all the p+p data for spin physics and a certain

Table 1. PHENIX data amount as of Dec. 2003.

	Run1 HI	Run2 HI p+p	Run3 HI p+p
raw data			
recorded (TB)	2.3	20 26	49 39
(transferred to CCJ)	2.3	7 26	– <sup>§</sup> 39
typ. file size (GB)	1.5	1.5 1.5	1.5 1.5
DST (version)	v05	v03 v01/2	v03 v03
produced (TB)	2.6	17.5 –	12.4 4.3
(transferred to CCJ)	2.6	– <sup>§</sup> 8.2	– <sup>§</sup> –
typ. file size (GB)	0.3–0.6	1.8 0.6	0.5 0.2
$\mu$ /nDST (version)	v05	v03 v01/2	
produced (TB)		– –	– –
(transferred to CCJ)		4 6.6	– –
typ. file size (GB)	0.1–0.2	0.3 0.1	– –

<sup>§</sup> transfer is on going

fraction of Heavy Ion (HI) data are also transferred. This principle was provisionally confirmed at the CCJ users meeting in Sep. 2003. While raw data and DST are transferred via tape solely by the CCJ administrator,  $\mu$ /nDST are transferred *via* network with significant cooperation from users.

The current configuration of CCJ is shown in Fig. 1. We have 176 PC nodes operated using Linux, 166 are calculation nodes and 10 are service nodes. Each calculation node has 1 GB of memory, 2 GB of swap area, 10–31 GB of local work area and dual CPU (Pentium III 700 MHz–1.4 GHz, Pentium 4 2.0 GHz). Red Hat 7.2/kernel 2.4.18 is operated on the calculation nodes, the same as RCF. Upgrading to Red Hat 8 is planned in Jan. 2004. We also have seven SUN servers oper-

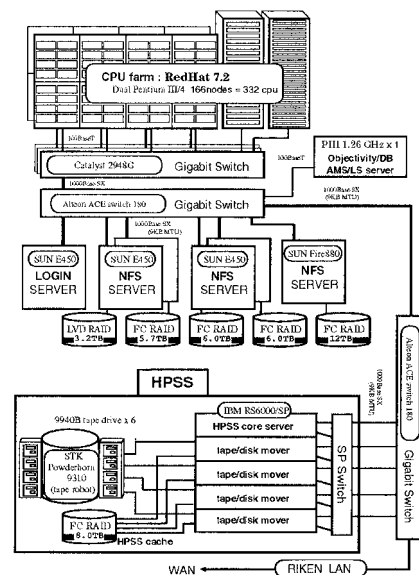


Fig. 1. Current configuration of CCJ.

\* Center for Nuclear Study, University of Tokyo

ated using Solaris, two are service nodes and five are data servers, which are connected to large RAID systems and operated as NFS servers. Service nodes are used for various purposes, for example, login server from WAN, database server for analysis, AFS client to share the PHENIX computing environment, controller of PC cluster, and monitoring of PC nodes and network.

HPSS is used as a mass storage system in CCJ, the same as RCF. Approximately 150 TB/450000 files of data are stored in CCJ-HPSS as of Oct. 2003. Five IBM RS6000/SP servers operated using AIX are used as HPSS core server and data/tape movers.

On the calculation nodes, LSF<sup>8)</sup> 4.2 is operated as a batch queueing system. Three general queues, *short/long/bg*, are categorized by CPU time limit, 200 minutes/1 day/7 days, respectively. Special queues for *production* (high priority), *largedisk* (dispatched to the nodes on which large disk/memory space remain) *etc.* are also set temporally or perpetually for special purposes. The priority of job dispatching in the queues is not 'first-in first-served' but is controlled by the fair-share policy of LSF, taking account of the CPU usage history by each user. Two job slots are assigned to each node because they have dual CPU. In the system, 20–30 job slots are kept for the *short* queue without being filled by longer jobs to maintain a shorter turnaround time for small-scale jobs. The number of running jobs in each queue is monitored using MRTG<sup>9)</sup> in addition to data flow between PCs and data servers or HPSS thus the state of the system is always watched by WEB.

The jobs submitted to CCJ are roughly categorized into two types, CPU bound and I/O bound. Typical CPU-bound jobs are simulation jobs (detector simulation and event generation) and event reconstruction (DST production) jobs. Typical I/O bound jobs are data reduction jobs, *i.e.*, making  $\mu$ DST (or nDST) from DST ( $\mu$ DST) and analysis of  $\mu$ /nDST, *i.e.*, reading the data and making small histogram files. In CCJ, such I/O bound jobs are limited by the I/O bandwidth of HPSS and/or RAID disks in which the required data are located. Particularly, concurrent NFS access from many PC nodes (typically more than 20) degrades the I/O throughput. In order to avoid such a situation, we use the *rcp* command to access the RAID disk. Jobs running on a PC have to transfer the data between the RAID and PC-local disk by *rcp*, and only work on the local disk. Actually, many concurrent *rcp*'s also degrade the throughput, hence we limit the number of maximum *rcp* processes on each data server. By the use of the limited *rcp*, I/O of RAID is maintained at 30–50 MB/s in contrast with NFS access which can achieve only 10 MB/s.

Hardware upgrades in this year are as follows. No CPUs were upgraded but several tens of motherboards were replaced to get rid of the node hanging-up

problem. FC RAID disks of 8 TB were newly connected to SUN Fire 880 and the total capacity was increased to approximately 33 TB. In HPSS, tape drives were replaced from four STK 9940A (I/O 10 MB/s, capacity 60 MB/cartridge) to six 9940B (30 MB/s, 200 MB/cartridge). All the data written in the 9940A format have already been rewritten in the 9940B format. Since we have 3000 tape cartridges, the total tape capacity is 600 TB currently. In the data duplication facility at RCF, two Redwood drives were replaced by two 9940B's and the host machine was also replaced, from IBM RS6000 F50 to IBM p630. The connection between RIKEN LAN to WAN was also replaced in June 2003, from IMnet (50 Mbps) to SINET (1 Gbps).

We have encountered the hardware problems described below this year. PC nodes encounter various hardware problems including problems of the fan, disk (itself and SCSI I/F board), memory, CPU and power supply. Approximately 15% of PC nodes (almost belong to older node group) suffered from such problems. Data servers also encounter hardware problems in the RAID controller, I/F PCI card between FC (fibre channel) RAID and server, FC GBIC and FC hub. To solve them, we needed to shutdown at least one data server per month on average. The simple break down of disks in the RAID system is not counted here because such disks are hot-swappable, *i.e.*, they can be replaced without stoppage of service. In spite of these problems, data on the disks have not been lost thus far.

We have proceeded now to a project of integrated operation between CCJ and the new RIKEN super-computer system. The new system includes 1024 nodes/2048 CPUs of a PC cluster system and we can use dedicated 128 nodes/256 CPUs in the cluster. Our data servers and HPSS can also be accessed by the new cluster nodes the same as for our old PC nodes. HPSS server machines will be replaced by seven IBM p630 servers and we can use eight 9940B tape drives connected to four data/tape movers and one tape robot (STK Powderhorn 9310) dedicatedly. The robot can handle approximately 5000 tape cartridges, thus we can extend the total tape capacity to 1 PB. The integrated system will be available in March 2004.

## References

- 1) <http://ccjsun.riken.go.jp/ccj/>  
Y. Watanabe et al.: RIKEN Accel. Prog. Rep. **36**, 262 (2003); T. Ichihara et al.: RIKEN Accel. Prog. Rep. **35**, 236 (2002).
- 2) <http://www.bnl.gov/rhic>
- 3) <http://www.phenix.bnl.gov>
- 4) <http://www.rhic.bnl.gov/RCF/>
- 5) <http://www.sdsc.edu/hpss/>
- 6) <http://doc.in2p3.fr/bbftp/>
- 7) <http://root.cern.ch>
- 8) <http://www.platform.com/products/LSF/>
- 9) <http://people.ee.ethz.ch/~oetiker/webtools/mrtg/>



# Azimuthal asymmetries in fragmentation processes at Belle

K. Hasuko, M. Grosse Perdekamp,\*<sup>1</sup> J. S. Lange,\*<sup>2</sup> A. Ogawa,\*<sup>3</sup> and V. Siegle\*<sup>4</sup>

In an unpolarized  $e^+e^-$  annihilation, nontrivial azimuthal asymmetries may exist, which determine novel chiral-odd fragmentation functions, such as the Collins-Heppelmann function,  $H_1^\perp$ ,<sup>1)</sup> and the two-pion interference fragmentation function,  $\delta q^h$ . We are extracting these functions using  $e^+e^-$  collision data from the Belle experiment<sup>2)</sup> at the KEK B-factory.<sup>3)</sup> These novel functions are also expected to be a powerful tool for accessing the quark transversity distribution of a proton,  $\delta q$ .<sup>4)</sup>

The fundamental observable for measurements of  $H_1^\perp$  in  $e^+e^- \rightarrow \pi^+\pi^-X$  ( $\pi^+$  and  $\pi^-$  should be in different jets) is the angle  $\phi_0$  between the ‘‘pion plane’’ formed by two pion momentum vectors  $\vec{p}_{\pi 1(2)}$  and the ‘‘reaction plane’’ formed by either of  $\vec{p}_{\pi 1(2)}$  and the beam axis.<sup>5) a)</sup> The angular dependence of a differential cross section is expressed as  $(1 + \cos^2 \theta^*) \times D_q^{\pi 1}(z_1)D_q^{\pi 2}(z_2) + \sin^2 \theta^* \cos(2\phi_0)H_1^\perp(z_1)H_1^\perp(z_2)$ , using the spin-averaged fragmentation function  $D_q^\pi(z)$ , the momentum fraction  $z_{1(2)}$ , and the center-of-mass angle between the incoming electron and the pion defining the reaction plane  $\theta^*$ .

We are studying on  $H_1^\perp$  using 32 million  $q\bar{q}$  data taken in the continuum region 60 MeV below the  $\Upsilon(4S)$  resonance. Details about the analysis method and event selection were reported in Ref. 6. We observed large background asymmetries in  $\cos(2\phi_0)$  distributions. The main background sources are (1) the limitation of detector acceptance and (2) gluon radiation. The background asymmetries arising from detector acceptance can be canceled by applying fiducial cuts for pions (see Fig. 1). We also used another method of eliminating the background by taking the

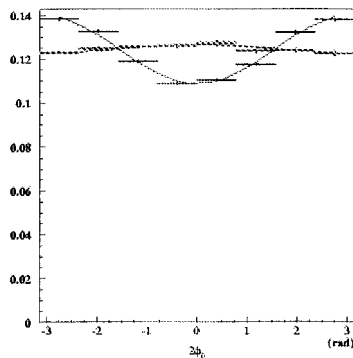


Fig. 1. Comparison of  $\cos(2\phi_0)$  dependences between raw (thin) and fiducial (thick) cuts.

ratio of asymmetry distribution between pion pairs selected under two contrary conditions (*e.g.* unlike-sign pairs and like-sign pairs); here, we can expect the same detector effects and other common systematics to be canceled while the difference in analyzing power for  $H_1^\perp$  remains.

Asymmetries arising from gluon radiation are expected to have  $Q_T$  dependence, where  $Q_T$  is the transverse momentum of a photon in the center-of-mass frame of two pions (Collins-Soper frame). Although these asymmetries have the same  $\cos(2\phi_0)$  dependence, they can be separated on the basis of  $Q_T$  dependence; the expected  $Q_T$  dependence on Collins and gluon radiation is illustrated in Fig. 2.

Detailed studies on background subtraction are nearly completed and extraction of  $H_1^\perp$  is in progress. The asymmetries are expected to have  $\sin^2 \theta^*$  dependence, which could help extract the relatively small asymmetries we are aiming at. We also plan to process on-resonance data (containing  $b\bar{b}$ ) to increase statistics and use  $b\bar{b}$  decays as a control sample. This study has been performed at RIKEN CCJ.

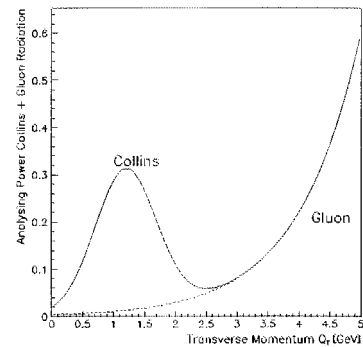


Fig. 2. Comparison of expected analyzing powers between  $H_1^\perp$  and gluon radiation as a function of  $Q_T$ .

## References

- 1) J. C. Collins: Nucl. Phys. B **396**, 161 (1993); J. C. Collins, S. F. Heppelmann, and G. Ladinsky: Nucl. Phys. B **420**, 563 (1994).
- 2) Belle Collaboration, S. Mori et al.: Nucl. Instrum. Methods Phys. Res. A **479**, 117 (2002).
- 3) KEK B Factory Design Report, KEK Rep. 95-7 (1995) (unpublished).
- 4) M. Grosse Perdekamp, A. Ogawa, K. Hasuko, J. S. Lange, and V. Siegle: Nucl. Phys. A **711**, 69 (2002).
- 5) D. Boer, R. Jakob, and P. J. Mulders: Phys. Lett. B **424**, 143 (1998).
- 6) K. Hasuko et al.: RIKEN Accel. Prog. Rep. **36**, 260 (2003).

\*<sup>1</sup> University of Illinois, USA

\*<sup>2</sup> University of Frankfurt, Germany

\*<sup>3</sup> Brookhaven National Laboratory, USA

\*<sup>4</sup> University of Heidelberg, Germany

a)  $\phi_{1(2)}$  are also defined using jet axis. Details can be seen in Ref. 6.

# Progress on precision measurement of fragmentation functions at Belle

V. Siegle,<sup>\*1</sup> J. S. Lange,<sup>\*2</sup> M. Grosse Perdekamp,<sup>\*3</sup> K. Hasuko, and A. Ogawa<sup>\*2,\*4</sup>

The Belle experiment at the asymmetric  $e^+e^-$  collider KEK-B at Tsukuba, Japan, is usually operating at  $\sqrt{s} = 10.58$  GeV, corresponding to the mass of the  $\Upsilon(4S)$  meson. The  $\Upsilon(4S)$  meson decays with a branching ratio of  $\sim 100\%$  into  $B\bar{B}$  pairs, providing a high statistics  $B$  meson sample for the study of, for example, CP violation and rare decays in the  $B$  meson system. For background studies,  $\sim 10\%$  of the data taking is performed at  $\sqrt{s} = 10.52$  GeV, 60 MeV below the  $\Upsilon(4S)$  resonance. Such data can be used for very accurate QCD studies.

The fragmentation function  $D_q^h(z, Q^2)$  denotes the probability of finding a hadron  $h$  in the fragmentation of a quark  $q$  ( $q = u, d, s, c, b$ ). The variable  $z$  denotes the fraction of momentum transferred from the quark to the hadron. In leading order QCD, the normalized hadronic differential cross section for a hadron  $h$  can be expressed by fragmentation functions  $\frac{1}{\sigma_0^h} \frac{d\sigma^{e^+e^- \rightarrow hX}}{dz} = \frac{\sum_q e_q^2 D_q^h(z)}{\sum_q e_q^2}$ , where  $e_q$  is the quark

charge. The available world data on the normalized hadronic cross section<sup>1)</sup> are shown in Fig. 1. It can be seen that the precision of the available data at high  $z$  is limited. In particular, at low  $\sqrt{s}$ , precise fragmentation function data are not available. We have investigated the possibility of re-measuring fragmentation functions at Belle utilizing the highly integrated luminosity available at KEK-B and the excellent particle identification capabilities of the Belle detector. Precision fragmentation functions would serve as input to a global QCD analysis of longitudinal spin asymmetries in inclusive hadron production at RHIC in polarized  $pp$  collisions.

Our preliminary results are very encouraging. As an example, we show the fragmentation function for charged pions in Fig. 2 on an arbitrary scale. The plot uses  $1.7 \times 10^5$  events, corresponding to 0.3% of the available statistics. For comparison, we have included parametrizations of fragmentation functions, obtained from global QCD fits to existing fragmentation function data. The full data set will extend to the highest  $z$  with good precision. The situation for kaon fragmentation functions is quite similar. At present, we are processing the full data sample and carrying out systematic error studies.

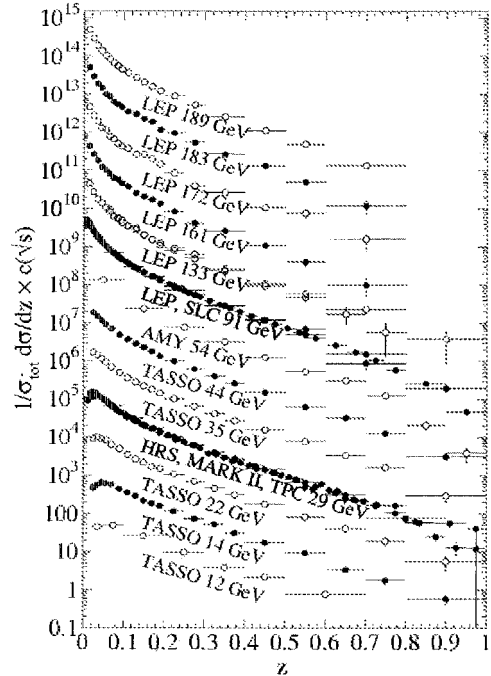


Fig. 1. World data set measurements of the normalized hadronic cross section.<sup>1)</sup>

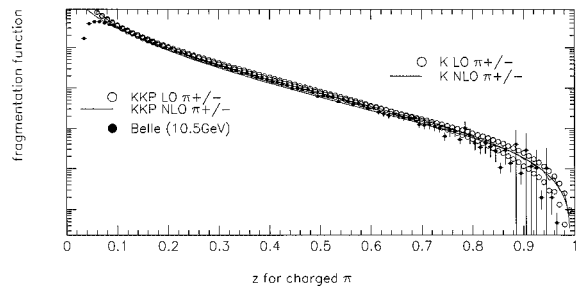


Fig. 2. Preliminary fragmentation function for charged pions for a data set of  $1.7 \times 10^5$  hadronic events at  $\sqrt{s} = 10.52$  GeV, compared to parametrizations from Kretzer<sup>2)</sup> and Kniehl, Krämer and Pötter.<sup>3)</sup> Only statistical errors are shown.

## References

- 1) O. Biebel, P. Nason, and B. R. Webber: hep-ph/0109282, Phys. Rev. D **66**, 010001 (2002).
- 2) S. Kretzer: Phys. Rev. D **62**, 054001 (2000).
- 3) B. A. Kniehl, G. Krämer, and B. Pötter: Nucl. Phys. B **582**, 514 (2000).

<sup>\*1</sup> University of Heidelberg, Germany

<sup>\*2</sup> University of Frankfurt, Germany

<sup>\*3</sup> University of Illinois, USA

<sup>\*4</sup> Brookhaven National Laboratory, USA

# Development of trigger and DAQ system for SVD2.0 at Belle

K. Hasuko

The Silicon Vertex Detector (SVD) plays an important role in the Belle experiment<sup>1)</sup> at the KEK B factory (KEKB).<sup>2)</sup> Although the basic performance of the previous SVD was satisfactory,<sup>3)</sup> further improvements will be achieved in the newest version of SVD, SVD2.0, installed in the summer of 2003.

Instead of the three layers in the previous version, SVD2.0 consists of four concentric cylindrical layers with a closer innermost layer ( $2.2 < r < 8.0$  cm). It contains 216 double-sided silicon strip detectors with two orthogonal-coordinate readouts (110K channels in total). The polar angle coverage is extended to be the nominal angular coverage of Belle. The front-end readout (VA1TA) chips are fabricated with  $0.35 \mu\text{m}$  process technology to improve radiation hardness ( $0.8 \mu\text{m}$  process technology in the previous version).

Considering there are 50% more readout channels and increasing beam currents at KEKB, the trigger rate is expected to rise up to 1 kHz; three times the bandwidth of the previous version is required. We developed a new DAQ system for SVD2.0. For easier implementation, handling and maintenance, we have employed a new scheme based on standard PCs, instead of the Motorola DSPs used in the previous version.<sup>4)</sup> The detailed setup of SVD2.0 DAQ and the trigger system can be found in Ref. 5.

The requirements for the new DAQ system are: to process data at a 1 kHz or faster, less than 5% of dead time at 1 kHz trigger rate and a data-flow rate of 10 MB/sec. To achieve these requirements, the DAQ system consists of 12 PCs (Xeon Pentium IV 2.4 GHz with Intel Compiler<sup>a)</sup>) using PCI interfaces (P-PCI board<sup>b)</sup>). The PCs receive event data from the flash ADC system via P-PCI boards in LVDS<sup>c)</sup> and perform data compression based on  $S/N$  ratio calculation and clustering.

The performance of the DAQ system has been examined with various occupancy levels (trigger rates) emulated by a random-pulse generator. The DAQ system including the event builder is confirmed to be able to process data at a 1.3 kHz trigger rate with 5% occupancy expected in SVD2.0. The total data size is measured to be 10.4 kB per event, which is manageable for the Belle data storage. The dead time is measured to be 5% at most under the same condition.

The trigger system has also been changed. To install the additional layer of SVD2.0, the innermost cathode strips of the Central Drift Chamber (CDC) had to be removed. They provided  $z$  (beam direction) information in the previous Level-1 (L1) trigger to suppress the beam-related backgrounds. Considering the expected beam backgrounds, additional trigger capability to compensate the loss of CDC  $z$  trigger is

necessary. Matching between CDC tracks and SVD segment hits has been employed to maintain a reasonable trigger rate for hadronic triggers.

For the SVD L1 trigger, the 128-OR'ed fast-shaped (shaping time of 75 to 300 ns) signal (TA) of the VA1TA chip is utilized. The SVD2.0 is divided into 18 track segments on the  $xy$  plane and coincidence conditions based on 3 out of 4 layer hits are prepared.

The SVD-L1 logic is implemented using a VME module containing XILINX FPGA. It receives 18 SVD-segment and 64 CDC-segment information and gives the matching results with reasonable clustering to the final L1 decision. It contains not only matching logic but timing adjustment, variable masks and a VME control interface. The trigger decision is made within  $1.7 \mu\text{sec}$ , satisfying the required latency of  $2.2 \mu\text{sec}$ .

Initial performance has been checked with cosmic-ray muons and we found that the system operates successfully. A typical event display is shown in Fig. 1. Physics runs have just started with the complete SVD2.0 system and detailed performance analysis is being continued.

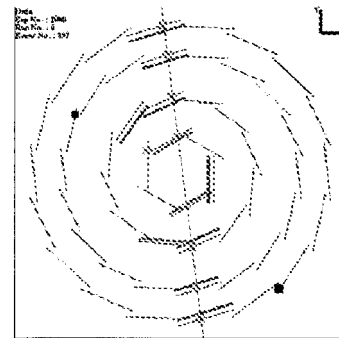


Fig. 1. Typical event of a cosmic-ray muon. Squares (circles) indicate the cluster hit of the cosmic-ray muon in the forward (backward) side of SVD2.0. The thick lines associated with ladders denote TA hits in VA1TA chips.

## References

- 1) Belle Collaboration, S. Mori et al.: Nucl. Instrum. Methods Phys. Res. A **479**, 117 (2002).
- 2) KEK B Factory Design Report, KEK Rep. 95-7 (1995) (unpublished).
- 3) R. Abe et al.: Nucl. Instrum. Methods Phys. Res. A **478**, 296 (2002); T. Kawasaki: Nucl. Instrum. Methods Phys. Res. A **494**, 94 (2002).
- 4) E. Banas et al.: Nucl. Instrum. Methods Phys. Res. A **469**, 364 (2001).
- 5) K. Hasuko: RIKEN Accel. Prog. Rep. **36**, 261 (2003).

a) version 6

b) manufactured by Fird Corporation

c) Low-Voltage Differential Signal

## Pumping $^{229m}\text{Th}$ by hollow-cathode discharge

H. Haba, M. Hara,\*<sup>1</sup> T. T. Inamura, Y. Kasamatsu,\*<sup>2</sup> H. Kikunaga,\*<sup>3</sup> T. Mitsugashira,\*<sup>1</sup> T. Nakanishi,\*<sup>3</sup>  
T. Ohtsuki,\*<sup>4</sup> A. Shinohara,\*<sup>2</sup> K. Takamiya,\*<sup>5</sup> A. Yokoyama,\*<sup>3</sup> and H. Yuki\*<sup>4</sup>

It was in 1976 that Kroger and Reich for the first time postulated the 1st excited state in  $^{229}\text{Th}$  at an energy of approximately 100 eV or less.<sup>1)</sup> Eighteen years later, Helmer and Reich revised such excitation energy to  $3.5 \pm 1.0$  eV.<sup>2)</sup> Meanwhile, Burke *et al.* suggested the existence of such an isomer by observing the angular distributions of the  $^{230}\text{Th}(d, t) ^{229}\text{Th}$  reaction.<sup>3)</sup> Their results are, however, not direct evidence for such an extremely low-lying isomer in  $^{229}\text{Th}$ . Several attempts have been carried out to obtain direct evidence for the isomer  $^{229m}\text{Th}$ . Because of its excitation energy comparable to the UV, mostly optical measurement has been carried out using  $^{233}\text{U}$  that decays to  $^{229g}\text{Th}$  (and  $^{229m}\text{Th}$  probably) by emission of  $\alpha$  particles.<sup>4-7)</sup> None of these attempts have been successful. Recently, two different types of attempts have been carried out to determine the lifetime of  $^{229m}\text{Th}$  by avoiding the huge background inevitably caused by the parent nucleus  $^{233}\text{U}$ .<sup>8,9)</sup> Unfortunately, their measurements are inconsistent with each other, and neither of them has provided clear evidence for the existence of  $^{229m}\text{Th}$ .

Here, we present a unique combination of a noble idea and the nuclear chemists' expertise, aiming at unprecedented achievements in studying the exotic isomer  $^{229m}\text{Th}$ . The noble idea is to make use of a well-established technique, hollow-cathode discharge tube, in atomic spectroscopy to populate the isomer in question; it is based on the Coulomb excitation of atomic nuclei and hyperfine interaction which are basically described with the same form of Hamiltonian of electromagnetic interaction.<sup>10,11)</sup> Eventually, this idea has been combined with Karpeshin's theoretical proposal,<sup>11,12)</sup> optical pumping with lasers, which is practically impossible because of the large experimental error in the excitation energy of  $^{229m}\text{Th}$  reported so far. In the present method, by contrast, there is no need to know exactly the excitation energies of atomic and nuclear states concerned. Now it seems very much probable to populate  $^{229m}\text{Th}$  through atomic states, and even population inversion will be realized.<sup>12)</sup>

When we designed the hollow-cathode discharge tube, we exercised special care to handle radioactive  $^{229m}\text{Th}$  and  $^{229g}\text{Th}$ . A schematic cross-sectional view of the tube is shown in Fig. 1. There is an empirical golden rule in designing to produce a well-localized plasma in the hollow:<sup>13)</sup> the ratio of the length of the

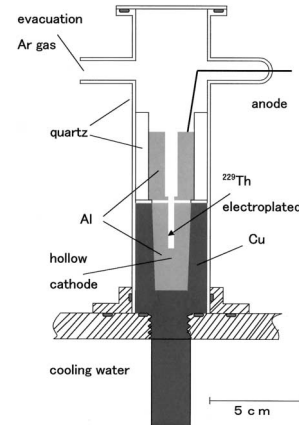


Fig. 1. Schematic cross-sectional view of our hollow-cathode discharge tube. Discharge Ar gas will be kept at a pressure of about  $10^2$  Pa. The discharge current will be about 100 mA.

hollow  $l$  to its diameter  $\phi$ ,  $l/\phi \gtrsim 4$  and the gap  $d$  between the anode surface and the cathode surface should be considerably smaller than  $\phi$ . Our present measures are  $l = 25$  mm,  $\phi = 5$  mm and  $d = 1$  mm. Cooling is effective not only for safety reason but also for localizing the plasma in the hollow.

The experiment will be made at the Oarai facility of Tohoku University with the world's radiochemically purest  $^{229}\text{Th}$  sample. This will be the first background-free measurement of  $\alpha$  particles and photons from  $^{229m}\text{Th}$ .

### References

- 1) L. A. Kroger and C. W. Reich: Nucl. Phys. A **259**, 29 (1976).
- 2) R. G. Helmer and C. W. Reich: Phys. Rev. C **29**, 1845 (1994).
- 3) R. G. Burke et al.: Phys. Rev. C **42**, R499 (1990).
- 4) G. M. Irwin and K. H. Kim: Phys. Rev. Lett. **79**, 990 (1997).
- 5) D. S. Richardson et al.: Phys. Rev. Lett. **80**, 3206 (1998).
- 6) S. B. Utter et al.: Phys. Rev. Lett. **82**, 505 (1999).
- 7) R. W. Shaw et al.: Phys. Rev. Lett. **82**, 1109 (1999).
- 8) E. Browne et al.: Phys. Rev. C **64**, 014311 (2001).
- 9) T. Mitsugashira et al.: J. Radioanal. Nucl. Chem. **255**, 63 (2003).
- 10) T. T. Inamura: Hyperfine Interact. **127**, 31 (2000).
- 11) T. T. Inamura, F. F. Karpeshin, and M. B. Trzhaskovskaya: Czech. J. Phys. **53**, B 349 (2003).
- 12) F. F. Karpeshin et al.: Phys. Lett. B **372**, 1 (1996).
- 13) B. Arcimowicz at Poznan Univ. Tech.: private communication.

\*<sup>1</sup> Oarai Branch, Institute for Materials Research, Tohoku University

\*<sup>2</sup> Graduate School of Science, Osaka University

\*<sup>3</sup> Graduate School of Science, Kanazawa University

\*<sup>4</sup> Laboratory of Nuclear Science, Tohoku University

\*<sup>5</sup> Research Reactor Institute, Kyoto University

## Study on beam instability due to space charge oscillation during longitudinal bunch compression

T. Kikuchi,<sup>\*1</sup> T. Katayama, M. Nakajima,<sup>\*2</sup> and K. Horioka<sup>\*2</sup>

Inertial confinement fusion is one of the energy production methods by controlled thermonuclear reactions. In the heavy ion inertial fusion (HIF), the generation and transport of intense heavy-ion beams are carried out by a particle accelerator. The Pb, Bi, Hg, and U ions of 4–10 GeV particle energy are candidates.<sup>1)</sup> The total beam current of 100 kA consists of many heavy-ion beams, and the pulse width of 10 ns is required for the effective implosion of a fuel pellet. In the final stage of the HIF accelerator system, the beam pulse must be longitudinally compressed from  $\sim 100$  to  $\sim 10$  ns. In the final beam bunching, the beam current is continuously increased due to the bunch compression, and the stability condition of the beam transport is also changed with increasing space charge effect. The bunch of heavy-ion beams should be transported and compressed without emittance growth and particle loss as much as possible for the final focusing to the target. However, these beam parameters have not yet been determined, because such space-charge-dominated beam dynamics could include many unknown behaviors. Consequently, the study of high-current and space-charge-dominated beam is crucial in HIF.

The beam dynamics was investigated during the longitudinal bunch compression in the final buncher of the HIF accelerator system.<sup>2–5)</sup> In this study, the pulse width of the beam bunch is compressed from 250 to 10 ns, so that the beam current increases linearly 400 A to 10 kA during the beam transport. For the simulation of the transverse beam dynamics during the longitudinal bunch compression, the transverse particle-in-cell method was used with a simple model of the beam current increase.<sup>3)</sup> The dilution of particle distribution in phase space was implied by the multiparticle simulation during the longitudinal bunch compression.<sup>2)</sup> Figure 1 shows the evolution of the emittance growth ratio  $\epsilon/\epsilon_i$ , which is the ratio of the transverse rms emittance to the initial one, during the final beam bunching along a number of lattice unit of 3 m length. The Kapchinskij-Vladimirskij (K-V), waterbag, Gaussian, semi-Gaussian, and parabolic distributions were assumed as the initial conditions of the transverse particle distribution. As shown in Fig. 1, the K-V and waterbag beams cause an abrupt emittance growth due to the instability induced by the space charge effect.<sup>3,4)</sup> The particle simulations showed the emittance growth accompanied by localized charge distri-

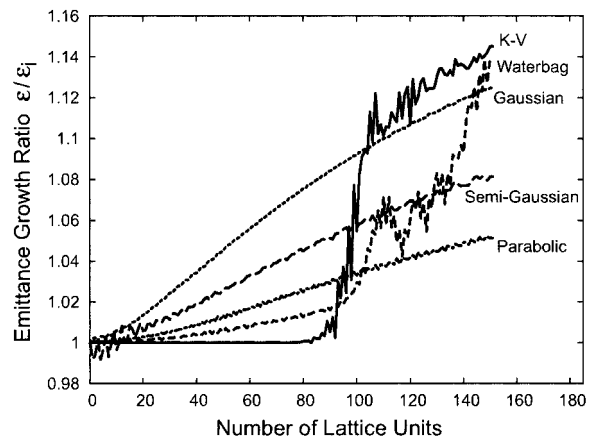


Fig. 1. Emittance growth ratio during the final beam bunching. Each line corresponds to the different initial distributions.

bution.<sup>3–5)</sup> It was found that the emittance growth indicated by Fig. 1 corresponds to the regime of the large growth rates of the axisymmetric flute perturbation.<sup>3,4)</sup> The comparison with the analytical estimation for the growth rate of the perturbation confirmed the importance of the role of space charge oscillation for the emittance growth. On the other hand, the simulation results at the other distributions indicated the gradual emittance increase without abrupt growth.

In the present paper, the transverse beam dynamics was investigated by the multiparticle simulation during the final beam bunching in the HIF accelerator. The initially K-V and waterbag distributed beams caused abrupt emittance growth due to the collective behavior of space-charge-dominated beams. On the other hand, it becomes clear that the initial Gaussian, semi-Gaussian, and parabolic beams may pass through the final beam bunching region without the influence of the instability induced by the space charge oscillation.

### References

- 1) J. J. Barnard et al.: Nucl. Instrum. Methods. Phys. Res. A **415**, 218 (1998).
- 2) T. Kikuchi, M. Nakajima, and K. Horioka: J. Plasma Fusion Res. **79**, 105 (2003).
- 3) T. Kikuchi, M. Nakajima, K. Horioka, and T. Katayama: accepted by Phys. Rev. Spec. Top. Accel. Beams.
- 4) T. Kikuchi, M. Nakajima, K. Horioka, and T. Katayama: Proc. 3rd Int. Conf. on Inertial Fusion Science and Applications, Monterey, USA, 2003-9, to be published.
- 5) T. Kikuchi, T. Katayama, M. Nakajima, and K. Horioka: Proc. 14th Symp. on Accelerator Science and Technology, Tsukuba, 2003-11 (2003), p. 398.

<sup>\*1</sup> Center for Nuclear Study, University of Tokyo

<sup>\*2</sup> Department of Energy Sciences, Tokyo Institute of Technology

# Production of intense $^{58}\text{Fe}$ and $^{64}\text{Ni}$ beams using MIVOC method

M. Kidera, T. Nakagawa, Y. Higurashi, T. Aihara, N. Suzuki, E. Ikezawa,  
O. Kamigaito, M. Kase, and Y. Yano

In RILAC, super heavy elements 108, 109, 110 and 111 were intensively researched from last summer to this summer. For these experiments, very stable and highly intense beams of  $^{58}\text{Fe}$  and  $^{64}\text{Ni}$  were required to produce these super heavy elements by using cold fusion reaction ( $^{58}\text{Fr}+^{208}\text{Pb}\rightarrow^{267}108+n$ ,  $^{58}\text{Fe}+^{209}\text{Bi}\rightarrow^{268}109+n$ ,  $^{64}\text{Ni}+^{208}\text{Pb}\rightarrow^{271}110+n$ ,<sup>1)</sup> and  $^{64}\text{Ni}+^{209}\text{Bi}\rightarrow^{272}111+n$ <sup>2)</sup>) which has a very small cross section of the order of picobarns.

One of the useful methods for the production of metal ion beams from ECRIS is the MIVOC method. Using the MIVOC method,<sup>3)</sup> it is possible to produce metal ions in the same manner as in the case of a gaseous element. Various kinds of metal ions have been successfully produced thus far using the MIVOC method from the RIKEN 18 GHz ECRIS. For the above mentioned long-term experiments, we succeeded in producing intense beams of  $^{58}\text{Fe}$  and  $^{64}\text{Ni}$  ions using the MIVOC method.

In the MIVOC method, volatile compounds containing metal atoms of interest in their molecular structure were used to release metallic gaseous elements. These compounds were placed in a separate vacuum chamber (MIVOC chamber) connected to the ECR plasma chamber. The compound vapor was allowed to diffuse into the plasma chamber. The MIVOC chamber was connected by a gas-feeding tube *via* a highly conductive regulation valve to control the flow rate of the compound vapor. Several 100 milligrams of the compound powder was placed at the bottom of the MIVOC chamber. Next, air and possible moisture in the MIVOC were evacuated until the vapor pressure in the MIVOC chamber become stable generally. With the compounds, gas pressure in the plasma chamber increased from  $\sim 1 \times 10^{-7}$  to  $\sim 5 \times 10^{-6}$  mbar. No gas-mixing method was applied during the experiments. In order to minimize contamination, the plasma chamber wall was covered with a thin aluminum tube of 1 mm thickness which is easily replaceable.

The  $^{58}\text{Fe}$  ion was produced from ferrocene ( $^{58}\text{Fe}(\text{C}_5\text{H}_5)_2$ ) in the following manner. Collaborating with the chemical analysis division in RIKEN, about 200 mg ferrocene was produced from 100 mg of 91.5% enrichment  $^{58}\text{Fe}$  oxide. Constructive crystallization was not carried out for the ferrocene; a compound of organic chemicals was used. The color of the powder was dark orange and the grain size was about 0.5 mm. The consumption rate of  $^{58}\text{Fe}$  was 1.2 mg/h during the beam time of 77 hours. The average beam intensity of  $^{58}\text{Fe}^{13+}$  was about  $15 e\mu\text{A}$  at an extraction voltage of 15.9 kV. The RF power was 500 W. The typical gas pressure was  $2.4 \times 10^{-6}$  Torr. The temperature

of the MIVOC chamber was controlled by the electric desk light, when the gas pressure was lower than  $1.0 \times 10^{-6}$  Torr.

The  $^{64}\text{Ni}$  ion was produced from nickelocene ( $^{64}\text{Ni}(\text{C}_5\text{H}_5)_2$ ) in the following manner. About 4 g of nickelocene was produced from 3 g of 97% enrichment  $^{64}\text{Ni}$  metal. Constructive crystallization was not carried out for the nickelocene. The color of the powder was dark green, and the grain size was about 0.5–2 mm. The beam times of  $^{64}\text{Ni}^{14+}$  and  $^{64}\text{Ni}^{13+}$  were about 400 and 2000 hours, respectively. 300–800 mg of nickelocene was placed in the MIVOC chamber once. The average consumption rate of  $^{64}\text{Ni}$  was about 1.2 mg/h. The average beam intensities of  $^{64}\text{Ni}^{14+}$  and  $^{64}\text{Ni}^{13+}$  were about  $17 e\mu\text{A}$  and  $40 e\mu\text{A}$ , respectively.

The gas pressure of the plasma chamber is very sensitive to room temperature, because the vapor pressure of nickelocene is strongly dependent on it. The change in gas pressure causes a rapid change in beam intensity. To minimize it, a new MIVOC chamber with

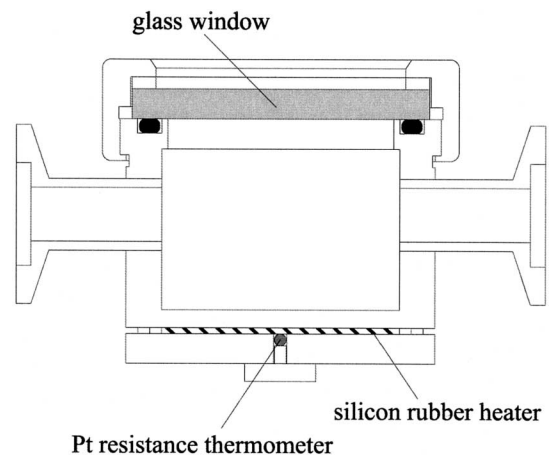


Fig. 1. Cross sectional view of new MIVOC chamber with temperature control.

Table 1. Typical main parameters of RIKEN 18 GHz ECRIS for the production of  $^{58}\text{Fe}$  and  $^{64}\text{Ni}$  using the MIVOC method.

	$^{58}\text{Fe}^{13+}$	$^{64}\text{Ni}^{14+}$	$^{64}\text{Ni}^{13+}$
Max. mirror magnetic field (T)			
Microwave injection side	1.4	1.4	1.4
Beam extraction side	1.0	1.1	1.1
Gas pressure (Torr)	$2.4\text{e-}6$	$1.7\text{e-}6$	$1.4\text{e-}6$
RF power (W)	500	450	500
Bias voltage of electrode (V)	-64	-50	-70
Extraction voltage (kV)	15.9	16.9	17.5
Beam intensity ( $e\mu\text{A}$ )	17	20	40

temperature control was developed for the  $^{64}\text{Ni}^{13+}$  experiment. Figure 1 shows the cross sectional view of the chamber. The chamber can be heated using a silicon rubber heater from room temperature to  $70^\circ\text{C}$ . A Pt resistance thermometer was placed on the heater to monitor the temperature. Gas pressure could be controlled by the temperature of the MIVOC chamber easily. The beam intensity of  $^{64}\text{Ni}^{13+}$  ions could be stably kept at more than  $30\text{ e}\mu\text{A}$  for a long term

operation.

The typical ECR parameters for the ferrocene and the nickelocene are listed in Table 1.

#### References

- 1) K. Morita et al.: Eur. Phys. J. A, in press.
- 2) K. Morita et al.: submitted to J. Phys. Soc. Jpn.
- 3) T. Nakagawa et al.: Nucl. Instrum. Methods Phys. Res. A **396**, 9 (1997).

## Optimization of magnetic field configuration for the production of Ar ions from RIKEN 18 GHz ECR ion source<sup>†</sup>

Y. Higurashi, T. Nakagawa, M. Kidera, T. Aihara,\* M. Kase, T. Kageyama, and Y. Yano

At RIKEN, the intense beams of multicharged heavy ions, such as Ar<sup>8+</sup>, Kr<sup>13+</sup>, Xe<sup>20+</sup> and U<sup>35+</sup>, are strongly in demand for the radioisotope beam (RIB) factory project.<sup>1)</sup> For this reason, we constructed the RIKEN 18 GHz electron cyclotron resonance ion source (RIKEN 18 GHz ECR ion source) in the mid-1990s and successfully produced intense beams of heavy ions.

Very recently, with respect to increasing the beam intensity from the ECR ion source, the importance of the magnetic field configuration and a few experimental results obtained using the superconducting ECR ion source have been reported.<sup>2)</sup> In 2001, we measured the beam intensities as a function of the minimum magnetic field strength of the mirror magnetic field ( $B_{min}$ ) and the beam extraction side ( $B_{ext}$ ) systematically for various heavy ions using the liquid-Helium free superconducting ECR ion source (RAMSES) at RIKEN and SHIVA at the University of Tsukuba.<sup>3-5)</sup> From these experimental results, we recognized that it is important not only to increase the magnetic field strength, but also to optimize the magnetic field configuration to increase the beam intensity. In particular, the minimum magnetic field strength ( $B_{min}$ ) of the magnetic mirror field plays an essential role in increasing the beam intensity. In these experiments, we observed the existence of an optimum value for  $B_{min}$  to maximize the beam intensity, and noted that this value is independent of the charge state of the heavy ions.<sup>3,4)</sup> The optimum value for  $B_{min}$  was 0.47–0.49 T for 18 GHz (RAMSES) and  $\sim 0.39$  T for 14 GHz (SHIVA) for the production of various multicharged heavy ions. We also observed that the magnetic field strength at the beam extraction side ( $B_{ext}$ ) affected the plasma confinement and the beam extraction conditions.<sup>4,5)</sup>

A detailed description of the RIKEN 18 GHz ECR ion source and its present performances is given in Ref. 6. The RIKEN 18 GHz ECR ion source has only two sets of solenoid coils to produce the mirror magnetic field. This means that we cannot control  $B_{min}$  and  $B_{ext}$ , independently. When choosing the optimum value for  $B_{min}$ ,  $B_{ext}$  may not be optimum for the production of Ar ions.

To overcome this problem, with respect to the experimental results described in Ref. 3, we fixed  $B_{min}$  to  $\sim 0.48$  T. Then we moved the plasma electrode position to maximize the extracted beam intensity. Figure 1 a) shows the magnetic field configuration for the

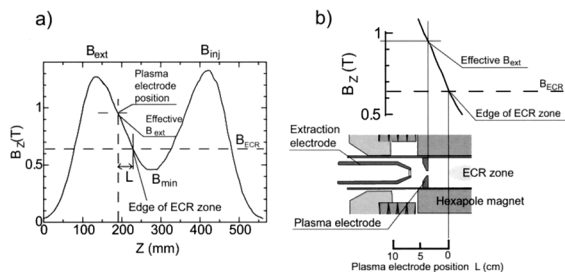


Fig. 1. a) Mirror magnetic field configuration for producing multicharged Ar ion beams; b) Schematic drawing of the plasma chamber around the plasma electrode position. Upper figure shows the magnetic mirror field of this region.

production of multicharged Ar ions. For the plasma confinement, the effective  $B_{ext}$  should not be the maximum magnetic field at the beam extraction side, but the magnetic field at the plasma electrode position shown in Fig. 1 b). This means that the optimum value for the effective  $B_{ext}$  for maximizing the beam intensity is strongly dependent on the plasma electrode position. The plasma electrode position also affects the plasma density at the electrode position<sup>7)</sup> and the beam extraction conditions.

Figure 2 shows the beam intensity of Ar<sup>9+</sup> as a function of plasma electrode position. The extraction voltage was 14 kV. The microwave power was 500 W. The plasma electrode position is defined in Fig. 1 b). The beam intensity gradually increases when moving the plasma electrode toward the ECR zone and then decreases as shown in Fig. 2. It seems that an optimum plasma electrode position exists to maximize the beam intensity of the multicharged Ar ions. Figure 3 shows the optimum plasma electrode position for maximizing

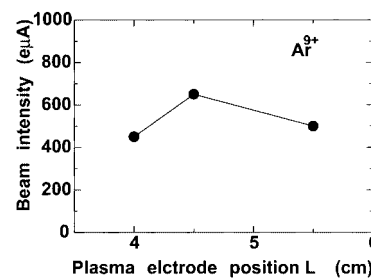


Fig. 2. Beam intensity of Ar<sup>9+</sup> ion as a function of plasma electrode position. The plasma electrode position  $L$  is defined in Fig. 1 b).

<sup>†</sup> Condensed from the article in Nucl. Instrum. Methods Phys. Res. A **510**, 206 (2003)

\* SHI Accelerator Service, Ltd.



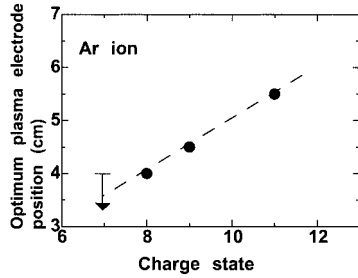


Fig. 3. Optimum plasma electrode position for maximizing the beam intensity as a function of Ar ions.

the beam intensity of different Ar charge state ions. The optimum plasma electrode position moves toward the ECR zone when the charge state becomes lower.

Figure 4 shows the strength of the effective  $B_{ext}$  and  $B_{min}$  for maximizing the beam intensities of Ar ions as a function of the charge state. The effective  $B_{ext}$  becomes higher as the charge state becomes higher. This tendency is the same as that in the experimental results obtained for the SHIVA ECR ion source.<sup>4)</sup> It may be due to the effect of the plasma confinement, which is dependent on the mirror ratio of the axial magnetic field strength.

Figure 5 shows the beam intensity of  $Ar^{8+,9+}$  ions as a function of microwave power. For the production of  $Ar^{8+}$  ions, the gas pressure of the plasma chamber was  $4 \times 10^{-6}$  Torr.  $B_{inj}$ ,  $B_{min}$  and  $B_{ext}$  were 1.4, 0.48 and 1.05 T, respectively. For  $Ar^{9+}$  ion production,

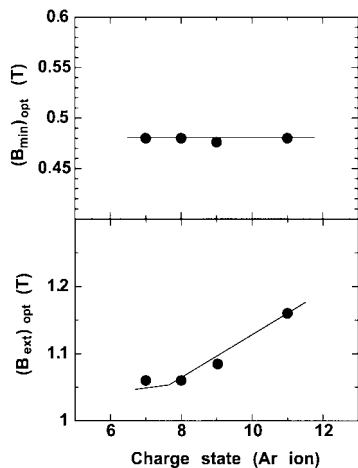


Fig. 4. Optimum  $B_{min}$  and  $B_{ext}$  for production of Ar ions as a function of the charge state of Ar ions.

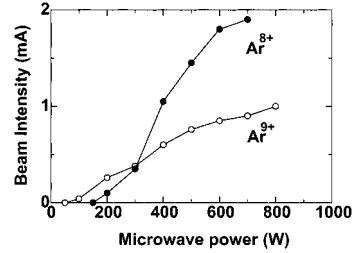


Fig. 5. Beam intensities of  $Ar^{8+,9+}$  ion beams as a function of microwave power. The ion source is tuned at the microwave power of 600 W.

the gas pressure was  $2.2 \times 10^{-6}$  Torr. The extraction voltage was 17 kV. The ion source was tuned at a microwave power of 600 W for both cases. In this experiment, we only changed the microwave power without changing the other parameters (gas pressure, magnetic field strength, extraction voltage and so on). It should be noted that the beam intensities were not saturated at the highest microwave power of 700 W in this experiment. This suggests that we would obtain a higher beam current at a higher microwave power. We successfully extracted 1.9 mA of  $Ar^{8+}$  and 1 mA of  $Ar^{9+}$  at 700–800 W microwave power. Before tuning  $B_{min}$ ,  $B_{ext}$  and the plasma electrode position, we obtained only 1 mA of  $Ar^{8+}$  at the microwave power of 500–600 W.<sup>6)</sup>

We successfully increased the beam intensity of  $Ar^{8+,9+}$  ions by optimizing  $B_{min}$ ,  $B_{ext}$  and the plasma electrode position. The beam intensity is strongly dependent on  $B_{ext}$  and the plasma electrode position. The optimum plasma electrode position moves toward the ECR zone when the charge state becomes lower. The optimum value of  $B_{ext}$  increases when the charge state becomes higher. The maximum extracted beam intensities for  $Ar^{8+,9+}$  ions were 1.9 and 1 mA at 17 kV extraction and the microwave power of 700–800 W, respectively.

#### References

- 1) Y. Yano: Indian J. Phys. **76S**, 1 (2002).
- 2) D. Hitz et al.: Rev. Sci. Instrum. **73**, 509 (2002).
- 3) H. Arai et al.: Nucl. Instrum. Methods Phys. Res. A **491**, 9 (2002).
- 4) T. Kurita et al.: Nucl. Instrum. Methods Phys. Res. B **192**, 429 (2002).
- 5) M. Imanaka et al.: Jpn. J. Appl. Phys. **41**, 3926 (2002).
- 6) Y. Higurashi et al.: Rev. Sci. Instrum. **73**, 598 (2002).
- 7) T. Nakagawa et al.: Jpn. J. Appl. Phys. **35**, 4077 (1996).

## Emittance measurement for intense beam of heavy-ions from RIKEN 18 GHz ECRIS<sup>†</sup>

Y. Higurashi, T. Nakagawa, M. Kidera, T. Aihara,\* M. Kase, and Y. Yano

Over the last decade, ECR ion sources (ECRIS) have been widely used as external ion sources for heavy-ion accelerators. In particular, ECRISs have become one of the key devices for the production of radio isotope beams (RI beams). Since the mid-1990s, RIKEN has undertaken the construction of a new accelerator complex for the RIKEN radioisotope beam factory (RIBF) project.<sup>1)</sup> In this project, the production of intense heavy-ion beams is an important factor in the generation of intense RI beams using projectile-like fragmentation. For these reasons, we tried to increase the beam intensity of medium charge-state, heavy-ions, such as  $\text{Ar}^{8+}$ ,  $\text{Kr}^{13+}$  and  $\text{Xe}^{20+}$ , for the RIKEN RIBF project. The final goal of this project was to produce at least  $1 \mu\text{A}$  on target from the p to U beams. To meet this requirement, we had to further develop the performance of the ECRIS. To increase the beam intensity from the accelerator, it is evident that the emittance is also an important physical value for the ECRIS. The emittance of the intense beam, *e.g.*,  $2 \text{ emA}$  of  $\text{Ar}^{8+}$ , should be enlarged by the space charge effect. To investigate this effect on the emittance and optimize the transmission coefficient of heavy-ion beams from the RIKEN 18 GHz ECRIS to the heavy-ion linac, we measured the emittance of the intense beam under various conditions.

A detailed description of the RIKEN 18 GHz ECR ion source and present performances are described in Ref. 2. A single 18 GHz, 1.5 kW klystron supplies microwave power to the source. The axial confinement of the plasma is obtained by two solenoid coils, which provide a magnetic mirror field. The maximum power consumption is 140 kW. The mirror ratio has a nominal value of  $\sim 3.0$  with  $B_{max} \sim 1.4 \text{ T}$ . The field strength at the surface of the hexapole magnets is approximately 1.4 T. Figure 1 shows a schematic drawing of the extraction system. The diameter of the plasma electrode hole and extraction puller are 10 and 16 mm, respectively. The distance between the two electrodes used ranges from 15 to 30 mm. The typical extraction voltage is from 10 to 20 kV. The typical beam intensity produced from RIKEN 18 GHz ECRIS is shown in Fig. 2. We successfully produced intense beams of heavy-ions. For example, the beam intensities of  $\text{Ar}^{8+}$ ,<sup>3)</sup>  $\text{Kr}^{13+}$  and  $\text{Xe}^{20+}$  are 2.0 emA, 0.6 emA and 0.3 emA, respectively.

Figure 3 shows a schematic drawing of the experimental setup for measurement of the beam emittance. As shown in this figure, we used a movable slit (defin-

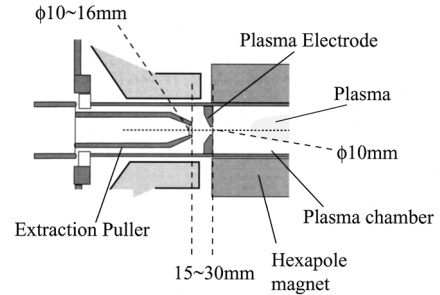


Fig. 1. Schematic drawing of the extraction system of the RIKEN 18 GHz ECRIS.

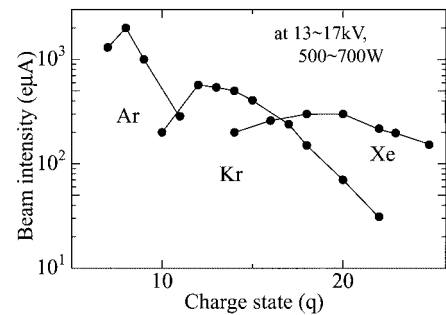


Fig. 2. Beam intensity of the Ar, Kr and Xe ions produced from the RIKEN 18 GHz ECRIS.

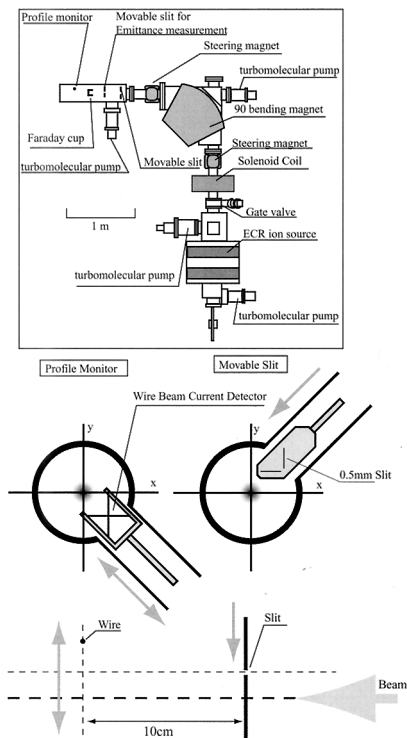


Fig. 3. Schematic drawing of the beam analyzing and profiling system for the RIKEN 18 GHz ECRIS.

<sup>†</sup> Condensed from the article in Rev. Sci. Instrum., in press  
\* SHI Accelerator Service, Ltd.

ing the beam position) and a movable thin wire (measurement of the beam position and intensity). The distance between the slit and the wire is 10 cm. We also installed a solenoid coil between the ion source and analyzing magnet for focusing the intense beam. Figure 4 shows the typical beam emittance ( $y$ - $y'$ ) of  $\text{Ar}^{11+}$  ions at an extraction voltage of 13 kV and an RF power of 510 W. The extracted current (the current of extraction voltage power supply) and beam current (the current of the faraday cup after the bending magnet) of  $\text{Ar}^{11+}$  ions were 4.1 mA and  $170 \text{ e}\mu\text{A}$ , respectively.

The ion beam emittance measurements in both the horizontal and vertical planes were performed for a wide mass range of ions. Figure 5 shows the normalized 99% emittance of the  $\text{Ar}^{8+}$  ions beam as a function of the extracted current of the ion source. It is clearly seen that the beam emittance gradually in-

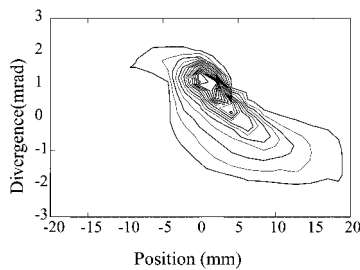


Fig. 4. Typical beam emittance ( $y$ - $y'$ ) of  $\text{Ar}^{11+}$  ions at an extraction voltage of 13 kV and an RF power of 510 W. The extracted current and beam current of  $\text{Ar}^{11+}$  ions were 4.1 mA and  $170 \text{ e}\mu\text{A}$ .

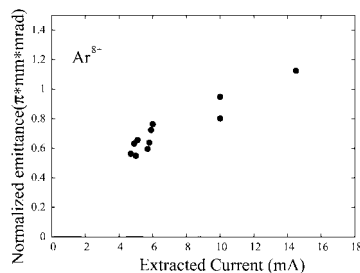


Fig. 5. Normalized beam emittance (99%) of  $\text{Ar}^{8+}$  ions as a function of extracted current.

creases from 0.5 to  $1.1 \pi\text{mm}\cdot\text{mrad}$ , with increasing extracted current from few mA to 14.5 mA. At a lower extracted current (3–4 mA), 90% of the  $\text{Ar}^{8+}$  beam could be accepted and accelerated by the RFQ linac at an extraction voltage of 20 kV. At the highest extracted current (14.5 mA), we obtained 1.5 e mA of the  $\text{Ar}^{8+}$  beam from the ion source at 17 kV extraction voltage. In this case, the beam emittance of  $\text{Ar}^{8+}$  was  $420 \pi\text{mm}\cdot\text{mrad}$  (unnormalized 99% emittance), which is very large compared to the acceptance of the RFQ linac ( $150 \pi\text{mm}\cdot\text{mrad}$ ). In order to accelerate the full beam of 1.5 e mA  $\text{Ar}^{8+}$  by RIKEN RFQ linac, we surely need the extraction voltage of higher than 60 kV.

At lower extracted current, the emittance was almost independent on it. For example, the emittance of  $\text{Xe}^{20+}$  ions were 0.47,  $0.45 \pi\text{mm}\cdot\text{mrad}$  for the extracted current of 3.5 and 1.5 mA, respectively. The voltage of the extraction was 13.2 kV for both cases. It may suggest that such low extracted currents ( $\leq 3 \text{ mA}$ ) do not affect the emittance very much.

We also measured the beam emittance of  $\text{Ta}^{20+}$  ions using the insertion method. The normalized beam emittance of the  $\text{Ta}^{20+}$  ions was  $0.85 \pi\text{mm}\cdot\text{mrad}$  at the extraction voltage of 14 kV, which is very large compared with the Xe ions at almost the same extracted current ( $\sim 2.9 \text{ mA}$ ). It is almost twice as large as that of  $\text{Xe}^{20+}$  (the normalized beam emittance of  $\text{Xe}^{20+}$  ions was  $0.47 \pi\text{mm}\cdot\text{mrad}$ ). Usually, we have to insert the Ta rod into the plasma deeply to produce Ta ions. because the melting point of Ta is very high ( $\sim 2800^\circ\text{C}$ ). Consequently the plasma and beam intensity become unstable. This instability may cause a large emittance of the Ta beam. To understand the effect of the instability of the plasma on the beam emittance, we need a systematic experiment for measurements of the plasma instability (or stability of beam) and beam emittance simultaneously.

#### References

- 1) Y. Yano: Proc. 15th Int. Conf. on Cyclotron and Their Applications, Caen, France, 1998-6 (IOP, Bristol, 1999), p. 696.
- 2) T. Nakagawa and Y. Yano: Rev. Sci. Instrum. **71**, 637 (2000).
- 3) Y. Higurashi, T. Nakagawa, M. Kidera, T. Aihara, M. Kase, and Y. Yano: Nucl. Instrum. Methods Phys. Res. A, in press.

## Control system for a Hyper ECR ion source

Y. Ohshiro,\* S. Watanabe,\* S. Yamaka,\* and T. Katayama

In 1999, a Hyper ECR ion source was moved from Tanashi to the RIKEN AVF cyclotron. The Hyper ECR ion source and a 10 GHz ECR ion source have been operated to deliver the beams of gaseous<sup>1)</sup> and metallic ions<sup>2)</sup> alternatively. The 10 GHz ion source has been operated under an RARF control system. This control system provides a sequence control system and a PC-based graphical remote control panel.

To facilitate the alternative operations of the two ion sources, we improved the control system of the Hyper ECR ion source because it was operated under a manual control system. A schematic of the new control system is illustrated in Fig. 1. As shown in Fig. 1, the

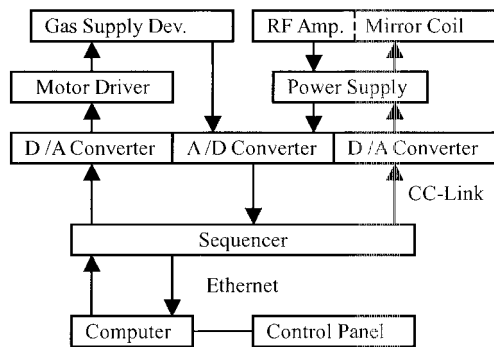


Fig. 1. Schematic of the remote control system.

standard voltages of the gas supply device, the power supply of the RF amplifier, and the exciting current source of the mirror coil are controlled by a pair of analog digital (A/D) and digital analog (D/A) converters regulated by the computer and sequencer.<sup>3)</sup>

A photograph of the control panel is shown in Fig. 2. The output ranges of power supplies covered by this control system are tabulated in Table 1. The main parameters such as the electric current and voltage of the power supply can be set on the graphical control panel. The control panel enables us the speedy operation of the Hyper ECR ion source in the manner similar to the 10 GHz ECR ion source.

To achieve interlocking between measuring devices such as a thermometer, cutoff relay of cooling water, vacuum gauge, power supply, and vacuum pumping system, a touch panel (GOT) system is introduced in

Table 1. Output ranges of power supplies.

Power supply name	Covering range
Mirror coil	0 ~ 600 A
RF amplifier	0 ~ 2 kW
Extraction electrode	0 ~ 50 kV
Einzel lens	0 ~ 20 kV
Quadrupole magnet	0 ~ 20 A
Analyzing magnet	0 ~ 200 A

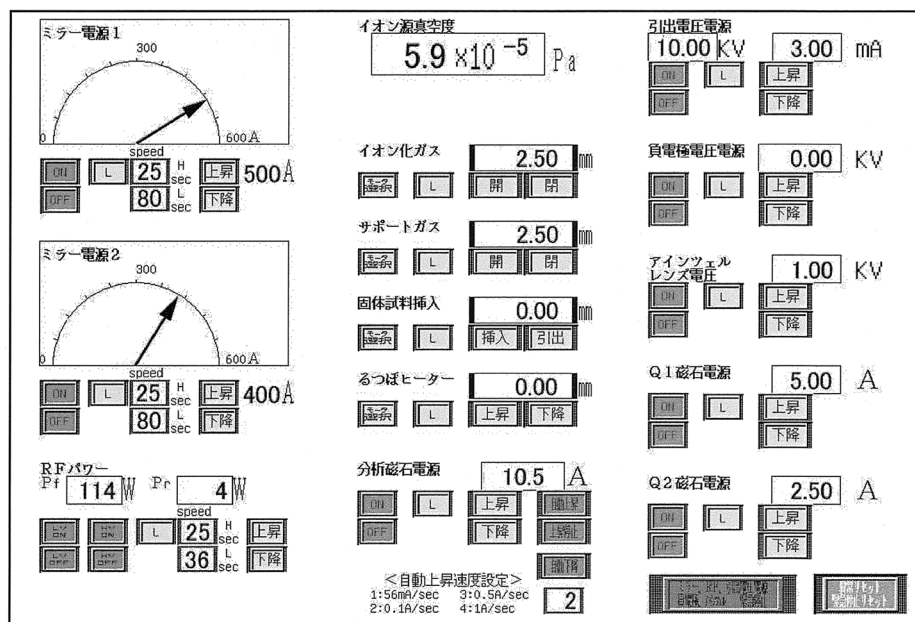


Fig. 2. Photograph of the control panel. (in Japanese)

\* Center for Nuclear Study, Graduate School of Science, University of Tokyo

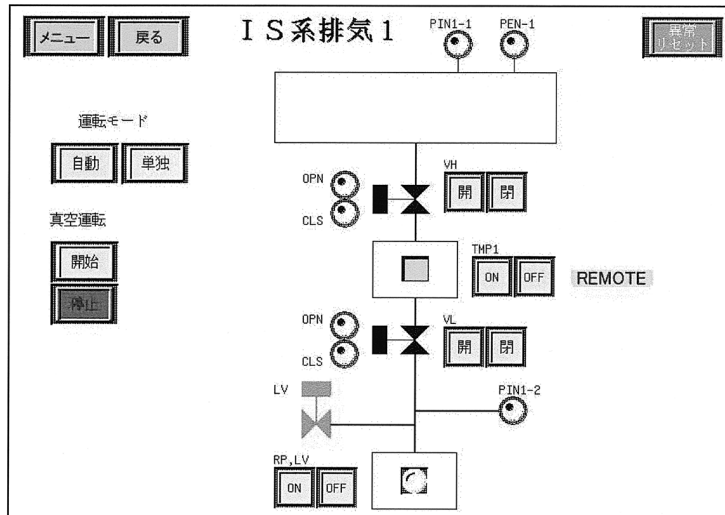


Fig. 3. Display of the touch panel. (in Japanese)

the Hyper ECR ion source. This GOT system is independent of the remote control system as shown in Fig. 1. Figure 3 shows the panel configuration with a display of a vacuum operating system. It can be operated automatically under good interlock conditions.

In 2002, we completed the installation of a remote/local control system for the Hyper ECR ion source. It enables the integration of all operating procedures of the Hyper ECR ion source. We have been able to speed up the operation with this system. Then, the

ion source as well as the 10 GHz ECR ion source has been routinely used for the delivery of multicharged ion beams to the AVF cyclotron.

#### References

- 1) Y. Ohshiro et al.: RIKEN Accel. Prog. Rep. **36**, 279 (2003).
- 2) T. Teranishi et al.: CNS Annu. Rep. **2001**, 7 (2002).
- 3) FX1s hardware manual, MITSUBISHI MELSEC-F.

## Improvement of power supplies for RARF beam transport magnets

M. Nagase, N. Fukunishi, E. Ikezawa, M. Kase, and Y. Yano

Power supplies for the bending magnets in the RIKEN Accelerator Research Facility (RARF) were fabricated in 1988 and had been in operation without any serious trouble. However, unstable behavior has sometimes arisen in recent years due to deterioration of circuit elements. In addition, stability of the output currents is becoming increasingly important, because recent unique experiments<sup>1)</sup> require beams with very high precision, *e.g.*, a parallel beam with an angular divergence less than 10 microradians. Output-current stability during an experimental program is crucial for such high-precision experiments. A sizable change of beam direction (100 microradians per day) was detected during an ion-channeling experiment. We hence measured the long-time stability of the output currents and found that the instabilities of several power supplies were greater than 100 ppm per 8 hours, which is the designed value.

Our detailed analysis revealed that the feedback control systems used to generate the constant output current encountered some trouble. The original feedback control system is illustrated in Fig. 1. The output current is detected by the shunt resistor. The temperature dependence of the shunt resistor is less than 10 ppm per Kelvin and the shunt resistor is directly cooled by water ( $35 \pm 1^\circ\text{C}$ ) controlled by a water chiller. The shunt resistor and related elements are put in the water, and their corrosion leads to the deterioration of characteristics. On the other hand, DAC and DC amplifier are contained in a box and heated using a thermostat oven. The average temperature in the box was designed to be  $45^\circ\text{C}$ . However, surface temperatures of several elements were found to be nearly  $70^\circ\text{C}$ . The heat had also significantly damaged several elements,

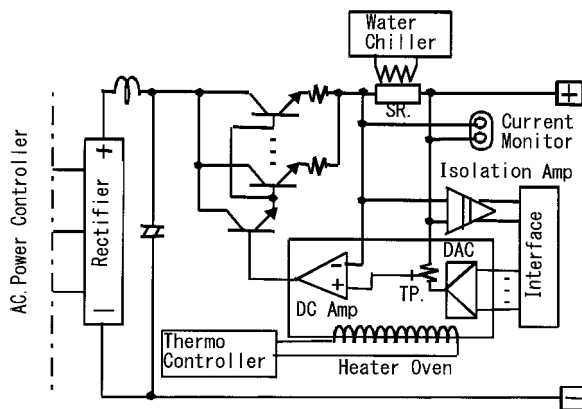


Fig. 1. Schematic diagram of feedback control system of the power supplies before modification. Trimmer potentiometer is abbreviated TP.

particularly chemical condensers and trimmer potentiometers. To solve the problems mentioned here, we decided to adopt a DC current transformer (DCCT) and a Peltier cooler, as shown in Fig. 2. The shunt resistor is replaced by the DCCT, which does not require cooling water and is free from the corrosion problem. The Peltier cooler holds the temperature of the DAC and the DC amplifier at  $25^\circ\text{C}$ . It is sufficiently low to avoid the heat-damage problem.

Modification of power supplies was performed by IDX Corporation during the routine maintenance period this summer. The fourteen power supplies listed in Table 1 were modified. The DCCT and the Peltier cooler were set on top of the power supply. The DCCTs used here are products of HITEC,<sup>2)</sup> and their specifications are listed in Table 2. Note that the temperature dependence of the total feedback control system is determined not only by the temperature dependence of the output current of the DCCT ( $< 0.15$  ppm/K), but also by that of the burden resistor monitoring the output current of the DCCT. The temperature dependence of the burden resistor is 5 ppm/K, hence we include it also in the thermostat chamber.

Because our modifications also changed the circuit constants, careful tuning was required, particularly to suppress hunching oscillations of output currents. The total cost of the present modifications is roughly the same as that to purchase two new power supplies.

The modified power supplies show sufficient long-time stability as shown in Fig. 3. The stability was better than 10 ppm per 8 hours for all the modified power supplies even when room temperature changed from  $28^\circ\text{C}$  to  $25^\circ\text{C}$  during the measurement. The measured stability corresponds to one-tenth the original value. There are two additional merits. First, the wa-

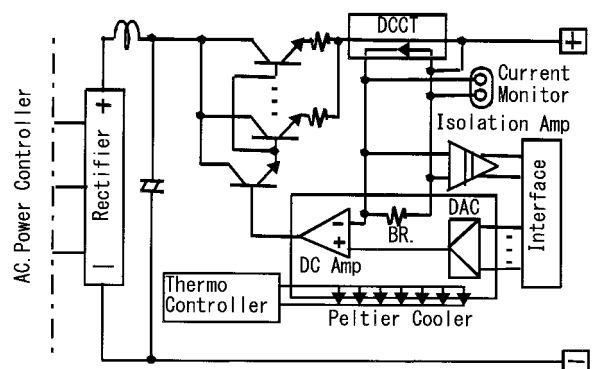


Fig. 2. Schematic diagram of feedback control system of the power supplies after modification. The abbreviation 'BR' indicates a burden resistor.

Table 1. List of power supplies modified in the present work. Under the “Type” column, SR and TR indicate saturable reactor and transistor type, respectively. Values of stability listed here are designed values before modification.

Power supply	Maximum current (A)	Maximum voltage (V)	Stability (ppm / 8H)	Resolution	Type
GARIS-D	600	160	100	<1%	SR+TR
A-DM2	600	60	100	16bit	SR+TR
A-DM3	200	60	100	16bit	SR+TR
I-D1	110	18	100	16bit	TR
I-D2	105	14	100	16bit	TR
C-DM1	400	50	100	16bit	SR+TR
C-DM3	400	50	100	16bit	SR+TR
C-DM4	400	50	100	16bit	SR+TR
C-DM5	400	60	100	16bit	SR+TR
C-DM7	300	90	100	16bit	SR+TR
C-DM8	300	90	100	16bit	SR+TR
C-DM9	300	90	100	16bit	SR+TR
C-DM10	300	60	100	16bit	SR+TR
C-DM11	300	60	100	16bit	SR+TR

Table 2. Specifications of DCCT used in the present modification.

System		MACC <sup>plus</sup>
Type		600 A
Primary Circuit	rated current (bipolar)	600 A
	permissible overcurrent (10s)	160 %
	short-circuit current (0.1s)	500 %
Output Circuit	rated output current / voltage	0.6 A
	output impedance	> 10 M $\Omega$
	output slew rate	> 200 A/ms
	small signal bandwidth (< 5% signal)	250 kHz
	RMS value of output noise (0~10 Hz)	< 0.5 ppm
	RMS value of output noise (0~10 kHz)	< 1 ppm
DC accuracy (offset error)	-initial (at 25°C)	< 8 ppm
	-versus temperature	< 0.15 ppm/K
	-versus time	< 4 ppm/yr

ter chiller that requires routine maintenance becomes unnecessary. Secondly, power consumption was reduced by 6 kW because the shunt resistors were no longer used.

The remaining power supplies in RARF are also old-fashioned and will suffer from the aging problem. Our

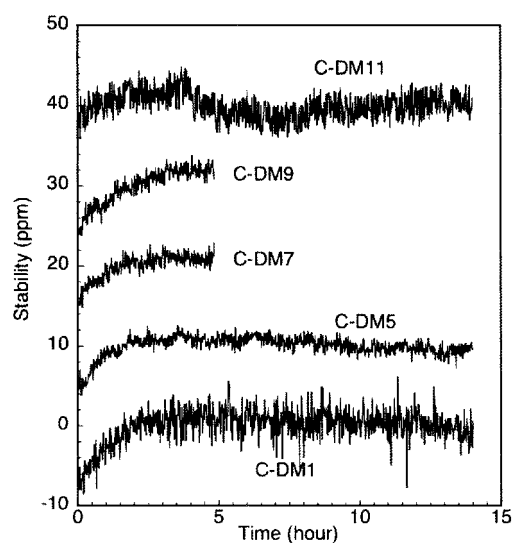


Fig. 3. Stability of power supplies modified here.

present success is a good example of improving the long-time stability of old-fashioned power supplies at reasonable cost.

#### References

- 1) Y. Nakai et al.: RIKEN Accel. Prog. Rep. **36**, 96 (2003); Nucl. Instrum. Methods Phys. Res. B **205**, 784 (2003).
- 2) MACC<sup>plus</sup>: <http://www.ppm.co.uk/HITEC37.htm>

## Design of vacuum pumping unit for RIBF beam transport lines

S. Yokouchi, M. Fujimaki, M. Hemmi, H. Isshiki,\* M. Nishida,\* K. Oyamada,\* and M. Kase

The vacuum pumping unit (VPU) for the RIBF beam transport (BT) lines has been developed. The VPU is composed of a turbomolecular pump (TMP), pneumatically driven gate valves, vacuum gauges, a local controller, and other vacuum components, and is connected to the beam diagnostic chamber of the BT line in sections that are divided by  $\phi 63$  mm gate valves (GV1, GV2) (see Figs. 1 and 2).

We selected a TMP fitted with grease-lubricated ball bearings, which has net pumping speed of 210 L/s for  $N_2$ . The TMP is designed to be connected to the beam diagnostic chamber at an installation angle of  $45^\circ$ , as shown in Fig. 2, since the grease-lubrication-type TMP can be operated in any orientation. If the TMP is connected to the bottom of the chamber (vertical attitude), the maintenance of the TMP would be very inconvenient because of the limited space, and if the TMP is connected to the side or top of the chamber (horizontal or upright attitude), it would be very difficult to carry out the alignment of BT line because the

TMP would interfere with the sighting of marks on the chamber.

The TMP is designed to be connected close to the beam diagnostic chamber *via* a  $\phi 100$  mm gate valve (VH) so that the effective pumping speed at the chamber is more than 150 L/s. For example, if an aluminum alloy beam duct of  $\phi 62$  mm  $\times$  10 m, whose outgassing rate after 100 hours of pumping is estimated to be about  $1 \times 10^{-7}$  Pam<sup>3</sup>/s/m<sup>2</sup>,<sup>1)</sup> is evacuated by this TMP, the average pressure along this duct is calculated to be less than  $7 \times 10^{-6}$  Pa. In practice, the gas load of the chamber and diagnostic devices, which are under development, must also be considered. Even if the gas load is five times as much as that of this duct, the increase in pressure due to it is about  $6 \times 10^{-6}$  Pa at most, and therefore the actual average pressure along this duct is expected to be less than  $2 \times 10^{-5}$  Pa. For this pressure range, the beam transmission in a BT line is expected to be more than 99%, assuming a cross section of  $1 \times 10^{-16}$  cm<sup>2</sup> and a beam path length of 100 m.

A set of one cold cathode gauge (PE1) and two Pirani gauges (PI1, PI2) is employed for the VPU in consideration of reliability and durability. By using these gauges, various signals of vacuum pressure for monitoring and interlocking are transmitted to the local controller and/or the control system.

Each VPU has a local controller for itself. Every component of the VPU can be locally operated and monitored at the controller according to sequence programs. Furthermore, both operation and monitoring of VPU components can be carried out remotely from the control console *via* an N-DIM interface card.<sup>2)</sup> The controller of one VPU is hard-wired with that of the adjacent VPU's to interchange the vacuum conditions for the operation of the GV1 (GV2).

We constructed a test bench of the VPU (see Fig. 2). The programs of the local controller were checked using this test bench. The vacuum chamber in Fig. 2, which was developed for the aluminum alloy beam diagnostic chamber for BT lines, involves two important techniques. One is precise electron beam (EB) welding of aluminum alloy, and the other is hardening of the seal surface of a knife edge flange made of aluminum alloy by melting copper into the base material with the EB. For the former, an accuracy within 0.2 mm was obtained in this work. The latter is being tested for evaluation.

### References

- 1) S. Yokouchi et al.: Proc. EPAC '90 (1990), p. 1332.
- 2) M. Fujimaki et al.: RIKEN Accel. Prog. Rep. 37, 279 (2004).

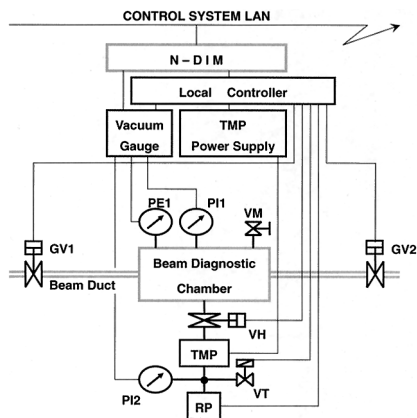


Fig. 1. Typical configuration of the VPU for BT lines.

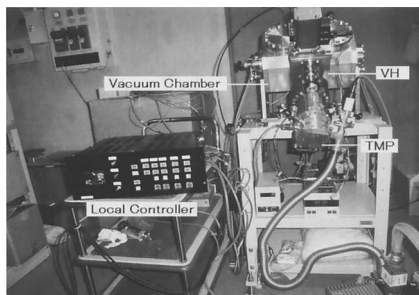


Fig. 2. Photograph of VPU test bench equipped with all VPU components except GV1 and GV2.

\* SHI Accelerator Service, Ltd.



## Longitudinal emittance measurement of the RRC beam

R. Taki,<sup>\*1</sup> H. Okamura,<sup>\*2</sup> N. Sakamoto, N. Fukunishi, H. Ryuto, K. Sekiguchi, and A. Goto

The correlation between kinetic energy and time spreads, *i.e.*, the longitudinal emittance, which is indispensable information for the operation of the RIBF, has been measured for the 3800-MeV <sup>40</sup>Ar beam from the RIKEN Ring Cyclotron (RRC). Because of the sinusoidal radio frequency (RF) field, the correlation is expected to have a quadratic form,  $T(\phi) = T_0 \cos \phi \simeq T_0(1 - \phi^2/2)$ , where  $\phi = 2\pi f_{\text{RF}} t$ . To cover the wide range of acceleration phase, the measurements were made by displacing the injection phase relative to the RF,  $\Delta\phi_{\text{inj}}$ , from  $-6^\circ$  to  $+4^\circ$  at a step of  $2^\circ$  (198 ps for  $f_{\text{RF}} = 28.1$  MHz). Also, the effect of phase compression in the RRC was observed. A radially increasing voltage distribution of the RF compresses the beam bunch size.<sup>1)</sup> The effect is formulated as  $\Delta\phi_{\text{ext}} = \Delta\phi_{\text{inj}} V_{\text{inj}}/V_{\text{ext}}$  and  $V_{\text{inj}}/V_{\text{ext}} = 1.6$  for the present experiment.

The experiment was carried out in the E4 experimental area using the magnetic spectrometer SMART.<sup>2)</sup> The beam accelerated by the AVF cyclotron and the RRC was transported to the scattering chamber. Particles were elastically scattered by a 25  $\mu\text{m}$  gold target, collimated at  $\theta = 2^\circ$  with an angular acceptance of 12 mrad, momentum-analyzed by the SMART and detected at the second focal plane by two plastic scintillation counters followed by a silicon position-sensitive detector (Si-PSD). The position resolution of Si-PSD was 1 mm and the time resolution of a pair of plastic scintillators was 100 ps (FWHM). Since the momentum dispersion of the SMART is  $-77$  mm/%, the relative energy resolution is estimated to be  $2.5 \times 10^{-4}$ . Energy spreads from energy-loss straggling in the target and kinematical broadening by the angular acceptance are negligibly small. The momentum dependence of time-of-flight from the RRC to the detector was corrected according to  $\delta t/t_0 = [-\gamma^{-2} + (\partial L/L_0)/(\partial p/p_0)] \delta p/p_0$ , where  $L_0 = 89.5$  m.  $\partial L/(\partial p/p_0)$  was determined to be  $-355$  mm/% so that the shift of time spectrum is proportional to the shift of injection time.

Figure 1 shows the result of longitudinal emittance. The quadratic correlation is clearly seen, but smeared by a fairly large spread of distribution. Particularly, the time spread, 700 ps (FWHM), is much larger than expected from both the detector resolution and acceleration mechanism. Its origin must be further studied.

The extraction phase with respect to the RF,  $\Delta\phi_{\text{ext}}$ , has been deduced from the centroid of the projected time spectra. The difference,  $\Delta\phi_{\text{ext}} - \Delta\phi_{\text{inj}}$ , is plotted as a function of  $\Delta\phi_{\text{inj}}$  in Fig. 2. The data approxi-

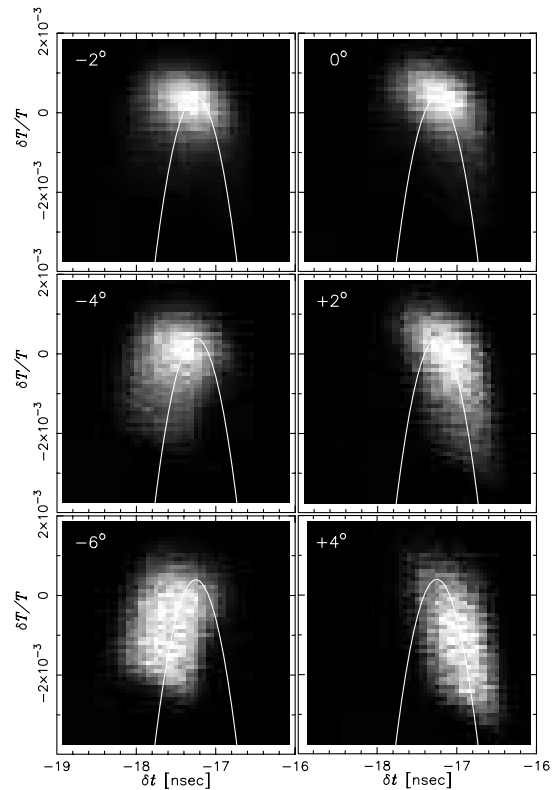


Fig. 1. Longitudinal emittance for various injection phases. The parabolic curve represents the RF.

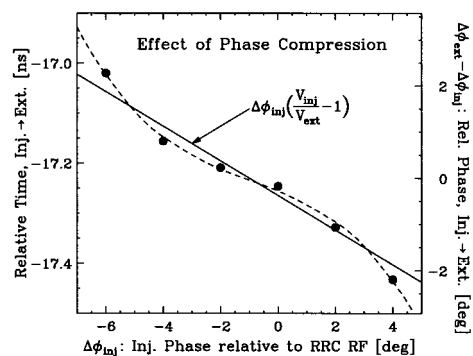


Fig. 2. Shift of time spectra relative to the injection ( $\Delta\phi_{\text{ext}} - \Delta\phi_{\text{inj}}$ ) plotted as a function of the shift of injection ( $\Delta\phi_{\text{inj}}$ ).

mately lie on a straight line expected from the phase compression effect, but the deviation indicates a higher order effect, the origin of which is a future problem.

### References

- 1) W. Joho: Part. Accel. **6**, 41 (1974).
- 2) T. Ichihara et al.: Nucl. Phys. A **569**, 287c (1994).

<sup>\*1</sup> Department of Physics and Astronomy, Michigan State University, USA

<sup>\*2</sup> Cyclotron and Radioisotope Center, Tohoku University

## Expansion of the control system for RARF

M. Kobayashi-Komiyama, I. Yokoyama, M. Fujimaki, J. Odagiri,\* T. Tanabe, and M. Kase

The basic operations of the RIKEN Accelerator Research Facility (RARF) are currently carried out by using the Experimental Physics and Industrial Control System (EPICS)<sup>1)</sup> without any serious problems.<sup>2)</sup> For more stable beam operation and system expansion gazing at the RIKEN radioisotope (RI) Beam Factory (RIBF) control, we carried out two important improvements of the EPICS control system last summer.

The first one is the EPICS upgrade. We replaced the EPICS base programs running on the server computer from R3.13.1 to R3.13.8. The reason why we selected EPICS base R3.13.8 was that it was the latest and most stable version at that time. By this upgrade, we can expect more stable beam operation. This was our first experience at renewing the base programs since we started using EPICS in our control system approximately four years ago. When we renewed the server computer about two years ago, we copied only the binary codes of the base programs from the old server computer and installed them on the new server computer. Unfortunately, it caused one problem, which was just the reason for last summer's EPICS upgrade. The problem is that we could not install recent application programs supported by the EPICS community in our system. The reason for this problem was considered to be due to some kind of mismatch between the old base programs and new application programs. By compiling the base programs on the server computer from scratch, we could add new functions to our con-


trol system. For example, we could install a timestamp record in our applications, which has made it very convenient to record a history of beam operation by using graphs and GUIs.

The second improvement is the system expansion. For the control of RIBF components, it was decided to introduce two types of Ethernet-based control interfaces into the EPICS control system. One is Programmable Logic Controller (PLC), which controls the RF system of cyclotrons and so on. The other one is Network-Device Interface Module (N-DIM), which is our original control device, developed to substitute for the CAMAC-CIM/DIM system.<sup>3)</sup> As shown in Table 1, N-DIM will be used for various purposes in the RIBF control system; to control all beam diagnostic equipment, all vacuum systems, the driving system for deflectors and so on. Furthermore, it is also planned to replace the CAMAC-CIM/DIM in the RARF with N-DIM gradually. Thus, we need to develop an N-DIM driver software to control them in EPICS.


We started to investigate how to develop the EPICS driver software for N-DIM in the summer of last year. We have already developed the EPICS driver software to control the OMRON PLC, CS1 last year and we have obtained data from them by using it. Thus, it is expected that it will not be difficult to develop driver software for N-DIM because it is a network controller as well as CS1. However, it is not a good idea to develop the driver software for N-DIM by the same

Table 1. Interface devices in RARF/RIBF.

	RARF			RIBF						
	RILAC	AVF/RRC	BT (existing)	fRC	BT (in Nishina)	BT in new building	IRC	SRC	Injection Line for Big-RIPS	Big-RIPS
Ion Source	Hard wire /WE 7000 (Yokogawa)	WE 7000 (Yokogawa)								
RF	PLC (Omron)	PLC (Sharp)	DIM	PLC (Omron)	not fixed	not fixed	PLC (Omron)	PLC (Omron)		
Magnet Power Supply	GP-IB/NIO/DIM	DIM	DIM/NIO*	DIM/NIO	NIO/DIM	NIO	NIO	NIO	NIO	NIO
Beam Diagnostics	DIM/N-DIM	DIM	DIM	N-DIM/DIM	N-DIM	N-DIM	N-DIM	N-DIM	N-DIM	not fixed
Driving Controller	DIM	DIM	DIM	N-DIM/DIM	N-DIM	N-DIM	PLC (Omron) /N-DIM	PLC (Mitsubishi) /N-DIM	not fixed	not fixed
Vacuum	N-DIM	PLC (Omron)	DIM	Local only	N-DIM	N-DIM	PLC (Omron)	PLC (Mitsubishi)	N-DIM	not fixed
Beam Interlock	Hard wire /PLC (Mitsubishi)	DIM	DIM	not fixed	not fixed	PLC (Mitsubishi)				
Cooling	Local only	Local only	Local Only	Local only	Local only	PLC (Mitsubishi)				

 : controlled by the existing EPICS system

\* NIO : Network-I/O (NDS)

 : will be controlled by the expanded existing EPICS system

\* High Energy Accelerator Research Organization (KEK)

method as that for CS1 because our method does not have the framework of EPICS for asynchronous I/O transactions. It is better to have an asynchronous driver for N-DIM because of the wait of a few moments to receive data from a beam diagnostic device. In other words, it is not a good idea to wait for a few moments in one task because it stops the flow of all tasks in Input Output Controller (IOC) during data acquisition. Thus, we decided to develop the driver software that has an asynchronous framework from scratch.

We developed a set of device/driver support modules for the EPICS to support N-DIM with the KEK control group. They also have an original controller based on Ethernet and the timing was matched for development of their driver software and for our requirements. Furthermore, we had a common requirement to control some kinds of PLCs as well as our original Ethernet-based controllers. We considered that it is essential that the drivers share as much of their codes as possible with sufficient flexibility for adapting to various proprietary communication protocols. Finally, the software consists of a common driver module, a common device support module, and a device-specific module for each of the devices to be supported. The common driver module encapsulates the details of the programming for communication over the network. The common device support module encapsulates the details of the framework of EPICS for asynchronous I/O transactions. We decided to implement the common modules in such a manner that the device specific modules can be implemented by using only standard UNIX libraries. As a result, it turned out that the developed device specific modules were compliant with both EPICS R3.13 on VxWorks and R3.14 on Linux.<sup>4)</sup> We started to develop driver software for Yokogawa PLC, FA-M3 at first because a large amount of FA-M3 would be used in the J-PARC project and we had an FA-M3 using for a test.

The development of the driver software was completed last summer. As for N-DIM, the device-specific module was developed from scratch, since it adopts the ASCII code, which was not used in any other software. It is confirmed that N-DIM operates in both the EPICS R3.13 on VxWorks and R3.14 on Linux environments. For R/D of the system, we newly introduced EPICS R3.14.1 on a Linux PC (Redhat 8) into the EPICS control system last summer to control nine N-DIMs installed in the new vacuum system in RILAC. The remarkable feature of the EPICS R3.14 on Linux PC system is that the Linux PC functions both as an operator interface and IOC in a control system, thus we can construct an EPICS control system solely by using it instead of a server computer and VxWorks on a VME computer. Therefore, we can de-

velop the N-DIM control system independently from the current control system of RARF. It was a significant advantage for us. In the current status, though some drawbacks of N-DIM itself were pointed out; no communication problems occurred under the condition that all N-DIMs scan all their digital and analog input (DI/AI) ports every 0.1 second. On the other hand, the Linux server PC also controls PLCs. There is a switch box controlled by FA-M3, and the new RF system in RILAC controlled by Omron PLC, CS1. The software for the CS1 was prepared very easily by using that for FA-M3 as a template.

In the RIBF, more than one hundred N-DIMs will be used to control the accelerator components. There are two candidate server computers in the current status, the HP-UX server and Linux server. Advantages and disadvantages of both systems are as follows;

Advantage of HP-UX server with EPICS R.3.13.8:

- Easy. Solely the adding of another VME to the existing control network enables the system extension.

Disadvantage of HP-UX server with EPICS R.3.13.8:

- When we add a new VME into the system, the license cost of the VxWorks is very high.

Advantage of Linux server with EPICS R.3.14.1:

- Cost-effective.
- It can be constructed independently from the current HP-UX system. In other words, multiple control networks divided into control blocks can exist in the system independently.

Disadvantage of Linux server with EPICS R.3.14.1:

- Difficult to maintain due to the high frequency of upgradation of its kernel version.

We have to select the server carefully by considering its functions, stability and future maintenance. We will examine the performance of both systems and choose the server machine for N-DIMs and PLCs in the near future.

#### References

- 1) <http://www.aps.anl.gov/epics/>
- 2) M. Kobayashi-Komiyama et al.: RIKEN Accel. Prog. Rep. **36**, 281 (2002).
- 3) M. Fujimaki et al.: RIKEN Accel. Prog. Rep. **37**, 279 (2004).
- 4) J. Odagiri et al.: Proc. 9th Int. Conf. on Accelerator and Large Experimental Physics Control System (ICALPECS 2003), Gyeongju, Korea, 2003-10, in printing.

## N-DIM as controller of devices for beam transport

M. Fujimaki, M. Kobayashi-Komiyama, I. Yokoyama, and M. Kase

A new control unit of N-DIM (shown in Fig. 1) has been developed for the devices installed in the beam transport of the RIBF. The control objects are the beam monitors such as Faraday cups and a beam profile monitors, and the vacuum pumping devices. A number of control units called DIM (the device interface module) have been used for the control of the above devices in the RARF. Because they are very old, it is unfavorable to extend the old DIM to the control of the new devices of the RIBF.

Considering the inconvenience associated with the old DIM, the new control unit of N-DIM was designed on the basis that the total control system would become very simple. To realize this, a communication interface between the N-DIM and an operation computer is made *via* an Ethernet network (general 10BASE-T/100BASE-TX). The N-DIM can be operated directly from other computers, even from other N-DIMs. this is a why the new unit was called as N-DIM (network DIM).

A block diagram for N-DIM is shown in Fig. 2. For the CPU, we used the SH4 fabricated by HITACHI, which is equipped with two kinds of memories (6 MB RAM and 1 MB ROM). The control software was produced in the  $\mu$ ITRON embedded on the N-DIM. We prepared approximately 20 command words consisting of three ASCII characters to be used in the operation of N-DIM. Moreover, the system may also be operated by logging in with telnet.

N-DIM is controlled by the socket connection of

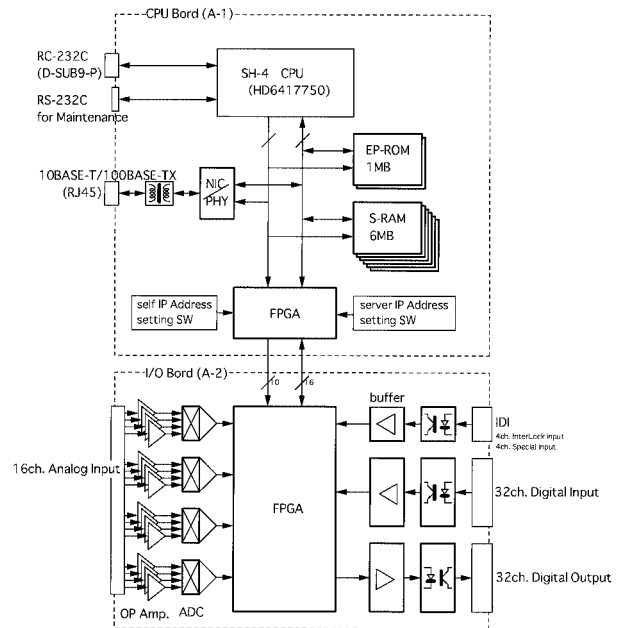


Fig. 2. Block diagram.

TCP/IP. The acquired data are sent to the control system inside the answer sentence of TCP/IP. When data are acquired continuously, they are sent in two ways. The data are stored as a file in the memory of the N-DIM and taken by the FTP connection, or such data, in units of small packets, can be sent by UDP/IP

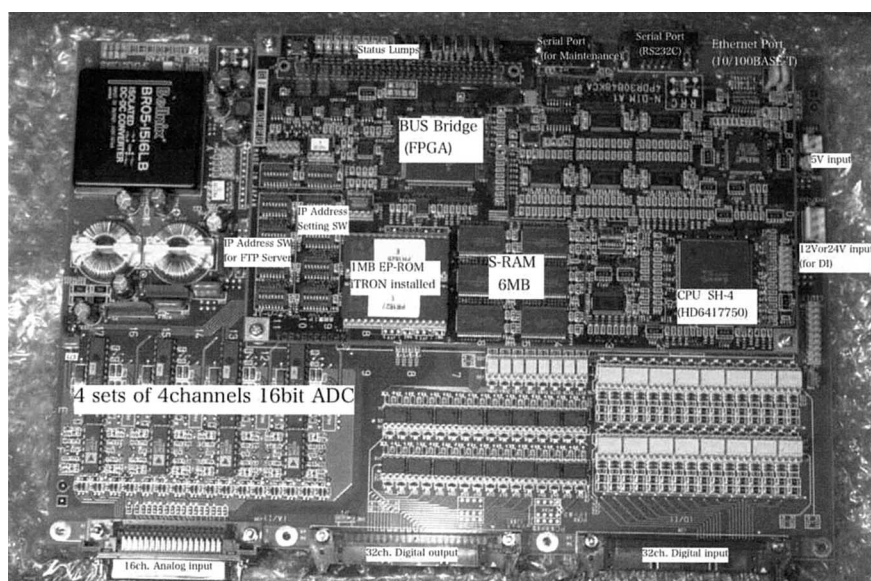


Fig. 1. N-DIM.

in the real-time scheme.

Whenever the N-DIM is switched on, it tries to connect to the application server, and an executive code is downloaded from the server by FTP. Using this function, new commands can be easily added to the N-DIM.

It is supposed that the N-DIM will be used for environmental radiant rays. S-RAM and EP-ROM are selected for the main memory. They have high tolerance to radiation in comparison with D-RAM and Flash-ROM. Besides, the clock of the CPU is used at a lower frequency than standard one, and the voltages of the data bus and the address bus are high in order to raise the noise margin.

The N-DIM has the following input and output specifications.

- (1) 32 ch digital inputs isolated with photocoupler
- (2) 32 ch digital outputs isolated with photocoupler
- (3) 16 ch analog inputs (14 bit accuracy and 200 kS/s sampling)

- (4) 8 ch Interrupt Inputs with photocoupler

The hardware connections of inputs and outputs are controlled by a logic circuit using FPGA. If necessary, the functions of inputs and outputs can be changed by the program on the FPGA. These functions can also be made compatible to the DIM using this program. The future exchange of the DIM, which will lose its usefulness soon, with the N-DIM is kept in mind. The interrupt inputs in item (4) can control some of the digital outputs directly. They can be used for interlock, for example. An additional circuit for the hardware interlock is unnecessary between the N-DIM and the controlled device.

A prototype of the N-DIM was produced in 2002 and a fundamental testing was carried out. In 2003, twenty sets of N-DIMs were fabricated. Some of them were installed on the beam line of RILAC to control a vacuum system and a beam profile monitor and a field test is now underway. About one hundred N-DIM units will be used in the RIBF.

## HIS: The radiation safety interlock system for the RIKEN RI Beam Factory

H. Sakamoto, S. Ito, T. Yamaki, S. Fujita, Y. Uwamino, and M. Kase

To ensure radiation protection at the RIKEN RI Beam Factory, two interlock systems will be installed. One is a radiation safety interlock system, HIS (Houshasen [which means “Radiation” in Japanese] Interlock System) which controls the radiation safety devices, and the other is BIS (Beam Interlock System) which protects the accelerator and the beam-line components. Their conceptual diagram is shown in Fig. 1. The devices for human safety are doubly monitored by the two systems independently. The beam will be immediately stopped, within 1 second, when either system detects any abnormality.

HIS was developed in 2003. This system initializes and controls all the devices connected to it, namely, radiation shutters, beam stoppers, radiation area monitors, shielding doors, beam status indicator, alarm siren, and so on.

HIS consists of five I/O stations and two personal computers (PCs). Figure 2 shows the concept. Each station has a programmable logic controller (PLC) which includes digital outputs, digital inputs and analog inputs. The concerned devices send their status to the five PLCs and receive the control signals from them, which are installed nearby. Actually, these signals connect the I/O boards of PLCs through multi-connectors. The use of connectors facilitates connection and disconnection of the station when we repair or test the system.

The stations are doubly connected between them *via* optical fibers. Moreover, one of the stations is also

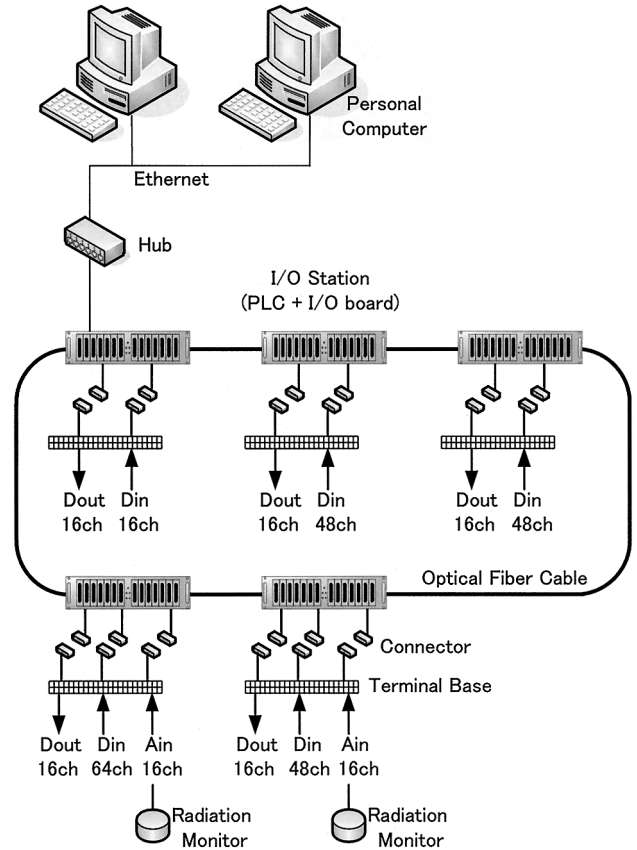


Fig. 2. Schematic of HIS.

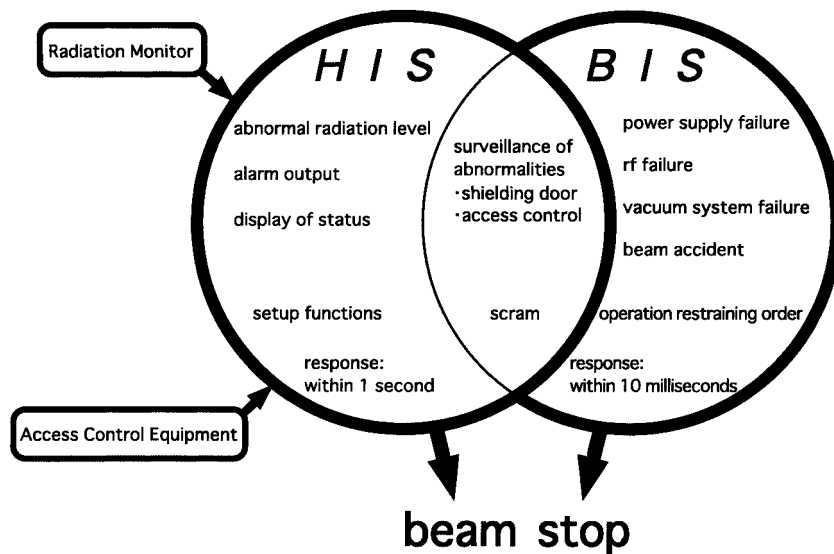


Fig. 1. Conceptual diagram of two interlock systems.

connected to a PC through the Ethernet. The PC is able to display the status of the whole system or of setup functions. The I/O record and the trend of the analog signals are saved and displayed on the PC. We can actually install the functional program ROMed on the PLC to improve the system reliability.

At the same time, we developed a testing apparatus that simulates the devices concerned that will be installed in the RIBF accelerator building. Due to this

apparatus, the debugging of the system logic can be performed before the construction of the whole system.

Henceforth, we have to verify the soundness of HIS and prepare the expansion of this system so that we can use it for the radiation control of the RIBF buildings. The expanded complete system will be installed in the RIBF accelerator and experiment buildings in 2005 at the earliest.

## Charge strippers for the RIKEN RI-Beam Factory

H. Ryuto, N. Inabe, N. Fukunishi, H. Hasebe,\* S. Yokouchi, M. Kase, A. Goto, and Y. Yano

A charge stripping scheme of the RIKEN RI-Beam Factory (RIBF) was presented in the previous report.<sup>1)</sup> According to the design modifications of the beam transport line from the RIKEN ring cyclotron (RRC) to the intermediate-stage ring cyclotron (IRC) *via* the fixed-frequency ring cyclotron (fRC), the stripping scheme was slightly changed. The points of change are described below. Experimental data on the charge-state distributions of  $^{136}\text{Xe}$  at 39 MeV/nucleon are also presented and compared with calculation values.

The third stripper section in the previous stripping scheme was planned to be used in both cases where ions are accelerated with the fRC and without the fRC. In the modified design (Fig. 1), the beam transport line from the fRC to the IRC does not pass through the previous third stripper section. Accordingly, the section previously numbered as third was renumbered as fourth, and the third stripper section was placed between the fRC and the IRC anew. The new third stripper section is used in the case only with the fRC, and the fourth stripper section is used in the case only without the fRC. The strippers placed at the new third and fourth sections are mainly characterised by the thicknesses of carbon foils and plates. As described in the previous report, uranium and xenon ions are planned to be stripped at the third stripper section by 14 mg/cm<sup>2</sup> and 20 mg/cm<sup>2</sup> thick carbon plates, respectively. On the other hand, the thickness of the stripper at the fourth section is required to be small in order to avoid a large energy loss aiming at the incident energy range of the IRC. Xenon ions are planned to be stripped by a 0.3 mg/cm<sup>2</sup> thick carbon foil (see below for details). A rotating carbon disk stripper for the third section is currently under development.

The charge-state distributions of  $^{136}\text{Xe}$  at 39 MeV/

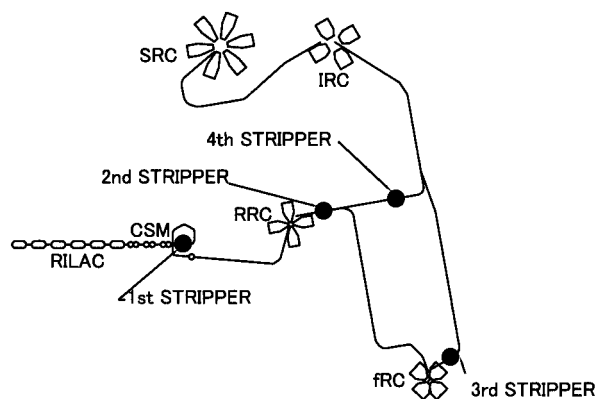


Fig. 1. Schematic of the RIBF.

nucleon, which corresponds to the incident energy of the fourth stripper section, were measured with strippers of various thicknesses. The xenon beam was bombarded on carbon foils, aramid films, and a polyimide film with thicknesses from 80  $\mu\text{g}/\text{cm}^2$  to 7 mg/cm<sup>2</sup>. Figure 2 shows the measured charge-state fractions. Solid and dashed lines indicate the GLOBAL<sup>2)</sup> and ETACHA<sup>3)</sup> calculations, respectively. Comparing the calculation values to the data, it is seen that the GLOBAL calculation well reproduces the data compared to the ETACHA calculation. According to the GLOBAL calculation, we can obtain  $^{136}\text{Xe}^{45+}$  by a 0.3 mg/cm<sup>2</sup> thick carbon foil with a 26% fraction.

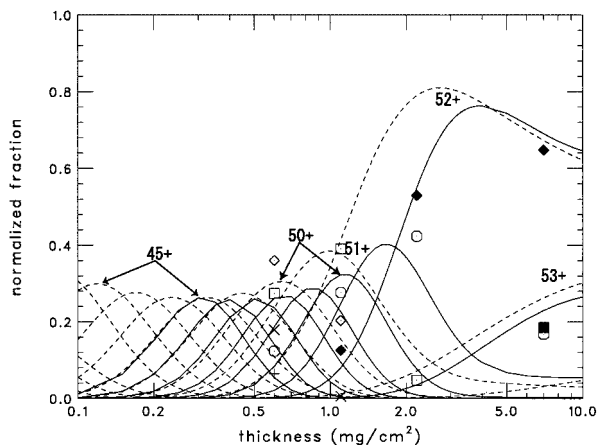


Fig. 2. Charge-state fractions of  $^{136}\text{Xe}$  at 39 MeV/nucleon stripped by carbon foils, aramid films, and a polyimide film. Horizontal and vertical axes indicate the thickness of the strippers and the charge-state fractions, respectively. Vertical cross, diagonal crosses, open diamonds, open squares, circles, solid diamonds, and solid square indicate the measured charge-state fractions from 47+ to 53+. The charge-state fractions are normalised by the area of the Gaussian fitted to the measured charge-state distribution. Solid and dashed lines indicate the calculations by GLOBAL and ETACHA, respectively.

### References

- 1) H. Akiyoshi, N. Inabe, N. Fukunishi, H. Hasebe, T. Chiba, M. Kase, and Y. Yano: RIKEN Accel. Prog. Rep. **36**, 292 (2003).
- 2) C. Scheidenberger, Th. Stöhlker, W. E. Meyerhof, H. Geissel, P. H. Mokler, and B. Blank: Nucl. Instrum. Methods Phys. Res. B **142**, 441 (1998).
- 3) J. P. Rozet, C. Stéphan, and D. Vernhet: Nucl. Instrum. Methods Phys. Res. B **107**, 67 (1996).

\* SHI Accelerator Service, Ltd.



## Low-power test of the IRC flattop resonator

N. Sakamoto, O. Kamigaito, S. Kohara, A. Goto, and Y. Yano

The flattop resonator for the IRC (Intermediate-stage Ring Cyclotron)<sup>1)</sup> has been constructed and low-power testing was carried out. The required frequency range and the maximum gap voltage of the resonator are from 72.0 to 121.5 MHz and 150 kV<sub>p</sub>, respectively.

A schematic of the resonator is shown in Fig. 1. The resonator is a single-gap type whose resonant frequency varies by two movable shoring plates. The shape of the resonator was designed and optimized by using the computer code MAFIA.

Figure 2 shows the resonant frequency of the fundamental mode. As shown in the figure, the movement of the shoring plates by a stroke of 790 mm varies the resonant frequency from 69 to 123 MHz. The resonant frequency predicted by MAFIA is lower than the measured frequency by 2% in the entire frequency range. The second and third higher modes appear around 120 and 190 MHz, respectively. The block tuner varies the resonant frequency by more than 0.5%.

Q-values and parallel shunt impedance (R<sub>s</sub>) are shown in Fig. 3. They are as large as 73% of the calculated values. R<sub>s</sub> values are obtained by electric-

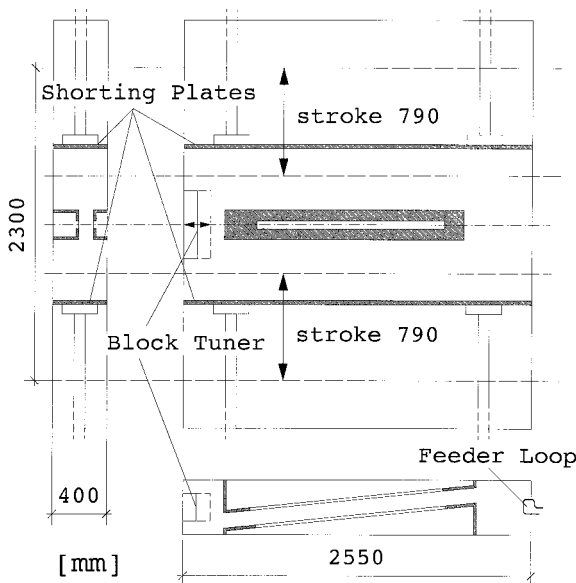


Fig. 1. Schematic of the IRC flattop resonator.

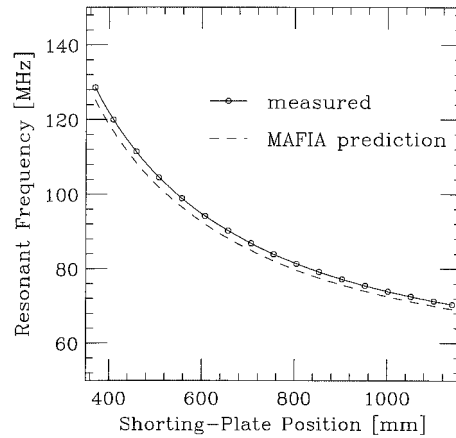


Fig. 2. Resonant frequency of the fundamental mode.

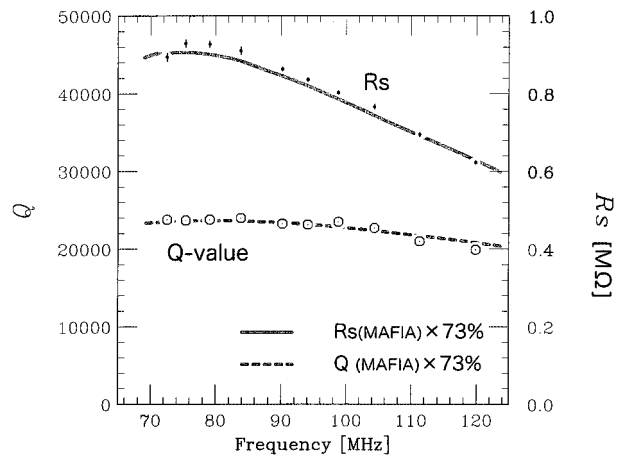


Fig. 3. Q-values and parallel shunt impedance.

field measurement using a perturbation method. At a frequency of 109.98 MHz, in the case of uranium 350 MeV/u acceleration, the wall loss is estimated to be 16 kW with a gap voltage of 150 kV<sub>p</sub>.

### References

- 1) N. Sakamoto et al.: Proc. 16th Int. Conf. on Cyclotrons and Their Applications, East Lansing, USA, 2001-5 (American Institute of Physics, 2001), p. 306.

## Status of booster ring cyclotrons for the RIKEN RI Beam Factory

A. Goto, H. Okuno, J. Ohnishi, N. Fukunishi, T. Tominaka, S. Fujishima,<sup>\*1</sup> K. Ikegami, N. Sakamoto, N. Inabe, Y. Miyazawa, S. Yokouchi, T. Fujinawa, T. Mitsumoto,<sup>\*2</sup> O. Kamigaito, H. Ryuto, H. Mikami,<sup>\*2</sup> M. Kase, and Y. Yano

In this report, the construction of a chain of booster ring cyclotrons consisting of the fRC, IRC and SRC for the RIKEN RI Beam Factory is described.

For the SRC, the fabrication of almost all its main components was completed in the spring of 2003 as scheduled. All the main coils (twelve sets) and trim coils (twenty-four sets) were fabricated within tolerances of  $\pm 1$  mm and  $\pm 2$  mm, respectively, for the positions of the centers of their cross sections. The stability of the power supplies for the main coils and trim coils was within 5 ppm per 8 h. The resonant frequencies and Q-values of the rf resonators were measured at the factory; the measured resonant frequencies were in agreement with the MAFFIA calculation within 1%, and the Q-values were 70–80% of the calculated ones in the entire frequency range. Figure 1 shows a photograph of the inside of the control Dewar vessel fabricated at the factory.

From the spring to the summer of 2003, all the completed components of the SRC, except for the cold mass such as the main coils and trim coils as well as warm poles, were delivered to the new accelerator building of RIKEN. More than 400 iron pieces for the yokes and magnetic shields (about 6,300 t in total) are now laid on the floors of both the SRC vault and the Big RIPS room. The cryostats and the control Dewar vessel are in the Big RIPS room. The power supplies for the sector magnets are set at the due places. The cryogenic cooling system consisting of one He refrigerator, three compressors and four reservoir tanks for He gas is also set in their proper places. The lower

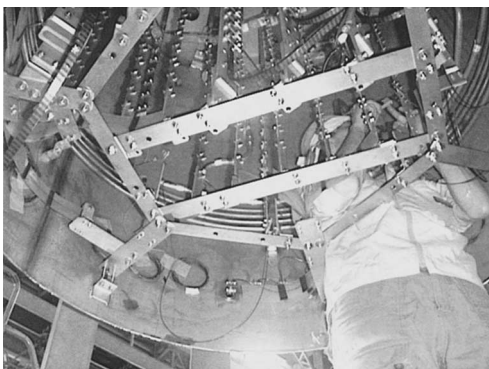


Fig. 1. Photograph of the inside of the control Dewar vessel being fabricated at the factory. The main coils and trim coils for the six sector magnets are connected in series.

<sup>\*1</sup> Ishikawajima-Harima Heavy Industries Co., Ltd.

<sup>\*2</sup> Sumitomo Heavy Industries, Ltd.

yokes and lower magnetic shield plates for one sector magnet were assembled in their proper places in the SRC vault. Figure 2 shows a photograph of the SRC vault that was taken in July 2003.

The completed superconducting bending magnet (SBM) for beam injection was tested at RIKEN in the autumn of 2003. It took about 100 h to cool the cold mass down from room temperature to 4.3 K. The SBM reached the designed field of 3.8 T in one quench. Magnetic field distributions along the beam axis were also measured.

In October 2003, the plumbing of the lines for the He refrigerator, compressors and reservoir tanks was started in the accelerator building. The assembly of the cold mass, *e.g.*, the attachment of the trim coil vessel, the 70 K thermal shields, temperature sensors, and strain gauges, to the main coil vessel was also started at the factory. The lower yokes and lower magnetic shields for the remaining five sector magnets are scheduled to be completed in the spring of 2004.

The installation and assembly of the IRC sector magnets were started in October 2003. For one and a half months, the lower parts including the yokes, poles, main coils, trim coils and beam chambers were assembled for all the four sector magnets. The sector magnets were set with an accuracy of 0.2 mm in both the horizontal and vertical directions. Figure 3 shows a photograph of the IRC vault that was taken in November 2003. The assembly of the remaining upper yokes and the installation of the rf resonators are scheduled to be completed by the end of 2003. The rf characteristics of the flattop resonator were mea-

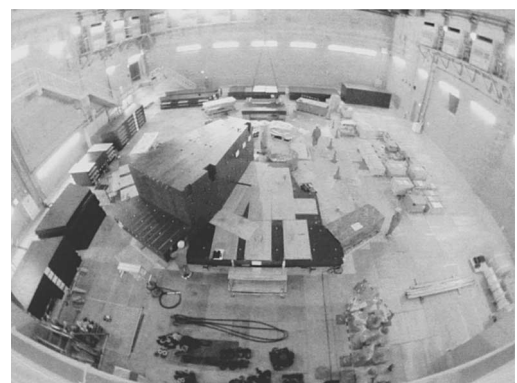


Fig. 2. Photograph of the SRC vault that was taken in July 2003. The assembled lower yokes and lower magnetic shields for one sector magnet can be seen along with some of other components temporarily delivered.



Fig. 3. Photograph of the IRC vault that was taken in November 2003. The lower parts have been assembled for all the four sector magnets.

sured at the factory; the measured resonant frequencies were higher than the MAFIA calculation by 2%, and the Q-values and shunt impedances were about 70% of the calculated ones in the entire frequency range.

An order was given to Sumitomo Heavy Industries, Ltd., regarding the fabrication of the fRC. As of November 2003, the machining of the yoke and pole pieces has been completed. Figure 4 shows a photo-

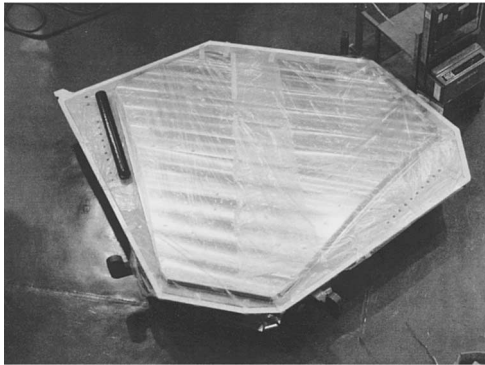


Fig. 4. Photograph of the completed pole as well as the vacuum chamber wall for the fRC.

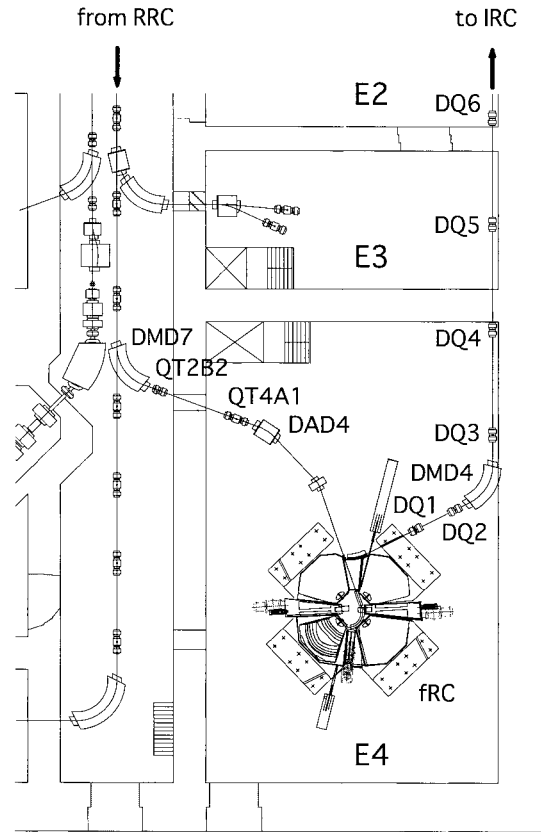


Fig. 5. Newly designed layout of the fRC as well as the injection and extraction beam lines.

graph of the completed pole as well as the vacuum chamber wall. The layout of the fRC as well as the injection and extraction beam lines has been changed; the beam transport line from the fRC to the IRC is planned to be set in experimental rooms E4, E3, E2 and E1. The newly designed layout is shown in Fig. 5.

The construction of the cooling water system for the new facility was started in October 2003; it is scheduled for completion by the spring of 2004.

# Magnetic field perturbations from the injection and the extraction elements of the RIKEN SRC and their correction

J. Ohnishi, H. Okuno, A. Goto, and Y. Yano

The magnetic elements used for the beam injection and extraction in the superconducting ring cyclotron (SRC) generate magnetic field perturbations on the isochronous field required for the beam acceleration. These magnetic field perturbations were calculated using the three-dimensional magnetic field calculation code "TOSCA" and their correction by the normal-conducting trim coils was simulated.

Figure 1 shows a schematic of the SRC injection and extraction elements and trajectory of the beam.<sup>1)</sup> The injection system consists of one superconducting bending magnet (SBM),<sup>2)</sup> two normal-conducting magnetic inflection channels (MIC1 and MIC2),<sup>3)</sup> and one electrostatic inflection channel (EIC). The extraction system consists of one electrostatic deflection channel (EDC), three normal-conducting magnetic deflection channels (MDC1, MDC2, and MDC3), and one normal-conducting extraction bending magnet (EBM).<sup>4)</sup>

To estimate the magnetic field perturbation, we carried out three-dimensional magnetic field calculations for the SRC with and without the injection and the extraction elements. We show the results for a 350 MeV/nucleon uranium beam in Fig. 2. The magnetic field perturbations on the first circulation orbit by the SBM and the MIC2, and on the last one by the EBM are illustrated in the figure. These three components are large compared with the perturbations from the other elements.

The magnetic field in the valley region of the cyclotron is in the direction opposite to that of the hill region and the field strength is approximately  $-74$  mT

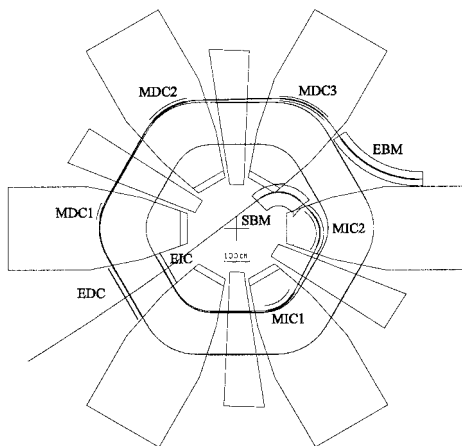


Fig. 1. Schematic of the injection and the extraction elements of the SRC.

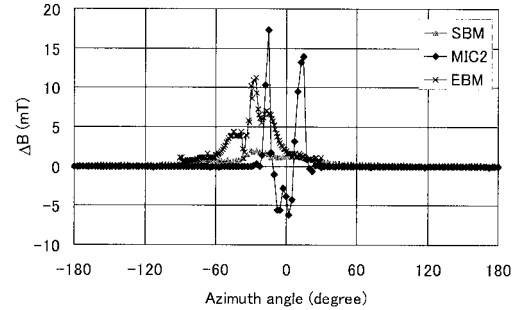


Fig. 2. Magnetic field perturbations on the first circulation orbit from the SBM and the MIC2 and on the last one from the EBM. Abscissa indicates azimuthal angle from the center of the sector magnet where the MIC2 is located.

and  $-58$  mT on the first and the last circulation orbit, respectively, at the center of the valley region. The direction of the error fields is the same as that of the sector field because iron yokes of the SBM and the EBM absorb the magnetic field in the valley region and reduce it. On the other hand, the error magnetic fields from the MIC2 can be corrected by the compensation coil, but they are not corrected perfectly because it is difficult to cancel the leakage field from both ends.

Figure 3 shows the radial distributions of the magnetic perturbations by the SBM, the MIC2, and the EBM averaged over the azimuthal direction. These error fields need to be corrected by 22 pairs of normal-conducting trim coils of the sector magnets<sup>5)</sup> so that the deviation from the isochronous field may be at the level of  $1 \times 10^{-4}$ . Figure 4 shows the magnetic field distributions generated by the normal-conducting trim coils. The current of each coil is 600 A. From these

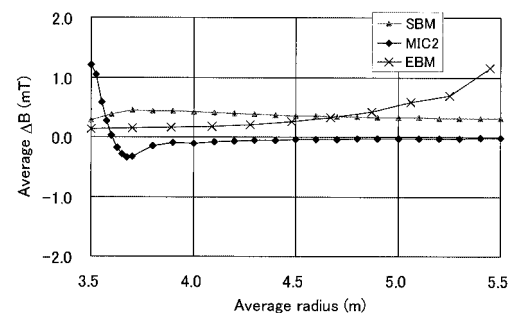


Fig. 3. Radial distributions of the azimuth average perturbation magnetic fields from the SBM, the MIC2, and the EBM.

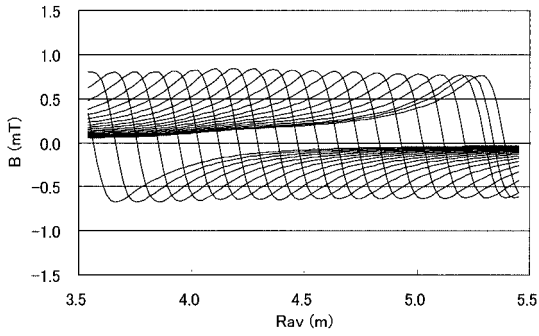


Fig. 4. Radial distributions of the azimuth average magnetic fields of 22 pairs of the normal-conducting trim coils. The current of each coil is 600 A. The magnetic fields were calculated assuming that the trim coils are air-core.

field distributions, the current set of the trim coils was determined by the least-square fitting so that the magnetic fields by the trim coils reduce markedly the per-

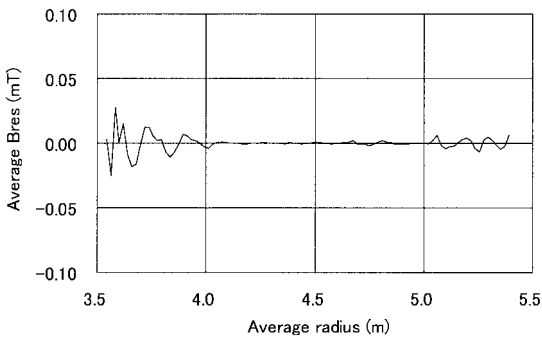


Fig. 5. Simulated residual magnetic field after the field correction by the normal-conducting trim coils.

turbation fields. Figure 5 shows the residual magnetic field distribution after the field correction by the trim coils. The residual magnetic field strength is found to be smaller than  $1 \times 10^{-4}$  of the average one on the beam orbit (1.3–1.4 T). Figure 6 shows the current values of the trim coils. They are within the capacity of the power supplies whose nominal currents are 600 A, 800 A, and 1200 A. Although the magnetic field perturbations from the injection and the extraction elements vary with the type of accelerated ions, a similar correction can be carried out.

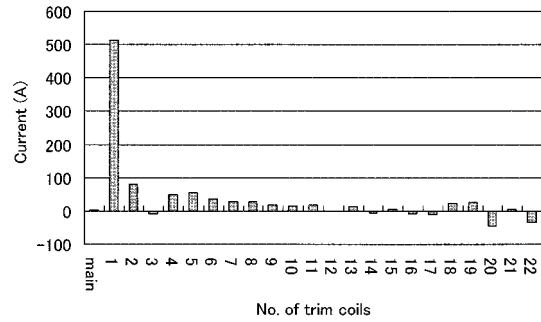


Fig. 6. Currents of the main and the normal-conducting trim coils required for the correction of the perturbation fields from the SBM, the MIC2, and the EBM.

#### References

- 1) S. Fujishima et al.: RIKEN Accel. Prog. Rep. **34**, 341 (2001).
- 2) H. Okuno et al.: IEEE Trans. Appl. Supercond. **12**, 192 (2002).
- 3) S. Fujishima et al.: IEEE Trans. Appl. Supercond. **12**, 63 (2002).
- 4) S. Fujishima et al.: Proc. 13th Symp. on Accelerator Science and Technology, Suita, 2001-10 (2001), p. 274.
- 5) A. Goto et al.: AIP Conf. Proc. **600**, 319 (2001).

## Cranes for RIBF

T. Fujinawa, T. Yamashita,<sup>\*1</sup> N. Yamasaki,<sup>\*1</sup> K. Kawamoto,<sup>\*2</sup> M. Kase, and Y. Yano

In the RI Beam Factory project, each facility (accelerator, magnet and other devices.) installed is considerably heavy in its weight. For instance, the SRC is estimated to be more than 8000 tons and the Big-RIPS radiation shield approaches 5000 tons. Each component of the facility will be brought into the factory from the manufacturer by a 30-ton trailer. Up to eight trailers are used per day. We have chosen and installed eight cranes (Table 1), for carrying, constructing, and maintenance. These cranes<sup>1)</sup> are arranged in the RI beam factory as shown in Fig. 1.

The common features for all cranes are as follows.

1. The inverter operation system adopted here, alleviates potential shock caused by starting and stopping, and significantly reduces energy consumption by 50%.<sup>2)</sup>
2. Usage of hoist motor reduces the size and weight of the cranes.
3. Both wired and wireless operations are available.
4. A high-resistant basket-type induction motor, which has a large starting torque and low striking current, has been adopted to endure constant inching operations. Those enabling it to start quickly and maintain low exothermic heat. Such features extend the lifetime of all equipment. The thermal relay protection is not necessary.
5. Since the electric power is supplied by a CGS<sup>3)</sup> bus bar, every crane can be operated even in case of a blackout.

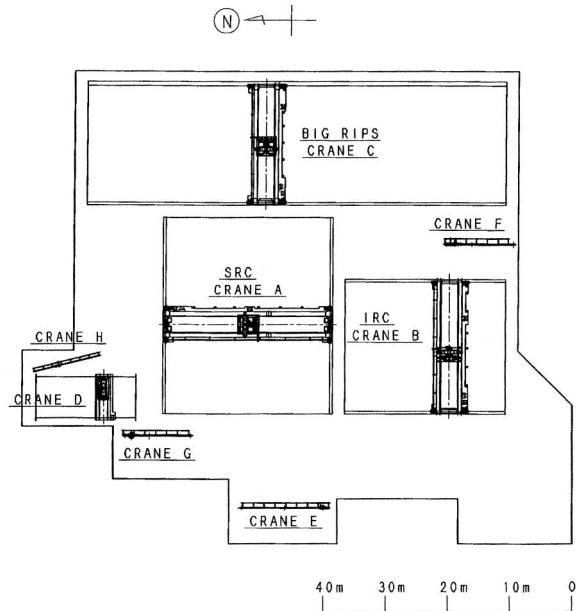


Fig. 1. Layout of all cranes in the RI beam factory.

The feature of each crane used is as follows.  
 SRC Crane A: A 60-ton crane is used based on function requirements and cost effectiveness. In order to minimize its size, the following amendments were made. (1) To minimize the clearance between the crane and the ceiling of the building, a single shaft for hook block was applied. (2) To reduce the height, the diameter of the wheels was halved but the number of e wheels was

Table 1. Crane specification.

Crane NO.	Crane A	Crane B	Crane C	Crane D	Crane E	Crane F	Crane G	Crane H
	SRC	IRC	Big-RIPS	Carry-In Entrance	Electrical Room 1	Cryogenic	Electrical Room 2	Carry-In Entrance
Type	§ <sup>1</sup> OTC	§ <sup>1</sup> OTC	§ <sup>1</sup> OTC	§ <sup>2</sup> BG	§ <sup>3</sup> TELPH	§ <sup>3</sup> TELPH	§ <sup>3</sup> TELPH	§ <sup>3</sup> TELPH
Rated Load (ton)	69/5t	35/5t	40/5t	40t	2.8t	10t	7.5t	2t
Span (m)	26.3	21	18.85	6.6	—	—	—	—
Lift	12.35/13.55	12.73/13.965	10.7/12.15	18	12.42	13.2	11.21	4.515
Operation	Wireless	Wireless	Wireless	Wireless	Wireless	Wireless	Wireless	Pendant
Rated Speed								
Main Hoist (m/min)	2.5	2.5	2.5	2.5	10	6	7	10
Aux.Hoist (m/min)	8	8	8	—	—	—	—	—
Traverse (m/min)	18	18	18	18	—	—	—	—
Travel (m/min)	18	18	18	18	25	15	15	25
Travel Rail	37 kg/m	37 kg/m	37 kg/m	37 kg/m	—	—	—	—
Electric Power	AC 200 V 50 Hz 3 ph							

§<sup>1</sup>OTC: Overhead travelling crane

§<sup>2</sup>BG: Bridge crane

§<sup>3</sup>TELPH: Telferage

<sup>\*1</sup> JFE Mechanical Co. Ltd. (Formerly Kawatetsu Machinery Co., Ltd.)

<sup>\*2</sup> Mitsubishi Electric Hoist Co.

doubled. (3) By separating the hoist motor unit from the cross travel equipment, their size was reduced 15%.

SRC Crane B: This is used for IRC erection and maintenance.

Big-RIPS Crane C: The size reduction is similar to that of SRC Crane A. By removing a part of the building walls, "dead space" was reduced by 65 cm.

Portal Shape Crane D: The crane is placed at the entrance and the most of the accelerator equipment is brought into the building by this crane.

Telpherage Crane E: This crane is used mainly for transporting electrical panels from the existing building to the RIBF building.

Cryogenic Crane F: This is used to handle Cryogenics.

Electric Room Crane G: This is used to transport electric panels, which were brought in by Crane D, to the electric rooms.

Carry-In Entrance Crane H: This is arranged due to the fact that the elevator floor was 1.1 meter higher than the entrance floor.

#### References

- 1) T. Nomura: *OASIS 2003 SPRING* (Kawatetsu Machinery Co., Ltd., Sougensya, Tokyo, 2003).
- 2) Mitsubishi Hoist Technical Report R-4 (2000).
- 3) T. Fujinawa et al.: RIKEN Accel. Prog. Rep. **36**, 310 (2003).

## Current status of the control system development at RIKEN RI-Beam Factory<sup>†</sup>

T. Tanabe, T. Masuoka, K. Yoshida, K. Kumagai, M. Kobayashi-Komiyama, T. Emoto, and M. Kase

The deployment of the Common Object Request Broker Architecture (CORBA)-based control system for RIKEN's RI-Beam Factory Project<sup>1)</sup> has started. Vendor independence, software sharing and interoperability are the main aims of the design. Abeans R2<sup>2)</sup> developed at Jozef Stefan Institute (JSI) of Slovenia has been connected to our CORBA servers running on VMEs *via* plug-ins. Oracle9i running on Linux is employed to store the data, operation loggings and device configurations. XMLs are utilized to set the configuration of each device from the DB to the equipment. The power supply (PS) controls are firstly deployed as well as RF monitor via Programmable Logic Controller (PLC).

The overall system architecture including some future extensions is shown in Fig. 1. The Java graphical user interface (GUI) programs work as a CORBA client only except for the alarm call-back function. Both server and client objects are in the application server (AS). Those in the VME are mostly servers except for the one which gets the parameter data from the database. The relational database management system (RDBMS) functions as the back end of the AS and cannot be accessed directly from other objects. GPIB wrapper and CORBA-EPICS server are still in the prototype stage and they will be field- tested in the coming months. Table 1 shows the list of hardware and

software used in the system.

Motorola's VME-CPU board (MVME2400) with 512MB RAM is chosen for the field controller. The

Table 1. List of the used hardware and software (those in bold characters are commercial software).

Equipment	Items	Used Software
Client PC (Java enabled)	OS	<b>Win2k/OS-X/Linux</b>
	Language	Java1.4
	CORBA	JacORB 1.4.1
Database [Dell PowerEdge 2650]	OS	<b>Miracle Linux 2.1</b>
	RDB Software	<b>Oracle 9i (9.0.1)</b>
Controller (VME64x) [Motorola MVME2400]	OS	<b>vxWorks5.4</b>
	Language	<b>C++ / C</b>
	ORB	<b>VisiBroker-RT 4.1c</b>
Application Server [Dell PowerEdge 4600]	XML Parser	libXML 2.5.2(modified)
	OS	<b>RH Linux AS 2.1</b>
	Language	GNU C++ / GNU C / Java1.4/ JDBC1.2
	Web server	Apache, Tomcat
	DNS	BIND
	NFS	Samba, Netatalk
	DHCP	dhcpcd
	ORB	MICO 2.3.10/ JacORB 1.4.1
Others	GNU Make	

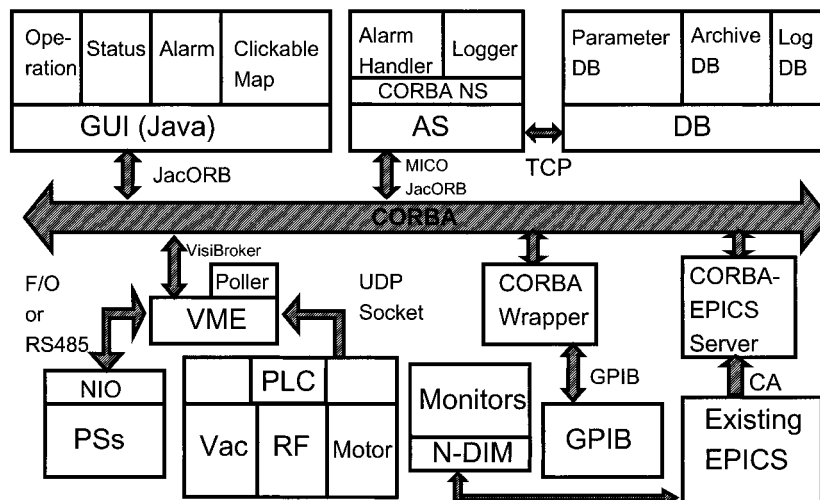


Fig. 1. System architecture.

<sup>†</sup> Condensed from the article in the Proc. 9th Int. Conf. on Accelerator and Large Experimental Physics Control System (ICALPCS'03), Gyeongju, Korea, 2003-10 (to be published)



VME64x crate (HS-SY013) has 15 slots and hot-swappable redundant power supplies for easy maintenance. It also has an alarm function for errors, and 5V35A, +12V4A, -12V1A; 3.3V25A of DC output can be used.

All the equipment-CORBA-objects are running in the VME including a poller program. There is only one type of program running in all the VME and the differences in terms of configurations and types of objects to be activated are determined from the DB data. Since VisiBroker-RT 4.1c does not support “wstring” type, Japanese characters cannot be handled in the same way as the Latin alphabet. Therefore, the unicode escape sequence was used to send Japanese via CORBA when necessary. The features of RT-CORBA such as “thread pool” and “server-declared CORBA priority” are employed to control the various task priorities. The PropertyResourceBundle class in Java is used to switch languages.

The NIO system comprises of the NIO-C master board in the VME crate and NIO-S slave boards which are located in the PSs.<sup>3)</sup> They can be connected to each other by serial communication of 2 Mbps either with SI fibre optical (F/O) cable in a star topology using branch boards or RS485 balanced serial cable in series. NIO-S has its CPU with a firmware running so it can be operated independently from the master, even if communication with it is severed. This concept has been carried over from the CAMAC-based I/O system that our existing facility utilizes. The firmware of NIO-S can also be downloaded from the host computer in order to ensure easy maintenance and modification.

Linux is used for the AS and the RDBMS. For the AS, Redhat Linux Advance Server 2.1 was chosen for its support availability. Oracle 9i for Linux is installed in Miracle Linux which is produced by a subsidiary of Oracle, Inc. and integrated support for both DB and OS are available. PS CORBA objects on any VME can be accessed and controlled by a CORBA client which in our case is the Power Supply (PS) Panel program made by JSI and modified by Cosylab. There are two types of screens; one for monitoring, and the other for setting-up and operating multiple PSs simultaneously. Individual PSPanel can be opened only through either of the above-mentioned screens. Each VME has many PS objects and it is inefficient for individual objects to ask the interoperable naming service (INS) for the interoperable object reference (IOR) every time the PSPanel is activated. The top screens for the PS control collect all the IORs at the beginning so that each individual PSPanel can immediately know where the object is. The setup information for each PS is sent to the PS object in terms of XML generated from the data from the RDBMS through JDBC. The UML Sequence diagram of PS Summary operation is given in

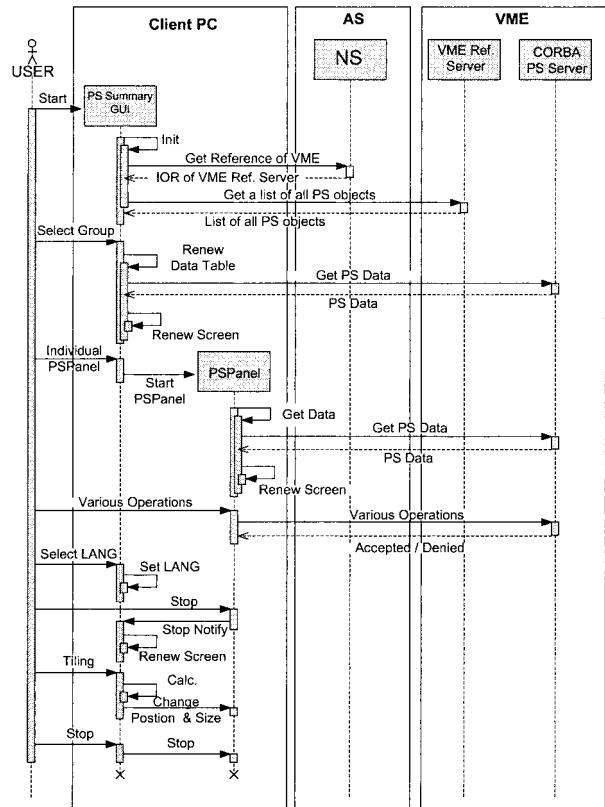


Fig. 2. Sequence diagram for PS summary operation.

Fig. 2.

The program for the polling runs in the VME and it sends the data to the logging object in the AS. This object writes the contents in both the shared memory and the DB. The Alarm Handler (AH) object will read the contents of the shared memory and report errors when the preset conditions are met. The RF monitor screen is also made of Abeans. The GUI program communicates with the PLC wrapper object<sup>4)</sup> which read/writes the data in the memory area of the PLC (OMRON SYSMAC CVM1/CV) through UDP with FINS commands that are provided by the manufacturer.

In summary, the world’s first RT-CORBA-based accelerator control system has been implemented at RIKEN. The fact that LHC accelerator controls at CERN have decided to use CORBA in their middleware guarantees more extensive use of it in the accelerator community in the future.

References

- 1) <http://ribfweb1.riken.go.jp/>
- 2) <http://www.cosylab.com/>
- 3) <http://www.ndssf.co.jp/>
- 4) <http://accelconf.web.cern.ch/AccelConf/ica01/papers/THAT003.pdf>

## Status of the BigRIPS separator project

T. Kubo, K. Kusaka, Y. Mizoi, A. Yoshida, and K. Yoshida

The in-flight radioactive isotope (RI) beam separator BigRIPS<sup>1)</sup> is being built to produce RI beams in the RI-beam factory (RIBF) project.<sup>2)</sup> The first RI-beam production using the BigRIPS is scheduled in late 2006. Nuclear physics experiments using RI beams will begin in early 2007. The use of in-flight fission of uranium beams at 350 MeV/nucleon is planned for the first RI-beam production.

Figure 1 shows a schematic of the BigRIPS separator, which is followed by RI-beam delivery lines and experimental setups. The construction of two BigRIPS separators, as shown in the figure, has been planned. This makes it possible to perform two different RI-beam experiments simultaneously by time-sharing of primary beams. One of the separators is a large-acceptance separator, indicated as BigRIPS-I in the figure, for which large-aperture superconducting quadrupole triplets are employed to achieve efficient collection of fission fragments. BigRIPS-I, including its RI-beam delivery lines, was funded, thus, some components of the magnet system are already being fabricated. The other is a medium-acceptance separator, indicated as BigRIPS-II, whose quadrupole magnets are room-temperature magnets. The basic design of BigRIPS-II has already been finished, including its RI-beam delivery lines, however, the funding is get unavailable. In this report we describe the fabrication status of the large-acceptance superconducting separator

BigRIPS-I. The design details of the BigRIPS separator are given in Ref. 1.

The large-acceptance BigRIPS forms a two-stage separator. The first stage separates and produces RI beams, while the second stage is used to tag isotope species of RI beams in an event-by-event mode. It consists of fourteen superconducting quadrupole triplets (STQ)<sup>3)</sup> and six room-temperature bending dipole magnets. The STQs and the dipole magnets are being fabricated by Toshiba Corporation and will be complete by early 2004. The five STQs in the first stage are cooled by liquid helium supplied by a large-scale, integrated cryogenic system through a transfer line,<sup>4)</sup> while the rest of the STQs are cooled by a small cooling system which is mounted on each cryostat of the quadrupole triplets.<sup>5)</sup> The large cryogenic system is being fabricated by Nippon Sanso Corporation and some of its components, such as compressors and buffer tanks, have already been installed in the RIBF building. The installation of the magnet system of the first stage, the five STQs including the cryogenic system and the two dipoles, will be complete by the end of March in 2004. The rest of the STQs and dipoles will be installed later in 2004 to 2005. A license which is required for building a large cryogenic system was issued in October 2003 by the Saitama municipal government. Figure 2 shows a photograph of the STQ with a small cooling system, which is being fabricated in a Toshiba

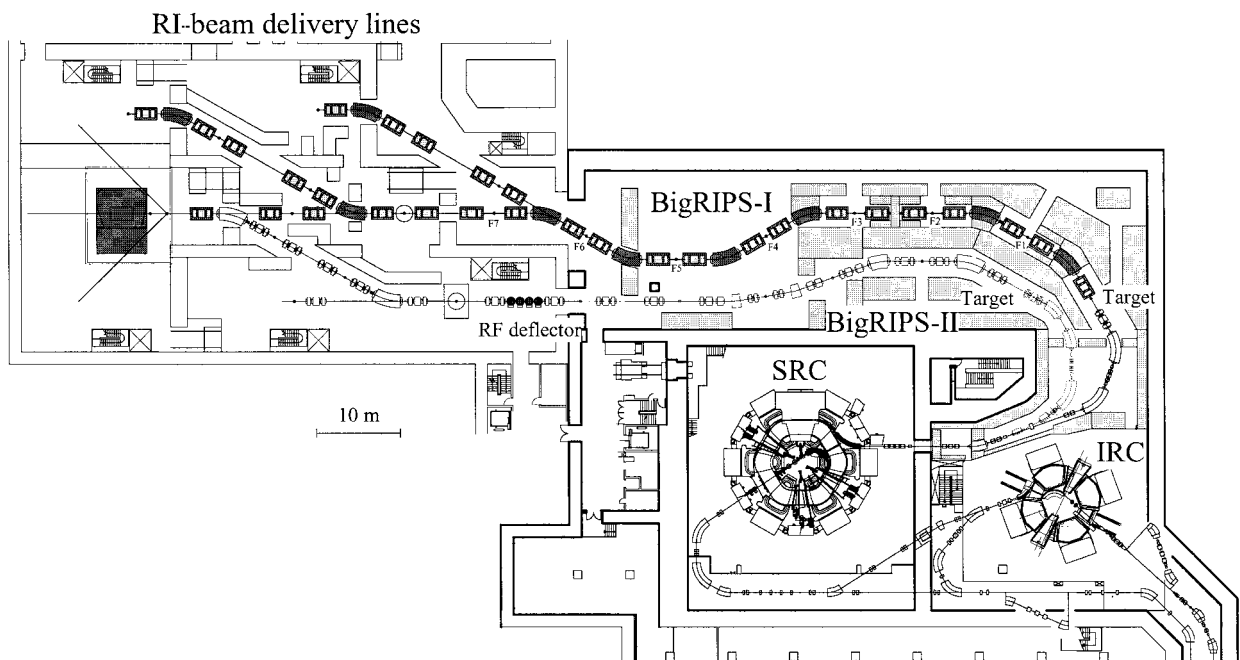


Fig. 1. Schematic of the BigRIPS separator. The BigRIPS is followed by RI-beam delivery lines and experimental setups.

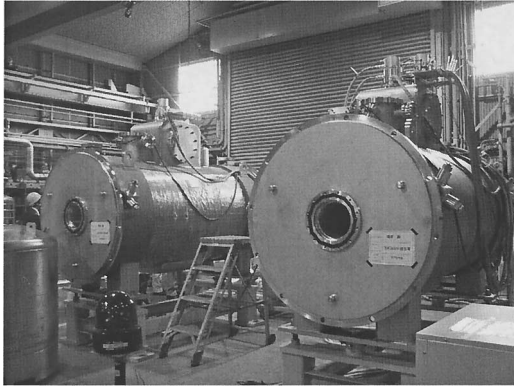


Fig. 2. STQs being fabricated in a Toshiba factory.

factory.

The STQs are of superferric type<sup>3)</sup> except for the first one which is placed right after the production target in the first stage. This first STQ is of air-core type, aiming at reducing neutron-radiation heat loads to the cryogenic system. Its design is also found in this progress report.<sup>6)</sup> A special current-lead system has been designed for the five STQs in the first stage, aiming at stable cooling of the current leads. Its design and testing are also found in this progress report.<sup>7)</sup>

The design study and development of a high-power beam dump and a high-power rotating-disk production target are under way. They are crucial since the expected beam power in the RIBF is as high as approximately 100 kW. A high-power beam dump in which swirl tubes are employed has been designed and its prototype for testing has been built. The development of the beam dump<sup>8,9)</sup> and production target<sup>10)</sup> is also found in this progress report.

The design of focal plane chambers, vacuum system, RI-beam diagnosis devices installed in the chambers, and beam-line detectors including the data-acquisition system are under way. The neutron-radiation shielding is also being designed.<sup>11)</sup> The RI-beam delivery lines that follow the BigRIPS have already been designed. The same superferric STQs equipped with the small cooling system and the same dipoles will be used for the delivery lines. The design of the BigRIPS control system is also under way. These devices will be fabricated and installed between 2004 and 2006.

#### References

- 1) T. Kubo: Nucl. Instrum. Methods Phys. Res. B **204**, 97 (2003).
- 2) Y. Yano et al.: AIP Conf. Proc. **600**, 161 (2001).
- 3) T. Hiramachi et al.: IEEE Trans. Appl. Supercond. **10**, 236 (2000); H. Kouzu et al.: RIKEN Accel. Prog. Rep. **34**, 350 (2001).
- 4) T. Kubo et al.: RIKEN Accel. Prog. Rep. **36**, 316 (2003).
- 5) K. Kusaka et al.: RIKEN Accel. Prog. Rep. **36**, 314 (2003).
- 6) K. Kusaka et al.: RIKEN Accel. Prog. Rep. **37**, 297 (2004).
- 7) N. Kakutani et al.: RIKEN Accel. Prog. Rep. **37**, 299 (2004).
- 8) Y. Mizoi et al.: RIKEN Accel. Prog. Rep. **37**, 303 (2004).
- 9) Y. Mizoi et al.: RIKEN Accel. Prog. Rep. **37**, 305 (2004).
- 10) A. Yoshida et al.: Nucl. Instrum. Methods Phys. Res. A **521**, 65 (2004); A. Yoshida et al.: RIKEN Accel. Prog. Rep. **37**, 295 (2004).
- 11) K. Yoshida et al.: RIKEN Accel. Prog. Rep. **37**, 301 (2004).

## Design study of the high-power production target for the Big-RIPS separator

A. Yoshida, Y. Mizoi, Y. Takahashi, T. Kubo, I. Tanihata, K. Yoshida, and K. Kusaka

A water-cooled rotating target system for the projectile fragment separator (Big-RIPS) in the RI Beam Factory (RIBF) has been developed. A prototype was constructed, and a test experiment using an  $^{40}\text{Ar}^{9+}$  beam with an energy of 24 MeV/nucleon and an intensity of 1.9 particle  $\mu\text{A}$  was performed.<sup>1)</sup> Simulation with the ANSYS code based on the finite element method could represent the data.<sup>2)</sup> A practical target system has been designed using the same simulation code.

The severest operating conditions for the production target in future Big-RIPS is a  $^{238}\text{U}$  primary beam with an energy of 350 MeV/nucleon and an intensity of 1 particle  $\mu\text{A}$  incoming onto a beryllium (Be) target with a 1-g/cm<sup>2</sup> 5.4 mm thickness (thickness/range = 0.36). The assumed beam-spot size of  $\phi$  1 mm in FWHM and an estimated total heat loss of 22 kW deposit quite a high energy with a density of 28 kW/mm<sup>2</sup> on the target surface and of 5.1 kW/mm<sup>3</sup> in a target volume. Under these conditions, adjustable parameters for the target design are disk size, rotation speed, and beam-spot position on the disk. A Be disk of 260 mm diameter and 4.4 mm thickness, and with a rotating speed of 500 rpm and a beam-spot position 10 mm from the edge of the water-cooled aluminum (Al) disk was designed as an expected parameter, because we have already constructed a prototype target disk of similar size. The beam-spot temperature dependence on these three parameters was investigated. A transversely Gaussian-shaped beam distribution with a size of  $\phi$  1 mm in FWHM was assumed and an energy loss function of the  $^{238}\text{U}$  beam in Be material was applied. Two types of boundary condition between the water-cooled Al disk and the cooling water were considered. One is an ideal case in which the temperature at the boundary was fixed at 25°C. The other is a realistic case in which the heat transfer coefficient at the boundary was 30 kW/(m<sup>2</sup>·K). From the result, the temperature distributions for both cases were almost the same. Thermal radiation from the surface of the Be disk was considered and a constant emissivity of 0.57 was used. Nonlinear time-dependent analysis was carried out taking the temperature dependence of heat conductivity and specific heat of the materials used into account. The typical heat conductivities and specific heats of the Be disk are 180 W/(m·K) and 1.98 J/(g·K) at room temperature, and 86 W/(m·K) and 2.89 J/(g·K) at 700°C.

Beam-spot temperature as a function of rotation speed is plotted in Fig. 1. When the rotation speed is faster than 300–500 rpm, the beam-spot temperature

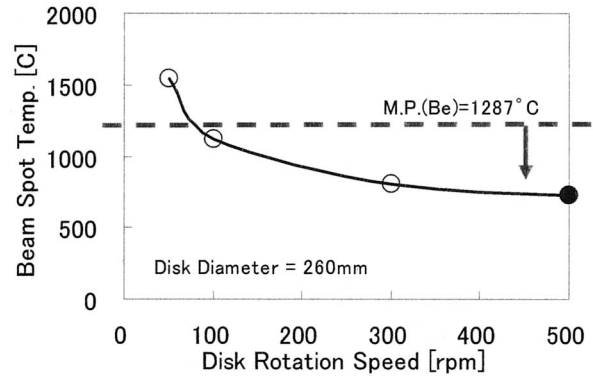


Fig. 1. Simulation result of beam-spot temperature as a function of disk rotation speed.

is sufficiently low compared to the Be melting temperature of 1287°C. Rotation speed does not considerably decrease beam-spot temperature at more than 500 rpm. The disk-size dependence of temperature is plotted in Fig. 2. The disk diameter being smaller than the expected parameter (260 mm in diameter) is not realistic because beam-spot temperature approaches the Be melting point. The temperature distribution in the radial direction including the beam spot is plotted in Fig. 3. As the beam-spot approaches the water-cooled Al disk, the temperature distribution of the Be disk decreases and we can get sufficient margin for both the melting temperatures of Be and Al.

From the result described above, the expected parameter of the rotating Be disk is acceptable even for the severest operating conditions. This applies to other operating conditions for primary beams lighter than

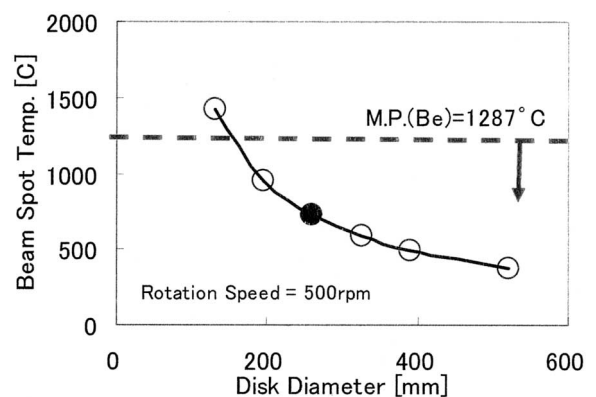


Fig. 2. Simulation result of beam-spot temperature as a function of disk diameter.

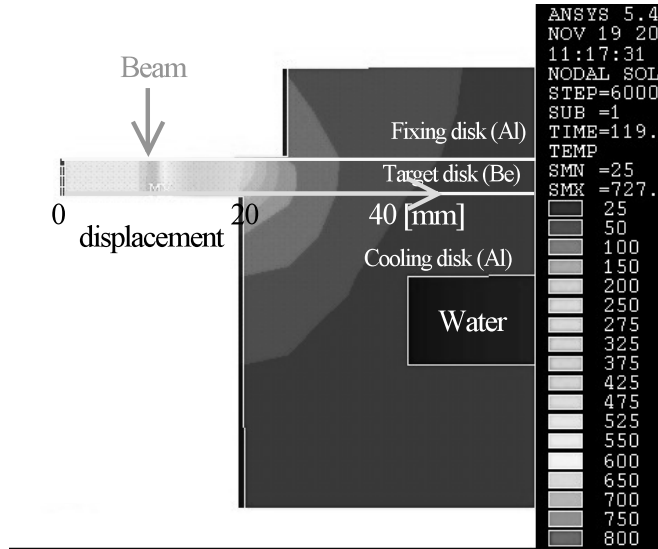
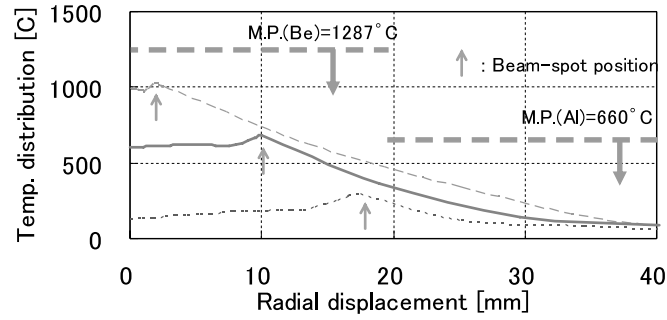


Fig. 3. Simulation result of temperature distribution in the radial direction of the target disk with changing the beam-spot position in the radial direction (up). Cross-sectional temperature distribution of the target disk near the beam spot (bottom) when the beam spot is 10 mm from the edge of the target disk.

the U beam, because such conditions are much less severe than the case discussed.

References

1) A. Yoshida et al.: RIKEN Accel. Prog. Rep. **34**, 188

(2001).  
 2) A. Yoshida et al.: RIKEN Accel. Prog. Rep. **35**, 152 (2002).

## Design of an air-core type superconducting quadrupole for the BigRIPS separator

K. Kusaka, T. Kubo, T. Tominaka, Y. Mizoi, K. Yoshida, A. Yoshida,  
N. Kakutani,\* T. Tsuchihashi,\* and K. Sato\*

Superconducting quadrupole magnets are to be used for the BigRIPS separator<sup>1)</sup> in the RI-beam factory project.<sup>2)</sup> Two types of superconducting magnets are planned for the BigRIPS. One is an iron-dominated (superferric) type in which quadrupole field distribution is mainly generated by hyperbolic cold iron poles. Superconducting coils are rigidly supported by a cold iron yoke.<sup>3)</sup> Since whole magnets are in the He vessel, its cryostat has simple structure and is characterized by small heat load, such that small cryocoolers are sufficient to keep coils superconducting.<sup>4)</sup>

The other is an air-core type in which only coils generate magnetic field. Since no cold iron is installed in the He vessel, its cold mass weight is much lower than that of the superferric type. With the smaller cold mass, the air-core magnets are adopted for the quadrupole triplet right after the production target, since it will be exposed to high neutron radiation from the target. The neutron radiation gives rise to significant additional heat load to the cold mass at 4.5 K in the He vessel. The smaller cold mass reduces the heat load to the cryogenic system. Furthermore, the quadrupoles right after the production target must have high field gradients in order to collect diverging RI beams efficiently. The air-core quadrupole is suitable for achieving high field gradients with good field quality without suffering magnetic saturation of iron poles. We here report the design of the air-core superconducting quadrupole triplet for the BigRIPS.

Figure 1 shows a schematic view of the superconducting coils forming a quadrupole triplet. The effective lengths and warm bore radii of three quadrupoles, P1, P2, and P3, are 500 mm, 800 mm, and 500 mm, and 90 mm, 120 mm, and 120 mm, respectively. The maximum field gradients of P1, P2, and P3 coils are

24 T/m, 20 T/m, and 20 T/m, respectively. The main parameters of quadrupoles are listed in Table 1.

As shown in Fig. 1, our coils have a racetrack shape and differ from a “ $\cos 2\theta$ ” type in which multistrand Rutherford cables are wound and compressed into a trapezoidal shape to form ideal current blocks. Since the requirement of uniformity of the field gradient is relatively moderate, we adopt a simple racetrack shape for easier coil winding. Sizes and positions of coils are optimized to maintain a single square racetrack coil per pole. Integrated 12-pole components scaled by the quadrupole component are estimated to be  $-4$ ,  $-2$ , and  $-2.8 \times 10^{-3}$  for P1, P2, and P3 coils, respectively.

We use a NbTi superconducting wire with a polyester-imide (PEI) insulator. PEI is chosen for the insulation material, because it is less sensitive to radiation than polyvinyl formal enamel (PVF) which is widely used for insulating superconducting wire. Since the nominal currents and resulting stored energies are high compared with those of the superferric type magnet, we use a rectangular wire instead of round ones. Table 2 summarizes the specifications of the superconducting wire.

Quench protection analysis is performed for the P2 coil whose stored energy is the highest. We have introduced a quench protection external resistor  $R_p$  connected in parallel in the excitation circuit. We assume that only one of the P2 coil quenches under the operating current of 625 A and magnetic field of 6.9 T. The current decays in  $\sim 5$  s and the maximum voltage and the temperature of the coil reach 897 (1361) V and 100 (117) K in the case of the external resistor  $R_p = 1.0$  (0.01)  $\Omega$ .

The winding of our flat racetrack coils are es-

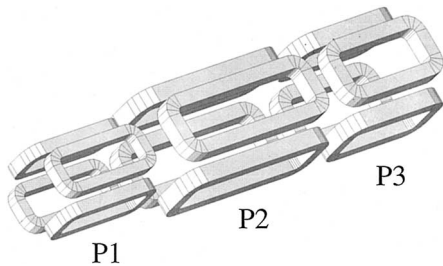


Fig. 1. Schematic of racetrack coils forming a quadrupole triplet.

Table 1. Main parameters of P1, P2 and P3 quadrupoles.

	P1	P2	P3
Effective magnetic length [m]	$\sim 0.5$	$\sim 0.8$	$\sim 0.5$
Warm clear bore radius [mm]	90	120	120
Max. field gradient [T/m]	24	20	20
Nominal current per pole [kA]	552	825	825
Number of turns	750	1320	1320
Nominal current [A]	735	625	625
Nominal current density [A/mm <sup>2</sup> ]	188	159	159
Straight length of coil [mm]	420	700	420
Max. field at coil [T]	6.0	6.9	7.0
Total length of coil [mm]	568	880	600
Inductance [H]	1.33	6.47	4.35
Stored energy [MJ]	0.36	1.26	0.85

\* Toshiba Corporation

Table 2. Main parameters of superconducting wire.

Conductor	NbTi
Bare conductor size [mm]	$2.28 \times 1.38$
Insulated size [mm]	$2.36 \times 1.46$
Insulator	PEI (Polyester-imide)
Cu/super ratio	1.33
Number of filaments	54
Filament diameter [ $\mu\text{m}$ ]	175
$I_c$ [A]	3300 at 5 T
	2700 at 6 T
	2100 at 7 T
	1450 at 8 T

essentially the same as that used for the superferric quadrupole triplets of the BigRIPS separator.<sup>1,2)</sup> Each coil is wound orderly on a mandrel by the wet winding method developed by Toshiba. Epoxy resin with fillers, which improves thermal conductivity and makes the thermal contraction rate similar to that of wire, is applied to coils by layer by layer.

Since the coils experience high magnetic field of  $|B| = 6\text{--}7\text{ T}$ , electromagnetic force acting on coil ends becomes much stronger than that of superferric magnets. Simulations based on the finite element method suggest that the entire outer circumference of the coil must be supported in order for the maximum shear stress not to exceed 10 MPa. If only the straight sections of the coil are supported, as in the case of superferric magnets, the maximum shear stress is estimated to be 22.7 MPa.<sup>a)</sup> We then introduced the stainless-steel nonmagnetic coil case to support coils.

Figure 2 shows a schematic view of the P2 coil case. The coils are supported by walls of the coil case with wedge sims and thin copper liners. The round coil ends are supported by the round stainless-steel spacers with wedge sims and liners made of glass and epoxy resin.

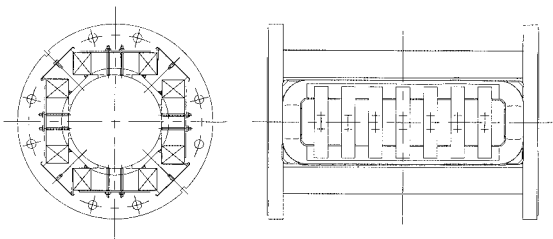


Fig. 2. Schematic view of P2 coil.

a) The maximum shear stress of the superferric magnet is 13 MPa.

FRP plates are attached to the coils for insulation, and the gap between coils and supporting materials is filled by the epoxy resin used in coil winding. The precision of the coil position is better than 0.5 mm. It should be noted that no preload to the coils is necessary, since the coils and the coil case contract almost at the same rate when they are cooled to 4.5 K.

Figure 3 shows a schematic cross sectional view of the cryostat. P1, P2, and P3 coils in their coil cases are connected rigidly to each other and form a quadrupole triplet. The He vessel, tightly connected to coil cases, is designed to be off-centered to use LHe efficiently. The He vessel, surrounded by the 80 K shield made of aluminum, is suspended by supporting rods made of CFRP or GFRP, and its position can be adjusted from outside the vacuum vessel. The end flanges of the vacuum vessel made of SS400 steel, play the role of a magnetic shield, so that stray field at the target position is less than 20 gauss. In the current port of the cryostat, newly designed gas-He cooled current leads are installed. Their design and R&D results are reported somewhere.<sup>5)</sup>

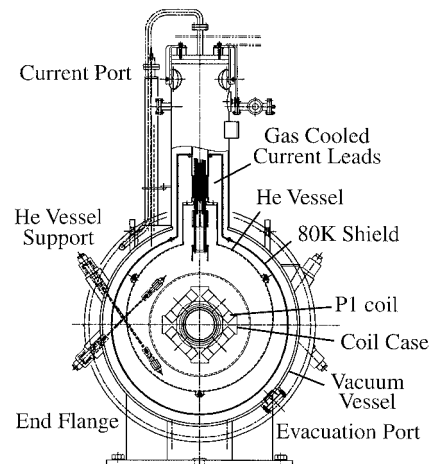


Fig. 3. Schematic view of cryostat.

#### References

- 1) T. Kubo: Nucl. Instrum. Methods Phys. Res. B **204**, 97 (2003).
- 2) Y. Yano et al.: AIP Conf. Proc. **600**, 161 (2001).
- 3) T. Hiramachi et al.: IEEE Trans. Appl. Supercond. **10**, 238 (2000).
- 4) K. Kusaka et al.: RIKEN Accel. Prog. Rep. **36**, 312 (2003).
- 5) N. Kakutani et al.: RIKEN Accel. Prog. Rep. **37**, 299 (2004).

## Gas-cooled current lead with multiple electrodes for BigRIPS superconducting quadrupoles

N. Kakutani,\* K. Kusaka, Y. Mizoi, A. Yoshida, K. Yoshida, T. Kubo, K. Ohsemochi,\*  
T. Yazawa,\* S. Monma,\* T. Kuriyama,\* and T. Tsuchihashi\*

Superconducting (SC) magnets for the BigRIPS in the RI beam factory project are used forming a quadrupole triplet with/without a superimposed sextupole coil. The three quadrupoles with/without sextupoles are installed in a single cryostat. While the coils are cooled by liquid helium, current leads are cooled by helium gas vapor. The electric currents are, in general, different among the coils in operation. This type of SC magnet, namely, a cryostat which contains more than two magnets, requires many gas channels for each current lead and complicated cooling gas control to prevent gas flow imbalance among the current leads. Furthermore, many gas channels require a larger current port and larger space for piping work.

We here report a new current lead for the BigRIPS SC magnets developed by Toshiba. It is a current lead with multiple electrodes in one cooling gas channel, with which no complicated multi-channel gas control is required. It also makes removal and installation work of magnets easier because the number of gas pipes is reduced. We shall report results of our R&D studies performed in Toshiba.

The newly developed current lead with multiple electrodes is shown in Fig. 1. The length of the lead, except the current input flange, is 816 mm and the diameter of the cylinder is 70 mm.

This current lead consists of four high-current electrodes for 800 A and a low-current electrode for 70 A positioned circularly in a cylinder. High-current electrodes correspond to the leads for the quadrupole coils and the low-current electrode corresponds to the lead for the sextupole coil. Each electrode is made of a bundle of phosphorous-deoxidized copper tubes. This current lead with multiple electrodes has the feature that

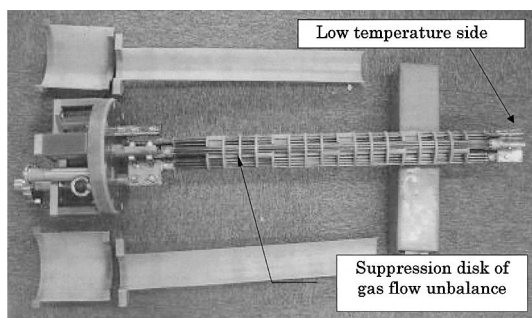


Fig. 1. Overview of gas cooled current lead with multiple electrodes.

cooling gas passes through spirally with disks vertically arranged across the electrodes. Therefore, cooling gas passes through all electrodes without concentrating around low-temperature electrodes, so that all the electrodes are well cooled even if the electric currents are different among electrodes.

The electric current excitation test of the lead was carried out in Toshiba. The maximum current for the test is 800 A for high-current electrodes. This current is sufficient for the BigRIPS SC magnets, whose maximum current is evaluated to be 733 A. The electric current excitation test of this lead was carried out by connecting the ends of the electrode in liquid helium bath with short-circuit bars. The schematic of the experimental setup is shown in Fig. 2.

The temperature distribution on the electrode was converted from the voltages measured by eight taps put on the electrode. Helium gas temperature is measured by thermo-couples and temperature sensors mounted on the electrode. Heat load was calculated from evaporated helium vapor mass flow. We measured the temperature and voltage in two kinds of excitation circuits. One is the “two-pole excitation” in which only two of the high-current electrodes are short-circuited and no current flows in the rest. The other is “four-pole excitation” in which the current flows in all of the high-current electrodes. We show, in Fig. 3, an example of the temperature distribution of the electrode with the excitation current of 800 A. Shown also are elec-

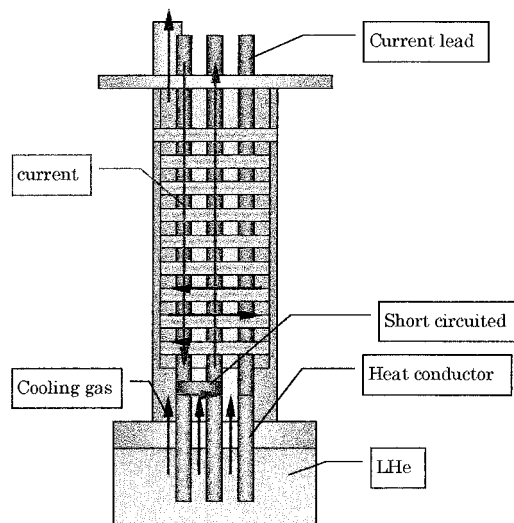


Fig. 2. Schematic of experiment.

\* Toshiba Corporation



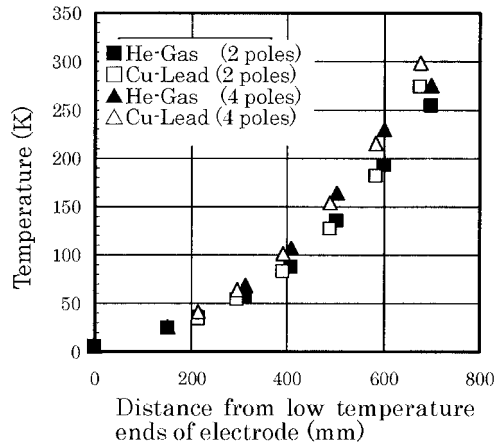


Fig. 3. Temperature change of the direction for current lead length (Current: 800 A).

trode and helium gas temperatures as functions of distance from the low-temperature side of the electrodes. A small difference between electrode and helium gas temperature is observed in both four-pole and two-pole excitations. In Fig. 4, heat load is shown as a function of current. The heat load for the four electrodes with a current of 800 A is evaluated to be 4.4 W. This value is lower than the twice of the ideal value,  $2 \times 3.3 = 6.6$  W, which is our design criterion. Heat load per electric current is then 1.3 mW/A and heat transfer efficiency between helium gas and current lead is evaluated to be

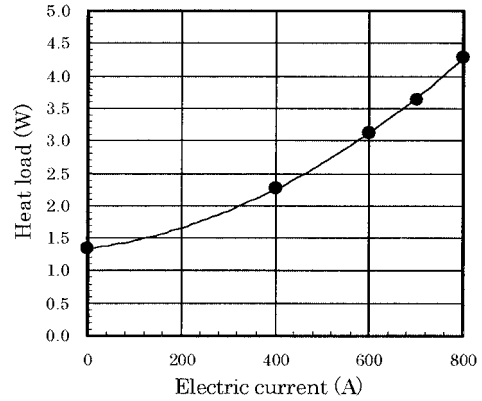


Fig. 4. Change of the heat leak by current.

0.8.<sup>1)</sup>

The gas-cooled current lead with multiple electrodes developed in Toshiba has been successfully tested. The multiple electrodes are efficiently cooled by helium vapor with a single gas channel. This newly developed current lead is going to be used in the SC quadrupole triplets in the BigRIPS. Five SC quadrupole triplets including air-core-type quadrupole triplet are now being fabricated in Toshiba.

References

- 1) M. N. Wilson: *Superconducting Magnets* (Clarendon Press, Oxford, 1983).

## Design of radiation shielding for the BigRIPS separator

K. Yoshida, T. Kubo, K. Kusaka, Y. Mizoi, A. Yoshida, E. Ideguchi,<sup>\*1</sup> and H. Kouzu<sup>\*2</sup>

Radiation shielding is one of the important issues in the design of a radioactive beam separator since huge radiation is expected to arise from the production target and the beam dump of the separator. The conceptual design of the shield has been made and was

published as a report.<sup>1)</sup> In the design, the BigRIPS separator will be placed in the big room of the east side of the underground of the accelerator building. The size of the room is 67.3 m long, 19.2 m wide and 14.0 m high. In the upper half of the separator, where strong

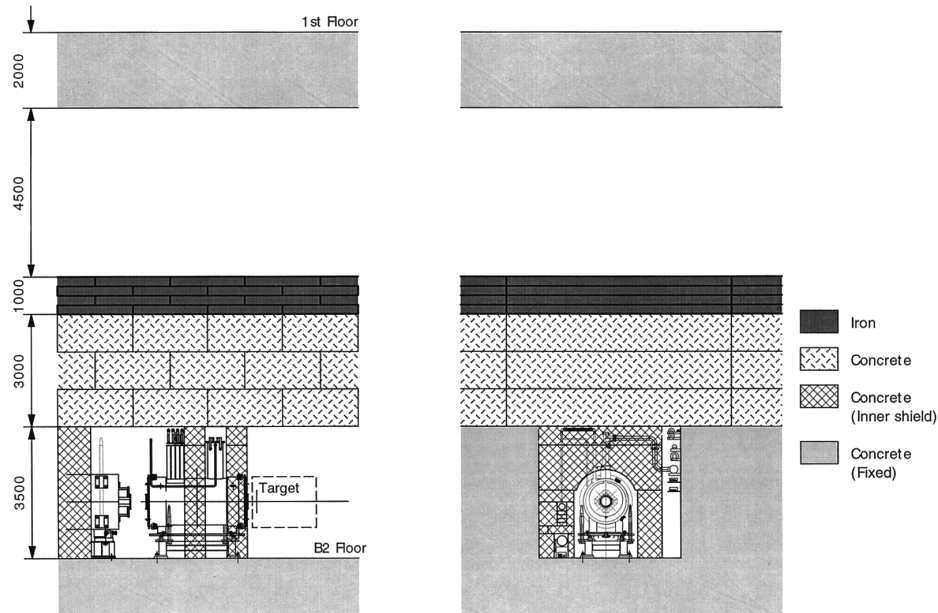


Fig. 1. Cross-sectional view of the shield around the first triplet Q-magnet of the BigRIPS separator.

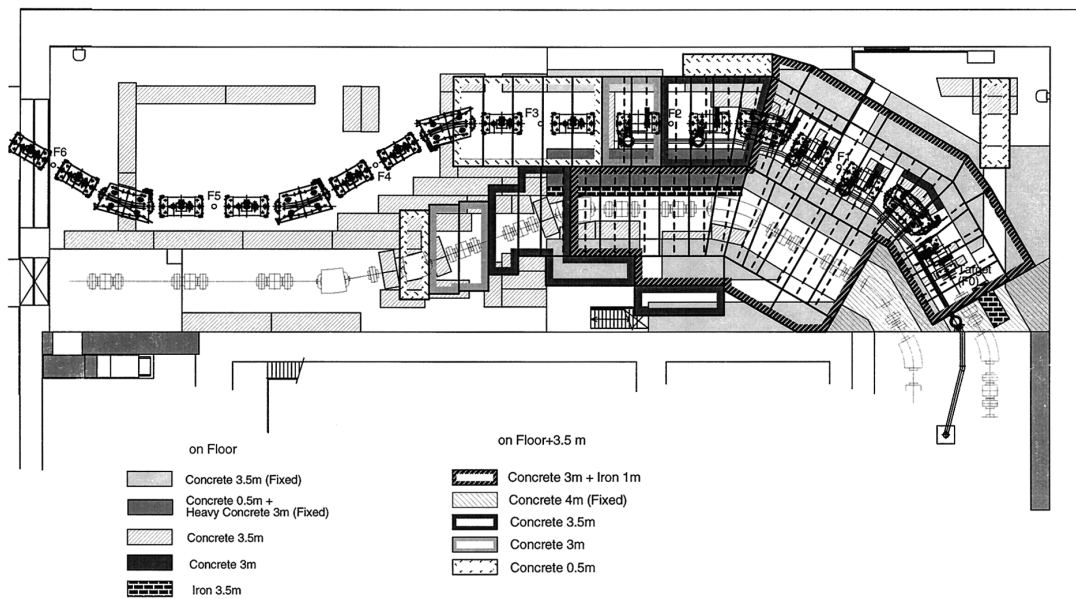


Fig. 2. Arrangement of shield blocks in the BigRIPS room.

<sup>\*1</sup> Center for Nuclear Study, University of Tokyo

<sup>\*2</sup> Toshiba Corporation

radiation is expected to arise, the fixed concrete walls with a height of 3.5 m are prepared on both sides of the separator. The concrete blocks with a maximum 5.5 m thickness covers the top of the separator. Instead of the 5.5 m thick concrete, the possibility of using iron blocks of 1 m thickness together with 3 m thick concrete blocks is suggested to save the necessary space.

The advanced design of the shield has been started based on the conceptual design. The discussion with the manufacturers shows that it is cost effective if the sizes of the blocks fulfill the following conditions:

- (1) Maximum size of the block is  $7\text{ m} \times 2.5\text{ m} \times 2.0\text{ m}$ .
- (2) Weight of the block should not exceed 30 tons.
- (3) Width of the block is a minimum of 1 m if the block is supported only at both ends.

In the original design, the typical block size was  $5.5\text{ m} \times 2.1\text{ m} \times 1.5\text{ m}$  and, hence, the size was reduced to

match the above condition. The protection of incidental equipments of the separator, such as the transfer tube of liquid He and their valves, is also considered in the design.

Figure 1 shows the cross-sectional view of the shields at the target area. The top of the target is covered with three layers of concrete blocks with a size of  $6\text{ m} \times 2\text{ m} \times 1\text{ m}$  together with four layers of iron blocks with a size of  $6\text{ m} \times 2\text{ m} \times 0.25\text{ m}$ . The shield blocks with elaborate shapes are placed around the magnet of the separator and protect the transfer tubes and the valves. The total arrangement of the blocks is shown in Fig. 2.

The further optimization of the design as well as the construction cost is now under way.

#### References

- 1) *Radiation Safety of RI Beam Factory*, RIBF Project Office, RIKEN, Wako, (2003).

# Conceptional design of the high-power beam dumps for BigRIPS

Y. Mizoi, T. Kubo, K. Kusaka, K. Yoshida, A. Yoshida, and T. Okuyama\*

Beam dumps for BigRIPS will be installed inside the vacuum chamber of the first dipole magnet (D1), and between D1 and the second superconducting triplet quadrupole magnet (STQ2). Figure 1 shows the schematic top view of these beam dumps and BigRIPS magnets, and the cross-sectional view of the beam dump inside the vacuum chamber.

Inside the vacuum chamber, vertically-tilted swirl- or screw-tube beam dumps<sup>1)</sup> are set at both ends in the horizontal plane in the vacuum chamber. Although the available space for the beam dump is limited, the tilted angle can be chosen to magnify the projected beam spot area on the beam dump so that the heat-flux density is sufficiently diluted for cooling. The promising tilted angle is approximately 9.8 degrees.

The beam dump between D1 and STQ2 is shown in Fig. 2. Its shape from the top view is that of a parallelogram with a corner angle of  $\Phi$ . The opening angle of the cross section is  $2\Theta$ . However the available space for this beam dump is limited, we can obtain the optimum shape to dilute the beam heat-flux density sufficiently by contriving its geometrical shape. The dilution factor by projection,  $F$ , is expressed as

$$F = \frac{1}{\sin \Theta} \times \frac{1}{\sin \Phi}. \tag{1}$$

Assuming that the available space between D1 and STQ2 is  $L$  and the beam spot diameter is  $2R$ ,  $F$  is

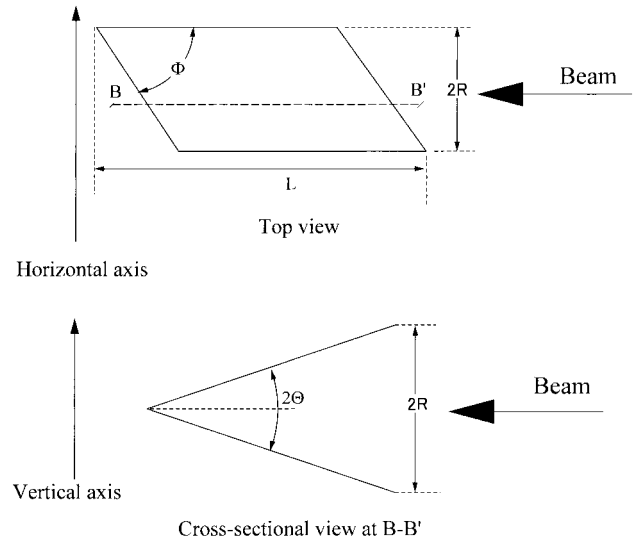


Fig. 2. Beam dump between D1 and STQ2. Its shape is useful for diluting the heat density not only horizontally but also horizontally.

expressed as

$$F = \frac{\sqrt{R^2 + \left(L - \frac{2R}{\tan \Phi}\right)^2}}{R} \times \frac{1}{\sin \Phi}. \tag{2}$$

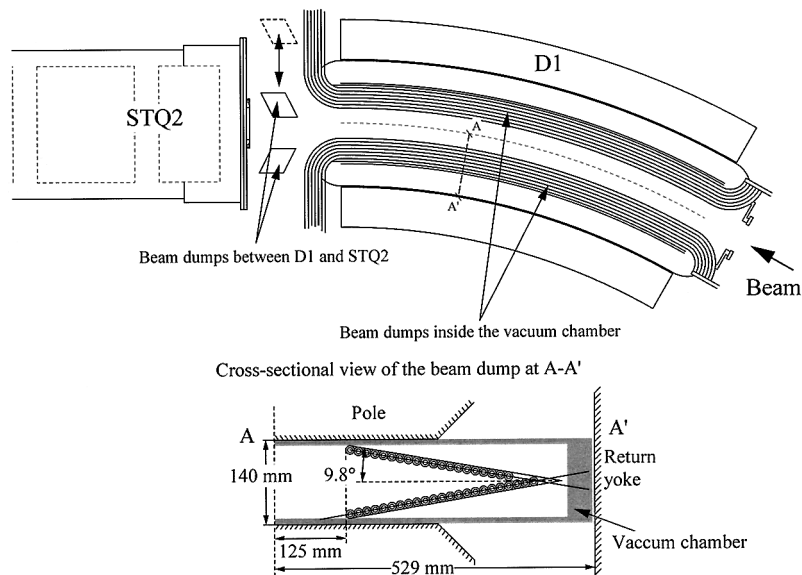


Fig. 1. Schematic top view of the beam dumps and BigRIPS magnets, and cross-sectional view of the beam dump inside the vacuum chamber. The beam dumps between D1 and STQ2 move horizontally according to  $B\rho$ . The available space between D1 and STQ2 is very limited.

\* Toshiba Corporation

Here, the maximum value of  $F$  can be derived from the differential equation of  $\partial F/\partial\Phi = 0$  under the condition of the limited values of  $L$  and  $R$ . We choose the preliminary values of  $L = 30$  cm and  $R = 2$  cm, then  $\Phi = 15$  degrees is obtained.

A promising material for the BigRIPS beam dump is CuCrZr which is also considered a candidate heat-sink material for ITER which can be used under high-heat-flux and high-neutron-flux conditions. Although

CuCrZr has sufficient heat-transfer coefficient and radiation hardness, we need to study the manufacturing process in relation to its mechanical hardness. We are continuing to research and develop high-power beam dumps.

#### References

- 1) Y. Mizoi et al.: RIKEN Accel. Prog. Rep. **36**, 318 (2003).

## Prototype of the high-power beam dump for BigRIPS

Y. Mizoi, T. Kubo, K. Kusaka, K. Yoshida, A. Yoshida, and T. Okuyama\*

We constructed a prototype beam-dump system in order to evaluate its cooling power for high-density heat flux. The prototype beam-dump system schematically shown in Fig. 1 consists of a prototype beam dump, a vacuum chamber, a high-pressure water pump ( $\sim 10$  atm), and measurement devices which are for water pressure and water temperature both inlet and outlet, and water flow at the outlet.

We are planning experiments using two heating methods for evaluating the ability of the prototype beam-dump system. One method is the laser-beam-irradiation heating method and the other is the heavy-ion-beam-irradiation heating method. Here, the prototype beam dump is the sample.

These methods are complementary to each other. In the former method, it is easy to control and monitor the irradiation area on the sample, although the absorbed power on it must be estimated indirectly due to its reflection. In the latter method, it is easy to estimate the deposited power on the sample, although the irradiation area on it is ambiguous.

A YAG or a CO<sub>2</sub> DC laser whose power is at least a few kW will be irradiated on the sample. Before the

experiment, we will measure the surface reflectance of the sample with a low-power laser beam in order to estimate the absorbed power. It is noted that the experiment with the laser beam irradiation can be performed in air without a vacuum chamber.

Heavy-ion beams, for example, <sup>40</sup>Ar with a power of approximately 2 kW (the energy is 24 MeV/nucleon and the intensity is 2 pμA) will be irradiated on the sample installed in the vacuum chamber.

In both experiments, the surface temperature of the sample will be monitored using an IR camera. In addition, thermocouples will be set near the irradiated area for the reference. The surface temperature of the sample will be measured as functions of heat-flux density, water temperature, water flow, and water pressure.

We will derive the cooling ability as a parameter of the heat-transfer coefficient of the sample from these data. Experimental results will be compared with the simulations<sup>1)</sup> and the feasibility will be demonstrated.

### References

- 1) Y. Mizoi et al.: RIKEN Accel. Prog. Rep. **36**, 318 (2003).

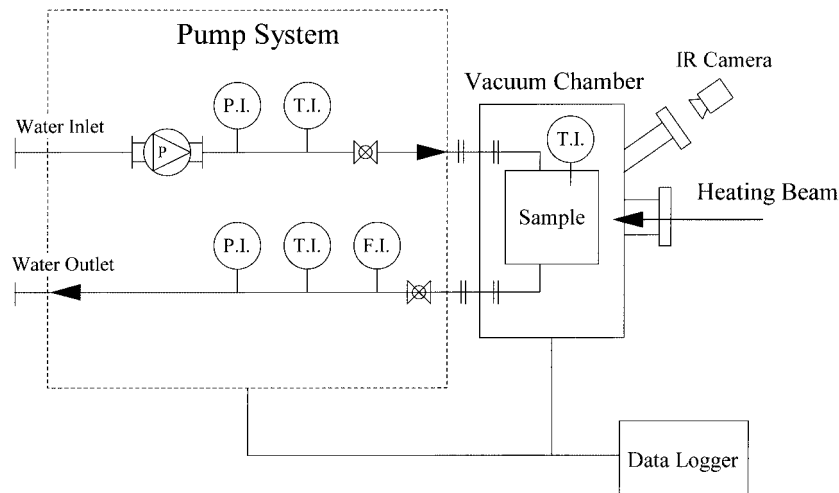


Fig. 1. Schematic diagram of the prototype beam-dump system. P: water pump, P.I.: pressure indicator, T.I.: temperature indicator, F.I.: flow indicator.

\* Toshiba Corporation

## Rf system with HOM damped cavity using SiC microwave absorbers for electron storage ring

T. Koseki and M. Izawa\*

An intense beam current is one of the essential characteristics for modern electron storage rings, such as high-luminosity colliders and high-brilliance synchrotron radiation sources. Evaluation and suppression of collective beam instabilities are very important issues in the storage rings. In particular, the solving the coupled-bunch instability due to higher order modes (HOMs) in rf cavity is a key task for achieving a high beam current limit. We have developed a 500 MHz rf cavity with a simple damped structure of HOMs.<sup>1,2)</sup> The cavity has a large diameter beam duct (140 mm) made of a silicon-carbide (SiC) microwave absorber. The HOMs are guided out of the cavity and dissipated by the absorber. The accelerating mode is not affected by the absorber since the frequency is sufficiently below the cutoff of the 140 mm duct. Figure 1 shows a schematic view of the damped cavity. The shunt impedance and the Q value for the accelerating mode are 7.7 MΩ and 44000, respectively. The available wall loss is 150 kW at maximum.

The damped cavities have been installed in the Photon Factory storage ring in KEK and pushed up the current limit of the ring to 800 mA, whereas the record current achieved with previously used cavities was approximately 500 mA.<sup>3)</sup> The damped cavity has also been installed and operated well in the New SUBARU ring, a 1.5 GeV synchrotron light source at the SPring-8 site. Recently, it was decided to adopt the cavity for the SAGA light source, a 1.4 GeV storage ring under construction in Tosu city, Saga prefecture.

In the damped cavity, HOMs with frequency lower than the cutoff frequency of the beam-duct cannot propagate in the beam duct. Some of the HOMs remain in the cavity with high impedance. For the reduction of impedances of the trapped modes, we have developed a simple HOM coupler<sup>4)</sup> as shown in Fig. 2.

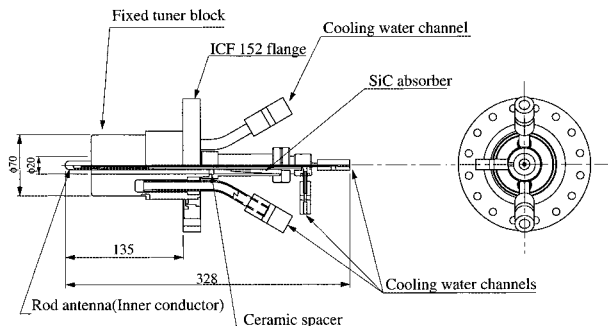


Fig. 2. HOM coupler.

It has a rod-shaped coupling antenna with a coaxial waveguide. The SiC piece attached to the end of the coaxial waveguide is made of the same material as the absorber at the SiC beam duct and absorbs the extracted HOM power. The copper block mounted on the ICF flange is used for detuning frequencies of a few trapped modes which are unable to couple with the rod antenna. In the center part of the cavity, there are two free ports at the side and bottom positions. The HOM couplers are attached to these free ports.

The damped cavity with the HOM coupler will be applied to the future Japanese high-brilliance synchrotron light source in the vacuum ultraviolet and soft X-ray region.<sup>5)</sup> The light source, called the Super SOR storage ring, is being designed by the nationwide collaboration of scientists and engineers from KEK, SPring-8, RIKEN, JAERI, UVSOR and universities in Japan. The circumference of the Super SOR ring is 280 m, the nominal emittance is 8 nm-rad and the required beam current is 500 mA at maximum. The ring has two 17-m long straight sections and twelve 6.2-m straight sections for intensive use of various kinds of insertion devices.

The rf system must provide sufficient accelerating voltage to compensate for the electron energy loss due to synchrotron radiation and to achieve a long beam lifetime. For the Super SOR ring, synchrotron radiation losses at the dipole magnets and the insertion devices are more than 100 kW with stored current of 500 mA. To replace the energy and to provide for a typical momentum acceptance of 3%, the peak accelerating voltage of 1.4 MV is required. Figure 3 shows calculated current dependence of rf power required for the accelerating voltage of 1.4 MV with two and three rf systems. In this calculation, the coupling coefficient between input coupler and the cavity is set to 1.7. Although stable operation with two rf systems is possi-

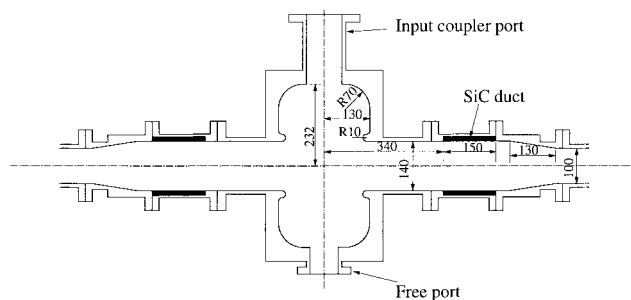


Fig. 1. Schematic view of the damped cavity.

\* High Energy Accelerator Research Organization (KEK)

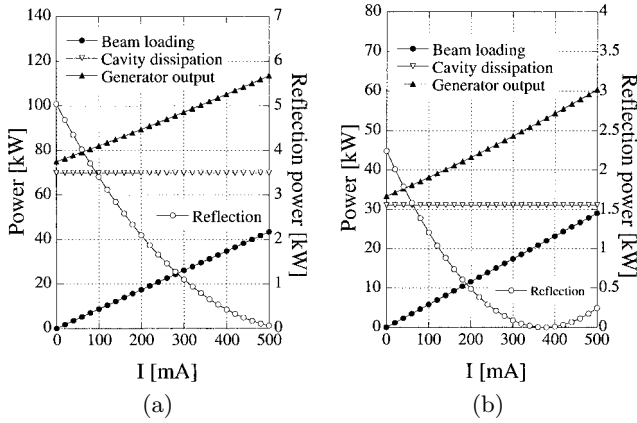


Fig. 3. Current dependence of rf power for (a) two rf system and (b) three rf system.

ble, unexpected trouble on one of the components may cause a long shutdown of the ring. Therefore, three rf systems operated under a moderate condition with a large safety margin are preferable.

Figure 4 shows the calculated longitudinal and transverse HOM impedances of the cavity. The critical impedances calculated by the Wang formalism<sup>6)</sup> for typical 1.8 GeV operation modes of the Super SOR ring are also indicated in the figure. The critical impedance denotes the impedance above which a coupled-bunch instability may occur at 500 mA. The HOMs with frequency higher than the cutoff frequency of the duct (1.64 GHz for TM01 and 1.26 GHz for TE11) are dissipated by the SiC duct and their impedances are reduced to the values below the critical impedances. For trapped modes, the impedances are damped by the HOM couplers. As shown in this figure, there are a

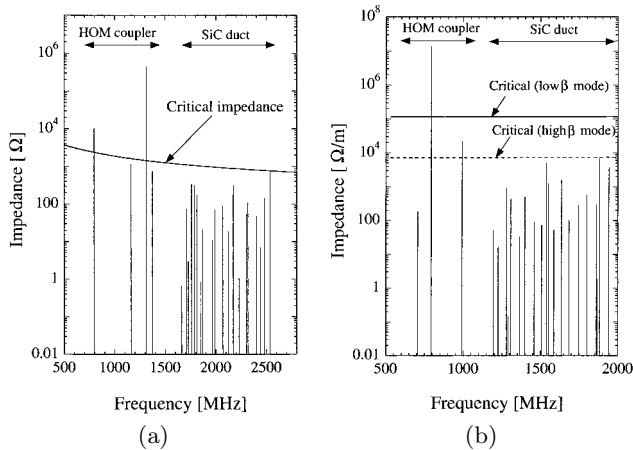


Fig. 4. Impedance of the damped cavity for (a) longitudinal and (b) transverse modes.

few surviving modes which cannot couple with the rod antenna of HOM coupler. The harmful ones among the surviving trapped modes are the longitudinal TM012-like mode (1312 MHz) and the transverse TM110-like mode (790 MHz). The TM110 mode, however, can be detuned easily so as not to induce the instabilities by choosing an appropriate length of the copper block of the HOM coupler. On the other hand, for the TM012 mode, the frequency shift by the copper block is not so large, and the detuning method is less effective. If a strong instability due to the TM012 mode occurs at the ring, an other method such as the bunch-by-bunch feedback method should be applied to suppress it.

Figure 5 shows a schematic layout of the rf station in the Super SOR ring. Three cavities are installed in one 6.2-m straight section. Each cavity is driven by one 200 kW klystron operating at 500.1 MHz. The power transmission system is composed of commercially available components of the WR1500 aluminum waveguide, a 100 kW dummy load and a circulator with 180 kW power capability.

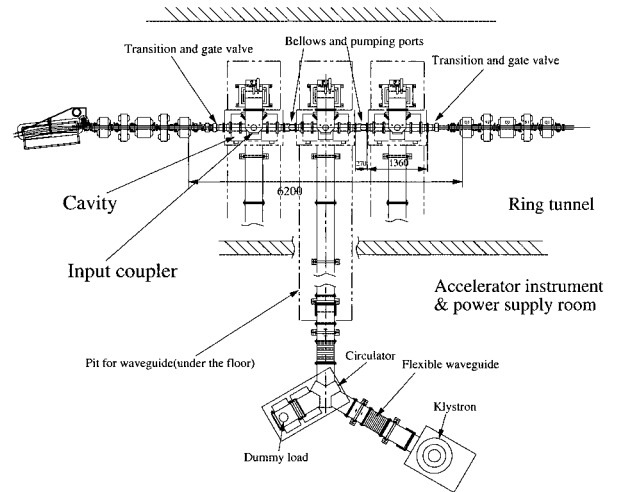


Fig. 5. Schematic layout of the rf station.

## References

- 1) T. Koseki, M. Izawa, and Y. Kamiya: *Rev. Sci. Instrum.* **66**, 1926 (1995).
- 2) T. Koseki: *Proc. Shanghai Symp. on Intermediate-Energy Light Source*, Shanghai, China, 2001-9, (Shanghai National Synchrotron Radiation Center (SSRC), 2001), p. 156.
- 3) M. Izawa et al.: *J. Synchrotron Radiat.* **5**, 369 (1998).
- 4) T. Koseki et al.: *Nucl. Instrum. Methods Phys. Res. A* **467/468**, 91 (2001).
- 5) *Vacuum Ultraviolet and Soft X-ray Synchrotron Light Source Project, Design Report* (Japanese Society for Synchrotron Radiation Research, Tokyo, 2002).
- 6) J. M. Wang: BNL-Rep. No. BNL-51302 (1980).



## Measurement of rf characteristics of magnetic-alloy-loaded cavity using cut-core configuration

M. Watanabe, Y. Chiba, K. Ohtomo,\* H. Tsutsui,\* T. Koseki, and T. Katayama

The accumulator cooler ring (ACR), a storage ring for the accumulation and cooling of RI beams, is being studied at RIKEN.<sup>1)</sup> In the ACR, an rf stacking method is used to capture injected RI beam bunches and to accumulate the beam to sufficient intensity.<sup>2)</sup> The stacking cavity is required to have a variable operation frequency from 20 to 40 MHz, rapid frequency sweep width of up to 0.4 MHz within 6 ms and maximum rf voltage of 50 kV. A combination of mechanical tuning of the center frequency and no-tuning broadband sweep around the center frequency using a low- $Q$  cavity is practical for our purpose. Recently, rf cavities using magnetic alloy (MA) cores have been developed at frequencies below 16 MHz.<sup>3-5)</sup> They have a marked broadband feature because of the low  $Q$  value of the MA cores. In the previous report,<sup>6)</sup> we presented the measured characteristics of the MA cores in the frequency range from 0.1 to 40 MHz. The  $Q$  value of MA is too low (less than 1) for use in the ACR stacking cavity, for which the  $Q$  value of several tens is suitable. To increase the effective  $Q$  value of a MA-loaded cavity, the use of a cut core with air gaps has been studied at several facilities.<sup>5,7)</sup> We have studied the rf characteristics of a cut-core-loaded cavity to examine its practicability in the frequency region of the ACR.

We fabricated a test vessel which has a coaxial structure comprising of copper as the outer conductor (O.D. = 450 mm) and aluminum as the inner conductor (I.D. = 132 mm). Figure 1 shows a schematic of the cut core in a test cavity. The core material is

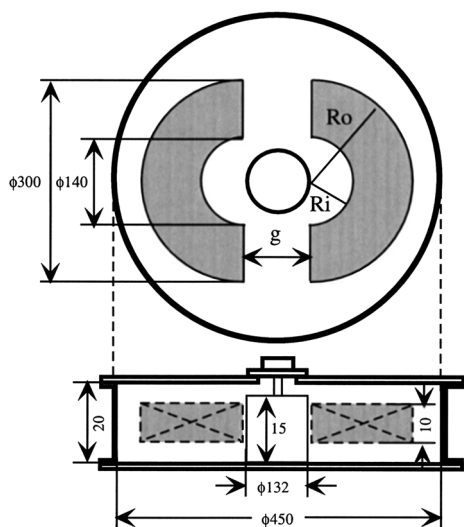


Fig. 1. Test vessel and cut core.

FINEMET (FT-3M) which is an iron-based nanocrystalline magnetic alloy made by Hitachi Metals, Ltd.<sup>8)</sup> The core is made of thin tape wound into a toroidal shape. The tapes are coated with SiO<sub>2</sub> for insulation. The size of the core of 140 mm I.D., 300 mm O.D. and 10 mm height is the actual size of the core to be used in the ACR stacking cavity. We set distances between the core and the inner walls of the cavity to be more than 5 mm to keep the stray capacitance small. The equivalent circuit of the cavity can be represented using a parallel  $LCR$  circuit; the admittance is given by

$$Y = 1/Rsh + j(\omega Cg - 1/\omega L), \tag{1}$$

where  $Rsh$  is shunt impedance,  $Cg$  is parasitic capacitance and  $L$  is inductance of the cavity. The parasitic capacitance  $Cg$  is estimated to be approximately 30 pF.

We measured the admittance of the cut-core-loaded cavity using a network analyzer (HP4195A) with an impedance test kit (HP41951A) in the frequency range from 1 to 50 MHz. Figures 2 and 3 show the gap dependences of  $Rsh$  and  $L$ , respectively. As shown in Fig. 2, a larger gap width gives a smaller  $Rsh$  value at a lower frequency. On the other hand,  $Rsh$  does not become very small by extending the gap width in the frequency region of ACR. As can be seen in Fig. 3,  $L$  remains almost constant with frequency for various gap widths. We try to explain these results using

$$L = (\mu_0 d)(Ro - Ri)/(2g) + k, \tag{2}$$

where  $\mu_0$  is the permeability in vacuum,  $g$  is the air

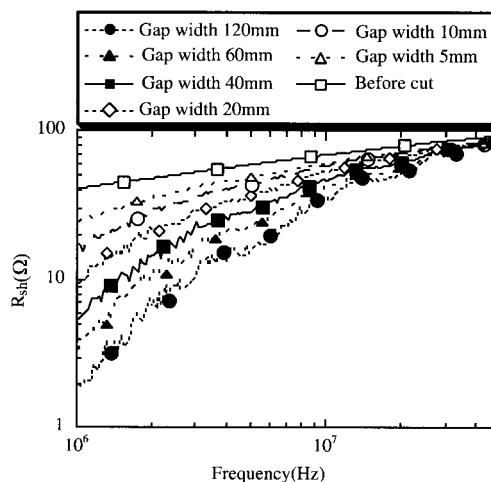


Fig. 2. Frequency vs. shunt impedance of the cut-core-loaded cavity.

\* Sumitomo Heavy Industries, Ltd.

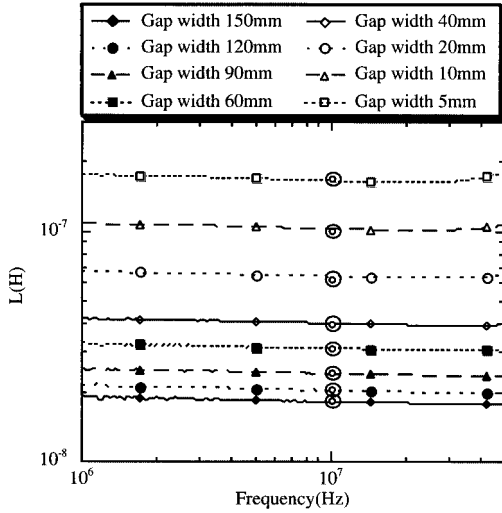


Fig. 3. Frequency vs. inductance of the cut-core-loaded cavity.

gap width between two circular halves of the core and  $R_i$ ,  $R_o$ , and  $d$  are the inner diameter, outer diameter and height of the core, respectively. This equation with  $k = 0$  is generally used for the approximate calculation of the magnetic circuit with an air gap in the low-frequency range. The  $k$  in Eq. (2) is introduced to correct the effect of leakage flux around the air gaps. For example, at the air gap width of 150 mm, the first term of Eq. (2) is calculated to be 3.4 nH, while the  $k$  is estimated to be 15 nH. We found that  $k = 8.75 \times 10^{-9}(2g)^{-0.45}$  gives the best fit of the measured data. The values calculated using Eq. (2) are plotted in Fig. 3 using double open circles.

Figure 4 shows gap dependence of the  $Q$  value, which is calculated by  $Q = Rsh/\omega L$ . As can be seen from the figure, it is more effective to expand the gap width at higher frequency. The  $Q$  value of approximately 20, which is the appropriate value for the ACR cavity, can be obtained at 30 MHz by choosing the air gap width of approximately 120 mm.

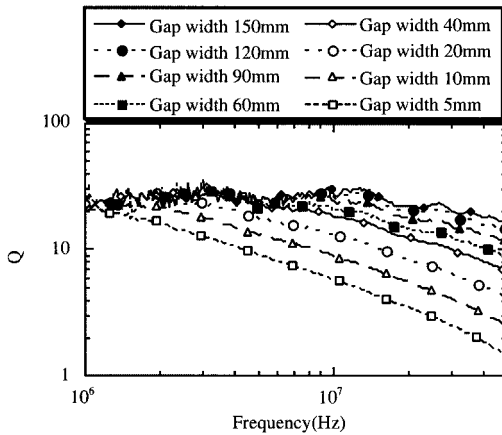


Fig. 4. Frequency vs.  $Q$  value of the cut-core-loaded cavity.

Figure 5 shows the relationship between the  $Q$  value and the total gap length divided by the average magnetic path length,  $2g/(2\pi\bar{r} + 2g)$ , for the frequency as a parameter. In this figure, the open marks indicate the regular-sized core (I.D. = 140 mm, O.D. = 300 mm, height = 10 mm) and the closed marks indicate a small-sized core, (I.D. = 140 mm, O.D. = 200 mm, height = 25 mm). From the fitted line, we obtain the empirical formula,

$$Q = a[2g/(2\pi\bar{r} + 2g)]^b, \quad (3)$$

$$a = 86.0f^{-0.182}, \quad b = 0.30f^{0.236},$$

where  $f$  is in MHz.

In these measurements, the power fed into the cavity was as low as 0.3 mW. Additional measurements at several higher input power levels up to 30 W for FT-3M were carried out using an rf source and an external high-power directional coupler together with the impedance analyzer. The measured results were almost the same as those of the low-power measurements as expected. Since the rf characteristics of FT-3M are stable up to high rf magnetic flux density of 0.2 T,<sup>9)</sup> the obtained data can be utilized for designing an actual cavity used at a high-power level.

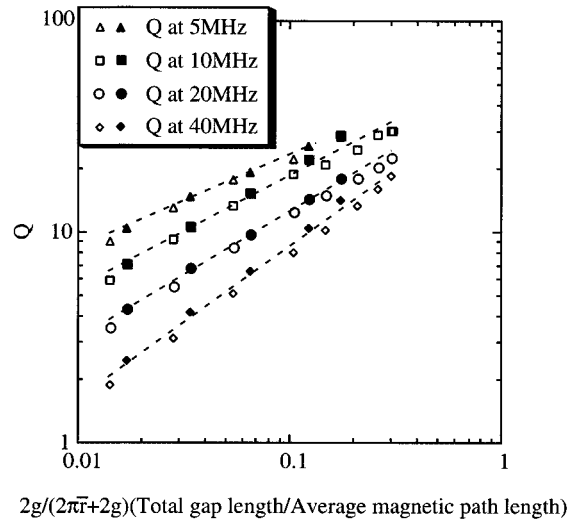


Fig. 5.  $Q$  value of the cut-core-loaded cavity for frequency as a parameter.

#### References

- 1) T. Katayama et al.: MUSES Conceptual Design Report (2000).
- 2) K. Ohtomo et al.: Proc. EPAC2000 (2000), p. 566.
- 3) Y. Mori et al.: Proc. EPAC98 (1998), p. 299.
- 4) M. Boehnke et al.: Proc. PAC1999 (1999), p. 851.
- 5) M. Yoshii et al.: Proc. EPAC2000 (2000), p. 984.
- 6) M. Watanabe et al.: RIKEN Accel. Prog. Rep. **36**, 325 (2003).
- 7) J. Dey et al.: Proc. PAC2001 (2001), p. 882.
- 8) Y. Yoshizawa et al.: J. Appl. Phys. **64**, 6047 (1988).
- 9) Y. Tanabe et al.: Proc. APAC98 (1998), p. 390.

## Development of an HTS-SQUID DC current monitor

T. Watanabe, S. Watanabe,\*1 T. Ikeda, Y. Sasaki,\*2 M. Kase, T. Kawaguchi,\*3 and T. Katayama

A highly sensitive cryogenic DC current monitor for the measurement of the intensity of faint beams, such as a radioisotope beam, was developed for the RIKEN RI beam factory project.<sup>1-4)</sup> This monitor is composed of a high-temperature superconducting (HTS) magnetic shield and an HTS current sensor including an HTS superconducting quantum interference device (SQUID), which are cooled by a low-vibration pulse-tube refrigerator. Since the principles of destructive detectors are based on the interaction between the beam and material, the beam is distorted by scattering or energy loss. However, the HTS-SQUID DC current monitor can measure the beam current nondestructively and avoid those problems. Both the HTS magnetic shield and the HTS current sensor based on Bi<sub>2</sub>-Sr<sub>2</sub>-Ca<sub>2</sub>-Cu<sub>3</sub>-O<sub>x</sub> (Bi-2223) were fabricated by dip-coating on a 99.9% MgO ceramic substrate. Recently, a prototype of the HTS-SQUID monitor was completed and we carried out the first measurements using DC heavy ion beams.

Prior to the measurements using heavy ion beams, we carried out an off-line test. The first output signal was observed using a feeding sine wave of 1 μA and 1 Hz into a Cu rod which was set in the beam chamber. Next, we confirmed that the measured beam current is not dependent on the beam position or beam radius by changing the position and the radius of the Cu rod. The dynamic range of this monitor was measured by changing the simulated beam current which was supplied into the Cu rod. The output voltage of the SQUID electronics as a function of the simulated beam current was measured and the dynamic range of 100 dB (from 1 μA to 0.1 A) was obtained by changing the feedback gain of the SQUID electronics.<sup>5,6)</sup> Furthermore, in order to investigate noise sources, not only the vibration originating from the ground but also that generated by the pulse-tube refrigerator itself was analyzed using accelerometers and an FFT in time and frequency domains. As a result, the amplitude of the vibration was found to be within 6 μm at the frequency band from 0.1 Hz to 20 Hz.

After completing the off-line test, we carried out the first beam test of the HTS-SQUID monitor which was installed in the beam transport line for the ECR ion source in the CNS experimental hall. The measurement was successfully performed and the system was removed to the beam transport line (E1 experimental hall) of the RIKEN Ring Cyclotron (RRC) to measure the current of a high-energy heavy ion beam

(Fig. 1). Figure 2 shows the measured signals of the HTS-SQUID monitor (above) and those of the Faraday cup monitor (below) where a 7 μA H<sup>+</sup> beam (a) and a 600 nA Ar<sub>40</sub><sup>17+</sup> beam (b) were used. The beams were pulsed and the zero level of the signals indicated that beams were stopped.

To improve the coupling between the input coil of the SQUID and the magnetic flux induced by the beam current, we are investigating the possibility of fabricating the HTS coil at the bridge circuit, and introducing a high permeability core in the SQUID chip. We aim to measure several nA beams nondestructively to make the system applicable to physics and biology experiments, and an ion implanter.

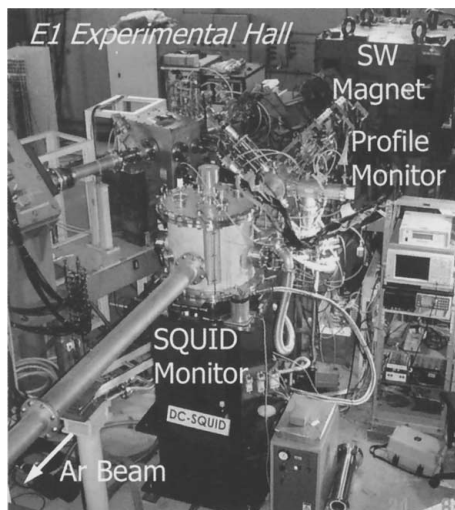


Fig. 1. Beam transport line (E1 experimental hall) of the RIKEN Ring Cyclotron (RRC).

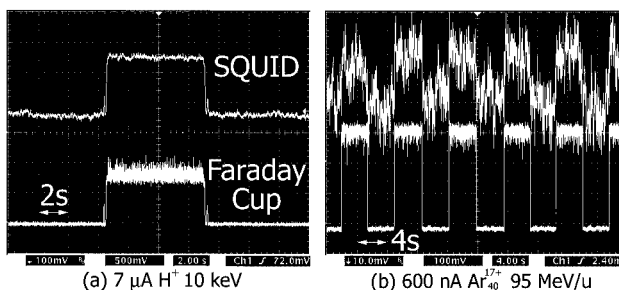


Fig. 2. Measured signals of the HTS-SQUID monitor (above) and those of the Faraday cup monitor (below) where a 7 μA H<sup>+</sup> beam (a) and a 600 nA Ar<sub>40</sub><sup>17+</sup> beam (b) were used.

\*1 Center for Nuclear Study, Graduate School of Science, University of Tokyo  
 \*2 Matsushita Electric Industrial Co. Ltd.  
 \*3 KT Science Ltd.

## References

- 1) T. Watanabe et al.: RIKEN Accel. Prog. Rep. **35**, 314 (2002).
- 2) T. Watanabe et al.: Proc. 8th European Particle Accelerator Conf., Paris, France, 2002-6, (EPS-IGA, 2003) p. 1995.
- 3) T. Watanabe et al.: RIKEN Accel. Prog. Rep. **36**, 331 (2003).
- 4) T. Watanabe et al.: CNS Annu. Rep. **59**, 71 (2003).
- 5) T. Watanabe et al.: Proc. 6th European Conf. on Applied Superconductivity 2003 (EUCAS 2003), Sorrento, Italy, 2003-9, to be published.
- 6) T. Watanabe et al.: Proc. 14th Symp. on Accelerator Science and Technology, Tsukuba, 2003-11, (KEK, 2003) p. 99.

## Feasibility of projectile-fragment-beam separation from a secondary beam in a storage ring<sup>†</sup>

M. Takanaka

An ion species of a beam is separated from a secondary beam of nuclear projectile fragments usually by using a projectile fragment separator in a transport line. At Radioisotope Beam Factory, the separated beam is planned to be injected and cooled in a storage ring before it is used for colliding experiments.<sup>1)</sup> The fragment separator has the side effect of enhancing the transverse emittance on the beam.<sup>2)</sup>

The new separation method proposed here, which does not have the side effect, is as follows. A secondary beam of nuclear projectile fragments is injected into a storage ring. After stochastic pre-cooling is applied to the beam, electron cooling is applied in order to separate ion species of the beams in the longitudinal phase space. A given ion species of the beam is rf-captured and accelerated for the sake of horizontal separation.

The space-charge effects on the separation have been studied using the simulation code that was developed to study bunch shortening of an electron-cooled ion beam.<sup>3)</sup> The longitudinal field is calculated approximately as

$$\frac{i}{2\pi} \sum_{k=0}^2 \left[ \frac{Z_{\parallel}^k}{n} \right]_{sp} \frac{dI^k}{ds}, \quad (1)$$

where  $s$  is the longitudinal coordinate,  $k$  the moment mode of the charge distribution (monopole, dipole, and quadrupole),  $\left[ \frac{Z_{\parallel}^k}{n} \right]_{sp}$  the longitudinal space-charge impedance when the transverse charge distribution is assumed to be Gaussian, and  $I^k$  the beam current.

The revolution time  $\tau$  of a particle with mass deviation  $\Delta m$  and momentum deviation  $\Delta p$  per charge has the following deviation  $\Delta\tau$ :

$$\frac{\Delta\tau}{\eta\tau} = \frac{\Delta p}{p} + \frac{\Delta m}{\eta\gamma^2 m} = \frac{\gamma^2 \Delta v}{v} + \frac{\Delta m}{\eta\gamma_t^2 m}, \quad (2)$$

where  $v$  is the velocity,  $\gamma = 1/\sqrt{1-v^2/c^2}$ ,  $\gamma_t$  is the transition gamma, and  $\eta$  is the slippage factor. If ion species of beams with different  $\Delta m$  are extremely stochastically cooled, they can all be overlapped in the  $\Delta\tau/\eta\tau$  space. When they are extremely electron-cooled or the velocity spread  $\delta v/v = 0$ , they are separated by  $\Delta m/\eta\gamma_t^2 m$  from the beam with  $\Delta m = 0$  in the  $\Delta\tau/\eta\tau$  space, or they circulate at their own revolution frequencies in the ring. Therefore, a given ion species of a beam can be rf-captured after electron cooling.

Using 40,000 macroparticles, particle tracking has been simulated in order to realize the separation pro-

cess after stochastic cooling (the series of electron cooling, rf capture, and acceleration). As a pre-cooled secondary beam, a 220 MeV/u beam of  $^{55}\text{Ni}^{28+}$ ,  $^{53}\text{Co}^{27+}$ , and  $^{51}\text{Fe}^{26+}$  fragments with the sixfold-rms momentum spread of  $10^{-3}$  and the rms transverse emittances of  $10^{-6}$  m rad starts to be electron-cooled. Simulated results of electron cooling in Fig. 1 show that, after electron cooling for 80 ms, the separation into the three ion species of beams in the  $\Delta\tau/\eta\tau$  space is dependent on the secondary-beam current. The higher the beam current, the larger the friction among ion species of beams that comes from the longitudinal charge-density fluctuation. Some of one ion species of a beam circulate together with the other ion species at their own revolution frequencies.

The  $\Delta\tau/\eta\tau$  separation between two neighboring beams is  $0.5 \times 10^{-4}$  after cooling. It takes 7 ms to rf-capture the  $^{53}\text{Co}^{27+}$  beam, with the rf voltage linearly increasing from 0 V with time, to produce the rf-bucket area of  $4\pi\delta p/p = 1.2\pi \times 10^{-4}$  (half-spread  $\delta p/p = 0.3 \times 10^{-4}$ ). The voltage reaches 66 V for a 180 m circumference of the ring and rf harmonics  $h = 40$ . During the capture, electron cooling is repeatedly switched off for 0.1 ms and on for 0.2 ms in order to suppress the whirling vortex of the bunched

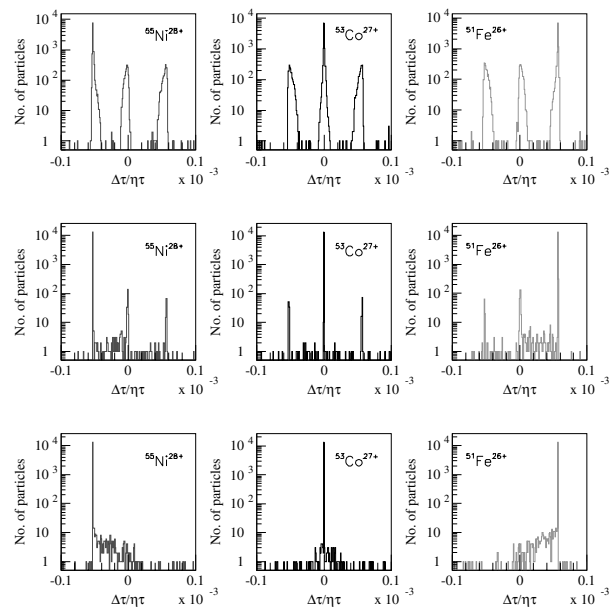


Fig. 1. Separation into ion species of beams in the  $\Delta\tau/\eta\tau$  space after electron cooling. The upper, the middle, and the lower panels are for the secondary-beam currents of 1 mA, 0.1 mA, and 0.01 mA, respectively.

<sup>†</sup> Condensed from the article in Proc. 14th Symp. on Accelerator Science and Technology, Tsukuba, 2003-11 (2003) p. 407.

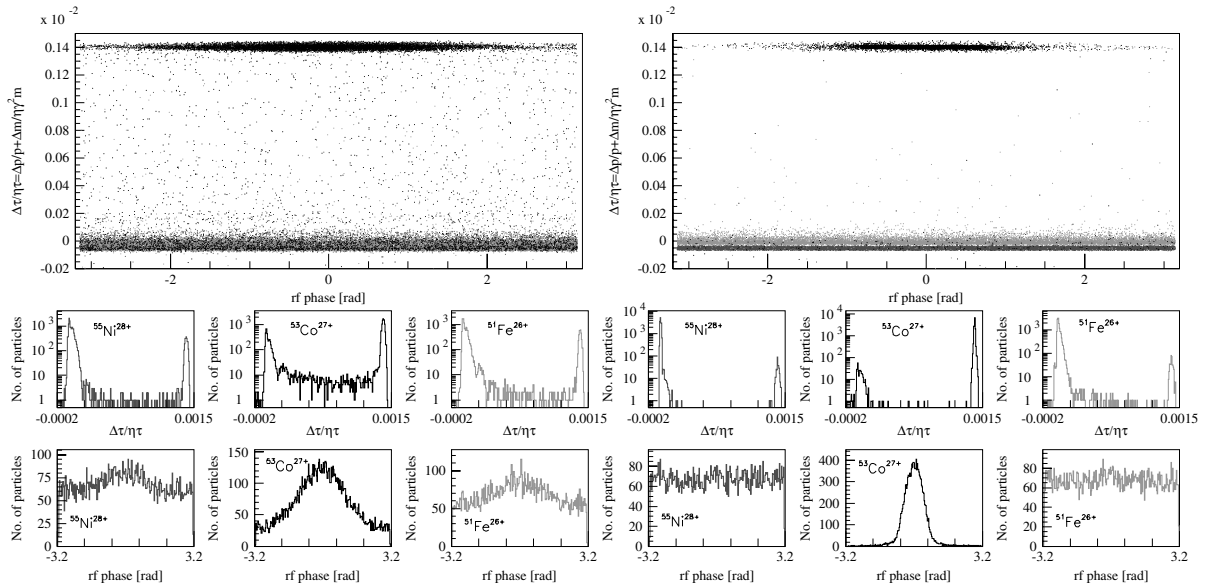


Fig. 2. Longitudinal phase-space distribution after pre-acceleration. The left and the right panels are for the secondary-beam currents of 1 mA and 0.1 mA, respectively.

beam in the rf bucket. Then, since the charge line density has few local peaks other than the main peak, the longitudinal space-charge effects can be lightened.

Pre-acceleration to make the momentum gain  $\Delta p/p = 1.4 \times 10^{-3}$  takes 17 ms with the rf-bucket area fixed and the electron-cooling turned off after the capture. The maximum rf voltage and synchronous phase are 273 V and 20 degree, respectively. Simulation results of the acceleration in Fig. 2 reveal that during the acceleration, the beam partially spills out of the rf bucket for the secondary-beam current of 1 mA, but not for that of 0.1 mA. Only the  $^{55}\text{Ni}^{28+}$  and the  $^{51}\text{Fe}^{26+}$  beam that circulated at the  $^{53}\text{Co}^{27+}$  revolution frequency at the end of electron cooling are seen to contaminate the separated  $^{53}\text{Co}^{27+}$  beam. The contamination rate is 2% for the secondary-beam current of 0.1 mA. The contamination is avoided when the secondary-beam current is less than about 0.01 mA, as is seen from Fig. 1.

The acceleration separates the  $^{53}\text{Co}^{27+}$  beam from the remaining beams by  $\Delta p/p = 1 \times 10^{-3}$  in the  $\Delta\tau/\eta\tau$  space, but not in the horizontal space because the transverse emittance is not very small ( $\epsilon_{rms} = 0.4 \times 10^{-6}$  m rad for the secondary-beam current of 1 mA). Next acceleration has to be applied to the separated beam with a larger rf bucket area corresponding

to  $\delta p/p = 1 \times 10^{-3}$  in order to make the separation greater and faster. The required rf voltage is higher by three orders than in the case of pre-acceleration. There is the option to use lower  $h$  for bunching again because the rf voltage can be high enough to shorten the acceleration time.

In conclusion, simulations using a particle-tracking simulation code have revealed that the novel separation of an ion species of a beam from a multicomponent beam in a storage ring has the following performance. The momentum of each ion species of a beam is not made perfectly monochromatic by electron cooling when longitudinal friction due to the charge-density fluctuation is induced in the multicomponent beam beyond a threshold of the secondary-beam current. Then, a species of a beam cannot be rf-captured without contamination due to the other species. The beam can be accelerated without spilling out of the rf bucket below about ten times the threshold.

#### References

- 1) T. Katayama et al.: Nucl. Phys. A **626**, 545 (1997).
- 2) C. C. Yun: RIKEN-AF-AC-30 (2001).
- 3) M. Takanaka: Phys. Rev. Spec. Top. Accel. Beams **6**, 104201 (2003).

## Numerical simulation of crystalline ion beam

H. Tsutsui,\*1 T. Katayama, I. Meshkov,\*2 A. Sidirin,\*2 A. Smirnov,\*2 E. Syresin,\*2 and D. Möhl\*3

After a simulation code for crystalline ion beams was developed in 2002, the code was applied to some ion rings such as the ESR ring<sup>1)</sup> and the TARN-II ring.<sup>2)</sup> This article is a summary of the results.<sup>3)</sup>

The ESR lattice functions and nominal parameters are shown in Fig. 1 and Table 1, respectively. There are two dispersion-free straight sections for electron cooling. Moreover, in order to reduce the transition gamma, dispersion function is high in the middle of the arc sections. Hence, the lattice functions are relatively complicated. In this ring, the 1D crystalline state of  $10^3 - 10^4$  ions was observed.<sup>1)</sup> The simulations using this code are in good agreement with the experiments, which were already shown last year.<sup>4)</sup>

Since we are interested in accumulating two orders of magnitude more (typically  $N = 10^6$ ) ions in the 1D crystalline state, we carried out simulations with increased cooling rate, expecting beam cooling technology innovation in the near future (Fig. 2). From the figure,  $N = 5 \times 10^5$  or more ions in the 1D state

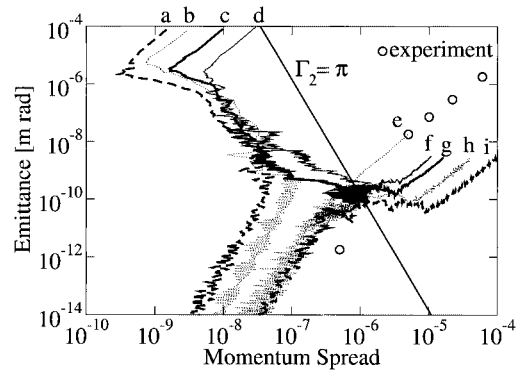


Fig. 2. Evolution of ion beam parameters during the cooling process for different initial emittances, momentum spreads, and cooling strengths, in the case of the ESR ring. The cooling strengths are  $\eta = 4 \times 10^{-2}$  (a, i),  $2 \times 10^{-2}$  (b, e, h),  $5 \times 10^{-3}$  (c, g), and  $2 \times 10^{-3}$  (d, f). The straight line corresponds to the criterion  $\Gamma_2 = \pi$  in Ref. 3.  $N = 5 \times 10^5$ . The one dimensional crystalline state is achieved when  $\eta \geq 2 \times 10^{-2}$ , irrespective of the initial beam emittance and momentum spread.

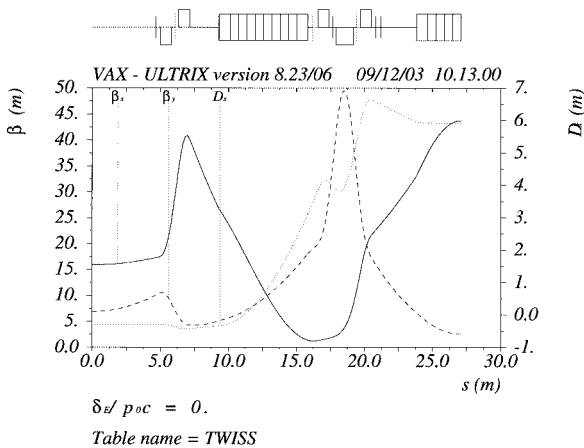


Fig. 1. Lattice functions of ESR.

Table 1. Nominal ring parameters used for the simulation study.

	ESR	TARN-II
Circumference (m)	108.36	77.76
Super-periodicity	2	6
Transition gamma	2.59	1.88
Tune (H/V)	2.27/2.27	1.67/1.81
Ion species	$^{197}\text{Au}^{79+}$	
Energy (MeV/u)	360	

\*1 Sumitomo Heavy Industries, Ltd.

\*2 Joint Institute for Nuclear Research, Russia

\*3 European Organization for Nuclear Research (CERN), Switzerland

can be achieved using an effective cooling system (a, b, e, h, i). Also, it is interesting that there is a forbidden low-momentum-spread region where the beam parameters make a detour (a, b, c, d). This is considered to be due to heating in the longitudinal direction by intrabeam scattering<sup>5)</sup> and longitudinal-horizontal coupling.

The TARN-II ring is considered to be desirable for making 2D or 3D crystalline states because the phase advance per cell can be lower than  $\pi/2$  by changing the strengths of the quadrupoles.<sup>6)</sup> The lattice functions of this ring are shown in Fig. 3, which are more regular

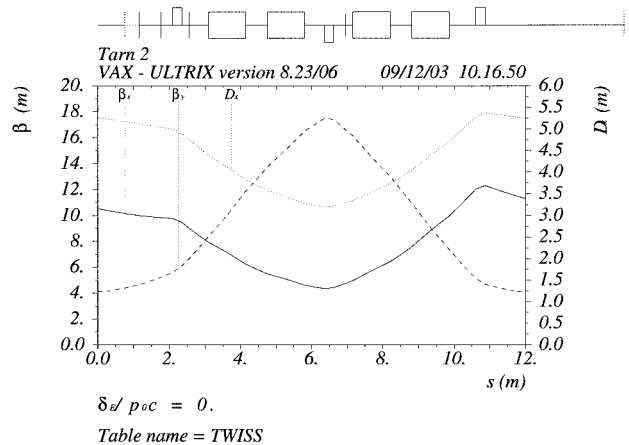


Fig. 3. Lattice functions of TARN-II.

than those of the ESR. We carried out simulations with nominal parameters as shown in Table 1.

The results are shown in Fig. 4. As in the ESR case, more than  $N = 5 \times 10^5$  particles can be accumulated in the 1D crystalline state, by using an effective cooling system. The difference between the two cases is that the required cooling strength for the TARN-II is relatively lower than that for the ESR. This is considered to come from the lattice flatness. Figure 5 shows the number of stored ions in the 1D crystalline state as

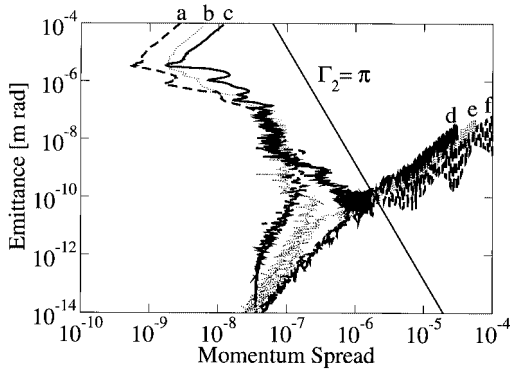


Fig. 4. Evolution of ion beam parameters during the cooling process for different initial emittances, momentum spreads, and cooling strengths, in the case of the TARN-II ion ring. The cooling strengths are  $\eta = 2 \times 10^{-2}$  (a, f),  $5 \times 10^{-3}$  (b, e), and  $2 \times 10^{-3}$  (c, d). The straight line corresponds to the criterion  $\Gamma_2 = \pi$  in Ref. 3.  $N = 5 \times 10^5$ . The one dimensional crystalline state is achieved when  $\eta \geq 5 \times 10^{-3}$ , irrespective of the initial beam emittance and momentum spread.

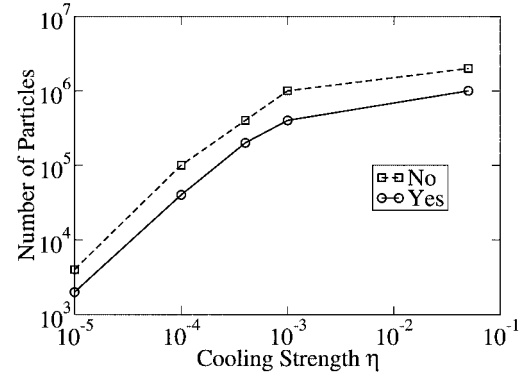


Fig. 5. Number of stored ions in the TARN-II ring as a function of longitudinal cooling strength (transverse ones are 10 times less), with (Yes) and without (No) ordering.

a function of the longitudinal cooling strength, in the case of the TARN-II ion ring. The number of particles is proportional to the strength at low cooling strength and saturates at around  $N = 10^6$ . This saturation is considered to be due to the space charge tune shift.<sup>7)</sup>

#### References

- 1) M. Steck et al.: Phys. Rev. Lett. **77**, 3803 (1996).
- 2) A. Noda: Proc. PAC87 (1987), p. 845.
- 3) I. Meshkov et al.: RIKEN-AF-AC-42 (2003).
- 4) H. Tsutsui et al.: RIKEN Accel. Prog. Rep. **36**, 327 (2003).
- 5) J. D. Bjorken and S. K. Mtingwa: Part. Accel. **13**, 115 (1983).
- 6) H. Okamoto: Private communication.
- 7) D. Möhl and T. Katayama: RIKEN-AF-AC-40 (2002).



## Routine work for radiation safety in the ring cyclotron facility

Y. Uwamino, S. Fujita, S. Ito, H. Sakamoto, T. Yamaki, T. Ito,<sup>\*1</sup> T. Nakamura,<sup>\*2</sup>  
T. Iwasa,<sup>\*2</sup> and M. Kase

We report here the residual radioactivity and leakage radiation level at the Ring Cyclotron Facility.

Residual radioactivities in the Ring Cyclotron Facility were measured at various locations using ionization-chamber survey meters.

The measurements were performed almost after every beam experiment as well as during the routine overhaul period. The routine overhaul period started immediately after the experiment which was carried out with the  $^{12}\text{C}$  beam of 92 MeV/nucleon in the E6 experimental vault from July 22 to 31, 2003. The dose rates at the deflectors in the injector AVF cyclotron and the Ring Cyclotron were found to be 0.5 mSv/h on Aug. 8, 2003 and 15 mSv/h on Aug. 29, 2003, respectively, during the overhaul period.

In addition to the above routine measurement, dose rates inside the injector AVF cyclotron were measured on March 19, 2003 after the new deflector had been installed and operated for a week. The dose rates were 3.5 mSv/h at the deflector and 4.0 mSv/h at the magnetic channel. A minor rearrangement was done with the deflector after the measurement.

During the period from Oct. 1, 2002 to Sept. 30, 2003, the dose rates were measured along the beam lines. Spots **a–z**, marked by bullets in Fig. 1, are the places where the dose rates exceeded  $30\ \mu\text{Sv/h}$ . Table 1 summarizes the observed dose rates and gives the dates when the measurements were performed. The maximum dose rate was found to be 20 mSv/h ( $20000\ \mu\text{Sv/h}$ ) at the beam duct in the beam distribution corridor denoted by **o** in Fig. 1. Whenever we observed a high dose rate, we roped off the area and posted a sign warning that it was dangerous to remain for a long time in that place.

We also continuously monitored the leakage radiation from the Ring Cyclotron Facility. Having analyzed the collected data of leakage neutrons, we found that the radiation levels in the controlled area were much lower than the allowable dose limit. The leakage of  $\gamma$ -rays and neutrons was below the detection limit of the environmental monitors. We evaluated the radiation level at the boundary of the accelerator facility using the monitor which was installed in the computer room on the ground floor immediately above a

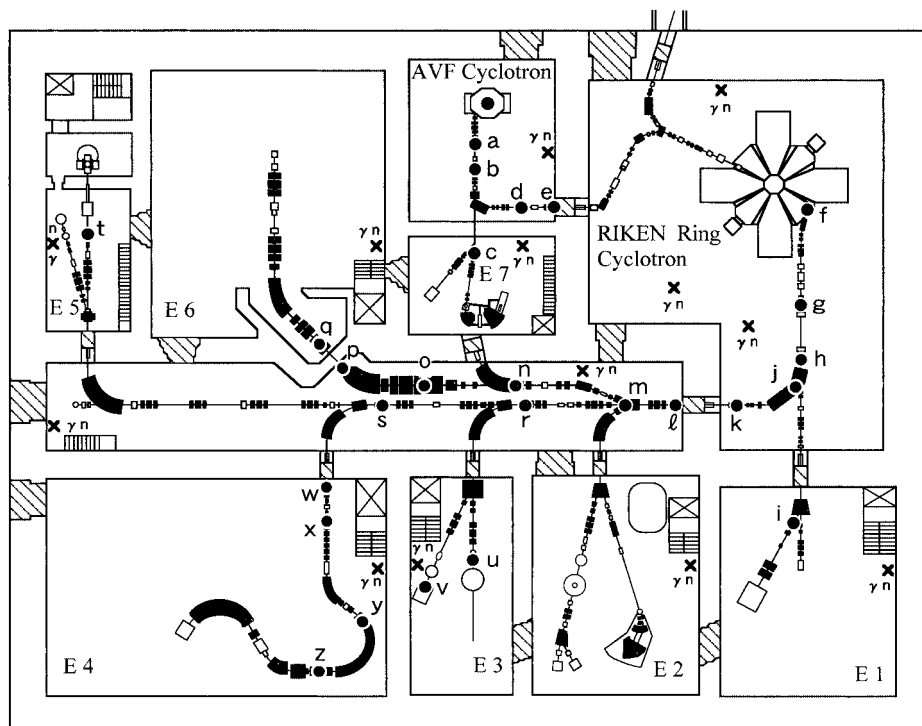


Fig. 1. Layout of the RIKEN Ring Cyclotron Facility as of 2003. Measured locations of residual radioactivities along the beam lines are shown by bullets **a–z**.

<sup>\*1</sup> Science Service, Inc.

<sup>\*2</sup> Tokyo University of Science

Table 1. Summary of the dose rates measured along the beam lines with ionization-chamber survey meters. Detection points **a-z** indicate the measured locations shown in Fig. 1.

Detection point	Measured dose rate ( $\mu\text{Sv/h}$ )	Date	Particle	Energy (MeV/u)	Intensity (enA)	Period (days)
<b>a</b>	60	Aug 1, '03	C-12	92	600	8
<b>b</b>	40	Aug 1, '03	C-12	92	600	8
<b>c</b>	50	Feb 14, '03	Ne-20	8.2	1500	7
<b>d</b>	55	Aug 1, '03	C-12	92	600	8
<b>e</b>	50	Aug 1, '03	C-12	92	600	8
<b>f</b>	380	Apr 4, '03	C-13	100	540	3
<b>g</b>	5500	Aug 1, '03	C-12	92	600	8
<b>h</b>	200	Aug 1, '03	C-12	92	600	8
<b>i</b>	45	Jun 30, '03	Ar-40	95	750	1
<b>j</b>	100	Aug 1, '03	C-12	92	600	8
<b>k</b>	180	Aug 1, '03	C-12	92	600	8
<b>l</b>	100	Aug 1, '03	C-12	92	600	8
<b>m</b>	720	Jan 30, '03	Ar-40	64	700	8
<b>n</b>	2000	Oct 31, '02	Ar-40	95	700	5
<b>o</b>	20000	Aug 1, '03	C-12	92	600	8
<b>p</b>	150	Apr 4, '03	C-13	100	540	3
<b>q</b>	30	Jun 20, '03	Kr-86	63	2600	18
<b>r</b>	65	Aug 1, '03	C-12	92	600	8
<b>s</b>	32	Apr 4, '03	C-13	100	540	3
<b>t</b>	40	May 26, '03	N-14	135	1	1
<b>u</b>	65	Feb 4, '03	P	210	1	1
<b>v</b>	280	Apr 14, '03	N-14	135	1600	1
<b>w</b>	80	May 1, '03	d	100	30	1
<b>x</b>	35	May 1, '03	d	100	30	1
<b>y</b>	40	May 1, '03	d	100	30	1
<b>z</b>	30	May 1, '03	d	100	30	1

bending magnet which guided the beams from the ring cyclotron vault to the distribution corridor. As a result, we obtained a radiation level of approximately  $5 \mu\text{Sv}/\text{year}$  which was much lower than the allowable dose limit ( $1 \text{mSv}/\text{year}$ ).

The routine operation of the Ring Cyclotron was started in April, 1987, and many experimenters, workers and visitors have entered the Nishina radiation con-

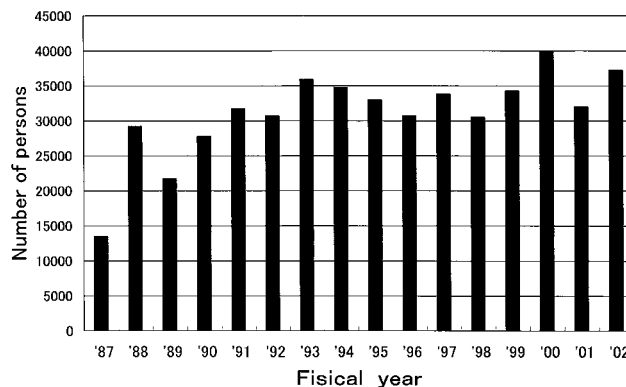


Fig. 2. Annual total number of persons who entered the Nishina radiation controlled area.

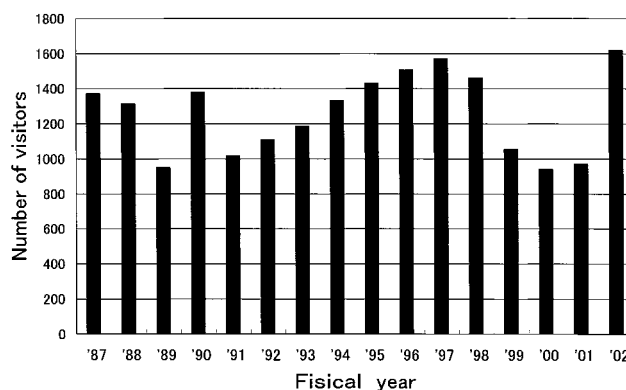


Fig. 3. Annual total number of visitors to Nishina radiation controlled area. “Visitors” do not include experimenters and workers.

trolled area. The annual total numbers of persons and visitors that entered the area are shown in Figs. 2 and 3, which are about 35000 and about 1500, respectively; their grand total numbers since 1987 are 497204 and 20230.

## VI. LIST OF PUBLICATIONS

### 1. Accelerator development and accelerator physics

- Y. Matsuda, K. Nagamine, T. Matsuzaki, K. Ishida, I. Watanabe, S. Nakamura, N. Kawamura, P. Bakule, P. Strasser, F. L. Pratt, Y. Miyake, K. Simomura, S. Makimura, and G. H. Eaton: “Upgrading the RIKEN-RAL Muon Facility”, *Hyperfine Interact.* **138**, 489–495 (2001).
- S. Kohara, A. Goto, O. Kamigaito, M. Kase, N. Sakamoto, S. Watanabe, and T. Katayama: “Construction of the flat-top acceleration system in the RIKEN AVF cyclotron”, *Proc. 13th Symp. on Accelerator Science and Technology, (RCNP, Osaka University), Suita, 2001–10, RCNP, Osaka University, Suita*, pp. 235–237 (2001).
- Y. Yano: “RIKEN RI beam factory project”, *Ind. J. Phys.* **76S**, 1–7 (2002).
- H. Ueno and K. Asahi: “Production of radioactive ion beams in the RIBF-RIPS configuration”, *Proc. RIKEN Symp. on Condensed Matter Studies with Radioactive Ion Beams, Wako, 2002–2*, edited by K. Asahi, Y. Kobayashi, and W. Sato, RIKEN, Wako, pp. 54–58 (2002).
- H. Watanabe: “High-spin isomer beams at RARF”, *Proc. RIKEN Symp. on Condensed Matter Studies with Radioactive Ion Beams, Wako, 2002–2*, edited by K. Asahi, Y. Kobayashi, and W. Sato, RIKEN, Wako, pp. 67–70 (2002).
- T. Watanabe, M. Kase, and T. Katayama: “Development of a highly sensitive beam current monitor with a SQUID and superconducting magnetic shield”, *Cryogenic Eng.* **38**, 509–521 (2003).
- M. Kidera, T. Nakagawa, S. Enomoto, K. Takahashi, R. Hirunuma, K. Igarashi, T. Ohyama, M. Fujimaki, E. Ikezawa, O. Kamigaito, M. Kase, and Y. Yano: “Accelerator mass spectrometry using electron cyclotron resonance ion source and heavy ion accelerator”, *Nucl. Study* **48**, 163–170 (2003).
- M. Takanaka: “Instability during bunch shortening of an electron-cooled beam”, *Phys. Rev. Spec. Top.: Accel. Beams* **6**, 104201-1–104201-10 (2003).
- M. Takanaka: “Feasibility of separation of an ion species of beam from a secondary beam in a storage ring”, *Proc. 14th Symp. on Accelerator Science and Technology, (KEK), Tsukuba, 2003–11, KEK, Tsukuba*, pp. 407–409 (2003).
- O. Kamigaito, M. Kase, N. Sakamoto, E. Ikezawa, S. Kohara, M. Fujimaki, T. Nakagawa, M. Kidera, Y. Higurashi, H. Ryuto, Y. Chiba, M. Hemmi, Y. Miyazawa, T. Chiba, T. Aihara, T. Ohki, H. Hasebe, H. Yamauchi, A. Uchiyama, K. Oyamada, A. Goto, and Y. Yano: “Present status of the RIKEN heavy-ion linac”, *Proc. 14th Symp. on Accelerator Science and Technology, (KEK), Tsukuba, 2003–11, KEK, Tsukuba*, pp. 708–710 (2003).
- S. Ozawa and M. Hamagaki: “Preparation of self-supporting boron films by electron-beam-excited plasma”, *Proc. 20th Symp. on Plasma Processing, (Division of Plasma Electronics, The Japan Society of Applied Physics), Nagaoka, 2003–1, The Japan Society of Applied Physics, Tokyo*, pp. 283–284 (2003).
- O. Kamigaito, M. Kase, E. Ikezawa, S. Kohara, N. Sakamoto, M. Fujimaki, T. Nakagawa, M. Kidera, Y. Higurashi, Y. Chiba, M. Hemmi, Y. Miyazawa, T. Chiba, T. Aihara, T. Ohki, H. Hasebe, H. Yamauchi, A. Uchiyama, K. Oyamada, and Y. Yano: “Present status of the RIKEN heavy-ion linac”, *Proc. 28th Linear Accelerator Meet. in Japan (LAM28), (J-PARC and others), Tokai-mura, 2003–7 ~ 8, JAERI, Tokai-mura*, pp. 22–24 (2003).
- T. Kikuchi, M. Nakajima, K. Horioka, and T. Katayama: “Transverse particle distributions of intense beams after final bunching for heavy ion inertial fusion”, *J. Plasma Fusion Res.* **80**, 87–88 (2004).

### 2. Nuclear physics and nuclear instrumentation

- K. Asahi, H. Ogawa, K. Sakai, A. Yoshimi, M. Tsuda, Y. Uchiyama, T. Suzuki, K. Suzuki, N. Kurokawa, M. Adachi, A. Yoshida, S. Fukuda, M. Notani, T. Kubo, H. Okuno, H. Sato, N. Fukunishi, N. Aoi, K. Yoneda, H. Iwasaki, N. Fukuda, M. Ishihara, H. Izumi, H. Ueno, T. Shimoda, S. Tanimoto, N. Takahashi, H. Miyatake, W.-D. Schmidt-Ott, and M. Schaefer: “Nuclear moments measurements with polarized radioactive beams”, *Application of Lasers in Atomic Nuclei Research: Proc. 4th Int. Workshop of Laser Spectroscopy on Beams of Radioactive Nuclei, (Joint Institute for Nuclear Research), Poznan, Poland, 1999–5, Joint Institute for Nuclear Research, Dubna*, pp. 127–134 (2000).
- H. Madokoro, J. Meng, M. Matsuzaki, and S. Yamaji: “Relativistic mean field description for the shears band mechanism in  $^{84}\text{Rb}$ ”, *Phys. Rev. C* **62**, 061301(R)-1–061301(R)-5 (2000).
- T. Suzuki and GSI-RIKEN-Kurchatov-Comenius Collaboration: “Measurements of interaction cross sections for nuclei far from stability at relativistic energies”, *AIP Conf. Proc.* **561**, 259–268 (2001).
- K. Asahi, K. Sakai, H. Ogawa, H. Ueno, Y. Kobayashi, A. Yoshimi, H. Miyoshi, K. Yogo, A. Goto, T. Suga, N. Imai, Y. Watanabe, K. Yoneda, N. Fukuda, N. Aoi, W.-D. Schmidt-Ott, G. Neyens, S. Teughels, A. Yoshida, T. Kubo, and M. Ishihara: “Nuclear moment studies with polarized radioactive nuclear beams”, *AIP Conf. Proc.* **570**, 109–118 (2001).
- H. Ogawa, K. Sakai, H. Ueno, T. Suzuki, K. Asahi, H. Miyoshi, M. Nagakura, K. Yogo, A. Goto, T. Suga,

- T. Honda, N. Imai, Y. Watanabe, K. Yoneda, A. Yoshimi, N. Fukuda, N. Aoi, Y. Kobayashi, W.-D. Schmidt-Ott, G. Neyens, S. Teughels, A. Yoshida, T. Kubo, and M. Ishihara: “Effective charge anomaly in neutron-rich nuclei revealed from spin-polarized RI beam experiments”, *AIP Conf. Proc.* **570**, 679–683 (2001).
- K. Asahi, Y. Kobayashi, H. Ueno, A. Yoshimi, W. Sato, H. Watanabe, H. Miyoshi, and D. Kameda: “Radioactive ion beams as microscopic probes into matter”, *Anal. Sci.* **17**, No. Suppl., i613–i616 (2001).
- K. Asahi, H. Ogawa, H. Ueno, Y. Kobayashi, W. Sato, A. Yoshimi, H. Watanabe, D. Kameda, H. Miyoshi, K. Sakai, N. Imai, K. Yoneda, Y. Watanabe, N. Fukuda, N. Aoi, A. Yoshida, T. Kubo, and M. Ishihara: “Nuclear moment studies with polarized radioactive nuclear beams”, *Hyperfine Interact.* **136/137**, 183–187 (2001).
- H. Ueno, W. Sato, H. Ogawa, N. Aoi, K. Yoneda, Y. Kobayashi, D. Kameda, H. Miyoshi, H. Watanabe, N. Imai, A. Yoshimi, J. Kaihara, and K. Asahi: “Development of a detector system for transient field experiments with radioactive isotope beams and a test experiment”, *Hyperfine Interact.* **136/137**, 211–214 (2001).
- M. Kato, H. Sugai, T. Hayashi, M. Nishi, M. Tanase, T. Matsuzaki, K. Ishida, and K. Nagamine: “Development of a compact tritium gas recycling system”, *Hyperfine Interact.* **138**, 397–401 (2001).
- J. Schaffner-Bielich, D. Kharzeev, L. McLerran, and R. Venugopalan: “Generalized scaling of the transverse mass spectrum at the relativistic heavy-ion collider”, *Nucl. Phys. A* **705**, 494–507 (2001).
- R. Kanungo, I. Tanihata, and A. Ozawa: “Possibility of enlarged core structure of  $N = 15$  neutron rich nuclei”, *Phys. Lett. B* **512**, 261–267 (2001).
- S. Sugimoto, K. Sumiyoshi, and H. Toki: “Relativistic Hartree-Bogoliubov approach for nuclear matter with nonlinear coupling terms”, *Phys. Rev. C* **64**, 054310-1–054310-5 (2001).
- K. Asahi: “RIKEN radioactive beam facility and polarized radioactive beams”, *Prog. Part. Nucl. Phys.* **46**, 321–333 (2001).
- A. Saito, S. Takeuchi, T. Motobayashi, Y. Ando, T. Gomi, Y. Higurashi, H. Kobayashi, M. Serata, K. Yamada, S. Shimoura, H. Iwasaki, M. Kurokawa, T. Teranishi, H. Ryuto, T. Minemura, S. Ozawa, Y. Yanagisawa, M. Ishihara, N. Aoi, H. Sakurai, Z. Fulop, M. Hirai, Y. Iwata, N. Iwasa, and Z. Liu: “Molecular states in neutron-rich beryllium isotopes”, *Clustering Aspects of Quantum Many-body Systems: Proc. Int. Symp. on Post-Symp. of YKIS01, Kyoto, 2001–11*, edited by A. Ohnishi and others, World Scientific, Singapore, pp. 39–42 (2002).
- H. Ogawa, K. Asahi, H. Ueno, K. Sakai, H. Miyoshi, D. Kameda, T. Suzuki, H. Izumi, N. Imai, Y. Watanabe, K. Yoneda, N. Fukuda, H. Watanabe, A. Yoshimi, W. Sato, N. Aoi, M. Nagakura, T. Suga, K. Yogo, A. Goto, T. Honda, Y. Kobayashi, W.-D. Schmidt-Ott, G. Neyens, S. Teughels, A. Yoshida, T. Kubo, and M. Ishihara: “Quenching of neutron E2 effective charge in neutron-rich nuclei and the ground state of  $^{17}\text{C}$ ”, *Eur. Phys. J. A* **13**, 81–85 (2002).
- A. Saito, S. Shimoura, S. Takeuchi, T. Motobayashi, H. Ryuto, Y. Ando, N. Aoi, Z. Fulop, T. Gomi, Y. Higurashi, M. Hirai, N. Iwasa, H. Iwasaki, Y. Iwata, H. Kobayashi, M. Kurokawa, Z. Liu, T. Minemura, S. Ozawa, H. Sakurai, M. Serata, T. Teranishi, K. Yamada, Y. Yanagisawa, and M. Ishihara: “Molecular states in  $^{12}\text{Be}$  and  $^{14}\text{Be}$ ”, *Exotic Nuclei and Atomic Masses: Proc. 3rd Int. Conf. on Exotic Nuclei and Atomic Masses (ENAM2001)*, (Department of Physics and Accelerator Laboratory of University of Jyväskylä), Hameenlinna, Finland, 2001–7, edited by J. Aysto and others, Springer Verlag, Heidelberg, p. 251 (2002).
- H. Koura, T. Tachibana, and M. Yamada: “Estimation of alpha-decay half-lives and fission barriers in the superheavy nuclidic region from the viewpoint of a new mass formula”, *Exotic Nuclei and Atomic Masses: Proc. 3rd Int. Conf. on Exotic Nuclei and Atomic Masses (ENAM2001)*, (Department of Physics and Accelerator Laboratory of University of Jyväskylä), Hameenlinna, Finland, 2001–7, edited by J. Aysto and others, Springer-Verlag, Heidelberg, p. 379 (2002).
- H. L. Yadav, S. Sugimoto, and H. Toki: “Relativistic mean field plus BCS approach to drip-line nuclei”, *Mod. Phys. Lett. A* **17**, 2523–2533 (2002).
- T. Wakasa, K. Hatanaka, T. Kawabata, T. Noro, H. Sakaguchi, M. Yosoi, Y. Fujita, G. Berg, T. Fujimura, H. Fujita, M. Ito, J. Kamiya, K. Nagayama, Y. Shimbara, H. Takeda, K. Tamura, H. Ueno, M. Uchida, and M. Uraki: “High resolution beam line for the grand raiden spectrometer”, *Nucl. Instrum. Methods Phys. Res. A* **482**, 79–93 (2002).
- H. Fujita, Y. Fujita, G. Berg, A. Bacher, C. Foster, K. Hara, K. Hatanaka, T. Kawabata, T. Noro, H. Sakaguchi, Y. Shimbara, T. Shinada, E. Stephenson, H. Ueno, and M. Yosoi: “Realization of matching conditions for high-resolution spectrometers”, *Nucl. Instrum. Methods Phys. Res. A* **484**, 17–26 (2002).
- K. Asahi, K. Sakai, H. Ogawa, H. Miyoshi, K. Yogo, A. Goto, T. Suga, H. Ueno, Y. Kobayashi, A. Yoshimi, A. Yoshida, T. Kubo, Y. Watanabe, N. Imai, K. Yoneda, N. Fukuda, N. Aoi, M. Ishihara, W.-D. Schmidt-Ott, G. Neyens, and S. Teughels: “Electromagnetic moments of neutron-rich nuclei measured with polarized radioactive ion beams”, *Nucl. Phys. A* **704**, 88c–97c (2002).
- H. Ueno, A. Yoshimi, W. Sato, H. Watanabe, K. Yoneda, Y. Kobayashi, A. Yoshida, T. Kubo, M.

- Ishihara, K. Asahi, H. Ogawa, H. Miyoshi, D. Kameda, T. Suga, K. Ohno, K. Sakai, K. Yogo, and N. Imai: “Magnetic moment of the ground state of  $^{17}\text{C}$ ”, *Perspectives in Heavy Ion Physics: Proc. 4th Italy-Japan Symp.*, Wako, Tokyo, 2001–9, edited by K. Yoshida, S. Kubono, I. Tanihata, and C. Signorini, World Scientific, Singapore, pp. 77–84 (2002).
- S. Motomura, Q. Pan, Y. Gounou, Y. F. Yang, S. Enomoto, Y. Yano, and K. Asahi: “Compton camera for multitracer”, *Perspectives in Heavy Ion Physics: Proc. 4th Italy-Japan Symp.*, Wako, Tokyo, 2001–9, edited by K. Yoshida, S. Kubono, I. Tanihata, and C. Signorini, World Scientific, Singapore, pp. 439–447 (2002).
- A. Yoshimi, K. Asahi, K. Sakai, K. Yogo, H. Ogawa, M. Tsuda, T. Suzuki, and M. Nagakura: “Nuclear spin maser with an artificial feedback mechanism”, *Phys. Lett. A* **304**, 13–20 (2002).
- R. Kanungo, I. Tanihata, and A. Ozawa: “Observation of new neutron and proton magic numbers”, *Phys. Lett. B* **528**, 58–64 (2002).
- S. Fujii, R. Okamoto, and K. Suzuki: “Shell-model calculations for  $^{16}_{\Lambda}\text{O}$  and  $^{17}_{\Lambda}\text{O}$  using microscopic effective interactions with  $\Sigma$  degrees of freedom”, *Phys. Rev. C* **66**, 054301-1–054301-10 (2002).
- M. Kitazawa, T. Koide, T. Kunihiro, and Y. Nemoto: “Precursor of color superconductivity in hot quark matter”, *Phys. Rev. D* **65**, 091504(R)-1–091504(R)-5 (2002).
- T. T. Takahashi, H. Sukanuma, Y. Nemoto, and H. Matsufuru: “Detailed analysis of the three-quark potential in SU(3) lattice QCD”, *Phys. Rev. D* **65**, 114509-1–114509-19 (2002).
- R. Kanungo, T. Suda, M. Chiba, N. Iwasa, S. Nishimura, A. Ozawa, C. Samanta, T. Suzuki, T. Yamaguchi, T. Zheng, and I. Tanihata: “Experimental evidence of core modification in the near drip-line nucleus  $^{23}\text{O}$ ”, *Phys. Rev. Lett.* **88**, 142502-1–142502-4 (2002).
- H. Miyoshi, H. Ueno, K. Asahi, H. Ogawa, J. Murata, K. Sakai, D. Kameda, Y. Kobayashi, W. Sato, A. Yoshimi, H. Watanabe, K. Yoneda, N. Imai, J. Kaihara, K. Shimada, and T. Koike: “Development of low energy polarized atomic beam”, *Proc. RIKEN Symp. on Condensed Matter Studies with Radioactive Ion Beams*, Wako, 2002–2, edited by K. Asahi, Y. Kobayashi, and W. Sato, RIKEN, Wako, pp. 61–66 (2002).
- W. Sato, H. Ueno, H. Watanabe, H. Ogawa, H. Miyoshi, N. Imai, A. Yoshimi, K. Yoneda, D. Kameda, Y. Kobayashi, and K. Asahi: “On-line TDPAC studies using the  $^{19}\text{O}$  beam”, *Proc. RIKEN Symp. on Condensed Matter Studies with Radioactive Ion Beams*, Wako, 2002–2, edited by K. Asahi, Y. Kobayashi, and W. Sato, RIKEN, Wako, pp. 71–75 (2002).
- H. Toki, S. Sugimoto, and K. Ikeda: “Relativistic mean-field theory with the pion in finite nuclei”, *Prog. Theor. Phys.* **108**, 903–916 (2002).
- M. Kitazawa, T. Koide, T. Kunihiro, and Y. Nemoto: “Chiral and color-superconducting phase transitions with vector interaction in a simple model”, *Prog. Theor. Phys.* **108**, 929–951 (2002).
- K. Iida, G. Watanabe, and K. Sato: “Formation of nuclear “pasta” in cold neutron star matter”, *Prog. Theor. Phys. Suppl.*, No. 146, pp. 514–519 (2002).
- A. Kohama, R. Seki, A. Arima, and S. Yamaji: “Model-independent determination of surface density distribution of unstable nuclei at radioactive beam facilities”, *Prog. Theor. Phys. Suppl.*, No. 146, pp. 577–578 (2002).
- H. Ogawa, K. Asahi, H. Ueno, H. Miyoshi, D. Kameda, N. Imai, K. Yoneda, H. Watanabe, T. Suga, K. Ohno, A. Yoshimi, W. Sato, K. Sakai, K. Yogo, Y. Kobayashi, A. Yoshida, T. Kubo, and M. Ishihara: “Assignment of the ground-state spin-parity for  $^{17}\text{C}$  through  $g$ -factor measurement”, *Prog. Theor. Phys. Suppl.*, No. 146, pp. 607–608 (2002).
- A. Saito, S. Shimoura, S. Takeuchi, T. Motobayashi, H. Ryuto, Y. Ando, N. Aoi, Z. Fulop, T. Gomi, Y. Higurashi, M. Hirai, N. Iwasa, H. Iwasaki, Y. Iwata, H. Kobayashi, M. Kurokawa, Z. Liu, T. Minemura, S. Ozawa, H. Sakurai, M. Serata, T. Teranishi, K. Yamada, Y. Yanagisawa, and M. Ishihara: “Molecular states in neutron-rich beryllium isotopes”, *Prog. Theor. Phys. Suppl.*, No. 146, pp. 615–616 (2002).
- Y. Motizuki: “Description: Element genesis - Solving the mystery (Video) revised ed.”, Image Science, Inc., Tokyo, (2002).
- K. Sekiguchi, H. Sakai, H. Okamura, A. Tamii, T. Uesaka, K. Suda, N. Sakamoto, T. Wakasa, Y. Satou, T. Ohnishi, K. Yako, S. Sakoda, H. Kato, Y. Maeda, J. Nishikawa, T. Saito, N. Uchigashima, N. N. Kalantar, and K. Ermisch: “Polarization transfer measurement for  $d$ - $p$  elastic scattering: a probe for three nucleon force properties”, *AIP Conf. Proc.* **675**, 711–714 (2003).
- H. Madokoro, T. Shimizu, and Y. Motizuki: “Global anisotropy versus small-scale fluctuations in neutrino flux in core-collapse supernova explosions”, *Astrophys. J.* **592**, 1035–1041 (2003).
- N. Dinh Dang: “Energies of the ground state and first excited  $0^+$  state in an exactly solvable pairing mode”, *Eur. Phys. J. A* **16**, 181–191 (2003).
- S. Motomura and S. Enomoto: “Development of multi-nuclide  $\gamma$ -ray emission imaging system GREI”, *J. Clin. Exp. Med.* **205**, 884–886 (2003).
- K. Ishida, K. Nagamine, T. Matsuzaki, and N. Kawamura: “Muon catalyzed fusion”, *J. Phys. G* **29**, 2043–2045 (2003).
- A. Kohama, R. Seki, A. Arima, and S. Yamaji: “Determination of matter surface distribution of neutron-rich nuclei”, *J. Phys. Soc. Jpn.* **72**, 2766–2780

- (2003).
- W. Sato, H. Ueno, H. Watanabe, H. Ogawa, H. Miyoshi, N. Imai, A. Yoshimi, K. Yoneda, D. Kameda, Y. Kobayashi, and K. Asahi: “On-line TDPAC studies with the  $^{19}\text{O}$  beam”, *J. Radioanal. Nucl. Chem.* **255**, 183–186 (2003).
- K. Sekiguchi, H. Sakai, H. Okamura, A. Tamii, T. Uesaka, K. Suda, N. Sakamoto, T. Wakasa, Y. Satou, T. Ohnishi, K. Yako, S. Sakoda, H. Kato, Y. Maeda, M. Hatano, J. Nishikawa, T. Saito, N. Uchigashima, N. N. Kalantar, and K. Ermisch: “Polarization transfer measurement for  $d$ - $p$  elastic scattering: To search for three nucleon force effects”, *Mod. Phys. Lett. A* **18**, 327–329 (2003).
- S. Yonai, T. Kurosawa, H. Iwase, H. Yashima, Y. Uwamino, and T. Nakamura: “Measurement of neutrons from thick Fe target bombarded by 210 MeV protons”, *Nucl. Instrum. Methods Phys. Res. A* **515**, 733–744 (2003).
- T. Motobayashi: “RI beam factory project at RIKEN”, *Nucl. Instrum. Methods Phys. Res. B* **204**, 736–738 (2003).
- T. Motobayashi: “Nuclear astrophysics experiments with high energy RI beams”, *Nucl. Phys. A* **718**, 101c–108c (2003).
- K. Oyamatsu and K. Iida: “Empirical properties of asymmetric nuclear matter to be obtained from unstable nuclei”, *Nucl. Phys. A* **718**, 363c–366c (2003).
- H. Madokoro, T. Shimizu, and Y. Motizuki: “Effects of anisotropy in neutrino radiation on the supernova explosion: More complicated patterns of anisotropy”, *Nucl. Phys. A* **718**, 458c–460c (2003).
- K. Iida and G. Baym: “Magnetic and rotational vortices in superfluid quark matter”, *Nucl. Phys. A* **718**, 697c–699c (2003).
- T. Motobayashi: “Coulomb dissociation studies for explosive hydrogen burning”, *Nucl. Phys. A* **719**, 65c–72c (2003).
- Z. Elekes, G. Kalinka, Z. Fulop, J. Gal, J. Molnar, G. Hegyesi, D. Novak, J. Vegh, T. Motobayashi, A. Saito, and Y. Yanagisawa: “Optimization of the performance of a CsI(Tl) scintillator + Si PIN photodiode detector for medium-energy light-charged particle hybrid array”, *Nucl. Phys. A* **719**, 316c–321c (2003).
- K. Sekiguchi, H. Sakai, H. Okamura, A. Tamii, T. Uesaka, K. Suda, N. Sakamoto, T. Wakasa, Y. Satou, T. Ohnishi, K. Yako, S. Sakoda, H. Kato, Y. Maeda, J. Nishikawa, T. Saito, N. Uchigashima, N. N. Kalantar, and K. Ermisch: “Polarization transfer measurement for  $d$ - $p$  scattering and three nucleon force effects”, *Nucl. Phys. A* **721**, 637c–640c (2003).
- S. Sugimoto, H. Toki, and K. Ikeda: “Surface pion condensation in finite nuclei”, *Nucl. Phys. A* **721**, 669c–672c (2003).
- K. Tanida, H. Akikawa, Y. Fukao, H. Hotchi, K. Imai, Y. Miura, K. Miwa, K. Mizunuma, S. N. Nakamura, M. Niiyama, S. Ota, S. K. Pranab, H. Takahashi, T. Takahashi, H. Tamura, S. Terashima, M. Togawa, and M. Ukai: “High-resolution  $\gamma$ -ray spectroscopy of hyperfragments produced by stopped  $\kappa$  reactions”, *Nucl. Phys. A* **721**, 999c–1002c (2003).
- S. Sugimoto, H. Toki, K. Ikeda, and N. P. Minkov: “Relativistic mean field theory with the pion for finite nuclei”, *Nucl. Phys. A* **722**, 360c–365c (2003).
- N. Dinh Dang and A. Arima: “Thermal quasiparticle correlations and continuum coupling in nuclei far from stability”, *Nucl. Phys. A* **722**, 383c–388c (2003).
- T. Yamaguchi, T. Zheng, A. Ozawa, M. Chiba, R. Kanungo, T. Kato, K. Morimoto, T. Ohnishi, T. Suda, Y. Yamaguchi, A. Yoshida, K. Yoshida, and I. Tanihata: “Momentum distributions of  $^{14}\text{C}$  and  $^{15}\text{C}$  fragments from  $^{16}\text{C}$  breakup”, *Nucl. Phys. A* **724**, 3–13 (2003).
- G. Watanabe, K. Iida, and K. Sato: “Erratum to: I. ‘thermodynamic properties of nuclear ‘pasta’ in neutron star crusts’ [Nucl. Phys. A 676 (2000) 455] and II. ‘Effects of neutrino trapping on thermodynamic properties of nuclear ‘pasta’ [Nucl. Phys. A 687 (2001) 512]”, *Nucl. Phys. A* **726**, 357–365 (2003).
- H. Watanabe, H. Ueno, D. Kameda, W. Sato, A. Yoshimi, H. Miyoshi, T. Kishida, Y. Kobayashi, A. Odahara, Y. Gounou, and K. Asahi: “g-Factor of the high-spin isomer in  $^{149}\text{Dy}$  and a multi-quasiparticle configuration caused by the  $N = 82$  core excitations”, *Nucl. Phys. A* **728**, 365–378 (2003).
- K. Sekiguchi, H. Sakai, H. Okamura, A. Tamii, T. Uesaka, K. Suda, N. Sakamoto, T. Wakasa, Y. Satou, T. Ohnishi, K. Yako, S. Sakoda, H. Kato, Y. Maeda, J. Nishikawa, T. Saito, N. Uchigashima, N. N. Kalantar, and K. Ermisch: “Polarization transfer measurement for deuteron-proton scattering and three nucleon force effects”, *Nuclear Many-Body and Medium Effects in Nuclear Interactions and Reactions: Proc. Kyudai-RCNP Int. Symp., (Osaka University RCNP and Kyushu University), Fukuoka, 2003–10*, edited by K. Hatanaka, T. Noro, K. Sagara, and others, World Scientific, Singapore, pp. 115–119 (2003).
- T. Matsuzaki, K. Nagamine, N. Kawamura, K. Ishida, Y. Matsuda, S. Nakamura, M. Kato, H. Sugai, M. Tanase, K. Kudo, N. Takeda, and G. H. Eaton: “Evidence for strong  $n$ - $\alpha$  correlations in the  $t+t$  reaction proved by the neutron energy distribution of muon catalyzed  $t$ - $t$  fusion”, *Phys. Lett. B* **557**, 176–183 (2003).
- Y. Yanagisawa, M. Notani, H. Sakurai, M. Kunibu, H. Akiyoshi, N. Aoi, H. Baba, K. Demichi, N. Fukuda, H. Hasegawa, Y. Higurashi, M. Ishihara, N. Iwasa, H. Iwasaki, T. Gomi, S. Kanno, M. Kurokawa, Y. Matsuyama, S. Michimasa, T. Minemura, Y. Mizoi,

- T. Nakamura, A. Saito, M. Serata, S. Shimoura, T. Sugimoto, E. Takeshita, S. Takeuchi, K. Ue, K. Yamada, K. Yoneda, and T. Motobayashi: “The first excited state of  $^{30}\text{Ne}$  studied by proton inelastic scattering in reversed kinematics”, *Phys. Lett. B* **566**, 84–89 (2003).
- K. Iida, K. Oyamatsu, and B. A. Sarhan: “Proton-nucleus elastic scattering and the equation of state of nuclear matter”, *Phys. Lett. B* **576**, 273–280 (2003).
- N. Dinh Dang and A. Arima: “Thermal quasiparticle correlations and continuum coupling in nuclei far from stability”, *Phys. Rev. C* **67**, 014304-1–014304-14 (2003).
- H. Miyatake, H. Ueno, Y. Yamamoto, N. Aoi, K. Asahi, E. Ideguchi, M. Ishihara, H. Izumi, T. Kishida, T. Kubo, S. Mitsuoka, Y. Mizoi, M. Notani, H. Ogawa, A. Ozawa, M. Sasaki, T. Shimoda, T. Shirakura, N. Takahashi, S. Tanimoto, and K. Yoneda: “Spin-parity assignments in  $^{15}\text{C}^*$  by a new method:  $\beta$ -delayed spectroscopy for a spin-polarized nucleus”, *Phys. Rev. C* **67**, 014306-1–014306-9 (2003).
- K. Yoneda, N. Aoi, H. Iwasaki, H. Sakurai, H. Ogawa, T. Nakamura, W.-D. Schmidt-Ott, S. Markus, M. Notani, N. Fukuda, E. Ideguchi, T. Kishida, S. Yamamoto, and M. Ishihara: “ $\beta$ -decay half-lives and  $\beta$ -delayed neutron multiplicities of the neutron drip-line nuclei  $^{19}\text{B}$ ,  $^{22}\text{C}$ , and  $^{23}\text{N}$ ”, *Phys. Rev. C* **67**, 014316-1–014316-7 (2003).
- A. Ozawa, Y. Yamaguchi, M. Chiba, R. Kanungo, K. Kimura, S. Momota, T. Suda, T. Suzuki, I. Tanihata, T. Zheng, S. Watanabe, T. Yamaguchi, and K. Yoshida: “Search for  $^{21}\text{B}$ ”, *Phys. Rev. C* **67**, 014610-1–014610-5 (2003).
- N. Dinh Dang, K. A. Vuong, T. Suzuki, and A. Arima: “Reply to the comment on the “authentic damping mechanism” of the phonon damping model”, *Phys. Rev. C* **67**, 029802-1–029802-2 (2003).
- H. Ogawa, K. Asahi, K. Sakai, T. Suzuki, H. Izumi, H. Miyoshi, M. Nagakura, K. Yogo, A. Goto, T. Suga, T. Honda, H. Ueno, Y. X. Watanabe, K. Yoneda, A. Yoshimi, N. Fukuda, Y. Kobayashi, A. Yoshida, T. Kubo, M. Ishihara, N. Imai, N. Aoi, S. Wolf-Dieter, G. Neyens, and S. Teughels: “Electric quadrupole moment of  $^{17}\text{B}$  and anomalous  $E2$  effective charges for neutron-rich nuclei”, *Phys. Rev. C* **67**, 064308-1–064308-9 (2003).
- N. Dinh Dang and A. Arima: “Modified Hartree-Fock-Bogoliubov theory at finite temperature”, *Phys. Rev. C* **68**, 014318-1–014318-18 (2003).
- N. Dinh Dang and A. Arima: “Pairing effect on the giant dipole resonance width at low temperature”, *Phys. Rev. C* **68**, 044303-1–044303-7 (2003).
- G. Watanabe and K. Iida: “Electron screening in the liquid-gas mixed phases of nuclear matter”, *Phys. Rev. C* **68**, 045801-1–045801-11 (2003).
- T. Sugihara: “Lattice chiral symmetry with hopping interactions”, *Phys. Rev. D* **68**, 034502-1–034502-4 (2003).
- F. Schumann, F. Hammache, S. Typel, F. Uhlig, K. Summerer, I. Bottcher, D. Cortina, A. Forester, M. Gai, H. Geissel, U. Greife, N. Iwasa, P. Koczon, B. Kohlmeyer, R. Kulesa, H. Kumagai, N. Kurz, M. Menzel, T. Motobayashi, H. Oeschler, A. Ozawa, M. Ptoskon, W. Prokopowicz, E. Schwab, P. Senger, F. Strieder, C. Sturm, Z. Sun, G. Surowka, A. Wagner, and W. Walus: “Coulomb dissociation of  $^8\text{B}$  and the low-energy cross section of the  $^7\text{Be}(p,\gamma)^8\text{B}$  solarfusion reaction”, *Phys. Rev. Lett.* **90**, 23501-1–23501-4 (2003).
- N. Kawamura, K. Nagamine, T. Matsuzaki, K. Ishida, S. Nakamura, Y. Matsuda, M. Tanase, M. Kato, H. Sugai, K. Kudo, N. Takeda, and G. H. Eaton: “Discovery of temperature-dependent phenomena of muon-catalyzed fusion in solid deuterium and tritium mixtures”, *Phys. Rev. Lett.* **90**, 043401-1–043401-4 (2003).
- A. A. Korshennikov, E. Nikolski, E. Kuzmin, A. Ozawa, K. Morimoto, F. Tokanai, R. Kanungo, I. Tanihata, N. Timofeyuk, M. S. Golovkov, A. S. Fomichev, A. M. Rodin, M. L. Chelnokov, G. M. Ter-Akopian, W. Mittig, P. Roussel-Chomaz, H. Savajols, E. Pollacco, A. A. Ogloblin, and M. V. Zhukov: “Experimental evidence for the existence of  $^7\text{H}$  and for a specific structure of  $^8\text{He}$ ”, *Phys. Rev. Lett.* **90**, 82501-1–82501-4 (2003).
- A. Toyoda, K. Ishida, K. Simomura, S. Nakamura, Y. Matsuda, W. Higemoto, T. Matsuzaki, and K. Nagamine: “New insights in muon-catalyzed  $dd$  fusion by using ortho-para controlled solid deuterium”, *Phys. Rev. Lett.* **90**, 243401-1–243401-4 (2003).
- H. Miyadera, K. Nagamine, K. Simomura, K. Nishiyama, H. Tanaka, K. Fukuchi, S. Makimura, and K. Ishida: “Dai Omega, a large solid angle axial focusing superconducting surface muon channel”, *Physica B* **326**, 265–269 (2003).
- H. Ryuto, N. Inabe, N. Fukunishi, H. Hasebe, M. Kase, and Y. Yano: “Charge stripping scheme in the RIKEN RI-beam factory”, *Proc. 14th Symp. on Accelerator Science and Technology, (KEK), Tsukuba, 2003–11, KEK, Tsukuba, pp. 551–553 (2003).*
- Y. Motizuki, H. Madokoro, and T. Shimizu: “Sensitivity of core-collapse supernovae to neutrino luminosity in cases of anisotropic neutrino radiation”, *Proc. 1st Yamada Symp. on Neutrinos and Dark Matter in Nuclear Physics (YS1-NDM03) (Web) (<http://ndm03.phys.sci.osaka-u.ac.jp/proc/index.htm>), Nara, 2003–6, edited by H. Ejiri and I. Ogawa, YS1-NDM03, pp. 281–286 (2003).*
- S. Ozawa and M. Hamagaki: “Preparation of boron films by sputtering with electron-beam-excited plasma”, *Proc. 7th Int. Symp. on Sputtering & Plasma Processes (ISSP 2003), Kanazawa, 2003–6, edited by N. Fujiwara, ISSP 2003, Kanazawa,*

- pp. 409–412 (2003).
- H. Watanabe, H. Ueno, D. Kameda, W. Sato, A. Yoshimi, H. Miyoshi, Y. Kobayashi, T. Kishida, K. Asahi, A. Odahara, and Y. Gounou: “g factor of the high-spin isomer in  $^{149}\text{Dy}$  and large oblate deformation induced by collapse of the  $N = 82$  core”, Proc. Int. Symp. on Frontiers of Collective Motions (CM2002), (Aizu University), Aizu-Wakamatsu, 2002–11, edited by H. Sagawa and H. Iwasaki, World Scientific, Singapore, pp. 355–360 (2003).
- K. Ishida, K. Nagamine, T. Matsuzaki, and N. Kawamura: “Highlights of muon catalyzed fusion experiments at RIKEN-RAL”, Proc. Int. Workshop on Exotic Atoms - Future Perspectives (EXA 2002), (Austrian Academy of Sciences), Vienna, Austria, 2002–11, Austrian Academy of Sciences Press, Vienna, pp. 175–184 (2003).
- T. Izubushi: “Domain wall fermions and chiral symmetry”, Proc. RBRC/CCAST Symp. on Spin Physics, Lattice QCD and RHIC Physics (CCAST-WL Workshop Ser., Vol. 151), (RBRC and CCAST), Beijing, China, 2003–4, CCAST, Beijing, pp. 11–40 (2003).
- Y. Motizuki: “RIBF nuclear astrophysics project: toward unified understanding of the mechanism of core-collapse supernovae and nucleosynthesis”, Proc. Workshop on Strategy of Astrophysical Nuclear Reaction Studies, (RIKEN), Wako, 2003–3, RIKEN, Wako, pp. 33–34 (2003).
- K. Oyamatsu and K. Iida: “Saturation of nuclear matter and radii of unstable nuclei”, Prog. Theor. Phys. **109**, 631–650 (2003).
- K. Koori, K. Iida, and K. Sato: “Upper limit on the mass of RX J1856.5-3754 as a possible quark star”, Prog. Theor. Phys. **109**, 765–780 (2003).
- L. Geng, H. Toki, S. Sugimoto, and J. Meng: “Relativistic mean field theory for deformed nuclei with pairing correlations”, Prog. Theor. Phys. **110**, 921–936 (2003).
- K. Koori, K. Iida, and K. Sato: “Possible quark star RX J1856.5-3754 and its mass”, Prog. Theor. Phys. Suppl., No. 151, pp. 181–185 (2003).
- A. Yoshida, T. Suda, T. Kubo, T. Ohtsuki, and H. Yuki: “A test of radiation hardness of magnetic fluid”, Res. Rep. Lab. Nucl. Sci. **36**, 111–114 (2003).
- K. Iida: “Compact stars: from observations to dense matter”, Soryushiron Kenkyu **106**, E33–E36 (2003).
- P. Bakule, Y. Matsuda, Y. Miyake, P. Strasser, K. Shimomura, S. Makimura, and K. Nagamine: “Slow muon experiment by laser resonant ionization method at RIKEN-RAL muon facility”, Spectrochim. Acta B **58**, 1019–1030 (2003).
- H. Watanabe, Y. Wakabayashi, Y. Gounou, T. Fukuchi, H. Ueno, W. Sato, A. Yoshimi, D. Kameda, H. Miyoshi, T. Kishida, Y. Kobayashi, T. Morikawa, S. Motomura, O. Kashiyama, K. Saito, A. Odahara, and K. Asahi: “Lifetime of a new high-spin isomer in  $^{150}\text{Dy}$ ”, Eur. Phys. J. A **19**, 163–167 (2004).
- Y. Motizuki and S. Kumagai: “ $^{44}\text{Ti}$  radioactivity in young supernova remnants: Cas A and SN 1987A”, New Astron. Rev. **48**, 69–73 (2004).
- M. Sekimoto, J. Chiba, H. Funahashi, H. Hamagaki, M. Ieiri, M. Ishino, M. Kitaguchi, S. Mihara, T. Miyashita, T. Murakami, R. Mutou, M. Naruki, M. Nomachi, K. Ozawa, F. Sakuma, O. Sasaki, T. Tabaru, K. Tanaka, S. Yamada, S. Yokkaichi, Y. Yoshimura, and H. Enyo: “Spectrometer for measurements of  $\phi$  mesons in nuclear matter produced through 12-GeV p+A reactions”, Nucl. Instrum. Methods Phys. Res. A **516**, 390–405 (2004).
- T. Sugihara: “Chiral symmetry on a lattice with hopping interactions”, Nucl. Phys. B (Proc. Suppl.) **129-130C**, 510–512 (2004).
- S. Sugimoto, H. Toki, and K. Ikeda: “Relativistic mean field theory with the pion for finite nuclei”, Nuclear Theory ’22: Proc. 22nd Int. Workshop on Nuclear Theory, (The Institute of Nuclear Research and Nuclear Energy of the Bulgarian Academy of Sciences), Rila Mountains, Bulgaria, 2003–6, edited by V. Nikolaev, Heron Press, Sofia, pp. 33–38 (2004).
- K. Yamada, T. Motobayashi, H. Ryuto, N. Aoi, Z. Fulop, T. Gomi, Y. Higurashi, N. Imai, N. Iwasa, H. Iwasaki, Y. Iwata, H. Kobayashi, M. Kurokawa, Z. Liu, T. Minemura, S. Ozawa, H. Sakurai, M. Serata, S. Shimoura, S. Takeuchi, T. Teranishi, Y. Yanagisawa, K. Yoshida, and M. Ishihara: “E1 strength of the subthreshold  $3/2^+$  state in  $^{15}\text{O}$  studied by Coulomb excitation”, Phys. Lett. B **579**, 265–270 (2004).
- Y. Ogawa, H. Toki, S. Tamenaga, H. Shen, A. Hosaka, S. Sugimoto, and K. Ikeda: “Chiral sigma model with pion mean field in finite nuclei”, Prog. Theor. Phys. **111**, 75–92 (2004).

### 3. Atomic and solid-state physics

- Y. Yoshida, Y. Kobayashi, F. Ambe, E. Yagi, X. Diao, J. Nakamura, H. Haesslein, A. Feinauer, T. Grund, A. Roeck, and A. Seeger: “Direct observation of self-interstitial motion in pure iron by  $^{56}\text{Fe}(\text{d},\text{p})^{57}\text{Fe}$  in-beam Mössbauer spectroscopy”, Defect Diffus. Forum **194/199**, 29–34 (2001).
- A. Igarashi, M. P. Faifman, and I. Shimamura: “Nonadiabatically coupled hyperspherical equations applied to the collisional spin flip of muonic hydrogen”, Hyperfine Interact. **138**, 77–83 (2001).
- F. Saito, Y. Nagashima, L. Wei, Y. Itoh, A. Goto, and T. Hyodo: “A high-efficiency positron moderator using electro-polished tungsten meshes”, Appl. Surf. Sci. **194**, 13–15 (2002).
- Y. Yoshida, Y. Kobayashi, A. Yoshida, X. Diao, S. Ogawa, K. Hayakawa, K. Yukihira, S. Fumio, and



- F. Ambe: "In-beam Mössbauer spectroscopy after GeV-ion implantation at an on-line projectile-fragment separator", *Hyperfine Interact.* **141/142**, 157–162 (2002).
- K. Kimura, S. Sharma, and A. Popov: "Fast electron-hole plasma luminescence from track-cores in heavy-ion irradiated wide-band-gap crystals", *Nucl. Instrum. Methods Phys. Res. B* **191**, 48–53 (2002).
- Y. Nakai: "Production of heavy fragment ions in collisions of C<sub>60</sub> with fast ions", *Proc. 22nd Int. Conf. on Photonic, Electronic and Atomic Collisions (ICPEAC 2001)*, Santa Fe, USA, 2001–7, Rinton Press, Princeton, pp. 665–674 (2002).
- D. P. van der Werf, M. Amoretti, G. Bonomi, A. Bouchta, P. D. Bowe, C. Carraro, C. L. Cesar, M. Charlton, M. Doser, V. Filippini, A. Fontana, M. C. Fujiwara, R. Funakoshi, P. Genova, J. S. Hangst, R. S. Hayano, L. V. Jorgensen, V. Lagomarsino, R. Landua, E. Lodi-Rizzini, M. Macri, N. Madsen, G. Manuzio, P. Montagna, H. Pruys, C. Regenfus, A. Rotondi, G. Testera, and A. Variola: "Transfer, stacking and compression of positron plasmas under UHV conditions", *AIP Conf. Proc.* **692**, 172–177 (2003).
- A. Igarashi, M. Kimura, I. Shimamura, and N. Toshima: "Positron annihilation and positronium formation: a unified theory in terms of a complex potential", *Butsuri* **58**, 528–532 (2003).
- I. Shimamura: "Hyperspherical coupled-channel method for Coulomb three-body continuum processes", *Frontiers in atomic, molecular and optical physics*, edited by S. P. Sen Gupta, S. S. Bhattacharyya, and S. C. Mukherjee, Allied Publishers PVT., New Delhi, pp. 141–170 (2003).
- E. Yagi: "The state of hydrogen in Nb-based Nb-Mo alloys analyzed by the channelling method", *ISIJ Int.* **43**, 505–513 (2003).
- M. Wada, Y. Ishida, T. Nakamura, Y. Yamazaki, T. Kambara, H. Oyama, Y. Kanai, T. Kojima, Y. Nakai, N. Oshima, A. Yoshida, T. Kubo, Y. Matsuo, Y. Fukuyama, K. Okada, T. Sonoda, S. Ohtani, K. Noda, H. Kawakami, and I. Katayama: "Slow RI-beams from projectile fragment separators", *Nucl. Instrum. Methods Phys. Res. B* **204**, 570–581 (2003).
- N. Oshima, T. Kojima, M. Niigaki, A. Mohri, K. Komaki, Y. Iwai, and Y. Yamazaki: "Development of a cold HCI source for ultra-slow collisions", *Nucl. Instrum. Methods Phys. Res. B* **205**, 178–182 (2003).
- Y. Iwai, Y. Kanai, Y. Nakai, T. Ikeda, H. Oyama, K. Ando, H. Masuda, K. Nishio, M. Nakao, H. Torii, K. Komaki, and Y. Yamazaki: "High-resolution soft X-ray spectroscopy of slow highly charged ions transmitted through a microcapillary target", *Nucl. Instrum. Methods Phys. Res. B* **205**, 762–766 (2003).
- Y. Nakai, T. Ikeda, Y. Kanai, T. Kambara, N. Fukunishi, T. Azuma, K. Komaki, Y. Takabayashi, and Y. Yamazaki: "Resonant coherent excitation of 94 MeV/u Ar<sup>17+</sup> ions channeling through a Si crystal", *Nucl. Instrum. Methods Phys. Res. B* **205**, 784–788 (2003).
- A. Hida, A. Iwase, Y. Mera, T. Kambara, and K. Maeda: "STM study of ion tracks created in GaAs by GeV Xe ion irradiation", *Nucl. Instrum. Methods Phys. Res. B* **209**, 140–144 (2003).
- K. Kimura: "Ultra-fast luminescence in heavy-ion track-cores in insulators: Electron-hole plasma", *Nucl. Instrum. Methods Phys. Res. B* **212**, 123–134 (2003).
- M. Koshimizu, K. Asai, and K. Kimura: "Time-resolved luminescence spectra of electron-hole plasma in ion-irradiated CdS", *Nucl. Instrum. Methods Phys. Res. B* **212**, 376–380 (2003).
- N. Yamanaka, Y. Kino, Y. Takano, H. Kudo, and A. Ichimura: "Enhancement of direct positron annihilation due to temporal capture by an atom", *Phys. Rev. A* **67**, 052712-1–052712-4 (2003).
- A. Igarashi, M. Kimura, I. Shimamura, and N. Toshima: "Inseparable positron annihilation and positronium formation on positron-atom collisions: Description in terms of an absorption potential", *Phys. Rev. A* **68**, 042716-1–042716-8 (2003).
- N. Yamanaka and Y. Kino: "Time-dependent coupled-channel calculation for elastic scattering of positrons by hydrogen atoms and helium ions", *Phys. Rev. A* **68**, 052715-1–052715-6 (2003).
- S. Ohira, K. Awaga, W. Fujita, I. Watanabe, and K. Nagamine: " $\mu$ SR study on a metal complex having a ferromagnetic linear chain *p*-NPNN-Cu(hfac)<sub>2</sub>", *Physica B* **326**, 568–571 (2003).
- M. Wada and Y. Yamazaki: "Technical developments toward antiprotonic atoms for nuclear structure studies of radioactive nuclei", *Nucl. Instrum. Methods Phys. Res. B* **214**, 196–200 (2004).
- #### 4. Radiochemistry, radiation chemistry, and radiation biology
- T. Ozaki, S. Ambe, T. Abe, and A. J. Francis: "Adsorption of radionuclides on silica and their uptake by rice plants from silica-multitracer solutions", *Biol. Trace Elem. Res.* **90**, 273–281 (2002).
- K. Igarashi, Y. Nakanishi, R. Hirunuma, S. Enomoto, and S. Kimuta: "Influence of NaFeEDTA and ferrous sulfate on the absorption of trace elements in everted intestinal segments of rats", *Biomed. Res. Trace Elem.* **13**, 322–323 (2002).
- T. Matsuyama, T. Abe, S. Yoshida, K. Koike, and T. Ebisuzaki: "A DNA polymorphism detection system by simulation using the *Arabidopsis* genome sequences -a virtual imaging restriction landmark genomic scanning", *DNA Polymorphism* **10**, 60–63 (2002).

- M. Hirate, A. Takeda, H. Tamano, S. Enomoto, and N. Oku: "Distribution of trace elements in the brain of EL (epilepsy) mice", *Epilepsy Res.* **51**, 109–116 (2002).
- Y. Kobayashi, Y. Yoshida, K. M. Kubo, Y. Yamada, A. Yoshida, H. Ogawa, H. Ueno, and K. Asahi: "In-beam Mössbauer studies of  $^{57}\text{Mn}$  using a secondary  $^{57}\text{Mn}$  beam and ion implantation", *Eur. Phys. J. A* **13**, 243–246 (2002).
- S. Goto, S. Morimoto, T. Kurobe, M. Izumi, N. Fukunishi, M. Watanabe, and F. Yatagai: "Delayed cell-cycle arrest following heavy-ion exposure", *Int. Congr. Ser.* **1236**, 317–318 (2002).
- T. Abe, T. Matsuyama, S. Sekido, I. Yamaguchi, S. Yoshida, and T. Kameya: "Chlorophyll-deficient mutants of rice demonstrated the deletion of a DNA fragment by heavy-ion irradiation", *J. Radiat. Res.* **43**, Suppl., S157–S161 (2002).
- S. Morimoto, M. Honma, and F. Yatagai: "Sensitive detection of LOH events in a human cell line after C-ion beam exposure", *J. Radiat. Res.* **43**, Suppl., S163–S167 (2002).
- Y. Yabushita, Y. Kanayama, T. Tarohda, R. Amano, and S. Enomoto: "Multitracer screening for in vivo element-element interrelations - Part I: Uptake of  $^{54}\text{Mn}$ ,  $^{46}\text{Sc}$ ,  $^{59}\text{Fe}$ ,  $^{58}\text{Co}$ ,  $^{65}\text{Zn}$ ,  $^{75}\text{Se}$ ,  $^{83}\text{Rb}$ ,  $^{85}\text{Sr}$  and  $^{88}\text{Zr}$  by brain and other organs of mice bred under Mn-deficient, -adequate and -excessive diets", *J. Radioanal. Nucl. Chem.* **253**, 93–99 (2002).
- S. Enomoto and R. Hirunuma: "Multitracer technology in biology", *Perspectives in Heavy Ion Physics: Proc. 4th Italy-Japan Symp.*, Wako, Tokyo, 2001–9, edited by K. Yoshida, S. Kubono, I. Tanihata, and C. Signorini, World Scientific, Singapore, pp. 468–479 (2002).
- Y. Kobayashi, K. M. Kubo, Y. Yamada, T. Saito, K. Katsumata, J. Miyazaki, H. Ueno, H. Ogawa, W. Sato, K. Yoneda, H. Watanabe, H. Miyoshi, D. Kameda, and K. Asahi: "Study on valence states of  $^{57}\text{Fe}$  arising from  $^{57}\text{Mn}$  implanted into  $\text{KMnO}_4$ ", *Proc. Specialist Research Meet. on New Developments in Solid State Physics with Probes of Radiations and Nuclei*, (Research Reactor Institute, Kyoto University), Kumatori, 2001–11, edited by S. Nasu, Y. Maeda, and Y. Kawase, Research Reactor Institute, Kyoto University, Osaka, pp. 20–23 (2002).
- K. Igarashi, Y. Nakanishi, R. Hirunuma, S. Enomoto, and S. Kimura: "Influence of NaFeEDTA and ferrous sulfate on the absorption of trace elements in rats everted intestinal segments", *Proc. Trace Nutr. Res.* **19**, 51–53 (2002).
- S. Morimoto, S. Goto, T. Kato, M. Izumi, M. Komiyama, N. Fukunishi, M. Honma, F. Hanaoka, and F. Yatagai: "Cellular responses to low dose heavy-ion exposure in human cells", *Radiat. Prot. Dosim.* **99**, 253–254 (2002).
- S. Goto, M. Watanabe, and F. Yatagai: "Delayed cell cycle progression in human lymphoblastoid cells after exposure to high-LET radiation correlates with extremely localized DNA damage", *Radiat. Res.* **158**, 678–686 (2002).
- T. Matsuyama: "RLGS profiling by computer simulation", *Regulation of Plant Growth and Development* **37**, 192–197 (2002).
- T. Ozaki, S. Ambe, T. Abe, and F. J. Arokiasamy: "Effect of humic acid on the bioavailability of radionuclides to rice plants", *Anal. Bioanal. Chem.* **375**, 505–510 (2003).
- S. Enomoto, H. Haba, R. Hirunuma, K. Igarashi, A. Nakayama, and S. Motomura: "Evolution of RI production technology for bio-trace elemental research using RIKEN accelerator research facility", *Biomed. Res. Trace Elem.* **14**, 359–361 (2003).
- K. Igarashi, R. Hirunuma, H. Haba, S. Enomoto, and S. Kimura: "Effects of carnosine for the absorption of iron and various trace elements in rats", *Biomed. Res. Trace Elem.* **14**, 379–380 (2003).
- T. Matsuyama, H. Saito, T. Abe, S. Yoshida, H. Kato, K. Koike, and T. Ebisuzaki: "*Arabidopsis* genome analysis by the virtual RLGS system", *DNA Polymorphism*, Vol.11, edited by Japanese Society for DNA Polymorphism Research, Toyo-shoten, Tokyo, pp. 65–67 (2003).
- F. Ambe, S. Ambe, and S. Enomoto: "Chapter 11: Tracer technique", *Handbook of Nuclear Chemistry*, Vol. 3: Chemical Application of Nuclear Reactions and Radiations, edited by A. Vertes, S. Nagy, and Z. Klencsar, Kluwer Academic Publishers, Dordrecht, pp. 443–474 (2003).
- T. Abe, H. Saito, and Y. Miyazawa: "Plant breeding by heavy-ion beam irradiation", *Isotope News*, No. 595, pp. 9–12 (2003).
- T. Takanami, Y. Zhang, H. Aoki, T. Abe, S. Yoshida, H. Takahashi, S. Horiuchi, and A. Higashitani: "Efficient repair of DNA damage induced by heavy ion particles in meiotic prophase I nuclei of *Caenorhabditis elegans*", *J. Radiat. Res.* **44**, 271–276 (2003).
- K. Matsumoto, I. Ui, R. Hirunuma, S. Enomoto, and K. Endo: "In vivo assessment of dynamics of various elements in living rat by using a multitracer", *J. Radioanal. Nucl. Chem.* **255**, 143–147 (2003).
- Y. Kobayashi, K. M. Kubo, Y. Yamada, T. Saito, H. Ueno, H. Ogawa, W. Sato, K. Yoneda, H. Watanabe, N. Imai, H. Miyoshi, and K. Asahi: "Valence states of  $^{57}\text{Fe}$  decayed from  $^{57}\text{Mn}$  implanted into  $\text{KMnO}_4$ ", *J. Radioanal. Nucl. Chem.* **255**, 403–406 (2003).
- K. Matsumoto, H. Nagashima, N. Sotogaku, R. Hirunuma, S. Enomoto, and K. Endo: "Affinity of various bio-trace elements to lipid membrane: In vivo and in vitro study using multitracer", *J. Radioanal. Nucl. Chem.* **255**, 489–493 (2003).
- T. Saito, Y. Kobayashi, K. M. Kubo, and Y. Yamada: "Development and application of parallel plate avalanche counter for in-beam Mössbauer spec-

- troscopy”, *J. Radioanal. Nucl. Chem.* **255**, 519–522 (2003).
- Y. Yabushita, Y. Kanayama, T. Tarohda, S. Enomoto, and R. Amano: “Multitracer screening for in vivo element-element interrelations Part II: Uptake of  $^{65}\text{Zn}$ ,  $^{46}\text{Sc}$ ,  $^{58}\text{Co}$ ,  $^{54}\text{Mn}$ ,  $^{75}\text{Se}$ ,  $^{83}\text{Rb}$ ,  $^{85}\text{Sr}$  and  $^{88}\text{Zr}$  by brain and other organs of mice bred under Zn-deficient, -adequate and -excessive diets”, *J. Radioanal. Nucl. Chem.* **256**, 481–488 (2003).
- T. Ozaki, S. Ambe, T. Abe, and F. J. Arokiasamy: “Uptake of short half-life radionuclides,  $^{28}\text{Mg}$ ,  $^{43}\text{K}$  and  $^{47}\text{Ca}$ , in carrot studied by the multitracer technique: Feasibility of utilization of the radionuclides in environmental research”, *J. Radioanal. Nucl. Chem.* **258**, 89–92 (2003).
- S. Yoshida, T. Abe, and Y. Yano: “Development of plant mutagenesis using ion beams irradiation”, *JAERI-Conf*, No. 2003-003, pp. 26–28 (2003).
- T. Soshi, S. Enomoto, and I. Yamaguchi: “Effect of microorganisms on the uptake of radionuclides by plant, application of the plant-microorganisms complex system to the phytoremediation”, *JAERI-Conf.*, No. 2003-010, pp. 272–276 (2003).
- R. Hirunuma and S. Enomoto: “Application of the multitracer technique: Transport of various elements in the pregnant rats and the fetus”, *JAERI-Conf.*, No. 2003-010, pp. 326–331 (2003).
- H. Haba, R. Hirunuma, and S. Enomoto: “Development of a gas-jet coupled multitarget system for multitracer production”, *JAERI-Conf.*, No. 2003-010, pp. 332–334 (2003).
- H. Kagami and T. Abe: “Training of the new UNSHUU mandarin orange by heavy ion irradiation”, *Kongetsu no Nougyou* **47**, No. 10, pp. 52–55 (2003).
- S. Yoshida, T. Abe, and N. Fukunishi: “Plant research at RIKEN Ring Cyclotron facilities”, *Korekarano Daigaku to Kenkyu Shisetsu Dai2hen: Seimeikagakuhen*, Research Institute of Educational Facilities and The Science News Ltd., Tokyo, pp. 7-1–7-11 (2003).
- T. Morishita, H. Yamaguchi, K. Degi, N. Shikazono, Y. Hase, A. Tanaka, and T. Abe: “Dose response and mutation induction by ion beam irradiation in buckwheat”, *Nucl. Instrum. Methods Phys. Res. B* **206**, 565–569 (2003).
- T. Matsuyama, M. Kimura, K. Koike, T. Abe, T. Nakano, T. Asami, T. Ebisuzaki, W. A. Held, S. Yoshida, and H. Nagase: “Global methylation screening in the *Arabidopsis thaliana* and *Mus musculus* genome: Applications of virtual image restriction landmark genomic scanning (Vi-RLGS)”, *Nucleic Acids Res.* **31**, 4490–4496 (2003).
- T. Abe, Y. Miyazawa, H. Saito, S. Yoshida, N. Fukunishi, H. Ryuto, and Y. Yano: “Utilization of heavy ion beam as a mutagen in plants”, *Proc. 14th Symp. on Accelerator Science and Technology*, (KEK), Tsukuba, 2003–11, KEK, Tsukuba, pp. 578–580 (2003).
- M. Saitoh, H. Komori, H. Sakamoto, M. Hatashita, K. Takagi, T. Abe, and S. Yoshida: “Mutation breeding using ion beams”, *Proc. 2nd 21Seiki Rengou Symp.: Kagakugijutsu to Ningen*, Tokyo, 2003–11, Ionics, Tokyo, pp. 77–78 (2003).
- H. Saito, Y. Miyazawa, Y. Yamamoto, K. Suzuki, T. Abe, N. Fukunishi, H. Ryuto, Y. Yano, and S. Yoshida: “Mutants induced by heavy-ion beam irradiation”, *Proc. 2nd 21Seiki Rengou Symp.: Kagakugijutsu to Ningen*, Tokyo, 2003–11, Ionics, Tokyo, pp. 79–80 (2003).
- T. Abe, Y. Miyazawa, K. Sakino, J. M. Wang, and S. Yoshida: “Heavy-ion beam mutagenesis for herbicide resistant plants”, *Proc. 30th Ann. Conf. on Plant Growth Regulation Soc. of America held jointly with the Japanese Soc. for Chemical Regulation Plants*, Vancouver, Canada, 2003–8, PGRSA, LaGrange, p. 185 (2003).
- S. Enomoto: “The multitracer technology in bio-trace elements research”, *Proc. Int. Symp. on Bio-Trace Elements 2002*, edited by S. Enomoto and Y. Seko, RIKEN, Wako, pp. 27–31 (2003).
- T. Nabekura, T. Minami, R. Hirunuma, S. Enomoto, and Y. Ito: “Expression of metallothionein in cataractous rat lens”, *Proc. Int. Symp. on Bio-Trace Elements 2002*, edited by S. Enomoto and Y. Seko, RIKEN, Wako, pp. 71–73 (2003).
- T. Ohyama, M. Koike, T. Ogi, Y. Kawamoto, H. Maetsu, H. Suganuma, M. Noguchi, K. Ishikawa, R. Hirunuma, S. Enomoto, and M. Yanaga: “Distribution of trace elements among subcellular fractions in livers of Zn-deficient mice”, *Proc. Int. Symp. on Bio-Trace Elements 2002*, edited by S. Enomoto and Y. Seko, RIKEN, Wako, pp. 80–82 (2003).
- T. Ogi, Y. Kawamoto, H. Maetsu, M. Koike, T. Ohyama, S. Enomoto, M. Noguchi, H. Suganuma, and M. Yanaga: “Effects of zinc content in a diet on concentrations of trace elements in organs and tissues of mice”, *Proc. Int. Symp. on Bio-Trace Elements 2002*, edited by S. Enomoto and Y. Seko, RIKEN, Wako, pp. 83–85 (2003).
- K. Igarashi, Y. Nakanishi, R. Hirunuma, S. Enomoto, and S. Kimura: “Biological interaction of various trace elements and NaFeEDTA as a food fortificant”, *Proc. Int. Symp. on Bio-Trace Elements 2002*, edited by S. Enomoto and Y. Seko, RIKEN, Wako, pp. 86–90 (2003).
- H. Yasui, T. Takino, J. Fugono, A. Nakayama, R. Hirunuma, S. Enomoto, and H. Sakurai: “Effect of vanadium treatment on tissue distribution of bio-trace elements in normal and streptozotocin-induced diabetic rats”, *Proc. Int. Symp. on Bio-Trace Elements 2002*, edited by S. Enomoto and Y. Seko, RIKEN, Wako, pp. 134–136 (2003).
- T. Soshi, S. Enomoto, and I. Yamaguchi: “Effect of microorganisms on the uptake of radionuclides

- by plant”, Proc. Int. Symp. on Bio-Trace Elements 2002, edited by S. Enomoto and Y. Seko, RIKEN, Wako, pp. 143–146 (2003).
- A. Nakayama, H. Yasui, H. Sakurai, R. Hirunuma, and S. Enomoto: “Distribution of biotrace elements in partially hepatectomized rats”, Proc. Int. Symp. on Bio-Trace Elements 2002, edited by S. Enomoto and Y. Seko, RIKEN, Wako, pp. 159–161 (2003).
- Y. Kobayashi, K. Kubo, Y. Yamada, T. Saito, W. Sato, H. Ueno, J. Murata, H. Watanabe, D. Kameda, H. Miyoshi, and K. Asahi: “Chemical states of Fe implanted into graphite”, Proc. Specialist Research Meet. on New Developments in Solid State Physics with Probes of Radiations and Nuclei (IV), (Research Reactor Institute, Kyoto University), Kumatori-cho, Osaka Pref., 2002–12, edited by S. Nasu, Y. Maeda, and Y. Kawase, Research Reactor Institute, Kyoto University, Kumatori-cho, Osaka Pref., pp. 18–21 (2003).
- T. Saito, Y. Kobayashi, and Y. Yamada: “Emission Mössbauer spectroscopic studies of absorbed  $^{57}\text{Co}$  atoms on graphite”, Proc. Specialist Research Meet. on New Developments in Solid State Physics with Probes of Radiations and Nuclei (IV), (Research Reactor Institute, Kyoto University), Kumatori-cho, Osaka Pref., 2002–12, edited by S. Nasu, Y. Maeda, and Y. Kawase, Research Reactor Institute, Kyoto University, Kumatori-cho, Osaka Pref., pp. 22–25 (2003).
- H. Yasui, Y. Adachi, J. Fugono, H. Haba, A. Nakayama, R. Hirunuma, S. Enomoto, and H. Sakurai: “Pharmacokinetic study on gastrointestinal absorption and disposition in the blood of  $^{48}\text{vanadium}$  and  $^{65}\text{zinc}$  in healthy rats using radio-tracer method”, Proc. Trace Nutr. Res. **20**, 5–8 (2003).
- K. Igarashi, Y. Nakanishi, R. Hirunuma, S. Enomoto, and S. Kimura: “Efficacy of NaFeEDTA for improving iron deficiency”, Proc. Trace Nutr. Res. **20**, 109–112 (2003).
- T. Abe: “Mutation breeding using heavy-ion irradiation”, Radiat. Ind., No. 99, pp. 17–22 (2003).
- H. Haba, K. Igarashi, R. Hirunuma, and S. Enomoto: “Multitracer technology and prospects of multitracer studies on the RIKEN RIBF project”, Radiochemistry News **8**, 9–13 (2003).
- S. Ambe, D. Abe, T. Ozaki, and F. Ambe: “Multitracer studies on the permeation of rare earth elements through a supported liquid membrane containing 2-ethylhexyl phosphonic acid-2-ethylhexyl ester (EHEHPA)”, Radiochim. Acta **91**, 217–221 (2003).
- S. Enomoto: “Developments of the multitracer technology as a simultaneous multi-elemental analysis and its evolution in RI-beam factory project”, Radioisotopes **52**, 631–647 (2003).
- T. Nabekura, T. Minami, R. Hirunuma, S. Enomoto, M. Tomohiro, Y. Ito, and S. Kitagawa: “Transport of trace elements in lenses of normal and hereditary cataract UPL rats”, Toxicology **191**, 227–232 (2003).

## 5. Material Analysis

- Y. Yoshida, Y. Kobayashi, K. Hayakawa, K. Yukihiro, F. Shimura, A. Yoshida, X. Diao, H. Ogawa, Y. Yano, and F. Ambe: “In-beam Mössbauer study of interstitial and substitutional  $^{57}\text{Mn}/^{57}\text{Fe}$  jumps in Si”, Defect Diffus. Forum **194/199**, 611–616 (2001).
- M. Hase, K. Ishioka, K. Ushida, and M. Kitajima: “Dephasing of coherent THz phonons in bismuth studied by femtosecond pump-probe technique”, Appl. Surf. Sci. **197/198**, 710–714 (2002).
- K. Ishioka, M. Hase, K. Ushida, and M. Kitajima: “Phonon dynamics in ion-irradiated graphite and GaAs”, Appl. Surf. Sci. **197/198**, 726–729 (2002).
- K. Ishioka, M. Hase, K. Ushida, and M. Kitajima: “Coherent acoustic phonon-defect scattering in graphite”, Physica B **316/317**, 296–299 (2002).
- K. Maeda, K. Hasegawa, H. Hamanaka, and M. Maeda: “Particle induced X-ray emission (PIXE) analysis using position-sensitive crystal spectrometers: application to chemical state analysis in air”, Adv. X-Ray Chem. Anal. Jpn. **34**, 89–113 (2003).
- M. Hase, K. Ishioka, M. Kitajima, and K. Ushida: “Ultrafast carrier and plasmon-phonon dynamics in ion-irradiated  $n$ -GaAs”, Appl. Phys. Lett. **82**, 3668–3670 (2003).
- K. Ishioka, M. Hase, M. Kitajima, and K. Ushida: “Coherent phonons in semimetals and semiconductors: Effects of irradiation-induced defects on relaxation dynamics”, J. Surf. Sci. Soc. Jpn. **24**, 288–294 (2003).
- M. Kitajima, M. Hase, K. Ishioka, and K. Ushida: “Application of time-domain vibrational spectroscopy to the study of defects in ion-implanted materials”, Nucl. Instrum. Methods Phys. Res. B **206**, 99–102 (2003).
- K. Hasegawa, K. Maeda, and H. Hamanaka: “A stacked detector system for rapid high-resolution PIXE analysis by a crystal spectrometer”, Trans. Soc. Instrum. Control Eng. **39**, 11–17 (2003).

## 6. RIKEN-BNL Collaboration

- S. Soff, S. A. Bass, and A. Dumitru: “Pion interferometry at RHIC: Probing a thermalized quark-gluon plasma?”, Phys. Rev. Lett. **86**, 3981–3984 (2001).
- A. Bazilevsky, G. M. Bunce, A. Deshpande, H. En’yo, Y. Goto, M. G. Perdekamp, N. Hayashi, T. Ichihara, K. Imai, M. Ishihara, B. V. Jacak, K. Kurita, Z. Li, Y. Mao, J. Murata, N. Saito, T. Sakuma, H. D. Sato, T. Shibata, M. Sugioka, A. Taketani, E. Taniguchi, J. Tojo, H. Torii, Y. Watanabe, S.

- Yokkaichi, and PHENIX Collaboration: “Measurement of the midrapidity transverse energy distribution from  $\sqrt{s_{NN}} = 130$  GeV Au+Au collisions at RHIC”, Phys. Rev. Lett. **87**, 052301-1–052301-6 (2001).
- V. W. Hughes, P. M. Gross, D. Kawall, W. Liu, K. Jungmann, and G. zu Putlitz: “Test of  $CPT$  and Lorentz invariance from muonium spectroscopy”, Phys. Rev. Lett. **87**, 111804-1–111804-4 (2001).
- Y. Goto: “First polarized proton collisions at PHENIX”, Acta Phys. Pol. B **B33**, 3767–3771 (2002).
- L. V. Bravina, E. E. Zabrodin, S. A. Bass, A. Faessler, C. Fuchs, M. I. Gorenstein, W. Greiner, S. Soff, H. Stocker, and H. Weber: “Chemical freeze-out parameters at RHIC from microscopic model calculation”, Nucl. Phys. A **698**, 383c–386c (2002).
- M. Stratmann and W. Vogelsang: “Partons and QCD in high-energy polarized pp collisions”, Nucl. Phys. B (Proc. Suppl.) **105**, 134–139 (2002).
- K. Kurita: “Proton-carbon CNI polarimeter for RHIC”, Nucl. Phys. B (Proc. Suppl.) **105**, 164–167 (2002).
- A. Bazilevsky, G. M. Bunce, A. Deshpande, H. En’yo, Y. Goto, M. G. Perdekamp, N. Hayashi, T. Ichihara, K. Imai, M. Ishihara, B. V. Jacak, K. Kurita, Z. Li, Y. Mao, J. Murata, N. Saito, T. Sakuma, H. D. Sato, T. Shibata, M. Sugioka, A. Taketani, E. Taniguchi, J. Tojo, H. Torii, Y. Watanabe, S. Yokkaichi, and PHENIX Collaboration: “Event-by-event fluctuations in mean  $p_T$  and mean  $e_T$  in  $\sqrt{s_{NN}} = 130$  GeV Au+Au collisions”, Phys. Rev. C **66**, 024901-1–024901-10 (2002).
- A. Bazilevsky, G. M. Bunce, A. Deshpande, H. En’yo, Y. Goto, M. G. Perdekamp, N. Hayashi, T. Ichihara, K. Imai, M. Ishihara, B. V. Jacak, K. Kurita, Z. Li, Y. Mao, J. Murata, N. Saito, T. Sakuma, H. D. Sato, T. Shibata, M. Sugioka, A. Taketani, E. Taniguchi, J. Tojo, H. Torii, Y. Watanabe, S. Yokkaichi, and PHENIX Collaboration: “Transverse-mass dependence of two-pion correlations in Au+Au collisions at  $\sqrt{s_{NN}} = 130$  GeV”, Phys. Rev. Lett. **88**, 192302-1–192302-6 (2002).
- A. Bazilevsky, G. M. Bunce, A. Deshpande, H. En’yo, Y. Goto, M. G. Perdekamp, N. Hayashi, T. Ichihara, K. Imai, M. Ishihara, B. V. Jacak, K. Kurita, Z. Li, Y. Mao, J. Murata, N. Saito, T. Sakuma, H. D. Sato, T. Shibata, M. Sugioka, A. Taketani, E. Taniguchi, J. Tojo, H. Torii, Y. Watanabe, S. Yokkaichi, and PHENIX Collaboration: “Measurement of single electrons and implications for charm production in Au+Au collisions at  $\sqrt{s_{NN}} = 130$  GeV”, Phys. Rev. Lett. **88**, 192303-1–192303-6 (2002).
- A. Bazilevsky, G. M. Bunce, A. Deshpande, H. En’yo, Y. Goto, M. G. Perdekamp, N. Hayashi, T. Ichihara, K. Imai, M. Ishihara, B. V. Jacak, K. Kurita, Z. Li, Y. Mao, J. Murata, N. Saito, T. Sakuma, H. D. Sato, T. Shibata, M. Sugioka, A. Taketani, E. Taniguchi, J. Tojo, H. Torii, Y. Watanabe, S. Yokkaichi, and PHENIX Collaboration: “Centrality dependence of  $\pi^{+/-}$ ,  $K^{+/-}$ ,  $p$  and  $\bar{p}$  production from  $\sqrt{s_{NN}} = 130$  GeV Au+Au collisions at RHIC”, Phys. Rev. Lett. **88**, 242301-1–242301-6 (2002).
- A. Bazilevsky, G. M. Bunce, A. Deshpande, H. En’yo, Y. Goto, M. G. Perdekamp, N. Hayashi, T. Ichihara, K. Imai, M. Ishihara, B. V. Jacak, K. Kurita, Z. Li, Y. Mao, J. Murata, N. Saito, T. Sakuma, H. D. Sato, T. Shibata, M. Sugioka, A. Taketani, E. Taniguchi, J. Tojo, H. Torii, Y. Watanabe, S. Yokkaichi, and PHENIX Collaboration: “Net charge fluctuations in Au+Au interactions at  $\sqrt{s_{NN}} = 130$  GeV”, Phys. Rev. Lett. **89**, 082301-1–082301-6 (2002).
- A. Bazilevsky, G. M. Bunce, A. Deshpande, H. En’yo, Y. Goto, M. G. Perdekamp, N. Hayashi, T. Ichihara, K. Imai, M. Ishihara, B. V. Jacak, K. Kurita, Z. Li, Y. Mao, J. Murata, N. Saito, T. Sakuma, H. D. Sato, T. Shibata, M. Sugioka, A. Taketani, E. Taniguchi, J. Tojo, H. Torii, Y. Watanabe, S. Yokkaichi, and PHENIX Collaboration: “Measurement of  $\Lambda$  and  $\bar{\Lambda}$  particles in Au+Au collisions at  $\sqrt{s_{NN}} = 130$  GeV”, Phys. Rev. Lett. **89**, 092302-1–092302-6 (2002).
- A. Bazilevsky, G. M. Bunce, A. Deshpande, H. En’yo, Y. Goto, M. G. Perdekamp, N. Hayashi, T. Ichihara, K. Imai, M. Ishihara, B. V. Jacak, K. Kurita, Z. Li, Y. Mao, J. Murata, N. Saito, T. Sakuma, H. D. Sato, T. Shibata, M. Sugioka, A. Taketani, E. Taniguchi, J. Tojo, H. Torii, Y. Watanabe, S. Yokkaichi, and PHENIX Collaboration: “Flow measurements via two-particle azimuthal correlations in Au+Au collisions at  $\sqrt{s_{NN}} = 130$  GeV”, Phys. Rev. Lett. **89**, 212301-1–212301-6 (2002).
- K. Sudo: “ $D$  meson production in neutrino DIS as a probe of polarized strange quark distribution”, AIP Conf. Proc. **675**, 370–374 (2003).
- N. Ishii and H. Suganuma: “A remark on the large difference between the glueball mass and  $T_c$  in quenched QCD”, Eur. Phys. J. A **17**, 77–82 (2003).
- K. Sudo: “Polarized parton distribution in neutrino induced heavy flavour production”, J. Phys. G **29**, 1955–1958 (2003).
- D. Cortina-Gil, J. Fernandez-Vazquez, F. Attallah, T. Baumann, J. Benlliure, M. J. G. Borge, L. Chulkov, C. Forssen, L. M. Fraile, H. Geissel, J. Gerl, K. Itahashi, R. Janik, B. Jonson, S. Karlsson, H. Lenske, S. Mandal, K. Markenroth, M. Meister, M. Mocko, G. Munzenberg, T. Ohtsubo, A. Ozawa, Y. Perfenova, V. Pribora, A. Richter, K. Riisager, R. Schneider, H. Scheit, G. Schreider, N. Shulgina, H. Simon, B. Sitar, A. Stolz, P. Strmen, K. Summerer, I. Szarka, S. Wan, H. Weick, and M. V. Zhukov: “Nuclear and Coulomb breakup of  $^8\text{B}$ ”, Nucl. Phys. A **720**, 3–19 (2003).
- K. Mawatari, T. Morii, S. Oyama, and K. Sudo: “DIS charged current  $\Lambda_c^+/\bar{\Lambda}_c^+$  production as a probe of  $\Delta s$

- and  $\Delta g$ ”, Nucl. Phys. A **721**, 380c–383c (2003).
- T. Izubushi and RRBC Collaboration: “Lattice QCD with dynamical domain wall quarks”, Nucl. Phys. B (Proc. Suppl.) **119**, 813–815 (2003).
- K. Adcox, A. V. Bazilevsky, G. M. Bunce, A. Deshpande, H. Enyo, Y. Goto, M. G. Perdekamp, N. Hayashi, T. Ichihara, K. Imai, M. Ishihara, B. V. Jacak, K. Kurita, Z. Liu, Y. Mao, J. Murata, N. Saito, T. Sakuma, H. Sato, T. Shibata, M. Sugioka, A. Taketani, E. Taniguchi, J. Tojo, H. Torii, Y. Watanabe, S. Yokkaichi, and PHENIX Collaboration: “Centrality dependence of the high  $p_T$  charged hadron suppression in Au+Au collisions at  $\sqrt{s_{NN}} = 130$  GeV”, Phys. Lett. B **561**, 82–92 (2003).
- T. Hirano and Y. Nara: “Pseudorapidity dependence of parton energy loss in relativistic heavy ion collisions”, Phys. Rev. C **68**, 064902-1–064902-5 (2003).
- Y. Hatta and T. Ikeda: “Universality, the QCD critical and tricritical point, and the quark number susceptibility”, Phys. Rev. D **67**, 014028-1–014028-12 (2003).
- S. Aoki, T. Izubushi, Y. Kuramashi, and Y. Taniguchi: “Perturbative renormalization factors in domain-wall QCD with improved gauge actions”, Phys. Rev. D **67**, 094502-1–094502-26 (2003).
- Y. Hidaka, O. Morimatsu, T. Nishikawa, and M. Ohtani: “Effect of the pion thermal width on the sigma spectrum”, Phys. Rev. D **68**, 111901-1–111901-5 (2003).
- S. S. Adler, Y. Akiba, A. V. Bazilevsky, G. M. Bunce, A. Deshpande, H. Enyo, D. E. Fields, B. Fox, Y. Goto, M. G. Perdekamp, T. Ichihara, K. Imai, M. Ishihara, O. Jinnouchi, N. Kamihara, H. Kobayashi, K. Kurita, Y. Mao, J. Murata, H. Onishi, K. Okada, N. Saito, H. Sato, T. Shibata, A. Taketani, K. Tanida, J. Tojo, H. Torii, Y. Watanabe, S. Yokkaichi, and PHENIX Collaboration: “Suppressed  $\pi^0$  production at large transverse momentum in central Au+Au collisions at  $\sqrt{s_{NN}} = 200$  GeV”, Phys. Rev. Lett. **91**, 072301-1–072301-6 (2003).
- T. Hirano and Y. Nara: “Back-to-back correlations of high- $p_T$  hadrons in relativistic heavy-ion collisions”, Phys. Rev. Lett. **91**, 082301-1–082301-4 (2003).
- S. S. Adler, Y. Akiba, A. V. Bazilevsky, G. M. Bunce, A. Deshpande, H. Enyo, D. E. Fields, B. Fox, Y. Goto, M. G. Perdekamp, T. Ichihara, K. Imai, M. Ishihara, O. Jinnouchi, N. Kamihara, H. Kobayashi, K. Kurita, Y. Mao, J. Murata, H. Onishi, K. Okada, N. Saito, H. Sato, T. Shibata, A. Taketani, K. Tanida, J. Tojo, H. Torii, Y. Watanabe, S. Yokkaichi, and PHENIX Collaboration: “Elliptic flow of identified Hadrons in Au+Au collisions at  $\sqrt{s_{NN}} = 200$  GeV”, Phys. Rev. Lett. **91**, 182301-1–182301-6 (2003).
- S. S. Adler, Y. Akiba, A. V. Bazilevsky, G. M. Bunce, A. Deshpande, H. Enyo, D. E. Fields, B. Fox, Y. Goto, M. G. Perdekamp, T. Ichihara, K. Imai, M. Ishihara, O. Jinnouchi, N. Kamihara, H. Kobayashi, K. Kurita, Y. Mao, J. Murata, H. Onishi, K. Okada, N. Saito, H. Sato, T. Shibata, A. Taketani, K. Tanida, J. Tojo, H. Torii, Y. Watanabe, S. Yokkaichi, and PHENIX Collaboration: “Midrapidity neutral-pion production in proton-proton collisions at  $\sqrt{s} = 200$  GeV”, Phys. Rev. Lett. **91**, 241803-1–241803-6 (2003).
- S. S. Adler, Y. Akiba, A. V. Bazilevsky, G. M. Bunce, A. Deshpande, H. Enyo, D. E. Fields, B. Fox, Y. Goto, M. G. Perdekamp, T. Ichihara, K. Imai, M. Ishihara, O. Jinnouchi, N. Kamihara, H. Kobayashi, K. Kurita, Y. Mao, J. Murata, H. Onishi, K. Okada, N. Saito, H. Sato, T. Shibata, A. Taketani, K. Tanida, J. Tojo, H. Torii, Y. Watanabe, S. Yokkaichi, and PHENIX Collaboration: “Scaling properties of proton and anti-proton production in  $\sqrt{s_{NN}} = 200$  GeV Au+Au collisions”, Phys. Rev. Lett. **92**, 172301-1–172301-6 (2003).
- N. Ishii, H. Sugauma, and H. Matsufuru: “Thermal width broadening of the  $0^{++}$  glueball spectrum near  $T_c$ ”, Prog. Theor. Phys. Suppl., No. 151, pp. 166–170 (2003).
- Y. Akiba: “Charm measurements at SPS and RHIC”, J. Phys. G **30**, S283–S293 (2004).
- Z. Li, H. Enyo, Y. Goto, V. Radeka, W. Chen, D. C. Elliott, T. Kawabata, M. Togawa, N. Saito, V. Rykov, K. Tanida, and J. Tojo: “Novel silicon strip-ixel detector for PHENIX upgrade”, Nucl. Instrum. Methods Phys. Res. A **518**, 300–304 (2004).
- A. Iwazaki, O. Morimatsu, T. Nishikawa, and M. Ohtani: “Color ferromagnetism of quark matter and quantum hall states of gluons in SU(3) gauge theory”, Phys. Lett. B **579**, 347–354 (2004).

## VII. LIST OF PREPRINTS

2003

RIKEN-AF-NP

- 442 R. Kanungo, M. Chiba, S. Adhikari, D. Fang, N. Iwasa, K. Kimura, K. Maeda, S. Nishimura, Y. Ogawa, T. Ohnishi, A. Ozawa, C. Samanta, T. Suda, T. Suzuki, Q. Wang, C. Wu, Y. Yamaguchi, K. Yamada, A. Yoshida, T. Zheng, and I. Tanihata: “Two-proton halo in  $^{17}\text{Ne}$ ”
- 443 H. Madokoro, T. Shimizu, and Y. Mochizuki: “Global anisotropy vs small-scale fluctuation of neutrino flux in supernova explosions”
- 444 A. A. Korsheninikov, E. Yu. Nikolskii, E. A. Kuzmin, A. Ozawa, K. Morimoto, F. Tokanai, R. Kanungo, I. Tanihata, N. K. Timofeyuk, M. S. Golovkov, A. S. Fomichev, A. M. Rodin, M. L. Chelnokov, G. M. Ter-Akopian, W. Mittig, P. Roussel-Chomaz, H. Savajols, E. Pollacco, A. A. Ogloblin, and M. V. Zhukov: “Experimental evidences for the existence of  $^7\text{H}$  and for a specific structure of  $^8\text{He}$ ”
- 445 T. Yamaguchi, T. Zheng, A. Ozawa, M. Chiba, R. Kanungo, T. Kato, K. Morimoto, T. Ohnishi, T. Suda, Y. Yamaguchi, A. Yoshida, K. Yoshida, and I. Tanihata: “Momentum distributions of  $^{14}\text{C}$  and  $^{15}\text{C}$  fragments from  $^{16}\text{C}$  breakup”
- 446 Y. Yanagisawa, M. Notani, H. Sakurai, M. Kunibu, H. Akiyoshi, N. Aoi, H. Baba, H. Demichi, N. Fukuda, K. Hasegawa, Y. Higurashi, M. Ishihara, N. Iwasa, H. Iwasaki, T. Gomi, S. Kanno, M. Kurokawa, Y. U. Matsuyama, S. Michimasa, T. Minemura, T. Mizoi, T. Nakamura, A. Saito, M. Serata, S. Shimoura, T. Sugimoto, E. Takeshita, S. Takeuchi, K. Ue, K. Yamada, and Motobayashi: “The first excited state in  $^{30}\text{Ne}$  studied by proton inelastic scattering in reversed kinematics”
- 447 N. Iwasa, T. Motobayashi, H. Sakurai, H. Akiyoshi, Y. Ando, N. Aoi, H. Baba, N. Fukuda, Zs. Fülöp, U. Futakami, T. Gomi, Y. Higurashi, K. Ieki, H. Iwasaki, T. Kubo, S. Kubono, H. Kinugawa, H. Kumagai, M. Kunibu, S. Michimasa, T. Minemura, H. Murakami, K. Sagara, A. Saito, S. Shimoura, S. Takeuchi, Y. Yanagisawa, K. Yoneda, and M. Ishihara: “In-beam  $\gamma$  spectroscopy of  $^{34}\text{Si}$  with deuteron inelastic scattering in reversed kinematics”
- 448 H. Ogawa, K. Asahi, K. Sakai, T. Suzuki, H. Izumi, H. Miyoshi, M. Nagakura, K. Yogo, A. Goto, T. Suga, T. Honda, H. Ueno, Y. X. Watanabe, K. Yoneda, A. Yoshimi, N. Fukuda, Y. Kobayashi, A. Yoshida, T. Kubo, M. Ishihara, N. Imai, N. Aoi, W.-D. Schmidt-Ott, G. Neyens, and S. Teughels: “Electric quadrupole moment of  $^{17}\text{B}$  and anomalous E2 effective charges for neutron-rich nuclei”
- 449 M. Ohtani, Y. Hidaka, O. Morimatsu, and T. Nishikawa: “Effect of pion thermal width on the spectral function of sigma meson”
- 450 N. Dinh Dang and A. Arima: “Modified Hartree-Fock-Bogoliubov theory at finite temperature”
- 451 K. Yamada, T. Motobayashi, H. Akiyoshi, N. Aoi, Zs. Fülöp, T. Gomi, Y. Higurashi, N. Imai, N. Iwasa, H. Iwasaki, Y. Iwata, H. Kobayashi, M. Kurokawa, Z. Liu, T. Minemura, S. Ozawa, H. Sakurai, M. Serata, S. Shimoura, S. Takeuchi, T. Teranishi, Y. Yanagisawa, K. Yoshida, and M. Ishihara: “E1 strength of the subthreshold  $3/2^+$  state in  $^{15}\text{O}$  studied by Coulomb excitation”
- 452 N. Imai, H. J. Ong, N. Aoi, H. Sakurai, K. Demichi, H. Kawasaki, N. Baba, Zs. Dombrádi, Z. Elekes, N. Fukuda, Zs. Fülöp, A. Gelberg, T. Gomi, H. Hasegawa, K. Ishikawa, H. Iwasaki, E. Kaneko, S. Kanno, T. Kishida, Y. Kondo, T. Kubo, K. Kurita, S. Michimasa, T. Minemura, M. Miura, T. Motobayashi, T. Nakamura, M. Notani, T. K. Ohnishi, A. Saito, S. Shimoura, T. Sugimoto, M. K. Suzuki, E. Takeshita, S. Takeuchi, M. Tamaki, K. Yoneda, H. Watanabe, and M. Ishihara: “Anomalously hindered E2 strength  $B(E2; 2_1^+ \rightarrow 0^+)$  in  $^{16}\text{C}$ ”
- 453 N. Dinh Dang and A. Arima: “Pairing effect on the giant dipole resonance width at low temperature”

- 454 T. Yamazaki, A. Dote, and Y. Akaishi: “Invariant-mass spectroscopy for condensed single- and double- $\bar{K}$  nuclear clusters to be formed as residues in relativistic heavy-ion collisions”
- 455 Z. Elekes, Zs. Dombrádi, A. Krasznahorkay, H. Baba, M. Csatlós, L. Csige, N. Fukuda, Zs. Fülöp, Z. Gácsi, J. Gulyás, N. Iwasa, H. Kinugawa, S. Kubono, M. Kurokawa, X. Liu, S. Michimasa, T. Minemura, T. Motobayashi, A. Ozawa, A. Saito, S. Shimoura, S. Takeuchi, I. Tanihata, P. Thirolf, Y. Yanagisawa, and K. Yoshida: “Decoupling of valence neutrons from the core in  $^{16}\text{C}$ ”

#### RIKEN-AF-AC

- 41 T. Ohkawa, Y. Chiba, M. Wakasugi, and T. Katayama: “Development of the kicker magnet for MUSES”
- 42 I. Meshkov, A. Sidorin, A. Smirnov, E. Syresin, T. Katayama, H. Tsutsui, and D. Mohl: “Simulation study of ordered ion beams”
- 43 R. A. Jameson, M. Okamura, and T. Katayama: “Desing of  $\geq 100$  MA  $\text{C}^{4+}$  RFQ for laser ion source”



## VIII. PAPERS PRESENTED AT MEETINGS

### 1. Accelerator development and accelerator physics

- M. Komiyama, M. Kase, T. Tanabe, M. Fujimaki, E. Ikezawa, M. Nagase, I. Yokoyama, and R. Abe: “New control system of the RIKEN ring cyclotron using EPICS”, 13th Symp. on Accelerator Science and Technology, (RCNP and ISIR, Osaka University), Suita, Oct. (2001).
- M. Kobayashi, K. Ushida, Y. Aoki, M. Mori, T. Kuribayashi, S. Kashiwagi, R. Kuroda, Y. Hama, and M. Washio: “Development of pulse radiolysis system with picosecond RF-gun in Waseda University”, 45th Symp. on Radiation Chemistry, Kasuga, Oct. (2002).
- R. Kuroda, S. Kashiwagi, A. Nagasawa, H. Kawai, M. Washio, Y. Hama, K. Ushida, J. Urakawa, and H. Hayano: “Development of a soft X-ray source for “water-window” region based on laser Compton scattering”, 58th Ann. Meet. of Physical Soc. of Japan, Sendai, Mar. (2003).
- H. Miyoshi, J. Murata, K. Asahi, H. Ueno, A. Yoshimi, H. Watanabe, D. Kameda, J. Kaihara, K. Shimada, W. Sato, S. Suda, T. Ito, and Y. Kobayashi: “Development of set-up for production of low energy spin-polarized RI beam(1)”, 58th Ann. Meet. of Physical Soc. of Japan, Sendai, Mar. (2003).
- K. Shimada, K. Asahi, T. Ito, H. Ueno, J. Kaihara, D. Kameda, Y. Kobayashi, W. Sato, S. Suda, J. Murata, A. Yoshimi, and H. Watanabe: “Development of set-up for production of low energy spin-polarized RI beam(2)”, 58th Ann. Meet. of Physical Soc. of Japan, Sendai, Mar. (2003).
- H. Ueno and K. Asahi: “Production of RIBs in the RIBF-RIPS configuration”, Workshop on RI Beam Factory and Research Plan, Wako, Mar. (2003).
- M. Kidera, T. Nakagawa, S. Enomoto, K. Takahashi, R. Hirunuma, K. Igarashi, T. Ohyama, M. Fujimaki, E. Ikezawa, O. Kamigaito, M. Kase, and Y. Yano: “Accelerator mass spectrometry using electron cyclotron resonance ion source and heavy ion accelerator”, Dai2kai Kogata Kasokuki Kenkyukai, (KEK), Tsukuba, July (2003).
- M. Kobayashi, K. Ushida, Y. Aoki, M. Mori, T. Kuribayashi, S. Kashiwagi, R. Kuroda, Y. Hama, and M. Washio: “Construction of pulse radiolysis system with a picosecond RF-gun at Waseda University”, Joint 6th ICFA Advanced & Novel Accelerators and 29th ICFA Advanced Beam Dynamics Workshop on Laser-Beam Interactions, Oxford, UK, July (2003).
- O. Kamigaito, M. Kase, E. Ikezawa, S. Kohara, N. Sakamoto, M. Fujimaki, T. Nakagawa, M. Kidera, Y. Higurashi, Y. Chiba, M. Hemmi, Y. Miyazawa, T. Chiba, T. Aihara, T. Ohki, H. Hasebe, H. Yamauchi, A. Uchiyama, K. Oyamada, and Y. Yano: “Present status of the RIKEN heavy-ion linac”, 28th Linear Accelerator Meet. in Japan (LAM28), (J-PARC and others), Tokai, July–Aug. (2003).
- M. Kidera, T. Aihara, Y. Higurashi, E. Ikezawa, O. Kamigaito, M. Kase, T. Nakagawa, N. Suzuki, and Y. Yano: “Production of intense  $^{58}\text{Fe}$ ,  $^{64}\text{Ni}$  beams using MIVOC method and new analyzing system of RIKEN 18 GHz ECRIS”, 10th Int. Conf. on Ion Sources (ICIS 2003), Dubna, Russia, Sept. (2003).
- T. Kikuchi, T. Katayama, K. Horioka, and M. Nakajima: “Dynamics and space charge effect during bunching processes of intense heavy-ion beam”, 2003 Fall Meet. of the Physical Soc. of Japan, Miyazaki and Okayama, Sept. (2003).
- T. Watanabe, S. Watanabe, T. Ikeda, M. Kase, Y. Sasaki, T. Kawaguchi, and T. Katayama: “Prototype of highly-sensitive cryogenic current comparator with HTS SQUID and HTS magnetic shield”, 6th European Conf. on Applied Superconductivity 2003 (EUCAS 2003), (Istituto Nazionale per la Fisica della Materia (INFN)), Napoli, Italy, Sept. (2003).
- F. Nagasawa, D. Ueyama, S. Kashiwagi, R. Kuroda, M. Washio, K. Ushida, H. Hayano, and J. Urakawa: “The development of the compact soft X-ray source using laser Compton scattering”, 46th Symp. on Radiation Chemistry, (Japanese Society of Radiation Chemistry), Hakone-machi, Kanagawa Pref., Sept. (2003).
- A. Goto, H. Okuno, J. Ohnishi, T. Tominaka, S. Fujishima, K. Ikegami, N. Fukunishi, Y. Miyazawa, T. Mitsumoto, and Y. Yano: “Sector magnets for the RIKEN superconducting ring cyclotron”, 18th Int. Conf. on Magnet Technology (MT-18), (National Institute for Materials Science), Morioka, Oct. (2003).
- T. Tanabe, T. Masuoka, K. Yoshida, K. Kumagai, M. Komiyama, T. Emoto, and M. Kase: “Current status of the control system development at RIKEN RI-Beam factory”, 9th Int. Conf. on Accelerator and Large Experimental Physics Control Systems (ICALEPCS 2003), Gyeongju, Korea, Oct. (2003).
- T. Kikuchi, T. Katayama, K. Horioka, and M. Nakajima: “Beam dynamics and instability in final beam bunching for heavy ion inertial fusion”, 14th Symp. on Accelerator Science and Technology (SAST03), (KEK), Tsukuba, Nov. (2003).
- T. Tanabe, K. Yoshida, T. Masuoka, M. Kase, K. Kumagai, and T. Emoto: “Development of RIBF accelerator power-supply controls using distributed object model”, 14th Symp. on Accelerator Science and Technology (SAST03), (KEK), Tsukuba, Nov. (2003).
- T. Watanabe, S. Watanabe, T. Ikeda, T. Katayama, M. Kase, T. Kawaguchi, and Y. Sasaki: “Development of a highly-sensitive and nondestructive beam

current monitor with HTS-SQUID and superconducting magnetic shield”, 14th Symp. on Accelerator Science and Technology (SAST03), (KEK), Tsukuba, Nov. (2003).

J. Ohnishi, T. Tominaka, H. Okuno, M. Nagase, and A. Goto: “Power supply system for the sector magnets of RIKEN superconducting ring cyclotron”, 14th Symp. on Accelerator Science and Technology (SAST03), (KEK), Tsukuba, Nov. (2003).

O. Kamigaito, M. Kase, N. Sakamoto, E. Ikezawa, S. Kohara, M. Fujimaki, T. Nakagawa, M. Kidera, Y. Higurashi, H. Ryuto, Y. Chiba, M. Hemmi, Y. Miyazawa, T. Chiba, T. Aihara, T. Ohki, H. Hasebe, H. Yamauchi, A. Uchiyama, K. Oyamada, A. Goto, and Y. Yano: “Present status of the RIKEN heavy-ion linac”, 14th Symp. on Accelerator Science and Technology (SAST03), (KEK), Tsukuba, Nov. (2003).

H. Ueno, K. Asahi, and A. Yoshimi: “Beam line for the production of spin-polarized RI beams”, Workshop on Experimental Apparatus Dedicated to the RIBF Project, Wako, Dec. (2003).

## 2. Nuclear physics and nuclear instrumentation

H. Madokoro, J. Meng, M. Matsuzaki, and S. Yamaji: “Shears bands in the  $A = 80$  mass region”, 2000 Spring Meet. of the Physical Soc. of Japan, Higashi Osaka, Mar. (2000).

H. Madokoro, J. Meng, M. Matsuzaki, and S. Yamaji: “Shears bands in the  $A = 80$  mass region II”, 55th Ann. Meet. of Physical Soc. of Japan, Niigata, Sept. (2000).

K. Sakai, K. Asahi, H. Ogawa, A. Goto, K. Yogo, T. Suga, H. Miyoshi, D. Kameda, M. Utsuro, K. Okumura, M. Hino, and A. Yoshimi: “A new method of UCN production using a spatially alternating magnetic field with spin flips”, 14th Int. Spin Physics Symp. (SPIN 2000), Osaka, Oct. (2000).

H. Madokoro, J. Meng, M. Matsuzaki, and S. Yamaji: “Relativistic tilted axis cranking model and its application to the shears bands in the  $A = 80$  region”, Workshop on Nuclear Structure of Unstable Nuclei, (Yukawa Institute of Theoretical Physics), Kyoto, Feb. (2001).

H. Madokoro, J. Meng, M. Matsuzaki, and S. Yamaji: “Relativistic Hartree-Bogoliubov study of shears bands in the  $A = 80$  region”, 56th Ann. Meet. of the Physical Soc. of Japan, Hachioji, Mar. (2001).

H. Madokoro, J. Meng, M. Matsuzaki, and S. Yamaji: “Magnetic rotation in the  $A = 80$  mass region”, RIKEN Workshop: Fuanteikakubutsuri ni mukete, Wako, Mar. (2001).

A. Saito: “Molecular states in neutron-rich nuclei  $^{12,14}\text{Be}$ ”, Workshop on Low-Energy Radioactive Nuclei Beams, (KEK), Tsukuba, Mar. (2001).

A. Saito, S. Shimoura, S. Takeuchi, T. Motobayashi,

H. Ryuto, Y. Ando, N. Aoi, Z. Fulop, T. Gomi, Y. Higurashi, M. Hirai, N. Iwasa, H. Iwasaki, Y. Iwata, H. Kobayashi, M. Kurokawa, Z. Liu, T. Minemura, S. Ozawa, H. Sakurai, M. Serata, T. Teranishi, K. Yamada, Y. Yanagisawa, and M. Ishihara: “Molecular states in  $^{12}\text{Be}$  and  $^{14}\text{Be}$ ”, 3rd Int. Conf. on Exotic Nuclei and Atomic Masses (ENAM 2001), Hameenlinna, Finland, July (2001).

R. Kanungo: “Observation of new proton and neutron magic numbers”, Int. Nuclear Physics Conf. (INPC2001), (University of California and Lawrence Berkeley National Laboratory), Berkeley, USA, July–Aug. (2001).

A. Saito: “Molecular states in neutron-rich be isotopes”, Cluster Physics and Unstable Nuclei, Wako, Aug. (2001).

J. Noaki: “Calculation of  $K \rightarrow \pi\pi$  decay amplitudes from  $K \rightarrow \pi$  matrix elements in quenched domain-wall QCD”, LATTICE2001: 19th Int. Symp. on Lattice Field Theory, (DESY Zeuthen and Humboldt-Universität zu Berlin), Berlin, Germany, Aug. (2001).

T. Blum: “ $\epsilon'$  from quenched lattice QCD”, 1st Joint Meet. of the Nuclear Physicists of the American and Japanese Physical Soc. (HAW01), (APS and JPS), Maui, USA, Oct. (2001).

Y. Nara, A. Krasnitz, and R. Venugopalan: “Gluon productions in classical SU(3) lattice gauge theory in high energy heavy ion collisions”, 1st Joint Meet. of the Nuclear Physicists of the American and Japanese Physical Soc. (HAW01), (APS and JPS), Maui, USA, Oct. (2001).

R. Venugopalan: “Initial conditions in heavy ion collisions”, 1st Joint Meet. of the Nuclear Physicists of the American and Japanese Physical Soc. (HAW01), (APS and JPS), Maui, USA, Oct. (2001).

R. Kanungo: “Modification of shell structure in unstable nuclei”, Yukawa Int. Seminar 2001 (YKIS01): Physics of Unstable Nuclei, (Yukawa Institute for Theoretical Physics, Kyoto University), Kyoto, Nov. (2001).

S. Sugimoto: “Relativistic mean field theory with pi meson field for finite nuclei”, Yukawa Int. Seminar 2001 (YKIS01): Physics of Unstable Nuclei, (Yukawa Institute for Theoretical Physics, Kyoto University), Kyoto, Nov. (2001).

R. Kanungo: “Modification of shell structure in nuclei far from stability”, DAE-BRNS Symp. on Nuclear Physics, (Department of Atomic Energy, Govt. of India), Kolkata, India, Dec. (2001).

H. Madokoro, J. Meng, M. Matsuzaki, and S. Yamaji: “Relativistic Hartree-Bogoliubov study of tilted axis rotation”, Seminar of Microscopic Description of Collective Motion in Nuclei, (Fukuoka University), Fukuoka, Dec. (2001).

H. Miyoshi, H. Ueno, K. Asahi, H. Ogawa, J. Murata, K. Sakai, D. Kameda, Y. Kobayashi, W. Sato, A.

- Yoshimi, H. Watanabe, K. Yoneda, N. Imai, J. Kaihara, K. Shimada, and T. Koike: “Development of low energy polarized RI atomic beam”, RIKEN Symp. on Condensed Matter Studies with Radioactive Ion Beams, Wako, Feb. (2002).
- H. Watanabe: “High-spin isomer beams at RARF”, RIKEN Symp. on Condensed Matter Studies with Radioactive Ion Beams, Wako, Feb. (2002).
- H. Ueno: “Production of radioactive ion beams in the RIBF-RIPS configuration”, RIKEN Symp. on Condensed Matter Studies with Radioactive Ion Beams, Wako, Feb. (2002).
- J. Murata: “RI beam buffering and the extraction towards ABS”, RIKEN Symp. on Condensed Matter Studies with Radioactive Ion Beams, Wako, Feb. (2002).
- R. Kanungo: “Proton scattering at RIKEN RI Beam Factory”, Workshop on Rare Isotope Physics at Storage Rings, (GSI and RIKEN), Hirscheegg, Austria, Feb. (2002).
- H. Madokoro, J. Meng, M. Matsuzaki, and S. Yamaji: “Relativistic Hartree-Bogoliubov study of chiral doublet bands in the odd-odd triaxial nuclei”, 57th Ann. Meet. of Physical Soc. of Japan, Kusatsu, Shiga Pref., Mar. (2002).
- T. Motobayashi: “RI beam factory project at RIKEN”, 14th Int. Conf. on Electromagnetic Isotope Separators and Techniques Related to their Applications, (TRIUMF), Victoria, Canada, May (2002).
- K. Asahi, H. Ueno, Y. Kobayashi, W. Sato, A. Yoshimi, H. Miyoshi, D. Kameda, K. Shimada, H. Ogawa, K. Sakai, H. Watanabe, N. Imai, Y. Watanabe, K. Yoneda, N. Fukuda, N. Aoi, A. Yoshida, T. Kubo, and M. Ishihara: “Spin polarized radioactive nuclei as probes in nuclear and condensed matter physics”, The Multilateral Symp. between the Korean Academy of Science and Technology (KAIST) and the Foreign Academies, Seoul, Korea, May (2002).
- A. Yoshimi and K. Asahi: “Nuclear spin maser with an artificial feedback for fundamental physics”, Advanced study institute on Symmetries and Spin (Paha-SPIN-2002), (Charles University), Prague, Czech, July (2002).
- T. Ichihara: “Observation of Isovector Giant Quadrupole Resonance (IVGQR) by the Charge-exchange reaction  $^{60}\text{Ni}(^{13}\text{C},^{13}\text{N})^{60}\text{Co}$  reaction at  $E/A = 100\text{ MeV}$ ”, RCNP Workshop on Nuclear Fouce and Nuclear Phys., (RCNP and ISIR, Osaka University), Ibaraki, July (2002).
- H. Madokoro, T. Shimizu, and Y. Motizuki: “Effects of anisotropy in neutrino radiation on the supernova explosion: More complicated patterns of anisotropy”, 7th Int. Symp. on Nuclei in the Cosmos, Fuji-Yoshida, July (2002).
- S. Fujii, R. Okamoto, and K. Suzuki: “Shell-model description of  $^{16}\text{O}$  with  $\Sigma$  degrees of freedom”, 16th Int. Conf. on Particles and Nuclei (PaNic02), (RCNP, Osaka University), Osaka, Sept.–Oct. (2002).
- S. Sugimoto: “Surface pion condensation in finite nuclei”, 16th Int. Conf. on Particles and Nuclei (PaNic02), (RCNP, Osaka University), Osaka, Sept.–Oct. (2002).
- S. Fujii, R. Okamoto, and K. Suzuki: “Effects of the parity-mixing intershell coupling on excited states in  $^{16}_{\Lambda}$ ”, 2002 Fall Meet. of the Physical Soc. of Japan, Tokyo, Sept. (2002).
- K. Morimoto, K. Morita, D. Kaji, Y. Zhao, H. Xu, A. Yoneda, T. Suda, A. Yoshida, E. Ideguchi, T. Zheng, T. Ohnishi, H. Haba, K. Katori, H. Kudo, and I. Tanihata: “Identification of  $^{234}\text{Bk}$  and  $^{230}\text{Am}$  with RIKEN GARIS”, 2002 Fall Meet. of the Physical Soc. of Japan, Tokyo, Sept. (2002).
- H. Ueno, W. Sato, H. Watanabe, A. Yoshimi, Y. Kobayashi, J. Murata, K. Asahi, H. Miyoshi, K. Shimada, and T. Saito: “Development of a detector system for the g-factor measurement on excited states of unstable nuclei”, Mini-Symp. on Nuclear Moments, Division of Nuclear Pysics 2002 Fall Meet. of the American Physical Soc., East Lansing, USA, Oct. (2002).
- K. Asahi, H. Ogawa, H. Miyoshi, D. Kameda, K. Sakai, H. Ueno, A. Yoshimi, H. Watanabe, W. Sato, Y. Kobayashi, Y. Watanabe, A. Yoshida, T. Kubo, M. Ishihara, N. Imai, N. Aoi, K. Yoneda, and N. Fukuda: “Electromagnetic moments of light neutron-rich nuclei”, Mini-Symp. on Nuclear Moments, Division of Nuclear Pysics 2002 Fall Meet. of the American Physical Soc., East Lansing, USA, Oct. (2002).
- H. Watanabe, H. Ueno, W. Sato, A. Yoshimi, T. Kishida, Y. Kobayashi, K. Asahi, D. Kameda, H. Miyoshi, A. Odawara, and Y. Gounou: “g factor and an oblate deformation of the  $I^P = 49/2^-$  high-spin isomer in  $^{149}\text{Dy}$ ”, Mini-Symp. on Nuclear Moments, Division of Nuclear Pysics 2002 Fall Meet. of the American Physical Soc., East Lansing, USA, Oct. (2002).
- A. Yoshida, K. Morita, K. Morimoto, D. Kaji, T. Kubo, Y. Takahashi, A. Ozawa, and I. Tanihata: “High-power rotating wheel targets at RIKEN”, 21st World Conf. the INTDS: Accelerator Target Technology for the 21th Century, Argonne, USA, Nov. (2002).
- K. Asahi, H. Ogawa, K. Sakai, H. Ueno, T. Suzuki, H. Izumi, H. Miyoshi, N. Imai, Y. Watanabe, K. Yoneda, M. Nagakura, K. Yogo, A. Goto, T. Suga, T. Honda, A. Yoshimi, N. Fukuda, N. Aoi, Y. Kobayashi, W.-D. Schmidt-Ott, G. Neyens, S. Teughels, A. Yoshida, T. Kubo, and M. Ishihara: “Quadrupole moments of B isotopes and anomalous E2 effective charges for neutron-rich nuclei”, Int. Symp. on Frontiers of Collective Motions (CM2002),

- (University of Aizu), Aizu-Wakamatsu, Nov. (2002).
- H. Watanabe, H. Ueno, D. Kameda, W. Sato, A. Yoshimi, H. Miyoshi, T. Kishida, Y. Kobayashi, A. Odawara, Y. Gounou, and K. Asahi: “g factor of the high-spin isomer in  $^{149}\text{Dy}$  and large oblate deformation induced by collapse of the  $N = 82$  core”, Int. Symp. on Frontiers of Collective Motions (CM2002), (University of Aizu), Aizu-wamakatsu, Nov. (2002).
- S. Sugimoto: “Relativistic mean field theory with pion for finite nuclei”, Int. Symp. on Physics of Unstable Nuclei (ISPUN02), (INST, Hanoi and IOP, Hanoi), Halong Bay, Vietnam, Nov. (2002).
- K. Iida: “Phenomenological aspects of dense quark matter”, 7th APCTP Winter School/3rd Dense Matter School, (APCTP), Pohang, Korea, Jan. (2003).
- K. Asahi, J. Murata, H. Miyoshi, K. Shimada, H. Ueno, W. Sato, T. Ito, and Y. Kobayashi: “Condensed matter studies using unstable nuclei as probe”, Materials Science Symp. on Heavy Ion Science in Tandem Energy Region, (JAERI), Tokai-mura, Jan. (2003).
- S. Ozawa and M. Hamagaki: “Preparation of self-supporting boron films by electron-beam-excited plasma”, The 20th Symposium on Plasma Processing, (Division of Plasma Electronics, JSAP), Nagasaki, Jan. (2003).
- H. Koura: “Current status of theoretical study for syntheses of superheavy nuclei in RIKEN (nuclear structure)”, Workshop on Synthesis of Superheavy Nuclei, Wako, Jan. (2003).
- T. Matsuzaki: “Evidence for strong (n- $\alpha$ ) correlations in the t+t reaction proved by the neutron energy distribution of muon catalyzed t-t fusion”, CNS-RIKEN Symp. on Continuum States of Few-Body Systems and Unstable Nuclei, and the Future, Wako, Feb. (2003).
- K. Sekiguchi, H. Sakai, H. Okamura, A. Tamii, T. Uesaka, K. Suda, N. Sakamoto, T. Wakasa, Y. Satou, T. Ohnishi, K. Yako, S. Sakoda, H. Kato, Y. Maeda, J. Nishikawa, T. Saito, N. Uchigashima, N. N. Kalantar, and K. Ermisch: “Measurement of heavy proton-proton elastic dispersion and three physical strength in a middle energy domain”, CNS-RIKEN Symp. on Continuum States of Few-Body Systems and Unstable Nuclei, and the Future, Wako, Feb. (2003).
- K. Iida: “Quark matter and compact stars”, Grants-in-Aid for Specially Promoted Research “New Development of Black Hole Astronomy” Workshop “Neutrinos and Supernovae”, Tokyo, Feb. (2003).
- H. Koura: “R-process nucleosynthesis from a viewpoint of nuclear physics -nuclear masses and nuclear fission-”, Grants-in-Aid for Specially Promoted Research “New Development of Black Hole Astronomy” Workshop “Neutrinos and Supernovae”, Tokyo, Feb. (2003).
- Y. Motizuki: “Mechanism of core-collapse supernova explosion and importance of nuclear physics”, Special lecture at Physics dept. of Kyoto University, Kyoto, Feb. (2003).
- Y. Motizuki: “Supernova explosion and synthesis of heavy elements”, Special lecture at Physics dept. of Kyoto University, Kyoto, Feb. (2003).
- H. Koura: “Syntheses and decays of superheavy nuclei predicted by a nuclear mass formula”, Workshop of Advanced Science Research Center, JAERI, Nuclear Physics and Nuclear Chemistry of Superheavy Elements, Tokai-mura, Feb. (2003).
- T. Motobayashi: “Spectroscopy of unstable nuclei around  $N = 8$  and  $N = 20$  by fast RI beams”, Workshop on Inelastic Scattering with Radioactive Nuclei, (KVI), Groningen, The Netherlands, Feb. (2003).
- T. Inamura and F. F. Karpeshin: “Bridging atomic and nuclear states in  $^{229}\text{Th}$ ”, 58th Ann. Meet. of Physical Soc. of Japan, Sendai, Mar. (2003).
- H. Koura: “Estimation of fission barriers and half-lives in the superheavy nuclidic region”, 58th Ann. Meet. of Physical Soc. of Japan, Sendai, Mar. (2003).
- H. Madokoro, T. Shimizu, and Y. Motizuki: “Global anisotropy vs small-scale fluctuation of neutrino flux in supernova explosion”, 58th Ann. Meet. of Physical Soc. of Japan, Sendai, Mar. (2003).
- K. Sekiguchi: “Heavy proton: Verification of the 3 physical strength effects by proton elastic dispersion measurement”, 58th Ann. Meet. of Physical Soc. of Japan, Sendai, Mar. (2003).
- D. Kameda, K. Asahi, H. Ueno, A. Yoshimi, H. Miyoshi, J. Murata, H. Watanabe, W. Sato, Y. Kobayashi, J. Kaihara, K. Shimada, S. Suda, and T. Ito: “Measurements of Spin Polarization of  $^{19}\text{C}$  and  $^{19}\text{N}$ ”, 58th Ann. Meet. of Physical Soc. of Japan, Sendai, Mar. (2003).
- K. Iida, K. Oyamatsu, and B. A. Sarhan: “Proton elastic scattering and the equation of state of nuclear matter”, 58th Ann. Meet. of Physical Soc. of Japan, Sendai, Mar. (2003).
- K. Yamada, T. Motobayashi, N. Aoi, H. Baba, K. Demichi, Z. Elekes, J. D. Gibelin, T. Gomi, H. Hasegawa, N. Imai, H. Iwasaki, S. Kanno, T. Kubo, K. Kurita, Y. Matsuyama, S. Michimasa, T. Minemura, M. Notani, T. Onishi, H. Ong, S. Ota, A. Ozawa, A. Saito, H. Sakurai, S. Shimoura, E. Takeshita, S. Takeuchi, M. Tamaki, Y. Togano, Y. Yanagisawa, K. Yoneda, and I. Tanihata: “Reduced transition probability  $B(E2)$  in proton-rich  $^{46}\text{Cr}$ ,  $^{50}\text{Fe}$ , and  $^{54}\text{Ni}$  studied by Coulomb excitation”, 58th Ann. Meet. of Physical Soc. of Japan, Sendai, Mar. (2003).
- A. Kohama: “Reflection of the tail region of the density distribution to the proton-nucleus elastic scattering cross section”, 58th Ann. Meet. of Physical Soc. of Japan, Sendai, Mar. (2003).

- S. Sugimoto, H. Toki, and K. Ikeda: “Relativistic Hartree-Fock theory with the pion for finite nuclei”, 58th Ann. Meet. of Physical Soc. of Japan, Sendai, Mar. (2003).
- S. Fujii, R. Okamoto, and K. Suzuki: “Shell structures of neutron-rich isotopes derived from modern nuclear forces”, 58th Ann. Meet. of Physical Soc. of Japan, Sendai, Mar. (2003).
- Y. Motizuki, T. Tachibana, and S. Goriely: “The r-process nucleosynthesis: development of reaction network code with specific attention to nuclear model information”, 58th Ann. Meet. of Physical Soc. of Japan, Sendai, Mar. (2003).
- K. Asahi, H. Miyoshi, D. Kameda, K. Shimada, H. Ueno, J. Murata, Y. Kobayashi, W. Sato, A. Yoshimi, and H. Watanabe: “Nuclear moments and condensed matter studies with polarized RI beams”, Exploratory Workshop on Polarized Radioactive Beams and Polarized Targets, (Institut de Recherches Subatomiques), Strasbourg, France, Mar. (2003).
- Y. Motizuki: “Retarded electron capture decay of  $^{44}\text{Ti}$  in plasma of supernova remnants”, Seminar at National Institute of Fusion Science, Toki, Mar. (2003).
- A. Saito: “Molecular resonances in  $^{12}\text{Be}$  and  $^{14}\text{Be}$ ”, Seminar of Molecular Structure from the Light Neutron-rich Nuclei to the Medium Heavy Nuclei, (RIKEN), Wako, Mar. (2003).
- Y. Motizuki: “RIBF nuclear astrophysics project: Towards understanding of supernova explosion mechanism and heavy element synthesis”, Workshop on Nuclear Astrophysics - Strategies for Astro Nuclear Reaction Studies, Wako, Mar. (2003).
- A. Ozawa: “Reaction cross-section measurements in RIBF”, Workshop on RI Beam Factory and Research Plan, Wako, Mar. (2003).
- Y. Motizuki: “How to make a good presentation in an international conference”, RIBF Nuclear Astrophysics Project Lecture Series 4, Wako, Apr. (2003).
- Y. Motizuki: “Towards unified paradigm of core-collapse supernovae and nucleosynthesis of heavy elements”, Sendai Nuclear Science Colloq., (Tohoku University), Sendai, Apr. (2003).
- A. Ozawa: “Physics for unstable nuclei”, TAC Seminar at University of Tsukuba, Tsukuba, Apr. (2003).
- R. Mutou, J. Chiba, H. Enyo, Y. Fukao, H. Funahashi, H. Hamagaki, M. Ieiri, M. Ishino, H. Kanda, M. Kitaguchi, S. Mihara, K. Miwa, T. Miyashita, T. Murakami, T. Nakura, M. Naruki, M. Nomachi, K. Ozawa, F. Sakuma, O. Sasaki, M. Sekimoto, T. Tabaru, K. Tanaka, M. Togawa, S. Yamada, S. Yokkaichi, and Y. Yoshimura: “Measurement of invariant mass spectra of vector meson decaying in nuclear matter at KEK-PS”, 8th Conf. on the Intersections of Particle and Nuclear Physics (CIPANP 2003), (Brookhaven National Laboratory), New York, USA, May (2003).
- Y. Motizuki: “ $^{44}\text{Ti}$  radioactivity in young supernova remnants: Cas A and SN 1987A”, Int. Workshop on Astronomy with Radioactivities 4th and Filling the Sensitivity Gap in MeV Astronomy, (Max-Planck-Institut fuer Extraterrestrische Physik), Seeon, Germany, May (2003).
- A. Ozawa: “Recent progress of interaction and reaction cross-section measurements”, WE-Heraeus-Seminar of Relativistic Structure Models for the Physics of Radioactive Nuclear Beams, (WE-Heraeus-Seminar), Bad Honnef, Germany, May (2003).
- Y. Ishida, M. Wada, Y. Matsuo, I. Tanihata, A. Casares, and H. Wollnik: “A multi-pass time-of-flight mass spectrometer of high resolving power”, 16th Int. Conf. on Ion Beam Analysis, (Bohmische Physical Society and others), Albuquerque, USA, June–July (2003).
- K. Ishida: “Non-particle physics with intense muon beams”, 5th Int. Workshop on Neutrino Factories & Superbeams (NuFact 03), (Columbia University), New York, USA, June (2003).
- T. Ichihara, M. Ishihara, H. Ohnuma, T. Niizeki, H. Satou, H. Okamura, S. Kubono, M. H. Tanaka, and Y. Fuchi: “Isovector quadrupole resonance observed in the  $^{60}\text{Ni}(^{13}\text{C}, ^{13}\text{N})^{60}\text{Co}$  reaction at  $E/A = 100\text{ MeV}$ ”, 8th Int. Conf. on Nucleus-Nucleus Collisions (NN 2003), (JINR), Moscow, Russia, June (2003).
- A. Ozawa: “Recent experiments for interaction and reaction cross-sections”, 8th Int. Conf. on Nucleus-Nucleus Collisions (NN 2003), (JINR), Moscow, Russia, June (2003).
- D. Kameda, K. Asahi, H. Ueno, A. Yoshimi, H. Watanabe, T. Hasegawa, H. Miyoshi, K. Shimada, J. Murata, Y. Kobayashi, G. Kato, S. Emori, W. Sato, and H. Ogawa: “Recent result from the nuclear moment measurement using a spin polarized radioactive beam”, 8th Int. Conf. on Nucleus-Nucleus Collisions (NN 2003), (Joint Institute for Nuclear Research), Dubna, Russia, June (2003).
- T. Gomi, T. Motobayashi, Y. Ando, N. Aoi, H. Baba, K. Demichi, Z. Elekes, N. Fukuda, Z. Fulop, U. Futakami, H. Hasegawa, Y. Higurashi, K. Ieki, N. Imai, M. Ishihara, K. Ishikawa, N. Iwasa, H. Iwasaki, S. Kanno, Y. Kondo, T. Kubo, S. Kubono, M. Kunibu, K. Kurita, Y. Matsuyama, S. Michimasa, T. Minemura, M. Miura, H. Murakami, T. Nakamura, M. Notani, S. Ota, A. Saito, H. Sakurai, M. Serata, S. Shimoura, T. Sugimoto, E. Takeshita, S. Takeuchi, Y. Togano, K. Ue, K. Yamada, Y. Yanagisawa, K. Yoneda, and A. Yoshida: “Study of the  $^{22}\text{Mg}(p,\gamma)^{23}\text{Al}$  reaction with the Coulomb-dissociation method”, 8th Int. Conf. on Nucleus-Nucleus Collisions (NN 2003), (JINR), Moscow, Russia, June (2003).
- Y. Yanagisawa, M. Notani, H. Sakurai, S. Shimoura,

- H. Iwasaki, S. Michimasa, K. Ue, M. Kurokawa, N. Iwasa, M. Kunibe, H. Baba, T. Gomi, A. Saito, T. Minemura, Y. Matsuyama, H. Higurashi, S. Kanno, M. Serata, E. Takeshita, S. Takeuchi, K. Yamada, H. Demichi, K. Hasegawa, H. Akiyoshi, N. Fukuda, K. Yoneda, N. Aoi, N. Imai, T. Sugimoto, T. Nakamura, M. Ishihara, and T. Motobayashi: "The first excited ofin  $^{30}\text{Ne}$  studied by proton inelastic scattering in reversed kinematics", 8th Int. Conf. on Nucleus-Nucleus Collisions (NN 2003), (JINR), Moscow, Russia, June (2003).
- K. Asahi: "Measurements of nuclear moments for light unstable nuclei", Gordon Research Conf. on Nuclear Chemistry, New London, USA, June (2003).
- T. Ichihara, M. Ishihara, H. Ohnuma, T. Niizeki, Y. Satou, H. Okamura, S. Kubono, M. H. Tanaka, and Y. Fuchi: "Isovector quadrupole resonance observed in the  $^{60}\text{Ni}(^{13}\text{C}, ^{13}\text{N})^{60}\text{Co}$  reaction at  $E/A = 100\text{ MeV}$ ", Int. Conf. on Collective Motion in Nuclei Under Extreme Conditions (COMEX 1), Paris, France, June (2003).
- Y. Motizuki: "Change of lifetime of  $^{40}\text{K}$  orbital electron capture beta-decay under ultra-high pressures", Seminar at Gono Laboratory of Kyushu University, (Nishinippon Institute of Technology), Fukuoka, June (2003).
- S. Ozawa and M. Hamagaki: "Preparation of boron films by sputtering with electron-beam-excited plasma", Seventh Int. Symp. on Sputtering & Plasma Processes, (The Vacuum Society of Japan), Kanazawa, June (2003).
- K. Sekiguchi, H. Sakai, H. Okamura, A. Tamii, T. Uesaka, K. Suda, N. Sakamoto, T. Wakasa, Y. Satou, T. Ohnishi, K. Yako, S. Sakoda, H. Kato, Y. Maeda, J. Nishikawa, T. Saito, N. Uchigashima, N. N. Kalantar, and K. Ermisch: "Measurement of polarization transfer coefficients for  $d-p$  scattering at intermediate energies and three nucleon force effects", 17th Int. IUPAP Conf. on Few-Body Problems in Physics, Durham, USA, June (2003).
- Y. Motizuki: "Sensitivity of core-collapse supernova explosions to neutrino luminosity (invited talk)", 1st Yamada Symp. on Neutrinos and Dark Matter in Nuclear Physics (NDM03), (Osaka University), Nara, June (2003).
- N. Dinh Dang: "Giant dipole resonance in hot nuclei", VIII Hispalensis Int. Summer School on Physics of Exotic Nuclear Physics, (University of Seville), Sevilla, Spain, June (2003).
- N. Dinh Dang: "Modified Hartree-Fock-Bogoliubov theory at finite temperature", VIII Hispalensis Int. Summer School on Physics of Exotic Nuclear Physics, (University of Seville), Sevilla, Spain, June (2003).
- S. Sugimoto, H. Toki, and K. Ikeda: "Relativistic mean field theory with the pion for finite nuclei", 22nd Int. Workshop on Nuclear Theory, (The Institute of Nuclear Research and Nuclear Energy of the Bulgarian Academy of Sciences), Rila Mountains, Bulgaria, June (2003).
- A. Yoshimi, K. Asahi, S. Emori, and M. Tsukui: "Nuclear spin oscillator and search for atomic EDM of  $^{129}\text{Xe}$ ", Advanced Studies Institute: Symmetries and Spin (Spin-Praha-2003), (Charles University), Prague, Czech, July (2003).
- M. Takashina: "A CDCC study of the breakup effect on  $^{11}\text{Be}$  elastic scattering", DREB 2003 Conf., (University of Surrey), Guildford, UK, July (2003).
- K. Iida: "Ginzburg-Landau approach to color superconductivity 30 min", Finite Density QCD, (RCNP, Osaka University), Nara, July (2003).
- T. Sugihara: "Realization of lattice chiral symmetry with hopping interactions", Int. Conf. on Color Confinement and Hadrons in Quantum Chromodynamics: Confinement 2003, Wako, July (2003).
- H. Ueno, K. Asahi, H. Ogawa, D. Kameda, H. Miyoshi, A. Yoshimi, H. Watanabe, K. Shimada, W. Sato, K. Yoneda, N. Imai, Y. Kobayashi, M. Ishihara, and W.-D. Schmidt-Ott: "Nuclear moments of nuclei in the neighborhood of the neutron drip line", Int. Conf. on the Labyrinth in Nuclear Structure, (NCSR Demokritos), Crete, Greece, July (2003).
- T. Sugihara: "Chiral symmetry on a lattice with hopping interactions", LATTICE 2003: 21st Int. Symp. on Lattice Field Theory, Tsukuba, July (2003).
- N. Ishii and H. Suganuma: "MEM analysis of glueball correlators at  $T > 0$ ", LATTICE 2003: 21st Int. Symp. on Lattice Field Theory, Tsukuba, July (2003).
- T. Izubushi: "The Kaon B parameter from two-flavor dynamical domain wall fermions", LATTICE 2003: 21st Int. Symp. on Lattice Field Theory, Tsukuba, July (2003).
- A. Ozawa: "Fast PID system and its applications", RIKEN Symp. on Advanced Signal Processing in Nuclear Physics, Wako, July (2003).
- Y. Motizuki: "Element genesis: Mystery in universe studying with RI", Seminar of Physics Department at Tokyo University of Science, Noda, July (2003).
- Y. Motizuki: "Core-collapse supernovae with anisotropic neutrino radiation", Int. Conf. in Honour of the 60th Birthday of Marcel Arnould: The Future Astronuclear Physics; From Microscopic Puzzles to Macroscopic Nightmares, (University Libre de Bruxelles), Brussels, Belgium, Aug. (2003).
- Y. Motizuki: "Required accuracy of mass and half-life measurements for the r-process nucleosynthesis", Int. Conf. in Honour of the 60th Birthday of Marcel Arnould: The Future Astronuclear Physics; From Microscopic Puzzles to Macroscopic Nightmares, (University Libre de Bruxelles), Brussels, Belgium, Aug. (2003).
- K. Sekiguchi, H. Sakai, H. Okamura, A. Tamii, T. Uesaka, K. Suda, N. Sakamoto, T. Wakasa, Y.

- Satou, T. Ohnishi, K. Yako, S. Sakoda, H. Kato, Y. Maeda, J. Nishikawa, T. Saito, N. Uchigashima, N. N. Kalantar, and K. Ermisch: “Measurement of deuteron-proton scattering at intermediate energies”, RCNP Workshop: Few Body Systems and Baryon-Baryon Interactions, Osaka, Aug. (2003).
- S. Fujii, H. Kamada, R. Okamoto, and K. Suzuki: “Application of low-momentum interaction to the calculation for few-nucleon systems”, RCNP Workshop: Few-Nucleon Systems and Baryon-Baryon Interaction, Ibaraki, Aug. (2003).
- H. Koura: “Stability and decay modes of superheavy elements from a viewpoint of atomic mass formulas”, Summer School of Nuclear Chemistry, (The Japan Society of Nuclear and Radiochemical Sciences), Daigo-cho, Ibaraki Pref., Aug. (2003).
- H. Koura: “Ground-state properties of heavy and superheavy nuclei predicted by nuclear mass models”, Tours Symp. on Nuclear Physics V (TOURS 2003), (Konan University), Tours, France, Aug. (2003).
- Y. Motizuki: “Radioactivity of the key isotope  $^{44}\text{Ti}$  in supernovae (invited talk)”, Tours Symp. on Nuclear Physics V (TOURS 2003), (Konan University), Tours, France, Aug. (2003).
- K. Iida: “Color superconductivity in finite quark matter”, YITP Workshop on Thermal Quantum Field Theories and Their Application, Kyoto, Aug. (2003).
- Z. Elekes, G. Kalinka, Z. Fulop, J. Gal, J. Molnar, G. Hegyesi, D. Novak, T. Motobayashi, A. Saito, and Y. Yanagisawa: “Optimization of the performance of a CsI(Tl) scintillator+Si PIN photodiode detector for medium-energy light-charged particle hybrid array”, 17th Int. Nuclear Physics Divisional Conf. of the European Physical Soc. (NPDC-17): Nuclear Physics in Astrophysics, (ATOMKI), Debrecen, Hungary, Sept.–Oct. (2003).
- Y. Motizuki: “Ionization and nucleosynthesis of  $^{44}\text{Ti}$  in Cassiopeia A”, 2003 Fall Ann. Meet. of Astrophysical Soc. of Japan, Matsuyama, Sept. (2003).
- S. Sugimoto, H. Toki, and K. Ikeda: “Application of charge-number- and parity-projected Hartree-Fock method for finite nuclei”, 2003 Fall Meet. of the Physical Soc. of Japan, Miyazaki and Okayama, Sept. (2003).
- S. Fujii, H. Kamada, R. Okamoto, and K. Suzuki: “Calculations for three- and four-nucleon systems using low-momentum interactions derived from realistic nucleon-nucleon forces”, 2003 Fall Meet. of the Physical Soc. of Japan, Miyazaki and Okayama, Sept. (2003).
- K. Iida and K. Oyamatsu: “Density dependence of the surface tension: nucleon density in the nuclear interior and neutron skin”, 2003 Fall Meet. of the Physical Soc. of Japan, Miyazaki and Okayama, Sept. (2003).
- A. Kohama: “Density shape dependence of the proton-nucleus elastic scattering cross section”, 2003 Fall Meet. of the Physical Soc. of Japan, Miyazaki and Okayama, Sept. (2003).
- H. Miyadera, K. Nagamine, K. Simomura, K. Nishiyama, H. Tanaka, Y. Ikeda, and K. Ishida: “Development of large solid angle axial focusing surface muon channel at KEK-MSL”, 2003 Fall Meet. of the Physical Soc. of Japan, Miyazaki and Okayama, Sept. (2003).
- H. Watanabe, Y. Gounou, B. Cederwall, N. Hokoïwa, M. Ishihara, M. Kibe, T. Kishida, K. Lagergren, A. Odahara, Z. Podolyak, T. Sasaki, and Y. Wakabayashi: “Experimental progress in the project of high-spin isomer beam at RIKEN”, 2003 Fall Meet. of the Physical Soc. of Japan, Miyazaki and Okayama, Sept. (2003).
- Y. Matsuda, P. Bakule, P. Strasser, Y. Miyake, K. Nagamine, K. Simomura, S. Makimura, M. Iwasaki, T. Matsuzaki, and K. Ishida: “Generation of slow muon beam at the RIKEN-RAL muon facility (II)”, 2003 Fall Meet. of the Physical Soc. of Japan, Miyazaki and Okayama, Sept. (2003).
- K. Ishida, K. Nagamine, T. Matsuzaki, N. Kawamura, Y. Matsuda, M. Iwasaki, H. Imao, M. Kato, H. Sugai, M. Tanase, S. Nakamura, K. Kudo, N. Takeda, and G. H. Eaton: “Muon catalyzed fusion experiment in D-T system at RIKEN-RAL Muon Facility: magnetic field effect”, 2003 Fall Meet. of the Physical Soc. of Japan, Miyazaki and Okayama, Sept. (2003).
- A. Yoshimi: “Nuclear spin maser with  $^{129}\text{Xe}$  and the search for the atomic EDM”, 2003 Fall Meet. of the Physical Soc. of Japan, Miyazaki and Okayama, Sept. (2003).
- K. Morimoto: “Recent status of super heavy element research at RIKEN”, 2003 Fall Meet. of the Physical Soc. of Japan, Miyazaki and Okayama, Sept. (2003).
- S. Fujii, R. Okamoto, and K. Suzuki: “Shell structures of neutron-rich O isotopes described with modern nucleon-nucleon interactions II”, 2003 Fall Meet. of the Physical Soc. of Japan, Miyazaki and Okayama, Sept. (2003).
- K. Suda, H. Okamura, T. Uesaka, H. Kumasaka, R. Suzuki, T. Ikeda, K. Itoh, H. Sakai, A. Tamii, K. Sekiguchi, K. Yako, Y. Maeda, M. Hatano, T. Saito, H. Kuboki, N. Sakamoto, and Y. Satou: “Study of spin-isospin responses in doubly magic nucleus  $^{16}\text{O}$ ”, 2003 Fall Meet. of the Physical Soc. of Japan, Miyazaki and Okayama, Sept. (2003).
- Y. Motizuki, T. Tachibana, and S. Goriely: “The r-process nucleosynthesis: difference produced by microscopic and semi-empirical mass formulae”, 2003 Fall Meet. of the Physical Soc. of Japan, Miyazaki and Okayama, Sept. (2003).
- T. Matsuzaki, K. Nagamine, N. Kawamura, K. Ishida, Y. Matsuda, M. Iwasaki, H. Imao, M. Kato, H. Sugai, M. Tanase, S. Nakamura, K. Kudo, N. Takeda, and G. H. Eaton: “n- $\alpha$  particle correla-

- tions observed in the muon catalyzed t-t fusion reactions”, 2003 Fall Meet. of the Physical Soc. of Japan, Miyazaki and Okayama, Sept. (2003).
- M. Kobayashi, K. Ushida, Y. Aoki, T. Kuribayashi, M. Kawaguchi, S. Kashiwagi, R. Kuroda, Y. Hama, and M. Washio: “Construction of pulse radiolysis system with a picosecond RF-gun at Waseda University”, 46th Symp. on Radiation Chemistry, (Japanese Society of Radiation Chemistry), Hakone, Sept. (2003).
- H. Watanabe, K. Asahi, H. Ueno, W. Sato, A. Yoshimi, Y. Kobayashi, J. Murata, T. Kishida, M. Ishihara, D. Kameda, H. Miyoshi, K. Shimada, Y. Gounou, T. Fukuchi, Y. Wakabayashi, T. Sasaki, M. Kibe, N. Hokoïwa, A. Odahara, B. Cederwall, K. Lagergren, and Z. Podolyak: “Application of the high-spin isomer beams to secondary fusion reaction and measurement of g-factors”, 6th Int. Conf. on Radioactive Nuclear Beams (RNB6), (Argonne National Laboratory), Argonne, USA, Sept. (2003).
- K. Yamada, T. Motobayashi, and I. Tanihata: “RF deflector system for proton-rich RI beams in RIKEN”, 6th Int. Conf. on Radioactive Nuclear Beams (RNB6), (Argonne National Laboratory), Argonne, USA, Sept. (2003).
- T. Matsuzaki, K. Nagamine, K. Ishida, N. Kawamura, H. Imao, Y. Matsuda, M. Iwasaki, M. Kato, H. Sugai, M. Tanase, S. Nakamura, K. Kudo, N. Takeda, and G. H. Eaton: “Strong n-alpha correlations in the t+t fusion reactions observed in the muon catalyzed t-t fusion”, Int. Conf. on FUSION3: From a Tunneling Nuclear Microscope to Nuclear Processes in Matter, (Tohoku University and others), Miyagi, Nov. (2003).
- H. Watanabe, K. Asahi, H. Ueno, W. Sato, A. Yoshimi, Y. Kobayashi, J. Murata, T. Kishida, M. Ishihara, D. Kameda, H. Miyoshi, K. Shimada, Y. Gounou, T. Fukuchi, M. Kibe, N. Hokoïwa, T. Sasaki, B. Cederwall, K. Lagergren, A. Odahara, Z. Podolyak, and Y. Wakabayashi: “Application of the high-spin isomer beams to secondary fusion reaction and measurement of g-factors”, Int. Symp. on A New Era of Nuclear Structure Physics (NENS03), (Niigata University), Kurokawa-mura, Niigata Pref., Nov. (2003).
- K. Iida, K. Oyamatsu, and B. A. Sarhan: “Deducing the density dependence of the symmetry energy from unstable nuclei”, Int. Symp. on A New Era of Nuclear Structure Physics (NENS03), (Niigata University), Kurokawa-mura, Niigata Pref., Nov. (2003).
- A. Kohama: “Determination of matter surface distribution of neutron-rich nuclei”, Int. Symp. on A New Era of Nuclear Structure Physics (NENS03), Kurokawa-mura, Niigata Pref., Nov. (2003).
- H. Miyoshi, K. Asahi, S. Emori, T. Haseyama, D. Kameda, G. Kato, Y. Kobayashi, J. Murata, H. Ogawa, K. Sakai, W. Sato, K. Shimada, H. Ueno, H. Watanabe, and W.-D. Schmidt-Ott: “Low-energy of polarized RI atomic beam”, Int. Symp. on A New Era of Nuclear Structure Physics (NENS03), (Niigata University), Kurokawa-mura, Niigata Pref., Nov. (2003).
- K. Sekiguchi: “Measurement of nucleon-deuteron scattering as a good probe to study three nucleon force”, Int. Symp. on A New Era of Nuclear Structure Physics (NENS03), (Niigata University), Kurokawa-mura, Niigata Pref., Nov. (2003).
- S. Fujii, R. Okamoto, and K. Suzuki: “Shell structures in nuclei around  $^{24}\text{O}$  described with modern nucleon-nucleon interactions”, Int. Symp. on A New Era of Nuclear Structure Physics (NENS03), (Niigata University), Kurokawa-mura, Niigata Pref., Nov. (2003).
- D. Kameda, K. Asahi, H. Ueno, A. Yoshimi, H. Watanabe, T. Haseyama, H. Miyoshi, K. Shimada, G. Kato, S. Emori, G. Kijima, Y. Kobayashi, J. Murata, W. Sato, and H. Ogawa: “g-factor measurement for  $^{19}\text{N}$ ”, Int. Symp. on A New Era of Nuclear Structure Physics (NENS03), (Niigata University), Niigata, Nov. (2003).
- T. Gomi, T. Motobayashi, Y. Ando, N. Aoi, H. Baba, K. Demichi, Z. Elekes, N. Fukuda, Z. Fulop, U. Futakami, H. Hasegawa, Y. Higurashi, K. Ieki, N. Imai, M. Ishihara, K. Ishikawa, N. Iwasa, H. Iwasaki, S. Kanno, Y. Kondo, T. Kubo, S. Kubono, M. Kunibu, K. Kurita, Y. Matsuyama, S. Michimasa, T. Minemura, M. Miura, H. Murakami, T. Nakamura, M. Notani, S. Ota, A. Saito, H. Sakurai, M. Serata, S. Shimoura, T. Sugimoto, E. Takeshita, S. Takeuchi, Y. Togano, K. Ue, K. Yamada, Y. Yanagisawa, K. Yoneda, and A. Yoshida: “Coulomb dissociation of  $^{23}\text{Al}$ : Study of the  $^{22}\text{Mg}(p,\gamma)^{23}\text{Al}$  reaction”, Int. Symp. on the Origin of Matter and Evolution of Galaxies 2003 (OMEG-03), (CNS, RIKEN and others), Wako, Nov. (2003).
- Y. Motizuki: “A proposal for nuclear  $\gamma$ -ray astronomy using NeXT satellite”, Science Meet. for the NeXT Satellite, (University of Tokyo), Tokyo, Nov. (2003).
- M. Takashina, M. Ito, Y. Kudo, S. Okabe, and Y. Sakuragi: “ $^{12}\text{C} + ^{12}\text{C} \rightarrow ^8\text{Be}_{g.s.} + ^{16}\text{O}_{g.s.}$  resonance reactions and multi-cluster states of highly excited  $^{24}\text{Mg}$  nucleus”, 8th Int. Conf. on Clustering Aspects of Nuclear Structure and Dynamics (CLUSTER'03), (RIKEN and Kyoto University), Nara, Nov. (2003).
- S. Sugimoto, K. Ikeda, and H. Toki: “Charge- and parity-projected Hartree-Fock study with the tensor force of light nuclei”, 8th Int. Conf. on Clustering Aspects of Nuclear Structure and Dynamics (CLUSTER'03), (RIKEN and Kyoto University), Nara, Nov. (2003).
- H. Ueno, K. Asahi, H. Ogawa, D. Kameda, H. Miyoshi, A. Yoshimi, H. Watanabe, K. Shimada, W. Sato, K. Yoneda, N. Imai, Y. Kobayashi, M. Ishihara, and



- W.-D. Schmidt-Ott: “Measurement of nuclear moments in the region of light neutron-rich nuclei”, 8th Int. Conf. on Clustering Aspects of Nuclear Structure and Dynamics (CLUSTER ’03), (RIKEN and Kyoto University), Nara, Nov. (2003).
- A. Kohama: “Neutron-rich nuclei and the proton-nucleus elastic scattering”, 8th Int. Conf. on Clustering Aspects of Nuclear Structure and Dynamics (CLUSTER ’03), (RIKEN and Kyoto University), Nara, Nov. (2003).
- K. Ikeda: “New mean field theory with parity and charge mixing for finite nuclei”, 8th Int. Conf. on Clustering Aspects of Nuclear Structure and Dynamics (CLUSTER ’03), (RIKEN and Kyoto University), Nara, Nov. (2003).
- K. Morimoto: “Status of super heavy element research using GARIS at RIKEN”, 8th Int. Conf. on Clustering Aspects of Nuclear Structure and Dynamics (CLUSTER ’03), (RIKEN and Kyoto University), Nara, Nov. (2003).
- A. Yoshimi, H. Ueno, W. Sato, H. Watanabe, Y. Kobayashi, J. Murata, H. Miyoshi, K. Shimada, and K. Asahi: “The g-factor measurement on excited states of unstable nuclei by a transient field method: development of a detector system”, 8th Int. Conf. on Clustering Aspects of Nuclear Structure and Dynamics (CLUSTER ’03), (RIKEN and Kyoto University), Nara, Nov. (2003).
- S. Yokkaichi: “Data processing in Nuclear/Particle Physics using Accelerator and PC cluster”, RIKEN Symp. on New Horizon on HPC, Wako, Dec. (2003).
- T. Sugihara: “Lattice representation of vector and chiral gauge theories”, YITP Workshop on Fundamental Problems and Applications of Quantum Field Theory, Kyoto, Dec. (2003).
- K. Iida, K. Oyamatsu, and B. A. Sarhan: “Deducing the density dependence of the symmetry energy from unstable nuclei”, YITP Workshop on Nuclear Matter under Extreme Conditions (Matter03), Kyoto, Dec. (2003).
- A. Kohama: “Determination of matter surface distribution of neutron-rich nuclei and effect of outer surface”, YITP Workshop on Nuclear Matter under Extreme Conditions (Matter03), Kyoto, Dec. (2003).
- R. Mutou, J. Chiba, H. Enyo, Y. Fukao, H. Funahashi, H. Hamagaki, M. Ieiri, M. Ishino, H. Kanda, M. Kitaguchi, S. Mihara, K. Miwa, T. Miyashita, T. Murakami, T. Nakura, M. Naruki, M. Nomachi, K. Ozawa, F. Sakuma, O. Sasaki, H. Sato, M. Sekimoto, T. Tabaru, K. Tanaka, M. Togawa, S. Yamada, S. Yokkaichi, and Y. Yoshimura: “Experimental signature of in-medium mass modification of vector mesons at normal nuclear density”, 17th Int. Conf. on Ultra-Relativistic Nucleus-Nucleus Collisions (Quark Matter 2004), (Lawrence Berkeley National Laboratory and others), Oakland, USA, Jan. (2004).
- S. Yokkaichi, K. Ozawa, and S. Sawada: “Vector meson measurements at J-PARC 50-GeV PS”, 17th Int. Conf. on Ultra-Relativistic Nucleus-Nucleus Collisions (Quark Matter 2004), (Lawrence Berkeley National Laboratory and others), Oakland, USA, Jan. (2004).
- A. Yoshimi, K. Asahi, S. Emori, and M. Tsukui: “Laser-polarized nuclei of  $^{129}\text{Xe}$  and the precise control of nuclear spin precession”, 2003 Conf. on Atom-Molecular Process in Cosmic Space, (JAXA), Sagamihara, Jan. (2004).
- Y. Motizuki: “Element genesis in the universe: How luckily we exist here”, Dai-13-Kai Housha-sen Riyou Sougou Symp., (Osaka Nuclear Science Association), Osaka, Jan. (2004).
- K. Asahi: “Polarized  $^3\text{He}$  gas as a polarizer and analyzer for the spin of low-energy neutron”, Int. Conf. on Neutron Optics (NOP2004), (MEXT), Tokyo, Jan. (2004).
- K. Iida: “Color superconductivity”, KEK Large Scale Simulation Program Workshop: Hadron Physics and Lattice QCD, Tsukuba, Jan. (2004).
- Y. Terada, Y. Motizuki, T. Tamagawa, K. Makishima, T. Takahashi, K. Yamaoka, Y. Okada, and S. Hong: “New physics expanded by observing nuclear  $\gamma$ -rays with the NeXT satellite”, 4th Space Science Symp., (JAXA/ISAS), Sagamihara, Jan. (2004).
- H. Miyoshi, K. Asahi, S. Emori, T. Haseyama, D. Kameda, G. Kato, Y. Kobayashi, J. Murata, H. Ogawa, K. Sakai, W. Sato, K. Shimada, H. Ueno, H. Watanabe, and W.-D. Schmidt-Ott: “Atomic beam method for the fragmentation-based radioactive beams”, 1st Tokyo Tech Physics COE Symp. on Spin and Quantum Structure in Hadrons, Nuclei and Atoms (SQS04), Tokyo, Feb. (2004).
- D. Kameda, K. Asahi, H. Ueno, A. Yoshimi, H. Watanabe, T. Haseyama, J. Murata, Y. Kobayashi, W. Sato, H. Miyoshi, K. Shimada, G. Kato, S. Emori, G. Kijima, T. Suga, H. Ogawa, K. Oono, K. Yoneda, N. Imai, A. Yoshida, T. Kubo, M. Ishihara, K. Yogo, and K. Sakai: “Nuclear moment studies with spin polarized radioactive beams from fragmentation reaction”, 1st Tokyo Tech Physics COE Symp. on Spin and Quantum Structure in Hadrons, Nuclei and Atoms (SQS04), Tokyo, Feb. (2004).
- A. Yoshimi, K. Asahi, S. Emori, and M. Tsukui: “Nuclear spin maser with a novel masing mechanism and its application to the search for an atomic EDM in  $^{129}\text{Xe}$ ”, 1st Tokyo Tech Physics COE Symp. on Spin and Quantum Structure in Hadrons, Nuclei and Atoms (SQS04), Tokyo, Feb. (2004).
- H. Watanabe, H. Ueno, A. Yoshimi, Y. Kobayashi, T. Kishida, Y. Gounou, A. Odahara, and T. Haseyama: “g-factor measurements of high-spin isomers and condensed matter studies using spin-aligned isomeric beams”, 1st Tokyo Tech Physics COE Symp. on Spin and Quantum Structure in Hadrons, Nuclei and Atoms (SQS04), Tokyo, Feb. (2004).

- and Atoms (SQS04), Tokyo, Feb. (2004).
- H. Madokoro, T. Shimizu, and Y. Motizuki: “2-D numerical simulation of core-collapse supernova explosions with Roe’s method in second order accuracy”, 2004 Spring Ann. Meet. of Astrophysical Soc. of Japan, Nagoya, Mar. (2004).
- Y. Motizuki and S. Kumagai: “Detectability of  $^{44}\text{Ti}$  nuclear  $\gamma$ -rays from SNR 1987A”, 2004 Spring Ann. Meet. of Astrophysical Soc. of Japan, Nagoya, Mar. (2004).
- H. Madokoro, T. Shimizu, and Y. Motizuki: “2-D numerical simulation of core-collapse supernova explosions with Roe’s method”, 59th Ann. Meet. of Physical Soc. of Japan, Fukuoka, Mar. (2004).
- Y. Motizuki: “Change in orbital-electron-capture beta-decay lifetime of  $^{40}\text{K}$  under ultra-high pressures”, 59th Ann. Meet. of Physical Soc. of Japan, Fukuoka, Mar. (2004).
- H. Watanabe, K. Asahi, H. Ueno, A. Yoshimi, T. Haseyama, T. Kishida, Y. Kobayashi, D. Kameda, H. Miyoshi, K. Shimada, Y. Gounou, and A. Odahara: “g-factor measurements of high-spin isomers and condensed matter studies with  $\gamma$ -TDPAD technique”, CNS-RIKEN Joint Symp. on Frontier of gamma-ray spectroscopy and its application, Wako, Mar. (2004).
- H. Watanabe, K. Asahi, H. Ueno, A. Yoshimi, Y. Kobayashi, T. Haseyama, T. Kishida, D. Kameda, H. Miyoshi, K. Shimada, S. Emori, G. Kato, Y. Gounou, and A. Odahara: “g-factor measurements of high-spin isomers and condensed matter studies using spin-aligned isomeric beams”, 5th Japan-China Joint Nuclear Physics Symp., (Kyushu University), Fukuoka, Mar. (2004).
- ### 3. Atomic and solid-state physics
- M. Wada: “On-line collection of energetic Li-8 ions by RF ion-guide”, Workshop on TRIUMF-TRAP: A facility for exotic and Highly Charged Ion Beams at ISAC, (TRIUMF (Canada’s National Laboratory for Particle and Nuclear Physics)), Vancouver, Canada, Apr. (2002).
- M. Wada: “Slow/trapped RI-beams from PF separators”, 14th Int. Conf. on Electromagnetic Isotope Separators and Techniques Related to their Applications, (TRIUMF), Victoria, Canada, May (2002).
- S. Ohira, K. Awaga, W. Fujita, I. Watanabe, and K. Nagamine: “ $\mu\text{SR}$  study on a metal complex having a ferromagnetic linear chain  $p\text{-NPNN}\cdot\text{Cu}(\text{hfac})_2$ ”, 9th Int. Conf. on Muon Spin Rotation/Relaxation/Resonance ( $\mu\text{SR}2002$ ), Williamsburg, USA, June (2002).
- S. Fujii: “Microscopic effective YN interaction for shell-model calculation and structure of  $^{16}_\Lambda\text{O}$ ”, Nuclear Theory Seminar at Chiba University, Chiba, June (2002).
- Y. Nagashima, F. Saito, Y. Ito, A. Goto, and T. Hyodo: “Study of X-ray emission by positron impact”, Workshop on Studies on Reliability of Advanced Pressure Boundary Materials Used in Extremely Severe Environments on Nuclear Energy Systems Research and Development of Advanced Positron Beam Applications: Functional Materials and Beam Technology, Takasaki, Aug. (2002).
- T. Kambara, K. Kageyama, Y. Kanai, T. Kojima, Y. Nakai, A. Yoneda, and Y. Yamazaki: “Elastic wave from GeV heavy-ion irradiations on solids”, 13th Int. Conf. on Ion Beam Modification of Materials (IBMM 2002), (The Japan Society of Applied Physics), Kobe, Sept. (2002).
- S. Ohira, K. Awaga, W. Fujita, I. Watanabe, and K. Nagamine: “ $\mu\text{SR}$  study on magnetic property of  $p\text{-NPNN}\cdot\text{Cu}(\text{hfac})_2$ ”, 2002 Fall Meet. of the Physical Soc. of Japan, Kasugai, Sept. (2002).
- T. Kojima, N. Oshima, M. Niigaki, A. Mohri, and Y. Yamazaki: “Creation of positron plasmas in ultra high vacuum environment”, 2002 Fall Meet. of the Physical Soc. of Japan, Kasugai, Sept. (2002).
- T. Kambara, Y. Kanai, Y. Nakai, T. Ikeda, N. Fukunishi, Y. Takabayashi, T. Azuma, K. Komaki, and Y. Yamazaki: “High-resolution spectroscopy of highly-charged ions utilizing a virtual-photon field in a single crystal”, 2002 Fall Meet. of the Physical Soc. of Japan, Kasugai, Sept. (2002).
- Y. Nagashima, F. Saito, Y. Ito, A. Goto, and T. Hyodo: “Measurement of inner-shell ionization cross sections by positron impact”, 2002 Fall Meet. of the Physical Soc. of Japan, Kasugai, Sept. (2002).
- M. Niigaki, T. Kojima, N. Oshima, and A. Mohri: “RIKEN HCI TRAP IV: Positron accumulation using a high-density electron plasma”, 2002 Fall Meet. of the Physical Soc. of Japan, Kasugai, Sept. (2002).
- A. Igarashi, M. Kimura, and I. Shimamura: “Positron annihilation in collisions with atoms: A solution to the pathological problem with the conventional theory”, 5th Asian Int. Seminar on Atomic and Molecular Physics (AISAMP 5), (Advanced Photon Research Center Kansai Research, JAERI), Nara, Oct. (2002).
- T. Hirade, N. Suzuki, F. Saito, A. Goto, and T. Hyodo: “Positronium formation at low temperatures”, 45th Symp. on Radiation Chemistry, Kasuga, Oct. (2002).
- I. Shimamura, A. Igarashi, and M. Kimura: “Annihilation of low energy positrons in hydrogen”, 17th Int. Conf. on the Application of Accelerators in Research and Industry (CAARI 2002), (University of North Texas), Denton, USA, Nov. (2002).
- K. Wada, Y. Nagashima, F. Saito, Y. Ito, A. Goto, and T. Hyodo: “Improvement of the positron spin polarization measurement using positron lifetime”, Specialist Research Meet. on Positron Beam Techniques and Condensed Matter, Kumatori-cho, Osaka

- Pref., Nov. (2002).
- Y. Nagashima, F. Saito, Y. Itoh, A. Goto, and T. Hyodo: "Ionization cross sections for Cu K-shell and Ag L-shell by positron impact", Specialist Research Meet. on Positron Beam Techniques and Condensed Matter, Kumatori-cho, Osaka Pref., Nov. (2002).
- M. Niigaki, T. Kojima, N. Oshima, A. Mohri, K. Komaki, and Y. Yamazaki: "Production of ultra-slow HCI beams sympathetically cooled by a cold positron plasma", 8th Japan-Russia Int. Symp. on Interaction of Fast Charged Particles with Solids, (Quantum Science and Engineering Center and Kyoto University), Kyoto, Nov. (2002).
- N. Oshima, T. Kojima, M. Niigaki, A. Mohri, K. Komaki, and Y. Yamazaki: "Development of positron accumulator for cooling highly charged ions", Scientific Meet. of the Research Reactor Institute, Kyoto University, Kumatori-cho, Osaka Pref., Nov. (2002).
- A. Igarashi, M. Kimura, and I. Shimamura: "Inseparable positron annihilation and positronium formation in positron-hydrogen collisions", JSPS-NSF and RIKEN Joint Workshop on Resonances in Physics, Chemistry and Biology (US-Japan Workshop), Hayama, Dec. (2002).
- Y. Nagashima, F. Saito, Y. Itoh, A. Goto, and T. Hyodo: "Si(Li) detector for the measurement of X-rays by positron impact", 17th Workshop on Radiation Detectors and Their Uses, (KEK), Tsukuba, Jan. (2003).
- K. Kimura: "Ultra fast luminescence in heavy-ion track cores in insulators: electron-hole plasma (invited talk)", 20th Int. Conf. on Atomic Collisions in Solids (ICACS 20), (University of Hyderabad and Institute of Physics, Bhubaneswar), Puri, India, Jan. (2003).
- S. Ohira: "Studies on magnetic properties of organic materials by using muon", RIKEN Symp. on Studies on Condensed Matter Physics, Atomic Physics, Hyperfine Interactions and Biomedical Sciences Using RIKEN Accelerators, Wako, Feb. (2003).
- M. Wada: "Efficient collection of energetic Li-8 ions by rf ion guide", Workshop on Physics Applications of Medical Use Particle Accelerator, (National Institute of Radiological Sciences), Chiba, Feb. (2003).
- E. Yagi, S. Koike, T. Matsumoto, T. Urai, N. Tajima, and K. Ogiwara: "Change of state of hydrogen in Nb-Mb alloys with Mo concentration", 58th Ann. Meet. of Physical Soc. of Japan, Sendai, Mar. (2003).
- Y. Nakai, Y. Kanai, Y. Iwai, Y. Yamazaki, H. Masuda, and K. Nishio: "Coincidence measurement of x-rays with final charge states of highly charged ions transmitted through a microcapillary target", 58th Ann. Meet. of Physical Soc. of Japan, Sendai, Mar. (2003).
- Y. Iwai, Y. Kanai, Y. Nakai, T. Ikeda, H. Oyama, K. Ando, H. Masuda, K. Nishio, M. Nakao, H. Torii, and K. Komaki: "High resolution soft X-ray spectroscopy using a single photon counting method", 58th Ann. Meet. of Physical Soc. of Japan, Sendai, Mar. (2003).
- S. Ohira, M. Tamura, R. Kato, and I. Watanabe: "Magnetic property of the [Pd(dmit)<sub>2</sub>] salts studied by the  $\mu$ SR method", 58th Ann. Meet. of Physical Soc. of Japan, Sendai, Mar. (2003).
- H. Shimada, Y. Nakai, H. Oyama, K. Ando, T. Kambara, A. Hatakeyama, and Y. Yamazaki: "Measurement of the momentum distributions of multiply charged ions produced by an intense laser", 58th Ann. Meet. of Physical Soc. of Japan, Sendai, Mar. (2003).
- M. Niigaki, T. Kojima, N. Oshima, A. Mohri, and Y. Yamazaki: "RIKEN HCI Trap V: Optimization of positron trapping with high-density electron plasma", 58th Ann. Meet. of Physical Soc. of Japan, Sendai, Mar. (2003).
- M. Hoshino, Y. Kanai, M. Yanagisawa, Y. Nakai, M. Kitajima, h. Tanaka, and Y. Yamazaki: "The state-selective angular distributions of single- and double-electron capture processes for X<sup>4+</sup> (X=C, N)-He collision in the energy range below 100 eV/q", 58th Ann. Meet. of Physical Soc. of Japan, Sendai, Mar. (2003).
- Y. Matsuo: "Spectroscopic behavior of atoms and ions in liquid and cold gas He", Chemistry in Quantum Condensed Phases, (Morino Foundation), Kyoto, Mar. (2003).
- N. Oshima, T. Kojima, M. Niigaki, A. Mohri, K. Komaki, and Y. Yamazaki: "Efficient positron trapping in a cryogenic vacuum with an electron plasma", Int. Conf. on Low Energy Antiproton Physics (LEAP'03), (Antimatter Science Project, University of Tokyo, RIKEN and KEK), Yokohama, Mar. (2003).
- M. Wada: "Technical developments toward antiprotonic radioactive nuclear atoms for nuclear structure study", Int. Conf. on Low Energy Antiproton Physics (LEAP'03), (Antimatter Science Project, University of Tokyo, RIKEN and KEK), Yokohama, Mar. (2003).
- N. Oshima: "Formation of a non-neutral positron plasma and its application", Mini Workshop on Generation of High-Energy Synchrotron Radiation by Superconducting Wiggler and Its Application, (SPRING-8), Harima, Mar. (2003).
- E. Yagi: "State of hydrogen in Nb-based bcc alloys", Symp. on the Role of Hydrogen in the Embrittlement of Structural Materials in the Environmental Atmosphere, (Iron and Steel Institute of Japan), Tokyo, Mar. (2003).
- M. Wada: "Deceleration and cooling of RI beams; from GeV to  $\mu$ eV", Int. Workshop on Beam Cooling and Related Topics (COOL03), (RIKEN and CNS), Yamanashi, May (2003).
- A. Takamine: "On-line test of an rf-ion guide for col-

- lecting energetic Li-8 beams”, Workshop on Slow RI-Beams and Related Topics, (RIKEN), Wako, May (2003).
- M. Wada: “The slow RI-beam facility at RIKEN RIBF”, Workshop on Slow RI-Beams and Related Topics, (RIKEN), Wako, May (2003).
- N. Nakamura: “Tokyo EBIT and possibility for highly charged RI ion”, Workshop on Slow RI-Beams and Related Topics, (RIKEN), Wako, May (2003).
- N. Ohshima: “Positron accumulation with an electron plasma”, 12th Int. Workshop on Low Energy Positron and Positronium Physics, (University of Aarhus), Sandbjerg, Denmark, July (2003).
- N. Yamanaka, Y. Kino, Y. Takano, H. Kudo, and A. Ichimura: “Enhancement of direct positron annihilation due to temporal capture during a collision”, 23rd Int. Conf. on Photonic Electronic and Atomic Collisions (ICPEAC 2003), Stockholm, Sweden, July (2003).
- H. Shimada, Y. Nakai, H. Oyama, K. Ando, T. Kambara, A. Hatakeyama, and Y. Yamazaki: “Measurement of the momentum distribution of argon ions produced by an intense laser light”, 23rd Int. Conf. on Photonic Electronic and Atomic Collisions (ICPEAC 2003), Stockholm, Sweden, July (2003).
- Y. Kanai, Y. Nakai, Y. Iwai, K. Nishio, H. Masuda, and Y. Yamazaki: “Measurements of X-rays from highly charged ion transmitted through a Ni microcapillary”, 23rd Int. Conf. on Photonic Electronic and Atomic Collisions (ICPEAC 2003), Stockholm, Sweden, July (2003).
- A. Takamine, M. Wada, Y. Ishida, T. Nakamura, T. Kambara, H. Oyama, Y. Kanai, T. Kojima, Y. Nakai, A. Yoshida, T. Kubo, Y. Matsuo, Y. Fukuyama, K. Okada, T. Sonoda, K. Noda, S. Ohtani, H. Kawakami, I. Katayama, and Y. Yamazaki: “On-line collection of energetic  $^8\text{Li}$  ions from a projectile fragment separator using an RF ion-guide”, 23rd Int. Conf. on Photonic Electronic and Atomic Collisions (ICPEAC 2003), Stockholm, Sweden, July (2003).
- A. Igarashi, M. Kimura, and I. Shimamura: “Positron annihilation and positronium formation: unified theory in term of a complex potential”, 23rd Int. Conf. on Photonic Electronic and Atomic Collisions (ICPEAC 2003), Stockholm, Sweden, July (2003).
- T. Nakamura, M. Wada, K. Okada, I. Katayama, S. Ohtani, and H. A. Schuessler: “Precision spectroscopy of the zeeman splittings of the  $^9\text{Be}^+ 2^2\text{S}_{1/2}$  hyperfine structure levels”, 23rd Int. Conf. on Photonic Electronic and Atomic Collisions (ICPEAC 2003), Stockholm, Sweden, July (2003).
- M. Hoshino, Y. Kanai, M. Yanagisawa, Y. Nakai, M. Kitajima, H. Tanaka, and Y. Yamazaki: “The state-selective angular distribution measurements of multi-electron capture in  $\text{X}^{4+}$  ( $\text{X}=\text{C}, \text{N}, \text{O}$ )-He collisions at 50-200 eV/ $q$ ”, 23rd Int. Conf. on Photonic Electronic and Atomic Collisions (ICPEAC 2003), Stockholm, Sweden, July (2003).
- I. Shimamura: “Divergence of the integral cross sections for electron and positron scattering by polar symmetric-top molecules”, Int. Symp. on Electron-Molecule Collisions and Swarms (EMS-03), (Charles University and Academy Sciences Czech Republic), Pruhonice, Czech, July–Aug. (2003).
- I. Shimamura: “Complex potential description of positron impact processes”, Int. Symp. on Electron-Molecule Collisions and Swarms (EMS-03), (Charles University and Academy Sciences Czech Republic), Pruhonice, Czech, July–Aug. (2003).
- N. Ohshima, T. Kojima, M. Niigaki, K. Komaki, and Y. Yamazaki: “Positron trapping with an electron plasma under ultra high vacuum conditions”, 40th Ann. Meet. on Radioisotopes and Radiation in the Physical Sciences and Industries, (Japan Radioisotope Association), Tokyo, July (2003).
- Y. Nagashima, F. Saito, Y. Ito, A. Goto, and T. Hyodo: “Detection of characteristic X-rays by positron impact”, 27th Ann. Meet. of the Soc. for Atomic Collision Research, Kyoto, Aug. (2003).
- Y. Iwai, Y. Kanai, Y. Nakai, T. Ikeda, H. Oyama, K. Ando, H. Masuda, K. Nishio, H. Torii, K. Komaki, and Y. Yamazaki: “High-resolution soft X-ray spectroscopy of 2.3 keV/u  $\text{N}^{6,7+}$  ions through microcapillary targets II”, 28th Ann. Meet. of the Soc. for Atomic Collision Research, Hachioji, Aug. (2003).
- Y. Iwai, Y. Nakai, Y. Kanai, T. Ikeda, H. Masuda, K. Nishio, and Y. Yamazaki: “Measurement of L X-ray of highly charged Ar ions transmitted through a microcapillary target”, 28th Ann. Meet. of the Soc. for Atomic Collision Research, Hachioji, Aug. (2003).
- I. Shimamura: “Nonadiabatic transitions for the formation of unstable products: An example of positronium formation and annihilation”, Moscow-Chernogolovka Workshop on Nonadiabatic Transitions in Quantum Mechanics, (Russian Research Centre Kurchatov Institute and others), Moscow and Chernogolovka, Russia, Aug. (2003).
- S. Ozawa, M. Wakasugi, M. Okamura, M. Serata, T. Koizumi, and T. Katayama: “Laser-induced fluorescence spectroscopy with highly charged ion beam produced by laser ion source”, 10th Int. Conf. on Ion Sources (ICIS 2003), Dubna, Russia, Sept. (2003).
- E. Yagi, S. Koike, T. Sugawara, T. Shishito, and K. Ogiwara: “Change of the state of hydrogen in Nb on alloying with Mo”, 2003 Fall Meet. of the Physical Soc. of Japan, Miyazaki and Okayama, Sept. (2003).
- I. Shimamura: “Divergence of the integral cross sections for electron and positron scattering by polar symmetric-top molecules”, 2003 Fall Meet. of the Physical Soc. of Japan, Miyazaki and Okayama, Sept. (2003).
- Y. Iwai, Y. Kanai, Y. Nakai, T. Ikeda, H. Oyama, K. Ando, H. Masuda, K. Nishio, H. Torii, K. Komaki,

- and Y. Yamazaki: “High-resolution soft X-ray spectroscopy of 2.3 keV/u  $N^{6,7+}$  ions through microcapillary targets II”, 2003 Fall Meet. of the Physical Soc. of Japan, Miyazaki and Okayama, Sept. (2003).
- E. Yagi, M. Yoshii, S. Koike, H. Matsuda, Y. Okada, K. Sakuma, K. Mori, S. Hagiwara, T. Sugawara, and T. Shishito: “Lattice location of hydrogen in Nb-Ta alloys”, 2003 Fall Meet. of the Physical Soc. of Japan, Miyazaki and Okayama, Sept. (2003).
- M. Hoshino, T. Kambara, Y. Kanai, S. Madzunkov, R. H. Schuch, and Y. Yamazaki: “Multi-electron transfer in close single collisions of slow highly-charged ions with atoms”, 2003 Fall Meet. of the Physical Soc. of Japan, Miyazaki and Okayama, Sept. (2003).
- N. Kuroda, M. Hori, H. Torii, A. Hatakeyama, N. Oshima, Y. Morishita, A. Mohri, Y. Yamazaki, and K. Komaki: “Observation of electrostatic modes of a mixed plasma of antiprotons and electrons”, 2003 Fall Meet. of the Physical Soc. of Japan, Miyazaki and Okayama, Sept. (2003).
- M. Wada, Y. Ishida, T. Nakamura, A. Takamine, Y. Nakai, T. Kojima, Y. Kanai, N. Oshima, H. Oyama, T. Kambara, A. Yoshida, T. Kubo, Y. Matsuo, Y. Fukuyama, K. Okada, T. Sonoda, K. Noda, H. Kawakami, S. Ohtani, I. Katayama, Y. Yamazaki, H. Wollnik, V. Varentsov, and P. Hostein: “Slow RI beam facility by using RF ion guide method”, 2003 Fall Meet. of the Physical Soc. of Japan, Miyazaki and Okayama, Sept. (2003).
- N. Oshima, T. Kojima, M. Niigaki, A. Mohri, K. Komaki, and Y. Yamazaki: “Study of a positron accumulation technique with an electron plasma”, 2003 Fall Meet. of the Physical Soc. of Japan, Miyazaki and Okayama, Sept. (2003).
- A. Takamine, M. Wada, Y. Ishida, T. Nakamura, Y. Nakai, T. Kojima, Y. Kanai, H. Oyama, T. Kambara, N. Oshima, A. Yoshida, T. Kubo, Y. Matsuo, Y. Fukuyama, K. Okada, T. Sonoda, K. Noda, H. Kawakami, S. Ohtani, I. Katayama, Y. Yamazaki, H. Wollnik, V. Varentsov, and P. Hostein: “The development of the system collecting energetic  $^8\text{Li}$  ions by means of the large He gas cell and rf field”, 2003 Fall Meet. of the Physical Soc. of Japan, Miyazaki and Okayama, Sept. (2003).
- N. Yamanaka and Y. Kino: “Time-dependent coupled channel calculation of positron elastic scattering”, 2003 Fall Meet. of the Physical Soc. of Japan, Miyazaki and Okayama, Sept. (2003).
- N. Yamanaka, Y. Kino, Y. Takano, H. Kudo, and A. Ichimura: “Direct positron annihilation in a dense gas”, ICPA-13: 13th Int. Conf. on Positron Annihilation (KYOTO 2003), Kyoto, Sept. (2003).
- N. Oshima, T. Kojima, M. Niigaki, A. Mohri, M. Inoue, K. Komaki, and Y. Yamazaki: “Positron accumulation efficiency with a combination of an electron plasma and an ion cloud”, ICPA-13: 13th Int. Conf. on Positron Annihilation (KYOTO 2003), Kyoto, Sept. (2003).
- Y. Yamazaki: “Antiproton-radioactive-isotope atom formation”, Meet. of the Users Group for Low-Energy Antiproton Physics at GSI, Darmstadt, Germany, Sept. (2003).
- T. Furukawa, Y. Matsuo, Y. Fukuyama, A. Hatakeyama, T. Kobayashi, H. Izumi, Y. Arakawa, I. Wakabayashi, K. Kawai, S. Morinobu, and T. Shimoda: “Spin polarization and relaxation of optically pumped atoms in superfluid helium”, 59th Ann. Meet. of Physical Soc. of Japan, Fukuoka, Mar. (2004).
- Y. Sakamaki, M. Hashimoto, Y. Fukai, K. Morita, J. Yuzuhara, M. Kato, S. Koike, and E. Yagi: “Stress-induced state of hydrogen in V-H system”, 59th Ann. Meet. of Physical Soc. of Japan, Fukuoka, Mar. (2004).

#### 4. Radiochemistry, radiation chemistry, and radiation biology

- Y. Kobayashi: “Valence states of  $^{57}\text{Fe}$  decayed from  $^{57}\text{Mn}$  implanted into  $\text{KMnO}_4$ ”, RIKEN Symp. on Condensed Matter Studies with Radioactive Ion Beams, Wako, Feb. (2002).
- T. Morishita, H. Yamaguchi, K. Degi, N. Shikazono, Y. Hase, A. Tanaka, and T. Abe: “Dose response and mutation induction by ion beam irradiation”, 13th Int. Conf. on Ion Beam Modification of Materials (IBMM 2002), Kobe, Sept. (2002).
- Y. Takahashi, C. Egawa, A. Hirakata, R. Hirunuma, and S. Enomoto: “Effect of surface diffusion on the diffusivity of various ions through porewater of granite”, 49th Ann. Meet. of the Geochemical Soc. of Japan, Kagoshima, Sept. (2002).
- M. Ito, Y. Takahashi, H. Mori, R. Hirunuma, S. Enomoto, and H. Shimizu: “Experimental study on the incorporation of Re and Os from seawater into sediments”, 49th Ann. Meet. of the Geochemical Soc. of Japan, Kagoshima, Sept. (2002).
- Y. Kanayama, S. Enomoto, and R. Amano: “Multi-tracer screening for RI delivery manner: Brain rubidium uptake bypassing blood-brain-barrier”, The 4th Ann. Meet./The 46th Symp. on Radiochemistry, Sapporo, Sept. (2002).
- T. Tsuji, R. Hirunuma, S. Enomoto, and R. Amano: “Radiochemical study of manganese concentration and its uptake behavior in brain: Their changes in fetal, suckling and developmental mice”, The 4th Ann. Meet./The 46th Symp. on Radiochemistry, Sapporo, Sept. (2002).
- T. Ohyama, M. Koike, T. Ogi, Y. Kawamoto, H. Maetsu, H. Suganuma, M. Noguchi, K. Ishikawa, R. Hirunuma, S. Enomoto, and M. Yanaga: “Sub-cellular distribution of trace elements in livers of Zn-deficient mice”, The 4th Ann. Meet./The 46th

- Symp. on Radiochemistry, Sapporo, Sept. (2002).
- W. Sato, H. Ueno, H. Watanabe, H. Ogawa, H. Miyoshi, N. Imai, A. Yoshimi, K. Yoneda, D. Kameda, Y. Kobayashi, K. Sueki, Y. Okubo, and K. Asahi: "TDPAC studies using probes implanted in powder C<sub>60</sub>", The 4th Ann. Meet./The 46th Symp. on Radiochemistry, Sapporo, Sept. (2002).
- Y. Kanayama, T. Tsuji, S. Enomoto, and R. Amano: "Differences in delivery manner of trace elements by some administration methods", 6th Conf. of the Int. Soc. for Trace Element Research in Humans (ISTERH), Quebec, Canada, Sept. (2002).
- T. Tsuji, T. Tarohda, Y. Kanayama, S. Enomoto, and R. Amano: "Elemental concentration and tracer uptake distribution of manganese and other elements in fetal, suckling and developmental mice", 6th Conf. of the Int. Soc. for Trace Element Research in Humans (ISTERH), Quebec, Canada, Sept. (2002).
- T. Yanagiya, N. Imura, S. Enomoto, and S. Himeno: "Manganese can alleviate cadmium cytotoxicity", 6th Conf. of the Int. Soc. for Trace Element Research in Humans (ISTERH), Quebec, Canada, Sept. (2002).
- S. Enomoto: "The multitracer technique: manufacturing and application to bio-trace elemental research", 6th Conf. of the Int. Soc. for Trace Element Research in Humans (ISTERH), Quebec, Canada, Sept. (2002).
- T. Matsuyama, T. Ebisuzaki, K. Koike, H. Kato, H. Saito, T. Abe, and S. Yoshida: "Arabidopsis genome analysis by the virtual RLGS system", 11th Meet. of the Japanese Soc. for DNA Polymorphism Research, Asahikawa, Oct. (2002).
- Y. Matsumoto, N. Umeda, H. Yin, M. Tomita, A. Enomoto, A. Morita, T. Mizukoshi, K. Sakai, Y. Hosoi, K. Ohtomo, and N. Suzuki: "Effects of hyperthermia on DNA-PK activity and radiosensitivity", 46th Ann. Meet. of the Japan Radiation Research Soc., Kyoto, Oct. (2002).
- T. Yanagiya, N. Imura, S. Enomoto, and S. Himeno: "Alleviation of cadmium cytotoxicity by manganese", Int. Symp. on Bio-Trace Elements 2002 (BITREL2002): Joint Symp. of RIKEN and Yamanashi Institute of Environmental Sciences, Wako and Fujiyoshida, Oct.–Nov. (2002).
- R. Hirunuma and S. Enomoto: "Application of the multitracer technique: Fetoplacental transport of various elements in pregnant rats", Int. Symp. on Bio-Trace Elements 2002 (BITREL2002): Joint Symp. of RIKEN and Yamanashi Institute of Environmental Sciences, Wako and Fujiyoshida, Oct.–Nov. (2002).
- K. Igarashi, Y. Nakanishi, R. Hirunuma, S. Enomoto, and S. Kimura: "Biological interaction of various trace elements and NaFeEDTA as a food fortificant", Int. Symp. on Bio-Trace Elements 2002 (BITREL2002): Joint Symp. of RIKEN and Yamanashi Institute of Environmental Sciences, Wako and Fujiyoshida, Oct.–Nov. (2002).
- A. Nakayama, H. Yasui, R. Hirunuma, and S. Enomoto: "Distribution of biotrace elements in partially hepatectomized rats", Int. Symp. on Bio-Trace Elements 2002 (BITREL2002): Joint Symp. of RIKEN and Yamanashi Institute of Environmental Sciences, Wako and Fujiyoshida, Oct.–Nov. (2002).
- T. Ohyama, M. Koike, T. Ogi, Y. Kawamoto, H. Maetsu, H. Suganuma, M. Noguchi, K. Ishikawa, R. Hirunuma, S. Enomoto, and M. Yanaga: "Distribution of trace elements among subcellular fractions in livers of Zn-deficient mice", Int. Symp. on Bio-Trace Elements 2002 (BITREL2002): Joint Symp. of RIKEN and Yamanashi Institute of Environmental Sciences, Wako and Fujiyoshida, Oct.–Nov. (2002).
- W. Ding, R. Hirunuma, and S. Enomoto: "Effect of insulin-enhancing action of vanadium on distribution of trace elements in the pre-diabetic stage and diabetic stages of KK mice", Int. Symp. on Bio-Trace Elements 2002 (BITREL2002): Joint Symp. of RIKEN and Yamanashi Institute of Environmental Sciences, Wako and Fujiyoshida, Oct.–Nov. (2002).
- T. Soshi, S. Enomoto, and I. Yamaguchi: "Effect of microorganisms on the uptake of radionuclides by plant", Int. Symp. on Bio-Trace Elements 2002 (BITREL2002): Joint Symp. of RIKEN and Yamanashi Institute of Environmental Sciences, Wako and Fujiyoshida, Oct.–Nov. (2002).
- H. Yasui, T. Takino, J. Fugono, A. Nakayama, R. Hirunuma, S. Enomoto, and H. Sakurai: "Effect of vanadium treatment on tissue distribution of biotrace elements in normal and streptozotocin-induced diabetic rats", Int. Symp. on Bio-Trace Elements 2002 (BITREL2002): Joint Symp. of RIKEN and Yamanashi Institute of Environmental Sciences, Wako and Fujiyoshida, Oct.–Nov. (2002).
- T. Ogi, Y. Kawamoto, H. Maetsu, M. Koike, T. Ohyama, S. Enomoto, M. Noguchi, H. Suganuma, and M. Yanaga: "Effects of zinc content in a diet on concentrations of trace elements in organs and tissues of mice", Int. Symp. on Bio-Trace Elements 2002 (BITREL2002): Joint Symp. of RIKEN and Yamanashi Institute of Environmental Sciences, Wako and Fujiyoshida, Oct.–Nov. (2002).
- T. Tsuji, R. Hirunuma, S. Enomoto, and R. Amano: "Elemental concentration and tracer uptake behavior of manganese in fetal, suckling, and developmental mice", Int. Symp. on Bio-Trace Elements 2002 (BITREL2002): Joint Symp. of RIKEN and Yamanashi Institute of Environmental Sciences, Wako and Fujiyoshida, Oct.–Nov. (2002).
- T. Nabekura, T. Minami, R. Hirunuma, S. Enomoto, and Y. Ito: "Expression of metallothionein in cataractous rat lens", Int. Symp. on Bio-Trace Elements 2002 (BITREL2002): Joint Symp. of RIKEN and Yamanashi Institute of Environmental Sciences,

- Wako and Fujiyoshida, Oct.–Nov. (2002).
- S. Enomoto: “The multitracer technology in bio-trace elements research”, Int. Symp. on Bio-Trace Elements 2002 (BITREL2002): Joint Symp. of RIKEN and Yamanashi Institute of Environmental Sciences, Wako and Fujiyoshida, Oct.–Nov. (2002).
- H. Tamano, A. Takeda, S. Enomoto, and N. Oku: “Zinc-65 imaging of rat brain tumors”, Int. Symp. on Bio-Trace Elements 2002 (BITREL2002): Joint Symp. of RIKEN and Yamanashi Institute of Environmental Sciences, Wako and Fujiyoshida, Oct.–Nov. (2002).
- K. Ushida, Y. Mizuntani, T. Kojima, Y. Yoshida, M. Miki, T. Kozawa, and S. Tagawa: “Acetone dimer radical cation: Reanalysis of formation dynamics”, 45th Symp. on Radiation Chemistry, Kasuga, Oct. (2002).
- T. Matsuyama, K. Koike, T. Ebisuzaki, S. Yoshida, H. Kato, H. Saito, and T. Abe: “Arabidopsis genome analysis by the virtual RLGS system”, 25th Ann. Meet. of the Molecular Biology Soc. of Japan, Yokohama, Dec. (2002).
- R. Hirunuma and S. Enomoto: “Application of the multitracer technique: Transport of various elements in the pregnant rats and the fetus”, Int. Symp. on Transfer of Radionuclides in Biosphere: Prediction and Assessment, (Crossover Research Promotion Council), Mito, Dec. (2002).
- H. Haba, R. Hirunuma, and S. Enomoto: “Development of a gas-jet coupled multitarget system for multitracer production”, Int. Symp. on Transfer of Radionuclides in Biosphere: Prediction and Assessment, (Crossover Research Promotion Council), Mito, Dec. (2002).
- T. Soshi, S. Enomoto, and I. Yamaguchi: “Effect of microorganisms on the uptake of radionuclides by plant, application of the microorganisms-plant complex system to the phytoremediation for radionuclides contamination”, Int. Symp. on Transfer of Radionuclides in Biosphere: Prediction and Assessment, (Crossover Research Promotion Council), Mito, Dec. (2002).
- T. Saito, Y. Kobayashi, K. M. Kubo, and Y. Yamada: “ $^{57}\text{Co}$  emission Mössbauer studies of the graphite surface”, Special Research Meet. on New Developments in Solid State Physics with Probes of Radiation and Nuclei, (Research Reactor Institute, Kyoto University), Kumatori-cho, Osaka Pref., Dec. (2002).
- Y. Kobayashi, K. M. Kubo, Y. Yamada, T. Saito, W. Sato, H. Ueno, J. Murata, H. Watanabe, H. Miyoshi, D. Kameda, and K. Asahi: “Chemical states of Fe implanted into graphite”, Special Research Meet. on New Developments in Solid State Physics with Probes of Radiation and Nuclei, (Research Reactor Institute, Kyoto University), Kumatori-cho, Osaka Pref., Dec. (2002).
- M. Kibe, Y. Gounou, S. Motomura, Q. Pan, S. Enomoto, and Y. Yano: “Characteristics of a stripped Ge detector”, 108th Ann. Meet. of Kyusyu Branch of The Physical Soc. of Japan, Fukuoka, Dec. (2002).
- H. Haba, K. Tsukada, M. Asai, K. Akiyama, A. Toyoshima, I. Nishinaka, S. Ichikawa, and Y. Nagame: “Anion exchange behavior of Nb, Ta, and Pa in hydrofluoric acid solutions: Model experiments for chemical characterization of element 105, dubnium”, Materials Science Symp. on Heavy Ion Science in Tandem Energy Region, (JAERI), Tokaimura, Jan. (2003).
- M. Tomita, S. Goto, F. Yatagai, and Y. Matsumoto: “A possible production of DNA clustered damage by space radiation”, 19th Space Utilization Symp., (The Institute of Space and Astronautical Science), Sagamihara, Jan. (2003).
- Y. Yamamoto, M. Kimura, H. Ryuto, N. Fukunishi, Y. Yano, T. Abe, and S. Yoshida: “Multiple pathways for light stress response of *Arabidopsis thaliana*”, Keystone Symp. on Plant Response to Abiotic Stress, Santa Fe, USA, Feb. (2003).
- Y. Kobayashi: “In-beam Mössbauer spectroscopy of Fe atoms implanted into graphite”, RIKEN Symp. on Studies on Condensed Matter Physics, Atomic Physics, Hyperfine Interactions and Biomedical Sciences Using RIKEN Accelerators, Wako, Feb. (2003).
- W. Sato, H. Ueno, H. Watanabe, H. Miyoshi, A. Yoshimi, D. Kameda, J. Kaihara, K. Shimada, T. Ito, S. Suda, Y. Kobayashi, and K. Asahi: “On-line EDPAC studies using the  $^{19}\text{F}$  probe (II)”, RIKEN Symp. on Studies on Condensed Matter Physics, Atomic Physics, Hyperfine Interactions and Biomedical Sciences Using RIKEN Accelerators, Wako, Feb. (2003).
- H. Haba: “Production of various radiotracers and their applications at the RIKEN accelerator facility”, RIKEN Symp. on Studies on Condensed Matter Physics, Atomic Physics, Hyperfine Interactions and Biomedical Sciences Using RIKEN Accelerators, Wako, Feb. (2003).
- H. Haba: “Heavy element chemistry in RIKEN: Present status and future plans”, Workshop of Advanced Science Research Center, JAERI, Nuclear Physics and Nuclear Chemistry of Superheavy Elements, Tokai-mura, Feb. (2003).
- R. Hirunuma, H. Haba, and S. Enomoto: “Development of a gas-jet coupled multitarget system and an automatic chemical separation apparatus for multitracer production”, 123rd Ann. Meet. of the Pharmaceutical Soc. of Japan, Nagasaki, Mar. (2003).
- H. Haba, K. Tsukada, M. Asai, K. Akiyama, A. Toyoshima, I. Nishinaka, S. Ichikawa, and Y. Nagame: “Anion exchange behavior of Nb, Ta, and Pa in hydrofluoric acid solutions: Model experi-

- ments for chemical characterization of element 105, dubnium”, 83rd Natl. Meet. of the Chemical Soc. of Japan, Tokyo, Mar. (2003).
- A. Toyoshima, K. Tsukada, H. Haba, M. Asai, K. Akiyama, I. Nishinaka, S. Ichikawa, Y. Nagame, M. Shigekawa, S. Goto, T. Kaneko, S. Ono, H. Kudo, Y. Oura, K. Sueki, M. Sakama, H. Kikunaga, N. Kinoshita, N. Tsuruga, A. Yokoyama, and A. Shinohara: “Anion-exchange behavior of Rf, Zr and Hf in HF solution”, 83rd Natl. Meet. of the Chemical Soc. of Japan, Tokyo, Mar. (2003).
- Y. Kobayashi: “In-beam Mössbauer spectroscopy using RI beams”, 83rd Natl. Meet. of the Chemical Soc. of Japan, Tokyo, Mar. (2003).
- S. Enomoto: “Evolution of next-generation multi-tracer production technology on the RI beam factory project: Development of multitracer gamma-ray emission imaging and new radiopharmaceuticals”, Workshop on RI Beam Factory and Research Plan, (RIKEN), Wako, Mar. (2003).
- Y. Kobayashi: “The applications of RI beam to materials science: In-beam Mössbauer spectroscopy”, Workshop on RI Beam Factory and Research Plan, (RIKEN), Wako, Mar. (2003).
- H. Haba, K. Tsukada, M. Asai, A. Toyoshima, K. Akiyama, I. Nishinaka, M. Hirata, T. Yaita, S. Ichikawa, Y. Nagame, A. Shinohara, S. Goto, T. Kaneko, H. Kudo, Y. Oura, H. Nakahara, K. Sueki, A. Yokoyama, M. Sakama, M. Schaedel, and J. V. Kratz: “Chemical characterization of rutherfordium by atom-at-a-time ion-exchange chromatography”, 6th Int. Conf. on Methods and Applications of Radioanalytical Chemistry (MARC VI), (American Nuclear Society), Hawaii, USA, Apr. (2003).
- K. Igarashi, Y. Nakanishi, R. Hirunuma, S. Enomoto, and S. Kimura: “The efficacy of NaFeEDTA for improving iron deficiency”, 20th Symp. on Trace Nutrients Research, Kyoto, May (2003).
- M. Tomita: “Imaging analysis of heavy-ion-induced DNA double-strand break”, RIKEN Symp. on New Development in Radiation Biology: Molecular Imaging of the Process of DNA Damage Induction and Its Repair, Wako, June (2003).
- S. Enomoto, H. Haba, R. Hirunuma, A. Nakayama, and K. Igarashi: “Evolution of next-generation multi-tracer technology: Manufacturing and application to bio-trace elemental research”, 13th Symp. on Roles of Metals in Biological Reactions, Biology and Medicine (SRM2003), (The Pharmaceutical Society of Japan), Chiba, June (2003).
- K. Igarashi, Y. Nakanishi, R. Hirunuma, S. Enomoto, and S. Kimura: “The efficacy of NaFeEDTA as a iron fortificant”, 13th Symp. on Roles of Metals in Biological Reactions, Biology and Medicine (SRM2003), (The Pharmaceutical Society of Japan), Chiba, June (2003).
- T. Abe, Y. Miyazawa, N. Fukunishi, S. Yoshida, K. Suzuki, and T. Kusumi: “A flower mutant of tobacco induced by heavy-ion beams”, Plant Biology 2003: The Ann. Meet. of the American Soc. of Plant Biologists, Honolulu, USA, July (2003).
- T. Kagawa, M. Kasahara, T. Abe, S. Yoshida, and M. Wada: “Functional analysis of *Acphot2* using mutants deficient in blue light-induced chloroplast avoidance movement of the fern *Adiantum capillus-veneris* L”, Plant Biology 2003: The Ann. Meet. of the American Soc. of Plant Biologists, Honolulu, USA, July (2003).
- M. Ono, H. Yokokawa, M. Matsugami, R. Amano, and S. Enomoto: “Behavior of bio-trace elements into the mouse brain by LPS administration”, 14th Ann. Meet. of the Japan Soc. for Biomedical Research on Trace Elements (JSBRTE2003), Osaka, July (2003).
- K. Igarashi, R. Hirunuma, H. Haba, S. Enomoto, and S. Kimura: “Effect of carnosine for the absorption of iron and various trace elements in rats”, 14th Ann. Meet. of the Japan Soc. for Biomedical Research on Trace Elements (JSBRTE2003), Osaka, July (2003).
- S. Enomoto, H. Haba, R. Hirunuma, K. Igarashi, A. Nakayama, and S. Motomura: “Evolution of RI production technology for bio-trace elemental research using RIKEN accelerator research facility”, 14th Ann. Meet. of the Japan Soc. for Biomedical Research on Trace Elements (JSBRTE2003), Osaka, July (2003).
- Y. Kanayama, T. Yanagida, S. Toyoda, R. Amano, and S. Enomoto: “Olfactory transport of Cs-137 by intranasal administration”, 14th Ann. Meet. of the Japan Soc. for Biomedical Research on Trace Elements (JSBRTE2003), Osaka, July (2003).
- M. Honma, W. Wang, M. Sakuraba, S. Tadokoro, M. Hayashi, M. Izumi, F. Hanaoka, and F. Yatagai: “Repair of DNA double strand breaks in human cells induced by restriction enzyme I-SceI”, 12th Int. Congr. of Radiation Research (ICRR 2003), (International Association for Radiation Research), Brisbane, Australia, Aug. (2003).
- M. Tomita, F. Yatagai, Y. Matsumoto, N. Suzuki, and Y. Hosoi: “Visualization of DNA clustered damage induced by heavy ion exposure”, 12th Int. Congr. of Radiation Research (ICRR 2003), (International Association for Radiation Research), Brisbane, Australia, Aug. (2003).
- Y. Matsumoto, Y. Hosoi, N. Suzuki, and M. Tomita: “XRCC4: a candidate for *in vivo* substrate of DNA-PK”, 12th Int. Congr. of Radiation Research (ICRR 2003), (International Association for Radiation Research), Brisbane, Australia, Aug. (2003).
- T. Abe, Y. Miyazawa, K. Sekino, J. Wang, and S. Yoshida: “Heavy-ion beam mutagenesis for herbicide resistant plants”, 30th Ann. Conf. on Plant Growth Regulation Soc. of America held jointly with The Japanese Soc. for Chemical Regulation Plants, Vancouver, Canada, Aug. (2003).



- M. Tomita, Y. Matsumoto, Y. Hosoi, and N. Suzuki: "Heavy-ion-induced DNA damages and its repair", Dai4kai Monbukagakusho Tokuteiryokikenkyu Gan bryoiki Wakate Workshop, Chino, Aug. (2003).
- Y. Hara, T. Kitaura, T. Abe, K. Sakamoto, Y. Miyazawa, and S. Yoshida: "Breeding of flower organ mutant by heavy-ion beam radiation to buds of rose", 104th Ann. Congr. of the Breeding Soc. of Japan, Kobe, Sept. (2003).
- K. Suzuki, T. Takeuchi, Y. Takatsu, Y. Miyazawa, H. Saito, T. Abe, and M. Kasumi: "Mutation breeding of spray-type Chrysanthemum I. Analysis on the shoot regeneration ability from the irradiated stem segments", 104th Ann. Congr. of the Breeding Soc. of Japan, Kobe, Sept. (2003).
- T. Abe: "Mutation breeding use in heavy-ion beam irradiation", 45th Symp. in 104th Congr. of the Breeding Soc. of Japan, Kobe, Sept. (2003).
- H. Yin, Y. Suzuki, Y. Matsumoto, M. Tomita, Y. Furusawa, A. Enomoto, A. Morita, M. Aoki, F. Yatagai, and Y. Hosoi: "Hyperthermic radiosensitization of chicken B lymphocyte DT40 and its derivatives lacking NHEJ and/or HR pathways of DNA DSB repair", 46th Ann. Meet. of the Japan Radiation Research Soc., Kyoto, Oct. (2003).
- M. Tomita, Y. Matsumoto, A. Naruto, Y. Hosoi, N. Suzuki, and F. Yatagai: "Role of DNA-dependent protein kinase in initial recognition of DNA double-strand breaks", 46th Ann. Meet. of the Japan Radiation Research Soc., Kyoto, Oct. (2003).
- Y. Kobayashi, T. Okada, H. Haba, S. Jimbo, T. Taniguchi, Y. Noro, and Y. Nagata: "99Ru Mössbauer spectroscopy of CaRuO<sub>3</sub>", The 5th Ann. Meet./The 47th Symp. on Radiochemistry, (The Japan Society of Nuclear and Radiochemical Sciences), Izumisano, Oct. (2003).
- K. Washiyama, Y. Kanayama, S. Kinuya, H. Haba, S. Enomoto, and R. Amano: "An application of bismuth isotopes for nuclear medicine", The 5th Ann. Meet./The 47th Symp. on Radiochemistry, (The Japan Society of Nuclear and Radiochemical Sciences), Izumisano, Oct. (2003).
- K. Kubo, Y. Kobayashi, T. Saito, Y. Yamada, Y. Sakai, H. Shoji, C. Yonezawa, H. Matsue, W. Sato, and M. Nakada: "Development of neutron in-beam Mössbauer spectroscopy", The 5th Ann. Meet./The 47th Symp. on Radiochemistry, (The Japan Society of Nuclear and Radiochemical Sciences), Izumisano, Oct. (2003).
- S. Enomoto, R. Hirunuma, H. Haba, K. Igarashi, and Y. Yano: "Evolution of the multitracer production technology on the RI beam factory project", The 5th Ann. Meet./The 47th Symp. on Radiochemistry, (The Japan Society of Nuclear and Radiochemical Sciences), Izumisano, Oct. (2003).
- Y. Kanayama, T. Yanagida, R. Amano, and S. Enomoto: "Olfactory transport of alkaline metal ions by intranasal administration (1): Direct brain uptake of 86Rb<sup>+</sup> and 137Cs<sup>+</sup>", The 5th Ann. Meet./The 47th Symp. on Radiochemistry, (The Japan Society of Nuclear and Radiochemical Sciences), Izumisano, Oct. (2003).
- T. Ohyama, K. Watanabe, N. Kinugawa, M. Yanaga, M. Noguchi, H. Suganuma, K. Ishikawa, R. Hirunuma, K. Takahashi, and S. Enomoto: "Searching for the metal binding factor responsible for a variation of concentration of trace elements under the Zn-deficient condition", The 5th Ann. Meet./The 47th Symp. on Radiochemistry, (The Japan Society of Nuclear and Radiochemical Sciences), Izumisano, Oct. (2003).
- W. Sato, H. Ueno, H. Watanabe, H. Miyoshi, A. Yoshimi, D. Kameda, J. Kaihara, K. Shimada, T. Ito, S. Suda, Y. Kobayashi, K. Asahi, and A. Shinohara: "c-Axis orientation dependence of TDPAC for a single-crystalline sample", The 5th Ann. Meet./The 47th Symp. on Radiochemistry, (The Japan Society of Nuclear and Radiochemical Sciences), Izumisano, Oct. (2003).
- T. Abe: "Mutation breeding with using ion beam irradiation", 7th Workshop on HPPA Development and Utilisation, (Korea Atomic Energy Research Institute), Daejeon, Korea, Oct. (2003).
- T. Matsuyama, H. Saito, T. Abe, S. Yoshida, K. Koike, and T. Ebisuzaki: "Arabidopsis genome analysis by the pattern matching system of virtual RLGS.", 12th DNA polymorphism, Tokyo, Nov. (2003).
- T. Abe, Y. Miyazawa, H. Saito, S. Yoshida, N. Fukunishi, H. Ryuto, and Y. Yano: "Utilization of heavy ion beams as a mutagen in plants", 14th Symp. on Accelerator Science and Technology (SAST03), (KEK), Tsukuba, Nov. (2003).
- M. Saito, H. Komori, H. Sakamoto, M. Hatashita, K. Takagi, T. Abe, and S. Yoshida: "Mutation breeding using ion beams", 2nd 21Seiki Rengou Symp.: Kagakugijutsu to Ningen, Tokyo, Nov. (2003).
- T. Abe, Y. Miyazawa, H. Saito, Y. Yamamoto, H. Ryuto, and N. Fukunishi: "Mutation breeding using ion beam irradiation", 2nd Workshop on Application for Ion Beam Biology, (JAERI), Takasaki, Nov. (2003).
- Y. Kobayashi, T. Okada, H. Haba, T. Taniguchi, Y. Nagata, and Y. Noro: "99Ru Mössbauer spectroscopy of CaRuO<sub>3</sub>", Special Research Meet. on New Developments in Solid State Physics with Probes of Radiation and Nuclei, (Research Reactor Institute, Kyoto University), Kumatori-cho, Osaka Pref., Nov. (2003).
- T. Matsuyama, T. Ebisuzaki, K. Koike, H. Ichida, H. Saito, T. Abe, and S. Yoshida: "Construction of the virtual RLGS system in Arabidopsis genome analysis", 26th Ann. Meet. of the Molecular Biology Soc. of Japan, Kobe, Dec. (2003).
- M. Tomita, Y. Matsumoto, A. Naruto, N. Suzuki, Y.

- Hosoi, and F. Yatagai: “Imaging analysis of heavy-ion-induced DNA damages”, 26th Ann. Meet. of the Molecular Biology Soc. of Japan, Kobe, Dec. (2003).
- Y. Kobayashi: “Magnetism of CaRuO<sub>3</sub> by means of 99Ru Mössbauer spectroscopy”, RIKEN Symp. on Studies on Condensed Matter Physics, Atomic Physics, Nuclear Chemistry, and Biology and Medicine Using RIKEN Accelerators, Wako, Jan. (2004).

## 5. Material Analysis

- A. Saeki, S. Seki, T. Sunagawa, K. Ushida, Y. Koizumi, T. Kozawa, and S. Tagawa: “Development of microwave absorption measurement for single molecular conductivity implemented for studies of nanotechnology using accelerators”, 28th Linear Accelerator Meet. in Japan (LAM28), (JAERI), Tokaimura, July (2003).
- H. Hamanaka, K. Maeda, K. Hasegawa, M. Tsuji, and S. Murao: “Chemical state analysis of Al in mica using a crystal spectrometer for PIXE”, 20th PIXE Symp., (The Japan Society for Particle Induced X-ray Emission (PIXE) Research), Kouchi, Sept. (2003).
- K. Mochiki, K. Okada, T. Matsuhisa, T. Toriyama, K. Kawasaki, K. Saneyoshi, K. Maeda, and K. Hasegawa: “Development of an X-ray detection system for WDX-PIXE using a two-dimensional CCD”, 20th PIXE Symp., (The Japan Society for Particle Induced X-ray Emission (PIXE) Research), Kouchi, Sept. (2003).
- K. Maeda, K. Hasegawa, M. Maeda, and H. Hamanaka: “Extension of the feasibility of a PIXE system using position-sensitive crystal spectrometers”, 20th PIXE Symp., (The Japan Society for Particle Induced X-ray Emission (PIXE) Research), Kouchi, Sept. (2003).
- A. Saeki, Y. Koizumi, S. Seki, T. Kozawa, S. Tagawa, T. Sunagawa, and K. Ushida: “Development of time-resolved microwave conductivity and light absorption spectroscopy and its application”, 46th Symp. on Radiation Chemistry, (Japanese Society of Radiation Chemistry), Hakone, Sept. (2003).
- H. Hamanaka, K. Maeda, and K. Hasegawa: “Improvement of the precision in PIXE measurement using a crystal spectrometer”, 22nd Symp. on Materials Science and Engineering Research Center of Ion Beam Technology, Hosei University, Koganei, Dec. (2003).
- ## 6. RIKEN-BNL Collaboration
- J. Schaffner-Bielich: “The role of strangeness in astrophysics”, Conf. of Strange Quarks in Matter (SQM2001), (The University of Frankfurt), Frankfurt, Germany, Sept. (2001).
- K. Originos: “Flavor singlet nucleon axial charge with domain wall fermions”, 1st Joint Meet. of the Nuclear Physicists of the American and Japanese Physical Soc. (HAW01), (APS and JPS), Maui, USA, Oct. (2001).
- H. Abuki, T. Hatsuda, and K. Itakura: “Momentum dependent gap in two flavor color superconductivity”, 1st Joint Meet. of the Nuclear Physicists of the American and Japanese Physical Soc. (HAW01), (APS and JPS), Maui, USA, Oct. (2001).
- S. A. Bass: “Partonic reaction dynamics at RHIC”, 1st Joint Meet. of the Nuclear Physicists of the American and Japanese Physical Soc. (HAW01), (APS and JPS), Maui, USA, Oct. (2001).
- K. Itakura, E. Iancu, and L. McLerran: “Solution to the small- $x$  evolution equation and saturation”, 1st Joint Meet. of the Nuclear Physicists of the American and Japanese Physical Soc. (HAW01), (APS and JPS), Maui, USA, Oct. (2001).
- Y. Goto: “First polarized proton collisions at PHENIX”, 10th Int. Workshop on Deep Inelastic Scattering (DIS2002), (Institute of Nuclear Physics, Krakow), Krakow, Poland, Apr.–May (2002).
- O. Jinnouchi, K. Kurita, N. Saito, J. Tojo, H. Enyo, K. Imai, I. G. Alekseev, A. Bravar, G. Bunce, R. Cadman, A. Deshpande, S. Dhawan, D. E. Fields, H. Huang, V. Hughes, G. Igo, V. P. Kanavets, J. Kiryluk, Z. Li, W. Lozowski, W. W. MacKay, Y. Makdisi, S. Rescia, T. Roser, H. Spinka, B. Surrow, D. N. Svirida, D. Underwood, and J. Wood: “RHIC pC CNI polarimeter: status and performance from the first collider run”, Advanced Study Institute: Symmetries and Spin, Praha-SPIN-2002, (Charles University), Praha, Czech, July (2002).
- Y. Nagashima, F. Saito, Y. Ito, A. Goto, and T. Hyodo: “Measurement of bremsstrahlung X ray by positron impact”, 39th Ann. Meet. on Radioisotopes and Radiation in the Physical Sciences and Industries, (Japan Radio Isotope Association), Tokyo, July (2002).
- Y. Goto: “Neutral pion measurements in polarized proton collisions from PHENIX at RHIC”, 16th Int. Conf. on Particles and Nuclei (PaNic02), (RCNP, Osaka University), Osaka, Sept.–Oct. (2002).
- H. Enyo: “Physics with RHIC spin collider”, 16th Int. Conf. on Particles and Nuclei (PaNic02), (RCNP, Osaka University), Osaka, Sept.–Oct. (2002).
- K. Hasuko, M. Grosse-Perdekamp, A. Ogawa, J. S. Lange, and V. Siegle: “Azimuthal asymmetries in fragmentation processes at KEKB”, 15th Int. Spin Physics Symp. (SPIN 2002), Long Island, USA, Sept. (2002).
- Y. Goto: “Prospects of the gluon polarization measurement at PHENIX”, 15th Int. Spin Physics Symp. (SPIN 2002), Long Island, USA, Sept. (2002).
- K. Okada and PHENIX Collaboration: “Single-spin transverse asymmetry in charged hadron production in  $\sqrt{s} = 200$  GeV p+p collisions at PHENIX”, 15th

- Int. Spin Physics Symp. (SPIN 2002), Long Island, USA, Sept. (2002).
- K. Okada and PHENIX Collaboration: “Performance of the new EMC-RICH Level-1-Trigger in PHENIX”, 2002 Fall Meet. of the Division of Nuclear Physics of the American Physical Soc., East Lansing, USA, Oct. (2002).
- N. Ishii: “Recent topics in lattice hadron physics”, Asia-Pacific Mini-Workshop on Lattice QCD, (Center for Computational Physics, University of Tsukuba), Tsukuba, Jan. (2003).
- N. Ishii, H. Matsufuru, and H. Suganuma: “Thermal glueballs at nonzero temperature from SU(3) anisotropic lattice QCD”, Tokyo-Adelaide Joint Workshop on Quarks, Astrophysics and Space Physics, (University of Tokyo), Tokyo, Jan. (2003).
- N. Ishii, H. Matsufuru, and H. Suganuma: “Thermal width of glueball at non-zero temperature”, U.S.-Japan Joint Workshop on Nuclear Chiral Dynamics, (Japan Society for the Promotion of Science and U.S. National Science Foundation), Honolulu, USA, Feb. (2003).
- K. Tanida: “Measurement of single transverse-spin asymmetry of inclusive charged particles by PHENIX BBC in polarized pp collision at  $\sqrt{s} = 200$  GeV”, 58th Ann. Meet. of Physical Soc. of Japan, Sendai, Mar. (2003).
- K. Sudo: “Nucleon spin structure in neutrino deep inelastic scattering”, The 26th Shikoku-Seminar, (Yukawa Institute for Theoretical Physics), Takamatsu, Apr. (2003).
- Y. Akiba: “Silicon vertex tracker upgrade of PHENIX experiment at RHIC”, 8th Conf. on the Intersections of Particle and Nuclear Physics (CIPANP 2003), New York, USA, May (2003).
- Y. Akiba and H. Suganuma: “Experimental results from RHIC”, Int. Conf. on Color Confinement and Hadrons in Quantum Chromodynamics: Confinement 2003, (Tokyo Institute of Technology and RIKEN), Wako, July (2003).
- M. Hirai: “ $\Delta g(x)$  uncertainty from prompt photon production”, 4th Circum-Pan-Pacific Symp. on High Energy Spin Physics (SPIN 2003), Seattle, USA, Aug. (2003).
- K. Sudo: “Single Spin Asymmetry in Inclusive D Meson Production at RHIC”, 4th Circum-Pan-Pacific Symp. on High Energy Spin Physics (SPIN 2003), Seattle, USA, Aug. (2003).
- T. Hirano: “Hydrodynamic model and hard probe”, 2003 Fall Meet. of the Physical Soc. of Japan, Miyazaki and Okayama, Sept. (2003).
- K. Sudo: “Single spin asymmetry in inclusive D meson production at RHIC”, 2003 Fall Meet. of the Physical Soc. of Japan, Miyazaki and Okayama, Sept. (2003).
- M. Ohtani: “Vortex excitation in color ferromagnetic phase”, 2003 Fall Meet. of the Physical Soc. of Japan, Miyazaki and Okayama, Sept. (2003).
- K. Tanida: “PHENIX upgrade”, VERTEX 2003: 12th Int. Workshop on Vertex Detection, (Brunel University), Windermere, UK, Sept. (2003).
- A. Kiyomichi and PHENIX Collaboration: “Radial flow study from identified hadrons spectra in Au + Au collisions at  $\sqrt{s_{NN}} = 200$  GeV”, 2003 Fall Meet. of the Division of Nuclear Physics of the American Physical Soc., Tucson, USA, Oct. (2003).
- J. Tojo, K. Aoki, H. Enyo, Y. Fukao, Y. Goto, J. Heuser, Z. Li, H. Onishi, H. Okada, V. Radeka, V. Rykov, N. Saito, F. Sakuma, M. Sekimoto, K. Tanida, M. Togawa, and Y. Watanabe: “Development of a novel silicon strip detector for PHIC-PHENIX detector upgrade”, IEEE Nuclear Science Symp. (NSS) and Medical Imaging Conf. (MIC), Portland, USA, Oct. (2003).
- Y. Akiba: “What we have learned from RHIC”, New Direction of Particle Physics (TEA03), (Yukawa Institute for Theoretical Physics, Kyoto University), Kyoto, Oct. (2003).
- T. Ikeda and Y. Hatta: “Quark number susceptibility at the critical end point”, 17th Int. Conf. on Ultra-Relativistic Nucleus-Nucleus Collisions (Quark Matter 2004), (Lawrence Berkeley National Laboratory), Oakland, USA, Jan. (2004).
- A. Kiyomichi and PHENIX Collaboration: “Radial flow study from identified hadron spectra in Au + Au collisions at  $\sqrt{s_{NN}} = 200$  GeV”, 17th Int. Conf. on Ultra-Relativistic Nucleus-Nucleus Collisions (Quark Matter 2004), Oakland, USA, Jan. (2004).
- T. Ikeda: “Memory effects in kinetic equation”, 59th Ann. Meet. of Physical Soc. of Japan, Fukuoka, Mar. (2004).

## IX. LIST OF SYMPOSIA

(Jan.–Dec. 2003)

- 1) Int. Workshop on Extreme Optics and Sensors  
14–17 Jan., Tokyo, Image Information Div. and Materials Fabrication Lab., RIKEN and MEXT
- 2) The Continuum States in the Few-body Systems and the Unstable Nuclei and Their Prospects  
20–22 Feb., Wako, RI Beam Science Lab., RIKEN and CNS
- 3) Nuclear Physics at RI Beam Factory  
4–5 Mar., Wako, Heavy Ion Nuclear Physics Lab., RIKEN
- 4) Workshop on Molecular Structure in the Region of Light Neutron-rich Nuclei to Medium Heavy Nuclei  
13–15 Mar., Wako, RI Beam Science Lab., RIKEN
- 5) Workshop on Strategy of Nuclear Astrophysics Research  
13–14 Mar., Wako, Heavy Ion Nuclear Physics Lab., RIKEN and National Astronomical Observatory, Japan
- 6) 4th RIKEN School on QCD “Topics on the Proton”  
26 Mar., Wako, Radiation Lab., RIKEN
- 7) Workshop on Slow RI-Beams and Related Topics  
16 May, Wako, Atomic Physics Lab., RIKEN
- 8) Int. Workshop on Beam Cooling and Related Topics (COOL03)  
19–23 May, Yamanakako, Beam Physics and Engineering Lab., RIKEN and CNS
- 9) New Development in Radiation Biology: Molecular Imaging of the Process of DNA Damage Induction and Its Repair  
26–27 June, Wako, Radioisotope Technology Div., RIKEN and Young Radiation Biologists’ Association in Japan
- 10) Int. Symp. on Color Confinement and Hadrons in Quantum Chromodynamics  
21–24 July, Wako, Radiation Lab., RIKEN and Tokyo Institute of Technology
- 11) Advanced Signal Processing in Nuclear Physics  
28 July, Wako, Heavy Ion Nuclear Physics Lab., RIKEN
- 12) RIKEN Cluster Project Workshop on Cluster Structure and Nuclear Force  
27–29 Aug., Wako, RI Beam Science Lab., RIKEN
- 13) Spectroscopy of Unstable Nuclei and Reaction Mechanism  
31 Oct.–1 Nov., Wako, Heavy Ion Nuclear Physics Lab., RIKEN
- 14) Collective Flow and QGP Properties  
17–19 Nov., New York, USA, RBRC, RIKEN
- 15) Origin of Matter and Evolution of the Galaxies (OMEG03)  
17–19 Nov., Wako, Heavy Ion Nuclear Physics Lab., RIKEN
- 16) Int. Conf. on Clustering Aspects of Nuclear Structure and Dynamics  
24–29 Nov., Nara, RI Beam Science Lab., RIKEN and University of Tokyo
- 17) High-pT Physics at RHIC  
2–6 Dec., New York, USA, RBRC, RIKEN

- 18) Experimental Apparatuses Being Constructed at RIBF  
26 Dec., Wako, RI Beam Science Lab., RIKEN

## X. LIST OF SEMINARS

(Jan.–Dec. 2003)

### RIKEN Nuclear-Physics Seminar

- 1) N. Dinh DANG, RIKEN (Wako), 18 Feb.  
“Modified Hartree-Fock-Bogoliubov theory”
- 2) W. J. Swiatecki, LBNL (USA), 18 Mar.  
“The physics of nucleus-nucleus fusion”
- 3) M. Takashina, RIKEN (Wako), 23 Apr.  
“ $^{11}\text{Be} \rightarrow ^{10}\text{Be} + n$  breakup effect on  $^{11}\text{Be}$  elastic scattering”
- 4) C. H. Fransen, Cologne University (Germany), 14 May  
“Nuclear multiphonon structures with mixed proton-neutron symmetry”
- 5) I. Hamamoto, University of Lund (Sweden)/NBI (Denmark), 24 July  
“Shell-structure and pair-correlation in nuclei close to the neutron drip line”
- 6) M. K. Gaidarov, Institute of Nuclear Research and Nuclear Energy (Bulgaria)/Kyushu University (Fukukoka), 6 Aug.  
“Nucleon-nucleon correlations and one-nucleon removal and inclusive proton-induced reactions”
- 7) H. Witala, Jagellonian University (Poland), 8 Aug.  
“Testing nuclear Hamiltonian with  $3N$  hadronic and electromagnetic processes”
- 8) Y. M. Zhao, Southeast University (China), 30 Oct.  
“Searching for the origin of spin zero ground states of atomic nuclei”
- 9) M. Pfutzner, Warszawa University (Poland), 2 Dec.  
“The discovery of the two-proton radioactivity”
- 10) Y. Abe, YITP, Kyoto University (Kyoto), 12 Dec.  
“Theoretical predictions of excitation functions for SHE”
- 11) T. R. Saitoh, GSI (Germany), 22 Dec.  
“Results from the RISING fast beam projects at GSI”
- 12) A. Gelberg, Institut für Kernphysik der Universität zu Köln (Germany), 22 Dec.  
“Gamow-Teller decay of the  $T = 1$  nucleus  $^{46}\text{Cr}$ ”

### Radiation Lab.

- 1) H. Abuki, University of Tokyo (Tokyo), 28 Jan.  
“Color superconductivity in Schwinger-Dyson approach”
- 2) T. Doi, Tokyo Institute of Technology (Tokyo), 4 Feb.  
“The quark-gluon mixed condensate  $g\langle\bar{q}\sigma Gq\rangle$  in lattice QCD”
- 3) H. Yokoya, Hiroshima University (Higashi Hiroshima), 7 Mar.  
“Lepton helicity distributions in polarized Drell-Yan process”
- 4) H. Matsufuru, Kyoto University (Kyoto), 11 Mar.  
“Towards precise lattice QCD computations for flavor physics: Heavy quark on anisotropic lattice”
- 5) Y. Aoki, RBRC (USA), 15 Apr.  
“Analyzing QCD with domain-wall fermions and an improved gauge field on the lattice”
- 6) L. Frankfurt, Tel Aviv University (Israel), 30 Apr.  
“Color transparency and color opacity phenomena”
- 7) Y. Hatta, Kyoto University (Kyoto), 30 Apr.  
“The QCD critical end-point”
- 8) L. Frankfurt, Tel Aviv University (Israel), 2 May  
“Color fluctuations in lepton, hadron and nuclear collisions”
- 9) J. Nagashima, Niigata University (Niigata), 20 May  
“Double spin asymmetries in large  $p_T$  hadron production in semi-inclusive DIS”
- 10) Y. Koike, Niigata University (Niigata), 20 May  
“Single spin asymmetries in pp and ep collisions”
- 11) K. Itakura, RBRC (USA), 27 May  
“Recent progress in the small  $x$  saturation physics”
- 12) H. Sato, KEK (Tsukuba), 27 May  
“Polarized beam acceleration in the J-PARC accelerator complex”
- 13) H. Kawamura, KEK (Tsukuba), 1 July  
“B meson wave functions in the heavy quark limit”

- 14) K. Hasuko, RIKEN (Wako), 1 July  
“Recent topics from Belle experiment”
- 15) Y. Nemoto, RBRC (USA), 4 Aug.  
“Pion electromagnetic form-factor with domain wall fermions”
- 16) C. Sasaki, Nagoya University (Nagoya), 17 Oct.  
“Vector manifestation of chiral symmetry: A new pattern for Wigner realization (with a short review on local gauge symmetry)”
- 17) D. Drechsel, Universität Mainz (Germany), 5 Nov.  
“The Gerasimov-Drell-Hearn sum rule and the nucleon spin structure in the resonance region”
- 18) G. Schnell, Tokyo Institute of Technology (Tokyo), 5 Nov.  
“Measurements of generalized Gerasimov-Drell-Hearn integral by HERMES”
- 19) O. Jinnouchi, RBRC (USA), 14 Nov.  
“Polarized p-C elastic scattering in CNI region, polarimetry at RHIC and AGS”
- 20) A. Taketani, RIKEN/RBRC (Wako/USA), 14 Nov.  
“Measurements of asymmetries in polarized proton-proton collisions at RHIC”
- 21) A. W. Thomas, Adelaide University (Australia), 9 Dec.  
“Recent results in neutrino physics without oscillations”
- 22) L. Frankfurt, Tel Aviv University (Israel), 16 Dec.  
“Ultra-peripheral collisions at LHC and RHIC”

#### RI Beam Science Lab.

- 1) Y. Motizuki, RIKEN (Wako), 11 Apr.  
“How to make a good presentation in an international conference”
- 2) H. Sakaguchi, Kyoto University (Kyoto), 28 May  
“Medium effects and density distributions in the intermediate energy proton elastic scattering”
- 3) S. Terashima, Kyoto University (Kyoto), 28 May  
“Neutron density distributions in Sn isotopes deduced from the proton elastic scattering at 295 MeV”
- 4) R. Diehl, Max-Planck-Institut fuer Extraterrestrische (Germany), 29 Nov.  
“Nuclear gamma-ray astronomy with

#### INTEGRAL”

#### Applied Nuclear Physics Lab.

- 1) Y. Hasegawa, Atominstytut der Oesterreichischen Universitaeten (Austria), 17 Jan.  
“Experimental test of Bell’s inequality with neutrons”

#### Atomic Physics Lab.

- 1) T. Morishita, University of Electro-Communications (Chofu), 29 Jan.  
“Double ionization of He with fast proton and antiproton impacts: Theoretical treatment of ss configuration with the hyperspherical coordinates method”
- 2) M. Fujiwara, RIKEN (Wako), 4 Apr.  
“Production and detection of cold antihydrogen atoms”
- 3) V. Varentsov, Radium Institute, St. Petersburg (Russia), 13 May  
“New techniques for buffer gas cooling and guiding of RI-beams”
- 4) V. Korobov, JINR, Dubna (Russia), 23 May  
“Antiprotonic helium, overview: Recent results and future problems”
- 5) J. Ullrich, Max Planck Institute fur Kernphysik (Germany), 19 June  
Atoms in intense laser fields
- 6) S. Kishimoto, KEK (Tsukuba), 3 Oct.  
“Observation of NEET by synchrotron x-rays”
- 7) J. Sternberg, University Tennessee (USA), 7 Nov.  
“Simple method for calculating three-body recombination rates in cold atoms: An adiabatic hyperspherical approach”
- 8) T. Gustafsson, State University of New Jersey (USA), 10 Nov.  
“Ion scattering studies of high dielectric constant materials”
- 9) L. Pichl, University of Aizu (Aizuwakamatsu), 25 Nov.  
“Predissociation rates for  $^1\Sigma^+$  and  $^3\Pi$  states AgH molecule”
- 10) M. Inokuti, Argonne National Laboratory (USA), 12 Dec.  
“The charm of radiation research”

## Beam Physics and Engineering Lab.

- 1) M. Tamba, RIKEN (Wako), 18 Mar.  
“Three dimensional ion implantation and production of DLC materials”
- 2) R. Jameson, LANL (USA), 25 Apr.  
“RFQ design for laser ion source (LIS) 100 mA C<sup>4+</sup> beam”
- 3) I. Meshkov, JINR (Russia), 9 May  
“Electron cooling studies and applications at Joint Institute for Nuclear Research”
- 4) M. Imanaka, CNS, University of Tokyo (Tokyo), 11 July  
“Effect of magnetic field configuration on the plasma of liquid-He-free superconducting ECR ion source”
- 5) T. Kikuchi, CNS, University of Tokyo (Tokyo), 7 Aug.  
“Final beam bunching for heavy ion inertial fusion”
- 6) K. Yamamoto, Tokyo Institute of Technology (Tokyo), 11 Sept.  
“Study of 2 MeV/u APF-IH linac”
- 7) S. M. Lund, LLNL/LBNL (USA), 10 Dec.  
“Bunch compression of intense heavy ion beam in rings”

## RIBF Project Office, Beam Dynamics Div., and Beam Tecnology Div.

- 1) G. Shirkov, JINR, Dubna (Russia), 19 June  
“Particle in cells simulations for ion source and accelerator”
- 2) G. Moritz, GSI (Germany), 17 Oct.  
“Superconducting magnets for the new facility for the rings of ions and antiprotons”

## Radioisotope Technology Div.

- 1) S. Kojima, RIKEN (Wako), 29 May  
“Molecular mechanisms of various disease: Molecular pathology of atherosclerosis, angiogenesis, and liver diseases using bioprobes”
- 2) A. Nakayama, RIKEN (Wako), 29 May  
“Molecular mechanisms of various disease: Investigation of development mechanism and new diagnostic method for chronic hepatic disorders based on bio-trace elements and metallothionein”
- 3) S. Motomura, RIKEN (Wako), 29 May

“Development and application of Compton camera: Development of multi-nuclide  $\gamma$ -ray emission imaging system”

- 4) H. Takeichi, RIKEN (Wako), 29 May  
“Development and application of Compton camera: Contemporary trends and prospects in brain research using PET and GREI”
- 5) T. Suzuki, Meiji Pharmaceutical University (Kiyose), 26 June  
“Study of detoxification mechanism to metals in cisplatin resistant cell line”
- 6) T. Ishii, National Institute of Radiological Sciences (Hitachinaka), 9 Oct.  
“In vivo chemical speciation of elements hyperaccumulated by marine organisms”

## RIKEN BNL Research Center

- 1) Z. Xu, BNL (USA), 7 Jan.  
“Characteristics of average transverse momentum in heavy ion collisions”
- 2) P. Kolb, Stony Brook University (USA), 17 Jan.  
“Spectroscopy of resonance decays in RHIC experiments”
- 3) S. Nussinov, Tel Aviv University (Israel), 22 Jan.  
“Physicist’s approach to complex problems”
- 4) Y. Nara, University of Arizona (USA), 24 Jan.  
“Energy loss and back-to-back correlations from hydro + jet model”
- 5) T. Blum, RBRC (USA), 30 Jan.  
“Lattice calculation of the lowest order hadronic contribution to the muon anomalous magnetic moment”
- 6) A. Accardi, Columbia University (USA), 4 Feb.  
“Is the color glass condensate just glauber shadowing?”
- 7) J. M. Resco, Ohio State University (USA), 5 Feb.  
“The electrical conductivity in hot QED”
- 8) P. Petreczky, BNL (USA), 7 Feb.  
“Lattice calculation of the properties of hot strongly interacting matter”
- 9) R. Fries, Duke University (USA), 11 Feb.  
“Hadronization in heavy ion collisions”
- 10) C. Rebbi, Boston University (USA), 12 Feb.  
“Semiclassical methods for the description of tun-



- neling in high-energy collisions”
- 11) H. Kowalski, DESY (Germany), 13 Feb.  
“An impact parameter saturation model”
  - 12) S. Weinstock, BNL (USA), 14 Feb.  
“Transport equations for electroweak baryogenesis”
  - 13) J. Ruppert, University of Frankfurt (Germany), 18 Feb.  
“Chiral symmetry restoration in linear sigma models with different numbers of quark flavors”
  - 14) H. Neuberger, Rutgers University (Germany), 19 Feb.  
“Large N reduction revisited”
  - 15) J. Manjavidze, JINR, Dubna (Russia), 21 Feb.  
“Thermalization effect in hadron collisions”
  - 16) K. Holland, UC San Diego (USA), 5 Mar.  
“Lattice QCD with fixed point fermions”
  - 17) D. Zschiesche, University of Frankfurt (Germany), 11 Mar.  
“Particle ratios from AGS to RHIC in an interacting hadronic model”
  - 18) T. Baltz, BNL/RBRC (USA), 13 Mar.  
“Coulomb corrections to electron positron pairs in heavy-ion reactions”
  - 19) I. Chiu, Columbia University (USA), 18 Mar.  
“Results from photon-hadron correlations in PHENIX”
  - 20) D. Diakonov, NORDITA (Denmark), 19 Mar.  
“Dyons in supersymmetric and ordinary Yang-Mills theory”
  - 21) E. Iancu, SPhT, Saclay (France), 20 Mar.  
“Deep inelastic scattering off the CGC: Geometric scaling, froissart bound, and all that”
  - 22) B. Kopeliovich, Regensburg University (Germany), 21 Mar.  
“High- $p_T$  hadrons at RHIC: energy loss or absorption?”
  - 23) D. Nomura, Durham University (UK), 26 Mar.  
“The sm prediction of  $g-2$  of the muon”
  - 24) A. Dumitru, University of Frankfurt (Germany), 27 Mar.  
“Polarized hyperons from pA collisions in the saturation regime”
  - 25) B. L. Ioffe, ITEP (Russia), 1 Apr.  
“Theoretical calculation of valence quark distributions in hadrons at low energy”
  - 26) G. Moore, University of Montreal (Canada), 2 Apr.  
“Transport and equilibration in ultrarelativistic plasmas”
  - 27) S. Jeon, McGill University (USA), 3 Apr.  
“Eta-prime mesons from gluon fusion”
  - 28) F. Zantow, University Bielefeld (Germany), 4 Apr.  
“Static quark-antiquark free energy and the renormalized Polyakov loop”
  - 29) F. Karsch, University Bielefeld (Germany), 8 Apr.  
“QCD thermodynamics at non-zero baryon density”
  - 30) D. Rainwater, DESY (Germany), 9 Apr.  
“LHC Higgs news: the good, the bad, and the maybe”
  - 31) B. Ioffe, ITEP (Russia), 10 Apr.  
“Formation of antideuterons in heavy ion collisions”
  - 32) M. Nardi, Turin University/INFN (Italy), 11 Apr.  
“Saturation effects in nuclear collisions”
  - 33) D. Molnar, Ohio State University (USA), 15 Apr.  
“Possible solution to the RHIC elliptic flow puzzle”
  - 34) I. Shovkovy, University of Frankfurt (Germany), 16 Apr.  
“Color superconductivity and compact stars”
  - 35) F. Gelis, SPhT, Saclay (France), 17 Apr.  
“pA collisions in the color glass condensate model”
  - 36) S. Klein, LBNL (USA), 18 Apr.  
“Vector meson interferometry and the EPR paradox with STAR”
  - 37) W. Soeldner, Regensburg University (Germany), 29 Apr.  
“Chiral symmetry restoration and the  $Z_3$  sectors of QCD”
  - 38) J. Bagger, Johns Hopkins University (USA), 8 May  
“TeV scale physics at a linear collider”

- 39) T. Hirano, RBRC (USA), 9 May  
“Dynamical parton energy loss in relativistic heavy ion collisions”
- 40) K. Itakura, RBRC (USA), 15 May  
“Gaussian effective theory at small  $x$  and its application to deep inelastic scattering”
- 41) N. Nikolaev, Juelich (Germany), 23 May  
“Nonlinear  $k_{\text{perp}}$  factorization for dijets and nuclear saturation: from DIS to nuclear collisions at RHIC”
- 42) A. Vourinen, Helsinki University (Finland), 28 May  
“The pressure of QCD at finite quark chemical potential”
- 43) I. Vitev, Iowa State University (USA), 29 May  
“D+Au and Au+Au reactions at RHIC: Manifestation of multiparton dynamics in dense nuclear matter”
- 44) H. Kowalski, BNL/Columbia University/DESY (USA/Germany), 5 June  
“An impact parameter dipole saturation model”
- 45) X. Wang, LBNL (USA), 19 June  
“Discovery of jet quenching and beyond”
- 46) R. Jaffe, MIT (USA), 11 July  
“On pentaquark states”
- 47) D. Teaney, BNL (USA), 17 July  
“Baryon number at small  $x$ ”
- 48) S. Bar-Shalom, Technion University (Israel), 30 July  
“Model independent analysis of Higgs Yukawa interactions *via* Higgs-heavy jet associated production”
- 49) S. Heinemeyer, University of Munich (Germany), 6 Aug.  
“New results for MSSM Higgs physics at the linear collider”
- 50) K. Splittorff, NBI (Denmark), 13 Aug.  
“Elitzur’s theorem and the sign problem”
- 51) J. Lenaghan, University of Virginia (USA), 14 Aug.  
“Instabilities in a non-equilibrium quark-gluon plasma”
- 52) T. Hatsuda, University of Tokyo (Japan), 15 Aug.  
“Lattice QCD study of hadrons in deconfined plasma”
- 53) M. Hayakawa, RIKEN/BNL (Wako/USA), 20 Aug.  
“Strong interaction effect on the muon’s  $g-2$  factor”
- 54) W. Roberts, Old Dominion University (USA), 21 Aug.  
“Aspects of pion photoproduction in the phenomenological lagrangian approach”
- 55) A. Stasto, DESY/Cracow (Germany/Poland), 22 Aug.  
“Solution of the Balitsky-Kovchegov equation at finite impact parameter”
- 56) J. Soffer, CPT Marseille (France), 28 Aug.  
“Implications of positivity for spin physics”
- 57) E. Leader, Imperial College London (UK), 3 Sept.  
“Can the polarization of the strange quark be positive? And why does it matter?”
- 58) T. Kucs, YITP, Stony Brook (USA), 18 Sept.  
“Beyond BFKL”
- 59) A. H. Hoang, “Max Plank Institute (Germany), 24 Sept.  
“NRQCD and top pair production at threshold”
- 60) M. Braun, St. Petersburg Nuclear Physics Institute (Russia), 26 Sept.  
“Nucleus-nucleus collisions in pQCD”
- 61) E. Shuryak, Stony Brook University (USA), 2 Oct.  
“Quark-gluon plasma at critical and supercritical coupling”
- 62) C. Gonzalez-Garcia, Stony Brook University (USA), 15 Oct.  
“Neutrino oscillations and the sunshine”
- 63) Y. Nemoto, RBRC (USA), 16 Oct.  
“Diquark fluctuations and pseudogap in color superconductivity”
- 64) E. Mottola, LANL (USA), 17 Oct.  
“Dark energy stars: How quantum mechanics can change classical black holes”
- 65) D. Marfatia, Boston University (USA), 22 Oct.  
“Physics of massive neutrinos”
- 66) A. Kusenko, UCLA/RBRC (USA), 23 Oct.  
“Pulsar velocities, neutrinos, and dark matter”

- 67) G. Kribs, IAS, Princeton (USA), 29 Oct.  
“Deforming supersymmetric technicolor”
- 68) A. Starinets, University of Washington, International (USA), 4 Nov.  
“String theory and kinetic coefficients of Yang-Mills plasma”
- 69) R. Mohapatra, Maryland University (USA), 5 Nov.  
“Neutrino mass, supersymmetry and grand unification”
- 70) Y. Hatta, Kyoto University/RBRC (Kyoto/USA), 6 Nov.  
“Linking the chiral and deconfinement phase transitions”
- 71) V. Guzey, Ruhr-University Bochum (Germany), 10 Nov.  
“Extraction of  $F_2^p - F_2^n$  at small x from deuteron collider data”
- 72) R. Kitano, IAS, Princeton (USA), 12 Nov.  
“Higgs mediated  $\mu$ -e conversion”
- 73) A. Mueller, Columbia University (USA), 13 Nov.  
“Fluctuations in high energy hard scattering in QCD”
- 74) R. Nouicer, BNL (USA), 14 Nov.
- 75) M. Golterman, S. F. State University (USA), 14 Nov.  
“On the phase diagram of quenched QCD with Wilson fermions”
- 76) A. Metz, Bochum University (Germany), 24 Nov.  
“Universality of T-odd fragmentation functions”
- 77) Y. Grossman, Technion/SLAC (Israel/USA), 3 Dec.  
“Sleptogenesis”
- 78) Y. Kuramashi, KEK (Japan), 4 Dec.  
“O(a) improvement for heavy quarks on the lattice”
- 79) Y. Nomura, UC Berkeley (USA), 10 Dec.  
“Grand unification in warped space”
- 80) D. Soper, University of Oregon (USA), 11 Dec.  
“Adding parton showers to NLO calculations”
- 81) K. Agashe, Johns Hopkins University (USA), 17 Dec.  
“Warped compactifications: Flavor, precision tests and grand unification”

## XI. LIST OF PERSONNEL

### Supervisor for RIKEN Accelerator Research Facility

*Supervisor*  
*Deputy Supervisor*

Hironichi KAMITSUBO  
Masayasu ISHIHARA

### Cyclotron Center

*Director*

Yasushige YANO

### Accelerator-based Research Group

*Director*

Tohru MOTOBAYASHI

### Experimental Equipment Sub-Group

*Sub-Group Leader*  
*Deputy Sub-Group Leader*

Masayuki KASE  
Tadashi KAMBARA

*Leader*

GARIS  
Atomic Collision Experiment  
Radioisotope Production  
SMART  
Plant Irradiation Technology  
Experimental Animal Irradiation  
RIPS  
Experimental Support  
Computing and Networking Management

Kosuke MORITA  
Tadashi KAMBARA  
Shuichi ENOMOTO  
Naruhiko SAKAMOTO  
Tomoko ABE  
Fumio YATAGAI  
Toshiyuki KUBO  
Tadashi KAMBARA  
Takashi ICHIHARA

### Experimental Research Sub-Group

*Sub-Group Leader (Non Nuclear Physics)*  
*Deputy Sub-Group Leader (Nuclear Physics)*

Yasunori YAMAZAKI  
Koichiro ASAHI

*Leader*

Nuclear Structure  
Nuclear Reaction  
Applied Nuclear Physics  
Atomic Science  
Animals and Cultured Cells Irradiation Research  
Plant Mutation Research  
Storage Ring  
Analysis on Trace Elements  
Detectors Development

Tohru MOTOBAYASHI  
Tohru MOTOBAYASHI  
Koichiro ASAHI  
Yasunori YAMAZAKI  
Fumio HANAOKA  
Shigeo YOSHIDA  
Takeshi KATAYAMA  
Yasushige YANO  
Hideto EN'YO

### Collaborative Research Sub-Group

*Sub-Group Leader*

Tohru MOTOBAYASHI

### RIBF Project Group

*Director*

Yasushige YANO

*Process Management*

*Leader*

Nobuhisa FUKUNISHI

*Construction Safety*

*Leader*

Atsushi YAMANAKA

### Accelerator Sub-Group

*Sub-Group Leader*  
*Deputy Sub-Group Leader*

Akira GOTO  
Nobuhisa FUKUNISHI

*Leader*

Project Management  
Ion-source Development  
RRC-system Upgrade  
Frc  
Irc  
SRC  
Cryogenics

Nobuhisa FUKUNISHI  
Takahide NAKAGAWA  
Osamu KAMIGAITO  
Naohito INABE  
Jun-ichi OHNISHI  
Hiroki OKUNO  
Kumio IKEGAMI

**Equipment Development Sub-Group**

*Sub-Group Leader*

*Deputy Sub-Group Leader*

Tohru MOTOBAYASHI

Toshiyuki KUBO

*Leader*

Counter System Development  
RIB Generator  
RI Spin Probe Facility Development  
SLOWRI  
SCRIT  
RI Ring  
Zero-degree Spectrometer  
Daimajin  
p-RIPS  
Networking and Data Processing Development  
Data Acquisition Technique Development

Toshimi SUDA  
Toshiyuki KUBO  
Koichiro ASAHI  
Michiharu WADA  
Masanori WAKASUGI  
Tohru MOTOBAYASHI  
Tohru MOTOBAYASHI  
Tohru MOTOBAYASHI  
Tohru MOTOBAYASHI  
Takashi ICHIHARA  
Yasushi WATANABE

**Safety Sub-Group**

*Sub-Group Leader*

Yoshitomo UWAMINO

**Cosmic Radiation Laboratory**

*Head*

Kazuo MAKISHIMA

*Members*

Hiroshi KATO  
Yukikatsu TERADA  
Ikuya SAKURAI\*

Toru TAMAGAWA  
Mitsuhiro KOHAMA\*

---

\* Contract Researcher

*Visiting Members*

Yasushi FUKAZAWA (Dept. Phys., Hiroshima Univ.)  
Tateo GOKA (JAXA)  
Soojing HONG (Dept. Phys., Saitama Univ.)  
Hokuto INOUE (JAXA)  
Madoka KAWAHARADA (Dept. Phys., Univ. Tokyo)  
Satoshi KAWASOE (Dept. Phys., Hiroshima Univ.)  
Yoshihito KOBAYASHI (JAXA)  
Motohide KOKUBUN (Dept. Phys., Univ. Tokyo)  
Hideki KOSHIISHI (JAXA)  
Jun'ichi KOTOKU (Dept. Phys., Univ. Tokyo)  
Haruhisa MATSUMOTO (JAXA)  
Takefumi MITANI (JAXA)  
Hiromasa MIYASAKA (Univ. Delaware, Bartol Res. Inst.)  
Masanori MORI (Dept. Phys., Saitama Univ.)  
Mio MURAKAMI (Dept. Phys., Univ. Tokyo)  
Motoki NAKAJIMA (Coll. Sci. Technol., Nihon Univ.)  
Kazuhiro NAKAZAWA (JAXA)  
Masanori OHNO (Dept. Phys., Hiroshima Univ.)  
Yuu OKADA (Dept. Phys., Univ. Tokyo)

Tadayuki TAKAHASHI (JAXA)  
Kazutaka YAMAOKA (Aoyama Gakuin Univ.)

## Radiation Laboratory

### *Head*

Hideto EN'YO

### *Members*

Yasuyuki AKIBA	Takashi ICHIHARA
Yuji GOTO	Masayasu OKAMURA
Yoshie OTAKE	Atsushi TAKETANI
Kiyoshi TANIDA	Yasushi WATANABE
Hiroaki ONISHI* <sup>1</sup>	Ryotaro MUTO* <sup>1</sup>
Junji TOJO* <sup>1</sup>	Hisayuki TORII* <sup>1</sup>
Tatsuya CHUJO* <sup>2</sup>	Kazumi HASUKO* <sup>2</sup>
Johann HEUSER* <sup>2</sup>	Masanori HIRAI* <sup>2</sup>
Noriyoshi ISHII* <sup>2</sup>	Hiroyuki KANO* <sup>2</sup>
Akio KIYOMICHI* <sup>2</sup>	Munehisa OTANI* <sup>2</sup>
Vladimir RYKOV* <sup>2</sup>	Kazutaka SUDO* <sup>2</sup>
Satoshi YOKKAICHI* <sup>2</sup>	

---

\*<sup>1</sup> Special Postdoctoral Researcher

\*<sup>2</sup> Contract Researcher

### *Visiting Members*

Igor ALEKSEEV (Phys. Dept., BNL, USA)  
Hiroyasu ASAMI (KEK)  
Masayuki ASAKAWA (Fac. Sci., Kyoto Univ.)  
Wolfgang BENTZ (Dept. Phys., Grad. Sch. Sci., Univ. Tokyo)  
Melynda BROOKS (LANL, USA)  
Muriel Jane BURWARD-HOY (Dept. Phys., State Univ. New York, Stony Brook, USA)  
Gianluca COLO (Univ. Milano, Italy)  
Norman CRIST (Columbia Univ., USA)  
Yoshihide FUCHI (KEK)  
Hirotsugu FUJII (Grad. Sch. Arts Sci., Univ. Tokyo)  
Yasuyuki GONO (Fac. Sci., Kyushu Univ.)  
Takashi HACHIYA (Fac. Sci., Hiroshima Univ.)  
Ikuko HAMAMOTO (Lund Inst. Technol., Univ. Lund, Sweden)  
Tetsuo HATSUDA (Fac. Sci., Univ. Tokyo)  
Yoshitaka HATTA (Fac. Sci., Kyoto Univ.)  
Naoki HAYASHI (JAERI)  
Arata HAYASHIGAKI (Dept. Phys., Grad. Sch. Sci., Univ. Tokyo)  
Kensuke HOMMA (Fac. Sci., Hiroshima Univ.)  
Takuma HORAGUCHI (Tokyo Inst. Technol.)  
Tomohiro HOTTA (Grad. Sch. Arts Sci., Univ. Tokyo)  
Kenichi IMAI (Fac. Sci., Kyoto Univ.)  
Michiko IMOTO (Lab. Phys., Coll. Sci. Technol., Nihon Univ.)  
Genming JIN (Inst. Modern Phys., Chin. Acad. Sci., China)  
Kaori KAKI (Fac. Sci., Shizuoka Univ.)  
Nobuyuki KAMIHARA (Tokyo Inst. Technol.)  
Takeo KAWASAKI (Fac. Sci., Niigata Univ.)  
Edouard KISTENEV (Phys. Dept., BNL, USA)  
Yuichiro KIYO (Grad. Sch. Sci., Tohoku Univ.)  
Jirou KODAIRA (Fac. Sci., Hiroshima Univ.)  
Yuji KOIKE (Fac. Sci., Niigata Univ.)  
Shunzo KUMANO (Fac. Sci. Eng., Saga Univ.)  
Teiji KUNIHICO (YITP, Kyoto Univ.)  
Yongil KWON (Seoul Natl. Univ., Korea)  
Zhong LIU (Inst. Modern Phys., Chin. Acad. Sci., China)  
Earle LOMON (Massachusetts Inst. Technol., USA)

Yajun MAO (Phys. Dept., BNL, USA)  
 Satoshi MATSUDA (Dept. Fund. Sci., Fac. Integr. Hum. Stud., Kyoto Univ.)  
 Tetsuo MATSUI (Grad. Sch. Arts Sci., Univ. Tokyo)  
 Yasuo MIAKE (Inst. Phys., Univ. Tsukuba)  
 Shoichi MIDORIKAWA (Fac. Eng., Aomori Univ.)  
 Toshiyuki MORII (Fac. Human Dev., Kobe Univ.)  
 Ludwig MUELLER (Phys. Dept., Univ. Padoba, Italy)  
 Tomofumi NAGAE (KEK)  
 Shoji NAGAMIYA (KEK)  
 Shogo NAKAMURA (Fac. Ed., Yokohama Natl. Univ.)  
 Akio OGAWA (Phys. Dept., BNL, USA)  
 Hiromi OKADA (Fac. Sci., Kyoto Univ.)  
 Kazuto OSHIMA (Gunma Natl. Coll. Technol.)  
 Ryutaro OOISHI (Inst. Phys., Univ. Tsukuba)  
 Qiangyan PAN (Inst. Modern Phys., Chin. Acad. Sci., China)  
 Edward PASCUZZI (Phys. Dept., BNL, USA)  
 Koichi SAITO (Tohoku Pharm. Univ.)  
 Naohito SAITO (Fac. Sci., Kyoto Univ.)  
 Fuminori SAKUMA (Fac. Sci., Kyoto Univ.)  
 Shoichi SASAKI (Fac. Sci., Univ. Tokyo)  
 Hikaru SATO (KEK)  
 Hiroki SATO (Fac. Sci., Kyoto Univ.)  
 Susumu SATO (Inst. Phys., Univ. Tsukuba)  
 Shinya SAWADA (KEK)  
 Markus SCHAEFER (Phys. Inst., Univ. Goettingen, Germany)  
 Andreas SCHAFER (Inst. Theor. Phys., Univ. Regensburg, Germany)  
 Wolf-Dieter SCHMIDT-OTT (Phys. Inst., Univ. Goettingen, Germany)  
 Bo SEDERWALL (Royal Inst. Technol., Sweden)  
 Michiko SEKIMOTO (KEK)  
 Toshiaki SHIBATA (Tokyo Inst. Technol.)  
 Kenta SHIGAKI (KEK)  
 Lucian STROE (Phys. Dept., Univ. Padoba, Italy)  
 Toru SUGITATE (Fac. Sci., Hiroshima Univ.)  
 Katsuhiko SUZUKI (Dept. Phys., Grad. Sch. Sci., Univ. Tokyo)  
 Tsuneo SUZUKI (Fac. Sci., Kanazawa Univ.)  
 Yasuhisa TAJIMA (Cycl. Radioisot. Cen., Tohoku Univ.)  
 Makoto TAKIZAWA (Showa Coll. Pharm. Sci.)  
 Manobu TANAKA (KEK)  
 Thomas THROWE (Phys. Dept., BNL, USA)  
 Manabu TOGAWA (Fac. Sci., Kyoto Univ.)  
 Takeshi TOYAMA (KEK)  
 Hidenori TOYOKAWA (JASRI)  
 Tsuneo UEMATSU (Dept. Fund. Sci., Fac. Integr. Human Stud., Kyoto Univ.)  
 Masashi WAKAMATSU (Lab. Nucl. Stud., Fac. Sci., Osaka Univ.)  
 Tomotsugu WAKASA (RCNP, Osaka Univ.)  
 Sebastian WHITE (Phys. Dept., BNL, USA)  
 Teruya YAMANISHI (Fac. Eng., Fukui Univ. Technol.)  
 Yoshiki YAMASHITA (Hirosaki Univ.)  
 Yoshiaki YASUI (KEK)  
 Koichi YAZAKI (Tokyo Women's Chr. Univ.)  
 Hiroshi YOKOYA (Fac. Sci. Hiroshima Univ.)  
 Koji YOSHIMURA (Int. Cen. Element. Part. Phys., Univ. Tokyo)  
 Naotaka YOSHINAGA (Fac. Sci., Saitama Univ.)  
 Masaru YOSOI (Fac. Sci., Kyoto Univ.)  
 Lihua ZHU (China Inst. Atom. Energy, China)

*Trainees*

Kazuya AOKI (Fac. Sci., Kyoto Univ.)  
 Hisato EGUCHI (Fac. Sci., Niigata Univ.)  
 Kouhei FUJIWARA (Fac. Sci., Niigata Univ.)

Koichi HASHIMOTO (Fac. Sci., Kanazawa Univ.)  
 Hiroki KANO (Tokyo Inst. Technol.)  
 Masahiro KONNO (Inst. Phys., Univ. Tsukuba)  
 Kentarou MAWATARI (Fac. Hum. Dev., Kobe Univ.)  
 Takahiro NAGAI (Fac. Sci. Eng., Saga Univ.)  
 Junji NAGASHIMA (Fac. Sci., Niigata Univ.)  
 Tomoaki NAKAMURA (Fac. Sci., Hiroshima Univ.)  
 Kenichi NAKANO (Tokyo Inst. Technol.)  
 Maya SHIMOMURA (Inst. Phys., Univ. Tsukuba)  
 Kohei SHOJI (Fac. Sci., Kyoto Univ.)  
 Noriyuki SUGITA (Fac. Sci., Hiroshima Univ.)  
 Satoshi TAKAGI (Inst. Phys., Univ. Tsukuba)  
 Junpei TAKANO (Tokyo Inst. Technol.)  
 Takashi WATANABE (Tokyo Inst. Technol.)  
 Choong-Jae YOON (Fac. Sci., Kyoto Univ.)

## RI Beam Science Laboratory

### *Head*

Tohru MOTOBAYASHI

### *Members*

Alexei A. KORSHENINNIKOV	Yukari MATSUO
Toshimi SUDA	Atsushi YOSHIDA
Koichi YOSHIDA	Akira OZAWA
Kouji MORIMOTO	Shunji NISHIMURA
Eiji IDEGUCHI	Akihisa KOHAMA
Yoshimitsu FUKUYAMA* <sup>1</sup>	Kei IIDA* <sup>1</sup>
Masaaki KIMURA* <sup>1</sup>	Yuji NISHI* <sup>1</sup>
Mizuki NISHIMURA* <sup>1</sup>	Tetsuya OHNISHI* <sup>1</sup>
Noritaka SHIMIZU* <sup>1</sup>	Satoshi SUGIMOTO* <sup>1</sup>
Deging FANG* <sup>2</sup>	Kiyomi IKEDA* <sup>2</sup>
Yoshihisa ISHIDA* <sup>2</sup>	Rituparna KANUNGO* <sup>2</sup>
Kensuke KUSAKA* <sup>2</sup>	Yuko MOTIZUKI* <sup>2</sup>
Toshimitsu YAMAZAKI* <sup>2</sup>	

---

\*<sup>1</sup> Special Postdoctoral Researcher

\*<sup>2</sup> Contract Researcher

### *Visiting Members*

Yasuhisa ABE (Yukawa Inst. Theor. Phys., Kyoto Univ.)  
 Yasuo AOKI (Fac. Sci., Univ. Tsukuba)  
 Shigeyoshi AOYAMA (Kitami Inst. Technol.)  
 Yoshihiro ARITOMO (JINR, Russia)  
 Richard BOYD (Ohio Univ., USA)  
 Rolf BROCKMANN (Inst. Phys., Univ. Mainz., Germany)  
 Antonio CASARES (Oak Ridge Lab., USA)  
 Masami CHIBA (Fac. Sci., Tohoku Univ.)  
 Llie CRUCCERU (Horia Inst. Eng., Romania)  
 Vivek DATAR (Bhabha Atom. Res. Cen., India)  
 Dean J. DAVID (CALTEC, USA)  
 Alla S. DEMIYANOVA (Kurchatov Inst. Atom. Energy, Russia)  
 Tadayoshi DOKE (Sci. Eng. Res Lab., Waseda Univ.)  
 Yoshiko ENYO (KEK)  
 Michael FAMIANO (Ohio Univ., USA)  
 Andrei FOMITCHEV (JNRF, Russia)  
 Takaaki FUKUOKA (Taisho Univ.)  
 Mamoru FUJIWARA (RCNP, Osaka Univ.)  
 Zsolt FÜLÖP (ATOMKI, Hungary)  
 Zoltan GACSI (ATOMKI, Hungary)  
 Yu-Cheng GE (Peking Univ., China)



Hans GEISSEL (GSI, Germany)  
 Mircea GIURGIU (Inst. Phys. Nucl. Eng., Romania)  
 Mikheil S. GOLOVKOV (Kurchatov Inst., Russia)  
 Sergei A. GONCHAROV (Kurchatov Inst., Russia)  
 Stephanoë GORIELY (Inst. Astron., Belgium)  
 Alexander GORINE (IHEO, Russia)  
 Ranjana GOSWAMI (Variable Energy Cycl. Cen. Calcutta, India)  
 Syuichi GUNJI (Yamagata Univ.)  
 Zhenhui HAN (Fudan Univ., China)  
 Toru HARADA (Fac. Sci. Inf., Sapporo Gakuen Univ.)  
 Nobuyuki HASEBE (Sci. Eng. Res. Lab., Waseda Univ.)  
 Jun HASEGAWA (Fac. Eng., Tokyo Inst. Technol.)  
 Michio HATANO (Fac. Sci., Univ. Tokyo.)  
 Nguyen Thuc HIEN (Hanoi Univ., Vietnam)  
 Satoru HIRENZAKI (Fac. Sci., Nara Women's Univ.)  
 Michio HONMA (Univ. Aizu)  
 Takatoshi HORIBATA (Fac. Sci., Aomori Univ.)  
 Shen HONG (Dept. Phys., Nankai Univ.)  
 Masakatu HORIGUCHI (Horiguchi Ironworks)  
 Hisashi HORIUCHI (Fac. Sci., Kyoto Univ.)  
 Akitsu IKEDA (Shizuoka Inst. Sci. Technol.)  
 Shigeru ISHIMOTO (KEK)  
 Naoyuki ITAGAKI (Fac. Sci., Univ. Tokyo)  
 Makoto ITO (Fac. Sci., Univ. Tsukuba)  
 Akira IWAMOTO (JAERI)  
 Naohisa IWASA (Fac. Sci., Tohoku Univ.)  
 Takuji IZUMIKAWA (Fac. Sci., Niigata Univ.)  
 Takeo IZUYAMA (Fac. Sci., Toho Univ.)  
 Dang-Xing JIANG (Peking Univ., China)  
 Masayasu KAMIMURA (Fac. Sci., Kyushu Univ.)  
 Toshiki KAJINO (Natl. Astron. Obs.)  
 Kiyoshi KATO (Fac. Sci., Hokkaido Univ.)  
 Jun KIKUCHI (Sci. Eng. Res. Lab., Waseda Univ.)  
 Kikuo KIMURA (Fac. Sci., Nagasaki Inst. Appl. Sci.)  
 Syunichi KITAHARA (Jumonji Women's Univ.)  
 Masanori KOBAYASHI (Sci. Eng. Res. Lab., Waseda Univ.)  
 Toshio KOBAYASHI (Fac. Sci., Tohoku Univ.)  
 Tetsuro KOMATSUBARA (Univ. Tsukuba)  
 Hiroyuki KOURA (Fac. Sci. Eng., Waseda Univ.)  
 Evgueni KOUZMINE (Kurchatov Inst., Russia)  
 Attila KRASZNAHORKAY (ATOMKI, Hungary)  
 Hidekazu KUMAGAI  
 Suresh KUMARU (Bhabha Atom. Res. Cen., India)  
 Khiem LE HONG (Inst. Phys., Natl. Cen. Sci. Technol., Vietnam)  
 Xing-Qing LI (Peking Univ., China)  
 Zhi-Huan LI (Peking Univ., China)  
 Hongfeng LU (Peking Univ., China)  
 Takahiro MIZUSAKI (Fac. Sci., Univ. Tokyo)  
 Koichi MARUYAMA (Kitazato Univ.)  
 Tomoyuki MARUYAMA (Nihon Univ.)  
 Toshiki MARUYAMA (JAERI)  
 Nobuyuki MATSUOKA (RCNP, Osaka Univ.)  
 Kensaku MATSUTA (Fac. Sci., Osaka Univ.)  
 Yoshitaka MATSUYAMA (Inst. Nucl. Stud., Univ. Tokyo)  
 Kenichi MATSUYANAGI (Grad. Sch. Sci., Kyoto Univ.)  
 Masayuki MATSUZAKI (Fac. Ed., Fukuoka Univ.)  
 Jie MENG (Peking Univ., China)  
 Souichi MIDORIKAWA (Fac. Eng., Aomori Univ.)  
 Kei MINAMISONO (Fac. Sci., Osaka Univ.)  
 Tadanori MINAMISONO (Fac. Sci., Osaka Univ.)

Wolfgang MITTING (GANIL, France)  
 Mototugu MIHARA (Fac. Sci., Osaka Univ.)  
 Tanu Ekanath MIRGULE (Bhabha Atom. Res. Cen., India)  
 Takashi MIYACHI (Fac. Sci. Eng., Waseda Univ.)  
 Yasuo MIYAKE (Fac. Sci., Univ. Tsukuba)  
 Osamu MIYAMURA (Fac. Sci., Hiroshima Univ.)  
 Sadao MOMOTA (Kochi Univ. Technol.)  
 Hiroaki MORITA (Horiguchi Ironworks)  
 Mitsuo MURAOKA (Fac. Sci., Aomori Univ.)  
 Atsushi MUTA (Inst. Phys., Univ. Tsukuba)  
 Kazuo MUTO (Inst. Sci., Chiba Univ.)  
 Hitoshi NAKADA (Fac. Sci., Chiba Univ.)  
 Takashi NAKATSUKASA (Fac. Sci., Tohoku Univ.)  
 Yoichi NOJIRI (Kochi Univ. Technol.)  
 Izumi NOMURA (Natl. Inst. Fusion Sci.)  
 Kengo OGAWA (Coll. Arts Sci., Chiba Univ.)  
 Masao OGAWA (Fac. Eng., Tokyo Inst. Technol.)  
 Yoko OGAWA (Fac. Sci., Osaka Univ.)  
 Alexei A. OGLOBLIN (Kurchatov Inst., Russia)  
 Akira OHNISHI (Fac. Sci., Hokkaido Univ.)  
 Naoki OHNISHI (Fac. Eng., Yamanashi Univ.)  
 Masahisa OHTA (Fac. Sci., Konan Univ.)  
 Hideaki OHTSU (Fac. Sci., Tohoku Univ.)  
 Takashi OHTSUBO (Fac. Sci., Niigata Univ.)  
 Narito OKABE (Fac. Sci., Hokkaido Univ.)  
 Hiroyuki OKADA (Sci. Eng. Res. Lab., Waseda Univ.)  
 Osamu OKUDAIRA (Fac. Sci. Eng., Waseda Univ.)  
 Kazuo OMATA (Inst. Nucl. Stud., Univ. Tokyo)  
 Akira ONO (Fac. Sci., Tohoku Univ.)  
 Makito OOI (Dept. Phys., Sch. Sci., Univ. Tokyo)  
 Shinsho ORYU (Fac. Sci. Technol., Tokyo Univ. Sci.)  
 Takaharu OTSUKA (Fac. Sci., Univ. Tokyo)  
 Diane REITZNER (Ohio Univ., USA)  
 Kazuhiro OYAMATSU (Aichi Shukutoku Univ.)  
 Emmanuel ROLACCO (EAC, France)  
 Zhou Zhang REN (Nanjing Univ., China)  
 Chamanz P. ROUSSEL (GANIL, France)  
 Hiroyuki SAGAWA (Univ. Aizu)  
 Harutaka SAKAGUCHI (Grad. Sch., Kyoto Univ.)  
 Hideyuki SAKAI (Fac. Sci., Univ. Tokyo)  
 Hirohisa SAKURAI (Yamagata Univ.)  
 Chhanda SAMANTA (Sala Inst. Nucl. Phys., Calcutta, India)  
 Badawy SARHAN (Cairo Univ., Egypt)  
 Hiromasa SASA (Horiguchi Ironworks)  
 Kimikazu SASA (Univ. Tsukuba)  
 Kenichi SATO (Dept. Phys., Tohoku Coll. Pharm)  
 Lee S. SCHROEDER (Laurence Berkeley Lab., USA)  
 Ryoichi SEKI (California Univ., USA)  
 Milena SERRA (Tech. Munich Univ., Germany)  
 Bradley M. SHERRIL (Michigan State Univ., USA)  
 Caiwan SHEN (Dept. Nucl. Phys., China Inst. At. Energy, China)  
 Michihiro SHIBATA (Nagoya Univ.)  
 Toru SHIBATA (Sci. Eng., Aoyama Gakuin Univ.)  
 Cosimo SIGNORINI (INEN, Italy)  
 Mickael SMITH (Inst. Oak Ridge, USA)  
 Koonin STEVEN (CALTEC, USA)  
 Masahiko SUGAWARA (Fund. Sci., Chiba Inst. Technol.)  
 Kohsuke SUMIYOSHI (Numazu Coll. Technol.)  
 Summerer KLAUS (GSI, Germany)  
 Akihiro SUZUKI (Shinshu Univ.)

Hideyuki SUZUKI (KEK)  
 Takeshi SUZUKI (Fac. Sci., Saitama Univ.)  
 Tsuneo SUZUKI (Fac. Sci., Kanazawa Univ.)  
 Toshio SUZUKI (Coll. Hum. Sci., Nihon Univ.)  
 Toshio SUZUKI (Fukui Univ.)  
 Yasuyuki SUZUKI (Fac. Sci., Niigata Univ.)  
 Takahiro TACHIBANA (Sen. High Sch., Waseda Univ.)  
 Koji TAKAHASHI (Inst. Max Plank, Germany)  
 Yutaka TAKAHASHI (RCNP, Osaka Univ.)  
 Masatoshi TAKANO (Sci. Eng. Res. Lab., Waseda Univ.)  
 Tadashi TAKEMASA (Kyoto Univ. Ed.)  
 Noboru TAKIGAWA (Fac. Sci., Tohoku Univ.)  
 Naoki TAJIMA (Fac. Sci., Fukui Univ.)  
 Kazuko TANABE (Otsu Women's Univ.)  
 Kazuhiro TANAKA (Med. Dept., Juntendo Univ.)  
 Takaya TANAKA (Fac. Sci., Saitama Univ.)  
 Kazuhiro TERASAWA (Fac. Sci. Eng., Waseda Univ.)  
 Hirokazu TEZUKA (Dept. Liberal Arts., Fac. Literature, Toyo Univ.)  
 Peter SHIROLF (Univ. Munich, Germany)  
 Mitsuru TOHYAMA (Kyorin Univ.)  
 Fuyuki TOKANAI (Fac. Sci., Yamagata Univ.)  
 Hiroshi TOKI (RCNP, Osaka Univ.)  
 Toshiaki TOMODA (Fac. Sci., Aomori Univ.)  
 Baeck TORBJOEN (Phys. Dept. Frescat., Sweden)  
 Jeffrey A. TOSTEVIN (Univ. Surry, India)  
 Yukio UCHIBORI (NIRS)  
 Yutaka UTSUNO (Tokai Res. Estab., JAERI)  
 Hiroaki UTSUNOMIYA (Fac. Sci., Konan Univ.)  
 Kalman VARGA (Inst. Oak Ridge, USA)  
 Takahiro WADA (Fac. Sci., Konan Univ.)  
 Masamiti WAKAI (Grad. Sch. Sci., Osaka Univ.)  
 Quanjin WANG (Peking Univ., China)  
 Martin WINKLER (GSI, Germany)  
 Cuie WU (Peking Univ., China)  
 Herman WOLLNIK (Oak Ridge Lab., USA)  
 Kazuhiro YABANA (Fac. Sci., Univ. Tsukuba)  
 Hirosuke YAGI (Fac. Sci., Univ. Tsukuba)  
 Kazunari YAMADA (Fac. Sci., Rikkyo Univ.)  
 Syoichi YAMADA (Fac. Sci., Univ. Tokyo)  
 Takayuki YAMAGUCHI (Fac. Sci., Univ. Saitama)  
 Yoshitaka YAMAGUCHI (Fac. Sci., Niigata Univ.)  
 Yoshio YAMAGUCHI (Inst. Nucl. Stud., Univ. Tokyo)  
 Yanlin YE (Peking Univ., China)  
 Alhassid YORANN (Yale Univ., USA)  
 Nobuaki YOSHIDA (Fac. Inf., Konan Univ.)  
 Naotaka YOSHINAGA (Fac. Sci., Saitama Univ.)  
 Akira YUNOKI (Toshiba Co.)  
 Tao ZHENG (Peking Univ., China)  
 Shan-Gi ZHOU (Peking Univ., China)

*Trainees*

Youhei ARAKAWA (Fac. Sci., Osaka Univ.)  
 Masayuki ASAEDA (Fac. Sci. Eng., Waseda Univ.)  
 Cholsong CHONG (Fac. Sci. Eng., Waseda Univ.)  
 Hiroki FUJIWARA (Fac. Sci., Osaka Univ.)  
 Yasuro FUNAKI (Fac. Sci., Kyoto Univ.)  
 Takeshi FURUKAWA (Fac. Sci., Osaka Univ.)  
 Naoki FUKUDA (Fac. Sci. Eng., Waseda Univ.)  
 Tetsuhito FUSE (Fac. Sci. Eng., Waseda Univ.)  
 Izumi HASHIMOTO (Fac. Sci., Osaka Univ.)

Kazuaki HASHIZUME (Fac. Sci., Konan Univ.)  
Masamichi HARUKI (Fac. Sci. Eng., Waseda Univ.)  
Masaru HIBINO (Fac. Sci. Eng., Waseda Univ.)  
Hiroshi HIGASHI (Fac. Sci. Eng., Waseda Univ.)  
Takuji HIRAMOTO (Fac. Sci. Eng., Waseda Univ.)  
Takehiro HOSOJIMA (Fac. Sci. Eng., Waseda Univ.)  
Tsutomu IGARASHI (Fac. Sci. Eng., Waseda Univ.)  
Akifumi IHARA (Fac. Sci. Eng., Waseda Univ.)  
Rinzo IIO (Fac. Sci. Eng., Waseda Univ.)  
Hiroshi ITO (Fac. Sci. Eng., Waseda Univ.)  
Tomomi KATO (Fac. Sci., Niigata Univ.)  
Nobuhiro KAJIWARA (Fac. Sci. Eng., Waseda Univ.)  
Yoshie KAWAMURA (Fac. Sci., Niigata Univ.)  
Eiichi KIHIRA (Fac. Sci. Eng., Waseda Univ.)  
Atushi KIYAMU (Ibaraki Univ.)  
Shingo KOBAYASHI (Fac. Sci. Eng., Waseda Univ.)  
Satoshi KODAIRA (Fac. Sci. Eng., Waseda Univ.)  
Takayuki KOIKE (Fac. Sci. Eng., Waseda Univ.)  
Ryo KOYAMA (Fac. Sci., Niigata Univ.)  
Shinichi KUMASHIRO (Fac. Sci., Osaka Univ.)  
Genei KURAZA (Fac. Sci. Eng., Waseda Univ.)  
Yohei MATSUDA (Fac. Sci., Tohoku Univ.)  
Makoto MATSUNAGA (Fac. Sci. Eng., Waseda Univ.)  
Takahiro MASUMURA (Fac. Sci. Eng., Waseda Univ.)  
Howard MEREDITH (Ohio Univ., USA)  
Daisuke MIKI (Fac. Sci. Eng., Waseda Univ.)  
Toshiya MIKI (Fac. Sci., Tohoku Univ.)  
Mitsuteru MIMURA (Fac. Sci. Eng., Waseda Univ.)  
Satoshi MURASAWA (Fac. Sci. Eng., Waseda Univ.)  
Atsushi NAGASHIMA (Fac. Sci. Eng., Waseda Univ.)  
Takashi NAGATOMO (Fac. Sci., Osaka Univ.)  
Yoshiki NAKASHIMA (Fac. Sci., Osaka Univ.)  
Yusuke NAKAMURA (Fac. Sci. Eng., Waseda Univ.)  
Fumihiko NISHIKIDO (Fac. Sci. Eng., Waseda Univ.)  
Takashi OKUDA (Fac. Sci., Tohoku Univ.)  
Masako OGURA (Fac. Sci., Osaka Univ.)  
Kazuki OHZEKI (Fac. Sci., Tohoku Univ.)  
Akihiro OKA (Fac. Sci. Eng., Waseda Univ.)  
Takashi OKUDA (Fac. Sci., Tohoku Univ.)  
Osamu OKUDAIRA (Fac. Sci. Eng., Waseda Univ.)  
Kiminori OZAKI (Fac. Sci. Eng., Waseda Univ.)  
Hisanori SAKABA (Fac. Sci. Eng., Waseda Univ.)  
Takao SAKAGUCHI (Fac. Sci. Eng., Waseda Univ.)  
Makoto SASAKI (Fac. Sci., Osaka Univ.)  
Kazunori SATO (Fac. Sci., Niigata Univ.)  
Yoko SEKI (Fac. Sci., Tohoku Univ.)  
Masatugu SEKIGUCHI (Fac. Sci., Tohoku Univ.)  
Atsuhito SHIINA (Fac. Sci. Eng., Waseda Univ.)  
Noritaka SHIMIZU (Fac. Sci., Univ. Tokyo)  
Tokukazu SHINOHARA (Fac. Sci., Tohoku Univ.)  
Wakako SHINOZAKI (Fac. Sci. Niigata Univ.)  
Hirofumi SOURU (Fac. Sci. Eng., Waseda Univ.)  
Edward SMITH (Ohio Univ., USA)  
Masa TAKAHASHI (Fac. Sci., Niigata Univ.)  
Atsushi TAKEMURA (Fac. Sci., Osaka Univ.)  
Haruyuki TAKEMURA (Fac. Sci. Eng., Waseda Univ.)  
Sunao TAKENAKA (Fac. Sci. Eng., Waseda Univ.)  
Masatoshi TAKENOUCI (Fac. Sci. Eng., Waseda Univ.)  
Motoyuki TANAKA (Fac. Sci. Eng., Waseda Univ.)  
Shinya TAZAWA (Fac. Sci., Tohoku Univ.)

Kazuhiro TERASAWA (Fac. Sci. Eng., Waseda Univ.)  
Satoru TERASAWA (Fac. Sci., Kyoto Univ.)  
Mariko TERASAWA (Natl. Astron. Obs.)  
Shigeru TERUHI (Fac. Sci. Eng., Waseda Univ.)  
Chikara TEZUKA (Fac. Sci. Eng., Waseda Univ.)  
Toru UZIE (Fac. Sci., Tohoku Univ.)  
Kiwamu WATANABE (Fac. Sci., Tohoku Univ.)  
Shigeo WATANABE (Fac. Sci., Niigata Univ.)  
Takashi YAKUSHIJI (Fac. Sci., Tohoku Univ.)  
Hiroyuki YAMAMOTO (Fac. Sci. Eng., Waseda Univ.)  
Masaki YAMASHITA (Fac. Sci. Eng., Waseda Univ.)  
Naoyuki YAMASHITA (Fac. Sci. Eng., Waseda Univ.)  
Junichi YASHIRO (Fac. Sci. Eng., Waseda Univ.)  
Jun YASUTANI (Fac. Sci. Eng., Waseda Univ.)  
Eriko YOKOYAMA (Fac. Sci. Eng., Waseda Univ.)  
Hideki YOSHIOKA (Fac. Sci. Eng., Waseda Univ.)

### Applied Nuclear Physics Laboratory

#### *Head*

Koichiro ASAHI

#### *Members*

Yoshio KOBAYASHI  
Akihiro YOSHIMI  
Hiroshi WATANABE\*2

Hideki UENO  
Tomohito HASEYAMA \*1

---

\*1 Special Postdoctoral Researcher

\*2 Contract Researcher

#### *Visiting Members*

Minoru ADACHI  
Yasuaki EINAGA (Fac. Sci. Eng., Keio Univ.)  
Hideaki IZUMI (Grad. Sch. Sci. Eng., Osaka Univ.)  
Kenya M. KUBO (Div. Natl. Sci., Int. Chr. Univ.)  
Hisanori MIYOSHI (Grad. Sch. Sci. Eng., Tokyo Inst. Technol.)  
Jiro MURATA (Fac. Sci., Rikkyo Univ.)  
Yujiro NAGATA (Coll. Sci. Technol., Aoyama Gakuin Univ.)  
Hiromichi NAKAHARA (Grad. Sch. Sci., Tokyo Metrop. Univ.)  
Jin NAKAMURA (Dept. Appl. Phys. Chem., Univ. Electro-Commun.)  
Saburo NASU (Grad. Sch. Eng. Sci., Osaka Univ.)  
Hiroshi OGAWA (Natl. Inst. Adv. Ind. Sci. Technol.)  
Takuya OKADA (Fac. Sci., Gakushuin Univ.)  
Hiroyuki SAGAWA (Math. Sci., Univ. Aizu)  
Wataru SATO (Grad. Sch. Sci., Osaka Univ.)  
Kenji SAKAI (Grad. Sch. Sci. Eng., Tokyo Inst. Technol.)  
Kenji SHIMADA (Fac. Sci., Tokyo Inst. Technol.)  
Tadashi SHIMODA (Grad. Sch. Sci. Eng., Osaka Univ.)  
Takashi TANIGUCHI (Coll. Sci. Technol., Aoyama Gakuin Univ.)  
Masahiko UTSURO (RCNP, Osaka Univ.)  
Yasuhiro YAMADA (Fac. Sci., Tokyo Univ. Sci.)  
Eiichi YAGI (Sch. Sci. Eng., Waseda Univ.)  
Yutaka YOSHIDA (Fac. Sci. Technol., Shizuoka Inst. Sci. Technol.)

#### *Trainees*

Syoken EMORI (Fac. Sci., Tokyo Inst. Technol.)  
Shinya FUKAGAI (Sch. Sci. Eng., Waseda Univ.)  
Shinichi HAGIWARA (Sch. Sci. Eng., Waseda Univ.)  
Tatsuya HAYASHI (Sch. Sci. Eng., Waseda Univ.)  
Naota HIGAMI (Sch. Sci. Eng., Waseda Univ.)

Takashi ITO (Fac. Sci., Tokyo Inst. Technol.)  
 Shimon JINBO (Coll. Sci. Technol., Aoyama Gakuin Univ.)  
 Daisuke KAMEDA (Grad. Sch. Sci. Eng., Tokyo Inst. Technol.)  
 Jou KAIHARA (Fac. Sci., Tokyo Inst. Technol.)  
 Gou KATO (Fac. Sci., Tokyo Inst. Technol.)  
 Gou KIJIMA (Fac. Sci., Tokyo Inst. Technol.)  
 Takaki KOIKE (Fac. Sci., Tokyo Inst. Technol.)  
 Akira KUMAKURA (Fac. Sci., Tokyo Univ. Sci.)  
 Hiroshi MATSUBA (Sch. Sci. Eng., Waseda Univ.)  
 Kazuya MIYAHARA (Sch. Sci. Eng., Waseda Univ.)  
 Jun MIYAZAKI (Grad. Sci., Tokyo Univ. Sci.)  
 Katsuhito MORI (Sch. Sci. Eng., Waseda Univ.)  
 Tetsuya NAKAGAWA (Fac. Sci., Tokyo Univ. Sci.)  
 Yuki NEMOTO (Fac. Sci., Tokyo Univ. Sci.)  
 Yoshinori OKADA (Sch. Sci. Eng., Waseda Univ.)  
 Takahiro OHTSUKA (Div. Natl. Sci., Int. Chr. Univ.)  
 Atsushi SAITO (Fac. Sci., Tokyo Univ. Sci.)  
 Takashi SAITO (Fac. Sci., Tokyo Univ. Sci.)  
 Kiwamu SAKUMA (Sch. Sci. Eng., Waseda Univ.)  
 Jyunko SUDA (Div. Natl. Sci., Int. Chr. Univ.)  
 Shinichi SUDA (Fac. Sci., Tokyo Inst. Technol.)  
 Chika SUGI (Sch. Sci. Eng., Waseda Univ.)  
 Masato TSUKUI (Fac. Sci., Tokyo Inst. Technol.)  
 Motoyasu YOSHII (Sch. Sci. Eng., Waseda Univ.)

## Atomic Physics Laboratory

### *Head*

Yasunori YAMAZAKI

### *Members*

Tadashi KAMBARA	Yasuyuki KANAI
Hitoshi OYAMA	Michiharu WADA
Takao M. KOJIMA	Yoichi NAKAI
Takane KOBAYASHI	Tokihiro IKEDA
Masaki OURA	Yoshio IWAI*
Nobuhiro YAMANAKA*	Makoto C. FUJIWARA*

---

\* Special Postdoctoral Researcher

### *Visiting Members*

Kozo ANDO  
 Takeo ARUGA (Tokai Res. Estab., JAERI)  
 Yohko AWAYA (Coll. Art Design Gen. Ed., Musashino Art Univ.)  
 Toshiyuki AZUMA (Dept. Phys., Tokyo Metrop. Univ.)  
 Joachim BURGDÖRFER (Vienna Univ. Technol., Austria)  
 Li CHEN (LASIM, Lyon Univ., France)  
 Yasuhiro CHIMI (Tokai Res. Estab., JAERI)  
 Atsushi HATAKEYAMA (Grad. Sch. Arts Sci., Univ. Tokyo)  
 Hiroyuki HIGAKI (Inst. Appl. Phys., Univ. Tsukuba)  
 Akira HITACHI (Kochi Med. Sch.)  
 Jiri HORACEK (Charles Univ., Czech)  
 Masamitsu HOSHINO (Grad. Sch. Sci. Eng., Sophia Univ.)  
 Roger HUTTON (Dept. Phys., Univ. Lund, Sweden)  
 Atsushi ICHIMURA (Inst. Space Astro. Sci.)  
 Akinori IGARASHI (Fac. Eng., Miyazaki Univ.)  
 Mitio INOKUTI (Argonne Natl. Lab., USA)  
 Keishi ISHII (Fac. Sci. Eng., Ritsumeikan Univ.)  
 Norito ISHIKAWA (Tokai Res. Estab., JAERI)  
 Akio ITOH (Fac. Eng., Kyoto Univ.)  
 Yoh ITOH (Fac. Sci., Josai Univ.)

Akihiro IWASE (Res. Inst. Adv. Sci. Tech., Osaka Prefec. Univ.)  
 Kensuke KAGEYAMA (Fac. Eng., Saitama Univ.)  
 Kenji KIMURA (Fac. Eng., Kyoto Univ.)  
 Mineo KIMURA (Fac. Eng., Yamaguchi Univ.)  
 Masashi KITAJIMA (Fac. Sci. Tech., Sophia Univ.)  
 Nobuo KOBAYASHI (Dept. Phys., Tokyo Metrop. Univ.)  
 Tetsuo KOIZUMI (Dept. Phys., Rikkyo Univ.)  
 Ken-ichiro KOMAKI (Grad. Sch. Arts Sci., Univ. Tokyo)  
 Kenichi KOWARI (Dept. Appl. Phys. Chem., Univ. Electro-Commun.)  
 Kenro KUROKI (Natl. Res. Inst. Police Sci.)  
 Michio MATSUZAWA (Dept. Appl. Phys. Chem., Univ. Electro-Commun.)  
 Koichiro MITSUKE (Inst. Mol. Sci.)  
 Akihiro MOHRI  
 Yuichiro MORISHITA (Electrotechnical Lab.)  
 Takeshi MUKOYAMA (Kansai Gaidai Univ.)  
 Kanetada NAGAMINE (Inst. Mater. Struc. Sci., KEK)  
 Nobuyuki NAKAMURA (Inst. Laser Sci., Univ. Electro-Commun.)  
 Takashi NAKAMURA (KEK)  
 Tetsuya NAKAZAWA (Tokai Res. Estab., JAERI)  
 Megumi NIIGAKI (Dept. Phys., Grad. Sch. Sci., Univ. Tokyo)  
 Tamio NISHIMURA (Dept. Chim., Univ. Roma, Italy)  
 Shunsuke OHTANI (Inst. Laser Sci., Univ. Electro-Commun.)  
 Nagayasu OSHIMA (Grad. Sch. Arts Sci., Univ. Tokyo)  
 Norio OKABAYASHI (Grad. Sch. Arts Sci., Univ. Tokyo)  
 Kunihiro OKADA (Fac. Sci. Technol., Sophia Univ.)  
 Satoru OKAYASU (Tokai Res. Estab., JAERI)  
 Kazuhiko OKUNO (Dept. Phys., Tokyo Metrop. Univ.)  
 Fumihisa ONO (Fac. Sci., Okayama Univ.)  
 Lukas PICHL (Found. Comput. Sci. Lab., Univ. Aizu)  
 Yi-Zhi QU (Univ. Sci. Technol. China, China)  
 Frank B. ROSMEJ (GSI, Germany)  
 Syuiti SAKAGUTI (Fac. Eng., Yamaguchi Univ.)  
 Akio SAKAI (Vacuum Products Co.)  
 Reinhold SCHUCH (Phys. Dept., Stockholm Univ., Sweden)  
 Hans A. SCHUESSLER (Texas A & M Univ., USA)  
 Noriyuki SHIMAKURA (Fac. Sci., Niigata Univ.)  
 Isao SHIMAMURA  
 Hiroya SUNO (Fac. Eng., Yamaguchi Univ.)  
 Aiko TAKAMINE (Dept. Phys., Grad. Sch. Sci., Univ. Tokyo)  
 Károly TÖKÉSI (ATOMKI, Hungary)  
 Hiroyuki TORII (Grad. Sch. Arts Sci., Univ. Tokyo)  
 Nobuyuki TOSHIMA (Inst. Appl. Phys., Univ. Tsukuba)  
 Hidetsugu TSUCHIDA (Fac. Sci., Nara Women's Univ.)  
 Kiyoshi UEDA (Res. Inst. Sci. Meas., Tohoku Univ.)  
 Victor VARENTSOV (V. G. Khlopin Radium Inst., Russia)  
 Akira YAGISHITA (KEK)  
 Yutaka YOSHIDA (Shizuoka Inst. Sci. Technol.)  
 Ken YOSHIKI FRANZÉN (Grad. Sch. Arts Sci., Univ. Tokyo)  
 Yaming ZOU (Shanghai Jiao Tong Univ., China)

#### *Trainees*

Pierre HOSTEINS (Univ. Paris XI-Orsay, France)  
 Masato INOUE (Dept. Phys., Grad. Sch. Sci., Univ. Tokyo)  
 Hiroaki KANEMITSU (Dept. Phys., Okayama Univ.)  
 Seiji KOMATSU (Dept. Phys., Okayama Univ.)  
 Chikara KONDOU (Dept. Phys., Grad. Sch. Sci., Univ. Tokyo)  
 Naofumi KURODA (Dept. Phys., Grad. Sch. Sci., Univ. Tokyo)  
 Takuya MAJIMA (Grad. Sch. Eng., Kyoto Univ.)  
 Saburou MASUGI (Dept. Phys., Tokyo Metrop. Univ.)  
 Tomoko MURANAKA (Dept. Phys., Tokyo Metrop. Univ.)

Hiroyuki SHIMADA (Dept. Phys., Grad. Sch. Sci., Univ. Tokyo)  
Tetsu SONODA (Grad. Sch. Sci., Tohoku Univ.)  
Masashi TERADA (Inst. Laser Sci., Univ. Electro-Commun.)

## Heavy Ion Nuclear Physics Laboratory

### *Head*

Tohru MOTOBAYASHI

### *Members*

Takashi ICHIHARA	Takashi KISHIDA
Yasushi WATANABE	Nori AOI
Yoshiyuki YANAGISAWA	Naoki FUKUDA* <sup>1</sup>
Nobuaki IMAI* <sup>1</sup>	Masaaki TAKASHINA* <sup>1</sup>
Satoshi TAKEUCHI* <sup>2</sup>	Meiko UESAKA-KUROKAWA* <sup>2</sup>

---

\*<sup>1</sup> Special Postdoctoral Researcher

\*<sup>2</sup> Contract Researcher

### *Visiting Members*

Masato ASAI (JAERI)  
Daniel BAZIN (Natl. Supercond. Cycl. Lab., Michigan State Univ., USA)  
Didier BEAUMEL (Paris-XI Univ., IPN-Orsay, France)  
Mottelson R BEN (NORDITA, Copenhagen, Denmark)  
Shawn BISHOP (JSPS)  
Yorick BLUMENFELD (Paris-XI Univ., IPN-Orsay, France)  
Peter von BRENTANO (Inst. fur Kern Phys., Univ. zu Koeln, Germany)  
Rick CASTEN (Phys. Dept., BNL, USA)  
Rangacharyulu CHILAKAMARRI (Univ. Saskatchewan, Canada)  
Zsolt DOMBRADI (Inst. Nucl. Res., Hung. Acad. Sci., Hungary)  
Zoltan ELEKES (Inst. Nucl. Res., Hung. Acad. Sci., Hungary)  
Francis A. BECK (CRN, Strasbourg, France)  
Mitsunori FUKUDA (Grad. Sch. Sci., Osaka Univ.)  
Tomokazu FUKUDA (Osaka Electro-Commun. Univ.)  
Kazuyoshi FURUTAKA (Jpn. Nucl. Cycl. Dev. Inst.)  
Zsolt FÜLÖP (Inst. Nucl. Res. Hung. Acad. Sci., Hungary)  
Janos GAL (Inst. Nucl. Res. Hung. Acad. Sci., Hungary)  
Adrian GELBERG (Inst. Kern Phys., Univ. Koeln, Germany)  
Johannes G. MESSCHENDORP (Univ. Groningen, The Netherland)  
Guan-Hua LIU (Inst. Modern Phys., China)  
Hisashi HORIUCHI (Fac. Sci., Kyoto Univ.)  
Akos HORVATH (Dept. Atom. Phys., Eotvos Lorand Univ., Hungary)  
Flocard HUBERT (CSNSM, Orsay, France)  
Munetake ICHIMURA (Univ. Air)  
Kazuo IEKI (Coll. Sci., Rikkyo Univ.)  
Tetsuro Ishii (JAERI)  
Jingbin LU (Fac. Sci., Kyushu Univ.)  
Gibelin J. DIDIER (Coll. Sci., Rikkyo Univ.)  
Tsuneyoshi KAMAE (Stanford Univ., USA)  
Zirouta KASAGI (Lab. Nucl. Sci., Tohoku Univ.)  
Seigo KATOU (Fac. Ed., Yamagata Univ.)  
Kazuyoshi KURITA (Coll. Sci., Rikkyo Univ.)  
Nasser KALANTAR-NAYESTANAKI (Univ. Groningen, The Netherland)  
Gabor KALINKA (Inst. Nucl. Res., Hung. Acad. Sci., Hungary)  
Victor LIMA (Paris-XI Univ., IPN-Orsay, France)  
Ken-ichi MATSUYANAGI (Fac. Sci., Kyoto Univ.)  
Shirou MITARAI (Fac. Sci., Kyushu Univ.)  
Hiroari MIYATAKE (KEK)  
Tsuneyasu MORIKAWA (JAERI)  
Shunpei MORINOBU (Fac. Sci., Kyushu Univ.)



Takeshi MURAKAMI (Natl. Inst. Radiol. Sci.)  
 Hiroyuki MURAKAMI (Coll. Sci., Rikkyo Univ.)  
 Vinodkumar Mayyan ATTUKALATHIL (Fac. Sci., Tokyo Inst. Technol.)  
 Alberto MENGONI (ENEA, Italy)  
 Peter MOLLER (Los Alamos Natl. Lab., USA)  
 Yasuki NAGAI (RCNP, Osaka Univ.)  
 Takashi NAKAMURA (Fac. Sci., Tokyo Inst. Technol.)  
 Shintaro NAKAYAMA (Fac. Integr. Arts Sci., Univ. Tokushima)  
 Takashi NIIZEKI (Tokyo Kasei Univ.)  
 Tetsuo NORO (Fac. Sci., Kyushu Univ.)  
 Atsuko ODAHARA (Nishinippon Inst. Technol.)  
 Hiroyuki OKAMURA (Grad. Sch. Sci., Tohoku Univ.)  
 Makito OOI (Fukui Univ.)  
 Masumi OOSIMA (JAERI)  
 Hikonojou ORIHARA (Cycl. Radioisot. Cen., Tohoku Univ.)  
 Broglia A. RICARD (Univ. Milano, Italy)  
 Chilakamarri RANGACHARYULU (Univ. Saskatchewan, Canada)  
 Akito SAITO (Coll. Sci., Rikkyo Univ.)  
 Harutaka SAKAGUCHI (Fac. Sci., Kyoto Univ.)  
 Hiroyuki SAKURAGI (Fac. Sci., Osaka City Univ.)  
 Hiroyoshi SAKURAI (Dept. Phys., Grad. Sch. Sci., Univ. Tokyo)  
 Yoshiteru SATOU (Fac. Sci., Tokyo Inst. Technol.)  
 Yoshifumi SHIMIZU (Fac. Sci., Kyushu Univ.)  
 Hazime SHIMIZU (Fac. Ed., Yamagata Univ.)  
 Shoko KANNO (Coll. Sci., Rikkyo Univ.)  
 Masahiko SUGAWARA (Chiba Inst. Technol.)  
 Yasuyuki SUZUKI (Fac. Sci., Niigata Univ.)  
 Toshio SUZUKI (Fac. Eng., Fukui Univ.)  
 Shuwei XU (Inst. Modern Phys., Chin. Acad. Sci., China)  
 Dorottya SOHLER (Inst. Nucl. Res., Hung. Acad. Sci., Hungary)  
 Yasuhisa TAJIMA (Cycl. Radioisot. Cen., Tohoku Univ.)  
 Eiichi TAKADA (Natl. Inst. Radiol. Sci.)  
 Tadayuki TAKAHASHI (Inst. Space Astronaut. Sci.)  
 Noboru TAKIGAWA (Grad. Sch. Sci., Tohoku Univ.)  
 Atsushi TAMII (RCNP, Osaka Univ.)  
 Atsushi TANOKURA (Fac. Sci. Technol., Sophia Univ.)  
 Atsuki TERAKAWA (Cycl. Radioisot. Cen., Tohoku Univ.)  
 Masahiro UNO (MEXT)  
 Kentarou YAKOU (Dept. Phys., Grad. Sch. Sci., Univ. Tokyo)  
 Ken-ichirou YONEDA (Natl. Supercond. Cycl. Lab., Michigan State Univ., USA)  
 Naotaka YOSHINAGA (Fac. Sci., Saitama Univ.)  
 Masaru YOSOI (Fac. Sci., Kyoto Univ.)

#### *Trainees*

Hidetada BABA (Coll. Sci., Rikkyo Univ.)  
 Ryosuke HADATE (Coll. Sci., Rikkyo Univ.)  
 Naho HOKOIWA (Fac. Sci., Kyushu Univ.)  
 Hooi Jin ONG (Dept. Phys., Grad. Sch. Sci., Univ. Tokyo)  
 Yuichi ICHIKAWA (Dept. Phys., Grad. Sch. Sci., Univ. Tokyo)  
 Kazuhiro ISHIKAWA (Fac. Sci., Tokyo Inst. Technol.)  
 Shoko KAWAI (Coll. Sci., Rikkyo Univ.)  
 Michiya KIBE (Fac. Sci., Kyushu Univ.)  
 Takayuki KINOSHITA (Coll. Sci., Rikkyo Univ.)  
 Yousuke KONDOU (Fac. Sci., Tokyo Inst. Technol.)  
 Hironori KUBOKI (Dept. Phys., Grad. Sch. Sci., Univ. Tokyo)  
 Yukie MAEDA (Dept. Phys., Grad. Sch. Sci., Univ. Tokyo)  
 Nobuyuki MATSUI (Coll. Sci., Rikkyo Univ.)  
 Yuichi MATSUYAMA (Coll. Sci., Rikkyo Univ.)  
 Hiroyuki NAKAYAMA (Dept. Phys., Grad. Sch. Sci., Univ. Tokyo)  
 Haruki NISHINO (Dept. Phys., Grad. Sch. Sci., Univ. Tokyo)

Takeo ONISHI (Dept. Phys., Grad. Sch. Sci., Univ. Tokyo)  
Takaaki SAITO (Dept. Phys., Grad. Sch. Sci., Univ. Tokyo)  
Shouta SAITO (Coll. Sci., Rikkyo Univ.)  
Hazuki SAKAI (Coll. Sci., Rikkyo Univ.)  
Tomoyuki SAKURADA (Coll. Sci., Rikkyo Univ.)  
Masaki SASANO (Dept. Phys., Grad. Sch. Sci., Univ. Tokyo)  
Junichi SATO (Coll. Sci., Rikkyo Univ.)  
Takashi SUGIMOTO (Fac. Sci., Tokyo Inst. Technol.)  
Hiroshi SUZUKI (Dept. Phys., Grad. Sch. Sci., Univ. Tokyo)  
Masaru SUZUKI (Dept. Phys., Grad. Sch. Sci., Univ. Tokyo)  
Daisuke SUZUKI (Dept. Phys., Grad. Sch. Sci., Univ. Tokyo)  
Yoshiyuki TAKAHASHI (Dept. Phys., Grad. Sch. Sci., Univ. Tokyo)  
Yasuhiro TOGANO (Coll. Sci., Rikkyo Univ.)  
Kazuma TSURUSAKI (Dept. Phys., Grad. Sch. Sci., Univ. Tokyo)  
Hirotaka UENO (Coll. Sci., Rikkyo Univ.)  
Naori UMEZAWA (Coll. Sci., Rikkyo Univ.)  
Kazuya URUSHIBARA (Coll. Sci., Rikkyo Univ.)  
Yasuo WAKABAYASHI (Fac. Sci., Kyushu Univ.)  
Takeshi WATANABE (Coll. Sci., Rikkyo Univ.)  
Kazunari YAMADA (Coll. Sci., Rikkyo Univ.)

### Magnetic Materials Laboratory

#### *Head*

Hidenori TAKAGI

#### *Members*

Masayuki HAGIWARA  
Hiroki YAMAZAKI  
Hiroyuki YAMASE\*<sup>1</sup>  
Hiroaki UEDA\*<sup>2</sup>

Hiroko KATORI  
Koshi TAKENAKA  
Katsuya IWAYA\*<sup>1</sup>

---

\*<sup>1</sup> Special Postdoctoral Researcher

\*<sup>2</sup> Contract Researcher

#### *Visiting Members*

Hirokazu TSUNETSUGU (Yukawa Inst. Theoretical Phys.)  
Masaaki MATSUDA (Natl. Inst. Mater. Sci.)

#### *Trainees*

Tomohiro TAKAYAMA (Adv. Mater. Sci., Univ. Tokyo)  
Haritoki SHIMURA (Adv. Mater. Sci., Univ. Tokyo)

### Muon Science Laboratory

#### *Head*

Masahiko IWASAKI

#### *Members*

Teiichiro MATSUZAKI  
Haruhiko OUTA  
Yasuyuki MATSUDA  
Takahisa KOIKE\*<sup>1</sup>  
Seiko OHIRA\*<sup>2</sup>

Katsuhiko ISHIDA  
Isao WATANABE  
Kenta ITAHASHI  
Patrick STRASSER\*<sup>2</sup>  
Pavel BAKULE\*<sup>2</sup>

---

\*<sup>1</sup> Special Postdoctoral Researcher

\*<sup>2</sup> Contract Researcher

#### *Visiting Members*

Tadashi ADACHI (Fac. Eng., Tohoku Univ.)  
Yoshitami AJIRO (Fac. Sci., Kyushu Univ.)

Jun AKIMITSU (Coll. Sci. Eng., Aoyama Gakuin Univ.)  
 Megumi AKOSHIMA (Adv. Inst. Sci. Technol.)  
 Juichiro ARAI (Tokyo Univ. Sci.)  
 Shingo ARAKI (Fac. Sci., Osaka Univ.)  
 Kunio AWAGA (Grad. Sch. Arts Sci., Univ. Tokyo)  
 George A. BEER (Univ. Victoria, Canada)  
 Hyoung Chan BHANG (Seoul Natl. Univ., Korea)  
 Ludmila Nikolaevna BOGDANOVA (Inst. Theor. Exp. Phys., Russia)  
 Tina M. BRIERRE (Inst. Metal Sci., Tohoku Univ.)  
 Tara Prasad DAS (State Univ. New York, USA)  
 Don FLEMING (TRIUMF, Canada)  
 Yutaka FUJII (Fac. Eng., Fukui Univ.)  
 Masaki FUJITA (Inst. Chem. Res., Kyoto Univ.)  
 Atsuko FUKAYA (IMR, Tohoku Univ.)  
 Makoto HAGIWARA (Fac. Eng. Design, Kyoto Inst. Technol.)  
 Wataru HIGEMOTO (KEK)  
 Masahiro HIRANO (JST)  
 Emiko HIYAMA (KEK)  
 Susumu IKEDA (KEK)  
 Shigeru ISHIMOTO (KEK)  
 Atsuko ITO  
 Ryosuke KADONO (KEK)  
 Masayasu KAMIMURA (Fac. Sci., Kyushu Univ.)  
 Mineo KATO (Tokai Res. Estab., JAERI)  
 Naritoshi KAWAMURA (KEK)  
 Yasushi KINO (Fac. Sci., Tohoku Univ.)  
 Youji KOIKE (Fac. Eng., Tohoku Univ.)  
 Yoshitaka KUNO (Fac. Sci., Osaka Univ.)  
 Hong LI (Michigan State Univ., USA)  
 Roderick MACRAE (Marian Coll., Indianapolis, USA)  
 Syunsuke MAKIMURA (KEK)  
 Goro MARUTA (Fac. Sci., Hokkaido Univ.)  
 Yasuhiro MIYAKE (KEK)  
 Satoshi N. NAKAMURA (Fac. Sci., Tohoku Univ.)  
 Takashi NAKAMURA (Fac. Sci., Tokyo Inst. Technol.)  
 Takayoshi NAKAMURA (Res. Inst. Electron. Sci., Hokkaido Univ.)  
 Takehito NAKANO (Fac. Sci., Osaka Univ.)  
 Nobuhiko NISHIDA (Fac. Sci., Tokyo Inst. Technol.)  
 Kusuo NISHIYAMA (KEK)  
 Yasuo NOZUE (Fac. Sci., Osaka Univ.)  
 Vassili V. PEREVOZCHIKOV (Russ. Fed. Nucl. Cen., Russia)  
 Leonid I. PONOMAREV (Kurchatov Inst., Russia)  
 Francis L. PRATT (RAL, UK)  
 Shinichi SAKAMOTO (Tokai Res. Estab., JAERI)  
 Ryoichi SEKI (California State Univ., USA)  
 Koichiro SHIMOMURA (KEK)  
 Vyacheslav G. STORCHAK (Kurchatov Inst., Russia)  
 Hiroyuki SUGAI (Tokai Res. Estab., JAERI)  
 Keiji TAKEDA (Fac. Sci., Hokkaido Univ.)  
 Masashi TAKIGAWA (Inst. Solid State Phys.)  
 Masakazu TANASE (Takasaki Res. Estab., JAERI)  
 Eiko TORIKAI (Fac. Eng., Yamanashi Univ.)  
 Akihisa TOYODA (KEK)  
 Kazuo UEDA (Inst. Solid State Phys.)  
 Kazuyoshi YAMADA (IMR, Tohoku Univ.)  
 A. A. YUKHIMCHUK (Russ. Fed. Nucl. Cen., Russia)  
 Johann ZMESKAL (IMEP, Austria)

*Trainees*

Soichiro ARIMURA (Fac. Sci., Osaka Univ.)

Aya HINO (Fac. Sci., Tohoku Univ.)  
Yutaka IKEDO (Fac. Eng., Yamanashi Univ.)  
Hiroshi IMAO (Fac. Sci., Univ. Tokyo)  
Mijung KIM (Seoul Natl. Univ., Korea)  
Yoshihiro KUBOTA (Fac. Sci., Tohoku Univ.)  
Sougo KUROIWA (Fac. Sci. Eng., Aoyama Gakuin Univ.)  
Satoru MATUISHI (Fac. Sci., Tokyo Inst. Technol.)  
Sadafumi NISHIHARA (Grad. Sch. Environ. Earth Sci., Hokkaido Univ.)  
Naoki OKI (Fac. Eng., Tohoku Univ.)  
RIADIANA (Fac. Eng., Tohoku Univ.)  
Hiroki SHIBATA (Fac. Sci., Tohoku Univ.)  
Hyeongryul SO (Seoul State Univ., Korea)  
Hiroyuki TANAKA (Fac. Sci., Nagoya Univ.)  
Maki YAMAZAWA (Fac. Sci. Eng., Aoyama Gakuin Univ.)

## Beam Physics and Engineering Laboratory

### *Head*

Takeshi KATAYAMA

### *Members*

Manabu HAMAGAKI	Tadashi KOSEKI
Masato NAKAMURA	Masahiro OKAMURA
Shuichi OZAWA* <sup>1</sup>	Akira SAKUMI* <sup>1</sup>
Masao TAKANAKA* <sup>2</sup>	Moritake TAMBA
Masao WATANABE* <sup>2</sup>	Tamaki WATANABE

---

\*<sup>1</sup> Special Postdoctoral Researcher

\*<sup>2</sup> Contract Researcher

### *Visiting Members*

Hiroshi AMEMIYA  
Yoshihiko CHIBA  
Yoshihide FUCHI (KEK)  
Tomonori FUKUCHI (CNS, Univ. Tokyo)  
Kevin Insik HAHN (Ewha Woman's Univ., Korea)  
Hideki HAMAGAKI (CNS, Univ. Tokyo)  
Tamio HARA (Toyota Technol. Inst.)  
Yuichi HASHIMOTO (Canon Inc.)  
Toshiyuki HATTORI (Res. Lab. Nucl. React., Tokyo Inst. Technol.)  
Jianjun HE (CNS, Univ. Tokyo)  
Eiji IDEGUCHI (CNS, Univ. Tokyo)  
Masashi IMANAKA (CNS, Univ. Tokyo)  
Masahide INUZUKA (CNS, Univ. Tokyo)  
Hironobu ISHIYAMA (KEK)  
Hironori IWASAKI (CNS, Univ. Tokyo)  
Robert A. JAMESON (Los Alamos Natl. Lab., USA)  
Daiya KAJI (CNS, Univ. Tokyo)  
Teruo KANEDA (Tokyo Electr. Univ.)  
Seigo KATO (Univ. Yamagata)  
Shigeki KATO (KEK)  
Souichiro KAMETANI (Waseda Univ.)  
Takahiro KAWABATA (CNS, Univ. Tokyo)  
Takashi KIKUCHI (CNS, Univ. Tokyo)  
Jongchan KIM (Seoul Univ., Korea)  
Ka-hae KIM (CNS, Univ. Tokyo)  
Yasuro KOIKE (Hosei Univ.)  
Shigeru KUBONO (CNS, Univ. Tokyo)  
Rubens Filho LICHTENTHALER (Sao Paulo Univ., Brazil)  
Takashi MATSUMOTO (CNS, Univ. Tokyo)  
Igor MESHKOV (JINR, Russia)

Shin'ichiro MICHIMASA (Univ. Tokyo)  
 Hirofumi MIYAZAKI (Sumitomo Heavy Ind. Ltd.)  
 Dieter MOEHL (CERN, Switzerland)  
 Toshihiro NISHIDA (Tokyo Inst. Technol.)  
 Masaki NISHIURA (Natl. Inst. Fusion Sci.)  
 Masahiro NOTANI (CNS, Univ. Tokyo)  
 Masao OGAWA (Tokyo Inst. Technol.)  
 Yoshiyuki OGURI (Res. Lab. Nucl. React., Tokyo Inst. Technol.)  
 Yukimitsu OHSHIRO (CNS, Univ. Tokyo)  
 Hiromi OKAMOTO (Hiroshima Univ.)  
 Kiyohiko OKAZAKI  
 Ken OYAMA (Univ. Tokyo)  
 Kyoichiro OZAWA (CNS, Univ. Tokyo)  
 Takao SAKAGUCHI (CNS, Univ. Tokyo)  
 Mitsuo SAKAI (CNS, Univ. Tokyo)  
 Takeshi SAKAKIBARA (Chuo Univ.)  
 Yuichi SAKAMOTO (Nichimen Co.)  
 Yuichiro SASAKI (Matsushita Electric Ind., Ltd.)  
 Masaki SERATA (Coll. Sci., Rikkyo Univ.)  
 Takaichi SHIMAZAKI (CNS, Univ. Tokyo)  
 Susumu SHIMOURA (CNS, Univ. Tokyo)  
 Anatoly SIDORIN (JINR, Russia)  
 Alexander SKRINSKY (ITEP, Russia)  
 Alexandre SMIRNOV (JINR, Russia)  
 Kazuo SUGII (Osaka Vacuum, Ltd.)  
 Masaharu SUZUKI (CNS, Univ. Tokyo)  
 Evgeny SYRESIN (JINR, Russia)  
 Motonobu TAKANO  
 Masahiko TANAKA (KEK)  
 Takashi TERANISHI (CNS, Univ. Tokyo)  
 Mariko TERASAWA (CNS, Univ. Tokyo)  
 Hiroshi TSUTSUI (Sumitomo Heavy Ind., Ltd.)  
 Meiko UESAKA (CNS, Univ. Tokyo)  
 Tomohiro UESAKA (CNS, Univ. Tokyo)  
 Guimaraes VALDIR (Sao Paulo Univ., Brazil)  
 Takashi WAKUI (CNS, Univ. Tokyo)  
 Shin-ichi WATANABE (CNS, Univ. Tokyo)  
 Yutaka WATANABE (KEK)  
 Meiqin XIAO (Fermi Natl. Accel. Lab., USA)  
 Kentaro YAKO (CNS, Univ. Tokyo)  
 Shoichi YAMAKA (CNS, Univ. Tokyo)  
 Kazuo YAMAMOTO (Tokyo Inst. Technol.)  
 Norio YAMAZAKI (CNS, Univ. Tokyo)  
 Katsuki YANO  
 Chong Cheoul YUN (Chung-Ang Univ., Korea)

#### *Trainees*

Taku GUNJI (Univ. Tokyo)  
 Takashi HASHIMOTO (Tokyo Univ. Sci.)  
 Tomoko ISHIKAWA (Tokyo Univ. Sci.)  
 Tadaaki ISOBE (Waseda Univ.)  
 Fukutaro KAJIHARA (Univ. Tokyo)  
 Koichi KATO (Waseda Univ.)  
 Tomoyuki KAWAMURA (Yamagata Univ.)  
 Narumi KURIHARA (Univ. Tokyo)  
 Eun Kyung LEE (Ewha Woman's Univ., Korea)  
 Ju Hahn LEE (Chung-Ang Univ., Korea)  
 Jun Young MOON (Chung-Ang Univ., Korea)  
 Daisuke NAGAE (Tokyo Inst. Technol.)  
 Megumi NIIKURA (Univ. Tokyo)

Shinya OGAWA (Tokyo Inst. Technol.)  
Susumu ODA (Univ. Tokyo)  
Shinsuke OTA (Kyoto Univ.)  
Junpei TAKANO (Tokyo Inst. Technol.)  
Hiroyuki SATO (Yamagata Univ.)  
Mituru TAMAKI (Univ. Tokyo)  
Yorito YAMAGUCHI (Waseda Univ.)

### Cellular Physiology Laboratory

#### *Head*

Fumio HANAOKA

#### *Members*

Fumio YATAGAI

#### *Visiting Members*

Koichi ANDO (Natl. Inst. Radiol. Sci.)  
Yoshiya FURUSAWA (Natl. Inst. Radiol. Sci.)  
Yoshimasa HAMA (Sci. Eng. Inst., Waseda Univ.)  
Nobutoshi ITOH (Fac. Sci., Univ. Tokyo)  
Tatsuaki KANAI (Natl. Inst. Radiol. Sci.)  
Kiyomi KASAI (Natl. Inst. Radiol. Sci.)  
Yasuhiko KOBAYASHI (JAERI)  
Hiroshi WATANABE (JAERI)  
Masami WATANABE (Fac. Pharm. Sci., Nagasaki Univ.)  
Shoji YAMASHITA (Natl. Saitama Hospital)

### Plant Functions Laboratory

#### *Head*

Shigeo YOSHIDA

#### *Members*

Tomoko ABE	Tomoki MATSUYAMA
Yutaka MIYAZAWA* <sup>1</sup>	Koichi SAKAMOTO* <sup>1</sup>
Hiroyuki SAITO* <sup>1</sup>	Yoshiharu YAMAMOTO* <sup>2</sup>

---

\*<sup>1</sup> Special Postdoctoral Researcher

\*<sup>2</sup> Contract Researcher

#### *Visiting Members*

Chang-Hyu BAE (Sunchon Natl. Univ., Korea)  
Koji FURUKAWA (Mukoyama Orchids Co. Ltd.)  
Misako HAMATANI (Hiroshima City Agr. Forest. Promot. Cen.)  
Yasuhide HARA (Kanagawa Inst. Agr. Sci.)  
Masanori HATASHITA (Wakasa Wan Energy Res. Cen.)  
Atsushi HIGASHITANI (Grad. Sch. Life Sci., Tohoku Univ.)  
Ichiro HONDA (Natl. Agr. Res. Cen., Min. Agr. Forest. Fish.)  
Mitsugu HORITA (Hokkaido Green-bio Inst.)  
Yuji ITO (Inst. Rad. Breeding, Natl. Inst. Agr. Res.)  
Hiroshi KAGAMI (Shizuoka Citrus Exp. Station)  
Toshiaki KAMEYA (Grad. Sch. Life Sci., Tohoku Univ.)  
Takeo KITAURA (Kanagawa Inst. Agr. Sci.)  
Kazumitsu MIYOSHI (Fac. Bioresource Sci., Akita Pref. Univ.)  
Toshikazu MORISHITA (Inst. Rad. Breeding, Natl. Inst. Agr. Res.)  
Jin Heui PARK (Coll. Life Environ., Sci., Korea Univ., Korea)  
Takiko SHIMADA (Res. Inst. Agr. Resources, Ishikawa Agr. Coll.)  
Masao SUGIYAMA (Hokko Chemical Ind. Co., Ltd.)  
Kazunori SUZUKI (Plant Biotech. Inst. Ibaraki Agr. Cen.)

Kenichi SUZUKI (Suntory Flowers Ltd.)  
Ken TOKUHARA (Dogashima Orchid Cen.)  
Takuji YOSHIDA (Takii Seed Co., Ltd.)  
Hisashi TSUJIMOTO (Fac. Agr., Tottori Univ.)  
Masao WATANABE (Fac. Agr., Iwate Univ.)

*Trainees*

Sadao GUNJI (Miyazaki Agr. Exp. Station)  
Tetsuji KINOSHITA (Miyazaki Agr. Exp. Station)  
Tomojiro KOIDE (RIKEN Vitamin Co., Ltd.)  
Eikou OYABU (Saga Agr., Exp. Station)  
Ryoko ONUMA (Fac. Sci., Tokyo Univ. Sci.)  
Minoru SAITO (Fukui Agr. Exp. Station)  
Kei-ichiro UENO (Kagoshima Biotech. Inst.)  
Tetsuya UMEKI (Miyazaki Agr. Exp. Station)

**CYCLOTRON CENTER**

*Chief Scientist*

Yasushige YANO

*Members*

Noritaka SHIMIZU\*<sup>1</sup>  
Nguyen DINH DANG\*<sup>2</sup>  
Hideki MADOKORO\*<sup>2</sup>

Satoru SUGIMOTO\*<sup>1</sup>  
Yuko MOTIZUKI\*<sup>2</sup>  
Kiyomi IKEDA\*<sup>3</sup>

---

\*<sup>1</sup> Special Postdoctoral Researcher  
\*<sup>2</sup> Contract Researcher  
\*<sup>3</sup> Temporary Employee

*Visiting Members*

Shinichiro FUJII (Fac. Sci., Univ. Tokyo)  
Hiroyuki KOURA (Fac. Sci. Eng., Waseda Univ.)  
Shoushichi MOTONAGA  
Shigeo NUMATA  
Takaharu OTSUKA (Fac. Sci., Univ. Tokyo)  
Mutsuko SASAKI  
Shuhei YAMAJI (Kanagawa Inst. Technol.)  
Yu-Min ZHAO (South East Univ., China)

**Beam Dynamics Division**

*Head*

Akira GOTO

*Members*

Takashi EMOTO  
Masanori WAKASUGI  
Koichi YOSHIDA  
Nobuhisa FUKUNISHI  
Naruhiko SAKAMOTO  
Kimiko SEKIGUCHI\*<sup>1</sup>  
Yutaka MIZOI\*<sup>2</sup>

Toshiyuki KUBO  
Osamu KAMIGAITO  
Atsushi YOSHIDA  
Jun-ichi OHNISHI  
Toshiyuki MINEMURA\*<sup>1</sup>  
Kensuke KUSAKA\*<sup>2</sup>

---

\*<sup>1</sup> Special Postdoctoral Researcher  
\*<sup>2</sup> Contract Researcher

*Visiting Members*

Yoshiaki CHIBA  
Takashi FUJISAWA (N. I. R. S.)  
Mitsuhiro FUKUDA (Takasaki Res. Estab., JAERI)

Toshihiro HONMA (N. I. R. S.)  
Shinji MACHIDA (KEK)  
Toshinori MITSUMOTO (Sumitomo Heavy Ind., Ltd.)  
Yoshiharu MORI (KEK)  
Hiroyuki OKAMURA (Dept. Phys., Saitama Univ.)  
Serguei VOROJTSOV (J. I. N. R., Dubna, Russia)

*Trainees*

Takahiro AKIYAMA (Dept. Phys., Saitama Univ.)  
Takashi HASEGAWA (Cycl. Radioisot. Cen., Tohoku Univ.)  
Motooki HOSOI (Dept. Phys., Saitama Univ.)  
Takuichiro IKEDA (Dept. Phys., Saitama Univ.)  
Keisuke ITOH (Dept. Phys., Saitama Univ.)  
Youhei SHIMIZU (RCNP, Osaka Univ.)  
Kenji SUDA (Dept. Phys., Saitama Univ.)  
Kousuke SUGAWARA (Dept. Phys., Saitama Univ.)  
Naoya SUGIMOTO (Cycl. Radioisot. Cen., Tohoku Univ.)  
Eri TAKESHITA (Coll. Sci., Rikkyo Univ.)  
Reiko TAKI (Michigan State Univ., USA)  
Yuji TAMESHIGE (RCNP, Osaka Univ.)

**Beam Technology Division**

*Head*

Masayuki KASE

*Members*

Kosuke MORITA	Takahide NAKAGAWA
Toshiya TANABE	Kiminori USHIDA
Jiro FUJITA	Kiyoshi OGIWARA
Makoto NAGASE	Tadashi KAGEYAMA
Shigeo KOHARA	Eiji IKEZAWA
Naohito INABE	Masaki FUJIMAKI
Keiko KUMAGAI	Shin FUJITA
Sachiko ITO	Kouji MORIMOTO
Yoshihide HIGURASHI* <sup>1</sup>	Masanori KIDERA* <sup>1</sup>
Akiko MASUDA* <sup>1</sup>	Hiromichi RYUTO* <sup>1</sup>
Tadashi FUJINAWA* <sup>2</sup>	Misaki KOMIYAMA* <sup>2</sup>
Hisao SAKAMOTO* <sup>2</sup>	Shigeru YOKOUCHI* <sup>2</sup>
Akira YONEDA* <sup>2</sup>	Ichiro YOKOYAMA* <sup>3</sup>
Kenichi YAMAGUCHI* <sup>3</sup>	Yoshitoshi MIYAZAWA* <sup>3</sup>
Tsutomu YAMAKI* <sup>3</sup>	

---

\*<sup>1</sup> Contract Researcher

\*<sup>2</sup> Contract Technical Scientist

\*<sup>3</sup> Temporary Employee

*Visiting Members*

Keisuke ASAI (Grad. Sch. Eng., Univ. Tokyo)  
Hiroaki ASAI (NASDA)  
Shinji BABA (NASDA)  
Sudeep BHATTACHARJEE (Univ. Wisconsin-Madison, USA)  
Toshiya CHIBA  
Alexander EREMINE (Flerov Lab. Nucle. React., Russia)  
Kaoru FURUSE (NASDA)  
Yasuyuki FUTAMI (N. I. R. S.)  
Shin-ichi GOTO (Fac. Sci., Niigata Univ.)  
Kichiji HATANAKA (RCNP, Osaka Univ.)  
Yuichi HATSUKAWA (Tokai Res. Estab., JAERI)  
Ryugo S. HAYANO (Fac. Sci., Univ. Tokyo)  
Masatake HEMMI



Yoshiya IIDE (NASDA)  
 Seiji IIO (Sumitomo Heavy Ind. Ltd.)  
 Naomi IKEDA (NASDA)  
 Hiroshi IKEZOE (Tokai Res. Estab., JAERI)  
 Takashi INAMURA  
 Masayuki ITO (Adv. Res. Inst. Sci. Eng., Waseda Univ.)  
 Ichiro KATAYAMA (KEK)  
 Kazuie KIMURA (Dept. Eng., Univ. Tokyo)  
 Osamu KOYAMA (Katagiri Eng. Co. Ltd.)  
 Satoshi KUBOYAMA (NASDA)  
 Hisaaki KUDO (Fac. Sci., Niigata Univ.)  
 Tadahiro KUROSAWA (Electrotech. Lab., Agency Ind. Sci. Tech.)  
 Toshikatsu MASUOKA (Nichizo Electric & Control Corp.)  
 Sumio MATSUDA (NASDA)  
 Hideo MIKAMI (Sumitomo Heavy Ind., Ltd.)  
 Tadanori MINAMISONO (Grad. Sch. Sci., Osaka Univ.)  
 Hiroari MIYATAKE (KEK)  
 Tetsuya MURAKAMI (Grad. Sch. Sci., Kyoto Univ.)  
 Yuki NAGAI (NASDA)  
 Noriaki NAKAO (KEK)  
 Toru NOMURA (KEK)  
 Jyun-ichi ODAGIRI (KEK)  
 Hideharu OHIRA (NASDA)  
 Koji OISHI (Shimizu Construction Co., Ltd)  
 Katsumi OKA (NASDA)  
 Hiromitsu OOTOMO (NASDA)  
 Kenshi SAGARA (Fac. Sci., Kyushu Univ.)  
 Hideyuki SAKAI (Dept. Phys., Sch. Sci., Univ. Tokyo)  
 Hiroki SATO (NASDA)  
 Eido SHIBAMURA (Saitama Pref. Jr. Coll.)  
 Osamu SHIMADA (NASDA)  
 Hiroyuki SHINDO (NASDA)  
 Tsutomu SHINOZUKA (Cycl. Radioisot. Cen., Tohoku Univ.)  
 Keisuke SUEKI (Inst. Chem., Univ. Tsukuba)  
 Isao SUGAI (KEK)  
 Masami SUZUKI (Irie Koken Co. Ltd.)  
 Sung Chang JEONG (KEK)  
 Hiroaki UTSUNOMIYA (Fac. Sci., Konan Univ.)  
 Masakazu WASHIO (Adv. Res. Inst. Sci. Eng., Waseda Univ.)  
 Yuji YAMAKAWA (Shimizu Construction Co., Ltd)  
 Yu-liang ZHAO (Inst. High Energy Phys., Beijing, China)

*Trainees*

Kentaro ASAI (Adv. Res. Inst. Sci. Eng., Waseda Univ.)  
 Masataka KOBAYASHI (Adv. Res. Inst. Sci. Eng., Waseda Univ.)  
 Masanori KOSHIMIZU (Dept. Eng., Grad. Sch. Eng., Univ. Tokyo)  
 Takehiko KURIBAYASHI (Adv. Res. Inst. Sci. Eng., Waseda Univ.)  
 Masakazu MORI (Adv. Res. Inst. Sci. Eng., Waseda Univ.)  
 Rei UMEBAYASHI (Dept. Eng., Grad. Sch. Eng., Univ. Tokyo)

**Radioisotope Technology Division**

*Head*

Fumio YATAGAI

*Members*

Kuniko MAEDA	Kazuya TAKAHASHI
Shuichi ENOMOTO	Hiroshige TAKEICHI
Masako IZUMI	Teruyo TSUKADA
Hiromitsu HABA* <sup>1</sup>	Takahiro YANAGIYA* <sup>1</sup>
Rieko HIRUNUMA* <sup>2</sup>	Kaori IGARASHI* <sup>2</sup>

Shigeko MORIMOTO\*<sup>2</sup>  
Akihiro NAKAYAMA\*<sup>2</sup>  
Takayuki SOSHI\*<sup>2</sup>

Shinji MOTOMURA\*<sup>2</sup>  
Qiangyan PAN\*<sup>2</sup>  
Masanori TOMITA\*<sup>2</sup>

---

\*<sup>1</sup> Special Postdoctoral Researcher

\*<sup>2</sup> Contract Researcher

*Visiting Members*

Ryohei AMANO (Fac. Med., Kanazawa Univ.)  
Sachiko AMARI (Washington Univ., USA)  
Wenjun DING (Colorado State Univ., USA)  
Kazutoyo ENDO (Showa Pharm. Univ., USA)  
Tatsunori FUKUMAKI (Japan NUS Co., Ltd.)  
Mika FUKUOKA (Tokyo Univ. Fish.)  
Sachiko GOTO (Sch. Pharm. Sci., Nagasaki Univ.)  
Ken-ichi HASEGAWA (Fac. Eng., Hosei Univ.)  
Hiroshi HIDAKA (Fac. Sci., Hiroshima Univ.)  
Seiichiro HIMENO (Fac. Pharm. Sci., Tokushima Bunri Univ.)  
Eiko HIRANO (Japan NUS Co., Ltd.)  
Masahiko HIRASAWA (Natl. Inst. Radiol. Sci.)  
Masamitsu HONMA (Natl. Inst. Health Sci.)  
Naoko IKEDA (Showa Women's Univ.)  
Hiroko INAGE (Int. Life Sci. Inst.)  
Nobuyoshi ISHII (Natl. Inst. Radiol. Sci.)  
Toshiaki ISHII (Natl. Inst. Radiol. Sci.)  
Atsushi ITO (Sch. Eng., Tokai Univ.)  
Hiroyuki KAGI (Grad. Sch. Sci., Univ. Tokyo)  
Kenji KAWABE (Kyoto Pharm. Univ.)  
Osamu KAWAGUCHI (Sch. Med., Keio Univ.)  
Tetsuya KAWATA (Fac. Med., Chiba Univ.)  
Masuo KONDOH (Showa Pharm. Univ.)  
Hideaki MAEKAWA (Natl. Inst. Infect. Dis.)  
Hiroshi MAEZAWA (Fac. Med. Technol., Univ. Tokushima)  
Ken-ichiro MATSUMOTO (Showa Pharm. Univ.)  
Yoshitaka MINAI (Cen. Art. Sci., Musashi Univ.)  
Takeshi MINAMI (Dept. Life Sci., Sch. Sci. Eng., Kinki Univ.)  
Tomohiro NABEKURA (Fac. Pharm. Sci., Niigata Univ. Pharm. Appl. Life Sci.)  
Yuichiro NAGAME (JAERI)  
Tomoko NAKANISHI (Grad. Sch. Agr. Life Sci., Univ. Tokyo)  
Yukiko NAKANISHI (Int. Life Sci. Inst.)  
van Chuyen NGUYEN (Jpn. Women's Univ.)  
Takehiko NOHMI (Natl. Inst. Health Sci.)  
Yasumitsu OGURA (Grad. Sch. Pharm. Sci., Chiba Univ.)  
Takeo OHNISHI (Fac. Biol., Nara Med. Univ.)  
Toshihiro OHTA (Fac. Life Sci., Tokyo Univ. Pharm. Life Sci.)  
Takuya OHYAMA (Grad. Sch. Sci. Technol., Shizuoka Univ.)  
Jun SAITO (Iwatsu Test Instruments Corp.)  
Tomofumi SAKURAGI (Natl. Inst. Radiol. Sci.)  
Hiromu SAKURAI (Kyoto Pharm. Univ.)  
Sadao SHIBATA (Natl. Inst. Radiol. Sci.)  
Hiroshi SHIMIZU (Fac. Sci., Hiroshima Univ.)  
Atsushi SHINOHARA (Dept. Chem., Grad. Sch. Sci., Osaka Univ.)  
Hiroyuki SUZUKI (RI Res. Cen., Chiba Univ.)  
Kazuo T. SUZUKI (Grad. Sch. Pharm. Sci., Chiba Univ.)  
Toshihiro SUZUKI (Meiji Pharm. Univ.)  
Keiko TAGAMI (Natl. Inst. Radiol. Sci.)  
Akihisa TAKAHASHI (Fac. Biol., Nara Med. Univ.)  
Masaaki TAKAHASHI (Grad. Sch. Agr. Biol. Sci., Osaka Pref. Univ.)  
Miho TAKAHASHI (Tokyo Univ. Fish.)  
Yoshio TAKAHASHI (Grad. Sch. Sci., Hiroshima Univ.)

Kaoru TAKAKURA (Div. Natural Sci., Int. Chr. Univ.)  
Atsushi TAKEDA (Sch. Pharm. Sci., Univ. Shizuoka)  
Haruna TAMANO (Sch. Pharm. Sci., Univ. Shizuoka)  
Tadayasu TOGAWA (Meiji Pharm. Univ.)  
Takehiro TOMITANI (Natl. Inst. Radiol. Sci.)  
Shigeo UCHIDA (Natl. Inst. Radiol. Sci.)  
Kohshin WASHIYAMA (Fac. Med., Kanazawa Univ.)  
Mineo YAMASAKI (Nara Med. Univ.)  
Makoto YANAGA (Fac. Sci., Shizuoka Univ.)  
Hiroyuki YASUI (Kyoto Pharm. Univ.)  
Akihiko YOKOYAMA (Fac. Sci., Kanazawa Univ.)  
Shigekazu YONEDA (Natl. Sci. Museum)  
Shozo YOSHIDA (Nara Med. Univ.)  
Takashi YOSHIMURA (Grad. Sch. Sci., Osaka Univ.)

#### *Trainees*

Yusuke ADACHI (Kyoto Pharm. Univ.)  
Jun FUGONO (Kyoto Pharm. Univ.)  
Jun FURUKAWA (Grad. Sch. Agr. Life Sci., Univ. Tokyo)  
Hiroko HASEGAWA (Grad. Sch. Sci., Osaka Univ.)  
Ryoichi HIRAYAMA (Grad. Sch. Sci. Tech., Chiba Univ.)  
Kenichi ISHIBASHI (Meiji Pharm. Univ.)  
Yoshiharu ISOBE (Dept. Radiol. Sci., Ibaraki Pref. Univ.)  
Yoshiyuki KAJITA (Fac. Sci., Shizuoka Univ.)  
Yousuke KANAYANA (Grad. Sch. Med. Sci., Kanazawa Univ.)  
Yoshitaka KASAMATSU (Grad. Sch. Sci., Osaka Univ.)  
Nobuyuki KINUGAWA (Grad. Sch. Sci. Technol., Shizuoka Univ.)  
Keiji MATSUO (Sch. Sci., Osaka Univ.)  
Tsutomu MATSUO (Fac. Sci. Eng., Waseda Univ.)  
Ryuji MINAYOSHI (Fac. Sci., Shizuoka Univ.)  
Aiko NARUTO (Fac. Life Sci., Tokyo Univ. Pharm. Life Sci.)  
Takanori OGI (Grad. Sch. Sci. Technol., Shizuoka Univ.)  
Shigeki OHATA (Meiji Pharm. Univ.)  
Toshitaka OKA (Fac. Sci. Eng., Waseda Univ.)  
Daisuke SAIKA (Sch. Sci., Osaka Univ.)  
Naoko SATOU (Meiji Pharm. Univ.)  
Momoko TAKAHASHI (Div. Natural Sci., Int. Chr. Univ.)  
Yuuki TANI (Grad. Sch. Sci., Osaka Univ.)  
Takae TSUJI (Grad. Sch. Med. Sci., Kanazawa Univ.)  
Makoto YATSUKAWA (Grad. Sch. Sci., Osaka Univ.)  
Hideaki YOSHIDA (Fac. Sci. Eng., Waseda Univ.)

### **Liquid Helium Service Division**

#### *Head*

Yasushige YANO

#### *Members*

Kumio IKEGAMI  
Hiroki OKUNO  
Ken-ichi KATO\*<sup>2</sup>

Masao OTAKE  
Toshiharu TOMINAKA\*<sup>1</sup>  
Kazushiro NAKANO\*<sup>2</sup>

---

\*<sup>1</sup> Contract Researcher

\*<sup>2</sup> Temporary Employee

#### *Visiting Members*

Toshiyuki MITO (Jpn. Nucl. Cycle Dev. Inst.)

## ADVANCED DEVELOPMENT AND SUPPORTING CENTER

### Planning and Promotion Team

#### *Head*

Katsumi SENOO

#### *Members*

Yuji IKEGAMI  
Yoshio NOMIYA  
Susumu SHIMODA  
Seigo SUGAHARA  
Teruo URAI  
Yutaka YAMADA

Tokuji KITSUNAI  
Tsunenobu SHIGA  
Akira SHIRAISHI  
Norio TAJIMA  
Shogo YAMADA

#### *Contract Members*

Naoe KANEKO  
Akira MATSUMOTO  
Tetsuji SASAMOTO  
Saburo TOKIWA  
Tokuji WATANABE

Ushizo KUBO  
Yuzo NIIOKA  
Kiyoji TAKAHASHI  
Sumio YAMAMOTO

### Beam Application Team

#### *Head*

Masaya IWAKI

#### *Members*

Tomohiro KOBAYASHI  
Kowashi WATANABE

Aiko NAKAO

## RESEARCH UNIT

### Image Information Research Unit

#### *Head*

Hirohiko M. SHIMIZU

#### *Members*

Hiromi SATO  
Yoshiyuki TAKIZAWA\*<sup>2</sup>  
Tomohiro ADACHI\*<sup>2</sup>  
Kazuaki IKEDA\*<sup>2</sup>  
Mario E. BERTAINA\*<sup>2</sup>

Shigetomo SHIKI\*<sup>1</sup>  
Masahiko KURAKADO\*<sup>2</sup>  
Takahiro MORISHIMA\*<sup>2</sup>  
Takenao SHINOHARA\*<sup>2</sup>

---

\*<sup>1</sup> Special Postdoctoral Researcher

\*<sup>2</sup> Contract Researcher

#### *Visiting Members*

Seiichirou ARIYOSHI (Grad. Univ. Adv. Stud.)  
Tadashi KIFUNE (Fac. Eng., Shinshu Univ.)  
Hiroaki MYOREN (Fac. Eng., Saitama Univ.)  
Takayuki OKU (JAERI)  
Kenji SAKAI (Dept. Phys., Tokyo Inst. Technol.)  
Tohru TAINO (Fac. Eng., Saitama Univ.)  
Fuyuki TOKANAI (Dept. Phys., Yamagata Univ.)

#### *Trainees*

Kouichi HOSHINO (Dept. Electr. Syst., Saitama Univ.)

## RIKEN BNL Research Center

### *Head*

Tsung-Dao LEE (Director)  
Nicholas P. SAMIOS (Deputy Director)  
Hideto EN'YO (RBRC Associate Director)

## Experimental

### *Group Leader*

Hideto EN'YO

### *Deputy Group Leader*

Gerry M. BUNCE

### *Members*

Yuji GOTO	Takashi ICHIHARA
Atsushi TAKETANI	Yasushi WATANABE
Kiyoshi TANIDA	Yasuyuki AKIBA
Abhay DESHPANDE* <sup>1</sup>	Douglas Edward FIELDS* <sup>2</sup>
Matthias GROSS PERDEKAMP* <sup>2</sup>	Masashi KANETA* <sup>3</sup>
Hisayuki TORII* <sup>4</sup>	Tsuguchika TABARU* <sup>4</sup>
Osamu JINNOUCHI* <sup>3</sup>	Kensuke OKADA* <sup>3</sup>
Brendan FOX* <sup>1</sup>	Hideyuki KOBAYASHI* <sup>4</sup>

### *Visiting Members*

Yoshinori FUKAO (Kyoto Univ.)  
Takuma HORAGUCHI (Tokyo Inst. Technol.)  
Kazuyoshi KURITA (Rikkyo Univ.)  
Naohito SAITO (Kyoto Univ.)  
Zheng LEE (BNL, USA)  
Viktor SIEGLE (Univ. Heidelberg, Germany)  
Jens S. LANGE (BNL, USA)  
Akio OGAWA (BNL, USA)

## Theory

### *Group Leader*

Tsung-Dao LEE

### *Deputy Group Leader*

Anthony J. BALTZ

### *Members*

Steffen A. BASS* <sup>2</sup>	Christopher DAWSON* <sup>1</sup>
Takashi IKEDA* <sup>4</sup>	Tetsufumi HIRANO* <sup>4</sup>
Yasumichi AOKI* <sup>3</sup>	Kazunori ITAKURA* <sup>3</sup>
Thomas BLUM* <sup>1</sup>	Rajagopal VENUGOPALAN* <sup>2</sup>
Sangyong JEON* <sup>2</sup>	Alexander KUSENKO* <sup>2</sup>
Yukio NEMOTO* <sup>3</sup>	Jun-ichi NOAKI* <sup>3</sup>
Stefan KRETZER* <sup>3</sup>	Thomas SCHAEFER* <sup>2</sup>
Mikhail A. STEPANOV* <sup>2</sup>	Takanori SUGIHARA* <sup>4</sup>
Ubirajara van KOLCK* <sup>2</sup>	Peter PETRECZKY* <sup>1</sup>
Tilo WETTIG* <sup>2</sup>	Werner VOGELSANG* <sup>1</sup>
Norikazu YAMADA* <sup>3</sup>	Taku IZUBUCHI* <sup>2</sup>

### *Visiting Members*

Miklos GYULASSY (Columbia Univ., USA)  
Robert L. JAFFE (Massachusetts Inst. Technol., USA)  
Robert MAWHINNEY (Columbia Univ., USA)  
Edward SHURYAK (State Univ. New York, Stony Brook, USA)

Shigemi OHTA (KEK)  
Hiroshi YOKOYA (Hiroshima Univ.)  
Yoshitaka HATTA (Kyoto Univ.)  
Konstantinos ORGINOS (Massachusetts Inst. Technol., USA)

*Administration*

Pamela ESPOSITO (Secretary)  
Rae GREENBERG (Assistant)  
Tammy Anne HEINZ (Secretary)  
Taeko ITO (Secretary)

*Administrative Manager*

Kiyofumi TSUTSUMI  
Motohide YOKOTA

*Deputy Administrative Manager*

Chiharu SHIMOYAMADA

---

\*<sup>1</sup> RIKEN BNL Fellow, \*<sup>2</sup> RHIC Physics Fellow,  
\*<sup>3</sup> Research Associate, \*<sup>4</sup> Special Postdoctoral Researcher

**SAFETY DIVISION**

*Head*

Hiroshi SAWA

*Deputy Director*

Masayuki SHIMAGAKI  
Makoto MIYAGAWA

**Laboratory Safety Section**

*Head*

Yoshitomo UWAMINO

*Members*

Hajime YOSHIKI  
Kunio FUKASAWA

Nobuyasu YAMAGISHI

**Research Ethics Section**

*Head*

Satoru KAGAYA

*Members*

Akira OZAKI  
Hiroko KATOU

Shigemi SHINOHARA  
Mika SUZUKI

## AUTHOR INDEX

- ABE Tomoko 阿部知子 113, 147, 148, 149, 150, 151, 152  
ABU-IBRAHIM Badawy 30  
ADACHI Tadashi 足立 匡 110  
ADACHI Yusuke 安達祐介 117  
AIDALA Christine 229  
AIHARA Toshimitsu 藍原利光 3, 265, 267, 269  
AKAISHI Yoshinori 赤石義紀 34  
AKEMANN Gernot 211  
AKIBA Yasuyuki 秋葉康之 232, 234, 236, 249, 251, 254  
AKIYAMA Kazuhiko 秋山和彦 130  
AKIYAMA Takahiro 秋山隆宏 159  
AKIYOSHI Hiromichi 秋吉啓充 47, 48, 49, 62  
ALEKSEEV Igor G. 245  
AMANO Ryohei 天野良平 116, 135  
AMEMIYA Hiroshi 雨宮 宏 36, 37, 38, 39, 40  
ANDO Kozo 安藤剛三 103  
ANDO Yoshiaki 安藤嘉章 47, 48, 66, 69  
AOI Nori 青井 考 44, 46, 47, 48, 49, 50, 53, 55, 56,  
57, 58, 59, 60, 62, 63, 66, 69, 76,  
77, 78, 153  
AOKI Kazuya 青木和也 251, 255  
AOKI Yasumichi 青木保道 220  
ARAI Masato 新井理太 134  
ARIMA Akito 有馬朗人 24, 25  
ASAHI Koichiro 旭 耕一郎 71, 79, 112, 160, 161, 170,  
171, 175  
ASAI Keisuke 浅井圭介 99, 101  
ASAI Masato 浅井雅人 130  
ASANO Nagayoshi 浅野長祥 118  
AZUMA Toshiyuki 東 俊行 95  
BABA Hidetada 馬場秀忠 46, 48, 49, 50, 53, 54, 55,  
56, 57, 58, 59, 60, 61, 62,  
63, 64, 66, 68, 69, 72, 74,  
75, 76, 77, 78, 155, 187  
BAKER Mark D. 254  
BAKULE Pavel 176  
BARISH Kenneth 255  
BASS Steffen A. 204  
BAUER Frank 229  
BAZILEVSKY Alexander 229, 231  
BAZIN Daniel 50, 59, 60  
BEAUMEL Didier 55, 63  
BENTZ Wolfgang 32, 33  
BHANG Hyeon-Chang 84  
BLUMENFELD Yorick 55, 63  
BOGDANOV Dmitri D. 41  
BOYD Richard N. 67  
BOYLE Peter A. 221  
BRÜCHLE Willy 130  
BRAVAR Allessandro 243, 245  
BROWN B. Alex 17  
BROWN David S. 225  
BUENKER Robert J. 94  
BUNCE Gerry 222, 243, 245  
CAMARD Xavier 240  
CASARES Antonio 163  
CHELNOKOV Maxim L. 41, 42, 43  
CHEN Dong 221  
CHIBA Masami 千葉将允 70  
CHIBA Yoshiaki 千葉好明 308  
CHIMI Yasuhiro 知見康弘 97  
CHRIST Norman H. 221  
CHUJO Tatsuya 中條達也 235, 237  
CIANCIOLO Vince 224  
CLARK Michael 221  
COHEN Sid D. 221  
CRISTIAN Calin 221  
d'ENTERRIA David 240  
DATTA Saumen 212  
DAVID Gabor 240  
DEMICHI Kimihiko 出道仁彦 46, 53, 56, 62, 66, 69, 76  
DESHPANDE Abhay 229, 246, 255, 256  
DHAWAN Satish 245  
DINH DANG Nguyen 24, 25  
DOMBRÁDI Zsolt 53, 54, 56, 61  
DONG Zhihua 221  
DOTÉ Akinobu 土手昭伸 34  
DUDNIK Oleksiy Volodimirovich 168  
DZORDZHADZE Vasily 224  
EATON Gordon H. 91  
EBIHARA Chiaki 海老原千晶 118  
ELEKES Zoltán 46, 53, 54, 55, 56, 61, 63, 66, 69, 76,  
77, 78  
EMORI Shoken 江守昭憲 71, 160, 171, 175  
EMOTO Takashi 江本 隆 81, 179, 291  
EN'YO Hideto 延與秀人 85, 86, 87, 222, 232, 249, 251,  
257  
ENOMOTO Shuichi 榎本秀一 113, 114, 115, 116, 117,  
118, 119, 120, 121, 122,  
123, 124, 125, 127, 128,  
130, 132, 134, 135, 136,  
137, 138, 139, 141  
EREMIN Vladimir 251  
ESUMI Shinichi 江角晋一 226

- FÜLÖP Zsolt 47, 48, 53, 54, 56, 61, 64, 66, 69  
 FAMIANO Michael A. 67  
 FANG Deqing 方 德清 51, 52, 70, 159  
 FIELDS Douglas E. 248  
 FOMICHEV Andrey S. 41, 42, 43  
 FOX Brendan 229, 231, 246  
 FRANKLIN Gregg 84  
 FRIES Rainer J. 204  
 FUGONO Jun 畚野 純 117  
 FUJII Makiko 藤井まき子 118  
 FUJII Masashi 藤井雅史 168  
 FUJII Shinichiro 藤井新一郎 22, 23  
 FUJIMAKI Masaki 藤巻正樹 3, 5, 275, 277, 279  
 FUJINAWA Tadashi 藤縄 雅 7, 285, 289  
 FUJISHIMA Shiro 藤島史郎 285  
 FUJITA Shin 藤田 新 281, 317  
 FUJIWARA Kohei 藤原康平 249  
 FUKAO Yoshinori 深尾祥紀 229, 246, 251  
 FUKAZAWA Yasushi 深沢泰司 88  
 FUKUCHI Tomonori 福地知則 46, 64, 74, 75, 77, 78, 79  
 FUKUDA Mitsunori 福田光順 51, 52  
 FUKUDA Naoki 福田直樹 50, 53, 55, 59, 60, 62, 63, 66, 69  
 FUKUNISHI Nobuhisa 福西暢尚 3, 5, 95, 143, 144, 145, 146, 273, 276, 283, 285  
 FUKUYAMA Yoshimitsu 福山祥光 173  
 FUKUZAWA Seiji 福澤聖児 5  
 FUTAKAMI Udai 二上宇内 66, 69  
 GARA Alan 221  
 GEISSEL Hans 156  
 GELBERG Adrian 53  
 GIBELIN Julien 54, 55, 56, 61, 63, 76  
 GILLITZER Albrecht 156  
 GLENN Andrew 224  
 GOKA Tateo 五家建夫 168  
 GOLOVKOV Mikhail S. 41, 42, 43  
 GOMI Tomoko 五味朋子 46, 47, 48, 49, 50, 53, 55, 56, 59, 60, 62, 63, 66, 69, 76  
 GOMIKAWA Kenji 五味川健治 84, 156  
 GONAI Takeru 郷内 武 152  
 GONO Yasuyuki 郷農靖之 64, 68, 75, 79, 136, 137, 138, 141  
 GORIELY Stephane 27  
 GORSHKOV Vladimir A. 41  
 GOTO Akira 後藤 彰 3, 5, 276, 283, 284, 285, 287  
 GOTO Shin-ichi 後藤真一 80, 130  
 GOTO Yuji 後藤雄二 229, 231, 232, 246, 249, 251, 254, 257  
 GROSSE PERDEKAMP Matthias 223, 255, 259, 260  
 GUIMARÃES Valdir 65  
 HABA Hiromitsu 羽場宏光 80, 111, 113, 114, 117, 120, 122, 123, 128, 130, 132, 135, 136, 263  
 HACHIYA Takashi 蜂谷 崇 236  
 HAHN Kevin Inskik 64  
 HAMAGAKI Hideki 浜垣秀樹 240, 257  
 HAMAGAKI Manabu 浜垣 学 177  
 HAMANAKA Hiromi 浜中廣見 191  
 HANAOKA Fumio 花岡文雄 143, 144  
 HARA Mitsuo 原 光雄 263  
 HASEBE Hiroo 長谷部裕雄 3, 7, 283  
 HASEBE Nobuyuki 長谷部信行 193  
 HASEGAWA Hirokazu 長谷川浩一 46, 50, 53, 56, 59, 60, 62, 66, 69, 76  
 HASEGAWA Kenichi 長谷川賢一 191  
 HASEYAMA Tomohito 長谷山智仁 71, 161, 171, 175  
 HASHIMOTO Koichi 橋本耕一 216  
 HASHIMOTO Tomonori 橋本知典 134  
 HASUKO Kazumi 蓮子和巳 259, 260, 261  
 HATANO Michio 波田野道夫 44, 181  
 HATTA Yoshitaka 八田佳孝 205  
 HAYANO Ryugo S. 早野龍五 84, 156  
 HAYASHI Takeshi 林 剛史 84  
 HE Jianjun 何 建軍 64, 65, 68, 72, 75  
 HEMMI Masatake 逸見政武 3, 275  
 HEUSER Johann M. 249, 250, 251, 254  
 HIGURASHI Yoshihide 日暮祥英 3, 5, 47, 48, 49, 62, 66, 69, 265, 267, 269  
 HIRAI Masaaki 平井正明 47, 48  
 HIRAI Masanori 平井正紀 197  
 HIRAI Toshiyuki 平井利幸 130  
 HIRAMOTO Takuji 平本卓嗣 193  
 HIRANO Tetsufumi 平野哲文 203  
 HIRASAWA Masahiko 平澤雅彦 141  
 HIRATA Masaru 平田 勝 130  
 HIRUNUMA Rieko 蛭沼利江子 113, 114, 115, 117, 119, 120, 123, 132, 135, 136, 139  
 HOKOIWA Naho 鉾岩奈穂 64, 68, 75  
 HOMMA Kensuke 本間謙輔 239  
 HONDA Ichiro 本多一郎 149  
 HONG Soojing 洪 秀徵 88, 167  
 HONMA Michio 本間道雄 17, 19  
 HORAGUCHI Takuma 洞口拓磨 229, 234  
 HORIKAWA Tai 堀川 敦 32  
 HORIOKA Kazuhiko 堀岡一彦 264  
 HORIUCHI Hisashi 堀内 昶 14



- HORVÁTH Ákos 54, 61  
HOSAKA Atsushi 保坂 淳 21  
HOSHINO Masamitsu 星野正光 105  
HOSOI Motooki 細井基興 159  
HOSTEINS Pierre 173  
HOWARD Meredith E. 67  
HUANG Haixin 245  
HUGHES Vernon 245  
ICHIHARA Takashi 市原 卓 189, 257  
ICHIKAWA Shin-ichi 市川進一 130  
ICHIKAWA Yuichi 市川雄一 44, 54, 61, 77, 78, 153  
IDEGUCHI Eiji 井手口栄治 46, 54, 61, 74, 75, 80, 301  
IEKI Kazuo 家城和夫 48, 49, 66, 69, 187  
IGARASHI Kaori 五十嵐香織 113, 114, 115, 132, 136, 139  
IGO George 245  
IIDA Kei 飯田 圭 30  
IIYAMA Masamitsu 飯山真充 125  
IKEDA Kiyomi 池田清美 12, 13, 20, 21  
IKEDA Naomi 池田直美 98  
IKEDA Takashi 池田 貴 208  
IKEDA Takuichiro 池田拓一郎 44, 45, 82  
IKEDA Tokihiro 池田時浩 95, 103, 104, 310  
IKEGAMI Kumio 池上九三男 285  
IKEZAWA Eiji 池沢英二 3, 5, 7, 265, 273  
IMAI Ken'ichi 今井憲一 232, 243  
IMAI Nobuaki 今井伸明 47, 48, 49, 50, 53, 56, 59, 60, 66, 69, 76, 153  
IMAO Hiroshi 今尾浩士 91  
INABE Naohito 稲辺尚人 3, 5, 98, 283, 285  
INAMURA Takashi Thomas 稲村 卓 263  
INOUE Hokuto 井上北斗 88  
INOUE Masato 井上正人 102  
ISHIBASHI Kenichi 石橋健一 120  
ISHIDA Carolina 74  
ISHIDA Katsuhiko 石田勝彦 90, 91, 176  
ISHIDA Yoshihisa 石田佳久 163, 173  
ISHIHARA Masayasu 石原正泰 46, 47, 48, 49, 50, 53, 56, 59, 60, 62, 66, 69, 77, 78  
ISHII Nobuyoshi 石井伸昌 124  
ISHII Noriyoshi 石井理修 32, 33, 213  
ISHIKAWA Katsutoshi 石川勝利 119  
ISHIKAWA Kazuhiro 石川和宏 53, 55, 63, 66, 69, 84  
ISHIKAWA Norito 石川法人 97  
ISHIMOTO Shigeru 石元 茂 84  
ISSHIKI Hiroshi 一色 博 5, 275  
ITAGAKI Naoyuki 板垣直之 49  
ITAHASHI Kenta 板橋健太 84, 90, 156  
ITO Makoto 伊藤 誠 12, 15  
ITO Masayuki 伊藤正之 128  
ITO Sachiko 伊藤祥子 281, 317  
ITO Toshiji 伊藤寿二 317  
ITO Yuji 伊藤祐司 151  
ITOH Keisuke 伊藤圭介 44, 45, 82  
IWAI Yoshio 岩井良夫 103, 104  
IWASA Naohito 岩佐直仁 46, 47, 48, 49, 51, 52, 54, 57, 58, 61, 62, 66, 69, 77, 78  
IWASA Tsutomu 岩佐 力 317  
IWASAKI Hironori 岩崎弘典 44, 46, 47, 48, 49, 53, 54, 56, 57, 58, 61, 62, 64, 66, 68, 69, 74, 75, 76, 77, 78, 153, 155  
IWASAKI Masahiko 岩崎雅彦 84, 90, 91, 109, 156, 176  
IWASE Akihiro 岩瀬彰宏 97  
IWATA Yoshiyuki 岩田佳之 47, 48  
IWAZAKI Aiichi 岩崎愛一 207  
IZAWA Masaaki 伊澤正陽 306  
IZUBUCHI Taku 出淵 卓 216, 217  
IZUMI Masako 泉 雅子 144, 145, 146  
IZUMIKAWA Takuji 泉川卓司 51, 52, 159  
JAYANTHI Udaya B. 167  
JEON Sangyong 錢 相蓉 201  
JIA Jianguyong 賈 江湧 233  
JIMBO Shimon 神保志文 111  
JINNOUCHI Osamu 陣内 修 225, 243, 245, 247, 257  
JOÓ Balint 221  
JUNG Chulwoo 221  
KACZMAREK Olaf 212  
KAGEYAMA Kensuke 蔭山健介 96  
KAGEYAMA Tadashi 影山 正 3, 5, 267  
KAJI Daiya 加治大哉 80, 132  
KAKUTANI Nobukazu 角谷暢一 297, 299  
KAMADA Hiroyuki 鎌田裕之 22  
KAMBARA Tadashi 神原 正 95, 96, 97, 105, 173  
KAMEDA Daisuke 亀田大輔 71, 79, 112, 161, 171, 175  
KAMETANI Soichiro 亀谷聡一朗 240  
KAMEYA Toshiaki 亀谷壽昭 150  
KAMIGAITO Osamu 上垣外修一 3, 5, 265, 284, 285  
KAMIHARA Nobuyuki 神原信幸 224  
KAMINAGA Shigeto 神長誉人 226  
KANAI Yasuyuki 金井保之 95, 96, 103, 104, 105, 173  
KANAMITSU Hiroaki 金光裕昭 97  
KANAYAMA Yousuke 金山洋介 135  
KANEKO Emi 金子恵美 53  
KANEKO Tetsuya 金子哲也 130  
KANETA Masashi 金田雅司 238

- KANNO Akira 菅野 明 150
- KANNO Shouko 菅野祥子 46, 48, 49, 53, 56, 57, 58,  
61, 62, 66, 69, 76, 77, 78
- KANO Hiroyuki 狩野博之 249, 253
- KANUNGO Rituparna 42, 43, 51, 52, 54, 61, 70, 77, 78,  
80
- KARSCH Frithjof 212
- KASAMATSU Yoshitaka 笠松良崇 134, 263
- KASE Masayuki 加瀬昌之 3, 5, 7, 98, 99, 101, 265,  
267, 269, 273, 275, 277,  
279, 281, 283, 285, 289,  
291, 310, 317
- KASHIYAMA Osamu 櫻山 修 79
- KASUMI Masakazu 霞 正一 152
- KATŌ Kiyoshi 加藤幾芳 12, 13
- KATAYAMA Ichiro 片山一郎 106, 173
- KATAYAMA Takeshi 片山武司 36, 37, 38, 39, 40, 107,  
264, 271, 308, 310, 314
- KATAYAMA Takeshi 片山武士 84
- KATO Go 加藤 剛 71, 171, 175
- KATO Hiroshi 加藤 博 167, 168
- KATO Koichi 加藤公一 240
- KATO Mineo 加藤岑生 91
- KATO Reizo 加藤礼三 109
- KATO Seigo 加藤静吾 64, 65, 68, 75
- KATO Toshiyuki 加藤俊幸 70
- KATORI Kenji 鹿取謙二 80
- KAWABATA Takahiro 川畑貴裕 44, 45, 82, 251
- KAWAGUCHI Takeo 川口武男 310
- KAWAHARADA Madoka 川原田 円 88
- KAWAI Shoko 河合祥子 54, 56, 61, 77, 78
- KAWAKAMI Hirokane 川上宏金 173
- KAWAMOTO Kanichi 川本完一 289
- KAWAMURA Naritoshi 河村成肇 91
- KAWASAKI Hiroaki 河崎洋章 53
- KAWASAKI Takeo 川崎健夫 249
- KIBE Michiya 木部道也 68, 75, 136, 137, 138
- KIDERA Masanori 木寺正憲 3, 5, 265, 267, 269
- KIJIMA Go 木島 剛 71, 171, 175
- KIKUCHI Kaori 菊地 郁 149
- KIKUCHI Takashi 菊池崇志 264
- KIKUNAGA Hidetoshi 菊永英寿 130, 134, 263
- KIM Changhoan 221
- KIM DongJo 224
- KIM Jong Chan 金 鍾贊 65
- KIM So-Young 150
- KIMURA Kazuie 木村一宇 99, 101
- KIMURA Kikuo 木村喜久雄 159
- KIMURA Masaaki 木村真明 14
- KIMURA Mineo 季村峯生 93, 94
- KIMURA Shuichi 木村修一 114, 115
- KINOSHITA Norikazu 木下哲一 130, 134
- KINUGAWA Nobuyuki 衣川信之 119
- KISHIDA Takashi 岸田 隆 53, 56, 75, 79
- KITAZAWA Masakiyo 北沢正清 206
- KIYOMICHI Akio 清道明男 235, 237, 257
- KOBAYASHI Hideyuki 小林秀幸 225
- KOBAYASHI Hiroshi 小林 寛 47, 48
- KOBAYASHI Kiyoshi 小林清志 5
- KOBAYASHI Masanori 小林正規 193
- KOBAYASHI Tomohiro 小林知洋 9
- KOBAYASHI Toshio 小林俊雄 50, 59, 60
- KOBAYASHI Yoshio 小林義男 71, 79, 111, 112, 171, 175
- KOBAYASHI-KOMIYAMA Misaki 小林-込山美咲 3, 5,  
277,  
279,  
291
- KOHAMA Akihisa 小濱洋央 31
- KOHAMA Mitsuhiro 小浜光洋 167
- KOHARA Shigeo 小原重夫 3, 5, 284
- KOIDE Tomoi 小出知威 206
- KOIKE Yoji 小池洋二 110
- KOIZUMI Tetsuo 小泉哲夫 107
- KOJIMA Takao M. 小島隆夫 96, 102, 173
- KOKUBUN Motohide 国分紀秀 88
- KOKUSEN Hisao 國仙久雄 125
- KOMAKI Ken-ichiro 小牧研一郎 95, 102, 103
- KOMATSU Seiji 小松征史 97
- KOMATSU Yu 小松 優 125, 127
- KOMATSUBARA Tetsuro 小松原哲郎 74
- KONDO Chikara 近藤 力 95
- KONDO Yousuke 近藤洋介 50, 53, 54, 55, 59, 60, 61,  
63, 66, 69, 84
- KONDOH Masuo 近藤昌夫 118
- KORSHENINNIKOV Alexey A. 41, 42, 43
- KOSEKI Tadashi 小関 忠 81, 179, 306, 308
- KOSHIMIZU Masanori 越水正典 99, 101
- KOTAKA Yasuteru 小高康熙 5
- KOTOKU Jun'ichi 古徳純一 167
- KOURA Hiroyuki 小浦寛之 11, 80
- KOUZU Hideo 神津秀雄 301
- KOYAMA Ryo 小山 亮 51, 52
- KRATZ Jens Von 130
- KRETZER Stefan 200
- KUBO Kenya M. 久保謙哉 112
- KUBO Toshiyuki 久保敏幸 50, 53, 55, 56, 59, 60, 63,  
66, 69, 74, 76, 77, 78, 173,  
293, 295, 297, 299, 301,

- 303, 305
- KUBOKI Hironori 久保木浩功 44, 45
- KUBONO Shigeru 久保野 茂 46, 48, 49, 57, 58, 64,  
65, 66, 68, 69, 72, 75,  
183
- KUBOYAMA Satoshi 久保山智司 98
- KUDO Hisaaki 工藤久昭 80, 130
- KUMAGAI Keiko 熊谷桂子 291
- KUNIBU Makoto 國分 誠 48, 49, 62, 66, 69
- KUNIHIRO Teiji 国広悌二 206
- KURAKADO Masahiko 倉門雅彦 157
- KURATA-NISHIMURA Mizuki 倉田-西村美月 65, 67,  
68, 72,  
75, 183
- KURITA Kazuyoshi 栗田和好 46, 53, 56, 57, 58, 66,  
69, 76, 77, 78, 81, 161,  
179, 243, 245, 247
- KURIYAMA Toru 栗山 透 299
- KUROKAWA Meiko 黒川明子 46, 48, 57, 58, 62, 74
- KUSAKA Kensuke 日下健祐 293, 295, 297, 299, 301,  
303, 305
- KUZMIN Evgueni A. 41, 42, 43
- LANGE Jens Soeren 259, 260
- LEE Chun-Sik 李 春植 64, 65, 68
- LEE Eun Kyung 李 恩敬 64
- LEE Ju-Hahn 李 柱漢 64, 65, 68
- LENZ Frieder 35
- LEVKOVA Ludmila 221
- LI Zheng 245, 249, 251
- LIAO Xiaodong 221
- LIHITENTHALER Rubens Filho 65
- LIMA Victor 55, 63
- LINDBERG Karl 156
- LIU Guo-Feng 221
- LIU Zhong 劉 忠 47, 48
- LOZOWSKI William 245
- MÖHL Dieter 314
- MÜLLER Berndt 204
- MACKAY William W. 245
- MADOKORO Hideki 間所秀樹 28
- MADZUNKOV Stojan 105
- MAEDA Kuniko 前田邦子 191
- MAEDA Yukie 前田幸重 44, 45
- MAIE Takeshi 真家武士 5, 7
- MAKDISI Yousef I. 243
- MAKIMURA Shunsuke 牧村俊助 176
- MAKISHIMA Kazuo 牧島一夫 88, 167
- MAKOCHEKANWA Casten 93
- MALYKHINA Tetyana Vasylivna 168
- MASUDA Hideki 益田秀樹 103, 104
- MASUOKA Toshikatsu 益岡俊勝 291
- MATSUDA Yasuyuki 松田恭幸 84, 90, 91, 176
- MATSUFURU Hideo 松古栄夫 219
- MATSUI Nobuyuki 松井信行 44, 45
- MATSUMOTO Haruhisa 松本晴久 168
- MATSUMOTO Takashi 松元貴志 240
- MATSUO Yukari 松尾由賀利 163, 173
- MATSUYAMA Tomoki 松山知樹 147
- MATSUYAMA Yuuichi U. 松山裕一 46, 48, 49, 56, 62,  
66, 69, 76
- MATSUZAKI Teiichiro 松崎禎市郎 90, 91, 176
- MAWHINNEY Robert D. 221
- MESHKOV Igor 314
- MICHIMASA Shin'ichiro 道正新一郎 46, 48, 49, 53,  
56, 57, 58, 62,  
64, 66, 68, 69,  
72, 74, 75, 76,  
77, 78, 155
- MIKAMI Hideo 三神英夫 285
- MILLER Katie 46
- MINEMURA Toshiyuki 峯村俊行 46, 47, 48, 49, 53,  
56, 57, 58, 62, 64,  
66, 69, 76
- MINEO Hirobumi 峯尾浩文 33
- MIODUSZEWSKI Saskia 240
- MITSUMOTO Toshiaki 三頭聰明 263
- MITSUMOTO Toshinori 密本俊典 285
- MITTIG Wolfgang 41, 42, 43
- MIURA Motooki 三浦元隆 50, 53, 59, 60, 66, 69
- MIYACHI Takashi 宮地 孝 193
- MIYAKE Yasuhiro 三宅康博 176
- MIYAMOTO Yutaka 宮本ユタカ 130
- MIYASAKA Hiromasa 宮坂浩正 88, 167
- MIYAZAWA Yoshitoshi 宮澤佳敏 285
- MIYAZAWA Yutaka 宮沢 豊 113, 149, 150, 151, 152
- MIYOSHI Hisanori 三好永哲 71, 79, 112, 161, 171, 175
- MIZOI Yutaka 溝井 浩 62, 293, 295, 297, 299, 301,  
303, 305
- MIZUSAKI Takahiro 水崎高浩 17, 19
- MOHRI Akihiro 毛利明博 102
- MONMA Shigeki 門間茂樹 299
- MOON Jun Young 文 俊永 64, 65, 68, 75
- MORIKAWA Tsuneyasu 森川恒安 79
- MORIMATSU Osamu 森松 治 207
- MORIMOTO Kouji 森本幸司 42, 43, 70, 74, 80
- MORISHIMA Yuki 森島由紀 98
- MORITA Kosuke 森田浩介 80
- MOTIZUKI Yuko 望月優子 27, 28

- MOTOBAYASHI Tohru 本林 透 1, 46, 47, 48, 49, 50,  
53, 54, 55, 56, 57,  
58, 59, 60, 61, 62,  
63, 66, 69, 76, 77,  
78
- MOTOMURA Shinji 本村信治 79, 136, 137, 138, 139,  
141
- MURAKAMI Hiroyuki 村上浩之 47, 66, 69
- MURAKAMI Tetsuya 村上哲也 46
- MURAO Satoshi 村尾 智 191
- MURASAWA Satoshi 村澤 哲 193
- MURATA Jiro 村田次郎 71, 161, 171, 175
- MUTO Ryotaro 武藤亮太郎 85, 86, 87
- MYO Takayuki 明 孝之 13
- NAGAME Yuichiro 永目諭一郎 130
- NAGAMINE Kanetada 永嶺謙忠 90, 91, 110, 176
- NAGASE Makoto 長瀬 誠 3, 5, 273
- NAGASHIMA Atsushi 永島 敦 193
- NAGATA Yujiro 永田勇二郎 111
- NAKAGAWA Takahide 中川孝秀 3, 5, 265, 267, 269
- NAKAHARA Hiromichi 中原弘道 130
- NAKAI Yoichi 中井陽一 95, 96, 103, 104, 173
- NAKAJIMA Mitsuo 中島充夫 264
- NAKAJIMA Motoki 中島基樹 167
- NAKAJIMA Noriaki 中島典昭 219
- NAKAMURA Takashi 中村貴志 106, 173
- NAKAMURA Takashi 中村隆司 48, 49, 50, 53, 55, 59,  
60, 62, 63, 66, 69, 84
- NAKAMURA Takeshi 仲村武志 317
- NAKAMURA Tomoaki 中村智昭 239
- NAKANISHI Takashi 中西 孝 263
- NAKAYAMA Akihiro 中山明弘 117, 121, 122
- NARA Yasushi 奈良 寧 203
- NARUKI Megumi 成木 恵 85, 86, 87
- NARUTO Aiko 成戸愛子 145
- NEMOTO Yukio 根本幸雄 206, 214, 219
- NIIGAKI Megumi 新垣 恵 102
- NIIKURA Megumi 新倉 潤 74, 77, 78, 155
- NIKOLSKII Evgueni Yu. 41, 42, 43
- NINOMIYA Kazuhiko 二宮和彦 134
- NISHI Yuji 西 勇二 67
- NISHIDA Minoru 西田 稔 5, 275
- NISHIKAWA Tetsuo 西川哲夫 207
- NISHIMURA Shunji 西村俊二 65, 67, 68, 72, 75, 183
- NISHINAKA Ichiro 西中一朗 130
- NISHINO Haruki 西野玄記 78
- NISHIO Kazuto 西尾和人 120
- NISHIO Kazuyuki 西尾和之 103, 104
- NOAKI Jun-Ichi 野秋淳一 218
- NODA Koji 野田耕司 173
- NOGUUCHI Motoko 野口基子 119
- NONAKA Chiho 野中千穂 204
- NORO Yoshihiko 野呂良彦 111
- NOTANI Masahiro 野谷将広 46, 53, 54, 56, 57, 58, 61,  
62, 64, 65, 66, 68, 69, 72,  
75, 76
- ODAGIRI Jun-ichi 小田切淳一 277
- ODAHARA Atsuko 小田原厚子 46, 64, 75, 79, 136,  
137, 138
- OGANESSIAN Yuri Ts. 41
- OGAWA Akio 小川暁生 259, 260
- OGAWA Yoko 小川洋子 21
- OGI Takanori 小木貴憲 119
- OGILVIE Craig A. 254
- OGIWARA Kiyoshi 荻原 清 9
- OGLOBLIN Alexey A. 41, 42, 43
- OHATA Shigeki 大畑茂樹 120
- OHIRA Hideharu 大平秀春 98
- OHIRA Seiko 大平聖子 109
- OHKI Tomonori 大木智則 3
- OHNISHI Hiroaki 大西宏明 89, 249, 251, 254
- OHNISHI Jun-ichi 大西純一 285, 287
- OHNISHI Tetsuya 大西哲哉 44, 51, 52, 54, 56, 61, 70,  
74, 80, 81, 159, 179
- OHNO Masanori 大野雅功 88
- OHSEMOCHI Koichi 大勢持光一 299
- OHSHIRO Yukimitsu 大城幸光 5, 271
- OHTA Koichi 太田浩一 35
- OHTA Ryuichi 太田隆一 5
- OHTA Shigemi 太田滋生 220, 221
- OHTANI Munehisa 大谷宗久 207
- OHTANI Shunsuke 大谷俊介 106, 173
- OHTOMO Kiyotaka 大友清隆 308
- OHTSUBO Takashi 大坪 隆 51, 52, 159
- OHTSUKI Tsutomu 大槻 勤 263
- OHYAMA Takuya 大山拓也 119
- OI Makito 大井万紀人 26
- OKA Katsumi 岡 克己 98
- OKADA Hiromi 岡田裕美 243, 251
- OKADA Hiroyuki 岡田宏之 193
- OKADA Kensuke 岡田謙介 229, 231, 233
- OKADA Kunihiro 岡田邦宏 106, 173
- OKADA Shinji 岡田信二 84
- OKADA Takuya 岡田卓也 111
- OKAMOTO Ryoji 岡本良治 22, 23
- OKAMURA Hiroyuki 岡村弘之 44, 276
- OKAMURA Masahiro 岡村昌宏 107, 241
- OKUDAIRA Osamu 奥平 修 193

- OKUNO Hiroki 奥野広樹 3, 5, 285, 287  
 OKUYAMA Toshihisa 奥山利久 303, 305  
 ONG Hooi Jin 王 惠仁 53, 56, 57, 58, 76, 77, 78, 153  
 ONISHI Takeo K. 大西健夫 44, 53, 76, 77, 78, 153  
 ONO Fumihisa 小野文久 97  
 ONO Mari 大野真里 116  
 ONO Sawako 小野佐和子 130  
 ORGINOS Konstantinos 220  
 OSHIMA Nagayasu 大島永康 102, 173  
 OTA Shinsuke 大田晋輔 46, 56, 57, 58, 66, 69, 74, 76,  
 77, 78, 155  
 OTOMO Hiromitsu 大友洋光 98  
 OTSUKA Takaharu 大塚孝治 17, 18, 19  
 OURA Yasuji 大浦泰嗣 130  
 OUTA Haruhiko 應田治彦 84  
 OYAMA Hitoshi 大山 等 103, 173  
 OYAMA Ken 大山 健 240  
 OYAMADA Kazuyuki 小山田和幸 3, 7, 275  
 OYAMATSU Kazuhiro 親松和浩 30  
 OZAWA Akira 小沢 顕 42, 43, 51, 52, 54, 56, 61, 70,  
 74, 76, 80, 159  
 OZAWA Kyoichiro 小沢恭一郎 240  
 OZAWA Shuichi 小澤修一 47, 48, 107, 177  
 PERSIKOV Valentin Kostyantynovich 168  
 PETER Jaen C. 80  
 PETRECZKY Peter 212  
 PETROV Konstantin 212, 221  
 POLLACCO Emanuel 42, 43  
 PURSCHKE Martin L. 240  
 QUINN Brian 84  
 RADEKA Veljko 251  
 READ Ken 224  
 REITZNER Diane 67  
 RESCIA Sergio 245  
 RODIN Aleksander M. 41, 42, 43  
 ROSER Thomas 245  
 ROUSSEL-CHOMAZ Patricia 41, 42, 43  
 RYKOV Vladimir L. 232, 249, 251, 254  
 RYUTO Hiromichi 龍頭啓充 3, 5, 143, 144, 146, 276,  
 283, 285  
 SAITO Akito 齋藤明登 46, 48, 49, 50, 53, 55, 56, 57,  
 58, 59, 60, 62, 63, 66, 69, 76,  
 77, 78  
 SAITO Hiroyuki 齋藤宏之 149, 150  
 SAITO Hiroyuki 齋藤宏之 113, 147, 151, 152  
 SAITO Naohito 齋藤直人 232, 243, 245, 246, 249, 251,  
 255  
 SAITO Shota 齋藤翔太 247  
 SAITO Takaaki 齋藤孝明 44, 45, 82  
 SAITOH Kohji 齋藤浩司 79  
 SAKAGUCHI Takao 坂口貴男 240  
 SAKAI Hazuki K. 酒井葉月 48, 56  
 SAKAI Hideyuki 酒井英行 44, 45, 82, 181  
 SAKAI Kenji 酒井健二 175  
 SAKAMA Minoru 阪間 稔 130  
 SAKAMOTO Hisao 坂本久雄 281, 317  
 SAKAMOTO Naruhiko 坂本成彦 3, 5, 44, 276, 284, 285  
 SAKAMOTO Yasunobu 坂本泰伸 187  
 SAKUMA Fuminori 佐久間史典 85, 86, 87, 251  
 SAKURAGI Yukinori 櫻木千典 15, 16  
 SAKURAI Hiromu 桜井 弘 117  
 SAKURAI Hiroyoshi 桜井博儀 46, 47, 48, 49, 50, 53,  
 54, 56, 57, 58, 59, 60,  
 61, 62, 66, 69, 76, 77,  
 78, 153  
 SAKURAI Ikuya 桜井郁也 167  
 SASAKI Takafumi 佐々木隆文 64  
 SASAKI Yuichirou 佐々木雄一朗 310  
 SASANO Masaki 笹野匡紀 44, 45  
 SATO Hiroki D. 佐藤博紀 224  
 SATO Hiroki 佐藤裕樹 98  
 SATO Hiromi 佐藤広海 157  
 SATO Kiyokazu 佐藤潔和 297  
 SATO Masaharu 佐藤将春 84  
 SATO Naoko 佐藤尚子 120  
 SATO Wataru 佐藤 涉 79, 134  
 SATOU Yoshiteru 佐藤義輝 44, 45, 55, 63, 77, 78  
 SAVAJOLS Herve 41, 42, 43  
 SCHÄFER Thomas 202  
 SCHÄDEL Matthias 130  
 SCHUCH Reinhold 105  
 SEKIGUCHI Kimiko 関口仁子 44, 45, 276  
 SEKIMOTO Michiko 関本美知子 251  
 SEKITA Masami 関田正實 125  
 SERATA Masaki 世良田真来 47, 48, 49, 62, 66, 69, 107  
 SHEN Hong 21  
 SHIBAMURA Eido 柴村英道 193  
 SHIBATA Sadao 柴田貞夫 134, 141  
 SHIBATA Toshi-Aki 柴田利明 224  
 SHIBUSAWA Satoshi 渋沢 哲 134  
 SHIGEKAWA Mitsuru 重川 充 130  
 SHIKI Shigetomo 志岐成友 157  
 SHIMADA Kenzi 島田健司 71, 161, 171, 175  
 SHIMADA Osamu 島田 修 98  
 SHIMAMURA Isao 島村 勲 94  
 SHIMIZU Hirohiko M. 清水裕彦 157  
 SHIMIZU Hiroshi 清水 洋 128  
 SHIMIZU Noritaka 清水則孝 18

- SHIMIZU Tetsuya 清水鉄也 28
- SHIMOMURA Koichiro 下村浩一郎 176
- SHIMOURA Susumu 下浦 享 46, 47, 48, 49, 50, 53,  
54, 56, 57, 58, 59, 60,  
61, 62, 64, 66, 69, 74,  
75, 76, 77, 78, 155,  
187
- SHINDO Miki 進藤美紀 84, 156
- SHINOHARA Atsushi 篠原 厚 130, 134, 263
- SHINOZAKI Wakako 篠崎和佳子 51, 52, 159
- SIDORCHUK Sergey I. 41
- SIDORIN Anatoly 314
- SIEGLE Viktor 259, 260
- SMIRNOV Alexandre 314
- SMITH Edward E. 67
- SO Hyoungyul 84
- SONODA Tetsu 園田 哲 173
- SPINKA Harold 245
- STEPANTSOV Sergey V. 41
- STEPHANOV Mikhail A. 195, 205
- STRASSER Patrick 84, 90, 176
- SUDA Kenji 須田健嗣 44, 45
- SUDA Toshimi 須田利美 51, 52, 70, 74, 80, 81, 179
- SUDOH Kazutaka 須藤和敬 196
- SUEKI Keisuke 末木啓介 80, 130
- SUGAI Hiroyuki 須貝宏行 91
- SUGANUMA Hideo 菅沼英夫 119
- SUGANUMA Hideo 菅沼秀夫 213, 219
- SUGAWARA Kousuke 菅原浩介 159
- SUGIHARA Takanori 杉原崇憲 210
- SUGIMOTO Satoru 杉本 聡 20, 21
- SUGIMOTO Takashi 杉本 崇 50, 53, 59, 60, 62, 66,  
69, 84
- SUMIYOSHI Kohsuke 住吉光介 29
- SUNO Hiroya 数納広哉 94
- SUZUKI Daisuke 鈴木大介 44
- SUZUKI Hideyuki 鈴木英之 29
- SUZUKI Hiroshi 鈴木 宏 77, 78, 153
- SUZUKI Kazunori 鈴木一典 152
- SUZUKI Kenji 鈴木賢二 22, 23
- SUZUKI Ken 鈴木 謙 84
- SUZUKI Masaru K. 鈴木 賢 53, 77, 78, 153
- SUZUKI Noriyuki 鈴木教之 265
- SUZUKI Shoji 鈴木祥仁 84
- SUZUKI Takatoshi 鈴木隆敏 84
- SUZUKI Takeshi 鈴木 健 51, 52, 61, 159
- SUZUKI Toshihiro 鈴木俊宏 120
- SVIRIDA Dmitry N. 245
- SYRESIN Evageny 314
- TABARU Tsuguchika 田原司睦 85, 86, 87, 249, 251
- TACHIBANA Takahiro 橘 孝博 27
- TAGAMI Keiko 田上恵子 123, 124
- TAKAHASHI Katsuhiko 高橋克彦 5
- TAKAHASHI Kazuya 高橋和也 119
- TAKAHASHI Masa 高橋 聖 51, 52
- TAKAHASHI Naruto 高橋成人 134
- TAKAHASHI Tadayuki 高橋忠幸 88
- TAKAHASHI Yoshio 高橋嘉夫 128
- TAKAHASHI Yutaka 高橋 豊 295
- TAKAMINE Aiko 高峰愛子 173
- TAKAMIYA Koichi 高宮幸一 263
- TAKANAKA Masao 高仲政雄 312
- TAKANO Junpei 高野淳平 241
- TAKASHINA Masaaki 高階正彰 15, 16
- TAKATSU Yasumasa 高津康正 152
- TAKAYANAGI Toshinobu 高柳俊伸 106
- TAKEDA Hiroyuki 竹田浩之 81, 179
- TAKEICHI Hiroshige 竹市博臣 113, 136, 137, 138,  
139, 140
- TAKESHITA Eri 竹下英里 46, 48, 49, 53, 54, 55, 56,  
57, 58, 61, 62, 63, 66, 69,  
76, 77, 78
- TAKETANI Atsushi 竹谷 篤 224, 225, 249, 251, 255
- TAKEUCHI Satoshi 武内 聡 46, 47, 48, 49, 53, 54,  
55, 56, 57, 58, 61, 62,  
63, 66, 69, 76, 77, 78,  
187
- TAKI Reiko 瀧 玲子 276
- TAKISAWA Aiko 滝沢愛子 159
- TAKIZAWA Yoshiyuki 滝澤慶之 157
- TAKYU Toshio 武弓利雄 151
- TAMAGAWA Toru 玉川 徹 167
- TAMAI Munetaka 玉井宗孝 240
- TAMAKI Mitsuru 玉城 充 46, 53, 56, 57, 58, 64, 74,  
76, 77, 78, 155
- TAMENAGA Setsuo 為永節雄 21
- TAMII Atsushi 民井 淳 44, 45, 181
- TAMURA Masafumi 田村雅史 109
- TANABE Shinzo 田辺信三 120
- TANABE Toshiya 田辺敏也 277, 291
- TANAKA Manobu 田中真伸 249
- TANASE Masakazu 棚瀬正和 91
- TANEMOTO Tsuyoshi 種本剛士 125
- TANIDA Kiyoshi 谷田 聖 227, 228, 229, 246, 249,  
251, 254
- TANIGUCHI Takashi 谷口貴士 111
- TANIHATA Isao 谷畑勇夫 41, 42, 43, 51, 52, 54, 61,  
67, 70, 72, 74, 76, 80, 159,

- 163, 183, 295
- TEGNER Per-Erik 156
- TER-AKOPIAN Gurgun M. 41, 42, 43
- TERADA Yukikatsu 寺田幸功 88, 167
- TERANISHI Takashi 寺西 高 46, 47, 48, 49, 55, 63,  
64, 65, 68, 72, 75
- THIES Michael 35
- THOMAS Antony Williams 32, 33
- TIMOFEYUK Natalia K. 42, 43
- TOGANO Yasuhiro 梶野泰宏 54, 55, 56, 61, 63, 66,  
69, 76, 77, 78
- TOGAWA Manabu 外川 学 232, 246, 249, 251
- TOGAWA Tadayasu 兎川忠靖 120
- TOJO Junji 東城順治 249, 251, 254
- TOKANAI Fuyuki 門叶冬樹 42, 43, 80
- TOKI Hiroshi 土岐 博 20, 21, 29
- TOMINAKA Toshiharu 富中利治 285, 297
- TOMITA Masanori 富田雅典 144, 145, 146
- TOMITANI Takehiro 富谷武浩 141
- TOMONO Dai 友野 大 84
- TORII Hiroyuki A. 鳥居寛之 103
- TORII Hisayuki 鳥井久行 229, 231, 238, 240
- TOYOSHIMA Atsushi 豊嶋厚史 130
- TSUCHIHASHI Takahiro 土橋隆博 297, 299
- TSUJI Masamichi 辻 正道 191
- TSUKADA Kazuaki 塚田和明 130
- TSUKADA Teruyo 塚田晃代 144, 145, 146
- TSUKIORI Noritoshi 月居憲俊 5
- TSUKUI Masato 津久井正人 160, 171, 175
- TSURUGA Naoya 釣賀直哉 130
- TSURUSAKI Kazuma 鶴崎一磨 78
- TSUTSUI Hiroshi 筒井裕士 36, 37, 38, 39, 40, 308, 314
- UCHIDA Shigeo 内田滋夫 123, 124
- UCHIHORI Yukio 内堀幸夫 167
- UCHIYAMA Akito 内山暁仁 3
- UE Koji 上 浩二 48, 49, 62, 64, 66, 69
- UENO Hideki 上野秀樹 71, 79, 112, 161, 170, 171, 175
- UENO Hirotaka 上野博隆 247
- UESAKA Meiko 上坂明子 47
- UESAKA Tomohiro 上坂友洋 44, 45, 82, 181
- UMETANI Shigeo 梅谷重夫 125, 127
- UNDERWOOD David 245
- UTSUNO Yutaka 宇都野 穰 19
- UWAMINO Yoshitomo 上養義朋 281, 317
- van KOLCK Ubirajara 209
- VARENTSOV Victor L. 165, 173
- VINODKUMAR Attukalathil Mayyan 50, 55, 59, 63, 84
- VOGELSANG Werner 198, 199
- WADA Michiharu 和田道治 106, 163, 165, 173, 185
- WAKABAYASHI Yasuo 若林泰生 64, 75, 79
- WAKASUGI Masanori 若杉昌徳 3, 5, 81, 107, 179
- WAKUI Takashi 涌井崇志 44, 181
- WALKER Philip M. 26
- WATANABE Ayako 渡部亜矢子 94
- WATANABE Hiroshi 渡邊 寛 53, 71, 75, 79, 112,  
161, 171, 175
- WATANABE Isao 渡邊功雄 109, 110
- WATANABE Kiwamu 渡辺極之 50, 59, 60
- WATANABE Masao 渡辺真朗 308
- WATANABE Shigeo 渡辺茂夫 52
- WATANABE Shin-ichi 渡辺伸一 271, 310
- WATANABE Tamaki 渡邊 環 310
- WATANABE Yasushi 渡邊 康 189, 249, 251, 257
- WATANABE Yoshiteru 渡辺善照 118
- WATANABE Yutaka X. 渡辺 裕 50, 59, 60
- WEICK Helmut 156
- WETTIG Tilo 211, 221
- WETZORKE Ines 212
- WHITTEN Chuck 245
- WIDMANN Eberhard 84
- WOLLNIK Hermann 163, 173
- WOLSKI Roman 41
- WOOD Jeffery 245
- WOODY Craig 240, 254
- WU Cuie 吴 翠娥 51, 52, 54, 61, 159
- XIE Wei 255
- XU Hushan 徐 珊瑚 80
- YAITA Tsuyoshi 矢板 毅 130
- YAKO Kentaro 矢向謙太郎 44, 45, 82
- YAKUSHIJI Takashi 薬師寺 崇 50, 59, 60
- YAMADA Hirohisa 山田裕久 125, 127
- YAMADA Kazunari 山田一成 46, 47, 48, 49, 56, 62,  
66, 69, 76, 187
- YAMADA Norikazu 山田憲和 215
- YAMADA Shoichi 山田章一 29
- YAMADA Yasuhiro 山田康洋 112
- YAMAGUCHI Azusa 山口あづさ 221
- YAMAGUCHI Kenichi 山口建一 7
- YAMAGUCHI Takayuki 山口貴之 70, 156
- YAMAGUCHI Yoshitaka 山口由高 51, 52, 54, 61, 70,  
159
- YAMAKA Shoichi 山家捷一 271
- YAMAKI Tsutomu 八巻 務 281, 317
- YAMAMOTO Yoshiharu Y. 山本義治 147, 148
- YAMANOUCHI Hiroaki 山ノ内宏昭 151
- YAMAOKA Kazutaka 山岡和貴 88, 167
- YAMASAKI Norichika 山崎訓史 289
- YAMASHITA Naoyuki 山下直之 193

YAMASHITA Takayuki 山下孝行 289  
 YAMAUCHI Hiromoto 山内啓資 3  
 YAMAZAKI Toshimitsu 山崎敏光 34, 84  
 YAMAZAKI Yasunori 山崎泰規 95, 96, 102, 103, 104,  
 105, 173  
 YANAGA Makoto 矢永誠人 119  
 YANAGISAWA Yoshiyuki 柳澤善行 44, 46, 47, 48, 49,  
 50, 54, 55, 56, 57,  
 58, 59, 60, 61, 62,  
 63, 64, 66, 68, 69,  
 75, 76, 77, 78  
 YANO Yasushige 矢野安重 3, 5, 7, 136, 137, 138, 139,  
 141, 179, 265, 267, 269,  
 273, 283, 284, 285, 287,  
 289  
 YASUDA Ken-ichiro 安田健一郎 130  
 YASUI Hiroyuki 安井裕之 117  
 YASUTANI Jun 安谷 純 193  
 YATAGAI Fumio 谷田貝文夫 143, 144, 145  
 YATSUKAWA Makoto 八津川 誠 134  
 YAZAKI Koichi 矢崎紘一 33, 35  
 YAZAWA Takashi 矢澤 孝 299  
 YEREMIN Alexander V. 80  
 YOKKAICHI Satoshi 四日市 悟 85, 86, 87, 257  
 YOKOKAWA Harumi 横川晴美 116  
 YOKOUCHI Shigeru 横内 茂 3, 5, 275, 283, 285  
 YOKOYA Hiroshi 横谷 洋 199  
 YOKOYAMA Akihiko 横山明彦 130, 134, 263  
 YOKOYAMA Ichiro 横山一郎 3, 5, 277, 279  
 YONEDA Akira 米田 晃 3, 5, 80, 96  
 YONEDA Ken-ichiro 米田健一郎 50, 53, 56, 59, 60, 62,  
 66, 69, 76  
 YONEYAMA Tetsu 米山 哲 84  
 YOSHIDA Atsushi 吉田 敦 54, 57, 58, 61, 66, 69, 70,  
 80, 173, 189, 293, 295,  
 297, 299, 301, 303, 305  
 YOSHIDA Koichi 吉田光一 47, 54, 55, 61, 63, 70, 74,  
 189, 291, 293, 295, 297,  
 299, 301, 303, 305  
 YOSHIDA Shigeo 吉田茂男 147, 148, 149, 150, 151, 152  
 YOSHIMI Akihiro 吉見彰洋 71, 79, 112, 160, 161, 170,  
 171, 175  
 YOUN Minyoung 尹 民榮 65  
 YUKI Hideyuki 結城英行 263  
 YUN Chong Cheoul 尹 鍾哲 64, 65  
 YUN Pil-Yong 150  
 ZANTOW Felix 212  
 ZHAO Yu-Liang 趙 宇亮 80  
 ZHENG Tao 鄭 涛 70, 80